

AN EXPLORATION OF MID- TO HIGH-VALENT TRANSITION METAL COMPLEXES
FOR APPLICATION TO CATALYSIS

By

Kelly E. Aldrich

A DISSERTATION

Submitted to
Michigan State University
in partial fulfillment of the requirements
for the degree of

Chemistry—Doctor of Philosophy

2019

ABSTRACT

AN EXPLORATION OF MID- TO HIGH-VALENT TRANSITION METAL COMPLEXES FOR APPLICATIONS TO CATALYSIS

By

Kelly E. Aldrich

The valency or oxidation state of a transition metal in a complex plays a large role in determining the reactivity of the complex. With transition metal chemistry, historically accessible chemistry has often focused on metals in a low oxidation state. However, transformations involving transition metals in high oxidation states are of equal importance in providing complex products for use in consumer products. Expanding the applications and understanding of transition metal complexes in high oxidation states is the focus of the research presented in this dissertation. Fundamental studies of how ligands interact with high valent metals is presented in chapters 2 and 3, where a chromium(VI) model complex has been used to study bonding interactions between this d^0 transition metal and phosphine ligands. Practical application of high valent titanium(IV) catalysts to C–N bond forming reactions is presented in chapters 4-6. Finally, chapters 7 and 8 focus on the changes in the character of M–N double bonds, with $M = \text{Fe}$ and Ru , as the metal is forced to higher oxidation states. Collectively, these studies demonstrate different approaches to the same general problems and questions of how chemists can better understand and utilize high valent transition metals to do catalytically-targeted transformations.

Dedicated to my family and friends

ACKNOWLEDGEMENTS

I would like to begin by thanking my Ph. D. advisor, Aaron. Over the last 4 years, I have been able to explore my projects in your lab without limitation. You have also supported my interest in writing. I've benefited greatly from the opportunity to write manuscripts and participate start to finish in the process of peer-reviewed publication. I appreciate all of the opportunities you have given me.

To my committee members, Prof. Mitch Smith, Prof. Ben Levine, and Prof. Tom Hamann, thank you for your guidance in navigating my Ph.D. Special thanks are necessary for Ben Levine. On several occasions he was willing to entertain my naïve questions about computational chemistry. Additionally, I would also like to thank Ben's former student, B. Scott Fales, for his efforts in performing CASSCF calculations with the iron and ruthenium imido systems discussed in Chapter 7.

I would like to thank Professor McCracken, both for assistance with EPR spectroscopy, as well as sharing his outlook on graduate school and careers. I've really enjoyed working with you over the last several years. Along those same lines, I would also like to thank Dr. Dan Holmes for his help with various NMR experiments. Without his help, I couldn't have climbed to the top of the user list in the subbasement. RIP Mutt.

To Dr. Richard Staples, I am so glad that I have had the opportunity to work with you. I have gotten to learn as much crystallography as I can handle and then some from collecting data on some pretty atrocious crystals. While your formal title is "academic expert", you have also been my guidance counselor, my cheerleader, and my friend. I'm very grateful to have had your support along my path to graduation.

I also don't think that I would have pursued graduate school without the influence of instructors that I had early in my undergraduate career. When I started undergrad, I was very lost in terms of what I wanted to do with my life and career. I started attending Bay de Noc Community College out of high school, and eventually gravitated toward science. The instructors that I encountered at Bay were phenomenal and encouraged me to pursue science further. The collective influence of Marc Labeau and Matt Krynicki is what first made me consider graduate school and a career in research. Although not my instructor at Bay, I would also like to thank Amy Anderson, my instructor for EMT certification while I was at Bay. She also showed me endless support, and her belief in my abilities helped me figure out that I was ready to explore what I wanted to study.

I need to thank past labmates, including Dhvani Kansal, Corbin Livingston, Nick Boersma, Cody Pasko, and Dr. Amrendra Singh. I want to give special thanks to Dr. Tanner McDaniel (aka Tanner McDanner). Often without realizing it, Tanner is an inspirational chemist. He has enthusiasm and curiosity for all things synthesis, and that enthusiasm is contagious. Talking chemistry with him often helped me find my motivation to tackle hard problems, and I will always be thankful for that.

Special thanks are also necessary for Dr. Brennan Billow. I can't count all the ways that you've helped me through my degree, but for all of the countless ways that you have supported me over the last several years, I'm very grateful.

Lastly, and most importantly, I want to thank my family. My sisters, Rachel and Emily, are my best friends, and grad school hasn't changed that. You guys pick me up when I'm down. My cats, Balthazar and Mr. Pockets, are always there for me, too, and coming home to their fluffy faces always helped me relax after a long day in lab.

Finally, I want to thank my parents. Nothing that I have achieved in the last 5 years would have been possible without them. They've always made it clear to me that the only limitations I should accept are those related to my own goals and ambitions, and that hard work can take me really far. Because of the appreciation they instilled in me for education., and their constant support and encouragement, I've been able to dedicate the last 5 years to pursuit of my Ph. D., and now pursue research as a fulltime career for the rest of my life. Thank you.

PREFACE

Transition metal catalysis is a wide and varied field which evolves every day. The types of transformations, metals used, and supporting fragments for the active metal, span the periodic table. The sheer number of catalyzed reactions that we know can be performed is astounding. Despite this diversity, there are still many important transformations that we 1) cannot do; 2) do not understand; or 3) can do, but very poorly in terms of atom economy, energy expended, and waste generated. Overcoming these limitations is one of the primary challenges facing the field today and is responsible for uniting the scientifically diverse community that deals with transition metal catalysis.

Over the last 5 years, working in the Odom Group at Michigan State, I have become part of this community. While each of the projects that I have focused on take different tactics in probing the behavior and reactivity of transition metal complexes, this theme underlies all of my experiments (and has helped focus my efforts when I find myself in the glovebox going on a synthesis rampage). Moving forward in my career, catalysis may not ever be the main objective of my research. But, learning how to think about chemistry in the mindset of catalysis, with all its complexities and subtle balances, will continue to shape the way I approach any scientific problem.

TABLE OF CONTENTS

LIST OF TABLES	xi
LIST OF FIGURES	xv
LIST OF SCHEMES	xxxviii
KEY TO SYMBOLS OR ABBREVIATIONS	xl
CHAPTER 1. INTRODUCTION	1
1.1 Traditional Approaches to Transition Metal Catalysis	1
1.2 Targeted Design of Catalysts: Ligand Donor Parameter	4
1.3 Expansion of “Ligands” in Organometallic Catalysis using Silica Supported Titanium Catalysts	8
1.4 Electronic Exploration of Unique Transition Metal Complexes: Valency Effects on Metal-Imide Bond Character.....	10
REFERENCES	13
CHAPTER 2. PROBING THE <i>IN SITU</i> DYNAMICS OF THE LDP SYSTEM WITH NEUTRAL LIGANDS	17
2.1 Introduction	17
2.2 Synthesis of $[\text{N}^i\text{Cr}(\text{N}^i\text{Pr}_2)_2(\text{PR}_3)][\text{X}]$ Complexes, Solvent Choice, and Initial Assessments of Solvent Effects	23
2.3 Direct Approaches to Characterize Ion Pairing: Diffusion Ordered Spectroscopy (DOSY NMR)	32
2.4 Other Solution State Investigations of Ion Proximity in Solution	42
2.5 Computational Investigation of Ion Pairing with PF_6^-	44
2.6 Entropic Complications in Ionic LDP Systems.....	47
2.7 Conclusions	52
2.8 Experimental	54
REFERENCES	191
CHAPTER 3. ANALYSIS OF THE DONOR ABILITIES OF PHOSPHINES TO HIGH VALENT METALS.....	197
3.1 Introduction	197
3.2 A Comparison of Traditional Phosphine Characteristics from Low-Valent Systems with LDP Results.....	201
3.3 Computational Analysis of the Electronic Structure of $[\text{N}^i\text{Cr}(\text{N}^i\text{Pr}_2)_2\text{PR}_3]^+$ Using Natural Bonding Orbital and Natural Resonance Theory	208
3.4 Modeling Approximations to Examine Stereoelectronic Control on LDP Value.....	217
3.5 Conclusions	220
3.6 Experimental	221
REFERENCES	265

CHAPTER 4. SILICA-GEL SUPPORTED TITANIUM CATALYSTS FOR C–N BOND FORMING REACTIONS ^{1,2}	269
4.1 Introduction	269
4.2 Preparation of Silica-gels with Varied Surface Hydroxyl Group Density	276
4.3 Performance of [Ti]200 and [Ti]700 as Intermolecular Hydroamination Catalysts	279
4.4 Application of [Ti]200 and [Ti]700 to Multicomponent Coupling Reactions	283
4.5 Use of Ti700 to Produce Functionalized Heterocycles	287
4.6 Exploration of Catalyst Reusability and Routes of Deactivation.....	288
4.7 Accidental Discovery of [Ti]700 Activity for Catalytic Guanylation of Carbodiimide	293
4.8 Conclusions	296
4.9 Experimental	298
REFERENCES	355
CHAPTER 5. REACTIVITY AND RATE LAW DETERMINATION OF A LIGAND-FUNCTIONALIZED SILICA-SUPPORTED TITANIUM CATALYST	361
5.1 Introduction	361
5.2 Activity of [Ti]700(X) for Three-Component Coupling Chemistry with a Variety of X ⁻ Ligands	365
5.3 One-pot-two-step Heterocycle Synthesis with [Ti]700(X)	370
5.4 3CC Reaction Kinetics for [Ti]700(X).....	372
5.5 Catalyst Poisoning and Recyclability	382
5.6 Poisoning Experiments and Controls for [Ti]700	384
5.7 Catalyst Recycling from Ti(X) ₃ /SiO ₂ ⁷⁰⁰ Precatalysts: Enhanced Recyclability through Poisoning.....	389
5.8 Conclusions	392
5.9 Experimental	393
REFERENCES	442
CHAPTER 6. HOMOGENEOUS TITANIUM CATALYZED IMINOAMINATION AND CATALYST DISPROPORTIONATION PROCESSES.....	446
6.1 Introduction	446
6.2 Kinetic Analysis of Iminoamination Catalyzed by Ti(dpm)(NMe ₂) ₂	448
6.3 Investigations into Catalyst Deactivation During Ti-Catalyzed Iminoamination.....	458
6.4 Modification of the Bis-Chelating Ancillary Ligand	464
6.5 Predicting What Ligands Lead to Stable Catalysts Versus Disproportionation.....	468
6.6 Conclusions	478
6.7 Experimental	479
REFERENCES	550
CHAPTER 7. AN EXPLORATION OF THE SYNTHESIS AND ELECTRONIC PROPERTIES OF RUTHENIUM AND IRON IMIDO COMPLEXES	554
7.1 Introduction	554
7.2 Synthesis and Oxidation of Terminal Ru Imido Complexes.....	560
7.3 Synthesis and Oxidation of Fe Imide Analogues	567
7.4 Exploration of a Trischelating Phosphine Ligand Platform for Fe and Ru Imides.....	570
7.5 Characterization of Cationic Ru ⁵⁺ , Fe ⁴⁺ , and Fe ⁶⁺ by EPR Spectroscopy (7.5).....	573

7.6	Computational Analysis Comparing Fe and Ru Analogues.....	583
7.7	Reactivity Studies with Fe5.....	588
7.8	Conclusions	592
7.9	Experimental	593
REFERENCES		671

CHAPTER 8. PURSUIT OF RUTHENIUM BIS(IMIDO) COMPLEXES AND HIGHER OXIDATION STATES

8.1	Introduction	677
8.2	Synthesis of Ru and Os κ_2 -diphenylhydrazido Complexes from Azobenzene	680
8.3	Thermal and Photochemical Reactivity of (κ_2 -diphenylhydrazido)Ru(PMe ₃) ₄	682
8.4	Synthesis of Ru(II)(1,4-diaryltetrazene)tris(trimethylphosphine) Complexes.....	689
8.5	Reactivity of Ru(II)(1,4-diaryltetrazene)tris(trimethylphosphine) Complexes	692
8.6	Synthetic Alterations of the Ru Platform: A Larger Phosphine Ligand	695
8.7	A Basic Reactivity Study with Ru1 and Comparison to Known Os Analogues.....	697
8.8	Conclusions	701
8.9	Experimental	702
REFERENCES		779

LIST OF TABLES

Table 2.1 The wide variety of complexes accessible through the general synthesis route. 3j and 3o were prepared using an alternate procedure in which the MX salt was TIPF ₆ , the solvent for the reaction was DCM, and the entire procedure was performed as a 1-pot reaction to facilitate total miscibility of the phosphine with the solvent. ^b The synthesis of 3p was conducted under the strict exclusion of MeCN, in DCM with TIBArF ₂₄ as a 1-pot procedure. Upon exposure of 3p to MeCN, 3p converts to 2 and PPh ₃ ligand.	23
Table 2.2 Cr1-P1 bond distances and N2-Cr1-N3 bond angles. ^a For those complexes were multiple bond distances/angles are given, there are two unique molecules in the asymmetric unit cell for these complexes.	26
Table 2.3 LDP values determined in two different NMR solvents with a variety of different PR ₃ ligands. All values reported here employ SbF ₆ ⁻ as the counter ion.	30
Table 2.4 Results of the DOSY NMR experiments utilizing various anions and the chromium(VI) cations 3a and 3f	39
Table 2.5 LDP values measured for 3a and 3f with a variety of anions in CDCl ₃ and CD ₃ CN. This illustrates the ion effect on the LDP measurement.	41
Table 2.6 Molecular weight calibration results for 3f [PF ₆] in several solvents and concentrations.	44
Table 2.7 Bond orders calculated for the PF ₆ ⁻ anion, showing H-bonding interaction effects on P – F bond orders.	46
Table 2.8 LDP values measured in CD ₃ CN with SbF ₆ ⁻ /PF ₆ ⁻ counter anions.	47
Table 2.9 Complexes 3f , 3j , and 3m which were used to determine experimental ΔS [‡] values for the ionic complexes in CD ₃ CN with the SbF ₆ ⁻ counter anion.	49
Table 2.10 Experimentally determined values of ΔH [‡] and ΔS [‡] for 3a-p BArF ₂₄ ⁻ salts in CDCl ₃	51
Table 2.11 Details from LDP measurements with various X ⁻ ligands in CDCl ₃	71
Table 2.12 Details from LDP measurements with various X ⁻ ligands in CD ₃ CN.	71
Table 2.13 Experimentally determined rate of Cr – N ⁱ Pr ₂ bond rotation, calculated ΔG [‡] , calculated LDP (where ΔS [‡] = -9 e.u.), and temperature of measurement.	72
Table 2.14 Molecular volumes calculated for various cations and anions from crystal structures using Olex Software.	75
Table 2.15 Experimental data from DOSY molecular weight calibrations with 3f [PF ₆].	76

Table 2.16 Experimentally measured rate of rotation and calculated ΔG^\ddagger for 1 determined across several different temperatures in CD ₃ CN.	81
Table 2.17 Various temperature measurements made to determine ΔS^\ddagger from experimental ΔG^\ddagger values for 3f [SbF ₆].	83
Table 2.18 Experimentally determined rate of Cr – N ⁱ Pr ₂ bond rotation and the calculated $\Delta G/H/S^\ddagger$	84
Table 2.19 Experimentally determined rate of rotation (k_{obs}) for the Cr – N ⁱ Pr ₂ bond in 3a-p salts with BARF ₂₄ ⁻ anion in CDCl ₃	85
Table 3.1 Experimentally determined ΔH^\ddagger values for 3a-p series of compounds in CDCl ₃ with BARF ₂₄ ⁻ counter anion and by the original method in CD ₃ CN with SbF ₆ ⁻	199
Table 3.2 The ΔH^\ddagger values determined for 3f , 3j , and 3m in both solvent/ion regimes and with the standard and experimentally determined ΔS^\ddagger values.	201
Table 3.3 Stereoelectronic parameters for phosphines in which σ (χ_d), π , and aromatic (Aryl) electronic effects are separated. θ is a steric term, which is essentially a modified TCA. ^{3, 15, 23}	204
Table 3.4 AN Values indicating the Lewis acidity of several compounds determined by the Guttmann-Beckett Method. ³⁷ ^a Measured in DCE, referenced to External O=P(Et) ₃ as 41.0 ppm.	208
Table 3.5 Natural Charges for NCr(NH ₂) ₂ PE ₃ ⁺ complexes	224
Table 3.6 Summary of Second Order Perturbation Interactions	245
Table 3.7 Total Charges on NCr(NH ₂) ₂ ⁺ fragment and PE ₃	246
Table 3.8 Sample variety of literature parameters available for stereoelectronic description of phosphine series under study. ³⁻¹¹	252
Table 4.1 General conditions for SiO ₂ ⁷⁰⁰ preparation from commercially available fumed silica.	278
Table 4.2 Substrate scope examined for hydroamination reactivity with [Ti]200 and [Ti]700. The general conditions outlined in the Scheme below apply to all reactions. ^{a,b}	282
Table 4.3 Iminoamination (3CC) substrate scope examined with [Ti]200 and [Ti]700. The general conditions outlined in Fig. 7, C apply to all reactions. ^{a,b}	287
Table 4.4 Hydroamination Results for the Coupling of 1-Octyne and Aniline with Recycled [Ti]200.	289
Table 5.1 Conditions screened for reaction order in each substrate and catalyst for heterogeneous catalyzed 3-component coupling of aniline, 1-octyne, and ^t BuNC. The initial catalyst and reagent amounts are listed by concentration (M).	373

Table 5.2 Estimated initial rates ($M^{-1}min^{-1}$) from the various conditions in Table 5.1. These estimates may be artificially low, as the reactions progressed far beyond 10% conversion in ~20 min.	374
Table 5.3 Ligands examined in Figure 5.8, showing LDP values of each phenoxide and the k_{obs} for the iminoamination reaction catalyzed with the given phenoxide as ligand (X) with [Ti]700(X).....	381
Table 5.4 ICP-OES analysis of various treatments for the [Ti]700 precatalyst material.	383
Table 5.5 Yields obtained from the hydroamination of 1-octyne and aniline using [Ti]700 precatalyst and 10 equiv of HX ligand added.	386
Table 5.6 Recycling experiments with 10 equiv of a variety of HX ligands added to the hydroamination of 1-octyne and aniline under the general conditions. Yields for the initial run with fresh catalyst (run 1), and a subsequent use (run 2) are shown.	390
Table 5.7 Results of reusing the [Ti]700 catalyst with 10 equiv of 5-fluoroindole (each trial) to perform the hydroamination of aniline and 1-octyne.	391
Table 5.8 Yield and regioselectivity observed for a variety of ligands screened for the iminoamination of aniline, 1-octyne, and CyNC.	401
Table 5.9 Yield and regioselectivity observed for a variety of ligands screened for the iminoamination of aniline, 1-phenylpropyne, and CyNC.....	402
Table 5.10 Yield and regioselectivity observed for a variety of ligands screened for the iminoamination of aniline, phenylacetylene, and CyNC.	403
Table 5.11 Examples of Graphical Method Application to Entries in Table 2.....	432
Table 5.12 Simulated rate constant and equilibrium constant values used to fit each set of experimental reaction traces. Good agreement is noted among the values, with small variances in some rate constants during fitting.	439
Table 5.13 Details of LDP value measurements (ΔH^\ddagger) for the 4-R-phenoxide ligands examined for electronic effects on [Ti]700(2,4,6-tri-tert-butylphenoxide) iminoamination catalysis.....	441
Table 6.1 Experimental conditions examined for kinetic analysis of $Ti(dpm)(NMe_2)_2$ catalyzed iminoamination. The general parameters from the reaction scheme below were applied. Amounts listed in the table are given as concentrations (molar).....	450
Table 6.2 Initial rates predicted for entries 1-3 with different orders in catalyst concentration. The values calculated for a fractional order appear to agree better with the experimentally observed initial rates shown in Fig. 6.4.....	455
Table 6.3 The ligand combinations listed in the table above, the heteroleptic $Ti(X)_2A_2$ complexes are noted quantitatively. This necessitates that K_{eq} is very large.....	469

Table 6.4 Values used to model the relationship of sterics and electronics to the equilibrium constant for the interconversion of the homoleptic and heteroleptic.....	475
Table 6.5 Experimentally determined diffusion coefficients (D) and calculated MW for Ti species for [Ti(OArCH ₂ ArO)(μ-Ntoly)] _x · 1/2 NHMe ₂ in C ₆ D ₆	532
Table 6.6 Experimental determination of diffusion coefficients (D) and calculated MW for Ti species for [Ti(dpm)(μ-Ntoly)] _x in C ₆ D ₆	533
Table 6.7 Experimentally determined diffusion coefficients (D) and calculated MW for the Ti species for Ti(OArCH ₂ ArO)(I) ₂ in C ₆ D ₆	534
Table 6.8 Experimentally determined diffusion coefficients (D) and calculated MW of the Ti species for Ti(OArCH ₂ ArO)(O ⁱ Pr) ₂ complex in C ₆ D ₆	535
Table 6.9 Combinations of parameters examined for fitting the dependence of K _{eq} on ΔLDP and % V _{bur}	548
Table 7.1 Table of relevant bond lengths and angles for Ru1	559
Table 7.2 Select bond lengths and angles from the single crystal X-ray structures for Ru3 and Ru2 , shown in Fig. 7.3.....	563
Table 7.3 Select bond distances and angles from the single crystal X-ray structures of Fe3* and Fe2* shown in Figure 7.7.	570
Table 7.4 Select bond distances and angles for the single crystal X-ray structures of Fe5 and Fe6 . Note that Fe6 has two unique molecules in the asymmetric unit; several of the bond lengths and angles show statistical differences, so both measurements are shown. Images of these structures are shown in Fig. 7.8.....	571
Table 7.5 Data from the X-ray crystal structures of several Fe and Ru-imide compounds for comparison to the computed optimized structures of Fe7 and Ru6	584
Table 7.6 N1-M-P angles (°) as optimized at the MP2 level of theory. The range spanned by each set of angles is also given.....	585
Table 8.1 Selected bond distances and angles from the single crystal structure of Ru5 in Fig. 8.10.....	692

LIST OF FIGURES

Figure 1.1 (top) A simple example of an olefin metathesis reaction, cross metathesis (CM) that can be catalyzed by Ru-carbene complexes. (bottom) Examples of several viable Ru catalysts competent for CM and other olefin metathesis reactions.	3
Figure 1.2 Illustration of the original Tolman system for phosphine parameterization. (left) The Ni(CO) ₃ PR ₃ complex was used to determine overall donor ability of a phosphine. (right) The system utilized to determine a steric profile for a given PR ₃ ligand where the metal–P bond length is 2.28 Å.	6
Figure 1.3 The NCr(N ⁱ Pr ₂) ₂ X scaffold used to measure the LDP value of a given X ligand. The illustration shows the rotation of one of the Cr–N ⁱ Pr ₂ bonds. The transition state (center) forces the amide lone pair into an antibonding orbital. The highlighted protons on the ⁱ Pr groups have unique chemical shifts. Their exchange, monitored by ¹ H NMR SST, facilitates the measurement of the rotation rate.	7
Figure 2.1 (<i>top</i>) Cr(VI) molecule used in the LDP system. (<i>bottom</i>) A selection of monoanionic ligands' LDP values. These values represent the overall donor ability of the X ligand, reflecting both σ and π interactions with high valent Cr(VI).	18
Figure 2.2 (<i>top</i>) The rotation monitored by ¹ H spin saturation transfer experiments to determine the LDP value for a ligand, X. The purple and green hydrogens exchange positions through the N–Cr bond rotation, allowing for saturation of one of the H signals to carry over to the other signal proportional to the rate of this rotation during the SST experiment (<i>bottom</i>). By experimentally determining this rotation rate, the enthalpic barrier to this rotation can be assessed, and $\Delta H^\ddagger = \text{LDP}$	19
Figure 2.3 General synthesis of the 3a-3p salts.	24
Figure 2.4 Plot of Tolman Cone Angle and Cr1 - P1 bond distances in X-ray crystal structures.	26
Figure 2.5 Crystal structure of 2 , showing the NCCH ₃ bound end-on through the N atom's lone pair. Ellipsoids are shown at 50% probability. H atoms are omitted for clarity. (Cr1-N1 1.533 Å; Cr1-N2 1.817 Å; Cr1-N3 1.816 Å; N2-Cr1-N3 121.85 °; Cr1-N4-13C 176.40 Å; N4-C13-C14 178.96; Cr1-N4 2.004 Å).	28
Figure 2.6 (<i>top</i>) Room temperature ¹ H NMR spectrum of NCr(N ⁱ Pr ₂) ₂ (OPh) showing broad resonances for the ⁱ Pr groups due to rapid Cr–N ⁱ Pr ₂ bond rotation. (<i>bottom</i>) Room temperature ¹ H NMR spectrum of [NCr(N ⁱ Pr ₂) ₂ PPhMe ₂][SbF ₆] showing sharp well-resolved resonances for the ⁱ Pr groups. The high barrier to rotation in this molecule prevents exchange of the ⁱ Pr Hydrogens leading to a static spectrum.	29
Figure 2.7 ¹⁴ N NMR spectra of 3f in CDCl ₃ with SbF ₆ ⁻ (left) and PF ₆ ⁻ (right) as counterions. (* = N ₂ reference at 309.6 ppm; a = amide shift; b = nitride shift).	32

Figure 2.8 A ^1H DOSY NMR spectrum in CD_3CN that contains several molecular species of different sizes. The diffusion coefficients are inversely proportional to the molecular sizes, with larger species diffusing more slowly than smaller ones.	34
Figure 2.9 The “weakly coordinating” anions used to examine ion pairing effects in the LDP system with $[\text{NCr}(\text{NiPr}_2)_2\text{PR}_3]^+$ cations.	35
Figure 2.10 ROESY NMR spectra for 3a $[\text{NCr}(\text{N}^i\text{Pr}_2)_2\text{PMe}_3][\text{BArF}_{24}^-]$ in CDCl_3 (<i>top</i>) and CD_3CN (<i>bottom</i>). Correlation between the cation and anion are noted in CDCl_3 , but these cross peaks are not observed in CD_3CN	38
Figure 2.11 Representation of the optimized 3a $[\text{PF}_6]$ structure showing electrostatic interactions between the F’s (teal) and ^iPr groups (pink).	46
Figure 2.12 ^1H ROESY NMR Spectrum of 3a $[\text{BPh}_4]$ in CDCl_3	78
Figure 2.13 ^1H ROESY NMR Spectrum of 3a $[\text{BPh}_4]$ in CD_3CN	79
Figure 2.14 The Eyring plot for SST measurements of 1 in CD_3CN	82
Figure 2.15 Eyring plot used for determining the ΔS^\ddagger value of $\text{Cr} - \text{N}^i\text{Pr}_2$ bond rotation in 3f $[\text{SbF}_6]$	83
Figure 2.16 ^1H NMR of 3b $[\text{SbF}_6]$ in CDCl_3	88
Figure 2.17 ^{13}C NMR of 3b $[\text{SbF}_6]$ in CDCl_3	89
Figure 2.18 ^{31}P NMR of 3b $[\text{SbF}_6]$ in CDCl_3	90
Figure 2.19 ^{19}F NMR of 3b $[\text{SbF}_6]$ in CDCl_3	91
Figure 2.20 ^1H NMR of 3c $[\text{SbF}_6]$ in CDCl_3	92
Figure 2.21 ^{13}C NMR of 3c $[\text{SbF}_6]$ in CDCl_3	93
Figure 2.22 ^{31}P NMR of 3c $[\text{SbF}_6]$ in CDCl_3	94
Figure 2.23 ^{19}F of 3c $[\text{SbF}_6]$ in CDCl_3	95
Figure 2.24 ^1H NMR of 3d $[\text{SbF}_6]$ in CDCl_3	96
Figure 2.25 ^{13}C NMR of 3d $[\text{SbF}_6]$ in CDCl_3	97
Figure 2.26 ^{31}P NMR of 3d $[\text{SbF}_6]$ in CDCl_3	98
Figure 2.27 ^{19}F NMR of 3d $[\text{SbF}_6]$ in CDCl_3	99
Figure 2.28 ^1H NMR of 3e $[\text{SbF}_6]$ in CDCl_3	100

Figure 2.29 ^{13}C NMR of 3e [SbF ₆] in CDCl ₃	101
Figure 2.30 ^{31}P NMR of 3e [SbF ₆] in CDCl ₃	102
Figure 2.31 ^{19}F NMR of 3e [SbF ₆] in CDCl ₃	103
Figure 2.32 ^{14}N NMR of 3e [SbF ₆] in CDCl ₃	104
Figure 2.33 ^1H NMR of 3f [SbF ₆] (PPhMe ₂) in CDCl ₃	105
Figure 2.34 ^{13}C NMR of 3f [SbF ₆] (PPhMe ₂) in CDCl ₃	106
Figure 2.35 ^{31}P NMR of 3f [SbF ₆] (PPhMe ₂) in CDCl ₃	107
Figure 2.36 ^{19}F NMR of 3f [SbF ₆] (PPhMe ₂) in CD ₃ CN.	108
Figure 2.37 ^{19}F NMR of 3f [SbF ₆] (PPhMe ₂) in CDCl ₃	109
Figure 2.38 ^{14}N NMR of 3f [SbF ₆] in CDCl ₃	110
Figure 2.39 ^1H NMR of 3g [SbF ₆] in CDCl ₃	111
Figure 2.40 ^{13}C NMR of 3g [SbF ₆] in CDCl ₃	112
Figure 2.41 ^{31}P NMR of 3g [SbF ₆] in CDCl ₃	113
Figure 2.42 ^{19}F NMR of 3g [SbF ₆] in CDCl ₃	114
Figure 2.43 ^1H NMR of 3h [SbF ₆] in CDCl ₃	115
Figure 2.44 ^{13}C NMR of 3h [SbF ₆] in CDCl ₃	116
Figure 2.45 ^{31}P NMR of 3h [SbF ₆] in CDCl ₃	117
Figure 2.46 ^{19}F NMR of 3h [SbF ₆] in CDCl ₃	118
Figure 2.47 ^1H NMR of 3i [SbF ₆] in CDCl ₃	119
Figure 2.48 ^{13}C NMR of 3i [SbF ₆] in CDCl ₃	120
Figure 2.49 ^{31}P NMR of 3i [SbF ₆] in CDCl ₃	121
Figure 2.50 ^{19}F NMR of 3i [SbF ₆] in CDCl ₃	122
Figure 2.51 ^1H NMR of 3j [PF ₆] in CDCl ₃	123
Figure 2.52 ^{13}C NMR of 3j [PF ₆] in CDCl ₃	124
Figure 2.53 ^{31}P NMR of 3j [PF ₆] in CDCl ₃	125

Figure 2.54 ^{19}F NMR of 3j [PF ₆] in CDCl ₃	126
Figure 2.55 ^{14}N NMR of 3j [PF ₆] in CDCl ₃	127
Figure 2.56 ^1H NMR of 3k [SbF ₆] in CDCl ₃	128
Figure 2.57 ^{13}C NMR of 3k [SbF ₆] in CDCl ₃	129
Figure 2.58 ^{31}P NMR of 3k [SbF ₆] in CDCl ₃	130
Figure 2.59 ^{19}F NMR of 3k [SbF ₆] in CDCl ₃	131
Figure 2.60 ^1H NMR of 3l [SbF ₆] in CDCl ₃	132
Figure 2.61 ^{13}C NMR of 3l [SbF ₆] in CDCl ₃	133
Figure 2.62 ^{31}P NMR of 3l [SbF ₆] in CDCl ₃	134
Figure 2.63 ^{19}F NMR of 3l [SbF ₆] in CDCl ₃	135
Figure 2.64 ^{14}N NMR of 3l [SbF ₆] in CDCl ₃	136
Figure 2.65 ^1H NMR of 3m [SbF ₆] in CDCl ₃	137
Figure 2.66 ^{13}C NMR of 3m [SbF ₆] in CDCl ₃	138
Figure 2.67 ^{31}P NMR of 3m [SbF ₆] in CDCl ₃	139
Figure 2.68 ^{19}F NMR of 3m [SbF ₆] in CDCl ₃	140
Figure 2.69 ^1H NMR of 3n [SbF ₆] in CDCl ₃	141
Figure 2.70 ^{13}C NMR of 3n [SbF ₆] in CDCl ₃	142
Figure 2.71 ^{31}P NMR of 3n [SbF ₆] in CDCl ₃	143
Figure 2.72 ^{19}F NMR of 3n [SbF ₆] in CDCl ₃	144
Figure 2.73 ^1H NMR of 3o [PF ₆] in CDCl ₃	145
Figure 2.74 ^{13}C NMR of 3o [PF ₆] in CDCl ₃	146
Figure 2.75 ^{31}P NMR of 3o [PF ₆] in CDCl ₃	147
Figure 2.76 ^{19}F NMR of 3o [PF ₆] in CDCl ₃	148
Figure 2.77 ^{14}N NMR of 3o [PF ₆] in CDCl ₃	149
Figure 2.78 ^1H NMR of 3p [BArF ₂₄] in CDCl ₃	150

Figure 2.79 ^{13}C NMR of 3p [BArF ₂₄] in CDCl ₃	151
Figure 2.80 ^{31}P NMR of 3p [BArF ₂₄] in CDCl ₃	152
Figure 2.81 ^{19}F NMR of 3p [BArF ₂₄] in CDCl ₃	153
Figure 2.82 ^1H NMR of 2 [SbF ₆] in CDCl ₃	154
Figure 2.83 ^{13}C NMR of 2 [SbF ₆] in CDCl ₃	155
Figure 2.84 ^{19}F NMR of 2 [SbF ₆] in CDCl ₃	156
Figure 2.85 ^{14}N NMR of 2 [SbF ₆] in CDCl ₃	157
Figure 2.86 ^1H NMR spectrum of 3f [PF ₆] in CDCl ₃	158
Figure 2.87 ^{13}C NMR spectrum of 3f [PF ₆] in CDCl ₃	159
Figure 2.88 ^{19}F NMR spectrum of 3f [PF ₆] in CDCl ₃	160
Figure 2.89 ^{31}P NMR of 3f [PF ₆] in CDCl ₃	161
Figure 2.90 ^{14}N NMR spectrum of 3f [PF ₆].....	162
Figure 2.91 ^1H NMR of 3f [BArF ₂₄] in CDCl ₃	163
Figure 2.92 ^{13}C NMR spectrum of 3f [BArF ₂₄] in CDCl ₃	164
Figure 2.93 ^{31}P NMR spectrum of 3f [BArF ₂₄] in CDCl ₃	165
Figure 2.94 ^{19}F NMR spectrum of 3f [BArF ₂₄] in CDCl ₃	166
Figure 2.95 ^{14}N NMR spectrum of 3f [BArF ₂₄] in CDCl ₃	167
Figure 2.96 ^1H NMR spectrum of 3f [BArF ₂₀] in CDCl ₃	168
Figure 2.97 ^{13}C NMR spectrum of 3f [BArF ₂₀] in CDCl ₃	169
Figure 2.98 ^{31}P NMR spectrum of 3f [BArF ₂₀] in CDCl ₃	170
Figure 2.99 ^{19}F NMR spectrum of 3f [BArF ₂₀] in CDCl ₃	171
Figure 2.100 ^{14}N NMR spectrum of 3f [BArF ₂₀] in CDCl ₃	172
Figure 2.101 ^1H NMR spectrum of 3f [Al(OC(CF ₃) ₃) ₄] in CDCl ₃	173
Figure 2.102 ^{13}C NMR spectrum of 3f [Al(OC(CF ₃) ₃) ₄] in CDCl ₃	174
Figure 2.103 ^{31}P NMR spectrum of 3f [Al(OC(CF ₃) ₃) ₄] in CDCl ₃	175

Figure 2.104 ^{19}F NMR spectrum of 3f [Al(OC(CF ₃) ₃) ₄] in CDCl ₃	176
Figure 2.105 ^{14}N NMR spectrum of 3f [Al(OC(CF ₃) ₃) ₄] in CDCl ₃	177
Figure 2.106 ^1H NMR spectrum of 3f [BPh ₄] in CDCl ₃	178
Figure 2.107 ^{13}C NMR spectrum of 3f [BPh ₄] in CDCl ₃	179
Figure 2.108 ^{31}P NMR spectrum of 3f [BPh ₄] in CDCl ₃	180
Figure 2.109 ^{14}N NMR spectrum of 3f [BPh ₄] in CDCl ₃	181
Figure 2.110 ^1H NMR spectrum of 3a [BArF ₂₄] in CDCl ₃	182
Figure 2.111 ^{13}C NMR spectrum of 3a [BArF ₂₄] in CDCl ₃	183
Figure 2.112 ^{31}P NMR spectrum of 3a [BArF ₂₄] in CDCl ₃	184
Figure 2.113 ^{19}F NMR spectrum of 3a [BArF ₂₄] in CDCl ₃	185
Figure 2.114 ^{14}N NMR spectrum of 3a [BArF ₂₄] in CDCl ₃	186
Figure 2.115 ^1H NMR spectrum of 3a [BPh ₄] in CDCl ₃	187
Figure 2.116 ^{13}C NMR spectrum of 3a [BPh ₄] in CDCl ₃	188
Figure 2.117 ^{31}P NMR spectrum of 3a [BPh ₄] in CDCl ₃	189
Figure 2.118 ^{14}N NMR spectrum of 3a [BPh ₄] in CDCl ₃	190
Figure 3.1 (<i>left</i>) The Ni(CO) ₃ PR ₃ complex used in to determine the TEP. (<i>right</i>) The model used to measure the Tolman Cone Angle of a given phosphine. The spheres represent a variety of R groups, and the P center and block are 2.28 Å apart.....	201
Figure 3.2 Resonance forms that contribute to the ground state electronic structure of traditional low-valent metal-phosphorous interactions.....	205
Figure 3.3 The synthetic scheme used to generate the O=P(Et) ₃ adduct with [NCr(N ⁱ Pr ₂) ₂] ⁺ . A high yield of the desired complex was isolated after recrystallization. (<i>right</i>) Preliminary crystal structure of [NCr(N ⁱ Pr ₂) ₂ (OP(Et) ₃)] [BArF ₂₄]; note, thermal ellipsoids are not shown due to the severe disorder in the structure. It provided only connectivity.....	208
Figure 3.4 Structures examined by NBO/NRT analysis.....	209
Figure 3.5 Resonance forms inherent to the CrN ₃ fragment from rearrangement of the lone pair electron density across the N ligands. These resonance forms and their electron rearrangements do not affect the nature of the Cr–P bonds, so they are summed as *Cr to focus resonance form discussion on the Cr–P interaction.....	210

Figure 3.6 NRT determined resonance forms accounting for 99% of the ground state of 3a* ..	211
Figure 3.7 Contribution of the two resonance forms that compose a dative interaction to the ground state electronic structure of 3m* and 3o*	212
Figure 3.8 Arrow pushing illustration relating α and γ in 3m* and 3o* . The example is shown here with 3m*	213
Figure 3.9 Arrow pushing illustration relating α and ϵ in 3m* and 3o* . The example is shown where with 3o*	214
Figure 3.10 Ground state electronic structures of 3m* and 3o* , including γ which shows negative hyperconjugation among the -OMe and -NMe ₂ ligands, as well as ϵ which is a new negative hyperconjugative resonance form involving the metal.....	214
Figure 3.11 NRT results for an aryl phosphine ligand. Similar to the ϵ resonance forms observed with 3m* and 3o* , electron density is pushed from one of the R groups into the Cr–P σ^* orbital.	216
Figure 3.12 A plot showing good correlation between experimental and modeled ΔH^\ddagger values for trialkyl phosphines fitted with χ_d and θ parameters.	219
Figure 3.13 All complexes 3a-p fitted with the model in Eq. 2. (Red = trialkyl, orange = monoaryl, green = diaryl, blue = heteroatom substituents).	220
Figure 3.14 Ground state resonance assignment to Cr fragment by NRT for [NCr(NH ₂) ₂ PMe ₂ Ph] ⁺	223
Figure 3.15 CHOOSE 1 geometry for NBO analysis.	224
Figure 3.16 CHOOSE 2 geometry for NBO analysis.	235
Figure 3.17 (left) CHOOSE1; (right) CHOOSE2.....	248
Figure 3.18 Correlation of %V _{bur} vs. Tolman Cone Angle for all phosphines used in model building (3a-o).	254
Figure 3.19 Steric profile from fit of trialkylphosphines (3a-e) using 2-parameter fit, Eq. 3.6.	255
Figure 3.20 Electronic profile from fit of trialkylphosphines (3a-e) using 2-parameter fit, Eq. 3.5.	256
Figure 3.21 Trialkylphosphine 2-parameter fit applied to total series: Electronic profile. (Orange squares = PR ₂ Ph; Green triangles = PPh ₂ R, Red circles = PR ₃ , Blue circles = P(OR) ₃ /P(NR ₂) ₃ .)	257
Figure 3.22 Trialkylphosphine 2-parameter fit applied to total series: Steric profile. (Orange squares = PR ₂ Ph; Green triangles = PPh ₂ R, Red circles = PR ₃ , Blue circles = P(OR) ₃ /P(NR ₂) ₃ .)	258

Figure 3.23 ^1H NMR of $[\text{NCr}(\text{N}^i\text{Pr}_2)_2(\text{OP}(\text{Et})_3)][\text{BArF}_{24}]$ in CDCl_3	260
Figure 3.24 ^{31}P NMR of $[\text{NCr}(\text{N}^i\text{Pr}_2)_2(\text{OP}(\text{Et})_3)][\text{BArF}_{24}]$ in CDCl_3	261
Figure 3.25 ^{19}F NMR of $[\text{NCr}(\text{N}^i\text{Pr}_2)_2(\text{OP}(\text{Et})_3)][\text{BArF}_{24}]$ in CDCl_3	262
Figure 3.26 ^{13}C NMR of $[\text{NCr}(\text{N}^i\text{Pr}_2)_2(\text{OP}(\text{Et})_3)][\text{BArF}_{24}]$ in CDCl_3	263
Figure 4.1 Reaction schemes to yield highly substituted nitrogen-based heterocycles using Ti-catalyzed iminoamination followed by simple organic ring-closing reactions. These processes are conducted as one-pot-two-step reactions from simple starting materials. ⁶	270
Figure 4.2 The combination of the LDP system using high valent Cr(VI) and our Ti(IV) hydroamination catalysts which has facilitated the development of a quantitative model describing the effects of ancillary ligands on catalytic rate.	272
Figure 4.3 The species that were targeted as potential precatalyst materials for hydroamination and iminoamination chemistry using a silica-supported, heterogeneous catalyst system.	276
Figure 4.4 The binding mode of Ti on the surface of SiO_2^{200} upon treatment with $\text{Ti}(\text{NMe}_2)_4$. For comparison, the bulk properties of the material reported by the Scott group is given along with the properties of the material we synthesized following their SiO_2^{200} preparation.	277
Figure 4.5 (top) Quartz tube used for silica gel prep with tube furnace setup. (bottom) Schematic for the preparation of the precatalyst material $[\text{Ti}]700$	278
Figure 4.6 Possible site variations in the coordination environment and binding modes for the two different catalysts, $[\text{Ti}]200$ and $[\text{Ti}]700$	279
Figure 4.7 Reaction conditions applied to the heterogeneous catalysts. The yields and regioselectivities listed here were observed with $[\text{Ti}]200$. The same trends were observed with $[\text{Ti}]700$, as well, with improvements in regioselectivities and yields at higher temperatures in dramatically shorter reaction times. Moving forward, the conditions for C were adopted as the general procedure.	281
Figure 4.8 General reaction scheme applied to the iminoamination reactions studied with $[\text{Ti}]200$ and $[\text{Ti}]700$	286
Figure 4.9 Proposed surface morphologies of used $[\text{Ti}]200$, after use in hydroamination reactions. Changes in the coordination environment could lead to changes in the regioselectivity ratio observed in the hydroamination products.	291
Figure 4.10 Ti complexes from the Richeson Group used for catalytic guanylation of carbodiimides and imide metathesis reactions. ^{47,48}	293
Figure 4.11 ^1H NMR of HA1^{red} in CDCl_3	319
Figure 4.12 ^{13}C NMR of HA1^{red} in CDCl_3	320

Figure 4.13 ^1H NMR of HA2 ^{red} in CDCl_3 .	321
Figure 4.14 ^{13}C NMR of HA2 ^{red} in CDCl_3 .	322
Figure 4.15 ^1H NMR of HA3 ^{red} .	323
Figure 4.16 ^1H NMR of HA4 in CDCl_3 .	324
Figure 4.17 ^{13}C NMR of HA4 in CDCl_3 .	325
Figure 4.18 ^1H NMR of HA7 ^{red} in CDCl_3 .	326
Figure 4.19 ^{13}C NMR of HA7 ^{red} in CDCl_3 .	327
Figure 4.20 ^1H NMR of HA8 ^{red} in CDCl_3 .	328
Figure 4.21 ^{13}C NMR of HA8 ^{red} in CDCl_3 .	329
Figure 4.22 ^1H NMR of HA12 ^{Red} in CDCl_3 .	330
Figure 4.23 ^{13}C NMR of HA12 ^{red} in CDCl_3 .	331
Figure 4.24 ^1H NMR of HA13 ^{red} in C_6D_6 .	332
Figure 4.25 ^{13}C NMR of HA13 ^{red} in C_6D_6 .	333
Figure 4.26 ^1H NMR of HA14 ^{red} in C_6D_6 .	334
Figure 4.27 ^{13}C NMR of HA14 ^{red} in C_6D_6 .	335
Figure 4.28 ^1H NMR of 3CC1 in CDCl_3 .	336
Figure 4.29 ^{13}C NMR of 3CC1 in CDCl_3 .	337
Figure 4.30 ^1H NMR of 3CC5 in CDCl_3 .	338
Figure 4.31 ^{13}C NMR of 3CC5 in CDCl_3 .	339
Figure 4.32 GC-MS of HA3 ^{red} .	340
Figure 4.33 GC-MS of crude HA11.	341
Figure 4.34 GC-MS of crude HA12.	342
Figure 4.35 Crude GC-MS trace of HA13.	343
Figure 4.36 HA14 crude GC-MS trace.	344
Figure 4.37 EI-MS Fragmentation Pattern for HA14(A).	345

Figure 4.38 EI-MS Fragmentation Pattern for HA14(B).....	346
Figure 4.39 GC-MS trace of HA14 ^{red}	347
Figure 4.40 EI-MS of HA14 ^{red} (A).....	348
Figure 4.41 EI-MS of HA14 ^{red} (B).....	349
Figure 4.42 GC-MS of 3CC1.....	350
Figure 4.43 GC-MS of 3CC5.....	351
Figure 4.44 Fragmentation patterns observed for 1-phenyl-3-cyclohexylurea.....	352
Figure 4.45 Fragmentation patterns observed in the HCl wash of used [Ti]700 catalyst after iminoamination which closely match those for 1-phenyl-3-cyclohexylurea.....	353
Figure 4.46 Fragmentation pattern observed in the HCl wash of used [Ti]700 catalyst after iminoamination, which closely matches 1,3-dicyclohexylurea.....	354
Figure 5.1 Proposed mechanism and rate law determined for homogeneous Ti(IV) hydroamination catalysts of the (A) ₂ Ti(X) ₂ variety; The integrated rate law is given, as well as the dependence of k _{obs} on both amine and Ti concentrations. ⁷ In the active species (A) stays bound to Ti while X's participate in protolytic cleavage to generate a Ti-imide active species.	362
Figure 5.2 (top) General reaction sequence for the 3-component coupling of an amine, alkyne, and isonitrile to yield 1,3-diimine tautomers. (bottom) The two catalysts typically utilized for this transformation.....	363
Figure 5.3 Effects of different HX ligands on the general 3CC reaction utilizing different alkynes: (top) The variety of HX ligands screened in the 3CC reactions; (bottom) Plots of the 3CC reaction products showing the regioisomer ratio versus % yield for each HX ligand examined. In the plots, burgundy diamonds correspond to bidentate ligands, while blue circles correspond to monodentate ligands. The best ligands for each alkyne are specified next to their respective points.....	368
Figure 5.4 The synthetic scheme (left) and single crystal X-ray structure of a 2-amino-3-cyanopyridine synthesized using [Ti]700(X).....	372
Figure 5.5 Plot of initial rates from the kinetic experiments shown in Table 5.1. The initial rates, determined from linear fits shown in the plot above, are listed in the table below. These rates are may be slower than the actual initial rates as they go far beyond 10% conversions.....	374
Figure 5.6 Order of catalyst and reagent dependence for rate law of the iminoamination reaction catalyzed by [Ti]700(X). Entry 1 represents the light purple points, with the following concentrations: 0.25 M aniline, 0.25 M CyNC, 0.51 M 1-octyne, and 0.012 M (5 mol%) Ti. It is plotted against the following entries, where the substrate alteration is indicated: 3 (green, 0.024 M (10 mol%) Ti), 5 (blue, 0.51 M CyNC), 4 (maroon, 0.51 M aniline), and 6 (aqua, 1.01 M 1-	

octyne) to demonstrate how different reagent concentrations affect the rate of the iminoamination reactions. For rough approximations of the initial rates, refer to Fig. 5.5.	376
Figure 5.7 Proposed catalytic cycle for [Ti]700(X) based on experimental kinetic data and KINSIM modeling. Note, in the figure, the green letters, rate constants, and equilibrium constants are from the KINSIM model. The deactivation step from A to J is based on experimental observations of 3CC reactivity with homogeneous Ti analogues (see Chapter 6).	378
Figure 5.8 Correlation between reaction rate and donor ability of X ⁻ in heterogeneous [Ti]700(X) catalyzed 3CC reactions. More electron-donating X ⁻ ligands seem to enhance the rate of the reaction by increasing the rate of formation of the active species from the resting state of the catalyst. (blue = ^t Bu, grey = H, orange = OMe, yellow = Br).	381
Figure 5.9 Poisoning experiments with pyrrole and 2- <i>tert</i> -butyl-4-methoxyphenol, showing very different catalyst activity with varying concentrations of the two different HX ligands.....	385
Figure 5.10 General hydroamination reaction and conditions applied to [Ti]700 catalyzed reactions with excess ligand additive (HX). Ligands examined in Table 5.5.....	386
Figure 5.11 A traditional homogeneous mechanism (i.e. Bergman or Doye) of hydroamination shown with a Ti catalyst (<i>top</i>), and a modified version of the mechanism where HX may participate in the deprotonation of the aza-titanacyclobutene intermediate and impact the equilibrium formation of the active Ti-imido species (<i>bottom</i>).	388
Figure 5.12 Crystal data and structure refinement for twin5.	396
Figure 5.13 Crystal data and structure refinement for tri_early2_a.	398
Figure 5.14 ¹ H NMR of 3CC1 in CDCl ₃ (isomeric mixture of A and B).	416
Figure 5.15 ¹³ C NMR of 3CC1 in CDCl ₃ (isomeric mixture of A and B).	417
Figure 5.16 gCOSY NMR of 3CC1 in CDCl ₃ (isomeric mixture of A and B).	418
Figure 5.17 GC trace of 3CC1 (A and B) and MS fragmentation pattern for 3CC1(A).	419
Figure 5.18 GC trace of 3CC1 (A and B) and MS fragmentation pattern for 3CC1(B).	420
Figure 5.19 ¹³ C NMR of 3CC2 in CDCl ₃	421
Figure 5.20 ¹³ C NMR of 3CC2 in CDCl ₃	422
Figure 5.21 gCOSY NMR of 3CC2 in CDCl ₃	423
Figure 5.22 GC trace and MS fragmentation pattern for 3CC2.	424
Figure 5.23 ¹ H NMR of 3CC3 in CDCl ₃	425

Figure 5.24 ^{13}C NMR of 3CC3 in CDCl_3 .	426
Figure 5.25 gCOSY NMR of 3CC3 in CDCl_3 .	427
Figure 5.26 ^1H NMR of $[\text{Cr}](\text{O-Ph-4-bromo})$ in CDCl_3 (room temperature).	428
Figure 5.27 ^1H NMR of $[\text{Cr}](\text{O-Ph-4-bromo})$ in CDCl_3 (-20 °C).	429
Figure 5.28 ^{13}C NMR of $[\text{Cr}](\text{O-Ph-4-bromo})$ in CDCl_3 (-20 °C).	430
Figure 5.29 Results from simulated reactions versus the experimentally determined concentrations of 3CC product over time, Entry 1.	435
Figure 5.30 Results from simulated reactions versus the experimentally determined concentrations of 3CC product over time, Entry 3.	436
Figure 5.31 Results from simulated reactions versus the experimentally determined concentrations of 3CC product over time, Entry 4.	437
Figure 5.32 Results from simulated reactions versus the experimentally determined concentrations of 3CC product over time, Entry 5.	438
Figure 5.33 Example simulation from KINSIM program.	440
Figure 6.1 Crude GCMS analysis of the iminoamination of 3,5-dimethylaniline, 1-phenylpropyne, and CyNC catalyzed by 10 mol% $\text{Ti}(\text{dpm})(\text{NMe}_2)_2$ (<i>left</i>) and 5 mol% $[\text{Ti}]700(2,6\text{-dimethylphenylamidate})$ (<i>right</i>). Note that the reaction catalyzed by $\text{Ti}(\text{dpm})(\text{NMe}_2)_2$ has a substantial peak at 8 min, which is the 3,5-dimethylaniline starting material, as well as a large peak at 18 min for hydroamination side product. The reaction catalyzed by $[\text{Ti}]700$ shows no other compounds in the GCMS trace (small peaks on baseline are polysiloxane column material from GC column).	447
Figure 6.2 The reaction traces of two homogeneous $\text{Ti}(\text{dpm})(\text{NMe}_2)_2$ catalyzed iminoamination reactions. Both reactions reach a maximum yield after about 12 h. With the high catalyst loading, there is even what appears to be a decrease in concentration of the product from the maximum measured concentration.	451
Figure 6.3 Graphical analysis of Entries 1-3 in Table 6.1. The plots are fitted with a fractional order (<i>top</i>) and first order (<i>bottom</i>) dependence. Similar fits result from both analyses.	454
Figure 6.4 Examination of the initial rates for Entries 1-3 from Table 6.1. The results suggest that the catalyst concentration may not be simple first-order in these concentration ranges.	455
Figure 6.5 Potential forms of titanium catalyst likely present in the catalytic iminoamination reaction mixture.	457

Figure 6.6 Isolation and structural characterization of the bridging $[\text{Ti}(\text{dpm})(\mu\text{-Ntoly})]_2$ complex. The single crystal X-ray structure is shown with ellipsoids at the 50% probability and H atoms omitted for clarity.	460
Figure 6.7 Various titanium species found to (or suspected of) react directly with the iminoamination product. This reactivity provides plausible means of titanium complex deactivation throughout the iminoamination reaction.	464
Figure 6.8 (<i>left</i>) ^1H NMR spectrum and (<i>right</i>) single crystal X-ray structure ⁴ of $\text{Ti}(\text{NMe}_2)_2(\text{OArCH}_2\text{ArO})$. The two protons on the methylene linker have unique positions due to the conformation of the 8-membered ring formed by the ligand with Ti, which is readily observed by the distinct doublets in the ^1H NMR spectrum. This trait applies to all of the complexes of the general form $\text{Ti}(\text{X})_2(\text{OArCH}_2\text{ArO})$ and makes them easy to observe and distinguish between by ^1H NMR.	466
Figure 6.9 The comproportionation reaction monitored by determination of the equilibrium constant K_{eq} . The 3 possible Ti species in equilibrium in these solutions are shown, including both starting materials and the only possible product.	473
Figure 6.10 Plot of K_{eq} vs. LDP of the X^- ligands in the $\text{Ti}(\text{OArCH}_2\text{ArO})(\text{X})_2$	474
Figure 6.11 A plot showing model-predicted versus experimental data relating the donor ability of a given X^- ligand to the equilibrium constant observed for formation of the heteroleptic species, $\text{Ti}(\text{X})_2(\text{OArCH}_2\text{ArO})$ (Fig. 6.15).	476
Figure 6.12 Potential ligands of interest that could avoid deactivation via ligand disproportionation as their donor abilities (LDP values) are predicted to be more and less donating than a chelated iminoamination product, potentially disfavoring ligand exchange reactions.	478
Figure 6.13 ^1H NMR of $\text{Ti}(\text{dpm})(\text{NMe}_2)_2$ and 3CC heated at 80 °C, 40 h in C_6D_6	489
Figure 6.14 ^1H NMR of $[\text{Ti}(\text{dpm})(\text{Ntoly})]_2$, $^t\text{BuNC}$ (xs), and 3CC in C_6D_6 , 80 °C at 6 h.	490
Figure 6.15 ^1H NMR of the $[\text{Ti}(\mu\text{-Ntoly})(\text{dpm})]_2$ with $^t\text{BuNC}$ <i>in situ</i> in C_6D_6	491
Figure 6.16 ^1H NMR of $[\text{Ti}(\text{OArCH}_2\text{ArO})(\mu\text{-Ntoly})]_2 \cdot \text{NHMe}_2$ after heating 16 h at 80 °C.	493
Figure 6.17 Proposed decomposition pathway and final products observed (top) and proposed (bottom) for the Ti-imide species upon heating with the iminoamination product in C_6D_6	495
Figure 6.18 ^1H NMR of $3\text{CC}(\text{A/B}) + [\text{Ti}(\text{OArCH}_2\text{ArO})(\text{Ntoly})]_2 \cdot \text{HNMe}_2$ heated for 0 h at 85 °C—showing no $\text{Ti}(\text{OArCH}_2\text{ArO})_2$	496
Figure 6.19 ^1H NMR of $3\text{CC}(\text{A/B}) + [\text{Ti}(\text{OArCH}_2\text{ArO})(\text{Ntoly})]_2 \cdot \text{HNMe}_2$ heated for 3 h at 85 °C—showing a small amount of $\text{Ti}(\text{OArCH}_2\text{ArO})_2$	497

Figure 6.20 ^1H NMR of $3\text{CC}(\text{A}/\text{B}) + [\text{Ti}(\text{OArCH}_2\text{ArO})(\text{Ntoly})]_2 \cdot \text{HNMe}_2$ heated for 48 h at 85°C —showing only $\text{Ti}(\text{OArCH}_2\text{ArO})_2$ as identifiable Ti species.....	498
Figure 6.21 ^1H NMR of the iminoamination reaction catalyzed by 20 mol% $\text{Ti}(\text{OArCH}_2\text{ArO})(\text{NMe}_2)_2$ in <i>tol-d</i> ₈ . Peaks at 11.2 and 10.4 ppm are for the two different regioisomers of the 3CC product. The large singlet at 3.97 ppm is Fc as internal standard. The peak at 3.35 ppm belongs to the $\text{Ti}(\text{OArCH}_2\text{ArO})_2$ disproportionation species.....	500
Figure 6.22 ^1H NMR of an isomeric mixture of 3CC(A) and (B) in CDCl_3	501
Figure 6.23 ^{13}C NMR of an isomeric mixture of 3CC _k (A) and (B) in CDCl_3	502
Figure 6.24 GCMS of 3CC isomers A and B; fragmentation pattern for A isomer.	503
Figure 6.25 GCMS of 3CC isomers A and B; fragmentation pattern for B isomer.	504
Figure 6.26 HRMS for isomeric mixture of 3CC.	505
Figure 6.27 ^1H NMR of the 4CC product in CDCl_3	506
Figure 6.28 ^{13}C NMR of the 4CC product in CDCl_3	507
Figure 6.29 GCMS of the 4CC product and MS fragmentation pattern.	508
Figure 6.30 HRMS of the 4CC product.	509
Figure 6.31 gCOSY NMR of the 4CC product in CDCl_3	510
Figure 6.32 HMBC NMR of 4CC in CDCl_3	511
Figure 6.33 ^1H NMR of $[\text{Ti}(\mu\text{-Ntoly})(\text{dpm})]_2$ in <i>tol-d</i> ₈ .(room temperature, high vac grease and hexane impurities).....	512
Figure 6.34 ^1H NMR of $[\text{Ti}(\mu\text{-Ntoly})(\text{dpm})]_2$ in <i>tol-d</i> ₈ .(-75 °C, high vac grease and hexane impurities).....	513
Figure 6.35 ^{13}C NMR of $[\text{Ti}(\mu\text{-Ntoly})(\text{dpm})]_2$ in <i>tol-d</i> ₈ .(room temperature, high vac grease and hexane impurities).....	514
Figure 6.36 ^1H NMR of $[\text{Ti}(\text{OArCH}_2\text{ArO})(\mu\text{-Ntoly})] \cdot \text{HNMe}_2$ in C_6D_6	515
Figure 6.37 ^{13}C NMR of $[\text{Ti}(\text{OArCH}_2\text{ArO})(\mu\text{-Ntoly})] \cdot \text{HNMe}_2$ in C_6D_6	516
Figure 6.38 ^1H NMR of $\text{Ti}(2,4\text{-di-tert-butyl-phenoxide})_4$ in C_6D_6	517
Figure 6.39 ^{13}C NMR of $\text{Ti}(2,4\text{-di-tert-butyl-phenoxide})_4$ in C_6D_6	518
Figure 6.40 Crystal data and structure refinement for earlyy2.	519

Figure 6.41 Crystal data and structure refinement for c2c_early_a.....	521
Figure 6.42 Crystal data and structure refinement for p21_c_a.....	523
Figure 6.43 Crystal data and structure refinement for rjs.	525
Figure 6.44 Crystal data and structure refinement for uc_a.....	527
Figure 6.45 Crystal data and structure refinement for early_a.	529
Figure 6.46 DOSY MW determination for $[\text{Ti}(\text{OArCH}_2\text{ArO})(\mu\text{-Ntoly})]_x \cdot 1/2 \text{NHMe}_2$ in C_6D_6	532
Figure 6.47 DOSY MW determination for $[\text{Ti}(\text{dpm})(\mu\text{-Ntoly})]_x$ in C_6D_6	533
Figure 6.48 DOSY MW determination of $\text{Ti}(\text{OArCH}_2\text{ArO})(\text{I})_2$ in C_6D_6	534
Figure 6.49 DOSY MW determination of $\text{Ti}(\text{OArCH}_2\text{ArO})(\text{O}^i\text{Pr})_2$ complex in C_6D_6	535
Figure 6.50 The graphical determination of reaction rate dependence on alkyne concentration. Purple spheres = 0.2 M (Entry 3); Red spheres = 1.0 M (Entry 4); Grey spheres = 0.4 M (Entry 5).	538
Figure 6.51 The graphical determination of reaction rate dependence on isonitrile concentration. Purple spheres = 0.2 M (Entry 3); Orange spheres = 0.4 M (Entry 6).	539
Figure 6.52 The graphical determination of reaction rate dependence on amine concentration. Purple spheres = 0.2 M (Entry 3); light blue spheres = 0.4 M (Entry 7); Green spheres = 1.0 M (Entry 8).	540
Figure 6.53 Reaction progress of two identical kinetics trials run with $\text{Ti}(\text{dpm})(\text{NMe}_2)_2$ and $\text{Ti}(\text{OArCH}_2\text{ArO})(\text{NMe}_2)_2$. Similar results were obtained with both catalysts under the conditions used for kinetics despite better performance of the $\text{Ti}(\text{OArCH}_2\text{ArO})(\text{NMe}_2)_2$ under normal conditions applied to a typical iminoamination reaction.	541
Figure 6.54 Equilibrium ligand exchange reaction used to determine K_{eq} experimentally. For reactions where K_{eq} is small, starting materials 1 and 2 were used. For reactions where K_{eq} was large, 3 could be prepared and isolated cleanly and was utilized in these experiments.	543
Figure 6.55 ^1H NMR of $\text{Ti}(\text{OArCH}_2\text{ArO})_2$ in C_6D_6	544
Figure 6.56 ^{13}C NMR of $\text{Ti}(\text{OArCH}_2\text{ArO})_2$ in C_6D_6	545
Figure 6.57 ^1H NMR of the equilibrium mixture of $\text{Ti}(\text{NMe}_2)_4$, $\text{Ti}(\text{NMe}_2)_2(\text{OArCH}_2\text{ArO})$, and $\text{Ti}(\text{OArCH}_2\text{ArO})_2$	546
Figure 6.58 ^1H NMR of the equilibrium mixture of $\text{Ti}(\text{OAr}^{4\text{-tert-butyl}})_4$, $\text{Ti}(\text{OAr}^{4\text{-tert-}}$ $\text{butyl})_2(\text{OArCH}_2\text{ArO})$, and $\text{Ti}(\text{OArCH}_2\text{ArO})_2$	547

Figure 6.59 Least Squares fit result for predicting K_{eq} from ΔLDP	549
Figure 7.1 Examples of terminal mono- and bis-imido Fe complexes in the literature. Note the prevalence of both bulky and chelating ligands, which stabilize these complexes. ²⁰⁻²⁸	557
Figure 7.2 (top) X-ray crystal structure of Ru1 with ellipsoids shown at 50% probability and H's omitted for clarity (N = blue, Ru = teal, P = pink). (bottom)	559
Figure 7.3 (top) Synthetic schemes for the synthesis of Ru2 and Ru3 . (bottom) X-ray crystal structure for Ru3 (left) (Ru(NAr)dppe(PMe ₃)) and Ru2 (right); ellipsoids shown at 50% probability, hydrogens omitted for clarity. For Ru2 , the two enantiomers co-crystallize and are disordered across the axis coincident with the P1–Ru1–P3 bond. Select bond lengths and angles are shown.	562
Figure 7.4 (top) Synthetic scheme for the production of Ru4 from Ru3 via oxidation with AgSbF ₆ (AgBARF ₂₄ can also be used). (bottom) X-ray crystal structure of the dimeric species with ellipsoids shown at 50% probability; H atoms and disordered counter anion omitted for clarity.	563
Figure 7.5 Proposed resonance contributors for Ru5 with radical distribution across the <i>ortho</i> and <i>para</i> positions of the imide aryl group.....	564
Figure 7.6 Synthesis procedure for Ru1* and Ru3* from <i>cis</i> -RuCl ₂ (PMe ₃) ₄ starting material. The crystal structure of Ru1* is shown with ellipsoids are shown at 50% probability; H atoms omitted for clarity.	566
Figure 7.7 (top) Synthesis of Fe analogues of Ru-imido complexes, Fe1 , Fe1* , Fe3 , and Fe3* . The side product, Fe2/2* , also results from this synthetic route, and is separated from Fe3/3* by several extractions and recrystallizations. (bottom) Crystal structures of Fe2* and Fe3* ; ellipsoids are shown at 50% probability with H atoms omitted for clarity. Note, Fe2* crystallizes in the C2/c spacegroup, with the crystallographic 2-fold axis bisecting the N1–Fe1–N1 and P1–Fe1–P1 angles. Thus, half of the molecule is symmetry generated.....	569
Figure 7.8 Synthesis of Fe5 and Fe6 by trapping the unstable Fe1 with the trischelating (PMe ₂ CH ₂) ₃ Si ^t Bu ligand. X-ray crystal structures of Fe5 and Fe6 are shown for comparison; ellipsoids are shown at 50% probability with H atoms and counteranion (Fe6) omitted for clarity.	572
Figure 7.9 M(III) cationic complexes examined by EPR spectroscopy. Fe6 is reasonably crystalline and has been characterized by single crystal X-ray crystallography. Ru4* and Fe4* are amorphous. The become oily when exposed to polar ethereal solvents, and attempts at crystallization generally produce powder solids.....	573
Figure 7.10 EPR spectra (black) of 2 different preparations of Fe4* (a and b), utilizing identical synthetic preparations. The insert shows a mixed Fe(III) radical species that seems to form as an impurity (or decomposition product) upon oxidation of Fe3* to Fe4*. The spectrum shown in a is relatively pure, while b shows the Fe(III) mixed radical impurity superimposed on the spectrum	

of Fe4*. Red traces represent simulated spectra. For more simulation details, see Experimental. Spectra were recorded at 10 K. 576

Figure 7.11 EPR spectra of two different preparations of Fe6 (black) and their simulated spectra (red), utilizing identical synthetic methods. Both samples show very similar characteristics, with about 75% Fe(III)-centered character and 25% ligand-centered radical with 14N hyperfine coupling. Two different lineshapes are noted in toluene (top) and 2-methylTHF (bottom), but the radical character has very similar properties in both spectra. Spectra were recorded at 10K 578

Figure 7.12 EPR spectra of two different samples of Ru5* (black) and their simulated spectra (red), utilizing identical synthetic methods. The samples are treated as a composite of two distinct paramagnetic centers—one centered on Ru(III) and one centered on the imide fragment. The two spectra show dramatically different proportions of each radical center in the sample. Spectrum (a) is about 90% Ru(III) and 10% ligand radical, whereas spectrum (b) shows about 30% Ru(III) character and 70% ligand radical. These spectra were taken from different batches of Ru5*, prepared following the same synthetic procedures. The relative distribution of radical character seems to be affected by synthesis and sample preparation of the compounds..... 580

Figure 7.13 The figure shows the radical localization in the Fe4*, Ru5*, and Fe6 cations. Note that with Fe4*, the cationic species is most accurately described by a single paramagnetic center. However, the Ru5* and Fe6 spectra could only be successfully modeled as a composite of two paramagnetic species, where both a metal- and ligand-centered radical contribute to the entire spectrum. 583

Figure 7.14 The orbital energies (defined as the negative ionization potential, as described in the text) of Fe7, Ru6, and Ru6_mod computed at the CASPT2 level of theory. Insets show the HOMO and HOMO-1 orbitals (SONOs of the cations, as described in the text). A green arrow indicates the bonding lobe of the HOMO of Ru6..... 586

Figure 7.15 Addition of CS₂ to the terminal Fe(II) imide, Fe5, results in the production of 2,6-diisopropylphenylthioisocyanate and an insoluble red species proposed to be [Fe(^tP₃)(μ-S)]₂. 590

Figure 7.16 Reaction of 2 equivalents of benzaldehyde with Fe5 produces a metalacyclic species which is chiral, and appears to be diamagnetic, low spin Fe(II). Based on bond lengths and angles in the crystal structure, the two oxygens coordinated to Fe appear anionic, with N1 best described as an imine. This means that loss of H₂ has occurred during the reaction. The crystal structure (*right*) is shown with ellipsoids at 50% probability. H's and one molecule of n-hexane in the lattice were omitted for clarity. (Fe1–O1 = 1.985 Å, Fe1–O2 = 1.858 Å, O1–C1 = 1.291 Å, C1–N1 = 1.297 Å, O2–C9 = 1.416 Å). 591

Figure 7.17 Results demonstrating the electronic basis of the distortion of Ru1 away from C_{3v} symmetry.⁴⁶ 596

Figure 7.18 ¹⁴N NMR of Ru1 in C₆D₆. 609

Figure 7.19 ¹H NMR of Ru2 in C₆D₆. 610

Figure 7.20 ¹³C NMR of Ru2 in d₈-THF. 611

Figure 7.21 ^{31}P NMR of Ru2 in d_8 -THF.	612
Figure 7.22 ^{14}N NMR of Ru2 in C_6D_6	613
Figure 7.23 ^1H NMR of Ru4 in CD_2Cl_2	614
Figure 7.24 ^{31}P NMR of Ru4 in CD_2Cl_2	615
Figure 7.25 ^{19}F NMR of Ru4 in CD_2Cl_2	616
Figure 7.26 ^1H NMR of Ru3 in C_6D_6	617
Figure 7.27 ^{13}C NMR of Ru3 in C_6D_6	618
Figure 7.28 ^{31}P NMR of Ru3 in C_6D_6	619
Figure 7.29 ^{14}N NMR of Ru3 in C_6D_6	620
Figure 7.30 ^1H NMR of Ru1* in C_6D_6	621
Figure 7.31 ^{13}C NMR of Ru1* in C_6D_6	622
Figure 7.32 ^{31}P NMR of Ru1* in C_6D_6	623
Figure 7.33 ^{14}N NMR of Ru1* in C_6D_6	624
Figure 7.34 ^1H NMR of Ru2* in C_6D_6	625
Figure 7.35 ^{13}C NMR of Ru2* in C_6D_6	626
Figure 7.36 ^{31}P NMR of Ru2* in C_6D_6	627
Figure 7.37 ^{14}N NMR of Ru2* in C_6D_6	628
Figure 7.38 ^1H NMR of Ru3* in C_6D_6	629
Figure 7.39 ^{13}C NMR of Ru3* in C_6D_6	630
Figure 7.40 ^{31}P NMR of Ru3* in C_6D_6	631
Figure 7.41 ^{14}N NMR of Ru3* in C_6D_6	632
Figure 7.42 ^{31}P NMR of Fe1 in THF (<i>in situ</i>).	633
Figure 7.43 ^{14}N NMR of Fe1 in THF (<i>in situ</i>).	634
Figure 7.44 ^1H NMR of Fe3 in C_6D_6	635
Figure 7.45 ^{13}C NMR of Fe3 in C_6D_6	636

Figure 7.46 ^{31}P NMR of Fe3 in C_6D_6	637
Figure 7.47 ^{14}N NMR of Fe3 in C_6D_6	638
Figure 7.48 ^{31}P NMR of Fe1* in C_6D_6	639
Figure 7.49 ^{14}N NMR of Fe1* in C_6D_6	640
Figure 7.50 ^1H NMR of Fe3* in C_6D_6	641
Figure 7.51 ^{13}C NMR of Fe3* in C_6D_6	642
Figure 7.52 ^{31}P NMR of Fe3* in C_6D_6	643
Figure 7.53 ^{14}N NMR of Fe3* in C_6D_6	644
Figure 7.54 ^1H NMR of Fe8 in C_6D_6	645
Figure 7.55 ^{31}P NMR of Fe8 in C_6D_6	646
Figure 7.56 ^1H NMR of the C_6D_6 soluble extracts from the reaction of Fe5 and CS_2 . The ^1H NMR shows H_2NAr and SCNAr	647
Figure 7.57 ^{31}P NMR of Fe5 + 1,1-dimethylhydrazine in C_6D_6 . The peak at 47 ppm is the starting Fe5 . The peak at 52 ppm is a new compound. (-49 is free triphos ligand).....	648
Figure 7.58 0.000109 M, THF	649
Figure 7.59 0.00022 M THF	650
Figure 7.60 0.00031 M, THF	651
Figure 7.61 0.00031 M, THF	652
Figure 7.62 0.00010 M, THF	653
Figure 7.63 0.00044 M, THF	654
Figure 7.64 0.000068 M, THF	655
Figure 7.65 0.000071 M, THF	656
Figure 7.66 0.000238 M, THF	657
Figure 7.67 0.00016 M, THF	658
Figure 7.68 Crystal data and structure refinement for Pbca.	660
Figure 7.69 CV for Fe3* in THF with TBAPF_6 electrolyte.	664

Figure 7.70 CV for Fe4* in THF with TBAPF6 electrolyte.....	665
Figure 7.71 CV for Fe5 in THF with TBAPF6 electrolyte.....	666
Figure 7.72 CV for Fe6 in THF with TBAPF6 electrolyte.....	667
Figure 7.73 CV for Ru3* in THF with TBAPF6 electrolyte.....	668
Figure 8.1 The synthetic procedure presented by Wilkinson and coworkers in 1992 which lead to the square planar d ⁴ Ru species on the right.	677
Figure 8.2 Examples of various Group 8 mono- and bis(imido) compounds.....	679
Figure 8.3 Illustration of the synthetic route proposed to access Ru-imido species in mid- to high oxidation states.....	681
Figure 8.4 (top) The X-ray crystal structure of Ru2 with ellipsoids shown at 50% probability; H atoms and solvent molecule omitted for clarity. (bottom) Synthetic procedure to yield (κ^2 -diphenylhydrazido)Ru(PMe ₃) ₄ from in situ reduced azobenzene and cis-RuCl ₂ (PMe ₃) ₄ . The same procedure can be utilized to produce the Os analogue of this compound.	681
Figure 8.5 The Ru(II) terminal hydride (Ru3) species produced upon heating Ru2. The single crystal X-ray structure is shown with ellipsoids at 50% probability; H atoms and solvent omitted for clarity.....	683
Figure 8.6 Plot of extinction coefficient (ϵ) versus wavenumber for the complexes Ru2 and Ru4 . Although the photolysis product absorbs more strongly than the starting material across most of the spectrum, full conversion is still achieved in these photolytic conversions. (Note that the sharp feature at ~15,000 cm ⁻¹ is due to the light source change in the UV-lamp).....	685
Figure 8.7 (<i>left</i>) Schematic showing the interconversion of Ru2 , Ru4 , and Ru3 . (<i>right</i>) ³¹ P NMR of photolysis solution to generate Ru4 . The inset shows the new ³¹ P resonances, while the sharp singlet at -62 ppm is free PMe ₃	686
Figure 8.8 Several possible products that were considered in identifying Ru4 . The chart shows the ΔG (blue) and ΔH (orange) values calculated for the conversion of Ru2 to the product number listed on the x-axis. Each complex is numbered and shown structurally on the right...	687
Figure 8.9 The single crystal X-ray structure of Ru2 shown (<i>left</i>) with thermal ellipsoids and (<i>right</i>) as the spacefilling model with van der Waals radii on all atoms. Notice that essentially none of the central Ru atom is visible from the spacefilling perspective, demonstrating the steric crowding in this molecule.....	689
Figure 8.10 (top) Single crystal X-ray structure of Ru5. Thermal ellipsoids are shown at 50% probability and H atoms and solvent were omitted for clarity and spacefilling model of Ru5 . (bottom) General synthetic scheme for making Ru(II) tetrazene complexes.	691

Figure 8.11 Single crystal X-ray structure of Ru(NAr) ₂ (PMe ₃) ₂ with ellipsoids shown at 50% probability and H atoms omitted for clarity.....	693
Figure 8.12 Absorption spectra for 0.002 M solutions of Ru5 (orange trace) and Ru1 (blue trace) in THF. The strong absorbance of the product (Ru1) across the UV-Vis spectrum likely contributes to the conversion limit of 25% in solution.	694
Figure 8.13 Reaction scheme to produce a Ru(II) imide species with bulkier phosphine ligands, PPhMe ₂ , and subsequent lack of reactivity upon addition of aryl azide.....	696
Figure 8.14 The formation of a 6-coordinate, C–H activated mesityl anilide species, resulting from an attempt to generate a terminal Ru(=NMe _s)(PPhMe ₂) ₃	697
Figure 8.15 Synthetic scheme presented by Schrock and coworkers to produce an (η ² -diphenylacetylene)Os(NAr) ₂ (Os10) complex. It is interesting that the compound doesn't exhibit nucleophilic or electrophilic behavior via interaction of the unsaturated C–C bond participants with the Os–N multiple bond. The same synthetic method was applied to produce Ru10	698
Figure 8.16 ¹⁴ N NMR of Ru10 (387.1 ppm) and Os10 (365.6 ppm).....	701
Figure 8.17 Fragment for Ru1 observed by HRMS.	710
Figure 8.18 ¹ H NMR spectrum of Ru(PhNNPh)(PMe ₃) ₄ · PhMe (Ru2) in C ₆ D ₆	724
Figure 8.19 ¹³ C NMR spectrum of Ru(PhNNPh)(PMe ₃) ₄ · PhMe (Ru2) in C ₆ D ₆	725
Figure 8.20 ³¹ P NMR spectrum of Ru(PhNNPh)(PMe ₃) ₄ · PhMe (Ru2) in C ₆ D ₆	726
Figure 8.21 ¹ H NMR spectrum of Ru4 (in situ) in C ₆ D ₆	727
Figure 8.22 ¹³ C NMR spectrum of Ru4 (in situ) in C ₆ D ₆	728
Figure 8.23 ³¹ P NMR spectrum of Ru4 (in situ) in C ₆ D ₆	729
Figure 8.24 ¹ H NMR spectrum of Ru3 in C ₆ D ₆	730
Figure 8.25 ¹³ C NMR spectrum of Ru3 in C ₆ D ₆	731
Figure 8.26 ³¹ P NMR spectrum of Ru3 in C ₆ D ₆	732
Figure 8.27 ¹ H NMR of Ru5 in C ₆ D ₆	733
Figure 8.28 ¹³ C NMR of Ru5 in C ₆ D ₆	734
Figure 8.29 ³¹ P NMR of Ru5 in C ₆ D ₆	735
Figure 8.30 ¹ H NMR of Ru6 in C ₆ D ₆	736
Figure 8.31 ¹³ C NMR of Ru6 in C ₆ D ₆	737

Figure 8.32 ^{31}P NMR of Ru6 in C_6D_6 .	738
Figure 8.33 ^1H NMR of Ru7 in C_6D_6 .	739
Figure 8.34 ^{13}C NMR of Ru7 in C_6D_6 .	740
Figure 8.35 ^{31}P NMR of Ru7 in C_6D_6 .	741
Figure 8.36 ^1H NMR of photolysis reaction containing a mixture of Ru1 , Ru5 (starting material), and H_2NAr (decomposition byproduct).	742
Figure 8.37 ^{31}P NMR spectrum of Ru1 (after extraction and repeated recrystallization) in C_6D_6 .	743
Figure 8.38 ^{13}C NMR spectrum of Ru1 in C_6D_6 .	744
Figure 8.39 ^{14}N NMR of Ru1 in C_6D_6 .	745
Figure 8.40 QTOF-HRMS fragmentation patterns (top) calculated and (bottom) experimental for Ru1 .	746
Figure 8.41 ^1H NMR spectrum of $\text{Ru}(\text{NAr})_2(\eta_2\text{-diphenylacetylene})$ containing diphenylacetylene (excess) and H_2NAr impurities.	747
Figure 8.42 ^{14}N NMR spectrum of $\text{Ru}(\text{NAr})_2(\eta_2\text{-diphenylacetylene})$ in C_6D_6 (in situ).	748
Figure 8.43 ^1H NMR of Ru8 in C_6D_6 .	749
Figure 8.44 ^{13}C NMR of Ru8 in C_6D_6 .	750
Figure 8.45 ^{31}P NMR of Ru8 in C_6D_6 .	751
Figure 8.46 ^1H NMR of Ru9 in C_6D_6 .	752
Figure 8.47 ^{13}C NMR of Ru9 in C_6D_6 .	753
Figure 8.48 ^{31}P NMR of Ru9 in C_6D_6 .	754
Figure 8.49 ^1H NMR of ArNPMe_3 in C_6D_6 .	755
Figure 8.50 ^{13}C NMR of ArNPMe_3 in C_6D_6 .	756
Figure 8.51 ^{31}P NMR of ArNPMe_3 in C_6D_6 .	757
Figure 8.52 ^1H NMR of Os3 in C_6D_6 .	758
Figure 8.53 ^{31}P NMR of Os3 in C_6D_6 .	759
Figure 8.54 ^{14}N NMR of $\text{Os}(\text{NAr})_2(\text{O})_2$.	760

Figure 8.55 ^{14}N NMR of $\text{Os}(\text{NAr})_2(\text{PMe}_3)_2$	761
Figure 8.56 ^{14}N NMR of $\text{Os}(\text{NAr})_2(\eta^2\text{-diphenylacetylene})$	762
Figure 8.57 Plot of ϵ vs wavenumber for Ru1 (0.000188 M in THF).....	763
Figure 8.58 Plot of ϵ vs wavenumber for Ru2 (0.00023 M in THF).....	764
Figure 8.59 Plot of ϵ vs wavenumber for Ru4 (0.00019 M in THF).....	765
Figure 8.60 Plot of ϵ vs. wavenumber for Ru5 (0.000203 M in THF).....	766
Figure 8.61 Plot of ϵ vs wavenumber for Ru6 (0.00030 M in THF).....	767
Figure 8.62 Plot of ϵ vs wavenumber for Ru7 (0.00031 M in THF).....	768
Figure 8.63 Photochemical irradiation setup utilizing a mercury arc lamp.....	769
Figure 8.64 Crystal data and structure refinement for p21c.	771
Figure 8.65 Crystal data and structure refinement for early_a.	773
Figure 8.66 Crystal data and structure refinement for KA_OsBisImido.	775
Figure 8.67 Crystal data and structure refinement for smalltwin5.	777

LIST OF SCHEMES

Scheme 4.1 One-pot-two-step quinoline synthesis of 2-methyl-3-phenyl-6-(<i>N,N</i> -dimethylamino)quinoline utilizing [Ti]700 to perform the initial iminoamination reaction.	288
Scheme 4.2 A typical iminoamination reaction utilizing [Ti]700 as the catalyst material and the organic residues found upon a mild acid-wash of the used catalyst material's surface.	292
Scheme 4.3 [Ti]700 catalyzed guanylation of 1,3-dicyclohexylcarbodiimide.	294
Scheme 4.4 HA Entry 1 synthesis and isolation.	305
Scheme 4.5 HA Entry 2 synthesis and isolation.	306
Scheme 4.6 HA entry 3 synthesis and isolation.	307
Scheme 4.7 HA entry 4 synthesis and isolation.	308
Scheme 4.8 HA entry 7 synthesis and isolation.	309
Scheme 4.9 HA entry 8 synthesis and isolation.	310
Scheme 4.10 HA entry 12 synthesis and isolation.	311
Scheme 4.11 HA entry 13 synthesis and isolation.	312
Scheme 4.12 HA entry 14 synthesis and isolation.	313
Scheme 4.13 Targeted synthesis of asymmetric urea species.	318
Scheme 5.1 Addition of Brønsted acidic HX ligands to [Ti]700 to generate [Ti]700(X) species.	365
Scheme 5.2 Iminoamination reaction examined with a variety of HX ligands.	367
Scheme 5.3 Quinoline synthesis using 5 mol% [Ti]700 with 5 mol% 2,6-dimethylphenylamidate as ligand.	370
Scheme 5.4 General conditions and substrates used to examine the iminoamination reaction with [Ti]700(X) catalyst.	373
Scheme 5.5 Iminoamination reaction catalyzed by [Ti]700 with 2,4,6-tri- <i>tert</i> -butylphenoxide.	407
Scheme 5.6 Iminoamination reaction catalyzed by [Ti]700 with 2,6-dimethylphenylamidate ligand and an internal alkyne.	409
Scheme 5.7 Iminoamination reaction catalyzed by [Ti]700 with 2,6-dimethylphenylamidate and an aromatic alkyne.	411

Scheme 5.8 Synthesis of 4-Br-phenoxide LDP complex.....	415
Scheme 6.1 General iminoamination reaction and substrates examined to determine the effect of each substrate on the rate of the overall reaction.	450
Scheme 6.2 The $\text{Ti}(\text{dpm})(\text{NMe}_2)_2$ complex reacts with the iminoamination product to yield an intractable mixture.	459
Scheme 6.3 No reaction was observed between the iminoamination product and the $[\text{Ti}(\text{dpm})(\mu\text{-Ntoly})]_2$	461
Scheme 6.4 Proposed decomposition pathway observed when both ${}^t\text{BuNC}$ and iminoamination product are added to the dimeric $[\text{Ti}(\text{dpm})(\mu\text{-Ntoly})]_2$	462
Scheme 6.5 Conversion of the $\mu\text{-Ntoly}$ species to a $\mu\text{-NAr}$ species upon the addition of an excess of H_2NAr . With a coordinated H_2NAr , there are several different pathways conceivable by which the anilides are exchanged by quick proton transfer steps.	463
Scheme 6.6 Iminoamination reaction catalyzed by $\text{Ti}(\text{OArCH}_2\text{ArO})(\text{NMe}_2)_2$ following standard reaction conditions.	467
Scheme 6.7 General equilibria observed for several $\text{Ti}(\text{IV})$ complexes that have been noted in the literature and through our observations.	469
Scheme 6.8 Production of 4CC product from iminoamination reaction mixture.	483
Scheme 6.9 Iminoamination reaction examined under different reaction conditions to probe the rate law and suggest optimal reaction conditions.	537
Scheme 8.1 Photochemical conversion to yield Ru1 from Ru5	711

KEY TO SYMBOLS OR ABBREVIATIONS

LDP	ligand donor parameter
THF	tetrahydrofuran
DCM	dichloromethane
DME	dimethoxyethane
Dppe	diphenylphosphino ethane
Tol	toluene
Bnz	benzene
<i>p</i> -cym	<i>para</i> -cymene
hex	hexanes
pent	pentanes
TEA	triethylamine
DBU	1,8-Diazabicyclo[5.4.0]undec-7-ene
COD	cyclooctadiene
r.t.	room temperature
NMR	nuclear magnetic resonance (spectroscopy)
SST	spin saturation transfer
DOSY	diffusion ordered spectroscopy
NOESY	nuclear overhauser effect spectroscopy
ROESY	rotating frame overhauser effect spectroscopy
MW	molecular weight
D	diffusion coefficient
GC	gas chromatography

MS	mass spectrometry
FID	flame ionization detector
ICP-OES	inductively coupled plasma optical emission spectroscopy
EA	elemental analysis
HRMS	high resolution mass spectrometry
EI	electrospray ionization
% V _{bur}	percent buried volume
θ	Tolman cone angle
e.u.	entropy units
DFT	density functional theory
NBO	natural bonding orbitals
NRT	natural resonance theory
MO	molecular orbital (theory)
HOMO	highest occupied molecular orbital
LUMO	lowest unoccupied molecular orbital
CV	cyclic voltammogram
UV	ultraviolet (radiation)
Vis	visible (radiation)
Std. dev.	Standard deviation
Dpm	5,5'-dimethyldipyrrolylmethane
Ar	2,6-diisopropylphenyl
Ar*	2,4,6-triisopropylphenyl
Mes	2,4,6-trimethylphenyl

$(\text{OArCH}_2\text{ArO})$	2,2'-Bis(4-methyl-6-tert-butylphenol)methane
ΔH^\ddagger	enthalpy of activation
ΔG^\ddagger	free energy of activation
ΔS^\ddagger	entropy of activation
BArF_{24}^-	tetrakis(3,5-(trifluoromethyl)phenyl)borane
BArF_{20}^-	tetrakis(2,3,4,5,6-fluoro-phenyl)borane
N_4^{R}	1,4-disubstituted tetrazene ligand

CHAPTER 1. INTRODUCTION

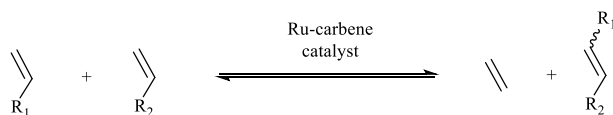
1.1 Traditional Approaches to Transition Metal Catalysis

It would be nice to think that good catalysts start with good design, but that's not usually the case. The discovery of good catalysts is often the result of serendipity. A typical catalytic reaction might start with the synthesis of an electronically interesting transition metal complex. Efforts to determine the details of the electronic structure for the complex may then be pursued, and include exploratory reactivity studies with the compound and a variety of reagents with different properties. Over the course of these reactivity studies, a reaction is discovered in which the transition metal complex or material acts as a catalytic reagent. With the newly discovered catalyst, chemists then turn to catalyst design principles for improvement of the catalytic reaction to achieve faster rate, improved selectivity, expanded substrate scope tolerance, higher yields, etc.

There are several good examples of this process of catalyst development in the literature. One well-known example is Grubbs' Ru catalyst for olefin metathesis. It was discovered in the 1960's that RuCl_3 was a precatalyst for olefin metathesis.^{1,2} Despite the fact that the active species in the catalytic cycle was not understood, application of this catalyst to industrial processes was undertaken in the late 1970's. Some 20-30 years later, Grubbs and coworkers published a well-understood molecular precatalyst with phosphine ligands.³ This species was modified several times by Grubbs and others in the following years until they developed the current generations of these Ru catalysts.⁴⁻⁹ With these successive changes, expansion of substrate tolerance, improved precatalyst tolerance to air and moisture, and additional controls were gained in the catalyst along the way.

This journey in catalyst development spans 50 years. While it has resulted in great improvements in the catalyst's abilities and diversification of substrates and applications, the history of this catalyst's development also demonstrates how much time and work goes into the optimization of an industrial catalyst that has a direct impact on society. From a chemistry perspective, the evolutionary process of Grubbs' catalyst has been fast and successful. But if we think about it in terms of society, 60 years is close to a human lifetime. When we consider that many consumer products, such as pharmaceuticals, take human lifetimes to develop, there is strong motivation to make catalyst development faster and more directed.

Cross Metathesis Catalyzed by Ru



Several Ru catalysts and precatalysts used for Olefin Metathesis Reactions

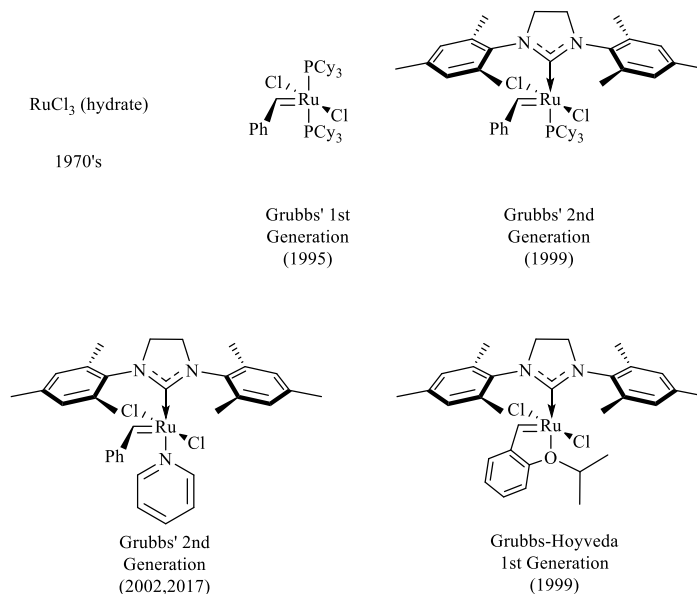


Figure 1.1 (top) A simple example of an olefin metathesis reaction, cross metathesis (CM) that can be catalyzed by Ru-carbene complexes. (bottom) Examples of several viable Ru catalysts competent for CM and other olefin metathesis reactions.

The real problem facing streamlined transition metal catalyst development is that no single rule can be applied to the entirety of the transition metal series, and to some extent, the properties of metal reactivity are related to the metal itself and cannot be changed (i.e. electronegativity or ionic radii). Rather, the most influential and general trends that exist among transition metal complexes is in the properties of the bonds that they make to other elements, and the subsequent effects that these bonds have on reactivity. Thus, the ligands in a catalytic system are where chemists can often exert the most control over the reactivity of a metal complex. This applies to ancillary ligands, or ligands which remain bound to a metal throughout the course of a reaction but

that do not directly participate in bond making or breaking, as well as ligands that participate directly in reactivity.

Collectively, the projects briefly introduced here and discussed in detail in this dissertation, touch on each step of catalyst development mentioned here: (1) identification of trends in metal-ligand bond interactions that correlate to the stereoelectronic nature of the ligands (Chapters 2 and 3); (2) experimental applications of these trends to catalytic systems, and the use of fundamental metal-ligand interaction models to predict catalyst behavior and improve it (Chapters 4-6); and (3) fundamental reactivity and discovery of new reactions through synthesis of electronically unique complexes (Chapters 7 and 8).

1.2 Targeted Design of Catalysts: Ligand Donor Parameter

Generally, some of the most well-understood transition metal chemistry is that of the noble metals, such as Pd, Pt, Rh, and Ir. These metals are essential to modern life, providing a variety of commodity chemicals and products from some of the most prolific anticancer drugs (i.e. cisplatin), to catalytic converters. Part of what makes these metals so successful as catalytic metals is their predictability, which is aided by the development of tools that guide their design and improvement (see below). One of the most powerful tools of this type is the ability to predict what effect changes to an ancillary ligand will render upon a catalyzed reaction. This predictive ability is contingent upon accurate parameterization of the properties of a series of ligands.

When considering ligand properties, two main aspects of the ligand–metal interaction dominate the minds of organometallic chemists: electronics and sterics of the ancillary ligands. Electronic properties stem from electron donor-acceptor interactions between the vacant or filled orbitals on the transition metal and the bonding atom of the ancillary ligand. Sterics (size) affect the amount of space available in the first coordination sphere of a metal, which heavily influences

substrate interactions with the metal during the course of a catalyzed reaction. Together, these two properties are the central pillars in tuning reactivity of metals.

To compare the effects of ligand properties on a catalyzed reaction, systematic parameterization of the electronic and steric properties of each ligand is needed to determine trends. A classic example of ligand parameterization is the Tolman Electronic Parameter and the Tolman Cone Angle (TEP and TCA).¹⁰⁻¹³ In what is now an iconic system of ligand classification, Tolman focused on quantifying the electron donor ability and size of a wide range of phosphine (PR_3) ligands.

In his initial study, a series of $\text{Ni}(\text{CO})_3\text{PR}_3$ complexes were synthesized, and the A_1 stretching frequencies (breathing mode) of the CO ligands was measured by IR spectroscopy. In this system, a more donating phosphine would result in more electron density on the metal, which results in greater π -backbonding to the CO ligands. This electron pushing is directly observable as an elongation in the CO bond, which correlates to a lower frequency C-O stretch in the IR spectrum. It is important to note that in this system, a phosphine with electron withdrawing R-groups, such as PX_3 ligands where X = halides, can also exhibit π -effects. The PR_3 will act as a π -acid, accepting electron density from the metal through an interaction dubbed negative hyperconjugation (see Chapter 3). This generates double-bond character between the ligand and metal ($\text{M}=\text{P}$) while pushing electron density onto the R groups. Thus, while a strong σ -donor will decrease the C-O stretching frequency, a strong π -acceptor will increase it by competing with the $\text{C}\equiv\text{O}$ ligands for π -backdonation. This makes the TEP a holistic electronic parameter which describes both σ - and π -donor abilities of PR_3 ligands.

In a similar way, Tolman also set about quantifying the size of PR_3 ligands. He used a 2.28 Å bond length, representing a typical $\text{Ni}^0\text{-P}$ bond length, and set the Ni as the origin point of a

conical section of space. He then arranged the PR_3 of interest into its tightest formation of the R groups and measured what the angle of the 3-dimensional cone of space was, occupied by the PR_3 ligand. This measurement became known as the Tolman Cone Angle (TCA) and is still invoked today to draw trends with PR_3 ligand sizes.

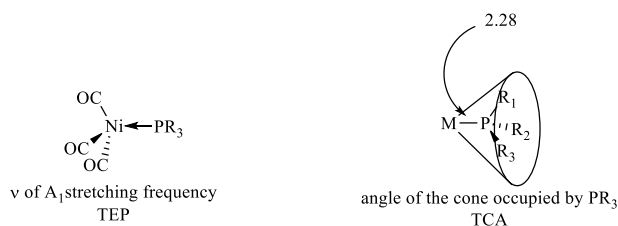


Figure 1.2 Illustration of the original Tolman system for phosphine parameterization. (left) The $\text{Ni}(\text{CO})_3\text{PR}_3$ complex was used to determine overall donor ability of a phosphine. (right) The system utilized to determine a steric profile for a given PR_3 ligand where the metal–P bond length is 2.28 Å.

As beautifully simplistic and broadly applicable as Tolman's parameterization system of PR_3 ligands is, there are of course limitations. One main limitation of Tolman's system has remained relatively poorly addressed. Tolman's system was designed for low-valent, late transition metals. There is no complementary system which addresses the donor ability of PR_3 ligands to high oxidation state, early transition metals. This problem can be more generally addressed to all ligands, not just phosphines. Few examples of systematic ligand effect studies exist with high valent (or high oxidation state) catalyst systems.

Generally speaking, high valent metals in high oxidation states, particularly those early in the transition metal series, have been neglected in fundamental studies of catalyst development and tool development of catalytic chemists. This is not due to a lack of these metals' significance as catalysts. For example, the group IV metals are utilized in processes such as Sharpless epoxidation and olefin polymerization.¹⁴⁻²⁰ Yet, despite their importance in these and other massive catalytic processes, systems such as Tolman's phosphine parameterization have not been developed for these early, high valent metals.

In response to the lack of predictive tools available to high valent transition metal catalysis, i.e. a complementary system to Tolman's where the metals used to study ligand properties are d^0 , the Odom group pioneered the Ligand Donor Parameter (LDP) system in 2012.²¹ This system is based on a 4-coordinate chromium(VI)nitride bis(diisopropylamide) fragment ($\text{NCr}(\text{N}^i\text{Pr}_2)_2$); the 4th coordination site to Cr in this fragment can be widely varied using straightforward synthetic techniques ($\text{NCr}(\text{N}^i\text{Pr}_2)_2\text{X}$). In the original, and several subsequent studies, X is a monoanionic ligand. This molecule is illustrated below in Fig. 3.²²⁻²⁴

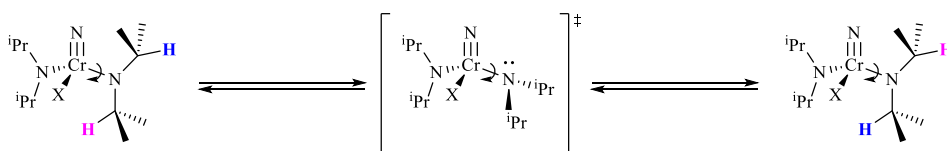


Figure 1.3 The $\text{NCr}(\text{N}^i\text{Pr}_2)_2\text{X}$ scaffold used to measure the LDP value of a given X ligand. The illustration shows the rotation of one of the $\text{Cr}-\text{N}^i\text{Pr}_2$ bonds. The transition state (center) forces the amide lone pair into an antibonding orbital. The highlighted protons on the ^iPr groups have unique chemical shifts. Their exchange, monitored by ^1H NMR SST, facilitates the measurement of the rotation rate.

In this system, the two N^iPr_2 ligands and the variable X ligand compete for vacant d-orbitals on Cr in the xy-plane. This electronic competition results in variable donation of the amide lone pairs to Cr. When X is a strong donor, less amide lone pair donation to Cr occurs, resulting in single-bond character between the Cr and N^iPr_2 ligands. In contrast, when X is a weak donor, more amide lone pair donation to Cr occurs, resulting in double-bond character between Cr and N^iPr_2 ligands. This variable donation of the amide lone pairs, leads to variability in $\text{Cr}-\text{N}$ bond character which changes the rate of $\text{Cr}-\text{N}$ bond rotation (for more details, see Chapters 2 and 3). This bond rotation rate is the experimental handle that we can use to make quantitative comparisons of donor ability of X to a high valent metal, analogous to the C–O stretching frequency noted in Tolman's system above.

More recently, a correlation with the LDP value of ancillary ligands of Ti(IV) hydroamination catalysts and the rate constant of the catalyzed reaction was established by our

group.²⁵ In fact, a quantitative model was developed that relates the rate constant of the reaction to the electronics (LDP) and sterics (% V_{bur}) for this specific reaction. Knowing the stereoelectronic parameters of candidate ligands provides the researcher a guide to making a faster catalyst while bypassing the need to synthesize and screen countless catalyst in order to start finding better ligands.²⁵

Having established what a valuable tool the LDP system can provide for high valent metal catalyst development, we wanted to broaden the scope of ligands parameterized using the LDP system. One category of ligands which we hadn't examined are neutral ligands, including amines, pyridines, nitriles, isonitriles, and phosphines. Such ligands are ubiquitous as ancillary ligands in catalytic systems, and their interactions with high valent metals have been largely ignored. The LDP system's synthetic variability and demonstrated utility with high valent metal systems led us to suspect it would be an ideal system with which to probe high-valent metal interactions with phosphines. We dedicated a lot of time and effort to determining how to transition the LDP system to the application of neutral ligands, using phosphines as the guinea pig ligands. The results of these studies, including efforts to establish systematic differences between the neutral Cr complexes with monoanionic X ligands, and the cationic Cr complex with neutral X ligands, are presented herein.^{26, 27}

1.3 Expansion of “Ligands” in Organometallic Catalysis using Silica Supported Titanium Catalysts

In addition to studies outlining the donor ability of various ligands to high valent metals, which has been a major focus in the Odom group over the last two decades, C–N bond forming reactions are another area of research interest.^{28, 29} Specifically, the development of homogeneous Ti species that catalyzed hydroamination, iminoamination, and hydrohydrazination has led to the

development of several catalysts which can perform these processes in moderate to high yields. Even when great care is taken to improve these catalysts through ligand design, this doesn't typically solve every problem. For example, problems that remain unsolved by ligand design and manipulation include: off-cycle resting states of catalyst species, catalyst species reactivity with products and substrates (deactivation), and separation of the catalyst from organic reaction mixtures (see Chapters 5 and 6).³⁰ These ongoing issues prompted us to pursue a new direction with these organometallic catalysts, specifically those for iminoamination: supported organometallic titanium species.

Specifically, we wanted to pursue silica-gel supported titanium species that retain similar coordination environments to homogeneous systems at the active titanium center, as heterogeneous catalysis of this sort has been shown an effective strategy for solving the problems mentioned above.³¹ This dramatic change in catalyst speciation, going from a typical homogeneous species to a silica-supported variant, we predicted, would render dramatic changes in the reactivity observed, in terms of reaction conditions, substrate tolerance, reaction times, etc. However, because the active metal sites retain a similar environment to the homogeneous catalysts, we also wondered if the tools developed with homogeneous systems²⁵ would apply to these heterogeneous titanium systems.

We were able to develop two variants of silica-supported titanium materials competent for C–N bond formation catalysis. The more highly dehydroxylated silica gel results in a material that can be ligand-functionalized, which provides rapid, selective, and nearly quantitative conversion of several sets of substrates to the iminoamination products. Practical application of this catalyst material has proven very promising, as these clean reactions with high conversion have provided heterocycle syntheses and isolation which are an improvement on their known homogeneous

analogues. This led to the ligand functionalization studies and kinetic analysis presented in Chapter 5, from which we can propose a mechanism for the catalyzed reaction using the heterogeneous catalyst.

Somewhat unexpectedly, these studies also lead us to reexamine the go-to homogeneous catalyst for similar transformations. Kinetic studies undertaken with $\text{Ti}(\text{dpm})(\text{NMe}_2)_2$ to perform iminoamination reactions catalytically, have guided ligand modifications to improve the rate of this catalyzed reaction. These studies provided a more reactive catalyst but also illustrated a gap in our understanding of ligand effect in the Ti(IV) hydroamination and iminoamination catalysts. This sparked investigations into ligand exchange reactions observed commonly with high valent transition metal complexes, based on our understanding of ligand donor abilities (LDP) to high valent transition metals.

Collectively, these studies of Ti(IV) C–N bond forming catalysts have illustrated that these Ti(IV) systems can benefit from the use of a solid-support. In addition, these studies have also demonstrated that new applications of the LDP system can improve our understanding of catalysts beyond simple rate and catalyst design correlations. Understanding metal-ligand interactions is as applicable to solid-state heterogeneous catalyst systems with isolated metal sites as it is in the homogeneous systems where they are typically studied. Indirectly, these studies have also produced a model of how ligand electronics influence ligand exchange reactions in the Ti(IV) catalyst systems, which can be directly applied to improve catalyst design and performance.

1.4 Electronic Exploration of Unique Transition Metal Complexes: Valency Effects on Metal-Imide Bond Character

Targeted ligand studies like those discussed with the Tolman system and LDP are highly useful with systems where a catalytic species has been identified and its general reactivity can be

established. This area of research does nothing to promote the discovery of new catalysts and reactivity, however.

Elements toward the middle of the d-block, Groups 5-8, tend to access a wide variety of oxidation states, which makes them unique. However, systematic studies of how the oxidation state of these metals might affect the nature of a bond to a given category of ligands are not common, which makes reactivity predictions difficult to make.

Specifically, one of the classes of ligands and associated reactivity that we are interested in is imidos. The C–N bond forming reactions studied by our research group involve titanium imido species, which are typically recognized as the active catalyst in these types of reactions. The subsequent catalytic activity observed with these systems is a result of [2 + 2] cycloaddition with an unsaturated C–C bond.³²⁻³⁵ This type of reactivity is typical of a high valent metal imide bond, however, in systems with late, low valent metal-imides, observed reactivity typically involves nucleophilic character at the nitrogen or the metal participating in the bond. With these pieces of knowledge in place, our next question is what happens in between? With a metal in a mid-valent oxidation state will a metal-imide bond react like those found in high or low valent systems? Or is there unique reactivity characterizing this middle-ground? With a late transition metal in a high oxidation state, how does the reactivity change as the oxidation state increases?

The group VIII metals are no exception to this knowledge gap, despite how many examples there are of M=NR complexes where M = Fe, Ru, or Os. Specifically, the chemistry of Fe imides has expanded rapidly in the last few decades, perhaps most especially due to interest in nitrogen fixation and related processes (see Chapter 7). By comparison, there fewer complexes known with osmium, and fewer still with ruthenium. In trying to make comparisons in reactivity, a lack of synthetic diversity, particularly with Ru became apparent. Thus, interest in these types of

complexes became multi-fold. First, we wanted to expand the synthetic diversity of these types of complexes. This work was begun in 2014³⁶ and has continued in the group until now. One of the main focuses of this aspect of these studies has been to push the Group VIII metal imide complexes into mid-valent oxidation states, where there are the fewest examples of known complexes.

As early studies were pursued, a second goal, in line with several of our overall interests emerged, which was to identify electronic structure changes associated with oxidation of the metal in a series of 4-coordinate terminal Fe and Ru imide complexes. Hoping to find answers to some of our fundamental questions about the nature of M=NR bonds and how they are affected by the oxidation state in the metal, synthetic and subsequent electronic studies have been undertaken with Fe(II) and Fe(III), as well as Ru(II), (III), and (IV) imide species. Studies focused on electronic structure changes upon oxidation of the metal have provided interesting insight about both Fe and Ru bonds to N. These results also highlight what has been experimentally observed across these and related studies, which is that synthetic difficulties are perhaps still the biggest hurdle to answering these basic questions about metal-imide bonds with the group VIII metals, as well as other metals in the middle of the d-block.

REFERENCES

REFERENCES

- (1) Michelotti, F. W.; Keaveney, W. P., Coordinated polymerization of the bicyclo-[2.2.1]-heptene-2 ring system (norbornene) in polar media. **1965**, *3* (3), 895-905.
- (2) Porri, L.; Rossi, R.; Diversi, P.; Lucherini, A., Ring-Opening polymerization of cycloolefins with catalysts derived from ruthenium and iridium. **1974**, *175* (11), 3097-3115.
- (3) Nguyen, S. T.; Johnson, L. K.; Grubbs, R. H.; Ziller, J. W., Ring-opening metathesis polymerization (ROMP) of norbornene by a Group VIII carbene complex in protic media. *J. Am. Chem. Soc.* **1992**, *114* (10), 3974-3975.
- (4) Vougioukalakis, G. C.; Grubbs, R. H., Ruthenium-Based Heterocyclic Carbene-Coordinated Olefin Metathesis Catalysts. *Chem. Rev.* **2010**, *110* (3), 1746-1787.
- (5) Mohr, B.; Lynn, D. M.; Grubbs, R. H., Synthesis of Water-Soluble, Aliphatic Phosphines and Their Application to Well-Defined Ruthenium Olefin Metathesis Catalysts. *Organometallics* **1996**, *15* (20), 4317-4325.
- (6) Grubbs, R. H.; Chang, S., Recent advances in olefin metathesis and its application in organic synthesis. *Tetrahedron* **1998**, *54* (18), 4413-4450.
- (7) Schwab, P.; France, M. B.; Ziller, J. W.; Grubbs, R. H., A Series of Well-Defined Metathesis Catalysts—Synthesis of $[\text{RuCl}_2(\text{CHR}')(\text{PR}_3)_2]$ and Its Reactions. **1995**, *34* (18), 2039-2041.
- (8) Nguyen, S. T.; Grubbs, R. H.; Ziller, J. W., Syntheses and activities of new single-component, ruthenium-based olefin metathesis catalysts. *Journal of the American Chemical Society* **1993**, *115* (21), 9858-9859.
- (9) Schwab, P.; Grubbs, R. H.; Ziller, J. W., Synthesis and Applications of $\text{RuCl}_2(\text{CHR}')(\text{PR}_3)_2$: The Influence of the Alkylidene Moiety on Metathesis Activity. *Journal of the American Chemical Society* **1996**, *118* (1), 100-110.
- (10) Tolman, C. A., Steric effects of phosphorus ligands in organometallic chemistry and homogeneous catalysis. *Chem. Rev.* **1977**, *77* (3), 313-348.
- (11) Tolman, C. A., Electron donor-acceptor properties of phosphorus ligands. Substituent additivity. *J. Am. Chem. Soc.* **1970**, *92* (10), 2953-2956.
- (12) Dias, P. B.; Depiedade, M. E. M.; Simoes, J. A. M., Bonding and Energetics of Phosphorus(III) Ligands in Transition-Metal Complexes. *Coord. Chem. Rev.* **1994**, *135*, 737-807.
- (13) Levason, W., Phosphine complexes of transition metals. In *Organophosphorus Compounds* (1990), Hartley, F. R., Ed. 1990.

- (14) Katsuki, T.; Sharpless, K. B., The first practical method for asymmetric epoxidation. *Journal of the American Chemical Society* **1980**, *102* (18), 5974-5976.
- (15) Heravi, M. M.; Lashaki, T. B.; Poorahmad, N., Applications of Sharpless asymmetric epoxidation in total synthesis. *Tetrahedron: Asymmetry* **2015**, *26* (8), 405-495.
- (16) Pfenninger, A., Asymmetric Epoxidation of Allylic Alcohols: The Sharpless Epoxidation. *Synthesis* **1986**, *1986* (02), 89-116.
- (17) Li, J. J., Sharpless asymmetric epoxidation. In *Name Reactions: A Collection of Detailed Mechanisms and Synthetic Applications Fifth Edition*, Springer International Publishing: Cham, 2014; pp 552-554.
- (18) Ziegler-Natta Catalysts. In *Kirk-Othmer Encyclopedia of Chemical Technology*.
- (19) Mülhaupt, R., Catalytic Polymerization and Post Polymerization Catalysis Fifty Years After the Discovery of Ziegler's Catalysts. *Macromolecular Chemistry and Physics* **2003**, *204* (2), 289-327.
- (20) Alt, H. G.; Köppl, A., Effect of the Nature of Metallocene Complexes of Group IV Metals on Their Performance in Catalytic Ethylene and Propylene Polymerization. *Chemical Reviews* **2000**, *100* (4), 1205-1222.
- (21) DiFranco, S. A.; Maciulis, N. A.; Staples, R. J.; Batrice, R. J.; Odom, A. L., Evaluation of donor and steric properties of anionic ligands on high valent transition metals. *Inorg. Chem.* **2012**, *51* (2), 1187-200.
- (22) Bemowski, R. D.; Singh, A. K.; Bajorek, B. J.; DePorre, Y.; Odom, A. L., Effective donor abilities of E-t-Bu and EPh (E = O, S, Se, Te) to a high valent transition metal. *Dalton Transactions* **2014**, *43* (32), 12299-12305.
- (23) Billow, B. S.; Bemowski, R. D.; DiFranco, S. A.; Staples, R. J.; Odom, A. L., Synthesis and Structure of Chromium(VI) Nitrido Cyclopentadienyl Complexes. *Organometallics* **2015**, *34* (18), 4567-4573.
- (24) Beaumier, E. P.; Billow, B. S.; Singh, A. K.; Biros, S. M.; Odom, A. L., A complex with nitrogen single, double, and triple bonds to the same chromium atom: synthesis, structure, and reactivity. *Chemical Science* **2016**.
- (25) Billow, B. S.; McDaniel, T. J.; Odom, A. L., Quantifying ligand effects in high-oxidation-state metal catalysis. *Nature Chemistry* **2017**, *9*, 837.
- (26) Aldrich, K. E.; Billow, B. S.; Holmes, D.; Bemowski, R. D.; Odom, A. L., Weakly Coordinating yet Ion Paired: Anion Effects on an Internal Rearrangement. *Organometallics* **2017**, *36* (7), 1227-1237.
- (27) Aldrich, K. E.; Billow, B. S.; Staples, R. J.; Odom, A. L., Phosphine interactions with high oxidation state metals. *Polyhedron* **2019**, *159*, 284-297.

- (28) Odom, A. L., New C-N and C-C bond forming reactions catalyzed by titanium complexes. *Dalton Transactions* **2005**, (2), 225-233.
- (29) Odom, A. L.; McDaniel, T. J., Titanium-Catalyzed Multicomponent Couplings: Efficient One-Pot Syntheses of Nitrogen Heterocycles. *Acc. Chem. Res.* **2015**, 48 (11), 2822-2833.
- (30) van Leeuwen, P. W. N. M., Decomposition pathways of homogeneous catalysts. *Applied Catalysis A: General* **2001**, 212 (1), 61-81.
- (31) Pelletier, J. D. A.; Basset, J.-M., Catalysis by Design: Well-Defined Single-Site Heterogeneous Catalysts. *Acc. Chem. Res.* **2016**, 49 (4), 664-677.
- (32) Pohlki, F.; Doye, S., The Mechanism of the [Cp₂TiMe₂]-Catalyzed Intermolecular Hydroamination of Alkynes. *Angew. Chem. Int. Ed.* **2001**, 40 (12), 2305-2308.
- (33) Walsh, P. J.; Hollander, F. J.; Bergman, R. G., Generation, alkyne cycloaddition, arene carbon-hydrogen activation, nitrogen-hydrogen activation and dative ligand trapping reactions of the first monomeric imidozirconocene (Cp₂Zr:NR) complexes. *J. Am. Chem. Soc.* **1988**, 110 (26), 8729-8731.
- (34) Johnson, J. S.; Bergman, R. G., Imidotitanium Complexes as Hydroamination Catalysts: Substantially Enhanced Reactivity from an Unexpected Cyclopentadienide/Amide Ligand Exchange. *J. Am. Chem. Soc.* **2001**, 123 (12), 2923-2924.
- (35) Nugent, W. A.; Mayer, J. M., *Metal-ligand multiple bonds: the chemistry of transition metal complexes containing oxo, nitrido, imido, alkylidene, or alkylidyne ligands*. Wiley: 1988.
- (36) Singh, A. K.; Levine, B. G.; Staples, R. J.; Odom, A. L., A 4-coordinate Ru(II) imido: unusual geometry, synthesis, and reactivity. *Chem. Commun.* **2013**, 49 (92), 10799-10801.

CHAPTER 2. PROBING THE *IN SITU* DYNAMICS OF THE LDP SYSTEM WITH NEUTRAL LIGANDS

2.1 Introduction^{1,2}

The ligand donor parameter (LDP) is an experimentally based system that allows for a quantitative comparison of the donor ability of various ligands to a high valent metal.¹ The system utilizes a chromium(VI)nitride bis(diisopropylamido) fragment, where the 4th coordination site can be occupied by the ligand of interest, (X^-). The system has been used to quantify the donor ability of a wide variety of anionic ligands, from amides to halogens.¹⁻⁵ A selection of these ligands and their LDP values are shown in Fig. 2.1.

As briefly mentioned in chapter 1, this system has three strongly donating nitrogen ligands. The Cr(VI) metal center, formally a d^0 metal, has empty d and s acceptor orbitals. The orientation of the ligands around the metal creates an electronic competition between the N^iPr_2 and the X^- ligand for the xy -plane centered acceptor orbitals.¹ When X^- is a strong donor and pushes more electron density into the acceptor orbitals on Cr, the amide ligands' lone pairs are localized on the nitrogens. Conversely, when X^- is a weak donor, Cr is electronically unsaturated, and so the amide ligands' lone pairs are donated to Cr through dative interaction. This variable donation from the N^iPr_2 ligands creates variable single- to double-bond character between N and Cr, which directly

¹ This work was done in collaboration with Dr. Brennan Billow. Both Brennan, and a former postdoc in the Odom Group, Dr. Ross Bemowski, had synthesized and partially characterized several $[NCr(N^iPr_2)_2(PR_3)][X]$ complexes prior to my inclusion on this project. Their efforts provided me with a good starting point as a first year in the group and Brennan's continued collaboration helped considerably in the results presented in this chapter and chapter 3. He is included as an author on the publications related to both chapters.

² The majority of this work has been previously published. The following articles are related to this research: Aldrich, K. E., et al. (2017). "Weakly Coordinating yet Ion Paired: Anion Effects on an Internal Rearrangement." *Organometallics* **36**(7): 1227-1237. Aldrich, K. E., et al. (2019). "Phosphine interactions with high oxidation state metals." *Polyhedron* **159**: 284-297.

effects the energetics of the barrier to rotation of the Cr–NⁱPr₂ bond. The weaker the X[−] donor, the more double-bond character there is in the ⁱPr₂N–Cr interaction and the higher the barrier to rotation, and vice versa.

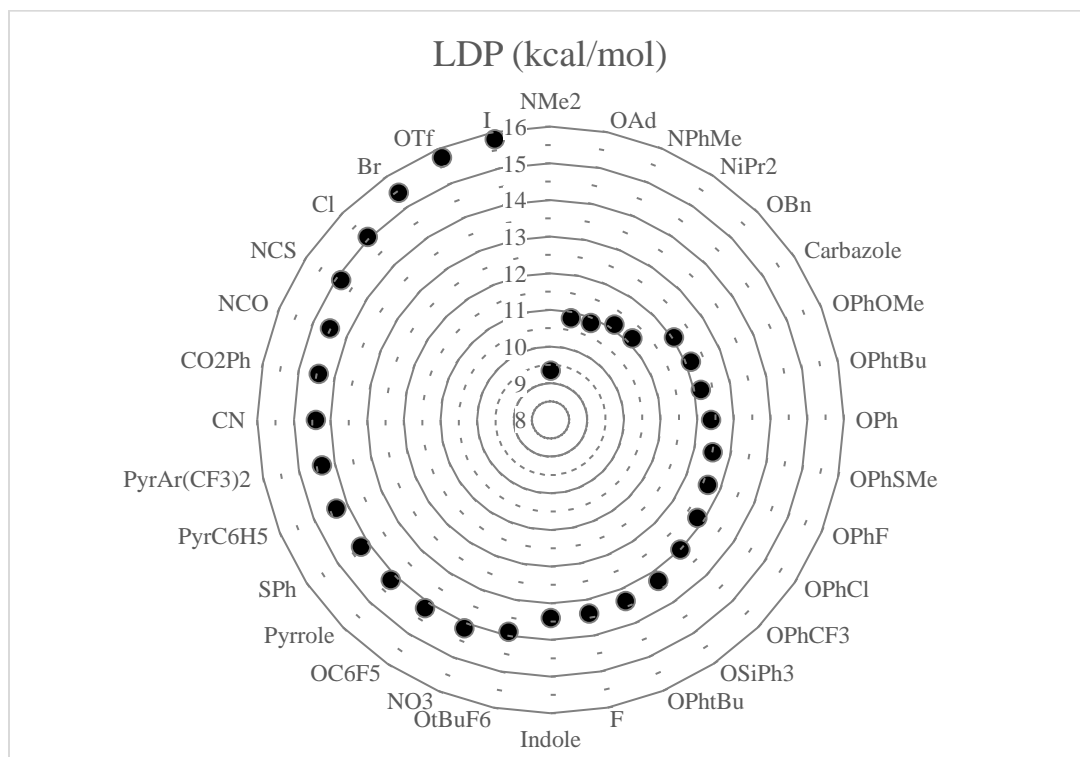
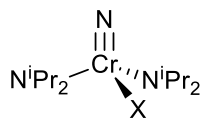


Figure 2.1 (*top*) Cr(VI) molecule used in the LDP system. (*bottom*) A selection of monoanionic ligands' LDP values. These values represent the overall donor ability of the X ligand, reflecting both σ and π interactions with high valent Cr(VI).

This barrier to rotation has a simple molecular orbital (MO) origin, which has been previously presented with DFT calculations.¹ The transition state for the Cr–NⁱPr₂ rotation puts the lone pair from the amide in an orientation to overlap with the π -bonding orbital of the Cr–nitride bond. This forces the amide lone pair into a π^* -orbital, evidenced by the pyramidalization of the optimized transition states for these molecules.¹ The energy of the ground state, specifically, how

localized the lone pair of the amide is in a bonding interaction, determines this energy difference and thus the energy of this rotation barrier with a given X^- ligand.¹

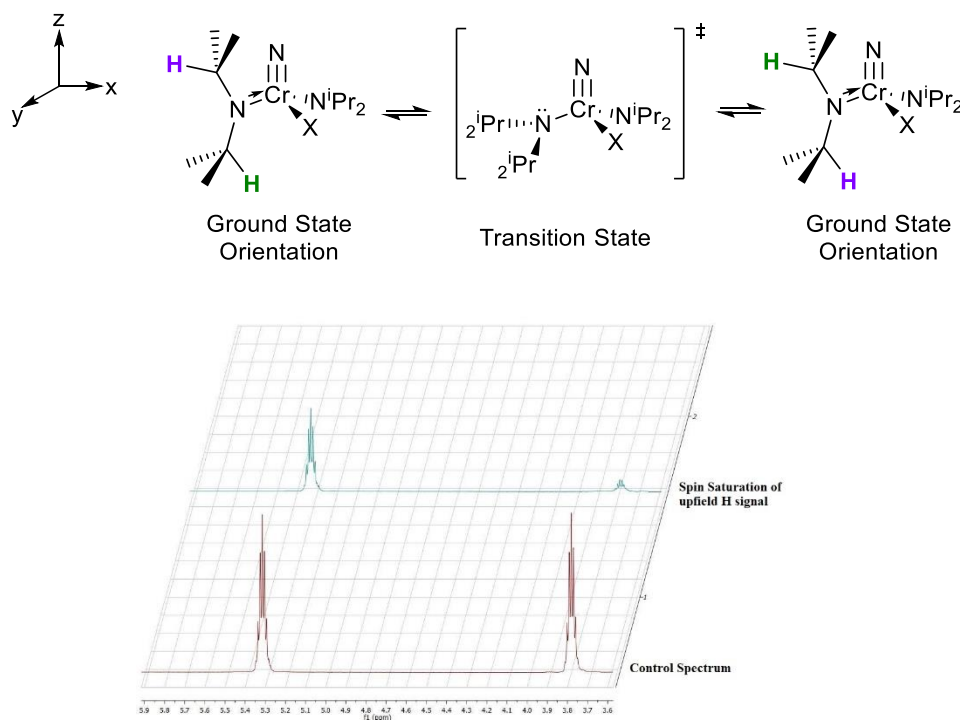


Figure 2.2 (*top*) The rotation monitored by ^1H spin saturation transfer experiments to determine the LDP value for a ligand, X. The purple and green hydrogens exchange positions through the N–Cr bond rotation, allowing for saturation of one of the H signals to carry over to the other signal proportional to the rate of this rotation during the SST experiment (*bottom*). By experimentally determining this rotation rate, the enthalpic barrier to this rotation can be assessed, and $\Delta H^\ddagger = \text{LDP}$.

The energies of these barriers to rotation for the X^- ligands examined have been easily studied over the temperature range amenable to NMR spectroscopy, the primary method used to measure LDP values. The methyne hydrogens on the ^iPr -groups sit in distinct positions in the ground state orientation of the $\text{NCr}(\text{N}^i\text{Pr}_2)_2(\text{X})$ molecules, giving them unique chemical shifts *syn* and *anti* to the Cr–nitride. During the rotation of the $-\text{N}^i\text{Pr}_2$ bond, these two Hydrogens exchange positions (and subsequently NMR shifts). With a simple ^1H NMR experiment, called spin saturation transfer (SST), the rate of exchange between these two sets of Hydrogens can be measured directly (Fig. 2.2). The rate of this rotation can be used in conjunction with the Eyring equation to find ΔG^\ddagger of rotation.¹

With monoanionic X^- ligands, the entropy of rotation, ΔS^\ddagger , was determined by measuring ΔG^\ddagger over a wide temperature range with several different X^- ligands. These measurements provided the assessment that, with small X^- ligands, ΔS^\ddagger is a small negative number (in e.u.). The experimentally measured ΔS^\ddagger for $X = \text{iodide}$ was the most accurate over the widest temperature range and was adopted as the official ΔS^\ddagger (-9 e.u.). With a value assigned to the entropic contribution to ΔG^\ddagger , we can calculate ΔH^\ddagger , a temperature-independent enthalpic barrier to rotation. This value is what we refer to as LDP. Note, because the temperature dependent factor has been removed, we can now directly compare the experimental values measured at any temperature.

The $\text{NCr}(\text{N}^i\text{Pr}_2)_2\text{X}$ measurements are done in solution, with little complication. When X^- is a monoanionic ligand, the complexes are neutral species overall. The complexes are soluble and stable in a variety of NMR solvents. Typically, the NMR solutions need to be chilled in order to obtain a reliable rate of rotation for the $\text{Cr}-\text{N}^i\text{Pr}_2$ bonds, so CDCl_3 became the solvent of choice for these measurements. With a neutral LDP molecule in a relatively nonpolar solvent, the solution behavior of these complexes has been consistent during LDP experiments.

In real catalytic systems, though, ligands have much greater variety than the ligand selection that has been examined with LDP. Some of the most common sets of ligands are those which are neutral and interact with metals via dative formation of σ -bonds. These ligands include things like CO, pyridines, phosphines, amines, nitriles, etc. Although some of these ligands, such as CO, are more common in low valent systems due to their propensity for π -backbonding with electron-rich metal centers, ligands like pyridines and phosphines are ubiquitous.^{6,7} Additionally, other species such as nitriles and isonitriles are relevant to catalytic systems as substrates, including with high valent catalyst species.^{8,9} In these cases, such substrates may interact with the active catalytic species via dative bond formation in various steps of a catalytic cycle.

To find an example of this, we need not look far. The Ti(IV)-catalyzed hydroamination and multicomponent coupling reactions studied by our group (and others), for example, contain high valent homogeneous Ti catalysts, as well as a variety of possible dative-donor ligands in the catalytic mixture.^{8, 10} Particularly, the donor ability of isonitriles in our iminoamination reaction (3CC) may affect the rates of our catalysts and bear relevance to future ligand design (vide supra, Chapters 5 and 6).⁸

We, therefore, wanted to turn our attention toward neutral ligands in the implementation of the LDP system. While several comprehensive ligand studies have been conducted that quantify ligand donor abilities to low valent metals (Tolman system^{11, 12} and spectrochemical series^{13, 14}), a complementary high valent system doesn't exist. The LDP system was the first to do this, but as demonstrated above, with X⁻ ligands. The bonding differences between M – L bonds (where L is a neutral ligand) in high valent versus low valent systems has never been systematically examined in a quantifiable manner.

To approach this task, we started with a class of neutral ligands which are well understood sterically and electronically, in both the bound and unbound configuration with low valent metals: phosphines (PR₃). Chadwick Tolman pioneered the parameterization of these ligands in terms of both sterics and electronics in his seminal work in the 1970's.^{11, 12} Since then, his system has been cited thousands of times and can be used to rationalize everything from reaction rates in catalyses where the phosphine is an ancillary ligand to simple substitution reactions.⁶

Of course, with improvements in instrumentation and computational methods, adjustments to his original parameterizations have been made. A trend in the field has moved toward differentiation of the electronic component of phosphine donor abilities into separate σ - and π -terms.¹⁵⁻¹⁸ This trend has produced systems such as the Quantitative Analysis of Ligand Effects,

established by Giering, Prock, and Poe.¹⁹⁻²² It has also sparked similar parameterization efforts for other ligands, such as NHC's, which have gained popularity in recent years.²³ While today, the Tolman values for new ligands are primarily determined using computational analyses in simple Ir or Rh molecular systems, the usefulness of these ligand classification schemes is difficult to overstate.²⁴ Given the vast knowledge of low-valent metal phosphine interactions—and more specifically, the detailed efforts that have gone into substituent effects from changing the PR₃ R-groups—phosphines seemed like an ideal place to start when crossing over to high valent systems.

We not only wanted to assess the quantitative donor ability of a variety of phosphine ligands to a high valent metal, but also address fundamental differences in high valent versus low valent bonding in these systems. For example, in a high valent metal-phosphine bond, the bond should be more covalent due to the high electronegativity of d⁰ early transition metals (i.e. χ_s of Cr(VI) = 3.37; Ti(IV) = 1.53^{14, 25}). Does this affect the σ -donor ability of phosphines relative to their donation in low valent metal interactions? Do changes to R groups produce the same trends in high valent interactions as have been observed in low valent systems?

We sought to address these questions directly using the experimental donor ability of phosphines determined by measuring the LDP values for these ligands. However, before we could put too much stock into the LDP measurements for a variety of PR₃ ligands using our Cr(VI) system, we needed to establish what effect the ionicity of these neutral ligand complexes would have on the solution state behavior of the LDP molecule. A detailed picture of ionicity based interactions in the solution-based system was critical to understanding our LDP measurements. Exchanging X⁻ for L ligands makes the Cr(VI) fragment a monocationic species with a counter anion. This change causes potentially massive differences in solution behavior of [NCr(NⁱPr₂)₂PR₃][X] salts versus neutral NCr(NⁱPr₂)₂X complexes.

2.2 Synthesis of $[\text{N}(\text{Cr}(\text{N}^i\text{Pr}_2)_2(\text{PR}_3))][\text{X}]$ Complexes, Solvent Choice, and Initial

Assessments of Solvent Effects

Synthesis of the $[\text{N}(\text{Cr}(\text{N}^i\text{Pr}_2)_2(\text{PR}_3))][\text{X}]$ salts was first undertaken by Brennan and Ross (see above), and proved to be straightforward and broadly applicable to a wide range of PR_3 complexes. They utilized AgSbF_6 to precipitate AgI from the $\text{N}(\text{Cr}(\text{N}^i\text{Pr}_2)_2\text{I})$ starting material (**1**) in MeCN. The AgI was removed by filtration, and in a second step, PR_3 can be added to displace MeCN and yield the $[\text{N}(\text{Cr}(\text{N}^i\text{Pr}_2)_2\text{PR}_3)][\text{SbF}_6]$ complex (**3**). The same general synthetic scheme, shown in Fig. 2.3, was utilized to produce almost all the derivatives shown in the table below. By altering the precipitation agent, the identity of the counterion, X^- , is easily changed.

Table 2.1 The wide variety of complexes accessible through the general synthesis route. **3j** and **3o** were prepared using an alternate procedure in which the MX salt was TlPF₆, the solvent for the reaction was DCM, and the entire procedure was performed as a 1-pot reaction to facilitate total miscibility of the phosphine with the solvent. ^bThe synthesis of **3p** was conducted under the strict exclusion of MeCN, in DCM with TlBARF₂₄ as a 1-pot procedure. Upon exposure of **3p** to MeCN, **3p** converts to **2** and PPh₃ ligand.

PMe_3	3a
P^nBu_3	3b
P^iBu_3	3c
P^iPr_3	3d
PCy_3	3e
PPhMe_2	3f
PPh_2Me	3g
PPhEt_2	3h
PPh_2Et	3i
$\text{PPh}_2^n\text{Bu}^a$	3j
PPh_2Cy	3k
PPhCy_2	3l
$\text{P}(\text{OEt})_3$	3m
$\text{P}(\text{O}^i\text{Pr})_3$	3n
$\text{P}(\text{NC}_4\text{H}_8)_3^a$	3o
PPh_3^b	3p

variants. Anomalous behavior with PPh₃ relative to other phosphines has been previously reported in the literature, where it is the lone derivative in a series of phosphine complexes that does not follow reaction kinetics characteristic of other phosphines.²⁶

These synthetic complications aside, we were able to synthesize 15 different [NCr(NⁱPr₂)₂(PR₃)]⁻[X] complexes with which to study phosphine donor properties with a d⁰ metal. These complexes readily crystallize from DCM or chloroform layered with a nonpolar solvent (Et₂O or pentane) at -35 °C, and all the PR₃ derivatives have been structurally characterized using X-ray diffraction. The complexes demonstrate predictable structural properties, with normal bond lengths observed for the NⁱPr₂ ligands and the nitride nitrogen. Additionally, there was no trend observed in the solid-state in terms of where the counterion sits relative to the Cr(VI) cation.

Despite this, two noteworthy elements of the structural data demonstrate the steric crowding in the system with PR₃ ligands. First, the Cr–P bond length increases roughly with the size of the phosphine (cone angle). A plot of this is shown in Fig. 2.4. Second, the N2–Cr1–N3 bond angle appears to get smaller as the PR₃ bound to Cr increases in size (Table 2.2). The results of the steric impacts on LDP measurement will be discussed in more detail in the next chapter.

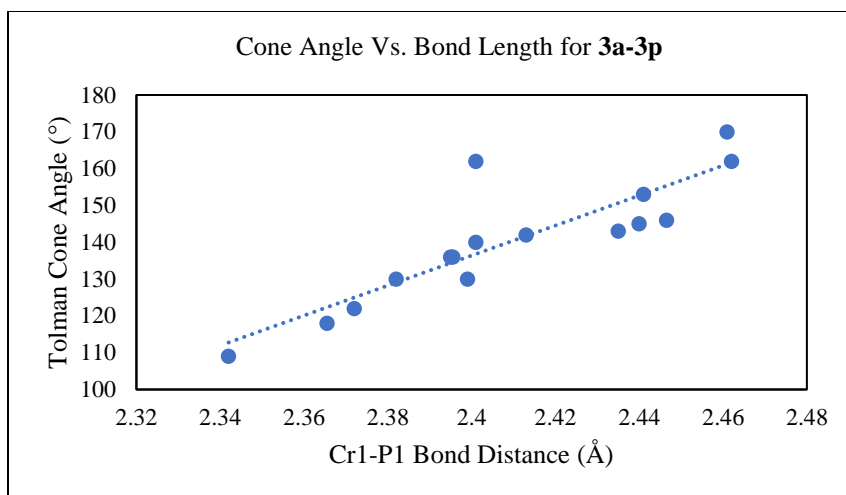


Figure 2.4 Plot of Tolman Cone Angle and Cr1 - P1 bond distances in X-ray crystal structures.

Table 2.2 Cr1-P1 bond distances and N2-Cr1-N3 bond angles. ^aFor those complexes were multiple bond distances/angles are given, there are two unique molecules in the asymmetric unit cell for these complexes.

3a^a		3i	
P-Cr	2.363/2.368	P-Cr	2.401
N2-Cr1-N3	124.22	N2-Cr1-N3	124.05
3b^a		3j	
P-Cr	2.399/2.392	P-Cr	2.413
N2-Cr1-N3	122.96/123.15	N2-Cr1-N3	123.1
3c		3k	
P-Cr	2.435	P-Cr	2.441
N2-Cr1-N3	121.41	N2-Cr1-N3	120.94
3d^a		3l	
P-Cr	2.452/2.472	P-Cr	2.401
N2-Cr1-N3	120.25/119.75	N2-Cr1-N3	121.49
3e		3m	
P-Cr	2.461	P-Cr	2.342
N2-Cr1-N3	119.24	N2-Cr1-N3	125.83
3f		3n^a	
P-Cr	2.461	P-Cr	2.381/2.383
N2-Cr1-N3	119.24	N2-Cr1-N3	125.08/122.77
3g		3o^a	
P-Cr	2.399	P-Cr	2.451/2.442
N2-Cr1-N3	124.02	N2-Cr1-N3	118.62/119.58
3h		3p	
P-Cr	2.395	P-Cr	2.44
N2-Cr1-N3	123.97	N2-Cr1-N3	121.73

Perhaps predictably, these $[\text{NCr}(\text{N}^i\text{Pr}_2)_2(\text{PR}_3)]^+$ salts are not very stable. Stored as solids at reduced temperatures, these complexes are stable for several weeks; they are generally yellow or orange powders, with the hue and intensity of the colors of the salts changing with different X^-

counter anions. When stored at room temperature or in solution, however, the complexes show signs of decomposition within 1 week. The counterion appears to have some bearing on stability such that $\text{SbF}_6^- < \text{PF}_6^- < \text{B}(\text{Ar})_4^-$; this trend was observed both in the solid state as well as in solution (Ar = C_6F_5 , 3,5-bis(CF_3)- C_6H_3 , or Ph) by examining old samples prepared with the different counter anions. The relative instability of these complexes has also made accurate elemental analysis unreliable. Samples prepared using standard air-sensitive EA techniques available at MSU have not resulted in reliable characterization using this method. To our knowledge, these are the first synthetic examples of isolated Cr(VI) cations and their extreme Lewis acidity (see Chapter 3) results in highly reactive complexes susceptible to decomposition pathways.

One other result of the syntheses of these complexes has been the isolation of **2** (the intermediate acetonitrile adduct produced from iodide extraction) and its full characterization. Nitriles by themselves are an interesting class of neutral ligands, and the successful isolation of **2** demonstrates that the synthesis used for the **3a-p** complexes here could easily be applied to the preparation of a series of L = NCR ligands. The crystal structure of **2** (Fig. 2.5) shows the nitrile coordinated to Cr datively through the N, with the Cr1–N4–C13 angle being approximately linear (176.04 °). Additionally, the N4–C13 bond distance is consistent with a covalent N≡C bond length (1.157 Å in free acetonitrile vs 1.137 Å in the bound form). Collectively, these two structural parameters suggest little to no π -interaction between Cr and NCCH₃, which characterizes NCCH₃ as a purely σ -donor in this interaction.

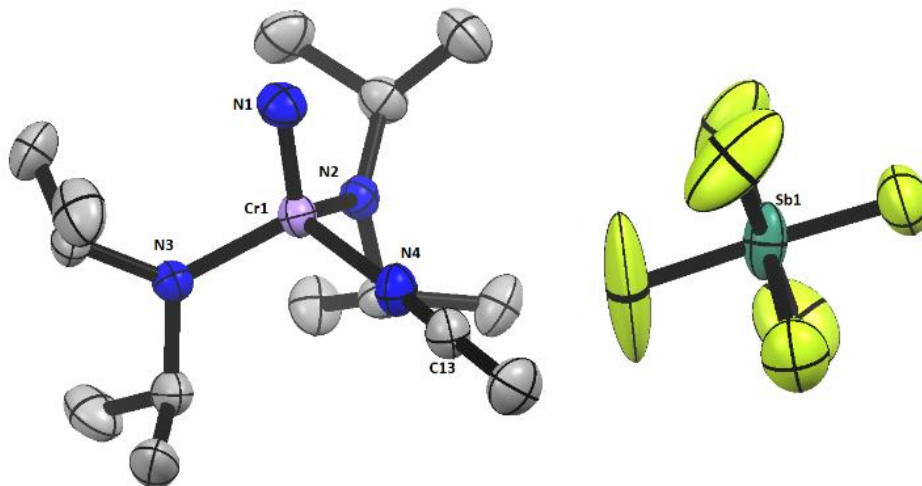


Figure 2.5 Crystal structure of 2, showing the NCCH₃ bound end-on through the N atom's lone pair. Ellipsoids are shown at 50% probability. H atoms are omitted for clarity. (Cr1-N1 1.533 Å; Cr1-N2 1.817 Å; Cr1-N3 1.816 Å; N2-Cr1-N3 121.85 °; Cr1-N4-13C 176.40 Å; N4-C13-C14 178.96; Cr1-N4 2.004 Å).

With a reliable synthetic route established to produce the $[\text{NCr}(\text{N}^i\text{Pr}_2)_2(\text{PR}_3)][\text{X}]$ complexes, with $[\text{X}] = \text{SbF}_6^-$, we began studying them in solution. Initially, we started with conditions similar to those used for the $\text{NCr}(\text{N}^i\text{Pr}_2)_2\text{X}$ complexes. NMR samples were prepared in CDCl_3 with concentrations of 0.025 M. Looking at a room temperature ^1H NMR spectrum for a phosphine salt (**3f**) compared to a moderately strong X^- ligand (OPh), we can see a dramatic difference. In **3f**, the $-\text{N}^i\text{Pr}_2$ methyne ($-\text{CH}-$) and methyl doublet peaks (CH_3) are well resolved and static, whereas these peaks in the $\text{NCr}(\text{N}^i\text{Pr}_2)_2(\text{OPh})$ spectrum are broad and fluctional due to their fast rotation (Fig. 2.6). Qualitatively this demonstrates that the phenol, in which rapid rotation occurs at room temperature, is a much better donor than the phosphine, with static N^iPr_2 groups at room temperature. Therefore, in order to get the Cr–N bond rotation in the phosphine complexes into a time regime that agrees with the NMR time scale, we needed to heat the samples. For a handful of the **3a-p** salts, this was not an issue, but for the majority, we were heating the samples to within a few degrees of the boiling point of the NMR solvent. In a few cases, even at 60 °C, bond rotation was still too slow to get measurable rotation rates.

the **3a-p** salts takes place in NCCH₃, we reasoned that solubility would be more than adequate in CD₃CN; additionally, this change gave us an additional 24 °C temperature threshold.

With a new solvent for measurement, we began remeasuring the LDP values for several **3** salts. However, the solvent change caused large differences in the LDP value between the two solvents. A selection of LDP values measured in both CDCl₃ and CD₃CN is shown in Table 2.3. In the most severe cases, the ΔLDP is 0.62 kcal/mol. Given the error margin typically quoted for LDP measurement (0.1 kcal/mol), these differences were far too large to amount to experimental errors. In previous experiments with NCr(NⁱPr₂)₂X complexes, no solvent dependence in the measured LDP values had been established. However, with the iconicity of the neutral ligand complexes, we suspected that ionicity-based solvent effects were impacting the measurements.

Table 2.3 LDP values determined in two different NMR solvents with a variety of different PR₃ ligands. All values reported here employ SbF₆⁻ as the counter ion.

Phosphine Complex (SbF ₆ ⁻)	LDP CDCl ₃ (kcal/mol)	LDP CD ₃ CN (kcal/mol)	Δ LDP
P(OEt) ₃	16.08	15.73	0.35
P(Me) ₃	17.23	16.64	0.59
PPhMe ₂	16.99	16.53	0.46
P(O ⁱ Pr) ₃	16.29	15.91	0.38
PPh ₂ Me	16.68	16.16	0.52
PPh ₂ Cy	17.04	16.43	0.61
P(ⁱ Pr) ₃	17.79*	17.17	0.62

*The temperature required to obtain an accurate rate of N-Cr bond rotation exceeded the boiling point of the solvent. This value is an estimate based on the rotation rate at the highest achievable temperature in CDCl₃.

Utilizing ¹⁴N NMR to characterize the complexes provided a clue as to why the LDP values measured in nonpolar CDCl₃ were higher than those measured in CD₃CN. A typical NCr(NⁱPr₂)₂X complex shows two resonances: the nitride appears between 900-1100 ppm and the amide appears between 200-400 ppm. The ¹⁴N NMR spectrum of several [NCr(NⁱPr₂)₂PR₃][SbF₆] complexes

exhibit only one resonance in CDCl_3 , which appears at about 450 ppm. This resonance has been assigned as the amide nitrogen. Deviation from the normal behavior for these complexes raised the question, why don't we observe a resonance for the nitride nitrogen? Structurally, there is no significant difference between the neutral $\text{N}(\text{N}^i\text{Pr}_2)_2\text{X}$ complexes and the $[\text{N}(\text{N}^i\text{Pr}_2)_2\text{PR}_3][\text{X}]$ complexes, so the lack of a nitride resonance seemed to be related to the ionicity.

^{14}N is a quadrupolar nucleus with a fast relaxation rate, so the most likely reason for the lack of a nitride resonance was enhanced relaxation which would broaden the signal into the baseline of the spectrum. The most abundant isotope of antimony is ^{121}Sb , which is also quadrupolar. Proximity of two quadrupolar nuclei can lead to coupling and subsequent enhancement of quadrupolar relaxation. It seemed likely that the nitride signal is diminished in CDCl_3 due to ion pairing which positions the SbF_6^- counterion close to the nitride nitrogen in solution.²⁷

28

Unfortunately, due to the large background resonance observed when CD_3CN is used as the NMR solvent, we could not compare between the two solvents directly. However, when the counterion is exchanged for one lacking a quadrupolar nucleus, the ^{14}N resonance for a nitride signal is observed in CDCl_3 . This was observed with both the PF_6^- and $\text{B}(\text{Ar})_4^-$ anions, and generally supports the conclusion that in the SbF_6^- salts, quadrupolar relaxation diminishes the nitride signal. This is illustrated by the spectra in Fig. 2.7.

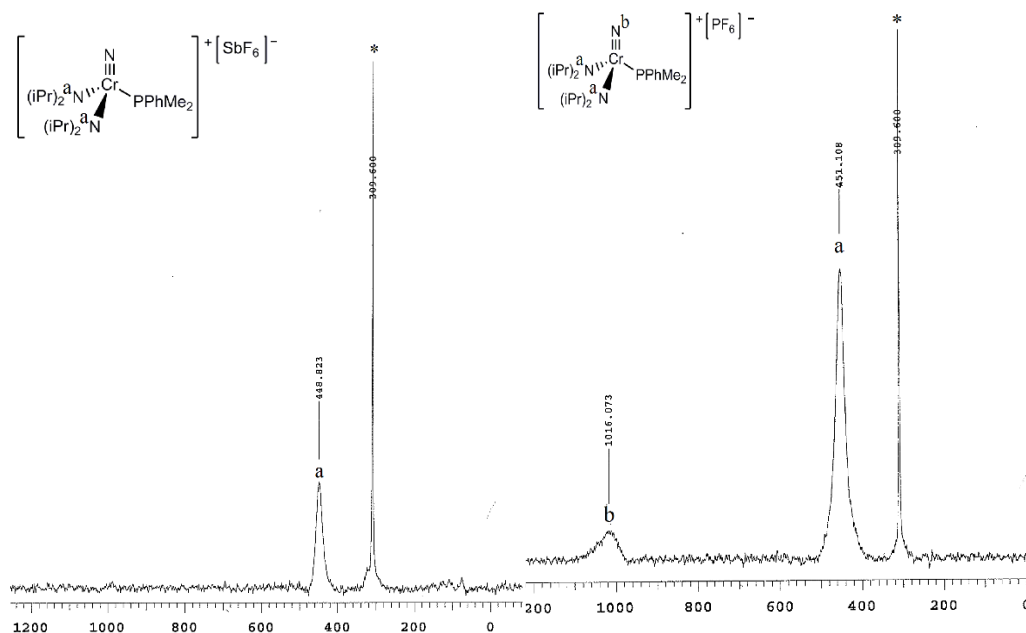


Figure 2.7 ^{14}N NMR spectra of **3f** in CDCl_3 with SbF_6^- (left) and PF_6^- (right) as counterions. (* = N_2 reference at 309.6 ppm; a = amide shift; b = nitride shift).

2.3 Direct Approaches to Characterize Ion Pairing: Diffusion Ordered Spectroscopy

(DOSY NMR)

With this piece of preliminary experimental evidence suggesting that, in CDCl_3 , tight ion pairing occurs, we needed a more direct approach to compare the solution state behaviors of the salts (**3**) in CDCl_3 versus CD_3CN . From initial observations and our understanding of the LDP measurement, we hypothesized that the difference was primarily that, in moving to the more polar CD_3CN solvent system, we were disrupting ion pairing. Thus, in the paired regime (CDCl_3) the counterion is close to the Cr cation in solution, inhibiting the rotation of the N^iPr_2 groups by sterically blocking them, while in the unpaired regime (CD_3CN) the ions are separated by fluctuational solvation spheres and the N^iPr_2 is unhindered in its rotation. This difference in the ion pairing behavior would then directly account for the differences observed in the LDP values measured in the two solvents with a given PR_3 .

The new problem became measuring ion pairing interactions. This has been a historically challenging problem to tackle experimentally, with early efforts focusing on conductivity measurements, potentiometry, or UV-Vis spectroscopy.²⁹⁻³² In some cases, correlation can even be drawn from solid state structures.³³ Advances in NMR spectroscopy in the last 15 years, however, have improved our ability to study complexes in solution. Specifically, methods that allow for through-space correlation (i.e. Nuclear Overhauser Effect) can show close contacts in tight ion pairs.³⁴⁻³⁷

Another NMR advancement, Diffusion Order Spectroscopy (DOSY) NMR, allows for the determination of the diffusion rate of species in solution. This can be used as an indirect way to determine if a cation and an anion are paired in solution, provided both ions have a readily observed NMR signal.^{34, 37-40} Two ions of different size should diffuse through solution at different rates. A simple equation relating diffusion rate and molecular size, the Stokes-Einstein equation, is shown in Eq. 2.1 and is a good approximation for regularly shaped molecules (i.e. spherical). From this equation, we can observe the size dependence.

$$D = \frac{k_B T}{6\pi\eta r} \quad (\text{Eq. 2.1})$$

Here the particle (molecular species) is assumed to be spherical, with a radius r , traveling through a medium with a viscosity of η . More elaborate models of diffusion that describe the motion of various shapes have been developed, but this equation can still be applied to simple molecules.^{41, 42} More importantly, it illustrates the inverse relationship between particle size (r) and diffusion rate (D). A practical demonstration of this effect is shown in Fig. 2.8, below, where several molecular species are in solution, and their diffusion rates have been determined by DOSY NMR spectroscopy. The larger the molecule, the more slowly it diffuses through solution, such that we know $\text{Et}_2\text{O} \sim \text{CHD}_2\text{CN} < \text{Ferrocene} < ((\text{H}_3\text{C})_3\text{Si})_4\text{Si} < \mathbf{3f}[\text{PF}_6]$.

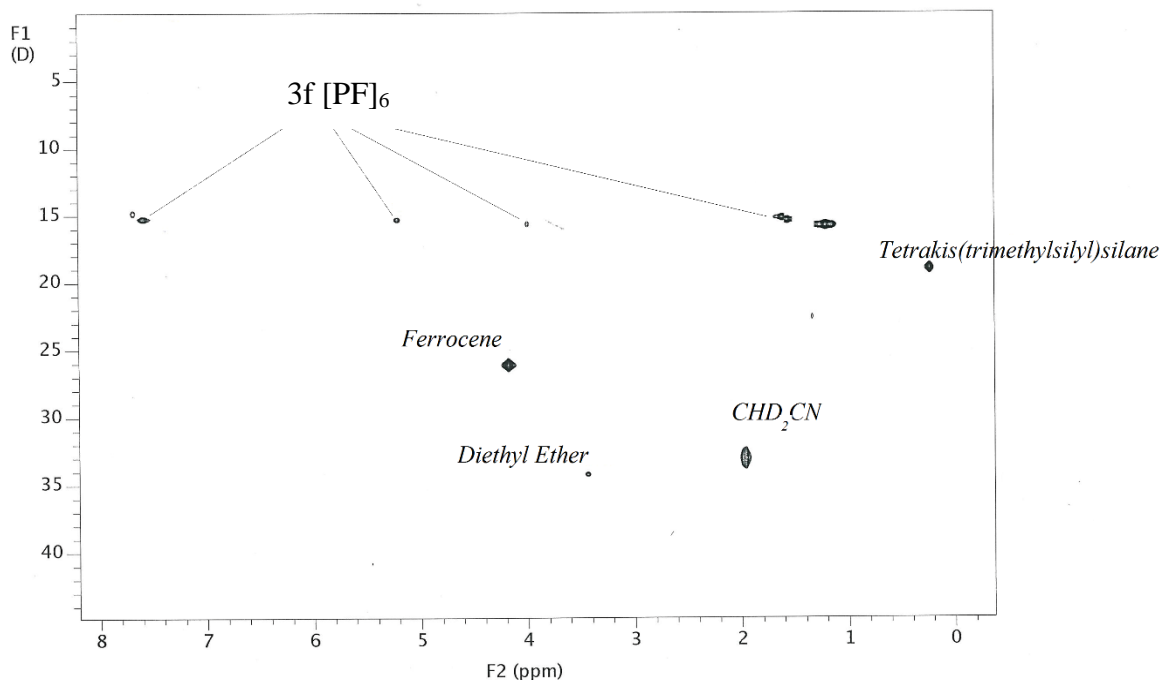


Figure 2.8 A ^1H DOSY NMR spectrum in CD_3CN that contains several molecular species of different sizes. The diffusion coefficients are inversely proportional to the molecular sizes, with larger species diffusing more slowly than smaller ones.

If two ions are separated, they should diffuse through solution at a rate inversely proportional to their independent hydrodynamic radii. However, if they are paired, they should exhibit the same hydrodynamic radius and diffuse at the same rate. Using a combination of these techniques (DOSY and NOE experiments) we set about determining whether the Cr(VI) cations and their counter anions were paired in the two NMR solvents examined.

Anions such as the $\text{B}(\text{Ar})_4^-$ were designed to replace anions such as SbF_6^- , PF_6^- and OTf^- , which have been shown to have limits to their “non-coordinating” tendencies.⁴³ The $\text{B}(\text{Ar})_4^-$ are generally regarded as the best “non-coordinating” anions available. This improvement has been achieved through extreme delocalization of charge, imparted to electronegative functional groups on the periphery of the anion. For example, in BArF_{24}^- , 8 CF_3 groups are spread out across the anion, bound to aromatic rings to delocalize the formal -1 charge of the molecular unit. In the LDP

system, we also hoped that perhaps these more diffuse anions would exhibit less ion pairing and solve the ion pairing issues in solutions simply. We had already undertaken synthetic efforts with three different anions: SbF_6^- , PF_6^- , and BArF_{24}^- . With these different counter anions, we had observed different ^{14}N NMR behaviors, and wondered if there were further differences in the solution state behaviors of these salts (**3**) dependent on the identity of the counterions. Thus we also further examined the ion pairing behavior of the Cr(VI) cations with several other “weakly coordinating” anions in both CDCl_3 and CD_3CN . The anions selected are shown in Fig. 2.9 below.

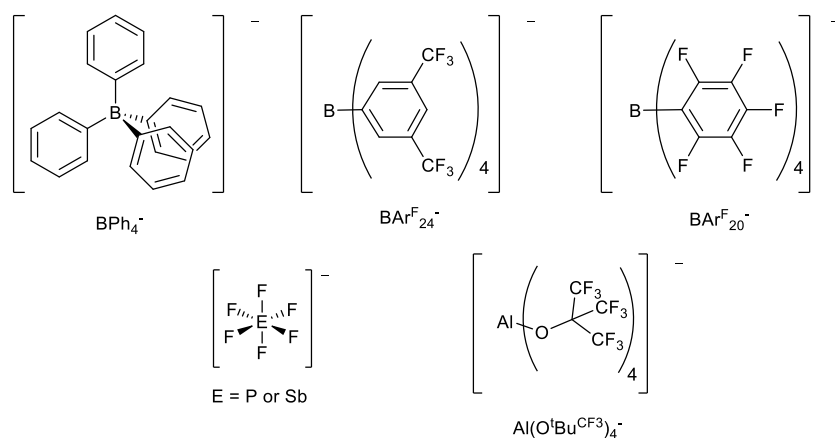


Figure 2.9 The “weakly coordinating” anions used to examine ion pairing effects in the LDP system with $[\text{NCr}(\text{NiPr}_2)_2\text{PR}_3]^+$ cations.

While diversifying the types of anions considered, we expanded the scope of the study beyond application to the LDP system.⁴⁴⁻⁴⁷ In doing so, however, we created a large number of potential complexes to make and study (>50). Therefore, we carefully selected two PR_3 species to serve as “model” complexes, representing the general behaviors of $[\text{NCr}(\text{N}^i\text{PR}_2)_2\text{PR}_3][\text{X}]$ complexes. Due to their simplicity in the ^1H NMR spectra, we chose the ligands PPhMe_2 (**3f**) and PMe_3 (**3a**) for our model complexes. For accurate DOSY or ROESY measurements, each species must present distinguishable peaks without overlap from other signals, and these ligands had provided resolved, well-separated spectra in which the ^1H peaks are easily distinguished and assigned.

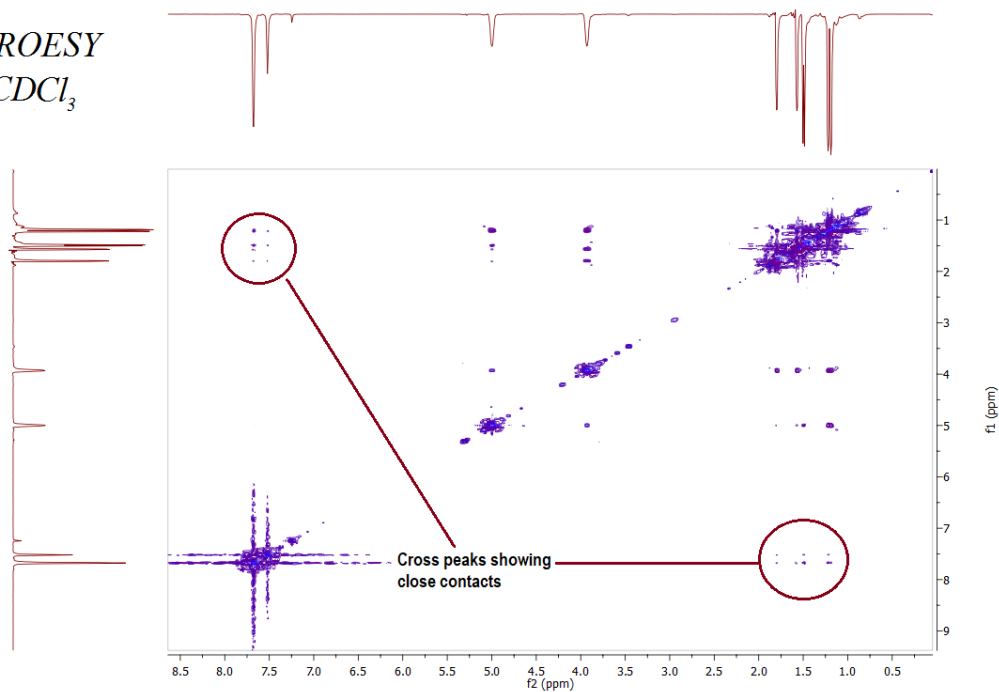
Considering the available NOE experiments that allow for detection of close contact between species in solution, we tried examining correlation between ^{19}F and ^1H signals from the anion and cation respectively using Heteronuclear Overhauser Effect Spectroscopy, (HOESY NMR). However, with many of the fluorinated anions, coupling induced odd and rapid relaxation properties of the ^{19}F nuclei, so we struggled to find adequate parameters for these NMR experiments. Additionally, due to the intermediate size of these species (1000 g/mol), their tumbling behavior in solution precludes good signal in a typical NOE experiment orientation.⁴⁸ To solve this problem, we looked at the $[\text{NCr}(\text{N}^i\text{Pr}_2)_2\text{PMe}_3][\text{BArF}_{24}]$ salt, using ^1H Rotating-frame Overhauser Effect Spectroscopy (ROESY NMR); the difference in the orientation and pulse sequence timing, going to the rotating frame experiment (^1H) versus a traditional NOESY or HOESY experiment, solves the signal intensity issues caused by molecular size. The BArF_{24}^- anion can be observed by its two sharp and unique ^1H NMR signals for the aromatic protons rather than by observing the ^{19}F signal.

With this salt, **3a** $[\text{BArF}_{24}]$, in CDCl_3 , we were able to observe pronounced cross peaks between the aliphatic signals of the $\text{Cr}(\text{VI})$ cation and the aromatic signals of the BArF_{24}^- anion in solution. These spectroscopic results are presented in Fig. 2.10. This provides direct evidence of proximity ($<5 \text{ \AA}$) for these two ions in solution and indicates a tight ion pair. By switching the solvent to CD_3CN , the cross peaks disappear. Of course, while negative evidence is often not informative, the results of these two experiments considered side-by-side certainly supported our hypothesis.

More interesting than the identification of ion pairing, this experiment also provides an idea of *how* the ions are paired. Cross peaks are observed between the BArF_{24}^- anion and the aliphatic Hydrogens of the ^iPr -groups as well as the PMe_3 ligand. This indicates that the ion

pairing, while tight, is non-site-specific. The pairing exists across the entire surface of both the cation and the anion rather than via one specific site on each anion with strong electrostatic attraction. Additionally, we were able to observe this tight ion pairing behavior in CDCl_3 with the BArF_{24}^- , which is one of the best and most diffuse anions in terms of minimizing its charge density. This direct observation made it seem highly likely that the ion pairing with diffuse anions is just as tight and substantial as that observed with the less diffuse anions. It also strongly indicates that there is no correlation between “weakly coordinating” characteristics and ion pairing.

ROESY
 $CDCl_3$



ROESY
 CD_3CN

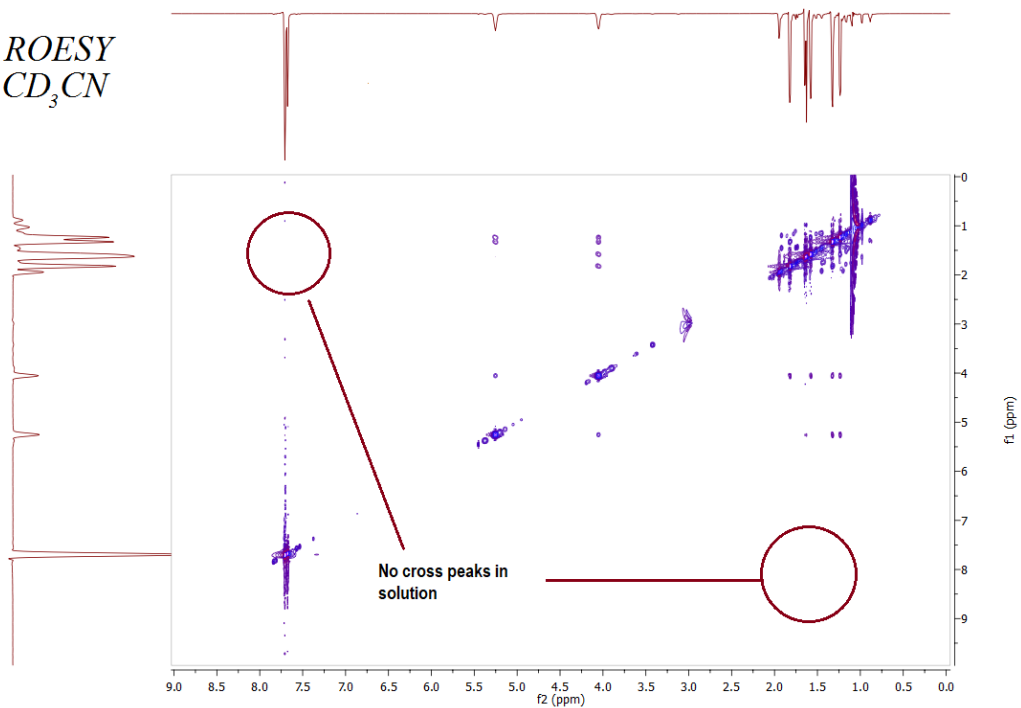


Figure 2.10 ROESY NMR spectra for **3a** $[NCr(N^iPr_2)_2PMe_3][BArF_{24}^-]$ in $CDCl_3$ (*top*) and CD_3CN (*bottom*). Correlation between the cation and anion are noted in $CDCl_3$, but these cross peaks are not observed in CD_3CN .

To verify this experimentally, we progressed to a DOSY study and examined each anion with one or both model cations, **3a** and **3f**. The results of the DOSY studies were very straightforward and informative. These results are highlighted in Table 2.4 below.

Table 2.4 Results of the DOSY NMR experiments utilizing various anions and the chromium(VI) cations **3a** and **3f**.

Complex	Anion	Solvent	Ion	D _{std}	D _{ion}	Ratio (D _{ion} :D _{Std})	Ratio (D _{+s} :D _{-s})
PPhMe ₂	PF ₆ ⁻	CDCl ₃	+	17.53	10.05	0.573	0.98 ±0.05
			-	14.92	8.73	0.584	
		CD ₃ CN	+	25.81	17.90	0.691	0.66 ±0.04
			-	28.2	29.63	1.051	
	BArF ₂₄ ⁻	CDCl ₃	+	14.79	6.35	0.429	1.04 ±0.07
			-	15.69	6.47	0.412	
		CD ₃ CN	+	21.69	14.21	0.658	1.14±0.03
			-	20.27	11.68	0.576	
	BArF ₂₀ ⁻	CDCl ₃	+	16.38	7.34	0.449	1.08 ±0.04
			-	12.25	5.10	0.416	
		CD ₃ CN	+	20.26	13.36	0.659	1.15 ±0.06
			-	19.75	11.30	0.572	
	Al(O ^t BuF ₉) ₄ ⁻	CDCl ₃	+	15.17	6.08	0.397	1.01 ±0.04
			-	13.65	5.35	0.392	
		CD ₃ CN	+	24.02	15.7	0.654	0.93 ±0.04
			-	20.46	14.48	0.708	
BPh ₄ ⁻	CDCl ₃	+	14.68	6.07	0.413	1.01 ±0.02	
		-	14.68	6.03	0.410		
	CD ₃ CN	+	22.53	14.89	0.661	0.98 ±0.02	
		-	22.53	15.12	0.671		
PMe ₃	BArF ₂₄ ⁻	CDCl ₃	+	15.72	6.47	0.41	1.02 ±0.04
			-	15.72	6.34	0.40	
		CD ₃ CN	+	21.29	11.68	0.56	0.76 ±0.02
			-	21.29	15.03	0.73	
	BPh ₄ ⁻	CDCl ₃	+	14.75	6.27	0.43	0.99 ±0.02
			-	14.75	6.32	0.43	
		CD ₃ CN	+	21.76	15.36	0.71	1.04 ±0.03
			-	21.76	14.75	0.68	

From the results in the table above (which are standardized against 1,3,5-tris(trifluoromethyl)benzene as internal standard when ^{19}F DOSY was used for the anion measurement), a common trend is observed for the CDCl_3 standardized diffusion coefficient ratios (cation : anion): they are all very close to 1. This indicates that the anionic and the cationic species are diffusing with identical rates in solution regardless of differences in ionic size. These results strongly indicate tight ion pairing with all anions examined in the nonpolar CDCl_3 system. Here again, the relative “coordinating” ability of the anions seems to have no effect on ion pairing.

A common trend is also observed from these results upon shifting to the more polar CD_3CN solvent system and repeating the DOSY measurements. The ratio of the standardized diffusion coefficients ($D_{+/s}:D_{-/s}$) diverge from 1 with a magnitude and direction proportional to the size difference of the ions. For example, PF_6^- is considerably smaller than the chromium(VI) cation in **3f**, so in acetonitrile the diffusion coefficient for the cation is smaller (i.e. diffuses slower) than that of the anion. The ratio of the diffusion coefficients therefore diverges from 1 and gets smaller, reflecting that the cation now diffuses considerably slower than the anion in solution. The only pair where the differences are less pronounced is the **3f** cation with BPh_4^- as the anion. However, due to the similarity of their molecular volumes (~ 400 vs. 300 \AA^3), this seems to be due to the detection limits of the technique. Thus, the results are not conclusive.

The results of the ROESY and DOSY NMR experiments are reinforced by the measured LDP values for each salt with different X^- in both CDCl_3 and CD_3CN . These values are shown in Table 2.5 below. With the different X^- examined, the LDP values in CDCl_3 are generally higher compared to the LDP values in CD_3CN . What is most interesting about these differences between solvents is that the magnitude seems to be completely dependent on the identity of X^- . For the compact anions (i.e. SbF_6^- and PF_6^-) a very large difference, $> 0.5 \text{ kcal/mol}$, is observed on

switching solvent. With the $B(\text{Ar})_4^-$ or aluminate anions, however, these differences are much smaller—in fact, within experimental error.

Table 2.5 LDP values measured for 3a and 3f with a variety of anions in CDCl_3 and CD_3CN . This illustrates the ion effect on the LDP measurement.

Complex	Anion	LDP (CDCl_3) (kcal/mol)	LDP (CD_3CN) (kcal/mol)
3f	SbF_6^-	16.99	16.53
	PF_6^-	19.96	16.53
	BArF_{24}^-	16.60	16.58
	BArF_{20}^-	16.64	16.62
	BPh_4^-	16.57	16.47
	$\text{Al}(\text{OC}(\text{CF}_3)_3)_4^-$	16.66	16.62
3a	SbF_6^-	17.24	16.64
	BPh_4^-	16.71	16.66
	BArF_{24}^-	16.86	16.65

From the ROESY results, BArF_{24}^- demonstrated non-site-specific ion pairing. From the similar impact on the LDP value observed with other borate and aluminate counterions, this behavior appears to be the norm for large diffuse anions in the system. The SbF_6^- counterion, on the other hand, diminishes the ^{14}N signal of the nitride ligand preferentially. Based on these results, we suspected that the large difference in the measured LDP variance between solvents with the small X^- anions was primarily caused by site-specific ion pairing. The SbF_6^- and PF_6^- anions have a specific part of the Cr cation where the electrostatic interaction is strongest, so the ions pair together in one specific orientation. If that orientation puts the X^- next to the $-\text{N}^i\text{Pr}_2$ ligands, as would be the case if the X^- sits above the Cr – nitride bond vector, the ion pairing would influence the measured LDP value more than ion pairing where the interaction is spread across the entire cation. After all, the LDP measurement is a bulk average of all the molecules in solution. Experimentally, this demonstrates that the difference in the mechanism of ion pairing can greatly impact the effects of ion pairing on processes such as internal rearrangements in the first

coordination sphere of an ionic complex. This is likely where the relative “coordinating” ability impacts ion pairing, where more charge-diffuse ions pair non-specifically and ions with more localized charge pair specifically.

Overall these experiments provide significant evidence that the Cr(IV) salts (**3**) are tightly ion paired to their counter anion in CDCl_3 , while in CD_3CN , the ions are separated and exhibit diffusion as free species in solution. These results agree well with the initial hypothesis, suggesting that steric interference from the paired counter anion is artificially raising the LDP values observed for the phosphine complexes in CDCl_3 .

2.4 Other Solution State Investigations of Ion Proximity in Solution

DOSY NMR to determine the diffusion rate of the ionic species in solution provided us with a clear qualitative picture of the fate of the Cr(VI) salts in solution with regards to their ion pairing. However, in order to get a more quantifiable sense of how unpaired the salts are in CD_3CN , we turned to an alternate DOSY technique in which the molecular weight of a species in solution can be calibrated with a series of internal standards.⁴⁹⁻⁵² This technique can be useful when determining if a molecular species is monomeric or dimeric in solution, for example. Similarly, with these ionic species in solution, there should be a noticeable difference in the calibrated molecular weight dependent on the pairing of the ions.

To utilize this technique, three internal standards which are inert, have unique NMR signals, and a wide range of molecular weights across the series of standards, were chosen. The diffusion coefficient of each molecule can then be plotted against the log of the molecular weight ($\log(\text{MW})$) to give a linear relationship, shown in Eq. 2.2 The experimentally determined diffusion coefficient for the unknown species of interest can then be calculated from the linear regression to provide the molecular weight in solution.

$$\log(D) = m(\log(MW)) + b \quad (\text{Eq. 2.2})$$

Here, D is the measured diffusion coefficient, MW = molecular weight, and m and b are the coefficients derived from linear regression. Of course, there is error associated with this experimental method, typically on the order of 5-20% relative error from the algorithm used to calculate diffusion from NMR signal attenuation. This raises an important point about the technique, which is that it's most useful in the determination of the molecular weight of a species *in situ* when the possible species are highly weight discrepant, such as a monomer vs. a dimer, where the molecular weight doubles.

For the purposes of determining the ion pairing behaviors within our system, we anticipated some challenges. The internal standards used are neutral species. Introducing additional ionic species would likely introduce non-innocence between the Cr salts in solution and the standards. However, because our species is charged and the standards are neutral, we suspected that there might be some complications with the absolute accuracy of the measurement. Specifically, the solvent interactions affecting the **3a-p** species in solution should be markedly different than those experienced by the neutral, high C–H composition standards examined due to the charge. We suspected that the association of a solvation sphere around the ionic species in solution would make these species manifest artificially high masses in solution.

The molecular weight determination of **3f** with PF_6^- as the counter anion was performed in CDCl_3 , $\text{C}_6\text{D}_5\text{Cl}$, and CD_3CN . We observed that the molecular weight determined for the chromium(VI) cation was highest in CDCl_3 and decreased as the polarity of the solvent increased. The weights are higher than the molecular weight of **3f** $[\text{PF}_6]$ (549.5 g/mol) or **[3f]⁺** (404 g/mol) in both solvents, suggesting there is a systematic difference in the behavior of the ionic compound

versus the neutral standards. However, a clear trend is still observed going from a nonpolar to a polar solvent.

Table 2.6 Molecular weight calibration results for **3f**[PF₆] in several solvents and concentrations.

Solvent	Concentration (M)	Dielectric Constant	Molecular Weight (g/mol)
CDCl ₃	0.025	4.91	693 ±114
C ₆ D ₅ Cl	0.025	5.62	628 ±21
CD ₃ CN	0.025	37.5	542 ±76
	0.01		578 ±93
	0.10		525 ±68

Looking at the series, in CDCl₃ the Cr(VI) cation fragment demonstrates a molecular weight of 693 g/mol, decreasing to 628 g/mol in C₆D₅Cl, and 542 g/mol in CD₃CN. This trend aligns with a reduction in ion pairing as the polarity of the solvent is increased. A molecular weight reduction of 151g/mol from 693 to 542 g/mol corresponds closely with the loss of PF₆⁻ (144 g/mol) on switching to the polar system. This trend supports the experimental observations made directly by analyzing the diffusion coefficients in Table 2.4.

There is a second possibility for why the ionic species have high molecular weights observed by this method. Aggregation, or the conglomeration of several pairs of ions, is a dynamic process which could also increase the observed molecular weight.^{40, 53} This process typically demonstrates concentration dependence, such that when the concentration of **3f**[PF₆] is increased in solution, more aggregation occurs. From Table 2.4, we can see that changing the concentration does not change the measured molecular weight, thus the high overall weights are not likely caused by aggregation. Solvent interaction differences between the ionic species of interest and the internal standards is the most likely culprit for these high molecular weights.

2.5 Computational Investigation of Ion Pairing with PF₆⁻

From experimental investigations, we had discovered several important pieces of information about the behaviors of these ionic species in solution, and the effect that this renders

on LDP measurements. As discussed above, large, diffuse anions such as BArF_{24}^- appear to pair to the Cr(VI) cations in a non-site-specific manner. However, the smaller, less diffuse counter anions have demonstrated different behavior according to LDP measurements and the effects observed with ^{14}N NMR.

Based on the ^{14}N NMR results with SbF_6^- , we suspected that the small, compact counter anions pair to the Cr(VI) cations in a site-specific manner. The point of contact between the two ions likely involves the nitride nitrogen on the Cr(VI) cation. From such an orientation, the N^iPr_2 groups' rotation is hindered, so an electrostatic interaction between these groups and the anion seemed likely. As no crystallographic interaction had been observed, and the properties of the anion and the inherent molecular weight of the compounds had led to difficulties in conducting HOESY NMR experiments, we turned to computational analysis to probe the nature of the ionic interaction with EF_6^- counter anions (E = Sb or P).

The structure of the Cr(VI) cation, **3f**, was optimized (starting from the crystallographic coordinates) using DFT, with the B3PW91 (and also with ωb97xd , which gave identical results) functional and 6-31G+(d,p) basis set on all atoms. With this optimized cation structure, the PF_6^- anion was then included in proximity to the cation; starting from several different orientations (i.e. above the Cr–nitride bond vector, below the Cr–nitride bond vector, next to the PR_3 group, and next to the N^iPr_2 groups), reoptimization was attempted.⁵⁴ These different orientations were each submitted for further optimizations. The only orientation from which the calculation would converge to an energy minimum was the orientation in which the PF_6^- anion was placed above the Cr–nitride bond vector. In this orientation, the structure quickly converged on an optimized geometry in which hydrogen bonding interactions exist between the ^iPr -groups and the fluorines of the PF_6^- .

This electrostatic interaction is most readily observed by considering the Mayer Bond Order for the P–F bonds (table 2.7). The 3-centered-4-electron bond that is oriented away from the Cr(VI) cation, F₆–P1–F₅, serves as a good reference point for comparison. In this bond, the bond order is calculated as 0.88. Relatively, the P–F₁ and P–F₂ bond orders are reduced (0.74 and 0.80 respectively), reflecting F₁ and F₂'s interaction with the cation.

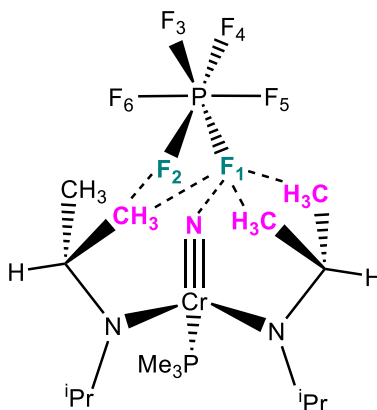


Figure 2.11 Representation of the optimized **3a**[PF₆] structure showing electrostatic interactions between the F's (teal) and ⁱPr groups (pink).

Table 2.7 Bond orders calculated for the PF₆[−] anion, showing H-bonding interaction effects on P – F bond orders.

P – F ₁ bond	Calculated Mayer Bond Order
F ₁	0.74
F ₂	0.80
F ₃	0.94
F ₄	0.94
F ₅	0.88
F ₆	0.88

The fluorines trans (F₃ and F₄) to these electron-density donor fluorines (F₁ and F₂) compensate for the shift of electron density in the P–F₁/F₂ bonds, by increasing their bond orders, such that both the P–F₃ and P–F₄ bond orders are 0.94 each. These substantial effects on the bonding in the PF₆[−] anion show the significance of these interactions, providing a logical reason

for the severe inhibition that ion pairing places on the rotation of the ⁱPr-groups with EF₆⁻ counterions. The computational results demonstrate clearly what the experimental results suggest, that with a compact PF₆⁻, the charge distribution on the cation and the anion lead to a specific orientation between the cation and the anion. This site-specific ion pairing leads to differences in the solution state of the ionic complexes compared to those where non-site-specific pairing occurs.

2.6 Entropic Complications in Ionic LDP Systems

Based on our efforts thus far to thoroughly understand the nature of ionic interactions in solution with the **3a-p** salts in the LDP system, it was determined that with a compact anion, in CD₃CN, ion pairing interactions were minimized. From this assessment, we thought that the system would lead to most purely electronic LDP values with the least amount of interference from ionic interactions in solution during the rotation barrier measurements. The LDP values of the series of Cr(VI) cations, **3a-o**, were measured with SbF₆⁻ or PF₆⁻ as the counter anion in CD₃CN (excluding **3p** due to instability with CD₃CN). The experimental values are listed in Table 2.8.

Table 2.8 LDP values measured in CD₃CN with SbF₆⁻/PF₆⁻ counter anions.

Compound Number	Phosphine Complex	Experimental ΔH‡ (kcal/mol)
3a	PMe ₃	16.64
3b	P ⁿ Bu ₃	16.77
3c	P ⁱ Bu ₃	17.13
3d	P ⁱ Pr ₃	17.17
3e	PCy ₃	17.27
3f	PPhMe ₂	16.53
3g	PPh ₂ Me	16.16
3h	PPhEt ₂	16.65
3i	PPh ₂ Et	16.15
3j	PPh ₂ ⁿ Bu	16.31
3k	PPh ₂ Cy	16.43
3l	PPhCy ₂	16.37
3m	P(OEt) ₃	15.73
3n	P(O ⁱ Pr) ₃	15.91
3o	P(NC ₄ H ₈) ₃	16.21

Before we could fully analyze these values, there was one other aspect of these complexes in solution that warranted further investigation: entropy. With the monoanionic X^- ligands typically examined in this system, it was previously determined that the entropy associated with N^iPr_2 rotation is a small negative number (e.u.) that is relatively constant regardless of the identity of X^- . In the **3a-p** salts, however, we had observed some concerning results that suggested either 1) the -9 e.u. determined with neutral Cr(VI) complexes was substantially different from ΔS^\ddagger in the ionic systems, or 2) the entropy for each **3a-p** complex was somehow dependent on the identity of PR_3 , and the assumption of constant ΔS^\ddagger was an oversimplification in these systems.

The first piece of evidence that caused concern about the accuracy of the entropy assumption within this system was that, for a few phosphine complexes, different LDP values were obtained at different temperatures. Furthermore, these differences were substantial. While a claimed error of ± 0.1 kcal/mol is typically assigned to LDP numbers, the measurement of these values is extremely precise; this error is largely attributed to our estimate of temperature calibration affecting the accuracy of the measurement. Two different researchers measuring the LDP value of two independently prepared batches of a given complex, on different instruments, making the measurement at different temperatures and on different days, typically yields numbers within 0.04 kcal/mol of one another. Additionally, these measurements are made in triplicate, with standard deviations typically below 0.02 kcal/mol. Consequently, differences on the order of those we had observed ($\Delta LDP = 0.4$ kcal/mol, $\Delta T = 10$ °C) were quite alarming. Therefore, the most likely source of error that we could attribute these differences to was entropy, a temperature dependent contributor to the ΔG^\ddagger of rotation.

Of course, measuring entropy experimentally is time-consuming and associated with strict limitations. In order to determine the entropy of the N^iPr_2 group rotation about the N–Cr bond, the

LDP value must be measured at several different temperatures. Generally, the wider the range of temperatures over which the ΔG^\ddagger can be determined, the more accurate the calculation of ΔS^\ddagger .^{1,55,56} (Note, ranges that come closer to absolute zero also make these calculations more accurate, but this property is not something that can be controlled by the experimenter) With the phosphine complexes **3a-p**, there is a very small range of temperatures over which the rotation is measurable on the NMR time scale, yet the complexes are stable enough to obtain accurate measurements without decomposition. Heating these complexes for extended time over 65 °C has been noted to release HN^iPr_2 , and even produce the bridging nitride-mixed valent Cr dimer that has been previously structurally characterized.⁵⁷ Consequently, for many of the phosphine complexes examined, this reliable temperature window for the determination of ΔS^\ddagger is a mere 10-20 °C.

By carefully selecting a few phosphine complexes in which the rotation barrier can be measured at lower temperatures, a wide enough variety of complexes was examined experimentally to elucidate the entropic behavior. Experimentally measured values of ΔS^\ddagger for **3f**, **3j**, and **3m**, with SbF_6^- as the counterion and CD_3CN solvent, are shown in Table 2.9 below.

Table 2.9 Complexes **3f**, **3j**, and **3m** which were used to determine experimental ΔS^\ddagger values for the ionic complexes in CD_3CN with the SbF_6^- counter anion.

Complex	Entropy (e.u.)	Temperature Range (°C)	Real ΔH^\ddagger (kcal/mol)
3f	4.7(0.5)	21.81	17.90
3j	25(5)	30.94	10.99
3m	38(4)	24.63	6.76

The complexes for which ΔS^\ddagger was measured span a relatively large range of electronic properties. They are all small phosphines, which was necessary to achieve the broader temperature ranges desired. The bulky phosphines require higher temperatures in order to achieve measurable rates of rotation in solution (see Chpt. 3). Even with only these 3 values, it is apparent that the entropy values are changing drastically depending on the PR_3 group in the complex under the

conditions that reduce ion pairing. These differences are far too significant to attribute to error in the measurement technique.

We suspected that these dramatic entropy differences, are a direct result of ionicity. In the polar solvent system utilizing CD_3CN , disruption of the electrostatic interaction between the cation and anion is achieved by replacing these charge-based interactions with directed dipole moment interactions with the solvent molecules. A specifically oriented arrangement of solvent molecules around each cation and anion in solution—solvation spheres—would likely impose a high degree of order in these solutions. Upon rotation of the N^iPr_2 group, the dipole moment of the Cr(VI) cation changes dramatically, which could in turn lead to a rearrangement of the solvation sphere. All these solvent rearrangements associated with the $\text{Cr-N}^i\text{Pr}_2$ rotation via the disruption of the solvation sphere would make the entropy of this rearrangement in each system unique; and in some cases this much order would likely produce a large value for ΔS^\ddagger . Therefore, it seemed likely that the LDP values determined with the $\text{SbF}_6^-/\text{CD}_3\text{CN}$ combination aren't strictly reliable at face value.

These experiments answered several questions about the entropic behavior of the ionic Cr(VI) complexes in solution and there was a logical explanation for the entropic differences observed with these complexes versus $\text{N}^i\text{Cr}(\text{N}^i\text{Pr}_2)_2\text{X}$ complexes. However, this raised several new questions, as well. Is this entropic variability a property of the ligands (PR_3)? Is it due to differences in the separation of the ion pair? Does pairing the ions make the variable entropic behavior more constant? If it is more constant, is it similar to the ΔS^\ddagger values determined with X^- ligands on Cr ? Potentially, answering some of these questions would assist in determining how to alleviate both ion pairing and entropic complications simultaneously. Thus, several additional entropy measurements were made.

To assess whether the variability in ΔS^\ddagger was due to PR_3 character, ion pair separation, or both, we examined the experimental ΔS^\ddagger values for the **3a-p** salts with the BArF_{24}^- anion. These ionic complexes exhibit ion pairing in CDCl_3 , however, the mechanism of the ion pairing (non site-specific) allows for bond rotation at lower temperatures than SbF_6^- , opening up the experimental temperature range. In fact, only 1 value in the **3a-p** series was not accessible within the temperature range provided by the $\text{BArF}_{24}^-/\text{CDCl}_3$ system (**3e**, PCy_3). These entropy values are shown in Table 2.10. From these values, it appears that the complexes have small, negative entropies of activation when ion-paired in CDCl_3 . The entropy ranges from -0.6 to -8.7 e.u. with an average of -4.7 e.u. Additionally, regardless of the PR_3 ligand, the values measured for ΔS^\ddagger are also tightly grouped.

Table 2.10 Experimentally determined values of ΔH^\ddagger and ΔS^\ddagger for **3a-p** BArF_{24}^- salts in CDCl_3 .

Phosphine Complex	Experimental ΔH^\ddagger (kcal/mol)	Experimental ΔS^\ddagger (e.u.) ^b	Phosphine Complex	Experimental ΔH^\ddagger (kcal/mol)	Experimental ΔS^\ddagger (e.u.) ^b
3a , PMe_3	18.71	-3.4 (1.0)	3i , PPh_2Et	17.98	-4.0 (1.0)
3b , P^nBu_3	18.91	-2.8 (1.0)	3j , PPh_2^nBu	18.17	-3.4 (1.0)
3c , P^iBu_3	17.76	-5.7 (1.0)	3k , PPh_2Cy	18.11	-5.5 (3.2)
3d , P^iPr_3	19.47	-3.0 (1.5)	3m , $\text{P}(\text{OEt})_3$	16.99	-6.1 (1.3)
3e , PCy_3	19.46	- ^a	3n , $\text{P}(\text{O}^i\text{Pr})_3$	17.12	-6.0 (1.2)
3f , PPhMe_2	18.79	-2.1 (1.1)	3o , $\text{P}(\text{NC}_4\text{H}_8)_3$	19.52	-0.6 (1.5)
3g , PPh_2Me	16.90	-8.2 (1.2)	3p , PPh_3	18.00	-4.1 (2.1)
3h , PPhEt_2	16.96	-6.7 (1.4)	Average	-	-4.7

^aThe value could not be determined experimentally because a temperature range of $<8^\circ\text{C}$ was available over which to measure bond rotation. ^bValues listed in parentheses are error approximations.

These results support the hypothesis that the deviations observed with **3f**, **3j**, and **3m** in CD_3CN are caused by the solvation interactions upon separation of the ion pair. However, whether the fluctuations in ΔS^\ddagger is caused by an additional ion effect or the properties of the PR_3 ligand remains to be seen. As one final piece of support for this hypothesis, we wanted to make sure that

the entropic differences observed between the two solvents were not simply the result of doing these measurements in CD₃CN, but rather originate from the ionic interactions with the solvent specifically. The ΔS^\ddagger values for NCr(NⁱPr₂)₂I (**1**) were measured in CDCl₃ and CD₃CN. The values that were obtained for this neutral Cr(VI) species in the two solvents were the same within error, -0.5 ± 1.0 and -1.3 ± 0.5 respectively. These values were determined over >40 °C temperature range, with 8 separate temperatures and ΔG^\ddagger determined in triplicate. The indistinguishable entropy behavior between solvents with a neutral molecule support our hypothesis that the deviations observed in the CD₃CN measurements of the [NCr(NⁱPr₂)₂PR₃][X] salts is due to ionic interactions with a polar solvent.

2.7 Conclusions

The solution state rotation barrier measurement, used to quantify ligand donor ability to a high valent metal in the LDP system, is highly sensitive to changes in solvent interactions. Neutral NCr(NⁱPr₂)₂X complexes analyzed in different solvents using ¹H spin saturation transfer demonstrate essentially no change in behavior, solvent to solvent. LDP values (ΔH^\ddagger) and the associated entropy of activation for the Cr–NⁱPr₂ bond rotation (ΔS^\ddagger) are consistent across highly different NMR solvents, suggesting little to no interaction between the Cr(VI) complexes and solvent during the bond rotation of interest.

Upon switching to a ligand set where X⁻ is replaced by neutral ligands, L = PR₃, we were able to synthesize a series of [NCr(NⁱPr₂)₂PR₃][X] salts, where X⁻ can be one of several weakly coordinating anions. These salts exhibit very different ΔH^\ddagger and ΔS^\ddagger values for Cr–NⁱPr₂ bond rotation in different solvents. Upon strategic investigation with a variety of experimental techniques, several interesting ionic effects were observed that affect the LDP measurement of PR₃ ligands in these complexes.

Highly diffuse, weakly coordinating anions such as $B(Ar)_4^-$ ions or aluminates ion pair with the Cr(VI) cation tightly in nonpolar solvents. This is contrary to the behavior of these anions portrayed by those who advocate the weak interaction or inertness that these anions exhibit with other species in solution. The ion pairing behavior is disrupted in a sufficiently polar solvent, such as CD_3CN , to the limits of our experimental detection. A charge-localized, weakly coordinating anion, such as SbF_6^- also forms a tight ion pair with the Cr(VI) cation in a nonpolar solvent. Also, similar to the diffuse anions, the ion pairing with SbF_6^- is disrupted in polar solvents.

What is much more interesting about the ion pairing behavior discovered with these two types of weakly coordinating anions is the difference in the mechanism of the pairing itself. With charge-diffuse anions, the ion pairing is non-site-specific, meaning that electrostatic attraction between the cation and the anion is dispersed across the surfaces of both molecules. With SbF_6^- , however, site specific pairing occurs, in which the ion pair exhibits a preferred contact point for pairing due to stronger electrostatic interactions between specific portions of the ions. In this system, the anion sits above the Cr–nitride bond vector, which causes the anion to directly impinge upon the N^iPr_2 groups' rotation about the Cr–N bonds.

In several ways, the LDP technique itself has proven to be a useful experimental tool for probing the ionic effects and solvent behaviors of these cationic Cr(VI) LDP complexes with several common weakly coordinating anions, X^- . This type of indirect observation with *in situ* ion effects is a valuable method for identifying 1) when ion pairing is affecting solution behaviors of organometallic complexes, and 2) the specifics of these effects, such as the mechanism of pairing.

2.8 Experimental

Instrumentation and facilities

All NMR spectra, including LDP and routine characterization data, were recorded utilizing the Max T. Rogers NMR Facility at Michigan State University. These include a UNITYplus 500 spectrometer equipped with a 5 mm switchable broadband probe operating at 36.12 MHz (^{14}N); a Varian Inova 500 spectrometer equipped with a 5 mm Pulse Field Gradient (PFG) switchable broadband probe operating at 499.84 MHz (^1H) and 470.28 MHz (^{19}F); a Varian Inova 600 spectrometer equipped with a 5 mm PFG switchable broadband probe operating at 599.89 MHz (^1H) and 564.30 MHz (^{19}F); and an Agilent DDR2 500 MHz NMR spectrometer equipped with a 5 mm PFG OneProbe operating at 499.84 MHz (^1H), 125.73 MHz (^{13}C), 469.96 MHz (^{19}F), and 202.35 (^{31}P). ^1H NMR chemical shifts are reported relative to residual CHCl_3 in CDCl_3 as 7.26 ppm. ^{13}C NMR chemical shifts are reported relative to natural abundance $^{13}\text{CDCl}_3$ in *d*-chloroform as 77.16 ppm. Single crystal X-ray diffraction data was collected in the Center for Crystallographic Research at MSU.4.2 operating with either Mo- or Cu- $\text{K}\alpha$.

General considerations

All syntheses were carried out under an N_2 atmosphere, using standard Schlenk techniques or in an MBraun glovebox. All reagents were stored in a glovebox after purification. Diethyl ether, acetonitrile, and dichloromethane were purified by passing them over a neutral alumina column under N_2 and stored over 3 Å molecular sieves. Chloroform was distilled from P_2O_5 under N_2 and stored over molecular sieves. Deuterated chloroform from Cambridge Isotope Laboratories was distilled from P_2O_5 under N_2 and stored over molecular sieves. Deuterated acetonitrile from

Cambridge Isotope Laboratories was distilled under N₂ from calcium hydride and stored over 3 Å molecular sieves.

The complex NCr(N¹Pr₂)₂I (**1**) was prepared according to the literature procedure.² Trimethyl-, dimethylphenyl-, and diphenylmethylphosphine were purchased from Aldrich Chemical Co. and used as received. Triethylphosphite and triisopropylphosphite were purchased from Aldrich Chemical Co. and distilled from Na₂SO₄ under reduced pressure. Triisobutylphosphine, diphenylcyclohexylphosphine, and phenyldicyclohexylphosphine were purchased from Strem Chemical Co. and used as received. Triisopropylphosphine purchased from Strem Chemical Co. was distilled from a 10 wt% solution in hexanes and stored over 3 Å molecular sieves. Tri(*n*-butyl)phosphine purchased from Strem Chemical Co. was distilled under N₂ and stored over 3 Å molecular sieves. Triphenyl-, phenyldiethyl-, diphenylethyl-, and tricyclohexylphosphine were purchased from Alfa Aesar and used as received. Silver hexafluoroantimonate (AgSbF₆) and thallium hexafluorophosphate (TlPF₆) were purchased from Sigma-Aldrich Chemical Co. and used as received. The KBArF₂₀ was supplied as a gift from Boulder Chemical Co. and was used as received. Thallium(I) BArF₂₄⁻ was prepared using the literature procedure.⁵⁸ The precipitation agent Ag[Al(OC(CF₃)₃)₄] was prepared according to literature procedures.⁵⁹

Tris(pyrrolidino)phosphine was synthesized by adding TMS-pyrrolidine (3.3 equiv) to trichlorophosphine (1 equiv) in cold (-78°C) diethyl ether solution and stirred for 3 h, over which time it was allowed to warm to room temperature.⁶⁰ Diphenyl(*n*-butyl)phosphine was synthesized by adding 1.7 M ⁿBuLi solution (1 equiv) to PPh₂Cl (1 equiv) in cold (-78°C) diethyl ether.⁶¹ In the literature preps for these phosphines, they were purified by distillation. However, the syntheses were carried out on much smaller scales than in the literature. Thus as an alternative method of

purification, the diphenyl(*n*-butyl)phosphine and the tris(pyrrolidino)phosphine, were run over a short plug of alumina for purification, which provided colorless oils that were pure by multi-nuclear NMR spectroscopy.

Adequate CHN was not obtained on the complexes under study despite many attempts. Their instability has been noted both in the solid state and in solution, and repeated attempts to obtain adequate CHN have demonstrated decomposition during attempts to transfer the sample to the combustion analysis instrument. The cationic Cr(VI) complexes have been characterized by NMR (^1H , ^{13}C , ^{31}P , ^{14}N , and ^{19}F), X-ray diffraction, and melting point. All experiments carried out with the chromium complexes in this study were conducted with X-ray quality single crystals to ensure purity.

Synthetic Procedures

General procedure for the synthesis of $[\text{NCr}(\text{N}^i\text{Pr}_2)_2\text{PR}_3][\text{SbF}_6]$ (3)

A 20 mL scintillation vial was charged with 1 equiv of **1**, acetonitrile (3 mL), and a Teflon-coated stirbar. This mixture was stirred at room temperature giving a dark red-orange solution. Separately, a solution of AgSbF_6 (1 equiv) was prepared in acetonitrile (1–2 mL). The AgSbF_6 solution was then added dropwise to the stirred solution of **1**. Upon addition, copious amounts of off-white precipitate formed, and the solution became dark brown. The resultant mixture was stirred for 20 min after complete addition of the Ag solution. The mixture was then filtered over Celite to remove the precipitate (AgI). The dark brown solution of **2** (filtrate) was once again stirred at room temperature and a solution of PR_3 (1–2 equiv) in acetonitrile (1–2 mL) was added. (Note: 1 equiv of the phosphine was used if it was a solid or high-boiling liquid phosphine that is

difficult to remove by recrystallization. 2 equiv of phosphine were used if PR₃ is a low-boiling liquid, easily removed under reduced pressure.)

Upon addition of PR₃, the solution quickly became yellow-orange. The reaction solution was stirred for 1 h at room temperature. The volatiles were then removed under reduced pressure to give a dark residue. This residue was rinsed with small aliquots of cold Et₂O (3x1 mL) to remove any unreacted **1**. The residue was once more dried under reduced pressure. The residue was dissolved in a minimal amount of CH₂Cl₂ or CHCl₃ and layered with Et₂O or *n*-pentane. The layered solution was then stored overnight at -35 °C to yield yellow-orange X-ray quality crystals. Note: [NCr(N^{*i*}Pr₂)₂PR₃][BArF₂₄] derivatives were synthesized in a similar fashion for LDP measurements in CDCl₃ and experimental determination of the entropies of activation. Instead of acetonitrile, DCM was generally used as solvent and TlBArF₂₄ replaced AgSbF₆ as the precipitation agent. With Tl⁺ instead of Ag⁺ the phosphine could be added to the initial solution for a 1-pot synthesis. The NMR data for each of these analogues is not reported, as all spectra except the ¹⁹F spectrum are very similar.

*Synthesis of 3a [NCr(N^{*i*}Pr₂)₂PMe₃][SbF₆]* Following the general procedure, the reaction was carried out with **1** (89 mg, 0.226 mmol), AgSbF₆ (78 mg, 0.226 mmol), and PMe₃ (35 mg, 0.460 mmol). This yielded **3a** (68.2 mg, 52.4%). Mp: 111–113 °C. ¹H NMR (500 MHz, CDCl₃): δ 5.42–5.29 (sept, 2H), 4.08–3.93 (sept, 2H), 1.86 (t, J = 4.6 Hz, 6H), 1.69 (d, J = 10.9 Hz, 9H), 1.61 (d, J = 6.3 Hz, 6H), 1.39 (d, J = 6.3 Hz, 6H), 1.27 (d, J = 9.0 Hz, 6H). ¹³C NMR (126 MHz, CD₃CN): δ 59.77 (s), 59.16 (s), 32.06 (s), 30.44 (s), 23.20 (d), 16.79 (s), 16.14 (s), 15.89 (s). ¹⁹F NMR (470 MHz, CDCl₃): δ -123.1 (d). ³¹P NMR (202 MHz, CDCl₃): δ 6.86 (s).

*Synthesis of [NCr(N^{*i*}Pr₂)₂P^{*n*}Bu₃][SbF₆] (3b)* Following the general procedure, the reaction was carried out with **1** (100 mg, 0.254 mmol), AgSbF₆ (87 mg, 0.254 mmol), and P^{*n*}Bu₃ (51.4 mg,

0.51 mmol). This yielded **3b** (83.1 mg, 46.4%). M.p.: 50 °C (dec.). ¹H NMR (500 MHz, CDCl₃): 7.70 (s, 1H), 7.52(s, 1H), 7.47 (ddd, J= 19.8, 9.9, 5.1 Hz, 1H), 4.95 (sept, J= 12.8, 6.4 Hz, 1H), 3.88 (sept, J= 12.5, 6.3 Hz, 1H), 1.87 (d, J= 10.3 Hz, 1H), 1.65 (d, J= 6.3 Hz, 1H), 1.56 (d, J= 6.3 Hz, 1H), 1.15 (d, J= 6.4 Hz, 1H), 1.10 (d, J= 6.4 Hz, 1H). ¹³C NMR (126 MHz, CDCl₃): 59.85 (d), 58.92, 32.48, 30.30, 25.79 (d), 24.92 (d), 24.56 (d), 23.87, 23.79, 13.85. ³¹P NMR (202 MHz, CDCl₃): 30.0. ¹⁹F NMR (470 MHz, CDCl₃): 106.55 to 137.63 (m).

Synthesis of [NCr(NⁱPr₂)₂PⁱBu₃][SbF₆] (3c) Following the general procedure, the reaction was carried out with **1** (50 mg, 0.127 mmol), AgSbF₆ (44 mg, 0.127 mmol), and PⁱBu₃ (36 mg, 0.254 mmol). This yielded **3c** (58.6 mg, 64.7%). M.p.: 150 °C (dec.). ¹H NMR (500 MHz, CDCl₃): 5.36 (sept, J= 12.4, 6.2 Hz, 2H), 4.00 (sept, J= 12.4, 6.2 Hz, 2H), 2.16 (dt, J= 18.8, 6.3 Hz, 3H), 1.97 (dd, J= 8.5, 6.3 Hz, 6H), 1.84 (d, J= 6.3 Hz, 6H), 1.57 (d, J= 6.2 Hz, 6H), 1.37 (d, J= 6.2 Hz, 6H), 1.32 (d, J= 6.2 Hz, 6H), 1.10 (d, J= 6.6 Hz, 18H). ¹³C NMR (126 MHz, CDCl₃): 59.50 (d), 59.09, 32.56 (d), 29.40, 25.02, 24.87, 23.94 (d), 23.74, 19.46. ³¹P NMR (202 MHz, CDCl₃): 32.8. ¹⁹F NMR (470 MHz, CDCl₃): -124.6 (m).

Synthesis of [NCr(NⁱPr₂)₂PⁱPr₃][SbF₆] (3d) Following the general procedure, the reaction was carried out with **1** (52 mg, 0.132 mmol), AgSbF₆ (45 mg, 0.132 mmol), and PⁱPr₃ (33.5 mg, 0.210 mmol). This yielded **3d** (33.5 mg, 40%). M.p.: 155 °C (dec.). ¹H NMR (500 MHz, CDCl₃): 5.41 (sept, J= 12.5, 6.2 Hz, 2H), 4.02 (sept, J= 12.6, 6.3 Hz, 2H), 2.46–2.34 (m, 3H), 1.84 (d, J= 6.4 Hz, 6H), 1.58 (d, J= 6.3 Hz, 6H), 1.43 (d, J= 7.2 Hz, 9H), 1.40 (d, J= 6.9 Hz, 15H), 1.34 (d, J= 6.2 Hz, 6H). ¹³C NMR (126 MHz, CDCl₃): 59.71, 59.24, 32.74, 29.58, 25.12 (d), 24.14, 23.94, 19.65.

^{31}P NMR (202 MHz, CDCl_3): 67.0. ^{19}F NMR (470 MHz, CDCl_3): -105.15 to -139.23 (m, J= 1809.1, 1654.8, 1457.8, 1258.2 Hz).

Synthesis of $[\text{NCr}(\text{N}^i\text{Pr}_2)_2\text{PCy}_3][\text{SbF}_6]$ (3e) Following the general procedure, the reaction was carried out with **1** (55 mg, 0.140 mmol), AgSbF_6 (48 mg, 0.140 mmol) and PCy_3 (40.5 mg, 0.140 mmol). This yielded **3e** (66 mg, 60%). M.p.: 117 °C (dec.). ^1H NMR (500 MHz, CDCl_3): 5.35 (sept, J= 12.4, 6.2 Hz, 2H), 4.02 (sept, J= 12.6, 6.3 Hz, 2H), 2.06 (dt, J= 21.0, 10.5 Hz, 6H), 1.99–1.86 (m, 16H), 1.83 (d, J= 6.3 Hz, 8H), 1.78 (s, 4H), 1.58 (d, J= 6.3 Hz, 10H), 1.56–1.41 (m, 6H), 1.39 (d, J= 6.2 Hz, 8H), 1.36 (d, J= 6.2 Hz, 8H), 1.35–1.11 (m, 16H). ^{13}C NMR (126 MHz, CDCl_3): 59.84, 59.22, 34.84 (d), 32.70, 29.75, 29.65, 27.60 (d), 25.84, 24.30, 23.75. ^{31}P NMR (202 MHz, CDCl_3): 56.9. ^{19}F NMR (470 MHz, CDCl_3): -123.19 (d, J= 3323.8 Hz).

Synthesis of $[\text{NCr}(\text{N}^i\text{Pr}_2)_2\text{PPhMe}_2][\text{SbF}_6]$ (3f) Following the general procedure, the synthesis was carried out with **1** (50 mg, 0.127 mmol, 1 equiv), AgSbF_6 (44 mg, 0.127 mmol, 1 equiv), and PPhMe_2 (35 mg, 0.253 mmol, 2 equiv). This yielded **3f** (56.4 mg, 68.4%) M.p.: 152–154 °C dec. ^1H NMR (500 MHz, CDCl_3): δ 7.62 (dd, J = 8.7, 3.1 Hz, 2H), 7.53 (s, 3H), 5.33 (sept, J = 23.2 Hz, 2H), 3.91 (dt, J = 12.0, 5.9 Hz, 2H), 1.99 (d, J = 10.3 Hz, 6H), 1.57 (dd, J = 11.1, 6.2 Hz, 12H), 1.31–1.17 (m, 13H). ^{13}C NMR (126 MHz, CDCl_3): δ 132.07 (s), 130.38 (d), 129.93 (d), 59.81 (d), 58.73 (s), 32.05 (s), 29.68 (s), 23.40 (s), 22.63 (s), 14.56 (s), 14.32 (s). ^{19}F NMR (470 MHz, CDCl_3): δ -122.13 (d, J = 5077.9 Hz). ^{31}P NMR (202 MHz, CDCl_3): δ 11.89 (s). ^{14}N NMR (36 MHz, CDCl_3): δ 448.8 (s).

Synthesis of $[\text{NCr}(\text{N}^i\text{Pr}_2)_2\text{PPh}_2\text{Me}][\text{SbF}_6]$ (3g) Following the general procedure, the reaction was carried out with **1** (50 mg, 0.127 mmol), AgSbF_6 (43 mg, 0.127 mmol), and PPh_2Me (50 mg, 0.250 mmol). This yielded **3g** (50.1 mg, 54.9%). M.p.: 138 °C. ^1H NMR (500 MHz, CDCl_3): 7.94–7.27 (m, 10H), 5.40 (sept, J= 11.6, 5.7 Hz, 2H), 3.89 (sept, J= 12.0, 5.9 Hz, 2H),

2.34 (d, J= 9.2 Hz, 3H), 1.89 (s, 1H), 1.55 (dd, J= 15.3, 6.2 Hz, 12H), 1.40(s, 3H), 1.27 (d, J= 6.0 Hz, 7H), 1.07 (d, J= 6.0 Hz, 6H). ^{13}C NMR (126 MHz, CDCl_3): 132.42 (d), 132.09, 131.79 (d), 130.70, 129.92(d), 129.21, 128.31, 127.93, 59.97 (d), 58.89, 31.99, 29.11, 23.05,22.25, 12.67 (d). ^{31}P NMR (202 MHz, CDCl_3): 20.7. ^{19}F NMR (470 MHz, CDCl_3): -107.41 to -139.91 (m). The X-ray diffraction study was carried out on the BArF_{24}^- salt, which gave single crystals and was made analogously to the SbF_6^- salt.

Synthesis of $[\text{NCr}(\text{N}^i\text{Pr}_2)_2\text{PPhEt}_2][\text{SbF}_6]$ (3h) Following the general procedure, the reaction was carried out with **1** (50 mg, 0.127 mmol), AgSbF_6 (43 mg, 0.127 mmol), and PPhEt_2 (34 mg, 0.246 mmol). This yielded **3h** (28.1 mg 33.1%). M.p.: 115 °C (dec.). ^1H NMR (500 MHz, CDCl_3): 7.64–7.50 (m, 5H), 5.21 (sept, J= 12.5, 6.3 Hz, 2H), 3.90 (sept, J= 12.5, 6.3 Hz, 2H), 2.48–2.33 (m, J= 15.0, 10.7, 7.5 Hz, 2H), 2.33–2.21 (m, 2H), 1.65 (d, J= 6.3 Hz, 6H), 1.57 (d, J= 6.3 Hz, 6H), 1.31–1.18 (m, 14H), 1.14 (d, J= 6.2 Hz, 6H). ^{13}C NMR (126 MHz, CDCl_3): 132.09, 130.87 (d), 130.25 (d), 59.65, 58.51, 31.88, 23.53, 22.34, 17.60(d), 7.16. ^{31}P NMR (202 MHz, CDCl_3): 34.9. ^{19}F NMR (470 MHz, CDCl_3): -123.30 (m).

Synthesis of $[\text{NCr}(\text{N}^i\text{Pr}_2)_2\text{PPh}_2\text{Et}][\text{SbF}_6]$ (3i) Following the general procedure, the reaction was carried out with **1** (100 mg, 0.254 mmol), AgSbF_6 (87 mg, 0.254mmol), and PPh_2Et (63 mg, 0.298 mmol). This yielded **3i** (94 mg, 51.6%). M.p.: 150 °C (dec). ^1H NMR (500 MHz, CDCl_3): 7.60 (dt, J= 11.6, 6.1 Hz, 6H), 7.45–7.28 (m, 4H), 5.20 (sept, J= 6.3 Hz, 2H), 3.93 (sept, J= 6.4 Hz, 2H), 2.62 (p, J= 7.3 Hz, 2H), 1.70 (d, J= 6.2 Hz, 6H), 1.56 (d, J= 6.2 Hz, 6H), 1.24 (d, J= 6.3 Hz, 6H), 1.11 (dt, J= 18.0, 7.4 Hz, 3H), 1.01 (d, J= 6.3 Hz, 6H). ^{13}C NMR (126 MHz, CDCl_3): 132.98

(d), 132.85 (d), 130.20 (d), 125.36 (d), 60.06, 59.07, 32.31, 29.49, 23.39, 22.60 (d), 22.34, 7.98 (d). ^{31}P NMR (202 MHz, CDCl_3): 35.3. ^{19}F NMR (470 MHz, CDCl_3): -122.12 (m).

Synthesis of $[\text{N}(\text{Pr}_2)_2\text{PPh}_2^{\text{n}}\text{Bu}][\text{PF}_6]$ (3j) A 20 mL scintillation vial was charged with **1** (100 mg, 0.254 mmol), CH_2Cl_2 (5 mL), diphenyl(*n*-butyl)phosphine (61 mg, 0.510 mmol), and a Teflon-coated stir bar. This solution was stirred at room temperature to give a dark red-orange solution. Separately, a suspension of TIPF_6 was prepared in 2 mL of CH_2Cl_2 . The TIPF_6 suspension was then added dropwise to the stirred solution of **1** and tris(pyrrolidinyl)phosphine. A yellow precipitate began to form on addition. After addition, the solution was stirred 3 h at room temperature. Then, the reaction mixture was filtered through Celite to remove the precipitate, and the bright orange filtrate was collected. The volatiles were removed from the filtrate under reduced pressure, leaving a dark residue. The residue was washed with cold Et_2O (31 mL), and the solution was again dried under reduced pressure. The residue was dissolved in a minimal amount of CH_2Cl_2 and layered with pentane. The layered solution was stored at $-35\text{ }^\circ\text{C}$ overnight to get X-ray quality orange crystals. This yielded **3j** (104 mg, 63%). M.p.: $74\text{--}77\text{ }^\circ\text{C}$ (dec). ^1H NMR (500 MHz, CDCl_3): 7.78–7.47 (m, 10H), 5.22 (sept, $J = 6.3$ Hz, 2H), 3.93 (sept, $J = 6.4$ Hz, 2H), 2.53 (q, $J = 7.8$ Hz, 2H), 1.69 (d, $J = 6.3$ Hz, 6H), 1.56 (d, $J = 6.2$ Hz, 6H), 1.38 (dq, $J = 23.9, 8.0, 7.6$ Hz, 4H), 1.25 (d, $J = 6.3$ Hz, 6H), 0.99 (d, $J = 6.3$ Hz, 6H), 0.84 (t, $J = 7.1$ Hz, 3H). ^{13}C NMR (126 MHz, CDCl_3): 132.89 (d), 132.80 (d), 130.23 (d), 125.81 (d), 60.11, 59.04, 32.29, 29.44, 29.05 (d), 25.67 (d), 23.99 (d), 23.33, 22.32, 13.60. ^{31}P NMR (202 MHz, CDCl_3): 32.7. ^{19}F NMR (470 MHz, CDCl_3): -73.41 (d, $J = 712.4$ Hz).

Synthesis of $[\text{N}(\text{Pr}_2)_2\text{PPh}_2\text{Cy}][\text{SbF}_6]$ (3k) Following the general procedure, the reaction was carried out with **1** (75 mg, 0.191 mmol), AgSbF_6 (68 mg, 0.195 mmol), and PPh_2Cy (63 mg, 0.230 mmol). This yielded **3k** (62.5 mg, 63.8%). M.p.: $168\text{ }^\circ\text{C}$ (dec). ^1H NMR (500 MHz,

CDCl₃): 7.63 (m, J= 15.0,7.8 Hz, 10H), 4.94 (sept, J= 6.2 Hz, 2H), 3.92 (sept, J= 6.3 Hz, 2H), 2.50–2.33 (m, 1H), 2.31–2.14 (m, 2H), 1.93–1.77 (m, 2H), 1.72 (d, J= 6.3 Hz, 6H), 1.57 (d, J= 6.2 Hz, 6H), 1.45–1.33 (m, 6H), 1.20 (d, J= 6.3 Hz, 6H), 1.02 (d, J= 6.2 Hz, 6H), 0.93–0.72 (m, 2H). ¹³C NMR (126 MHz, CDCl₃): 133.77 (d, J= 10.2 Hz), 132.89, 129.85 (d, J= 10.2 Hz), 123.03 (d, J= 42.8 Hz), 59.92 (d, J= 1.8 Hz), 58.90,36.94 (d, J= 22.4 Hz), 32.14 (d, J= 1.8 Hz), 29.05, 26.63 (d, J= 12.5 Hz), 25.46, 23.34, 22.39. ³¹P NMR (202 MHz, CDCl₃): 45.2. ¹⁹F NMR (470 MHz, CDCl₃): 106.76-136.05 (m). The X-ray diffraction study was done with the BPh₄⁻ salt, which gave single crystals and was made analogously to the SbF₆⁻ salt.

Synthesis of [NCr(NⁱPr)₂PPhCy₂][SbF₆] (3l) Following the general procedure, the reaction was carried out with **1** (52 mg, 0.132 mmol), AgSbF₆ (45 mg, 0.132 mmol), and PPhCy₂ (48.3 mg, 0.176 mmol). This yielded **3l** (58.2 mg, 56.1%). M.p.: 115 °C (dec). ¹H NMR (500 MHz, CDCl₃): 7.79–7.37 (m, 5H), 5.38 (sept, J= 12.2, 6.1 Hz, 2H), 3.99 (sept, J= 12.2, 6.0 Hz, 2H), 2.34 (d, J= 8.7 Hz, 2H), 1.91 (d, J= 21.6 Hz, 8H), 1.77 (d, J= 6.2 Hz,8H), 1.60 (d, J= 6.2 Hz, 6H), 1.44–1.05 (m, 24H). ¹³C NMR (126 MHz, CDCl₃): 132.89 (d), 132.49, 130.01 (d), 122.36 (d),59.96, 59.02, 34.31 (d), 32.28, 29.37, 28.32, 28.04, 27.17–26.56 (m), 25.52, 23.50, 23.19. ³¹P NMR (202 MHz, CDCl₃): 49.8. ¹⁹F NMR (470 MHz, CDCl₃): -108.70 to -142.59 (m).

Synthesis of [NCr(NⁱPr)₂P(OEt)₃][SbF₆] (3m) Following the general procedure, the reaction was carried out with **1** (100 mg, 0.254 mmol), AgSbF₆ (87 mg, 0.254 mmol), and P(OEt)₃ (43 mg, 0.26 mmol). This yielded **3m** (48.2 mg, 28.3%). M.p.: 149–150 °C. ¹H NMR (500 MHz, CDCl₃): 5.36 (sept, J= 12.6,6.3 Hz, 2H), 4.24 (p, J= 7.1 Hz, 6H), 4.03 (sept, J= 12.5, 6.1 Hz,2H), 1.87 (d, J= 6.3 Hz, 6H), 1.60 (d, J= 6.3 Hz, 6H), 1.45–1.35 (m,18H), 1.28 (d, J= 6.3 Hz, 9H). ¹³C

NMR (126 MHz, CDCl₃): 65.06(d), 60.32 (d), 59.19, 32.14, 30.46, 23.17, 22.81, 16.29 (d). ³¹P NMR (202 MHz, CDCl₃): 122.6. ¹⁹F NMR (470 MHz, CDCl₃): -122.86 (m).

Synthesis of [NCr(NⁱPr)₂P(OⁱPr)₃][SbF₆] (3n) Following the general procedure, the reaction was carried out with **1** (50 mg, 0.127 mmol), AgSbF₆ (43 mg, 0.127 mmol), and P(OⁱPr)₃ (38 mg, 0.182 mmol). This yielded **3n** (44.3 mg, 51%). M.p.: 138–140 °C. ¹H NMR (500 MHz, CDCl₃): 5.35 (dt, J= 12.6,6.3 Hz, 2H), 4.89–4.70 (m, 3H), 4.05 (dt, J= 12.5, 6.2 Hz, 2H), 1.92(d, J= 6.3 Hz, 6H), 1.56 (d, J= 6.3 Hz, 6H), 1.41 (d, J= 6.2 Hz, 18H),1.38 (d, J= 6.3 Hz, 6H), 1.30 (d, J= 6.3 Hz, 6H). ¹³C NMR (126 MHz, CDCl₃): 75.15 (d), 59.98 (d), 59.26, 32.48, 29.97, 24.11(d), 23.00 (d). ³¹P NMR (202 MHz, CDCl₃): 119.1. ¹⁹F NMR (470 MHz, CDCl₃): -122.86 (m).

Synthesis of [NCr(NⁱPr)₂P(NC₄H₈)₃][PF₆] (3o) A 20 mL scintillation vial was charged with **1** (100 mg,0.254 mmol), CH₂Cl₂ (5 mL), tris(pyrrolidinyl)phosphine (61 mg,0.510 mmol), and a Teflon-coated stir bar. This solution was stirred at room temperature to give a dark red-orange solution. Separately, a suspension of TlPF₆ was prepared in CH₂Cl₂ (2 mL). The TlPF₆ suspension was then added dropwise to the stirred solution of **1** and tris(pyrrolidinyl)phosphine. A yellow precipitate began to form on addition. Upon complete addition, the solution was stirred 3 h at room temperature. Then, the reaction mixture was filtered over Celite to remove the precipitate, and the orange filtrate was collected. The volatiles were removed from the filtrate under reduced pressure, leaving a dark residue. The residue was washed with cold Et₂O (3x1 mL) and was again dried under reduced pressure. The residue was dissolved in a minimal amount of CH₂Cl₂ and layered with pentane. The layered solution was stored at -35 °C overnight to get X-ray quality orange crystals of **3o** (102 mg, 61.5%). M.p.: 145–147 °C (dec). ¹H NMR (500 MHz, CDCl₃): 5.29 (sept, J= 12.1, 6.0 Hz, 2H),3.99 (sept, J= 12.0, 5.9 Hz, 2H), 3.14 (d, J= 4.5 Hz, 12H), 1.89 (s,12H), 1.85 (d, J= 6.2 Hz, 6H), 1.48 (d, J= 6.1 Hz, 6H), 1.37–1.29 (m, 12H). ¹³C NMR (126

MHz, CDCl₃) 58.81, 58.62, 47.56 (d), 33.04, 29.17, 25.97 (d), 23.54, 22.75. ³¹P NMR (202 MHz, CDCl₃): 103.1. ¹⁹F NMR (470 MHz, CDCl₃): 73.85 (d, J=712 MHz).

Synthesis of [NCr(NⁱPr₂)₂PPh₃][BArF₂₄] (3p) A 20 mL scintillation vial was charged with **1** (100 mg, 0.254 mmol), a Teflon-coated stir bar, CH₂Cl₂ (2 mL) and PPh₃ (64.5 mg, 0.250 mmol). Separately, TIBArF₂₄ (282 mg, 0.254 mmol) was dissolved in 2 mL of CH₂Cl₂. The TIBArF₂₄ solution was then added dropwise to the stirred chromium solution, resulting in rapid formation of a yellow precipitate. Upon complete addition, the reaction was stirred for 8 h at room temperature. Then, the reaction was filtered over Celite to remove the precipitate, and the orange filtrate was collected. The volatiles were removed from the filtrate under reduced pressure resulting in a brown residue. The residue was washed with cold pentane, and the volatiles were removed under reduced pressure. The residue was dissolved in minimal amount of Et₂O and layered with pentane and stored at -35 °C overnight to get X-ray quality orange crystals of **3p** (292 mg, 35.4%). From the X-ray diffraction study the structure of the cation could be gleaned but had full molecule disorder; in addition, the BArF₂₄⁻ was severely disordered. Consequently, the structure is of poor quality. M.p.: 110–112 °C (dec.). ¹H NMR (500 MHz, CDCl₃): 7.71 (s, 8H), 7.66–7.42 (m, 16H), 4.95 (sept, J= 12.6, 6.3 Hz, 2H), 3.87 (sept, J= 12.6, 6.3 Hz, 2H), 1.76 (d, J= 6.3 Hz, 6H), 1.54 (d, J= 6.3 Hz, 6H), 1.13 (d, J= 6.3 Hz, 6H), 0.76 (d, J= 6.3 Hz, 6H). ¹³C NMR (126 MHz, CDCl₃): 161.83 (dd), 134.93, 133.61 (d), 133.13 (d), 130.11 (d), 129.03 (d), 127.93, 126.31, 125.85 (d), 123.60, 121.43, 117.61, 59.97 (d), 59.77 (d), 32.51 (d), 29.19, 22.95, 21.96. ³¹P NMR (202 MHz, CDCl₃): 35.0. ¹⁹F NMR (470 MHz, CDCl₃): 62.42 (s).

Synthesis of [NCr(NⁱPr₂)₂NCCH₃][SbF₆] (2) A 20 mL scintillation vial was charged with **1** (50 mg, 0.127 mmol), a Teflon-coated stir bar, CH₂Cl₂ (4 mL), and acetonitrile (60 μL). The solution was stirred at room temperature to give a dark red-orange solution. Separately, AgSbF₆

(43 mg, 0.125 mmol) was suspended in CH₂Cl₂ (2 mL). The AgSbF₆ suspension was then added dropwise to the chromium solution, resulting in rapid formation of an off-white precipitate. Upon complete addition, the solution was stirred 3 h at room temperature. Then, the reaction mixture was filtered over Celite to remove the precipitate, and the red filtrate was collected. The volatiles were removed from the filtrate under reduced pressure, leaving a dark brown residue. The residue was washed with cold Et₂O (3x1 mL), and once again, the volatiles were removed under reduced pressure. The residue was dissolved in a minimal amount of CH₂Cl₂ and layered with Et₂O. This solution was stored overnight at -35 °C to give X-ray quality red-orange crystals of **2** (30.9 mg, 43.5%). M.p.: 126–129 °C (dec.). ¹H NMR (500 MHz, CDCl₃): 5.57 (sept, J = 7.5, 6.7 Hz, 2H), 4.07 (sept, J = 6.2 Hz, 2H), 2.58 (s, 3H), 2.02 (d, J = 6.2 Hz, 6H), 1.52 (d, J = 6.2 Hz, 6H), 1.39 (d, J = 6.2 Hz, 6H), 1.20 (d, J = 6.3 Hz, 6H). ¹³C NMR (126 MHz, CDCl₃): 60.34 (d), 59.87, 31.15, 30.91, 22.40, 22.25. ¹⁹F NMR (470 MHz, CDCl₃): 123.79 (m).

Additional Complexes Studied for Ion Pairing Effects

Synthesis of 3a[BArF₂₄]. A 20 mL scintillation vial was charged with **1** (50 mg, 0.127 mmol, 1 equiv), PMe₃ (0.301 mmol, 2.4 equiv), 3 mL of DCM, and a magnetic stir bar. To the stirred solution was added a solution of TlBArF₂₄ (135 mg, 0.127 mmol, 1 equiv) in 1 mL of DCM. Upon addition, a copious amount of yellow precipitate formed, and the solution went from dark red to bright orange. This solution was stirred for 3 h at room temperature. The TlI precipitate was removed by filtration through Celite, and the bright orange filtrate was concentrated under reduced pressure. The concentrated solution was layered with pentane and chilled to -35 °C, which afforded X-ray-quality crystals (92.6 mg, 60.4%). Mp: 93 °C (dec.). ¹H NMR (500 MHz, CDCl₃): 7.69 (s, 8H), 7.53 (s, 4H), 5.01 (sept, J = 12.8, 6.4 Hz, 2H), 3.95 (sept, J = 12.5, 6.3 Hz, 2H), 1.82 (d, J = 6.3 Hz, 6H), 1.59 (d, J = 6.3 Hz, 6H), 1.51 (d, J = 10.6 Hz, 9H), 1.22 (dd, J = 14.2, 6.4 Hz, 14H).

^{13}C NMR (126 MHz, CDCl_3): 161.62 (q), 134.73 (s), 129.60–128.24 (m), 124.50 (q), 117.46 (s), 59.61 (s), 59.04 (s), 31.92 (s), 30.23 (s), 22.97 (s), 15.89 (s), 15.64 (s). ^{19}F NMR (470 MHz, CDCl_3): -62.35 (s). ^{31}P NMR (202 MHz, CDCl_3): 7.16 (s). ^{14}N NMR (36 MHz, CDCl_3): 1010.7 (s), 449.4 (s).

Synthesis of 3a[BPh₄]. A scintillation vial was charged with **1** (75 mg, 0.191 mmol, 1 equiv), 3 mL of acetonitrile, and a magnetic stir bar. To this stirred solution was added a suspension of AgBPh₄ (82 mg, 0.191 mmol, 1 equiv) in 1 mL of DCM. This solution was stirred for 3 h at room temperature. During this time the solution changed color from dark red-orange to dark brown, and an off-white precipitate was formed. The precipitate was removed by filtration through Celite. The dark brown filtrate was stirred, and a solution of 30 mg of PMe₃ (0.394 mmol) in 1 mL of acetonitrile was added. This solution was stirred for 1 h at room temperature and then dried in vacuo. The residue was rinsed with several small aliquots of diethyl ether and dried under reduced pressure once again. The complex was dissolved in a minimal amount of DCM, layered with diethyl ether, and chilled to -35 °C, which afforded orange crystals (25.8 mg, 20.5%). Mp: 93–95 °C (dec.). ^1H NMR (500 MHz, CDCl_3): 7.44 (s, 8H), 7.05 (s, 8H), 6.90 (s, 4H), 4.84 (sept, J = 12.6, 6.3 Hz, 2H), 3.88 (dt, J = 12.6, 6.1 Hz, 2H), 1.76 (d, J = 6.2 Hz, 6H), 1.55 (d, J = 6.2 Hz, 7H), 1.18 (t, J = 6.1 Hz, 13H), 1.08 (d, J = 10.8 Hz, 9H). ^{13}C NMR (126 MHz, CDCl_3): 164.37 (q), 136.47 (s), 125.78 (s), 121.89 (s), 59.56 (s), 58.79 (s), 32.11 (s), 30.41 (s), 23.39 (s), 15.70 (s), 15.45 (s). ^{31}P NMR (202 MHz, CDCl_3): 8.02 (s). ^{14}N NMR (36 MHz, CDCl_3): 1015.9 (s), 446.4 (s).

Synthesis of 3f[PF₆]. A 20 mL scintillation vial was charged with **1** (50 mg, 0.127 mmol, 1 equiv), a magnetic stir bar, PPhMe₂ (35 mg, 0.253 mmol, 2 equiv), and 3 mL of acetonitrile. To this stirred solution was added a solution of TIPF₆ (44.3 mg, 0.127 mmol, 1 equiv) in 1 mL of

acetonitrile. Upon addition, copious amounts of yellow precipitate formed, and the solution went from dark red-orange to a lighter orange. This solution was stirred for 3 h at room temperature. The TII precipitate was filtered off the bright orange solution through Celite, and the filtrate was pumped to dryness under reduced pressure. The residue was crystallized with CH₂Cl₂/pentane at -35 °C, which afforded X-ray-quality orange crystals (64.8 mg, 48.3%). Mp: 172–174 °C (dec). ¹H NMR (500 MHz, CDCl₃): 7.69–7.58 (m, 2H), 7.52 (dd, J = 5.6, 2.9 Hz, 3H), 5.39 (sept, J = 12.5, 6.3 Hz, 2H), 3.91 (sept, J = 12.5, 6.2 Hz, 2H), 1.99 (d, J = 10.3 Hz, 6H), 1.56 (dd, J = 8.7, 6.4 Hz, 12H), 1.24 (d, J = 6.2 Hz, 12H). ¹³C NMR (126 MHz, CDCl₃): 132.26 (d), 130.68 (d), 130.13 (d), 59.98 (d), 58.94 (s), 32.28 (d), 29.92 (s), 23.65 (s), 22.89 (s), 14.69 (d). ¹⁹F NMR (470 MHz, CDCl₃): -72.21 (d, J = 719.7 Hz). ³¹P NMR (202 MHz, CDCl₃): 12.35 (s), -130.77 to -156.42 (sept). ¹⁴N NMR (36 MHz, CDCl₃): 1016.1 (s), 451.1 (s).

Synthesis of 3f[BArF₂₄]. A 20 mL scintillation vial was charged with **1** (50 mg, 0.127 mmol, 1 equiv), PPhMe₂ (35 mg, 0.253 mmol, 2 equiv), 3 mL of DCM, and a magnetic stir bar. To this stirred solution was added a solution of TIBArF₂₄ (135 mg, 0.127 mmol, 1 equiv) in 1 mL of DCM. Upon addition, copious amounts of yellow precipitate formed, and the solution went from dark red-orange to transparent bright orange. The solution was stirred for 3 h at room temperature. The TII precipitate was filtered through Celite, and the bright orange filtrate was concentrated in vacuo. The concentrated solution in DCM (~1 mL) was layered with pentane and chilled to -35 °C overnight to obtain X-ray-quality orange crystals (62 mg, 38.5%). Mp: 115 °C (dec.). ¹H NMR (500 MHz, CDCl₃): 7.70 (s, 8H), 7.52 (s, 5H), 7.51–7.40 (m, 4H), 4.95 (sept, J = 12.8, 6.4 Hz, 2H), 3.88 (sept, J = 12.5, 6.3 Hz, 2H), 1.87 (d, J = 10.3 Hz, 6H), 1.65 (d, J = 6.3 Hz, 6H), 1.56 (d, J = 6.3 Hz, 6H), 1.15 (d, J = 6.4 Hz, 6H), 1.10 (d, J = 6.4 Hz, 6H). ¹³C NMR (126 MHz, CDCl₃): 164.34–159.48 (m), 134.76 (s), 132.65 (s), 130.15 (d), 129.65 (d), 128.87 (d),

127.77 (s), 125.60 (s), 123.43 (s), 121.26 (s), 117.46 (s), 59.70 (s), 59.00 (s), 31.85 (s), 29.71 (s), 23.07 (s), 22.27 (s), 14.86 (d). ^{19}F NMR (470 MHz, CDCl_3): -62.38 (s). ^{31}P NMR (202 MHz, CDCl_3): 12.74 (s). ^{14}N NMR (36 MHz, CDCl_3): 1008.5 (s), 445.8 (s).

Synthesis of 3f[BArF₂₀]. A 20 mL scintillation vial was charged with **1** (60 mg, 0.153 mmol, 1 equiv), PPhMe₂ (42 mg, 0.303 mmol, 2 equiv), 3 mL of DCM, and a magnetic stir bar. To this stirred solution was added a solution of KBArF₂₀ (110 mg, 0.153 mmol) in 1 mL of DCM. This reaction mixture was stirred for 8 h at room temperature. Over the course of the reaction, the dark red-orange, cloudy solution slowly cleared and became bright orange as a yellow precipitate formed. The KI precipitate was removed by filtration through Celite, and the bright orange solution was concentrated under reduced pressure. The concentrated filtrate (~1 mL) was layered with pentane (~2 mL) and chilled to -30 °C overnight to yield X-ray quality orange crystals (46 mg, 27.8%). Mp: 135 °C (dec.). ^1H NMR (600 MHz, CDCl_3): 7.61–7.40 (m, 4H), 5.01 (sept, $J = 12.8$, 6.4 Hz, 2H), 3.91 (sept, $J = 12.5$, 6.2 Hz, 2H), 1.90 (d, $J = 10.3$ Hz, 6H), 1.66 (d, $J = 6.3$ Hz, 6H), 1.58 (d, $J = 6.3$ Hz, 6H), 1.21 (d, $J = 6.4$ Hz, 6H), 1.16 (d, $J = 6.4$ Hz, 6H). ^{13}C NMR (126 MHz, CDCl_3): 148.30 (d), 137.28 (t), 132.78 (s), 130.31 (d), 129.92 (d), 128.52 (d), 59.97 (d), 59.15 (s), 32.08 (d), 29.88 (s), 23.35 (s), 22.47 (d), 14.88 (d). ^{19}F NMR (470 MHz, CDCl_3): -132.56 (s), -163.03 (d, $J = 17.7$ Hz), -166.84 (s). ^{31}P NMR (202 MHz, CDCl_3): 12.92 (s). ^{14}N NMR (36 MHz, CDCl_3): 1010.3 (s), 448.5 (s).

Synthesis of 3f[Al(OC(CF₃)₃)₄]. A 20 mL scintillation vial was charged with **1** (100 mg, 0.254 mmol, 1 equiv), 3 mL of acetonitrile, and a magnetic stir bar. To this was added a solution of AgAl(OC(CF₃)₃)₄ (273 mg, 0.254 mmol, 1 equiv) in 1 mL of acetonitrile. The resultant solution was stirred for 1 h at room temperature, during which time a yellowish precipitate formed, and the solution darkened from red-orange to brown. The AgI was removed by filtration through Celite,

and the filtrate was once again stirred. To the stirring filtrate was added a solution of PPhMe₂ (35 mg, 0.254 mmol, 1 equiv) in 1 mL of acetonitrile. This solution was stirred at room temperature for 2 h, changing slightly in color from dark brown to dark orange-brown. The solution was dried under reduced pressure, and the residue was washed with several aliquots of cold pentane. The solids were again dried under reduced pressure and dissolved in a minimal amount of chloroform. This concentrated solution was layered with pentane and chilled to -35 °C, which afforded yellow crystals (183 mg, 52.5%). Removal of all traces of solvent from the aluminate complex (without decomposing the complex) was difficult, and solvent peaks were identified in the NMR spectra. Mp: 136–138 °C. ¹H NMR (500 MHz, CDCl₃): 7.68–7.43 (m, 5H), 5.02 (sept, J = 6.4 Hz, 2H), 3.93 (sept, J = 6.1 Hz, 2H), 1.94 (d, J = 10.3 Hz, 7H), 1.68 (d, J = 6.3 Hz, 6H), 1.60 (d, J = 6.3 Hz, 6H), 1.23 (d, J = 6.4 Hz, 8H), 1.20 (d, J = 6.4 Hz, 6H). ¹³C NMR (126 MHz, CDCl₃): 132.85 (d), 130.35 (d), 129.88 (d), 128.51 (d), 121.35 (q), 60.00 (d), 59.19 (s), 32.03 (d), 29.85 (s), 23.22 (s), 22.40 (d), 14.80 (s), 14.21 (s). ¹⁹F NMR (470 MHz, CDCl₃): -75.49 (s). ³¹P NMR (202 MHz, CDCl₃): 12.71 (s). ¹⁴N NMR (36 MHz, CDCl₃): δ 980.5 (s), 452.6 (s).

Synthesis of 3f[BPh₄]. A 20 mL scintillation vial was charged with **1** (100 mg, 0.254 mmol, 1 equiv), 3 mL of acetonitrile, and a magnetic stir bar. To this was added a suspension of AgBPh₄ (108 mg, 0.254 mmol, 1 equiv) in 1 mL of DCM. The resultant solution was stirred for 3 h at room temperature, during which time an off-white precipitate formed, and the solution darkened from red-orange to brown. The AgI was removed by filtration through Celite, and the filtrate was once again stirred. To the stirred filtrate was added a solution of PPhMe₂ (70 mg, 0.506 mmol, 2 equiv) in 1 mL of acetonitrile. This solution was stirred at room temperature for 1 h, changing slightly in color from dark brown to dark orange-brown. The solution was dried under reduced pressure, and the residue was rinsed with several small aliquots of diethyl ether. The residue was dried again and

dissolved in a minimal amount of DCM. This concentrated solution was layered with diethyl ether and chilled to $-35\text{ }^{\circ}\text{C}$ overnight, affording bright orange crystals (23.4 mg, 12.7%). Mp: $84\text{ }^{\circ}\text{C}$ (dec.). ^1H NMR (600 MHz, CDCl_3): 7.49 (dt, $J = 6.5, 3.2\text{ Hz}$, 1H), 7.43 (dd, $J = 11.4, 3.6\text{ Hz}$, 1H), 7.31–7.25 (m, 2H), 7.00 (t, $J = 6.1\text{ Hz}$, 9H), 6.86 (s, 4H), 4.81 (dt, $J = 12.7, 6.4\text{ Hz}$, 2H), 3.79 (dt, $J = 12.5, 6.3\text{ Hz}$, 2H), 1.52 (dd, $J = 11.9, 6.3\text{ Hz}$, 13H), 1.39 (d, $J = 10.3\text{ Hz}$, 6H), 1.14 (d, $J = 6.4\text{ Hz}$, 6H), 1.04 (d, $J = 6.3\text{ Hz}$, 6H). ^{13}C NMR (126 MHz, CDCl_3): 164.38 (q), 136.49 (d), 132.16 (d), 130.23 (m), 125.65 (d), 121.80 (d), 59.88 (s), 58.75 (s), 32.06(s), 29.74 (s), 23.48 (s), 23.71 (s), 14.08 (s). ^{31}P NMR (202 MHz, CDCl_3): 13.60 (s). ^{14}N NMR (36 MHz, CDCl_3): 1006.8 (s), 445.9 (s).

Additional Experimental Data for LDP Measurements

Table 2.11 Details from LDP measurements with various X⁻ ligands in CDCl₃.

LDP Measurements CDCl ₃						
Cation	Anion	Experimental Rate	ΔG [‡] (kcal/mol)	ΔH [‡] (kcal/mol)	Standard Deviation	Temp (°C)
3f	PF ₆	0.38	19.90	16.96	0.07	-- ^a
	BArF ₂₄	0.41	19.50	16.60	0.02	49.28
	BArF ₂₀	0.24	19.50	16.64	0.01	43.70
	Al(O ^t BuF ₉) ₄	0.23	19.51	16.66	0.01	43.84
	BPh ₄	0.40	19.47	16.57	0.01	48.44
	SbF ₆	0.16	19.87	16.99	-- ^b	45.86
3a	BArF ₂₄	0.32	19.78	16.86	0.01	51.32
	BPh ₄	0.46	19.64	16.71	0.01	52.77
	SbF ₆	0.11	20.11	17.24	-- ^b	45.86

Table 2.12 Details from LDP measurements with various X⁻ ligands in CD₃CN.

LDP Measurements CD ₃ CN						
Cation	Anion	Experimental Rate	ΔG [‡] (kcal/mol)	Δ [‡] H (kcal/mol)	Standard Deviation	Temp (°C)
3f	PF ₆	0.56	19.46	16.53	0.01	52.01
	BArF ₂₄	0.38	19.47	16.58	0.01	48.02
	BArF ₂₀	0.25	19.47	16.62	0.01	43.92
	Al(O ^t BuF ₉) ₄	0.25	19.47	16.62	0.01	43.84
	BPh ₄	0.46	19.36	16.47	0.01	48.44
	SbF ₆	0.57	19.46	16.53	0.01	52.04
3a	BArF ₂₄	0.38	19.54	16.65	0.03	45.96
	BPh ₄	0.34	19.55	16.66	0.01	48.15
	SbF ₆	0.58	19.59	16.64	0.03	54.31

Table 2.13 Experimentally determined rate of Cr – NⁱPr₂ bond rotation, calculated ΔG^\ddagger , calculated LDP (where $\Delta S^\ddagger = -9$ e.u.), and temperature of measurement.

Phosphine	Compound number	Rate Constant (s ⁻¹)	ΔG^\ddagger (kcal/mol)	LDP (kcal/mol)	Std. Dev.	Temperature (°C)
PMe ₃	3a ^a	0.58	19.59	16.64	0.03	54.31
P ⁿ Bu ₃	3b	0.36	19.69	16.77	0.005	51.13
P ⁱ Pr ₃	3c ^a	0.46	20.14	17.13	0.02	62.90
P ⁱ Bu ₃	3d	0.52	20.19	17.17	0.02	60.72
PCy ₃	3e ^a	0.43	20.32	17.29	0.03	62.96
PPhMe ₂	3f	0.57	19.46	16.53	0.01	52.04
PPh ₂ Me	3g	0.33	18.96	16.16	0.01	34.71
PPhEt ₂	3h	0.45	19.58	16.65	0.02	51.46
PPh ₂ Et	3i	1.16	19.09	16.15	0.02	53.62
PPh ₂ ⁿ Bu	3j	0.4	19.16	16.31	0.008	43.71
PPh ₂ Cy	3k	1.01	19.41	16.43	0.02	57.36
PPhCy ₂	3l	0.54	19.26	16.37	0.02	48.25
P(OEt) ₃	3m ^a	0.48	18.5	15.73	0.02	34.88
P(O ⁱ Pr) ₃	3n ^a	1.15	18.81	15.91	0.04	48.82
P(NC ₄ H ₈) ₃	3o	0.68	19.1 ^b	16.21	0.05	— ^b
PPh ₃	3p	0.65	19.13	16.24 (15.95) ^c	0.03	48.10
NCCH ₃	2	1.02	17.95	15.19	0.01	33.33

^aLDP value in CD₃CN was measured via *in situ* generated species stabilized with excess phosphine. ^bMeasured LDP was taken in multiple trials, taking a single measurement on three different samples due to compound instability. As a result, three different temperatures were calibrated, one for each separate run. The reported ΔG^\ddagger is approximate, as it is an average from 3 (close) temperatures. However, the LDP, ΔH^\ddagger , for each run was fully calculated with the calibrated temperature for that run, before an average was taken of the final LDP values. ^cThe LDP value for PPh₃ was measured in CDCl₃, as the chromium complex with PPh₃ is completely unstable in CD₃CN. The value reported in parenthesis is the model predicted LDP value (CD₃CN).

DOSY Experiments:

General Considerations The Varian Dbppste_cc (DOSY bipolar pulse pair simulated spin echo convection corrected) pulse sequence was utilized for all experiments except for the ^{19}F DOSY measurements of the $\mathbf{3f}[\text{BArF}_{20}]$ salt. For this complex, the large chemical shift range led to phasing and modulation issues under the normal Dbppste_cc strategy. As a result, an alternate experiment was developed by adapting the Oneshot_CHORUS pulse sequence developed by Morris, et. al.⁶² This experiment was utilized in order to obtain reliable ^{19}F DOSY data without suffering from the limited bandwidth of excitation of standard DOSY experiments.

All spectra were multiplied by weighted exponential of 10 Hz and baseline corrected before applying DOSY Processing. Standard DOSY processing as supplied by the vendor was used based on peak heights and with compensation for non-uniform gradients.

Convection Effects Due to the need to compare each compound via two different nuclei, two separate DOSY experiments were run for each compound (except $\mathbf{3f}[\text{BPh}_4]$, $\mathbf{3a}[\text{BPh}_4]$, and $\mathbf{3a}[\text{BArF}_{24}]$). The parameter differences between the ^1H and ^{19}F DOSY experiments for a given compound (relaxation delay, acquisition time, gradient length, diffusion delay, etc.) gave rise to inconsistencies in data. These inconsistencies were traced back to convection differences between successive experiments. By running convection corrected pulse sequences and including internal standards in each experiment, the convection effects have been eliminated, such that multiple trials of the same compound provide diffusion coefficients within experimental error.

The internal standard for all experiments was chosen based on the simplicity of its resonance in both ^1H and ^{19}F NMR (one sharp singlet by each method), and the uniqueness of the resonances relative to the resonances of the chromium complexes. For these purposes, 1,3,5-tris(trifluoromethyl)benzene was utilized as the internal standard. The diffusion coefficients

measured are presented as ratios to the internal standard's diffusion coefficient from the same experiment. This ratio can then be used to compare the diffusion rate of the anion and cation for a chromium complex without the complication of convection differences between experiments.

As a result of the much more complex pulse sequence required by the **3f**[BArF₂₀] complex to obtain DOSY signal, convection correction in the pulse sequence was not feasible. As a result, the experiment was run at 18 °C in CDCl₃, and utilizing a capillary tube for both solvents (as capillary tubes have been shown to reduce the effects of convection substantially compared to a standard 5 mm NMR tube).² Consistent diffusion values were verified by ¹H NMR of the compound running the non-convection-corrected experiment under the same conditions, allowing for the ¹⁹F measurement to continue with minimal residual convection effects anticipated.

Table 2.14 Molecular volumes calculated for various cations and anions from crystal structures using Olex Software.

OLEX Molecular Volume (Å ³)	
326	3f
301	3a
68	PF ₆ ⁻
293	BPh ₄ ⁻
564	BArF ₂₄ ⁻
536	Al(O ^t BuF ₆) ₄ ⁻
411	BArF ₂₀ ⁻

Molecular Weight Calibration Following literature methods, the molecular weight of **3f**[PF₆] was probed using DOSY techniques. The internal molecular weight standards chosen for the experiment included diethyl ether, ferrocene, and tetrakis(trimethylsilyl)silane. The experiments were performed utilizing a capillary tube (2 mm) to further reduce any convection errors in the experiments and improve accuracy.

Table 2.15 Experimental data from DOSY molecular weight calibrations with **3f**[PF₆].

	Compound	MW (g/mol)	Diffusion Coefficient (m²/s *10⁻¹⁰)	Error	log MW	log D
0.025 M CD ₃ CN	Diethyl Ether	74.12	37.64	0.09	1.869935	1.57565
	Ferrocene	180.04	25.83	0.07	2.255369	1.412124
	TMS ₄ Si	320.84	18.24	0.05	2.506289	1.261025
	Cr-fragment	542	14.47	0.04	2.734353	1.160469
0.1 M CD ₃ CN	Diethyl Ether	74.12	38.18	0.09	1.869935	1.581836
	Ferrocene	180.04	25.73	0.07	2.255369	1.41044
	TMS ₄ Si	320.84	18.45	0.05	2.506289	1.265996
	Cr-fragment	525	14.745	0.04	2.720234	1.168645
0.01M CD ₃ CN	Diethyl Ether	74.12	37.12	0.09	1.869935	1.569608
	Ferrocene	180.04	26.62	0.07	2.255369	1.425208
	TMS ₄ Si	320.84	19.59	0.05	2.506289	1.292034
	Cr-fragment	578	15.54	0.04	2.761599	1.191451
0.025 M CDCl ₃	Diethyl Ether	74.12	25.35	0.75	1.869935	1.403978
	Ferrocene	180.04	18.79	0.51	2.255369	1.273927
	TMS ₄ Si	320.84	14.33	0.54	2.506289	1.156246
	Cr-fragment	694	10.93	0.53	2.841356	1.03862
0.025 M C ₆ D ₅ Cl	Diethyl Ether	74.12	19.21	0.09	1.869935	1.283527
	Ferrocene	180.04	11.83	0.07	2.255369	1.072985
	TMS ₄ Si	320.84	8.46	0.05	2.506289	0.92737
	Cr-fragment	628	5.84	0.04	2.797865	0.766413
0.025 M CD ₃ CN (45 °C)	CD ₃ CN residual	44.07	59.12	0.09	1.644143	1.771734
	Ferrocene	180.04	34.15	0.07	2.255369	1.533391
	TMS ₄ Si	320.84	24.24	0.05	2.506289	1.384533
	Cr-fragment	579	19.425	0.04	2.762472	1.288361

ROESY Experiments with 3a[BArF₂₄] and 3a[BPh₄] A Varian Inova 600 spectrometer equipped a 5 mm pulse-field-gradient (PFG) switchable broadband HCN probe, operated at 25 °C. The ROESY spectra were acquired with a spectral width of 9596 Hz in both F2 and F1. The preacquisition delay was set to 2 s. The mixing time was 0.35 ms. A total of 256 increments with 64 transients per increment were collected, containing 2878 data points. Linear prediction to 512 data points was applied to F1 prior to 2D processing. Gaussian multiplication was applied to both F1 and F2 dimensions.

For both complexes examined by ROESY NMR(**3a**[BArF₂₄]⁻ and **3a**[BPh₄]⁻), it appears that in CDCl₃ there are small correlation peaks between the aromatic protons of the anion (BArF₂₄⁻ and BPh₄⁻) and the aliphatic peaks of the phosphine and diisopropylamido methyl groups. This suggests that in a non-polar solvent, the anion is sufficiently close to the cation in solution to allow for observable NOE signal (~7Å). Such behavior supports the analysis of ion pairing in CDCl₃, which was by DOSY and LDP analysis.

The results in CD₃CN for the two complexes show no observable correlation peaks under the same experimental regime as applied to the samples in CDCl₃. While lack of signal is not a positive identifier, there is no evidence of ion pairing between the chromium fragment and the counterion. This also agrees with DOSY and LDP analyses for the compounds. The **3a**[BArF₂₄] results are shown in above in the text. The spectra of **3a**[BPh₄] are shown below.

{2}BPh₄ ROESY CDCl₃

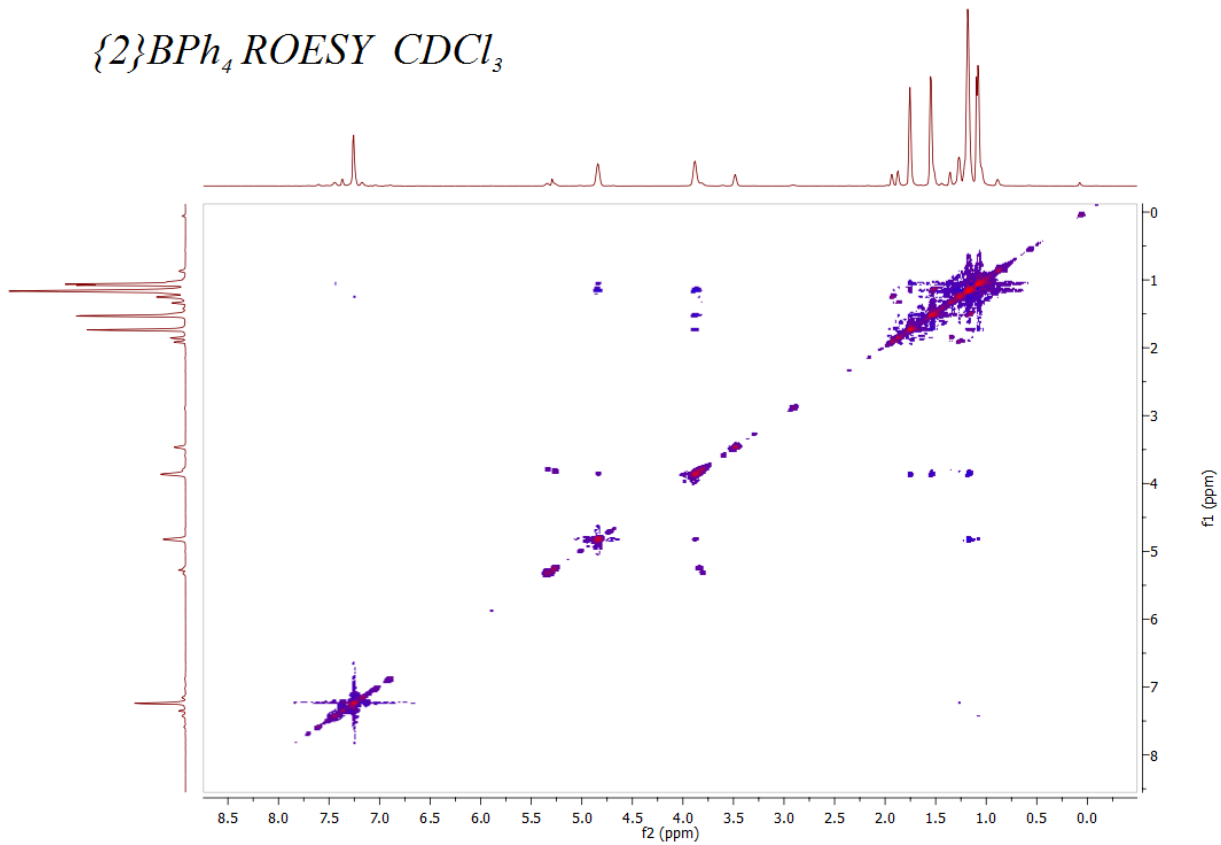


Figure 2.12 ¹H ROESY NMR Spectrum of **3a**[BPh₄] in CDCl₃.

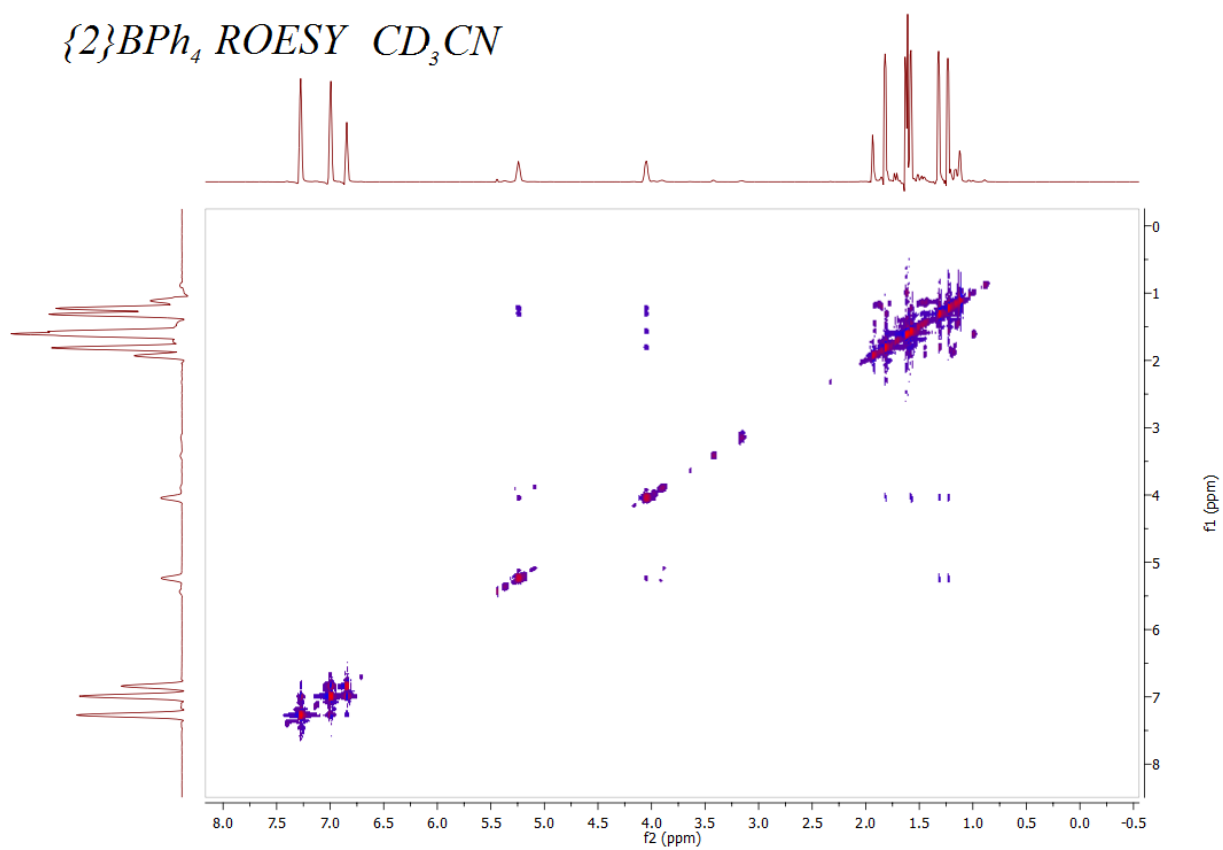


Figure 2.13 ¹H ROESY NMR Spectrum of **3a**[BPh₄] in CD₃CN.

Experimental Determinations of ΔS^\ddagger

General Considerations for Measuring ΔS^\ddagger Experimental measurements of entropy with the LDP system have previously been conducted by two different methods.¹ In this study, due to the temperatures at which measurement occurs, it was most practical to utilize the determination of the rate of $-N^iPr_2$ by Spin Saturation Transfer 1H NMR, over a range of temperatures, and then use the Eyring equation to determine the ΔS^\ddagger by monitoring change in ΔG^\ddagger as a function of temperature (K). Experimentally, this consists of performing the Spin Saturation Transfer 1H NMR experiment at 4 or more different temperatures, and plotting $\ln(k_{obs}/T)$ vs. $1/T$, where k_{obs} is the experimental rate of amide rotation and T is temperature in K. The parameters $\sim\Delta H^\ddagger$ and ΔS^\ddagger were then derived from the slope and intercept of the Eyring plots, respectively. Standard treatment of the data was used to approximate errors in these values, which were relatively small for the series of measurements presented here.²

The values determined in CD_3CN for the **3f**, **3j**, and **3m** salts of SbF_6^- were the complexes that could be measured accessible temperature range over which the SST measurement could be performed. At low temperatures, the amide rotation is too slow to observe the rate accurately, while at higher temperatures, the samples thermally decompose in solution during the measurement. Similar issues were faced with the **3a-o** salts with $BArF_{24}^-$ as the anion. Lower limits of rotation, thermal instability, and the low boiling point of the NMR solvent ($CDCl_3$) all limited the accessible experimental temperature range for these derivatives.

Table 2.16 Experimentally measured rate of rotation and calculated ΔG^\ddagger for **1** determined across several different temperatures in CD₃CN.

Temp (K)	k (s ⁻¹)	ΔG^\ddagger
281.93	0.0225	18.60
	0.0235	18.57
	0.0230	18.58
289.49	0.0528	18.62
	0.0533	18.61
	0.0539	18.61
296.05	0.1098	18.62
	0.1120	18.61
	0.1135	18.60
302.45	0.2289	18.60
	0.2227	18.61
	0.2282	18.60
308.99	0.3920	18.68
	0.3863	18.69
	0.3879	18.69
315.32	0.8478	18.59
	0.8615	18.58
	0.8332	18.61
318.65	1.0545	18.66
	1.0398	18.67
	1.0444	18.67
323.14	1.7011	18.62
	1.6799	18.63
	1.6618	18.64

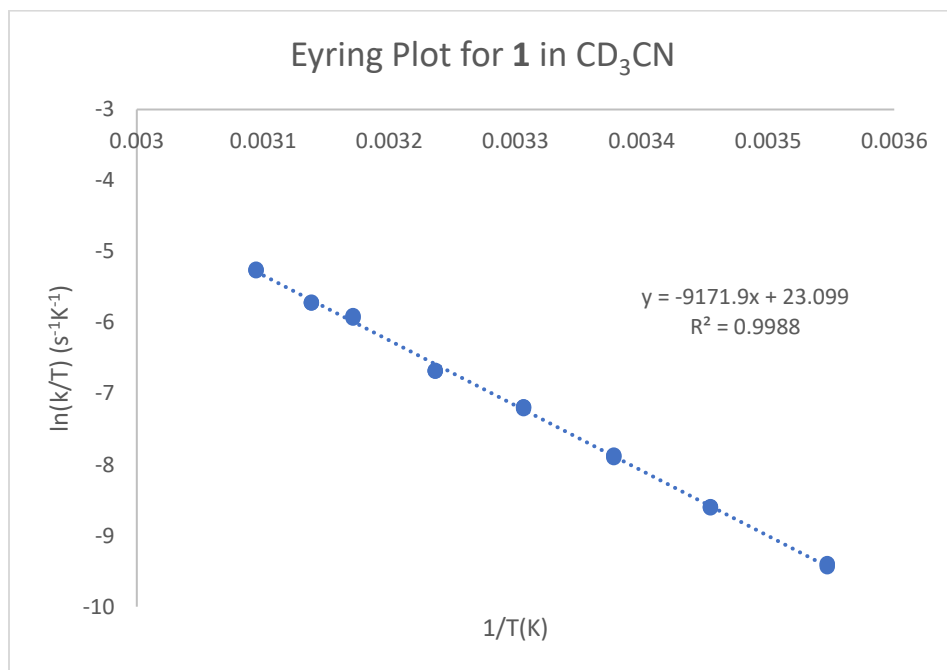


Figure 2.14 The Eyring plot for SST measurements of **1** in CD₃CN.

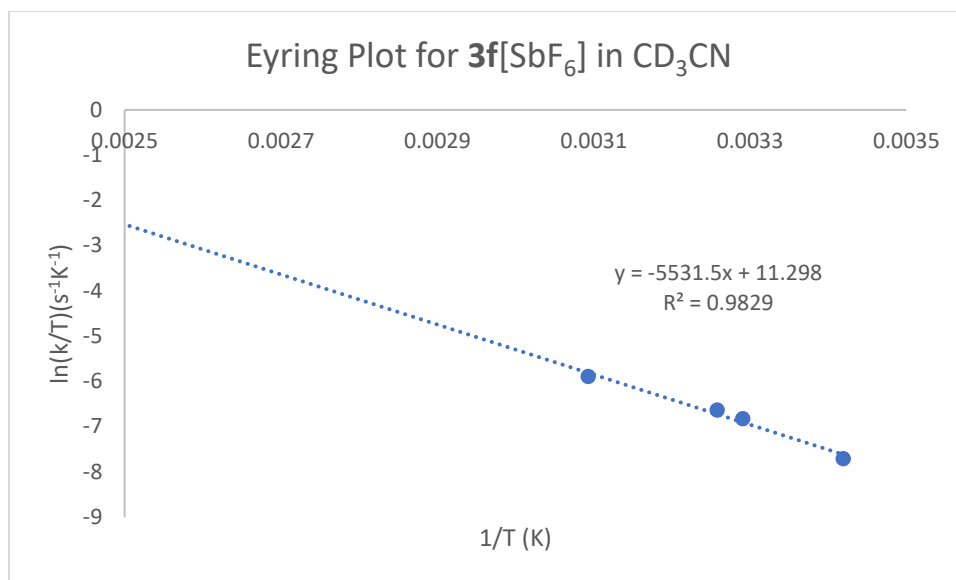


Figure 2.15 Eyring plot used for determining the ΔS^\ddagger value of Cr – NiPr₂ bond rotation in $3f[SbF_6]$.

Table 2.17 Various temperature measurements made to determine ΔS^\ddagger from experimental ΔG^\ddagger values for $3f[SbF_6]$.

	T	k	ΔG^\ddagger	1/T	ln(k/T)
1	306.91	0.39765	18.54415	0.003258	-6.63454
2	303.87	0.333047	18.4615	0.003291	-6.8276
3	292.46	0.131258	18.28714	0.003419	-7.70892
4	323.29	0.912213	19.0339	0.003093	-5.88755
Avg	306.6325				

Table 2.18 Experimentally determined rate of Cr – NⁱPr₂ bond rotation and the calculated $\Delta G^\ddagger/H/S^\ddagger$.

Phosphine	Compound No.	Temp (K)	k _{obs} (s ⁻¹)	$\sim\Delta H^\ddagger$ (kcal/mol)	ΔS^\ddagger (e.u.)	ΔG^\ddagger (kcal/mol)
PPhMe ₂	3f	325.21	0.5585	17.90	-4.76	19.47
		315.33	0.2395			19.39
		339.07	2.0544			19.44
		303.40	0.0728			19.35
PPh ₂ ⁿ Bu	3j	306.91	0.3977	10.99	-24.68	18.53
		303.87	0.3330			18.47
		292.46	0.1313			18.30
		323.29	0.9122			19.04
P(OEt) ₃	3m	308.08	0.4840	6.76	-37.88	18.50
		299.79	0.3800			18.13
		291.51	0.22410			17.92
		283.45	0.1762			17.54

Table 2.19 Experimentally determined rate of rotation (k_{obs}) for the Cr – NⁱPr₂ bond in **3a-p** salts with BArF₂₄⁻ anion in CDCl₃.

Phosphine	Compound No.	Temp (K)	k_{obs} (s ⁻¹)	$\sim\Delta H^\ddagger$ (kcal/mol)	ΔS^\ddagger (e.u.)	ΔG^\ddagger (kcal/mol)
PMe ₃	3a	306.72	0.0546	18.71	-3.38	19.74
		314.28	0.1112			19.80
		321.75	0.2339			19.81
		331.44	0.5776			19.83
P ⁿ Bu ₃	3b	316.58	0.1385	18.91	-2.83	19.81
		323.91	0.2928			19.80
		328.85	0.4429			19.84
		331.50	0.5650			19.85
P ⁱ Bu ₃	3c	311.08	0.1229	17.76	-5.66	19.53
		317.52	0.2324			19.55
		325.68	0.4635			19.62
		332.79	0.8692			19.64
P ⁱ Pr ₃	3d	321.19	0.0831	19.48	-2.95	20.44
		325.46	0.1305			20.42
		330.03	0.1965			20.45
		333.42	0.2657			20.47
PPhMe ₂	3f	306.87	0.0862	18.79	-2.13	19.47
		313.81	0.1725			19.50
		321.80	0.3916			19.48
		329.32	0.7432			19.54
PPh ₂ Me	3g	309.76	0.3302	16.29	-8.22	18.84
		321.19	0.8478			18.95
		325.46	1.2066			18.99
		330.03	1.8105			18.99
PPhEt ₂	3h	306.80	0.1828	16.96	-6.66	19.01
		314.15	0.3635			19.05
		321.99	0.6844			19.14
		327.88	1.1946			19.14
PPh ₂ Et	3i	306.94	0.1340	17.97	-3.99	19.21
		314.10	0.2757			19.22
		321.78	0.5657			19.25
		329.55	1.0834			19.30
PPh ₂ ⁿ Bu	3j	302.66	0.08587	18.18	-3.38	19.20
		310.09	0.1818			19.22
		316.58	0.3413			19.24
		323.91	0.6663			19.27

Table 2.19 (cont'd)

PPh ₂ Cy	3k	312.26	0.0879	18.11	-5.54	19.81
		321.05	0.1753			19.95
		328.85	0.3896			19.93
		331.50	0.5007			19.93
P(OEt) ₃	3m	298.42	0.1010	16.98	-6.13	18.83
		308.83	0.2896			18.86
		319.22	0.7419			18.92
		329.60	1.6656			19.02
P(O ⁱ Pr) ₃	3n	311.08	0.2987	17.12	-6.03	18.98
		317.52	0.5025			19.06
		325.68	1.0674			19.08
		332.79	1.9091			19.12
P(NC ₄ H ₈) ₃	3o	306.80	0.0599	19.52	-0.52	19.69
		314.15	0.1387			19.65
		321.99	0.2852			19.70
		327.88	0.5127			19.69
PPh ₃	3p	306.87	0.1139	18.00	-4.13	19.30
		313.81	0.2493			19.27
		321.80	0.4866			19.35
		329.32	0.9393			19.38

X-ray Crystallography

All crystal structures have been deposited with the Cambridge Structural Database. The following CCDC numbers have been assigned to the structures referenced in this work 1552070-84 (**2** and **3b-3e** and **3g-3p**), 1544906-10 (**3a** and **3f** salts with various X^-).

NMR Spectra of 2 and 3a-3

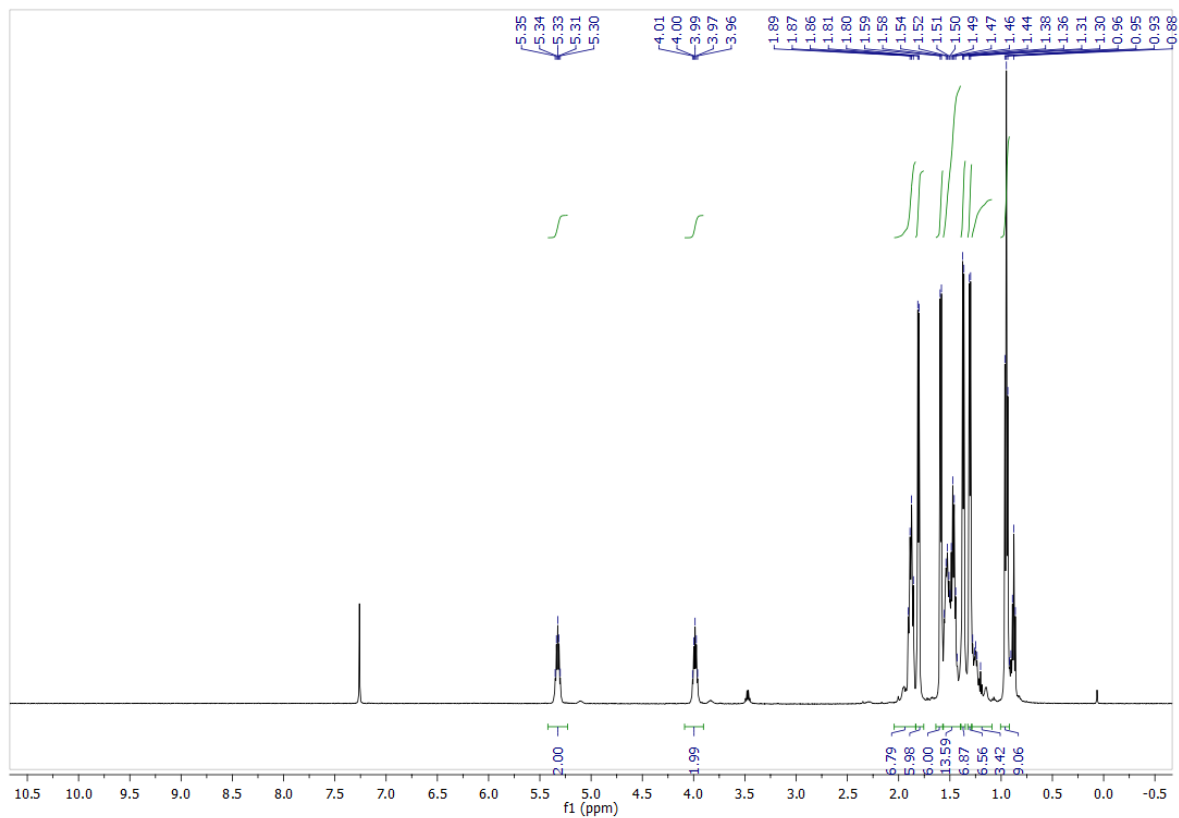


Figure 2.16 ^1H NMR of $3\text{b}[\text{SbF}_6]$ in CDCl_3 .

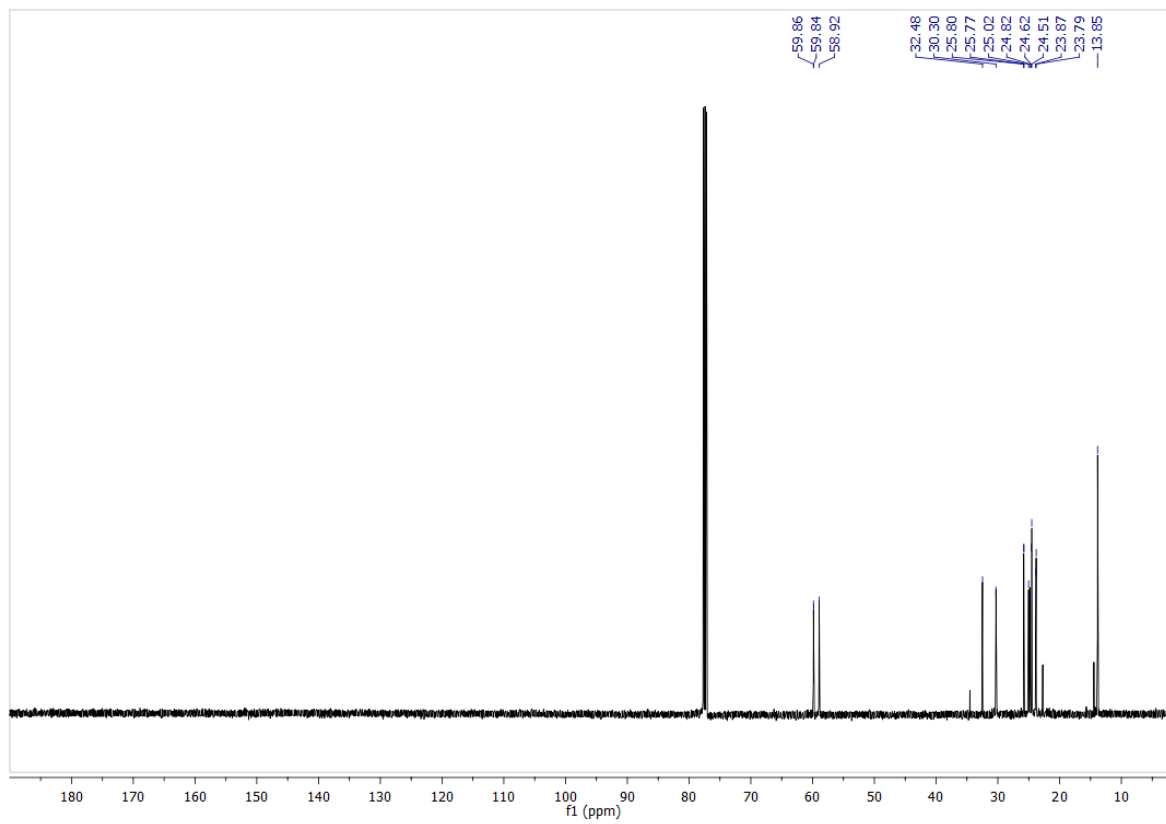


Figure 2.17 ^{13}C NMR of $\mathbf{3b}[\text{SbF}_6]$ in CDCl_3 .

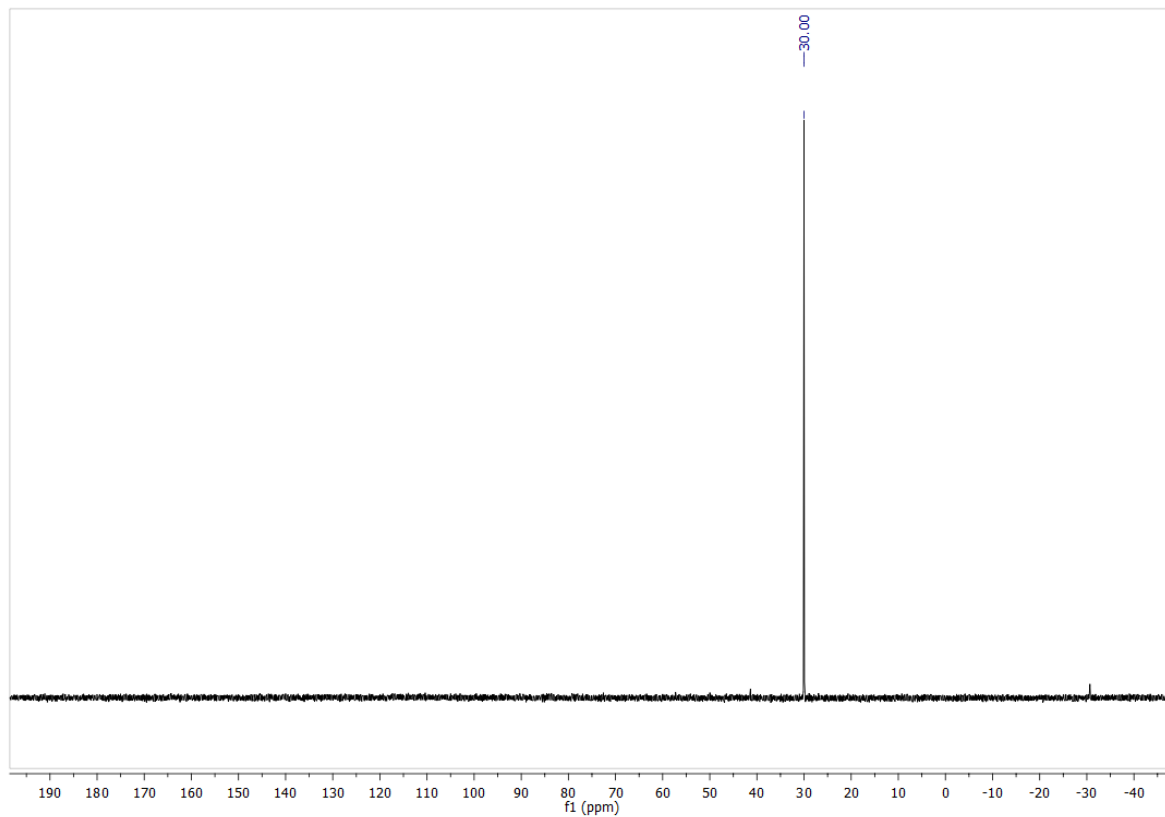


Figure 2.18 ^{31}P NMR of **3b**[SbF_6] in CDCl_3 .

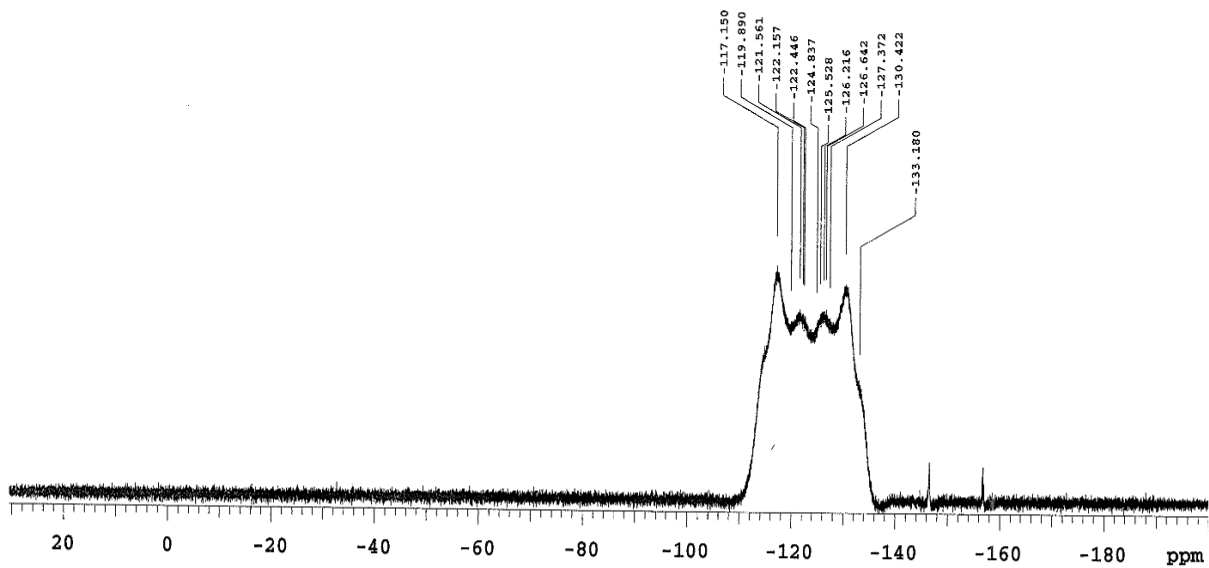


Figure 2.19 ^{19}F NMR of $3\text{b}[\text{SbF}_6]$ in CDCl_3 .

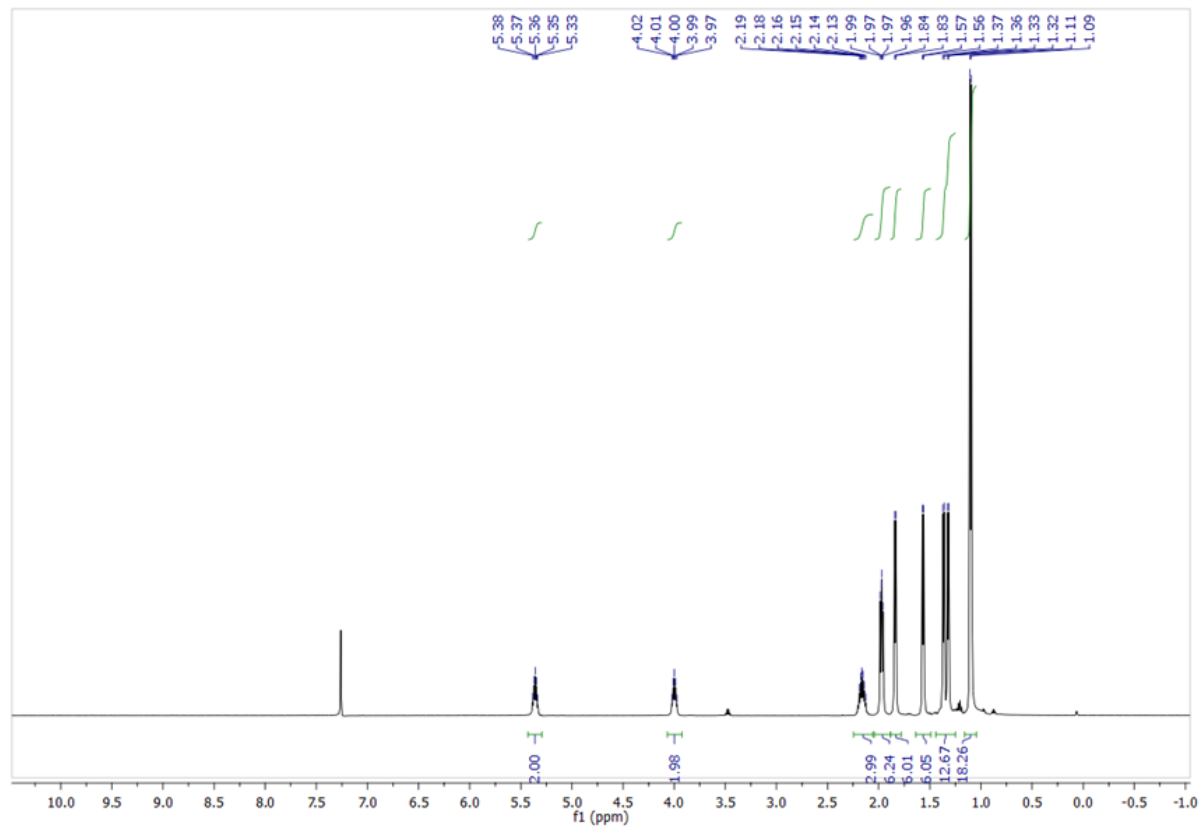


Figure 2.20 ^1H NMR of $3\text{c}[\text{SbF}_6]$ in CDCl_3 .

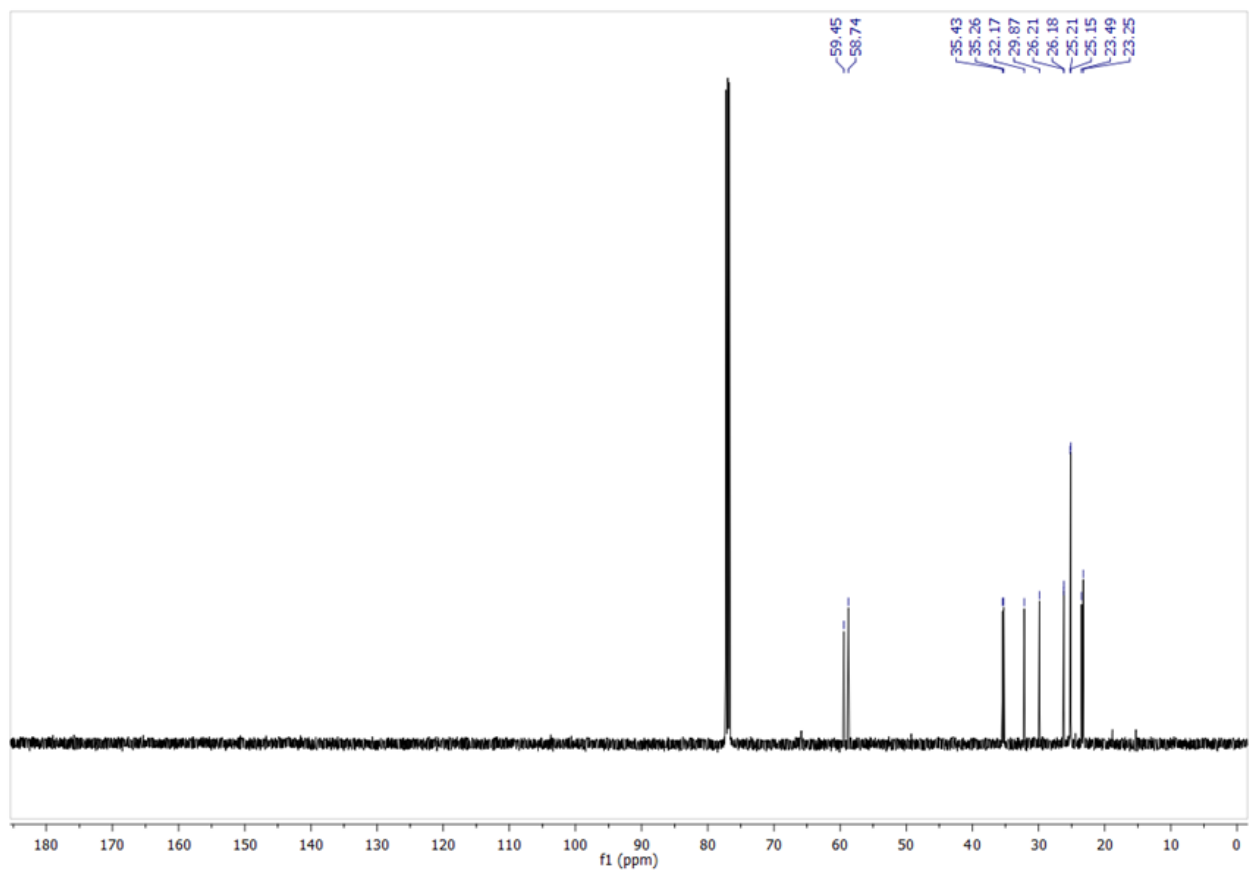


Figure 2.21 ^{13}C NMR of $3\text{c}[\text{SbF}_6]$ in CDCl_3 .

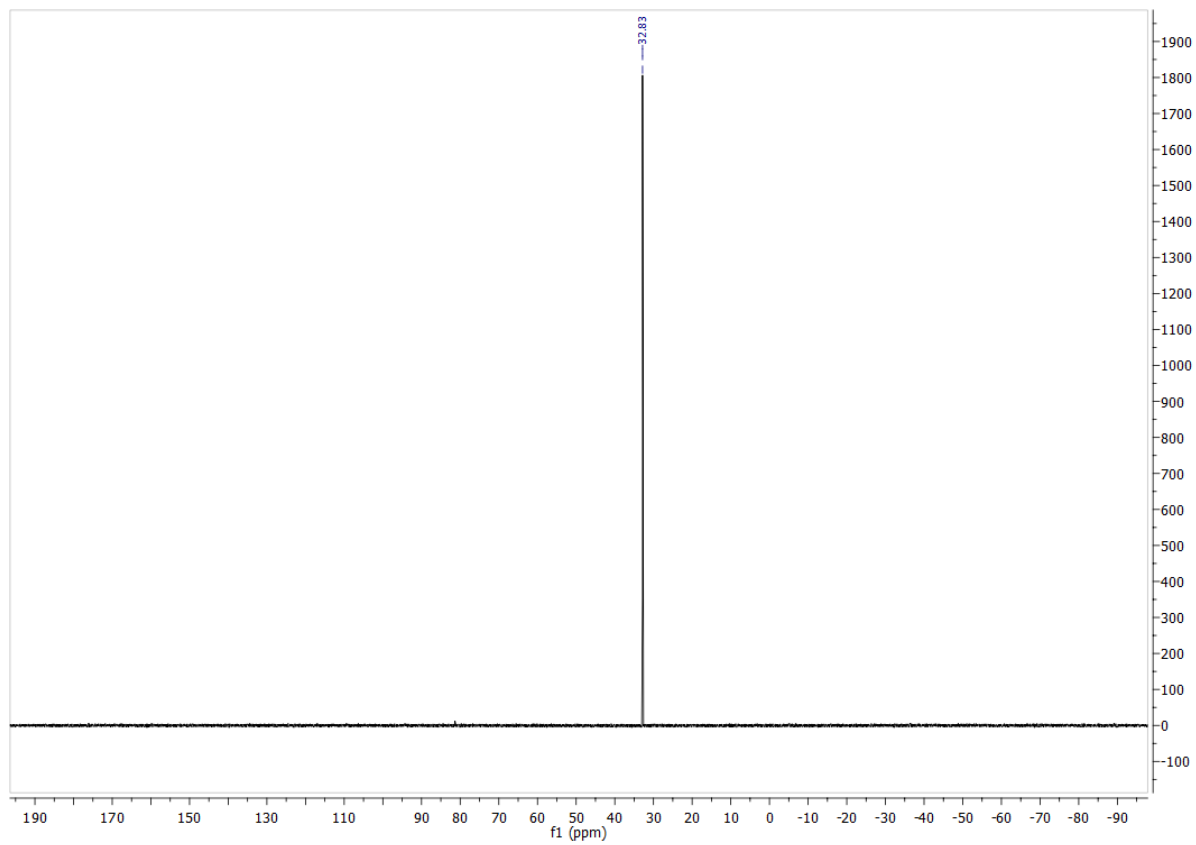


Figure 2.22 ^{31}P NMR of $3\text{c}[\text{SbF}_6]$ in CDCl_3 .

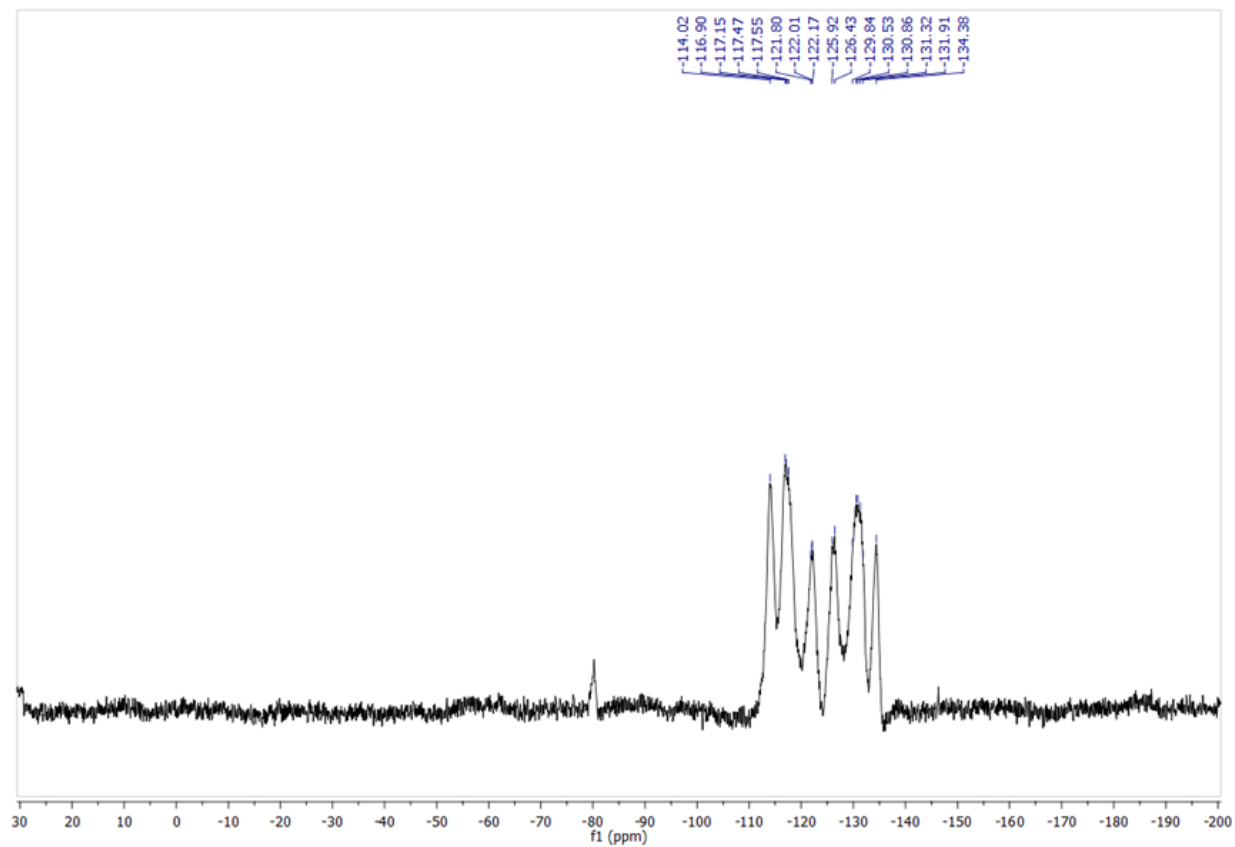


Figure 2.23 ^{19}F of $3\text{c}[\text{SbF}_6]$ in CDCl_3 .

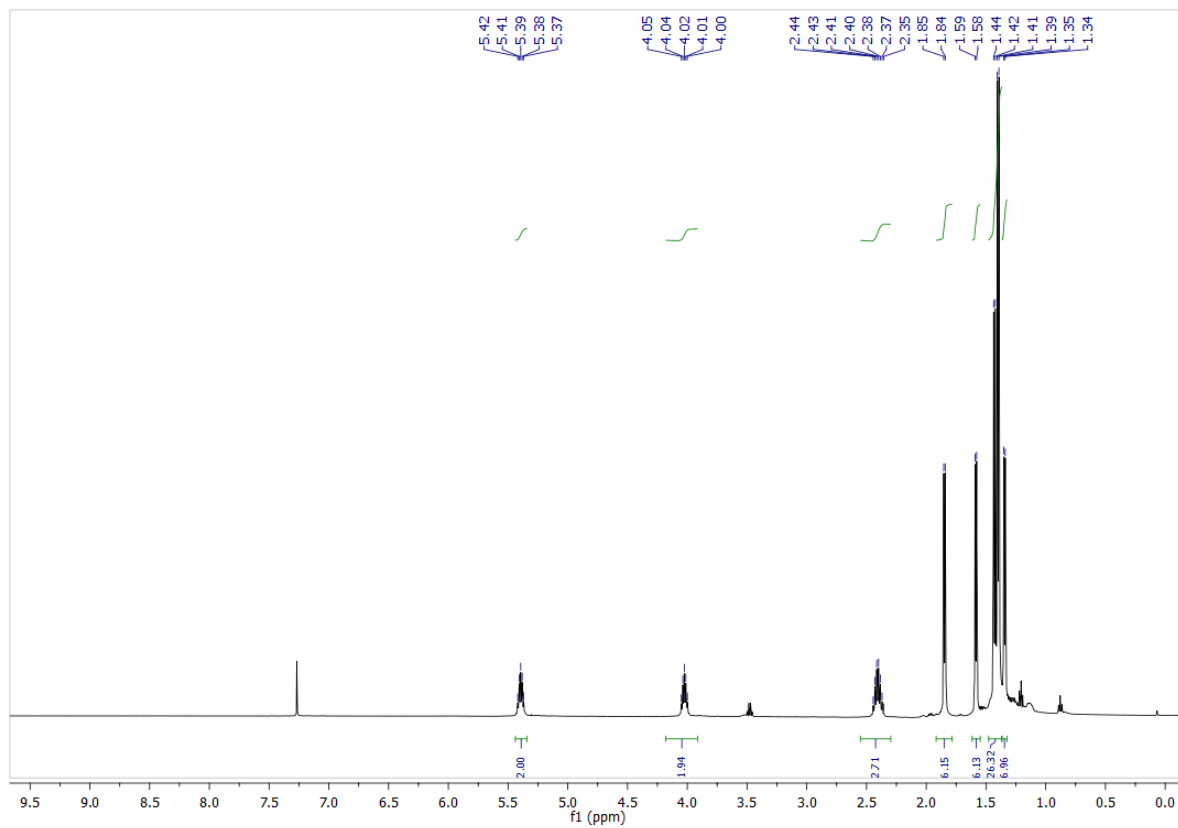


Figure 2.24 ^1H NMR of $3\text{d}[\text{SbF}_6]$ in CDCl_3 .

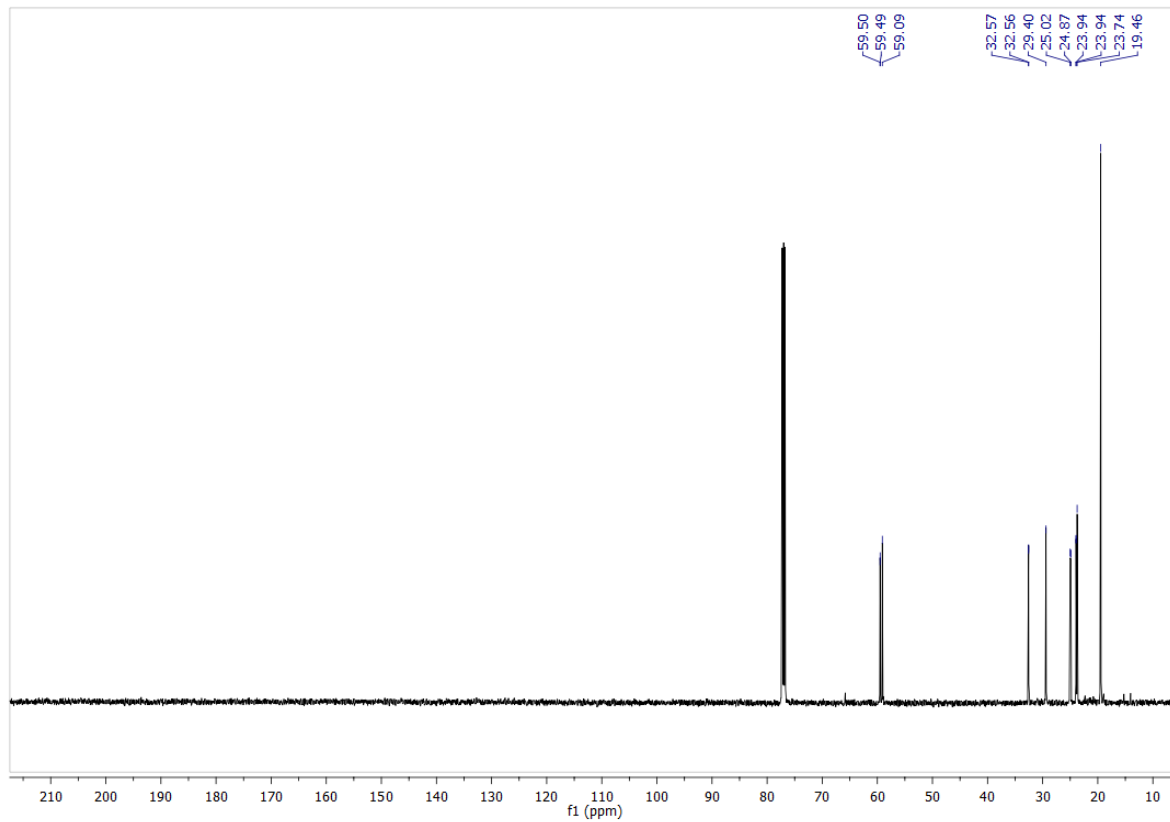


Figure 2.25 ^{13}C NMR of **3d**[SbF₆] in CDCl₃.

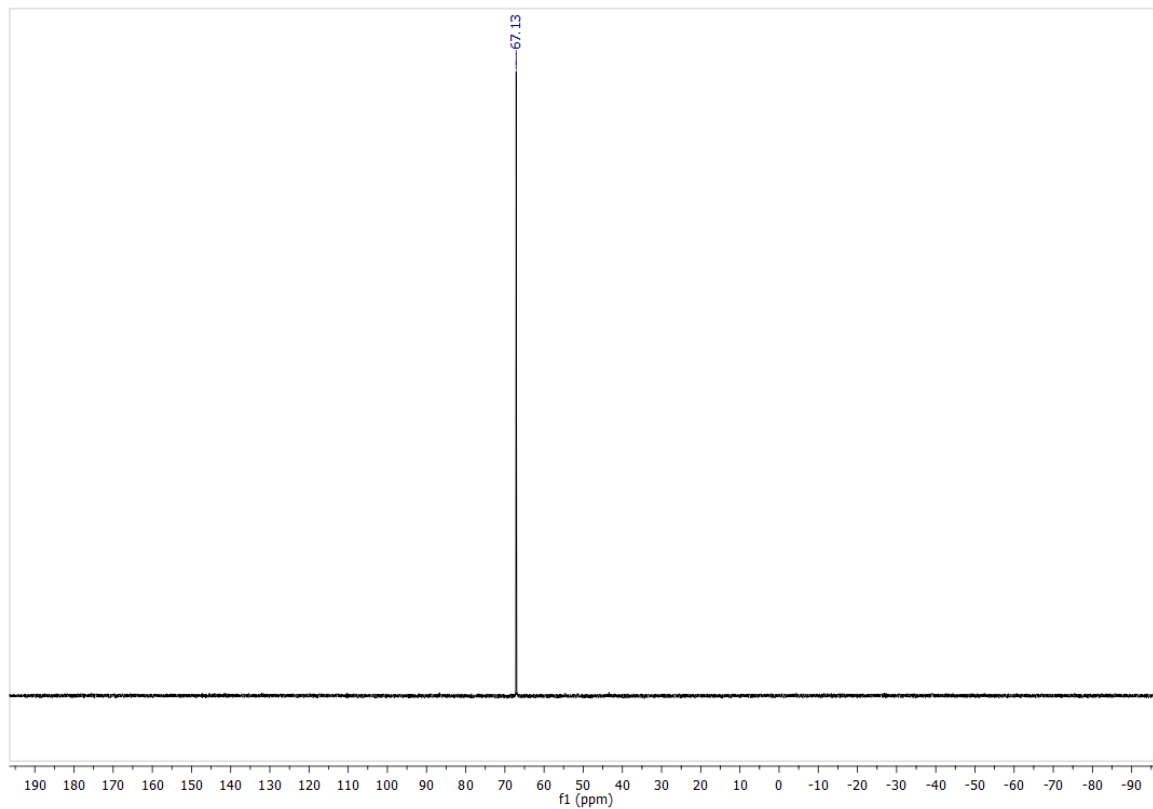


Figure 2.26 ^{31}P NMR of **3d**[SbF₆] in CDCl₃.

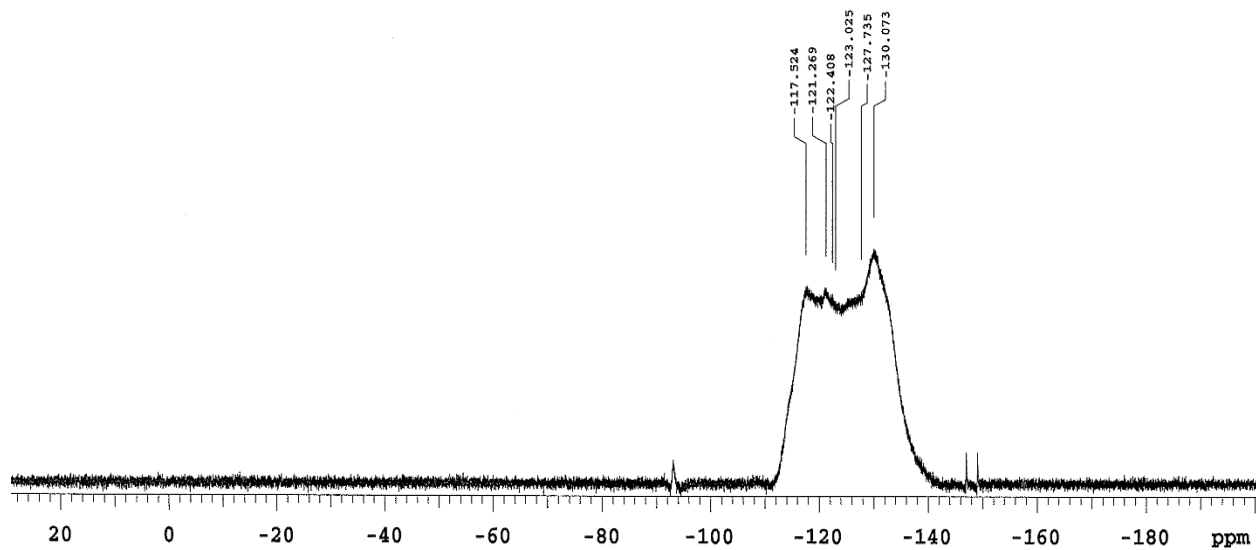


Figure 2.27 ^{19}F NMR of $3\text{d}[\text{SbF}_6]$ in CDCl_3 .

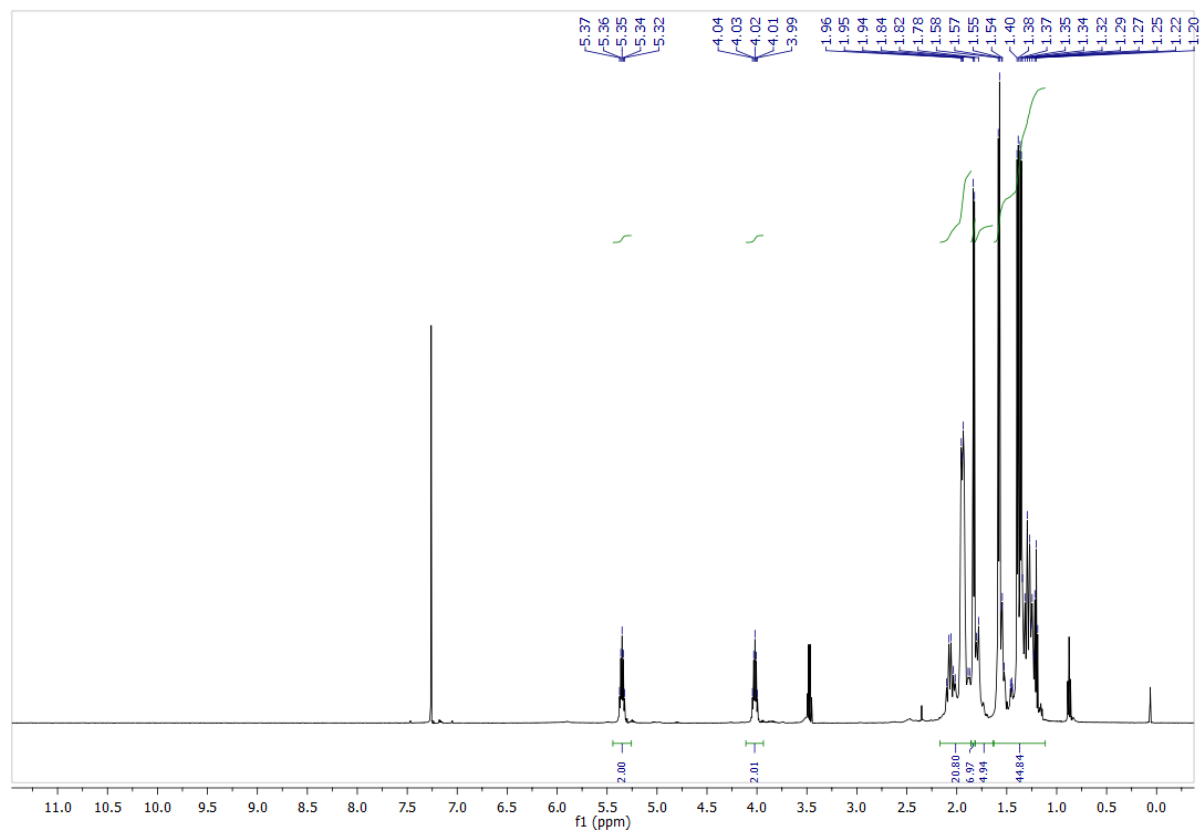


Figure 2.28 ^1H NMR of $3\text{e}[\text{SbF}_6]$ in CDCl_3 .

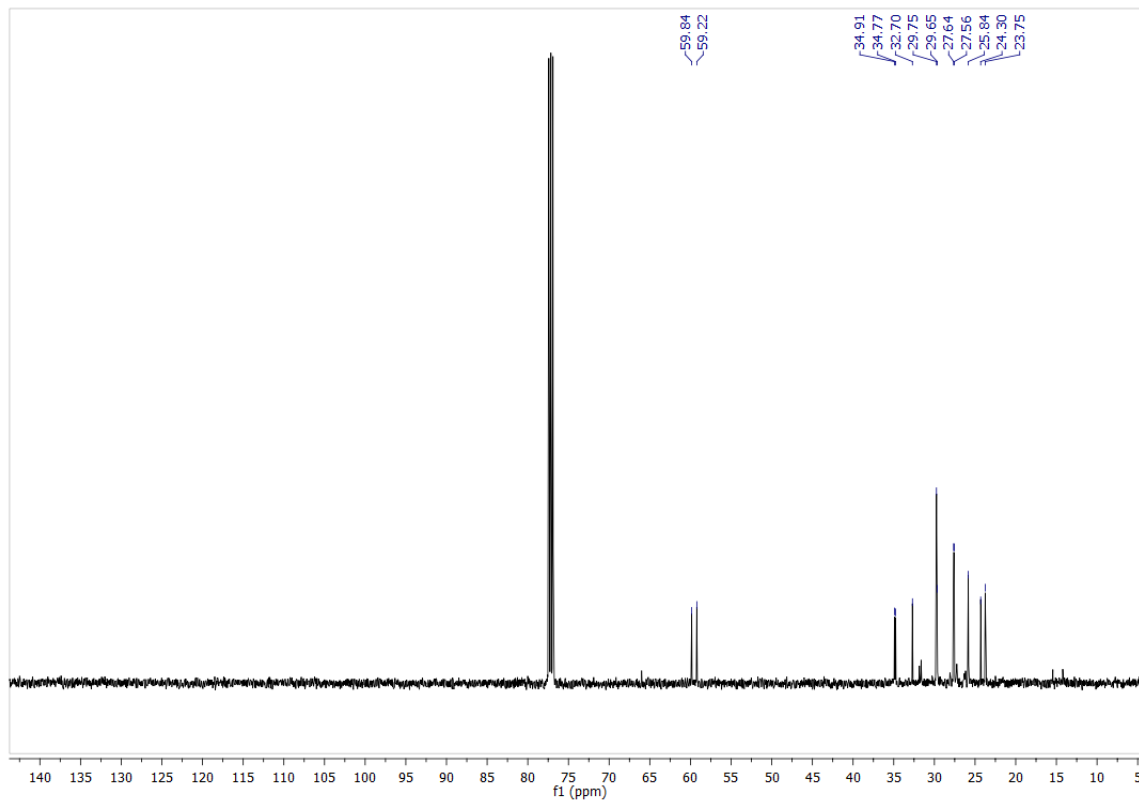


Figure 2.29 ^{13}C NMR of $3\text{e}[\text{SbF}_6]$ in CDCl_3 .

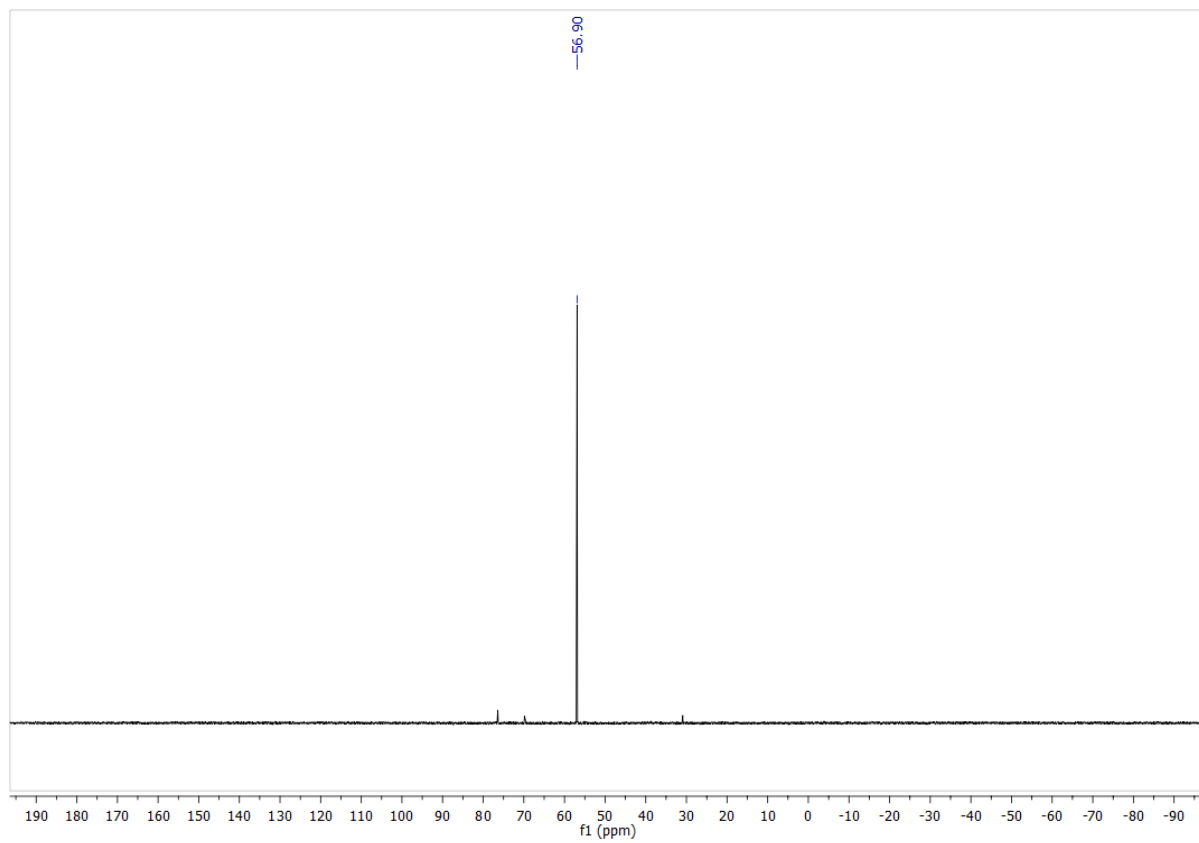


Figure 2.30 ^{31}P NMR of $3\mathbf{e}[\text{SbF}_6]$ in CDCl_3 .

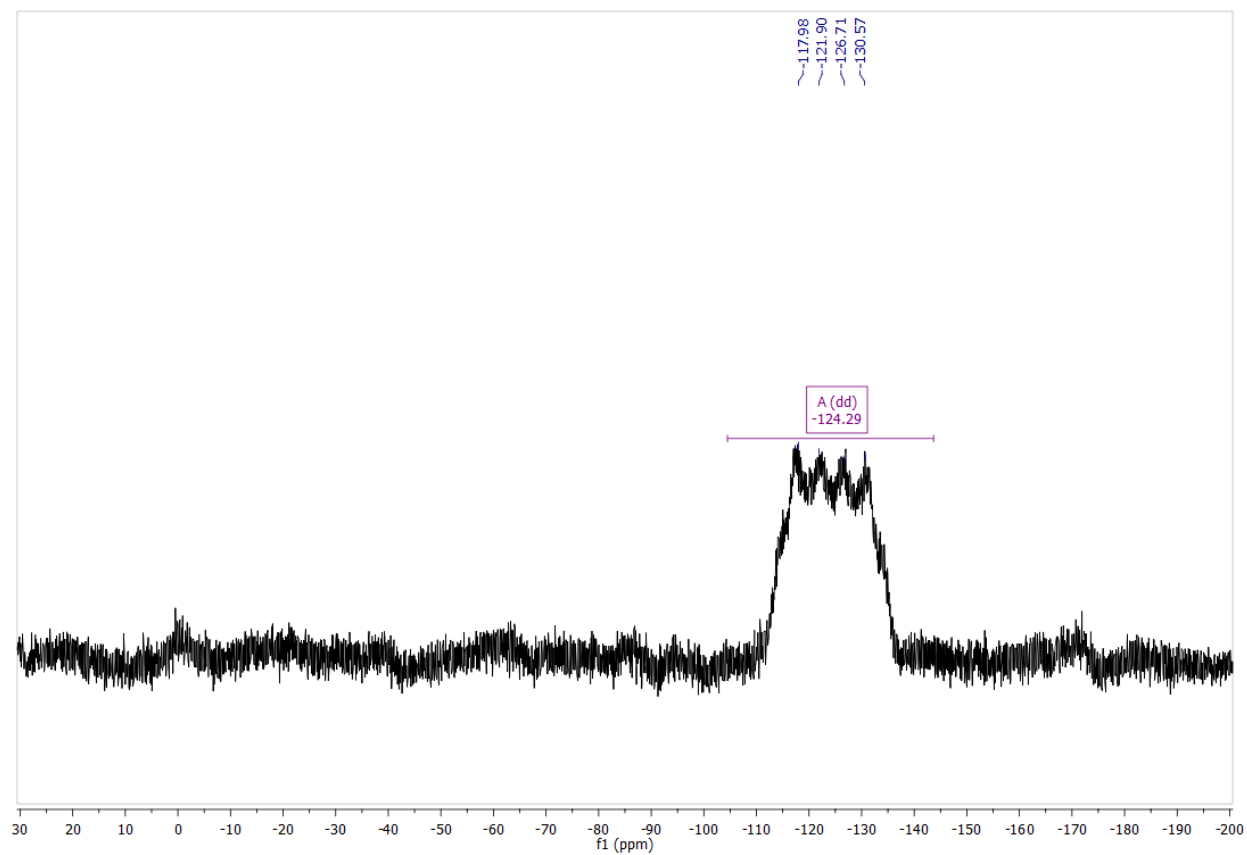


Figure 2.31 ^{19}F NMR of $3\text{e}[\text{SbF}_6]$ in CDCl_3 .

$\{\text{NCr}(\text{N}^i\text{Pr}_2)_2\text{PCy}_3\}\text{SbF}_6$ CDCl_3 ^{14}N NMR

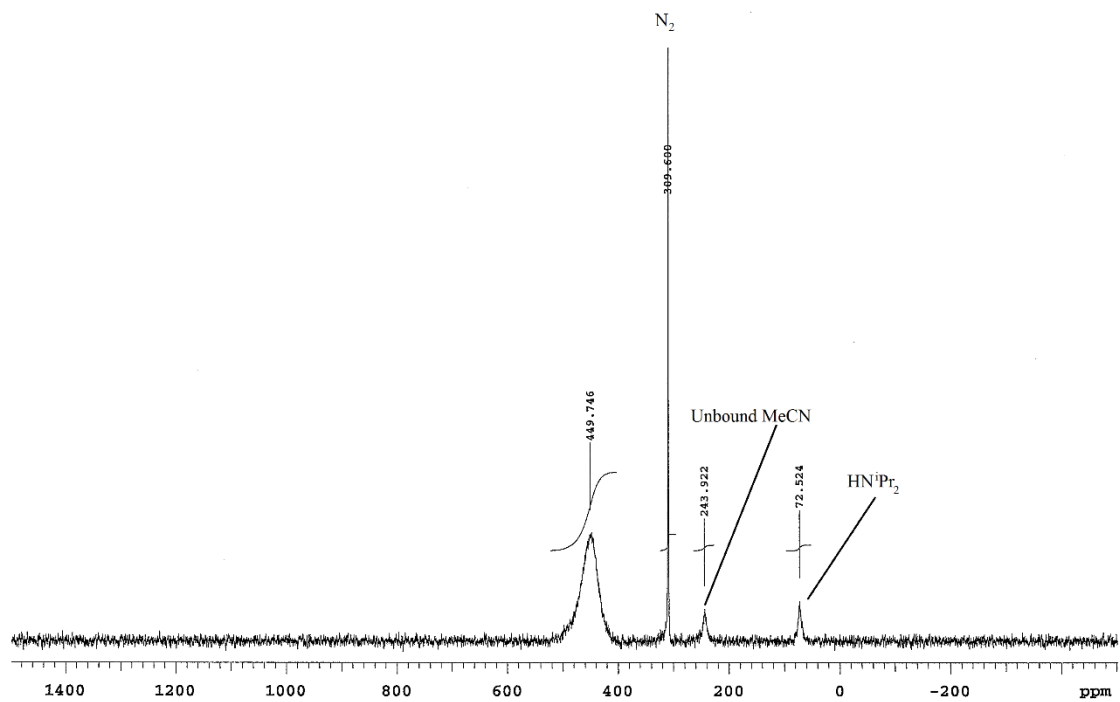


Figure 2.32 ^{14}N NMR of $\mathbf{3e}[\text{SbF}_6]$ in CDCl_3 .

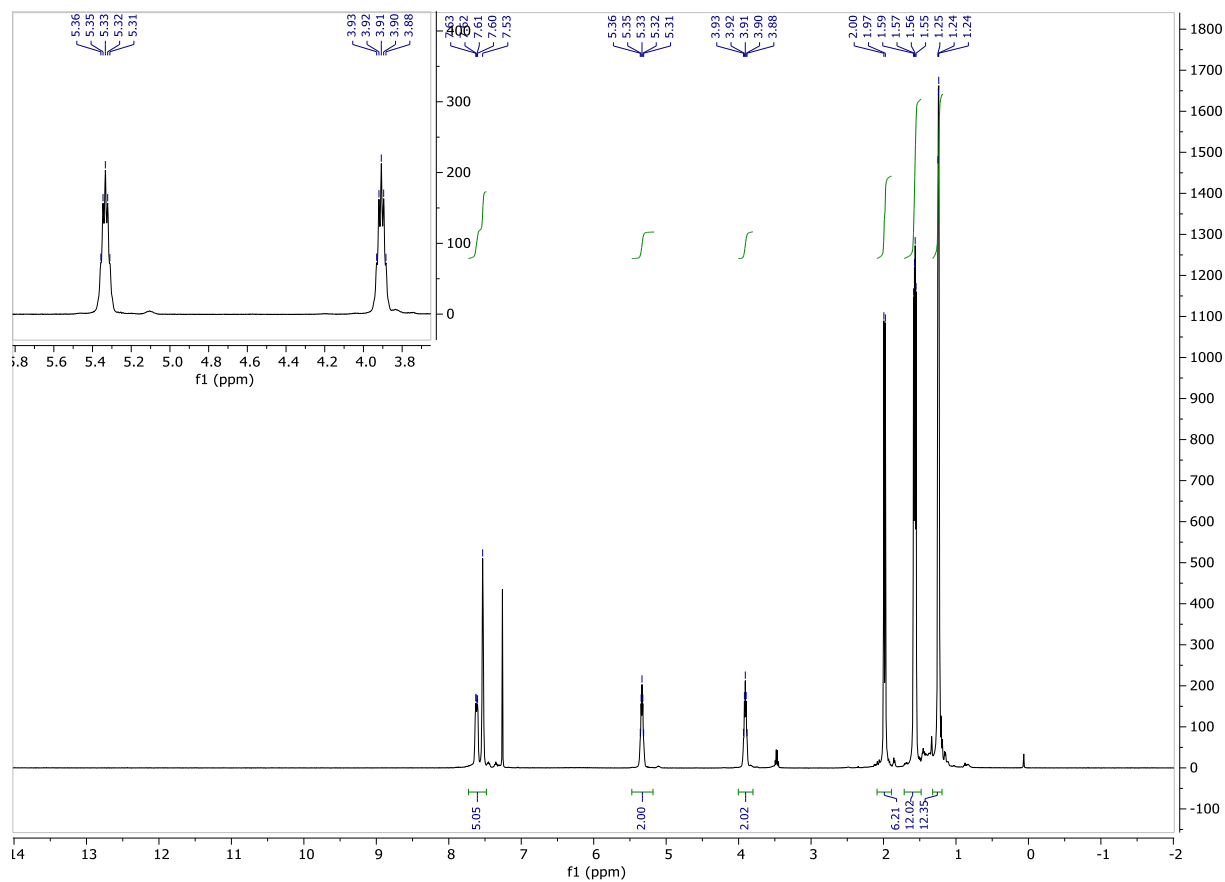


Figure 2.33 ^1H NMR of $3f[\text{SbF}_6]$ (PPhMe₂) in CDCl_3 .

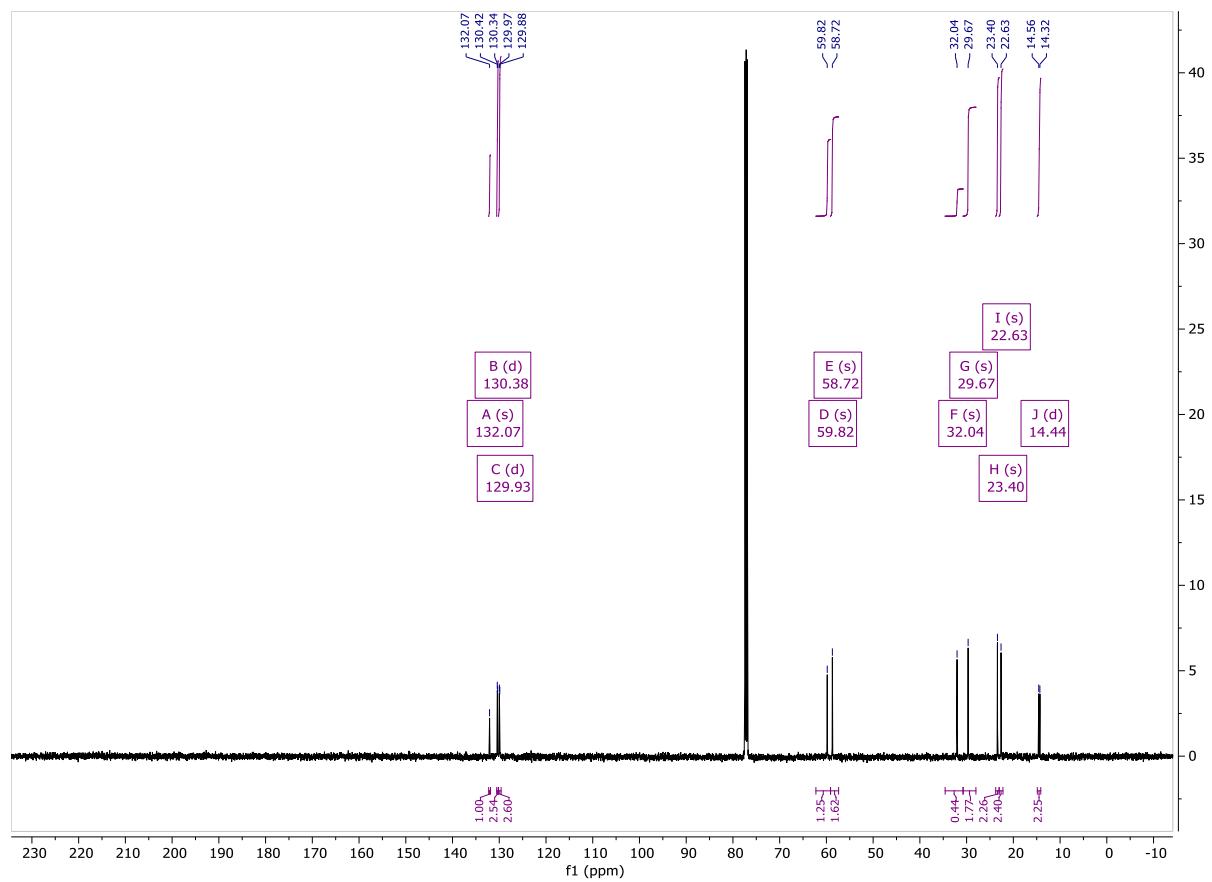


Figure 2.34 ^{13}C NMR of $3\mathbf{f}[\text{SbF}_6]$ (PPhMe_2) in CDCl_3 .

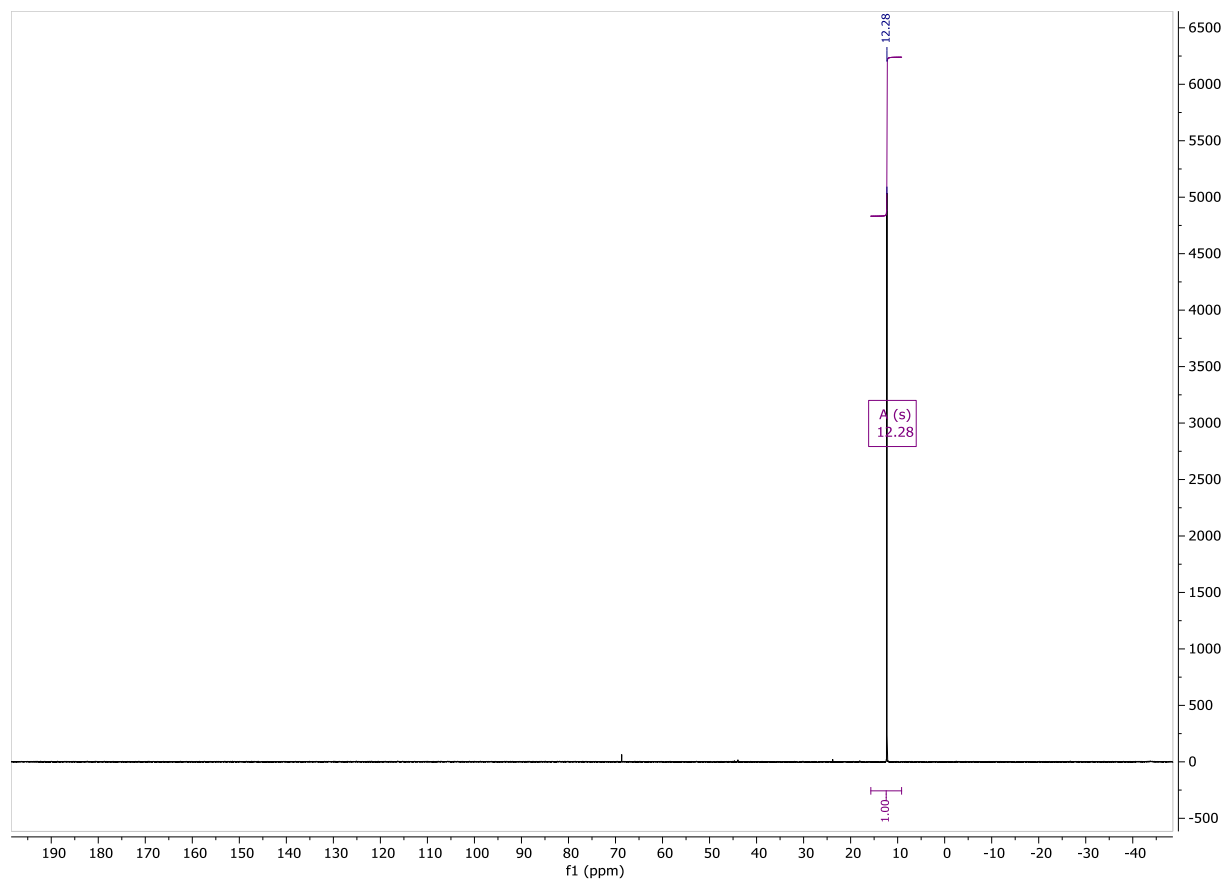


Figure 2.35 ^{31}P NMR of $3\mathbf{f}[\text{SbF}_6]$ (PPhMe_2) in CDCl_3 .

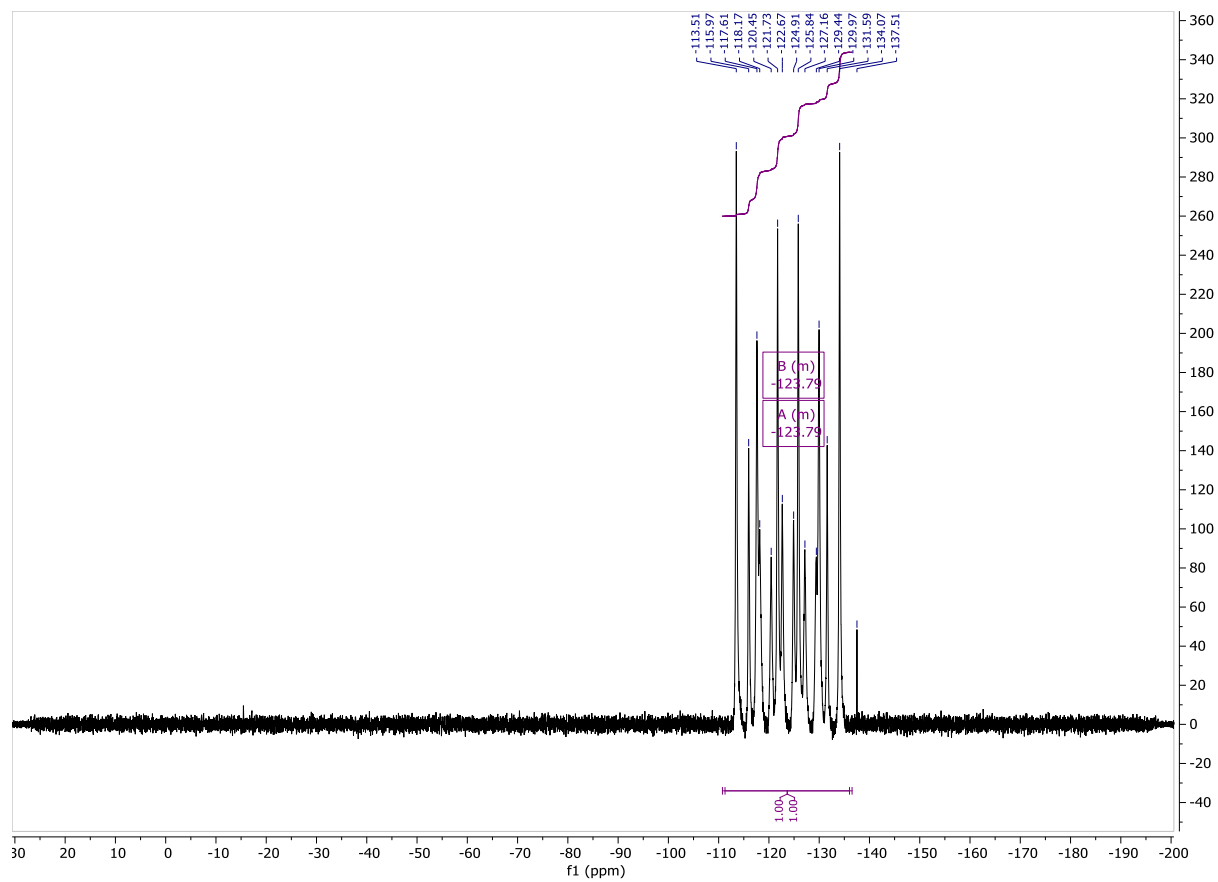


Figure 2.36 ^{36}F NMR of $3\mathbf{f}[\text{SbF}_6]$ (PPhMe_2) in CD_3CN .

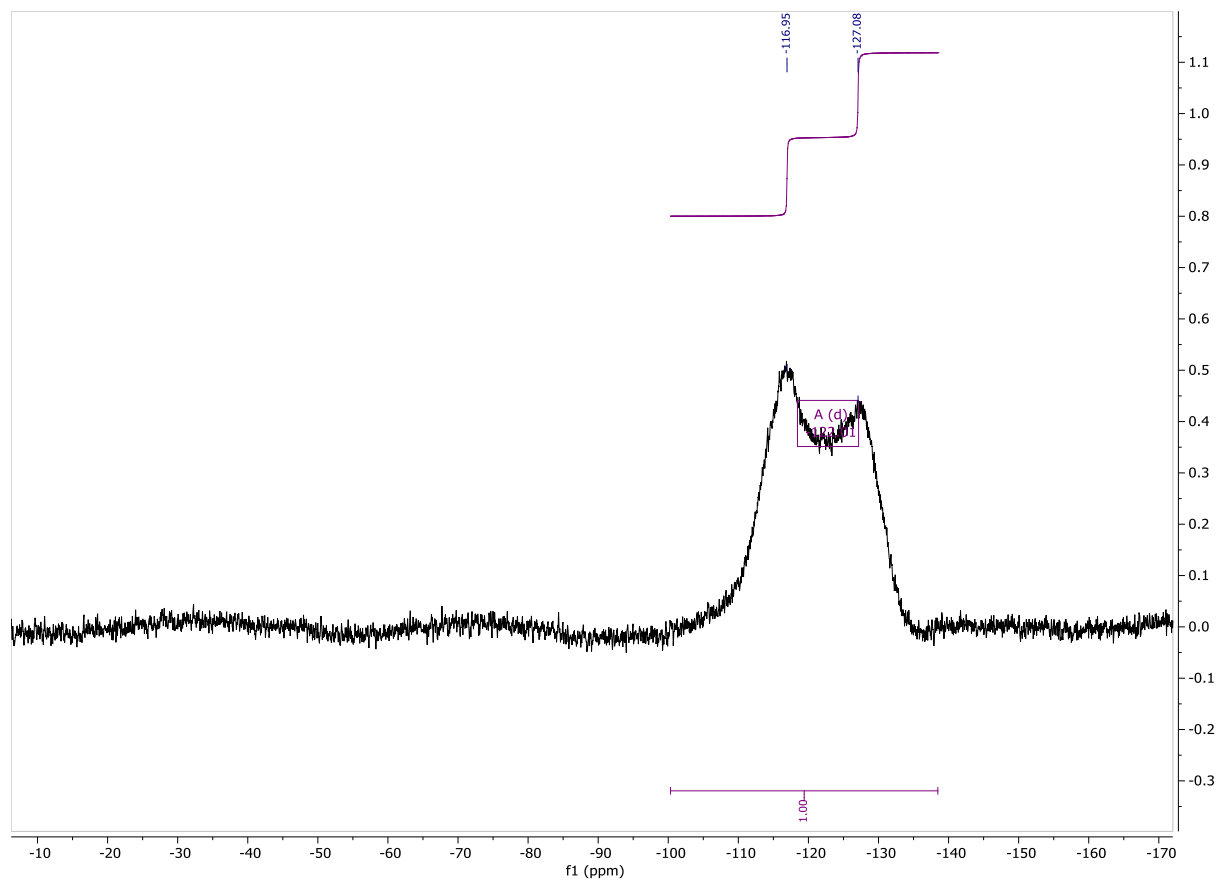


Figure 2.37 ^{19}F NMR of $3\text{f}[\text{SbF}_6] (\text{PPhMe}_2)$ in CDCl_3 .

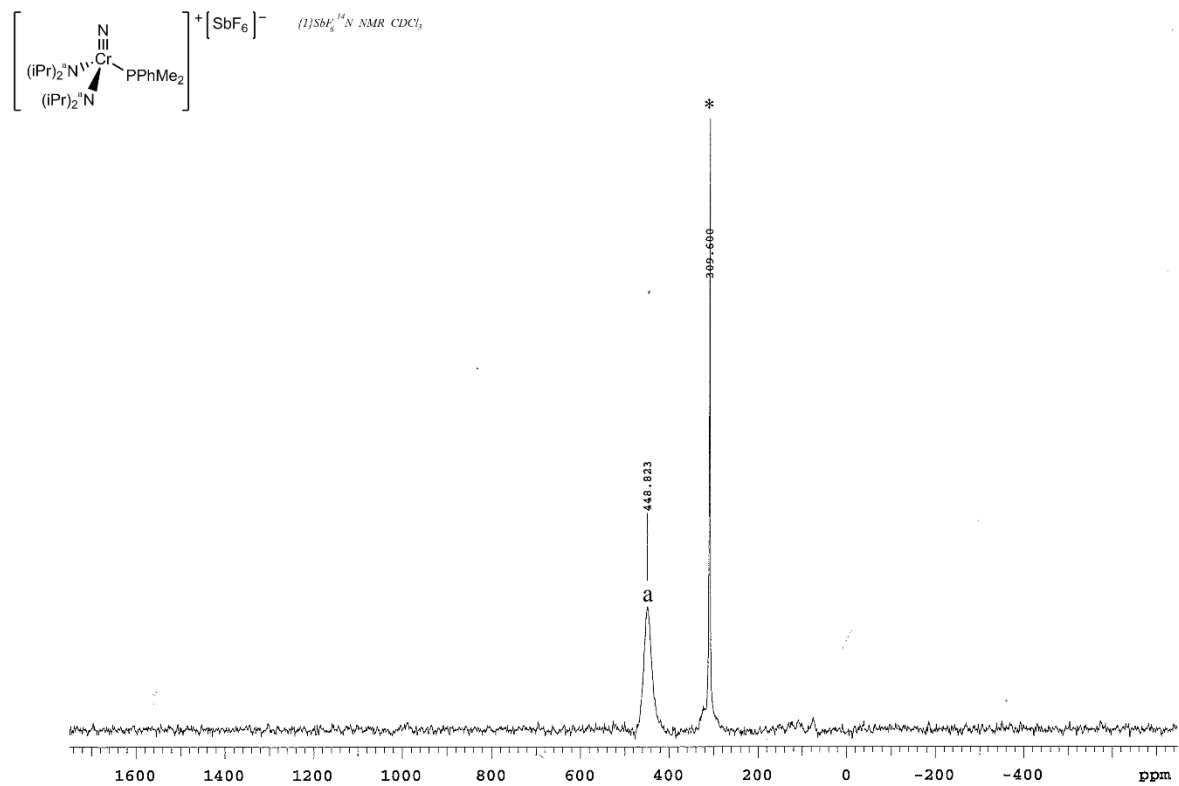


Figure 2.38 ^{14}N NMR of $3f[\text{SbF}_6]$ in CDCl_3 .

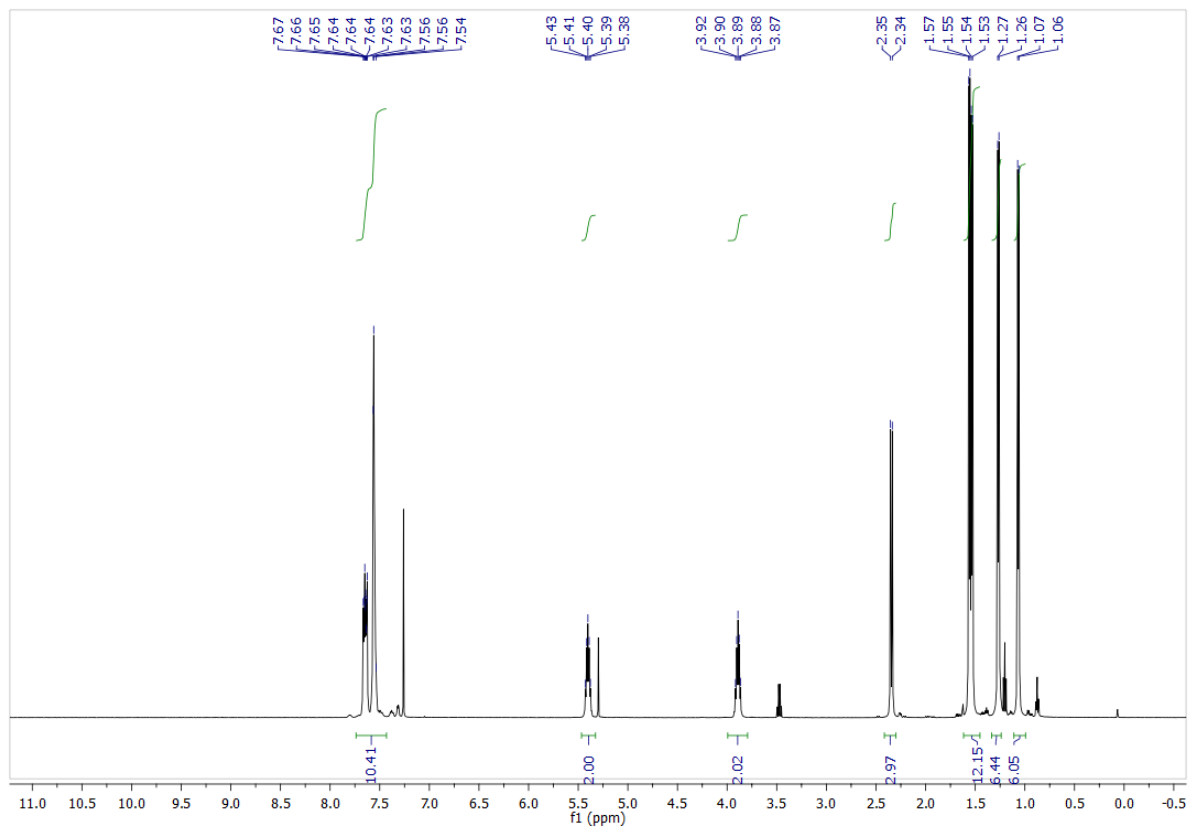


Figure 2.39 ^1H NMR of $3\mathbf{g}[\text{SbF}_6]$ in CDCl_3 .

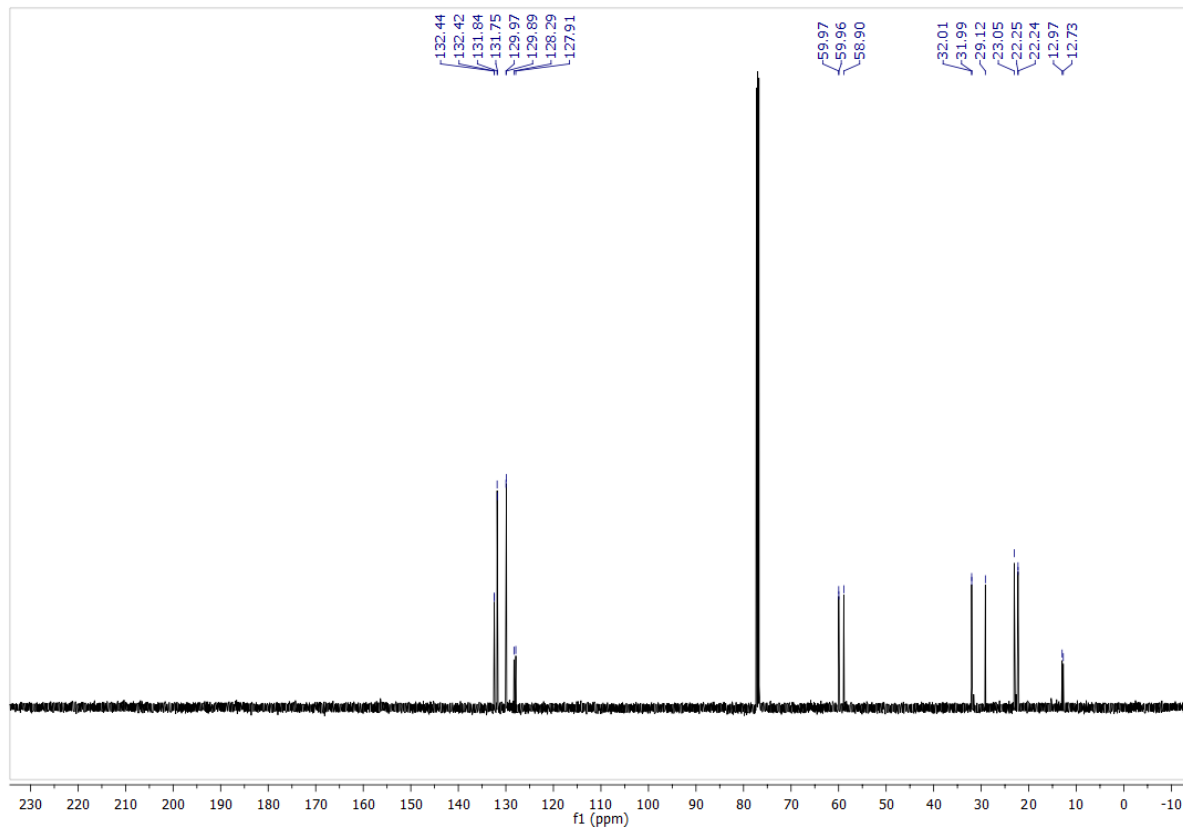


Figure 2.40 ^{13}C NMR of $3\text{g}[\text{SbF}_6]$ in CDCl_3 .

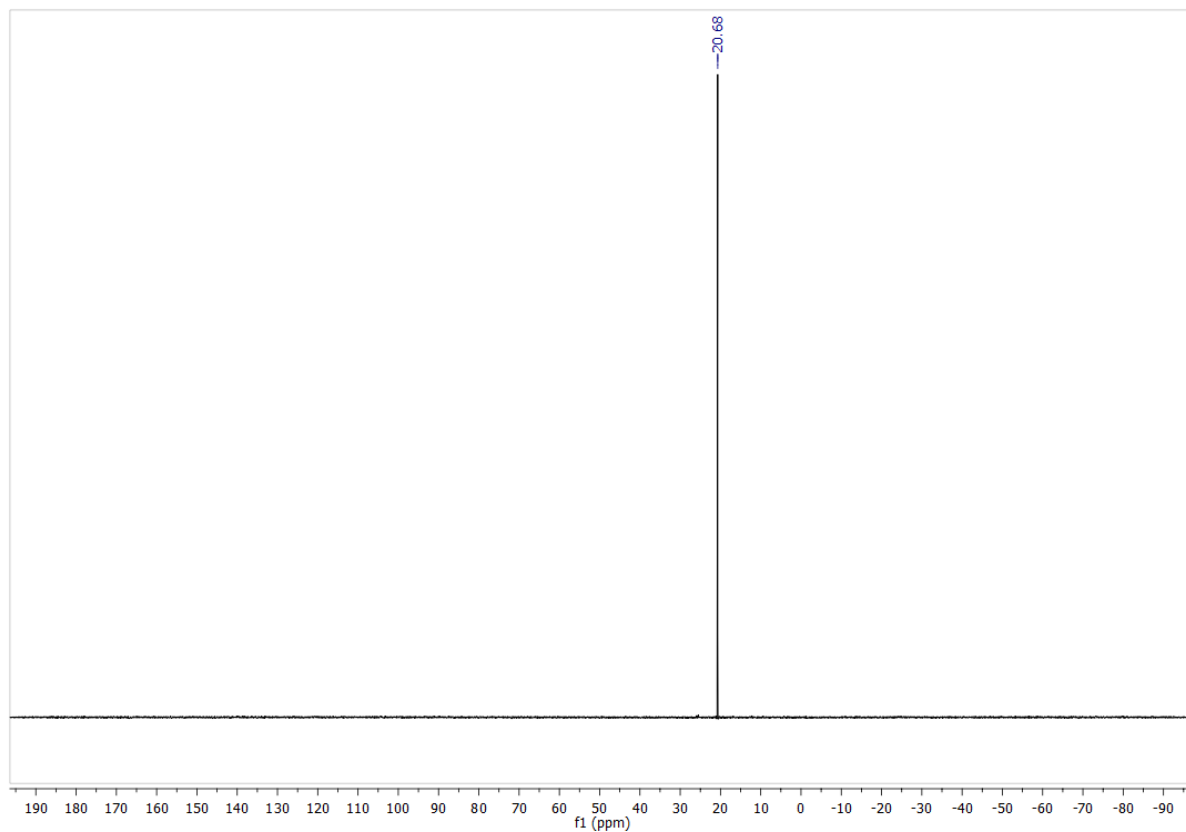


Figure 2.41 ^{31}P NMR of $3\mathbf{g}[\text{SbF}_6]$ in CDCl_3 .

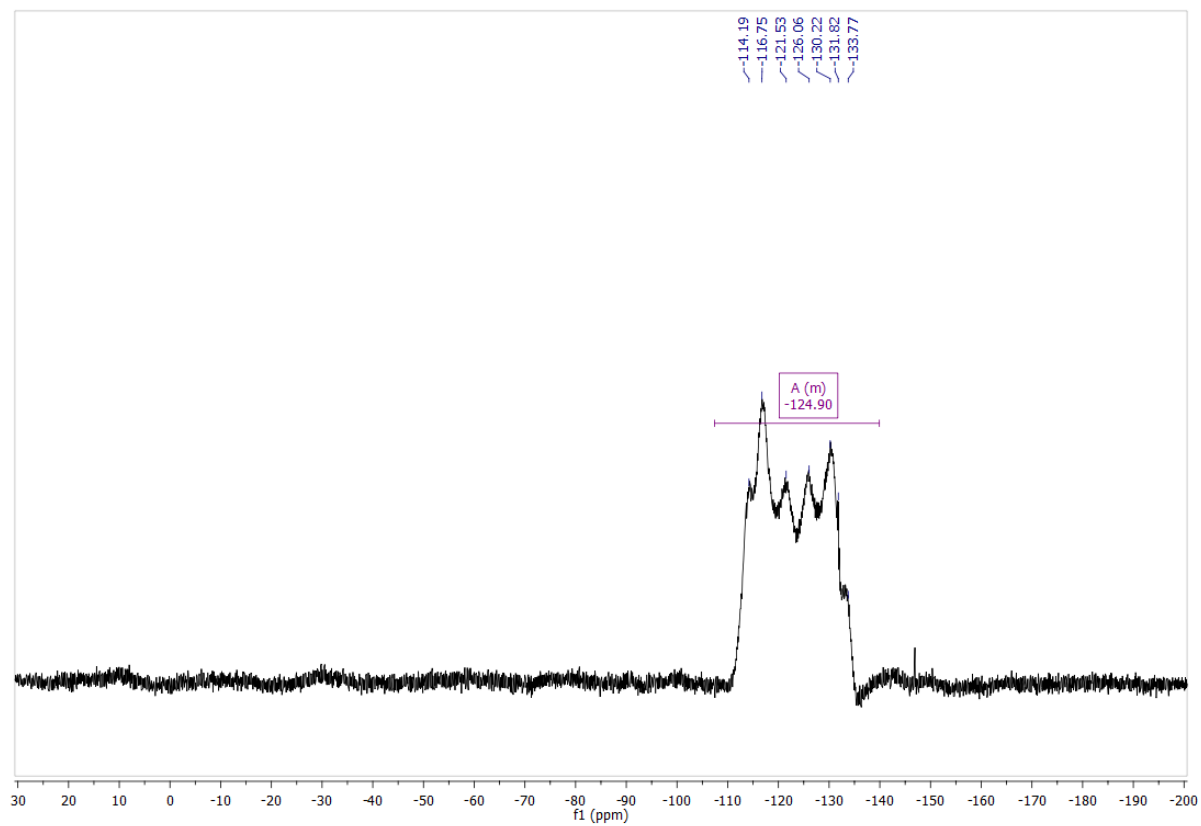


Figure 2.42 ^{19}F NMR of $3\text{g}[\text{SbF}_6]$ in CDCl_3 .

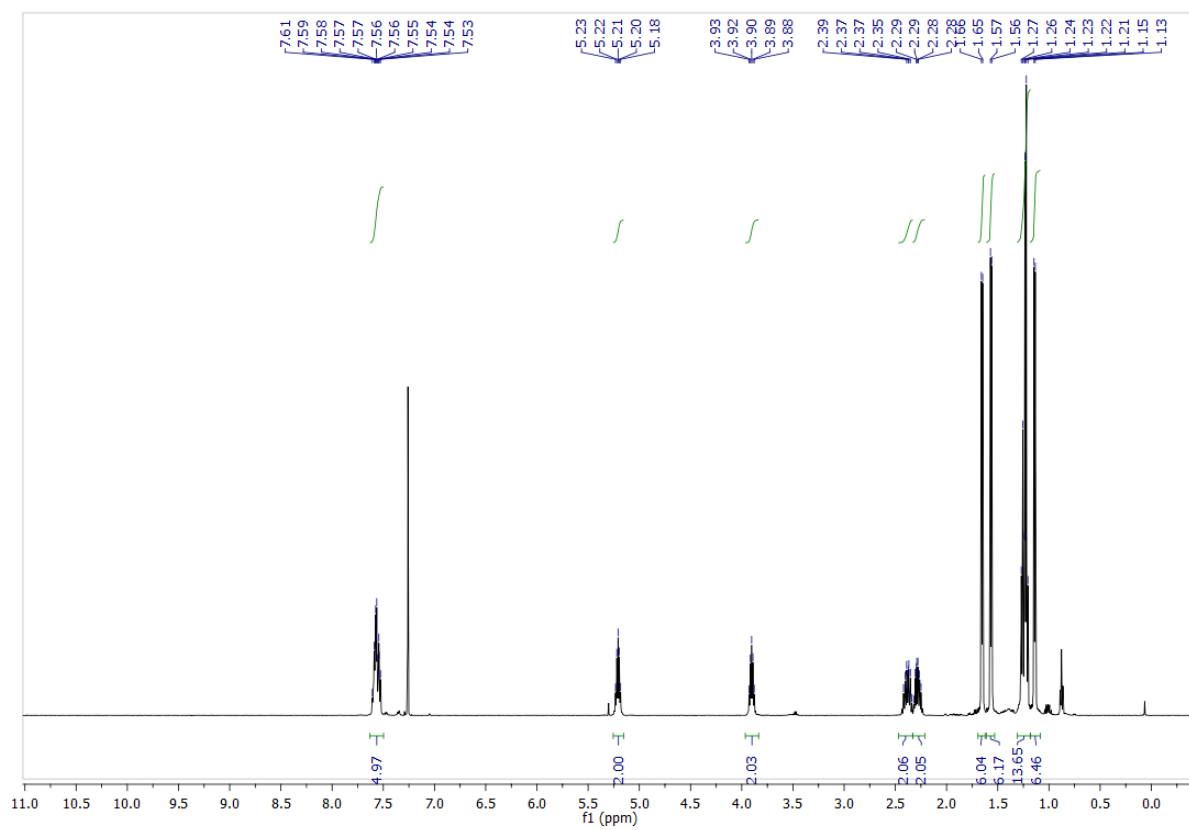


Figure 2.43 ^1H NMR of $3\text{h}[\text{SbF}_6]$ in CDCl_3 .

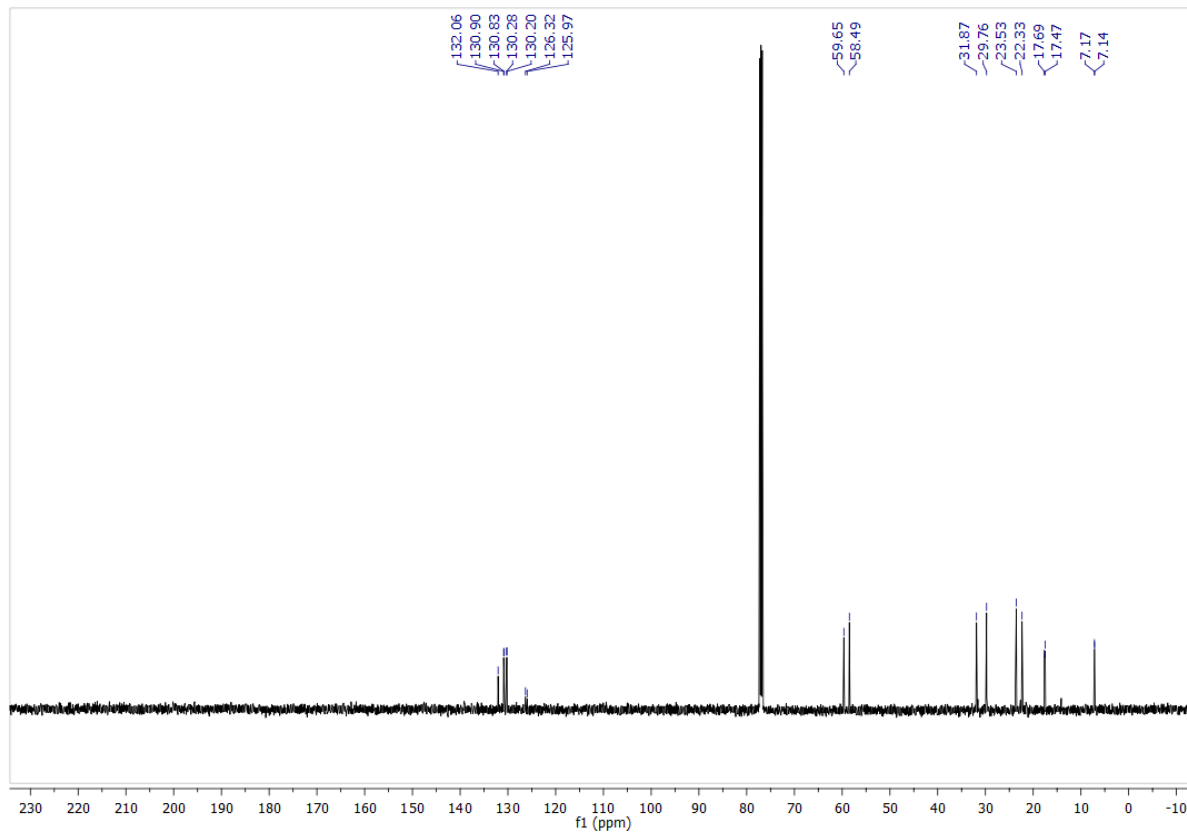


Figure 2.44 ^{13}C NMR of $3\mathbf{h}[\text{SbF}_6]$ in CDCl_3 .

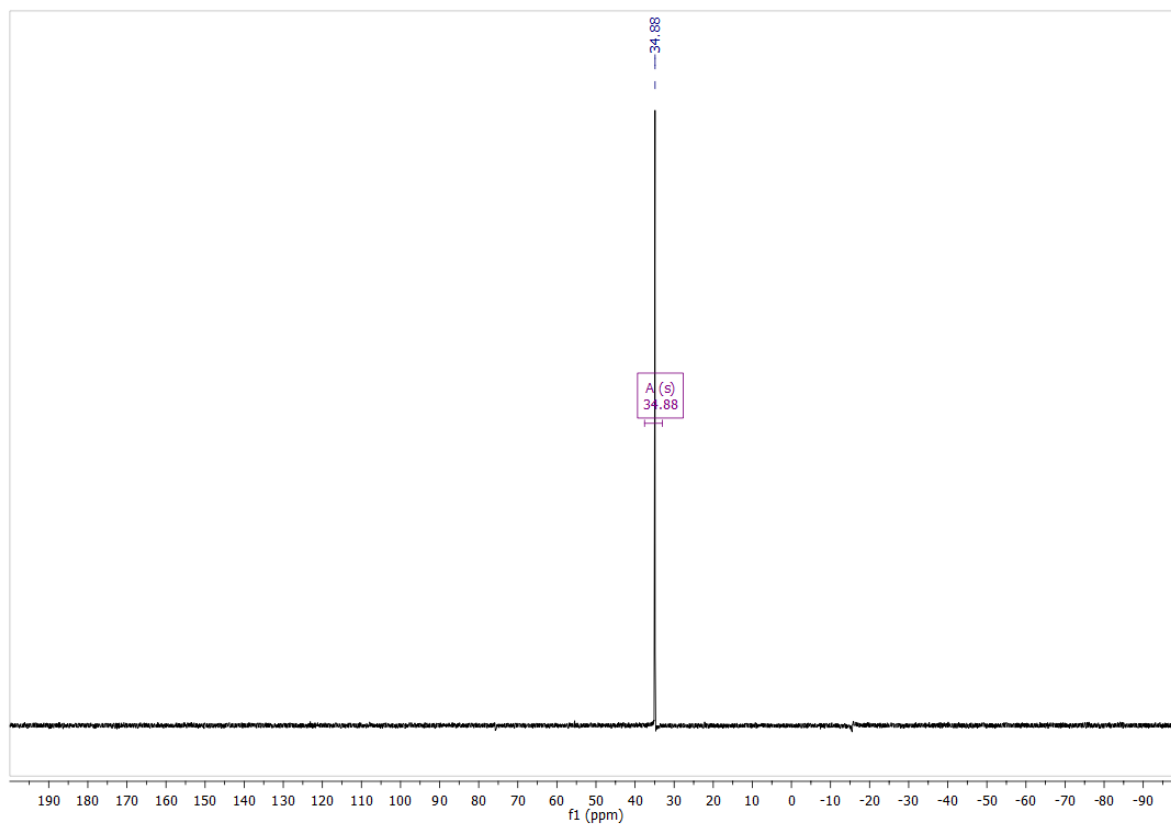


Figure 2.45 ^{31}P NMR of $3\mathbf{h}[\text{SbF}_6]$ in CDCl_3 .

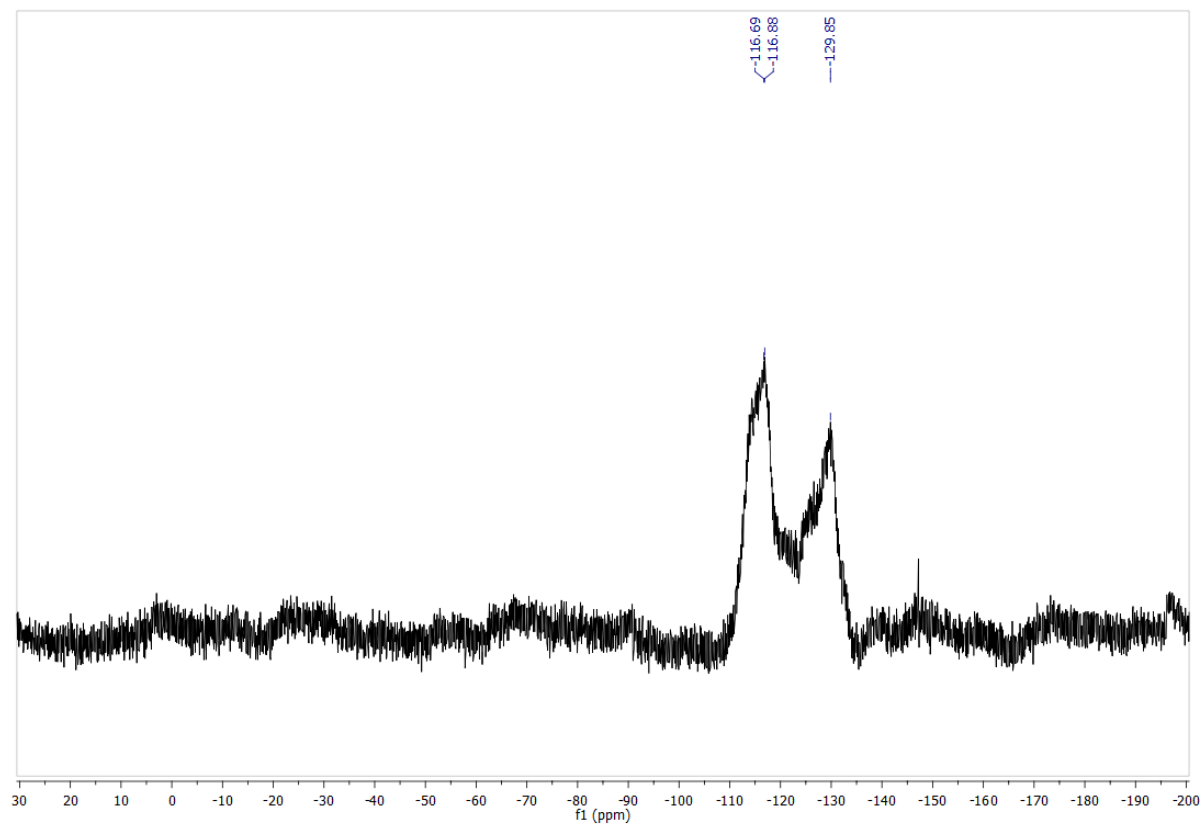


Figure 2.46 ^{19}F NMR of $3\mathbf{h}[\text{SbF}_6]$ in CDCl_3 .

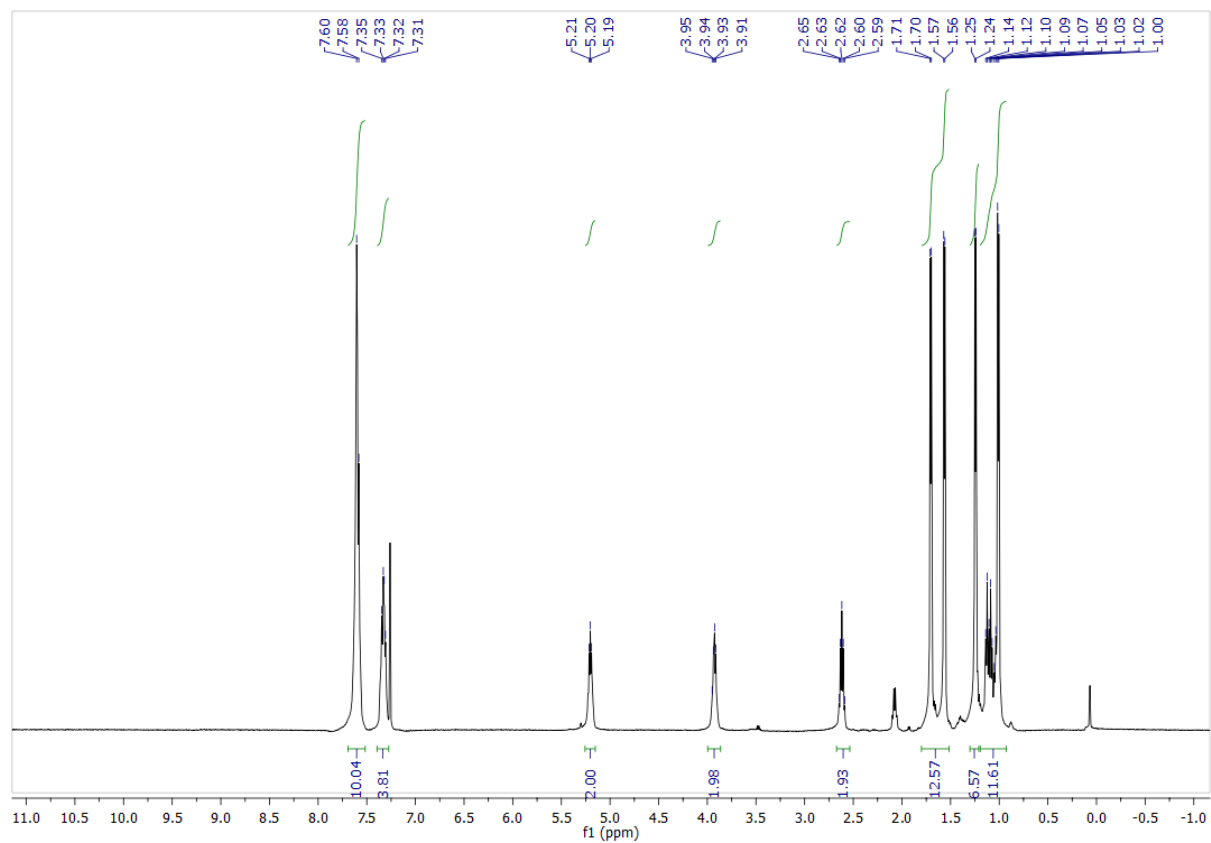


Figure 2.47 ^1H NMR of $3\mathbf{i}[\text{SbF}_6]$ in CDCl_3 .

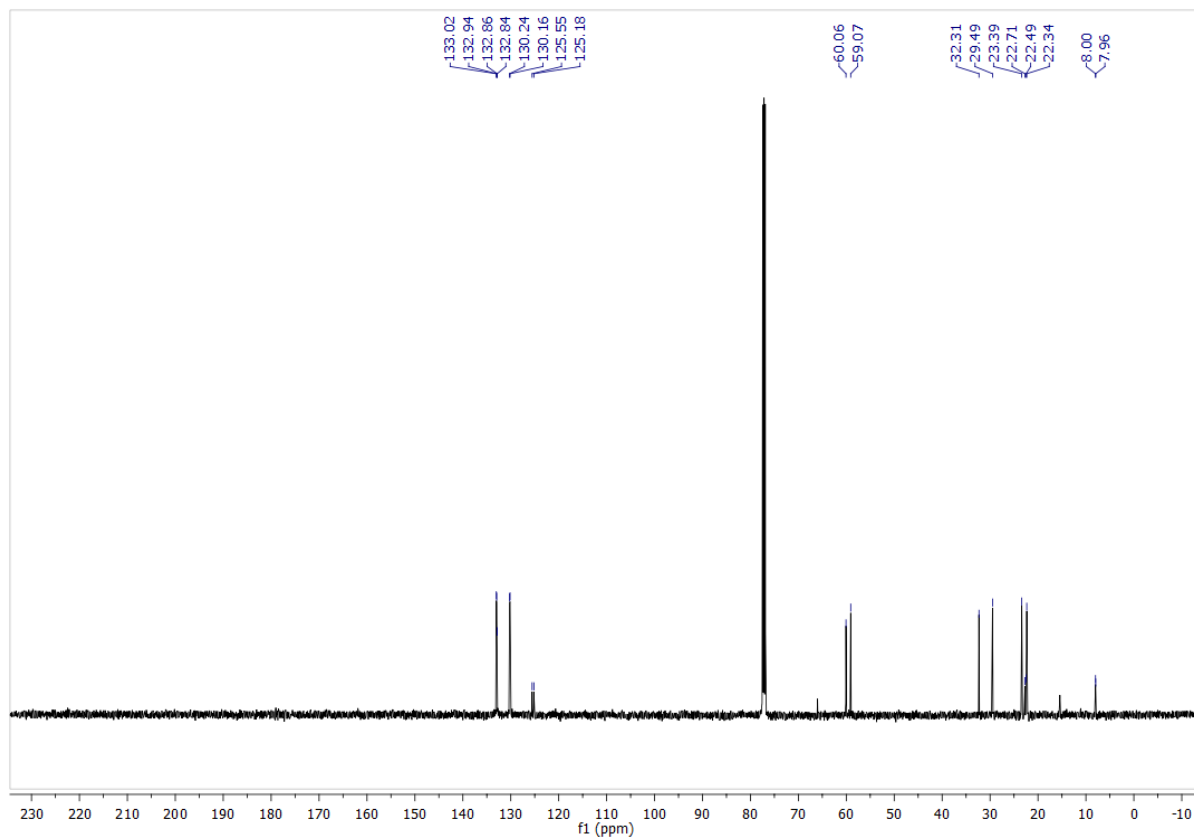


Figure 2.48 ^{13}C NMR of $3i[\text{SbF}_6]$ in CDCl_3 .

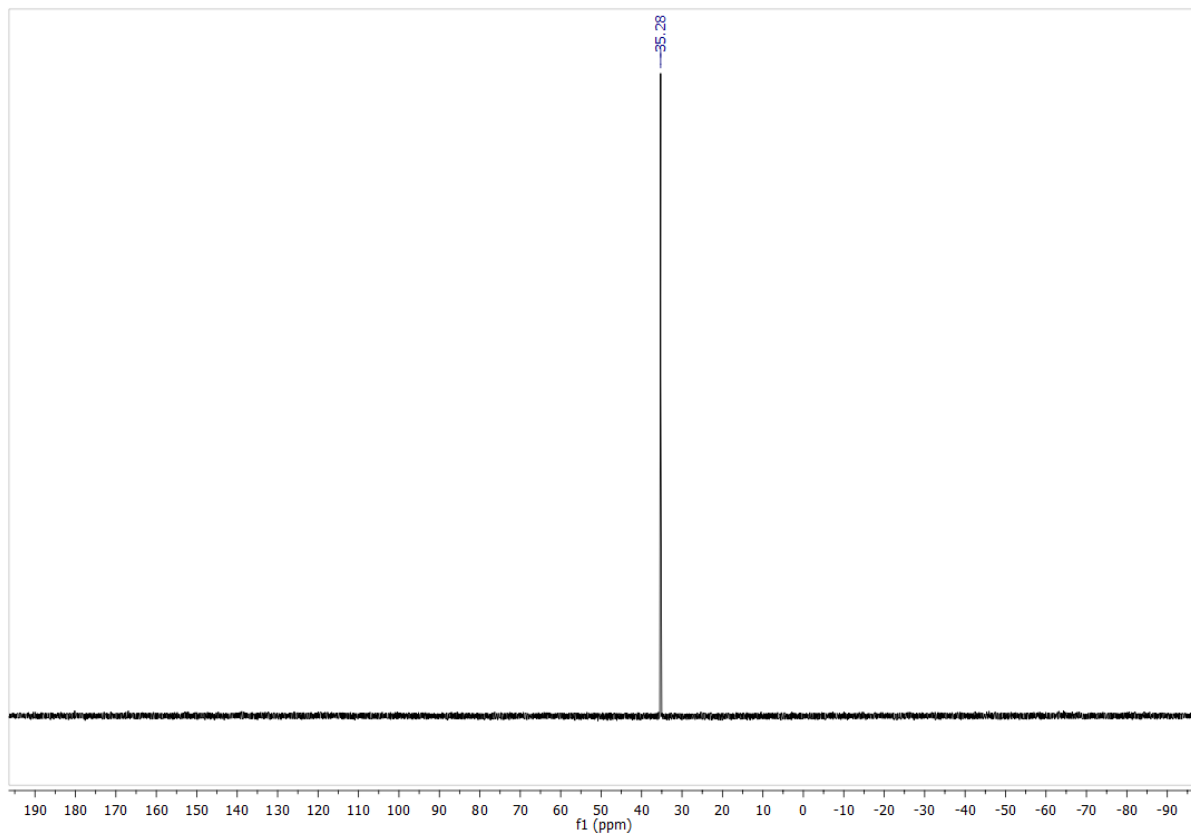


Figure 2.49 ^{31}P NMR of $3i[\text{SbF}_6]$ in CDCl_3 .

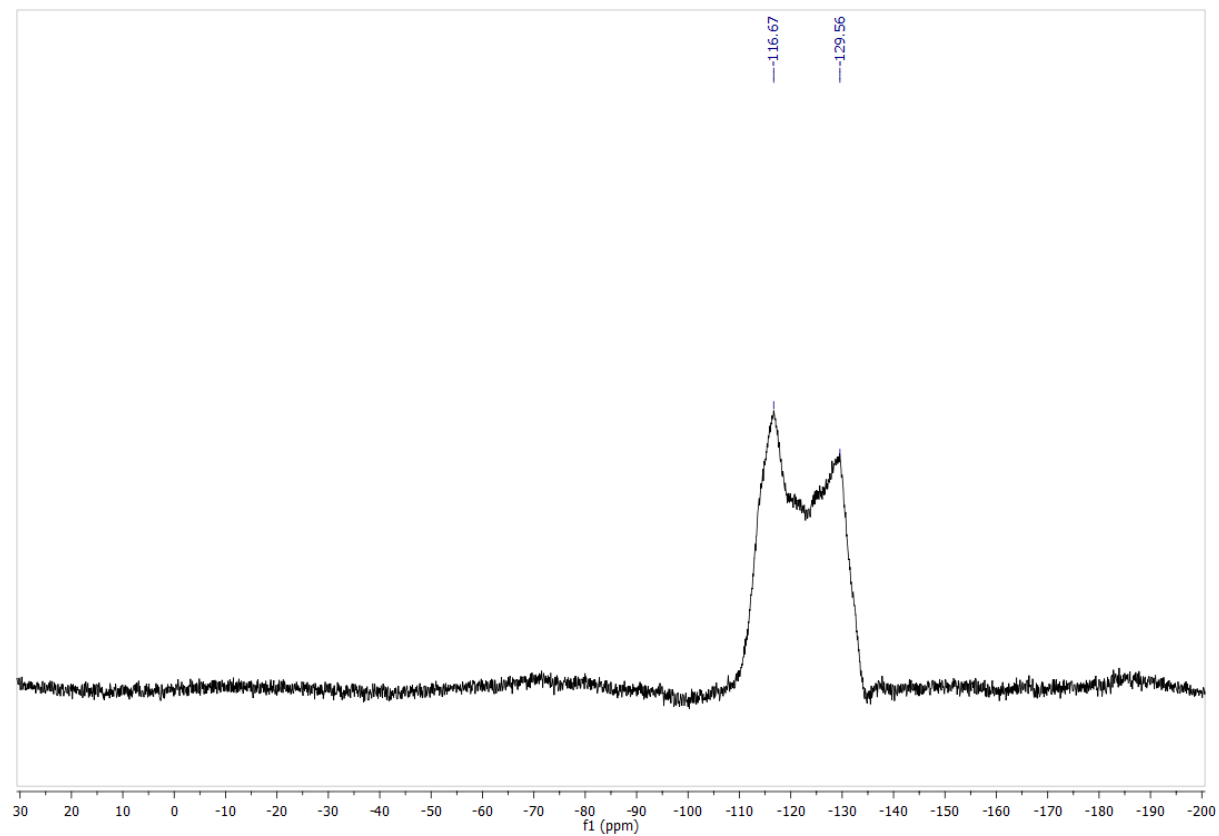


Figure 2. ^{19}F NMR of $3i[\text{SbF}_6]$ in CDCl_3 .

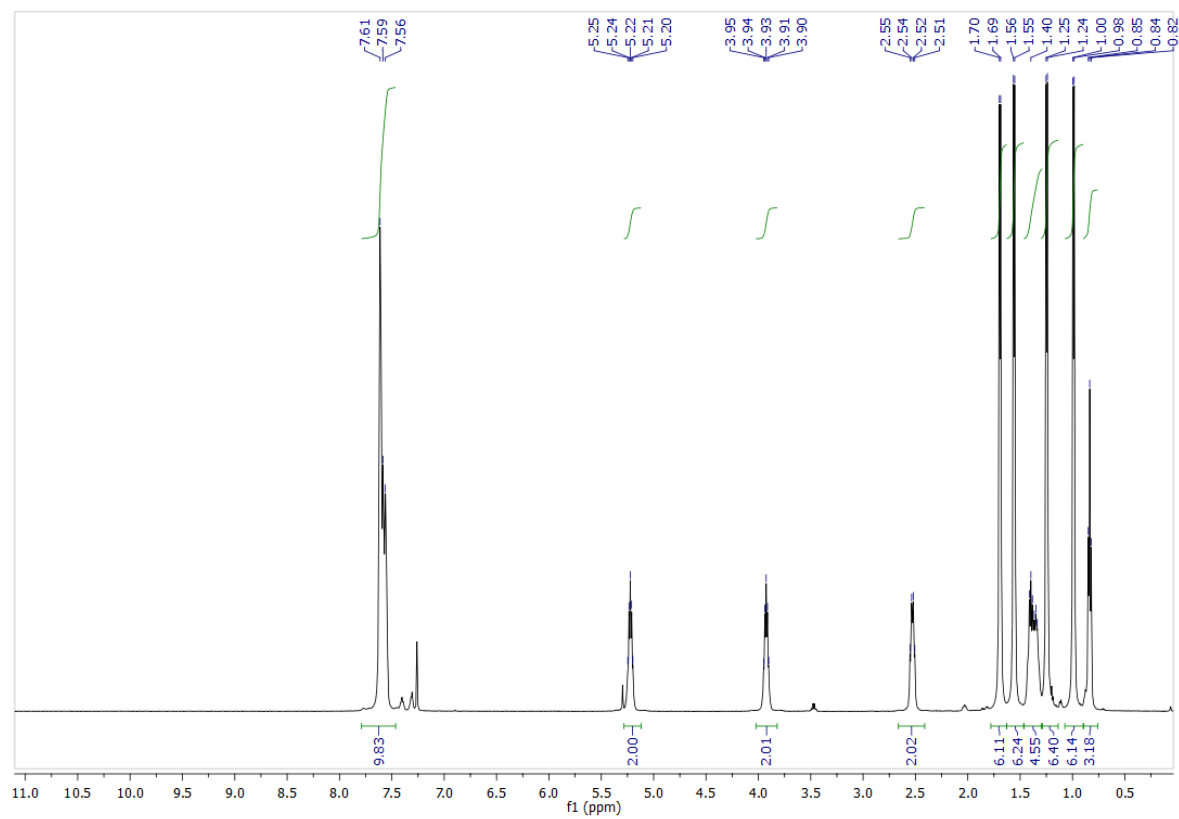


Figure 2.51 ^1H NMR of **3j**[PF₆] in CDCl₃.

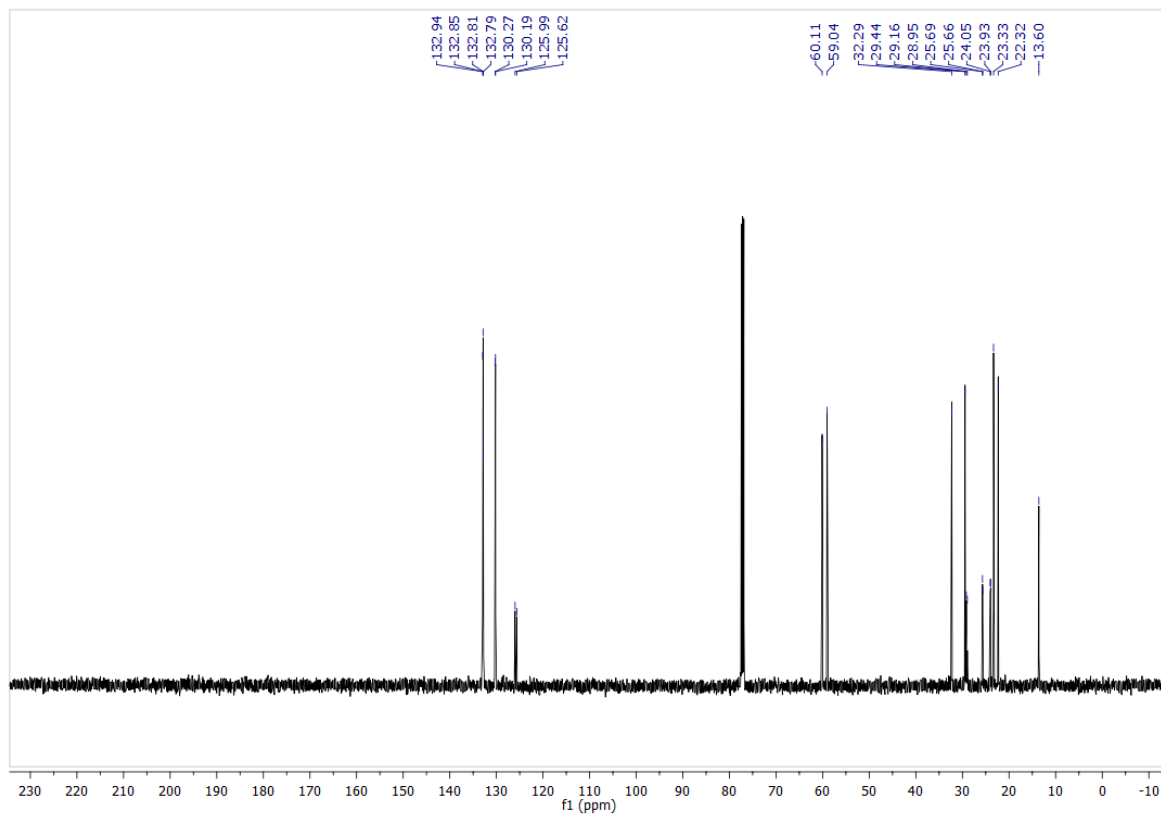


Figure 2.52 ^{13}C NMR of **3j**[PF₆] in CDCl₃.

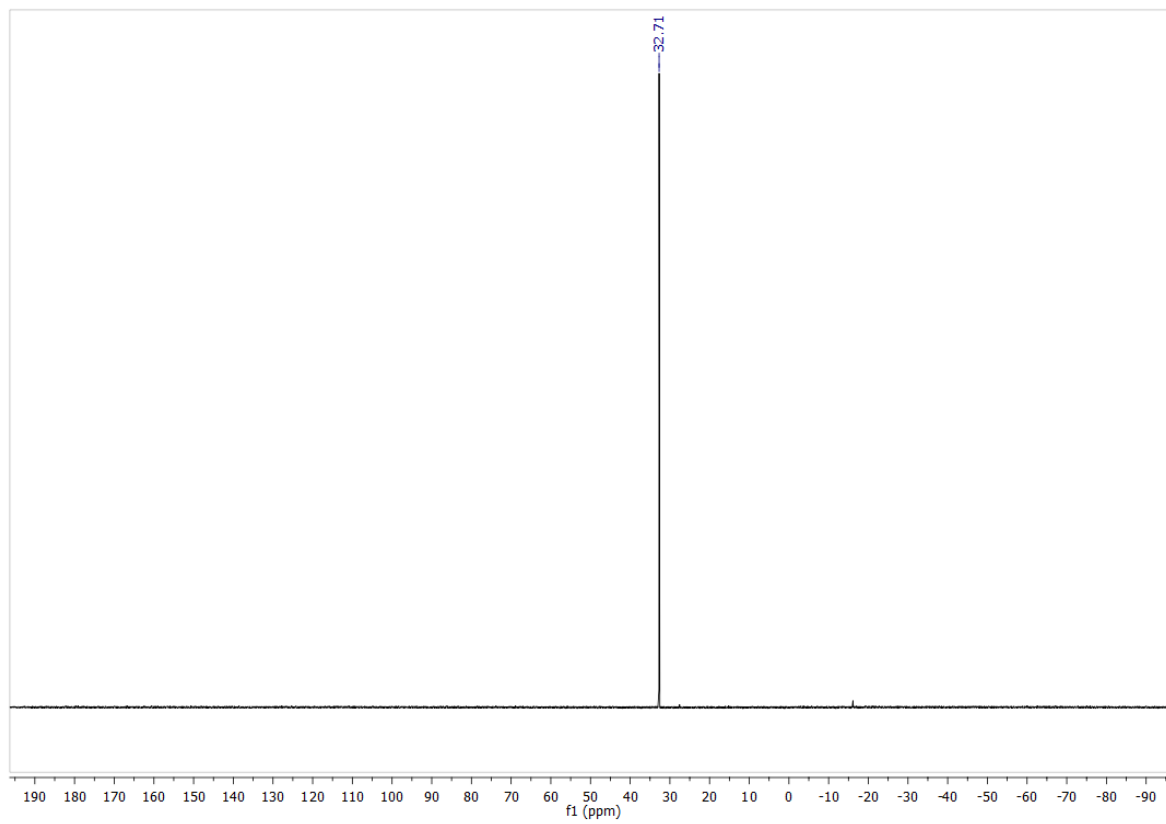


Figure 2.53 ^{31}P NMR of **3j**[PF₆] in CDCl₃.

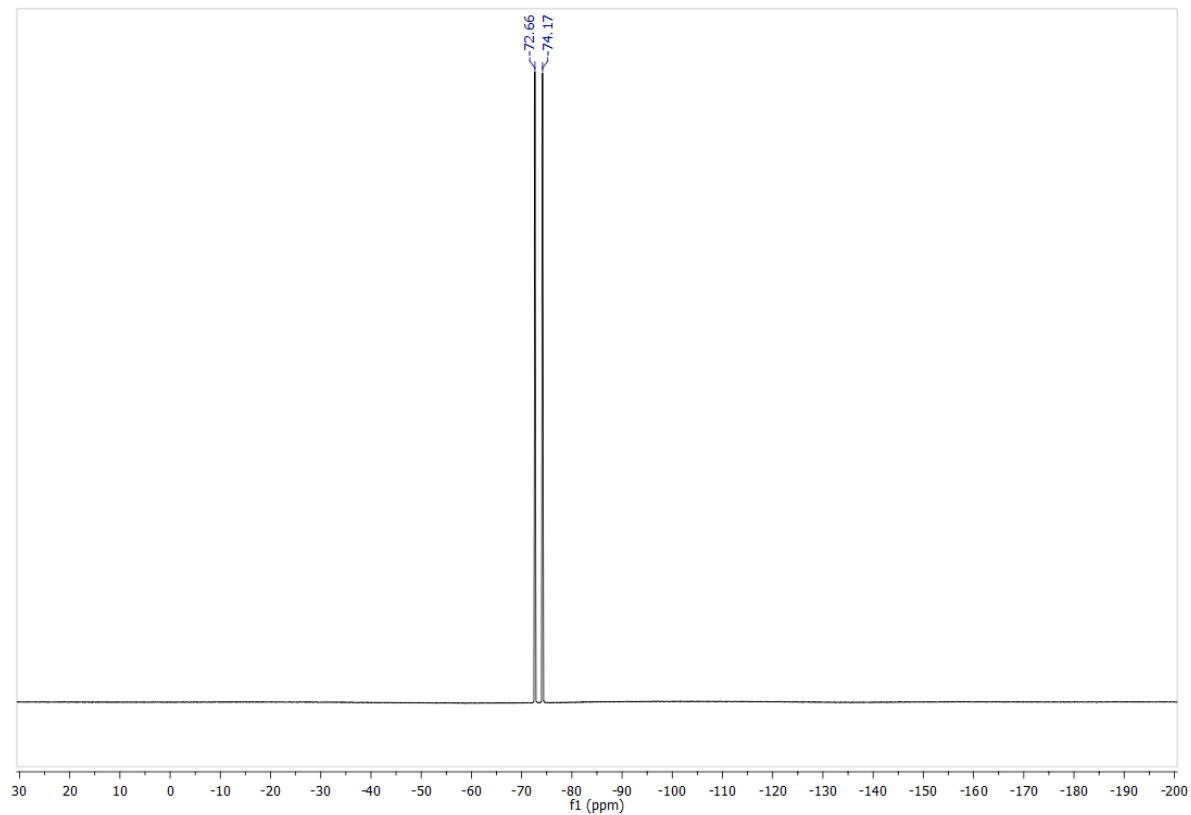


Figure 2.54 ^{19}F NMR of **3j**[PF₆] in CDCl₃.

$\{\text{NCr}(\text{N}^i\text{Pr})_2\text{PPh}_2^o\text{Bu}\}\text{PF}_6$ CDCl_3 ^{14}N NMR

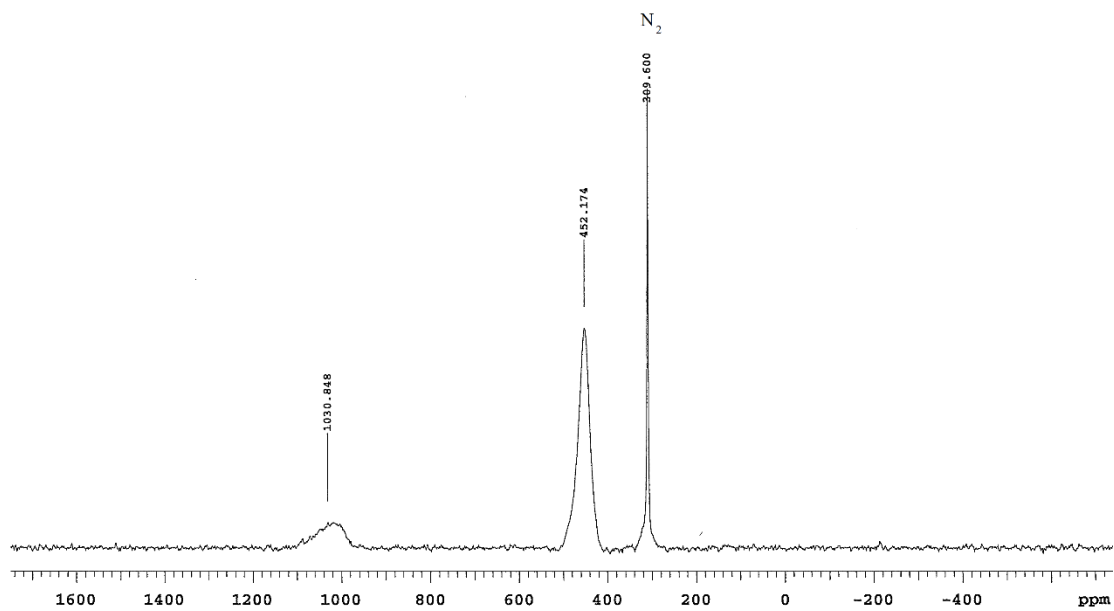


Figure 2.55 ^{14}N NMR of **3j**[PF_6] in CDCl_3 .

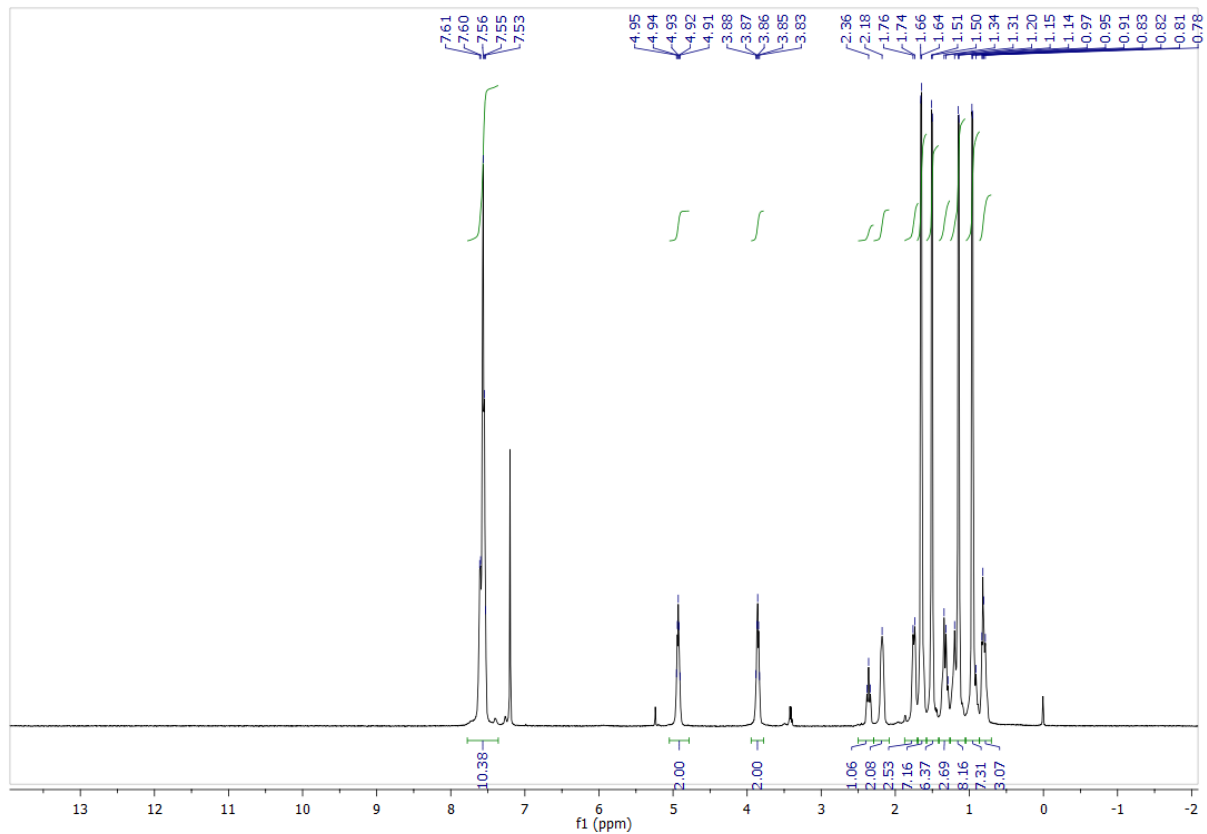


Figure 2.56 ^1H NMR of $3\mathbf{k}[\text{SbF}_6]$ in CDCl_3 .

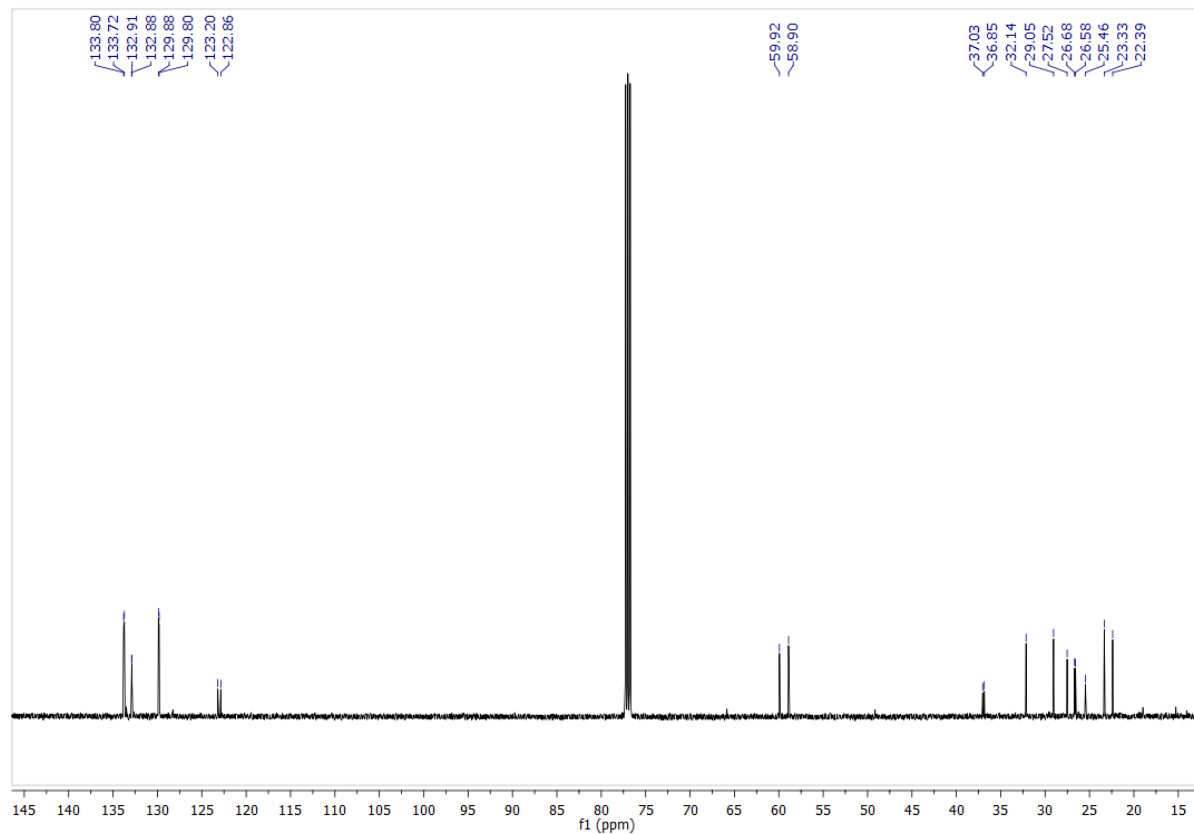


Figure 2.57 ^{13}C NMR of $3\mathbf{k}[\text{SbF}_6]$ in CDCl_3 .

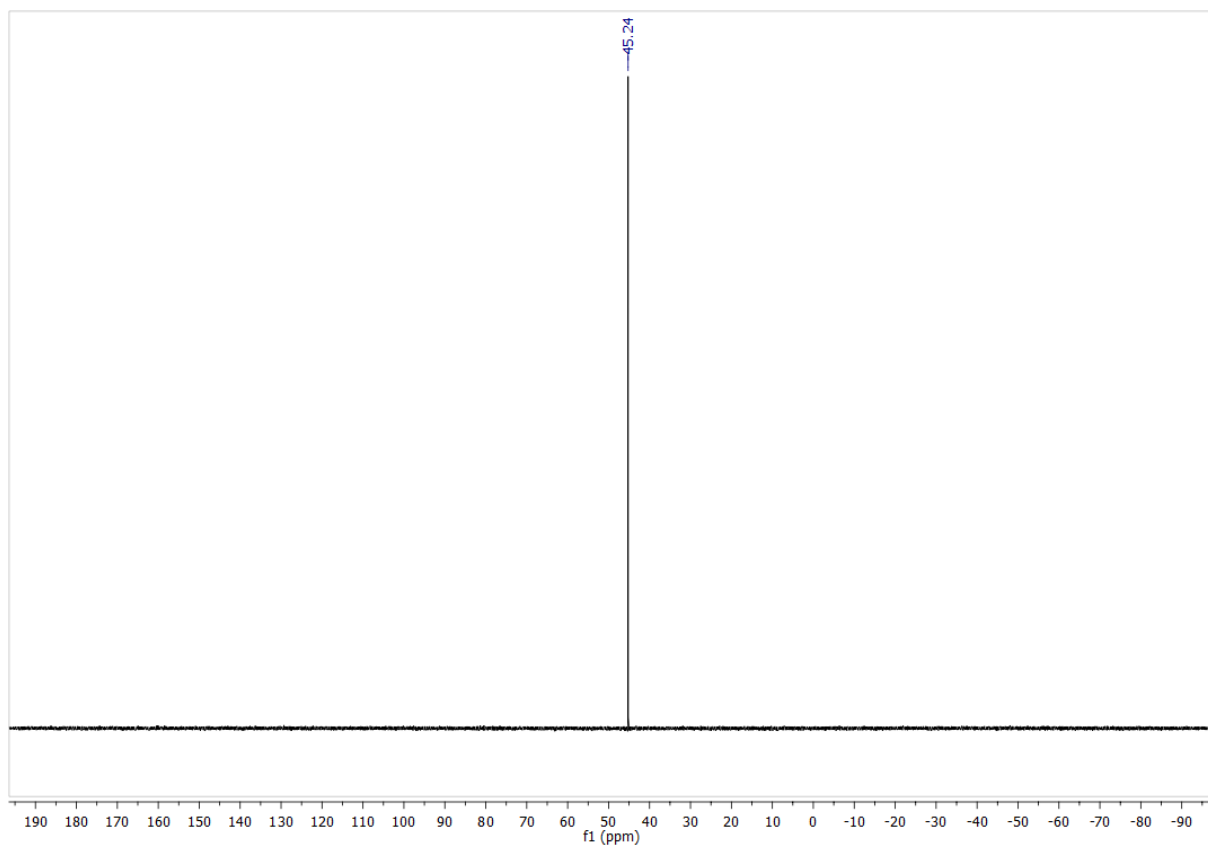


Figure 2.58 ^{31}P NMR of **3k**[SbF₆] in CDCl₃.

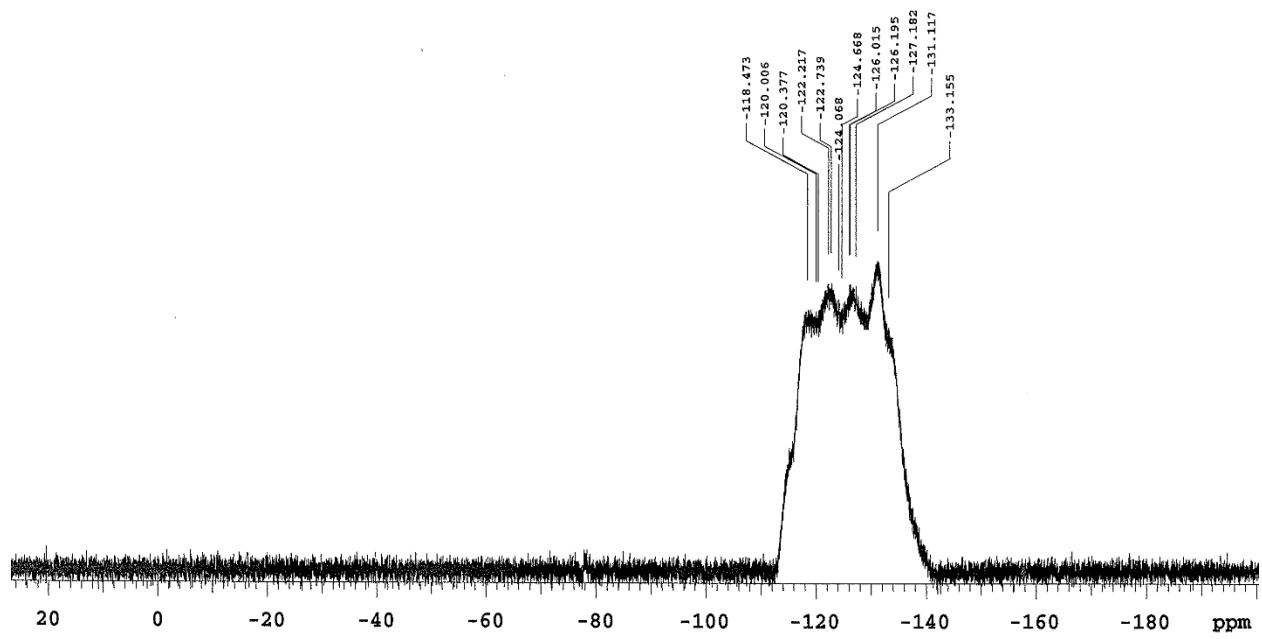


Figure 2.59 ^{19}F NMR of $3\mathbf{k}[\text{SbF}_6]$ in CDCl_3 .

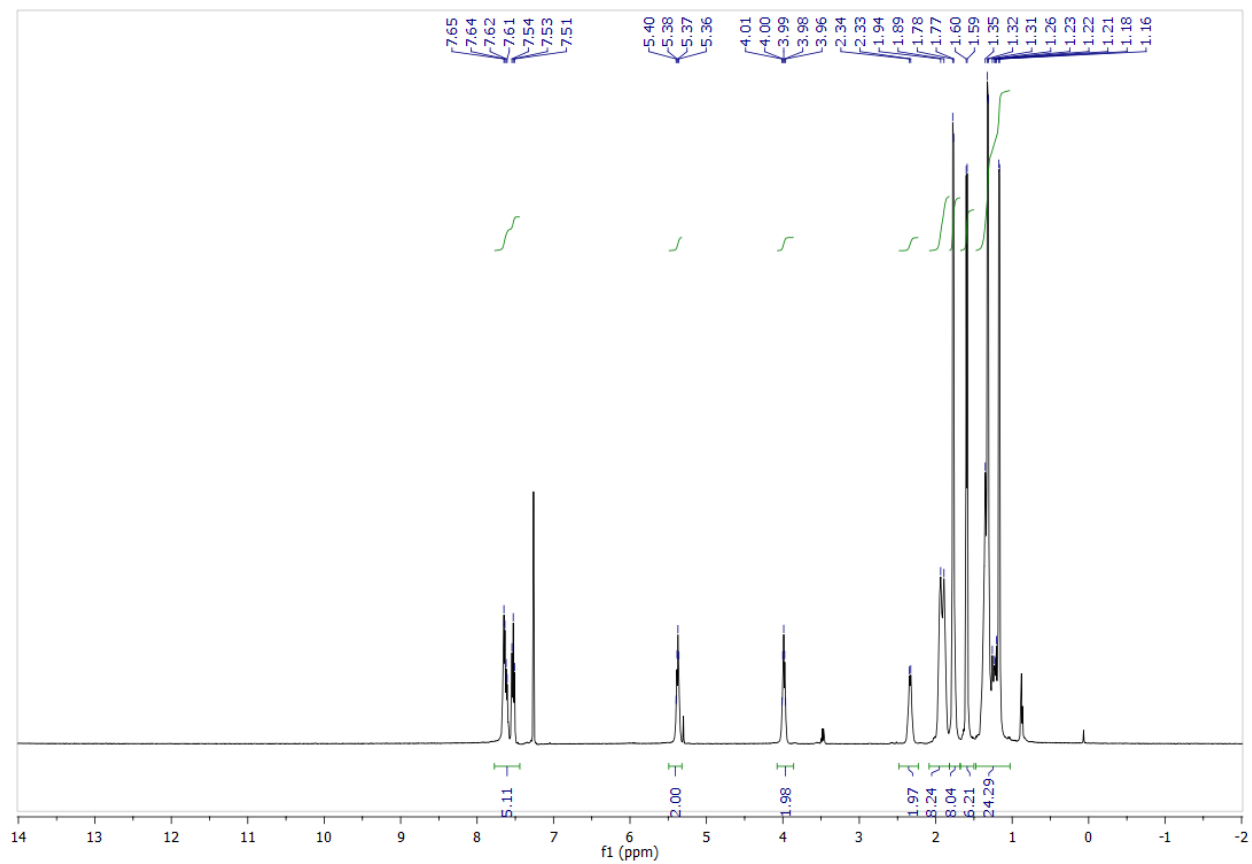


Figure 2.60 ^1H NMR of $3\text{I}[\text{SbF}_6]$ in CDCl_3 .

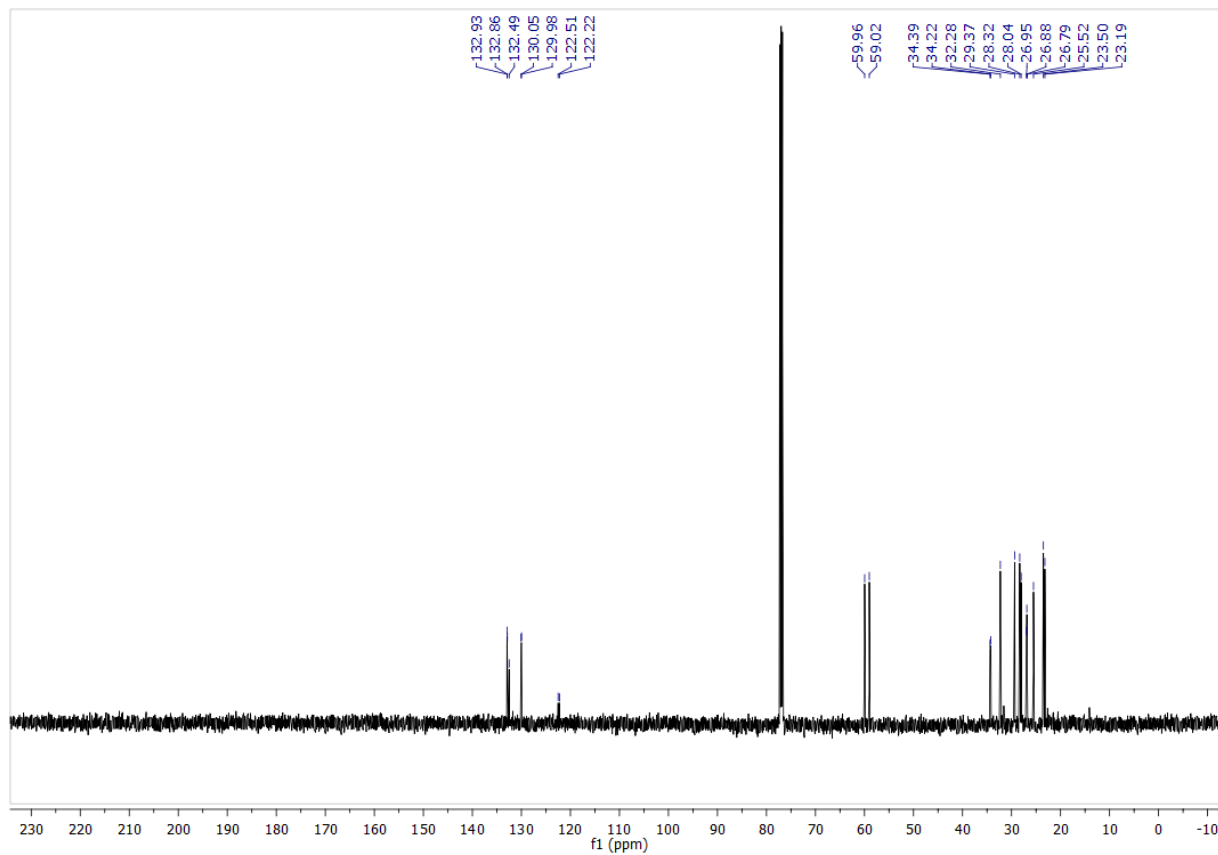


Figure 2.61 ^{13}C NMR of $3\text{I}[\text{SbF}_6]$ in CDCl_3 .

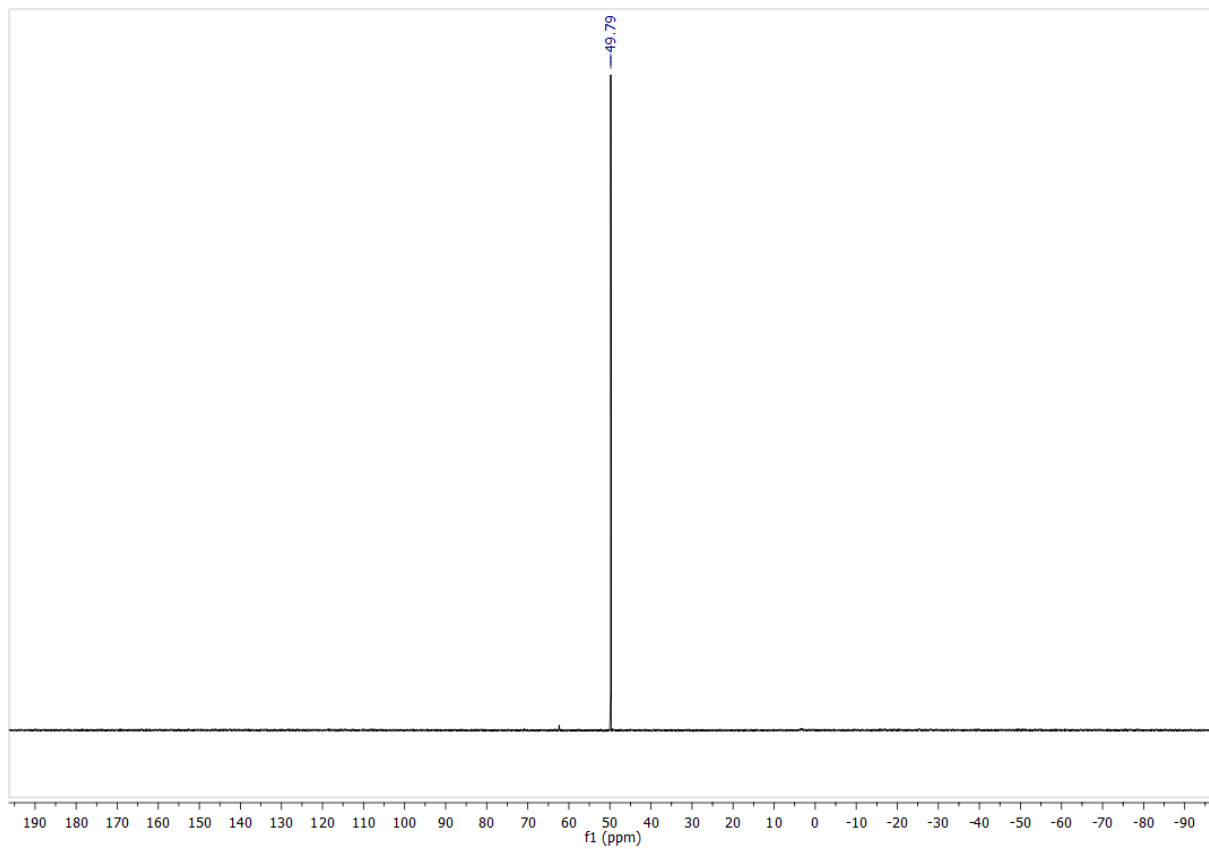


Figure 2.62 ^{31}P NMR of $3\text{I}[\text{SbF}_6]$ in CDCl_3 .

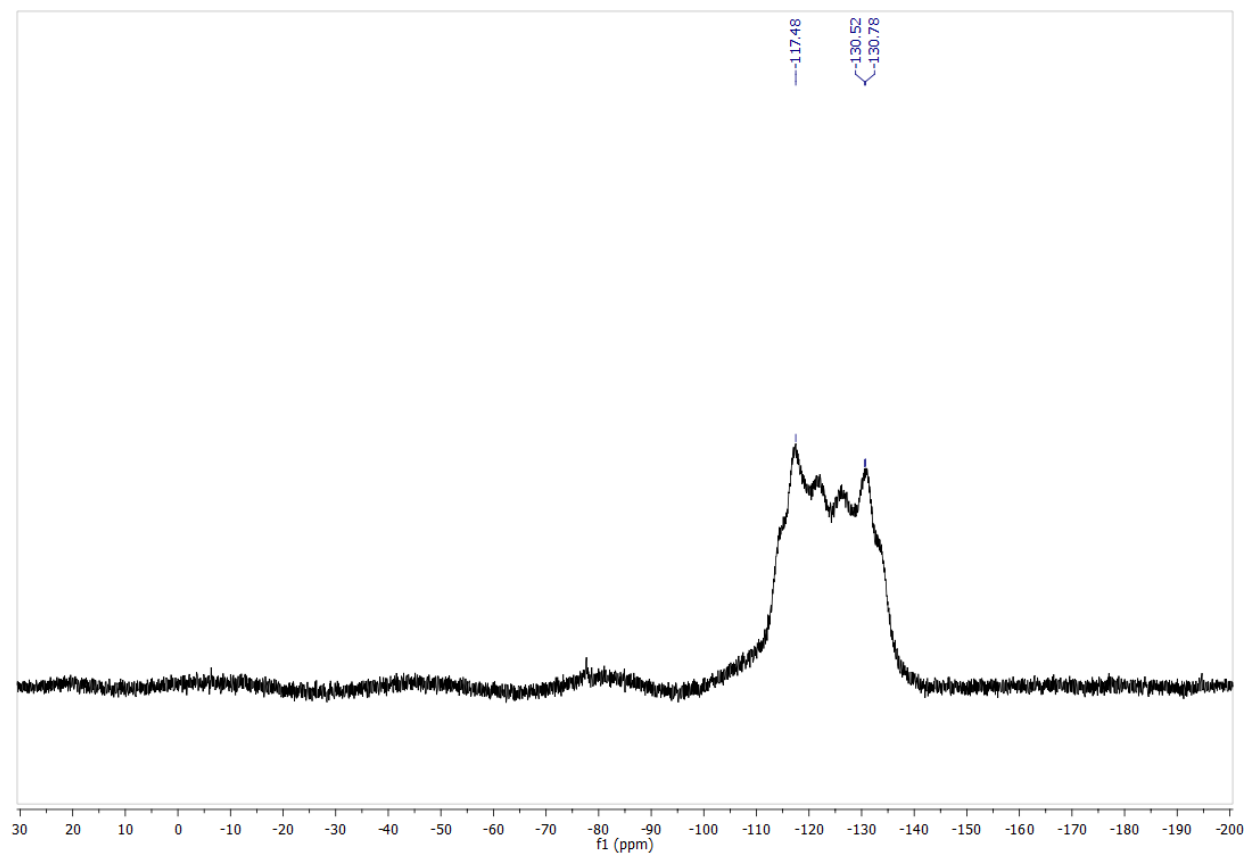


Figure 2.63 ^{19}F NMR of $3\text{I}[\text{SbF}_6]$ in CDCl_3 .

$\{\text{NCr}(\text{N}^i\text{Pr}_2)_2\text{PCy}_2\text{Ph}\}\text{SbF}_6$ CDCl_3 ^{14}N NMR

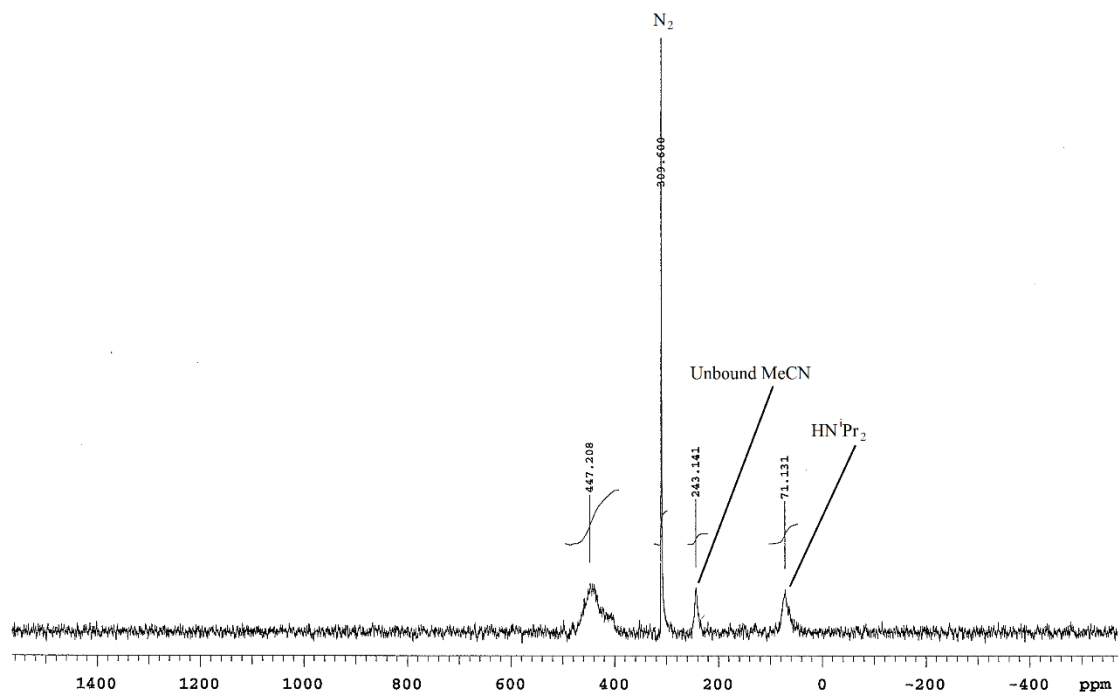


Figure 2.64 ^{14}N NMR of **3I**[SbF_6] in CDCl_3 .

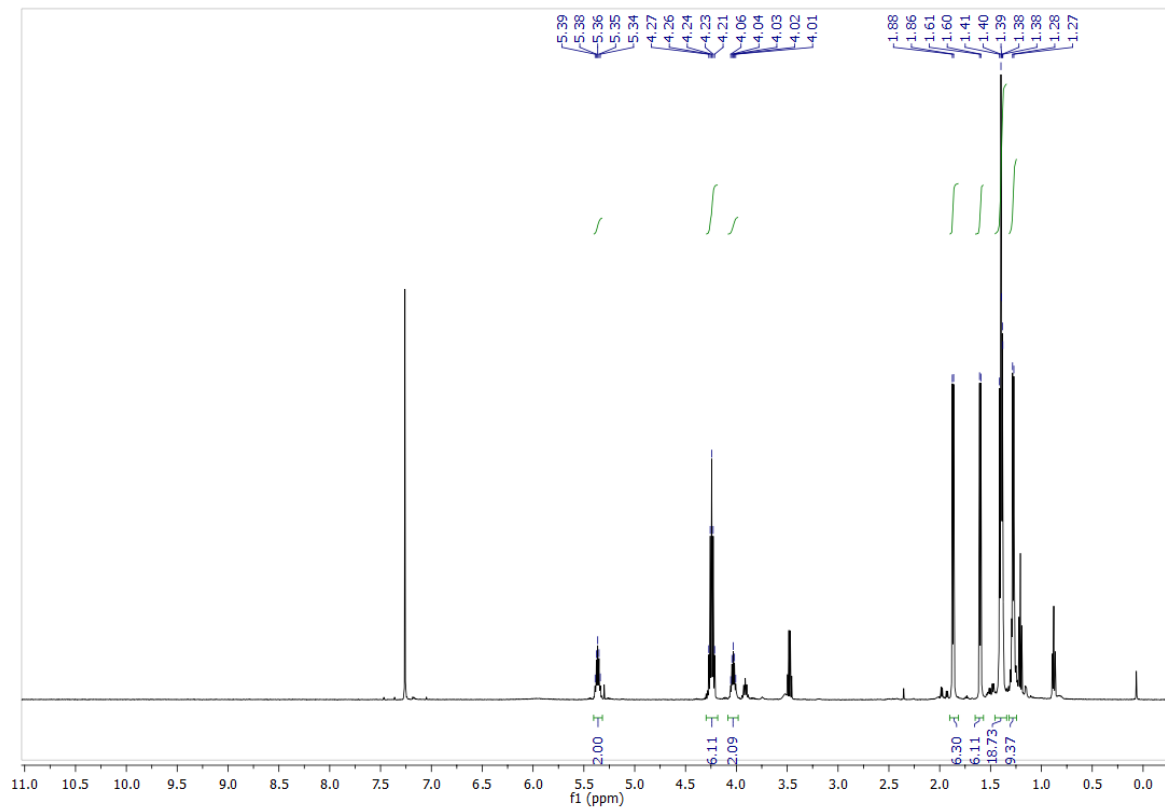


Figure 2.65 ^1H NMR of **3m**[SbF₆] in CDCl₃.

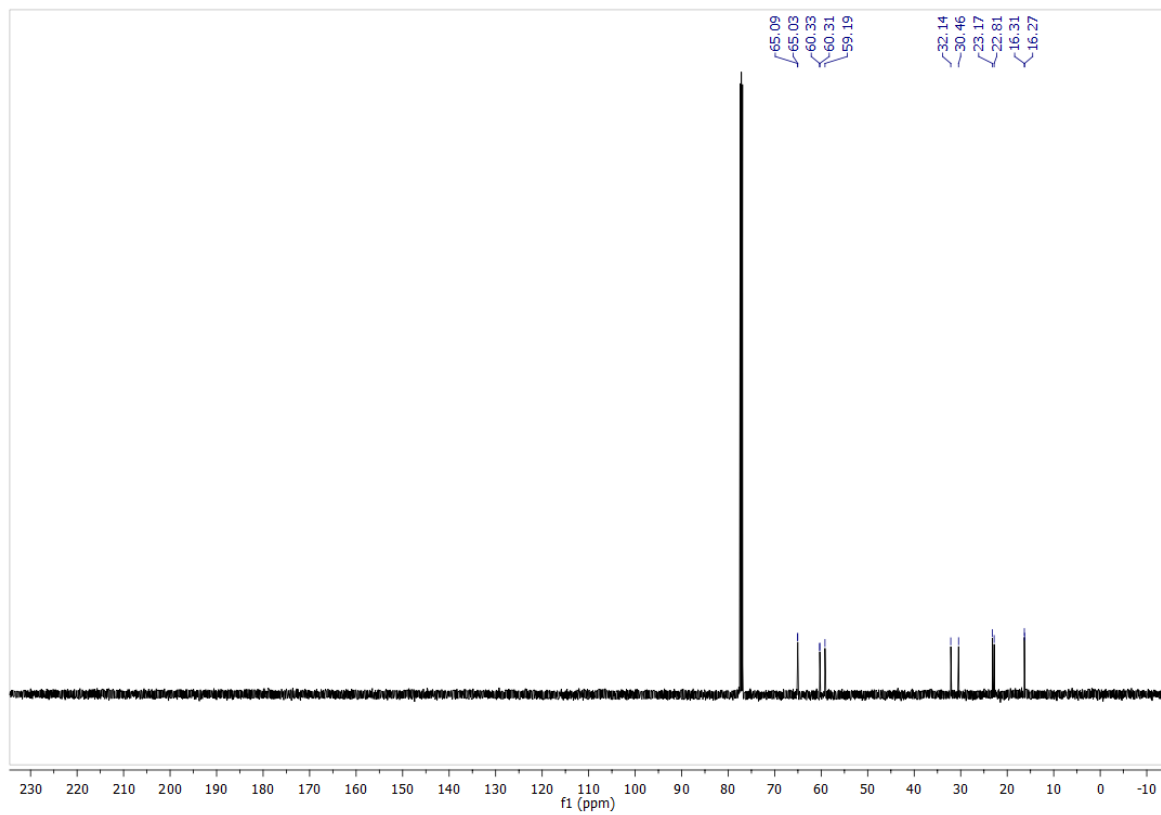


Figure 2.66 ^{13}C NMR of $3\text{m}[\text{SbF}_6]$ in CDCl_3 .

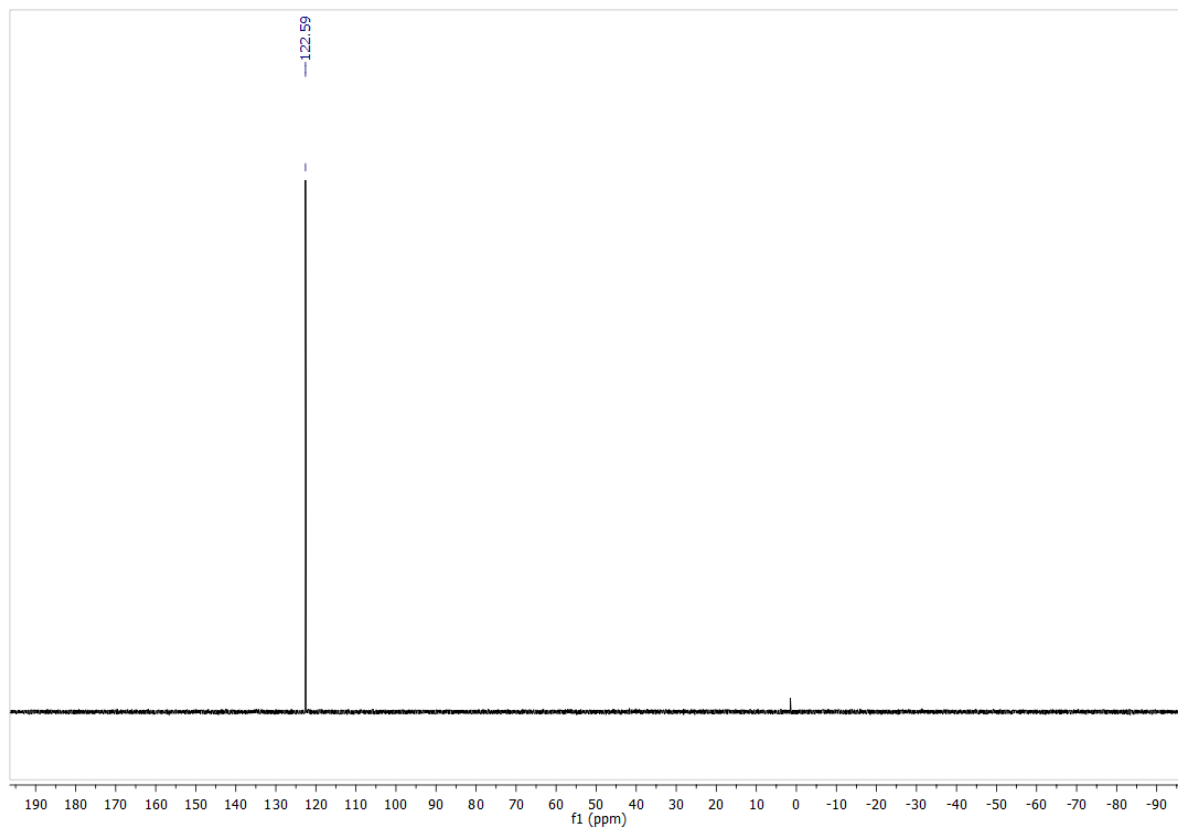


Figure 2.67 ^{31}P NMR of $3\mathbf{m}[\text{SbF}_6]$ in CDCl_3 .

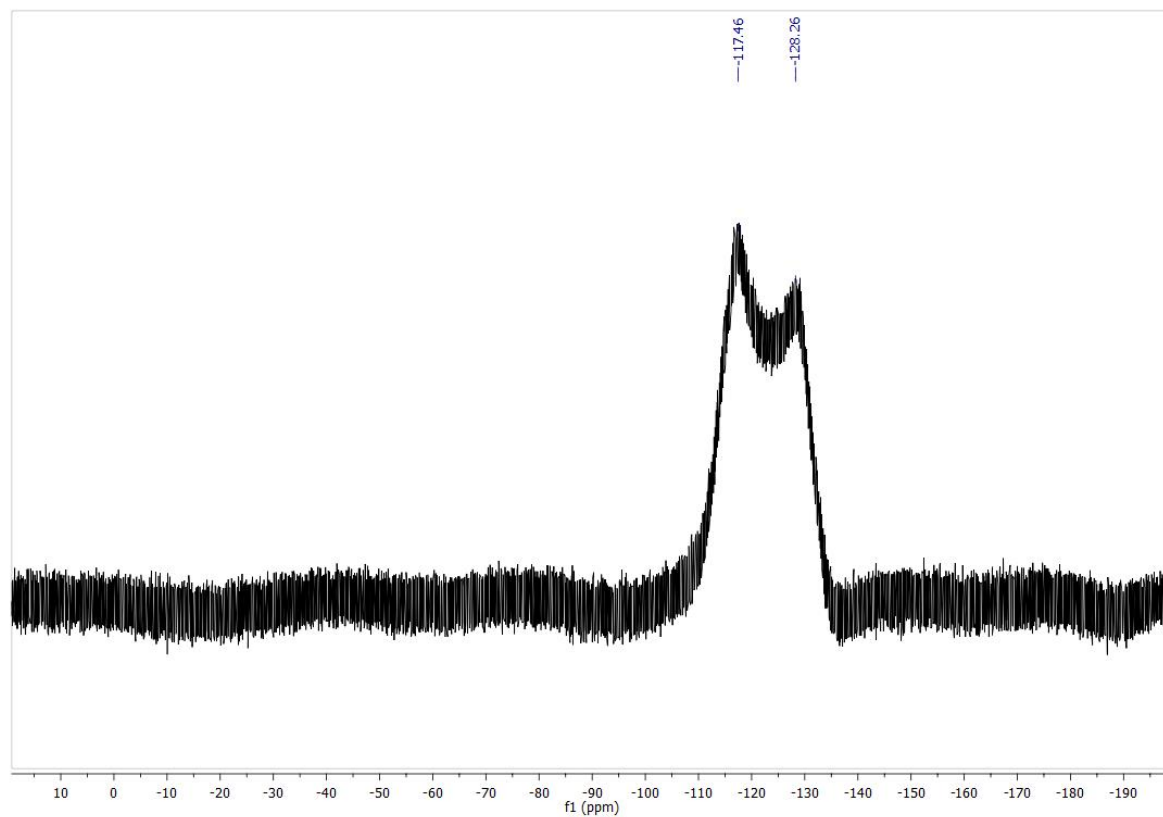


Figure 2.68 ^{19}F NMR of $3\mathbf{m}[\text{SbF}_6]$ in CDCl_3 .

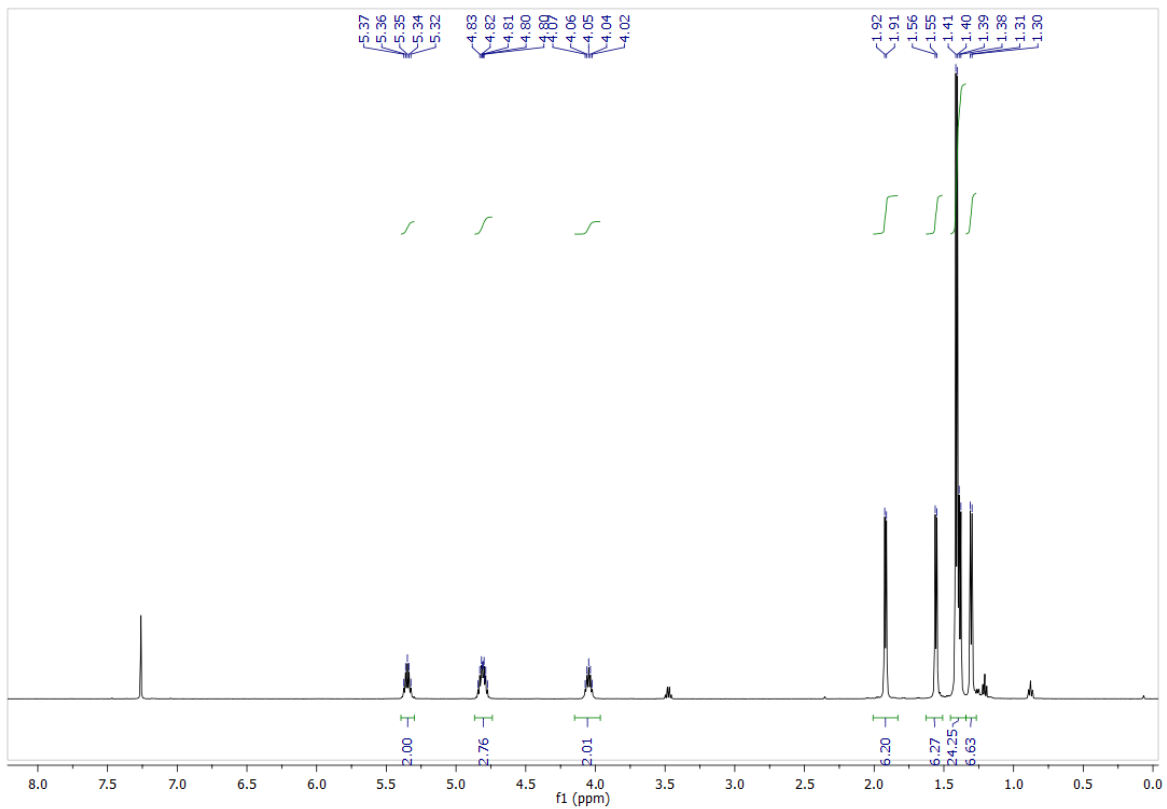


Figure 2.69 ^1H NMR of $3\mathbf{n}[\text{SbF}_6]$ in CDCl_3 .

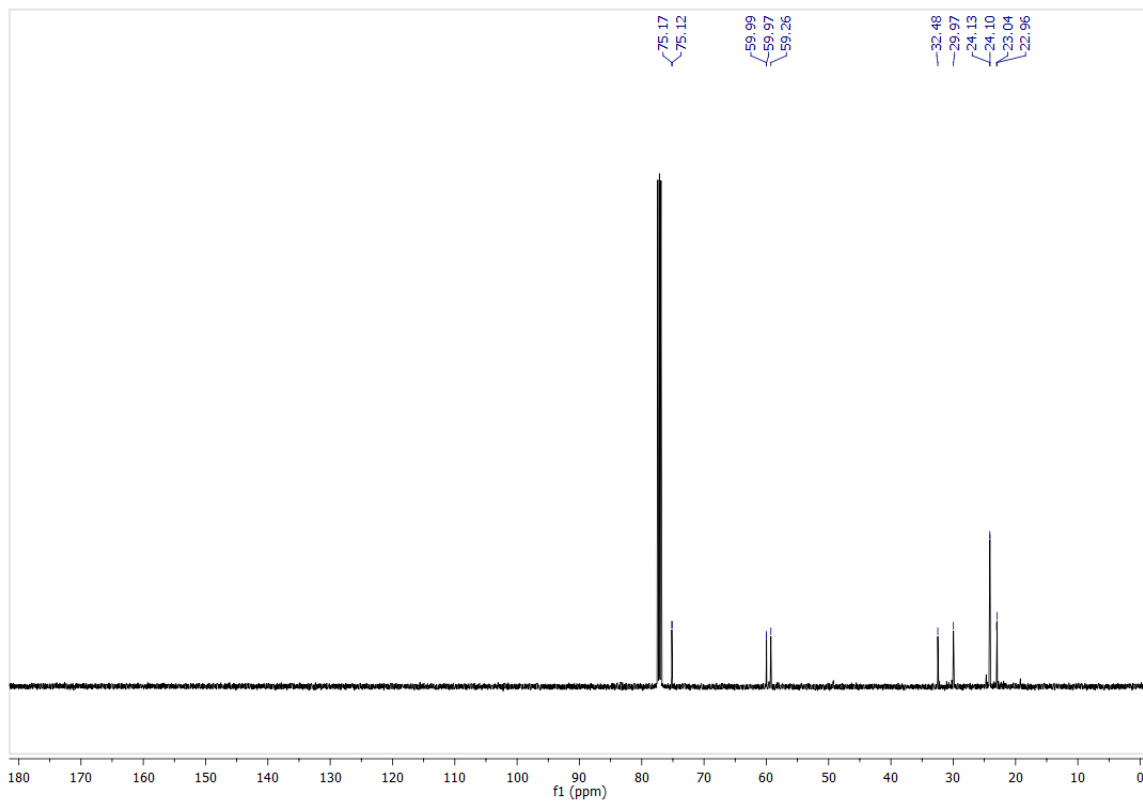


Figure 2.70 ^{13}C NMR of $3n[\text{SbF}_6]$ in CDCl_3 .

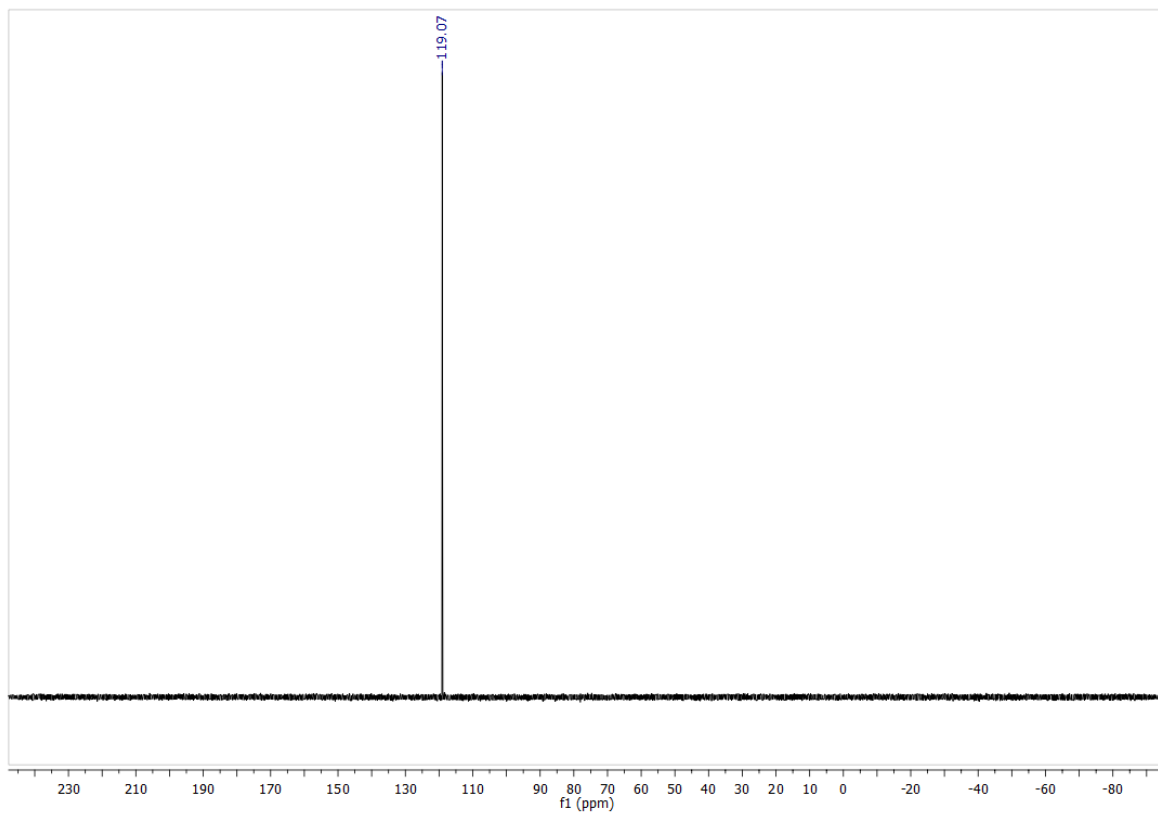


Figure 2.71 ^{31}P NMR of $3\mathbf{n}[\text{SbF}_6]$ in CDCl_3 .

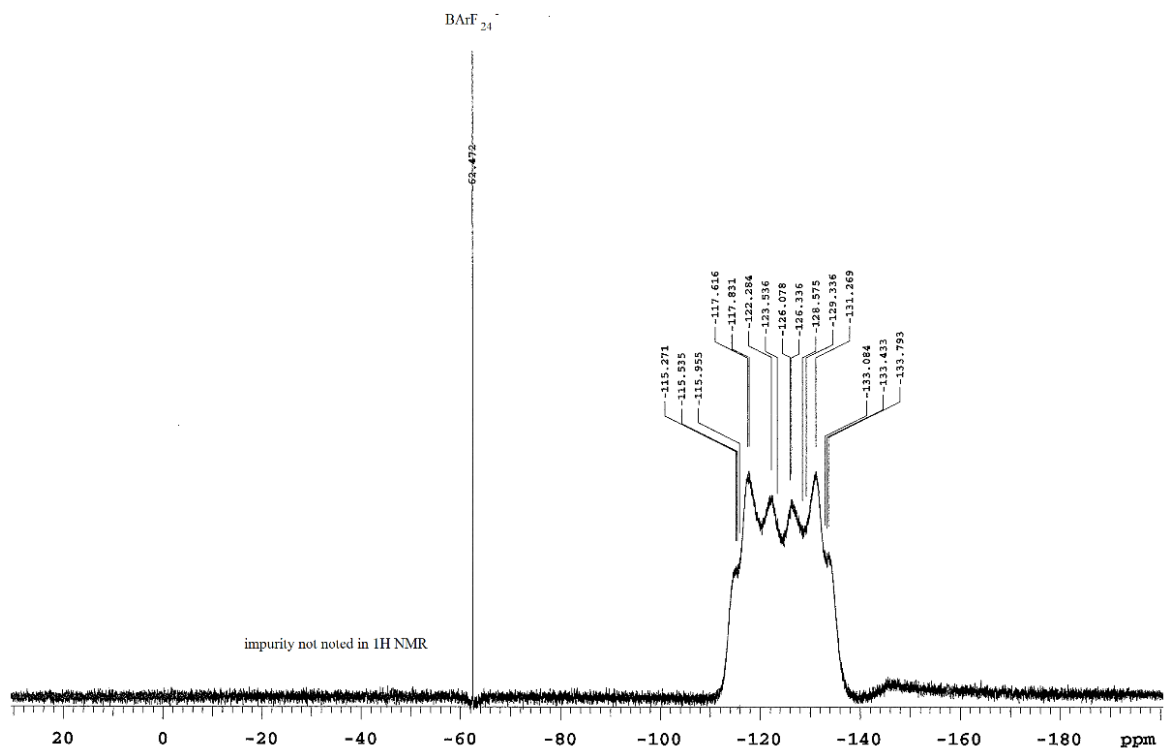


Figure 2.72 ^{19}F NMR of $3n[SbF_6]$ in $CDCl_3$.

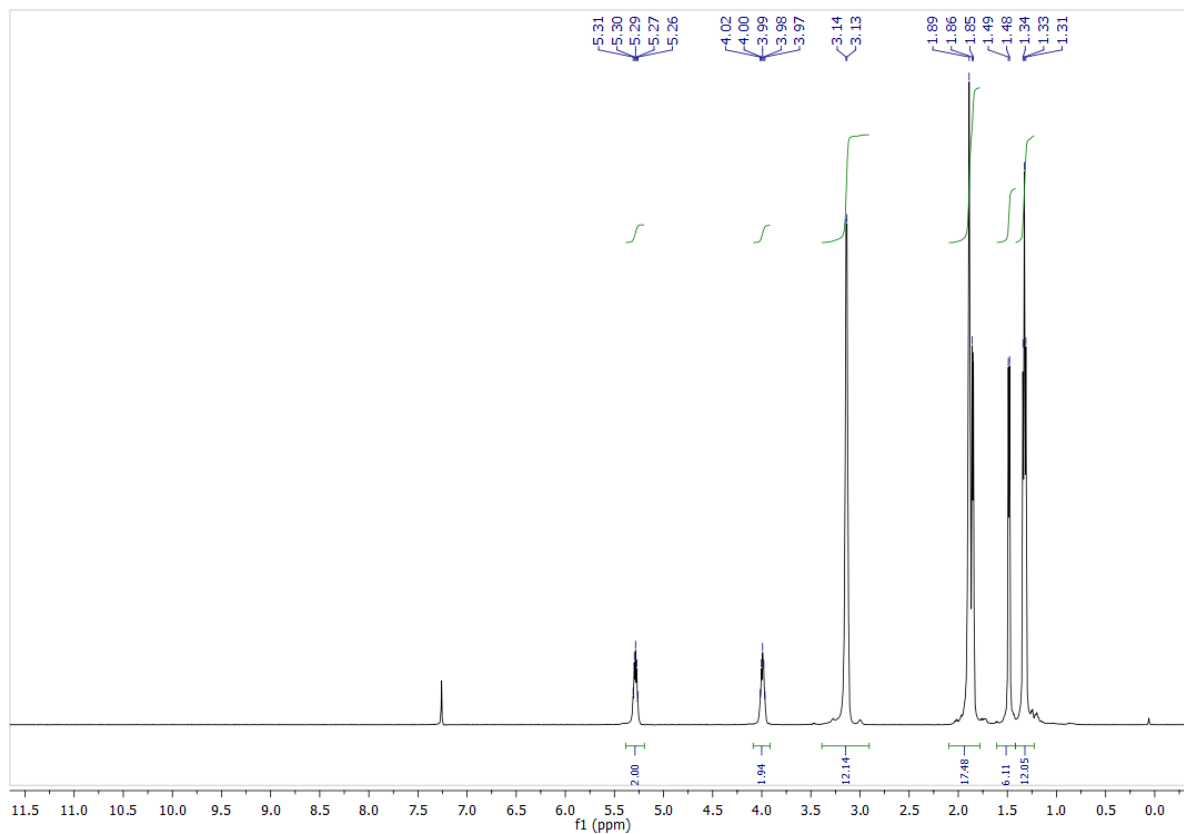


Figure 2.73 ^1H NMR of $3\text{o}[\text{PF}_6]$ in CDCl_3 .

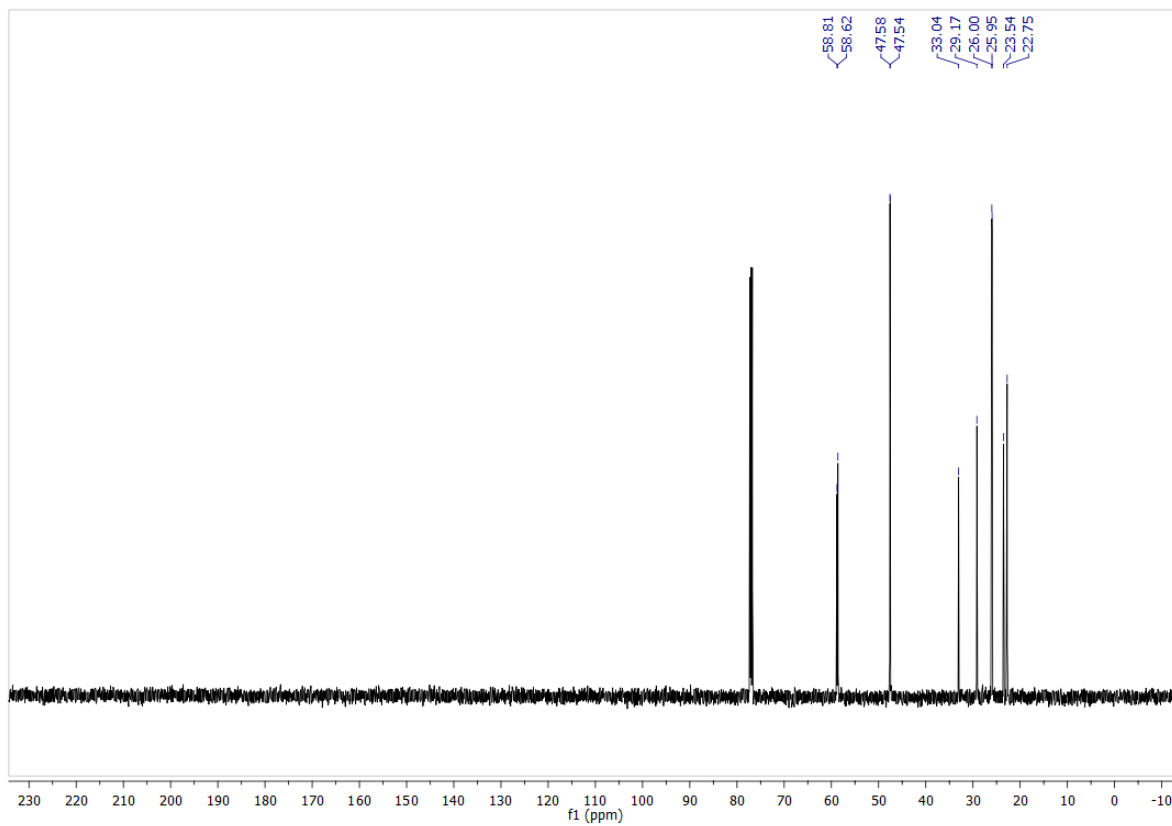


Figure 2.74 ^{13}C NMR of $30[\text{PF}_6]$ in CDCl_3 .

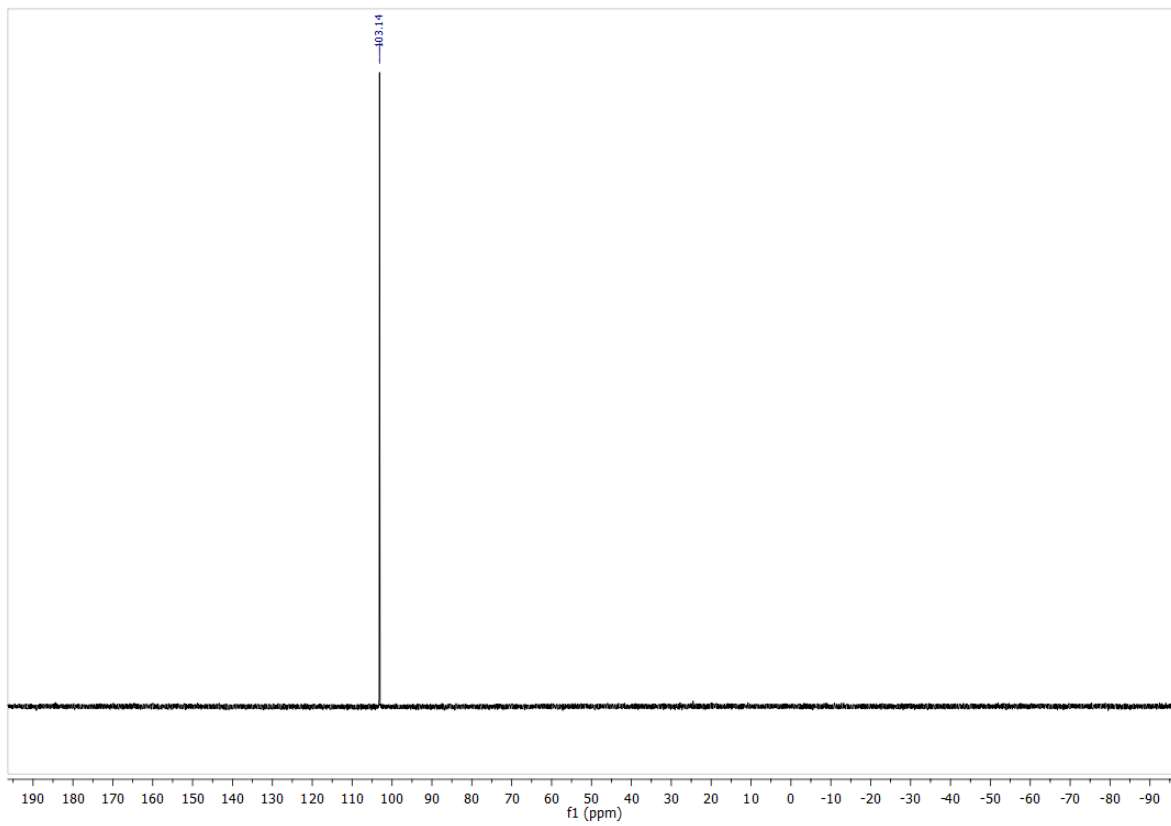


Figure 2.75 ^{31}P NMR of **3o**[PF₆] in CDCl₃.

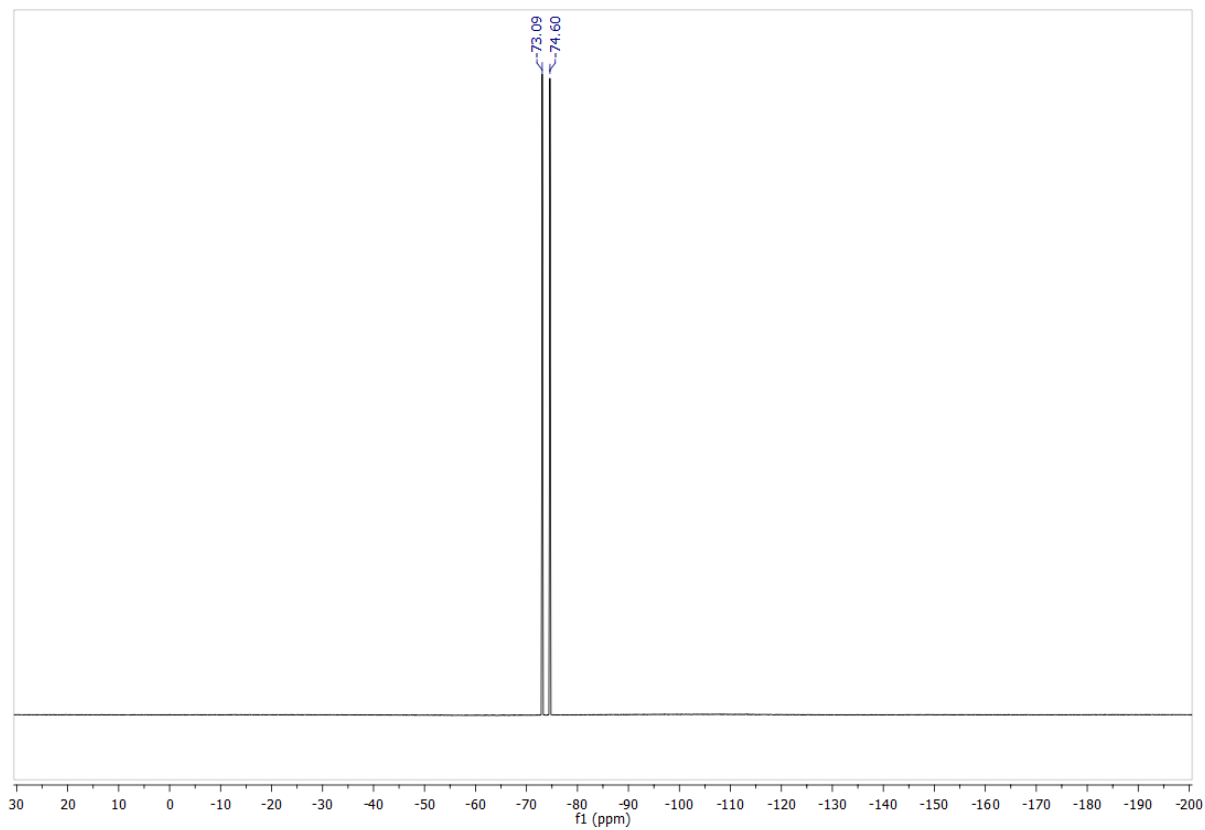


Figure 2.76 ^{19}F NMR of $3\mathbf{o}[\text{PF}_6]$ in CDCl_3 .

$\{NCr(N^iPr_2)_2P(NC_4H_9)_3\}PF_6$ $CDCl_3$ ^{14}N NMR

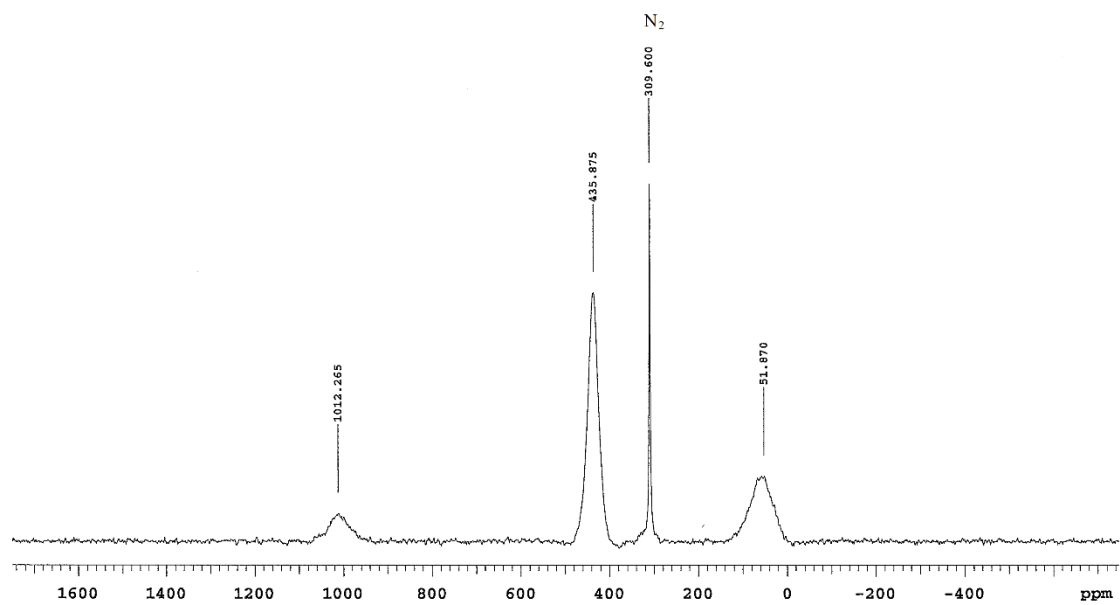


Figure 2.77 ^{14}N NMR of **30**[PF_6] in $CDCl_3$.

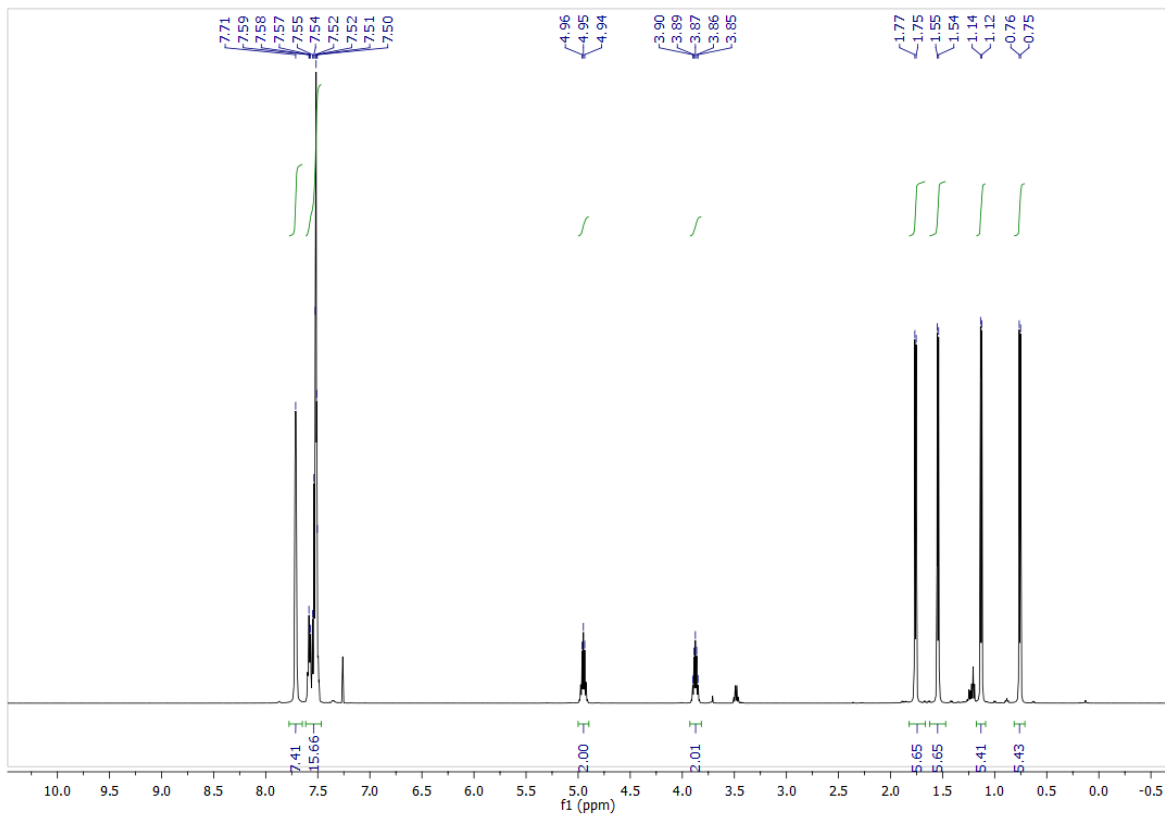


Figure 2.78 ^1H NMR of $3\text{p}[\text{BArF}_{24}]$ in CDCl_3 .

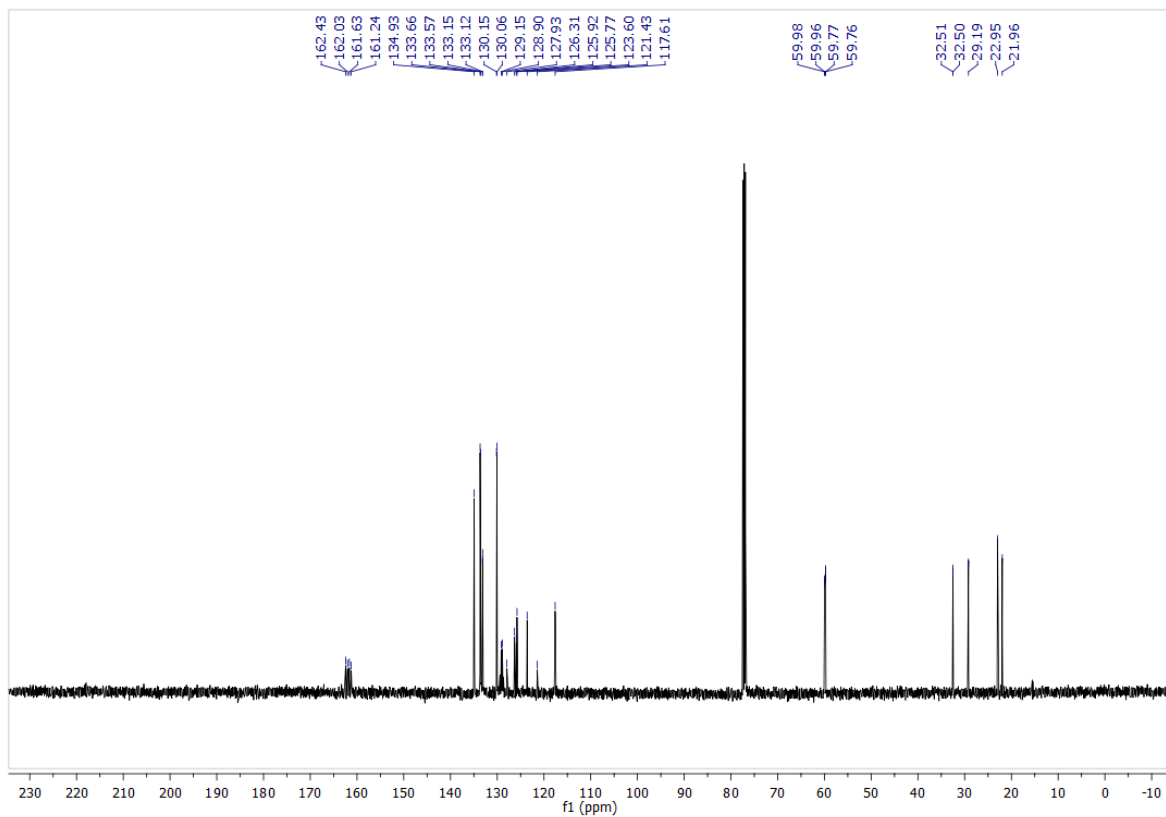


Figure 2.79 ^{13}C NMR of $3\text{p}[\text{BArF}_{24}]$ in CDCl_3 .

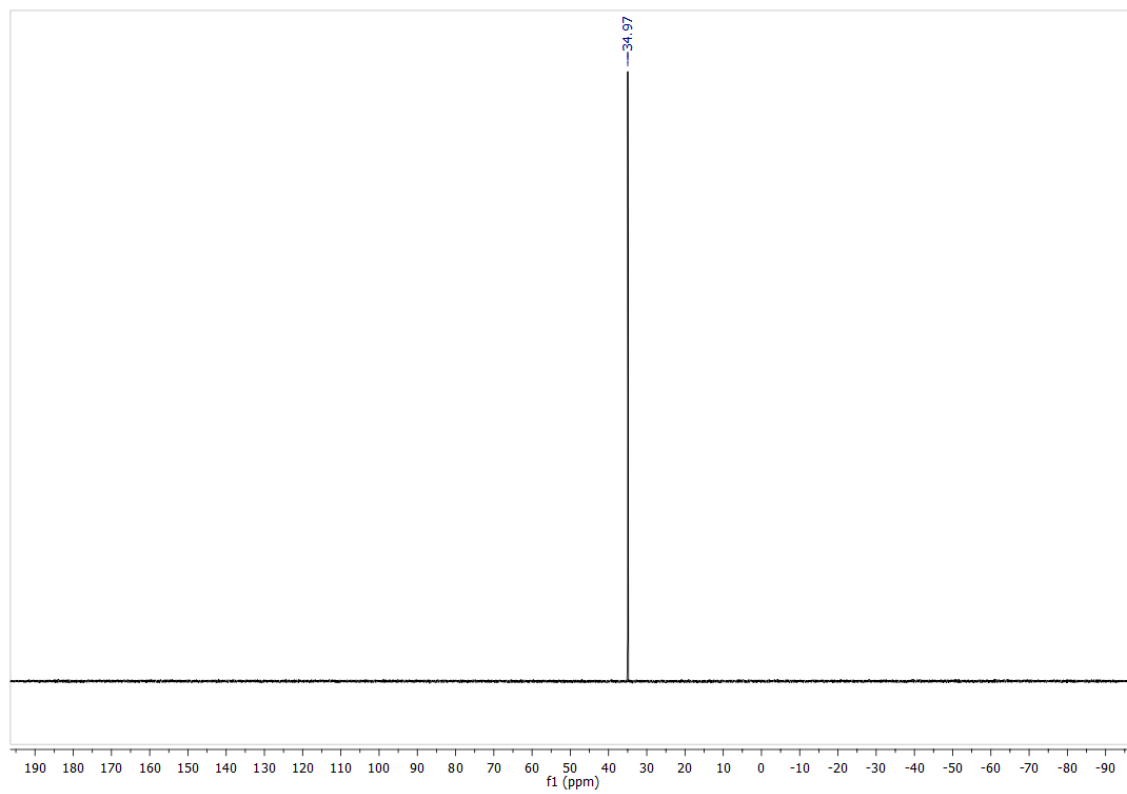


Figure 2.80 ^{31}P NMR of **3p**[BArF₂₄] in CDCl₃.

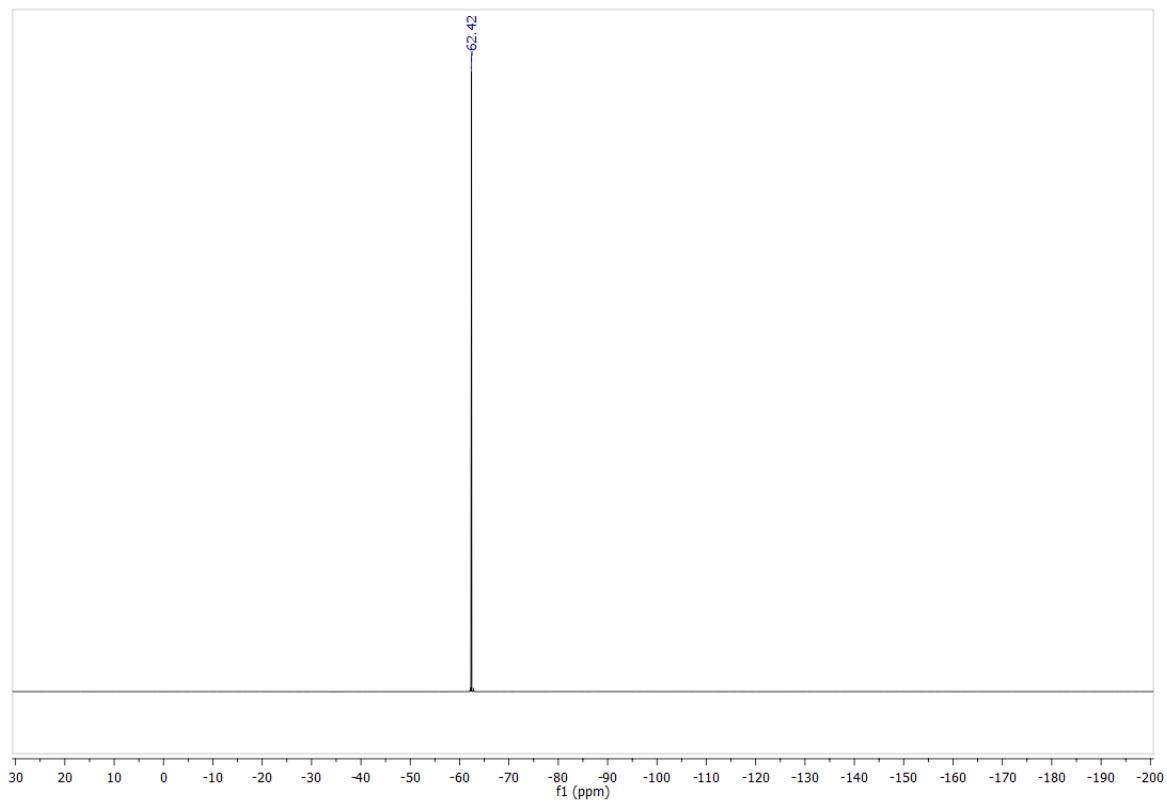


Figure 2.81 ^{19}F NMR of $3\mathbf{p}[\text{BArF}_{24}]$ in CDCl_3 .

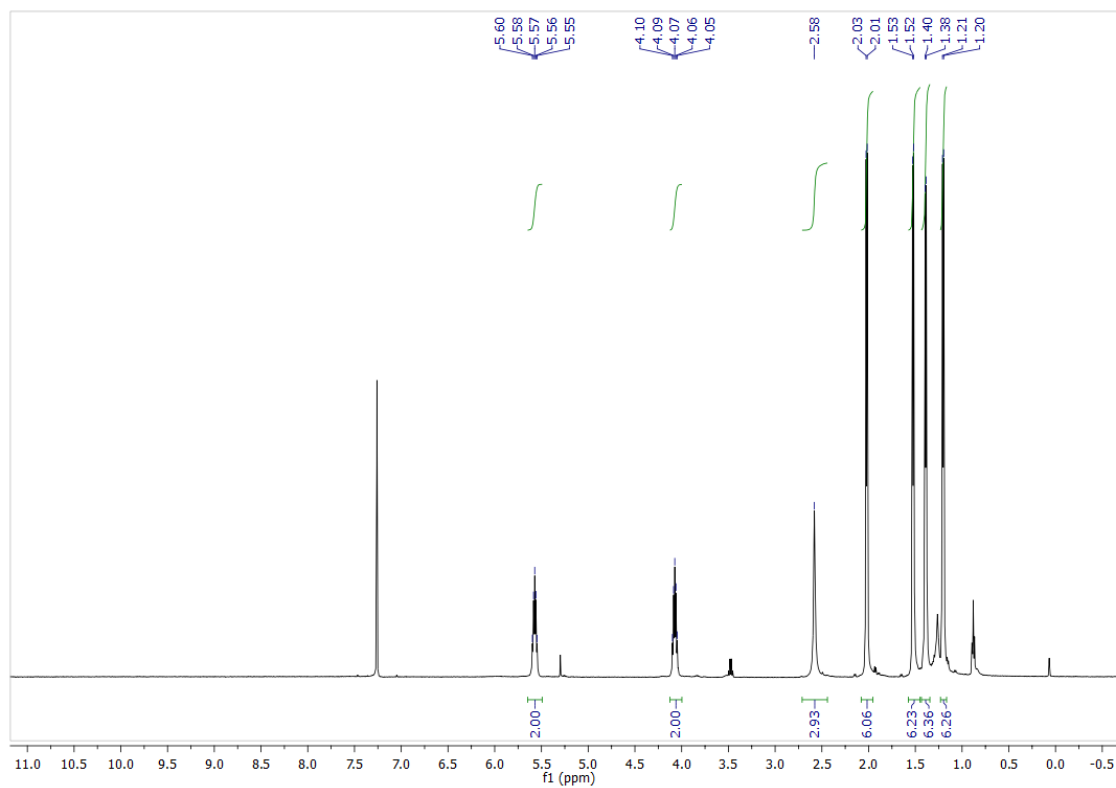


Figure 2.82 ^1H NMR of $2[\text{SbF}_6]$ in CDCl_3 .

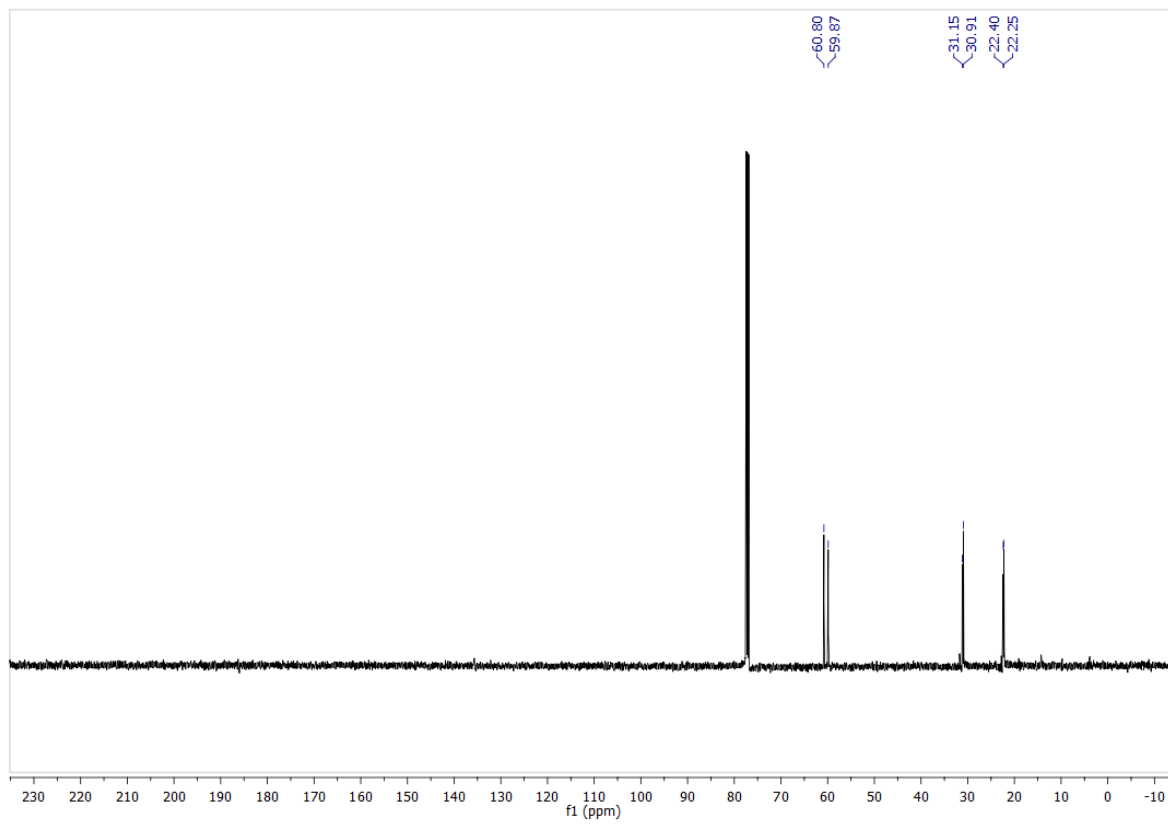


Figure 2.83 ^{13}C NMR of $2[\text{SbF}_6]$ in CDCl_3 .

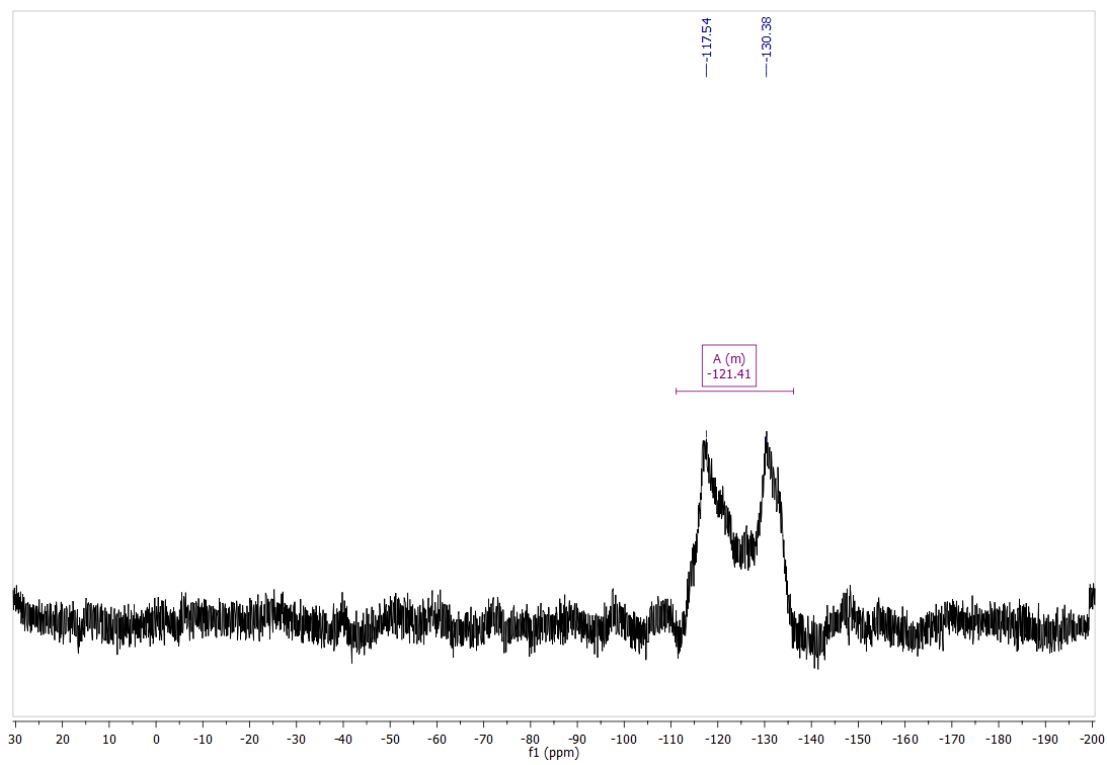


Figure 2.84 ^{19}F NMR of $2[\text{SbF}_6]$ in CDCl_3 .

$\{\text{NCr}(\text{N}^i\text{Pr}_2)_2\text{NCCH}_3\} \text{SbF}_6$ CDCl_3 ^{14}N NMR

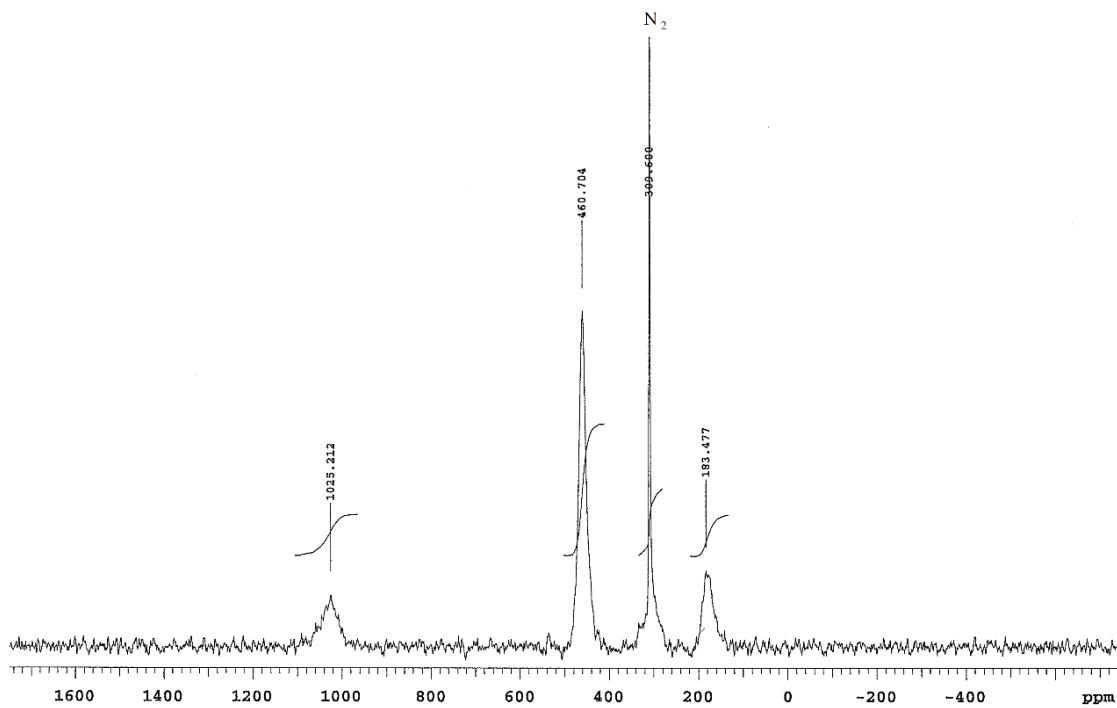


Figure 2.85 ^{14}N NMR of $2[\text{SbF}_6]$ in CDCl_3 .

NMR Spectra of Additional Complexes Utilized for Ion Pairing Studies

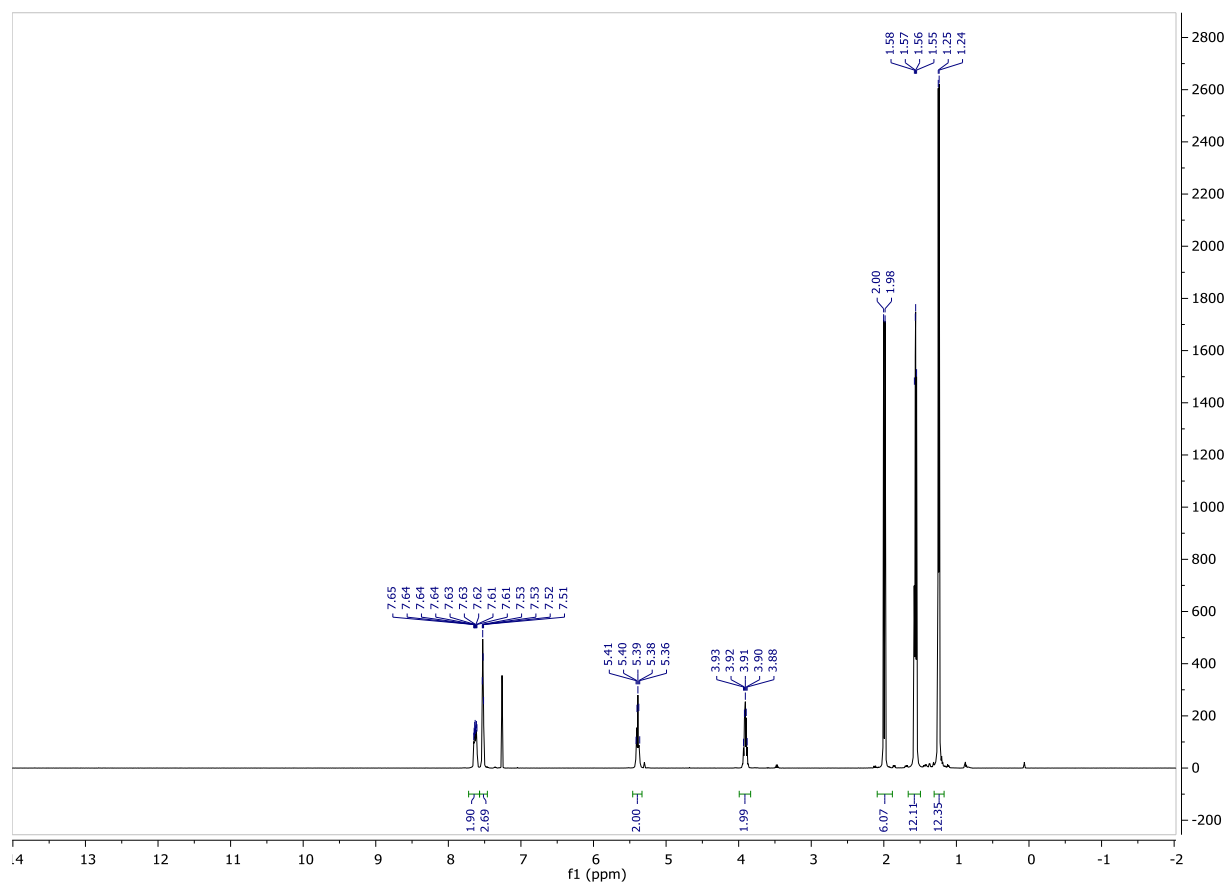


Figure 2.86 ^1H NMR spectrum of $3f[\text{PF}_6]$ in CDCl_3 .

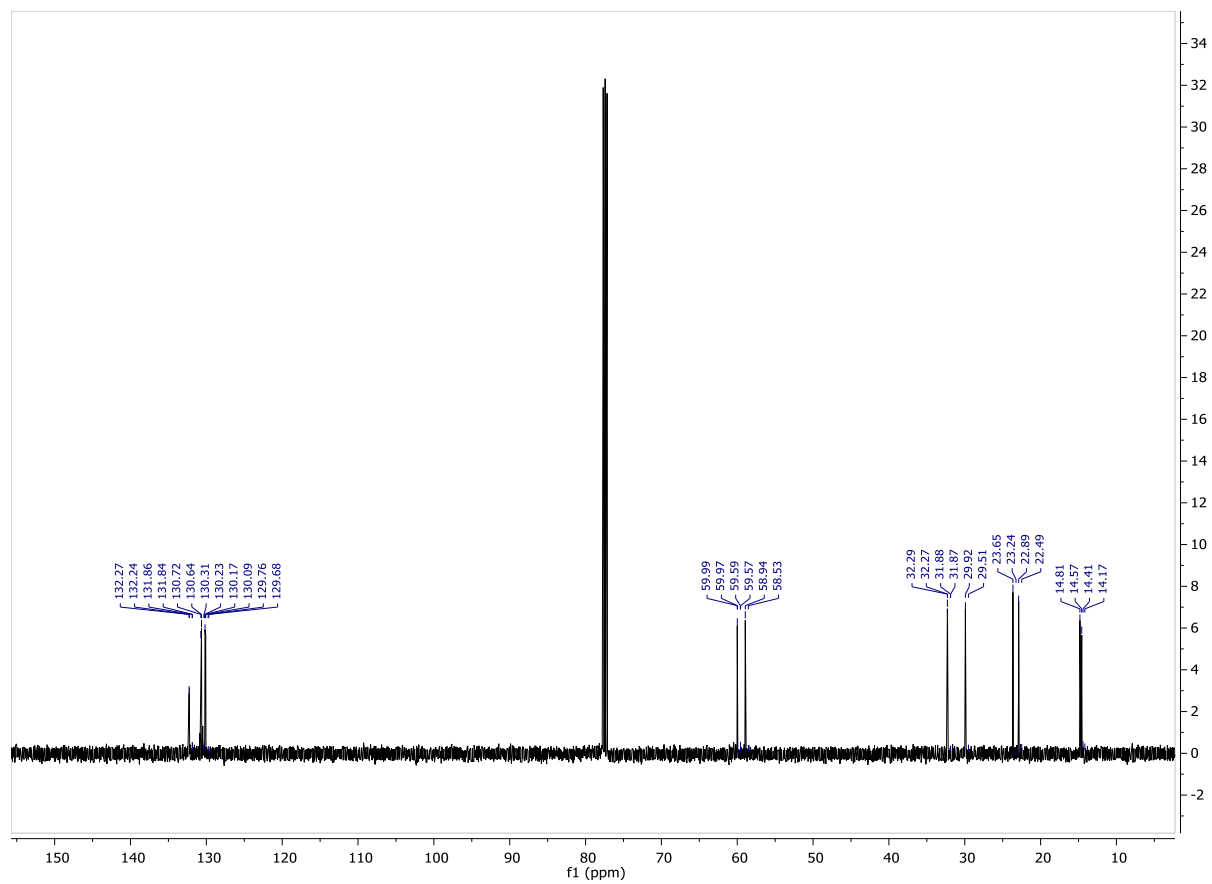


Figure 2.87 ^{13}C NMR spectrum of $3\mathbf{f}[\text{PF}_6]$ in CDCl_3 .

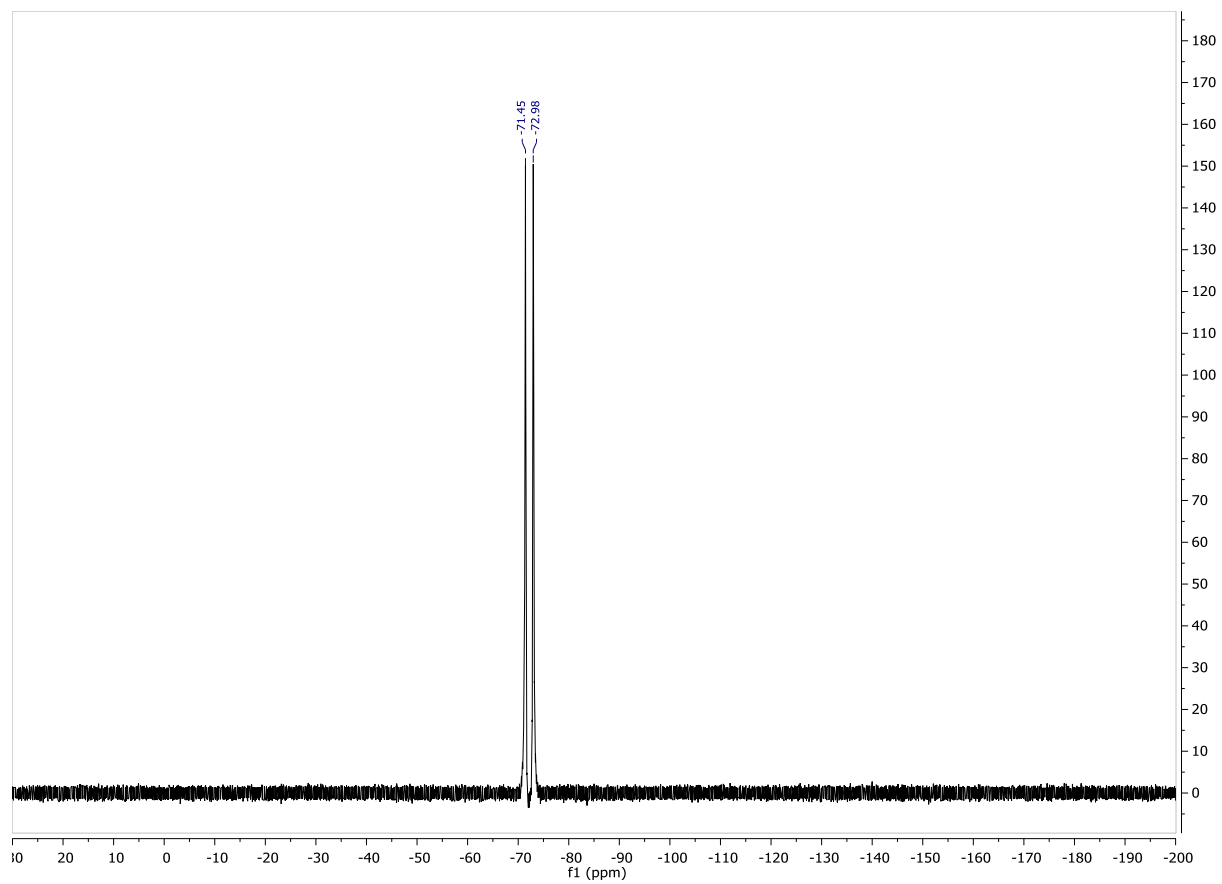


Figure 2.88 ^{19}F NMR spectrum of **3f**[PF₆] in CDCl₃

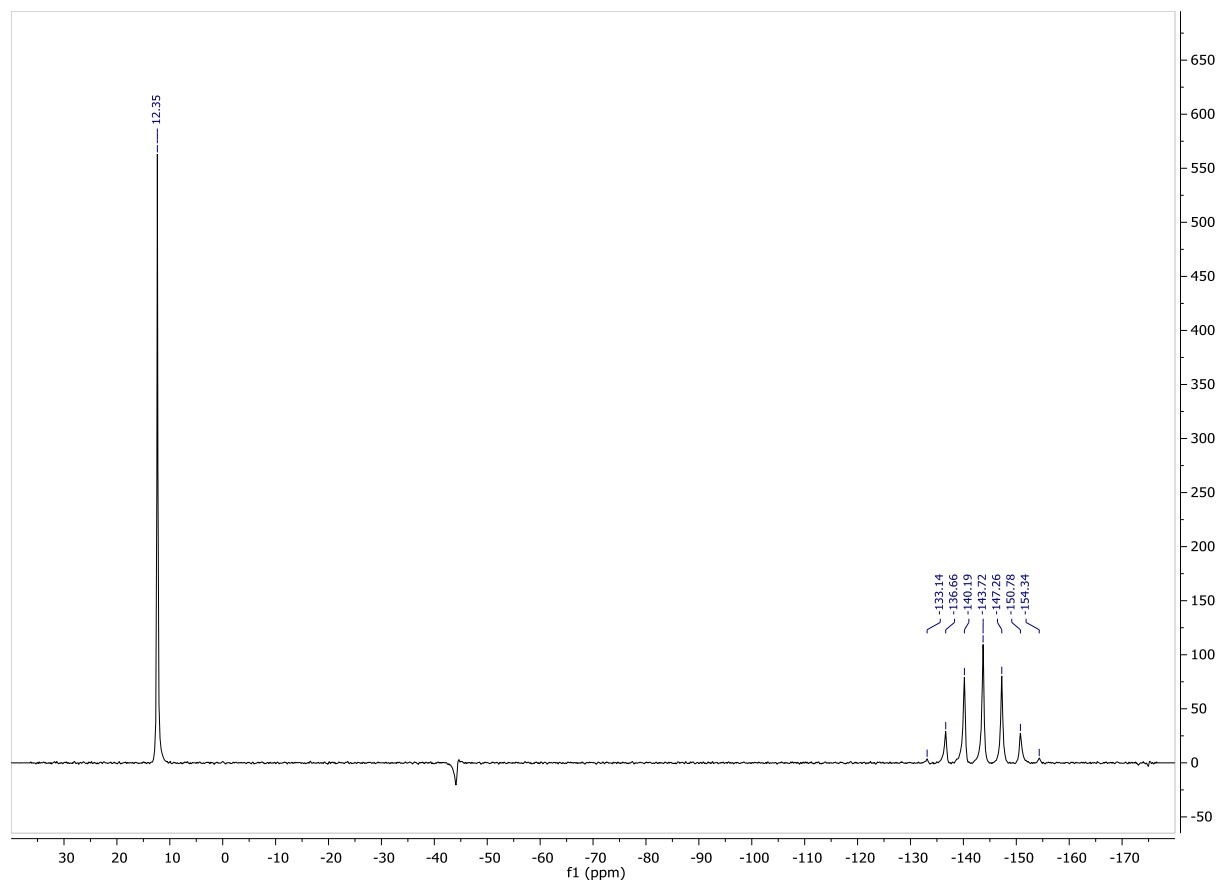
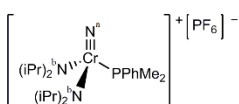


Figure 2.89 ^{31}P NMR of **3f**[PF₆] in CDCl₃.



$\{1\}\text{PF}_6^{14}\text{N NMR CDCl}_3$

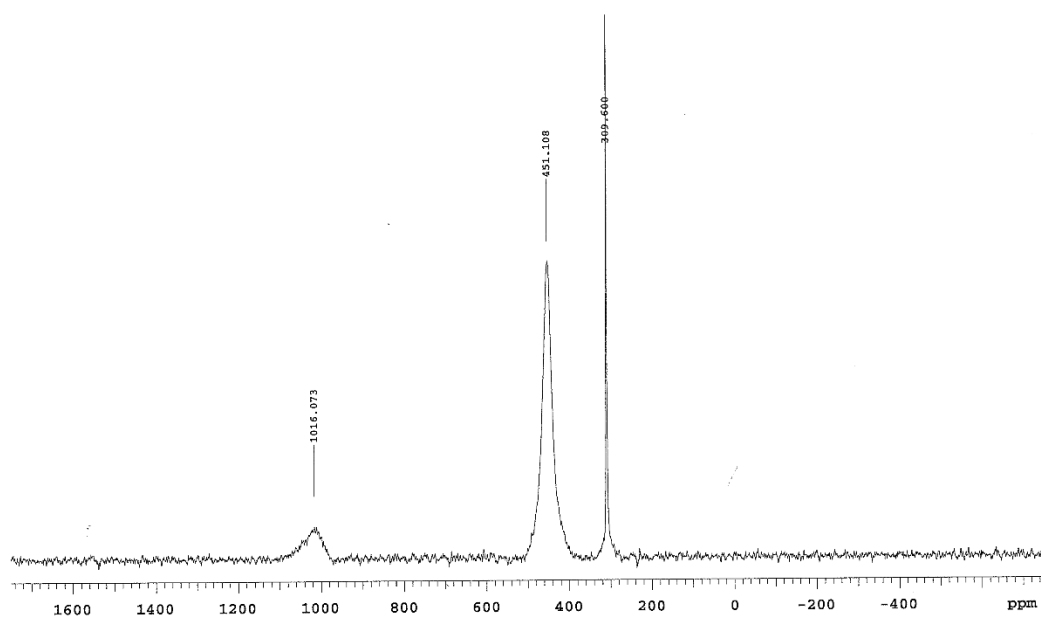


Figure 2.90 ^{14}N NMR spectrum of $3\mathbf{f}[\text{PF}_6]$.

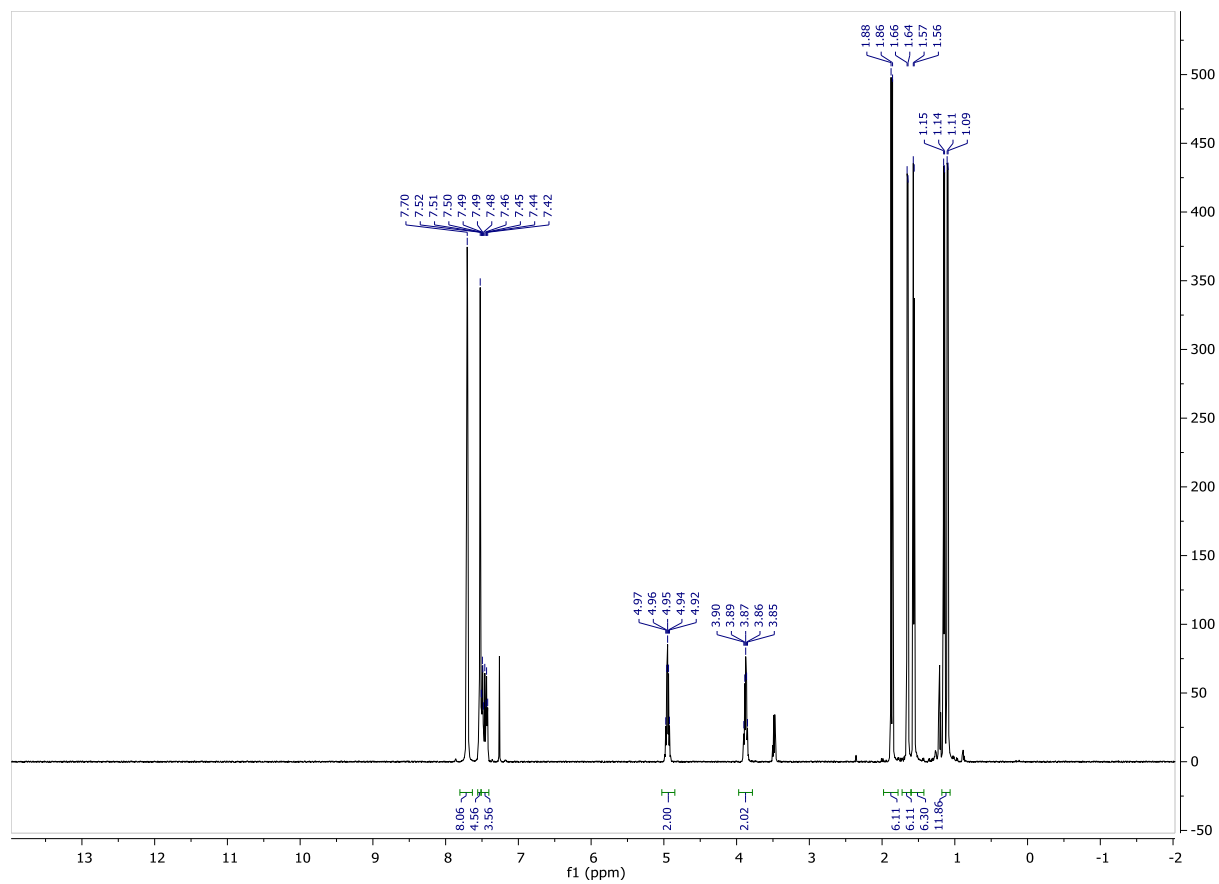


Figure 2.91 ^1H NMR of $3f[\text{BArF}_{24}]$ in CDCl_3 .

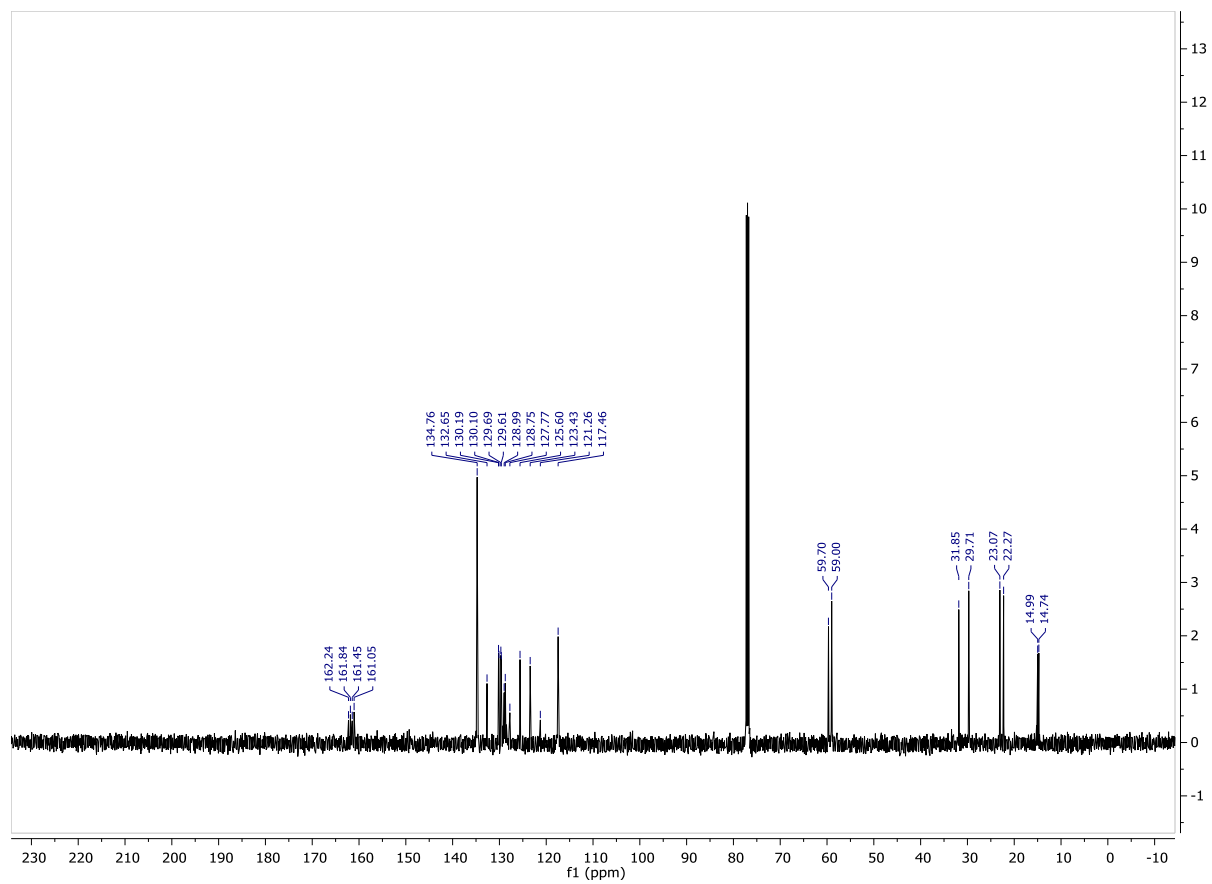


Figure 2.92 ^{13}C NMR spectrum of **3f**[BArF₂₄] in CDCl₃.

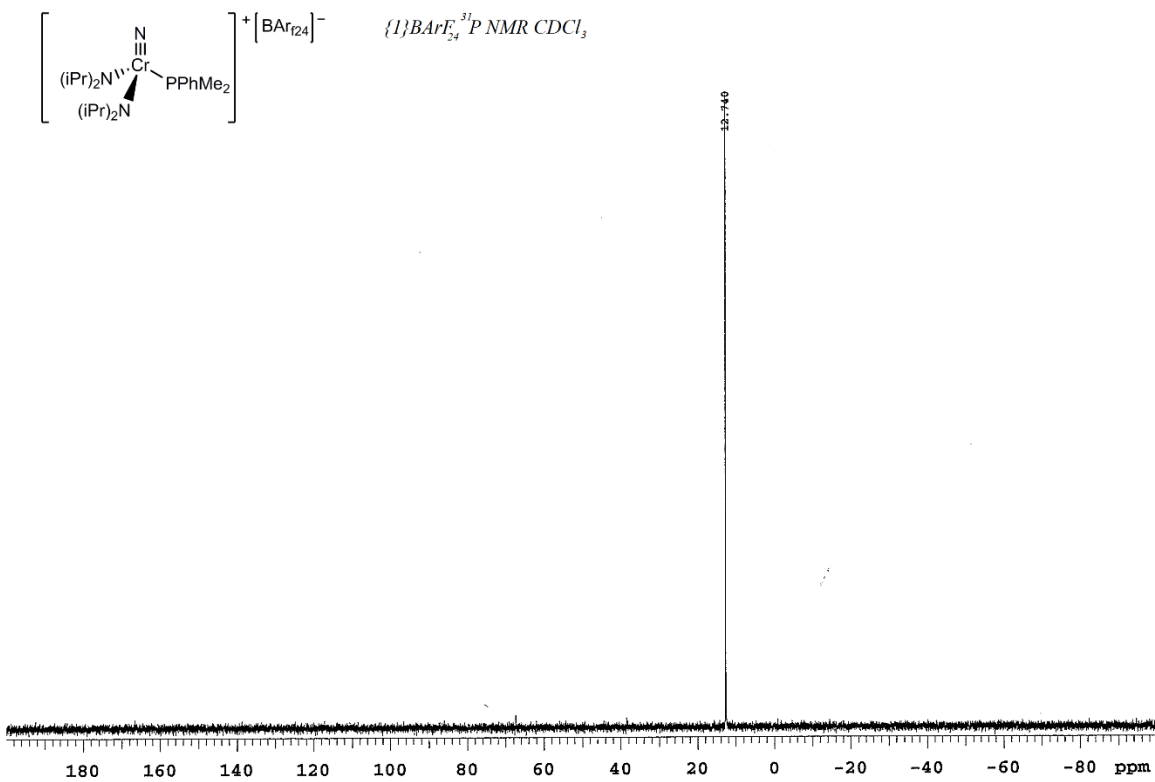


Figure 2.93 ^{31}P NMR spectrum of **3f**[BArF₂₄] in CDCl₃.

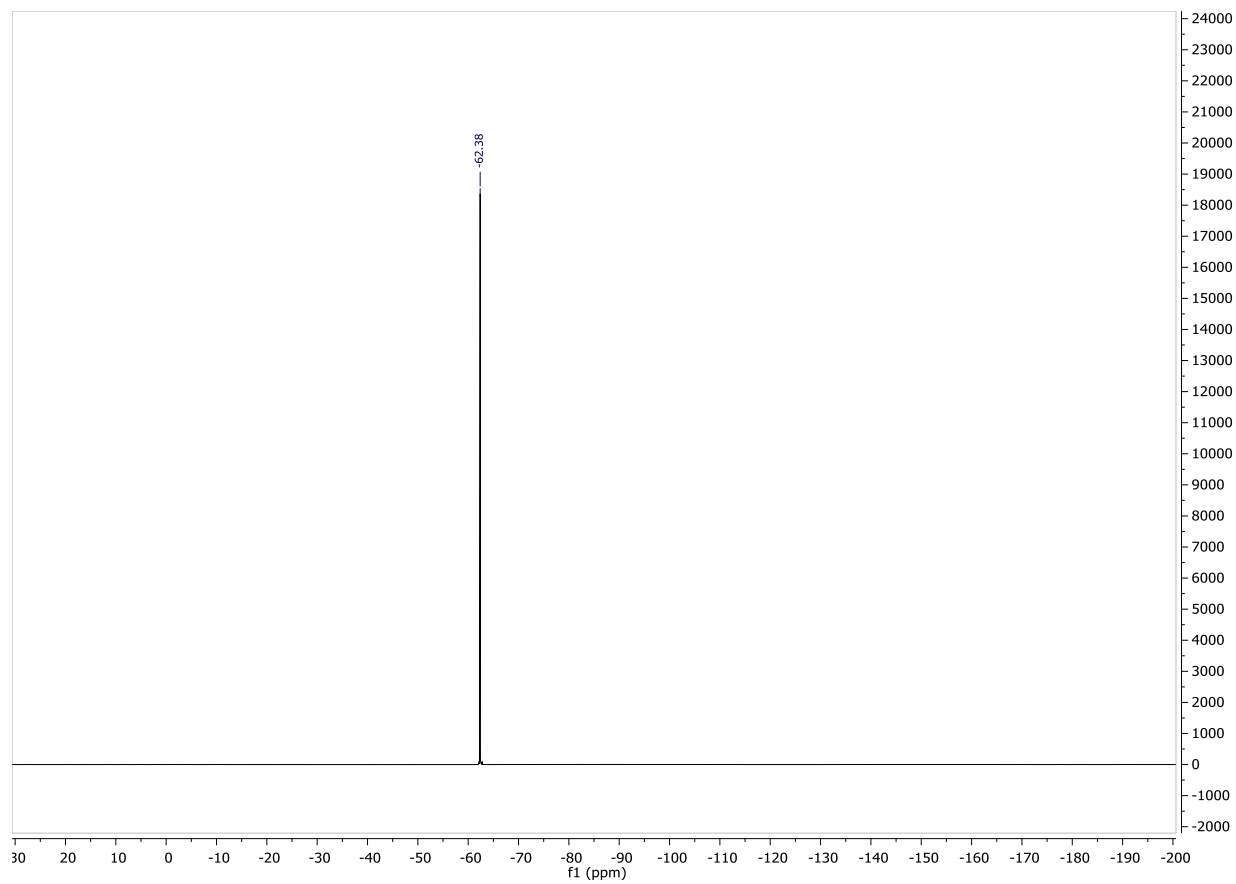


Figure 2.94 ^{19}F NMR spectrum of **3f**[BArF₂₄] in CDCl₃.

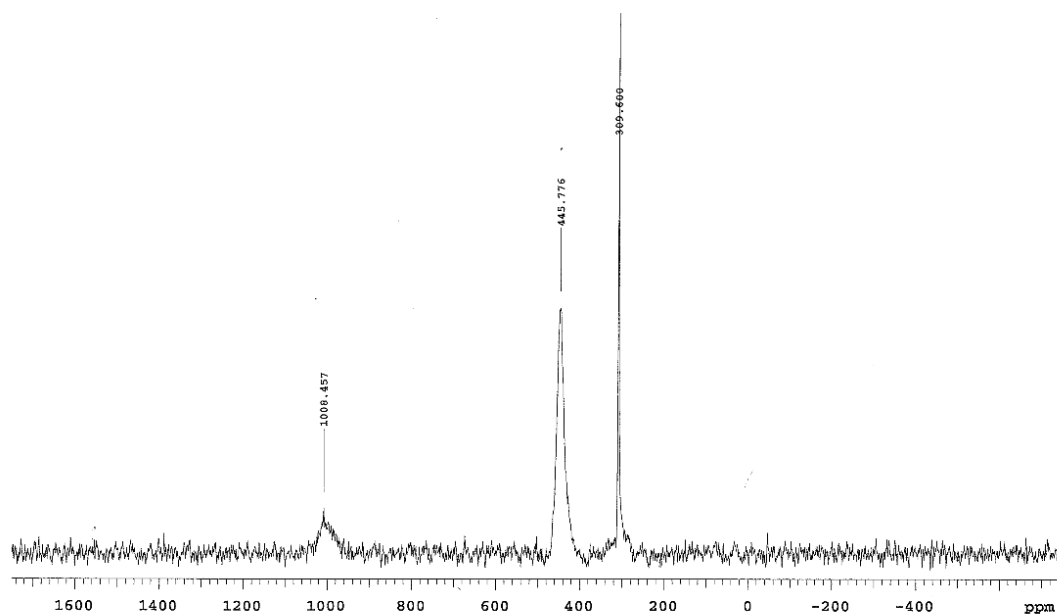
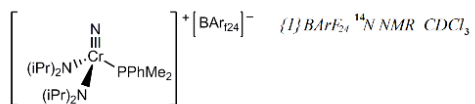


Figure 2.95 ^{14}N NMR spectrum of $3\mathbf{f}[\text{BArF}_{24}]$ in CDCl_3 .

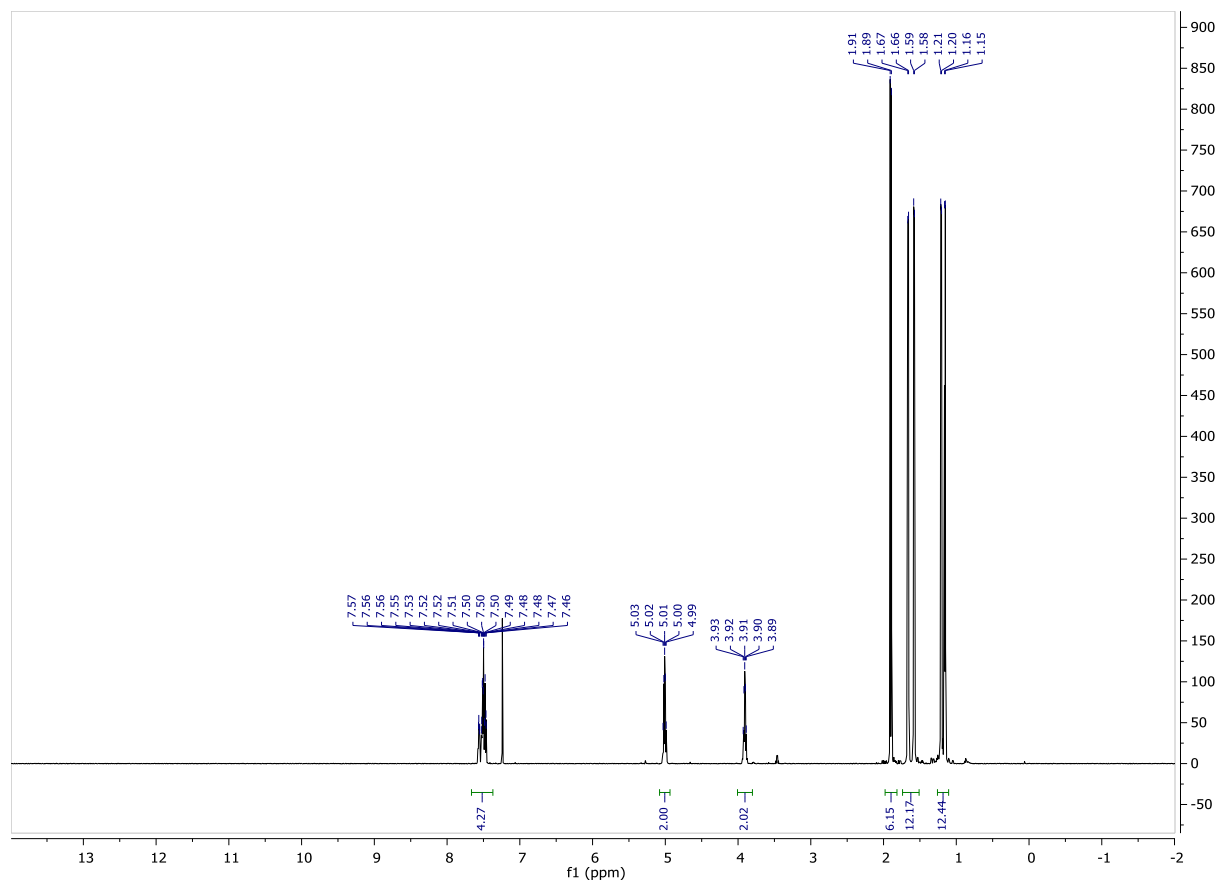


Figure 2.96 ^1H NMR spectrum of $3\text{f}[\text{BArF}_{20}]$ in CDCl_3 .

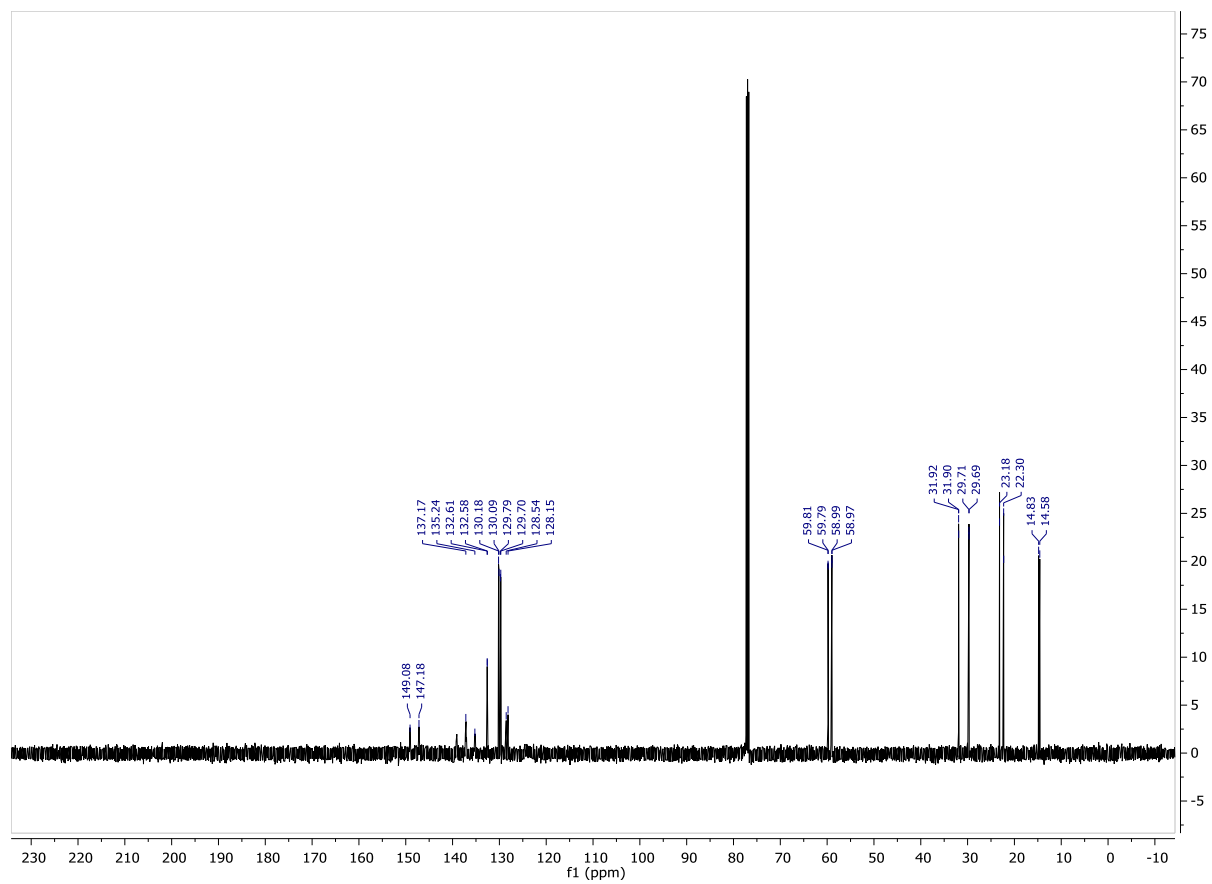


Figure 2.97 ^{13}C NMR spectrum of $3f[\text{BArF}_{20}]$ in CDCl_3 .

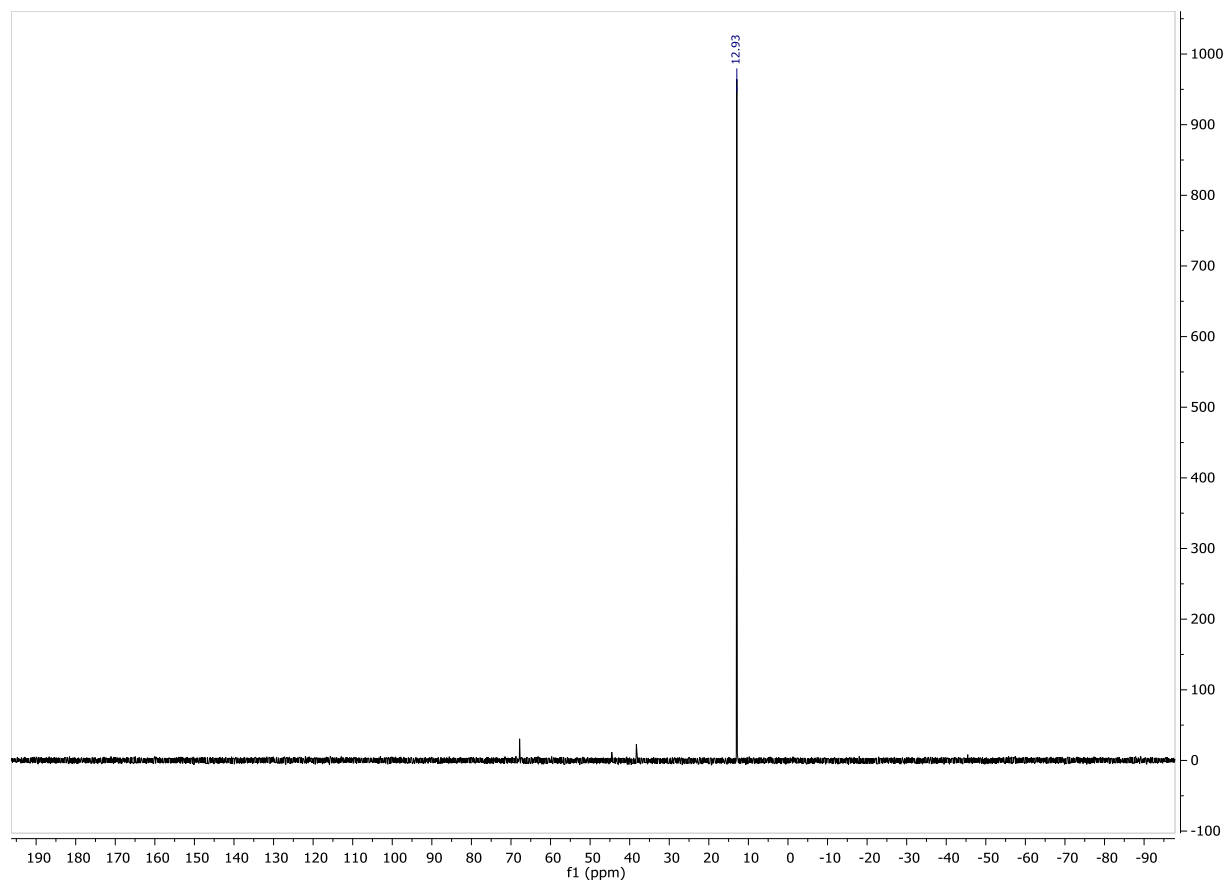


Figure 2.98 ^{31}P NMR spectrum of **3f**[BArF₂₀] in CDCl₃.

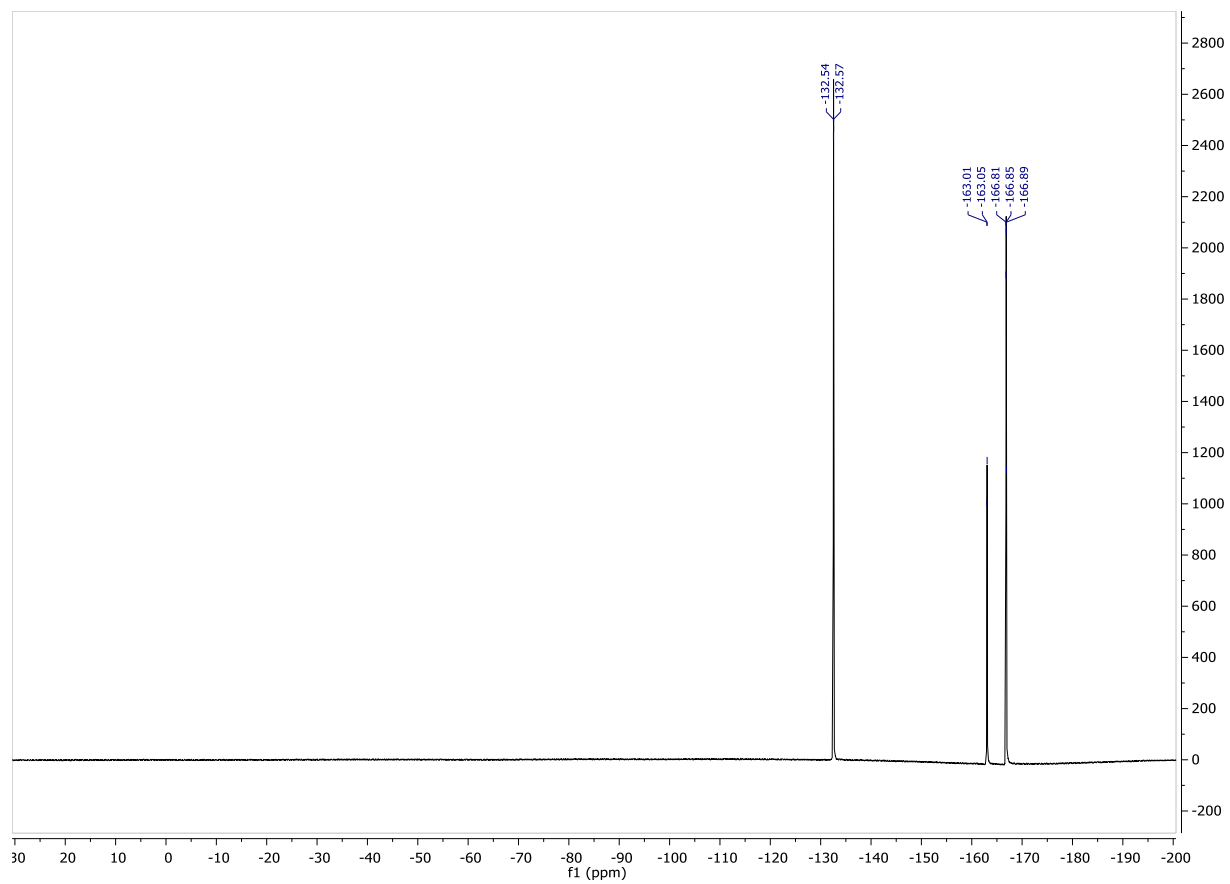


Figure 2.99 ^{19}F NMR spectrum of $3\mathbf{f}[\text{BArF}_{20}]$ in CDCl_3 .

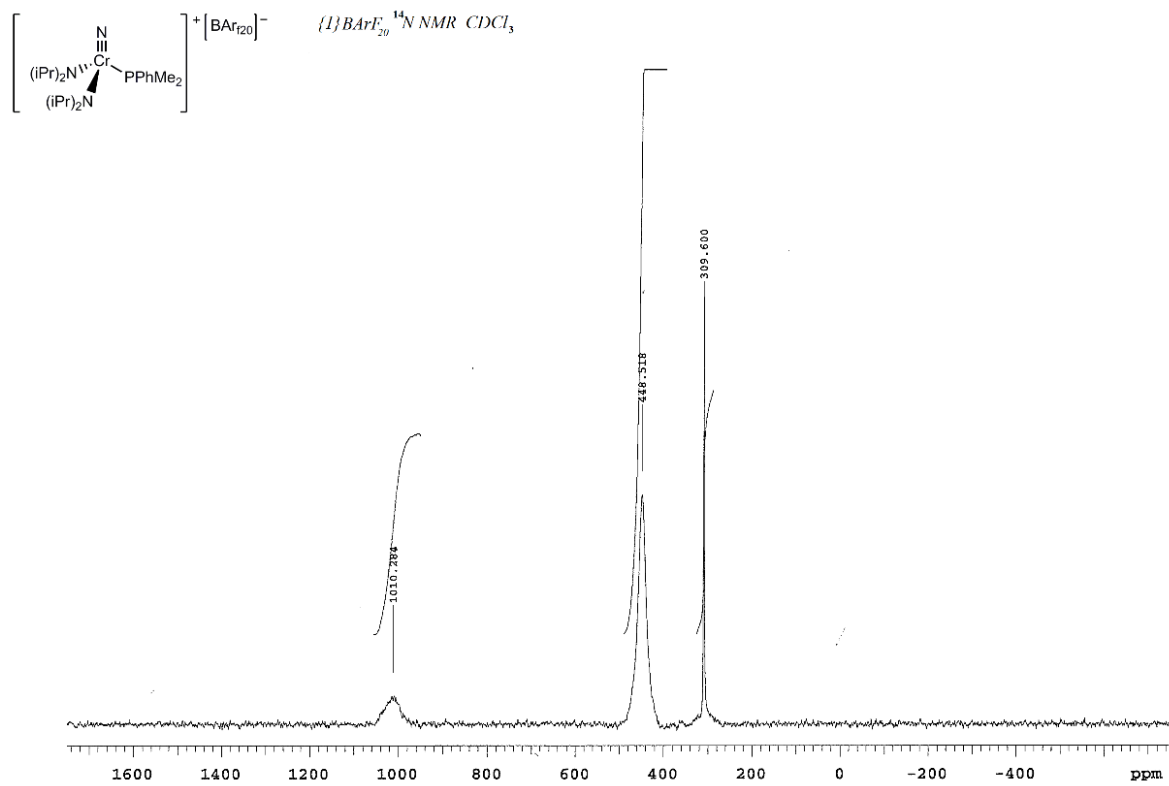


Figure 2.100 ^{14}N NMR spectrum of **3f**[BArF₂₀] in CDCl₃.

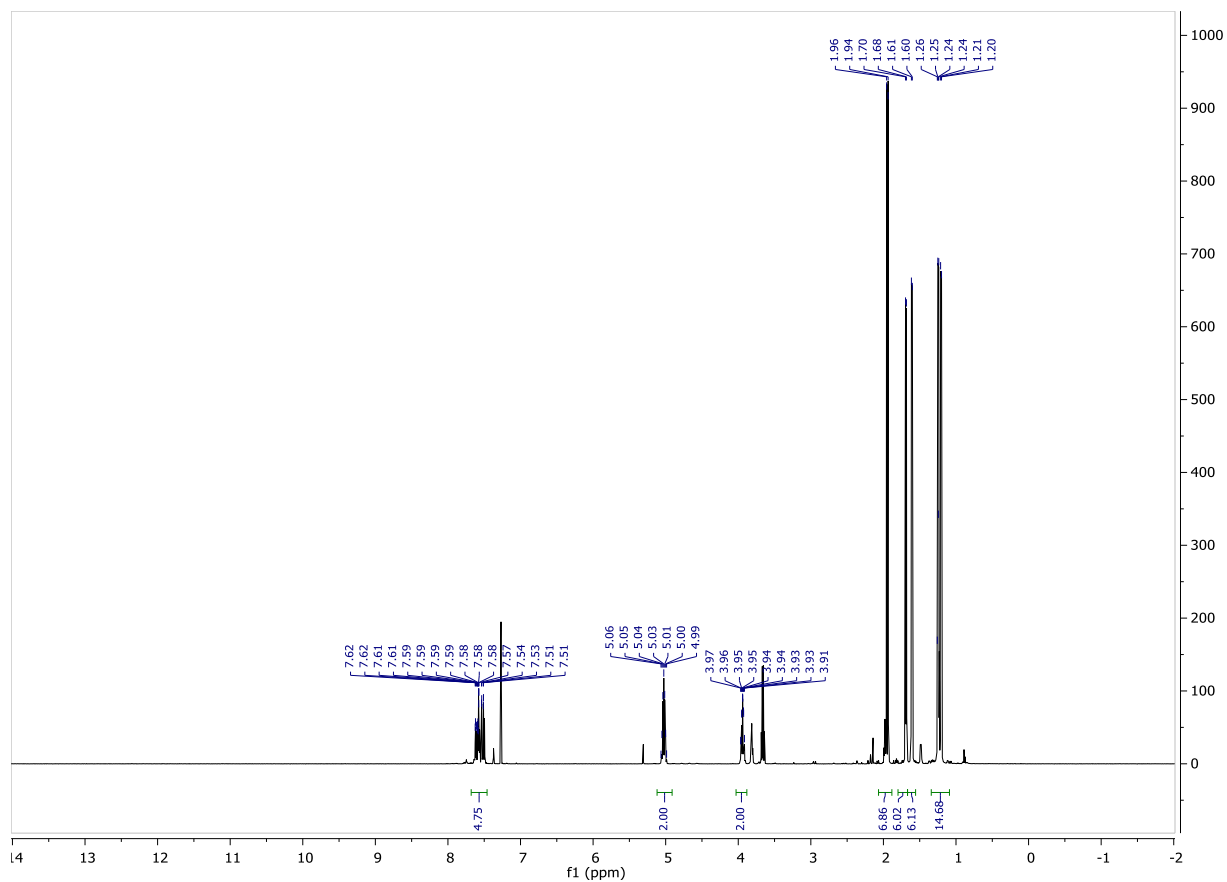


Figure 2.101 ^1H NMR spectrum of $3\text{f}[\text{Al}(\text{OC}(\text{CF}_3)_3)_4]$ in CDCl_3 .

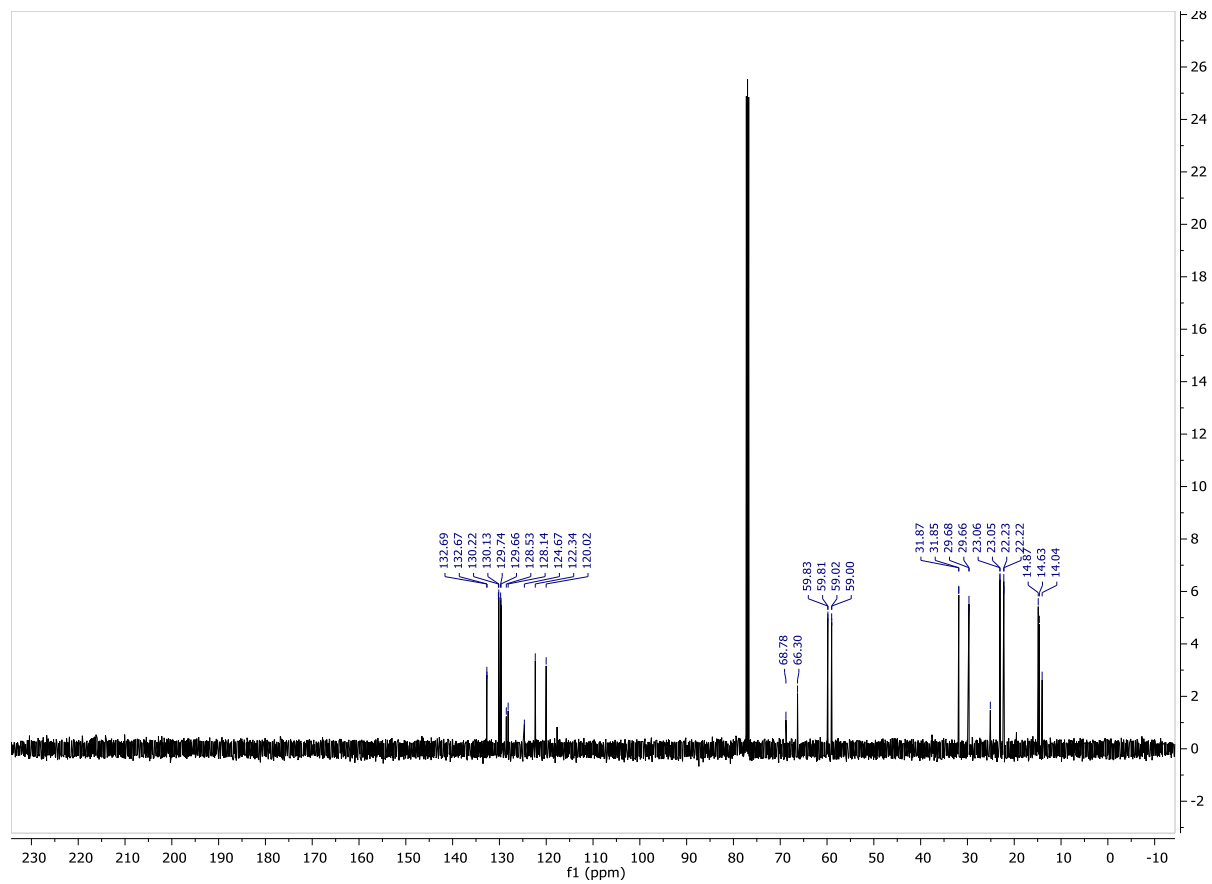


Figure 2.102 ^{13}C NMR spectrum of $3\mathbf{f}[\text{Al}(\text{OC}(\text{CF}_3)_3)_4]$ in CDCl_3 .

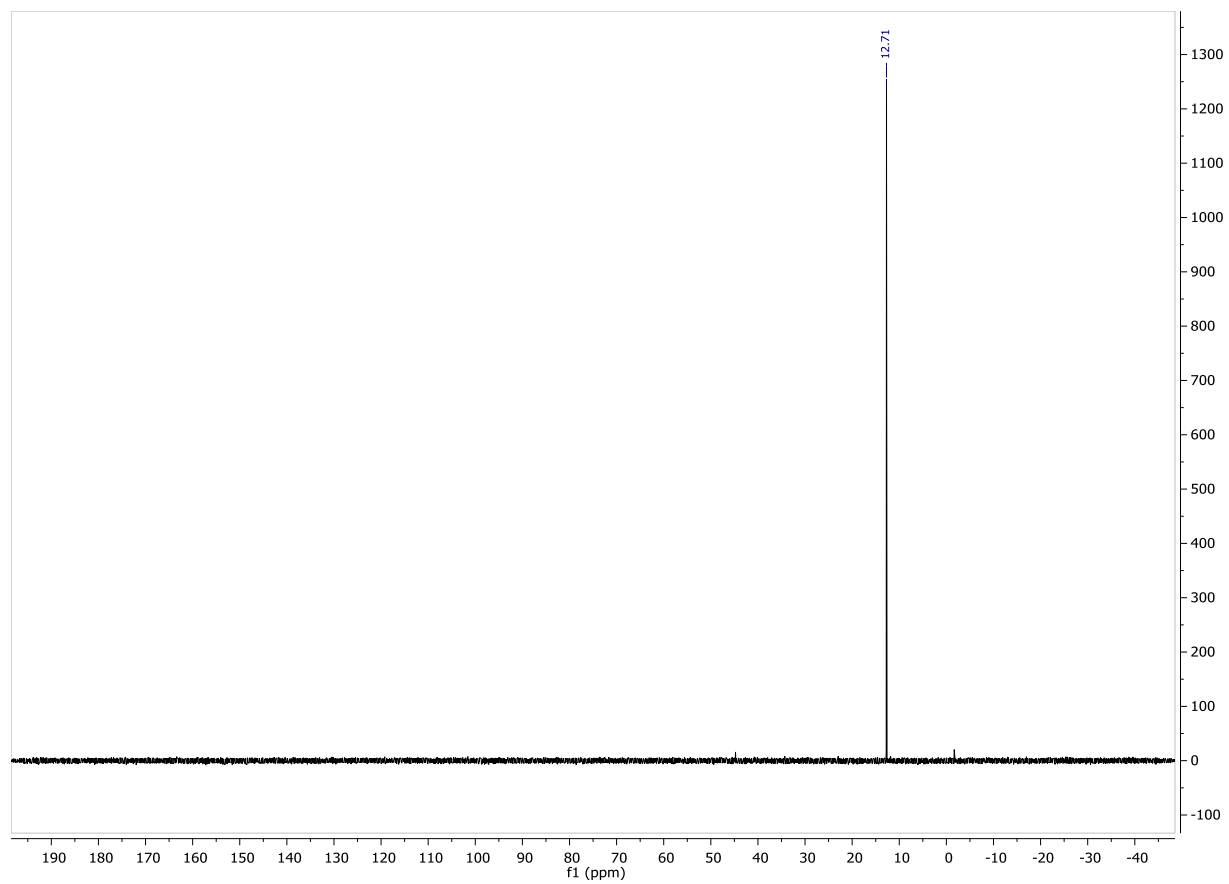


Figure 2.103 ^{31}P NMR spectrum of $3\mathbf{f}[\text{Al}(\text{OC}(\text{CF}_3)_3)_4]$ in CDCl_3 .

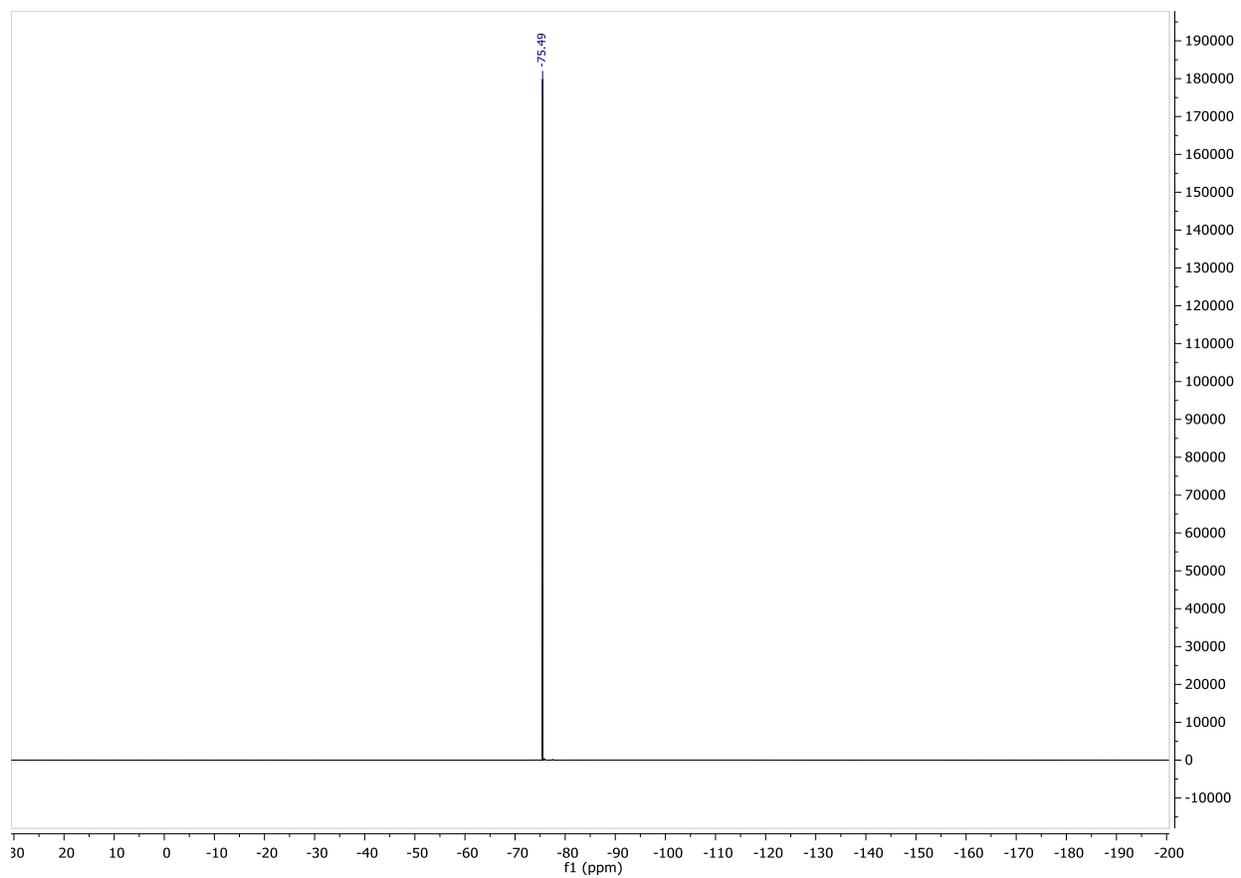


Figure 2.104 ^{19}F NMR spectrum of $3\mathbf{f}[\text{Al}(\text{OC}(\text{CF}_3)_3)_4]$ in CDCl_3 .

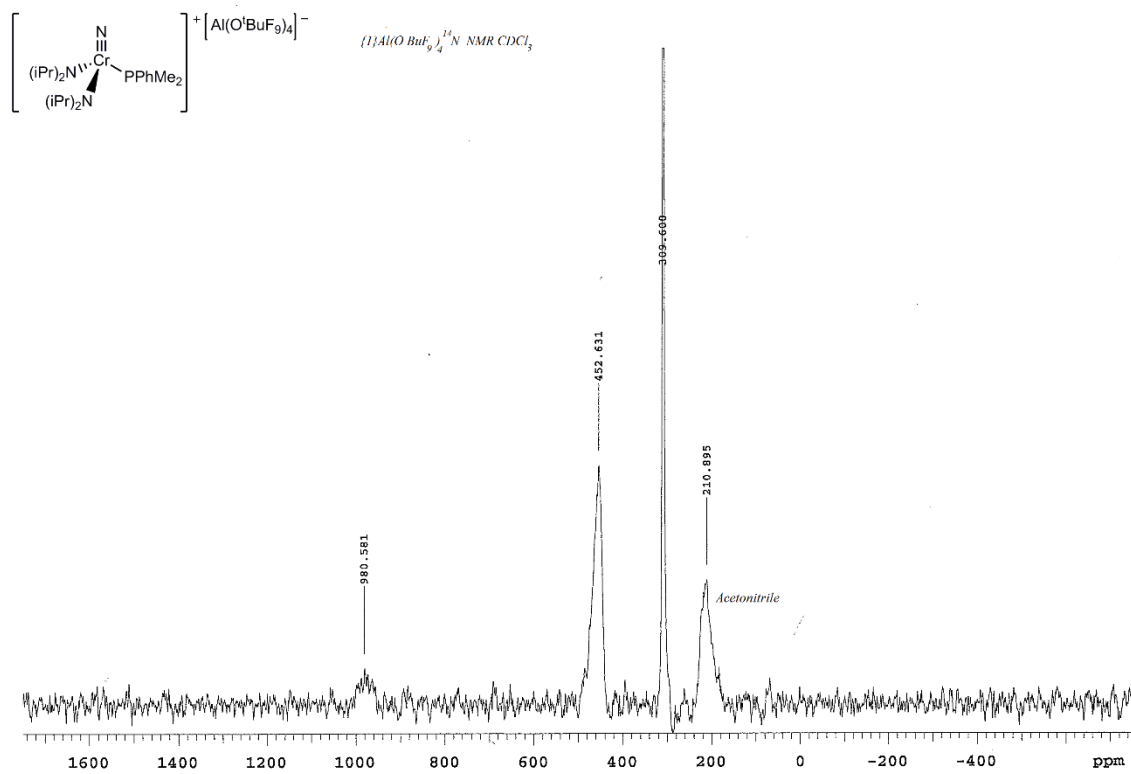


Figure 2.105 ^{14}N NMR spectrum of $3\mathbf{f}[\text{Al}(\text{OC}(\text{CF}_3)_3)_4]$ in CDCl_3 .

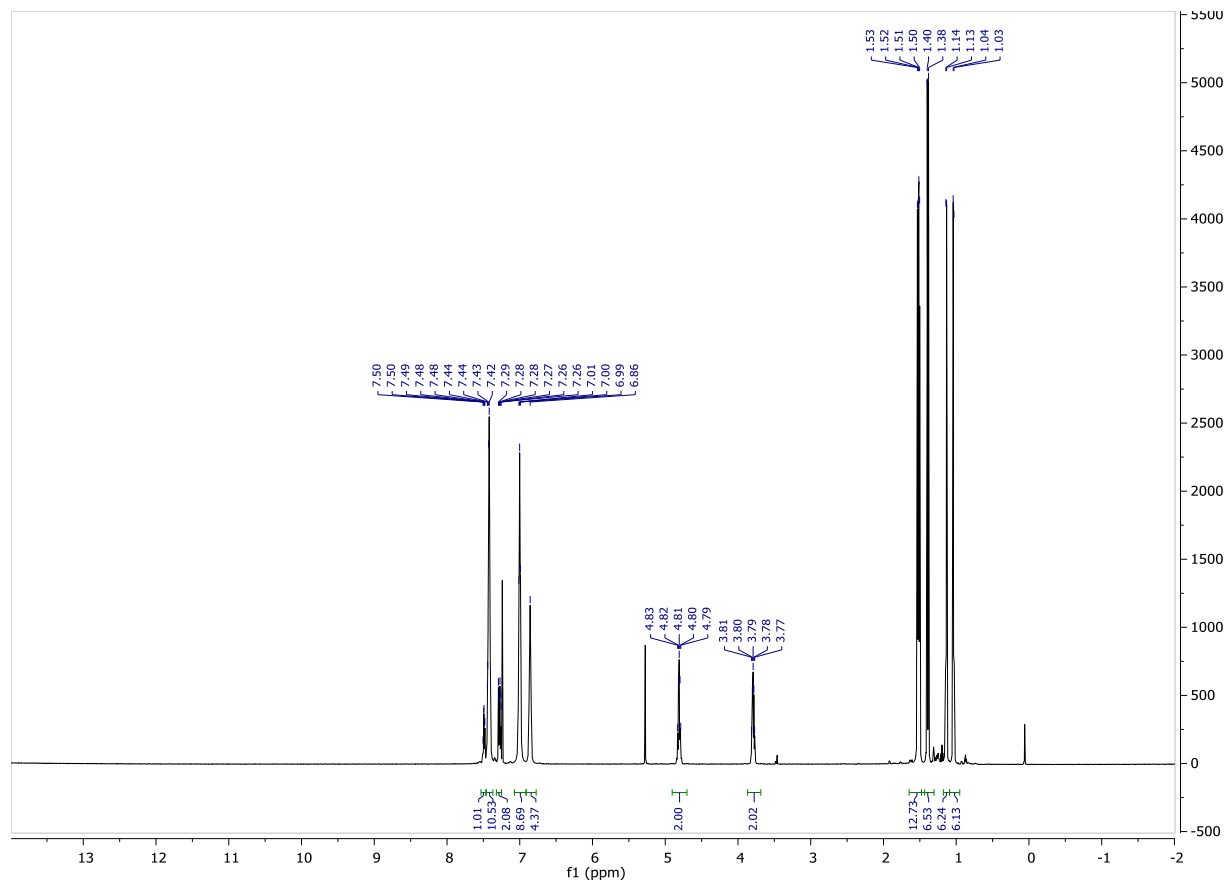


Figure 2.106 ^1H NMR spectrum of $3\text{f}[\text{BPh}_4]$ in CDCl_3 .

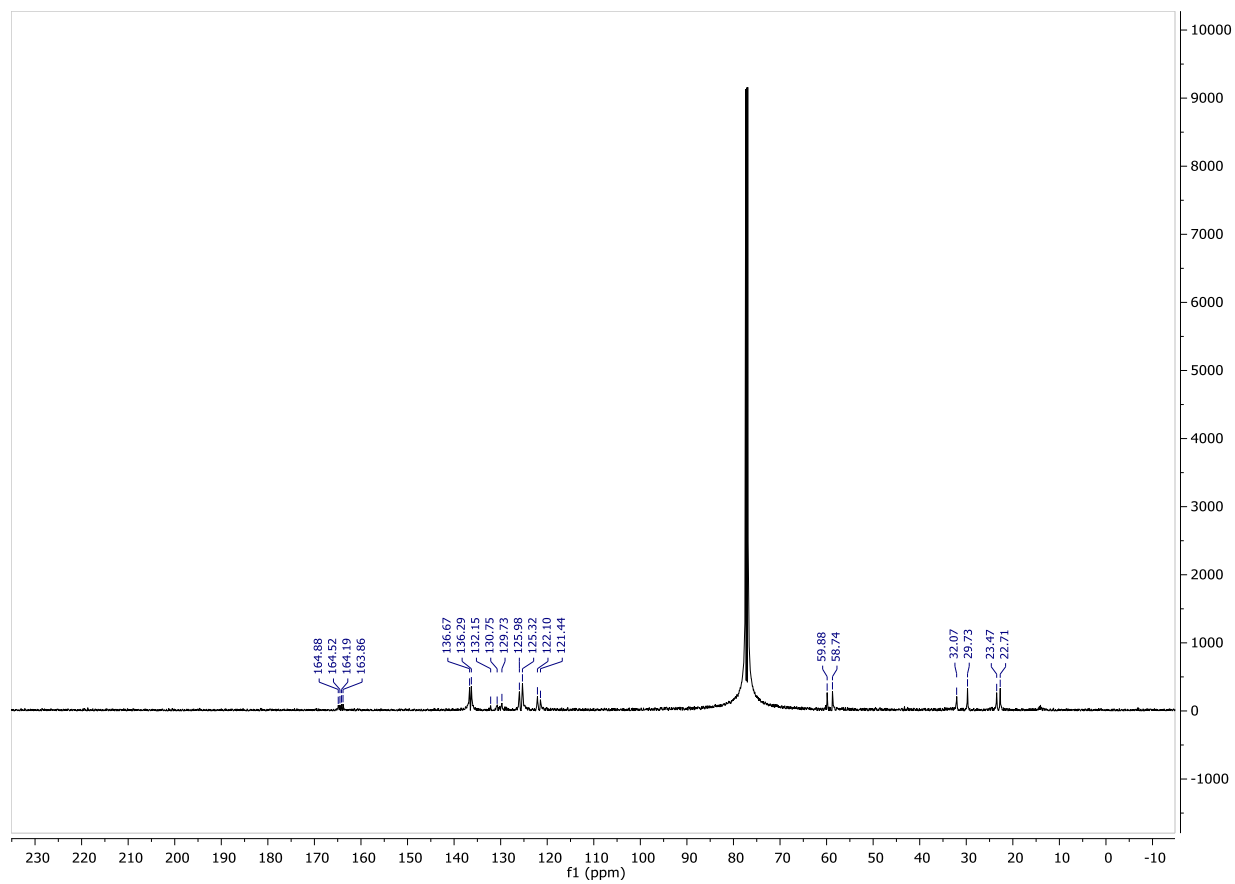


Figure 2.107 ^{13}C NMR spectrum of $3\mathbf{f}[\text{BPh}_4]$ in CDCl_3 .

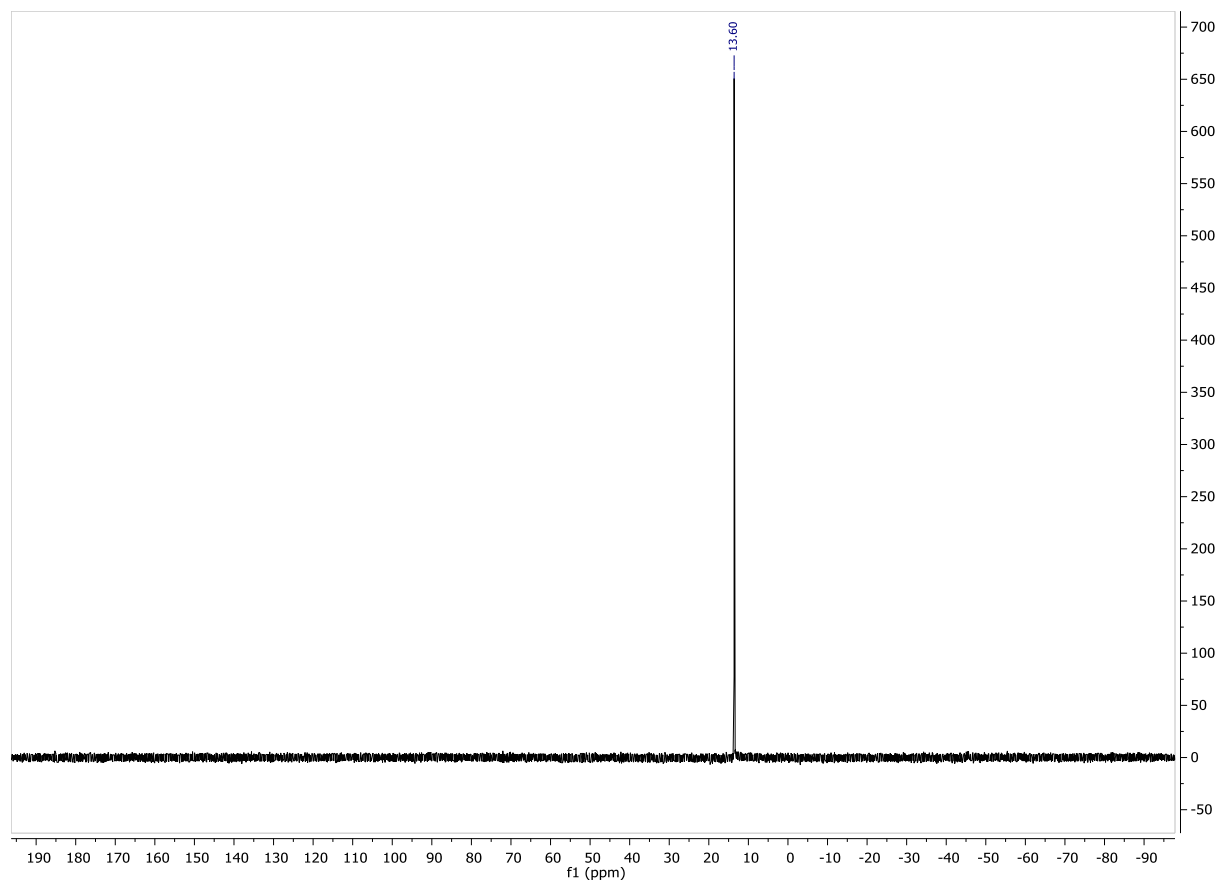


Figure 2.108 ^{31}P NMR spectrum of $3f[\text{BPh}_4]$ in CDCl_3 .

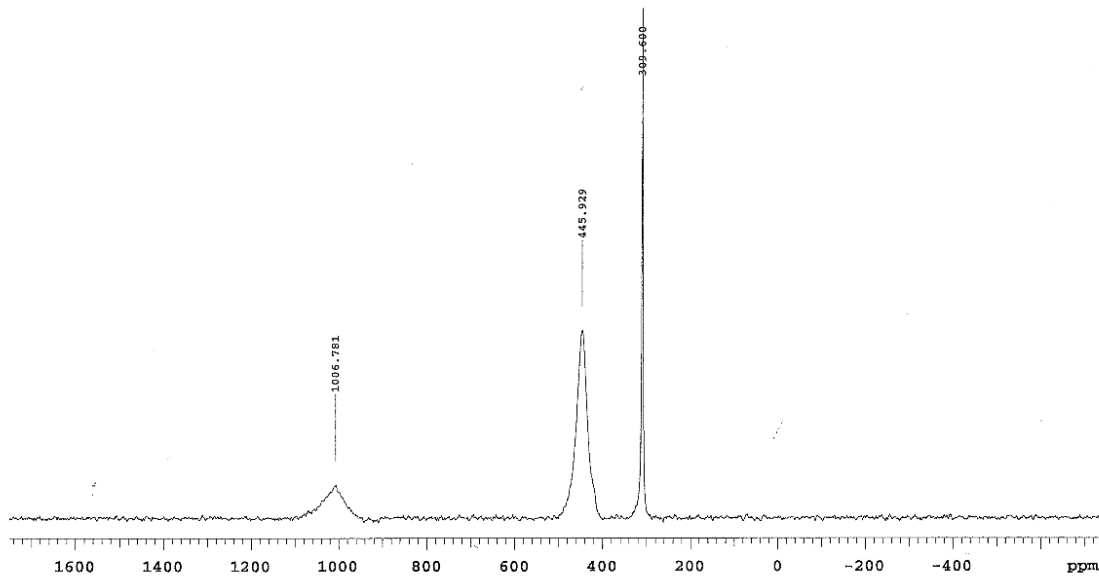
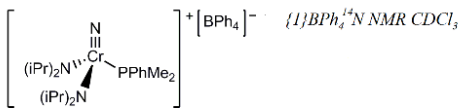


Figure 2.109 ^{14}N NMR spectrum of $3\mathbf{f}[\text{BPh}_4]$ in CDCl_3 .

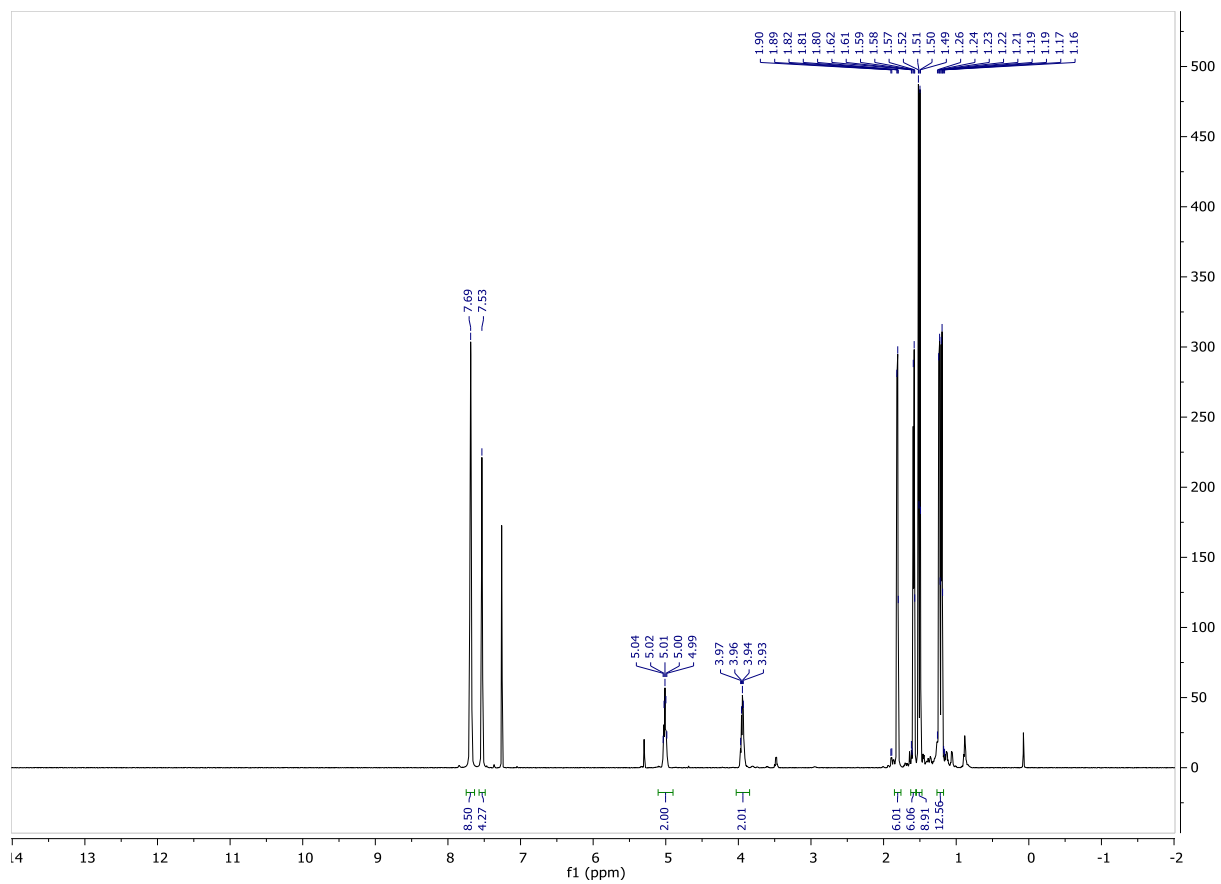


Figure 2.110 ^1H NMR spectrum of $3\mathbf{a}[\text{BArF}_2\mathbf{4}]$ in CDCl_3 .

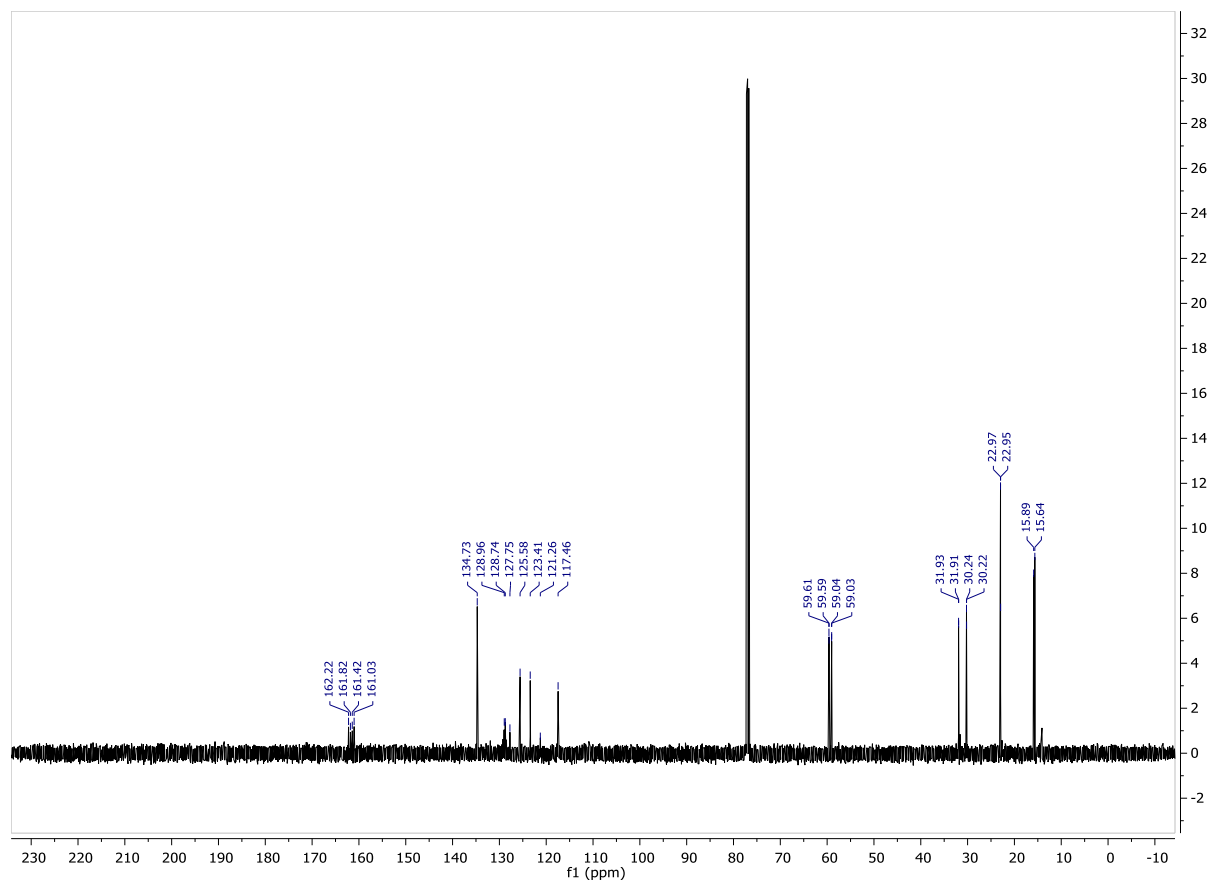


Figure 2.111 ^{13}C NMR spectrum of $3\mathbf{a}[\text{BArF}_{24}]$ in CDCl_3 .

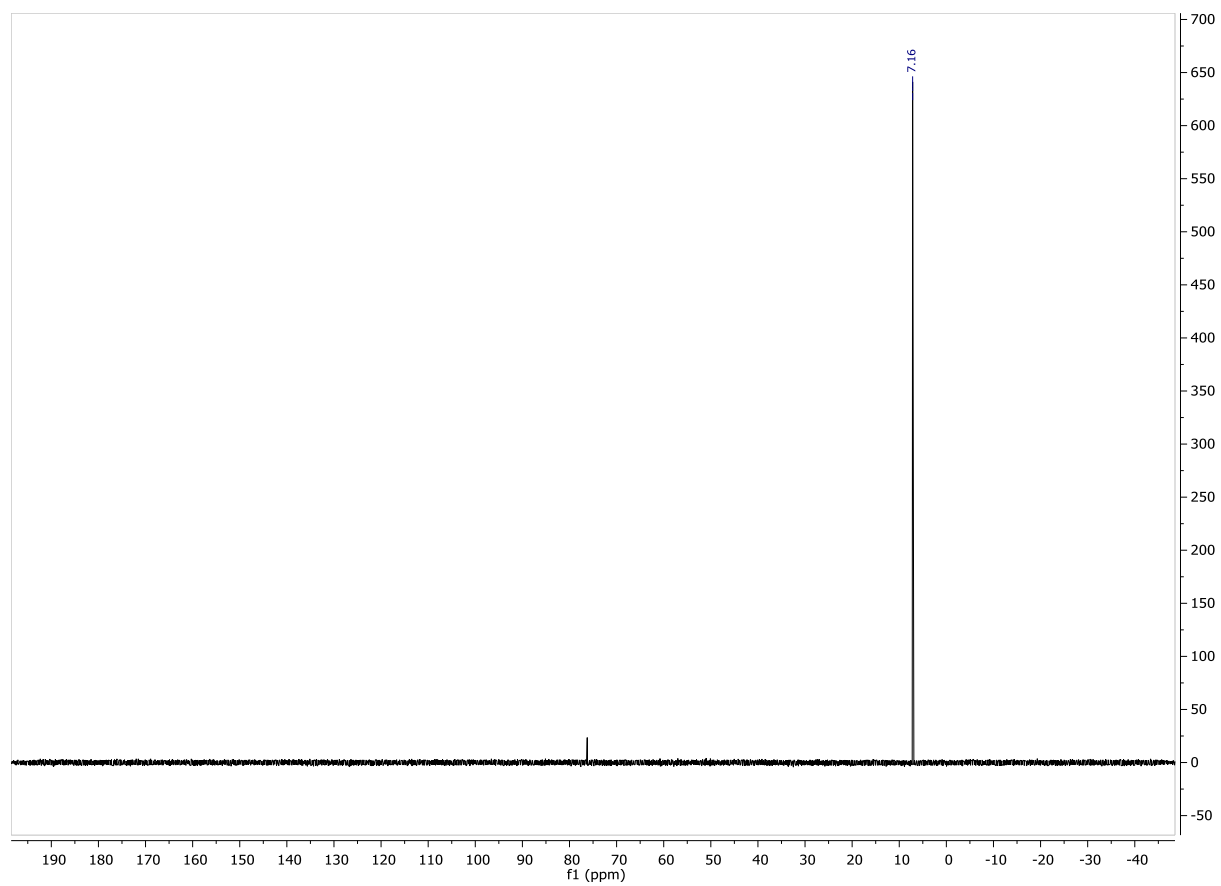


Figure 2.112 ^{31}P NMR spectrum of **3a**[BArF₂₄] in CDCl₃.

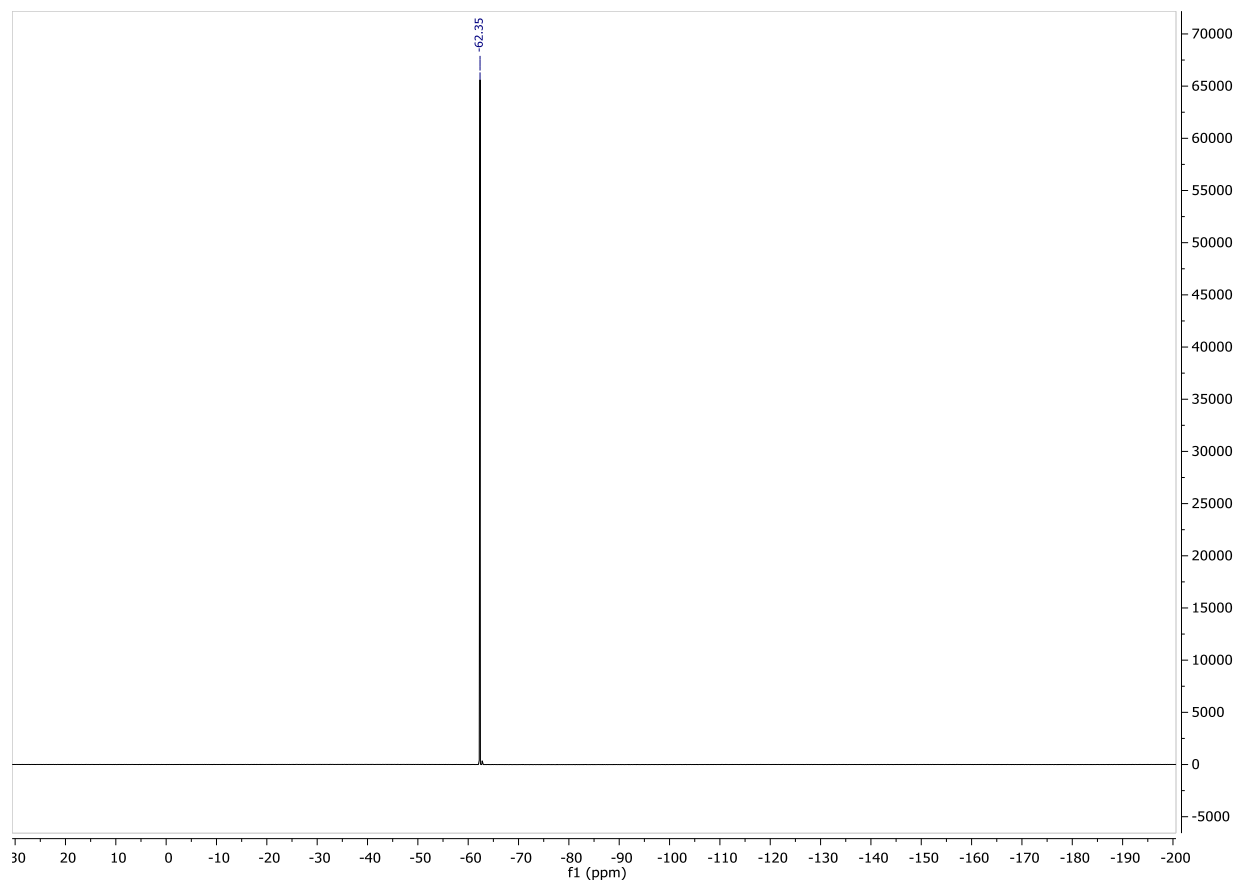


Figure 2.113 ^{19}F NMR spectrum of **3a**[BArF₂₄] in CDCl₃.

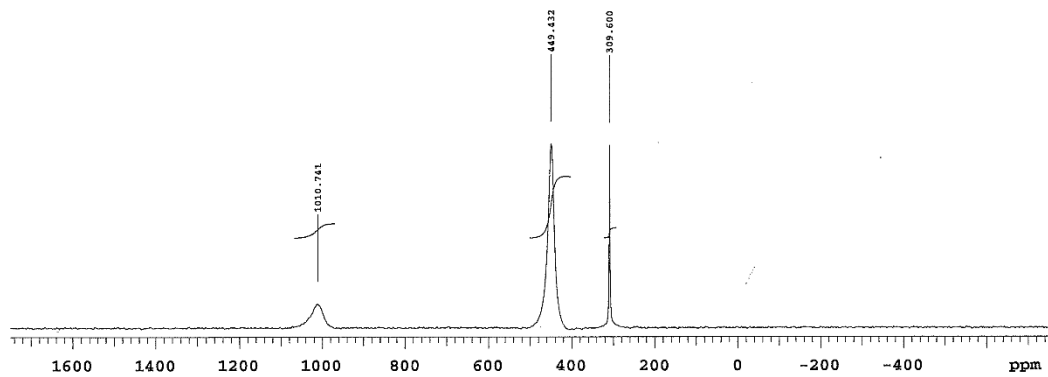
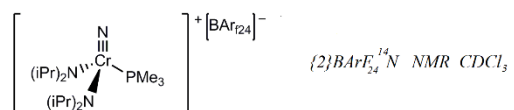


Figure 2.114 ¹⁴N NMR spectrum of **3a**[BArF₂₄] in CDCl₃.

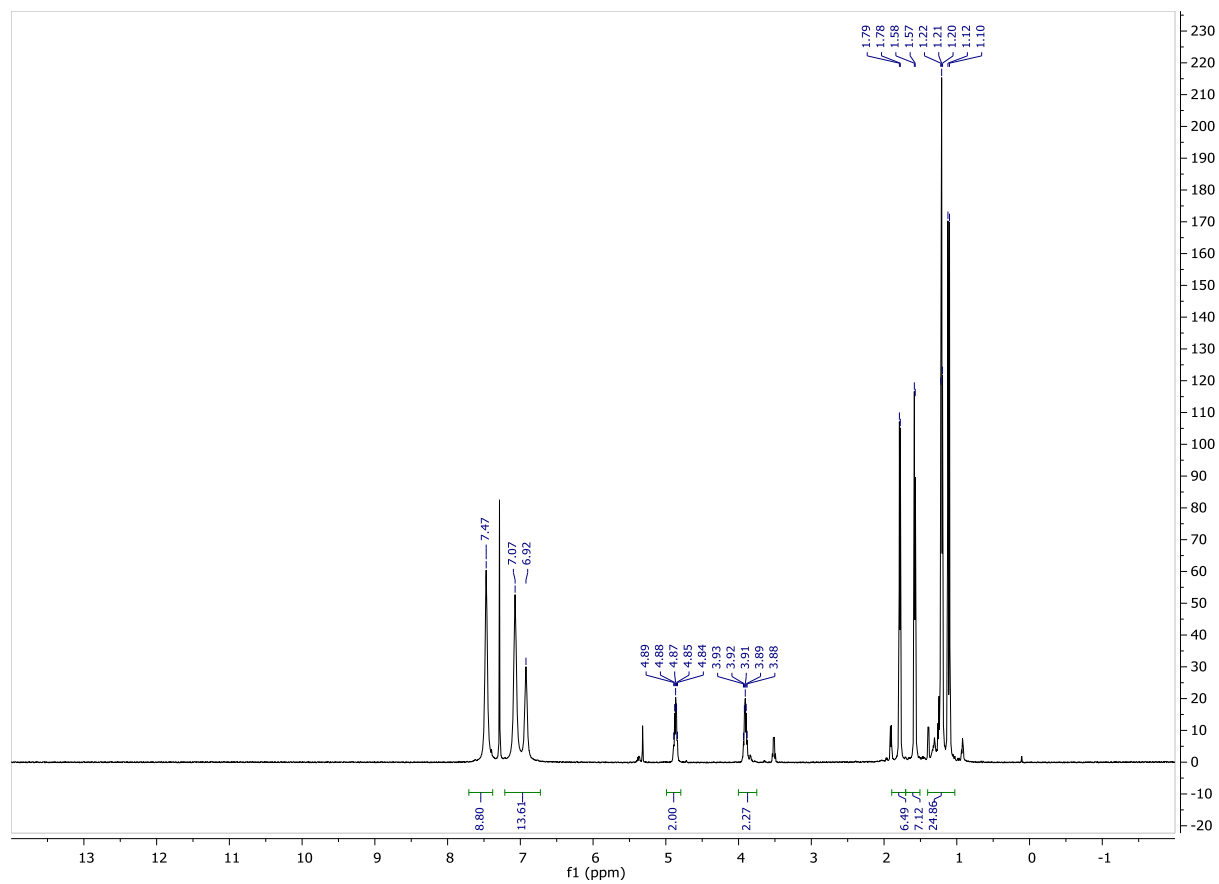


Figure 2.115 ^1H NMR spectrum of $3\mathbf{a}[\text{BPh}_4]$ in CDCl_3 .

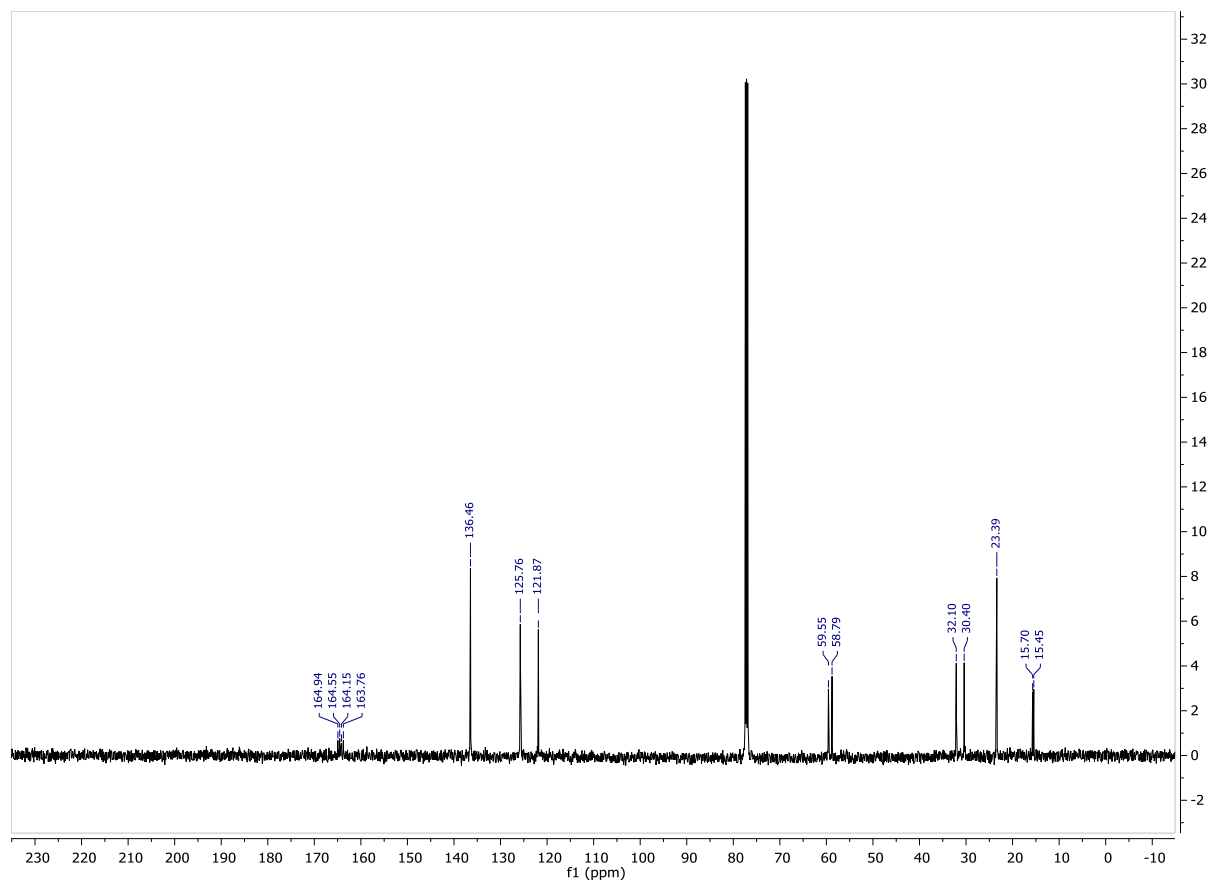


Figure 2.116 ^{13}C NMR spectrum of $3\mathbf{a}[\text{BPh}_4]$ in CDCl_3 .

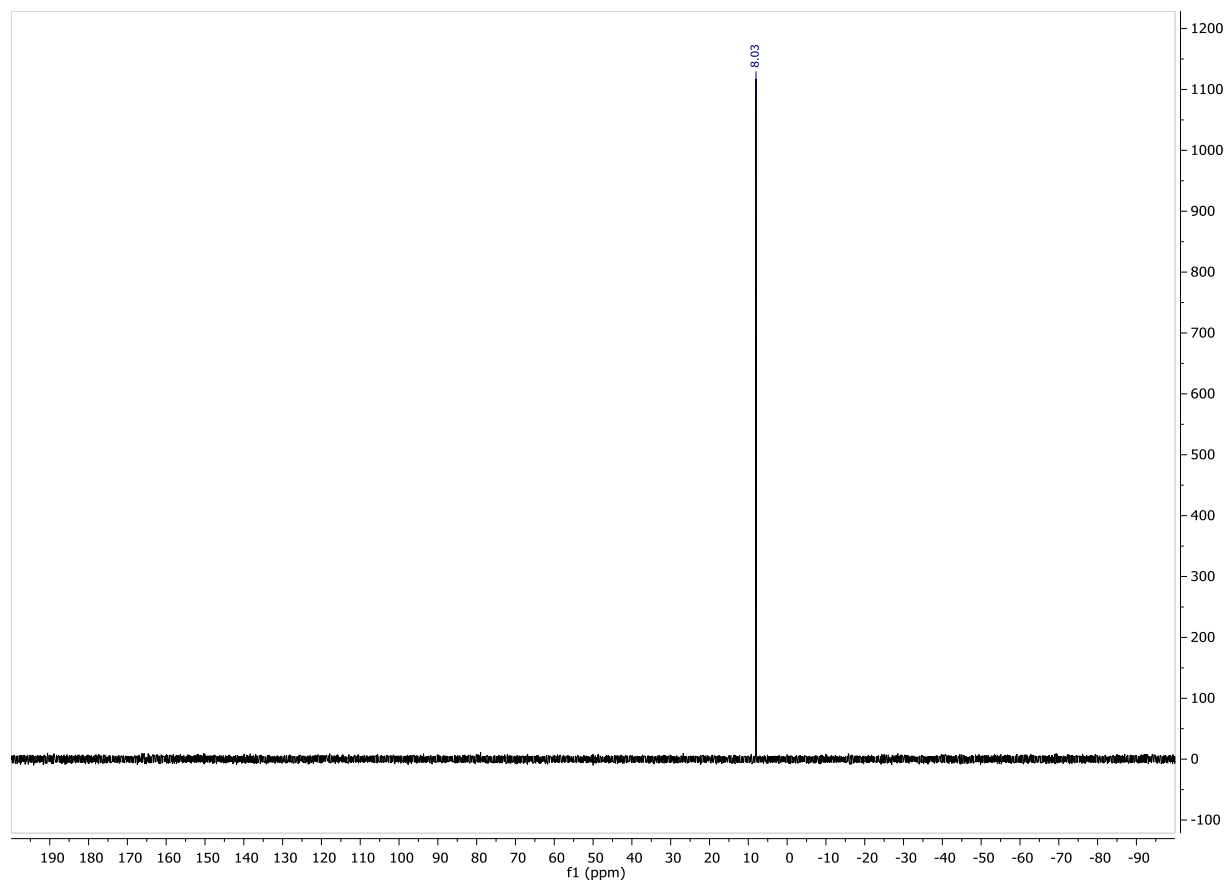


Figure 2.117 ^{31}P NMR spectrum of **3a**[BPh₄] in CDCl₃.

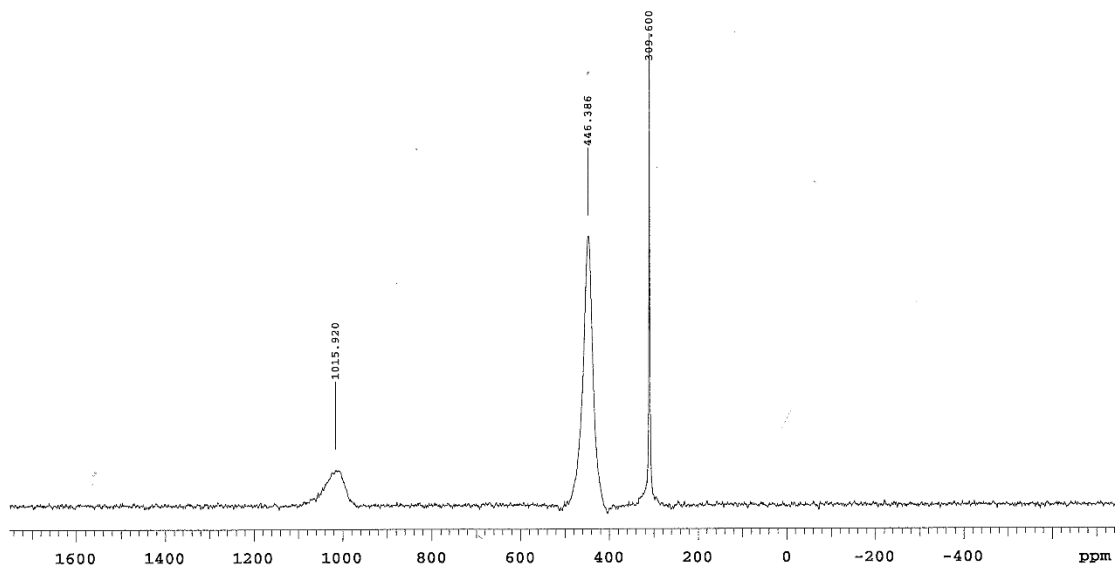
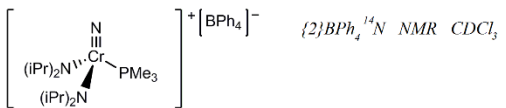


Figure 2.118 ^{14}N NMR spectrum of $3\mathbf{a}[\text{BPh}_4]$ in CDCl_3 .

REFERENCES

REFERENCES

- (1) DiFranco, S. A.; Maciulis, N. A.; Staples, R. J.; Batrice, R. J.; Odom, A. L., Evaluation of donor and steric properties of anionic ligands on high valent transition metals. *Inorganic chemistry* **2012**, *51* (2), 1187-200.
- (2) Billow, B. S.; Bemowski, R. D.; DiFranco, S. A.; Staples, R. J.; Odom, A. L., Synthesis and Structure of Chromium(VI) Nitrido Cyclopentadienyl Complexes. *Organometallics* **2015**.
- (3) Bemowski, R. D.; Singh, A. K.; Bajorek, B. J.; DePorre, Y.; Odom, A. L., Effective donor abilities of E-t-Bu and EPh (E = O, S, Se, Te) to a high valent transition metal. *Dalton transactions* **2014**, *43* (32), 12299-12305.
- (4) Beaumier, E. P.; Billow, B. S.; Singh, A. K.; Biros, S. M.; Odom, A. L., A complex with nitrogen single, double, and triple bonds to the same chromium atom: synthesis, structure, and reactivity. *Chemical Science* **2016**.
- (5) Billow, B. S.; McDaniel, T. J.; Odom, A. L., Quantifying ligand effects in high-oxidation-state metal catalysis. *Nature Chemistry* **2017**, *9*, 837.
- (6) Dias, P. B.; de Piedade, M. E. M.; Simões, J. A. M., Bonding and energetics of phosphorus (III) ligands in transition metal complexes. *Coordination Chemistry Reviews* **1994**, *135–136* (0), 737-807.
- (7) Levason, W., Phosphine complexes of transition metals. In *Organophosphorus Compounds (1990)*, Hartley, F. R., Ed. 1990.
- (8) Odom, A. L.; McDaniel, T. J., Titanium-Catalyzed Multicomponent Couplings: Efficient One-Pot Syntheses of Nitrogen Heterocycles. *Accounts of Chemical Research* **2015**, *48* (11), 2822-2833.
- (9) Porter, J. R.; Wirschun, W. G.; Kuntz, K. W.; Snapper, M. L.; Hoveyda, A. H., Ti-Catalyzed Regio- and Enantioselective Synthesis of Unsaturated α -Amino Nitriles, Amides, and Acids. Catalyst Identification through Screening of Parallel Libraries. *Journal of the American Chemical Society* **2000**, *122* (11), 2657-2658.
- (10) Odom, A. L., New C-N and C-C bond forming reactions catalyzed by titanium complexes. *Dalton transactions* **2005**, (2), 225-233.
- (11) Tolman, C. A., Electron donor-acceptor properties of phosphorus ligands. Substituent additivity. *Journal of the American Chemical Society* **1970**, *92* (10), 2953-2956.
- (12) Tolman, C. A., Steric effects of phosphorus ligands in organometallic chemistry and homogeneous catalysis. *Chemical Reviews* **1977**, *77* (3), 313-348.

- (13) Tsuchida, R., Absorption Spectra of Co-ordination Compounds. I. *Bull. Chem. Soc. Jpn.* **1938**, *13* (5), 388-400.
- (14) Wulfsberg, G., *Inorganic Chemistry*. **1987**.
- (15) Drago, R. S.; Dadmun, A. P., Dual-parameter substituent constants, .DELTA.Ex and .DELTA.Cx, for the correlation of physicochemical measurements. *Journal of the American Chemical Society* **1993**, *115* (19), 8592-8602.
- (16) Vogel, G. C.; Drago, R. S., The ECW Model. *Journal of Chemical Education* **1996**, *73* (8), 701.
- (17) Suresh, C. H.; Koga, N., Quantifying the Electronic Effect of Substituted Phosphine Ligands via Molecular Electrostatic Potential. *Inorganic chemistry* **2002**, *41* (6), 1573-1578.
- (18) Allman, T.; Goel, R. G., The basicity of phosphines. *Canadian Journal of Chemistry* **1982**, *60* (6), 716-722.
- (19) Golovin, M. N.; Rahman, M.; Belmonte, J. E.; Giering, W. P., QUANTITATIVE SEPARATION OF SIGMA-COMPONENTS AND PI-COMPONENTS OF TRANSITION-METAL PHOSPHORUS BONDING AND THE APPLICATION OF LIGAND EFFECTS IN ORGANOMETALLIC CHEMISTRY. *Organometallics* **1985**, *4* (11), 1981-1991.
- (20) Wilson, M. R.; Woska, D. C.; Prock, A.; Giering, W. P., THE QUANTITATIVE-ANALYSIS OF LIGAND EFFECTS (QALE) - THE ARYL EFFECT. *Organometallics* **1993**, *12* (5), 1742-1752.
- (21) Poe, A. J., The tuning of P-donor ligands: the aryl and other pendent group effects (PGEs) revisited. *Dalton transactions* **2009**, (11), 1999-2003.
- (22) Rahman, M. M.; Liu, H. Y.; Prock, A.; Giering, W. P., QUANTITATIVE-ANALYSIS OF LIGAND EFFECTS (QALE) .2. STERIC AND ELECTRONIC FACTORS INFLUENCING TRANSITION-METAL PHOSPHORUS(III) BONDING. *Organometallics* **1987**, *6* (3), 650-658.
- (23) Nelson, D. J.; Nolan, S. P., Quantifying and understanding the electronic properties of N-heterocyclic carbenes. *Chemical Society Reviews* **2013**, *42* (16), 6723-6753.
- (24) Setiawan, D.; Kalescky, R.; Kraka, E.; Cremer, D., Direct Measure of Metal–Ligand Bonding Replacing the Tolman Electronic Parameter. *Inorganic chemistry* **2016**.
- (25) Sanderson, R. T., Principles of electronegativity Part I. General nature. *Journal of Chemical Education* **1988**, *65* (2), 112.
- (26) Davis, M. F.; Clarke, M.; Levason, W.; Reid, G.; Webster, M., Tin(IV) Fluoride Complexes with Tertiary Phosphane Ligands – A Comparison of Hard and Soft Donor Ligands. **2006**, *2006* (14), 2773-2782.
- (27) Mason, J., *Multinuclear NMR*. Plenum Press: New York [etc.], 1987.

- (28) Mason, J., Nitrogen nuclear magnetic resonance spectroscopy in inorganic, organometallic, and bioinorganic chemistry. *Chemical Reviews* **1981**, *81* (3), 205-227.
- (29) Marcus, Y.; Hefter, G., Ion Pairing. *Chemical Reviews* **2006**, *106* (11), 4585-4621.
- (30) Hefter, G., When spectroscopy fails: The measurement of ion pairing. In *Pure and Applied Chemistry*, 2006; Vol. 78, p 1571.
- (31) Fuoss, R. M., Conductance-concentration function for the paired ion model. *The Journal of Physical Chemistry* **1978**, *82* (22), 2427-2440.
- (32) Kameda, Y.; Ebina, S.; Amo, Y.; Usuki, T.; Otomo, T., Microscopic Structure of Contact Ion Pairs in Concentrated LiCl- and LiClO₄-Tetrahydrofuran Solutions Studied by Low-Frequency Isotropic Raman Scattering and Neutron Diffraction with ⁶Li/⁷Li Isotopic Substitution Methods. *The Journal of Physical Chemistry B* **2016**, *120* (20), 4668-4678.
- (33) Diaz-Torres, R.; Alvarez, S., Coordinating ability of anions and solvents towards transition metals and lanthanides. *Dalton transactions* **2011**, *40* (40), 10742-10750.
- (34) Pregosin Paul, S., NMR spectroscopy and ion pairing: Measuring and understanding how ions interact. In *Pure and Applied Chemistry*, 2009; Vol. 81, p 615.
- (35) Pregosin, P. S., NMR diffusion methods in inorganic and organometallic chemistry. In *Spectroscopic Properties of Inorganic and Organometallic Compounds: Techniques, Materials and Applications, Volume 42*, The Royal Society of Chemistry: 2012; Vol. 42, pp 248-268.
- (36) Fernández, I.; Martínez-Viviente, E.; Pregosin, P. S., Multinuclear PGSE Diffusion and Overhauser NMR Studies on a Variety of Salts in THF Solution. *Inorganic chemistry* **2005**, *44* (15), 5509-5513.
- (37) Pregosin, P. S., Applications of NMR diffusion methods with emphasis on ion pairing in inorganic chemistry: a mini-review. *Magnetic Resonance in Chemistry* **2016**, n/a-n/a.
- (38) Macchioni, A., Ion Pairing in Transition-Metal Organometallic Chemistry. *Chemical Reviews* **2005**, *105* (6), 2039-2074.
- (39) Brand, T.; Cabrita, E. J.; Berger, S., Intermolecular interaction as investigated by NOE and diffusion studies. *Progress in Nuclear Magnetic Resonance Spectroscopy* **2005**, *46* (4), 159-196.
- (40) Bellachioma, G.; Ciancaleoni, G.; Zuccaccia, C.; Zuccaccia, D.; Macchioni, A., NMR investigation of non-covalent aggregation of coordination compounds ranging from dimers and ion pairs up to nano-aggregates. *Coordination Chemistry Reviews* **2008**, *252* (21-22), 2224-2238.
- (41) Macchioni, A.; Ciancaleoni, G.; Zuccaccia, C.; Zuccaccia, D., Determining accurate molecular sizes in solution through NMR diffusion spectroscopy. *Chemical Society Reviews* **2008**, *37* (3), 479-489.

- (42) Chen, H. C.; Chen, S. H., Diffusion of crown ethers in alcohols. *The Journal of Physical Chemistry* **1984**, *88* (21), 5118-5121.
- (43) Honeychuck, R. V.; Hersh, W. H., Coordination of "noncoordinating" anions: synthesis, characterization, and x-ray crystal structures of fluorine-bridged hexafluoroantimonate(1-), tetrafluoroborate(1-), and hexafluorophosphate(1-) adducts of [R₃P(CO)₃(NO)W]⁺. An unconventional order of anion donor strength. *Inorganic chemistry* **1989**, *28* (14), 2869-2886.
- (44) Metz, M. V.; Sun, Y.; Stern, C. L.; Marks, T. J., Weakly Coordinating Al-, Nb-, Ta-, Y-, and La-Based Perfluoroaryloxymetalate Anions as Cocatalyst Components for Single-Site Olefin Polymerization. *Organometallics* **2002**, *21* (18), 3691-3702.
- (45) Hamilton, G. L.; Kang, E. J.; Mba, M.; Toste, F. D., A Powerful Chiral Counterion Strategy for Asymmetric Transition Metal Catalysis. *Science* **2007**, *317* (5837), 496.
- (46) Brak, K.; Jacobsen, E. N., Asymmetric Ion-Pairing Catalysis. *Angewandte Chemie International Edition* **2013**, *52* (2), 534-561.
- (47) Ohmatsu, K.; Ito, M.; Kunieda, T.; Ooi, T., Ion-paired chiral ligands for asymmetric palladium catalysis. *Nature Chemistry* **2012**, *4*, 473.
- (48) Claridge, T., High Resolution NMR Spectroscopy in Organic Chemistry. *Elsevier* **2008**, Chpt 8.
- (49) Lane, E. M.; Chapp, T. W.; Hughes, R. P.; Glueck, D. S.; Feland, B. C.; Bernard, G. M.; Wasylshen, R. E.; Rheingold, A. L., Synthesis of Gold Phosphido Complexes Derived from Bis(secondary) Phosphines. Structure of Tetrameric [Au(MesP(CH₂)₃PMes)Au]₄. *Inorganic chemistry* **2010**, *49* (8), 3950-3957.
- (50) Li, D.; Kagan, G.; Hopson, R.; Williard, P. G., Formula Weight Prediction by Internal Reference Diffusion-Ordered NMR Spectroscopy (DOSY). *Journal of the American Chemical Society* **2009**, *131* (15), 5627-5634.
- (51) Li, D.; Keresztes, I.; Hopson, R.; Williard, P. G., Characterization of Reactive Intermediates by Multinuclear Diffusion-Ordered NMR Spectroscopy (DOSY). *Accounts of Chemical Research* **2009**, *42* (2), 270-280.
- (52) Neufeld, R.; Stalke, D., Accurate molecular weight determination of small molecules via DOSY-NMR by using external calibration curves with normalized diffusion coefficients. *Chemical Science* **2015**, *6* (6), 3354-3364.
- (53) Rocchigiani, L.; Macchioni, A., Disclosing the multi-faceted world of weakly interacting inorganic systems by means of NMR spectroscopy. *Dalton transactions* **2016**, *45* (7), 2785-2790.
- (54) Clot, E., Ion-Pairing in Organometallic Chemistry: Structure and Influence on Proton Transfer from a Computational Perspective. **2009**, *2009* (16), 2319-2328.

- (55) Leskowitz, G. M.; Ghaderi, N.; Olsen, R. A.; Pederson, K.; Hatcher, M. E.; Mueller, L. J., The Amide Rotational Barrier in Isonicotinamide: Dynamic NMR and Ab Initio Studies. *The Journal of Physical Chemistry A* **2005**, *109* (6), 1152-1158.
- (56) Schneider, A.; Hommel, G.; Blettner, M., Linear regression analysis: part 14 of a series on evaluation of scientific publications. *Deutsches Arzteblatt international* **2010**, *107* (44), 776-782.
- (57) Odom, A. L.; Cummins, C. C.; Protasiewicz, J. D., Nitric Oxide Cleavage: Synthesis of Terminal Chromium(VI) Nitrido Complexes via Nitrosyl Deoxygenation. *Journal of the American Chemical Society* **1995**, *117* (24), 6613-6614.
- (58) Park, J. G.; Jeon, I.-R.; Harris, T. D., Electronic Effects of Ligand Substitution on Spin Crossover in a Series of Diiminoquinonoid-Bridged FeII₂ Complexes. *Inorganic chemistry* **2015**, *54* (1), 359-369.
- (59) Krossing, I., The Facile Preparation of Weakly Coordinating Anions: Structure and Characterisation of Silverpolyfluoroalkoxyaluminates AgAl(ORF)₄, Calculation of the Alkoxide Ion Affinity. *Chemistry – A European Journal* **2001**, *7* (2), 490-502.
- (60) Wiesler, W. T.; Caruthers, M. H., Synthesis of Phosphorodithioate DNA via Sulfur-Linked, Base-Labile Protecting Groups¹. *The Journal of Organic Chemistry* **1996**, *61* (13), 4272-4281.
- (61) Kermagoret, A.; Braunstein, P., SHOP-type nickel complexes with alkyl substituents on phosphorus, synthesis and catalytic ethylene oligomerization. *Dalton transactions* **2008**, (6), 822-831.
- (62) Power, J. E.; Foroozandeh, M.; Moutzouri, P.; Adams, R. W.; Nilsson, M.; Coombes, S. R.; Phillips, A. R.; Morris, G. A., Very broadband diffusion-ordered NMR spectroscopy: 19F DOSY. *Chemical communications* **2016**, *52* (42), 6892-6894.

CHAPTER 3. ANALYSIS OF THE DONOR ABILITIES OF PHOSPHINES TO HIGH VALENT METALS

3.1 Introduction^{3,4}

In the previous chapter, several of the complications created by using neutral ligands in the LDP system were presented. Ion pairing effects in the $[\text{NCr}(\text{N}^i\text{Pr}_2)_2\text{PR}_3][\text{X}]$ salts in nonpolar solvents artificially increase the measured barrier to Cr–NⁱPr₂ bond rotations. This effect is not systematic, which causes *variable* increases in the experimentally determined donor ability, precluding an easy correction to the ΔH^\ddagger values. Conversely, when the rotation barrier of the Cr–NⁱPr₂ bond in these ionic complexes are examined in a more polar solvent system (CD₃CN) the ion pairing effect is reduced. This is reflected in the reduction of the measured LDP values in CD₃CN versus CDCl₃. The polar solvent disrupts the ion pairing in the $[\text{NCr}(\text{N}^i\text{Pr}_2)_2\text{PR}_3][\text{X}]$ salts, removing the steric and electrostatic inhibition of Cr–NⁱPr₂ bond rotation by the anion.

However, ion pair disruption is accomplished at the expense of the consistency associated with the entropy of activation, ΔS^\ddagger , when the LDP complex is neutral ($\text{NCr}(\text{N}^i\text{Pr}_2)_2\text{X}$) or an ion paired salt.¹ Due to the instability of the $[\text{NCr}(\text{N}^i\text{Pr}_2)_2\text{PR}_3][\text{X}]$ salts and experimental limitations on the temperatures needed to induce the bond rotation, ΔS^\ddagger cannot be determined for each complex in the **3a-p** series (Fig. 2.3). Even if these measurements were experimentally feasible, it is not clear what exactly the activation energies mean in these measurements where the ions are unpaired and solvation appears to be the controlling factor.

³ The work presented in this chapter was done in collaboration with Dr. Brennan Billow.

⁴ The results presented in this chapter have been published in the following article: Aldrich, K. E., Billow, B. S., Staples, R. J., Odom, A. L., (2019). "Phosphine interactions with high oxidation state metals." *Polyhedron* **159**: 284-297.

Thus, while we had collected two complete sets of LDP values, one in CD₃CN with the SbF₆⁻ counter anion and the other in CDCl₃ with the BArF₂₄⁻ counter anion, we were uncertain exactly what the LDP values meant. In CDCl₃, we suspected that the ion pairing interference could cause the measurements to be errant by up to 0.7 kcal/mol (See Chapter 2), but because these deviations aren't uniform, they can't be subtracted or ignored. In CD₃CN, several of the measured PR₃ LDP values vary with temperature and our investigations into the entropy of activation for several of these compounds demonstrate that ΔS^\ddagger varies greatly in this system on a case-by-case basis. For reference, both sets of LDP values are shown in Table 3.1.

Table 3.1 Experimentally determined ΔH^\ddagger values for **3a-p** series of compounds in CDCl_3 with BArF_{24}^- counter anion and by the original method in CD_3CN with SbF_6^- .

Compound Number	Phosphine Complex	Experimental ΔH^\ddagger (kcal/mol) CDCl_3	Experimental ΔS^\ddagger (e.u.) CDCl_3	Experimental ΔH^\ddagger (kcal/mol) ^c CD_3CN
3a	PMe_3	18.71	-3.4 (1.0)	16.64
3b	P^nBu_3	18.91	-2.8 (1.0)	16.77
3c	P^iBu_3	17.76	-5.7 (1.0)	17.13
3d	P^iPr_3	19.47	-3.0 (1.5)	17.17
3e	PCy_3	19.46	- ^a	17.27
3f	PPhMe_2	18.79	-2.1 (1.1)	16.53
3g	PPh_2Me	16.9	-8.2 (1.2)	16.16
3h	PPhEt_2	16.96	-6.7 (1.4)	16.65
3i	PPh_2Et	17.98	-4.0 (1.0)	16.15
3j	PPh_2^nBu	18.17	-3.4 (1.0)	16.31
3k	PPh_2Cy	18.11	-5.5 (3.2)	16.43
3l	PPhCy_2	-	-	16.37
3m	P(OEt)_3	16.99	-6.1 (1.3)	15.73
3n	P(OiPr)_3	17.12	-6.0 (1.2)	15.91
3o	$\text{P(NC}_4\text{H}_8)_3$	19.52	-1.0 (1.5)	16.21
3p	PPh_3	18	-4.1 (2.1)	- ^b
Average		-	-4.7	-

^aMeasurable rotation rate did not occur until $\sim 55^\circ\text{C}$ so Eyring plot analysis of different ΔG^\ddagger values over a range of temperatures could not be performed. ^b**3p** decomposes to **2** and PPh_3 in the presence of acetonitrile so an LDP of the complex in CD_3CN could not be determined. ^cValues represent ΔH^\ddagger values determined in the typical manner of LDP, where ΔS^\ddagger was set equal to -9 e.u.

However, drawing comparisons between the two sets of ΔH^\ddagger without focusing on the exact values, two major trends struck us as significant. First, adding more phenyl substituents to a phosphine appears to make the phosphine a stronger donor. This trend is contrary to the steric effects we would predict in the system, as adding phenyl groups to PR_3 ligands makes them bulkier and more rigid, which should raise the LDP value.^{1, 2} In terms of electronics this, is also contrary (vide supra), as phenyl groups are typically regarded as electron withdrawing. Second, the P(OR)_3 ligands, which are typically regarded as π -acids with low valent metals (i.e. accept electron density via π -backbonding), are two of the best donors in either system.

Additionally, if we consider these trends in light of the three $[\text{NCr}(\text{N}^i\text{Pr}_2)_2\text{PR}_3][\text{SbF}_6^-]$ complexes for which ΔS^\ddagger was determined experimentally, in the absence of ion pairing effects—**3f**, **3j**, and **3m**—the relative ordering of these LDP values remains unchanged in all 3 systems. These results are shown in Table 3.2. It is clearly observed that under all 3 versions of ΔH^\ddagger determination, the value for **3m** is lowest, meaning it is the best donor, and the value for **3f** is the highest, indicating that it is the worst overall donor.

Again, we hesitated to put too much confidence in the LDP values in Table 3.1 or 3.2, because we knew that complications across both sets of values may interfere with accurate analysis and subsequent interpretations of bonding interactions. However, if we consider specific values in which ion pairing raises the ΔH^\ddagger values, with CDCl_3 and $\text{X}^- = \text{BArF}_{24}^-$, several direct comparisons make these perceived trends seem substantial and worth further consideration.

As an example, the ΔH^\ddagger values for **3a** and **3m** are 18.71 and 16.99 kcal/mol, respectively. The phosphines are roughly the same size (*vide supra*) so the primary difference in their donor abilities should be electronic. Despite the fact that PMe_3 is far more σ -electron-rich than $\text{P}(\text{OEt})_3$, $\text{P}(\text{OEt})_3$ is a far better donor according to these values.³ Even if we consider an exaggerated scenario, and say the ΔH^\ddagger for $\text{P}(\text{OEt})_3$ (**3m**) is unaffected by ion pairing but that the value for PMe_3 (**3a**) is raised artificially by up to 1 kcal/mol, there is still a substantial difference between the two values (0.7 kcal/mol), which suggests $\text{P}(\text{OEt})_3$ is a better donor in our high valent system. Taking a more realistic approach to the likely effects that ion pairing with BArF_{24}^- have on the ΔH^\ddagger measurement, both values are likely increased by 0.1-0.5 kcal/mol with this non-site-specific ion pairing counter anion (refer to Chapter 2). Therefore, while we can't precisely quantify *how much better* $\text{P}(\text{OEt})_3$ is than PMe_3 in terms of donor ability, the 1.7 kcal/mol margin seems significant enough that the trend is real.

Table 3.2 The ΔH^\ddagger values determined for **3f**, **3j**, and **3m** in both solvent/ion regimes and with the standard and experimentally determined ΔS^\ddagger values.

PR ₃	Complex	ΔH^\ddagger (CD ₃ CN, SbF ₆ ⁻) ^a	ΔS^\ddagger (CD ₃ CN, SbF ₆ ⁻) ^b	ΔH^\ddagger (CD ₃ CN, SbF ₆ ⁻) ^c	ΔS^\ddagger (CD ₃ CN, SbF ₆ ⁻) ^c	ΔH^\ddagger (CDCl ₃ , BArF ₂₄ ⁻) ^c	ΔS^\ddagger (CDCl ₃ , BArF ₂₄ ⁻) ^c
PPhMe ₂	3f	16.53	-9	17.90	-5	18.79	-2.1
PPh ₂ ⁿ Bu	3j	16.31	-9	10.99	-25	18.17	-3.4
P(OEt) ₃	3m	15.73	-9	6.76	-38	16.99	-6.1

^aThe ΔH^\ddagger values shown here are following the standard LDP practices, with the assumed $\Delta S^\ddagger = -9$ e.u. ^b ΔS^\ddagger determined from NCr(NⁱPr₂)₂X system. ^cThe fully experimentally determined enthalpic and entropic parameters for activation derived from Eyring plots with the experimental rates of rotation.

3.2 A Comparison of Traditional Phosphine Characteristics from Low-Valent Systems with LDP Results

As mentioned briefly in chapter 2, PR₃ ligands are some of the most well-understood ligands used in transition metal chemistry. Their characterization as ligands is primarily based on an electronic parameter and a steric parameter. This concept was first presented in a systematic way by Chadwick Tolman. In his system there was the Tolman Electronic Parameter (TEP, χ) and the Tolman Cone Angle (TCA, θ), with both parameters determined experimentally from a Ni⁰(CO)₃PR₃ complex (or representative model for sterics).⁴⁻⁶

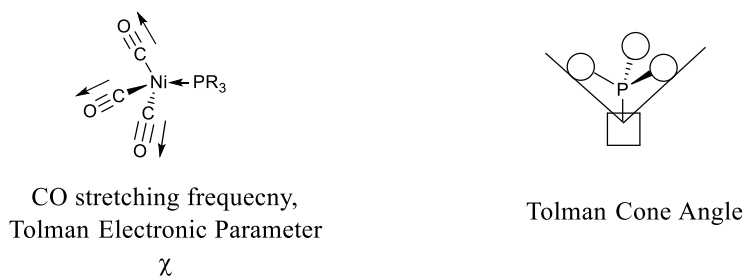


Figure 3.1 (*left*) The Ni(CO)₃PR₃ complex used in to determine the TEP. (*right*) The model used to measure the Tolman Cone Angle of a given phosphine. The spheres represent a variety of R groups, and the P center and block are 2.28 Å apart.

The electronic parameter, χ , was derived from the A₁ CO stretching frequency. Donation from the PR₃ group increases the electron density at the already electron rich Ni⁰ metal center; the Ni⁰ then allocates more electron density into the π -backbonding interactions between Ni and the CO ligands, elongating the CO bonds and decreasing the frequency of the CO stretches. By

comparison, a less donating PR_3 ligand exhibits less backbonding, less C–O bond elongation, and to higher frequency CO stretches. This property is readily observed and serves as a direct indicator of the donor ability of PR_3 ligands.⁴

The steric parameter was based on CPK models (spacefilling) in which the P atom of a given PR_3 ligand was centered on a pin above a pivot 2.85 cm (scaled from 2.28 Å). A protractor was used to determine the angle subtended throughout the rotation of the ligand around the pin. The largest θ value measured was taken as the TCA. When there was flexibility in the PR_3 model, the R groups were constrained to their tightest configuration for determination of θ , giving approximations that were generally reproducible within a few degrees.^{5, 6}

In the last 50 years, since Tolman's initial investigations and subsequent parameterization, IR spectroscopy has advanced, as has the treatment of discrete electronic effects. This has led directly to the modification, and ultimately the separation, of Tolman's original electronic descriptor into separate σ - and π -electronic contributions as well as other expansions in the way we classify phosphines as electron donors.⁷⁻²¹ Despite these criticisms and alterations, the utility of this system of ligand parameterization is hard to dispute considering the number of citations for both the TEC and TCA.⁵ In fact, the TCA is still widely used for a relative comparison of size, and the use of alternate steric descriptors (i.e. % V_{bur} or solid G) mostly stems from the specifics of the complex used and/or personal preferences.^{9, 22}

Again, these parameterizations have been accomplished using low valent metals (Ni, Pd, $\text{Fe}^{0/+2}$, etc) in mind. However, to determine whether these PR_3 ligands are behaving the same way in our high valent system as they do in these low valent systems in the literature, these parameters serve as a useful tool. If there are no differences in the M–P interaction caused by the valency of

⁵ References 2-4 have over 3,000 citations.

the metal, the stereoelectronic parameters used to describe PR₃ ligands in low valent systems should also describe the interactions in high valent systems.

In our high valent Cr(VI) system with low ($\sim C_s$) symmetry, we know that both σ and π orbitals participate and are heavily mixed.¹ Therefore, for comparison, we wanted to consider a system in which these two parameters are separated so we could distinguish the role of each of these electronic factors separately in the holistic LDP values. For reference, the QALE system's description of stereoelectronic parameters, in which σ , π , and even aromatic effects are considered separately, was selected for comparison purposes between low and high valent interactions. These values for the PR₃ ligands across the series of **3a-p** complexes are listed in Table 3.3, below.

Table 3.3 Stereoelectronic parameters for phosphines in which σ (χ_d), π , and aromatic (Aryl) electronic effects are separated. θ is a steric term, which is essentially a modified TCA.^{3, 15, 23}

Compound Number	PR ₃	χ_d	π	Aryl	θ (°)	ΔH^\ddagger (CDCl ₃)	ΔH^\ddagger (CD ₃ CN)
3a	PMe ₃	8.55	0	0	118	18.71	16.64
3b	P ⁿ Bu ₃	5.25	0	0	136	18.91	16.77
3c	P ⁱ Bu ₃	5.7	0	0	143	17.76	17.13
3d	P ^t Pr ₃	3.45	0	0	160	19.47	17.17
3e	PCy ₃	1.4	0	0	170	19.46	17.27
3f	PPhMe ₂	10.5	0	1.0	122	18.79	16.53 (17.90)
3g	PPh ₂ Me	12.6	0	2.2	136	16.90	16.16
3h	PPhEt ₂	8.6	0	1.1	136	16.96	16.65
3i	PPh ₂ Et	11.1	0	2.3	140	17.98	16.15
3j	PPh ₂ ⁿ Bu	11.3	0	2.1	143	18.17	16.31 (10.99)
3k	PPh ₂ Cy	9.1	0	1.6	153	18.11	16.43
3l	PPhCy ₂	5.7	0	1.6	162	-	16.37
3m	P(OEt) ₃	15.8	2.9	1.1	109	16.99	15.73 (6.76)
3n	P(O ⁱ Pr) ₃	13.4	2.9	1.3	130	17.12	15.91
3o	P(NC ₄ H ₈) ₃	-1.4	0.9	-0.6	146	19.52	16.21
3p	PPh ₃	13.25	0	2.7	145	18.00	-

It is important to clarify that, like the Tolman system, the QALE system's primary donor parameter describing σ -bond formation, χ_d , is based on the donor ability of PⁱBu₃ as the zero point reference.^{4, 12} With this σ -electron rich donor's perturbation on the CO stretching frequency as zero, a higher χ_d value correlates with a less donating phosphine. Thus, by these parameters, of the PR₃ ligands listed above, P(NC₄H₈)₃ is the most donating while P(OEt)₃ is the least donating. Additionally, both the π and Aryl parameters typically represent Lewis acidic or electron withdrawing effects in low valent systems.

Considering these parameters from the literature, which specifically describe traditional low-valent M–P bonding interactions, it's easy to see why the low LDP values (good donor abilities) of ligands such as aryl phosphines and especially the phosphites (**3m** and **3n**) relative to the trialkyls (**3a-e**) are so surprising. Both types of PR₃ donors have electron withdrawing R groups and considerably diminished σ -donor abilities relative to the trialkyl's. If we consider the manner of the bonding involved in an aryl or -OR substituted PR₃ ligand's electron withdrawing ability,

these arguments typically hinge upon π -backbonding. In a π interaction between an electron rich metal center and a π -acidic PR_3 , a filled d-orbital on the metal pushes electron density into an appropriately oriented P–R σ^* orbital. This interaction is illustrated in Fig. 3.2 and leads to the resonance form ϕ , shown below. Together with the resonance forms α and β , that characterize dative donation of the P's lone pair to M, this summarizes the bonding picture of a M–P bond in a low valent complex.^{21, 24-30}

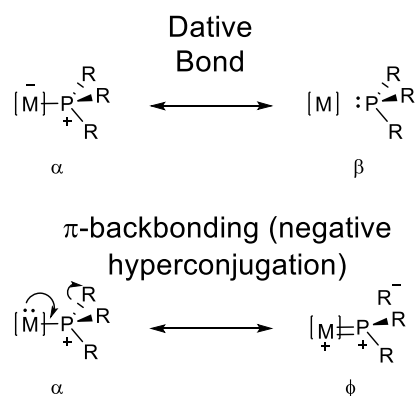


Figure 3.2 Resonance forms that contribute to the ground state electronic structure of traditional low-valent metal-phosphorous interactions.

Presumably, the ϕ interaction is heavily diminished in high valent M–P bonds, especially when the metal is d^0 . Formally, any participation of ϕ in the electronic structure of a high valent M–P bond is populated by donation from or mixing with an M–X bonding orbital in these complexes (where X is another ligand).³¹ Where symmetry or energy discrepancies prevent such a bonding-to-antibonding orbital interaction, the participation of ϕ would be essentially 0%. Simply omitting the π -acceptor ability of these phosphines, however, doesn't account for the increased donor ability of these traditionally π -acidic PR_3 ligands. Based on the experimental evidence, it seemed likely that some other interaction, not readily observed with low valent metals, was leading to an enhancement of these PR_3 ligands' donor abilities.

Considering the fundamental properties of low and high valent metals, their inherent Lewis acid-base characteristics are markedly different. Low valent metals are electron rich and can delocalize their *d* (and *s*) orbital electron density onto their ligands. High valent metals, on the other hand, are typically regarded as Lewis acids. In fact, simple molecular compounds of high valent transition metals (i.e. TiCl_4) are utilized for Lewis acid catalyzed (mediated) organic transformations.³¹⁻³³ The exact Lewis acidity or basicity of highly dissimilar compounds is a hard comparison to make outside of an experimental handle such as pK_a or ionization potentials.

However, this gave us the idea that perhaps in the M-P bonds with high valent metals there is a role reversal observed relative to low valent M-P bonds. Specifically, we suspected that this could happen with regards to the π -interactions. With a high valent metal, lacking electron density in the *s* and *d* orbitals, the metal may act as the Lewis acid (π -acid) and the PR_3 ligand may act as the Lewis base (π -base). If this were the case, a PR_3 ligand such as $\text{P}(\text{OEt})_3$, which has electronegative heteroatoms bound to P has stored π -electron density (oxygen lone pairs). Similarly, aryl groups bound to P have aromatic π -electron density. With an electron deficient metal bound to P, these substituents, which act as electron-withdrawing groups in low valent interactions, may act as electron donating groups, through simple negative hyperconjugation interactions where the metal is the recipient of additional electron density. Such an interaction could strongly enhance the donor ability of such ligands, despite poor σ -donor ability from the P's lone pair of electrons. Based on this idea, we decided to pursue computational investigations that might elucidate the electronic interactions of these ligands with a high valent metal.

Before we got carried away with interpreting calculations, we sought experimental evidence to support our hypothesis that the Cr(VI) metal center utilized in the LDP system is in fact a strong Lewis acid. A piece of experimental evidence supporting the proposed inversion of

the Lewis acid-base dynamic with PR₃ ligands—one free of the solvent effects impacting the LDP measurements—seemed necessary in light of our losing fight against ion pairing and unpredictable ΔS^\ddagger values. It would unify all of the qualitative pieces of evidence that we had collected while probing the *in situ* dynamics of the **3a-p** salts. With this motivation looked for a way to determine the Lewis acidity of the Cr(VI) in our system with a quantitative experimental technique.

To determine the Lewis acidity of [NCr(NⁱPr₂)₂]⁺ a convenient method for probing the Lewis acidity of various species in solution, which utilizes ³¹P NMR, was pursued. This method, known as the Gutmann Parameter or Gutmann-Beckett Method, requires the synthesis of the tri(ethyl)phosphine oxide adduct of the Lewis acid in question.³⁴⁻³⁸ Upon binding through the oxygen of the O=P(Et)₃, inductive effects caused by the donation of electron density from the O to the Lewis acidic species produce a shift in the ³¹P NMR signal for the O=P(Et)₃. Therefore, when the O=P(Et)₃ is bound to a Lewis acid, the ³¹P signal shifts downfield; the extent of this shift can be related to the Lewis acidity by the following equation (Eq. 3.1).

$$AN = 2.21 * (\delta(ppm) - 41.0) \quad (\text{Eq. 3.1})$$

In this equation AN, or acceptor number, is the value indicating Lewis acidity (aka Gutmann parameter). The higher the value, the more Lewis acidic a species is. Since the system was originally designed to probe the Lewis acidity of various solvents, the ³¹P NMR shift of 41.0, which is the value observed for O=P(Et)₃ “interacting” with *n*-hexane, serves as the zero-point reference. The coefficient of 2.21 scales the ³¹P NMR shifts such that the AN for SbCl₅ is set to 100 ($\delta = 86.1$ ppm). For reference, the AN’s for a selection of commonly regarded strong Lewis acids is listed in Table 3.4 with Fig. 3.3.

Table 3.4 AN Values indicating the Lewis acidity of several compounds determined by the Guttmann-Beckett Method.³⁷ ^aMeasured in DCE, referenced to External O=P(Et)₃ as 41.0 ppm.

Compound	³¹ P δ (ppm)	AN
B(C ₆ F ₅) ₃	78.0	82
BF ₃ ·Et ₂ O	80.9	88.5
SbCl ₅	86.1	100
BCl ₃	88.7	106
BBr ₃	90.3	109
BI ₃	92.9	115
TiCl ₄	72.7	70
AlCl ₃	80.3	87
NiCr(N ⁱ Pr ₂) ₂ ⁺	86.2	100 ^a

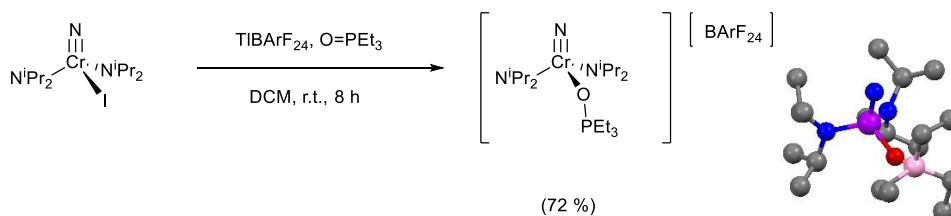


Figure 3.3 The synthetic scheme used to generate the O=P(Et)₃ adduct with [NiCr(NⁱPr₂)₂]⁺. A high yield of the desired complex was isolated after recrystallization. (*right*) Preliminary crystal structure of [NiCr(NⁱPr₂)₂(OP(Et)₃)]⁺[BARF₂₄]⁻; note, thermal ellipsoids are not shown due to the severe disorder in the structure. It provided only connectivity.

Using this technique, we were able to synthesize and isolate the [NiCr(NⁱPr₂)₂(O=P(Et)₃)]⁺[BARF₂₄]⁻ salt and determine the ³¹P NMR shift for the bound phosphine oxide species. The shift of 86.2 ppm correlates to an AN of 100, which is the same as the highly acidic SbCl₅. The experimental verification of such strongly Lewis acidic character from the [NiCr(NⁱPr₂)₂]⁺ fragment offers support for the following computational results. The relative electron deficiency of the metal is substantial enough that it is one of the primary factors determining the bonding interactions between the Cr(VI) and its ligands.

3.3 Computational Analysis of the Electronic Structure of [NiCr(NⁱPr₂)₂PR₃]⁺ Using Natural Bonding Orbital and Natural Resonance Theory

Calculations to examine the details of the bonding interactions between Cr and the PR₃ ligands under study in the LDP system were carried out using MSU's HPCC platform. For the purposes of our studies, we found it necessary to abridge the NⁱPr₂ ligands, substituting the ⁱPr-

groups for hydrogens.⁶ Similarly, two of the PR₃ ligand R groups (**3m*** and **3o***) were slightly abridged for ease of optimization of the structures. With **3m*** and **3o***, the extended alkyl portions of the R groups on the PR₃ ligand caused difficulties in geometry optimization, so they were appended to smaller versions of electronically similar PR₃ ligands. In all cases, the first coordination sphere of the Cr and the atoms bound directly to P were unaltered. Our model complexes followed the form [NCr(NH₂)₂PR₃]⁺. To achieve diversity of the R groups in the PR₃ ligands, the following model PR₃ ligands were examined: PMe₃ (**3a***), PPhMe₂ (**3f***), P(OMe)₃ (**3m***), and P(NMe₂)₃ (**3o***). These model complexes are shown in Fig. 3.4.

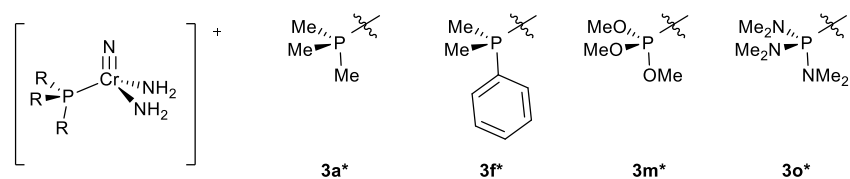


Figure 3.4 Structures examined by NBO/NRT analysis.

The general approach to these calculations started with geometry optimization for each structure. The initial structural models input for optimization were based on modified versions of the X-ray structures of the closest **3** derivatives characterized. These model compound structures were optimized using DFT with the B3PW91 functional and 6-311G+(d,p) basis set on all atoms, with Gaussian09.³⁹ Upon successful optimization, each structure was analyzed using the NBO6 program.⁴⁰ Through this program, local NRT calculations that included the Cr atom, all three N's, the P atom, and its direct substituent atoms on each molecule, were performed (see experimental for more specifics).

⁶ Brennan performed several sets of calculations looking at ΔG^\ddagger values for the -NR₂ rotations, where R = H, Me, or ⁱPr. From his efforts, little difference was noted among the different R groups in the trends and absolute values calculated for ΔG^\ddagger , but increasing the R group complexity dramatically increased computational time. Therefore, we opted to use H's in these calculations, especially because we were considering only orbital interactions rather than energies.

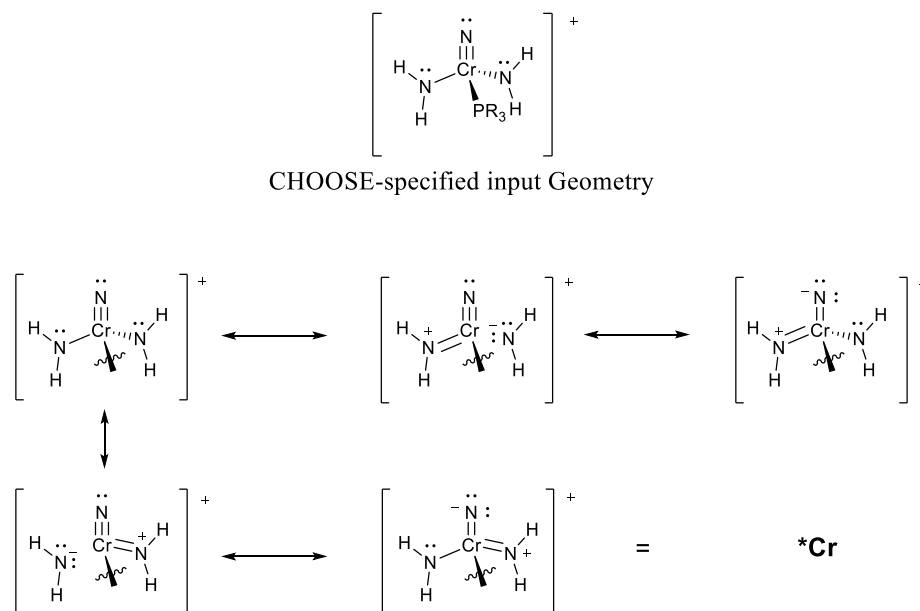


Figure 3.5 Resonance forms inherent to the CrN_3 fragment from rearrangement of the lone pair electron density across the N ligands. These resonance forms and their electron rearrangements do not affect the nature of the Cr–P bonds, so they are summed as *Cr to focus resonance form discussion on the Cr–P interaction.

Before discussing the results of the NRT calculations specifically, it is worth noting that, because we included the three N ligands in the NRT list, these N's participate in resonance. However, the various rearrangements that can occur via electron reorganization of the N lone pairs and bonds to Cr do not directly affect the character of the Cr–P bond. For example, whether N2 versus N3 has a lone pair, the same electronic interaction occurs between Cr and P. Therefore, when electron density shifts among the N ligands, but the Cr–P bond and the PR_3 bonds are the same, we have summed the total contributions of these resonance forms to focus discussion on the Cr–P bond. This treatment is summarized in Fig. 3.5.

By most descriptions, PMe_3 is a simple ligand. In trialkyl phosphines, the P–C σ^* orbitals are high in energy and participate very little in their bonding interactions, even in low valent systems. Consequently, these PR_3 ligands are typically regarded as simple σ -donors.²⁴ Knowing this we started our NBO/NRT analysis with $\mathbf{3a}^*$. Unsurprisingly, with the PMe_3 ligand bound to our Cr^* model, the resulting bonding picture is very simple. According to NBO/NRT calculations,

>99% of the ground state electronic structure can be described by two resonance forms. The first, α , simply includes σ -bond formation from dative donation of the P lone pair to Cr, which accounts for 69% of the electronic structure. The second, β , is the unbound form of the dative bond, where no lone pair donation from P to Cr occurs (alternatively, population of Cr–P σ^* orbital). This electronic description is a nearly perfect example of a purely dative interaction and these results are summarized in Fig. 3.6.²⁶

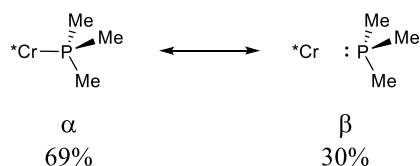


Figure 3.6 NRT determined resonance forms accounting for 99% of the ground state of **3a***.

This bonding picture, generated by NBO and represented by NRT, served as a nice check for the system and application of resonance theory to this low symmetry system. With these results, we next sought to analyze slightly more complicated systems, **3m*** and **3o***. In both systems, we first identified the contributions of the same α and β resonance forms identified for **3a***. The contribution of these resonance forms, the components of a classic dative bond, are shown in Fig. 3.7.

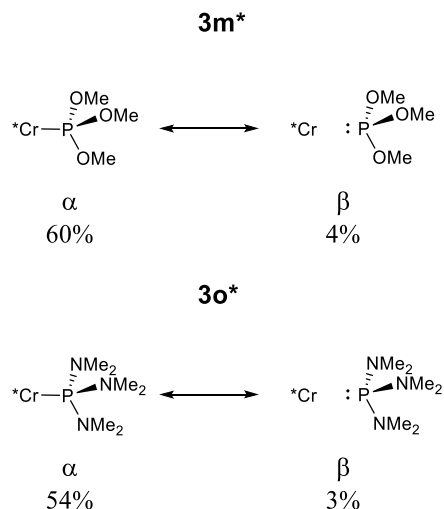


Figure 3.7 Contribution of the two resonance forms that compose a dative interaction to the ground state electronic structure of **3m*** and **3o***.

According to the NRT analysis of these complexes only ~60% of the ground state electronic structure is described by these resonance forms. Most interesting is that the contribution of the β form is substantially decreased, making up less than 5% of the ground state structure in both compounds. This alone lends support to the increased donor ability of these phosphines, as it suggests an increased bond order between the PR_3 and Cr in these structures relative to **3a***. But what accounts for the remaining 30% of the electronic ground state?

Closer inspection of the NRT results shows two additional resonance forms that contribute substantially to the overall ground state. The first structure, γ , is one that is invoked for low valent systems, as well. When heteroatom-containing R groups are substituents on P in a PR_3 ligand, negative hyperconjugation allows for lone pair donation from one substituent into the $\text{P}-\text{R} \sigma^*$ orbital with one of the other substituents. This creates double bond character between P and R_1 (donor), while R_2 dissociates with negative charge (acceptor).^{24, 30} The introduction of this resonance form, was not surprising, but can be considered to contribute to the increased donor ability, again by taking the place of β contribution, increasing the overall bond order between Cr

and P. This is represented by γ in Fig. 3.10 and is shown by the arrow pushing diagram in Fig. 3.8, below.

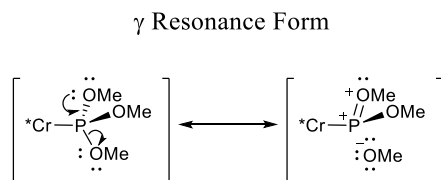


Figure 3.8 Arrow pushing illustration relating α and γ in $\mathbf{3m}^*$ and $\mathbf{3o}^*$. The example is shown here with $\mathbf{3m}^*$.

One final resonance form that appears to contribute substantially to the ground state electronic structures with $\text{P}(\text{OMe})_3$ and $\text{P}(\text{NMe}_2)_3$ is the form ϵ . This resonance form does not appear in literature describing PR_3 interactions with low valent metals. In this resonance form, a lone pair on a heteroatom substituent donates electron density into the Cr–P σ^* orbital. In this way, ϵ is similar to γ . However, instead of negative hyperconjugation between R groups, this constitutes negative hyperconjugation with the metal! This pushes a lone pair of electron density onto the Cr^* fragment. Arrow pushing that represents this electron redistribution is shown below in Fig. 3.9, as well as in Fig. 3.10 as the ϵ resonance form.

ϵ Resonance Form



Figure 3.9 Arrow pushing illustration relating α and ϵ in **3m*** and **3o***. The example is shown where with **3o***.

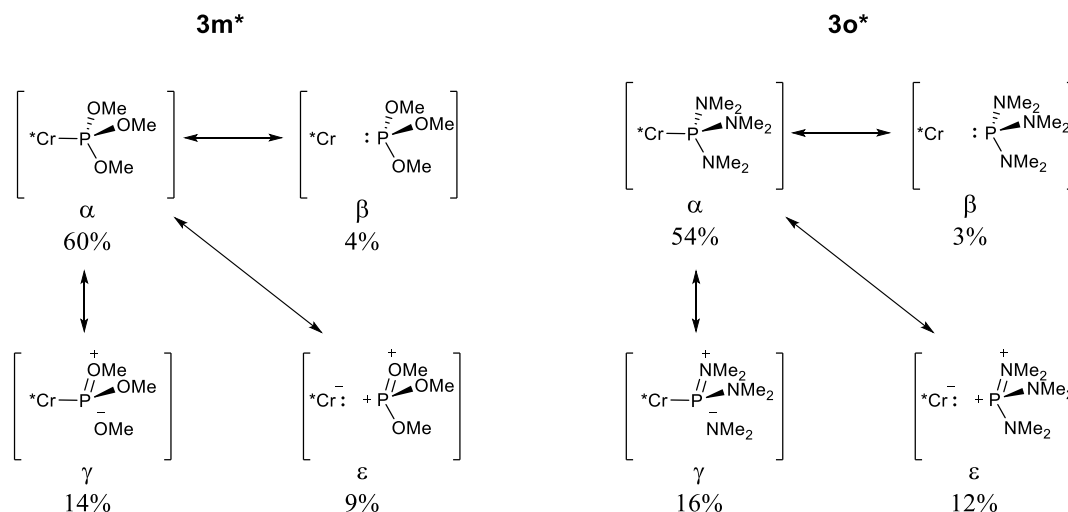


Figure 3.10 Ground state electronic structures of **3m*** and **3o***, including γ which shows negative hyperconjugation among the -OMe and -NMe₂ ligands, as well as ϵ which is a new negative hyperconjugative resonance form involving the metal.

The observation of this new resonance form, ϵ , is particularly interesting, as it directly increases the electron density on the Cr* fragment by a full electron pair. This resonance form is very similar to γ , in principle, and we would propose that it is facilitated by the extreme Lewis acidity of the Cr(VI) metal center. Another way to think about this phenomenon is to consider what happens to the electronegativity of an atom as it is oxidized. Looking at the Sanderson electronegativities of the different oxidation states of Cr, for example, the following values are assigned: Cr(II) = 1.24, Cr(III) = 1.66, Cr(IV) = 2.29, Cr(V) = 2.83, and Cr(VI) = 3.37.⁴¹ As the metal becomes increasingly oxidized, the electronegativity increases substantially. In fact, on the Sanderson scale, the electronegativity of Cr(VI) is comparable to that of oxygen or nitrogen. When the metal in an M–P bond is sufficiently oxidized, the advent of resonance form ϵ seems like a

complementary resonance form to γ . In high valent systems, where the electronegativity of the highly oxidized metal is comparable to that of the heteroatom substituents on P, the metal begins to participate in negative hyperconjugation.

These calculations have provided electronic structures which support the possibility that, in interactions with high valent metals, bonding interactions occur which increase the electron density on the metal. First, the contribution of γ decreases the contribution of β to the overall ground state electronic structure. Second, ε directly increases the electron density donated from the PR_3 fragment to the CrN_3 fragment via negative hyperconjugation from the substituents on P to the metal. Note that in the LDP system, the contribution of ε to the ground state electronic structure would result in more lone pair electron density on the amide ligands and a reduced barrier to $\text{Cr-N}^i\text{Pr}_2$ bond rotation.

With a clear picture of the bonding interactions that make up a total of ~90% of the ground state electronic structure in $\mathbf{3m}^*$ and $\mathbf{3o}^*$, we examined $\mathbf{3f}^*$. We suspected that in the aryl phosphines, something similar to the ε interaction noted in the “ π -acidic” PR_3 ligands of $\mathbf{3m}^*$ and $\mathbf{3o}^*$ might be increasing their electron donor abilities. NRT calculations were performed on $\mathbf{3f}^*$ in a slightly different manner compared to the other complexes. Due to the massive number of possible resonance forms enabled by the inclusion of the entire phenyl ring on the PPhMe_2 ligand, the NBO6 program could not run the NRT calculation. Inclusion of the entire PPhMe_2 ligand was crucial to the analysis, so in order to free-up more space in the NRT calculations, we froze the nitrogen ligands using the CHOOSE keyword (see Experimental). Only the Cr, P, and P substituent groups were included in the local NRT calculation.

With the Cr-N interactions frozen, the calculation involving the aromatic ring was able to run successfully. The results of the NRT calculation for $\mathbf{3f}^*$ are shown below in Fig. 3.11. Similar

to the ϵ resonance form, donation of π -electron density from the phenyl ring into the P–Cr σ^* orbital, was observed for **3f***. We would note that, because a slightly different method was used for **3f***, due to the limits of the NRT calculation, comparing the percentages from this calculation to those for **3a***, **3m***, and **3o*** may not be valuable. Also of note is the fact that, because the other R groups are methyl's in this case, the γ resonance form was not observed.

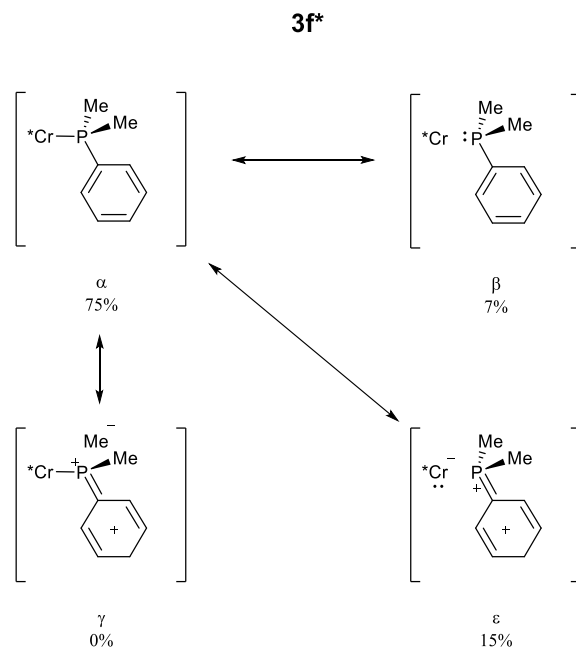


Figure 3.11 NRT results for an aryl phosphine ligand. Similar to the ϵ resonance forms observed with **3m*** and **3o***, electron density is pushed from one of the R groups into the Cr–P σ^* orbital.

The NRT results are consistent with the energies of several orbital interactions in the Second Order Perturbation Theory List (SOPT). These analyses show very small π -backbonding interactions within all 4 complexes (~ 3 kcal/mol = E2). Interestingly, these donations from filled Cr–N nitride and amide bonds into P–R σ^* orbitals are very similar despite radically different R substituents, in terms of their stabilization abilities for this type of interaction. Additionally, there are substantial stabilization energies for the orbital interactions describing γ (~ 75 kcal/mol) and ϵ (~ 12 kcal/mol) interactions for **3m*** and **3o***. These substantial energies support the interpretation of the NRT results with these complexes.

Finally, examination of the optimized structures **3a***, **3m***, **3o***, and **3f***, by Mayer Bond Order⁴² analysis suggests that the Cr–P bond orders increase in the order **3a*** < **3f*** < **3m***~**3o***. There is consistency across several aspects of the calculations suggesting that, in fact, based on the electronic structure, there is an explanation for how PR₃ ligands which are poor donors in low valent metal systems are much better donors to high valent metals.

3.4 Modeling Approximations to Examine Stereoelectronic Control on LDP Value

Despite complications with both sets of experimental ΔH^\ddagger values, determined for **3a-p**, calculations had pointed to real electronic effects causing improved donation from traditionally poor PR₃ ligands. With the ΔH^\ddagger values determined in CD₃CN, where ion pairing effects were eliminated, the main concern was entropic inconsistencies. Knowing this, we were still unable to determine if the experimentally measured entropies in this system for **3f**, **3j**, and **3m** were actually relevant to the Cr–NⁱPr₂ bond rotation. For example, when we consider the actual ΔH^\ddagger and ΔS^\ddagger values determined from the Eyring plot of the rotation rate of the Cr–NⁱPr₂ bond in **3m**[SbF₆] at several different temperatures, we end up with a ΔH^\ddagger value of 6.76 kcal/mol. In the simplest scenario where the ΔH^\ddagger and ΔS^\ddagger values measured here have the same meaning as those in the NCr(NⁱPr₂)₂X system, this means that P(OEt)₃ is a better donor than (NMe₂) (See Chapter 2, Fig. 2.6). We know this isn't true just by looking at the room temperature ¹H NMR spectra of the two complexes. In this case, just as the ΔS^\ddagger value is affected by the solvation sphere, the ΔH^\ddagger value seems similarly affected by solvent.

The values of ΔS^\ddagger are consistent when the ions are paired in the [NCr(NⁱPr₂)₂PR₃][BArF₂₄] salts with CDCl₃, and similar to the values observed in the NCr(NⁱPr₂)₂X system.¹ Therefore, we don't suspect that the actual ΔS^\ddagger value for the [NCr(NⁱPr₂)₂PR₃]⁺ bond rotation is actually different in this system. With this suspicion, we set about trying to model the stereoelectronic effects of

each PR₃ for the trialkyl phosphines with the ΔH^\ddagger values observed with X⁻ = SbF₆⁻ in CD₃CN. For this purpose, we left the $\Delta S^\ddagger = -9$ e.u. in place. Given the similarity of the PR₃ ligands where R = alkyls, we suspected that the real ΔS^\ddagger value for these complexes should be similar. Additionally, all 5 experimental measurements were conducted at similar temperatures (within 10 °C), so small entropy differences over this small temperature range would not have a large impact on the ΔH^\ddagger calculated.

The stereoelectronic properties of the trialkyl phosphines, as mentioned above are generally regarded as simple; they are σ -donors, but due to the covalency of the P–C bonds and the elements' similar electronegativities, the P–C σ^* orbitals are high in energy and participate very little in bonding. Therefore, if we consider even an elaborate parameterization system, such as QALE, only two terms are needed to parameterize **3a-e**. This assumption was verified with the [NCr(NⁱPr₂)₂PR₃]⁺ system via the computational analysis with NRT. By this method, we found that 99% of the electronic ground state is composed of a pure dative interaction. Therefore, based on our own experimental and literature evidence, we elected to examine a simple 2-parameter fit, considering σ -electron donor ability and sterics.

Using χ_d to represent the electronic properties of the PR₃ (R = alkyl) ligands and θ to represent the steric properties of the ligands, a least squares fit was applied, with ΔH^\ddagger fitted as the dependent term. The model then fits Eq. 3.2, below.

$$\Delta H^\ddagger = 11.98 + 0.135(\chi_d) + 0.030(\theta) \quad (\text{Eq. 3.2})$$

According to the model, both electronic donor ability and sterics make sizable contributions to determining the overall ΔH^\ddagger value for each PR₃ ligand. We can verify that the model fits the data well by plotting the experimental versus modeled ΔH^\ddagger values (or the steric and electronic profiles). The fit shown in Fig. 3.12 demonstrates good correlation between the

experimental and model predicted ΔH^\ddagger values suggesting that the least squares fit in Eq. 3.2 is an accurate predictor of the donation ability for the trialkyl phosphines. Furthermore, the model makes chemical sense. According to Eq. 2, as the size of PR_3 increases, ΔH^\ddagger also increases. This is the logical results as a larger ligand on Cr will lead to steric hindrance of the measured bond rotation. Likewise, as the χ_d parameter increases and the PR_3 ligand becomes less σ -electron donating, the ΔH^\ddagger value also increases. Since dative donation of the lone pair is the only significant bonding interaction between Cr and PR_3 with a trialkyl substituted P, this correlation is also logical. These trends are signified by the (+) coefficients in Eq. 3.2.

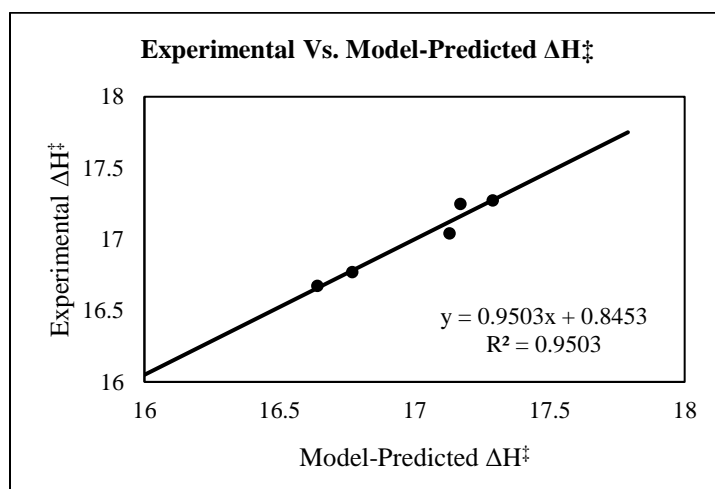


Figure 3.12 A plot showing good correlation between experimental and modeled ΔH^\ddagger values for trialkyl phosphines fitted with χ_d and θ parameters.

We tried to apply this simple, 2-parameter model, with the coefficients fitted from the trialkyls in Eq. 3.2, to the entire series of electronically diverse PR_3 ligands in the series **3a-p**. This does not produce good correlation. In fact, the data series looks like a nearly random scatter plot (Fig. 3.13). When we begin dissecting this scatter more closely, it resembles several of the plots shown by Giering and Prock in the QALE system, where there are stepwise deviations from the model based on the types of R groups.¹⁵ This is highlighted in the color coding in the figure below. This observation directly supports the conclusion that different electronic factors are likely

affecting the measured ΔH^\ddagger values here, and that these effects appear to be related to systematic alterations in the R groups on the PR_3 ligands. While further quantitative fittings with these data were not pursued, considering the remaining issues with entropy complications, these findings are in agreement with both computational and experimental observations.

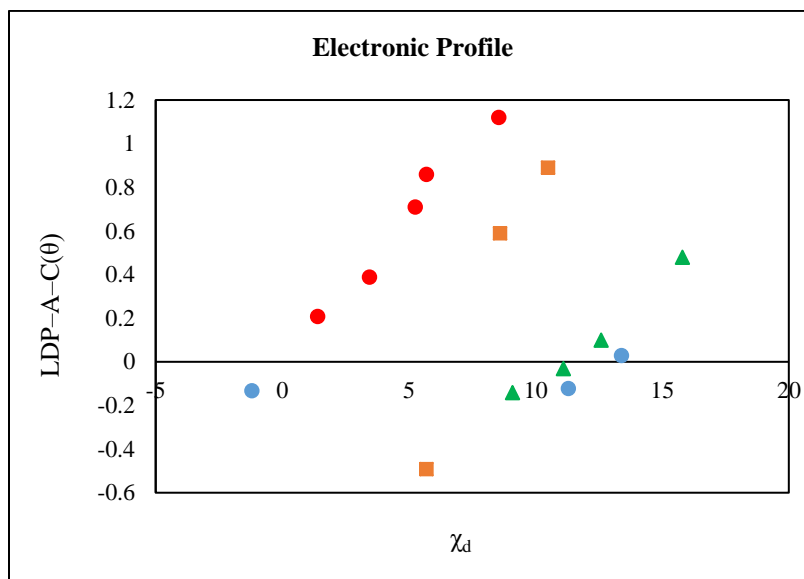


Figure 3.13 All complexes **3a-p** fitted with the model in Eq. 2. (Red = trialkyl, orange = monoaryl, green = diaryl, blue = heteroatom substituents).

3.5 Conclusions

Obviously, from the experimental LDP data, we couldn't construct a concrete stereoelectronic model detailing the exact *quantitative effect* of each electronic property of a PR_3 ligand on the donor ability of that ligand. However, the fact that the aryl and heteroatom substituted phosphines do not fit Eq. 2, supports the assessment that these phosphines have additional electronic properties affecting their bonding interactions with Cr. Qualitatively, this agrees with the calculations and initial observations made for both series of ΔH^\ddagger values examined. Despite ongoing difficulties in experimentally determining the true donor abilities of these PR_3 ligands, without solvent effects caused by ionicity, the methods presented here that examine the Cr- PR_3 bonding interaction consistently point toward the same conclusion. PR_3 ligands that are poor

donors for traditional low valent metals are strong donors for high valent metals due to the enhanced Lewis acidity and electronegativity of a highly oxidized metal.

Specifically, from the NRT calculations, orbital interactions which facilitate this enhancement in donor ability were discovered. With our high valent metal system, a form of negative hyperconjugation, whereby π -bonding or lone pair electron density from an R group populates the Cr–P σ^* orbital, delocalizes electron density onto the Cr. This effectively makes ligands which have this π -bonding (aryl) or lone pair (heteroatom) electron density better donors to metal centers which are Lewis acidic, electronegative, or electron deficient (i.e. high valent).

These findings demonstrate that the interactions of ligands with metal centers in drastically different oxidation states can completely change the role of the ligand in the bonding interaction with the metal. It also points toward the risks of extending chemical intuition built on an understanding of metal-ligand interactions with low valent systems to high valent ones. The fundamental differences in the types of interactions are potentially quite substantial and could lead the unsuspecting researcher completely off target when attempting to manipulate metal complex behaviors through ancillary ligand selection. Experimental investigations to probe the differences in high valent metal interactions with a wider variety of ligand types is a necessary endeavor to advance catalysis with these metals. For the purposes of quantifying the fundamental bonding effects discovered in these studies, it is likely that a neutral high valent metal system is needed to experimentally verify the enhanced donor abilities of phosphites and aryl phosphines.

3.6 Experimental

General Considerations

All complexes discussed in this chapter were previously characterized and discussed in Chapter 2. Additionally, details on ion pairing behavior and other NMR measurements are

included in Chapter 2, which should be referenced for further information. The exception to this is the phosphine oxide complex utilized for determination of the Gutmann Parameter, the AN. Details on this complex are provided below.

Calculations All calculations were carried out at the High Performance Computing Center (HPCC) through Michigan State University's Institute for Cyber-Enabled Research. DFT optimizations were performed using Gaussian09 with B3PW91 and the 6-311G+(d,p) basis for all chromium and main group compounds. The NBO and local NRT (*vide infra*) calculations were performed using NBO6. The phosphine complexes were analyzed using $\text{NCr}(\text{NH}_2)_2\text{PE}_3^+$ as a model in order to reduce the amount of computational time required for optimization.

To focus on the interactions of the bound ligand atom (P) to the metal and simplify the NRT analysis, we chose to localize the NRT calculations on the metal and all atoms bound directly to it. The first substituent atoms on the phosphorus atom, directly bound in E through P–E σ -bond, were also included. Primarily, the localization only eliminates inclusion of the hydrogens on the amide ligands in the Cr(VI) model and alkyl carbons and hydrogens on the distal portions of the E groups. So, for example, in the $[\text{NCr}(\text{NH}_2)_2\text{PMe}_3]^+$ cation, the NRT included the chromium, three nitrogens, phosphorus, and the three carbons in the methyl groups. This method allowed for the calculations to focus on the first coordination sphere interactions with chromium and the phosphine ligand's substituent orbital participation without generating hundreds of resonance forms dealing with charge distribution among distal protons and similar effects which do not involve rearrangement of the electron density at the metal.

The only exception to this NRT method was made for $[\text{NCr}(\text{NH}_2)_2\text{PMe}_2\text{Ph}]^+$. The full phenyl ring was crucial to examining the impact of an aromatic substituent on phosphorus, so all carbons in the Ph group were included in the calculation. However, too many resonance forms

were found during these calculations. Consequently, the structure below was used with the CHOOSE keyword, and resonance forms localized on the chromium, phosphorus, and all carbons in the phosphine ligand were calculated.

The default applications of NRT then locked the N interactions of the CrN₃ portion of the fragment as shown below. This arrangement is roughly the average for the resonance forms available by N inclusion, which we have been summing together into a single “*Cr”); this denotes resonance isolated to the N’s. As noted previously, the NRT analysis was intended to focus on the Cr–P interaction. Additionally, the resonance of the Cr–N bonds behaves predictably based on other calculations performed, and do not alter the interactions of Cr and P. Thus, we do not believe that this adjustment to the method lead to substantially different treatment of those atoms included in the local NRT.

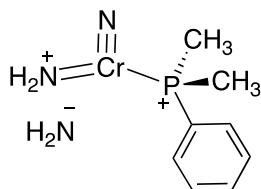


Figure 3.14 Ground state resonance assignment to Cr fragment by NRT for [NCr(NH₂)₂PMe₂Ph]⁺.

Additional Analysis from the NBO Calculations:

Below is a list of the atomic charges assigned by NBO for the atoms considered in the NBO calculations. Note that since any change in the electron density at Cr is delocalized across the entire CrN₃ fragment, the changes in the charges should be relatively small in magnitude. Thorough analysis and overemphasis of the differences noted in these calculated charges, especially in the

absence of a valid assignment of error for these calculated values, is neither highly informative nor recommended. However, the values are listed below for transparency.

Table 3.5 Natural Charges for $\text{NCr}(\text{NH}_2)_2\text{PE}_3^+$ complexes

Complex	NBO Charge by Atom							
	Cr	P	N1 ^a	N2 ^b	N3 ^b	R ^c	R ^c	R ^c
$[\text{Cr}]\text{PMe}_3^+$	0.57790	1.05257	-0.05995	-0.85567	-0.92391	-0.92391	-0.91721	-0.91721
$[\text{Cr}]\text{POMe}_3^+$	0.53725	1.94464	-0.07349	-0.8703	-0.86708	-0.84327	-0.83297	-0.83121
$[\text{Cr}]\text{PPhMe}_2^+$	0.58370	1.08700	-0.07261	-0.84814	-0.86036	-0.92910	-0.91149	-0.38288
$[\text{Cr}]\text{P}(\text{NMe}_2)_3^+$	0.54956	1.74058	-0.06175	-0.87353	-0.86802	-0.84567	-0.86371	-0.87116

^aN1 = nitride nitrogen. ^bN2/3 = amide nitrogens. ^cR = C or E bound to P.

For the default bonding in the $\text{NCr}(\text{NH}_2)_2\text{PE}_3^+$ molecules, NBO chose the following structure for 3 of the 4 molecules:

CHOOSE 1 (picked by NBO)

Cr-N1 triple bond

Cr-N2 double bond

Cr-N3 double bond

Cr-P single bond

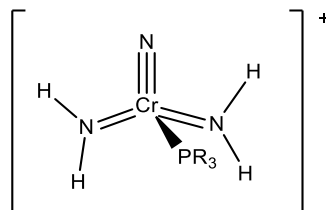


Figure 3.15 CHOOSE 1 geometry for NBO analysis.

This arrangement was not the default for P(NMe₂)₃ but was easily selected with an appropriate CHOOSE command added to the input file.

Results from the “SECOND ORDER PERTURBATION THEORY ANALYSIS OF FOCK MATRIX IN NBO BASIS” are presented below for each PE₃ examined using this above bonding configuration. The type of interaction, Donor-acceptor, and reported E2 value (kcal/mol) are reported.



N1 = nitride, N2/3 = amide, C6/10/14 = Me C's

Donor	Acceptor	E (kcal/mol)
π backbonding		
LP1 N1	BD*1 P2-C6	0.74
BD2 Cr-N2	BD*1 P2-C14	2.33
BD2 Cr-N1	BD*1 P2-C6	3.07
BD3 Cr-N1	BD*1 P2-C14	0.64
BD3 Cr-N1	BD*1 P2-C10	0.64
BD2 Cr-N3	BD*1 P2-C10	2.33
	Total	9.75 (avg 3.25/CH₃)

Resonance form γ: Negative hyperconjugation among R groups

BD1 P2-C6	BD*1 P2-C10	1.31
BD1 P2-C6	BD*1 P2-C14	1.31
BD1 P2-C10	BD*1 P2-C14	1.27
BD1 P2-C10	BD*1 P2-C6	1.33
BD1 P2-C14	BD*1 P2-C10	1.27
BD1 P2-C14	BD*1 P2-C6	1.33
	Total	7.82 (avg 2.60/CH₃)

Resonance form ϵ : Negative hyperconjugation from P-R to Cr

BD1 P2-C14	BD*1 Cr1-P2	1.50
BD1 P2-C10	BD*1 Cr1-P2	1.50
	Total	3.00



N1 = nitride, N2/3 = amide, O3/4/15 = OMe O's

Donor	Acceptor	E (kcal/mol)
π backbonding		
LP1 N1	BD1* P1-O3	0.72
BD2 Cr-N2	BD1* P1-O4	2.53
BD2 Cr-N3	BD1* P1-O3	1.27
BD3 Cr-N1	BD1* P1-O4	0.82
BD3 Cr-N1	BD1* P1-O15	0.75
BD2 Cr-N2	BD1* P1-O15	1.98
	Total	8.07 (avg 2.7/OMe)

Resonance form γ : Negative hyperconjugation among R groups

BD1 P1-O15	BD1* P1-O3	4.28
BD1 P1-O15	BD1* P1-O3	1.98
BD1 P1-O4	BD1* P1-O3	2.28
BD1 P1-O4	BD1* P1-O14	4.12
BD1 P1-O3	BD1* P1-O4	2.63
BD1 P1-O3	BD1* P1-O15	1.23
LP2 O15	BD1* P1-O3	1.31
LP2 O15	BD1* P1-O4	8.91
LP1 O15	BD1* P1-O3	6.46
LP1 O15	BD1* P1-O4	1.39
LP2 O4	BD1* P1-O3	13.61
LP1 O4	BD1* P1-O15	6.74
LP2 O3	BD1* P1-O15	6.79
LP2 O3	BD1* P1-O4	11.90
LP1 O3	BD1* P1-O15	2.43
LP1 O3	BD1* P1-O4	1.51
	Total	77.57 (avg 25.9/OMe)

Resonance form ϵ : Negative hyperconjugation from P-R to Cr

BD1 P1-O15	BD1* P1-Cr	1.21
BD1 P1-O3	BD1* P1-Cr	1.69
LP2 O15	BD1* P1-Cr	3.59
LP1 O15	BD1* P1-Cr	0.56
LP2 O4	BD1* P1-Cr	2.14
LP1 O4	BD1* P1-Cr	1.52
LP1 O3	BD1* P1-Cr	0.84
	Total	11.55



N1 = nitride, N2/3 = amides, C5/20 = Me C's, C9 = Ph carbon

Donor	Acceptor	E (kcal/mol)
π backbonding		
LP1 N1	BD1* P-C5	0.82
BD2 Cr-N2	BD1* P-C20	2.63
BD2 Cr-N3	BD1* P-C9	2.36
BD2 Cr-N1	BD1* P-C5	3.26
BD3 Cr-N1	BD1* P-C5	0.56
BD3 Cr-N1	BD1* P-C5	0.71
Total		10.3 (avg 3.4/C)

Resonance form γ: Negative hyperconjugation among R groups

BD1 P-C5	BD1* P-C9	1.04
BD1 P-C5	BD1* P-C20	1.24
BD1 P-C9	BD1* P-C5	1.46
BD1 P-C9	BD1* P-C20	1.28
BD1 P-C20	BD1* P-C9	0.91
BD1 P-C20	BD1* P-C5	1.17
BD2 C9-C10	BD1* P-C20	2.90
Total		10 (avg 3.3/C)

Resonance form ϵ : Negative hyperconjugation from P-R to Cr

BD1 P-C5	BD1* Cr-P	1.59
BD1 P-C9	BD1* Cr-P	1.23
BD1 P-C20	BD1* Cr-P	1.70
BD2 C9-C10	BD1* Cr-P	1.46
	Total	5.98



N6 = nitride, N5/7 = amide, N3/4/8 = P(NMe₂)₃ N's

Donor	Acceptor	E (kcal/mol)
π backbonding		
LP1 N6	BD1* P-N4	1.50
BD2 Cr-N5	BD1* P-N3	1.74
BD2 Cr-N6	BD1* P-N4	1.19
BD3 Cr-N6	BD1* P-N3	0.99
BD1 Cr-N7	BD1* P-N8	0.54
BD2 Cr-N7	BD1* P-N3	0.53
BD2 Cr-N7	BD1* P-N8	1.96
	Total	8.5 (avg 2.8/NMe₂)

Resonance form γ : Negative hyperconjugation among R groups

LP1 N3	BD1* P-N4	2.32
LP1 N3	BD1* P-N8	6.23
LP1 N4	BD1* P-N3	11.79
LP1 N4	BD1* P-N8	5.35
LP1 N8	BD1* P-N3	1.59
LP1 N8	BD1* P-N4	14.61
BD1 P-N3	BD1* P-N4	2.82
BD1 P-N3	BD1* P-N8	2.95
BD1 P-N4	BD1* P-N3	2.13
BD1 P-N4	BD1* P-N8	1.78
BD1 P-N8	BD1* P-N3	2.60
BD1 P-N8	BD1* P-N4	1.89
	Total	53.7 (avg 17.9/NMe₂)

Resonance form ϵ : Negative hyperconjugation from P-R to Cr

LP1 N3	BD1* Cr-P	4.64
LP1 N8	BD1* Cr-P	1.55
BD1 P-N3	BD1* Cr-P	0.97
BD1 P-N4	BD1* Cr-P	1.35
BD1 P-N8	BD1* Cr-P	0.93
	Total	9.44

We know in the LDP system ($\text{NCr}(\text{N}^i\text{Pr}_2)_2\text{PE}_3^+$) the Cr-NⁱPr₂ bonds are between double and single bonds in character.¹³ In light of this, we wanted to see how the second order perturbation theory interactions and their energies would change with an alternate bonding arrangement. The CHOOSE command was used to assign each of the $\text{NCr}(\text{NH}_2)_2\text{PE}_3^+$ complexes the following bonds and lone pairs:

CHOOSE 2

Cr-N1 triple bond

Cr-N2 single bond

Cr-N3 single bond

Cr-P single bond

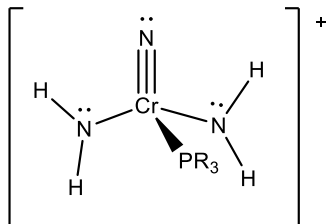


Figure 3.16 CHOOSE 2 geometry for NBO analysis.

Results from the “SECOND ORDER PERTURBATION THEORY ANALYSIS OF FOCK MATRIX IN NBO BASIS” are presented below for each PE₃ examined using this above bonding configuration. The type of interaction, Donor-acceptor, and reported E2 value (kcal/mol) are reported.

[NCr(NH₂)₂PMe₃]⁺ (**3a***)

N4 = nitride, N3/5 = amide, C6/10/14 = Me C's

Donor	Acceptor	E (kcal/mol)
π backbonding		
LP1 N3	BD1* P-C6	0.85
LP1 N4	BD1* P-C6	0.74
LP1 N5	BD1* P-C10	0.85
BD1 Cr-N3	BD1* P-C14	0.78
BD3 Cr-N4	BD1* P-C6	2.65
BD1 Cr-N5	BD1* P-C10	0.78
	Total	6.65 (2.2/Me)
Negative hyperconjugation among R groups		
BD1 P-C6	BD1* P-C10	1.31
BD1 P-C6	BD1* P-C14	1.31
BD1 P-C10	BD1* P-C6	1.33
BD1 P-C10	BD1* P-C14	1.27
BD1 P-C14	BD1* P-C6	1.33
BD1 P-C14	BD1* P-C10	1.27
	Total	7.82 (2.6/Me)

Negative hyperconjugation from P-R to Cr

BD1 P-C6	BD1* Cr-P	1.74
BD1 P-C10	BD1* Cr-P	1.64
BD1 P-C14	BD1* Cr-P	1.64
	Total	5.02



N13 = nitride, N12/14 = amide, O3/4/15 = OMe O's

Donor	Acceptor	E (kcal/mol)
π backbonding		
LP1 N12	BD1* P-O4	1.13
LP1 N13	BD1* P-O3	0.72
LP1 N14	BD1* P-O15	0.99
BD1 Cr-N12	BD1* P-O4	0.65
BD3 Cr-N13	BD1* P-O3	0.93
	Total	4.42 (1.5/OMe)

Negative hyperconjugation among R groups

LP1 O3	BD1* P-O4	1.51
LP1 O3	BD1* P-O15	2.43
LP2 O3	BD1* P-O4	11.90
LP2 O3	BD1* P-O15	6.79
LP1 O4	BD1* P-O15	6.74
LP2 O4	BD1* P-O3	13.61
LP1 O15	BD1* P-O3	6.46
LP1 O15	BD1* P-O4	1.39
LP2 O15	BD1* P-O3	1.31
LP2 O15	BD1* P-O4	8.91
BD1 P-O3	BD1* P-O4	2.63
BD1 P-O3	BD1* P-O15	1.23
BD1 P-O4	BD1* P-O3	2.28
BD1 P-O4	BD1* P-O15	4.12
BD1 P-O15	BD1* P-O3	4.28
BD1 P-O15	BD1* P-O4	1.98
	Total	77.57 (25.9/OMe)

Negative hyperconjugation from P-R to Cr

LP1 O3	BD1* Cr-P	0.93
LP1 O4	BD1* Cr-P	1.63
LP2 O4	BD1* Cr-P	2.39
LP2 O15	BD1* Cr-P	4.03
BD1 P-O3	BD1* Cr-P	1.92
BD1 P-O15	BD1* Cr-P	1.34
	Total	12.24



N6 = Nitride, N5/7 = amide, N3/4/8 = P(NMe₂)₃ N's

Donor	Acceptor	E (kcal/mol)
π backbonding		
BD3 Cr-N6	BD1* P-N4	1.17
LP1 N7	BD1* P-N8	1.55
LP1 N6	BD1* P-N4	1.50
LP1 N5	BD1* P-N3	1.38
	Total	5.6 (1.9/NMe₂)
Negative Hyperconjugation among R groups		
LP1 N3	BD1* P-N4	2.32
LP1 N3	BD1* P-N8	6.23
LP1 N4	BD1* P-N3	11.79
LP1 N4	BD1* P-N8	5.35
LP1 N8	BD1* P-N3	1.59
LP1 N8	BD1* P-N4	14.61
BD1 P-N3	BD1* P-N4	2.82
BD1 P-N3	BD1* P-N8	2.95
BD1 P-N4	BD1* P-N3	2.13
BD1 P-N4	BD1* P-N8	1.78
BD1 P-N8	BD1* P-N3	2.60
BD1 P-N8	BD1* P-N4	1.89
	Total	53.7 (avg 17.9/NMe₂)

Negative hyperconjugation from P-R to Cr

LP1 N3	BD1* Cr-P	5.61
LP1 N8	BD1* Cr-P	1.82
BD1 P-N3	BD1* Cr-P	1.19
BD1 P-N4	BD1* Cr-P	1.60
BD1 P-N8	BD1* Cr-P	1.10
	Total	11.32



N24 = nitride, N3/4 = amide, C5/20 = Me, C9 = Ph

Donor	Acceptor	E (kcal/mol)
π backbonding		
LP1 N3	BD1* P-C20	0.92
LP1 N4	BD1* P-C9	0.99
LP1 N24	BD1* P-C5	0.82
BD1 Cr-N3	BD1* P-C20	0.89
BD1 Cr-N4	BD1* P-C9	0.77
BD3 Cr-N24	BD1* P-C5	2.79
	Total	7.18 (2.4/C)
Negative hyperconjugation among R groups		
BD1 P-C5	BD1* P-C9	1.04
BD1 P-C5	BD1* P-C20	1.24
BD1 P-C9	BD1* P-C5	1.46
BD1 P-C9	BD1* P-C20	1.28
BD1 P-C20	BD1* P-C9	0.91
BD1 P-C20	BD1* P-C5	1.17
BD2 C9-C10	BD1* P-C20	2.90
	Total	10 (3.3/C)

Negative hyperconjugation from P-R to Cr

BD1 P-C5	BD1* Cr-P	1.75
BD1 P-C9	BD1* Cr-P	1.41
BD1 P-C20	BD1* Cr-P	1.84
BD2 C9-C10	BD1* Cr-P	1.74
	Total	6.74

Table 3.6 Summary of Second Order Perturbation Interactions

PR ₃	Interaction type	CHOOSE1 E2 (kcal/mol)	CHOOSE2 E2 (kcal/mol)
PMe ₃	π -backbonding	9.8 (3.3)	6.7 (2.2)
	β	38.1	27.21
	γ	7.8 (2.6)	
	ϵ	3.0	5.0
P(OMe) ₃	π -backbonding	8.1 (2.7)	4.4 (1.5)
	β	38.98	22.21
	γ	77.6 (25.9)	
	ϵ	11.5	12.2
P(NMe ₂) ₃	π -backbonding	8.5 (2.8)	5.6 (1.9)
	β	41.66	38.76
	γ	53.7 (17.9)	
	ϵ	9.4	11.3
PPhMe ₂	π -backbonding	10.3 (3.4)	7.2 (2.4)
	β	39.13	29.23
	γ	10.0 (3.3)	
	ϵ	6.0	6.7

Discussion of Natural Charges

The electronic competition created between the two amide ligands and the PE₃ ligand, for donation into Cr's vacant acceptor orbitals, should result in a fairly constant charge on Cr. This should result in very similar natural charges in Cr for all four of the NCr(NH₂)₂PE₃⁺ cations examined by NBO. In fact, this seems to be the case, as there are only very small differences in the natural charge assigned to Cr in the four different cations, with the largest difference being

only 0.046. Additionally, similar contributions of negative charge are located on the N ligands in each structure as well.

Generally, we know that the charge on Cr should remain relatively constant despite shifts in the electron densities between the metal and the ligands. Thus, it is most informative if we consider the $\text{NCr}(\text{NH}_2)_2^+$ fragment separate from the PE_3 fragment. Examining the molecule in this piecewise fashion, the charge distribution agrees with the bonding interactions suggested by NRT. In terms of total charge, there is more total positive charge on the $\text{NCr}(\text{NH}_2)_2^+$ fragment in the PMe_3 derivative, suggesting that PMe_3 is the least donating PE_3 . The amount of positive charge decreases in the order $\text{PMe}_3 > \text{P}(\text{OMe})_3 \sim \text{PPhMe}_2 > \text{P}(\text{NMe}_2)_3$. These results are summarized in the table below. Again, while the differences here are small in absolute terms, the trend agrees with the NRT calculations, with PMe_3 being the poorest donor to Cr.

Table 3.7 Total Charges on $\text{NCr}(\text{NH}_2)_2^+$ fragment and PE_3 .

PE_3	Charge on $\text{NCr}(\text{NH}_2)_2^+$	Charge on PE_3
PMe_3	0.38051	0.61949
$\text{P}(\text{OMe})_3$	0.33423	0.66577
$\text{P}(\text{NMe}_2)_3$	0.29951	0.70049
PPhMe_2	0.32444	0.67556

Potentially the largest absolute differences come from the charges localized on the P atoms. The natural charges are most informative when we compare the charge on P in the unbound ligands relative to the charge when the ligand is bound to the CrN_3 fragment. Similar changes are noted for $\text{P}(\text{OMe})_3$ and $\text{P}(\text{NMe}_2)_3$. The free phosphite has a charge of +1.504 localized on P, while the phosphite bound to Cr has a charge of +1.945; the $\text{P}(\text{NMe}_2)_3$ has a free charge of +1.312 on P, and a charge of +1.740 when bound to Cr. In both cases, the P has increased in positive charge by about 0.43. By comparison, the charge on P in free PMe_3 is +0.737, while the charge on the bound phosphine is +1.053. The difference with the P charge with PMe_3 is only about +0.316. At the

same time, the substituent atoms bound directly to P in all 3 cases have essentially the same charge when the ligand is bound or unbound (Δ 0.01-0.03 in total charge per E). This suggests that the increased positive shift in the natural charge on P in $\text{P}(\text{OMe})_3$ and $\text{P}(\text{NMe}_2)_3$ is related to the Cr–P interaction and is the result of greater donation (higher degree of oxidation) from P to Cr in these cases. The charge density analysis provided by NBO is in agreement with the suggested bonding interactions provided by the NRT calculations, however, the charge density doesn't give details about the nature of the orbitals or types of bonds that facilitate donation from each PE_3 to the metal center.

Discussion of Second Order Perturbation Theory Interactions

CHOOSE Bonding Arrangements

The second order perturbation theory (SOPT) list was analyzed after performing the NBO calculations with two different bonding arrangements. The first, which was the default chosen by the NBO program for 3 of the 4 input structures (CHOOSE1), displays a Cr–N triple bond with the nitride, Cr–N double bonds with both amide groups, and a Cr–P single bond. In this arrangement, the maximum potential for classical π -backbonding will be reached, as this places the most filled π -bonding orbitals in proximity to the P–E σ^* orbitals.

Because we know from experiments using $\text{NCr}(\text{N}^i\text{Pr}_2)_2\text{PE}_3^+$ that the Cr–N amide bonds are most accurately described with a bond order between 1 and 2,¹³ we show the same NBO results for a different bonding arrangement. In CHOOSE2, the model cation has a Cr–N triple bond with the nitride and a Cr–P single bond; however, the two Cr–N bonds to the amide ligands were specified as single bonds, which results in a lone pair on each amide nitrogen.

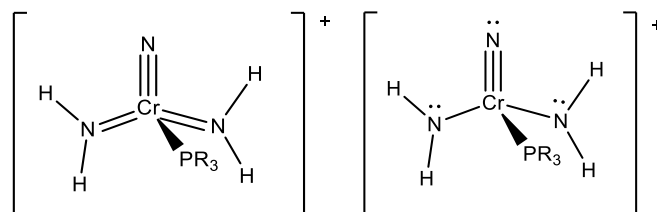


Figure 3.17 (left) CHOOSSE1; (right) CHOOSSE2

Comparing the SOPT analysis between the two different structural arrangements is quite informative. First, pushing the π -bonding electrons in the Cr–N double bonds with the amides, out on the amide nitrogens decreases the amount of π -backbonding in each structure to ~ 2 kcal/mol per P–E σ^* . At the same time, other interactions which donate electron density to Cr are increased (i.e. more participation of ϵ). This exercise has thus provided a nice electronic check on the system as it is interpreted by NBO. In these types of $\text{NCr}(\text{NR}_2)_2\text{X}$ systems, a decrease in electronic donation from the X ligand results in an increase in donation from the amides; conversely, an increase in the electronic donation from X results in a decrease in donation from the amide ligands. This push-and-pull or electronic competition is directly observable in these forced bond changes of the initial NBO structure. Overall these results agree very well with the previous MO calculations done with the $\text{NCr}(\text{NR}_2)_2\text{X}$ system, as well as chemical intuition.¹

A Comparison of SOPT and NRT Results

Perhaps most important in terms of the second order perturbation theory results, is the fact that the predominant interactions from the NRT results are readily recognized in the SOPT interactions. Interactions which correlate with resonance forms β , γ , and ϵ were found to participate to different amounts for each cation.

In the SOPT list, the starting structure has a Cr–P single bond. The stabilization energies found for the Cr–P σ to σ^* interaction in all the PE_3 ligands in CHOOSSE1 are close to 40 kcal/mol. Upon switching to CHOOSSE2, there is a common trend in these stabilization energies, as they all

decrease going to the less electronically saturated Cr. This means that as electron donation from the amides is removed, the contribution of the Cr–P σ to σ^* donation is decreased, resulting in an increased bond order between Cr and P.

The γ interactions remain unchanged between CHOOSE1 and CHOOSE2, supporting the fact that these delocalizations are primarily ligand based and dependent on the properties of the R group on PR_3 . The magnitudes of these energies are much smaller (order of magnitude) in the PMe_3 and PPhMe_2 compared to the P(OMe)_3 and $\text{P(NMe}_2)_3$ cases. For P(OMe)_3 and $\text{P(NMe}_2)_3$, the total stabilization energy from these interactions is quite substantial, calculated to be 77 and 54 kcal/mol, respectively. Considered per P-R interaction, these energies are still quite large, at 26 and 17 kcal/mol. These large energies arise from a well-established electronic behavior associated with heteroatom substituted phosphine ligands; these values serve as a comparative tool to evaluate the magnitude of the stabilization energies of other interactions.

Aside from the large “ β ” and “ γ ” contributions, the “ ϵ ” interaction was also found to participate in each of the 4 structures. This contribution is the largest for P(OMe)_3 and $\text{P(NMe}_2)_3$, in the range of 10-12 kcal/mol. In both cases, the stabilization energy of this interaction increases in CHOOSE2 compared to CHOOSE1. This trend reflects the need to increase donation from the PR_3 ligand to compensate for the reduced donation from the amide l.p.’s. The contribution from ϵ is about half as large in PPhMe_2 (≈ 6 kcal/mol) as it is in P(OMe)_3 and $\text{P(NMe}_2)_3$ and is only 3 kcal/mol with PMe_3 in CHOOSE1. Again, with both phosphines, the contribution of ϵ increases in CHOOSE2, thus the overall trend is the same among the series. The same delocalizations of electron density, whether via donor acceptor interactions in the second order perturbation list, or with formal resonance forms in the NRT calculations, are readily observed with both methods.

In addition to the resonance forms found in NRT, we also examined the SOPT list for ϕ interactions—classical π -backbonding. NRT does not show any evidence of ϕ from the CrN_3 fragment to the PE_3 ligand. However, these interactions are observed in the SOPT list, with smaller energies than those observed for any of the other interactions (1-3 kcal/mol). It is interesting to note that the magnitude of the ϕ interaction decreases in the order $\text{PPhMe}_2 > \text{PMe}_3 > \text{P(OMe)}_3 > \text{P(NMe}_2)_3$. This is somewhat counterintuitive when considering the electronegativities of the R groups bound to P, but perhaps is a reflection of the error in the calculations rather than a real trend. Overall, it seems that these interactions are small, potentially contributing very little to the overall electronic structure of the molecule.

The point raised above regarding the magnitude of the stabilization energies for the ϕ resonance form raises another valid point, which is: how much does each of these interactions matter to the overall electronic structure in these cations? The NRT calculations give weighted % values indicating the piecewise contribution of each resonance form, while the SOPT list gives stabilization energies that correlate to the amount of delocalizations.

β and γ interactions appear substantial for both starting structures by SOPT. There is one discrepancy in these forms, and it comes from the magnitude of the β interaction in the $\text{P(NMe}_2)_3$ case. The stabilization energy in CHOOSE2 is still rather large (> 38 kcal/mol), in contrast to the low percentage that NRT gives for this same delocalization (3%). The trends observed for the other three phosphines agree between both methods, so it seems that generally, β contributes less to the overall electronic structure when other delocalizations are available to participate. Absolute quantification from these methods, however, seems unwise.

It seems that the ε stabilization energies observed by NBO are far more substantial than π -backbonding for P(OMe)_3 and $\text{P(NMe}_2)_3$ (10-12 vs 1-2 kcal/mol respectively). If we compare both

ϕ and ε to the stabilization energy of γ , for example, the values for ϕ interactions are about 10% of γ while the values for ε are closer to 50% of γ in both $\text{P}(\text{OMe})_3$ and $\text{P}(\text{NMe}_2)_3$. Based on this comparison, it seems that SOPT suggests a greater contribution from ε in these molecules than γ . Perhaps like the conclusions drawn about the contribution of β , above, absolute quantification of the contribution of ε is not prudent. But rather, we can conclude that this form of delocalization (ε) is generally observed in both methods, and to a degree that seems significant to the electronic structure.

Modeling Approach

General Considerations

Modeling the discrete components contributing to the $\sim\Delta\text{H}^\ddagger$ value as a holistic stereoelectronic parameter follows the general form (Eq. 3.3):

$$LDP = a + b(x_1) + c(x_2) + \dots + m_n(x_i) \quad (\text{Eq. 3.3})$$

The $\sim\Delta\text{H}^\ddagger$ value is broken into a constant value, a , and a series of terms x_1 through x_i , each representing unique stereoelectronic properties of the ligand. These properties are weighted by coefficients (b - m_n) to scale relative importance of each property in determining the overall $\sim\Delta\text{H}^\ddagger$ value.

The $\sim\Delta\text{H}^\ddagger$ values were determined experimentally. However, in order to fully solve the equation, we then need a series of stereoelectronic parameters, to take the place of x_1 - x_i in the equation. Available in the literature are a wide variety of descriptors of the steric and electronic properties of phosphines. In terms of electronics, these properties include Tolman Electronic Parameter (χ), pK_a , IE, σ -donor ability, π -acidity, etc.³⁻¹¹ In terms of sterics, descriptors like cone angle (θ), percent buried volume ($\%V_{\text{bur}}$), or the solid G angles are adequate descriptors of ligand

size. By examining combinations of these descriptors, summing to the $\sim\Delta H^\ddagger$ term, we can start building the model for $\sim\Delta H^\ddagger$ (Table 3.8).

Table 3.8 Sample variety of literature parameters available for stereoelectronic description of phosphine series under study.³⁻¹¹

Phosphine	χ^{FT}	pK _a	E°	V _{min}	PA (kJ/mol)	χ_d	TCA	E _{ar}	π_a	% Vbur ^a
PMe ₃	8.55	8.55	-0.3593	-43.02	945	8.55	118	0	0	22.6
P(ⁿ Bu) ₃	5.25	8.43	-0.3994	-43.71	–	5.25	136	0	0	25.8
P(ⁱ Bu) ₃	5.7	7.97	-0.3939	-44.8	–	5.7	143	0	0	28.6
P(^t Pr) ₃	3.45	–	-0.4406	-44.47	–	3.45	162	0	0	28.7
PCy ₃	1.4	9.7	-0.4597	-44.99	1018	1.4	170	0	0	32.4
PPhMe ₂	10.6	6.5	-0.317	-40.41	961	10.5	122	1	0	23.7
PPh ₂ Me	12.1	4.56	-0.2674	-36.76	964	12.6	130	2.2	0	25.5
PPhEt ₂	9.3	6.25	-0.3426	-40.76	–	8.6	136	1.1	0	25.3
PPh ₂ Et	11.3	4.9	–	–	–	11.1	140	2.3	0	25.6
PPh ₂ ⁿ Bu	11.1	5	–	–	–	11.3	142	2.1	0	25.2
PPh ₂ Cy	–	5.05	–	–	–	9.1	153	1.6	0	26.9
PPhCy ₂	–	–	–	–	–	5.7	162	1.6	0	28.0
P(OEt) ₃	20.9	3.35	-0.1551	-27.85	924 ^b	15.7	109	1.1	2.9	23.4
P(O ⁱ Pr) ₃	19.05	4	–	–	–	13.4	130	1.3	2.9	25.7
P(NC ₄ H ₈) ₃	–	–	–	–	1015 ^c	-1.2	146	-0.6	0.9	28.1

^aTaken with the standard 3.5 Å radius from the metal center, including hydrogens. ^bP(OMe)₃ treated as electronic surrogate. ^cP(NMe₂)₃ treated as electronic surrogate

In the equation shown above, the coefficients can then be solved for by applying a least-squares fit to the chosen series of parameters for x_i and the measured $\sim\Delta H^\ddagger$ values for the series of phosphines. With the least squares fit giving real number values to the weighting coefficients, we can rationalize, based on the properties with which each parameter correlates, whether the effect rendered on $\sim\Delta H^\ddagger$ makes chemical sense.

Goodness of fit with a given set of parameters can generally be determined by looking at three different metrics:

- 1) Electronic profile
- 2) Steric profile
- 3) Model predicted LDP value

The “profiles” are essentially the component contribution to LDP. The profile for the electronic parameter is demonstrated in the following equation:

$$b(\chi) = LDP - a - c(x_2) - \dots - m_n(x_i) \quad (\text{Eq. 3.4})$$

Plotting the contribution of the electronic term ($b(\chi)$) versus the electronic parameter (χ) should then show very strong correlation if the fit is a good descriptor, with the slope of the line equal to the weighting parameter, b . Any fitting parameter can be examined in this manner. Provided the profiles demonstrate good correlation, the model should be able to predict the $\sim\Delta H^\ddagger$ value based on the coefficients and the stereoelectronic parameters (x_{1-x_i}) utilized. Plotting the $\sim\Delta H^\ddagger$ values calculated by solving the full equation (Eq. 3.3) against the experimentally measured $\sim\Delta H^\ddagger$ values will ideally give a plot with intercept of zero and a slope of one. Evaluating our model by examination of the steric, electronic, and model-predicted $\sim\Delta H^\ddagger$ allows for quantitative determination of the accuracy of the parameter system selected in modeling the $\sim\Delta H^\ddagger$.¹²

Parameter Selection

As mentioned above, there is an abundance of literature parameters that serve as both electronic and steric descriptors of the phosphine ligands. With such a large selection available, it can be a challenge to select parameters and incorporate them into a model for phosphine behavior. Selection of the best electronic donation parameter was based the trialkylphosphines examined in the system. It is generally assumed that trialkylphosphines are the simplest phosphines electronically and should provide the simplest interaction with the $\text{NCr}(\text{N}^i\text{Pr}_2)_2$ -cation. Good agreement with the trialkyls *should* at least correlate to good representation of the σ -donor ability. Steric parameters were evaluated similarly, by examining the trialkylphosphines for the best correlation with each steric descriptor available.

As an illustration of how important the starting stereoelectronic parameters are, Fig. 3.18 shows the differences between two of the steric parameters considered for the series of phosphines (**3a-3o**). In this case, poor correlation is noted between %V_{bur} and TCA. Again, this illustrates that careful parameter selection is needed to get appropriate representation of the ligands in our system. Based on this method, the best descriptors of a simple electronic term (σ -donor descriptor) and sterics were the χ_d value from the QALE system and cone angle ($\theta/^\circ$), respectively.

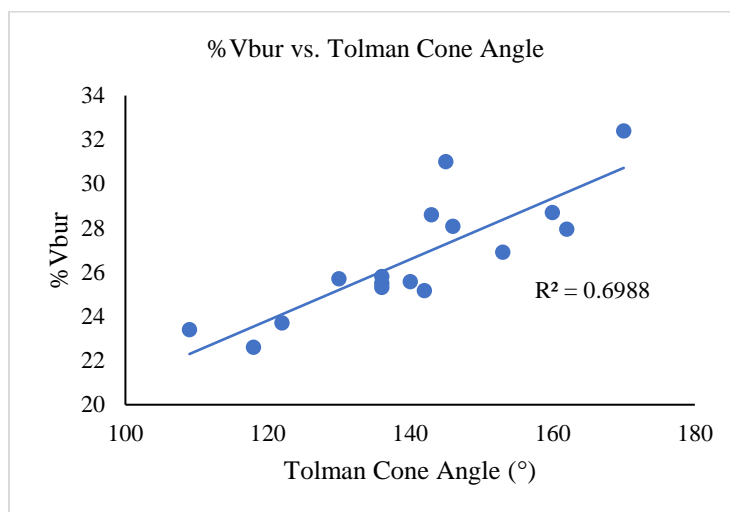


Figure 3.18 Correlation of %V_{bur} vs. Tolman Cone Angle for all phosphines used in model building (**3a-o**).

Model Building

Unfortunately, due to entropic and ion pairing complications with the variety of solvent/anion combinations examined with the salts **3a-o**, a full stereoelectronic model, which compiles the wide variety of phosphine complexes synthesized, wasn't possible. The 5 trialkylphosphines **3a-e**, however, were examined under the assumption that their similar polarity R groups would interact in a similar manner with solvents, and these compounds would have a similar entropic contribution. A stereoelectronic fit accounting for σ -donor ability and size, was performed using a least squares fit, following the shortened form of the general equation (Eq. 3.3) in Eq. 3.5.

$$LDP = a + b(\chi_d) + c(\theta) \quad (\text{Eq. 3.5})$$

Here, the term χ_d is the σ -donation term derived from the QALE system of phosphine parameterization. It is scaled similar to Tolman's Electronic Parameter, with smaller values of χ_d indicating better donors. The steric term, θ , is the Tolman Cone Angle. These parameters provide excellent correlation with the LDP system, with the solved values for the weighting parameters shown in Eq. 3.6.

$$LDP = 11.98 + 0.135(\chi_d) + 0.030(\theta) \quad (\text{Eq. 3.6})$$

In addition to the high R^2 values observed below in the steric and electronic profiles for this fit of **3a-e**, these plots also demonstrate good correlation through the intercepts, each close to zero, and the slopes of each profile matching closely to the fitted coefficients c and b respectively.

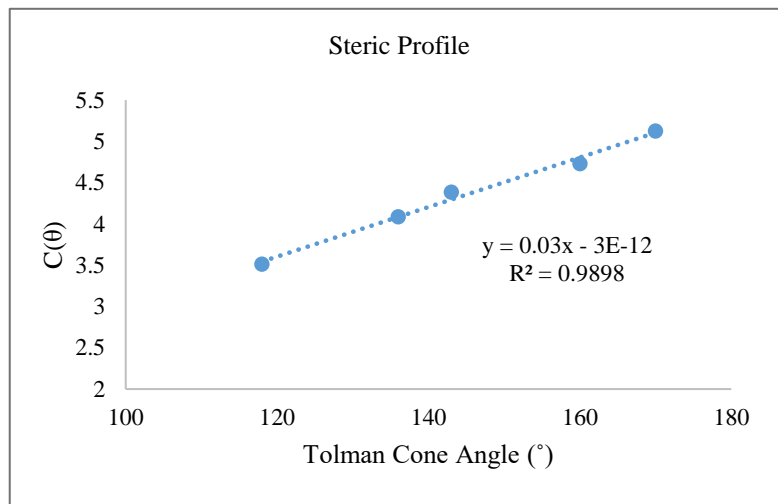


Figure 3.19 Steric profile from fit of trialkylphosphines (**3a-e**) using 2-parameter fit, Eq. 3.6.

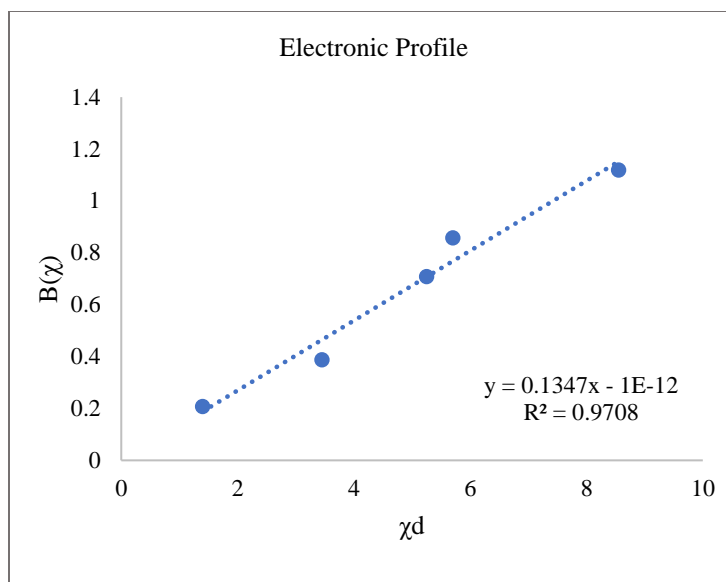


Figure 3.20 Electronic profile from fit of trialkylphosphines (**3a-e**) using 2-parameter fit, Eq. 3.5.

The application of the trialkylphosphine-derived 2-parameter model (Eq. 3.5) to the entire series of phosphines shows significant deviation in both the steric and electronic profiles (Fig. 3.21 and 3.22). Primarily, this demonstrates that more than a size parameter and σ -donor ability must be considered when describing the donation of more diverse phosphines to a high valent metal. In the Cr(VI) system here, these deviations with more complex aryl and heteroatom substituents on phosphorous could be due to genuine electronic effects such as π -interactions, or these could also be manifestations of entropic differences when looking at $\sim\Delta H^\ddagger$ in the unpaired regime (CD_3CN with $\text{X}^- = \text{SbF}_6^-$). Consequently, expansion of the model to include more diverse stereoelectronic parameters of these phosphines is not a reliable method of determining interactions with the metal distinct from solvent effects.

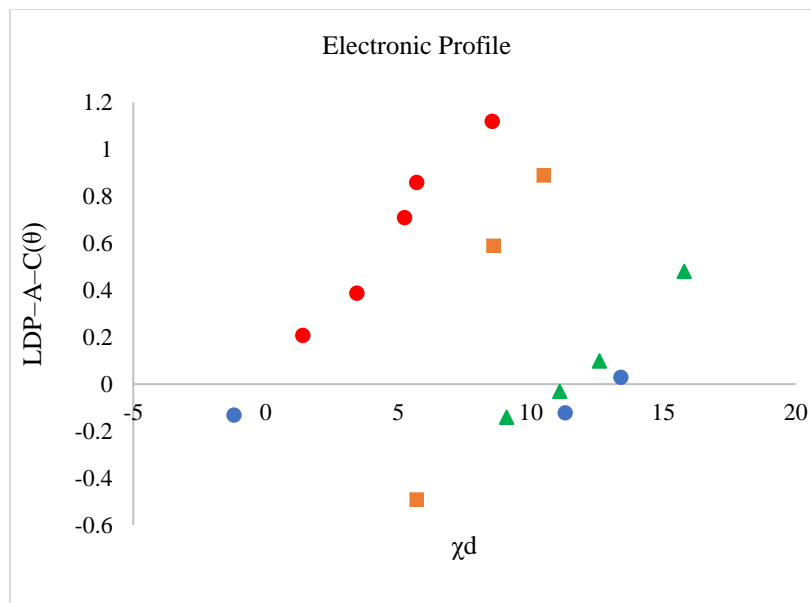


Figure 3.21 Trialkylphosphine 2-parameter fit applied to total series: Electronic profile. (Orange squares = PR₂Ph; Green triangles = PPh₂R, Red circles = PR₃, Blue circles = P(OR)₃/P(NR₂)₃.)

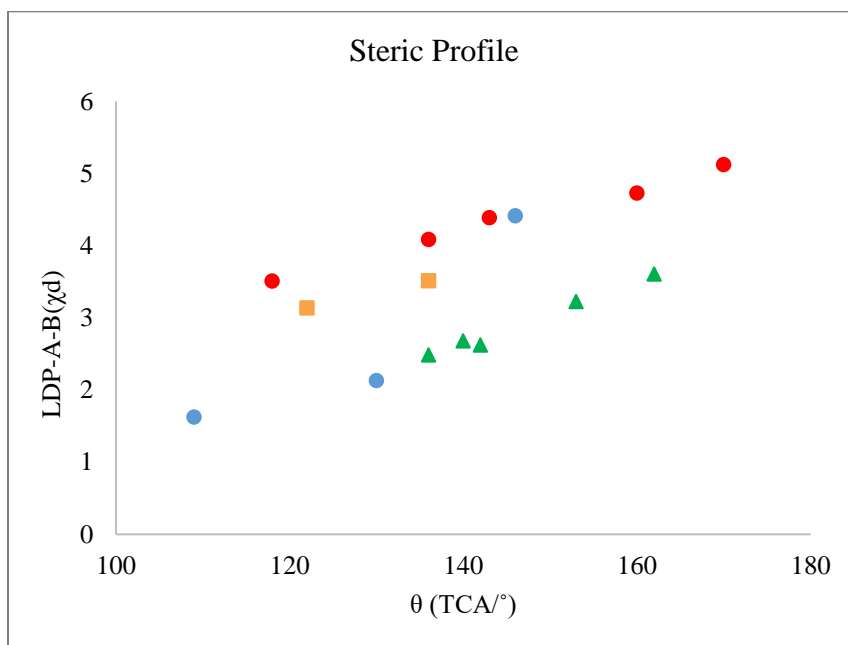


Figure 3.22 Trialkylphosphine 2-parameter fit applied to total series: Steric profile. (Orange squares = PR₂Ph; Green triangles = PPh₂R, Red circles = PR₃, Blue circles = P(OR)₃/P(NR₂)₃.)

Synthetic considerations

All manipulations were performed in an MBraun glovebox under N₂ atmosphere. NCr(NⁱPr₂)₂I was prepared according to literature procedures.⁴³ TIBArF₂₄ was prepared according to literature procedures.⁴⁴ The triethylphosphine oxide was purchased from Alfa Aesar and used as received. The solvents DCM and Et₂O were dried by passage over activated alumina and sparged with N₂ prior to use. The NMR solvent CDCl₃ as well as the DCE used to record the Gutmann parameter measurement were dried over P₂O₅ and distilled under N₂ prior to use.

Synthesis of [NCr(NⁱPr₂)₂(OP(Et)₃)] [BArF₂₄]: A scintillation vial was charged with 50 mg of NCr(NⁱPr₂)₂I (0.127 mmol, 1 equiv), 3 mL DCM, a stir bar, and 17 mg OP(Et)₃ (0.127 mmol, 1 equiv). The solution was stirred at room temperature and to it was added 135 mg TIBArF₂₄ (0.127 mmol, 1 equiv), as a solution in 2 mL DCM. The dark brown-orange solution rapidly turned bright orange and precipitated a yellow solid. The mixture was stirred 4 h at room temperature. The precipitate was removed by filtration over Celite and the filtrate was dried under reduced pressure. The precipitate was dissolved in a minimum amount of DMC, filtered over Celite, and layered with n-pentane. The layered solution was stored at -35 °C overnight to yield small, twinned (and disordered) crystals of [NCr(NⁱPr₂)₂(OP(Et)₃)] [BArF₂₄] (115 mg, 72%). ¹H NMR (500 MHz, Chloroform-*d*): 7.77–7.67 (m, 9H), 7.54 (s, 4H), 5.09 (sept, *J* = 6.5 Hz, 2H), 3.89 (sept, *J* = 6.3 Hz, 2H), 2.00–1.80 (m, 12H), 1.44 (d, *J* = 6.3 Hz, 6H), 1.15 (dd, *J* = 6.5, 1.5 Hz, 12H), 1.14–1.03 (m, 9H). ¹³C NMR (126 MHz, Chloroform-*d*) 163.70–160.02 (m), 134.74, 128.92 (d, *J* = 30.1 Hz), 125.57, 123.40, 117.47, 59.68, 58.20, 30.43 (d, *J* = 39.4 Hz), 21.50, 21.00, 17.86, 17.35, 4.82 (d, *J* = 5.0 Hz). ³¹P NMR (202 MHz, Chloroform-*d*) 86.15. ¹⁹F NMR (470 MHz, Chloroform-*d*) -62.42.

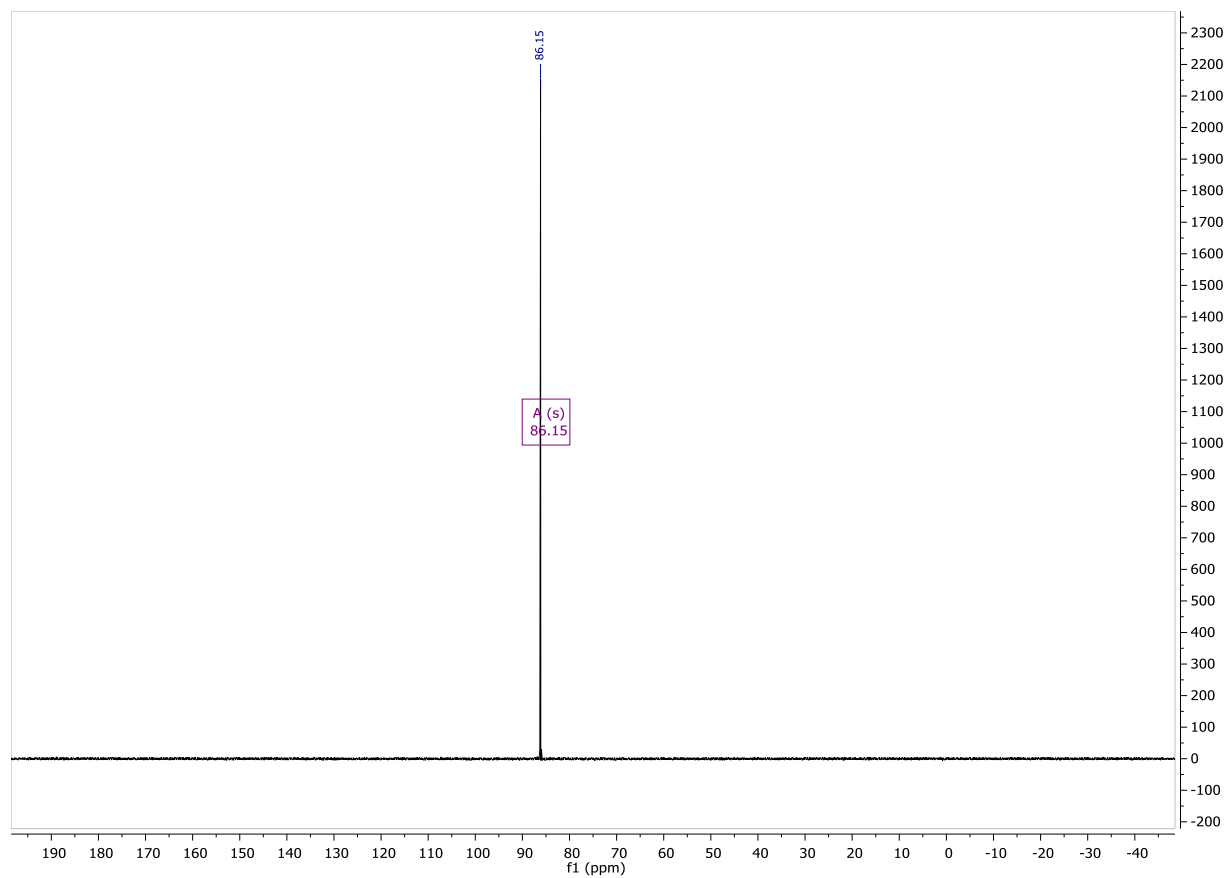


Figure 3.24 ^{31}P NMR of $[\text{NCr}(\text{N}^i\text{Pr}_2)_2(\text{OP}(\text{Et})_3)][\text{BArF}_{24}]$ in CDCl_3 .

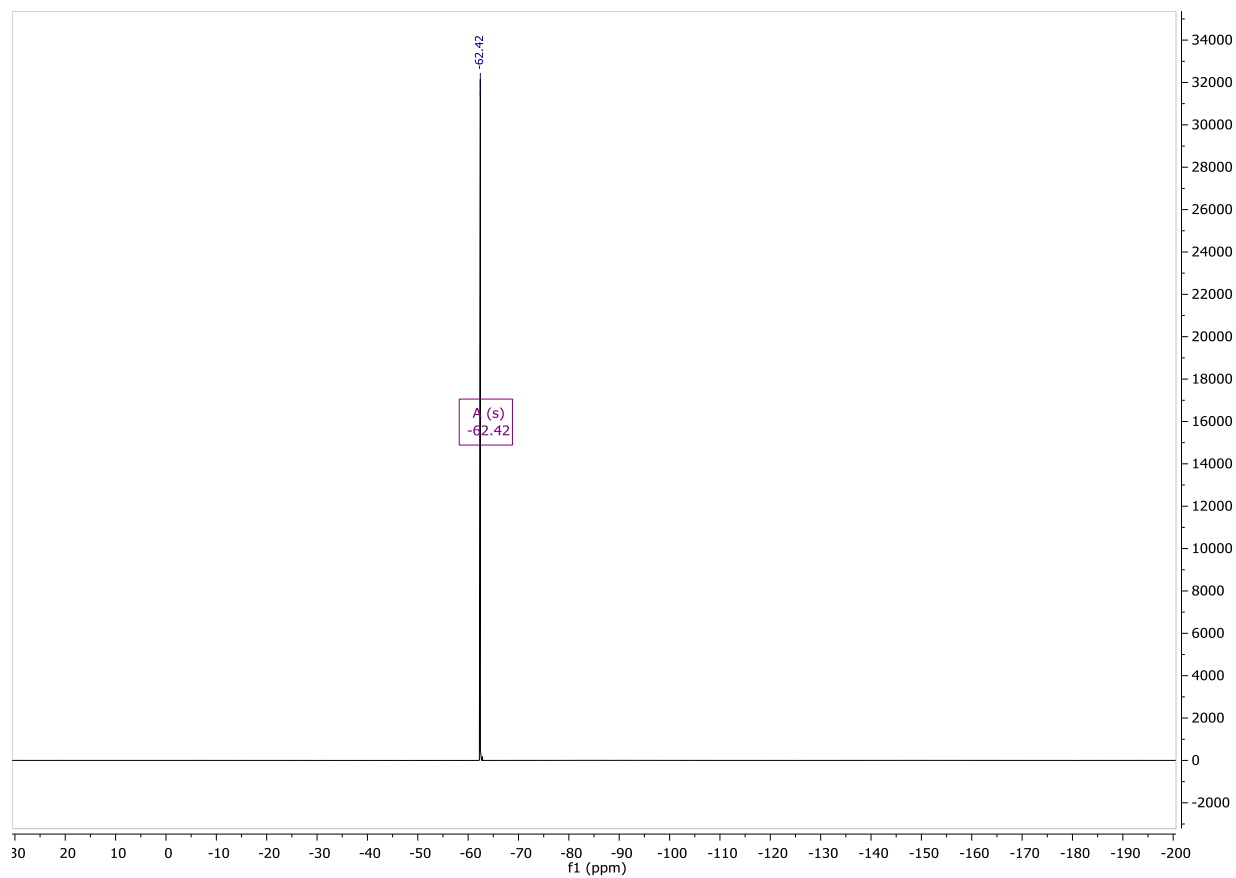


Figure 3.25 ^{19}F NMR of $[\text{NCr}(\text{N}^i\text{Pr}_2)_2(\text{OP}(\text{Et})_3)][\text{BArF}_{24}]$ in CDCl_3 .

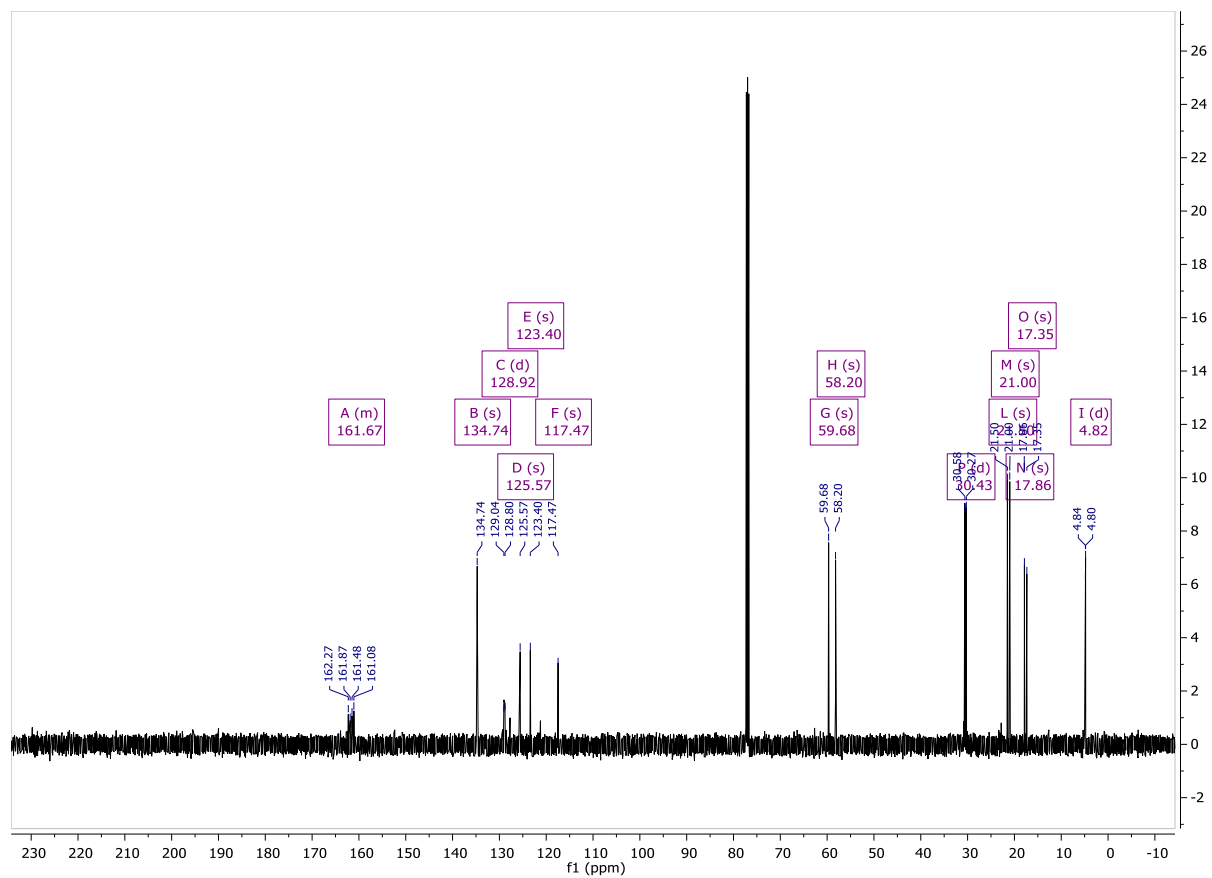


Figure 3.26 ^{13}C NMR of $[\text{NCr}(\text{N}^i\text{Pr}_2)_2(\text{OP}(\text{Et})_3)][\text{BArF}_{24}]$ in CDCl_3 .

REFERENCES

REFERENCES

- (1) DiFranco, S. A.; Maciulis, N. A.; Staples, R. J.; Batrice, R. J.; Odom, A. L., Evaluation of donor and steric properties of anionic ligands on high valent transition metals. *Inorganic chemistry* **2012**, *51* (2), 1187-200.
- (2) Billow, B. S.; McDaniel, T. J.; Odom, A. L., Quantifying ligand effects in high-oxidation-state metal catalysis. *Nature Chemistry* **2017**, *9*, 837.
- (3) Fernandez, A. L.; Reyes, C.; Prock, A.; Giering, W. P., The stereoelectronic parameters of phosphites. The quantitative analysis of ligand effects (QALE). *Journal of the Chemical Society-Perkin Transactions 2* **2000**, *5*, 1033-1041.
- (4) Tolman, C. A., Electron donor-acceptor properties of phosphorus ligands. Substituent additivity. *Journal of the American Chemical Society* **1970**, *92* (10), 2953-2956.
- (5) Tolman, C. A., Steric effects of phosphorus ligands in organometallic chemistry and homogeneous catalysis. *Chemical Reviews* **1977**, *77* (3), 313-348.
- (6) Tolman, C. A., Phosphorus ligand exchange equilibriums on zerovalent nickel. Dominant role for steric effects. *Journal of the American Chemical Society* **1970**, *92* (10), 2956-2965.
- (7) Bartik, T.; Himmler, T.; Schulte, H. G.; Seevogel, K., Substituenteneinflüsse auf die basizität von phosphorliganden in R₃P-Ni(CO)₃-komplexen. *Journal of Organometallic Chemistry* **1984**, *272* (1), 29-41.
- (8) Kalescky, R.; Kraka, E.; Cremer, D., New Approach to Tolman's Electronic Parameter Based on Local Vibrational Modes. *Inorganic chemistry* **2014**, *53* (1), 478-495.
- (9) Dias, P. B.; de Piedade, M. E. M.; Simões, J. A. M., Bonding and energetics of phosphorus (III) ligands in transition metal complexes. *Coordination Chemistry Reviews* **1994**, *135-136* (0), 737-807.
- (10) Drago, R. S., .DELTA.E-.DELTA.C Analysis of Phosphine Basicity. *Organometallics* **1995**, *14* (7), 3408-3417.
- (11) Vogel, G. C.; Drago, R. S., The ECW Model. *Journal of Chemical Education* **1996**, *73* (8), 701.
- (12) Golovin, M. N.; Rahman, M.; Belmonte, J. E.; Giering, W. P., QUANTITATIVE SEPARATION OF SIGMA-COMPONENTS AND PI-COMPONENTS OF TRANSITION-METAL PHOSPHORUS BONDING AND THE APPLICATION OF LIGAND EFFECTS IN ORGANOMETALLIC CHEMISTRY. *Organometallics* **1985**, *4* (11), 1981-1991.

- (13) Rahman, M. M.; Liu, H. Y.; Prock, A.; Giering, W. P., Quantitative analysis of ligand effects. 2. Steric and electronic factors influencing transition-metal-phosphorus(III) bonding. *Organometallics* **1987**, *6* (3), 650-658.
- (14) Rahman, M. M.; Liu, H. Y.; Eriks, K.; Prock, A.; Giering, W. P., Quantitative analysis of ligand effects. Part 3. Separation of phosphorus(III) ligands into pure σ -donors and σ -donor/ π -acceptors. Comparison of basicity and σ -donicity. *Organometallics* **1989**, *8* (1), 1-7.
- (15) Wilson, M. R.; Woska, D. C.; Prock, A.; Giering, W. P., THE QUANTITATIVE-ANALYSIS OF LIGAND EFFECTS (QALE) - THE ARYL EFFECT. *Organometallics* **1993**, *12* (5), 1742-1752.
- (16) Poe, A. J., The tuning of P-donor ligands: the aryl and other pendent group effects (PGEs) revisited. *Dalton transactions* **2009**, (11), 1999-2003.
- (17) Fernandez, A. L.; Reyes, C.; Prock, A.; Giering, W. P., The stereoelectronic parameters of phosphites. The quantitative analysis of ligand effects (QALE). *J. Chem. Soc., Perkin Trans. 2.* **2000**, (5), 1033-1041.
- (18) Allman, T.; Goel, R. G., The basicity of phosphines. *Canadian Journal of Chemistry* **1982**, *60* (6), 716-722.
- (19) Ardizzoia, G. A.; Brenna, S., Interpretation of Tolman electronic parameters in the light of natural orbitals for chemical valence. *PCCP* **2017**, *19* (8), 5971-5978.
- (20) Köhl, O., Predicting the net donating ability of phosphines—do we need sophisticated theoretical methods? *Coordination Chemistry Reviews* **2005**, *249* (5–6), 693-704.
- (21) Leyssens, T.; Peeters, D.; Orpen, A. G.; Harvey, J. N., Insight into metal-phosphorus bonding from analysis of the electronic structure of redox pairs of metal-phosphine complexes. *New Journal of Chemistry* **2005**, *29* (11), 1424-1430.
- (22) Wu, K.; Doyle, A. G., Parameterization of phosphine ligands demonstrates enhancement of nickel catalysis via remote steric effects. *Nature Chemistry* **2017**, *9*, 779.
- (23) Fernandez, A.; Reyes, C.; YingLee, T.; Prock, A.; Giering, W. P.; Haar, C. M.; Nolan, S. P., Assessing the stereoelectronic properties of pyrrolyl phosphines and related ligands. The quantitative analysis of ligand effects (QALE). *J. Chem. Soc., Perkin Trans. 2.* **2000**, (7), 1349-1357.
- (24) Mitoraj, M. P.; Michalak, A., σ -Donor and π -Acceptor Properties of Phosphorus Ligands: An Insight from the Natural Orbitals for Chemical Valence. *Inorganic chemistry* **2010**, *49* (2), 578-582.
- (25) Leyssens, T.; Peeters, D.; Orpen, A. G.; Harvey, J. N., How Important Is Metal–Ligand Back-Bonding toward YX₃ Ligands (Y = N, P, C, Si)? An NBO Analysis. *Organometallics* **2007**, *26* (10), 2637-2645.

- (26) Parkin, G., Valence, Oxidation Number, and Formal Charge: Three Related but Fundamentally Different Concepts. *Journal of Chemical Education* **2006**, 83 (5), 791.
- (27) Orpen, A. G.; Connelly, N. G., Structural systematics: the role of P-A σ^* orbitals in metal-phosphorus π -bonding in redox-related pairs of M-PA₃ complexes (A = R, Ar, OR; R = alkyl). *Organometallics* **1990**, 9 (4), 1206-1210.
- (28) Orpen, A. G.; Connelly, N. G., Structural evidence for the participation of P-X σ^* orbitals in metal-PX₃ bonding. *Journal of the Chemical Society, Chemical Communications* **1985**, (19), 1310-1311.
- (29) Fey, N.; Orpen, A. G.; Harvey, J. N., Building ligand knowledge bases for organometallic chemistry: Computational description of phosphorus(III)-donor ligands and the metal-phosphorus bond. *Coordination Chemistry Reviews* **2009**, 253 (5), 704-722.
- (30) Pacchioni, G.; Bagus, P. S., Metal-phosphine bonding revisited. σ -Basicity, π -acidity, and the role of phosphorus d orbitals in zerovalent metal-phosphine complexes. *Inorganic chemistry* **1992**, 31 (21), 4391-4398.
- (31) Kobayashi, S.; Manabe, K., Development of Novel Lewis Acid Catalysts for Selective Organic Reactions in Aqueous Media. *Accounts of Chemical Research* **2002**, 35 (4), 209-217.
- (32) Houk, K. N.; Strozier, R. W., Lewis acid catalysis of Diels-Alder reactions. *Journal of the American Chemical Society* **1973**, 95 (12), 4094-4096.
- (33) Jung, M. E.; Chang, J. J., Enantiospecific Formal Total Synthesis of (+)-Fawcettimine. *Organic Letters* **2010**, 12 (13), 2962-2965.
- (34) Mayer, U.; Gutmann, V.; Gerger, W. J. M. f. C. C. M., The acceptor number — A quantitative empirical parameter for the electrophilic properties of solvents. **1975**, 106 (6), 1235-1257.
- (35) Gutmann, V.; Steininger, A.; Wychera, E. J. M. f. C. u. v. T. a. W., Donorstärken in 1,2-Dichloräthan. **1966**, 97 (2), 460-467.
- (36) Beckett, M. A.; Strickland, G. C.; Holland, J. R.; Sukumar Varma, K., A convenient n.m.r. method for the measurement of Lewis acidity at boron centres: correlation of reaction rates of Lewis acid initiated epoxide polymerizations with Lewis acidity. *Polymer* **1996**, 37 (20), 4629-4631.
- (37) Beckett, M. A.; Brassington, D. S.; Coles, S. J.; Hursthouse, M. B., Lewis acidity of tris(pentafluorophenyl)borane: crystal and molecular structure of B(C₆F₅)₃-OPe_t₃. *Inorganic Chemistry Communications* **2000**, 3 (10), 530-533.
- (38) Sivaev, I. B.; Bregadze, V. I., Lewis acidity of boron compounds. *Coordination Chemistry Reviews* **2014**, 270-271, 75-88.

- (39) Frisch, M. J.; Trucks, G. W.; Schlegel, H. B.; Scuseria, G. E.; Robb, M. A.; Cheeseman, J. R.; Scalmani, G.; Barone, V.; Mennucci, B.; Petersson, G. A.; Nakatsuji, H.; Caricato, M.; Li, X.; Hratchian, H. P.; Izmaylov, A. F.; Bloino, J.; Zheng, G.; Sonnenberg, J. L.; Hada, M.; Ehara, M.; Toyota, K.; Fukuda, R.; Hasegawa, J.; Ishida, M.; Nakajima, T.; Honda, Y.; Kitao, O.; Nakai, H.; Vreven, T.; Montgomery Jr., J. A.; Peralta, J. E.; Ogliaro, F.; Bearpark, M. J.; Heyd, J.; Brothers, E. N.; Kudin, K. N.; Staroverov, V. N.; Kobayashi, R.; Normand, J.; Raghavachari, K.; Rendell, A. P.; Burant, J. C.; Iyengar, S. S.; Tomasi, J.; Cossi, M.; Rega, N.; Millam, N. J.; Klene, M.; Knox, J. E.; Cross, J. B.; Bakken, V.; Adamo, C.; Jaramillo, J.; Gomperts, R.; Stratmann, R. E.; Yazyev, O.; Austin, A. J.; Cammi, R.; Pomelli, C.; Ochterski, J. W.; Martin, R. L.; Morokuma, K.; Zakrzewski, V. G.; Voth, G. A.; Salvador, P.; Dannenberg, J. J.; Dapprich, S.; Daniels, A. D.; Farkas, Ö.; Foresman, J. B.; Ortiz, J. V.; Cioslowski, J.; Fox, D. J. *Gaussian 09*, Gaussian, Inc.: Wallingford, CT, USA, 2009.
- (40) NBO 6.0. E. D. Glendening, J., K. Badenhoop, A. E. Reed, J. E. Carpenter, J. A. Bohmann, C. M. Morales, C. R. Landis, and F. Weinhold., *Theoretical Chemistry Institute, University of Wisconsin, Madison* (2013).
- (41) Sanderson, R. T., Principles of electronegativity Part I. General nature. *Journal of Chemical Education* **1988**, 65 (2), 112.
- (42) Mayer, I., Program "BORDER" version 1.0. *Program "BORDER" version 1.0, (Chemical Research Center, Hungarian Academy of Sciences), Budapest* **2005**.
- (43) Billow, B. S.; Bemowski, R. D.; DiFranco, S. A.; Staples, R. J.; Odom, A. L., Synthesis and Structure of Chromium(VI) Nitrido Cyclopentadienyl Complexes. *Organometallics* **2015**.
- (44) Park, J. G.; Jeon, I.-R.; Harris, T. D., Electronic Effects of Ligand Substitution on Spin Crossover in a Series of Diiminoquinonoid-Bridged FeII₂ Complexes. *Inorganic chemistry* **2015**, 54 (1), 359-369.

CHAPTER 4. SILICA-GEL SUPPORTED TITANIUM CATALYSTS FOR C–N BOND FORMING REACTIONS^{1,2}

4.1 Introduction

In 2001, the Odom group published studies that demonstrated the electronic structure of $\text{Ti}(\text{NMe}_2)_2(\text{dpm})$ ($\text{dpm} = 2,2'$ -pyrrolylmethane) complexes and their potential applications to hydroamination-based reaction chemistry.³⁻⁵ These efforts mark the starting point for what has become an extensive body of research conducted in the following 2 decades, by various members of the Odom group, into Ti(IV) catalysts for C–N bond formation reactions.⁶⁻⁸ Primarily, three different varieties of C–N bond forming reactions have been the focus of these catalyst development efforts: (1) hydroamination, coupling amines and alkynes; (2) hydrohydrazination, coupling hydrazines and alkynes; and (3) multicomponent coupling reactions originating from 1 and 2, where more complex organic products are yielded via the inclusion of an additional coupling partner. In particular, the multicomponent coupling reactions are of interest to the broader organic synthesis and biological chemistry communities, as many of these multicomponent coupling products can be readily functionalized to yield highly-substituted heterocyclic compounds.^{6,9-15} A highlight of some of this chemistry, based on iminoamination, is featured in Fig. 4.1 below.

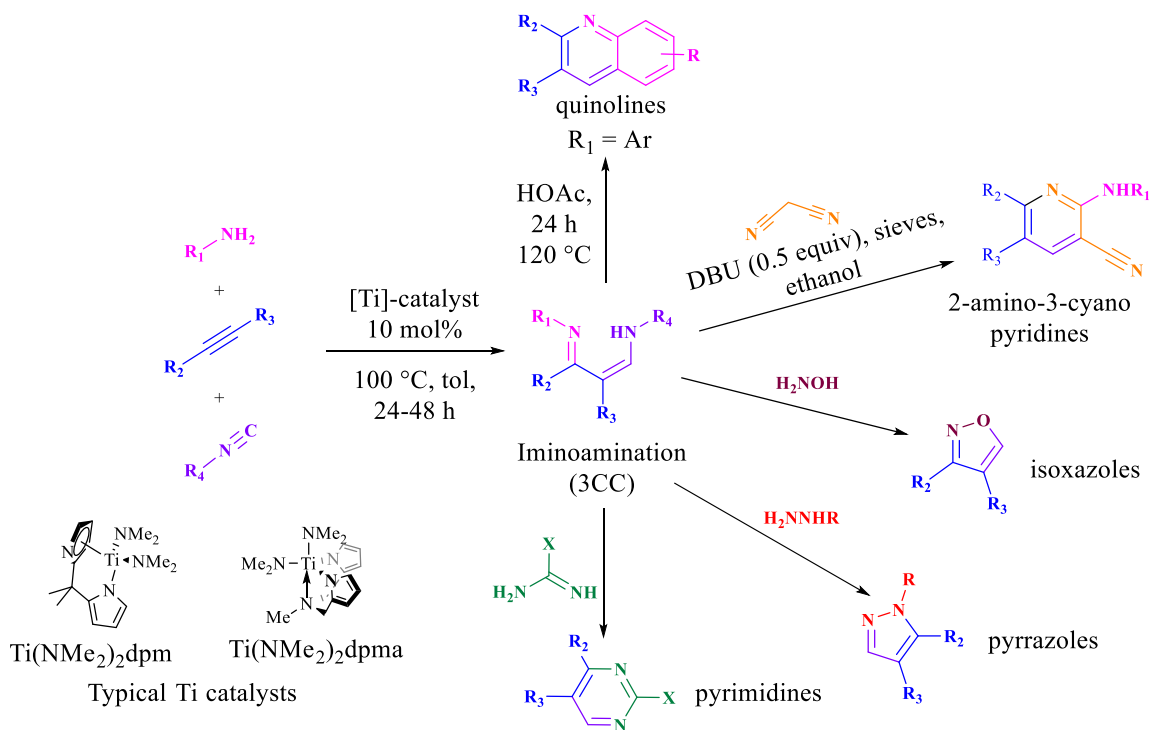


Figure 4.1 Reaction schemes to yield highly substituted nitrogen-based heterocycles using Ti-catalyzed iminoamination followed by simple organic ring-closing reactions. These processes are conducted as one-pot-two-step reactions from simple starting materials.⁶

Several of the products shown in Fig. 4.1, including substituted quinolines and 2-amino-3-cyanopyridines, have led to collaborations within the department and the university to explore the biological activity of these complex organic products. Many of the quinoline compounds, which can be produced in 1-pot-2-step reaction sequences using Ti(IV) catalyzed C–N bond forming reactions starting from simple, cheap, commercially available starting materials, are sub-micromolar inhibitors of the human proteasome.⁹ This finding is very interesting due to the relevance of the human proteasome in many human diseases. Additionally, moieties such as these heterocycles are commonly observed in natural products; employment of these catalyses is a potential tool to basic organic synthesis problems pursuing natural products.¹⁰

Several other groups have been pursuing similar chemistry with Group-4 transition metal catalysts and deserve mention here. The Schafer group at UBC has pursued ligand design and

product functionalization, in addition to expanded substrate tolerance in hydroamination and similar C–N bond forming reactions utilizing homogeneous Ti and Zr catalysts.^{16,17} The Tonks group at University of Minnesota has recently been expanding the C–N bond forming chemistry and multicomponent coupling capacity of Mountford's catalyst in the one-pot synthesis of tetra-substituted pyrroles from alkynes and azobenzene. Of course, these more recent advances have benefited from early work in the field by the Bergman, Mountford, Bercaw, and Doye groups, which provided fundamental mechanistic investigations and footholds for future catalyst design and development.¹⁸⁻²¹

For several of the heterocyclic compounds accessible through Group-4 transition metal catalyzed reaction pathways, complex organic reaction routes could likely lead to the same or similar compounds. However, using the Ti(IV) catalysts developed in our group and other groups, these reactions are 1 to 2 steps and frequently provide moderate to high yields of the desired heterocycles.⁶ Unfortunately, there are limitations with these homogeneous Ti(IV) catalysts, which have been discovered in the last several years. Thus, some significant barriers remain along the pathway to optimization of these catalytic reactions with a broad range of substrates, higher turnover frequencies, and increased regioselectivity.

A very fundamental example of one such limitation has been demonstrated by the multidisciplinary study undertaken by Dr. Brennan Billow and Dr. Tanner McDaniel during their time in the Odom Group. In this study, the rates of various Ti(IV) hydroamination catalysts were found to correlate with the electronic donor ability (LDP) and size (% V_{bur}) of the ancillary ligands on Ti.²² With the electronic and steric parameters for each ligand determined utilizing our Cr(VI) LDP system,²³ the rate of a Ti-catalyst bearing a given ancillary ligand can be predicted using the equation shown below (Fig. 3.2).

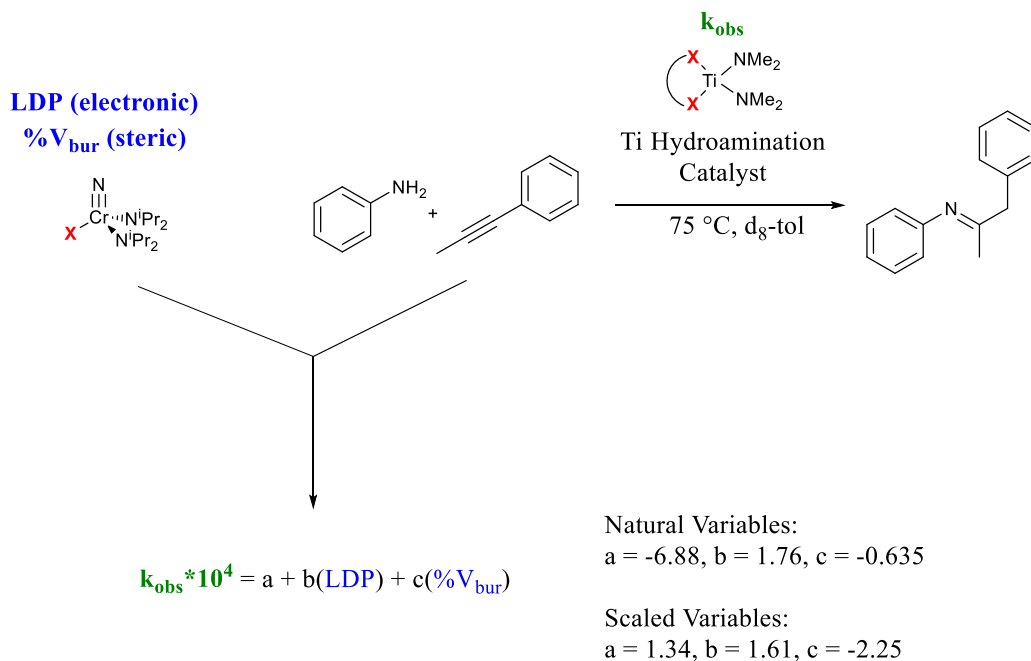


Figure 4.2 The combination of the LDP system using high valent Cr(VI) and our Ti(IV) hydroamination catalysts which has facilitated the development of a quantitative model describing the effects of ancillary ligands on catalytic rate.

According to this model, a more electron deficient ancillary ligand results in faster catalyst turnover, as demonstrated by the positive coefficient for the LDP (electronic) term; as LDP increases, the X⁻ ligand is a poorer donor, and multiplied by the positive coefficient this increases k_{obs} . This fits mechanistically with the proposed rate-limiting step of imine formation via hydroamination being protonation of the intermediate metallacycle; a more Lewis acidic Ti may enhance the rate of that protonation step. Conversely, as the steric term gets larger, indicating more crowding in the first coordination sphere of Ti, the rate of the catalyst decreases. This is indicated by the negative coefficient modulating the effect of the steric descriptor on k_{obs} .²²

While the successful development of this predictive model was a triumph, several complications resulted from these studies which highlight some of the limits of homogeneous systems. For example, based on its relatively high LDP value (~14 kcal/mol) and its small steric profile (%V_{bur}~23%), 2-thionaphthol was predicted to be an excellent ancillary ligand, resulting in

a fast k_{obs} . However, when the $\text{Ti}(\text{NMe}_2)_2(2,2'\text{-di(thionaphthol)})$ catalyst was prepared and the k_{obs} measured experimentally, the performance was quite poor with next to no product formation.

Upon further analysis it was determined that the complex exists as a thiol-bridged dimer in the solid state. Even in the presence of excess aniline at elevated temperatures, the dimerized form persists in solution.²⁴ Consequently, a definitive form for the catalytically active species cannot be assigned, as one of two scenarios (or both at the same time) are likely occurring. If the active species is actually monomeric, its concentration in solution is fleeting and low due to the equilibrium process with the dimeric species. Again, by *in situ* experimental indications, the dimer is the major species in solution. If the active species is in fact the dimer, its kinetics are very different from the monomeric analogues that were used to build the model for the study, and therefore the predictive capability of the model fails to account for these differences.

Regardless of the active species, a ligand which was predicted to yield a fast k_{obs} turned out to be the worst catalyst (slowest) examined in the study. Dimerization processes are by no means exclusive to the catalysts in this system and are a common issue across a wide variety of homogeneous transition metal catalyzed reactions, reducing the concentration of active species *in situ*. Easy ways to circumvent these processes, however, are not common and typically involve synthetic strategies related to ligand design that disfavor dimer formation (i.e. adding steric bulk to block molecular contacts between two molecular metal complexes in solution).

Many other examples of ligand-design-limited alterations to homogeneous Ti(IV) catalysts for these and similar reactions include ligand non-innocence, ligand comproportionation and disproportionation reactions (see Chapter 6), and introduction of competing side reactions with radical changes in ligand design. These sorts of results are only discovered after careful ligand

design, synthesis, isolation, and attachment to the transition metal has occupied hours or days of a chemist's time in the laboratory.

Many of the problems plaguing these homogeneous Ti systems have a simple solution. Dimerization and ligand exchange interactions are not problems in heterogeneous systems. In some types of heterogeneous catalysts, the active metal is immobilized on a solid support or within a porous 3-dimensional matrix. In covalent materials like MOFs or many types of nanomaterials, the "ligands" are typically electronegative elements that compose the structure of the solid material itself making bonds to a metal. They are not nearly as susceptible to the same types of exchange reactions and dynamic processes that a homogeneous catalyst might undergo. There are a handful of recent examples in the literature where heterogeneous catalyst systems have been used to perform hydroamination reactions, including nanoparticles and gel-supported systems.²⁵⁻²⁷

One type of heterogeneous catalyst that has appeal for application to C–N bond forming reactions is silica-gel supported organometallic catalysts. Over the last few decades, both the Coperet, Basset, and Scott groups (among others) have pioneered thorough characterization and mechanistic understanding of catalytically active organometallic complexes immobilized on silica surfaces via Si–O–M linkages.²⁸⁻³⁴ For example, in collaboration with Schrock, the Coperet group has extensively characterized the properties and catalytic ability of a silica-gel supported high-valent molybdenum alkylidene, a replica of Schrock's homogeneous species which catalyzes olefin metathesis.³⁵⁻³⁸ Even examples of silica-supported lanthanide catalysts and a silica supported Zn catalyst have recently been reported for intramolecular hydroamination.^{39,40}

This type of catalyst system has the potential to directly solve many of the problems that so heavily diminish the success of the homogeneous catalysts discussed above. Unlike many heterogeneous catalysts, however, silica-supported systems offer the benefit of maintaining a

similar coordination environment around the active metal to homogeneous analogues. The preservation of the catalytically active metal's coordination sphere facilitates the translation of mechanistic and intuitive understanding built on homogeneous analogues over the last several decades, to the development of similar reaction chemistry with these heterogeneous materials.³⁵ It has also been demonstrated that silica-supported catalysts are good candidates for things like catalyst recycling and reactivation.⁴¹ These are features we sought to extend to hydroamination and iminoamination catalysts but which are also relatively impractical with homogeneous systems. Put simply, heterogeneous catalysts are far more robust than homogeneous counterparts, so even simple things like higher reaction temperatures or higher reaction concentrations seemed like potential routes to improve catalyst performance, in terms of rate.

With these potential benefits offered by moving to a catalyst system using a silica-support, we decided to explore the reactivity of silica-supported Ti materials. Our only synthetic requirement in these supported systems was the preservation of two protolytically active sites in the Ti coordination sphere. Generally, we would expect a Ti–O bond, such as those that would be produced by grafting $\text{Ti}(\text{NR}_2)_4$ precursors to a silica surface, are going to resist protonation by the relatively weak proton sources such as the primary amines utilized in hydroamination and iminoamination reactions (pK_a : H_2NPh ~30; $(\text{Si})\text{O-H}$ ~5). With this forethought, we knew that a maximum of 2 surface interactions per Ti was likely needed to preserve the desired reactivity at the metal.

We also suspected that there would be large differences in the reactivity of Ti sites bound through 1 versus 2 Ti–O–Si linkages. In the simplest organometallic view, each bond to the surface is like a large siloxide ligand. When two of these interactions are achieved, the Ti then has a very different set of “ancillary ligands” relative to a Ti that has one surface interaction and one

additional protolytically active ligand, such as an -NHP_h fragment, in the reaction solution. The differences in this ligand set are dramatic both in terms of sterics and electronics. Keeping these ideas in mind, we set about preparing two different materials that would offer the two different surface site environments. The targeted species are shown below in Fig. 4.3 to assess the reactivity of such surface-bound species for C–N bond forming reactions.

Targeted Silica-Supported Ti(NMe₂)_n species

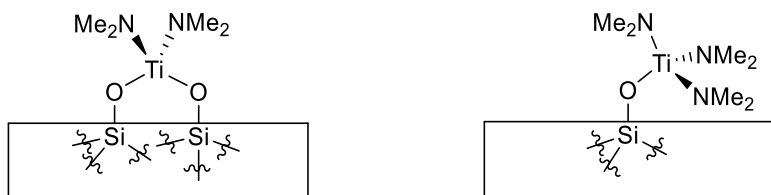


Figure 4.3 The species that were targeted as potential precatalyst materials for hydroamination and iminoamination chemistry using a silica-supported, heterogeneous catalyst system.

4.2 Preparation of Silica-gels with Varied Surface Hydroxyl Group Density

In 2001, the Scott group at UCSB published the preparation of a material that they characterized as a Ti(IV) bis(dimethylamido) complex bound to the silica surface through two Ti–O–Si linkages each. A depiction of this surface is shown in Fig. 4.4.⁴²

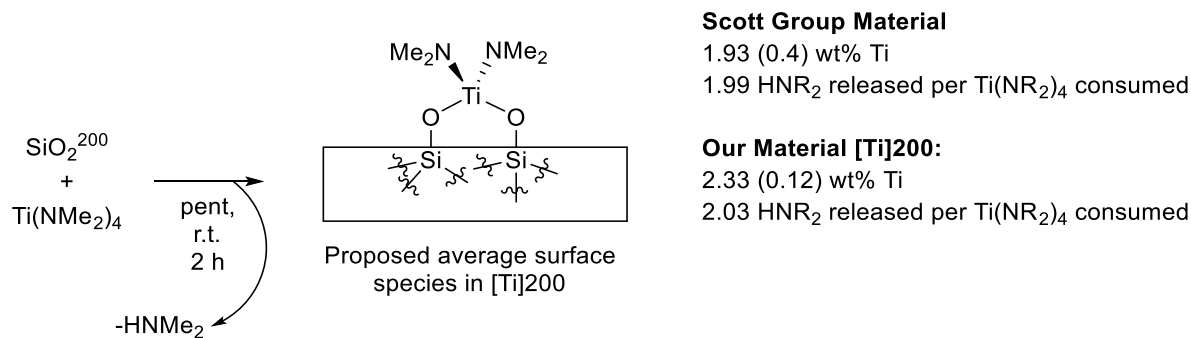


Figure 4.4 The binding mode of Ti on the surface of SiO_2^{200} upon treatment with $\text{Ti}(\text{NMe}_2)_4$. For comparison, the bulk properties of the material reported by the Scott group is given along with the properties of the material we synthesized following their SiO_2^{200} preparation.

Scott's procedure for preparing the silica-gel is straightforward and requires minimal dehydroxylation. After compacting the fumed silica (surface area $200 \pm 25 \text{ m}^2/\text{gram}$), it is heated to $200 \text{ }^\circ\text{C}$ under vacuum for 8 h to provide SiO_2^{200} . According to Scott's preparation, this provides a material which liberates 1.99 ± 0.04 equiv HNR₂ per mole of $\text{Ti}(\text{NR}_2)_4$ consumed, and a Ti content of $1.93 \pm 0.4 \text{ wt}\%$ when saturated with $\text{Ti}(\text{NMe}_2)_4$.⁴² In our hands, this preparation led to a very similar material with $0.52 \text{ mmol Si-O-H sites per gram}$ or $1.6 \text{ Si-O-H sites per nm}^2$; this correlates with liberation of 2.03 ± 0.12 equiv HNR₂ per mole of $\text{Ti}(\text{NR}_2)_4$ consumed according to NMR titration of SiO_2^{200} with $\text{Ti}(\text{NEt}_2)_4$. When treated with $\text{Ti}(\text{NMe}_2)_4$, our material shows $2.33 \pm 0.12 \text{ wt}\%$ Ti by ICP-OES analysis. The properties of the two materials are the same within error.

Preparation of the silica-gel leading to a much lower concentration of terminal Si-O-H sites requires much harsher conditions. Fortunately, using a quartz tube fitted with a gas adapter and a tube furnace in the Hamann group's labs, slight modification of the existing literature procedures resulted in highly dehydroxylated silica-gel.²⁸ This involves heating compacted silica-gel under vacuum at a temperature of $700 \text{ }^\circ\text{C}$ for several hours; repeat batches of SiO_2^{700} prepared in this manner have demonstrated consistent results following the protocol outlined in Table 4.1, below.

Table 4.1 General conditions for SiO_2^{700} preparation from commercially available fumed silica.

Temperature (°C)	Ramp rate (°C/min)	Time (min)	Atmosphere
20-500	5	96	Air
500	–	240	Air
500	–	720	Vacuum
500-700	1.33	150	Vacuum
700	–	480	Vacuum
700-20	≈ 4	180	Vacuum

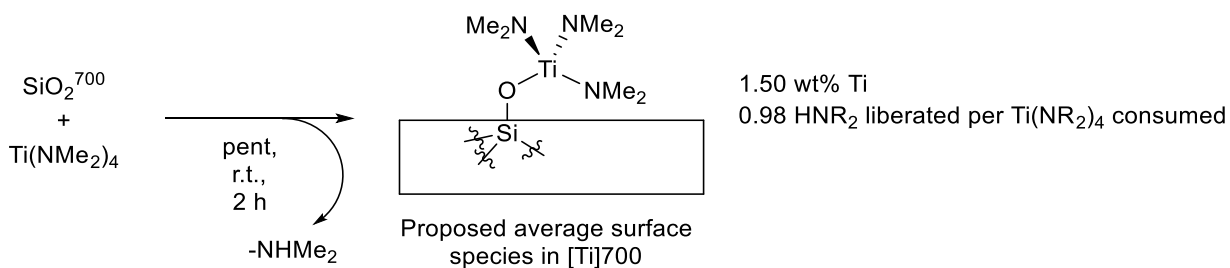


Figure 4.5 (top) Quartz tube used for silica gel prep with tube furnace setup. (bottom) Schematic for the preparation of the precatalyst material [Ti]700.

Calibration of the surface with $\text{Ti}(\text{NET}_2)_4$ and quantification of the Ti content of the SiO_2^{700} , when treated with $\text{Ti}(\text{NMe}_2)_4$ and measured by ICP-OES spectroscopy, provides values consistent with a low Ti concentration. The calibration stoichiometry suggests that, on average, each Ti is bound to the silica-gel surface through a single Ti–O–Si; these NMR titrations show that 0.98 ± 0.04 equiv of HNR₂ is liberated per equiv of $\text{Ti}(\text{NR}_2)_4$ consumed. The subsequent Si–O–H concentration was determined to be 0.31 ± 0.05 mmol per gram of SiO_2^{700} or 0.9 ± 0.1 Si–O–H sites per nm²; when saturated with $\text{Ti}(\text{NMe}_2)_4$ this correlates with 1.53 ± 0.07 wt% Ti. These properties provide characterization data for the material in terms of its bulk properties. Of course,

there is still the possibility that each individual Ti site on the silica-gel surface could possess one of several variations in the local Ti environment.

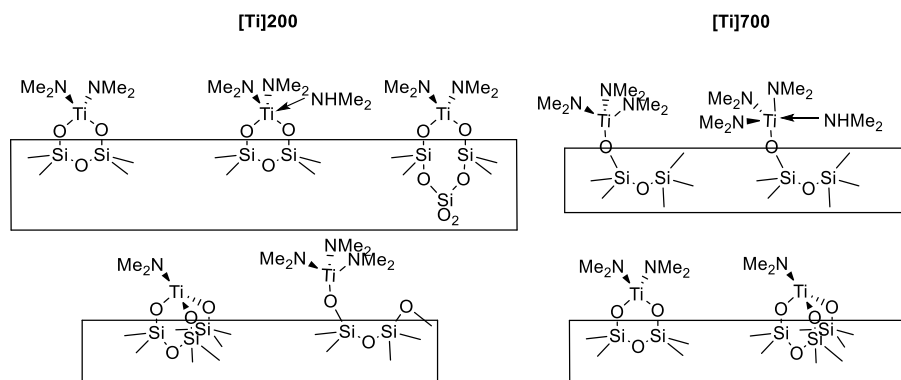


Figure 4.6 Possible site variations in the coordination environment and binding modes for the two different catalysts, [Ti]200 and [Ti]700.

These possible differences in the local Ti environment on the silica surface could induce differences in the potential active catalytic species, however, they do not preclude catalysis (i.e. each Ti has at least 2 proteolytically cleavable sites). Thus, we began screening this material, [Ti]700, as well as the [Ti]200 for catalysis. In the future, it would be very interesting to look at these and other relevant materials (vide supra) by advanced solid-state NMR techniques, which could provide insight related to Ti speciation on the surface.^{30,43} This technology is not available at MSU, and would require collaboration with an external group, such as a national lab. With this acknowledgement out of the way, note that our chemistry and rationale proceeds with the simplest assumption that the stoichiometry of the bulk material represents the average Ti site in the material.

4.3 Performance of [Ti]200 and [Ti]700 as Intermolecular Hydroamination Catalysts

As a starting point for hydroamination reactions, similar conditions were used to those employed previously with homogeneous catalysts. Using 10 mol% catalyst loading at 110 °C in toluene, both catalysts, [Ti]200 and [Ti]700, demonstrated slow production of the hydroamination product of aniline and 1-hexyne. Since one of the main benefits of a heterogeneous catalyst over a homogeneous one is the increased stability, we increased the temperature of the reaction to 140

°C. This dramatically accelerated the rate of the reactions in addition to increasing the with this dimerized form persisting in solution, regioselectivity observed in the products with both the [Ti]200 and [Ti]700 catalyst materials.

With increased temperatures demonstrating such a marked improvement in catalyst performance, the temperature was again increased to 180 °C. The solvent for the reaction was changed from toluene to *p*-cymene, to retain similar properties but raise the boiling point of the solvent; likewise, the alkyne substrate was swapped for 1-octyne so higher concentrations of alkyne would remain in solution rather than vaporizing into the reaction headspace, provided by the increased boiling point. These changes provided another dramatic improvement in catalyst performance. The [Ti]200, for example, now performs the hydroamination of aniline and 1-octyne in 98% yield in under 40 min with only 5 mol% catalyst loading. Similar improvements were noted with the [Ti]700, as well. Fundamentally, needing higher reaction temperatures to achieve catalyst activation in a system with mixed-phase substrates and catalyst is not uncommon; interaction of catalyst and substrate across phases can increase the barrier to initiate reactions.

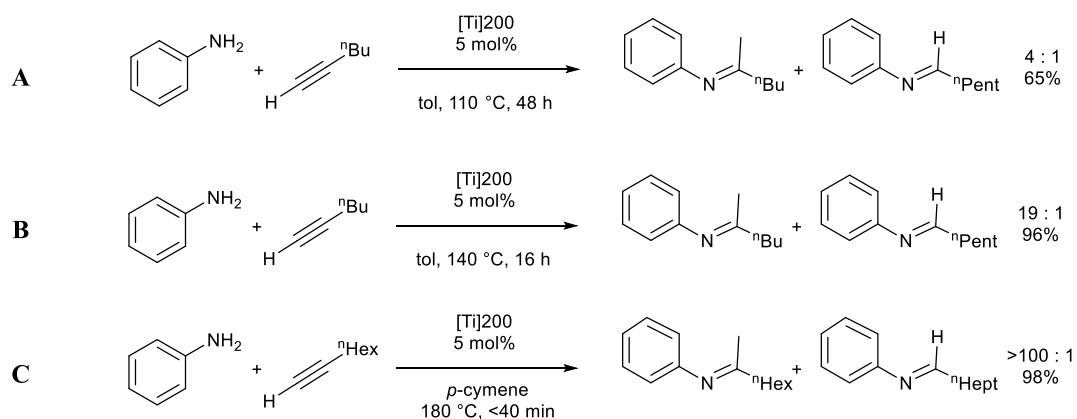
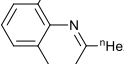
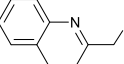
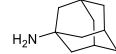
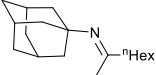
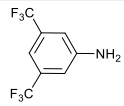
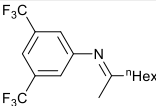
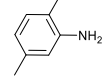
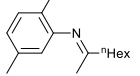
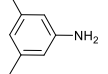
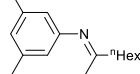
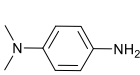
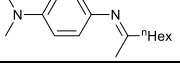
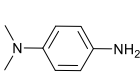
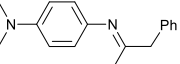


Figure 4.7 Reaction conditions applied to the heterogeneous catalysts. The yields and regioselectivities listed here were observed with [Ti]200. The same trends were observed with [Ti]700, as well, with improvements in regioselectivities and yields at higher temperatures in dramatically shorter reaction times. Moving forward, the conditions for C were adopted as the general procedure.

Using these conditions (C), a series of hydroamination reactions were performed with both catalysts to evaluate functional group tolerance in both the amine and alkyne substrates. Both catalysts demonstrate high yields for hydroamination with aniline, and bulky, electron-rich anilines (entries 1-4, 7, 8, and 11-14). This is true with both 1-octyne and 1-phenylpropyne as coupling partners. Both catalysts also demonstrate high regioselectivities for these reactions, as well, showing selectivity to the limits of our detection in many cases (Table 4.2). These results provided promising reactivity that suggested many of the reactions we were interested in pursuing with iminoamination (i.e. aniline as the amine coupling partner) could lead to high yields in regioselectivities in heterocyclic products down the line.

Table 4.2 Substrate scope examined for hydroamination reactivity with [Ti]200 and [Ti]700. The general conditions outlined in the Scheme below apply to all reactions.^{a,b}

Entry	Amine	Alkyne	Hydroamination Product	[Ti]200 Yield (Regioselectivity)	[Ti]700 Yield (Regioselectivity)	
1		${}^n\text{Hex}-\text{C}\equiv\text{C}-\text{H}$		98 (>100:1)	92 (>100:1)	
2		$\text{Ph}-\text{C}\equiv\text{C}-\text{H}$		92 (8.7:1)	92 (15:1)	
3		$\text{Ph}-\text{C}\equiv\text{C}-\text{Ph}$		67 (6.7:1)	33 (28:1)	
4		$\text{Ph}-\text{C}\equiv\text{C}-\text{Ph}$		92 (NA)	93 (NA)	
5		${}^n\text{Hex}-\text{C}\equiv\text{C}-\text{H}$		24 (24:1)	11 (1:1)	
6		$\text{Ph}-\text{C}\equiv\text{C}-\text{H}$		trace (NA)	34 (2.1:1)	
7		${}^n\text{Hex}-\text{C}\equiv\text{C}-\text{H}$		99 (>100:1)	85 (43:1)	
8		$\text{Ph}-\text{C}\equiv\text{C}-\text{H}$		99 (>17:1)	91 (100:1)	
9		${}^n\text{Hex}-\text{C}\equiv\text{C}-\text{H}$		7 (3:1)	0	
10				trace (NA)	28 (>100:1)	
11				92 (>100:1)	69 (60:1)	
12				91 (48:1)	59 (>100:1)	
13				92 (>100:1)	86 (>100:1)	
14			$\text{Ph}-\text{C}\equiv\text{C}-\text{H}$		99 (>100:1)	80 (>100:1)

^aYields reported were measured by GC/FID using external calibrations of the reduced derivatives of the hydroamination products shown in the figure. For those species with low yield, the next closest derivative was used to estimate the yield. ^bTimes for each reaction varied, from under 40 min for entry 1 to 14 h for entry 4. For specific reaction times, see experimental.

Both catalysts also show similar limitations. Specifically, tolerance toward alkyl amines and electron deficient aniline as coupling partners is low, with incredibly low yields; in fact, yields were so poor that no attempt was made to isolate products from these reactions. The regioisomers drawn in the table, therefore, are representative examples rather than an assignment of the observed regioisomer preference for these reactions. Overall, catalyst performance for hydroamination is very similar between the two materials, [Ti]200 and [Ti]700.

While there are many catalysts available in the literature that are capable of hydroamination, many at much milder conditions, we think this catalyst system offers a unique advantage. If imines are needed as intermediates in a multi-step synthesis, these reactions are clean and high yielding with the [Ti]700/200 systems, such that *in situ* reactions from their imine products would likely proceed successfully. At the same time, use of a solid catalyst means that after the reaction is complete, removal of the catalyst requires only a simple filtration. The organic filtrate can then be conveniently taken on to the next step in a reaction pathway without fear of remaining contaminants from the HA catalyst in solution with the products. Especially given how easy it is to make [Ti]200, these benefits make its use for even routine hydroamination catalysis attractive, especially as the first step in a multi-step sequence.

4.4 Application of [Ti]200 and [Ti]700 to Multicomponent Coupling Reactions

In the previous section, both [Ti]200 and [Ti]700 show comparable performance in hydroamination reactions. When using these catalysts for iminoamination, the three-component coupling (3CC) of an amine, an alkyne, and an isonitrile, their abilities are vastly different. Similar to the hydroamination reactions, several sets of conditions were probed, and while the catalysts showed product formation at lower temperatures (110 °C and 140 °C), this product formation was

extremely slow. Thus, similar reaction conditions as those presented for hydroamination were adopted for iminoamination, as shown in Fig. 4.8.

These reaction conditions limit the choice of isonitrile coupling partner. At 180 °C, isonitrile decomposition was noted with aryl and bulky alkyl (octyl, 1,1-2,2-tetramethyl-propyl, and *tert*-butyl) groups on the isonitrile. Only CyNC, with its high boiling point and reduced propensity to undergo alkyl eliminations (which had been observed when reactions were attempted with ^tBuNC), was able to withstand the high reaction temperatures.

With the [Ti]200 catalyst, however, even at elevated temperatures, relatively small amounts of product were observed with many sets of substrates. This is demonstrated by several of the entries in Table 4.3, below. Examining the series of reactions in entries 1-3, it seems that steric protection of the aniline derivative at either or both *ortho*-positions on the aniline's phenyl ring is necessary to promote formation of the 3CC product. This is because the side reaction to generate formamidine, which is an off-cycle product, or the hydroamination products are competing with 3CC production.^{6,8} The rates of side product formation are particularly high with an unprotected aniline, generating a very substantial amount of formamidine with these substrates.

Typically, in homogeneous reactions, the amount of off-cycle formamidine production can be reduced with the use of ^tBuNC, which slows the rate of formamidine production relative to other processes in the iminoamination reaction. However, as noted above, this substrate had already proven incompatible with the reaction conditions. As such, the bulky aniline derivatives are really the only substrates that are compatible with [Ti]200 for iminoamination chemistry.

Switching catalyst to the [Ti]700, every aspect of the catalysis is improved. The [Ti]700 catalyst material gives even higher yields than the [Ti]200 catalyzed reactions with the bulky aniline derivatives, with entries 1 and 2, giving 94% and 72% yield, respectively, in 48 h.

Additionally, the [Ti]700 can perform couplings with 1-phenylpropyne much more readily than the [Ti]200 material (entry 5), and it can even provide high yields of the 3CC product coupling aniline and 1-phenylpropyne with CyNC. Note, this reaction also appears much faster, as 88% yield is generated in only 16 h. Overall, the iminoamination reactions catalyzed by [Ti]700 are much cleaner than any of the reactions catalyzed by the [Ti]200 as well, with very little formamidine or hydroamination observed by GCMS and GCFID of the crude reaction mixtures.

There is only one real limitation remaining with the [Ti]700 as a catalyst for iminoamination: the catalyst does not couple small aniline derivatives (i.e. aniline or 4-NMe₂-aniline) with terminal alkylalkynes well (1-octyne). These substrates show very low yields with substantial side product formation. The catalyst also falls short with alkyl amine derivatives such as CyNH₂; this is true even when considering just the simple hydroamination reaction, so this is a direct failure of the iminoamination reaction so much as an inherent substrate intolerance of these types of catalysts. To qualify [Ti]700 as a universal iminoamination catalyst for a broad range of substrates, these substrate intolerances need to be overcome. As an iminoamination catalyst for anilines with 1-phenylpropyne or phenylacetylene, however, this material appears to perform with similar success to the best homogeneous catalysts for these reactions. This class of compounds alone is quite valuable for application to quinoline synthesis, for example, and certainly demonstrates the potential of this type of catalyst in performing these C–N bond forming reactions quickly and cleanly.

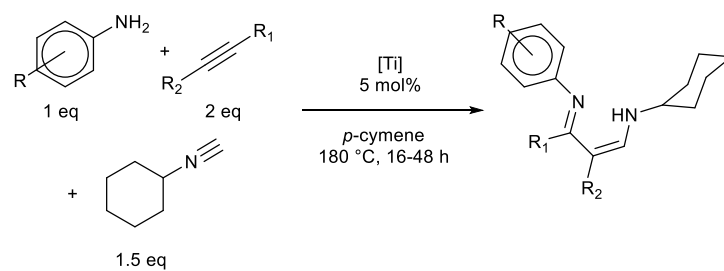
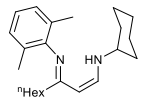
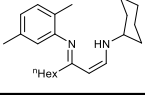
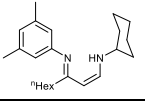
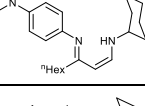
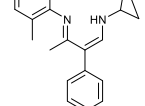
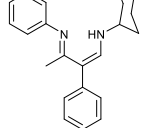
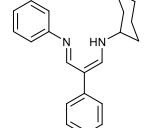


Figure 4.8 General reaction scheme applied to the iminoamination reactions studied with [Ti]200 and [Ti]700.

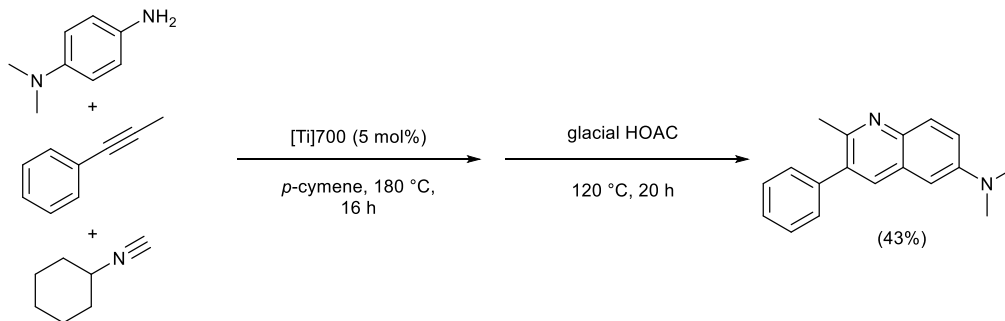
Table 4.3 Iminoamination (3CC) substrate scope examined with [Ti]200 and [Ti]700. The general conditions outlined in Fig. 7, C apply to all reactions.^{a,b}

Entry	Amine	Alkyne	Iminoamination (3CC) Product	[Ti]200 Yield (Regioselectivity)	Byproducts	[Ti]700 Yield (Regioselectivity)	Byproducts
1				51 (5.2:1)	14% HA, 10% FA	94 (6.6:1)	6% HA
2				50 (>100:1)	16% HA, 10% FA	71 (>100:1)	trace FA
3				7 (>100:1)	13% HA, 10% FA	33 (1.5:1)	trace FA
4				12 (3.3:1)	31% HA, 10% FA	8 (>100:1)	16% HA
5				36 (6.8:1)	8% HA, 6% FA	61 (3.0:1)	5% HA (18% aniline)
6				NA	NA	88 (10.3:1)	(10% aniline)
7				NA	NA	52 (6.3:1)	Alkyne Trimerization

^aYields reported were measured by GCFID using external calibrations of the reduced derivatives of the hydroamination products shown in the figure. For those species with low yield, the closest derivative in terms of molecular formula, was used to estimate the yield by GCFID. ^bTimes for each reaction varied, from under 40 min for entry 1 to 14 h for entry 4. For specific reaction times, see experimental.

4.5 Use of Ti700 to Produce Functionalized Heterocycles

To demonstrate the practicality of [Ti]700 as an iminoamination catalyst, the 1-pot-2-step quinoline synthesis, previously developed by the Odom group with homogeneous Ti catalysts, was repeated here with [Ti]700.^{9,44} The reaction scheme shown below produced the targeted quinoline in 43% yield utilizing 5 mol% [Ti]700. The total reaction time of both steps together was 36 hours.



Scheme 4.1 One-pot-two-step quinoline synthesis of 2-methyl-3-phenyl-6-(*N,N*-dimethylamino)quinoline utilizing [Ti]700 to perform the initial iminoamination reaction.

Compared to the original synthesis of this quinoline, the synthesis of the quinoline utilizing [Ti]700 is, in many ways, an improvement. The 3CC reaction was catalyzed with 10 mol% of the homogeneous catalyst ($\text{Ti}(\text{NMe}_2)_2(\text{dpm})$) and took 24 hours to complete, followed by a 24 h conversion to the quinoline using acetic acid. This provided 50% yield of the targeted quinoline. The yields of the two Ti-catalyzed reactions are comparable, but the [Ti]700 catalyzed reaction took less time and half the catalyst loading. The results of the quinoline synthesis not only demonstrates that [Ti]700 performs well enough to be practically employed in routine synthesis of heterocycles, but also shows that [Ti]700 performs these iminoamination based reactions on the same level as some of our best homogeneous variants.

4.6 Exploration of Catalyst Reusability and Routes of Deactivation

As mentioned in the introduction, another appealing aspect of heterogeneous catalysts, specifically those supported on a silica or metal-oxide surface, is their potential to be recycled or reused. The physical ease with which the catalyst can be removed from a complex, solvated organic reaction mixture facilitates recovery of the catalyst material, something which is a far greater challenge with homogeneous systems. Additionally, a recent example from the Sadow group demonstrates the ability to reactivate a silica-supported Zr catalyst with a mild reductant (HBpin) after it has been exposed to air.⁴¹

Attempts were made with both [Ti]200 and [Ti]700 catalysts to recycle the material. Despite the similarity in structure of the materials, two very different responses were noted for the when reusing them in subsequent catalytic reactions. With [Ti]200 catalyzing the hydroamination of aniline and 1-octyne (entry 1, Table 1), the catalyst can be filtered off the crude reaction mixture, washed with pentane, dried under reduced pressure, and added to a second hydroamination reaction. The second round provides a yield comparable to the first round. This process was repeated for a total of 5 uses of the catalyst, with the third round showing a slight decrease in yield; by the 4th round, the yield has been reduced to about half of the original yield; and by round 5, the catalyst is close to complete deactivation, showing fewer than 5 turnovers relative to the original loading.

Interestingly, as the yield gradually tapers off, the regioselectivity also decreases (by about 1 order of magnitude total) with each use of the catalyst. When the used catalyst material was “regenerated” by adding Ti(NMe₂)₄ after the 5th use of the catalyst, the yield makes a dramatic recovery. However, it still isn’t quite as high as the initial yields and the regioselectivity is relatively low (7.3:1 vs. >100:1) compared to the initial use. These results are highlighted in Table 4.4.

Table 4.4 Hydroamination Results for the Coupling of 1-Octyne and Aniline with Recycled [Ti]200.

Trial Number	Yield (%)^a	Regioselectivity Ratio
1	98	>100:1
2	96	32:1
3	90	14:1
4	44	10:1
5	23	10:1
6 ^b	71	7.3:1

^aReported yields are GC-FID yields. ^bPrior to running experiment 6, the catalyst material was treated with Ti(NMe₂)₄ to “regenerate” the material.

Unfortunately, we don't have the means to examine every possible occurrence at the surface that may be changing the nature of the catalyst, reducing regioselectivity and yield across multiple uses of the catalyst. One detrimental effect of catalyst recycling that we *were* able to identify is that over the course of a single hydroamination reaction, a measurable quantity of the Ti metal is leached from the surface of the catalyst. ICP-OES analysis of used [Ti]200, that has been through 1 round of hydroamination, demonstrates a 10% reduction in Ti (wt%) content. Successive uses of the same catalyst material strip more of the active metal away, leading to a decrease in catalyst loading with each reuse. This phenomenon agrees with the observations presented in the table above, including a recovery in the reaction yield upon re-exposure of the SiO₂²⁰⁰ support to a molecular Ti source.

We don't firmly understand the mechanism of Ti removal from the surface, but one possible contribution to this process may be the alkyne trimerization that appears as an off-cycle side reaction in hydroamination catalyses. One of the proposed steps in this type of catalyze reactions includes a temporary reduction of the metal, which we think could weaken the Ti metal's bond to the surface. This hypothesis is currently very speculative and is simply our best guess as to what is different between the [Ti]200 and the [Ti]700, which does not demonstrate loss of the metal (see below).

The only aspect of the [Ti]200 recycling experiments that is not necessarily explained by the Ti leaching from the catalyst material is the change in the regioselectivity noted. While a change in the catalyst loading could certainly alter the observed regioisomer ratio of the products, this change could also be the result of other changes in the material. For example, if the Ti on the catalyst material is labile, it may be rearranging to form different coordination environments (Fig. 4.9). One could even envision the formation of dimers, like those observed by Scott and coworkers

when they used $\text{Ti}(\text{O}^i\text{Pr})_4$ to synthesize $\text{Ti}(\text{O}^i\text{Pr})_2/\text{SiO}_2^{200}$.⁴⁵ While this type of interaction isn't typical in a heterogeneous system like this, we know that Ti comes off the surface during these reactions with [Ti]200. The liberated Ti, once in solution, could exhibit behaviors more typical of homogeneous species. This type of rearrangement could certainly result in changes in the reactivity, including regioselectivity.

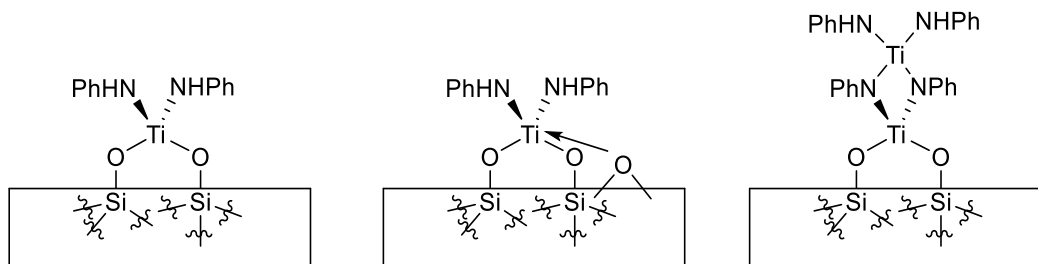
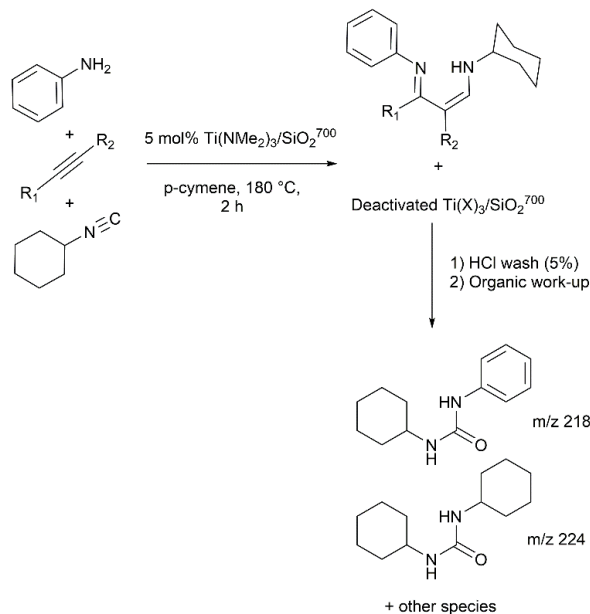


Figure 4.9 Proposed surface morphologies of used [Ti]200, after use in hydroamination reactions. Changes in the coordination environment could lead to changes in the regioselectivity ratio observed in the hydroamination products.

When we tried to reuse the [Ti]700 material, very different results were observed. There was no loss of Ti, determined by ICP-OES analysis of used catalyst material, within the error of our detection techniques. Despite this, only a trace (<5%) of the hydroamination or iminoamination products were observed upon a second use of the catalyst material. This was the case with a variety of different substrates examined for reuse with either reaction.

Careful analysis of the crude reaction solutions by GCMS didn't indicate the cause of the catalyst poisoning. As of yet, we have no clear experimental indication of why the catalyst is "poisoned" and ceases catalytic function after a single round of hydroamination. However, there is some precedence with homogeneous Ti systems that catalyze hydroamination reactions, to deactivate via the generation of thermodynamically stable, metallacyclic species. Specifically, Mountford and coworkers have demonstrated that double-insertion of alkyne into the Ti-imide double bond can result in an isolable product that is not readily cleaved from Ti in the presence of excess amine (i.e. a proton source).^{21,46} While this product (aniline + 2 equiv alkyne) has not been

directly observed in the crude reaction solutions of any hydroamination reactions catalyzed by [Ti]700, if the product were irreversibly bound to the Ti on the silica surface, it may not appear in



Scheme 4.2 A typical iminoamination reaction utilizing [Ti]700 as the catalyst material and the organic residues found upon a mild acid-wash of the used catalyst material's surface.

solution. Thus, the lack of GC evidence means that a deactivation event of this nature is still possible in the [Ti]700 system.

There is slightly more experimental evidence suggesting the source of the catalyst poisoning in the iminoamination. Again, there were no obvious indications of catalyst poisoning products in the crude reaction mixtures by GCMS analysis. With [Ti]700 used for iminoamination reactions, surface extractions or washing with dilute HCl solutions provided evidence of new organic residues. While several of the new masses observed by GCMS remain unidentified, two masses match those of 1-phenyl-3-cyclohexylurea and 1,3-dicyclohexylurea. This suggests that the isocyanide is potentially non-innocent toward the active Ti metal, as CyNC is the only source for a cyclohexyl functional group in the reaction.

Unfortunately, with only these complexes identified in surface extractions, a working mechanism for the deactivation process has not been fully pieced-together. Additionally, because

an acidic, aqueous wash is required to remove the surface residues, it is likely that what is on the surface, actually poisoning the catalyst, is transformed upon removal by the species present in the HCl solution. Thus, although we have identified the urea species by GCMS, they may exist in a different form on the surface of the material. Here again, the application of solid-state NMR, or even (stringently) air-free IR spectroscopy would be highly beneficial to our understanding of these poisoning events.

4.7 Accidental Discovery of [Ti]700 Activity for Catalytic Guanylation of Carbodiimide

While trying to figure out how the [Ti]700 is poisoned by iminoamination, we came across a few interesting studies in the literature. In 2003, Richeson and coworkers published two studies in which the interactions of carbodiimides and terminal Ti–imido species were examined. In the first study, they observed metathesis of the C–N double bonds of the carbodiimide with the Ti–N double bond.⁴⁷ In a second study, catalytic production of substituted guanidines was achieved with a primary amine, a carbodiimide, and catalytic Ti–imide species bearing guanidine ancillary ligands.⁴⁸ This catalytic reaction is depicted in Scheme 4.3. Similar guanylation reactions have been reported using alternate Ti–imide systems since that time.

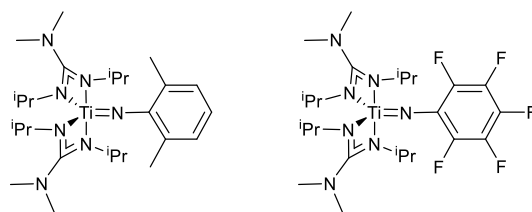
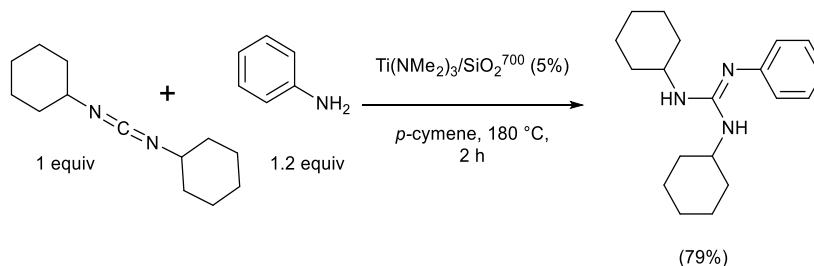


Figure 4.10 Ti complexes from the Richeson Group used for catalytic guanylation of carbodiimides and imide metathesis reactions.^{47,48}

We wondered if in fact a guanidine-like species was able to form in the crude reaction mixture from CyNC and aniline, and if, subsequently, guanidine or a carbodiimide could shut down the catalytic activity of [Ti]700. A stoichiometric reaction between [Ti]700, carbodiimide, and an excess of aniline was heated for 2 h, and the crude solution analyzed by GCMS. Two

products were noted. First, a small amount of 1-cyclohexyl-3-phenyl-carbodiimide was noted, the metathesis product of $\text{Ti}=\text{NPh}$ and 1,3-dicyclohexylcarbodiimide. Second, a very large amount of 1,2-dicyclohexyl-3-phenylguanidine was also observed. When the reaction was repeated with 5 mol% [Ti]700, 1 equiv 1,3-dicyclohexylcarbodiimide, and 1.2 equiv H_2NPh , an isolated yield of 79% of the 1,2-dicyclohexyl-3-phenylguanidine was obtained in 2 h of reaction time (Scheme 4.3).



Scheme 4.3 [Ti]700 catalyzed guanylation of 1,3-dicyclohexylcarbodiimide.

The fact that the [Ti]700 catalyst can produce guanidines catalytically from aniline and carbodiimides is an interesting discovery on its own and certainly supports exploratory reactivity studies with the catalyst material. For example, with this specific reaction, the homogeneous catalyst $\text{Ti}(\text{dpm})(\text{NMe}_2)_2$ can also generate guanidine when combined with aniline and carbodiimide, but it cannot do so catalytically, as the dpm ligand is displaced by the guanidine product. This happens even stoichiometrically, where the crude reaction solution shows only H_2dpm and the guanidine produced can only be observed after washing the reaction solution with water and performing an organic work-up.

Because the [Ti]700 is supported on a silica surface, interactions between the product and the Ti metal are only of concern if they constitute irreversible bonding interactions. In the case of something like a guanidine product, however, binding of the guanidine to Ti and its removal by protonation are likely equilibria processes, that appear to avoid shutting down the catalyst irreversibly. Thus, this direct comparison in reactivity between a homogeneous catalyst and the heterogeneous [Ti]700 system demonstrates one of the major strategic advantages of the [Ti]700

material as a C–N bond forming catalyst. Exploration of other reactions where the product may be destabilizing to a homogeneous catalyst could be similarly productive with [Ti]700.

With the knowledge that our catalyst can generate guanidine following the pathway demonstrated by Richeson, we returned to the original hypothesis, that guanidine could be generated in the reaction as a side product and that it could inhibit the catalyst from performing iminoamination. Upon addition of 20 mol% guanidine to a 3CC reaction (Entry 6, Table 2), we did note a decreased yield of the 3CC product over the same reaction time. Relative to entry 6, where 88% yield was observed, the same reaction with 20 mol% 1,3-dicyclohexyl-2-phenylguanidine added provides a yield of only 45% in the same amount of time. While this suggests that guanidine does in fact inhibit the reaction, presumably by reducing the concentration of active Ti sites available by acting as a chelating ligand, it does not shut down catalysis completely. Since the recycling experiments demonstrate complete deactivation, we concluded this was not likely the source of the catalyst poisoning (or at least not the major source).

One other aspect of the catalytic reaction mixture that seemed necessary to consider—since we have experimental evidence suggesting that isonitrile contributes to the poisoning phenomena in the 3CC reactions—is an interaction between H₂NPh and CyNC, perhaps mediated by Ti but unique from the pathway through which formamidine is generated. In recent years, reports of these types of reactions have been made. In 2015, Ji and coworkers published a report in which a primary amine and an isonitrile can be coupled to generate carbodiimides in up to 93% yield using catalytic I₂ and an oxidant (cumene hydroperoxide, CHP).⁴⁹ Using a similar approach, Bez reported in 2018 that ureas can be synthesized directly through an I₂ mediated coupling of an amine and an isonitrile, using DMSO as oxidant.⁵⁰ One step in this proposed pathway includes an off-cycle equilibrium between one of the intermediates and carbodiimide.

To get an idea if this type of process could be responsible for the poisoning we observe in the [Ti]700 system, we looked at the potential of carbodiimide to inhibit the 3CC reaction. Similar to the experiment with guanidine, described above, 0.2 equiv of CyNCNCy was added to the reaction mixture to generate 3CC Entry 6 (Table 4.2). Here again, some product was observed, but with carbodiimide in the reaction mixture, a yield of only about 10% was observed, relative to 88% without carbodiimide. This is a much more dramatic reduction in catalyst activity than was observed with the guanidine added directly. This evidence, when considered with the observation that urea species were removed from the surface of the used catalyst upon a mild acid wash, makes the formation of carbodiimide-like intermediates forming in the reaction mixture seem like a probable source of catalyst deactivation.

Obviously, many details of how this process may occur are unclear. Specifically, in our system, there is no clear source of oxidant, aside from the SiO₂ support itself. At the same time, generation of these poisonous species in no way appears catalytic; so perhaps we are witnessing our catalyst material taking the reactants down one of these coupling pathways (amine + isonitrile) where the whole process gets stuck prior to oxidation of an unsaturated intermediate species. Of course, much of this is speculative, and short of stringent ¹³C NMR on the surface pre- and post-reaction, it is difficult to draw many well-founded conclusions. Further efforts to access recyclability with the catalyst material may then meet with the greatest success through condition optimization efforts, whereby the conditions for poisoning would be avoided altogether.

4.8 Conclusions

Based on the results presented above, we've learned a lot about the potential of these silica-supported Ti catalysts for C–N bond formation. The easily prepared [Ti]200, which requires only access to a basic vacuum-oven is an excellent hydroamination catalyst for aromatic primary amines

and a variety of alkynes. These reactions provide high yields and regioselectivities with these substrates and offer the benefit of easily removed catalyst material. For both the rapid synthesis of imines and the synthesis of imines for further functionalization, [Ti]200 offers an attractive means of producing the desired product. Additionally, these reactions can be performed with lower catalyst loadings than similar homogeneous systems.

Where the [Ti]200 catalyst begins to fail is for iminoamination chemistry. The catalyst isn't selective for production of the 3CC product over other possible byproducts in the reaction. While the best results were achieved with bulky derivatives (i.e. entries 1 and 2 above, Table 4.2), even with these substrates, large amounts of the hydroamination and formamidine byproducts were still observed in relatively high concentrations in the reaction mixtures. This makes the prospect of using the catalyst for these iminoamination reactions much less attractive.

By contrast, the [Ti]700 catalyst is average in terms of its hydroamination ability, it is a good catalyst for iminoamination reactions between aromatic primary amines and aromatic alkynes. The product yields are moderate to high and the byproduct yields are low. Additionally, with aniline as the amine and aromatic alkynes, these reactions are much faster than previously thought, with reaction times around 16 h showing high yields and almost complete consumption of the starting materials. Using iminoamination catalyzed by [Ti]700, we were able to demonstrate the utility of this catalyst system for practical synthesis of heterocycle synthesis. Following the 1-pot-2-step synthesis of quinolines which we developed with homogeneous Ti catalyst, the [Ti]700 system was able to provide a similar final yield with a faster total reaction time and half the catalyst loading. These results demonstrate that even a very simple silica-supported Ti catalyst is capable of improving upon the known homogeneous systems.

Of course, even with the [Ti]700 system, shortcomings have still been discovered. Primarily, we would still like to overcome the substrate limitations (sterically unprotected anilines coupled to 1-octyne and tolerance of alkyl primary amines). Achieving a highly reusable catalyst, that provides high yields and regioselectivities across several uses of the same batch of catalyst material is still an end goal in switching to a heterogeneous catalyst system. These goals encouraged us to explore further modification of the catalyst that enhanced its performance (Chapter 5).

4.9 Experimental

General Considerations

All syntheses and handling of materials were carried out under an inert N₂ atmosphere, either in an MBraun glovebox or by standard Schlenk technique. Any handling of materials in air is specified. Generally, this was limited to column chromatography and preparation of some GC and all ICP samples.

Fumed SiO₂ was purchased from Sigma Aldrich and used as received (200 ± 25 m²/g, Lot # SLBT0198). The following solvents were purchased commercially and dried prior to use: *para*-cymene was dried over CaH₂ and distilled under vacuum prior to use; pentanes and toluene were dried by passage over activated alumina and sparged with N₂ prior to use; tetrahydrofuran was purchased commercially, dried over sodium, and distilled under N₂ prior to use. The NMR solvent C₆D₆ was purchased from Sigma Aldrich, dried over CaH₂, and distilled under N₂ prior to use. All dried solvents were stored in an N₂ glovebox until use. For routine isolated product characterization, CDCl₃ was purchased from Cambridge Isotopes and used as received.

Ti(NMe₂)₄ and Ti(NEt₂)₄ were purchased from Gelest and used as received. Aniline, 2,6-dimethylaniline, 2,5-dimethylaniline, 3,5-dimethylaniline and 3,5-bis(trifluoromethyl)aniline

were purchased commercially, dried over an appropriate drying agent (see purification of laboratory chemicals, 7th ed.), and distilled under vacuum prior to use. The amines NH₂Cy and 1-NH₂Ad were purchased commercially and dried before use. The alkynes phenylacetylene, 1-phenylpropyne, and 1-octyne were purchased from Alfa and dried over Na₂SO₄, then distilled under N₂ before use. Diphenylacetylene was recrystallized from dry solvents before use. Cyclohexylisonitrile was prepared according to literature procedures.⁵¹ SiO₂²⁰⁰ was prepared according to Scott's published procedure.⁴²

NMR Titration A J-Young tube was loaded with SiO₂^{200/700} (approx. 100 mg), Ti(NEt₂)₄, and hexamethyldisiloxane internal standard as a 2.0 mL solution in C₆D₆. The tube was sealed and transferred to a sonicator. The mixture was sonicated for approximately 1 h, and the solids allowed to settle. The mixture was then examined by ¹H NMR (gain = 36, relaxation delay = 30 s) and the integral for NEt₂H versus Ti(NEt₂)₄ in solution was evaluated relative to the internal standard. This allowed determination of how much NHEt₂ had evolved from the reaction of Ti(NEt₂)₄, and by correlation, terminal Si-OH site quantity on the silica surface. This also indicated the surface density of Ti, and by comparing NHEt₂ generated versus Ti(NEt₂)₄ consumed, the average binding mode for the Ti was determined. The surface loading based on this titration was verified by ICP-OES.

ICP-OES Analysis for Ti Content Sample preparation consisted of digesting a known mass of [Ti]200 or [Ti]700 catalyst (approx. 100 mg) in 2 mL of concentrated HNO₃. The digests were allowed to sit for 4 h under ambient conditions before dilution with deionized water and centrifuging. The liquid portion of the sample was removed, and the solids washed with 2 aliquots of deionized water, which was again centrifuged, and the liquid portions collected. The combined liquid portions were diluted to a known volume, and further dilution with a 2% HNO₃ was carried

out as needed to get sample concentrations within the limits of detection of the instrument (0-6 ppm for Ti). A 1000 ppm Ti ICP standard in 2% HNO₃ was purchased from Sigma-Aldrich and used as received to prepare an external calibration curve. The [Ti]200/700 samples were then measured in triplicate, and quantified from the external calibration, allowing for the mass of titanium in each sample to be determined.

Preparation of SiO₂⁷⁰⁰ An OTF-1200X-S (MTI Corporation) high temperature furnace was utilized in the preparation of the SiO₂⁷⁰⁰. The fumed SiO₂ purchased from Sigma, was poured into a 1 L beaker. To this was added DI water, and this mixture was stirred until it formed a homogenous slurry. This slurry was air-dried for 48 h, and then transferred to a 140 °C glassware oven for an additional 48 h. The resulting SiO₂ was compact and clumpy. The material was then ground with a mortar and pestle until a finely divided, free-flowing powder resulted. 15 g of this material could be loaded into a quartz tube closed at one end and fitted with a gas-adapted ball-and-socket joint at the other end (borosilicate glass). The loaded quartz tube was placed in the tube furnace, taking care to center the SiO₂ over the heating element. The heating and atmosphere protocol listed in Fig. 4.5 was then followed to de-hydroxylate the SiO₂. After the tube was cooled to room temperature, it was sealed under vacuum and transferred to an N₂ atmosphere glovebox. The material was stored in sealed containers in the glovebox until further use.

Ti(NEt₂)₄ titrations of the material following reported procedure (above) provide a surface density Si-OH determination of 0.00031 ± 0.00005 mol/g SiO₂⁷⁰⁰ or 0.90 ± 0.11 Si-OH sites/nm². This correlates to a predicted Ti loading of 1.46 ± 0.12 wt %.

Preparation of [Ti]200 From Ti(NEt₂)₄ titrations, the surface abundance of Si-OH sites was estimated (0.00052 mol/g). A 125 mL Erlenmeyer flask was charged with 4g of SiO₂²⁰⁰ and 30 mL of pentanes. The slurry was stirred and 1.2 equiv of Ti(NMe₂)₄ (560 mg) was added

dropwise. The mixture was stirred for 4 h at room temperature during which time the colorless silica turned yellow. The solids were collected by filtration, rinsed with 20 mL of benzene, and dried under vacuum. The material was stored in an N₂ glovebox in a sealed container and used as needed. *ICP-OES*: 2.33 % Ti (\pm 0.12).

Preparation of [Ti]700 From Ti(NEt₂)₄ titrations the surface abundance of Si-OH sites was estimated (0.00031 mol/g). A 125 mL Erlenmeyer flask was charge with 6 g of SiO₂⁷⁰⁰ and 30 mL of pentanes. The slurry was stirred and 1.2 equiv of Ti(NMe₂)₄ (500 mg) was added dropwise. The mixture was stirred for 4 h at room temperature during which time the colorless silica turned yellow. The solids were collected by filtration, rinsed with 20 mL of benzene, and dried under vacuum. The material was stored in an N₂ glovebox in a sealed container and used as needed *ICP-OES*: 1.50 % Ti (\pm 0.07).

General Hydroamination Procedure with [Ti]200 A pressure tube was charged with 5 mol % [Ti]200 (100 mg) and a Teflon stir bar. A 1.0 mL solution containing 1 mmol NH₂R and 1-2 mmol Alkyne in *p*-cymene was then added to the pressure tube, which was sealed and transferred from the glovebox to a preheated aluminum block (180 °C). The pressure tube was heated for the desired amount of time with magnetic stirring. Upon reaction completion, the pressure tube was centrifuged, compacting the [Ti]200 into a pellet at the bottom of the tube. This leaves a transparent yellow to orange solution which was decanted and used for GC/MS or GC/FID analysis.

General 3CC Prodcedure with [Ti]200 A pressure tube was charged with 5 mol % [Ti]200 (100 mg) and a Teflon stir bar. A 1.50 mL solution containing 1 mmol NH₂R, 1-2 mmol alkyne, and 1.5 mmol CyNC in *p*-cymene was then added to the pressure tube, which was sealed and transferred from the glovebox to a preheated aluminum block (180 °C). The pressure tube was heated for the desired amount of time with magnetic stirring. Upon reaction completion, the

pressure tube was centrifuged, compacting the [Ti]200 into a pellet at the bottom of the tube and leaving a transparent yellow to orange solution which was decanted and used for GC/MS or GC/FID analysis.

General Hydroamination Procedure with [Ti]700 A 15 mL pressure tube was charged with 163 mg $\text{Ti}(\text{NMe}_2)_3/\text{SiO}_2^{700}$ (5 mol%), a stir bar, and 1.0 mL *p*-cymene. Separately, a volumetrically prepared 1.0 mL solution of 1 mmol NH_2R and 2 mmol alkyne was prepared. This solution was added to the catalyst mixture in the pressure tube, which was sealed and transferred from the glovebox to a preheated aluminum block (180 °C). The reaction was heated with magnetic stirring for 40 min-12 h. The pressure tube was ambiently cooled to room temperature, and centrifuged to compact the $\text{Ti}(\text{NMe}_2)_3/\text{SiO}_2^{700}$ into an orange-brown pellet at the bottom of the tube. The pressure tube was transferred back to the glovebox and the liquids decanted. The crude solution was utilized for GC analysis.

General 3CC Procedure with [Ti]700 A 15 mL pressure tube was charged with 163 mg $\text{Ti}(\text{NMe}_2)_3/\text{SiO}_2^{700}$ (5 mol%), a stir bar, and 1.0 mL *p*-cymene. Separately, a volumetrically prepared 1.0 mL solution of 1 mmol NH_2R , 1.5 mmol CyNC, and 2 mmol alkyne was prepared. This solution was added to the catalyst mixture in the pressure tube, which was sealed and transferred from the glovebox to a preheated aluminum block (180 °C). The reaction was heated with magnetic stirring for 12-36 h. The pressure tube was ambiently cooled to room temperature, and centrifuged to compact the $\text{Ti}(\text{NMe}_2)_3/\text{SiO}_2^{700}$ into an orange pellet at the bottom of the tube. The pressure tube was transferred back to the glovebox and the liquids decanted. The crude solution was utilized for GC analysis.

General Procedure: Recycling Experiments The general procedure for HA or 3CC was followed for set-up of the initial reaction with either [Ti]200 or [Ti]700. Upon completion of the

initial reaction (run 1), the pressure tube was cooled ambiently, centrifuged, and returned to the glovebox. The catalyst material was collected by filtration and thoroughly rinsed (20 mL aromatic solvent followed by 20 mL hexane). The catalyst material was dried under vacuum and loaded into a new pressure tube with a stir bar. The reagent solution for a second reaction (run 2) was then loaded into the tube. The tube was sealed and returned to heat (180 °C, aluminum well plate), and the process repeated as many times as needed. The filtrate solutions were reserved for GC analysis.

General Notes about Quantification and Product Characterization:

Reduced derivatives of the hydroamination products were isolated from catalyzed reactions with [Ti]200. These isolated derivatives provided evidence for the favored regioisomer (NMR) and allowed for verification of retention times by GC-MS. The isolated derivatives were also utilized to generate GC-FID calibration curves of the hydroamination products, which allowed for further quantification of hydroamination yields by GC analysis in crude reaction solutions and products identification by GC retention times. For those hydroamination products which could not be isolated from the catalyzed reaction mixtures due to poor yield, quantification was performed using the next closest isolated hydroamination derivatives.

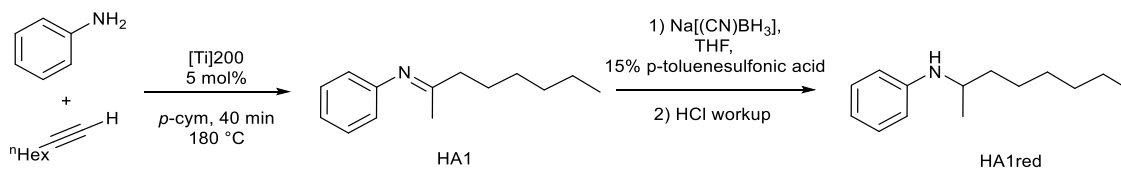
Similarly, iminoamination products were quantified in the crude reaction mixture using GC-FID analysis. Both 3CC1 and 3CC5 were successfully isolated from these catalyzed iminoamination reactions. The compounds were characterized by NMR, which allowed for regioisomer identification. They were used to provide GC-FID calibration curves, allowing for further quantification of similar 3CC derivatives in the crude reaction solutions, using GC-FID analysis. Retention times confirmed product identity by GC-MS.

Reduction of Hydroamination Products and Isolation of Amine Derivatives HA products (with which GC-FID calibrations were performed) were isolated from 3 mmol scales of

the starting amine, following the General Procedure listed in the Experimental section. The resulting imine products were reduced to their respective amine derivatives for isolation. In a glovebox, the crude reaction mixture was decanted from the solid catalyst, which was rinsed with 5 mL of THF. The THF wash and crude *p*-cymene solution were combined with 2 equiv of Na[B(CN)H₃] (6 mmol) and another 10 mL of THF in a Schlenk flask, and the reaction was transferred to a Schlenk line. The reaction mixture was stirred and 15 mol% *p*-toluenesulfonic acid was added. The reaction was stirred 4 h at room temperature, after which time 5 mL of 2 M HCl solution was added and stirring was continued for an additional hour. The solution was neutralized (pH 7-8) and extracted with Et₂O (3 x 30 mL). The volatiles were removed from the extracted organic layer by rotary evaporation to give a viscous yellow oil, which was purified by column chromatography (typically silica gel basified with NEt₃ using a hexane/EtOAc gradient as eluent).

Amine Derivative for Hydroamination Entry 1:⁵²

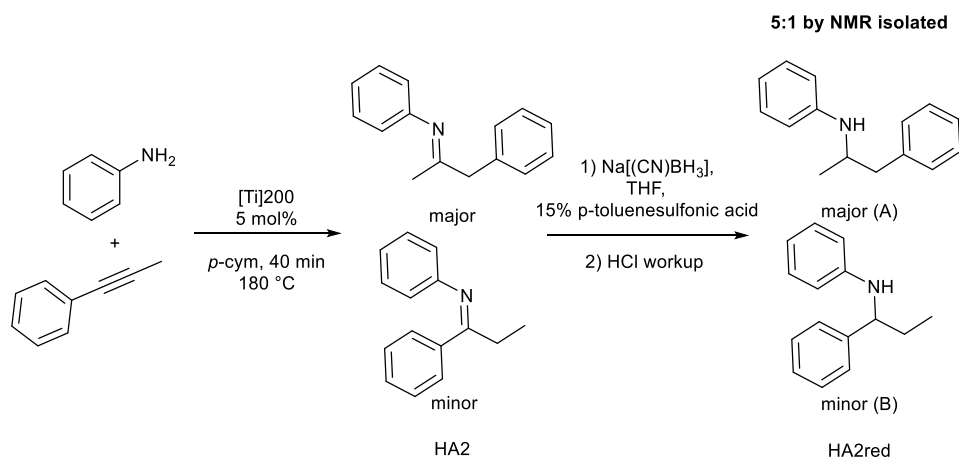
¹H NMR (500 MHz, 21 °C, CDCl₃): 7.17 (dd, *J* = 8.6, 7.3 Hz, 2H), 6.67 (t, *J* = 7.2 Hz, 1H), 6.61–6.57 (m, 2H), 3.46 (sextet, *J* = 6.2 Hz, 1H), 1.63–1.52 (m, 1H), 1.47–1.23 (m, 11H), 1.19 (d, *J* = 6.3 Hz, 3H), 0.89 (t, 3H). ¹³C NMR (126 MHz, 21 °C, CDCl₃): 147.83, 129.39, 116.84, 113.17, 48.58, 37.38, 32.01, 29.53, 26.29, 22.82, 20.96, 14.27. Yield: 51% (yellow oil)



Scheme 4.4 HA Entry 1 synthesis and isolation.

Amine Derivative for Hydroamination Entry 2:^{53,54}

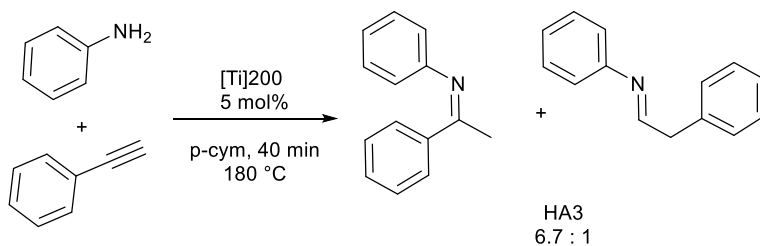
¹H NMR (500 MHz, 21 °C, CDCl₃): δ *major isomer A* (aliphatic): 6.80–6.71 (t, $J = 7.3$ Hz, 3H), 6.68 (d, $J = 8.7$, 2H), 3.91–3.76 (m, 1H), 2.99 (dd, $J = 13.4, 4.7$ Hz, 1H), 2.75 (dd, $J = 13.4, 7.3$ Hz, 1H), 1.20 (d, $J = 6.4$ Hz, 3H). ¹H NMR (500 MHz, 21 °C, CDCl₃): δ *minor isomer B* : 7.15–7.10 (m, 2H), 6.56 (d, $J = 7.6$ Hz, 2H), 4.27 (t, $J = 6.7$ Hz, 1H), 1.94–1.72 (m, 2H), 1.00 (t, $J = 7.4$ Hz, 3H). Aromatic region of isomeric mixture also shows the following overlapping multiplets: δ 7.41–7.31 (m), 7.29–7.26 (m), 7.26–7.22 (m). ¹³C NMR (126 MHz, 21 °C, CDCl₃): *isomeric mixture*: δ 147.52, 147.23, 143.94, 138.57, 129.54, 129.40, 129.10, 128.51, 128.35, 126.90, 126.50, 126.30, 117.19, 117.12, 113.36, 113.24, 59.72, 49.34, 42.30, 31.71, 20.22, 10.89. Yield: 33% (yellow oil)



Scheme 4.5 HA Entry 2 synthesis and isolation.

Amine Derivative for Hydroamination Entry 3:⁵⁵

HA3^{red}: Both isomers of HA3^{red} have been previously reported in the literature. Difficulties were encountered in isolating one or both regioisomers of HA3^{red} from the alkyne trimerization byproduct that inevitably forms due to the excess of alkyne needed to force the reaction to completion. After repeated column chromatography, the major isomer was determined from matching peaks in ¹H NMR to reports by Kato, et. al., referenced to the retention times of the two isomers in the crude reduction mixture. Identification is shown below, by GCMS and ¹H NMR identification in the impure mixture. This sample was not utilized for *in situ* quantification of the yield of this reaction. Rather it served only to identify the major regioisomer. ¹H NMR (500 MHz, Chloroform-d): 7.36–7.32 (m, 2H), 7.28 (t, J = 8.5, 6.8 Hz, 2H), 7.20 (m, J = 5.5, 1.8 Hz, 1H), 7.06 (t, J = 7.3 Hz, 2H), 6.61 (t, J = 7.3 Hz, 1H), 6.52–6.43 (m, 2H), 4.52–4.40 (m, 1H), 3.99 (s(br), 1H), 1.48 (d, J = 6.7 Hz, 3H).

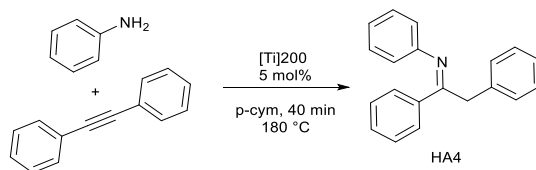


Scheme 4.6 HA entry 3 synthesis and isolation.

Hydroamination Entry 4 (Imine product):⁵⁶

¹H NMR (500 MHz, CDCl₃): 7.97 (dd, *J* = 8.0, 1.7 Hz, 2H), 7.40 (d, *J* = 7.7 Hz, 3H), 7.37–7.31 (t, 2H), 7.25 (s, 2H), 7.21–7.14 (m, 1H), 7.12 (m, 3H), 6.90–6.85 (d, *J* = 7.0 Hz, 2H), 4.12 (s, 2H).

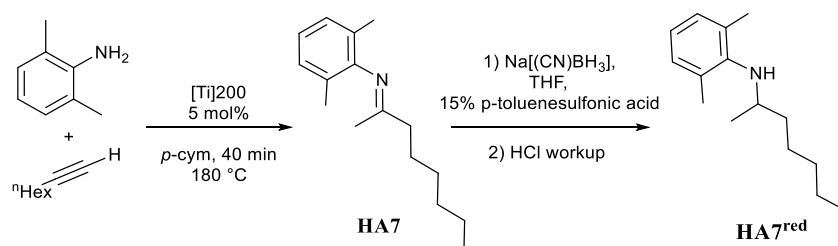
¹³C NMR (126 MHz, 21 °C, CDCl₃): 166.27, 151.11, 138.32, 137.14, 130.39, 129.03, 128.65, 128.43, 128.38, 128.11, 126.30, 123.43, 119.14, 36.27. Yield: 57 %, pale yellow crystalline solid



Scheme 4.7 HA entry 4 synthesis and isolation

Amine Derivative of Hydroamination Entry 7:⁵⁷

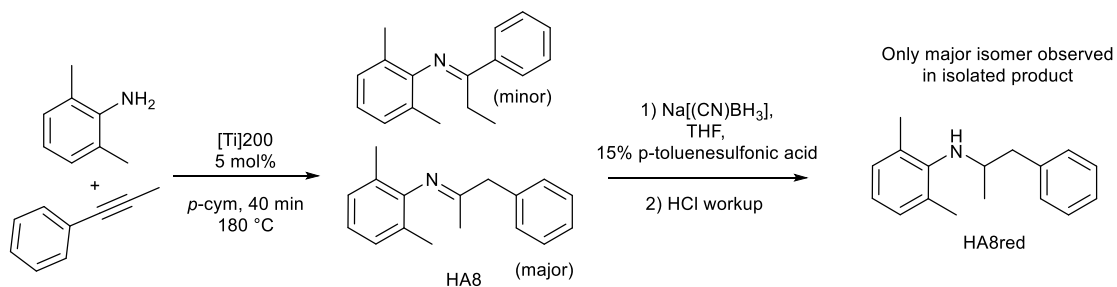
¹H NMR (500 MHz, 21 °C, CDCl₃): δ 6.98 (d, *J* = 7.5 Hz, 2H), 6.79 (t, *J* = 7.5 Hz, 1H), 3.31–3.22 (m, 1H), 2.82 (s, 1H), 2.26 (s, 6H), 1.62–1.48 (m, 1H), 1.45–1.35 (m, 3H), 1.32–1.24 (m, 7H), 1.05 (d, *J* = 6.3 Hz, 3H), 0.89 (t, *J* = 6.8 Hz, 3H). ¹³C NMR (126 MHz, 21 °C, CDCl₃): δ 145.21, 128.86, 128.79, 121.00, 52.42, 38.48, 31.87, 29.51, 26.45, 22.64, 21.37, 19.11, 14.10. Yield: 34% (yellow oil)



Scheme 4.8 HA entry 7 synthesis and isolation.

Amine Derivative of Hydroamination Entry 8:⁵⁸

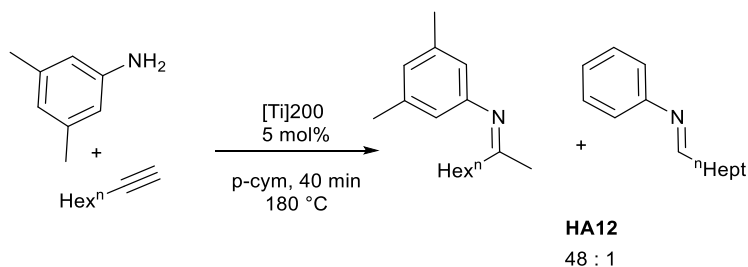
¹H NMR (500 MHz, 21 °C, CDCl₃): δ 7.34–7.27 (m, 2H), 7.24–7.16 (m, 2H), 7.00 (d, *J* = 7.4 Hz, 2H), 6.82 (t, *J* = 7.5 Hz, 1H), 3.66–3.41 (sextet, *J* = 6.2 Hz, 1H), 2.95 (dd, *J* = 13.0, 4.7 Hz, 2H), 2.56 (ddd, *J* = 12.9, 8.5, 1.8 Hz, 1H), 2.25 (s, 6H), 1.06 (d, *J* = 6.3 Hz, 3H). ¹³C NMR (126 MHz, 21 °C, CDCl₃): δ 144.88, 139.51, 129.51, 129.32, 129.00, 128.38, 126.23, 121.53, 54.18, 44.53, 20.93, 19.19. Yield: 52% (yellow oil) (1 mmol scale)



Scheme 4.9 HA entry 8 synthesis and isolation.

Amine Derivative of Hydroamination Entry 12:

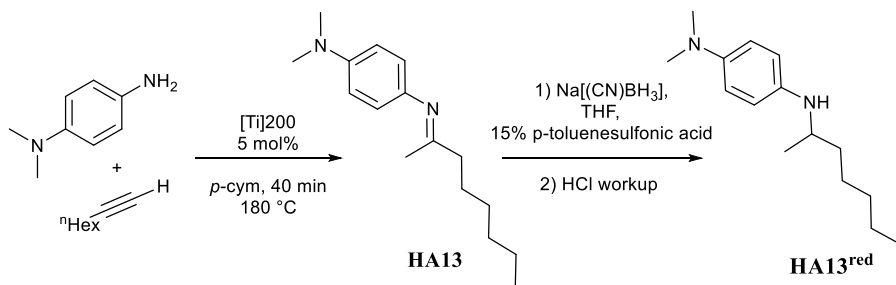
No spectral data for HA12^{red} was found reported in the literature. The spectral data support the structural assignment shown below. ¹H NMR (500 MHz, Chloroform-d): 6.33 (s, 1H), 6.22 (s, 2H), 3.43 (pent, J = 6.3 Hz, 1H), 3.33 (s, 1H), 2.23 (d, J = 2.1 Hz, 6H), 1.63–1.45 (m, 2H), 1.42–1.21 (m, 14H), 1.15 (d, J = 6.3 Hz, 3H), 0.89 (m, 6H). ¹³C NMR (126 MHz, Chloroform-d): 147.77, 138.87, 118.72, 110.93, 48.33, 37.31, 31.84, 29.36, 26.13, 22.64, 21.53, 20.89, 14.11. EI-MS: m/z HA12 231 (base 160); HA12^{red} 233 (base 148). Yield: 120 mg (1 mmol scale), 52 % (yellow oil).



Scheme 4.10 HA entry 12 synthesis and isolation.

Amine Derivative of Hydroamination Entry 13:

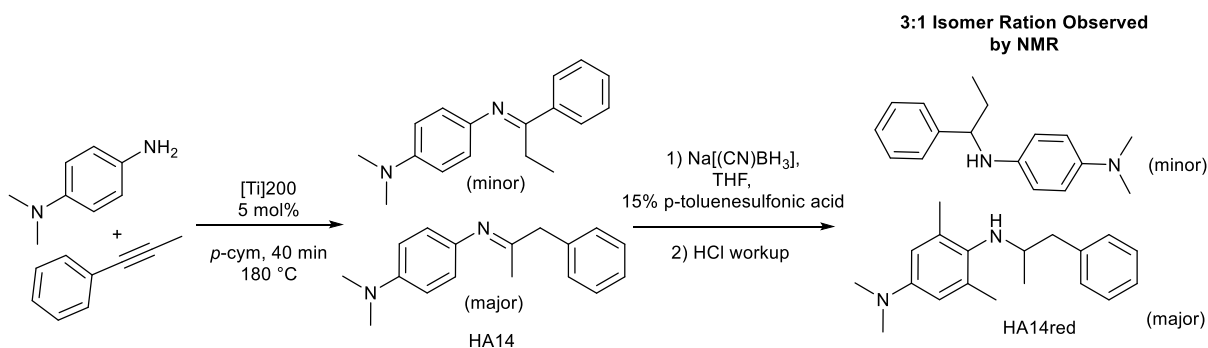
^1H NMR (500 MHz, 21 °C, benzene- d_6): 6.77 (d, $J = 8.8$ Hz, 2H), 6.58 (d, $J = 8.8$ Hz, 2H), 3.31 (sextet, $J = 6.2$ Hz, 1H), 2.61 (s, 6H), 1.47–1.37 (m, 2H), 1.34–1.19 (m, 10H), 1.03 (d, $J = 6.2$ Hz, 3H), 0.90 (t, $J = 7.0$ Hz, 3H). ^{13}C NMR (126 MHz, 21 °C, benzene- d_6): 144.43, 140.81, 116.32, 115.40, 49.69, 42.20, 37.69, 32.31, 29.89, 26.60, 23.09, 21.10, 14.39, 1.44. Yield: 19 % (reddish oil).



Scheme 4.11 HA entry 13 synthesis and isolation.

Amine Derivative of Hydroamination Entry 14:

^1H NMR (500 MHz, 21 °C, benzene- d_6): (*major A*) 7.23 (d, $J = 7.9$ Hz, 1H), , 7.12–7.04 (m, 4H), 6.76 (d, $J = 8.2$ Hz, 2H), , 6.58 (d, $J = 8.4$ Hz, 2H), 3.58 (sextet, $J = 6.0$ Hz, 1H), 2.77 (dd, $J = 13.3, 4.7$ Hz, 1H), 2.62 (s, 6H), 2.46 (dd, $J = 13.6, 7.6$ Hz, 1H), 0.95 (d, $J = 6.3$ Hz, 3H). ^1H NMR (500 MHz, 21 °C, benzene- d_6): (*minor B*) 7.14 (s, 2H (5)), 6.62 (d, $J = 8.7$ Hz, 0.67H (2)), 6.51 (d, $J = 8.3$ Hz, 0.57H (2)), 4.07 (t, $J = 6.7$ Hz, 0.29H (1)), 2.53 (s, 1.65H (6)), 1.55 (quintet, $J = 7.5$ Hz, 0.65H (2)), 1.18 (dt, $J = 6.9, 1.9$ Hz, 0.22H (1)), 0.78 (t, $J = 7.4$ Hz, 0.90H (3)). ^{13}C NMR (126 MHz, 21 °C, benzene- d_6) isomeric mixture: 144.18, 144.06, 140.02, 139.74, 138.98, 129.50, 128.29, 128.15, 127.96, 126.58, 126.01, 115.82, 115.60, 115.25, 114.90, 60.40, 50.20, 42.13, 41.68, 41.64, 31.60, 19.89, 10.54. Yield: 24% (orange oil)



Scheme 4.12 HA entry 14 synthesis and isolation.

Isolation of 3CC1 Isomer:

A sample of one of the isomers of 3CC1 was isolated from the reaction of $\text{Ti}(\text{NMe}_2)_2\text{dpm}$ (20 mol%) as catalyst, 2,6-dimethylphenylaniline (1) (1 equiv, 3 mmol), 1-octyne (1 equiv, 3 mmol), and cyclohexylisocyanide (1.5 equiv, 4.5 mmol) in toluene at 110 °C. The crude reaction mixture was concentrated, and 3CC1 was separated by column chromatography (basified alumina, gradient pentane:Et₂O) to yield 235 mg of the product. This sample was used to quantify GC/FID yields for the other 3CC compounds synthesized by [Ti]200.

The NMR and MS characterization are consistent with similar derivatives isolated in previous studies by our group. Yield: 235 mg, (24%, orange oil). ¹H NMR (500 MHz, CDCl₃): 9.89 (s, 1H), 7.02 (d, J = 7.4 Hz, 2H), 6.85 (t, J = 7.5 Hz, 1H), 6.71 (d, J = 7.8 Hz, 1H), 4.68 (d, J = 7.7 Hz, 1H), 3.00 (s, 1H), 2.05 (s, 6H), 1.93-1.84 (m, 3H), 1.75-1.68 (m, 2H), 1.55 (m, 2H), 1.41-1.08 (m, 18H), 0.94-0.87 (m, 2H), 0.82 (t, J = 7.1 Hz, 3H). ¹³C NMR (126 MHz, CDCl₃): 170.52, 149.54, 145.16, 128.46, 127.65, 121.77, 90.73, 57.00, 34.63, 34.38, 31.64, 29.53, 27.74, 25.64, 24.84, 22.57, 18.71, 14.17. EI-MS: m/z 340 (base 255).

Assessment of purity for use as GCFID quantification sample: Elemental analysis Calc'd for C₂₃H₃₆N₂ (3CC product above): C, 81.12; H, 10.66; N, 8.23. Based on ¹H and ¹³C NMR, an impurity of 13 mol% triethylamine (TEA) is evident in the isolated 3CC product, as a result of basifying the column material used to separate the crude reaction mixture. Even after extended time under reduced pressure, the TEA remains present in the 3CC sample, likely due to hydrogen bonding interactions with the 3CC amine moiety. This amount of TEA impurity correlates to a modified molecular formula of C₂₃H₃₆N₂·0.13(C₆H₁₅N). Comparison of the anticipated elemental analysis results with this impurity versus the experimentally determined elemental analysis is shown below: Elemental analysis Calc'd for C₂₃H₃₆N₂·0.13(C₆H₁₅N): C, 80.75; H, 10.81; N, 8.43.

Found: C, 80.34; H, 10.52; N, 7.99. The results match closely with the molecular formula including the proportional amount of TEA observed by NMR. The FID calibration samples were adjusted for this impurity.

Isolation of 3CC5:

An authentic sample of one of the regioisomers of 3CC5 was isolated in a similar way as described above. This compound was used to calibrate the GCFID response for 3CC5. Characterization data for this product are shown below.

Isolated 3CC Isomer of Iminoamination Entry 5: Yield: 185 mg (53%, 1 mmol). ^1H NMR (500 MHz, CDCl_3) 10.42 (s, 1H), 7.32 (t, $J = 7.6$ Hz, 2H), 7.28–7.23 (m, 2H), 7.23–7.17 (m, 1H), 7.08 (d, $J = 7.5$ Hz, 2H), 6.90 (t, $J = 7.5$ Hz, 1H), 6.85 (s, 1H), 3.07 (sextet, $J = 9.2, 4.5$ Hz, 1H), 2.13 (s, 6H), 1.98–1.87 (m, 2H), 1.79–1.70 (m, 3H), 1.60 (s, 3H), 1.31 (m, 6H). ^{13}C NMR (126 MHz, CDCl_3) 165.82, 150.63, 147.53, 142.32, 130.52, 128.68, 127.98, 125.36, 122.31, 121.58, 107.65, 57.81, 34.52, 25.50, 24.96, 24.62, 20.33. EI-MS: m/z 346 (base 331). Elemental Analysis Calc'd for $\text{C}_{24}\text{H}_{30}\text{N}_2$: C, 83.19; H, 8.73; N, 8.08. Found: C, 82.82; H, 8.56; N, 7.62.

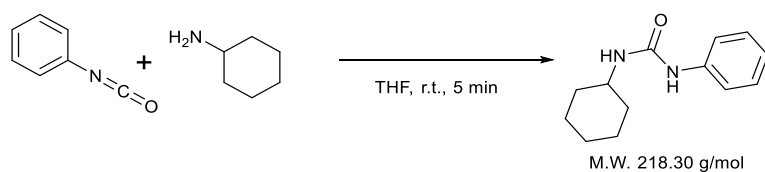
Investigations into Catalyst Deactivations

After running a 3CC reaction following the general procedure, the contents of the pressure tube were centrifuged to compact the catalyst material into a tight pellet at the bottom of the tube. In air, the organic phase was removed, and the catalyst material washed several times with hexanes (3 * 5 mL), vortexing and centrifuging with each wash. The catalyst material was air-dried and then washed with 3 mL of a dilute (10%) HCl solution. The HCl aliquot was then neutralized to pH 7-8 with sodium bicarbonate solution, and extracted with Et₂O, followed by EtOAc. The organic extracts were combined and examined by GCMS.

The GC results show several new compounds in the HCl wash not observed in the organic phase while some remain unidentified, two masses appear with m/z 218 and 224. In particular, the mass of 218 was determined to closely match that of 1-phenyl-3-cyclohexyl-urea. The urea was independently synthesized by literature procedures,⁵⁹ and the retention time and fragmentation pattern determined on the same instrument as the authentic samples. The synthesized urea and the peak observed with the same mass in the HCl wash display very similar retention times and fragmentation patterns. Thus, we believe this is likely the identity of the organic residue. Likewise, the m/z 224 peak has the same mass as 1,3-dicyclohexylurea. GC/MS fragmentation patterns are shown below (Fig. 4.44-4.46).

While other species are also examined in the HCl wash extract of the catalyst material, from the identification of the urea species, and the observation that both cyclohexyl and phenyl groups are involved, we know that an off-cycle interaction between anilide and the cyclohexylisocyanide are leading to new and previously undetected reactivity. Also of note is the fact that these species are not observed in the hexanes washes of the catalyst material. Only once an aqueous acid is added to the catalyst material do these species appear, which suggests that they

are tightly bound to the surface. The types of ligand-metal interactions that can be drawn between an carbodiimide-like species or a urea species and a metal would make for good ligands for a Ti(IV) metal center, and may be related to the catalyst poisoning observed in these reactions.



Scheme 4.13 Targeted synthesis of asymmetric urea species.

Spectra of Isolated Hydroamination and 3CC Derivatives

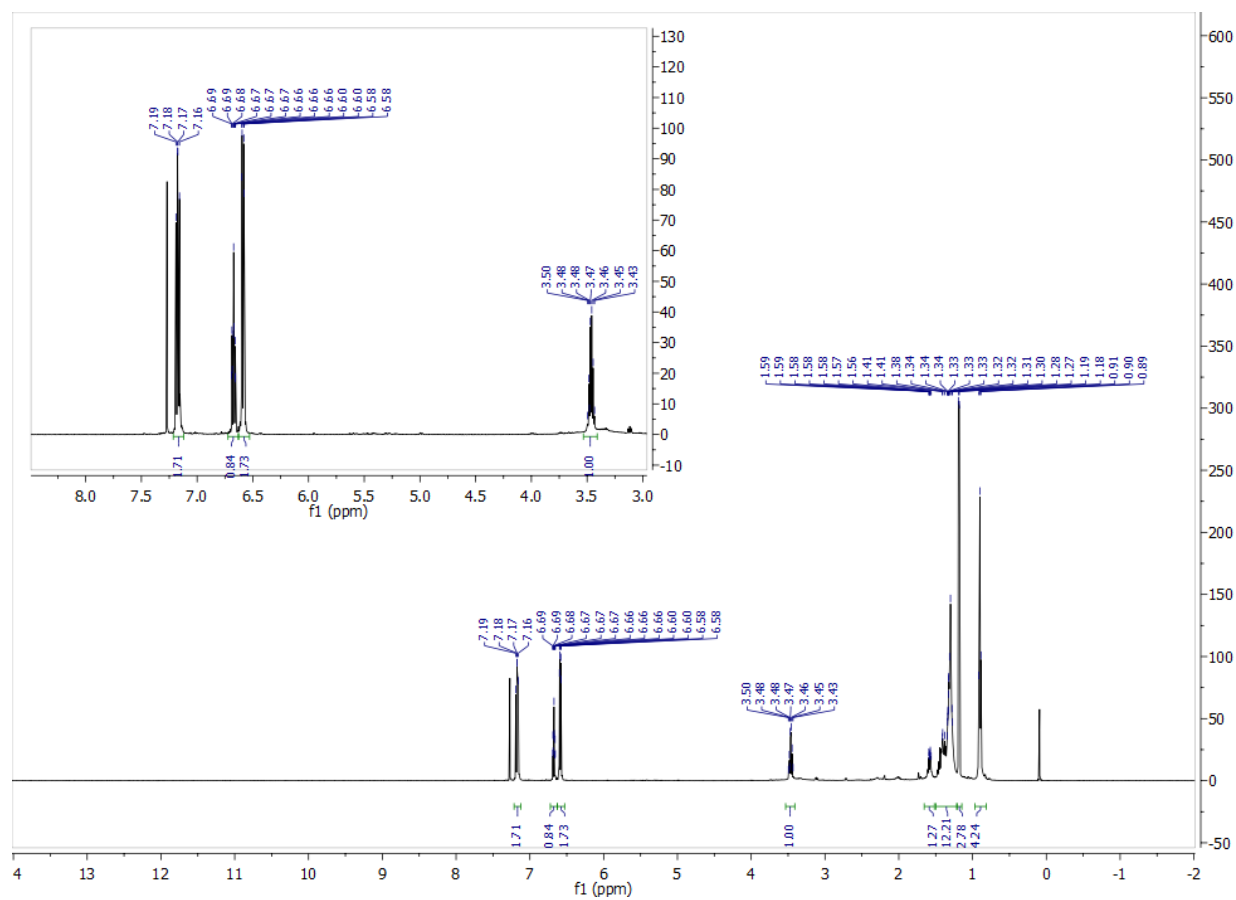


Figure 4.11 ^1H NMR of HA1^{red} in CDCl_3 .

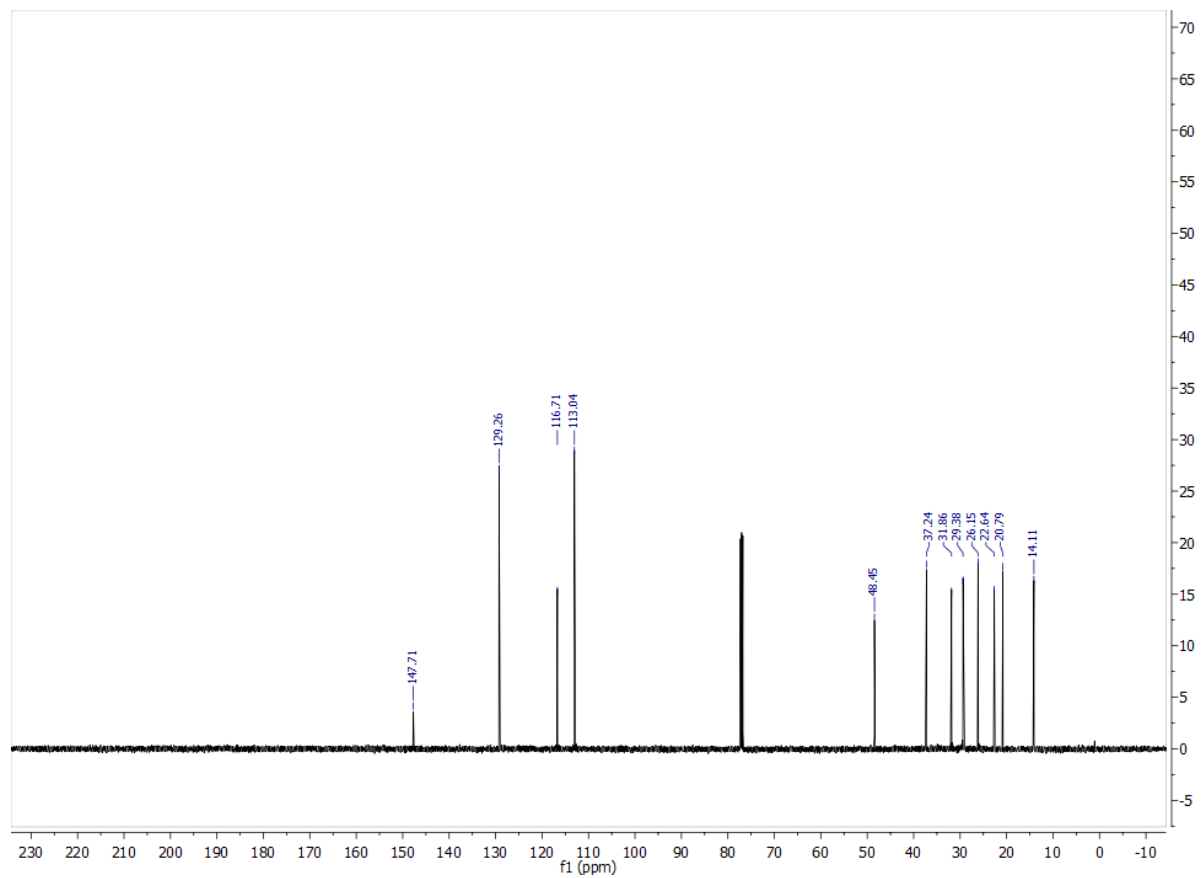


Figure 4.12 ^{13}C NMR of HA1^{red} in CDCl_3 .

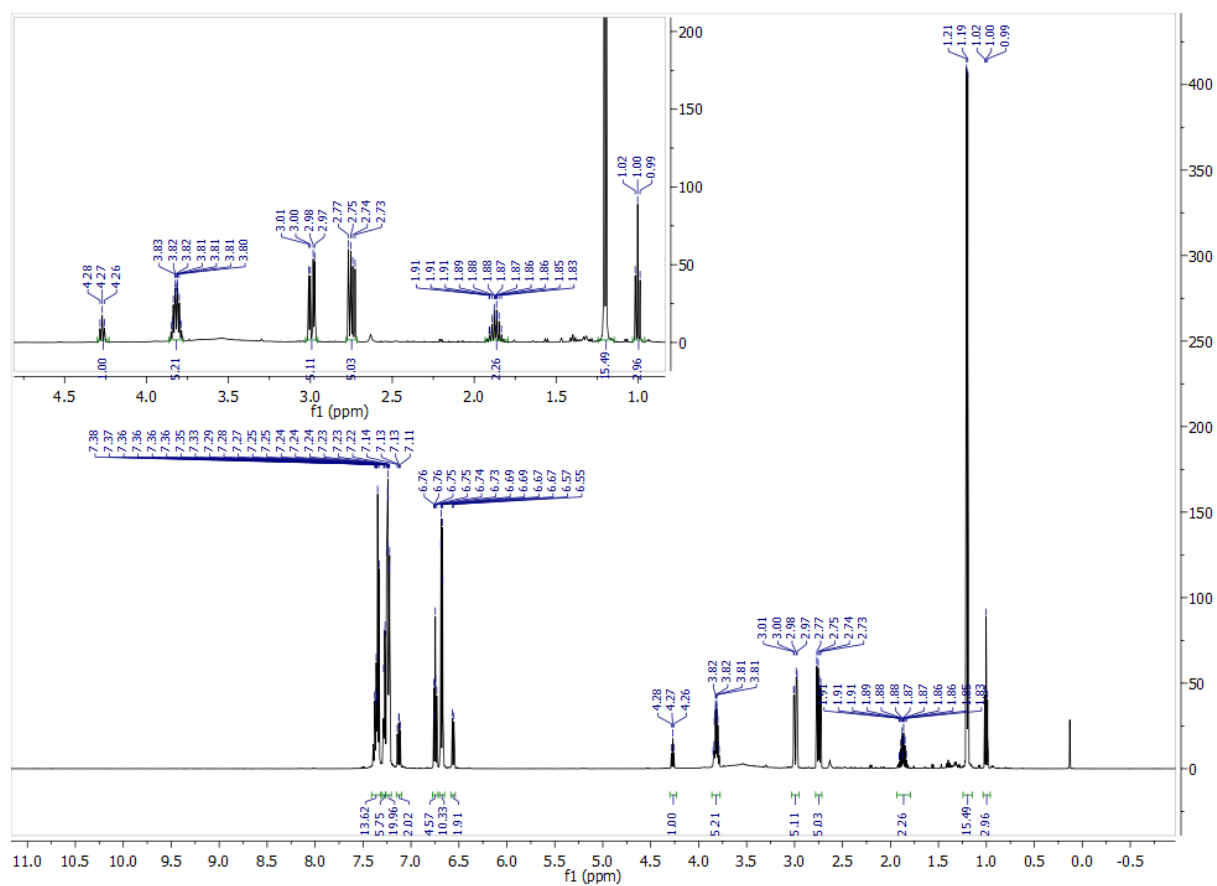


Figure 4.13 ¹H NMR of HA2^{red} in CDCl₃.

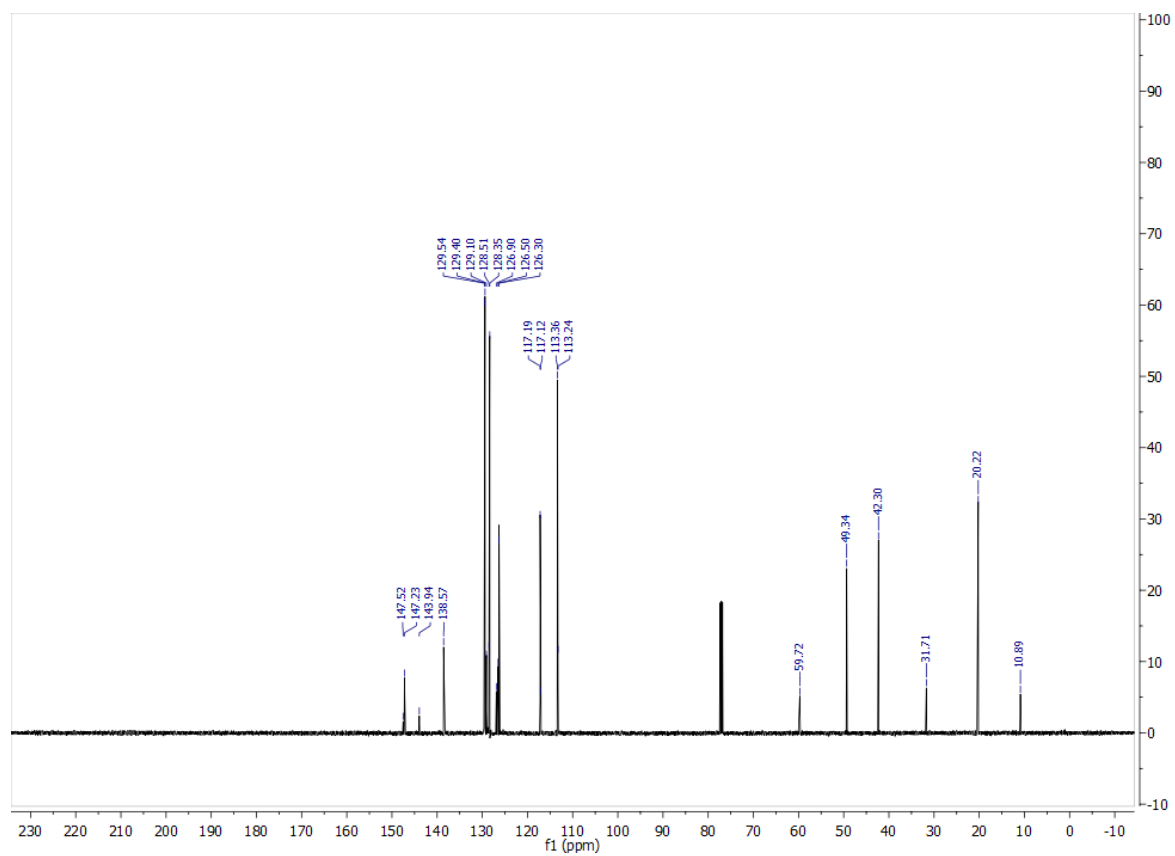


Figure 4.14 ^{13}C NMR of HA2^{red} in CDCl_3 .

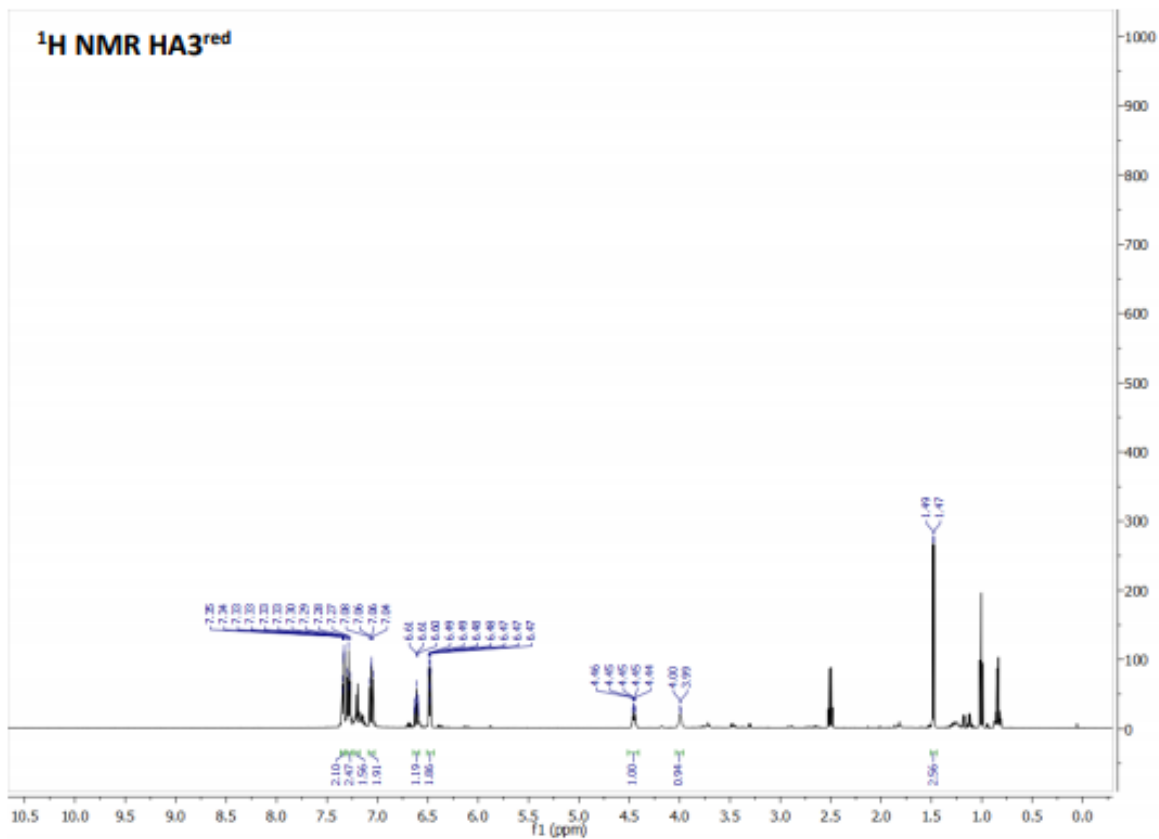


Figure 4.15 ¹H NMR of HA3^{red}

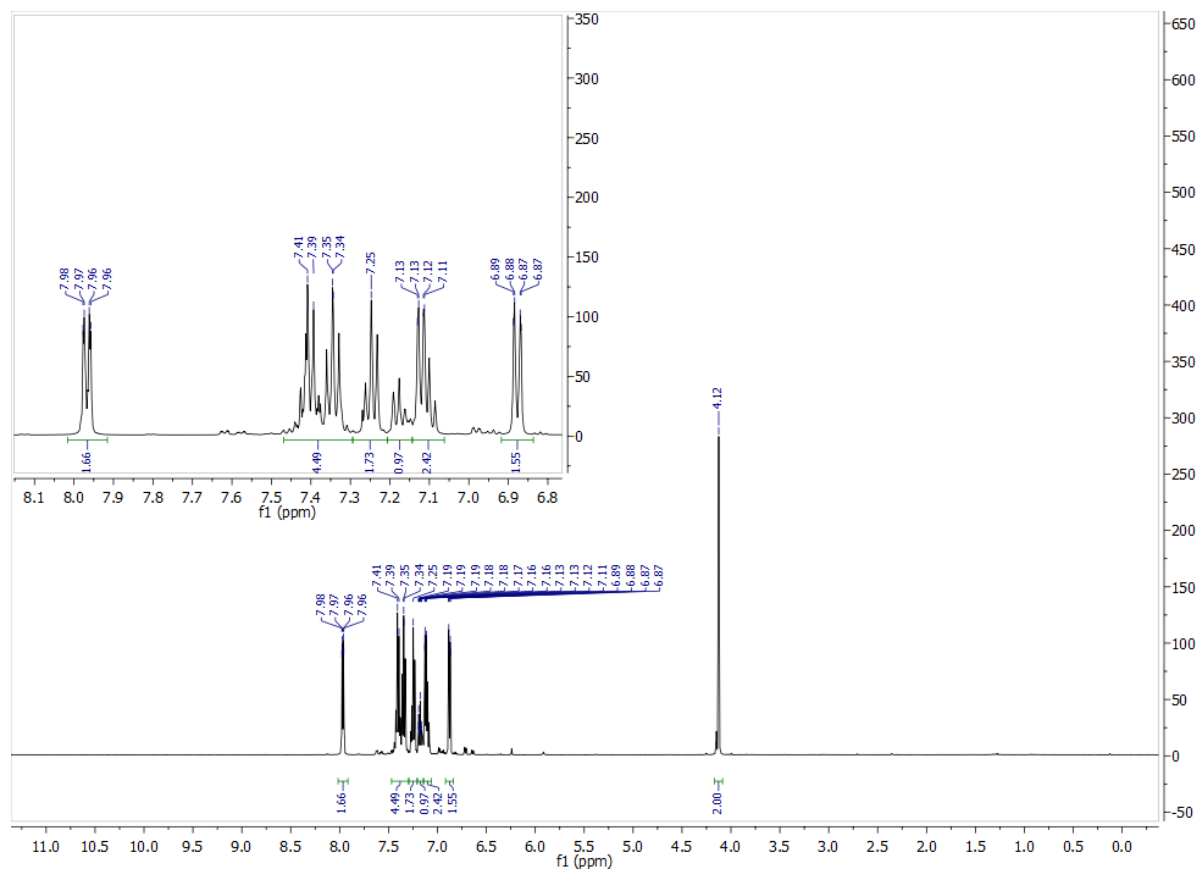


Figure 4.16 ^1H NMR of HA4 in CDCl_3 .

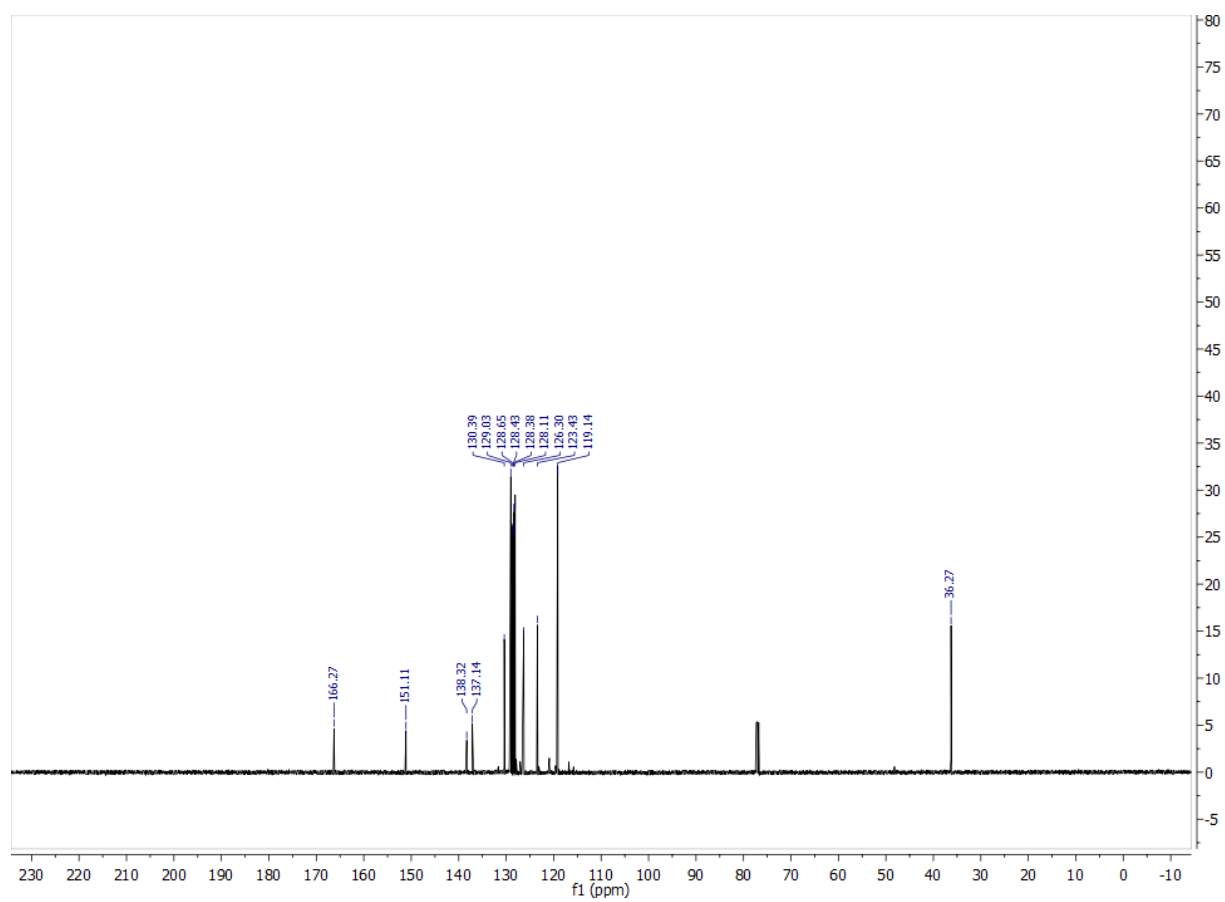


Figure 4.17 ^{13}C NMR of HA4 in CDCl_3 .

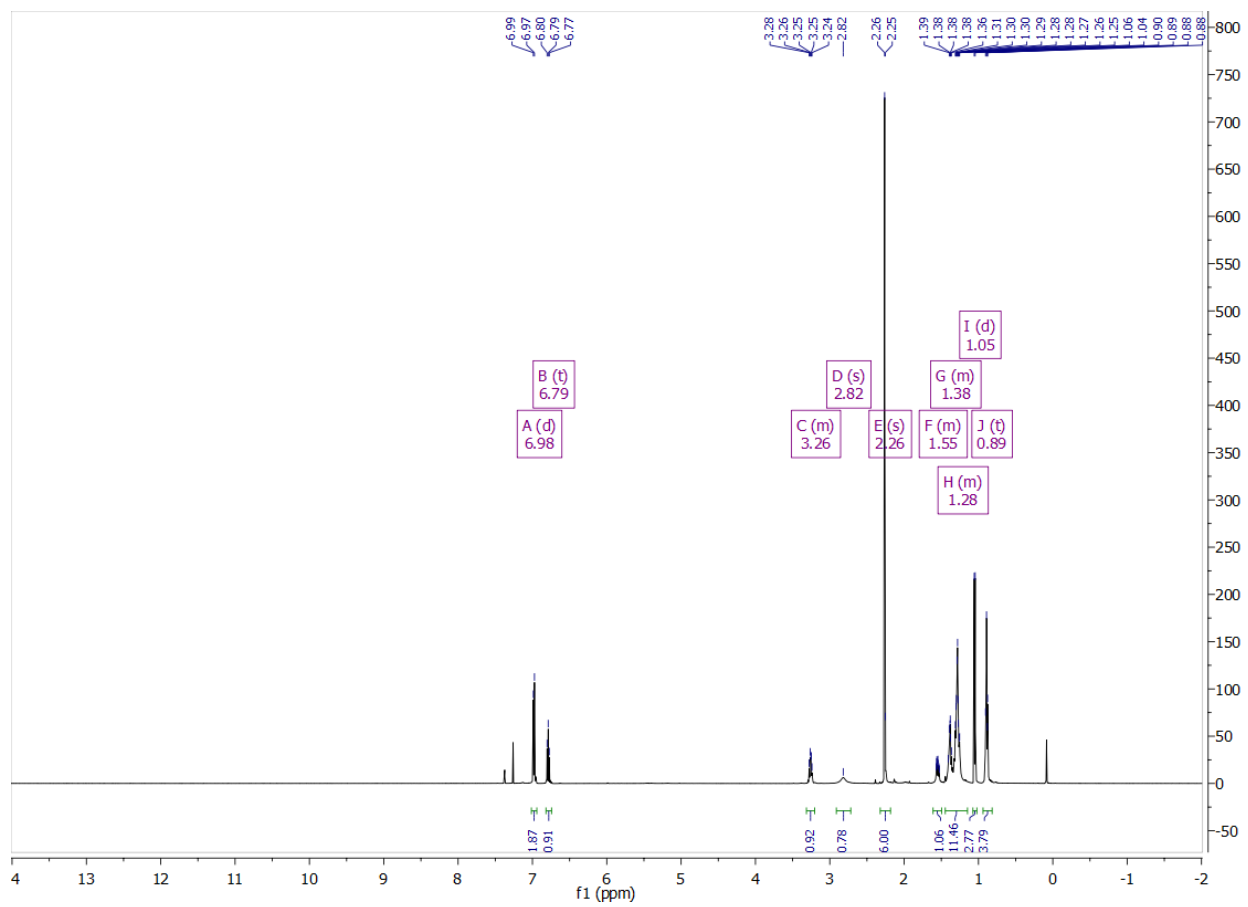


Figure 4.18 ^1H NMR of HA7^{red} in CDCl_3 .

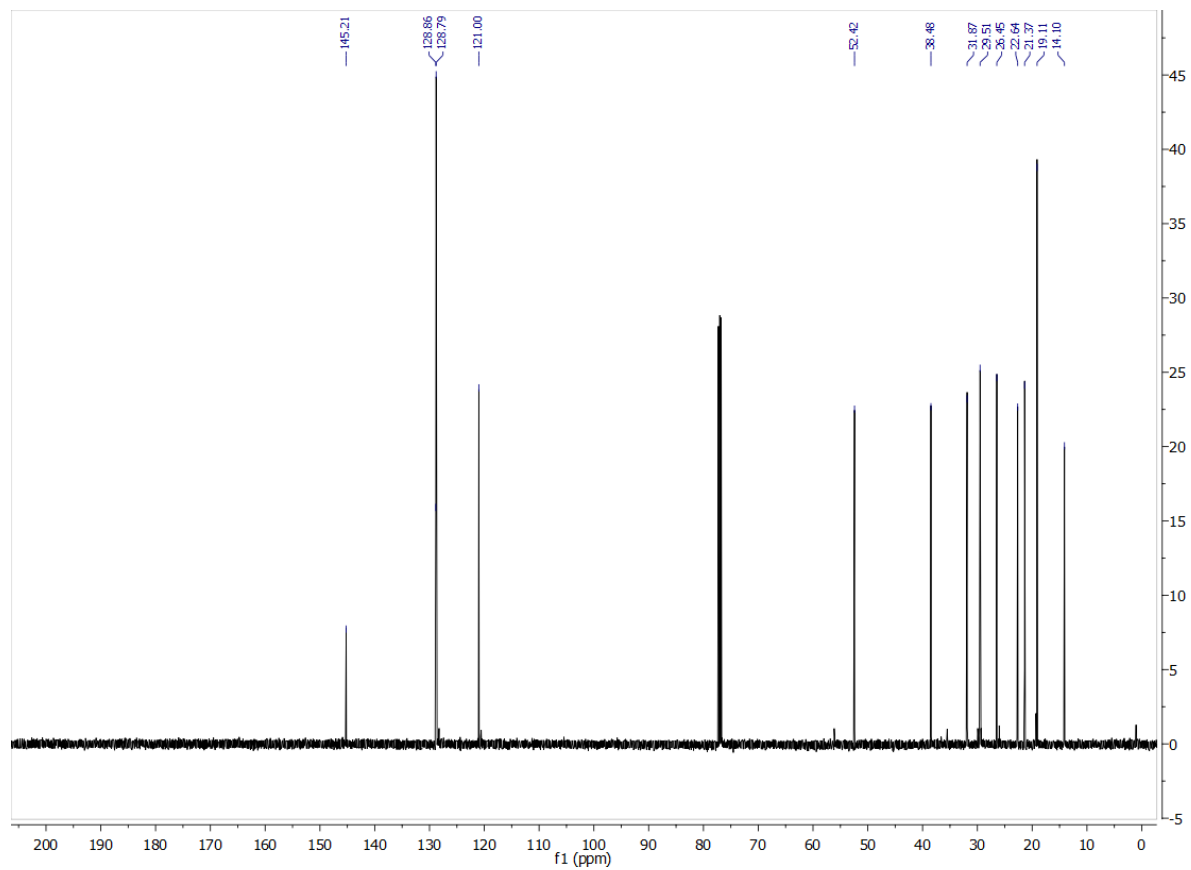


Figure 4.19 ^{13}C NMR of HA7^{red} in CDCl_3 .

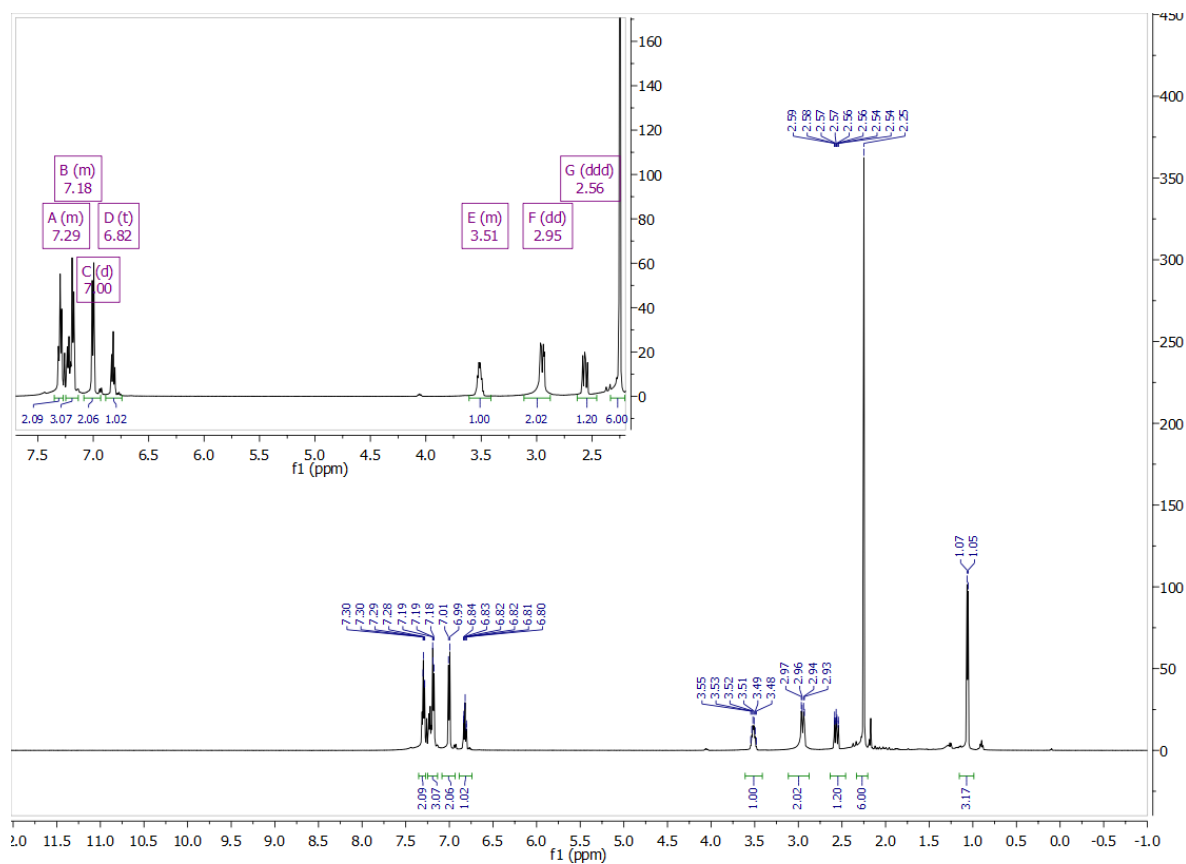


Figure 4.20 ^1H NMR of HA8^{red} in CDCl_3 .

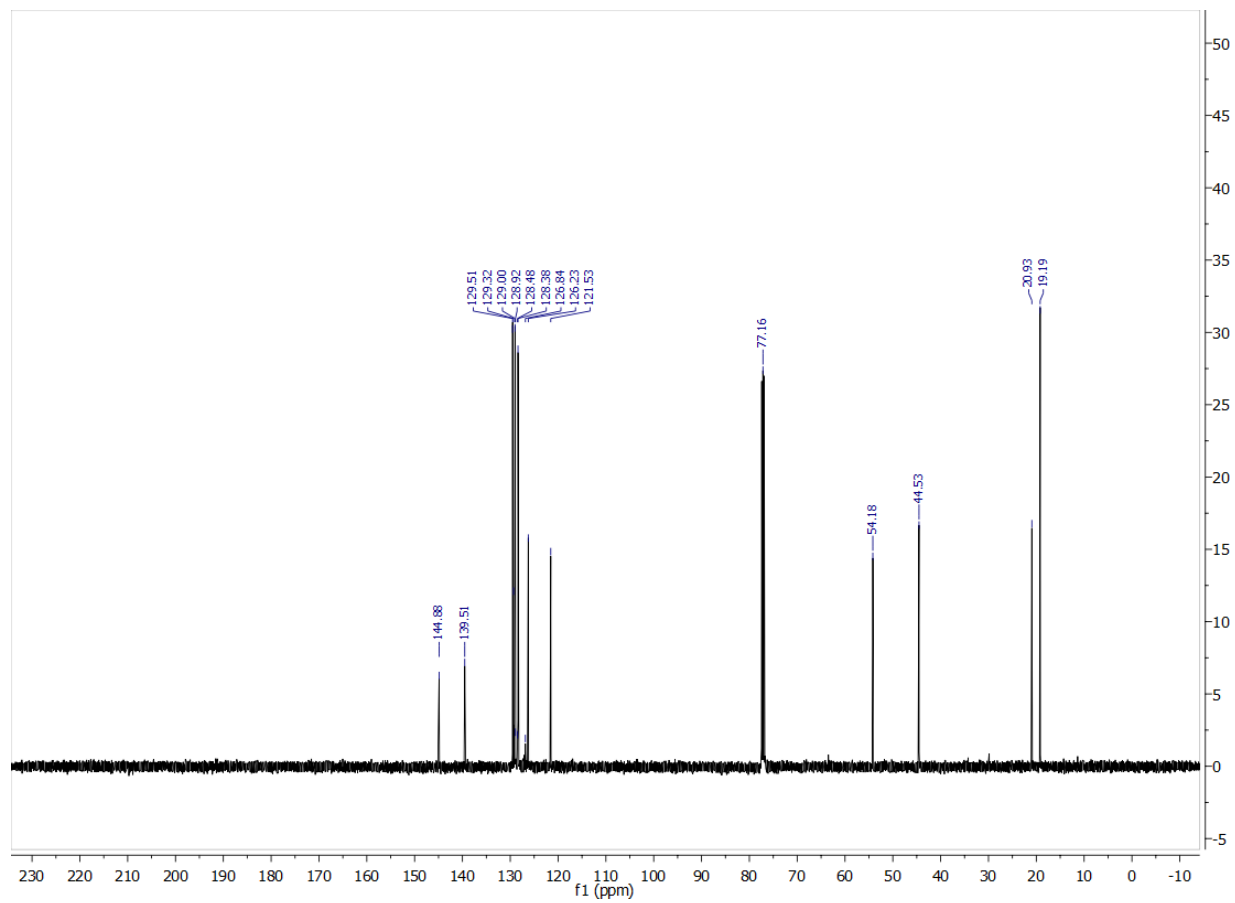


Figure 4.21 ^{13}C NMR of HA8^{red} in CDCl_3 .

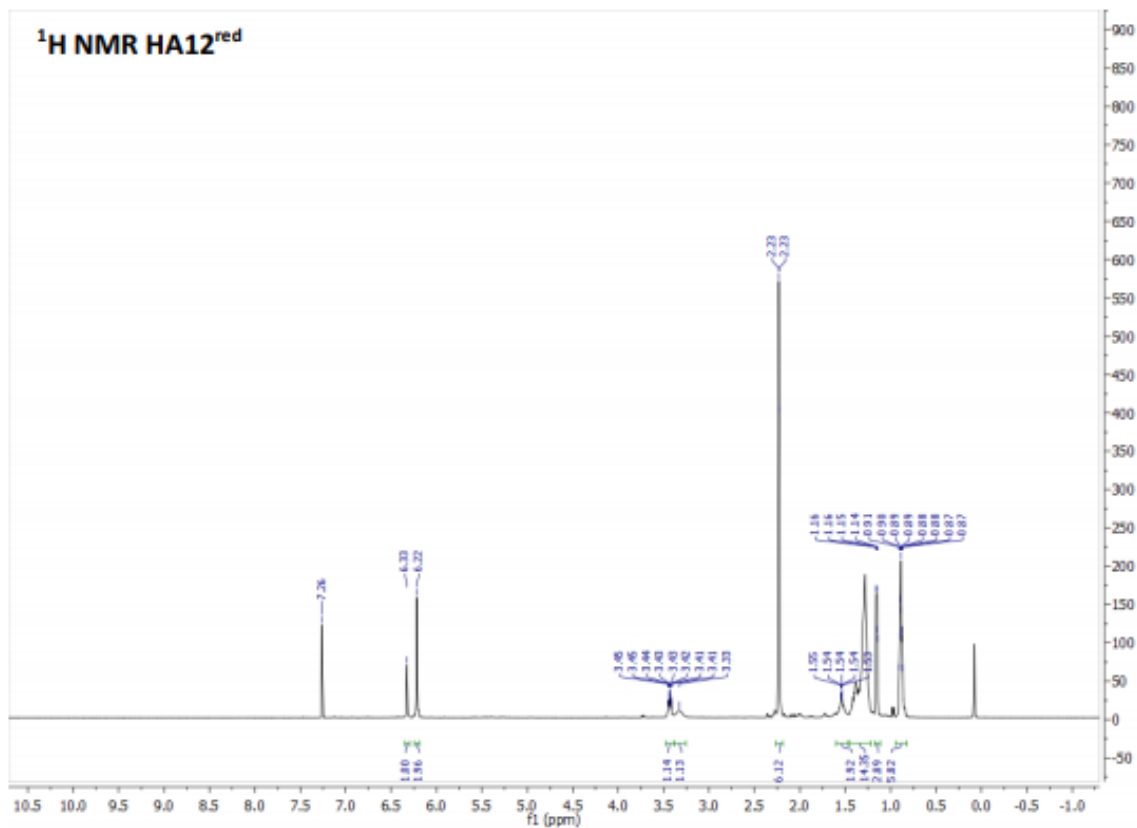


Figure 4.22 ¹H NMR of HA12^{Red} in CDCl₃.

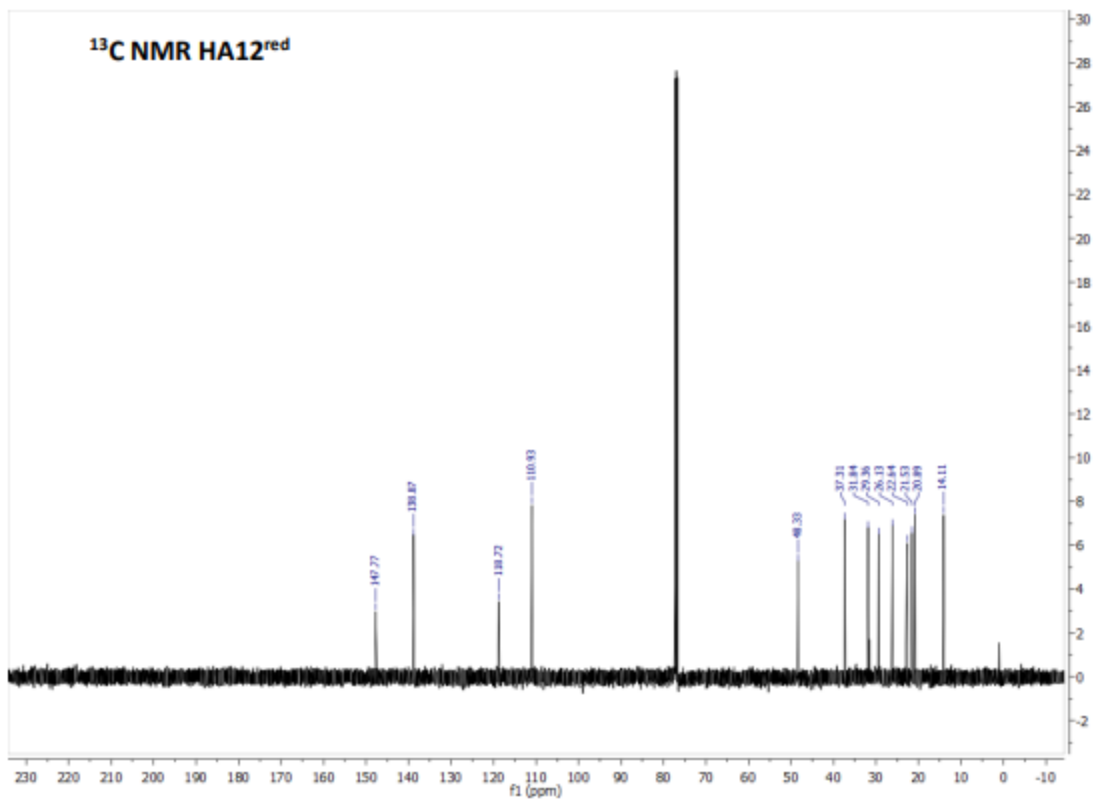


Figure 4.23 ¹³C NMR of HA12^{red} in CDCl₃.

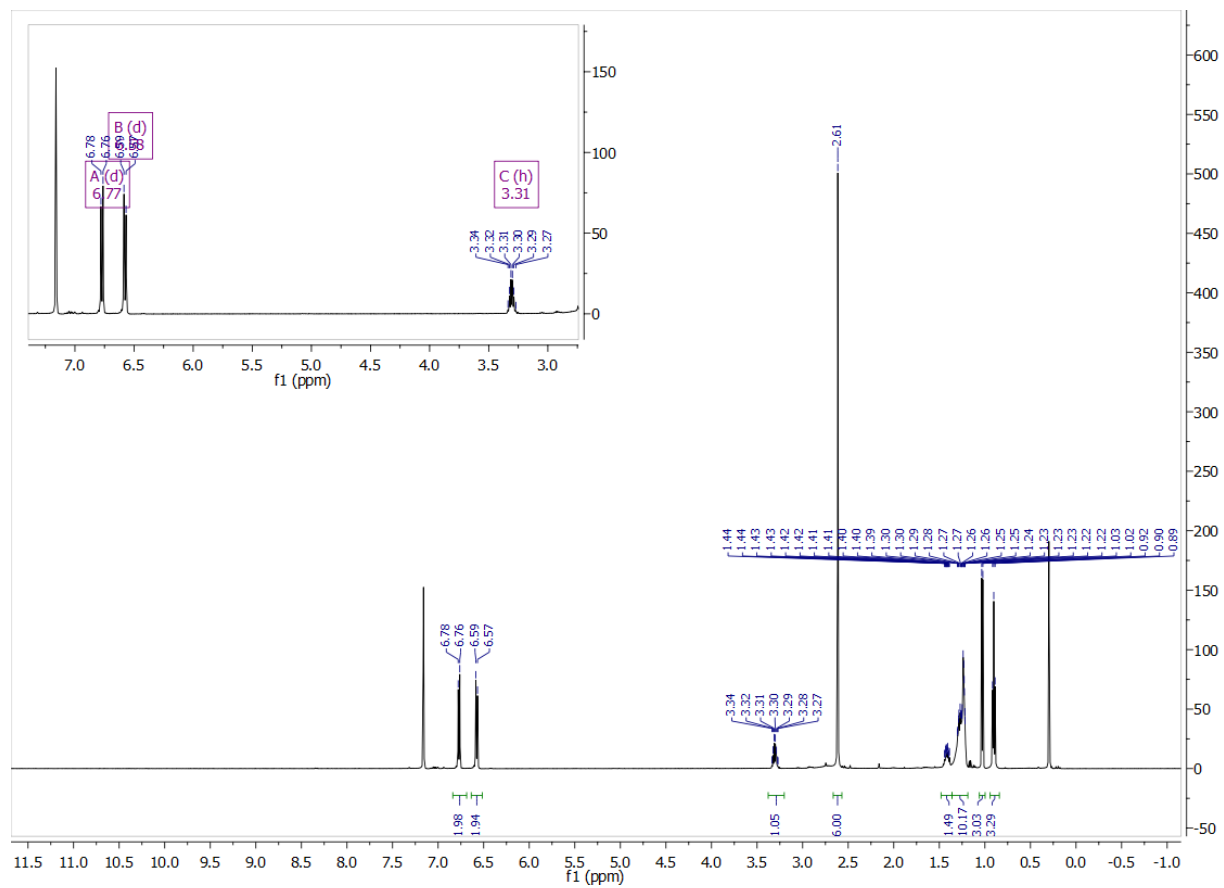


Figure 4.24 ^1H NMR of HA13^{red} in C_6D_6 .

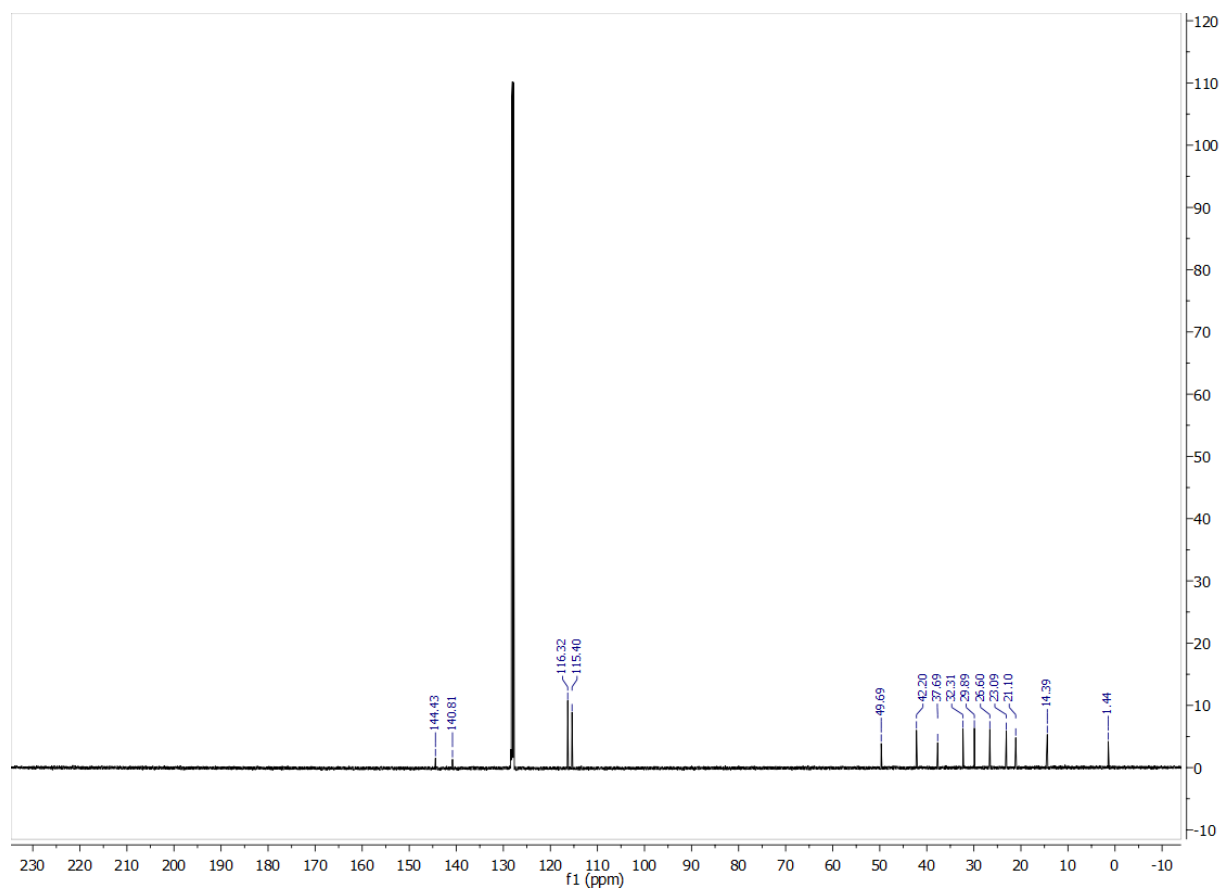


Figure 4.25 ^{13}C NMR of HA13^{red} in C_6D_6 .

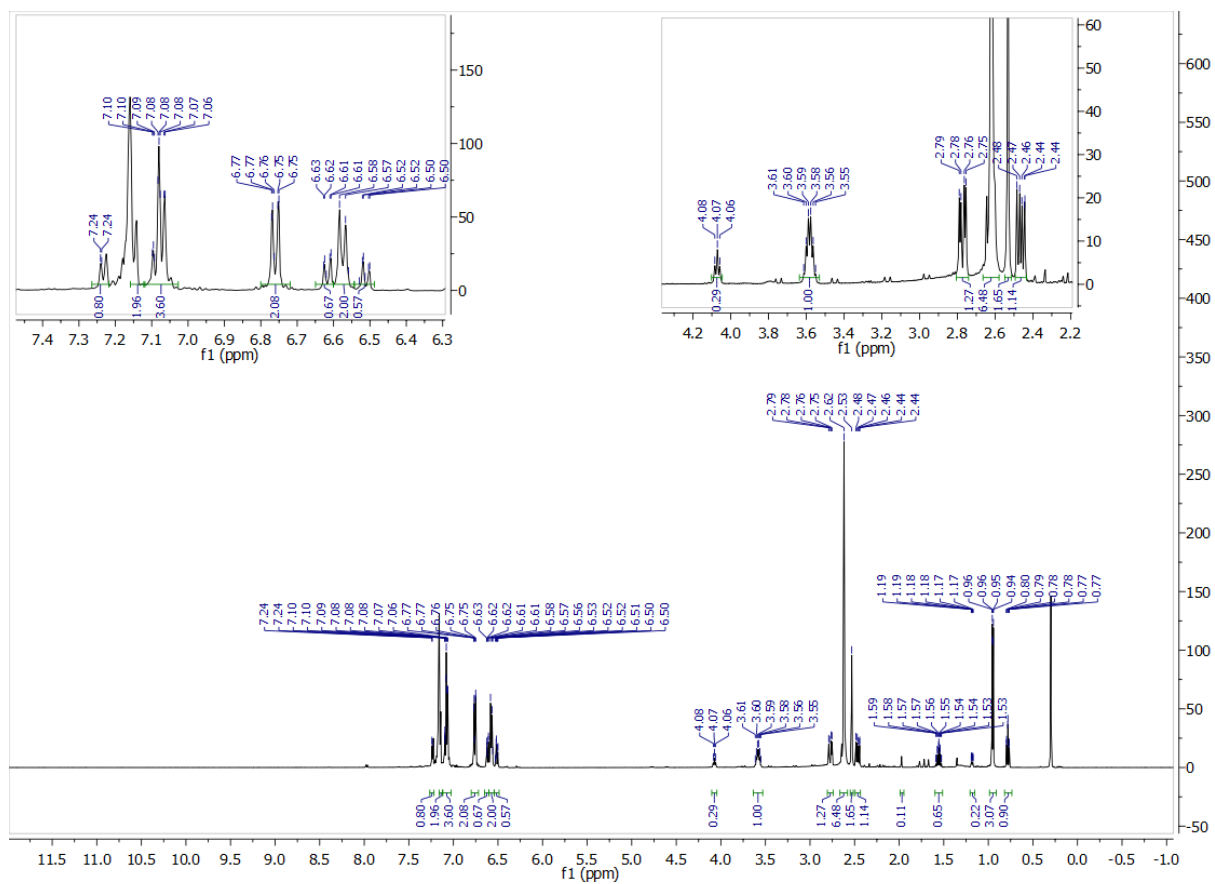


Figure 4.26 ^1H NMR of HA14^{red} in C_6D_6 .

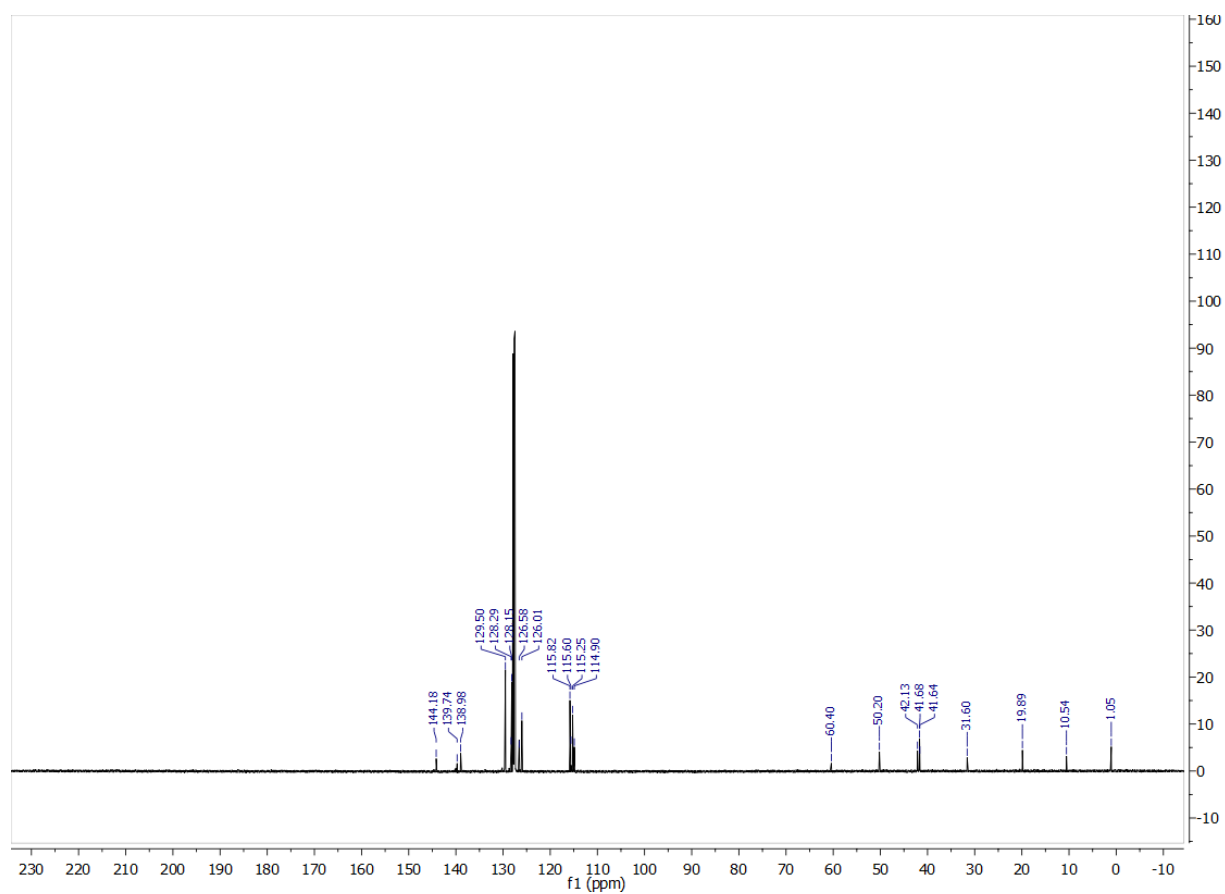


Figure 4.27 ^{13}C NMR of HA14^{red} in C_6D_6 .

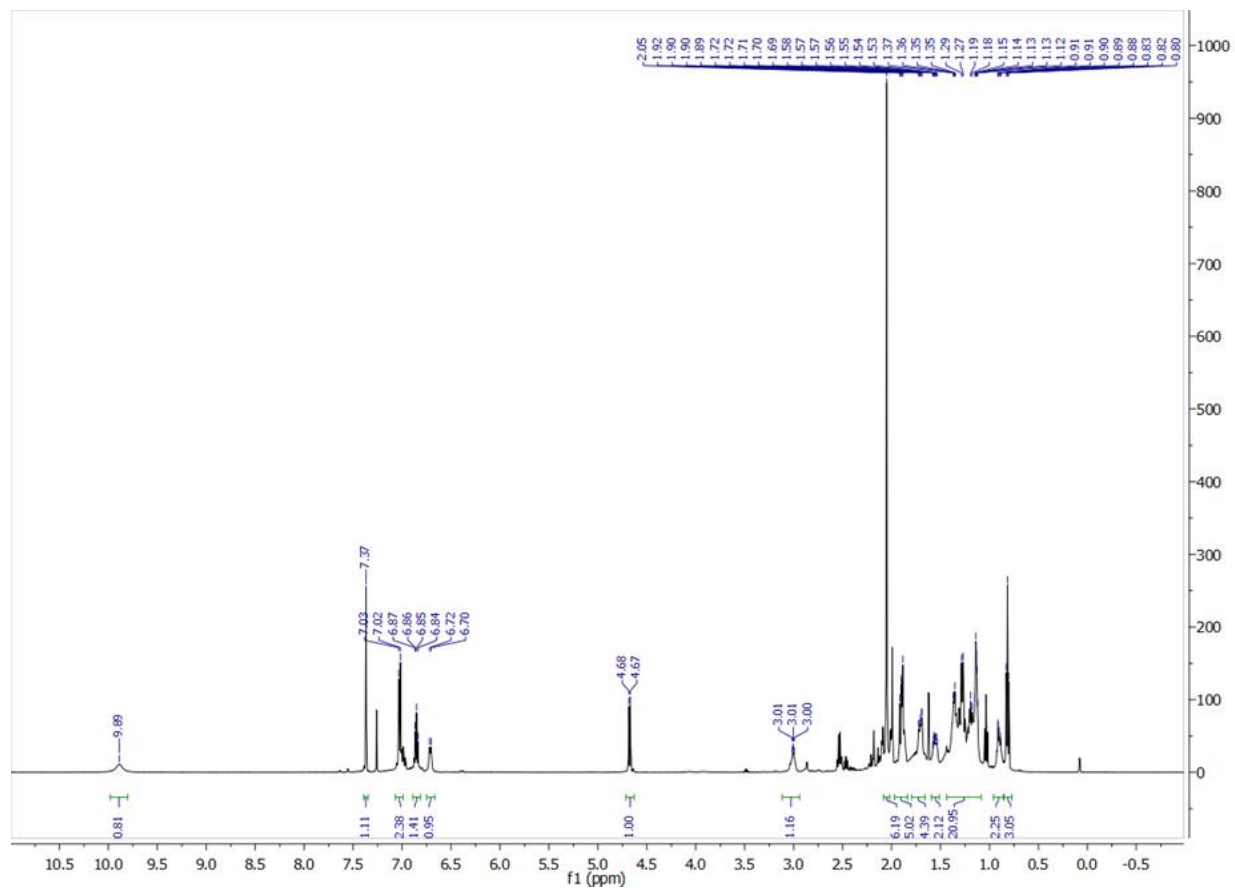


Figure 4.28 ^1H NMR of 3CC1 in CDCl_3 .

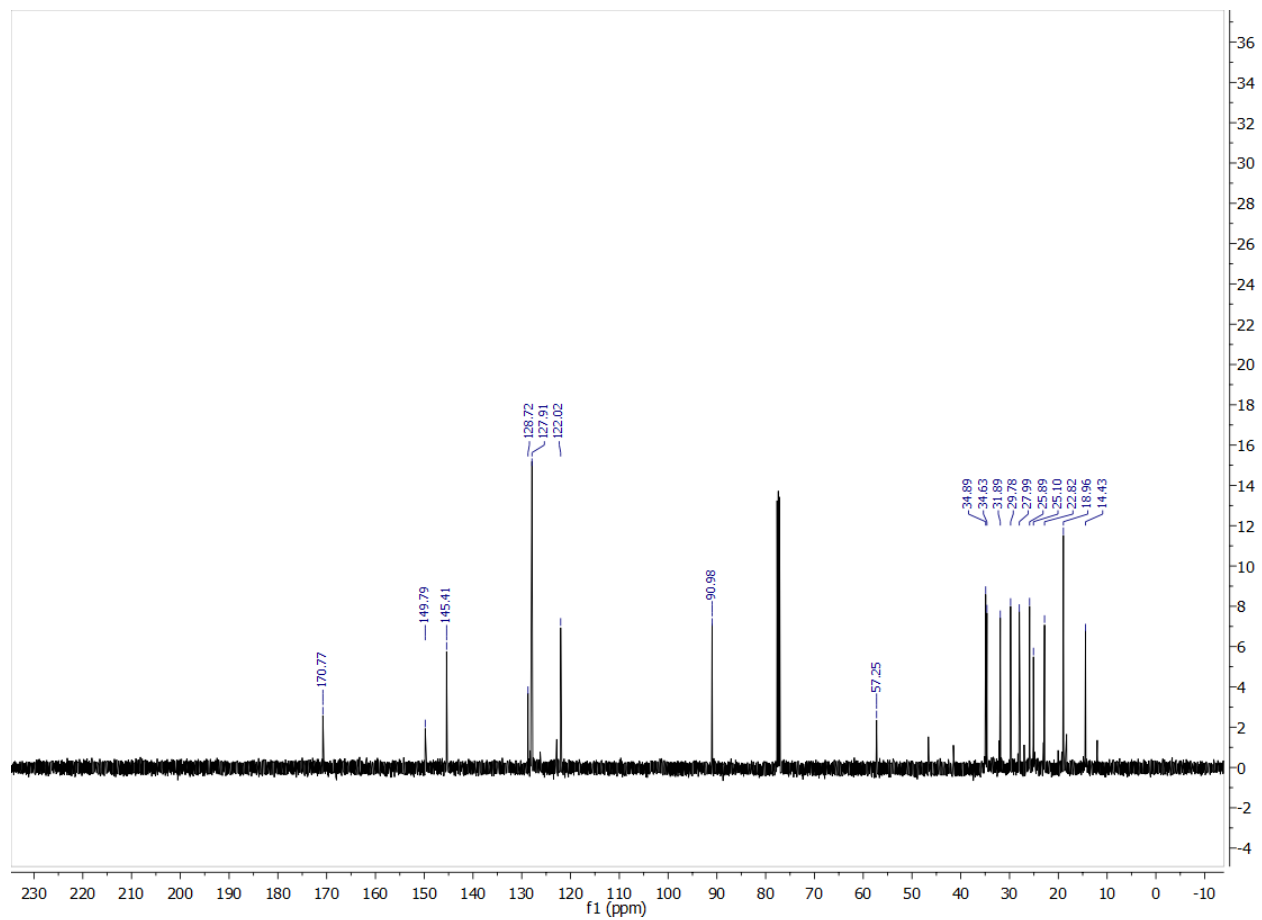


Figure 4.29 ^{13}C NMR of 3CC1 in CDCl_3 .

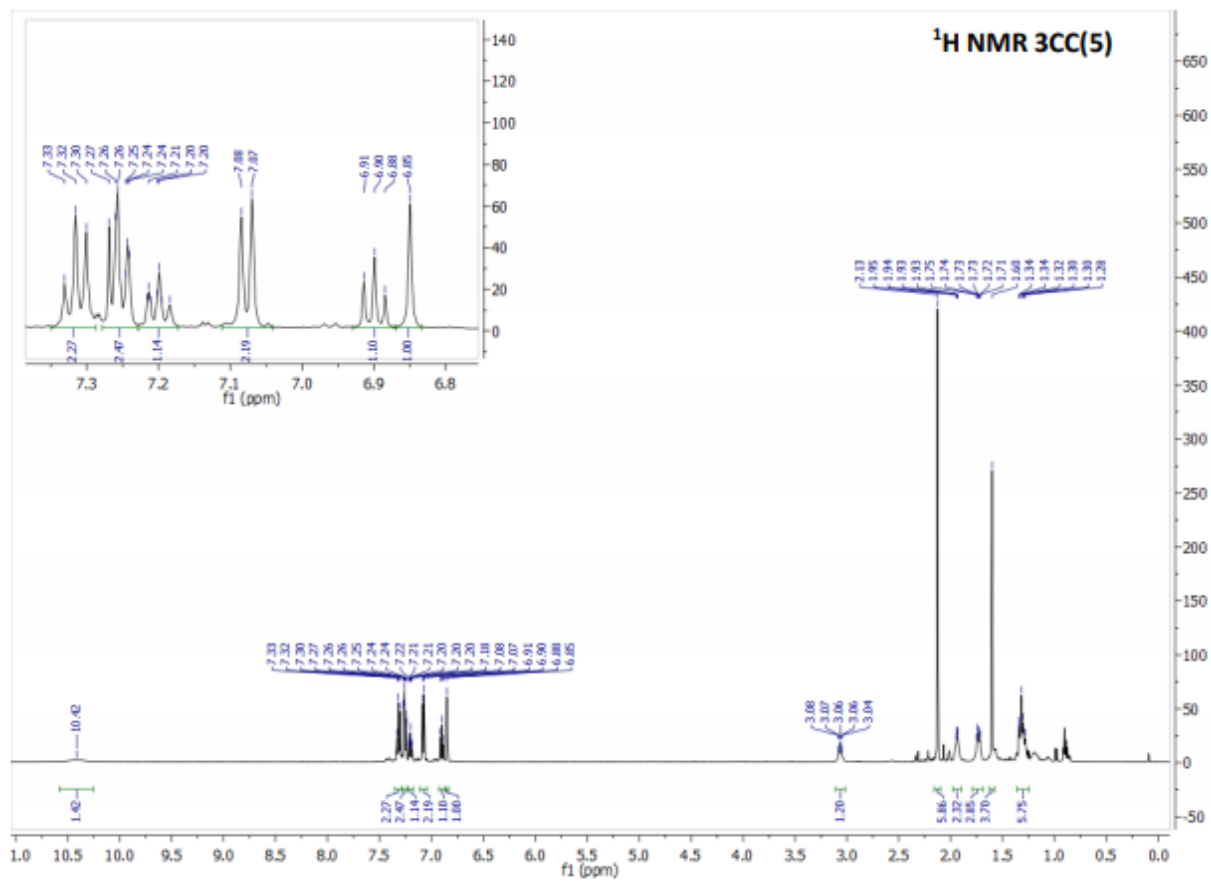


Figure 4.30 ¹H NMR of 3CC5 in CDCl₃.

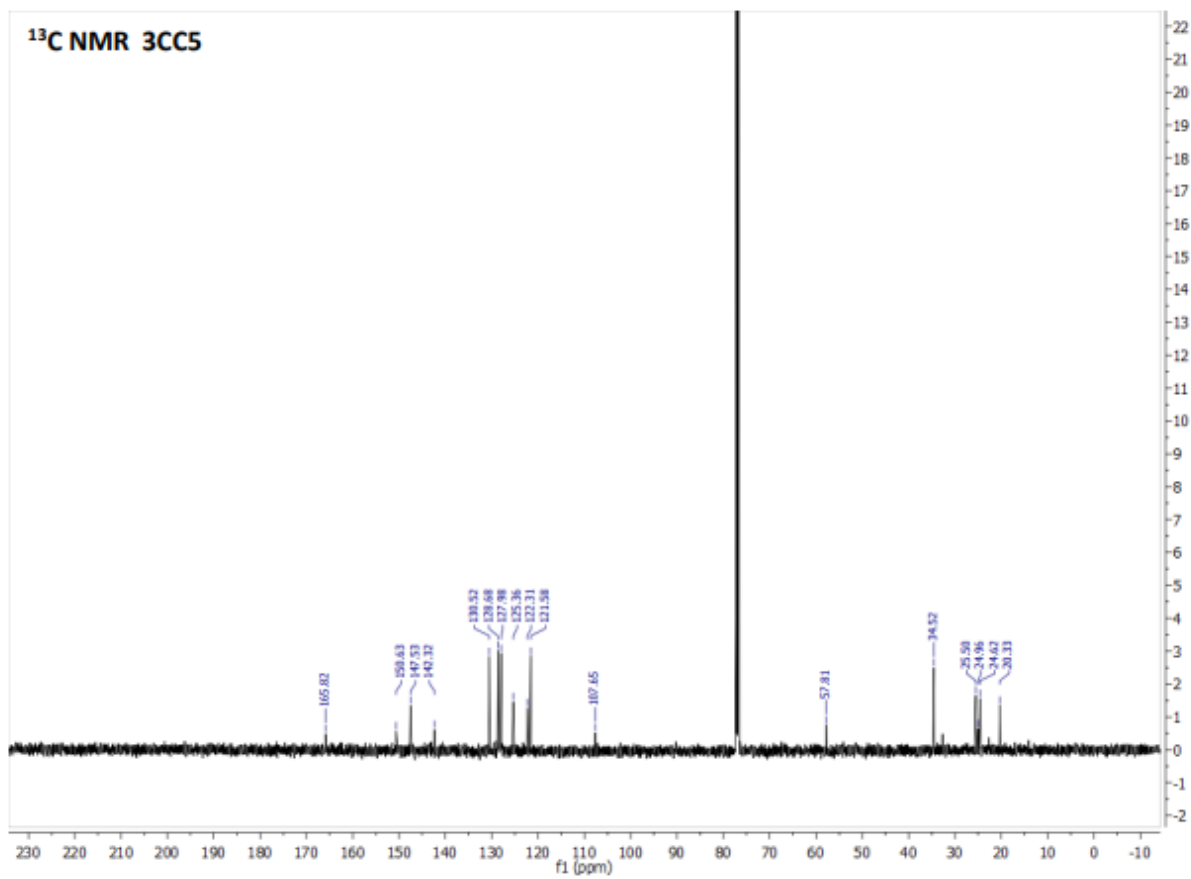


Figure 4.31 ¹³C NMR of 3CC5 in CDCl₃.

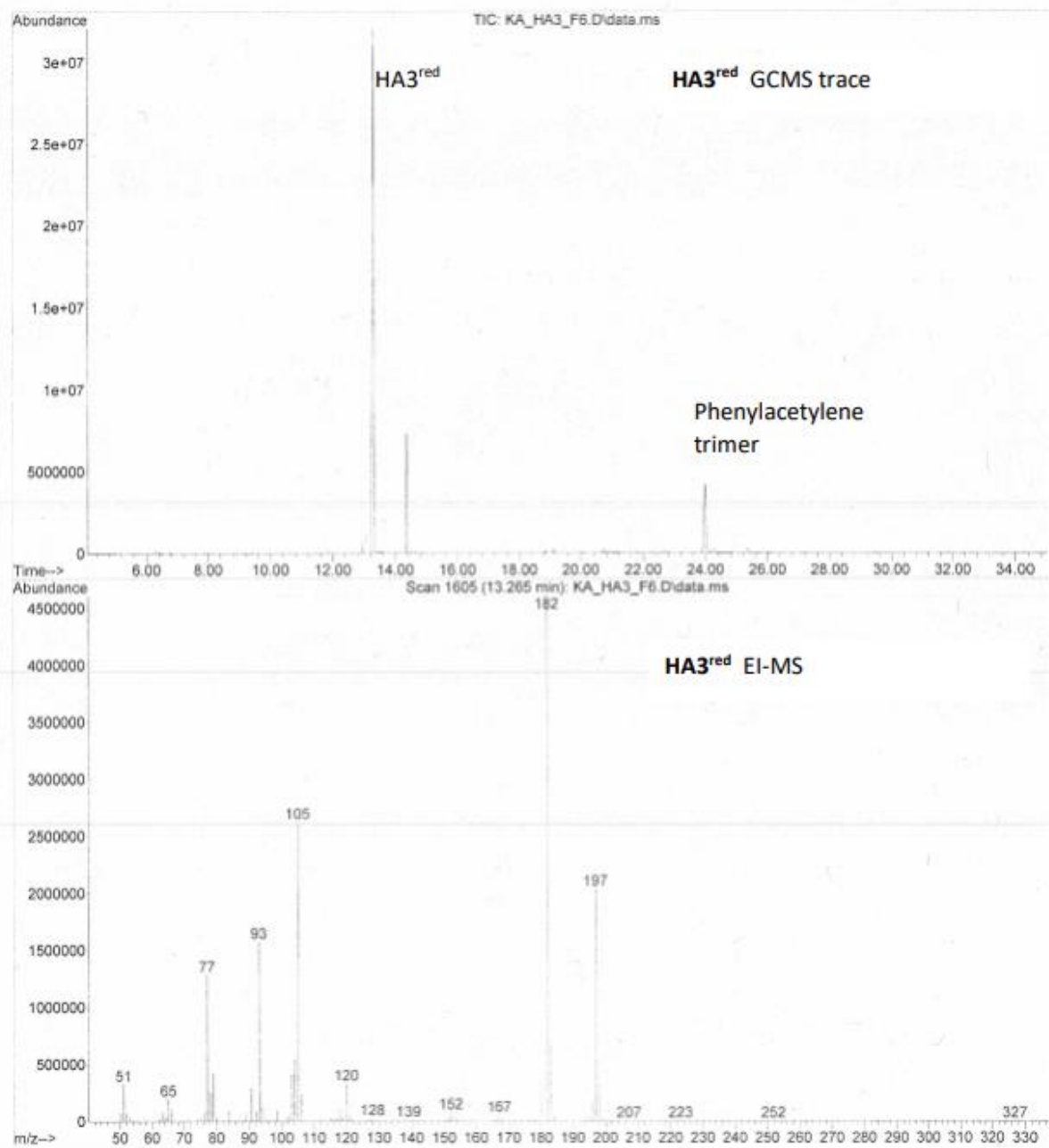


Figure 4.32 GC-MS of HA3^{red}.

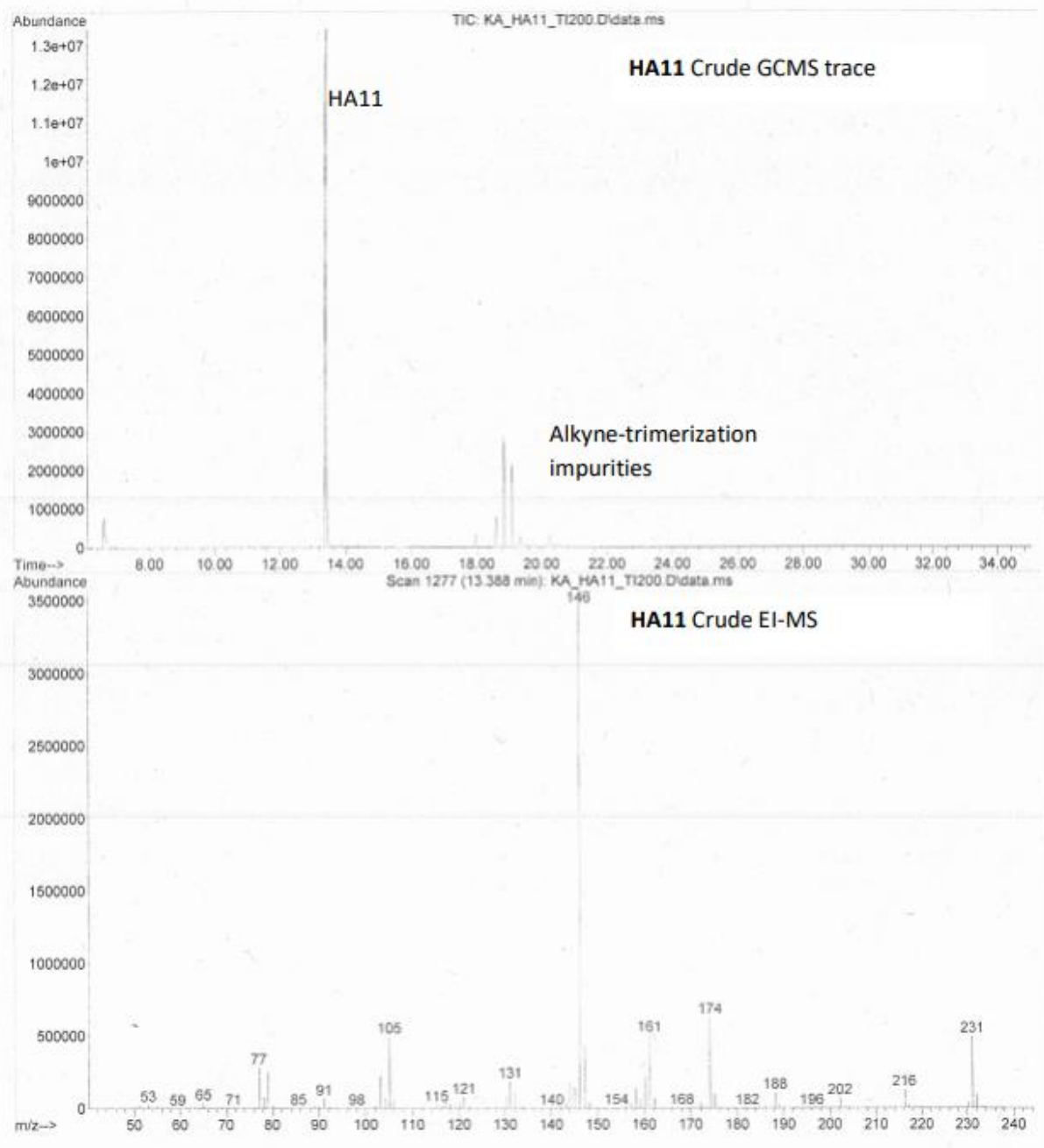


Figure 4.33 GC-MS of crude HA11

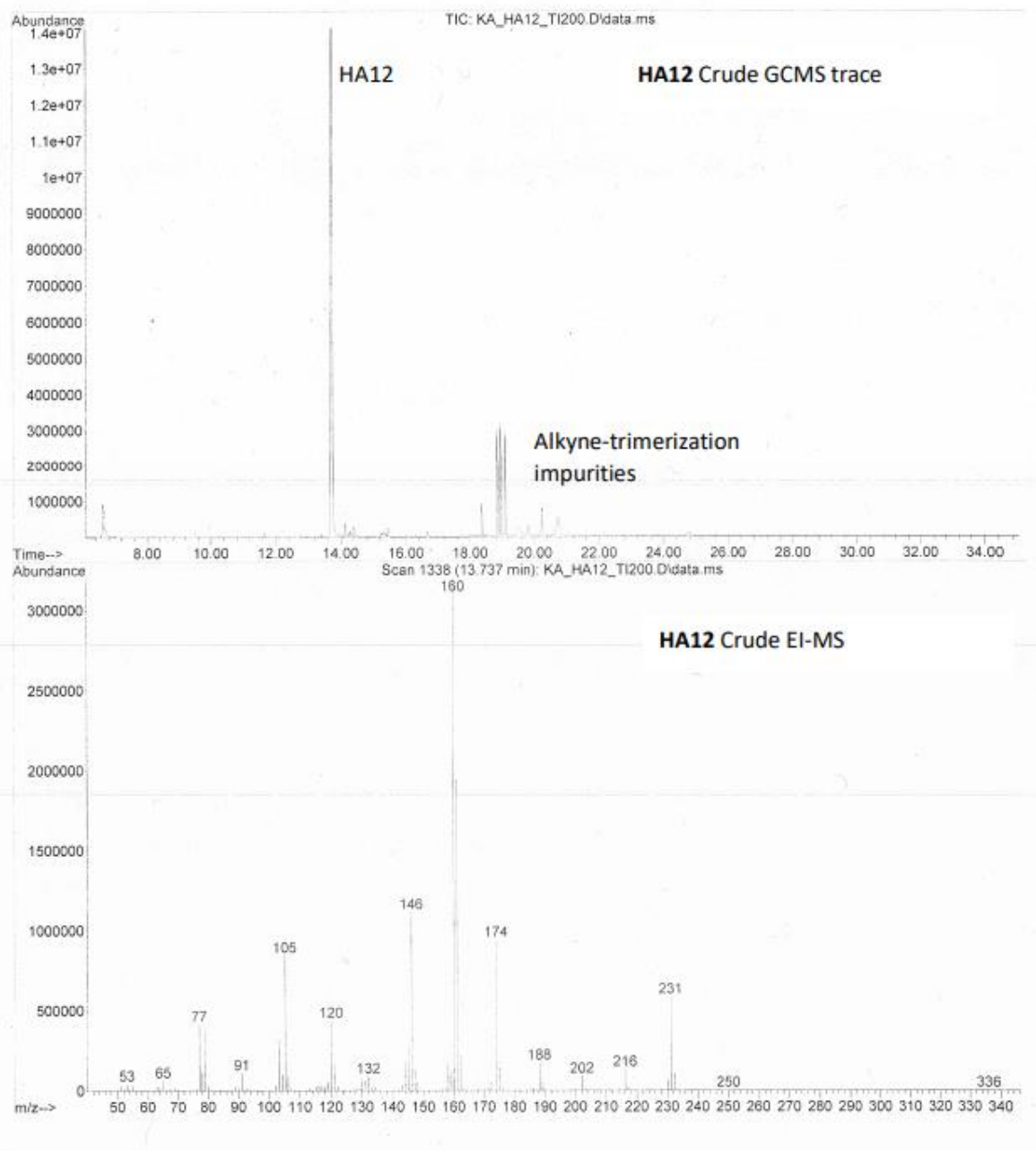


Figure 4.34 GC-MS of crude HA12.

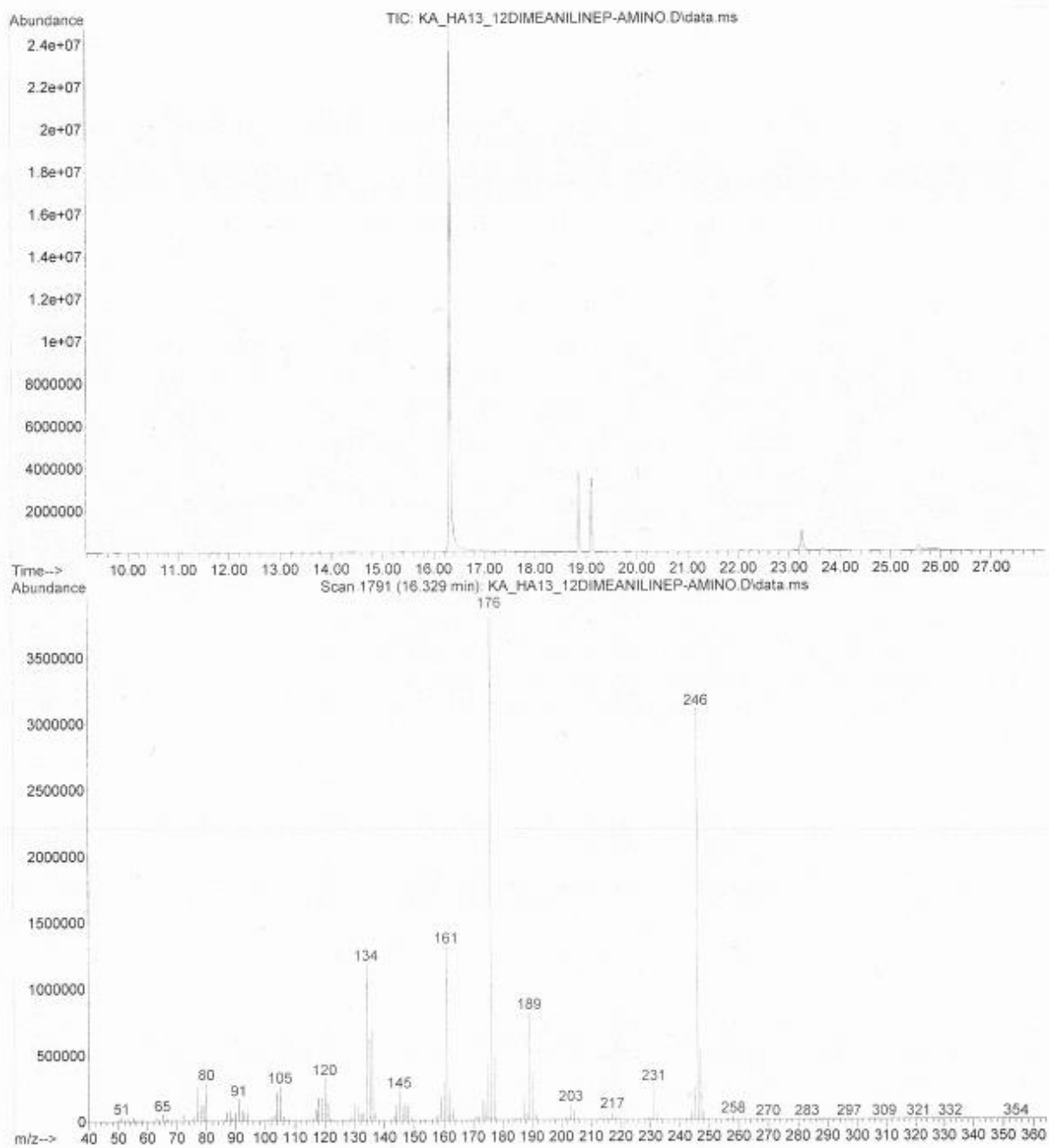


Figure 4.35 Crude GC-MS trace of HA13.

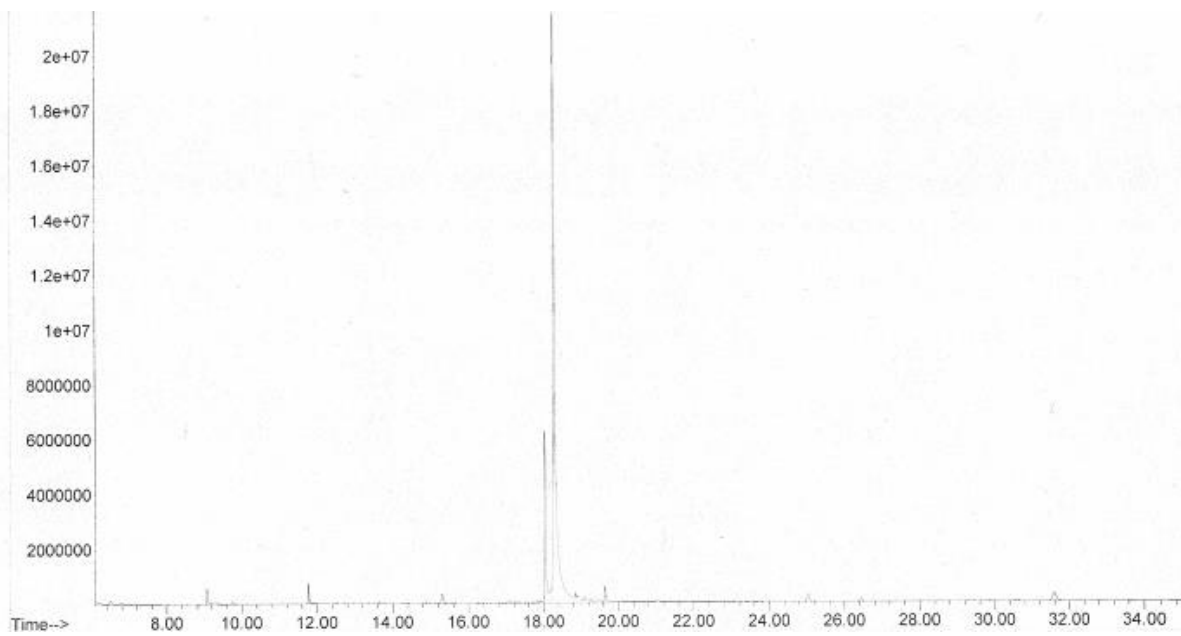


Figure 4.36 HA14 crude GC-MS trace.

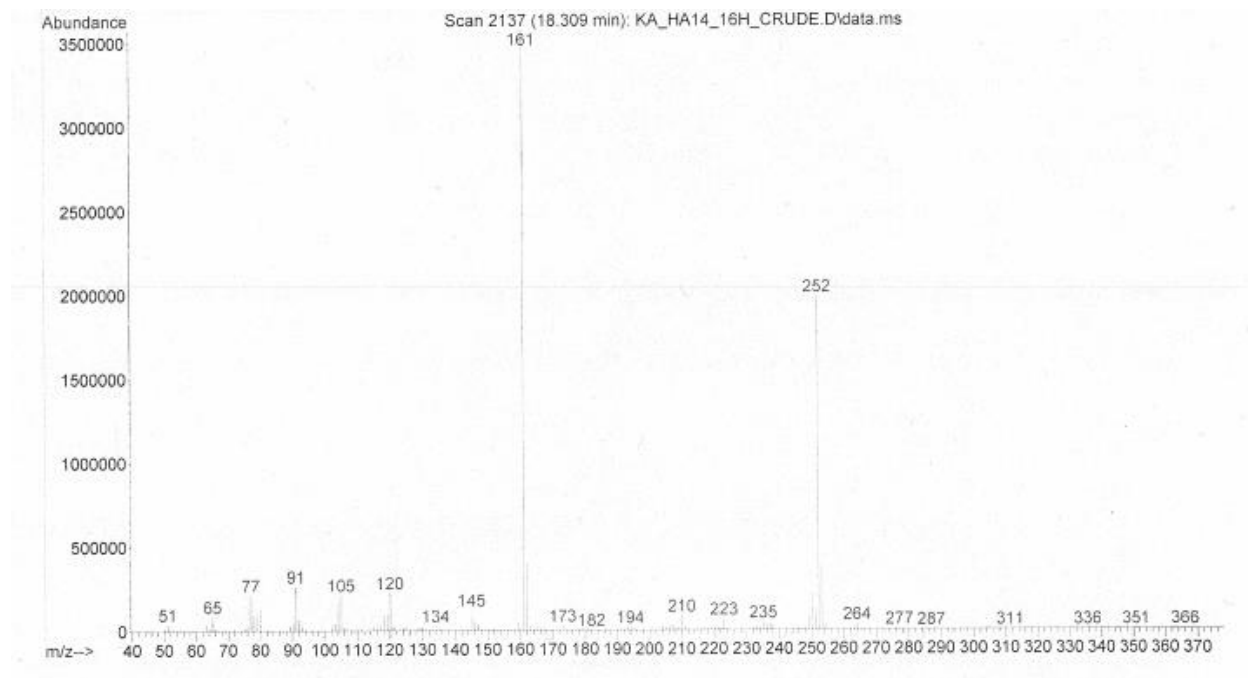


Figure 4.37 EI-MS Fragmentation Pattern for HA14(A).

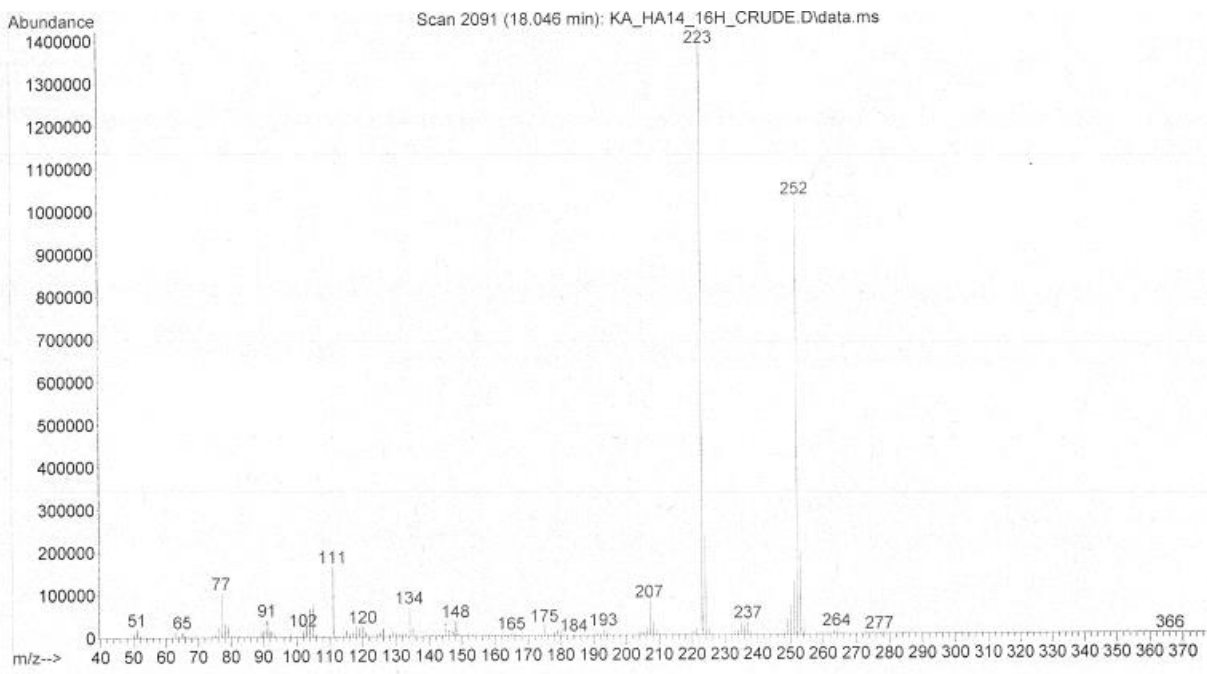


Figure 4.38 EI-MS Fragmentation Pattern for HA14(B).

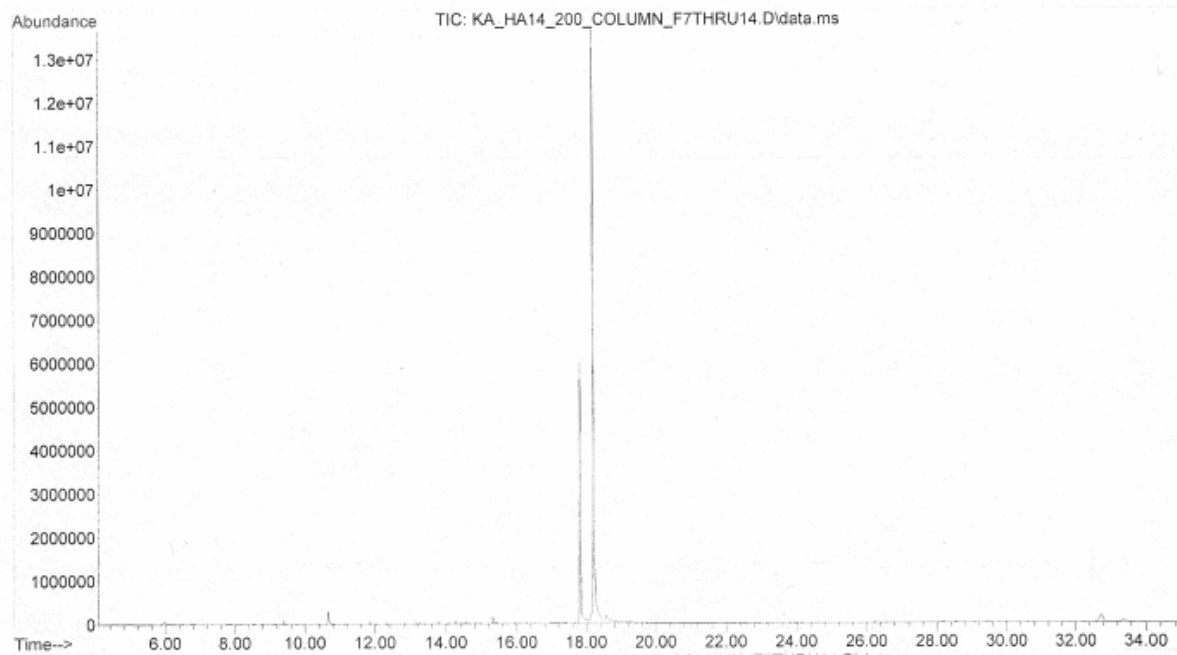


Figure 4.39 GC-MS trace of HA14^{red}.

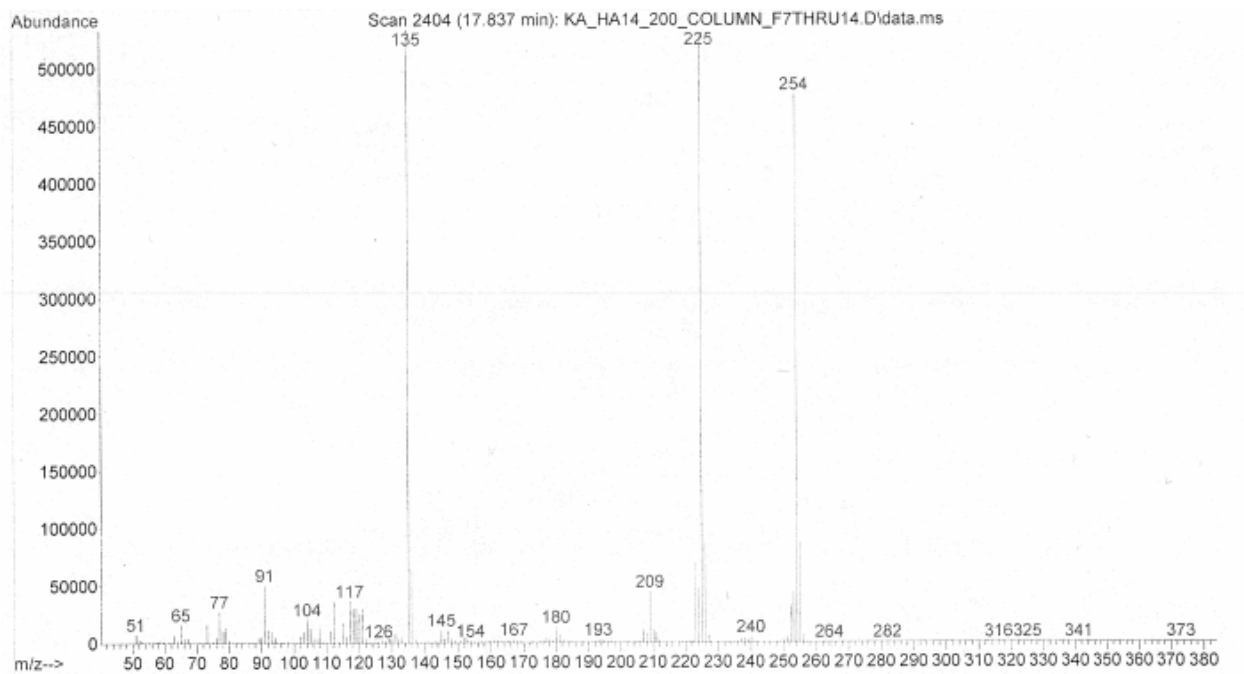


Figure 4.40 EI-MS of HA14^{red}(A).

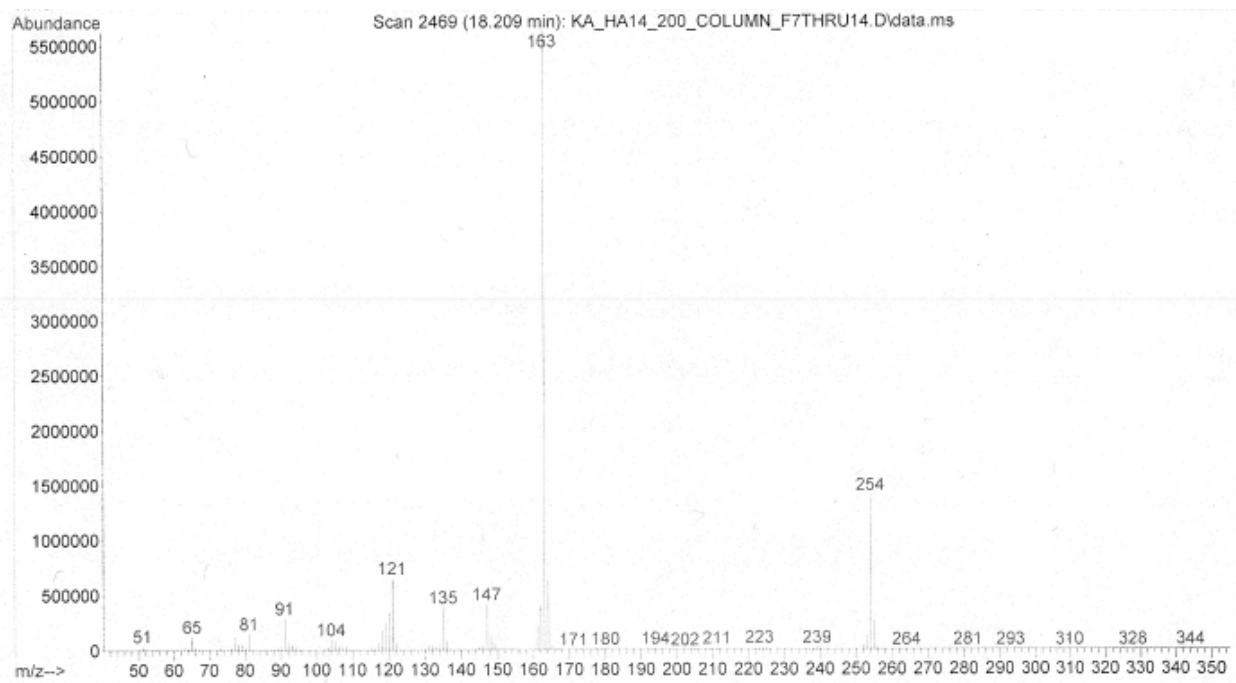
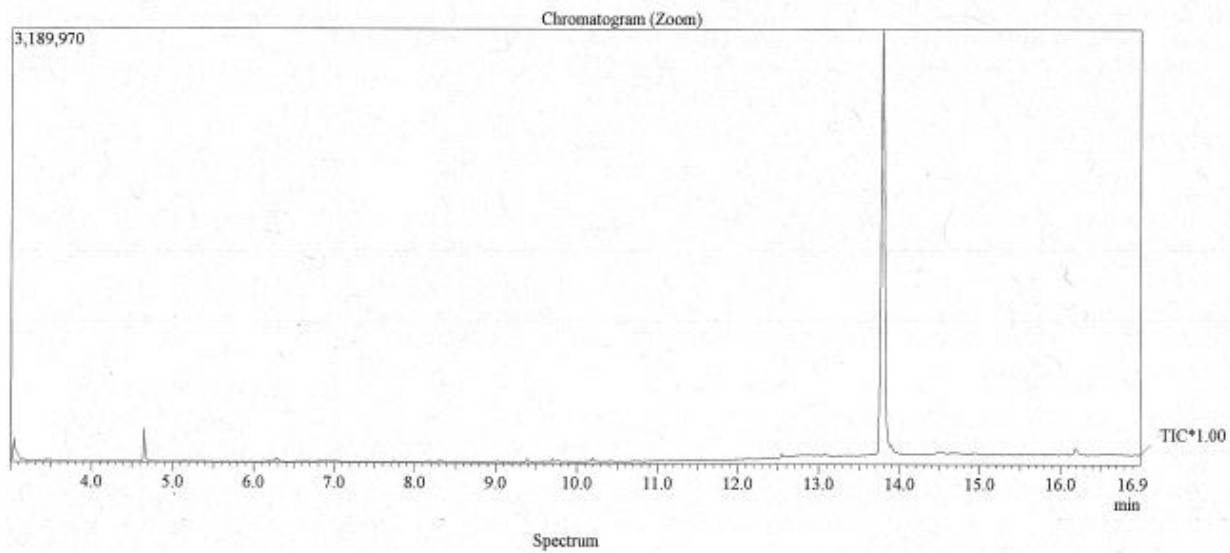


Figure 4.41 EI-MS of HA14^{red}(B).



Line#:1 R. Time:13.800(Scan#:2161)
MassPeaks:462
RawMode:Single 13.800(2161) BasePeak:255.10(176663)
BG Mode:None Group 1 - Event 1 Scan

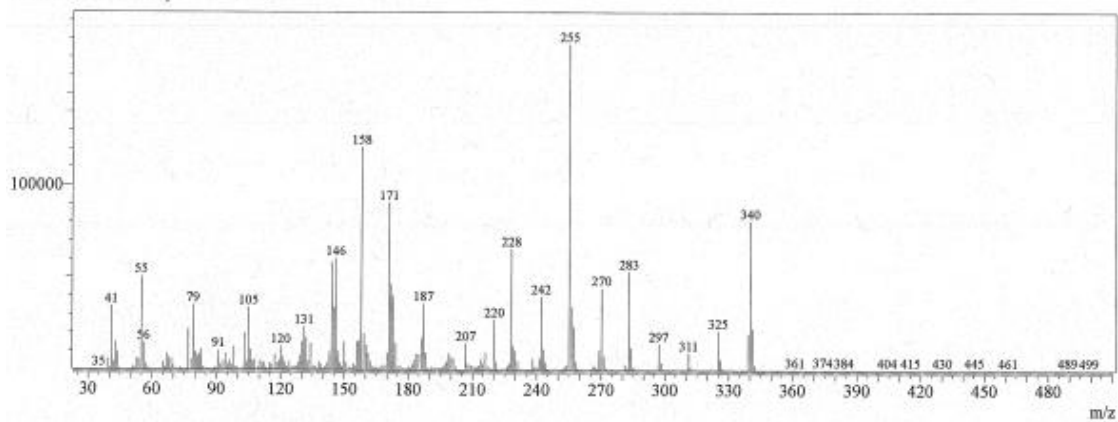


Figure 4.42 GC-MS of 3CC1.

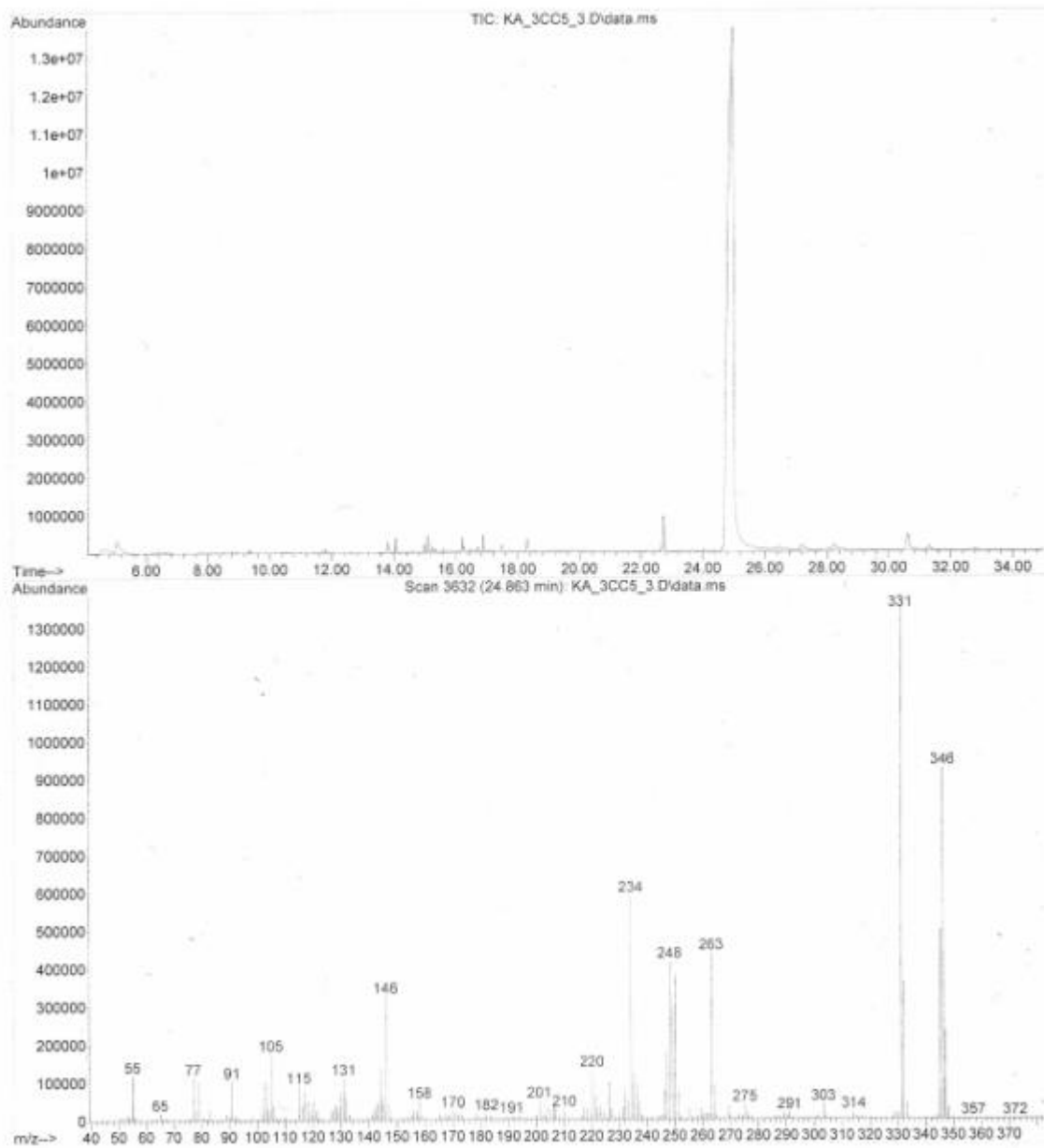


Figure 4.43 GC-MS of 3CC5.

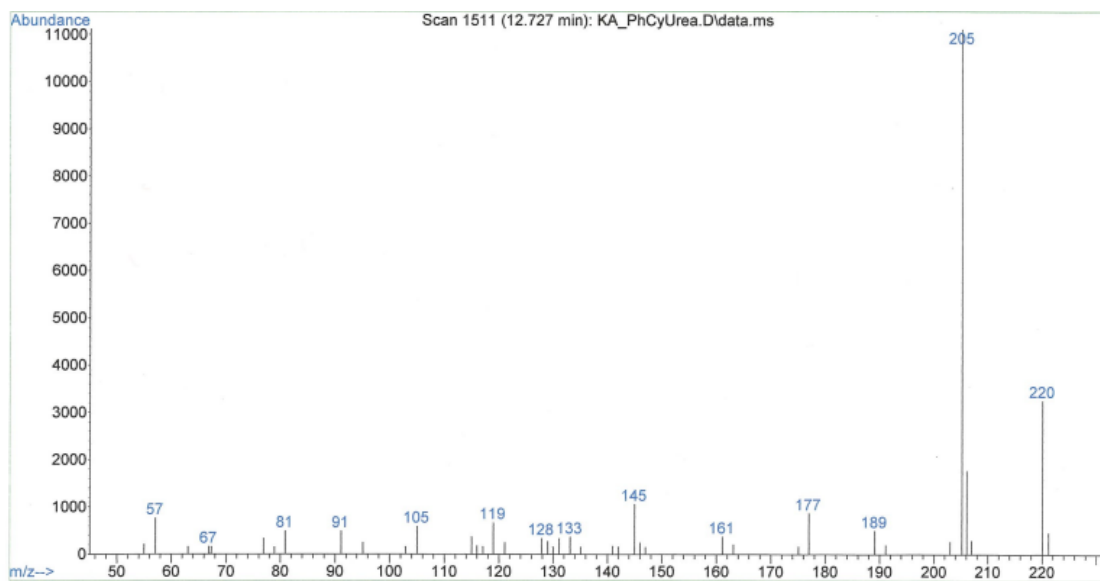
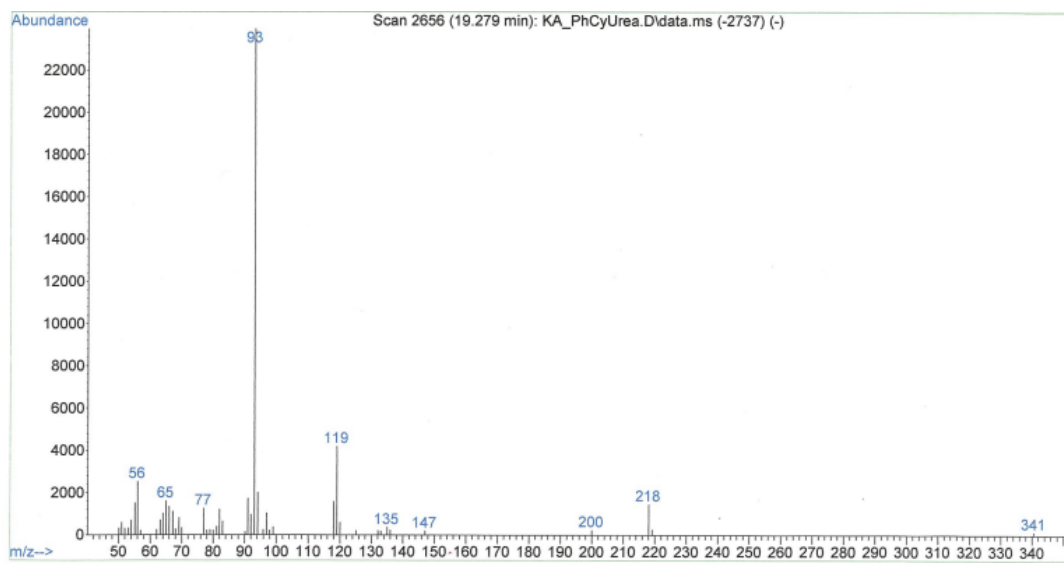


Figure 4.44 Fragmentation patterns observed for 1-phenyl-3-cyclohexylurea.

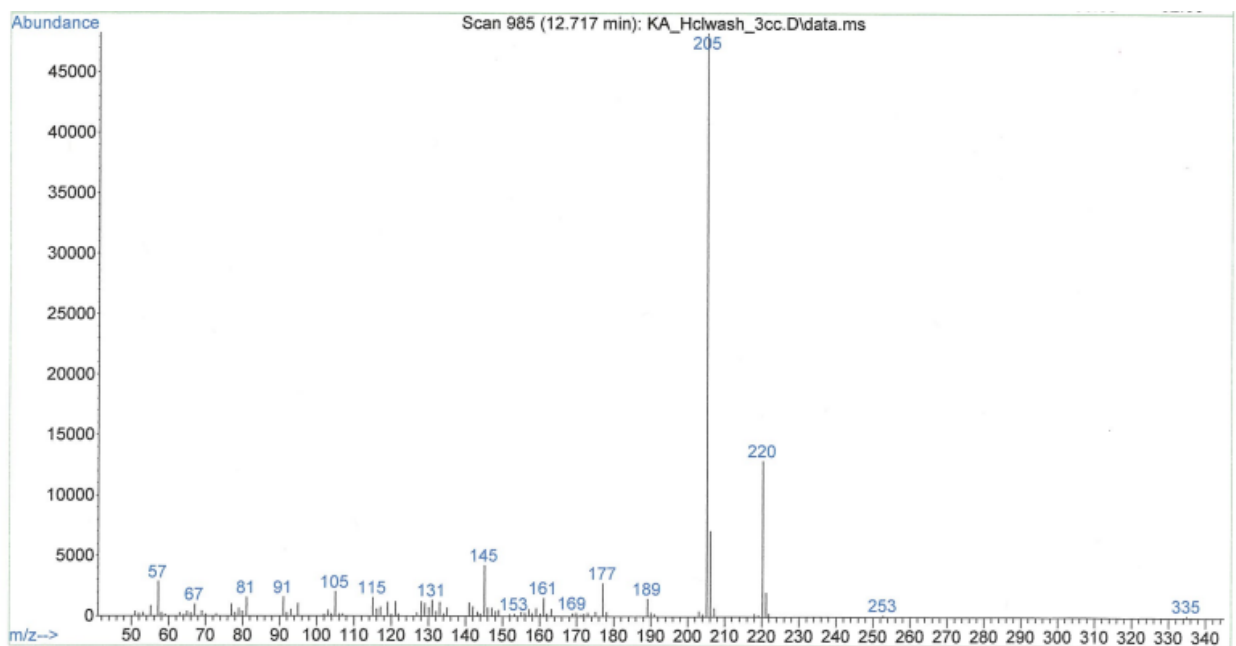
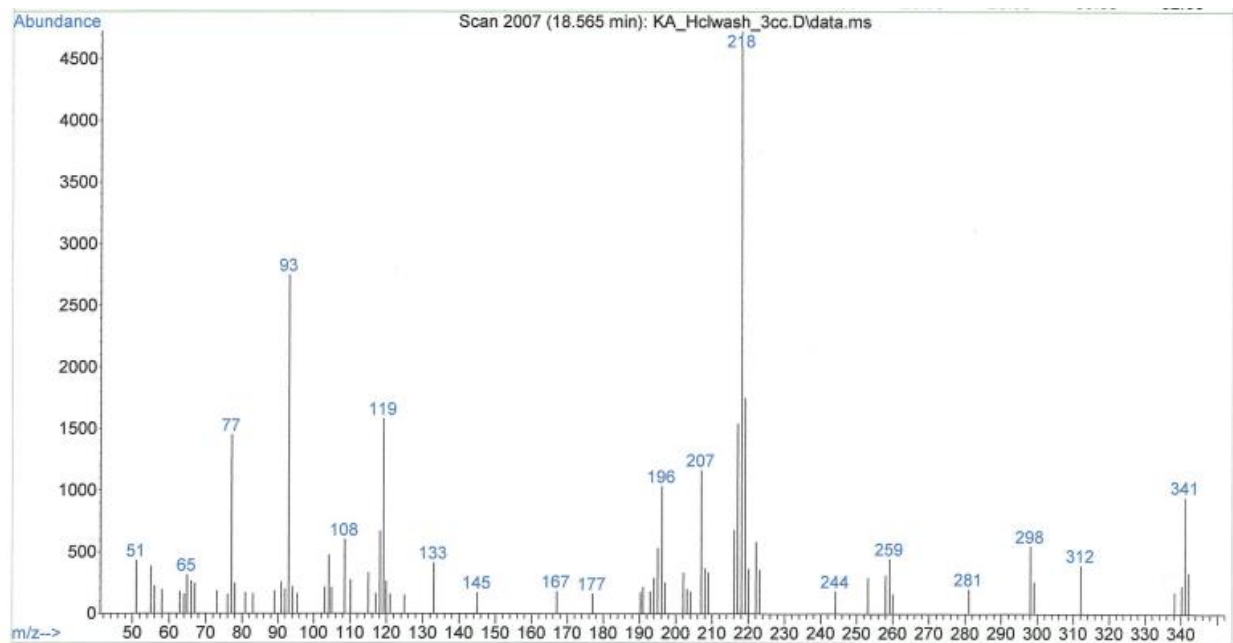


Figure 4.45 Fragmentation patterns observed in the HCl wash of used [Ti]700 catalyst after iminoamination which closely match those for 1-phenyl-3-cyclohexylurea.

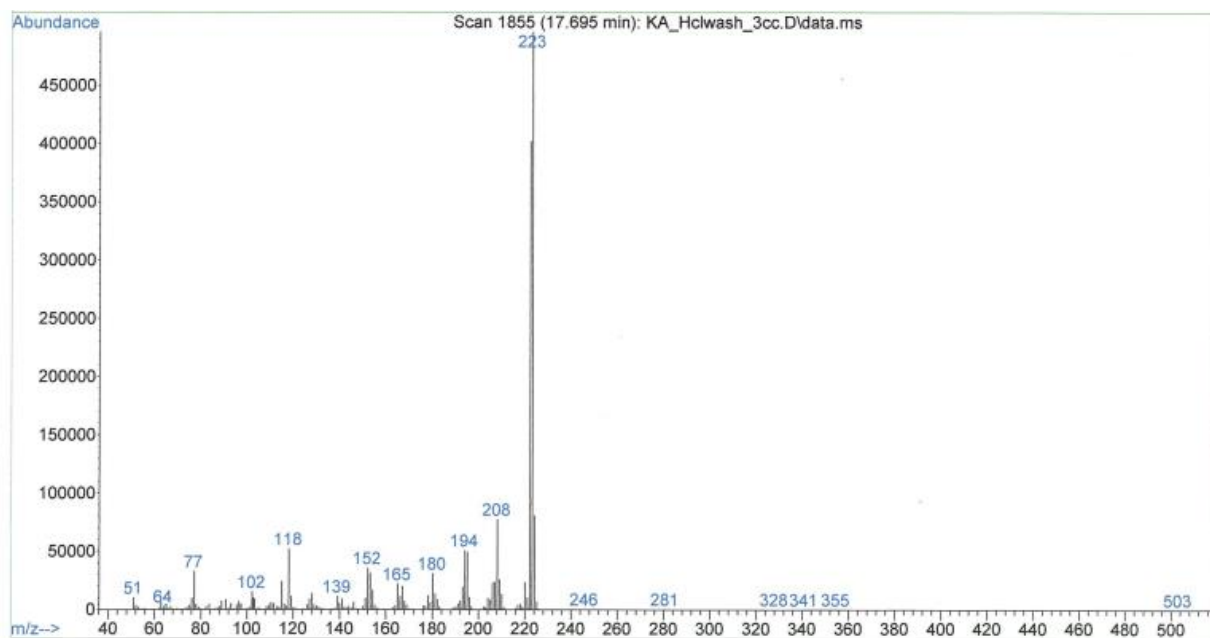


Figure 4.46 Fragmentation pattern observed in the HCl wash of used [Ti]700 catalyst after iminoamination, which closely matches 1,3-dicyclohexylurea.

REFERENCES

REFERENCES

Note: The original research presented in this chapter has been, in parts, published in the peer-reviewed articles under references 1 and 2 below.

- (1) Aldrich, K. E.; Odom, A. L. Titanium-Catalyzed Hydroamination and Multicomponent Coupling with a Simple Silica-Supported Catalyst. *Organometallics* 2018, DOI:10.1021/acs.organomet.8b00313 10.1021/acs.organomet.8b00313.
- (2) Aldrich, K. E., Odom, A. L., Low surface density silica-supported Ti precatalyst for C-N bond forming reactions. Submitted, 2019.
- (3) Harris, S. A.; Ciszewski, J. T.; Odom, A. L. Titanium η^1 -Pyrrolyl Complexes: Electronic and Structural Characteristics Imposed by the N,N-Di(pyrrolyl- α -methyl)-N-methylamine (dpma) Ligand. *Inorganic chemistry* 2001, 40 (9), 1987.
- (4) Cao, C.; Ciszewski, J. T.; Odom, A. L. Hydroamination of Alkynes Catalyzed by a Titanium Pyrrolyl Complex. *Organometallics* 2001, 20 (24), 5011.
- (5) Shi, Y.; Hall, C.; Ciszewski, J. T.; Cao, C.; Odom, A. L. Titanium dipyrrolylmethane derivatives: rapid intermolecular alkyne hydroamination. *Chemical communications* 2003, DOI:10.1039/B212423H 10.1039/B212423H(5), 586.
- (6) Odom, A. L.; McDaniel, T. J. Titanium-Catalyzed Multicomponent Couplings: Efficient One-Pot Syntheses of Nitrogen Heterocycles. *Accounts of Chemical Research* 2015, 48 (11), 2822.
- (7) Odom, A. L. New C-N and C-C bond forming reactions catalyzed by titanium complexes. *Dalton transactions* 2005, DOI:10.1039/B415701J 10.1039/B415701J(2), 225.
- (8) Cao, C.; Shi, Y.; Odom, A. L. A Titanium-Catalyzed Three-Component Coupling To Generate α,β -Unsaturated β -Iminoamines. *Journal of the American Chemical Society* 2003, 125 (10), 2880.
- (9) McDaniel, T. J.; Lansdell, T. A.; Dissanayake, A. A.; Azevedo, L. M.; Claes, J.; Odom, A. L.; Tepe, J. J. Substituted quinolines as noncovalent proteasome inhibitors. *Bioorganic & Medicinal Chemistry* 2016, 24 (11), 2441.
- (10) Majumder, S.; Gipson, K. R.; Staples, R. J.; Odom, A. L. Pyrazole Synthesis Using a Titanium-Catalyzed Multicomponent Coupling Reaction and Synthesis of Withasomnine. 2009, 351 (11-12), 2013.
- (11) Majumder, S.; Odom, A. L. Titanium catalyzed one-pot multicomponent coupling reactions for direct access to substituted pyrimidines. *Tetrahedron* 2010, 66 (17), 3152.

- (12) Barnea, E.; Majumder, S.; Staples, R. J.; Odom, A. L. One-Step Route to 2,3-Diaminopyrroles Using a Titanium-Catalyzed Four-Component Coupling. *Organometallics* 2009, 28 (13), 3876.
- (13) Dissanayake, A. A.; Odom, A. L. Regioselective conversion of alkynes to 4-substituted and 3,4-disubstituted isoxazoles using titanium-catalyzed multicomponent coupling reactions. *Tetrahedron* 2012, 68 (3), 807.
- (14) Dissanayake, A. A.; Staples, R. J.; Odom, A. L. Titanium-Catalyzed, One-Pot Synthesis of 2-Amino-3-cyano- pyridines. *Advanced Synthesis & Catalysis* 2014, 356 (8), 1811.
- (15) Pasko, C. M.; Dissanayake, A. A.; Billow, B. S.; Odom, A. L. One-pot synthesis of pyrroles using a titanium-catalyzed multicomponent coupling procedure. *Tetrahedron* 2016, 72 (9), 1168.
- (16) Lui, E. K. J.; Brandt, J. W.; Schafer, L. L. Regio- and Stereoselective Hydroamination of Alkynes Using an Ammonia Surrogate: Synthesis of N-Silylenamines as Reactive Synthons. *Journal of the American Chemical Society* 2018, 140 (15), 4973.
- (17) Hao, H.; Thompson, K. A.; Hudson, Z. M.; Schafer, L. L. Ti-Catalyzed Hydroamination for the Synthesis of Amine-Containing π -Conjugated Materials. 2018, 24 (21), 5562.
- (18) Walsh, P. J.; Baranger, A. M.; Bergman, R. G. Stoichiometric and catalytic hydroamination of alkynes and allene by zirconium bisamides $\text{Cp}_2\text{Zr}(\text{NHR})_2$. *Journal of the American Chemical Society* 1992, 114 (5), 1708.
- (19) Johnson, J. S.; Bergman, R. G. Imidotitanium Complexes as Hydroamination Catalysts: Substantially Enhanced Reactivity from an Unexpected Cyclopentadienide/Amide Ligand Exchange. *Journal of the American Chemical Society* 2001, 123 (12), 2923.
- (20) Pohlki, F.; Doye, S. The Mechanism of the $[\text{Cp}_2\text{TiMe}_2]$ -Catalyzed Intermolecular Hydroamination of Alkynes. 2001, 40 (12), 2305.
- (21) Hazari, N.; Mountford, P. Reactions and Applications of Titanium Imido Complexes. *Accounts of Chemical Research* 2005, 38 (11), 839.
- (22) Billow, B. S.; McDaniel, T. J.; Odom, A. L. Quantifying ligand effects in high-oxidation-state metal catalysis. *Nature Chemistry* 2017, 9, 837.
- (23) DiFranco, S. A.; Maciulis, N. A.; Staples, R. J.; Batrice, R. J.; Odom, A. L. Evaluation of donor and steric properties of anionic ligands on high valent transition metals. *Inorganic chemistry* 2012, 51 (2), 1187.
- (24) Aldrich, B., Holmes, Bemowski, Odom.
- (25) Ng, E.-P.; Law, S.-P.; Mukti, R. R.; Juan, J.-C.; Adam, F. Hydroamination of cyclohexene enhanced by ZnCl_2 nanoparticles supported on chiral mesoporous silica. *Chemical Engineering Journal* 2014, 243, 99.

- (26) Davaasuren, B.; Emwas, A.-H.; Rothenberger, A. MAu₂GeS₄-Chalcogel (M = Co, Ni): Heterogeneous Intra- and Intermolecular Hydroamination Catalysts. *Inorganic chemistry* 2017, 56 (16), 9609.
- (27) Sengupta, M.; Bag, A.; Das, S.; Shukla, A.; Konathala, L. N. S.; Naidu, C. A.; Bordoloi, A. Reaction and Mechanistic Studies of Heterogeneous Hydroamination over Support-Stabilized Gold Nanoparticles. 2016, 8 (19), 3121.
- (28) Copéret, C.; Comas-Vives, A.; Conley, M. P.; Estes, D. P.; Fedorov, A.; Mougél, V.; Nagae, H.; Núñez-Zarur, F.; Zhizhko, P. A. Surface Organometallic and Coordination Chemistry toward Single-Site Heterogeneous Catalysts: Strategies, Methods, Structures, and Activities. *Chemical Reviews* 2016, 116 (2), 323.
- (29) Copéret, C.; Chabanas, M.; Petroff Saint-Arroman, R.; Basset, J.-M. Cover Picture: *Angew. Chem. Int. Ed.* 2/2003. 2003, 42 (2), 129.
- (30) Blanc, F.; Copéret, C.; Lesage, A.; Emsley, L. High resolution solid state NMR spectroscopy in surface organometallic chemistry: access to molecular understanding of active sites of well-defined heterogeneous catalysts. *Chemical Society Reviews* 2008, 37 (3), 518.
- (31) Coperet, C. C–H Bond Activation and Organometallic Intermediates on Isolated Metal Centers on Oxide Surfaces. *Chemical Reviews* 2010, 110 (2), 656.
- (32) Barman, S.; Merle, N.; Minenkov, Y.; De Mallmann, A.; Samantaray, M. K.; Le Quémener, F.; Szeto, K. C.; Abou-Hamad, E.; Cavallo, L.; Taoufik, M. et al. Well-Defined Silica Grafted Molybdenum Bis(imido) Catalysts for Imine Metathesis Reactions. *Organometallics* 2017, DOI:10.1021/acs.organomet.7b00115 10.1021/acs.organomet.7b00115.
- (33) Samantaray, M. K.; Dey, R.; Kavitate, S.; Basset, J.-M. In *C-H Bond Activation and Catalytic Functionalization II*; Dixneuf, P. H.; Doucet, H., Eds.; Springer International Publishing: Cham, 2016, DOI:10.1007/3418_2015_139 10.1007/3418_2015_139.
- (34) Goldsmith, B. R.; Peters, B.; Johnson, J. K.; Gates, B. C.; Scott, S. L. Beyond Ordered Materials: Understanding Catalytic Sites on Amorphous Solids. *ACS Catalysis* 2017, DOI:10.1021/acscatal.7b01767 10.1021/acscatal.7b01767, 7543.
- (35) Schrock, R. R.; Copéret, C. Formation of High-Oxidation-State Metal–Carbon Double Bonds. *Organometallics* 2017, 36 (10), 1884.
- (36) Conley, M. P.; Forrest, W. P.; Mougél, V.; Copéret, C.; Schrock, R. R. Bulky Aryloxide Ligand Stabilizes a Heterogeneous Metathesis Catalyst. 2014, 53 (51), 14221.
- (37) Solans-Monfort, X.; Copéret, C.; Eisenstein, O. Metallacyclobutanes from Schrock-Type d⁰ Metal Alkylidene Catalysts: Structural Preferences and Consequences in Alkene Metathesis. *Organometallics* 2015, 34 (9), 1668.

- (38) Pucino, M.; Inoue, M.; Gordon, C. P.; Schowner, R.; Stöhr, L.; Sen, S.; Hegedüs, C.; Robé, E.; Tóth, F.; Buchmeiser, M. R. et al. Promoting Terminal Olefin Metathesis with a Supported Cationic Molybdenum Imido Alkylidene N-Heterocyclic Carbene Catalyst. *2018*, *57* (44), 14566.
- (39) Le Roux, E.; Liang, Y.; Storz, M. P.; Anwender, R. Intramolecular Hydroamination/Cyclization of Aminoalkenes Catalyzed by Ln[N(SiMe₃)₂]₃ Grafted onto Periodic Mesoporous Silicas. *Journal of the American Chemical Society* 2010, *132* (46), 16368.
- (40) Cook, A. K.; Copéret, C. Alkyne Hydroamination Catalyzed by Silica-Supported Isolated Zn(II) Sites. *Organometallics* 2018, *37* (9), 1342.
- (41) Eedugurala, N.; Wang, Z.; Chaudhary, U.; Nelson, N.; Kandel, K.; Kobayashi, T.; Slowing, I. I.; Pruski, M.; Sadow, A. D. Mesoporous Silica-Supported Amidozirconium-Catalyzed Carbonyl Hydroboration. *ACS Catalysis* 2015, *5* (12), 7399.
- (42) Beaudoin, M.; Scott, S. L. Spontaneous Evolution of Silica-Supported Ti Amide Fragments to Imine and Imido Complexes. *Organometallics* 2001, *20* (2), 237.
- (43) Walder, B. J.; Berk, C.; Liao, W.-C.; Rossini, A. J.; Schwarzwälder, M.; Pradere, U.; Hall, J.; Lesage, A.; Copéret, C.; Emsley, L. One- and Two-Dimensional High-Resolution NMR from Flat Surfaces. *ACS Central Science* 2019, DOI:10.1021/acscentsci.8b00916 10.1021/acscentsci.8b00916.
- (44) Majumder, S.; Gipson, K. R.; Odom, A. L. A Multicomponent Coupling Sequence for Direct Access to Substituted Quinolines. *Organic Letters* 2009, *11* (20), 4720.
- (45) Bouh, A. O.; Rice, G. L.; Scott, S. L. Mono- and Dinuclear Silica-Supported Titanium(IV) Complexes and the Effect of TiOTi Connectivity on Reactivity. *Journal of the American Chemical Society* 1999, *121* (31), 7201.
- (46) Vujkovic, N.; Fillol, J. L.; Ward, B. D.; Wadepohl, H.; Mountford, P.; Gade, L. H. Insertions into Azatitanacyclobutenes: New Insights into Three-Component Coupling Reactions Involving Imidotitanium Intermediates. *Organometallics* 2008, *27* (11), 2518.
- (47) Ong, T.-G.; Yap, G. P. A.; Richeson, D. S. Catalytic C–N bond metathesis of carbodiimides by group 4 and 5 imido complexes supported by guanidinate ligands. *Chemical communications* 2003, DOI:10.1039/B308710G 10.1039/B308710G(20), 2612.
- (48) Ong, T.-G.; Yap, G. P. A.; Richeson, D. S. Catalytic Construction and Reconstruction of Guanidines: Ti-Mediated Guanylation of Amines and Transamination of Guanidines. *Journal of the American Chemical Society* 2003, *125* (27), 8100.
- (49) Zhu, T.-H.; Wang, S.-Y.; Tao, Y.-Q.; Ji, S.-J. Synthesis of Carbodiimides by I₂/CHP-Mediated Cross-Coupling Reaction of Isocyanides with Amines under Metal-Free Conditions. *Organic Letters* 2015, *17* (8), 1974.
- (50) Bora, P.; Bez, G. Chemoselective isocyanide insertion into the N–H bond using iodine–DMSO: metal-free access to substituted ureas. *Chemical communications* 2018, *54* (60), 8363.

- (51) Ugi, I. M., R.; Lipinski, M.; Bodesheim, F.; Rosendahl, F. Cyclohexyl Isocyanide. *Org. Synth.* 1961, 41, 13.
- (52) Khedkar, V.; Tillack, A.; Beller, M. A Dramatic Effect of Aryloxo Ligands on the Titanium-Catalyzed Hydroamination of Alkynes. *Organic Letters* 2003, 5 (25), 4767.
- (53) Heydari, A.; Khaksar, S.; Esfandyari, M.; Tajbakhsh, M. A novel one-pot reductive amination of aldehydes and ketones with lithium perchlorate and zirconium borohydride–piperazine complexes. *Tetrahedron* 2007, 63 (16), 3363.
- (54) Pei, D.; Wang, Z.; Wei, S.; Zhang, Y.; Sun, J. S-Chiral Sulfinamides as Highly Enantioselective Organocatalysts. *Organic Letters* 2006, 8 (25), 5913.
- (55) Kato, H.; Shibata, I.; Yasaka, Y.; Tsunoi, S.; Yasuda, M.; Baba, A. The reductive amination of aldehydes and ketones by catalytic use of dibutylchlorotin hydride complex. *Chemical communications* 2006, DOI:10.1039/B610614E 10.1039/B610614E(40), 4189.
- (56) Anderson, L. L.; Arnold, J.; Bergman, R. G. Catalytic Hydroamination of Alkynes and Norbornene with Neutral and Cationic Tantalum Imido Complexes. *Organic Letters* 2004, 6 (15), 2519.
- (57) Buil, M. L.; Esteruelas, M. A.; López, A. M.; Mateo, A. C. Preparation of Half-Sandwich Alkyl–Titanium(IV) Complexes Stabilized by a Cyclopentadienyl Ligand with a Pendant Phosphine Tether and Their Use in the Catalytic Hydroamination of Aliphatic and Aromatic Alkynes. *Organometallics* 2006, 25 (17), 4079.
- (58) Heutling, A.; Pohlki, F.; Doye, S. [Ind₂TiMe₂]: A General Catalyst for the Intermolecular Hydroamination of Alkynes. 2004, 10 (12), 3059.
- (59) Lin, B.; Waymouth, R. M. Urea Anions: Simple, Fast, and Selective Catalysts for Ring-Opening Polymerizations. *Journal of the American Chemical Society* 2017, 139 (4), 1645.

CHAPTER 5. REACTIVITY AND RATE LAW DETERMINATION OF A LIGAND-FUNCTIONALIZED SILICA-SUPPORTED TITANIUM CATALYST

5.1 Introduction

An introduction to some of the possible Ti-catalyzed C–N bond forming reactions was discussed in Chapter 4.¹⁻⁶ While many simple C–N bond forming reactions have relatively simple mechanisms and simple rate laws, others are quite complex. As an example, the rate law determined by Doye for Ti-catalyzed hydroamination (Fig. 5.1) suffers from not one, but two equilibrium processes which reduce the effective concentration of the active species (Ti-imide) and hinder the rate of the overall reaction.⁷ Of note is that one of these processes is a dimerization, a process inherent to many active homogeneous catalyst systems, of which several examples with Ti are known.⁸⁻¹³

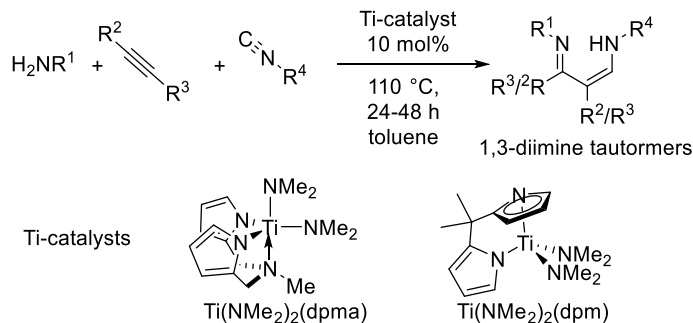


Figure 5.2 (top) General reaction sequence for the 3-component coupling of an amine, alkyne, and isonitrile to yield 1,3-diimine tautomers. (bottom) The two catalysts typically utilized for this transformation.

A wide variety of iminoamination (3CC) products can be synthesized using the Ti-catalysts shown above, with dipyrrolyl ligands under homogeneous conditions. However, in these homogeneous catalyst systems, little can be done if a substrate leads to side reactions, and the regioselectivity is not readily manipulated. Additionally, with the homogeneous nature of these systems, it is likely that similar catalyst deactivation pathways and potential off-cycle occupation of the Ti catalyst to those demonstrated by Doye¹⁸ also contribute to catalyst deactivation and effective reduction of loading in these reactions (*vide supra*).

With the goal of improving on some of these catalyst issues, we set out to perform this same type of chemistry with heterogeneous catalysts. Thus, the work highlighted in Chapter 4 was inspired, to move to a heterogeneous system but maintain similar coordination environment—and corresponding reactivity—to the well-studied homogeneous catalysts. The initial results obtained with the two different catalyst variants that we synthesized, [Ti]200 and [Ti]700, suggested that this was a fruitful direction to explore for Ti-catalyzed iminoamination.

While these catalysts are both competent for hydroamination, [Ti]200 is a poor catalyst for iminoamination. On the other hand, [Ti]700 is a decent iminoamination catalyst for both terminal and internal aromatic alkynes coupled with aromatic primary amines. In fact, with aniline, 1-phenylpropyne, and CyNC, a yield of 88% was noted in only 16 h. This result not only

demonstrates a dramatic improvement in iminoamination ability relative to the [Ti]200, which is severely substrate-scope-limited, but also demonstrates catalytic ability comparable to the best homogeneous catalysts for the same reaction at lower catalyst loadings. Some challenges still remained to making the material a general iminoamination catalyst capable of dramatically improving upon the ability of the homogeneous systems.

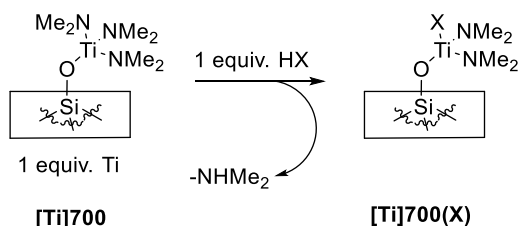
The first issue remaining with these silica-supported catalysts, specifically [Ti]700 is a limited substrate scope tolerance. The catalyst cannot perform iminoamination between an unsubstituted aniline and a terminal alkyl alkyne, such as 1-octyne. Additionally, with both heterogeneous catalysts, intolerance to alkyl primary amines had been observed. Finally, we also had evidence for catalyst deactivation, as the material was not able to be recycled (i.e. multiple runs of the reaction catalyzed by a single batch of material).

Considering traditional high-valent transition metal mechanisms for these reactions, i.e. Bergman's mechanism for Zr(IV) catalyzed hydroamination^{19,20} or Doye's mechanism for Ti(IV)⁷ shown above, only 2 protolytically active sites are necessary on the metal in order to form the active metal-imide species. Alternatively, a mechanism such as Marks' mechanism for Ln-based hydroamination, requires a single Ln–N bond where olefin or alkyne insertion can occur.²¹

Following either path, the Ti sites in [Ti]700 have more protolytically cleavable NMe₂ ligands than each site needs to undergo these types of C–N bond forming reactions. This leads to the possibility of ligand functionalization of the surface-bound metal to *tune reactivity* while maintaining the active sites necessary for reactivity. Capitalizing on this idea, we decided to pursue ligand functionalization of the [Ti]700 catalyst for three component coupling chemistry. We suspected this would be an easy route to tuning the substrate tolerance and subsequent selectivity in the products of iminoamination yielded in [Ti]700 catalyzed reactions.

5.2 Activity of [Ti]700(X) for Three-Component Coupling Chemistry with a Variety of X⁻ Ligands

Operating under the assumption that the surface-bound Ti sites are catalyzing HA and 3CC, with a Ti-imide active species, we hypothesized that two protolytically active sites are needed to maintain the catalytic activity of the silica-supported Ti species. With [Ti]700, 3 protolytically active sites remain on Ti after binding to the surface. Theoretically, we can add 1 stoichiometric equivalent (relative to Ti) of an irreversibly bound Brønsted acidic species, HX, to our Ti catalyst to protonate one NMe₂ ligand to liberate NHMe₂. Removal of one NMe₂ still maintains a Ti site that is active for the desired catalysis. In this manner, a variety of HX species can be utilized as ligand additives to functionalize the surface-bound titanium sites, providing the catalyst species [Ti]700(X). The addition of these ligands should result in dramatic differences in the reactivity of the Ti species, just as ancillary ligand design affects the performance of homogeneous catalysts. This approach is illustrated in Scheme 5.1.



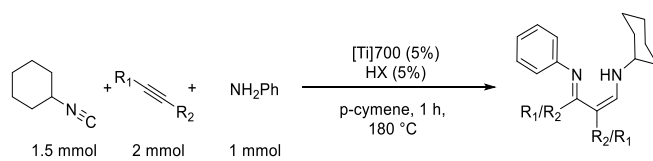
Scheme 5.1 Addition of Brønsted acidic HX ligands to [Ti]700 to generate [Ti]700(X) species.

We began screening the 3CC reactions of aniline and CyNC with 4 different alkynes, employing a variety of HX species as ligand additives. Note, in terms of the overall reaction stoichiometry, we are adding 5 mol% HX, or a 1:1 ratio of Ti to HX. Overall, the ligands we chose to examine in these initial studies are similar to those which have yielded competent catalysts in homogeneous systems, such as phenoxides, pyrrolides, or amidate ligands.^{2, 22, 23} The goal was to examine commercially available or easily synthesized ligands (1 step reactions from cheap starting

materials), in keeping with the “green nature” and simplicity of the [Ti]700 catalyst material and the intent to avoiding time-intensive ligand design and preparation. Even with these simple ligands, the effects of HX addition to these Ti-catalyzed iminoamination reactions is dramatic.

The reaction times with HX additives are incredibly fast. With many combinations of substrates and HX ligands, the 3CC reactions now provide yields of >90% in less than 1 h of reaction time! For comparison, even with the best homogeneous catalyst, these reactions typically take on the order of 24 h to complete. Additionally, large changes in the regioselectivity of the catalyst can be observed depending on the identity of HX, within each set of substrates. This is demonstrated well by Scheme 5.2 and Fig. 5.3, which shows the yields of the different 3CC reactions examined at 1 h reaction times, using a variety of different HX ligands. Tables that list each of these results can be found in the Experimental but are shown graphically here for ease of discussion.

Because the parent precatalyst, [Ti]700, catalyzes the 3CC reactions of aniline and CyNC with both 1-phenylpropyne and phenylacetylene, in the absence of HX, we can compare the overall regioselectivity and rates of these reactions with HX included, to the parent catalyst.²⁴ This provides a complete picture of how the ligand additives affect catalyst performance. In both cases, it is apparent that the rate of these reactions is dramatically enhanced with the inclusion of a ligand additive. For example, even though 1-phenylpropyne is an internal alkyne, with the right ligands, we see over 90% yield of the iminoamination products in under 1 h. Namely, [Ti]700(X), where X = 2,6-dimethylphenylamidate, gives the 3CC products in 99% yield in only 1 h with a regioselectivity of 10.2:1. In direct comparison to the [Ti]700, which takes 16 h to reach 88% completion with a very similar regioselectivity of 10.3:1, the rate increase upon inclusion of HX is readily apparent.



Scheme 5.2 Iminoamination reaction examined with a variety of HX ligands.

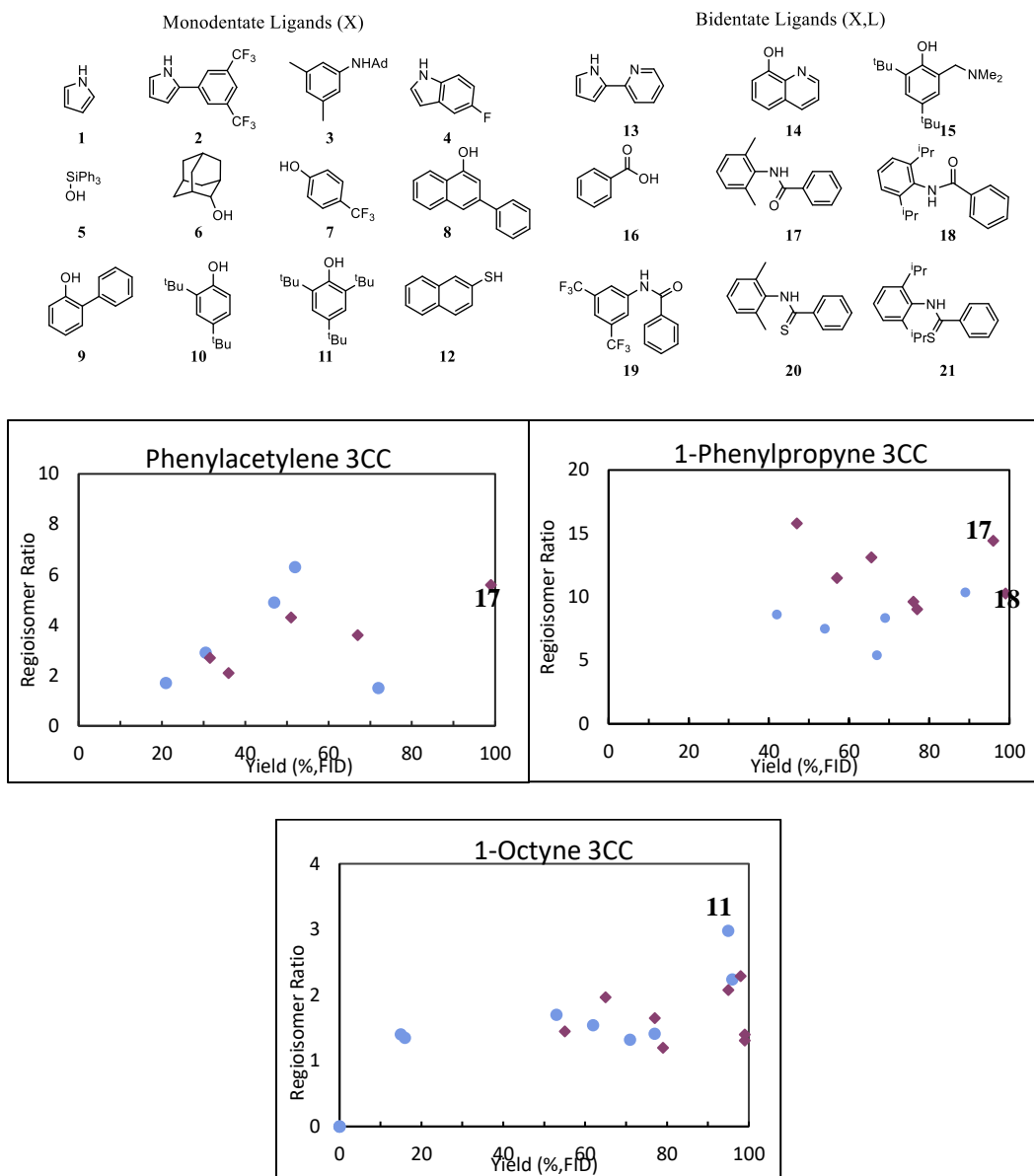


Figure 5.3 Effects of different HX ligands on the general 3CC reaction utilizing different alkynes: (top) The variety of HX ligands screened in the 3CC reactions; (bottom) Plots of the 3CC reaction products showing the regioisomer ratio versus % yield for each HX ligand examined. In the plots, burgundy diamonds correspond to bidentate ligands, while blue circles correspond to monodentate ligands. The best ligands for each alkyne are specified next to their respective points.

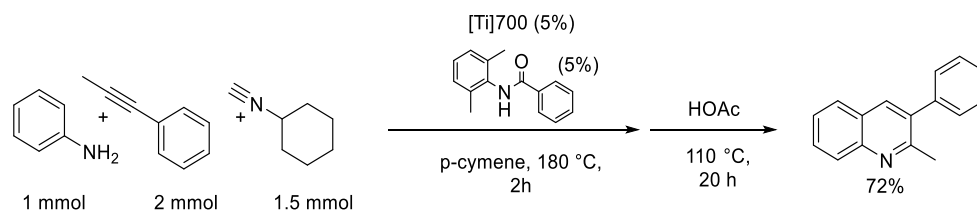
A very comparable trend is noted with phenylacetylene as the coupled alkyne. The [Ti]700 provides a yield of 52% in 18 h, with a regioselectivity of 6.3:1. Yet when [Ti]700(X) is used as the catalyst, again where X = 2,6-dimethylphenylamidate, we observe a yield of 99% in 1 h with a regioselectivity of 5.6:1. It is also worth noting that with phenylacetylene, the inclusion of the

ligand greatly reduces the propensity for side reactions. With [Ti]700, we see 18% of the aniline remaining after 18 h; between the 3CC product and the unreacted aniline, however, only 70% of the initial aniline has been accounted for, with the remaining 30% going to hydroamination (~15%), formamidine production (~5%), and other side products. Additionally, alkyne trimerization is also observed by GC analysis. While the reduction in side product formation with 1-phenylpropyne is less substantial than it is with phenylacetylene upon addition of HX ligand to the catalytic 3CC reactions, it is still observed (on the order of <5%). Thus overall, the 3CC reactions using [Ti]700 catalysts appear to offer 3 major advantages: (1) faster rates, (2) higher yields, and (3) reduction in side product formation.

The advantages of ligand inclusion continue to grow when we consider one of the substrate-limited reactions with [Ti]700: the coupling of aniline and CyNC with a terminal alkyl alkyne, 1-octyne. This reaction with [Ti]700 had previously yielded only side products, but did not show formation of the desired 3CC products.^{17,24} Switching to [Ti]700(X), however, has provided a number of catalytic species that can do this transformation in high yields (See Fig. 5.3). Now the main limitation in this reaction is the relatively low regioselectivity, which has previously been observed when utilizing a terminal alkyl alkyne, such as 1-hexyne as the coupling partner (*vide supra*).¹⁴ Despite this regioselectivity limitation, we do see vast opportunity to increase the regioselectivity, as changing the HX ligands in this reaction results in large changes in this ratio. Thus, finding a selective catalyst may simply require a slightly different ligand from the classes examined here. Also, it is still an improvement over homogeneous systems and their inherent regioselectivity, which is close to 1:1 (*vide supra*).

5.3 One-pot-two-step Heterocycle Synthesis with [Ti]700(X)

Quantification of organic products in catalyzed reactions via *in situ* techniques (i.e. GC analysis calibrated against authentic isolated products) is valuable and provides detailed information about the species in reaction solutions. However, for the Ti-catalyzed iminoamination reactions discussed above, product isolation remains the primary objective for the functionalized heterocycles that can proceed directly from the iminoamination products. To evaluate the practical usability of the [Ti]700(X) catalyst system, we pursued product isolation of a previously synthesized quinoline (using the one-pot-two-step method) produced with homogeneous systems, to provide direct comparison with a [Ti]700(X) reaction.^{25, 26} Scheme 5.2 describes the reaction, which provided an isolated quinoline yield of 72% after column chromatography (previously 53%).²⁵ This synthesis demonstrates that the high yields, high regioselectivities, and limited amounts of side products formed with reactions catalyzed by the silica-supported Ti could result in higher yields and more readily purified products than many previous homogeneous catalysts.



Scheme 5.3 Quinoline synthesis using 5 mol% [Ti]700 with 5 mol% 2,6-dimethylphenylamidate as ligand.

Another functionalization of interest is the formation of 2-amino-3-cyanopyridines in a similar 1-pot-2-step reaction.²⁷ The original report of this complex, produced through Ti-catalyzed iminoamination, employed $\text{Ti}(\text{dpm})(\text{NMe}_2)_2$ (10 mol%) as the catalyst and required a 24 h iminoamination step, followed by a 2 h ring-closure reaction. Additionally, in the original report, the product pyridine was characterized as a waxy brown solid. Attempts to repeat the synthesis, as originally reported, have failed in the hands of several researchers. Highly impure reaction

mixtures result and isolation of the product from the reaction mixtures is quite challenging. This synthetic method, utilizing 10 mol% $\text{Ti}(\text{dpm})(\text{NMe}_2)_2$ does provide product, as an oily, colored residue with residual impurities by NMR, GC-MS, and TLC.

There are several places where the synthesis of the 2-amino-3-cyano pyridines could be encountering challenges to reproducibility on each experimental run. Specifically, the second step to transform the iminoamination product into the final pyridine has not been optimized and still includes 3 Å molecular sieves (perhaps to prevent unintentional hydration). It has been directly observed by GCMS of the crude iminoamination reaction mixture that with $\text{Ti}(\text{dpm})(\text{NMe}_2)_2$, the iminoamination reaction produces byproducts and doesn't go to completion; regardless of additional reaction steps and their influence in compromising the yield, this observation suggests fundamental problems with the formation of the iminoamination product in the first step. However, the impure product and reproducibility issues are a major concern.

Using $[\text{Ti}]700(\text{Amidate}^{2,6\text{-dimethyl}})$, the coupling of 3,5-dimethylaniline, CyNC, and 1-phenylpropyne, followed by base-catalyzed pyridine formation with malononitrile takes a total of 4 h of reaction time (Fig. 5.4). The resulting pyridine product was isolated in 70% yield after these 2 steps. While a slight impurity was noted in the product by NMR, recrystallization of the pale-yellow solid from a dilute hexane solution yields extremely pure, X-ray quality crystals of the pyridine. This synthesis as well as the crystal structure are shown in Fig. 5.4, below, and have provided a very reliable route to isolation of a clean, crystalline pyridine product, suitable for use in biological studies.

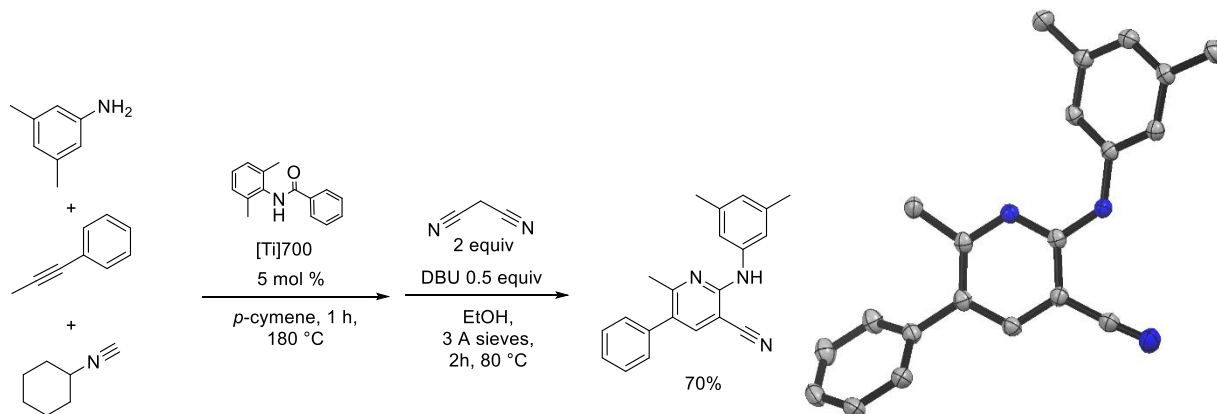


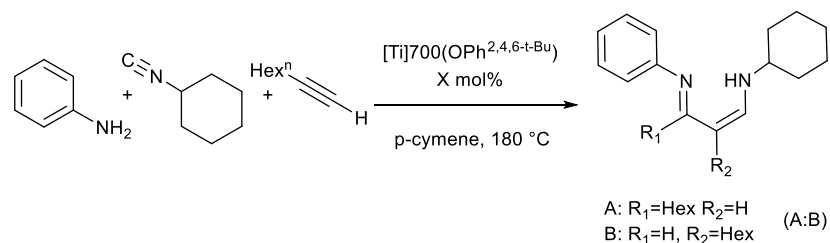
Figure 5.4 The synthetic scheme (left) and single crystal X-ray structure of a 2-amino-3-cyanopyridine synthesized using [Ti]700(X).

This investigation and application of the [Ti]700(X) system to the synthesis of complex heterocycles clearly demonstrates that the catalyst system is of practical use in the laboratory for isolation of targeted organic molecules. It also demonstrates that the improvements in the iminoamination step—cleaner reactions with fewer byproducts, consumption of limiting reagents, inertness of the catalyst toward subsequent functionalization steps—all add up to better results with the heterogeneous catalyst system compared to the homogeneous systems with certain substrates.

5.4 3CC Reaction Kinetics for [Ti]700(X)

To gain insight into how the [Ti]700(X) system is outperforming the homogeneous systems, we wanted to probe the rate law for the Ti-catalyzed iminoamination reaction. Following the simple graphical method of Bures, to analyze a reaction for order in reagents and catalyst, the modifications listed in Table 2 were made to the reaction under study.^{28, 29} Utilizing $X^- = 2,4,6$ -tri-*tert*-butylphenoxide as the ancillary ligand, a very clean and rapid reaction suitable for kinetic analysis, was achieved with aniline, 1-octyne, and CyNC as the coupling partners. Note that the concentration of the reactions examined for kinetic analysis were about $\frac{1}{2}$ of the concentration typically used for one of our standard heterogeneous catalyzed reaction. This allowed for a slower

reaction that was more amenable to sampling the amount of product over time (i.e. the reaction continued to run for longer than 1 h), as well as conservation of materials.



Scheme 5.4 General conditions and substrates used to examine the iminoamination reaction with [Ti]700(X) catalyst.

Table 5.1 Conditions screened for reaction order in each substrate and catalyst for heterogeneous catalyzed 3-component coupling of aniline, 1-octyne, and ^tBuNC. The initial catalyst and reagent amounts are listed by concentration (M).

Entry	Ti(NMe ₂) ₂ (X)/SiO ₂ ⁷⁰⁰ (mol%)	H ₂ NPh	CyNC	1-Octyne	Total Conversion to 3CC (%) ^b	Regioisomer Ratio (A:B)	Hydroamination Byproduct (%)
1	0.012 (5)	0.25	0.25	0.51	83	2.9:1	16
2 ^a	0.006 (2.5)	0.25	0.25	0.51	8	1.8:1	3
3	0.024 (10)	0.25	0.25	0.51	83	3.4:1	15
4	0.012 (5)	0.51	0.25	0.51	54	2.1:1	9
5	0.012 (5)	0.25	0.51	0.51	61	3.2:1	8
6	0.012 (5)	0.25	0.25	1.01	58	3.0:1	7
7 ^c	0.012 (5)	0.25	0.25	0.51	59	2.9:1	8

^aWith less than 5 mol% catalyst loading, a large amount of formamidine is produced; in fact the forward rate of formamidine formation is in excess of that of 3CC formation (18% vs. 8%). With 5 mol% or more catalyst loading, essentially no formamidine formation is observed, and 3CC is the only reaction with substantial forward progress after the initial heating period. ^bThis is the conversion observed after approximately 100 minutes of reaction time. Typically, the reaction progress has begun to plateau at this point; note in entries 1 and 3 this yield correlates to consumption of the limiting reagent. ^cIn addition to the reagents listed in the table, an initial 3CC concentration was included in this reaction mixture (0.02 M) to probe for 3CC inhibition on the reaction.

The graphical analyses provided by the experiments listed in Table 5.1, present some complications. First, there appears to be hydroamination occurring rapidly at the beginning of the reaction while the solution is reaching thermal equilibrium with the aluminum well-plate. In Entry 1 for example, the first reaction sample at 10 minutes shows a HA concentration of 0.02 M (8%), while at the end of the reaction at 100 minutes, there is a HA product concentration of 0.04 M (16%). As much HA product is produced in the first 10 minutes as is produced throughout the remaining 90 minutes of reaction time. This indicates that HA initiates with the heterogeneous

catalyst at a lower temperature relative to iminoamination. However, when the temperature for iminoamination is reached, it becomes the predominant reaction catalyzed in this complex mixture, by an order of magnitude.

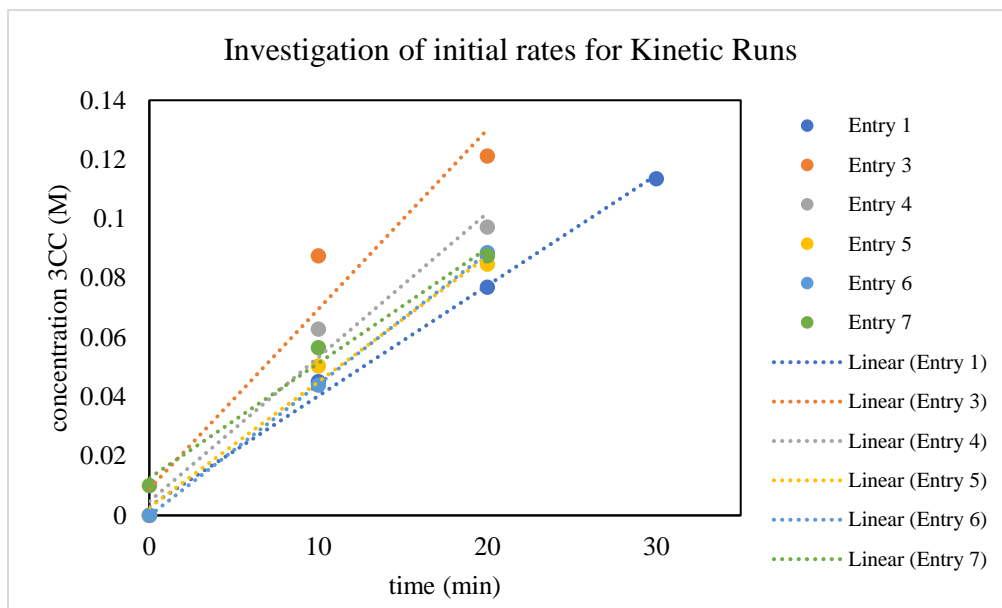


Figure 5.5 Plot of initial rates from the kinetic experiments shown in Table 5.1. The initial rates, determined from linear fits shown in the plot above, are listed in the table below. These rates may be slower than the actual initial rates as they go far beyond 10% conversions.

Table 5.2 Estimated initial rates ($M^{-1}min^{-1}$) from the various conditions in Table 5.1. These estimates may be artificially low, as the reactions progressed far beyond 10% conversion in ~20 min.

Entry Number	Initial Rate	R ²
1	0.004	0.99
3	0.008	0.93
4	0.005	0.97
5	0.004	0.99
6	0.004	0.99
7	0.004	1

Also note that total conversion was not being reached under several of the conditions listed in Table 5.1. With the conditions in Entries 1 and 3, we noted essentially quantitative conversion of the H₂NPh starting material into a combination of 3CC products and HA side product (99% and 98%) respectively. However, in many of the other entries in Table 5.1, we noted a similar problem, with the average reaction consuming only about 70% of the initial H₂NPh starting material. This,

along with other observations from the graphical analysis of the kinetics, suggests that catalyst deactivation is an issue in this system. Given that Entries 1 and 3 reached total conversion, the relative rate of deactivation with the heterogeneous catalyst under these conditions is certainly a better match when compared to homogeneous catalysts (see Chapter 6), but it complicates the rate law analysis substantially. For these reasons, a plot of the initial rates extracted from the kinetic runs shown in Table 5.1, is presented in Fig. 5.5 and Table 5.2, for comparison.

There are some clear relationships between the rate law and the substrates used in the reaction. Primarily, upon graphical analysis of Entries 1 and 4 and 1 and 5, we noted that there appears to be inverse 1st-order on both the concentration of aniline and isonitrile in the reaction (Fig. 5.6). There appears to be a zeroth order dependence in alkyne (Entries 1 and 6), looking at the graphical order and initial rates observed. All three of these reactions present less total conversion than Entry 1. The graphically determined rate law is summarized in Eq. 5.1, below. With the aniline and isonitrile concentrations and their perceived inverse first order dependence, this makes sense. Increasing the concentrations of these substrates decreases the overall rate of the reaction and makes the deactivation process (or processes) catch up with the catalyst faster than it did under the conditions in Entry 1.

$$Rate = k[Ti][H_2NR]^{-1}[CyNC]^{-1} \quad (\text{Eq. 5.1})$$

Initially it seemed less obvious how a zeroth order dependence was possible with alkyne, yet lower conversion was achieved. This may suggest that the alkyne concentration directly affects the rate of the deactivation of the catalyst; this interaction remains a possibility, as the means of catalyst deactivation are not yet fully understood (See Chapter 4).

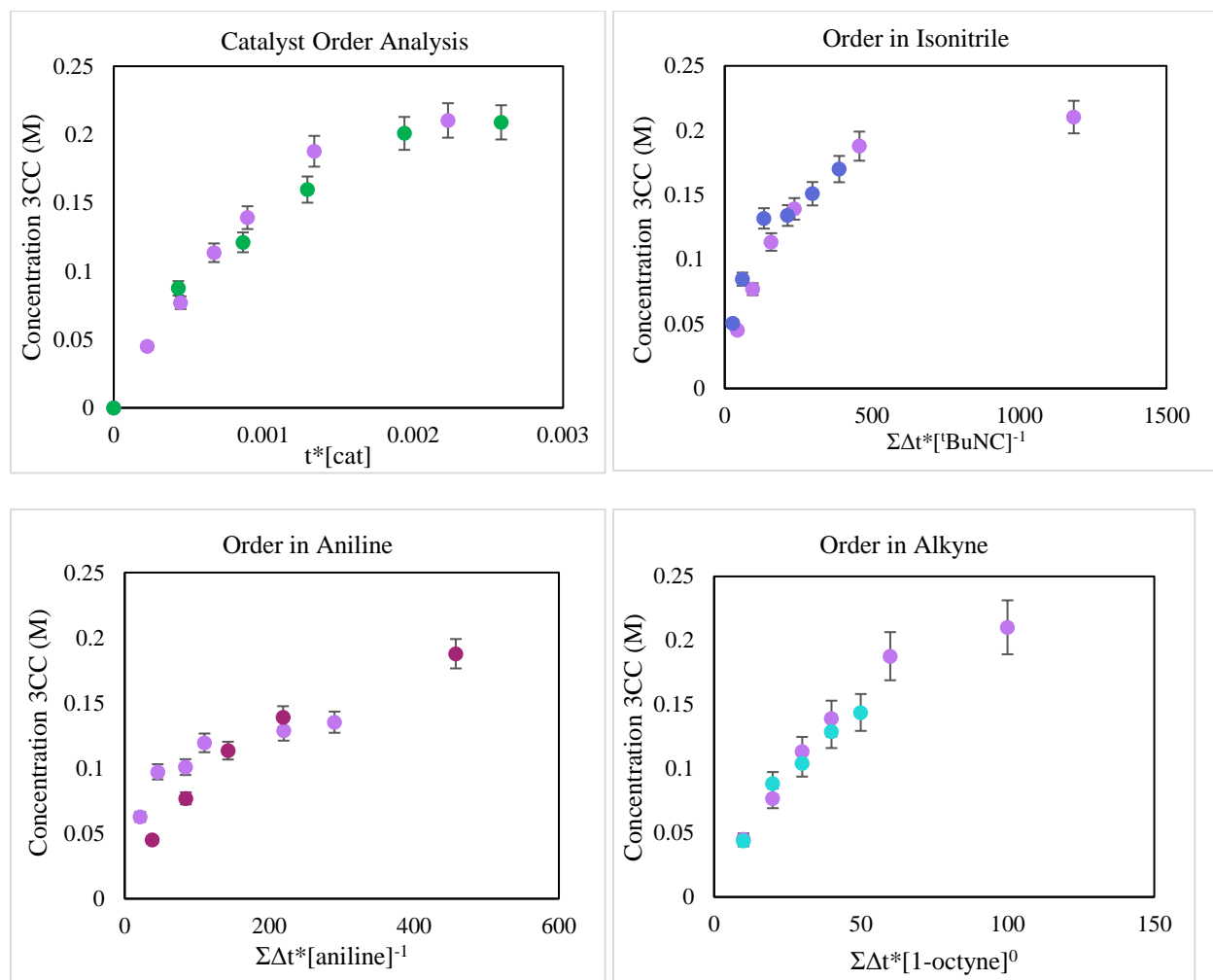


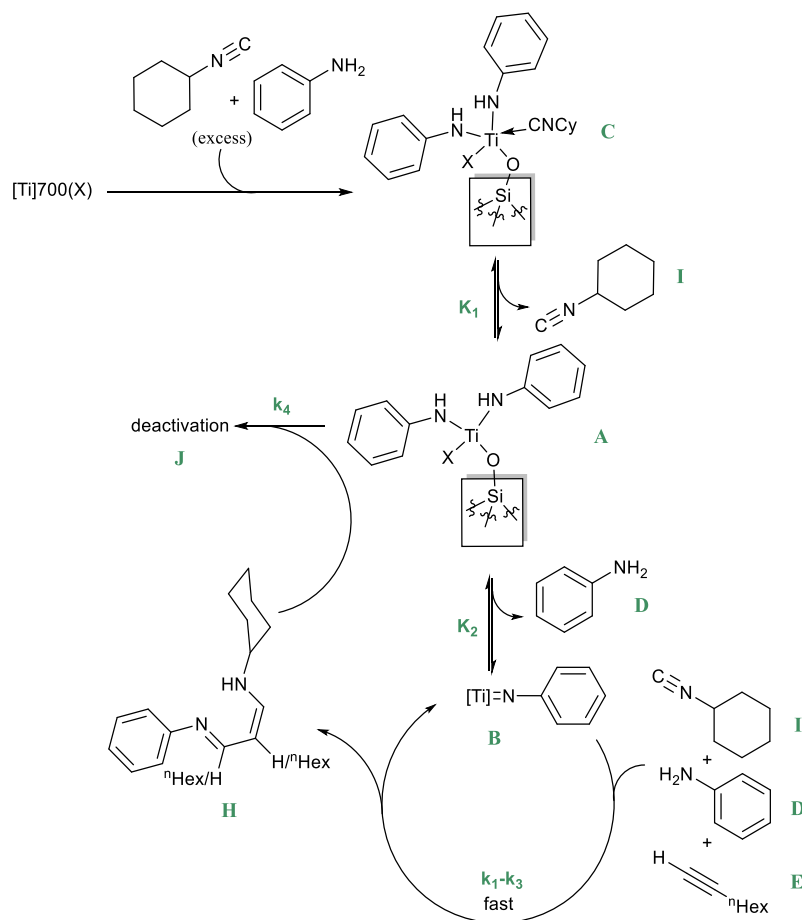
Figure 5.6 Order of catalyst and reagent dependence for rate law of the iminoamination reaction catalyzed by [Ti]700(X). Entry 1 represents the light purple points, with the following concentrations: 0.25 M aniline, 0.25 M CyNC, 0.51 M 1-octyne, and 0.012 M (5 mol%) Ti. It is plotted against the following entries, where the substrate alteration is indicated: 3 (green, 0.024 M (10 mol%) Ti), 5 (blue, 0.51 M CyNC), 4 (maroon, 0.51 M aniline), and 6 (aqua, 1.01 M 1-octyne) to demonstrate how different reagent concentrations affect the rate of the iminoamination reactions. For rough approximations of the initial rates, refer to Fig. 5.5.

Finally, according to the graphical analysis method, it seems that the rate is first-order dependent on catalyst concentration. There also doesn't appear to be an obvious inhibitory relationship with the [3CC] and reaction rate as both Entries 1 and 7 demonstrate similar rates, but again, similar to Entry 6 (excess 1-octyne), a lower conversion is achieved with Entry 7 compared to Entry 1.

We specify that the rate law shown above describes the initial rate of the reaction because this simple equation assumes a constant catalyst concentration. As a consequence, it fails to accurately represent the catalyst deactivation that occurs throughout the course of the reaction. To obtain a more accurate idea of what happens in the reaction, start-to-finish, we turned to kinetic simulations. Using the kinetic data outlined in Table 5.1, we attempted to model the proposed mechanism of the iminoamination reaction using KinSim software.

The mechanism we propose, and the corresponding rate law probed using KINSIM are shown in Fig. 5.6 (See Experimental for more information). Based on the experimental observations and the rate law, the rate determining step appears to be generation of the active catalytic species from the “resting state” of the catalyst, which we approximate as species **C** in Fig. 5.7, below. This resting state appears to be a SiO–Ti(NHPh)₂(CNCy) species—such that generation of the Ti-imide species, which initiates the coupling for generating the 3CC product, is inhibited by CyNC and aniline.

We propose that dissociation of 1 equivalent of H₂NPh and 1 equivalent of CNCy is required before the [Ti]700 supported sites reach the active imido form of the catalyst, from which the catalytic cycle can be entered. This interpretation is consistent with the inverse-first-order or inhibitory dependence of the rate upon the concentrations of H₂NPh and CyNC. As a result, the individual rates of any given step in the presumably multi-step conversion of the three substrates (aniline, alkyne, and isonitrile) into the coupled product may not play a determining role in the overall rate. Since these steps appear fast relative to the formation of the active catalytic species, the actual 3-component coupling can therefore be treated effectively as a single rapid step. This results in the assumption that the first step in the iminoamination cycle ([2+2] cycloaddition of alkyne to the Ti-imide π bond) occurs each time the active Ti-imide is generated.



$$rate = k[Ti][CyNC]^{-1}[H_2NPh]^{-1} \quad \text{where } k \text{ is determined by } k_4, K_1, \text{ and } K_2$$

Figure 5.7 Proposed catalytic cycle for [Ti]700(X) based on experimental kinetic data and KINSIM modeling. Note, in the figure, the green letters, rate constants, and equilibrium constants are from the KINSIM model. The deactivation step from A to J is based on experimental observations of 3CC reactivity with homogeneous Ti analogues (see Chapter 6).

From a practical standpoint, of improving the reaction rate, we took a more qualitative approach. Thus, regardless of the full rate equation, the suggestion that formation of the active imido is the rate-limiting step, and that this step is dependent on CyNC dissociation and H₂NPh, led us to reconsider the effects of the X⁻ ancillary ligand on the rates of the [Ti]700(X) catalysts. Specifically, we wondered if increasing the electronic donor ability of the X⁻ ligand would lead to more labile interactions with datively bound CyNC and facilitate a faster equilibrium between a (SiO₂⁷⁰⁰)Ti(NHPh)₂(CNCy)(X) species and the proposed active Ti-imide. According to the rate

law derived from our graphical analyses, rendering these changes stands to greatly improve the rate of the 3CC reaction.

In order to test this hypothesis, we turned to the Ligand Donor Parameter system. This system uses a Cr(VI), d^0 model complex to experimentally determine quantitative electronic donor abilities of various X^- ligands to a high valent metal, as discussed in Chapters 1-3.^{30, 31} Previously, it has been demonstrated that these LDP values, determined for X^- ligands on Cr(VI), correlate very well with the electronic effects of ancillary ligands on Ti(IV) hydroamination catalyst.²² The extension of LDP analysis of ligand effects in this heterogeneous system aligns well with the previous studies, as we are still examining the electronic effects of X^- ancillary ligands on a Ti(IV) catalyst.

The easiest way to make these comparisons while maintaining similar conversions and preventing the reintroduction of side reaction competition in the catalyzed 3CC reaction, is to alter the periphery of the X^- ligand to render subtle electronic changes. This allows the ligands to remain isosteric and result in similar bond distances and steric profiles around the active metal. A series of 2,6-di-*tert*-butyl-4-R-phenols were used as the X^- ligands in the [Ti]700(X) catalyst material. A list of the phenols used is displayed in Fig. 5.8. Our strategy of maintaining the same steric profile around the metal and changing only the R group on the phenols did result in comparable conversions, without the observation of additional byproducts in the reaction mixtures (relative to 2,4,6-tri-*tert*-butylphenol). Any observed changes in the rates of the catalysts is also directly related to the electronic donor ability of the ligand alone, without the additional complication of steric effects on the rate.

Comparing the LDP values for the ligands examined, listed in Fig. 5.8, the relative donor ability is ordered such that $R = \text{OMe} > \text{H} \sim \text{tBu} > \text{Br}$. Looking at the measured k_{obs} (initial) for

each of the catalyst generated with these ancillary ligands, or the plots of the reaction traces also shown in Fig. 5.8 and Table 5.3, we see that the rate of the catalyst follows the same order. This supports our hypothesis, that making the metal center more electron-rich by increasing the donor ability of the ancillary X^- ligand increases the rate of active species formation, and thus increases the rate of the overall reaction. This also supports the possibility that, with the right ligand(s), the catalyst may be able to achieve rates that allow it to outpace catalyst deactivation processes.

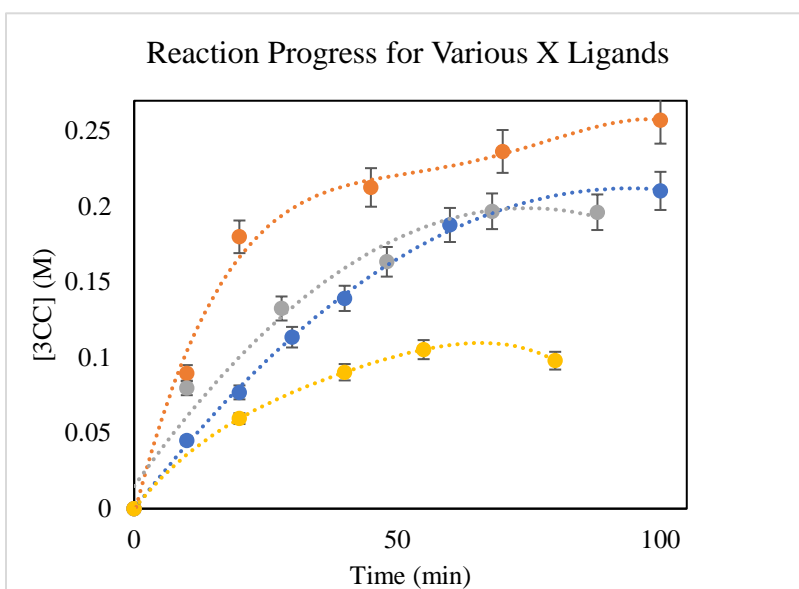
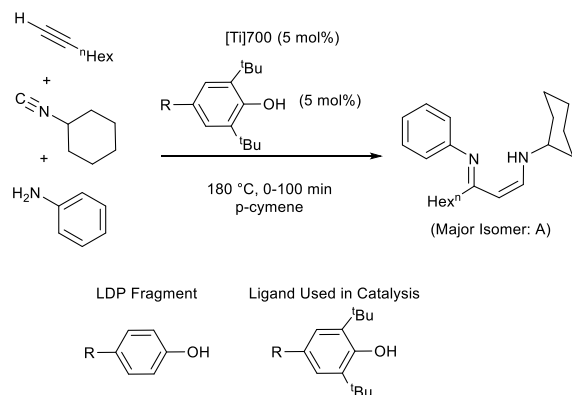


Figure 5.8 Correlation between reaction rate and donor ability of X^- in heterogeneous $[Ti]700(X)$ catalyzed 3CC reactions. More electron-donating X^- ligands seem to enhance the rate of the reaction by increasing the rate of formation of the active species from the resting state of the catalyst. (blue = t -Bu, grey = H, orange = OMe, yellow = Br).

Table 5.3 Ligands examined in Figure 5.8, showing LDP values of each phenoxide and the k_{obs} for the iminoamination reaction catalyzed with the given phenoxide as ligand (X) with $[Ti]700(X)$.

Entry	R	LDP (kcal/mol)	$k_{obs}(\text{initial})$ (s^{-1})	Trace color
1	t Bu	12.01	0.00006	Blue
2	H	11.98	0.00008	Grey
3	OMe	11.71	0.00010	Orange
4	Br	12.18	0.00004	Yellow

5.5 Catalyst Poisoning and Recyclability

Recyclability of the catalyst material was one of our initial goals in moving toward heterogeneous Ti based catalysts for these hydroamination and multicomponent coupling reactions. Previously, utilizing [Ti]200, it was determined that the catalyst cannot be perfectly recycled, as Ti is leached from the surface of the SiO₂²⁰⁰ support. It was also determined that this leaching of the active metal originates from interaction with alkyne substrate, and while modest reusability is noted for a few iterations of a given reaction, both the yield and regioselectivity of the catalyst suffer with repeated use of the catalyst material.

The recyclability of [Ti]700 species was also examined, and initial results demonstrated only trace amounts of product generated upon a second use of the catalyst material. This was the case for both HA or 3CC reactions. Even with the inclusion of a variety of HX type ligands, the [Ti]700(X) is not recyclable. Our initial suspicion was that the [Ti]700(X) and the [Ti]700 material may suffer from loss of the active metal via interaction with substrates, similar to the [Ti]200. However, by examining the Ti concentration in a variety of [Ti]700(X) samples (and [Ti]700, see Chapter 4), after use in a catalytic reaction, there appeared to be no statistically significant loss of Ti from the material. The results of these analyses, which utilized ICP-OES spectroscopy to determine the Ti concentration in the used catalyst samples, is shown in Table 5.4.

Table 5.4 ICP-OES analysis of various treatments for the [Ti]700 precatalyst material.

Ti(X)₃/SiO₂⁷⁰⁰ species	ICP determined Ti wt% (±)	Material Evaluation
[Ti]700(OPh ^{2,4,6-tri-tbutyl})	1.53 (0.06)	Within error of calculated Ti wt%
[Ti]700(pypyr)	1.38 (0.05)	
[Ti]700(2,6-dimethylphenylamidate)	1.36 (0.04)	
[Ti]700(OSiPh ₃)	1.38 (0.04)	
[Ti]700	1.42 (0.03)	
Ti(X)₃/SiO₂⁷⁰⁰ species	ICP Ti wt% calculated (±)	
As-prepared [Ti]700	1.46 (0.12)	
Used [Ti]700(X) ^a	1.46-1.35 (0.11)	

^aA range is provided for the calculated wt% Ti for used [Ti]700(X) because different speciation may occur on the Ti sites after a reaction. (i.e. there are 3 coordination sites that could be occupied by X⁻, NHPPh⁻, CyNC, etc.).

Without evidence of Ti loss, we then suspected that, similar to our suspicions about [Ti]700, stable surface species were forming on the active Ti sites. Under the standard 3CC conditions, there is both excess alkyne and excess cyclohexylisonitrile. Either of these species, or any product generated in the reaction mixture, could form non-innocent interactions with the metal that would lead to metallocycles forming on the catalyst surface, for example. Such species may not easily re-enter our catalytic cycle via generation of a Ti-imido simply by addition of more substrates, similar to what we observed with [Ti]700 (See Chapter 4).

With non-innocent substrates, potentially adjusting the ratio of the three substrates in the 3CC reaction would reduce these side reactions that lead to deactivation of the catalyst. Both decreasing the amount of CyNC used (1 equiv) in the reaction and increasing the amount of aniline so that it was no longer the limiting reagent (2 equiv), resulted in lower yields than those achieved with the general 3CC conditions. Additionally, the catalyst material recovered from these reactions had still been deactivated. Unfortunately, this simple strategy was not effective at preserving the

activity of the Ti sites. In light of the kinetic analyses, this result is somewhat unsurprising, as both CyNC and H₂NPh demonstrate inverse first order dependence in the rate law; thus, with these conditions, the total reaction rate is likely lower than it was with the initial reaction conditions.

5.6 Poisoning Experiments and Controls for [Ti]700

Note, for these poisoning experiments and regeneration attempts, a simpler hydroamination reaction was examined, as opposed to iminoamination. The general reaction scheme for this hydroamination reaction is outlined in the header for Table 5.3. In these “poisoning” experiments, the equilibrium formation of the active Ti–imido species is systematically altered by the addition of an *excess* of HX compounds. The HX compounds compete with NH₂Ph, as ligands that occupy the active sites on Ti. We would predict that as more of the HX species is added, the concentration of inactive species such as Ti(X)₃/SiO₂⁷⁰⁰ will increase relative to the proposed active species, Ti(=NR)X/SiO₂⁷⁰⁰. This shift should be directly observed by a reduction in the rate of catalysis and/or a decreased overall yield.

With the closely related [Ti]200, addition of 1.2 equiv of pyrrole to the catalyst decreased the performance of the catalyst to about 20% of the activity of the un-poisoned catalyst for the hydroamination of 1-phenylpropyne and aniline. This finding, in combination with the observation that *N*-methyl-aniline does not react with [Ti]200, served to support the assumption that generation of an imido species is needed to facilitate the catalysis.

With [Ti]700, the addition of 1 equiv of HX results in the formation of [Ti]700(X), which retains two protolytically active sites (two NMe₂ ligands), and is an active catalyst with comparable activity to the original [Ti]700, resulting in high overall yields for hydroamination of aniline and 1-octyne. The addition of more equivalents of HX, does indeed decrease the overall yields of these reactions, but by a surprisingly small amount. As an example, Fig. 5.9 shows the yield obtained

with 3 different amounts of pyrrole added to the [Ti]700 catalyst. We see that the [Ti]700 and the [Ti]700(pyrrolide) give similar overall results, both with yields over 90%. When 10 equivalents of pyrrole was added, which is enough pyrrole to “poison” the catalysts 3 times over, we still observe >80% yield in less than 1 h. Even with the inclusion of up to 40 equiv of pyrrole, which is 2.5 times the amount of H₂NPh in the reaction mixture, we still observed 70% yield in 1 h.

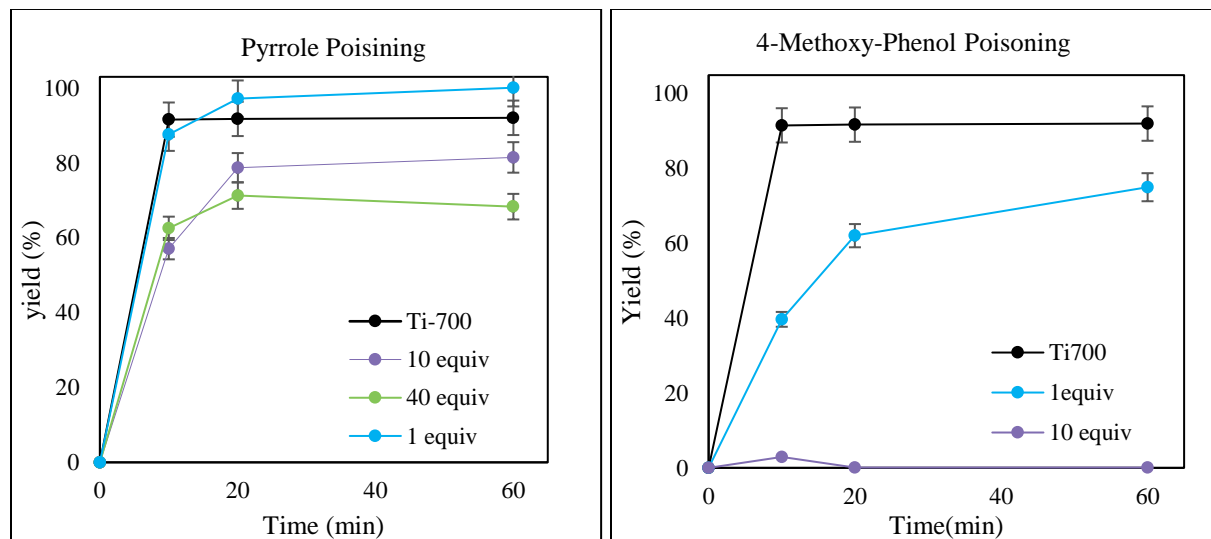


Figure 5.9 Poisoning experiments with pyrrole and 2-*tert*-butyl-4-methoxyphenol, showing very different catalyst activity with varying concentrations of the two different HX ligands.

These results starkly contrast the observations with [Ti]200, and we sought to determine whether this resilience to poisoning was a general trait with the [Ti]700 or was inherently related to some property of the specific HX ligand used, in this instance pyrrole. Since in the 3CC ligand screenings, phenols generally performed well as ligands, addition of a substituted phenol to the HA reaction was first examined for comparison. Similar to the pyrrole reaction, 1 equivalent of the phenol results in catalyst performance similar to that of [Ti]700. However, the catalytic activity is eliminated when 10 equivalents of phenol was added. This experiment suggests that the properties of HX determine whether the equilibria favor inactive species such as $\text{Ti}(\text{X})_3/\text{SiO}_2^{700}$ or the active $\text{Ti}(=\text{NR})\text{X}/\text{SiO}_2^{700}$, where aniline displaces X^- and the Ti species can enter the catalytic cycle.

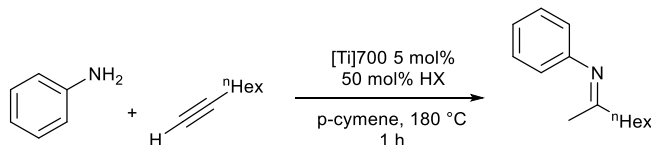


Figure 5.10 General hydroamination reaction and conditions applied to [Ti]700 catalyzed reactions with excess ligand additive (HX). Ligands examined in Table 5.5.

Table 5.5 Yields obtained from the hydroamination of 1-octyne and aniline using [Ti]700 precatalyst and 10 equiv of HX ligand added.

Entry	HX (10 equiv)	LDP (kcal/mol)	pK _a	%V _{bur}	% yield HA1	Regioisomer Ratio
1	pyrrole	13.64	17(20)	20.4	81	52:1
2	2- <i>tert</i> -butyl-4-methoxyphenol	11.82 ^a	~10	21.5	0	-
3	<i>tert</i> -butanol	10.59	17	21.0 ^c	0	-
4	2-aryl ^(CF₃) -pyrrole	14.32 ^b	-	27.9	86	11.8:1
5	2-thionaphthol	13.99	~5	22.3	33	46.4:1
6	2,6-dimethylphenylamidate	15.02 ^b	-	30.4	27	4.7:1
7	2,2'-pyridinylpyrrole	13.64(pyr)/>15 (Py)	-	25.6 ^d	76	4.4:1
8	5-fluoroindole	13.16	-	22.2	88	56:1
9	3-methylindole	12.49	-	22.6	74	6.5:1
10	2,3-dimethylindole	11.38	-	25.1	73	>100:1
11	3-methyl-5-methoxyindole	12.22	-	22.6	62	13.7:1

^aLDP listed is that for 2-methyl-4-methoxyphenol. ^bLDP value is artificially increased by steric affects in the measurement. ^cApproximated from a close derivative. ^dCalculated %V_{bur} based on DFT optimized structure. See the SI for more details.

Looking at the two HX ligands initially examined, there are four major differences that could likely affect the equilibrium processes: boiling point, pK_a of the acidic H, donor ability of X⁻ as a ligand to a high valent metal, and sterics.^{22, 30} With these four factors in mind, a series of experiments in which different HX ligands, where the above 4 properties were varied, are used in excess (10 equiv) in the hydroamination of aniline and 1-octyne. The results, shown in Table 5.5 span a considerable range for these 4 properties and suggest some correlations between the properties listed above and the equilibrium.

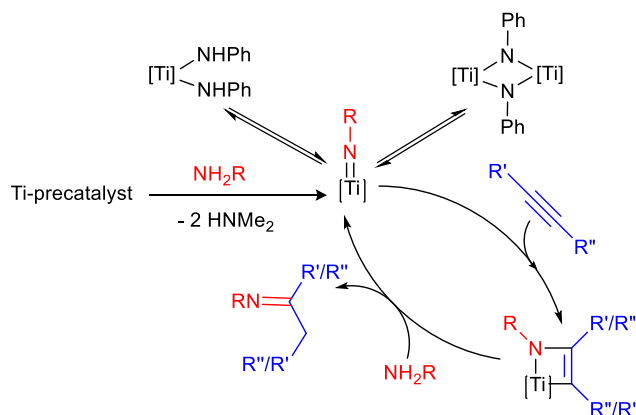
For these comparisons, pK_a values for each ligand (or a close derivative) were referenced from the literature. The terms describing donor ability to Ti (LDP) and size (%V_{bur}) are parameters derived from a Cr(VI) model complex in the Ligand Donor Parameter system.^{22, 30} This system was thoroughly discussed in chapters 2 and 3. These parameters to describe donor ability and size

of a given X^- ligand on a high valent metal have previously shown excellent correlation to homogeneous Ti hydroamination catalysts.²² Thus, it seems these ligand property descriptors could be informative here, in determining what ligand properties are affecting the formation of the active Ti species with this heterogeneous system.

Two of the ligand properties appear to have little effect on the equilibrium properties of the X^- ligands in this system. First, the data provided by this small group shows no correlation between size and the metric which provides an estimate of the equilibrium between $Ti(X)_3/SiO_2^{700}$ and $Ti(=NR)X/SiO_2^{700}$, which here is the yield of hydroamination product (%) after 1 h. Even taken to the extreme, we note that the bidentate pypyr ligand outperforms many substantially smaller ligands, yet at the same time, many of the small ligands are also high-yielding. Additionally, it does not appear that the boiling point of the ligand, or relative volatility, is hugely important. Both pyrrole and t BuOH, for example boil well below the reaction temperature, at 130 °C and 83 °C respectively. Despite the fact that both ligands will be vaporized to some extent, when free in solution, under the reaction conditions, pyrrole facilitates equilibrium with aniline, while t BuOH halts catalytic activity.

The donor ability of the X^- ligand and the pK_a seem to be exhibiting the greatest affect over the equilibrium processes here. To some extent, this makes sense, as pK_a is indicative of the σ -donor ability of X^- , while the donor ability used here is a wholistic parameter which sums both σ and π effects. There is a degree of inherent relation between the two descriptors. However, as ligand exchange in this system also involves protonation/deprotonation events, pK_a may also play other roles in the thermodynamic and kinetic controls of the ligand exchanges on Ti, specific to proton behavior. An illustration of how the X^- ligands may be impacting the catalytic cycle is shown in Fig. 5.11, which is a modified version of the Bergman mechanism for hydroamination.

a) Traditional Homogeneous Mechanism



b) Modified Mechanism

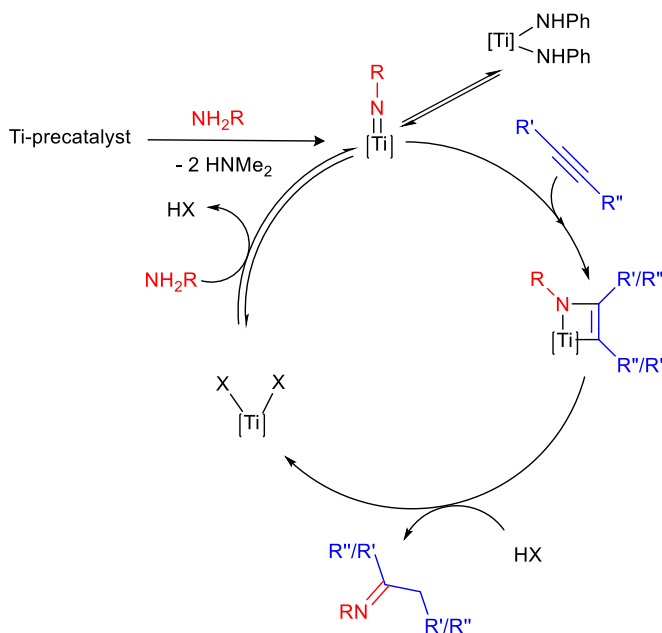


Figure 5.11 A traditional homogeneous mechanism (i.e. Bergman or Doye) of hydroamination shown with a Ti catalyst (*top*), and a modified version of the mechanism where HX may participate in the deprotonation of the aza-titanacyclobutene intermediate and impact the equilibrium formation of the active Ti-imido species (*bottom*).

Comparing Entries 1, 2, 3, and 10 from Table 5.5 provides a few insights. First, looking at 1 and 3, the two ligands have similar pK_a values but different donor abilities as ligands. This suggests that the donor abilities of these ligands to Ti impact the equilibrium, with the stronger donor shutting down the equilibrium entirely (Entry 3), favoring the $Ti(X)_3/SiO_2^{700}$ species by

equilibrium. Now looking at Entries 2 and 10, these HX ligands have much more similar donor abilities but very different pK_a values. HX in Entry 10 has an LDP value lower than that of HX in Entry 2, meaning it is a slightly better overall donor to the metal; however, the pK_a of HX in Entry 10 is much higher than that of HX in Entry 2. In this case, we see that Entry 10 allows for much more product formation than Entry 2, which completely shuts down the catalysis (74% vs 0%). Collectively, these comparisons suggest that a higher LDP (weaker overall donor) and a higher pK_a (less acidic proton, more σ -donating X^-) are needed to access the equilibrium regime in which the active $Ti(=NR)X/SiO_2^{700}$ species can be formed in the presence of excess HX (10 equiv). If the HX of choice is too donating to Ti as the conjugate base X^- , or the conjugate base is not easily protonated by aniline, no equilibrium is observed, and thus no hydroamination product is observed.

5.7 Catalyst Recycling from $Ti(X)_3/SiO_2^{700}$ Precatalysts: Enhanced Recyclability through Poisoning

Perhaps more interesting than identifying trends in these equilibria presented in the previous section, is the application of these equilibria to the catalyst as a means of recycling it for multiple uses. We know that even with an excess of these HX type ligands, some portion of the Ti sites can reach the $Ti(=NR)X/SiO_2^{700}$ active species through equilibrium formation, and the reaction can progress. However, when the Ti sites are not active in the cycle, they presumably resemble $Ti(X)_3/SiO_2^{700}$. By using the right X^- ligand, which has a weak enough Ti-X interaction (in terms of equilibria) that the imido can be formed, but a strong enough Ti-X interaction to outcompete the binding of excess substrate(s) when the reaction nears completion, we may be able to prevent irreversible surface-bound species from forming, and thus prevent the deactivation of the catalyst.

Based on the ligand property screening for active HX equilibria, we were able to narrow in on the range of LDP values and pK_a values that will likely lead to productive hydroamination as opposed to shutting down the catalysis. Ligands such as pyrroles and indoles are in the ideal range for both donor ability and pK_a of the acidic proton. With a selection of several of these ligands, we examined the ability of the catalysts to be recycled. Based on the results in Table 5.4, we can see that this technique, of including excess ligand in the hydroamination reaction, does in fact preserve catalytic activity for a second use of the catalyst material. Interestingly, upon a second use, we observed changes in the regioselectivity of the product with all but one of the X⁻ ligands employed. The best result was observed with 5-fluoroindole; more reuses of this catalyst material were pursued.

Table 5.6 Recycling experiments with 10 equiv of a variety of HX ligands added to the hydroamination of 1-octyne and aniline under the general conditions. Yields for the initial run with fresh catalyst (run 1), and a subsequent use (run 2) are shown.

HX	Run Number	Yield (%)	Regioisomer Ratio
pyrrole	1	81	51.8 : 1
	2	9	4.2 : 1
pypyr	1	76	48.8 : 1
	2	39	7.2 : 1
3-methyl-5-methoxyIndole	1	62	13.7 : 1
	2	15	9.1 : 1
2,3-dimethylindole	1	74	>100 : 1
	2	56	5.1 : 1
3-methylindole	1	73	6.5 : 1
	2	56	6.6 : 1
5-fluoroindole	1	88	55 : 1
	2	74	6.5 : 1

Upon additional reuses of the 5-fluoroindole doped catalysts we see the yield progressively decrease (Table 5.6). This result is similar to the observed reusability with [Ti]200, where loss of the catalytically active metal was observed across 5 uses of the material. Likewise, with the [Ti]700(5-F-indole) species, after 5 runs, ICP-OES analysis indicates about a 30% loss of the mass of Ti present in the catalyst material. This suggests that *two* different mechanisms of catalyst

deactivation, minimally, are contributing to the loss of catalytic activity upon several uses of the material. The first is a slow loss of the catalytically active metal and the second is a buildup of inhibitory species. In this case, the inhibitory species could be interaction of substrates with the catalyst material in a non-innocent way or from an interaction with the high concentrations of X^- on the heterogeneous catalyst.

Table 5.7 Results of reusing the [Ti]700 catalyst with 10 equiv of 5-fluoroindole (each trial) to perform the hydroamination of aniline and 1-octyne.

Catalyst Trial	% yield of hydroamination product	Regioselectivity Ratio
1	86	>100 : 1
2	73	6.6 : 1
3	56	5.6 : 1
4	2	1 isomer
5	Not observed	N/A

Based on these results, this strategy to preserve the catalyst's activity across several uses of the material shows promise but is far from a perfect solution to catalyst recyclability. Experimentally, these observations demonstrate that there can be competitive binding to the active metal between the doped ligand and the other substrates in solution. While the high concentrations of ligand can preserve some of the metal sites, it is likely via an equilibrium exchange with protic species in solution. Eventually (i.e. with enough usage of the catalyst) the majority of the Ti sites succumb to irreversible binding with other species in solution; while the excess ligand concentration slows this process down, it still catches up with the material after several uses. At the same time, this also enables surface extraction of the active metal. This suggests that adjusting the ligand concentration in solution during the catalytic reactions may be one means by which to optimize the reactions and lead to improved reusability, but even with ligands that show high rates of exchange with the catalyst, there is a limit to the amount that can be productively added.

5.8 Conclusions

Exploration of the catalytic activity of the [Ti]700 material with the addition of ligands has provided several big improvements to the overall performance of this material. Reaction times have been dramatically reduced, such that iminoamination with several different sets of substrates provides over 90% yield of the desired product(s) in less than 1 hour of reaction time. Additionally, the regioselectivity of the catalyst can be dramatically altered based on the identity of the ligand. The practical advantage of these catalysts has also been demonstrated by the high yields obtained with the one-pot-two-step production of complex heterocycles (quinolines and 2-amino-3-cyanopyridines) utilizing [Ti]700(X) species.

Experimental determination of the rate law governing the iminoamination reaction with [Ti]700(X) has also given us insight into what strategies may improve the rates of these catalysts even further. It appears that formation of the active Ti-imide species is rate-limiting, with inverse-first-order dependence on both aniline and isonitrile concentration. However, rate increases were noted by increasing the electron-donor ability of the ancillary X^- ligand. This suggests that a more donating ancillary ligand increases the equilibrium-based formation of the active Ti-imide relative to the “resting state” of the catalyst.

Based on the observation of slow catalyst deactivation over the course of the iminoamination reaction, even small rate increases stand to improve the overall conversion observed in these reactions. This observation of catalyst deactivation agrees with previous observations that both [Ti]700 and [Ti]700(X) are not reusable after a single application to iminoamination catalysis. Non-innocence of both products and reactants are suspected to contribute to these deactivation pathways.

Preliminary investigations show that running hydroamination reactions with [Ti]700(X) in the presence of a substantial excess of HX ligand species facilitates the some reusability of the material—or rather that the excess ligand slows down the rate of deactivation. Eventually, i.e. after several runs, all of the Ti sites do still become deactivated, and this is accompanied by a loss of some of the active metal. So, while this strategy is far from a perfect system by which to facilitate catalyst reuse, it provides experimental evidence that by manipulating the reaction conditions, we may be able to prolong the life of the catalyst in solution. Achieving perfect reusability, especially with iminoamination, will require further study.

5.9 Experimental

General Considerations

All manipulations involving catalytic reaction set-up and catalyst material handling were carried out under inert atmosphere (N₂), either in an MBraun glovebox or using standard Schlenk technique. Manipulations in air were primarily limited to preparation of ICP samples, organic product handling, and catalytic product isolation via column chromatography.

The catalyst material, [Ti]700, was prepared according to procedures listed in Chapter 4. The preparation of the [Ti]700X variants was generally performed *in situ*, as described below. The solvents n-hexane, toluene, and n-pentane were dried by passage over an activated alumina column and sparging with N₂ prior to use. The solvents *p*-cymene and C₆D₆ were dried over CaH₂ and distilled under vacuum and N₂, respectively, prior to use. The solvents used for column chromatography, organic workup, and routine complex characterization (GC or NMR) included hexanes, ethyl acetate, ether, triethylamine, and CDCl₃. These complexes were purchased commercially and used as received.

All substrates employed in catalytic reactions were dried prior to use. The alkynes, 1-octyne, 1-phenylpropyne, and phenylacetylene were purchased from Alfa Aesar, dried over Na_2SO_4 , and distilled under N_2 prior to use. Aniline and 3,5-dimethylaniline were dried over CaH_2 and distilled under vacuum prior to use. Cyclohexylisocyanide was synthesized according to literature procedures.³²

The following phenol ligands were purchased from commercial vendors: phenol; 4-methoxyphenol; 2-*tert*-butylphenol; 2,4,6-tri-*tert*-butylphenol; 2,6-di-*tert*-butyl-4-bromophenol; 2,6-di-*tert*-butylphenol; 2-phenylphenol; and 8-hydroxyquinoline. All phenols were purified by sublimation under reduced pressure prior to use. The following pyrrole and indole ligands were purchased from commercial vendors: pyrrole, 2,3-dimethylindole, 3-methylindole, and 5-fluoroindole. These ligands were dried azeotropically with toluene using a Dean-Stark apparatus prior to use. Additionally, 1-adamantanol, triphenylsilanol, 2-thionaphthol, and benzoic acid were also purchased from commercial vendors. These ligands were purified by sublimation prior to use. The amidate and thioimidate ligands were synthesized from published procedures.^{33, 34} 2-(*N,N*-dimethylaminomethyl)-4,6-di-*tert*-butylphenol was synthesized via a Mannich reaction.³⁵ 3-phenyl-1-naphthalenol was donated by the Wulff group at MSU.

The 2-aryl-substituted pyrroles, 2-(3,5-bis(trifluoromethyl)phenyl)pyrrole and 2-pyridinylpyrrole, were synthesized using Suzuki reactions between the Boc-protected-boronic acid-substituted pyrrole derivatives and halogenated aryl groups.^{36, 37} These ligands are the only ones considered that were more involved than a single step or aren't commercially available. However, these ligands were of interest due to the results they've previously demonstrated with our Ti-catalyzed C–N bond formation chemistry.

NMR Solution phase NMR was utilized to perform the SiO_2^{700} surface titration experiments, as well as routine characterization of isolated products from catalytic reactions. Routine characterization spectra were obtained using an Agilent DDR2 500 MHz NMR spectrometer equipped with a 5 mm PFG OneProbe operating at 499.84 MHz (^1H) and 125.73 MHz (^{13}C). ^1H NMR titrations of the SiO_2^{700} with $\text{Ti}(\text{NEt}_2)_4$ was performed using a Varian Inova 500 spectrometer equipped with a 5mm pulse-field-gradient (PFG) switchable broadband probe operating at 499.84 MHz (^1H). ^1H NMR chemical shifts were referenced to residual CHCl_3 in CDCl_3 as 7.26 ppm, or residual C_6HD_5 in C_6D_6 as 7.16 ppm. ^{13}C NMR chemical shifts are reported relative to $^{13}\text{CDCl}_3$ as 77.16 ppm, or $(^{13}\text{C})\text{C}_5\text{D}_6$ as 128.06 ppm.

X-ray Crystallography X-ray crystal structure data was collected at the Center for Crystallographic Research at MSU. The data was collected using either Mo or $\text{Cu-K}\alpha$ radiation.

NCr(NⁱPr₂)₂(OⁱPh-4-Br) Single Crystal X-ray Data Details

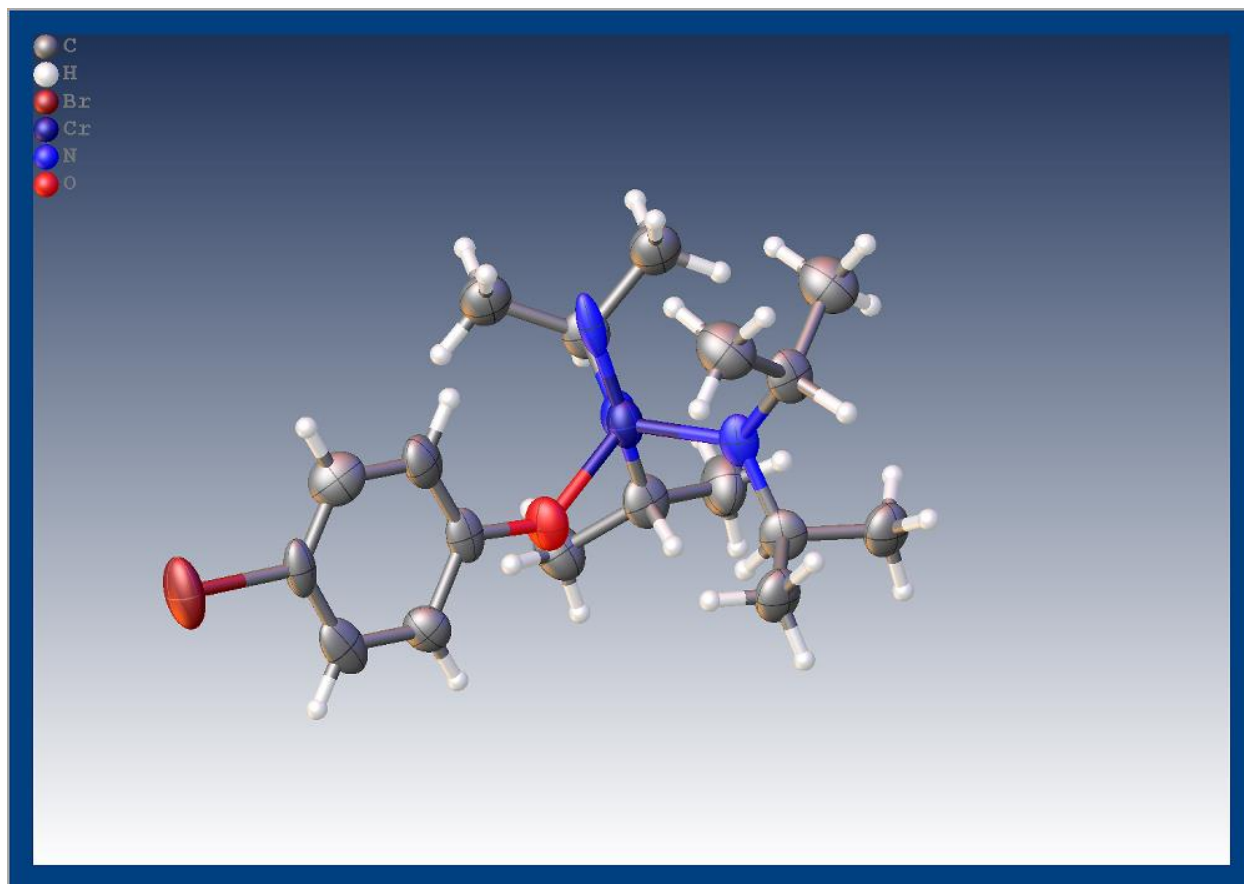


Figure 5.12 Crystal data and structure refinement for twin5.

Identification code	twin5
Empirical formula	C ₁₈ H ₃₂ BrCrN ₃ O
Formula weight	438.37
Temperature/K	173(2)
Crystal system	monoclinic
Space group	P2 ₁ /n
a/Å	9(2)
b/Å	9.228

$c/\text{\AA}$	25.647
$\alpha/^\circ$	90
$\beta/^\circ$	93.26
$\gamma/^\circ$	90
Volume/ \AA^3	2150(473)
Z	4
$\rho_{\text{calc}}/\text{g/cm}^3$	1.355
μ/mm^{-1}	2.400
F(000)	912.0
Crystal size/ mm^3	$0.498 \times 0.375 \times 0.144$
Radiation	MoK α ($\lambda = 0.71073$)
2Θ range for data collection/ $^\circ$	3.182 to 55.204
Index ranges	$-11 \leq h \leq 11, 0 \leq k \leq 11, 0 \leq l \leq 33$
Reflections collected	8059
Independent reflections	8059 [$R_{\text{int}} = ?$, $R_{\text{sigma}} = 0.1118$]
Data/restraints/parameters	8059/0/196
Goodness-of-fit on F^2	1.066
Final R indexes [$I \geq 2\sigma(I)$]	$R_1 = 0.1189$, $wR_2 = 0.3042$
Final R indexes [all data]	$R_1 = 0.1578$, $wR_2 = 0.3279$
Largest diff. peak/hole / $e \text{\AA}^{-3}$	1.70/-1.36

(2-[(3,5-dimethylphenyl)amino]-6-methyl-5-phenyl-nicotinonitrile) Single Crystal X-ray

Data Details

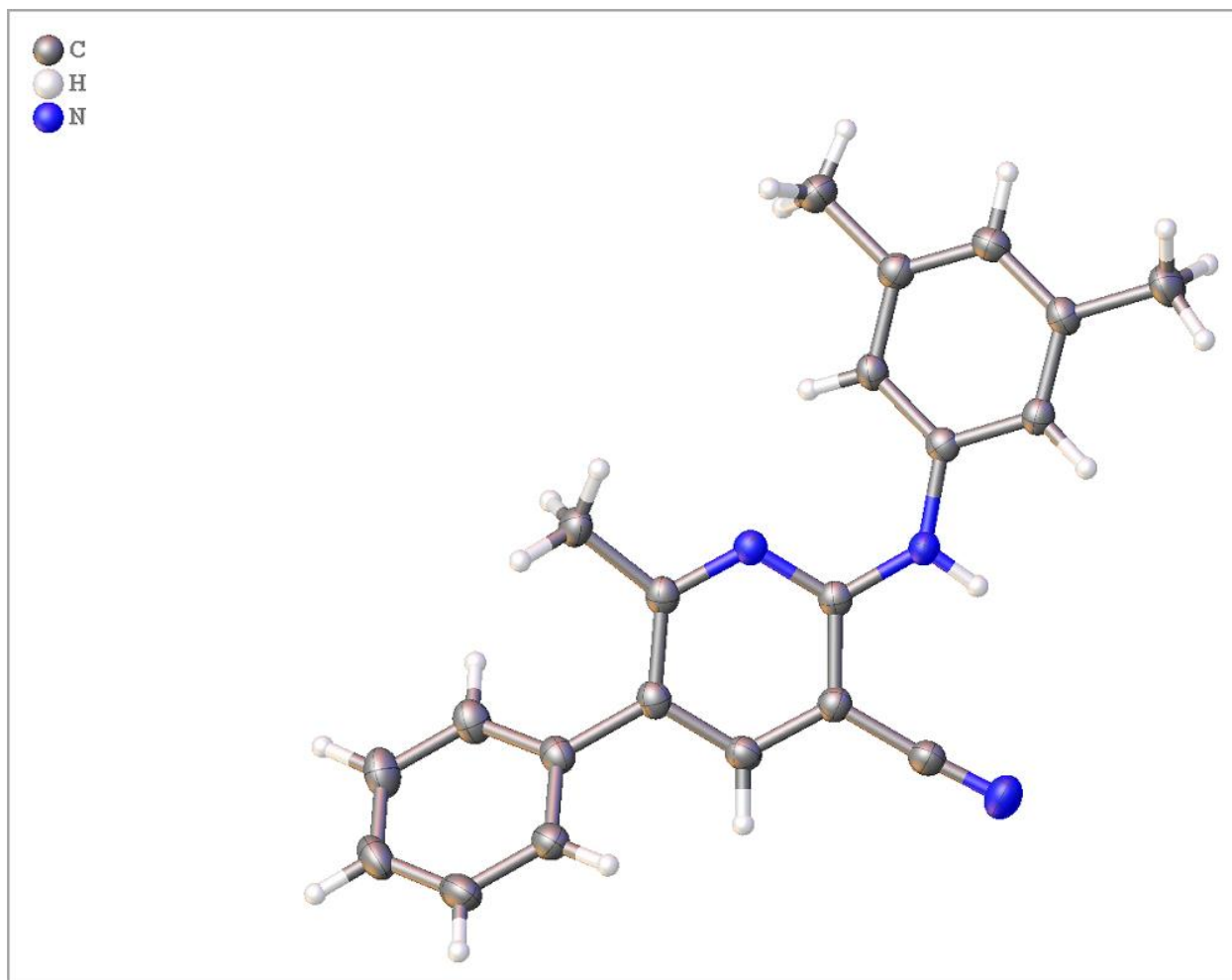


Figure 5.13 Crystal data and structure refinement for tri_early2_a.

Identification code	tri_early2_a
Empirical formula	C ₂₁ H ₁₉ N ₃
Formula weight	313.39
Temperature/K	172.99
Crystal system	triclinic
Space group	P-1

a/Å	8.0856(3)
b/Å	9.8636(3)
c/Å	12.1249(5)
α /°	66.347(2)
β /°	82.136(3)
γ /°	70.711(2)
Volume/Å ³	836.03(6)
Z	2
ρ_{calc} /cm ³	1.245
μ /mm ⁻¹	0.579
F(000)	332.0
Crystal size/mm ³	0.655 × 0.302 × 0.12
Radiation	CuK α (λ = 1.54178)
2 Θ range for data collection/°	7.96 to 144.658
Index ranges	-9 ≤ h ≤ 9, -12 ≤ k ≤ 12, -14 ≤ l ≤ 13
Reflections collected	14176
Independent reflections	3142 [R _{int} = 0.0280, R _{sigma} = 0.0239]
Data/restraints/parameters	3142/0/293
Goodness-of-fit on F ²	1.027
Final R indexes [I ≥ 2 σ (I)]	R ₁ = 0.0363, wR ₂ = 0.0959
Final R indexes [all data]	R ₁ = 0.0403, wR ₂ = 0.1000
Largest diff. peak/hole / e Å ⁻³	0.19/-0.19

GC Experiments and *in situ* Quantification GCMS data was collected on an Agilent 5973 MSD with a 6890N series GC. GCFID data was collected on a Hewlett Packard 6890 series GC system, and standardized against dodecane as an internal standard. The iminoamination products were quantified *in situ* by utilizing GCFID calibration curves generated with authentic samples of the isolated products for each derivative, standardized against internal dodecane.

ICP-OES ICP data was collected on a Varian 710es ICPOES spectrometer. A 1000 ppm Ti ICP standard in 2% HNO₃ was purchased from Sigma and used as received to prepare an external calibration curve. The Ti-SiO₂²⁰⁰ samples were then measured in triplicate, and quantified from the external calibration, allowing for the mass of Ti in each sample to be determined.

Catalytic Reactions

General Iminoamination Procedure with [Ti]700(X): A 15 mL pressure tube was charged with [Ti]700 (0.05 mmol, 163 mg), HX ligand (0.05 mmol), 1.0 mL *p*-cymene, and a stir bar. This mixture was stirred for 5 min at room temperature. To the catalyst mixture was added a separate 1.0 mL solution of H₂NPh (1 mmol, 93 mg), alkyne (2 mmol), and CyNC (1.5 mmol, 164 mg) in *p*-cymene. The pressure tube was sealed and transferred from the glovebox to a preheated 180 °C aluminum block. The tube was heated with stirring for 1 h; after the reaction was complete, the tube was removed from heat and cooled ambiently to room temperature. The pressure tube was centrifuged, compacting the catalyst material into a pellet at the bottom of the tube. The organic reaction solution was removed (by pipette) from the catalyst material for GC analysis.

Table 5.8 Yield and regioselectivity observed for a variety of ligands screened for the iminoamination of aniline, 1-octyne, and CyNC.

	Ligand	Yield (%)	Regioselectivity
monodentate	pyrrole	0	na
	2,4-di- ^t Buphenol	77	1.41:1
	2-thionaphthol	16	1.35:1
	2-Ar ^{CF₃} -pyrrole	15	1.4:1
	2,4,6-tri- ^t Buphenol	95	2.98:1
	<i>p</i> -CF ₃ -phenol	0	Na
	Ph ₃ SiOH	96	2.24:1
	1/2 vapol	71	1.32:1
	AdOH	62	1.54:1
	No ligand	0	Na
bidentate	2-phenylphenol	53	1.7:1
	6-dimethylAmino-2,4-di- ^t Bu-phenol	98	2.29:1
	2,6-dimethylphenylamidate	99	1.31:1
	8-hydroxyquinoline	77	1.65:1
	pypyr	79	1.2:1
	2,6-dimethylphenylthioamidate	95	2.08:1
	dipp-thioamidate	65	1.97:1
	dipp-amidate	99	1.4:1
	Ar(CF ₃) ₂ -amidate	55	1.45:1
Benzoic acid	0 ^a	na	

^aLarge amount of formamidine product noted in this reaction, but no iminoamination product.

Table 5.9 Yield and regioselectivity observed for a variety of ligands screened for the iminoamination of aniline, 1-phenylpropyne, and CyNC.

	Ligand	Yield (%)	Regioselectivity
monodentate	2,4,6-tri- ^t Buphenol	67	5.4:1
	HOSiPh ₃	54	7.5:1
	NHAdAr	69	8.34:1
	2,4-di- ^t Buphenol	42	8.6:1
	NH ₂ Ph or CyNC	89	10.35:1
bidentate	2,6-dimethylphenylamidate	99	10.28:1
	6-dimethylaminomethyl-2,4-di- ^t Bu-phenol	47	15.8:1
	2,6-dimethylphenylthioamidate	66	13.1:1
	8-hydroxyquinoline	57	11.5:1
	pypyr	76	9.64:1
	Dipp-Amidate	96	14.43:1
	Dipp-Thioamidate	77	9.04:1

Table 5.10 Yield and regioselectivity observed for a variety of ligands screened for the iminoamination of aniline, phenylacetylene, and CyNC.

	Ligand	Yield (%)	regioselectivity
monodentate	2,4,6-tri- ^t BuPhOH	72	1.5:1
	2,4-di- ^t Buphenol	21	1.7:1
	NHAdAr	47	4.89:1
	2-phenyl-phenol	31	2.9:1
	aniline/CyNC	52	6.3:1
bidentate	6-dimethylaminomethyl- 2,4-di- ^t Bu-phenol	31.5	2.7:1
	diip-amidate	67	3.6:1
	pypyr	51	4.3:1
	2,6-dimethylphenylamidate	99	5.6:1
	2,6-dimethylphenylthioamidate	36	2.1:1

General Procedure for Catalyst Recycling (Iminoamination) An initial reaction with the catalyst material was set up and performed according to the general procedure above. After the reaction was finished and centrifuged, the pressure tube was transferred back to the glovebox and the organic reaction solution was decanted for GC analysis. The catalyst material was rinsed with benzene (5 mL) and pentane (5 mL) on a fritted funnel. The material was briefly dried under vacuum and transferred to a new pressure tube. 1.0 mL of *p*-cymene was added and the catalyst material was stirred. To this mixture was added a volumetrically prepared 1.0 mL solution containing H₂NPh (1 mmol, 93 mg), alkyne (2 mmol), and CyNC (1.5 mmol, 164 mg) in *p*-cymene. The pressure tube was sealed and transferred to an aluminum block (180 °C) and the reaction heated, with stirring, for 1 hour. The reaction solution was centrifuged and the organic solution was then decanted and analyzed by GCMS and GCFID. (Note, even when the rinsing and filtration steps were omitted, the same results were observed on a second use with a variety of ligands and different substrates, such that <5% 3CC yield was observed on subsequent runs).

General Procedure for Catalyst Recycling (Hydroamination with excess HX Added) A 15 mL pressure tube was charged with 163 mg of [Ti]700 (0.05 equiv, 0.05 mmol), a stir bar, the HX ligand of interest (0.5 equiv, 0.5 mmol) and 1.0 mL of *p*-cymene. This mixture was stirred for 5 min at room temperature and a 1.0 mL solution containing 93 mg H₂NPh (1 equiv, 1 mmol) and 220 mg 1-octyne (2 equiv, 2 mmol) in *p*-cymene was added. The pressure tube was sealed and transferred to a 180 °C aluminum well plate. The reaction was heated and stirred for 1 h; it was cooled ambiently, centrifuged and returned to the glovebox. The organic solution was decanted for GC analysis (trial 1). The catalyst material was rinsed with benzene (5 mL) and pentane (5 mL) on a fritted funnel. The catalyst was dried under reduced pressure and transferred to a new pressure

tube. The HX ligand and substrates were added in the same manner as the initial run and the reaction performed again (trial 2). This process was repeated again as necessary.

General Procedure for Kinetic Analysis For kinetics runs, monitored by GC, 6-8 trials of each set of reaction conditions in Table 1 were prepared. To achieve consistency across the reactions, the catalyst material was prepared prior to the reactions. In an Erlenmeyer flask, 2 g of [Ti]700 (0.62 mmol) was stirred as a suspension in toluene (20 mL). To this suspension was added 162 mg of 2,4,6-tri-*tert*-butylphenol (0.62 mmol). The suspension was stirred for a total of 1 h at room temperature after addition. The catalyst material was collected by filtration and dried under reduced pressure. This pre-formed catalyst was used in the kinetics experiments. The following description of a reaction set-up utilizes the amounts from Entry 1 of Table 5.1 as a representative example of how these reactions were run.

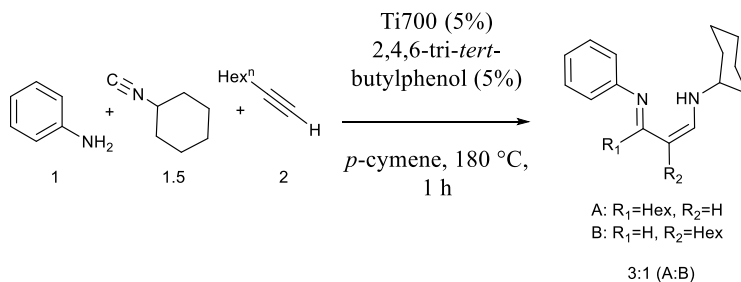
Representative Kinetic Procedure with Conditions from Entry 1 8 separate pressure tubes were charged with 88 mg of [Ti]700(OPh^{2,4,6-tri-*tert*-butyl}) (0.025 mmol, 0.05 equiv) and a stir bar. To each tube 2.0 mL of a volumetrically prepared solution in *p*-cymene that was 0.25 M H₂NPh (0.5 mmol, 1 equiv), 0.25 M CyNC (0.5 mmol, 1 equiv) and 0.51 M 1-octyne (1 mmol, 2 equiv) and 0.05 M dodecane (as internal standard for GC analysis), was added. The tubes were sealed and transferred from the glovebox to a 180 °C aluminum well plate. At timed intervals from 0-100 min, samples were removed from heat and analyzed by GC-MS and GC-FID to identify reaction products and quantify the amount of iminoamination product in solution.

Note, the tubes contain small amounts of solution and cool rapidly. Based on previous observations, we know that by the time the reaction temperature has reached 140 °C, the catalyzed reaction will have slowed by 1-2 orders of magnitude. No specific quenching step was taken upon removal of reaction vessels from heat, as cooling the reaction sufficiently eliminates further

catalytic activity, and opening the reaction vessel at 180 °C is not advisable. As soon as the tube was cool enough to handle, it was opened to air, thus killing any residual active catalyst.

Product Isolation from Catalytic Reactions:

Iminoamination with H₂NPh, 1-octyne, and CyNC



Scheme 5.5 Iminoamination reaction catalyzed by [Ti]700 with 2,4,6-tri-*tert*-butylphenoxide.

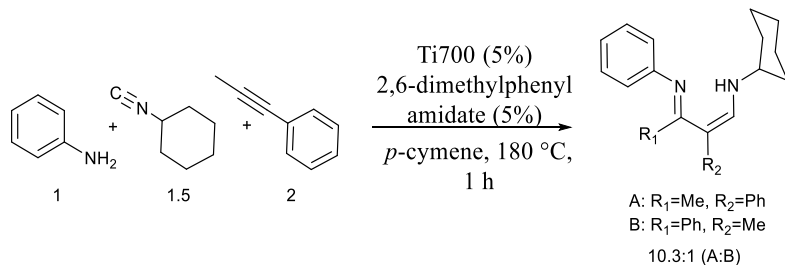
Synthetic Procedure A A 15 mL pressure tube was charged with 320 mg [Ti]700 (0.05 equiv, 0.1 mmol), a stir bar, 1 mL *p*-cymene, and 26 mg of 2,4,6-tri-*tert*-butylphenol (0.05 equiv, 0.1 mmol). This mixture was stirred for 5 min at room temperature. Then a 2 mL solution containing 186 mg H₂NPh (1 equiv, 2 mmol), 327 mg CyNC (1.5 equiv, 3 mmol), and 440 mg 1-octyne (2 equiv, 4 mmol), was added to the pressure tube. The tube was sealed and transferred to a 180 °C aluminum block, where it was heated and stirred for 1 h. The reaction was cooled and centrifuged to compact the catalyst material at the bottom of the tube. The crude reaction solution was decanted and the 3CC compound isolated by column chromatography (Alumina, Hexanes(1%TEA) gradient from 0-30% Et₂O). The 3CC product was isolated as a yellowish oil as an isomeric mixture of A and B (yield: 330 mg, 53%).

HRMS: QTOF EI (positive ion) calc'd for C₂₁H₃₃N₂: 313.2644; found: 313.2641. ¹H NMR (500 MHz, CDCl₃) 9.90 (s, 1H), 6.98 (q, *J* = 8.4 Hz, 1H), 6.80 (d, *J* = 7.8 Hz, 1H), 6.72 (d, *J* = 7.8 Hz, 1H), 4.67 (d, *J* = 7.8 Hz, 1H), 3.04 (dt, *J* = 17.3, 5.6 Hz, 1H), 2.57 (t, *J* = 7.8 Hz, 0H), 2.21–2.09 (m, 2H), 1.93–1.70 (m, 1H), 1.63–1.54 (m, 1H), 1.45 (dd, *J* = 10.0, 5.1 Hz, 2H), 1.30 (s, 4H), 1.23–1.15 (m, 3H), 0.89 (t, *J* = 6.5 Hz, 2H), 0.82 (t, *J* = 7.1 Hz, 2H). ¹³C NMR (126 MHz, CDCl₃) 170.83, 153.60, 151.46, 147.52, 147.09, 145.38, 129.32, 128.61, 122.01, 121.53, 117.60, 91.82,

62.96, 57.11, 34.94, 34.55, 33.77, 33.13, 32.71, 31.78, 31.60, 31.33, 29.45, 29.02, 28.92, 28.80, 25.87, 25.66, 24.82, 24.64, 22.79 (d, $J = 12.9$ Hz), 22.61, 14.30, 14.19.

gCOSY NMR correlation list: ^1H NMR (500 MHz, CDCl_3) 7.28, 7.31, 6.81, 7.27, 7.27, 4.67, 1.82, 1.86, 1.89, 1.29, 1.60, 1.60, 1.49, 1.50, 1.46, 1.46, 1.45, 1.30, 3.02, 3.06, 1.30, 2.58, 2.58, 2.58, 1.18, 1.17, 1.85, 1.17, 1.84, 2.15, 3.06, 1.84, 2.15, 1.82, 2.14, 1.77, 1.79, 1.76, 3.02, 0.88, 1.87, 3.02, 0.83, 0.82, 0.82, 1.45, 1.30, 1.30, 1.22, 1.22. ^1H NMR (500 MHz, CDCl_3) 8.26, 7.49, 7.25, 6.98, 6.80, 6.72, 3.05, 3.05, 3.02, 3.01, 2.59, 2.56, 2.37, 2.33, 2.17, 2.14, 2.14, 1.90, 1.88, 1.83, 1.72, 1.62, 1.59, 1.56, 1.56, 1.50, 1.49, 1.48, 1.46, 1.45, 1.44, 1.43, 1.42, 1.41, 1.39, 1.33, 1.33, 1.32, 1.32, 1.30, 1.28, 1.28, 1.24, 1.21, 1.19, 1.16, 0.90, 0.87, 0.84, 0.81.

Iminoamination with H₂NPh, 1-phenylpropyne, and CyNC:



Scheme 5.6 Iminoamination reaction catalyzed by [Ti]700 with 2,6-dimethylphenylamidate ligand and an internal alkyne.

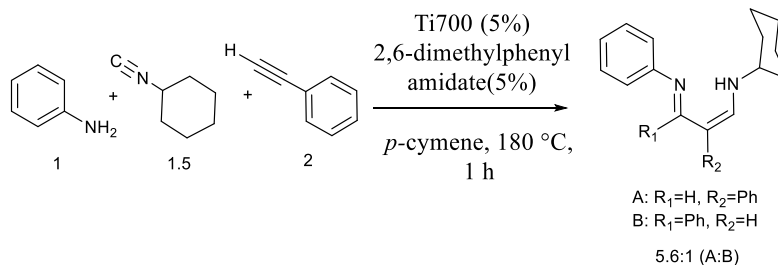
Synthetic Procedure: A 15 mL pressure tube was charged with 326 mg [Ti]700 (0.05 equiv, 0.1 mmol), 28 mg of 2,6-dimethylphenylamidate (0.05 equiv, 0.1 mmol), a magnetic stir bar, and 1 mL *p*-cymene. The mixture was stirred for 5 minutes, and then a 2.0 mL *p*-cymene solution containing 186 mg aniline (2 mmol, 1 equiv), 327 mg of CyNC (3 mmol, 1.5 equiv), and 348 mg of 1-phenylpropyne (3 mmol, 1.5 equiv) was also added to the pressure tube. The tube was sealed and transferred from the glovebox to a preheated, 180 °C aluminum block. The tube was heated, with stirring, for 1 h. The pressure tube was removed from heat and allowed to ambiently cool to room temperature. The contents were centrifuged and the liquid portion decanted. This crude reaction solution was separated by column chromatography (Al₂O₃, Hex(1% TEA), gradient Et₂O from 0 to 20%) to yield 410 mg (64%) of the major regioisomer (A) as a yellow oil. Note, the isolated product contains only the main regioisomer (A) to the limits of detection of our GC instruments and NMR.

HRMS: QTOF EI (positive ion) calc'd for C₂₂H₂₇N₂: 319.2174; found: 319.2164. ¹H NMR (500 MHz, CDCl₃) 10.75 (s, 1H), 7.34–7.28 (m, 4H), 7.27 (d, *J* = 1.6 Hz, 2H), 7.22–7.17 (m, 1H), 7.03 (m, 1H), 6.92 (s, 1H), 6.91–6.87 (m, 2H), 3.09–3.01 (m, 1H), 1.95–1.87 (m, 3H), 1.83 (s, 3H), 1.75 (d, *J* = 3.3 Hz, 4H), 1.57 (s, 4H), 1.43–1.27 (m, 4H). ¹³C NMR (126 MHz, CDCl₃) δ

165.82, 150.63, 147.53, 142.32, 130.52, 128.68, 127.98, 125.36, 122.31, 121.58, 107.65, 34.52, 25.50, 24.96, 24.62, 20.33.

*g*COSY NMR Correlation List: ^1H NMR (500 MHz, CDCl_3) δ 6.94, 6.93, 7.32, 7.31, 7.31, 7.30, 7.31, 1.36, 1.33, 1.91, 3.08, 1.81, 1.94, 1.71. ^1H NMR (500 MHz, CDCl_3) δ 7.33, 7.30, 7.21, 7.18, 7.05, 7.01, 6.89, 1.92, 1.75, 1.39, 1.37, 1.36, 1.33, 1.30.

Iminoamination of H₂NPh, phenylacetylene, and CyNC:



Scheme 5.7 Iminoamination reaction catalyzed by [Ti]700 with 2,6-dimethylphenylamidate and an aromatic alkyne.

Synthetic Procedure: A 15 mL pressure tube was charged with 326 mg [Ti]700 (0.05 equiv, 0.1 mmol), 28 mg of 2,6-dimethylphenylamidate (0.05 equiv, 0.1 mmol), a magnetic stir bar, and 1 mL *p*-cymene. The mixture was stirred for 5 minutes, and then a 2.0 mL *p*-cymene solution containing 186 mg aniline (2 mmol, 1 equiv), 327 mg of CyNC (3 mmol, 1.5 equiv), and 306 mg of phenylacetylene (3 mmol, 1.5 equiv) was also added to the pressure tube. The tube was sealed and transferred from the glovebox to a preheated, 180 °C aluminum block. The tube was heated, with stirring, for 1 h. The pressure tube was removed from heat and allowed to ambiently cool to room temperature. The contents were centrifuged and the liquid portion decanted. This crude reaction solution was separated by column chromatography (Al₂O₃, Hex(1% TEA), gradient Et₂O from 0 to 20%) to yield 312 mg (51%) of the major regioisomer (A) as a yellow oil. Note, the isolated product contains only the main regioisomer (A) to the limits of detection of our GC instruments and NMR.

HRMS: QTOF EI (positive ion) calc'd for C₂₁H₂₅N₂: 305.2018; found: 305.2015. ¹H NMR (500 MHz, CDCl₃) 11.65 (s, 1H), 8.17 (d, *J* = 2.9 Hz, 1H), 7.59 (d, *J* = 2.9 Hz, 1H), 7.40–7.28 (m, 6H), 7.23–7.16 (m, 1H), 7.12 (dd, *J* = 8.5, 1.1 Hz, 2H), 7.08 (td, *J* = 7.3, 1.2 Hz, 1H), 3.25 (ddt, *J* = 13.5, 9.3, 3.9 Hz, 1H), 2.02–1.91 (m, 2H), 1.86–1.78 (m, 2H), 1.68–1.62 (m, 2H), 1.52 (m, 2H), 1.48–1.38 (m, 2H). ¹³C NMR (126 MHz, CDCl₃) 152.48, 150.72, 149.33, 140.95, 129.23, 128.60, 125.48, 124.67, 123.24, 119.10, 106.34, 34.55, 31.62, 25.60, 24.40.

*g*COSY NMR Correlation List: ¹H NMR (500 MHz, CDCl₃) δ 7.59, 8.18, 7.27, 7.11, 7.32, 7.35, 1.06, 1.52, 1.42, 1.36, 1.85, 3.24, 2.09, 1.82, 1.62, 2.55, 2.56, 1.32. ¹H NMR (500 MHz, CDCl₃) δ 8.17, 7.59, 7.19, 7.13, 7.12, 7.07, 2.55, 1.96, 1.83, 1.64, 1.56, 1.52, 1.48, 1.39, 1.34, 1.07, 1.04, 0.89.

1-Pot-Two-Step Quinoline Synthesis:

A 15 mL pressure tube was charged with 163 mg of [Ti]700 (0.05 equiv, 0.05 mmol), 13 mg 2,6-dimethylphenylamidate (0.05 equiv, 0.05 mmol), a stir bar, and 1.0 mL *p*-cymene. The mixture was stirred for 5 min at room temperature. A 1.0 mL solution of 93 mg H₂NPh (1 equiv, 1 mmol), 232 mg 1-phenylpropyne (2 equiv, 2 mmol), and 164 mg CyNC (1.5 equiv, 1.5 mmol) was added to the catalyst mixture and the pressure tube was sealed. The tube was transferred from the glovebox to a preheated 180 °C aluminum block and heated with stirring for 2 h. The tube was cooled ambiently to room temperature and then 2 mL of glacial acetic acid was added to the pressure tube. The tube was resealed and heated at 120 °C for an additional 10 h.

The tube was removed from heat and the contents neutralized with sodium bicarbonate solution once cooled (pH 7-8). The neutralized mixture was extracted with EtOAc and the organic layer concentrated by rotary evaporation to give provide a viscous brown residue. The crude residue was purified by column chromatography (silica, Hexanes(1%TEA)-Hexanes(1%TEA)/EtOAc) yielding the product as an red oil (158 mg, 72%). The compound matches literature reports by ¹H NMR, ¹³C NMR, and HRMS.

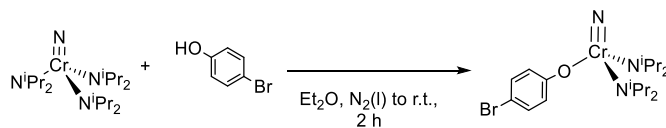
HRMS: QTOF EI (positive ion) calc'd for C₁₆H₁₄N: 220.1126; found: 220.1129. ¹H NMR (500 MHz, CDCl₃) 8.08 (d, *J* = 8.4 Hz, 1H), 7.97 (s, 1H), 7.79 (d, *J* = 8.0 Hz, 1H), 7.70 (t, *J* = 8.4, 6.9 Hz, 1H), 7.53–7.45 (m, 3H), 7.45–7.39 (m, 3H), 2.68 (s, 3H). ¹³C NMR (126 MHz, CDCl₃) 157.38, 146.98, 139.87, 136.14, 135.74, 129.37, 129.21, 128.43, 128.36, 127.60, 127.45, 126.84, 126.06, 24.56.

One-pot-Two-Step Synthesis of a 2-amino-3-cyano-pyridine (2-[(3,5-dimethylphenyl)amino]-6-methyl-5-phenyl-nicotinonitrile):

A 15 mL pressure tube was charged with 163 mg of [Ti]700 (0.05 equiv, 0.05 mmol), 13 mg of 2,6-dimethylphenylamidate (0.05 equiv, 0.05 mmol), a stir bar, and 1.0 mL of *p*-cymene and the mixture was stirred for 5 min at room temperature. A 1.0 mL solution containing 121 mg of 3,5-dimethylaniline (1 equiv, 1 mmol), 116 mg of 1-phenylpropyne (1 equiv, 1 mmol), and 109 mg CyNC (1 equiv, 1 mmol) was then added to the catalyst mixture. The pressure tube was sealed and transferred from the glovebox to a heated aluminum block (180 °C). The reaction was heated for 2 h with stirring before it was cooled ambiently to room temperature. To the cooled reaction solution was added 125 mg of malononitrile (2 equiv, 2 mmol) and 75 mg of DBU (0.5 equiv, 0.5 mmol) with 2 mL of dry EtOH and 200 mg of activated 3 Å molecular sieves. This provided 228 mg (70%) of the product as a yellow solid that matched the reported ¹H and ¹³C NMR spectra, but which also contained *p*-cymene and hexanes. The product was washed with cold hexanes and then recrystallized from hexane at -20 °C. This yielded 88 mg (28%) of X-ray quality single crystals. ¹H and ¹³C NMR spectra of the crystalline solid were extremely pure.

¹H NMR (500 MHz, CDCl₃) 7.62 (s, 1H), 7.44 (dd, *J* = 8.0, 6.6 Hz, 3H), 7.39 (d, *J* = 7.1 Hz, 1H), 7.33 (s, 2H), 7.32–7.26 (m, 2H), 6.91 (s, 1H), 6.76 (s, 1H), 2.48 (s, 4H), 2.35 (s, 7H). ¹³C NMR (126 MHz, CDCl₃) 160.29, 154.31, 142.18, 138.85, 138.70, 138.29, 129.18, 128.70, 128.01, 127.71, 125.36, 118.05, 116.82, 90.39, 24.23, 21.62.

Synthesis of $\text{NCr}(\text{N}^i\text{Pr}_2)_2(\text{OPh-4-Br})$



Scheme 5.8 Synthesis of 4-Br-phenoxide LDP complex.

Synthetic Procedure: A scintillation vial was charged with 50 mg of $\text{NCr}(\text{N}^i\text{Pr}_2)_3$ (0.127 mmol, 1 equiv), a stir bar, and 4 mL of Et_2O . This solution was chilled in a liquid nitrogen Coldwell for 10 minutes. A solution containing 24 mg of 4-Br-phenol in 1 mL of Et_2O was added to the chilled chromium solution in a dropwise manner. The reaction rapidly changed color from beet to an orangish-red hue. The reaction was allowed to come to room temperature, with stirring, for 2 h. The volatiles were removed under reduced pressure to yield a dark red powdery residue. This residue was dissolved in a minimal amount of pentane and filtered over Celite. This solution was chilled at $-35\text{ }^\circ\text{C}$ for 2 days to yield a fine, powdery precipitate, which was the product. 43 mg of the product (72%) was collected and used for LDP measurements, elemental analysis, and NMR characterization of the complex. X-ray quality crystals were grown from a concentrated solution of the Cr complex in toluene, layered with *n*-hexane at $-35\text{ }^\circ\text{C}$, over the course of 7 days.

$^1\text{H NMR}$ (500 MHz, CDCl_3) 7.22 (d, $J = 8.8\text{ Hz}$, 2H), 6.83 (d, $J = 8.8\text{ Hz}$, 2H), 5.04 (septet, $J = 6.5\text{ Hz}$, 2H), 3.75 (septet, $J = 6.4\text{ Hz}$, 2H), 1.85 (d, $J = 6.2\text{ Hz}$, 6H), 1.46 (d, $J = 6.3\text{ Hz}$, 6H), 1.15 (d, $J = 6.4\text{ Hz}$, 12H). $^{13}\text{C NMR}$ (126 MHz, CDCl_3) 165.93, 131.60, 119.56, 110.65, 58.46, 55.59, 30.50, 30.24, 21.48, 21.20. *Elemental analysis* calc'd for $\text{CrOBrC}_{18}\text{H}_{32}\text{N}_3$: C, 49.32; H, 7.36; N, 9.59. Found: C, 49.09; H, 7.41; N, 9.33.

Spectral Data

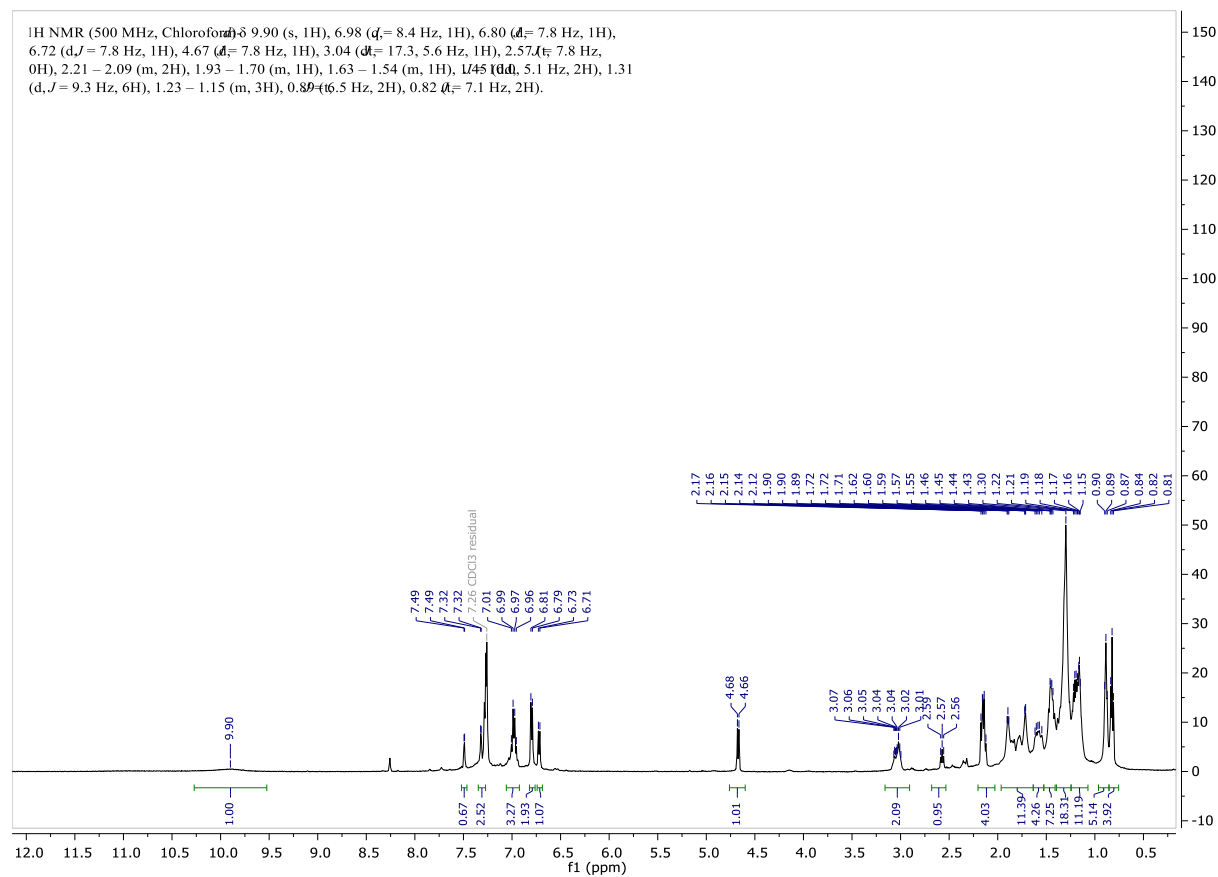


Figure 5.14 ¹H NMR of 3CC1 in CDCl₃ (isomeric mixture of A and B).

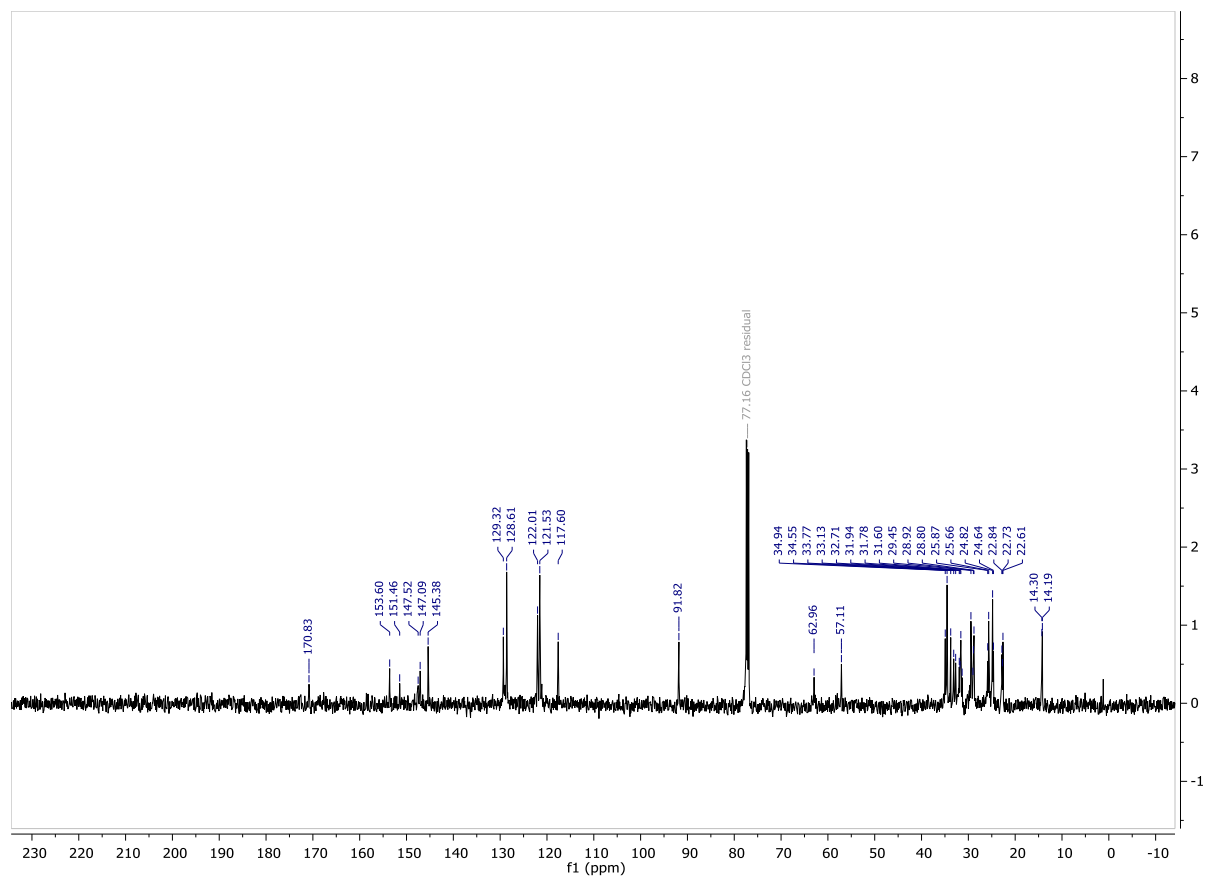


Figure 5.15 ^{13}C NMR of 3CC1 in CDCl_3 (isomeric mixture of A and B).

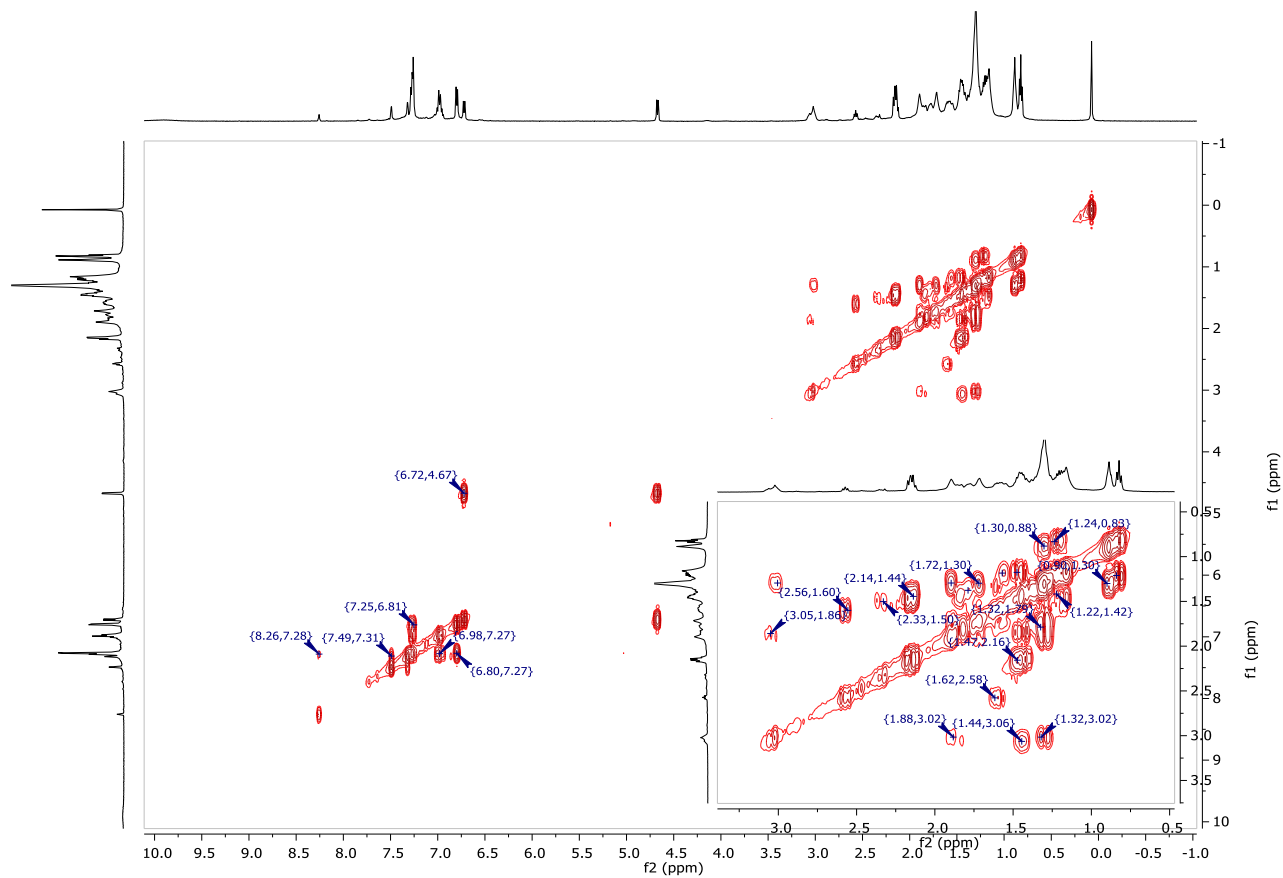


Figure 5.16 gCOSY NMR of 3CC1 in CDCl₃ (isomeric mixture of A and B).

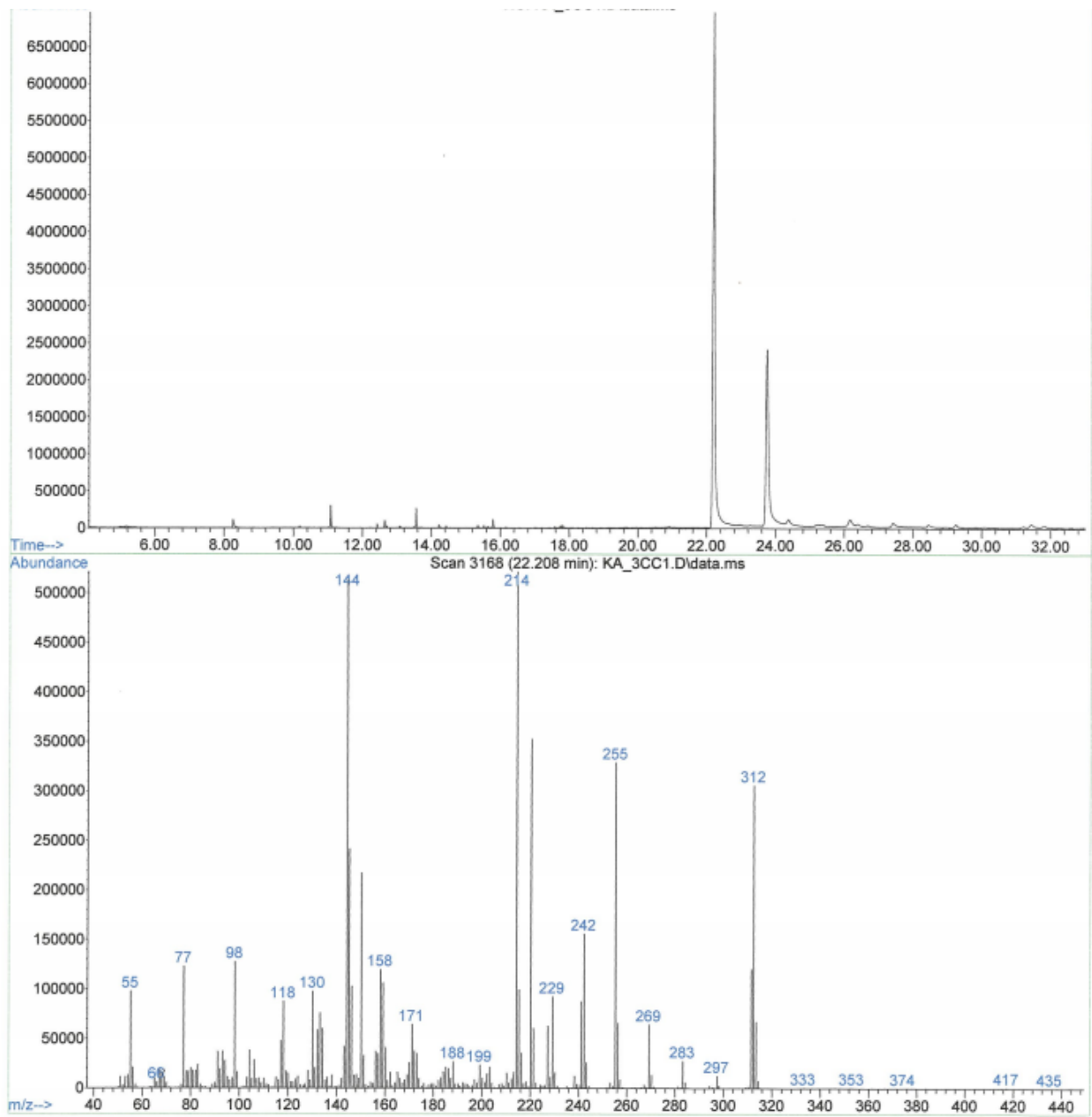


Figure 5.17 GC trace of 3CC1 (A and B) and MS fragmentation pattern for 3CC1(A).

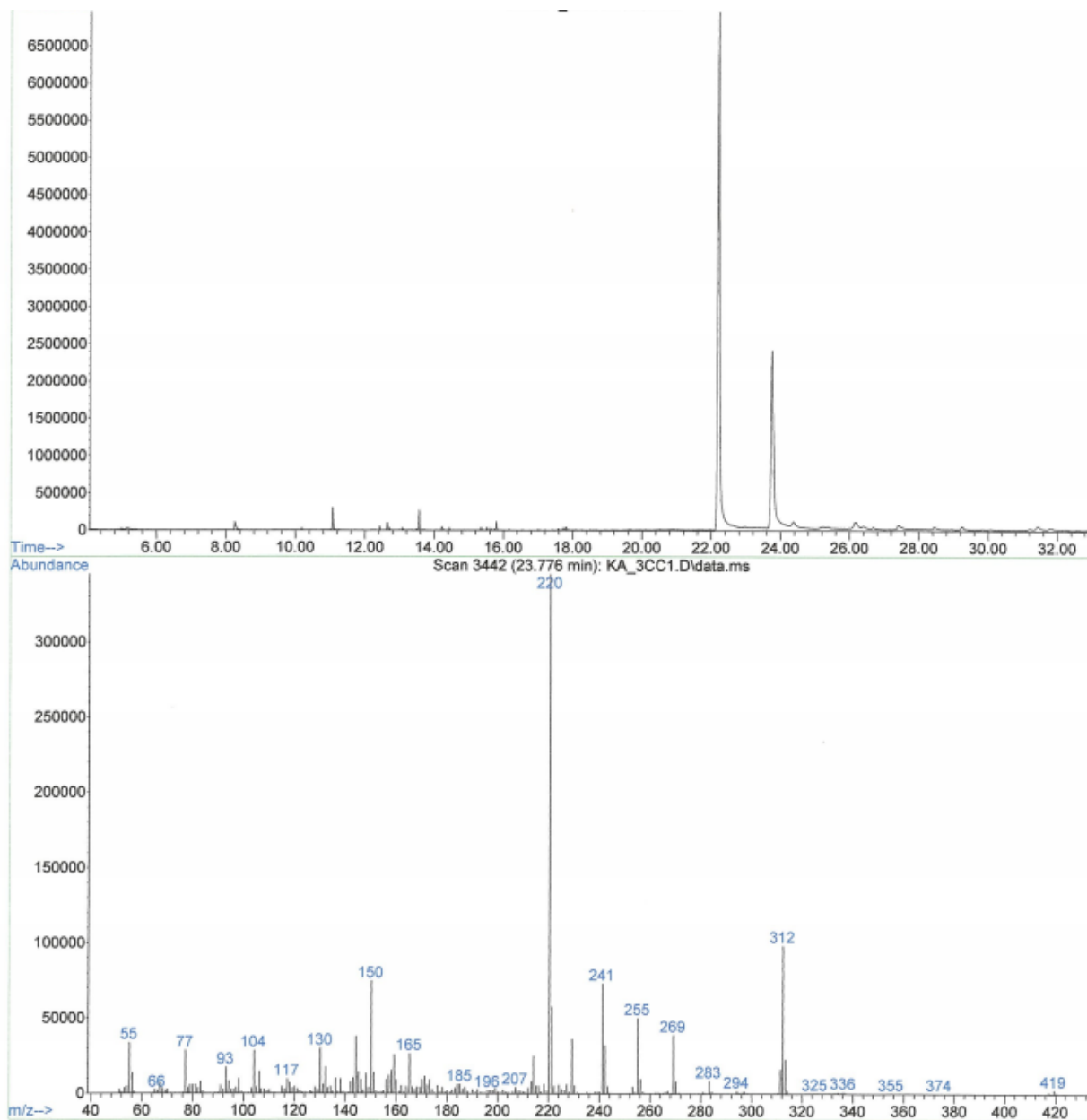


Figure 5.18 GC trace of 3CC1 (A and B) and MS fragmentation pattern for 3CC1(B).

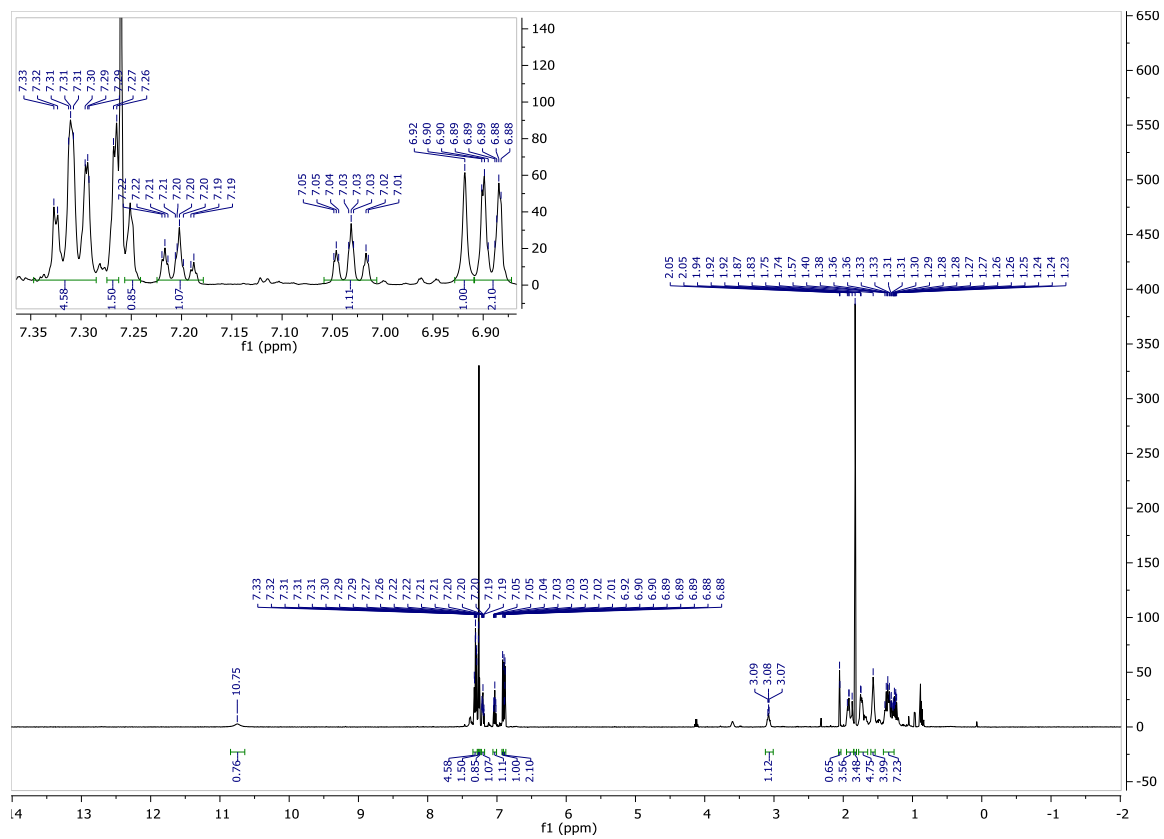


Figure 5.19 ^{13}C NMR of 3CC2 in CDCl_3 .

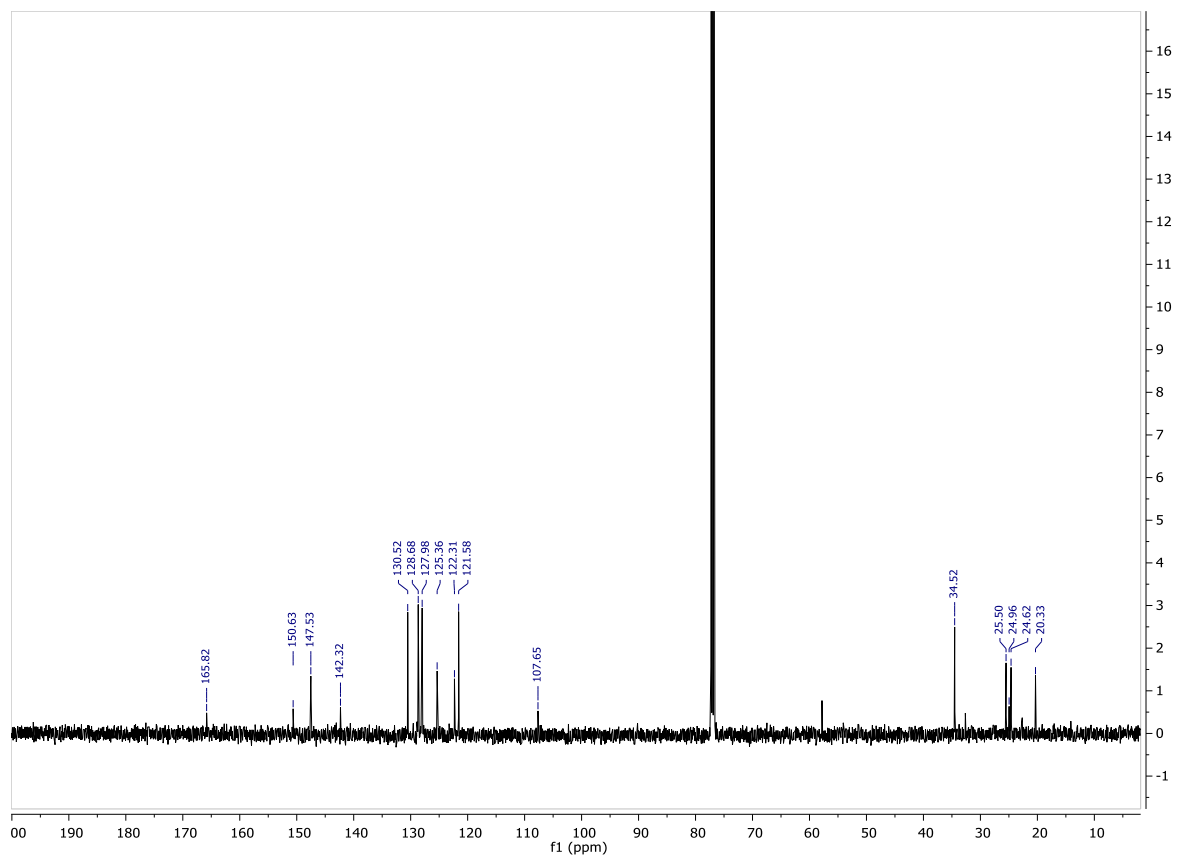


Figure 5.20 ^{13}C NMR of 3CC2 in CDCl_3 .

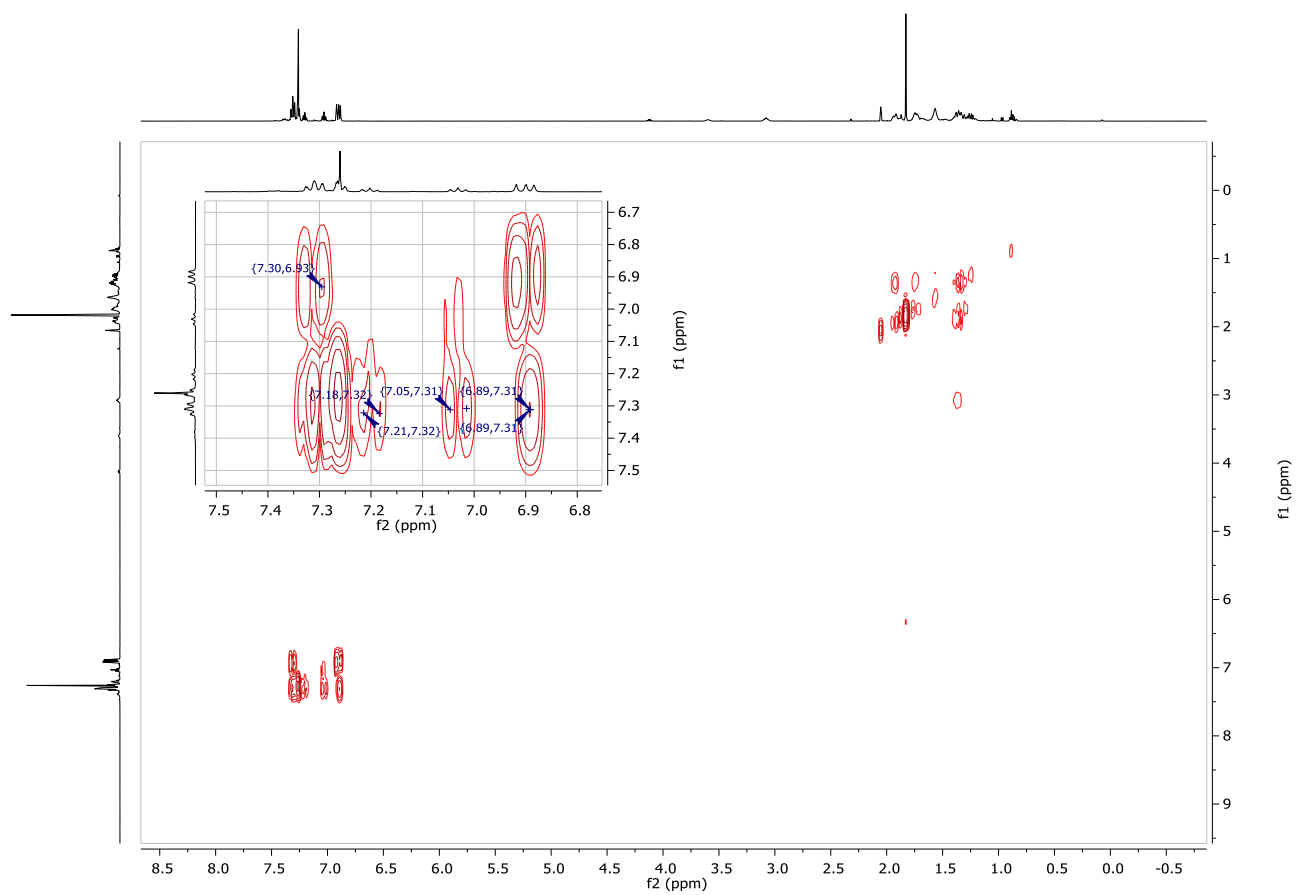


Figure 5.21 gCOSY NMR of 3CC2 in CDCl₃.

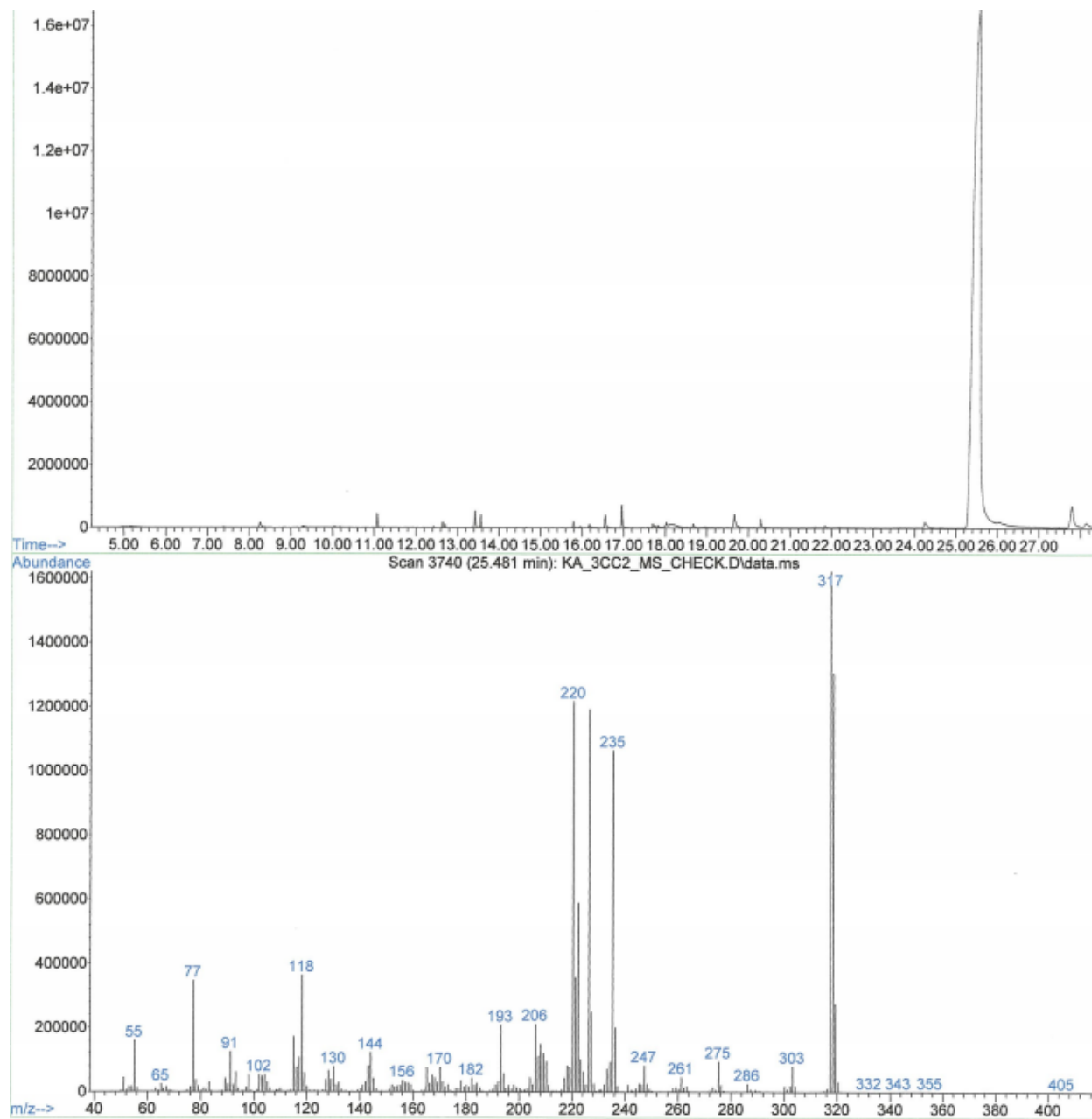


Figure 5.22 GC trace and MS fragmentation pattern for 3CC2.

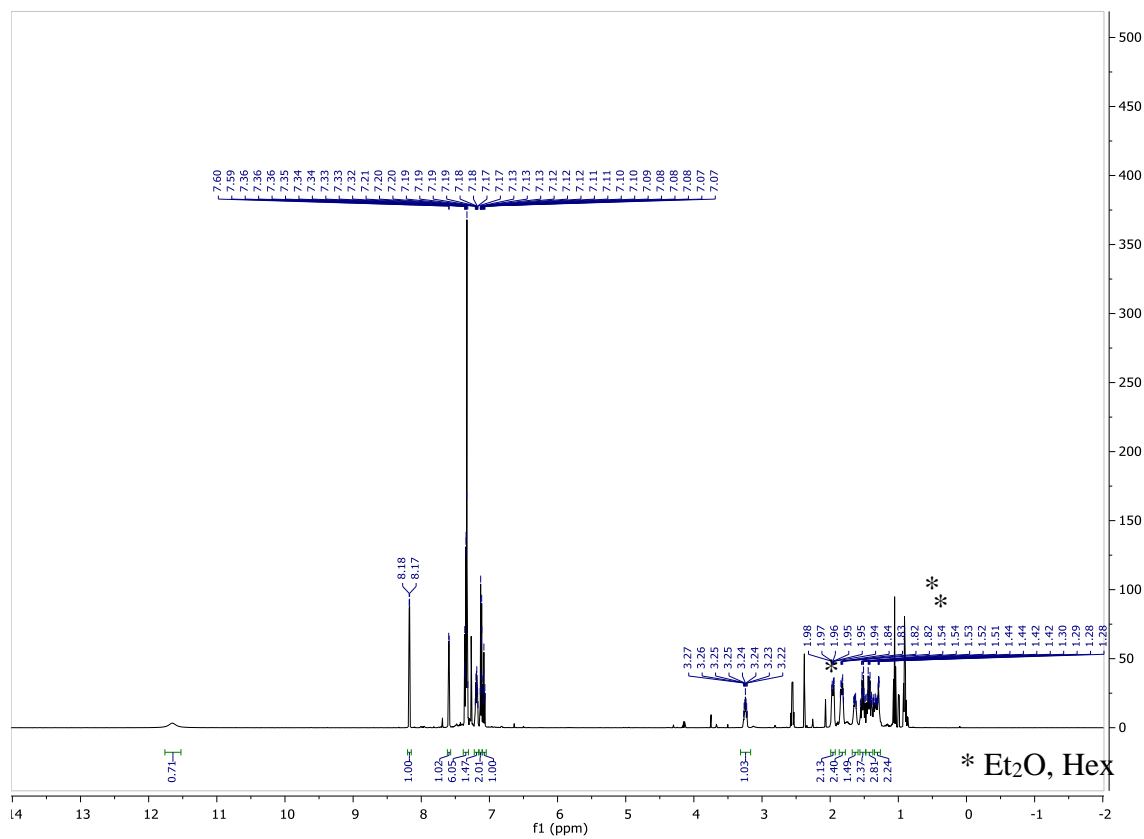


Figure 5.23 ^1H NMR of 3CC3 in CDCl_3 .

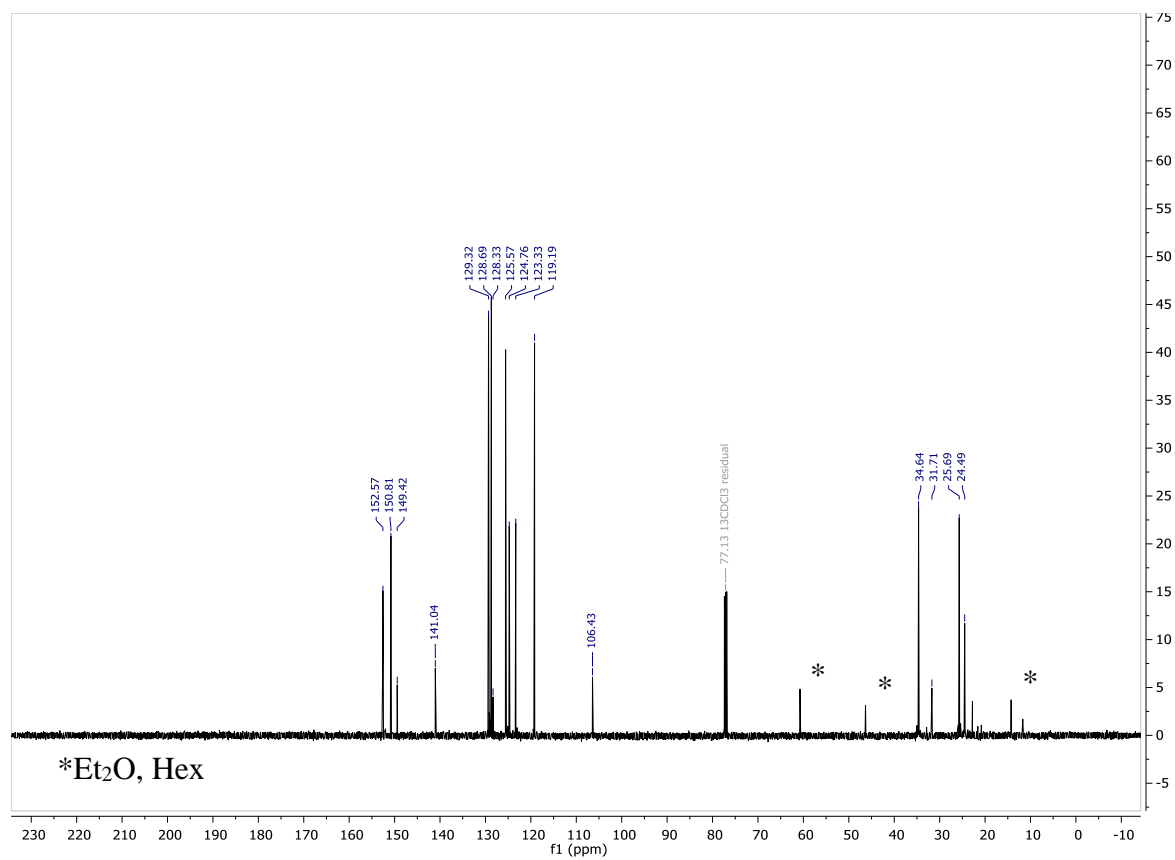


Figure 5.24 ¹³C NMR of 3CC3 in CDCl₃.

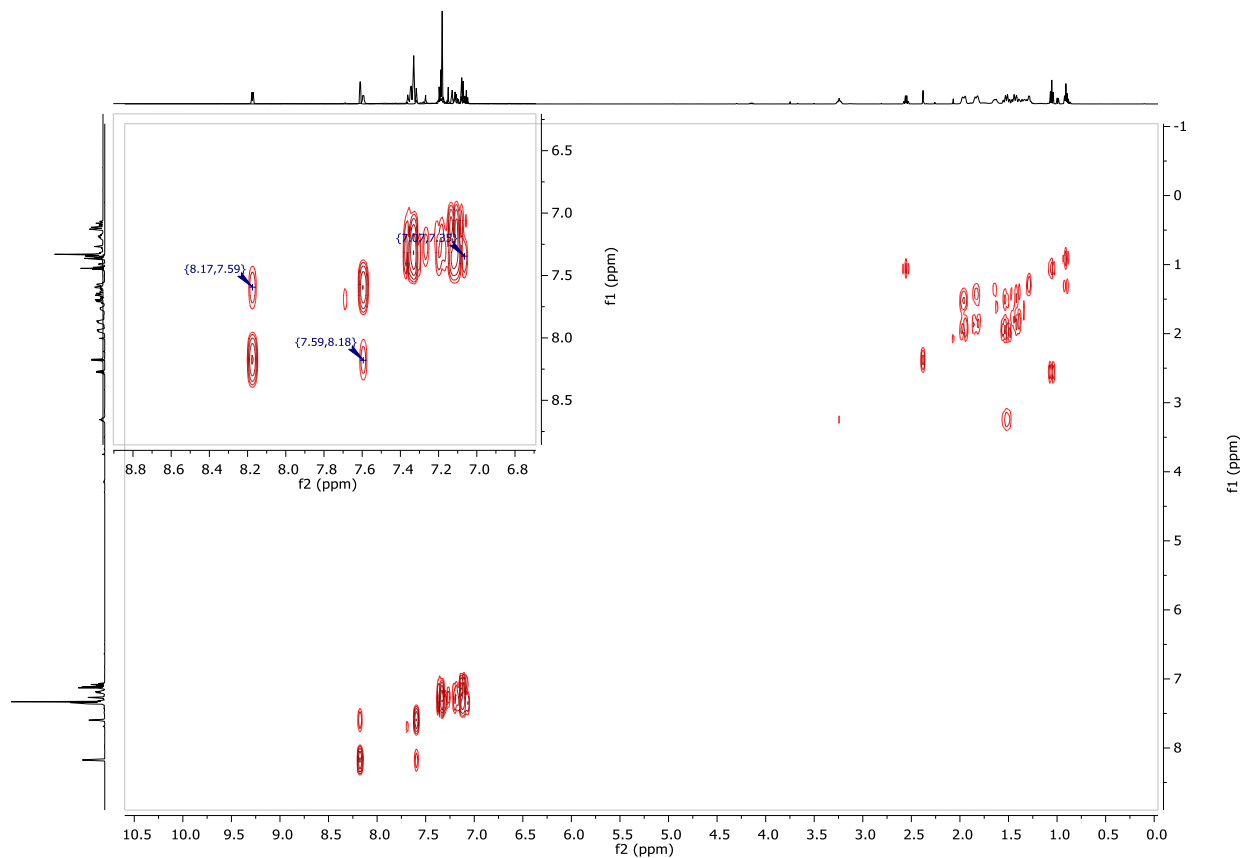


Figure 5.25 gCOSY NMR of 3CC3 in CDCl₃.

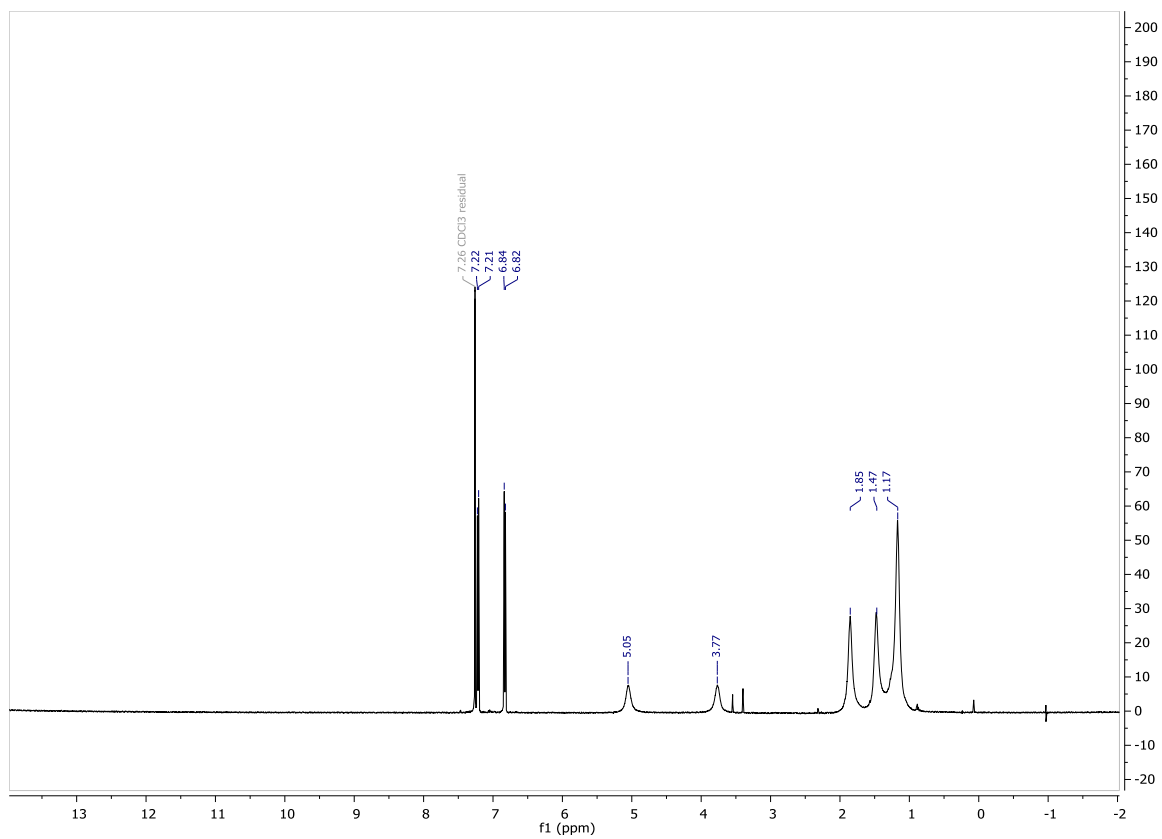


Figure 5.26 ^1H NMR of $[\text{Cr}](\text{O-Ph-4-bromo})$ in CDCl_3 (room temperature).

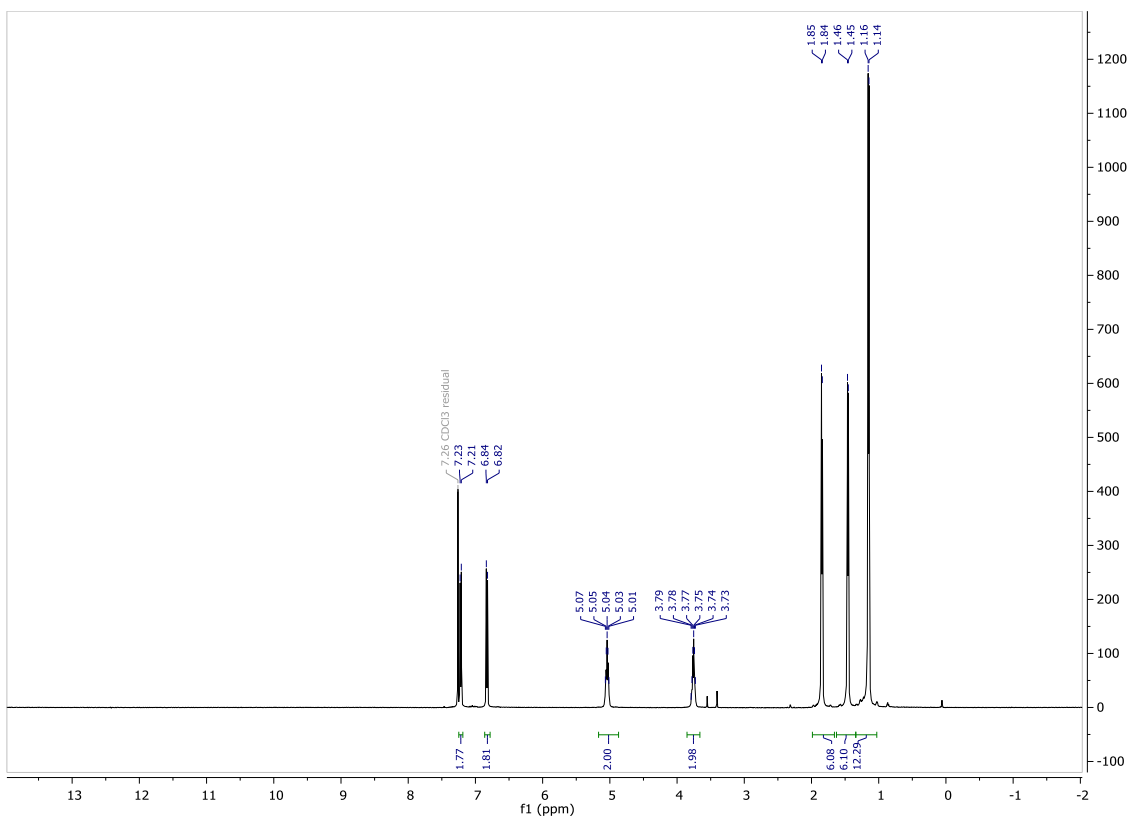


Figure 5.27 ^1H NMR of $[\text{Cr}](\text{O-Ph-4-bromo})$ in CDCl_3 ($-20\text{ }^\circ\text{C}$).

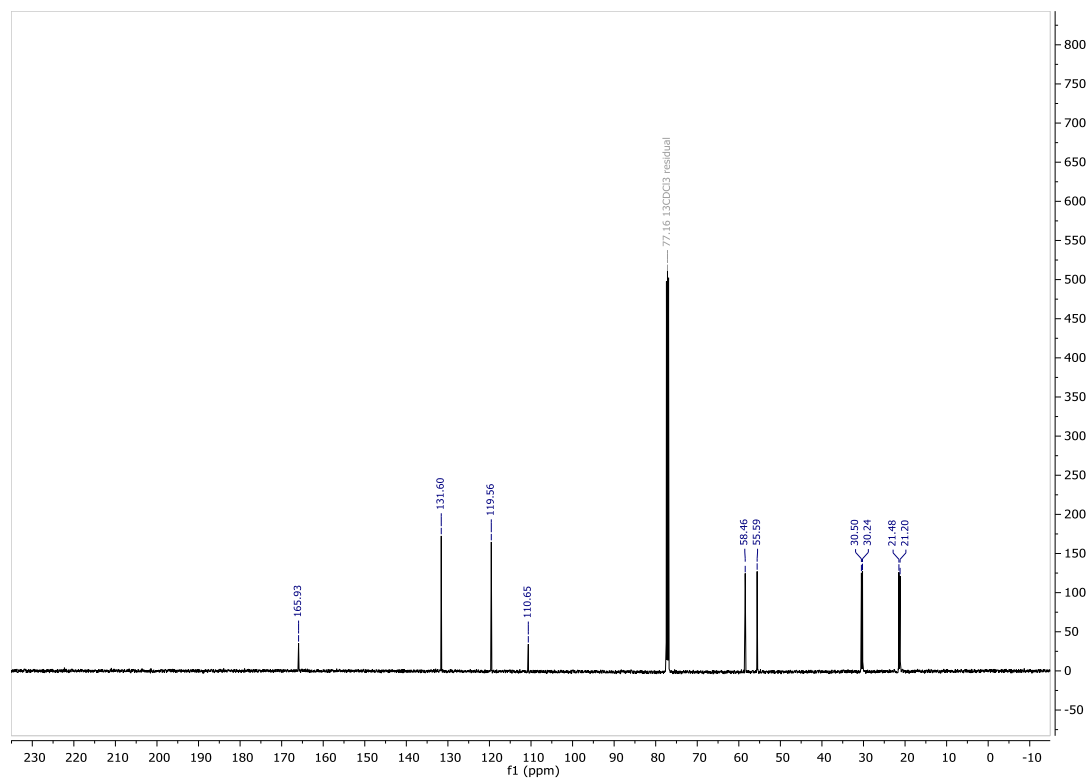


Figure 5.28 ^{13}C NMR of $[\text{Cr}](\text{O-Ph-4-bromo})$ in CDCl_3 ($-20\text{ }^\circ\text{C}$).

Graphical Method to Determine Order in Catalyst and Reagents:

The method utilized to analyze the experimental data graphically applies time-normalization to the x-axis, such that the variable concentration for each reagent is accounted for. The time-normalized reagent concentration is plotted against the concentration of product or consumption of a starting material (other than the one under study) across the time points sampled. The catalyst concentration dependence determined via the same method is treated differently, as catalyst concentration is assumed to be *constant* throughout the reaction. Using the following formula (Equation 5.2), the x-axis values for time-normalized concentration in the reagent under study can be calculated for the period of time between two sampled points.²⁹

$$x_n(t) = \sum_{i=1}^n \Delta t * \left(\frac{([A]_n + [A]_{n-1})}{2} \right)^m \quad (\text{Eq. 5.2})$$

In this equation, [A] is the concentration of A, the species under study. This effectively demonstrates the way the change in species A over time changes the rate of product formation.

According to the literature, application of this method is not advisable if, “the quantity of catalyst is unknown or if it changes in an unknown way during the reaction. This problem is particularly important when there are fast catalyst deactivation processes.”²⁸ In this system, we know that the catalyst deactivates under certain reaction conditions; however, this deactivation process does not appear to be rapid relative to the generation of product under many conditions (Table 5.1). This is specifically apparent at the beginning of each reaction. Comparisons between the full graphical analysis for order in catalyst, and traditional $k_{\text{obs}}(\text{initial})$ observation, agree quite well. Thus, we feel confident in the assessment that these reactions are first-order in catalyst. Plots of the graphical method results for each reagent, as well as catalyst concentration, are shown in Fig. 5.7. Examples of the applied graphical method functions are shown below in Table 5.9.

Table 5.11 Examples of Graphical Method Application to Entries in Table 2.

Entry	sample	time	3cc	t*[cat] ⁿ
1	0	0	0	0
	1	10	0.045079	0.00022316
	2	20	0.076953	0.00044632
	3	30	0.113497	0.00066948
	4	40	0.139191	0.00089263
	6	60	0.187779	0.00133895
	8	100	0.21032	0.00223159
2	0	0	0	0
	1	10	0.087487	0.00043111
	2	20	0.121113	0.00086223
	3	30	0.159726	0.00129334
	4	45	0.200862	0.00194001
	6	60	0.208921	0.00258668
Entry	sample	time	3cc	x _n (t) 1-octyne
1	0	0	0	10
	1	10	0.045079	20
	2	20	0.076953	30
	3	30	0.113497	40
	4	40	0.139191	60
	6	60	0.187779	100
	8	100	0.21032	-
6	0	0	0	10
	1	10	0.043931	20
	2	20	0.088563	30
	3	30	0.104307	40
	4	40	0.129061	50
	5	50	0.143897	-
Entry	sample	time	3cc	x _n (t) H ₂ NPh
1	0	0	0	38.0300973
	1	10	0.045079	84.4857829
	2	20	0.076953	142.683592
	3	30	0.113497	218.742693
	4	40	0.139191	457.667275
	6	60	0.187779	1731.10317
	8	100	0.21032	-

Table 5.11 (cont'd)

4	0	0	0	22.9614895
	1	10	0.062778	49.5168329
	2	20	0.097242	91.6754708
	3	35	0.100878	117.994244
	4	45	0.11943	227.298338
	5	85	0.128889	297.690438
	6	110	0.135292	-

Application of KINSIM Modeling Program:

The KINSIM modeling program, published by JPlus Consulting was used to simulate kinetics experiments, analyzing for rate constants and equilibrium processes following the proposed mechanism (Fig. 5.7). The simulated trace showing concentration of 3CC is represented by the bright blue line (H). Plotting this trace against the experimental data points, for product concentration vs. time, allows for a direct comparison of the modeled kinetic behavior versus the experimentally observed behavior.

With this method, and the reaction processes outlined in Fig. 5.7, the following plots were obtained, where K_1 , K_2 , and the forward rate constants described are kept relatively constant between the different reaction conditions examined. The values assigned to each equilibrium or rate constant are provided in the associated Table.

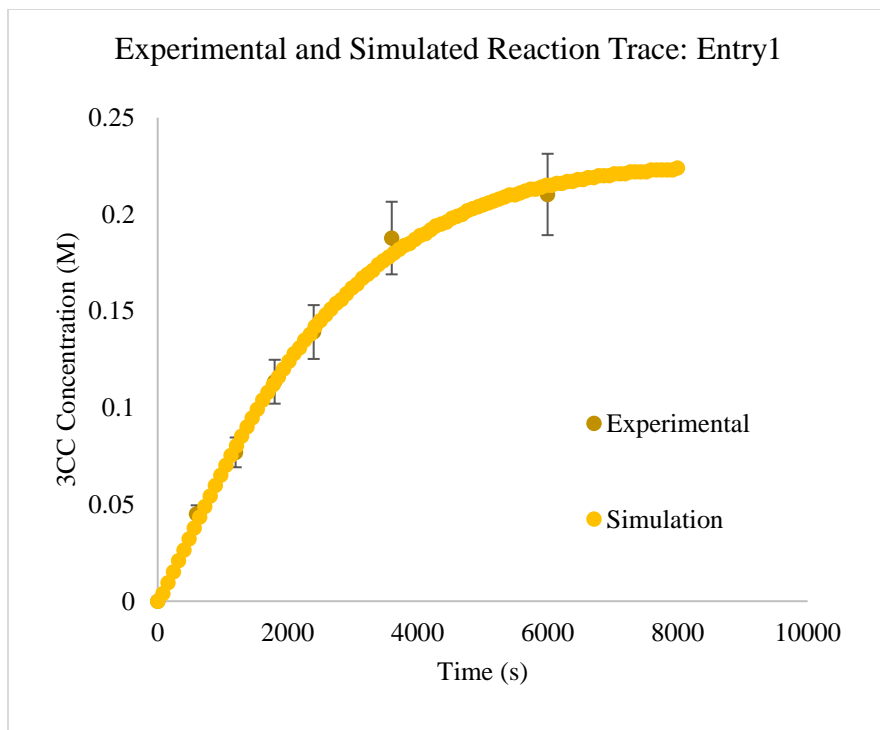


Figure 5.29 Results from simulated reactions versus the experimentally determined concentrations of 3CC product over time, Entry 1.

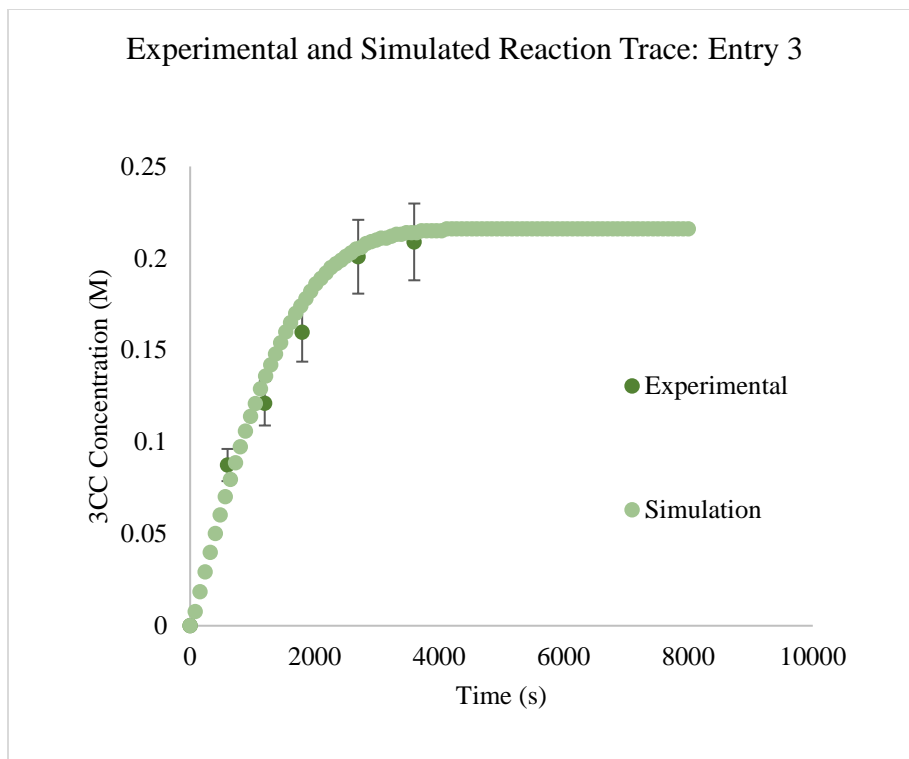


Figure 5.30 Results from simulated reactions versus the experimentally determined concentrations of 3CC product over time, Entry 3.

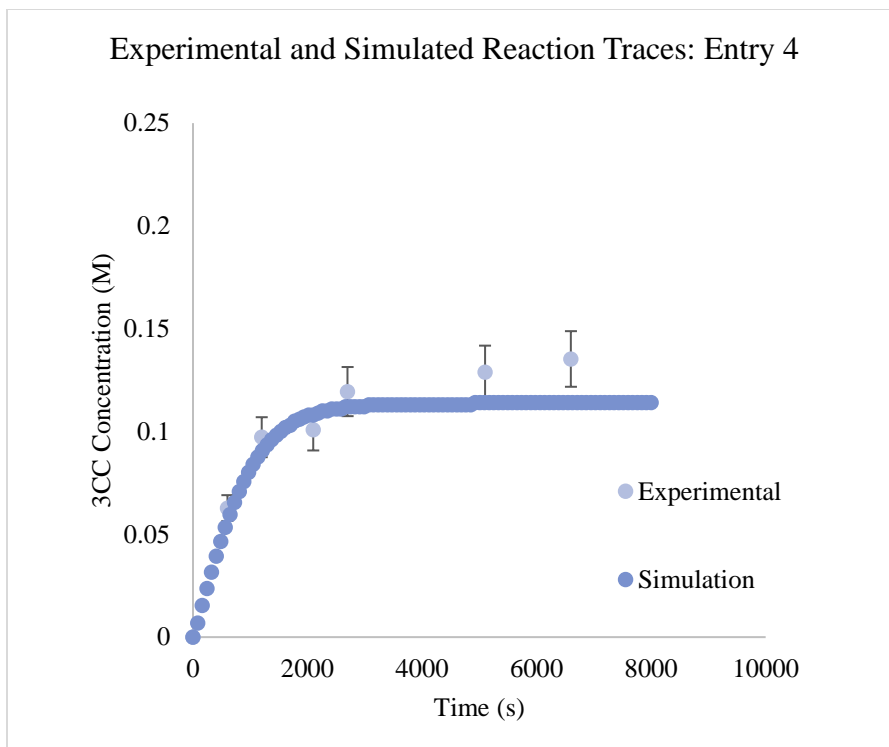


Figure 5.31 Results from simulated reactions versus the experimentally determined concentrations of 3CC product over time, Entry 4.

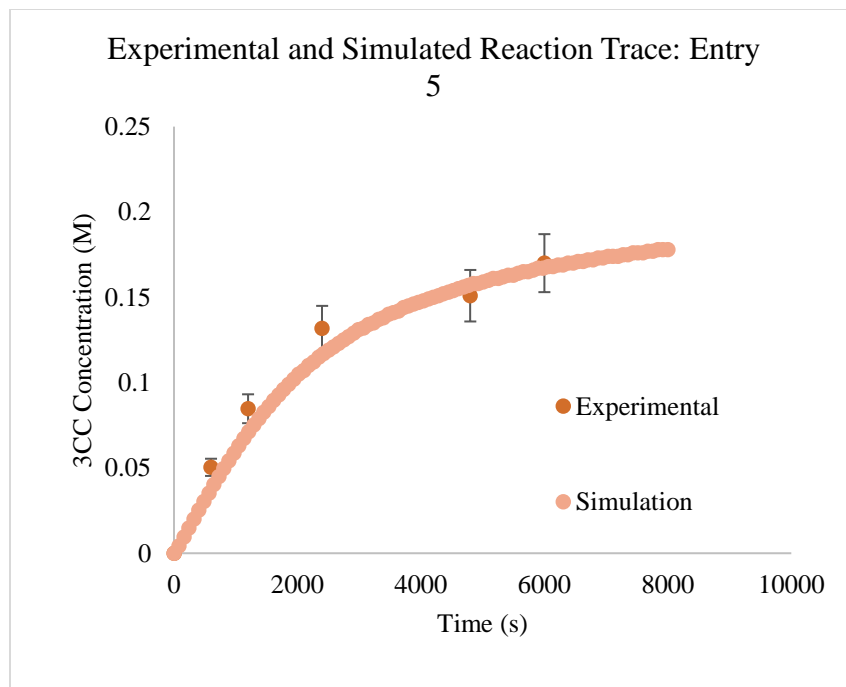


Figure 5.32 Results from simulated reactions versus the experimentally determined concentrations of 3CC product over time, Entry 5.

Table 5.12 Simulated rate constant and equilibrium constant values used to fit each set of experimental reaction traces. Good agreement is noted among the values, with small variances in some rate constants during fitting.

E5				E4					
A+I	=	C	K1	1	A+I	=	C	K1	1
B+D	=	A	K2	1.55	B+D	=	A	K2	1.5
B+E	>	F	k1	0.58	B+E	>	F	k1	0.8204
F+I	>	G	k2	0.3472	F+I	>	G	k2	0.3472
G+D	>	H+B	k3	0.367	G+D	>	H+B	k3	0.367
B+H	>	J	k4	0	B+H	>	J	k4	0
A+H+D	>	J	k5	0.3584	A+H+D	>	J	k5	0.1469
E3				E1					
A+I	=	C	K1	1	A+I	=	C	K1	1
B+D	=	A	K2	1.55	B+D	=	A	K2	1.55
B+E	>	F	k1	0.3952	B+E	>	F	k1	0.5507
F+I	>	G	k2	0.28	F+I	>	G	k2	0.3472
G+D	>	H+B	k3	0.296	G+D	>	H+B	k3	0.367
B+H	>	J	k4	0	B+H	>	J	k4	0
A+H+D	>	J	k5	0.296	A+H+D	>	J	k5	0.2278

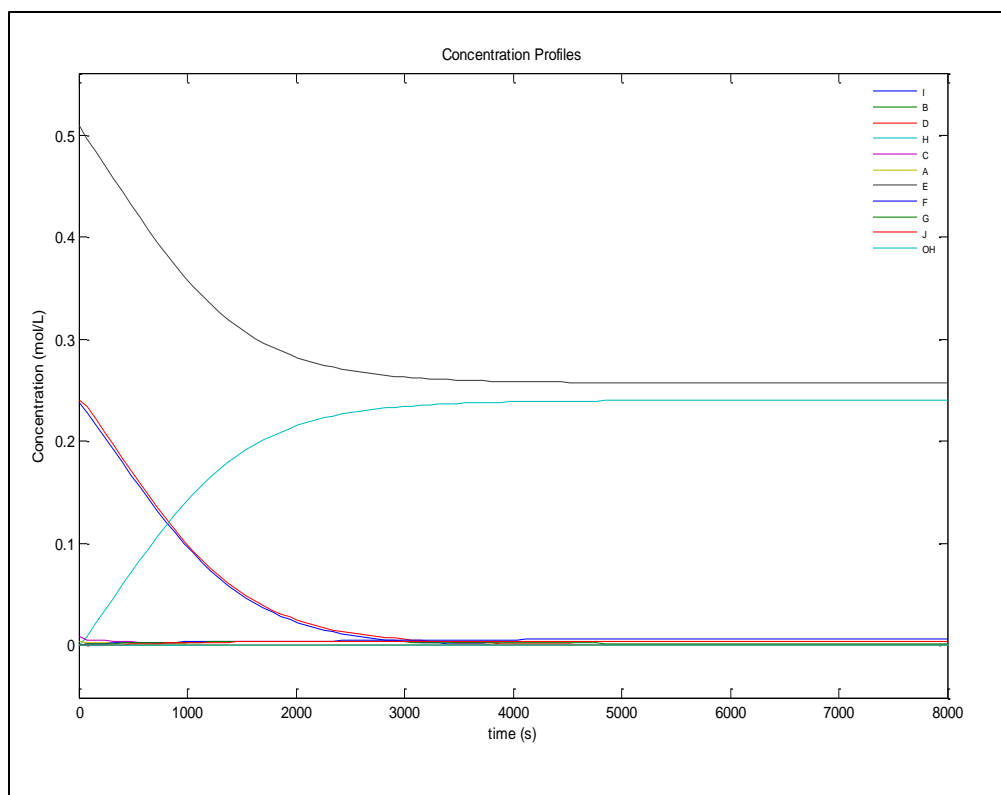


Figure 5.33 Example simulation from KINSIM program.

LDP Data:

All other complexes were synthesized as previously reported.³⁰ These complexes include $\text{NCr}(\text{N}^i\text{Pr}_2)_2(\text{O}^i\text{Ph-4-}^t\text{Bu})$, $\text{NCr}(\text{N}^i\text{Pr}_2)_2(\text{O}^i\text{Ph})$, and $\text{NCr}(\text{N}^i\text{Pr}_2)_2(\text{O}^i\text{Ph-4-OMe})$. The Cr complexes were then used to perform a series of ^1H NMR experiments that allow for the Cr- N^iPr_2 bond's barrier to rotation to be measured experimentally.³⁰

Table 5.13 Details of LDP value measurements (ΔH^\ddagger) for the 4-R-phenoxide ligands examined for electronic effects on [Ti]700(2,4,6-tri-tert-butylphenoxide) iminoamination catalysis.

Complex	Rate(s^{-1})	ΔG^\ddagger (kcal/mol)	T (K)	ΔH^\ddagger (kcal/mol)	Std. Deviation
4-Br-OPh	1.17	14.41	249.1	12.17	0.009
4-piperazino-OPh	1.76	13.90	243.8	11.70	0.005
OPh	-	14.27	254.7	11.98	-
4- t Bu-OPh	1.86	14.26	250.5	12.01	0.004
4-OMe-OPh	-	13.91	245.3	11.71	0.008

REFERENCES

REFERENCES

- (1) Odom, A. L., New C-N and C-C bond forming reactions catalyzed by titanium complexes. *Dalton transactions* **2005**, (2), 225-233.
- (2) Odom, A. L.; McDaniel, T. J., Titanium-Catalyzed Multicomponent Couplings: Efficient One-Pot Syntheses of Nitrogen Heterocycles. *Acc. Chem. Res.* **2015**, *48* (11), 2822-2833.
- (3) Davis-Gilbert, Z. W.; Tonks, I. A., Titanium redox catalysis: insights and applications of an earth-abundant base metal. *Dalton transactions* **2017**, *46* (35), 11522-11528.
- (4) Gilbert, Z. W.; Hue, R. J.; Tonks, I. A., Catalytic formal [2+2+1] synthesis of pyrroles from alkynes and diazenes via TiIII/TiIV redox catalysis. *Nature Chemistry* **2015**, *8*, 63.
- (5) Vujkovic, N.; Ward, B. D.; Maisse-François, A.; Wadepohl, H.; Mountford, P.; Gade, L. H., Imido-Alkyne Coupling in Titanium Complexes: New Insights into the Alkyne Hydroamination Reaction. *Organometallics* **2007**, *26* (23), 5522-5534.
- (6) Hazari, N.; Mountford, P., Reactions and Applications of Titanium Imido Complexes. *Accounts of Chemical Research* **2005**, *38* (11), 839-849.
- (7) Pohlki, F.; Doye, S., The Mechanism of the [Cp₂TiMe₂]-Catalyzed Intermolecular Hydroamination of Alkynes. **2001**, *40* (12), 2305-2308.
- (8) Rosner, T.; Le Bars, J.; Pfaltz, A.; Blackmond, D. G., Kinetic Studies of Heck Coupling Reactions Using Palladacycle Catalysts: Experimental and Kinetic Modeling of the Role of Dimer Species. *Journal of the American Chemical Society* **2001**, *123* (9), 1848-1855.
- (9) van Leeuwen, P. W. N. M., Decomposition pathways of homogeneous catalysts. *Applied Catalysis A: General* **2001**, *212* (1), 61-81.
- (10) Proutiere, F.; Aufiero, M.; Schoenebeck, F., Reactivity and Stability of Dinuclear Pd(I) Complexes: Studies on the Active Catalytic Species, Insights into Precatalyst Activation and Deactivation, and Application in Highly Selective Cross-Coupling Reactions. *Journal of the American Chemical Society* **2012**, *134* (1), 606-612.
- (11) Evans, D.; Yagupsky, G.; Wilkinson, G., The reaction of hydridocarbonyltris(triphenylphosphine)rhodium with carbon monoxide, and of the reaction products, hydridodicarbonylbis(triphenylphosphine)rhodium and dimeric species, with hydrogen. *Journal of the Chemical Society A: Inorganic, Physical, Theoretical* **1968**, (0), 2660-2665.
- (12) Bonds, W. D.; Brubaker, C. H.; Chandrasekaran, E. S.; Gibbons, C.; Grubbs, R. H.; Kroll, L. C., Polystyrene attached titanocene species. Preparation and reactions. *Journal of the American Chemical Society* **1975**, *97* (8), 2128-2132.

- (13) Bercaw, J. E.; Marvich, R. H.; Bell, L. G.; Brintzinger, H. H., Titanocene as an intermediate in reactions involving molecular hydrogen and nitrogen. *Journal of the American Chemical Society* **1972**, *94* (4), 1219-1238.
- (14) Cao, C.; Shi, Y.; Odom, A. L., A Titanium-Catalyzed Three-Component Coupling To Generate α,β -Unsaturated β -Iminoamines. *Journal of the American Chemical Society* **2003**, *125* (10), 2880-2881.
- (15) Vujkovic, N.; Fillol, J. L.; Ward, B. D.; Wadepohl, H.; Mountford, P.; Gade, L. H., Insertions into Azatitanacyclobutenes: New Insights into Three-Component Coupling Reactions Involving Imidotitanium Intermediates. *Organometallics* **2008**, *27* (11), 2518-2528.
- (16) Barnea, E.; Majumder, S.; Staples, R. J.; Odom, A. L., One-Step Route to 2,3-Diaminopyrroles Using a Titanium-Catalyzed Four-Component Coupling. *Organometallics* **2009**, *28* (13), 3876-3881.
- (17) Aldrich, K. E.; Odom, A. L., Titanium-Catalyzed Hydroamination and Multicomponent Coupling with a Simple Silica-Supported Catalyst. *Organometallics* **2018**.
- (18) Severin, R.; Doye, S., The catalytic hydroamination of alkynes. *Chemical Society Reviews* **2007**, *36* (9), 1407-1420.
- (19) Walsh, P. J.; Baranger, A. M.; Bergman, R. G., Stoichiometric and catalytic hydroamination of alkynes and allene by zirconium bisamides $\text{Cp}_2\text{Zr}(\text{NHR})_2$. *Journal of the American Chemical Society* **1992**, *114* (5), 1708-1719.
- (20) Johnson, J. S.; Bergman, R. G., Imidotitanium Complexes as Hydroamination Catalysts: Substantially Enhanced Reactivity from an Unexpected Cyclopentadienide/Amide Ligand Exchange. *Journal of the American Chemical Society* **2001**, *123* (12), 2923-2924.
- (21) Gagne, M. R.; Marks, T. J., Organolanthanide-catalyzed hydroamination. Facile, regiospecific cyclization of unprotected amino olefins. *Journal of the American Chemical Society* **1989**, *111* (11), 4108-4109.
- (22) Billow, B. S.; McDaniel, T. J.; Odom, A. L., Quantifying ligand effects in high-oxidation-state metal catalysis. *Nature Chemistry* **2017**, *9*, 837.
- (23) Ayinla, R. O.; Schafer, L. L., Bis(amidate) titanium precatalyst for the intermolecular hydroamination of allenes. *Inorg. Chim. Acta* **2006**, *359* (9), 3097-3102.
- (24) Aldrich, O., Low surface density silica-supported Ti precatalyst for C-N bond forming reactions. **2019**.
- (25) Majumder, S.; Gipson, K. R.; Odom, A. L., A Multicomponent Coupling Sequence for Direct Access to Substituted Quinolines. *Organic Letters* **2009**, *11* (20), 4720-4723.

- (26) McDaniel, T. J.; Lansdell, T. A.; Dissanayake, A. A.; Azevedo, L. M.; Claes, J.; Odom, A. L.; Tepe, J. J., Substituted quinolines as noncovalent proteasome inhibitors. *Bioorganic & Medicinal Chemistry* **2016**, *24* (11), 2441-2450.
- (27) Dissanayake, A. A.; Staples, R. J.; Odom, A. L., Titanium-Catalyzed, One-Pot Synthesis of 2-Amino-3-cyano-pyridines. *Advanced Synthesis & Catalysis* **2014**, *356* (8), 1811-1822.
- (28) Burés, J., A Simple Graphical Method to Determine the Order in Catalyst. **2016**, *55* (6), 2028-2031.
- (29) Burés, J., Variable Time Normalization Analysis: General Graphical Elucidation of Reaction Orders from Concentration Profiles. **2016**, *55* (52), 16084-16087.
- (30) DiFranco, S. A.; Maciulis, N. A.; Staples, R. J.; Batrice, R. J.; Odom, A. L., Evaluation of donor and steric properties of anionic ligands on high valent transition metals. *Inorganic chemistry* **2012**, *51* (2), 1187-200.
- (31) Bemowski, R. D.; Singh, A. K.; Bajorek, B. J.; DePorre, Y.; Odom, A. L., Effective donor abilities of E-t-Bu and EPh (E = O, S, Se, Te) to a high valent transition metal. *Dalton transactions* **2014**, *43* (32), 12299-12305.
- (32) Ugi, I. M., R.; Lipinski, M.; Bodesheim, F.; Rosendahl, F., Cyclohexyl Isocyanide. *Org. Synth.* **1961**, *41*, 13.
- (33) Webster, R. L.; Noroozi, N.; Hatzikiriakos, S. G.; Thomson, J. A.; Schafer, L. L., Titanium pyridonates and amidates: novel catalysts for the synthesis of random copolymers. *Chemical communications* **2013**, *49* (1), 57-59.
- (34) Lui, E. K. J.; Brandt, J. W.; Schafer, L. L., Regio- and Stereoselective Hydroamination of Alkynes Using an Ammonia Surrogate: Synthesis of N-Silylenamines as Reactive Synthons. *Journal of the American Chemical Society* **2018**, *140* (15), 4973-4976.
- (35) Möhrle, H.; Schake, D., Heterocyclische Spirocyclohexadienone aus substituierten Phenolen / Heterocyclic Spirocyclohexadienones from Substituted Phenols. In *Zeitschrift für Naturforschung B*, 1995; Vol. 50, p 1859.
- (36) Rieth, R. D.; Mankad, N. P.; Calimano, E.; Sadighi, J. P., Palladium-Catalyzed Cross-Coupling of Pyrrole Anions with Aryl Chlorides, Bromides, and Iodides. *Organic Letters* **2004**, *6* (22), 3981-3983.
- (37) Mishra, S. J.; Ghosh, S.; Stothert, A. R.; Dickey, C. A.; Blagg, B. S. J., Transformation of the Non-Selective Aminocyclohexanol-Based Hsp90 Inhibitor into a Grp94-Selective Scaffold. *ACS Chemical Biology* **2017**, *12* (1), 244-253.

CHAPTER 6. HOMOGENEOUS TITANIUM CATALYZED IMINOAMINATION AND CATALYST DISPROPORTIONATION PROCESSES

6.1 Introduction^{7,8}

Kinetic analysis of the heterogeneous catalyst, [Ti]700(X), provided insight that allowed for targeted enhancement of the observed catalytic rate for iminoamination (see Chapter 5). Parallel studies with the homogeneous titanium catalysts that we typically use to perform iminoamination reactions had never been undertaken. In part, this is because we foresaw several complications with performing kinetic analysis with these reactions, as typically in homogeneous iminoamination (3CC), substantial portions of hydroamination and formamidine side products are noted.^{1, 2} Even the four component coupling product, 4CC (aniline + alkyne + isonitrile + isonitrile), 2,3-diaminopyrrole is often noted in small concentrations in the crude iminoamination reaction mixtures.³ Some of these side products can be reduced by careful substrate selection, but generally speaking, the homogeneous iminoamination reactions are not as clean as their heterogeneous counterparts. An illustrative example of this is shown in Fig. 6.1.

⁷ This project was picked up where a former group member, Dhvani Kansal, left investigations into Ti(IV) complex disproportionation and comproportionation reactions. She prepared and fully characterized several complexes and some of her data will be discussed in this chapter.

⁸ The work presented in this chapter is being prepared for submission to *Faraday Discussions*: Aldrich, K. E., Kansal, D., Odom, A. L., "Title of paper," 2019.

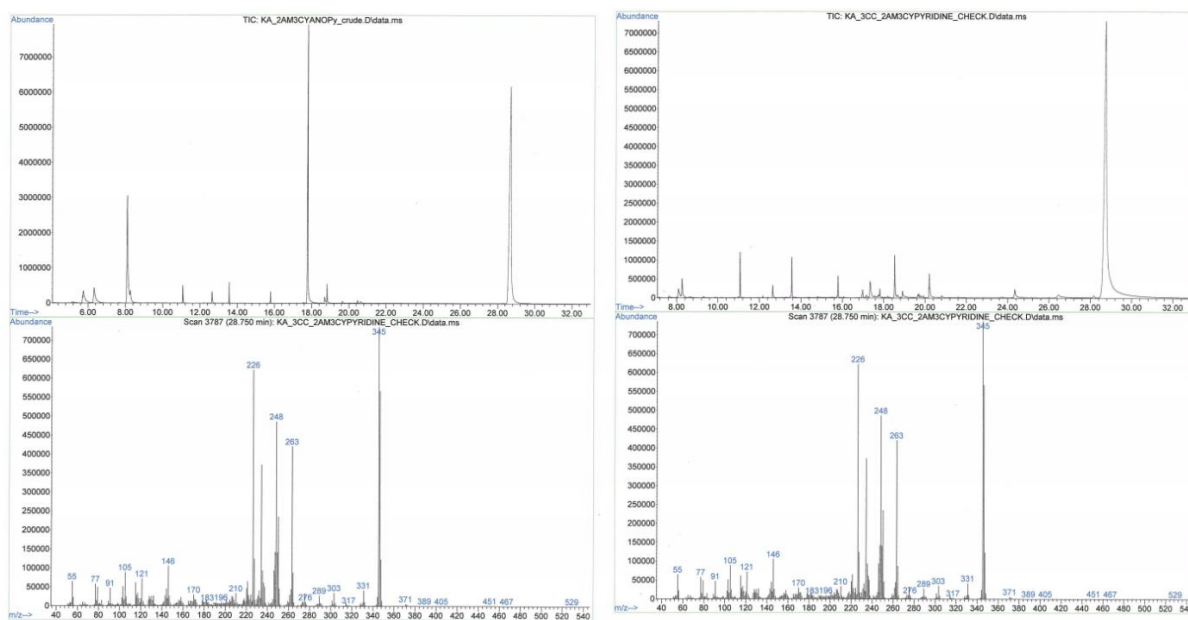


Figure 6.1 Crude GCMS analysis of the iminoamination of 3,5-dimethylaniline, 1-phenylpropyne, and CyNC catalyzed by 10 mol% $\text{Ti}(\text{dpm})(\text{NMe}_2)_2$ (left) and 5 mol% $[\text{Ti}]700(2,6\text{-dimethylphenylamidate})$ (right). Note that the reaction catalyzed by $\text{Ti}(\text{dpm})(\text{NMe}_2)_2$ has a substantial peak at 8 min, which is the 3,5-dimethylaniline starting material, as well as a large peak at 18 min for hydroamination side product. The reaction catalyzed by $[\text{Ti}]700$ shows no other compounds in the GCMS trace (small peaks on baseline are polysiloxane column material from GC column).

At the same time, a lot of work has been done in the Odom group to demonstrate how detailed understanding and quantitative classification of ligand donor ability and steric profiles can be used to predict how ancillary ligand properties will affect the rate of high valent metal catalysts.⁴⁻⁸ Highly specific studies correlating ancillary ligand properties with the rate of various $\text{Ti}(\text{IV})$ hydroamination catalysts, mentioned in previous chapters, for example, clearly indicate that electron-deficient, small ancillary ligands will produce faster catalysts.⁴ In theory, using the same techniques we should be able to predict what types of ligands will make Ti -catalyzed iminoamination reactions faster. However, to effectively employ these same techniques, a much more thorough understanding of the iminoamination mechanism is needed to inform about what the slow step of the reaction is and how to speed it up. This would facilitate logical changes in ligand design that target this reaction step specifically.

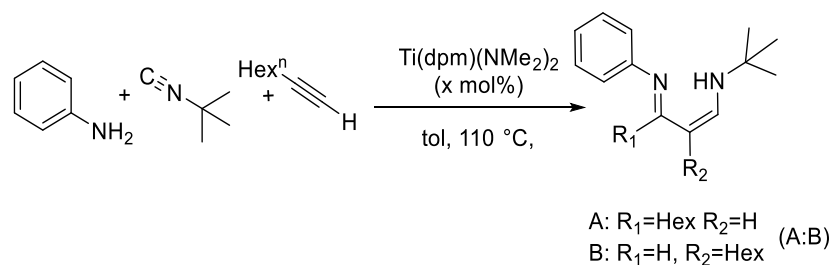
A general mechanism for this reaction has previously been proposed. As discussed below, we think several pieces of this proposed reaction are accurate. In addition to the reaction steps within the cycle, many of the concepts discussed in Chapter 5 (i.e. the off-cycle Ti species similar to those in the Doye Ti-catalyzed hydroamination mechanism and the [Ti]700(X) catalyzed iminoamination reaction) will be referenced here.

6.2 Kinetic Analysis of Iminoamination Catalyzed by $\text{Ti}(\text{dpm})(\text{NMe}_2)_2$

With the end goal of using mechanistic insights to guide catalyst design, by correlating ligand properties and effects on reaction rate, we set out to determine the rate law that describes the iminoamination reaction. The general reaction studied kinetically is shown above Table 6.1. Due to the messy nature of these reactions, discussed above, we elected to observe reaction progress by GC rather than NMR. The yields listed in Table 1, which shows the conditions of each kinetic trial, are GCFID yields quantified by external calibration of the isolated iminoamination product and standardized against dodecane. This allowed for clean observation (and quantification) of the product (both isomers), the hydroamination side product, and starting materials all in the crude reaction solution.

Note that the substrates for the reaction were carefully selected. Initial screenings at the kinetic concentrations examined CyNC as an alternative isonitrile, as well as 1-phenylpropyne and phenylacetylene as alternative alkynes. The smaller isonitrile led to the production of large quantities of formamidine (i.e. >30% overall yield of formamidine) and compromised the quality of the data that could be inferred about the iminoamination reaction. Switching to the larger ^tBuNC substrate reduced this problem substantially. In fact, in most of the kinetics runs shown in Table 1, the formamidine byproduct was noted in trace amounts by GCMS and showed negligible quantitation by GCFID.

The aromatic alkynes examined were originally considered because with the (dpm)Ti(NMe₂)₂ precatalyst, relatively high regioselectivities have been observed in the coupling of aromatic alkynes.^{1, 2, 9-12} Thus, we would only have to consider a single regioisomer of the desired product. Despite higher selectivity in the 3CC product yielded with these alkynes, the overall yields and conversions are much poorer. Additionally, substantial hydroamination is observed with these alkynes (up to 35% yield of hydroamination product with 1-phenylpropyne) along with alkyne trimerization. When a terminal alkyl alkyne (1-octyne) was examined instead, much lower quantities of hydroamination byproduct(s) were observed; alkyne trimerization processes were eliminated as well. While this does result in two regioisomers being produced in roughly a 1:1 ratio, we were willing to compromise on selectivity to get cleaner reactions that should provide purer kinetic data describing iminoamination. Additionally, since there is essentially no regioselectivity with this alkyne, the assumption that the rate of formation of either regioisomer is the same, is experimentally supported. (Also, provided that the [2 + 2] cycloaddition isn't rate determining, selectivity shouldn't affect the rate).



Scheme 6.1 General iminoamination reaction and substrates examined to determine the effect of each substrate on the rate of the overall reaction.

Table 6.1 Experimental conditions examined for kinetic analysis of Ti(dpm)(NMe₂)₂ catalyzed iminoamination. The general parameters from the reaction scheme below were applied. Amounts listed in the table are given as concentrations (molar).

Entry	Ti(dpm)(NMe ₂) ₂ (mol%)	H ₂ NPh	^t BuNC	1-octyne	Total Conversion to 3CC (%)	Regioisomer Ratio (A:B)	Hydroamination Byproduct (%) ^c
1	0.02 (10%)	0.20	0.20	0.20	63	1.0:1	4
2	0.04 (20%)	0.20	0.20	0.20	57	1.2:1	8
3	0.01 (5%)	0.20	0.20	0.20	63	0.9:1	3
4	0.01 (5%)	0.20	0.20	0.40	65	0.9:1	3
5	0.01 (5%)	0.20	0.20	1.00	63	1.0:1	2
6 ^a	0.01 (5%)	0.20	0.40	0.20	61	0.9:1	3
7	0.01 (5%)	0.40	0.20	0.20	77	0.9:1	4
8	0.01 (5%)	1.00	0.20	0.20	80	0.8:1	4
9 ^b	0.01 (5%)	0.20	0.20	0.20	0	na	0

^aThis sample, with additional ^tBuNC relative to the other three component coupling reagents, shows a measurable amount of the 4CC (H₂NPh+1-octyne+2^tBuNC), a double insertion of the isonitrile on intermediate Ti-metalloacycles which produces a 2,3-diaminopyrrole.³ ^bThis run included 0.02 M 3CC product, added to the reaction mixture with the isonitrile and alkyne prior to heating samples. No product was detectable in the samples by GC analysis. ^cThe hydroamination product generated appears to be during the initial heating period when the reaction comes to temperature. The amount of HA observed was generated between reaction initiation and the first sample analyzed, suggesting that after the induction period, the rate of HA is negligible compared to 3CC production.

With substrate options evaluated and selected, the reaction conditions listed in Table 6.1 were examined, sampling over a reaction period of 0-24 h. One issue with the catalyst that was immediately recognized is deactivation. Consider the reaction trace shown below for Entry 3. At 24 h, there is still excess of every starting material observed by GCFID, however, the yield for iminoamination product has essentially plateaued and the forward reaction progress has ceased.

This deactivation could even be observed visually with many of the kinetics solutions, with a color change in the reaction solutions going from an opaque brown color early in the reaction to a transparent orange color by 24 h. This color change appears to correlate with deactivation of the

Ti catalyst (see below). As a consequence of this deactivation, most of the conditions in Table 6.1 show only about 60% total conversion to the iminoamination product. Given this complication, utilization of the graphical analysis method should be approached cautiously; results obtained via graphical analysis were compared to plots of the initial rates and generally gave good agreement for the assessed order.^{13, 14} Plots for the graphical analysis results discussed here that aren't shown in associated figures are provided in the Experimental section.

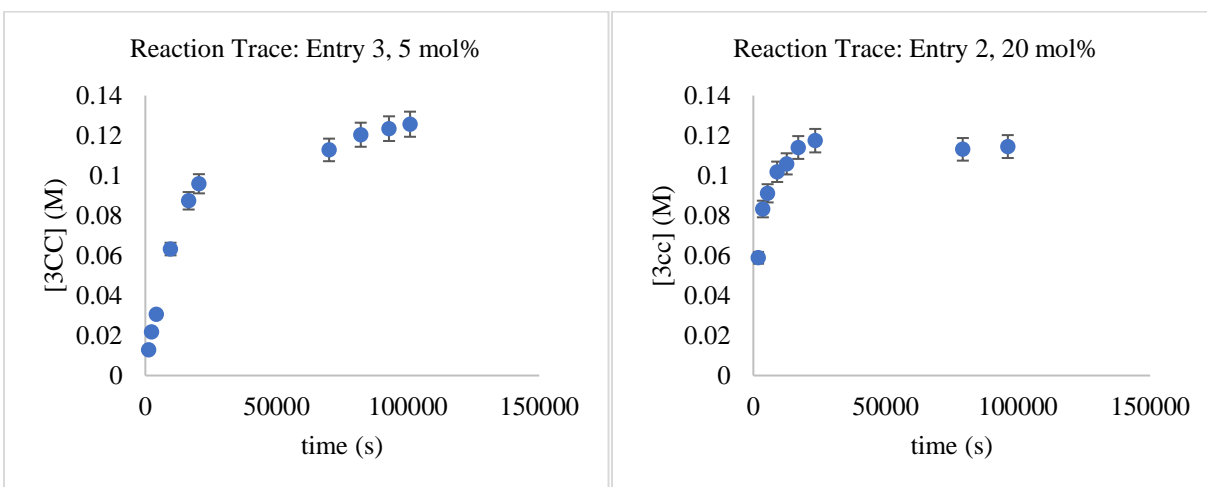


Figure 6.2 The reaction traces of two homogeneous $\text{Ti}(\text{dpm})(\text{NMe}_2)_2$ catalyzed iminoamination reactions. Both reactions reach a maximum yield an after about 12 h. With the high catalyst loading, there is even what appears to be a decrease in concentration of the product from the maximum measured concentration.

Under the reaction conditions shown in Table 6.1, Entry 3 was used as the baseline of comparison for determining the order of substrates as they affect the reaction rate. Analysis of the order in alkyne, comparing Entries 3 and 5, showed a zeroth order dependence. Similarly, isonitrile concentration dependence appears straightforward, as the reaction appears to be zeroth order in both reagents by comparison of Entries 3 and 6. However, there are three additional concentrations to consider in relation to their influence on the overall reaction rate: titanium concentration, aniline concentration, and the concentration of the product itself (3CC).

The graphical method suggests that there is a fractional order in aniline concentration. The best visual agreement is observed when the concentration of aniline is raised to a power of ~ 0.6 .

Graphically, this raises the question, is this value really $\frac{1}{2}$ -order in aniline, or first order in aniline, as the graphical method doesn't provide an effective way of determining the error for order estimation. Assuming there is a fractional order in aniline, we can envision several mechanistic explanations that might lead to this dependence appearing in the rate law.

Assessing the order-dependence between the reaction rate and product concentration, however, proved to be impossible to measure experimentally. As indicated by Entry 9, a kinetic run was attempted where the isolated $3CC_k$ was introduced into the reaction mixture with the substrates. However, upon addition of the solution containing $tBuNC$, 1-octyne, and the $3CC_k$ product to the solution containing the $Ti(dpm)(NMe_2)_2$ precatalyst and H_2NPh , the solution rapidly went from the typical opaque brown color of the iminoamination reactions to transparent orange. Upon heating the reaction mixture, no catalytic product formation was observed, even after 24 h. Thus, it appears that inclusion of $3CC$ prior to heating the reaction mixture results in total deactivation of the catalyst.

This observation supports what we had already suspected with regards to the catalyst instability and deactivation. Some form, or forms, of the catalyst can react with the product generated, and while this seems to take time when the solution is at reaction temperature, at room temperature, this reaction is rapid and irreversible in the presence of the iminoamination reagents. While, in understanding the kinetics data, experimental evidence of this deactivation pathway (catalyst + iminoamination product) was important to obtain, we were unable to experimentally determine the order of this deactivation under the conditions of the reaction. However, it is likely that an additional term (i.e. $k_{obs}[Ti][3CC]$) should be included as a second term in the most accurate description of the rate law.

Finally, there is the relationship between rate and catalyst concentration. Upon initial assessment, it seemed like a first order dependence in catalyst concentration provided the best overlap for Entries 1-3. A plot that shows the results of the graphical overlap produced by this order dependency is shown below in Fig. 6.3. However, this would provide a rate law that is first order in catalyst and fractional order in aniline concentration. While attempts were made to rationalize these results mechanistically, I was unconvinced that any of these explanations fully agreed with the experimental data, and after reading about some examples of reactions in which an off-cycle dimerization affects the order observed in catalyst concentration, I decided to reexamine the graphical method data for Entries 1-3.

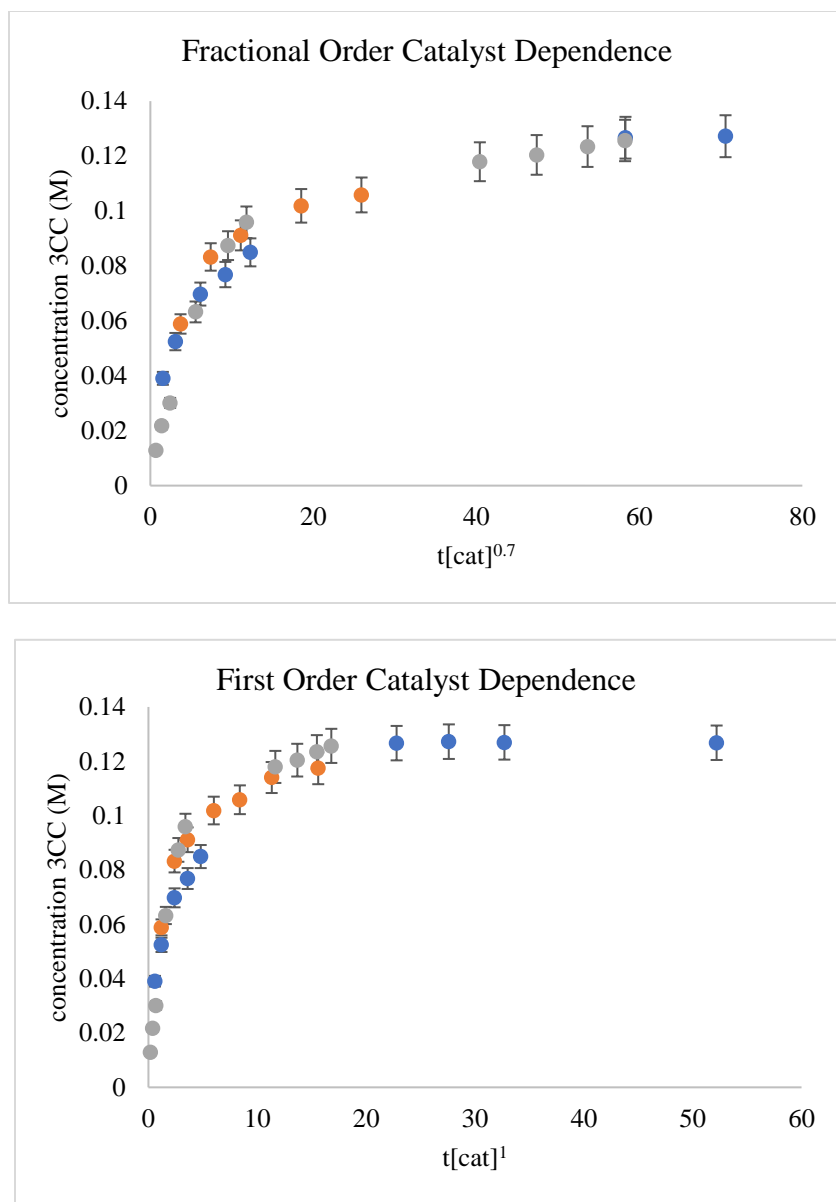


Figure 6.3 Graphical analysis of Entries 1-3 in Table 6.1. The plots are fitted with a fractional order (*top*) and first order (*bottom*) dependence. Similar fits result from both analyses.

Previously, it had been observed that a first-order dependence seemed more accurate than a half-order dependence, and the residual deviations between the points in the plot of the first order dependence were attributed to experimental error. This error could include simple errors associated with the measurements, as well as the small amount of hydroamination generated during the initial heating period; it also seems reasonable to anticipate error due to complicating factors that could arise directly from catalyst deactivation. However, if the data is examined with a fractional order

dependence, similar—or arguably what looks like slightly better agreement—is obtained graphically for Entries 1-3. Specifically, in the plot shown above (Fig. 6.3), all three Entries were fitted with an exponent of ~ 0.7 . These results are also presented below by examining the initial rates from the experimental kinetic runs (Entries 1-3), as well as the predicted k_{initial} values for both 0.7 and first-order dependence on catalyst concentration.

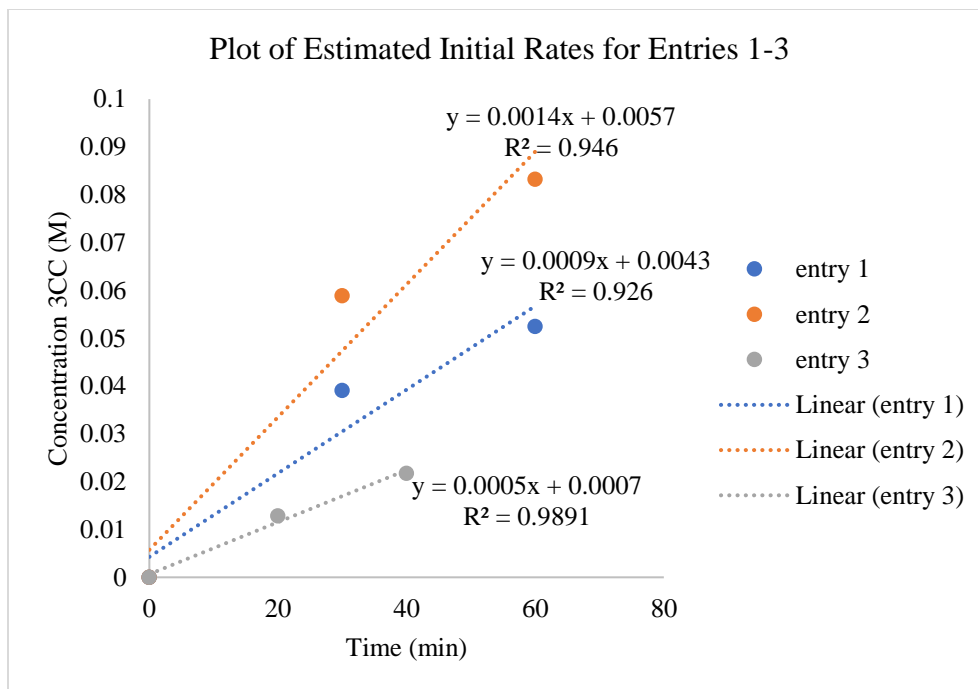


Figure 6.4 Examination of the initial rates for Entries 1-3 from Table 6.1. The results suggest that the catalyst concentration may not be simple first-order in these concentration ranges.

Table 6.2 Initial rates predicted for entries 1-3 with different orders in catalyst concentration. The values calculated for a fractional order appear to agree better with the experimentally observed initial rates shown in Fig. 6.4.

Entry	k_{initial} (0.7 order)	k_{initial} (first order)
3	0.00054	0.00054
1	0.00088	0.0011
2	0.0014	0.0022

The graphical analysis has generated a basic rate law of the form shown in Eq. 6.1, for the range of reaction conditions examined so far. However, several big questions about iminoamination still remain.

$$rate = k_{obs}[Ti]^{0.7}[PhNH_2]^{0.6} \quad (\text{Eq. 6.1})$$

Additional studies are currently ongoing, but it is worth noting that the resulting fractional orders observed via the graphical order analysis are very similar to what is observed in a Heck coupling reaction described in the graphical method studies by Bures.^{13, 15} This example is from a study by Blackmond and coworkers, in which the kinetic effects of the catalyst and substrate concentrations for the Pd-catalyzed Heck coupling of *p*-bromobenzaldehyde and butylacrylate were examined. In their system, an off-cycle dimerization of the active Pd species is observed, where the forward equilibrium constant for dimer formation is very large. This creates two extreme regimes in the catalytic system. One regime dominates when catalyst concentration is high, and the dimerization process is facilitated. Under these conditions, half-order dependence between metal complex concentration, [Pd], and the reaction rate is noted. The second regime dominates catalyst concentration is extremely low. Under these conditions, dimerization—an inherently bimolecular process, which is second order in metal—is reduced to the extent that the overall reaction rate then appears first-order in [Pd]. Between these two extremes, changes to the catalyst concentration can present orders from 0.5-1.

In these Ti systems, other studies investigating the behaviors of related complexes in solution implicate off-cycle formation of a dimeric Ti species, bridged by imide ligands, $[Ti(dpm)(\mu\text{-NPh})]_2$.^{16, 17} These Ti systems also indicate the potential for a bis(amide) speciation, as an equilibrium species that can form $Ti(dpm)(=\text{NPh})$ and the aniline substrate. A depiction of these potential processes is shown in Fig. 6.5. This process also takes the metal off-cycle. As was observed in the Blackmond studies, other studies of the Heck reaction, and other homogeneous catalytic systems with these off-cycle dimerization pathways, I wondered if these competitive off-cycle equilibrium processes were also manifesting here as fractional orders in the rate law.

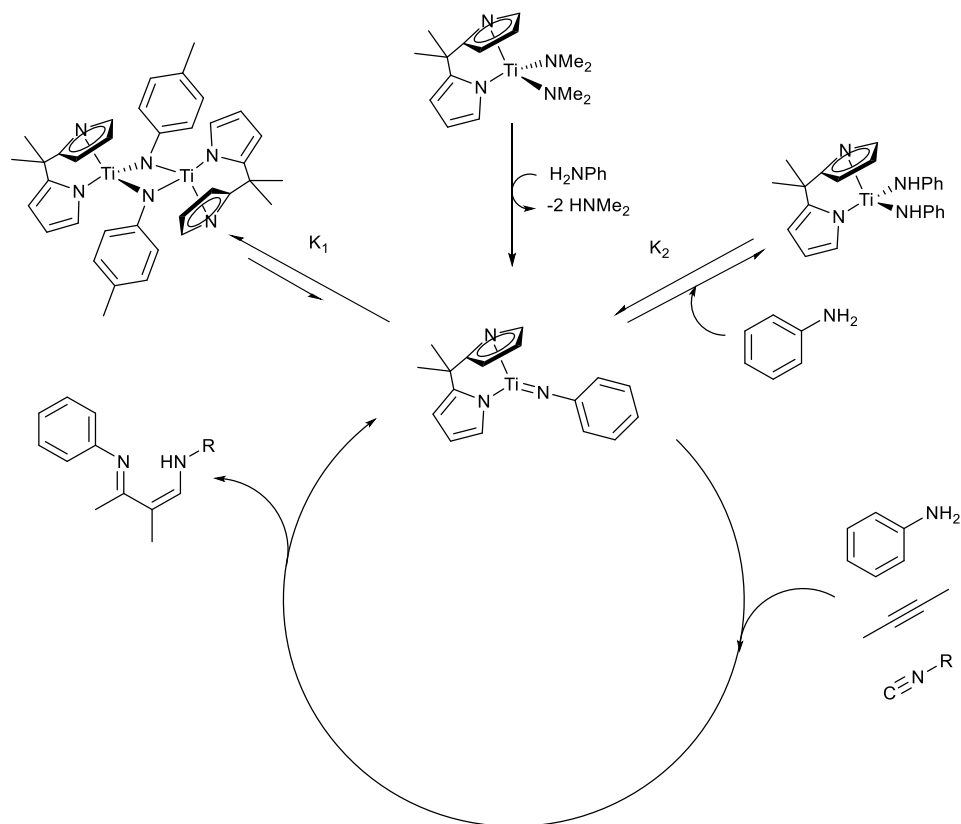


Figure 6.5 Potential forms of titanium catalyst likely present in the catalytic iminoamination reaction mixture.

If these off-cycle processes and their equilibrium constants are causing fractional dependences in the rate law, it is possible that under dramatically different reaction conditions, we will observe a different experimental rate law. Specifically, if the dimerization process is exerting a dominant influence over the rate of the catalysis under the concentrations examined, $[Ti] = 0.01\text{--}0.04\text{ M}$ (5–20 mol%), we would expect that at much lower concentrations, the propensity for dimerization will be reduced. This may result in a return to truly first-order behavior, as has been observed with these types of mechanisms in the literature.^{13, 15} Conversely, going to higher catalyst concentrations, we would expect the dependence on $[Ti]$ to approach true half-order dependence. The issue with the kinetic experiments presented in Table 6.1 then becomes that they were examined over too narrow a range of conditions. For example, in the Pd systems for Heck couplings, >2 orders of magnitude were spanned in catalyst concentrations.

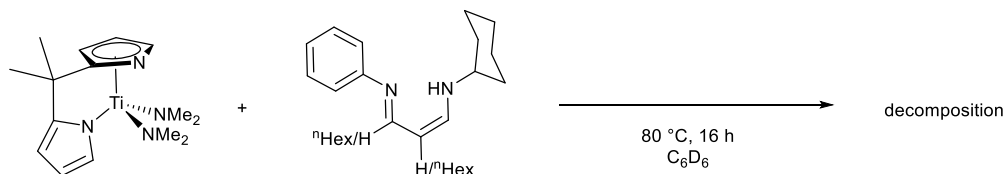
Expansion of the catalytic conditions examined via these kinetic studies is currently underway. Of the two potentially fractional orders, the more challenging of the two to probe experimentally will likely be the concentration dependence for H₂NPh. We've established that a higher aniline concentration correlates with higher conversion, seemingly preserving the catalyst by slowing its decomposition over time. This is consistent with off-cycle formation of the Ti(dpm)(NHPH)₂ equilibrium, provided that this species does not react to directly result in decomposition. Thus, we've done the experiments with relatively high concentrations of H₂NPh, because these are favorable in a practical sense to the generation of the iminoamination product. However, running experiments at low concentrations of H₂NPh is likely to encourage decomposition, as well as potentially encouraging side-product formation.

Finally, from the rate equation that has been experimentally determined, and the suspected role of off-cycle pathways that appear to have a substantial effect on the rate, it is hard to firmly rule out the possibility that under alternate conditions, the rate will be determined by whatever step within the catalytic cycle, represented by a single arrow above, is slowest. It is common for the rate law of a reaction, where competitive reactions take some of the active metal off-cycle, to be altered by dramatic reaction conditions changes.

6.3 Investigations into Catalyst Deactivation During Ti-Catalyzed Iminoamination

Primary among our unanswered questions at this point was, how does the catalyst deactivate? We have several pieces of evidence suggesting the involvement of the iminoamination product itself. This product, after all, is a tautomer of the ubiquitous nacnac or 1,3-diketimine ligand class, so it is reasonable to assume it will have an affinity for binding to transition metals. This binding may then facilitate other reactivity, which leads to irreversible destruction of catalytically competent Ti species in solution. There are several potential forms of the titanium

catalyst, shown in Fig. 6.5, from which this decomposition may originate. We tried to investigate these possibilities in turn to get a better idea of what exactly occurs between point A, the active catalyst, and point B, total deactivation



Scheme 6.2 The $\text{Ti}(\text{dpm})(\text{NMe}_2)_2$ complex reacts with the iminoamination product to yield an intractable mixture.

Several stoichiometric *in situ* reactions, between various potential titanium species in solution and the iminoamination product, were examined. First, we considered whether the precatalyst was stable toward the product. $\text{Ti}(\text{dpm})(\text{NMe}_2)_2$ and the iminoamination product were combined in a ratio of 1:1.5 in C_6D_6 . The sample was heated in a J-young tube for 16 h, at which time the solution was examined by ^1H NMR. The heated solution is a mess, showing an unidentifiable mixture of products with $\text{Ti}(\text{dpm})(\text{NMe}_2)_2$ not clearly identifiable after heating. While it is unclear exactly what forms during this interaction, it's apparent that the initial precatalyst is not intact after 16 h of heating at 80 °C with 3CC (Scheme 6.2).

This was a start, but due to the order of addition of the reagents when setting up an iminoamination reaction, the titanium species in solution are likely a combination of the $[\text{Ti}(\text{dpm})(\mu\text{-NPh})_2]$ and the $\text{Ti}(\text{NHPH})_2(\text{dpm})$ complex. There may also be the proposed active species, $\text{Ti}(\text{dpm})(\text{NPh})$. Of course, datively bound H_2NPh and $^t\text{BuNC}$ could also be present interacting with these species, as well. At any rate, the relevance of titanium species reacting with the iminoamination product is greater when we start closer to the species present in the authentic iminoamination reaction mixture. To that end, the dimeric bridging imido species was synthesized using H_2Ntolyl and $\text{Ti}(\text{dpm})(\text{NMe}_2)_2$. The single crystal X-ray structure of this species is shown below in Fig. 6.6. Note that the molecule has a center of inversion, such that only half the molecule

appears in the asymmetric unit, with the other half of the molecule generated by symmetry in the solid-state structure.

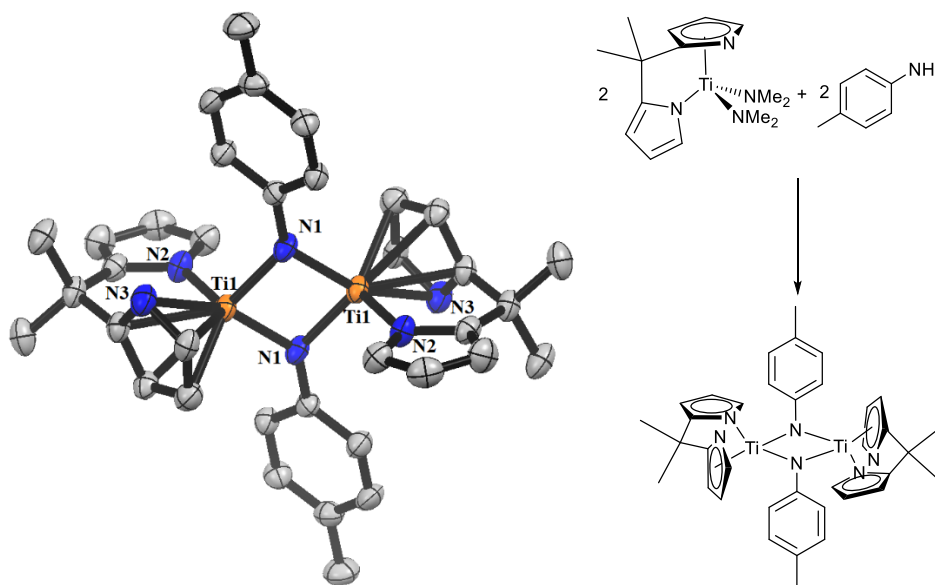
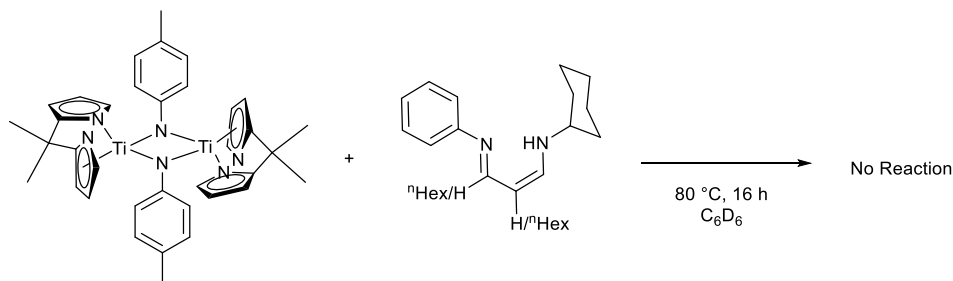


Figure 6.6 Isolation and structural characterization of the bridging $[\text{Ti}(\text{dpm})(\mu\text{-Ntoly})]_2$ complex. The single crystal X-ray structure is shown with ellipsoids at the 50% probability and H atoms omitted for clarity.

Another interesting feature of this species is that within each dpm ligand, one pyrrole ligand binds η_1 while the other binds η_5 . Rapid interconversion of the two pyrrole rings, a haptotropic shift or exchange, causes the ^1H NMR to appear broad at room temperature, as a result of the fluxionality. Even down to $-75\text{ }^\circ\text{C}$, some broadness in the aromatic and aliphatic signals (CH_3 signals from the dpm linkers) is observed. However, at this low temperature, the spectrum can be assigned (see Experimental, Fig. 6.33-35).

Attempts to characterize the complex *in situ* using ^1H DOSY NMR provided a calibrated molecular weight of $463 (\pm 51)$ g/mol. This molecular weight is intermediate to the monomer and the dimer molecular weights, and it is unclear whether this is a result of an exchange between the monomer and dimer in solution or if it is a result of inaccurate calibration due to the broadness of the peaks that we are trying to observe. Additionally, as the peaks remain broad, it is hard to rule out the presence of other species at room temperature (i.e. $\text{Ti}(\text{dpm})(\text{NHPh})_2$). However, these

results suggest that it doesn't completely dissociate to a monomeric species in solution at room temperature.

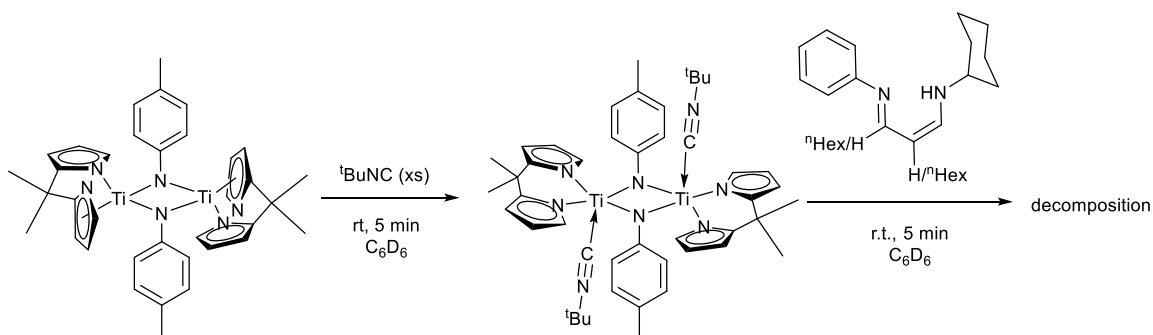


Scheme 6.3 No reaction was observed between the iminoamination product and the [Ti(dpm)(μ -Ntolyl)]₂.

When the isolated dimeric titanium species is combined with an excess of the iminoamination product and heated in C₆D₆, no reaction is observed over the course of several hours (Scheme 6.3). This suggests that one of the other possible Ti species in solution is responsible for reacting with the iminoamination product. Given that the precatalyst reacts with the iminoamination product, we suspected that the Ti(NHPh)₂(dpm) complex was a likely candidate for reaction with the iminoamination product. Additionally, the proposed active species—which in theory is the most reactive form of the titanium in the reaction mixture—may also undergo these undesired reactions. Thus, we kept looking, trying to mimic any titanium species that may exist in the catalytic reaction solutions.

The addition of roughly 3 equivalents of ^tBuNC to isolated [Ti(dpm)(μ -Ntolyl)]₂ renders an interesting spectroscopic change. The peaks on the dpm ligand sharpen considerably and are clearly observed at room temperature. This likely indicates coordination of the isonitrile to the Ti center, which is supported by the ¹H NMR, as well. Only 4 aromatic peaks appear, which indicates that each pyrrole ring on the dpm ligands is equivalent (and one is coincident with a doublet peak from the tolyl group); likewise, the CH₃ groups on the dpm linker are also equivalent.

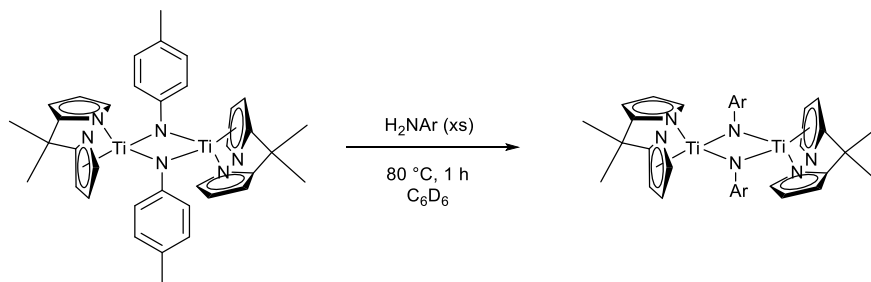
This compound, $[\text{Ti}(\text{dpm})(\text{CN}^t\text{Bu})(\mu\text{-Ntoly})]_2$, reacts rapidly with iminoamination product in solution at room temperature. Upon adding the iminoamination product to an NMR sample of the isonitrile adduct, the compounds have reacted in the time it takes to walk a sample to the NMR instrument (Scheme 6.4).



Scheme 6.4 Proposed decomposition pathway observed when both $^t\text{BuNC}$ and iminoamination product are added to the dimeric $[\text{Ti}(\text{dpm})(\mu\text{-Ntoly})]_2$.

In somewhat separate experiments, we determined that $[\text{Ti}(\text{dpm})(\mu\text{-Ntoly})]_2$ when heated with an excess of a different aniline in solution for 1 h at $80\text{ }^\circ\text{C}$ quantitatively exchanges the H_2Ntoly with the new aniline. This was observed with 3,5-dimethylaniline and 2-fluoro-5-methylaniline. When the dimer was heated with an excess of H_2Ntoly for 48 h at $80\text{ }^\circ\text{C}$, the dimeric complex even appears to undergo exchange with the dpm ligand. These observations suggest that, even if the dimer is present in relatively high concentrations in the iminoamination mixture, relative to other titanium species, it can still undergo rapid exchange (Scheme 6.5).

Before concluding anything specific, we can say that generally, there appears to be a competition for the $\text{Ti}(\text{dpm})$ species formed in the iminoamination solution between the product being generated versus deactivation processes. This fundamentally requires a faster or more robust catalyst in order to provide full conversion to products. Otherwise, the catalyst will be deactivated well before all the starting materials are consumed.



Scheme 6.5 Conversion of the μ -Ntolyl species to a μ -NAr species upon the addition of an excess of H_2NAr . With a coordinated H_2NAr , there are several different pathways conceivable by which the anilides are exchanged by quick proton transfer steps.

Based on these initial investigations into the nature of the deactivation reactions, there are several suspected pathways from which these titanium complexes can likely lose their activity and fall off the catalytic cycle. While the dimeric $[\text{Ti}(\text{dpm})(\mu\text{-Ntolyl})]_2$ complex doesn't appear to react directly with the iminoamination product, all of the following species appear to lead to reactivity with the iminoamination product: $\text{Ti}(\text{NHPh})_2(\text{dpm})$, $\text{Ti}(\text{dpm})(\text{NPh})$, and $[\text{Ti}(\text{dpm})(\text{CN}^t\text{Bu})(\mu\text{-Ntolyl})]_2$. As is evident from the reaction traces from the kinetic runs, these deactivation processes have a profound effect on the rate observed in these reactions and the final conversion. Subsequently they cannot be ignored when considering catalyst design in these systems. A summary of the suspected pathways of decomposition that we have observed through these stoichiometric NMR-scale experiments is shown in Fig. 6.7.

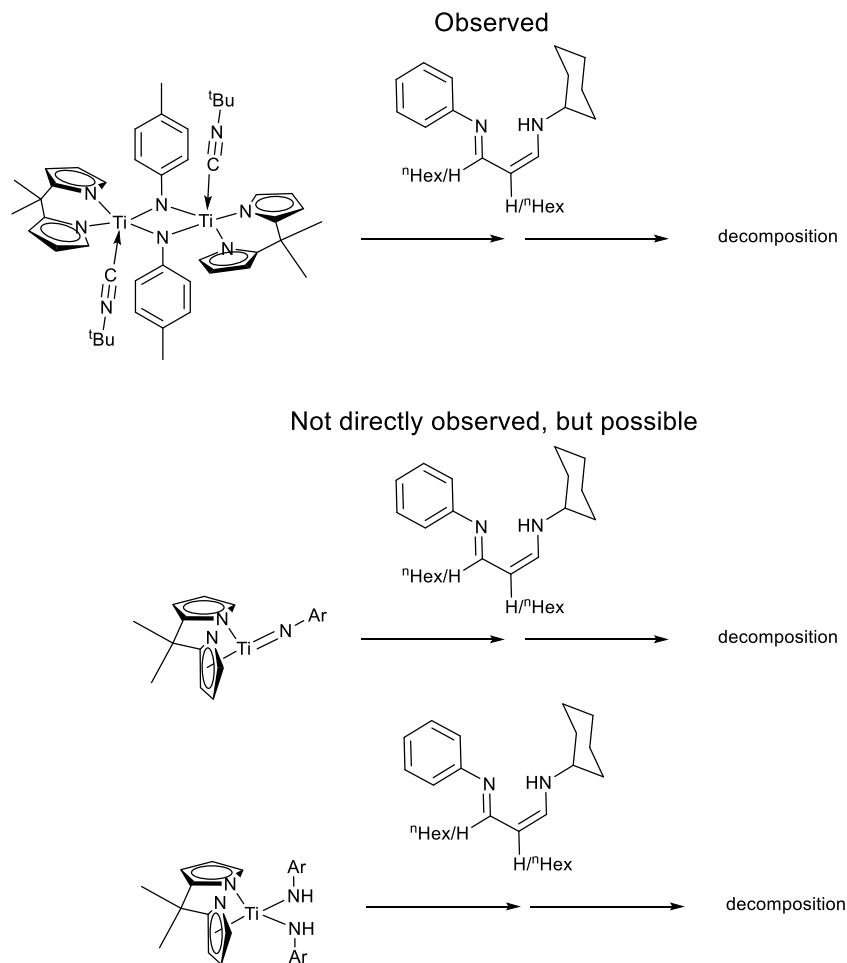


Figure 6.7 Various titanium species found to (or suspected of) react directly with the iminoamination product. This reactivity provides plausible means of titanium complex deactivation throughout the iminoamination reaction.

6.4 Modification of the Bis-Chelating Ancillary Ligand

With the information gleaned from kinetic studies (Sections 6.2 and 6.3), we suspected that a modification to the ancillary ligand could be beneficial for several reasons. One of these reasons relates to catalyst stability. As discussed in the previous sections, the $\text{Ti}(\text{dpm})(\text{NMe}_2)_2$ catalyst reacts with the iminoamination product, and potentially other species in the reaction mixture, leading to deactivation of the titanium catalyst. We thought that a more donating ancillary ligand with a lower pK_a might be less susceptible to substitution or protonation by other species in the reaction mixture.

We also reasoned that, regardless of the slow step of the reaction sequence, shown above in Fig. 6.5, Ti species other than the active catalyst exist in solution. Namely, there is the dimeric Ti-species and the Ti(Bis(amide)), which are both off-cycle species that reduce the amount of catalytically active metal in solution. Moving to an ancillary ligand that is more electron-rich should serve to push equilibria with the off-cycle species (where the Lewis acidic Ti, picks up other ligands in solution to increase its electron density) toward the catalytically active terminal imido complex, resulting in faster rates of iminoamination.

To that end, we considered some of the other precatalysts that had been examined by the group previously for other applications. One bischelating ancillary ligand that seemed promising, which performed poorly as a hydroamination catalyst due to its strong donor ability and steric bulk, was 2,2'-methylenebis(6-*tert*-butyl-4-methylphenoxide) (OArCH₂ArO).⁴ A “normal” scale iminoamination experiment (1 mmol H₂NPh/1.5 mmol ^tBuNC/ 1.5 mmol 1-octyne, 2 mL toluene, 5 mol% catalyst (0.025 M)) was performed using Ti(OArCH₂ArO)(NMe₂)₂. GC analysis of the crude reaction mixture revealed 72% yield of the 3CC products, 10% yield of hydroamination, with the remainder going to the 2,3-diaminopyrrole (4CC). While this result shows a substantial amount of byproduct, it more importantly shows consumption of the limiting reagent. Thus, despite the generation of some side products, this catalyst demonstrates higher relative activity, as no leftover H₂NPh is observed in the reaction solution.

Running the reaction again under the significantly more dilute conditions for Entry 3 in Table 6.1 (0.2 M in each reagent, 0.01M Ti(dpm)(NMe₂)₂), and monitoring reaction progress by GC, a very similar reaction trace was noted for the Ti(OArCH₂ArO)(NMe₂)₂ catalyst relative to Ti(dpm)(NMe₂)₂, with the yield maxing out at about 60%. Overall, the rates are very similar, too (see experimental). This suggests that the Ti-catalyst is still suffering from deactivation, regardless

of what we predicted would be a more stable ancillary ligand in the presence of the iminoamination product among other acidic protic species.

One additional benefit of the (-OArCH₂ArO-) ligand, over dpm, is that it has readily identified NMR signals in an uncrowded region of the NMR spectrum. The bisphenoxide ligand, when bound to 4-coordinate Ti, results in distinct ¹H NMR shifts for the two hydrogens on the -CH₂- linker. The chelate forms an 8-membered ring with the metal, such that two unique environments are created for the two protons (diastereotopic). This is shown in the figure below (Fig. 6.8).^{18, 19}

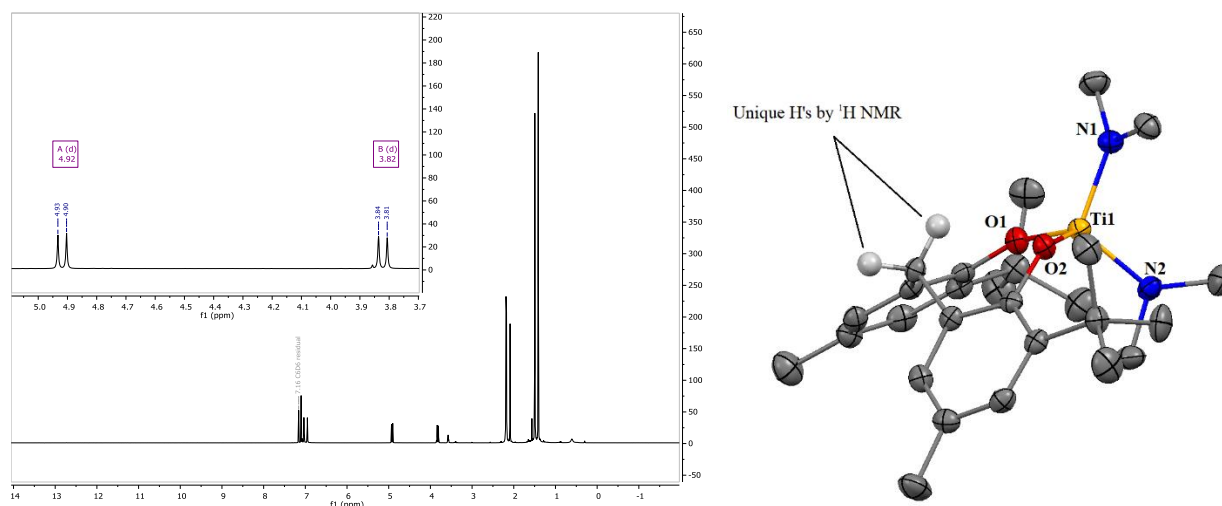
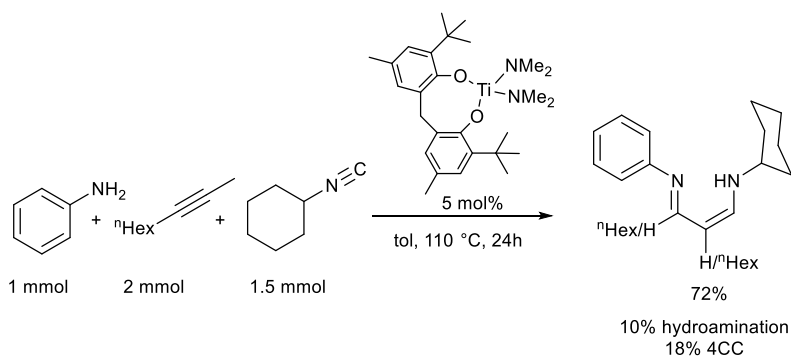


Figure 6.8 (*left*) ¹H NMR spectrum and (*right*) single crystal X-ray structure⁴ of Ti(NMe₂)₂(OArCH₂ArO). The two protons on the methylene linker have unique positions due to the conformation of the 8-membered ring formed by the ligand with Ti, which is readily observed by the distinct doublets in the ¹H NMR spectrum. This trait applies to all of the complexes of the general form Ti(X)₂(OArCH₂ArO) and makes them easy to observe and distinguish between by ¹H NMR.

Taking advantage of these inherent ligand properties, an NMR scale iminoamination reaction using 20 mol% Ti(OArCH₂ArO)(NMe₂)₂ was examined in tol-d₈, to try to directly determine the fate of the catalyst in solution. Unlike in the Ti(dpm)(NMe₂)₂, where free H₂dpm ligand is observed in solution after heating the catalysts with 3CC and isonitrile, with Ti(OArCH₂ArO)(NMe₂)₂ no dissociated or free chelating ligand is observed in the reaction mixture. Rather, after 16 h of heating, 45% yield of the iminoamination product was observed,

along with 10 mol% of $\text{Ti}(\text{OArCH}_2\text{ArO})_2$ (i.e. $\frac{1}{2}$ of the original Ti added to the solution). The other 10 mol% of the catalyst could not be directly identified but presumably has picked up a variety of N-bound ligand species in solution from the reactants and products of the catalysis (See Experimental).

This observation demonstrates two consequences of switching from the (dpm) to the (OArCH₂ArO) ligand: 1) while the ligand is stable with respect to maintaining coordination to Ti (as opposed to dissociation to the free ligand) the properties of the ligand have also opened up disproportionation pathways, and 2) with full catalyst deactivation observed on the order of 16 h of reaction time, the enhanced reactivity of this catalyst in the normal scale reaction is even more impressive in terms of the rate of the reaction when the catalyst is still active. The latter observation really suggests that further ligand modification could result in a much faster catalyst, provided the stability issues with the catalyst can be overcome.



Scheme 6.6 Iminoamination reaction catalyzed by $\text{Ti}(\text{OArCH}_2\text{ArO})(\text{NMe}_2)_2$ following standard reaction conditions.

These experiments support our kinetically-derived hypothesis that more electron-rich bischelating ancillary ligands can potentially improve the performance of homogeneous Ti(IV) iminoamination catalysts. However, the marked difference in the means of catalyst deactivation upon transitioning from the dpm to (OArCH₂ArO) bischelating ancillary ligand raised several additional questions with regards to ligand design. Is disproportionation a decomposition pathway

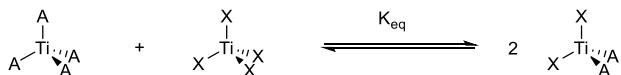
that is related to the electronics of the ligand? If this phenomenon is general, can we predict what ligands will be susceptible to these decomposition pathways? Are there other ligand design strategies that can prevent these ligand-exchange reactions from compromising the catalysts while maintaining catalyst stability toward the reaction products? In order to effectively search for promising ancillary ligand candidates to improve the iminoamination reaction, we need answers to some of these questions.

6.5 Predicting What Ligands Lead to Stable Catalysts Versus Disproportionation

Considering the precedence in the literature and our own experiences with Ti(IV) species, the results described in the previous section were not surprising. Ti(IV) complexes have been noted, with a variety of different X^- ligands, to undergo ligand dis- and comproportionation reactions. For example, mixing $Ti(NMe_2)_4$ with $TiCl_4$ in equal proportions results in quantitative generation of the heteroleptic $Ti(NMe_2)_2Cl_2$ species in minutes at room temperature.²⁰ Likewise, these comproportionation reactions can even facilitate formation of the heteroleptic complexes with chelating bis(amide) ligands and $TiCl_4$,²¹ the same observation can be made with $Ti(OR)_4$ and TiX_4 ($R = Cy$ or iPr , $X = Cl$ or Br), and can even be utilized as a synthetic methodology to yield heteroleptic species of the general form $Ti(A)_{4-n}(X)_n$.²²⁻²⁴ Another example which highlights the same phenomenon if the mixed ligand, heteroleptic compound being preferred, is $Ti(dpm)(NMe_2)_2$. We note that no ligand disproportionation occurs to produce the homoleptic species, even when the compound is heated in C_6D_6 for several weeks at 85 °C (Scheme 6.7 summarizes these ligand exchange processes).

Ultimately, understanding these ligand processes is critical to improving our ability to select and design better ancillary ligands for both improvements in catalyst rate and stability. While these processes have been observed and acknowledged for decades, and early transition metal

chemists are all too familiar with these complications in synthesizing complexes, no systematic study to show correlation or causation has been undertaken.^{25, 26}



Scheme 6.7 General equilibria observed for several Ti(IV) complexes that have been noted in the literature and through our observations.

Table 6.3 The ligand combinations listed in the table above, the heteroleptic Ti(X)₂A₂ complexes are noted quantitatively. This necessitates that K_{eq} is very large.

Ligand Sets where K _{eq} >> 1,000		LDP (kcal/mol)	
A ⁻	X ⁻	NMe ₂	9.34
NMe ₂	Cl	O ⁱ Pr	10.56
O ⁱ Pr	Cl	Cl	14.97
OCy	Cl	Br	15.45
O ⁱ Pr	Br	Pyr (dpm)	13.64
NMe ₂	dpm	OCy	-

With these motivations in mind, we set out to determine what ligand properties lead to ligand exchanges in the Ti(IV) complexes of interest. Looking at the complexes mentioned above, we noticed a common theme among the ligand combinations that demonstrate rapid comproportionation to produce exclusively the heteroleptic Ti(X)₂(A)₂ complexes. With Ti(NMe₂)₄ and TiCl₄, for instance, the NMe₂ and Cl ligands have very different donor abilities with LDP values of 9.34 and 14.97 kcal/mol respectively.^{5, 27} With these highly different ligands bound to each Ti(IV) species, the ligands rapidly exchange to form the Ti(NMe₂)₂Cl₂ complex, where each Ti has two electron rich NMe₂ ligands and two electron-poor Cl ligands. This results in Ti centers with the same electron density than existed in the two individual starting materials.

Again, approaching this problem from the other direction, we can consider Ti(dpm)(NMe₂)₂. Each half of the dpm chelate donates similar electron density to a pyrrole ligand, which has an LDP value of 13.64 kcal/mol (bound η₁ to Cr), while again, the NMe₂ ligands have an LDP value of 9.34 kcal/mol. This is still a very large difference in donor abilities between the

X^- and A^- ligands in the Ti complex, and so the species does not demonstrate any reversion to the $Ti(dpm)_2$ or $Ti(NMe_2)_4$ parent homoleptic complexes, which would relegate the two Ti centers to experience highly discrepant electronic environments. Thus, in reactions utilizing $Ti(dpm)(NMe_2)_2$ as precatalyst, no disproportionation to make $Ti(N)_4$ and $Ti(dpm)_2$ has been observed (N = any nitrogen-bound ligand in reaction mixture).

A tendency for metal complexes to undergo these ligand exchange process to produce more equivalent electronic environments at any given metal atom in an entire system may have a very simple thermodynamic explanation. Ionic bonds are stronger than covalent bonds. In a system like $TiCl_4$ and $Ti(NMe_2)_4$ the Ti should form more ionic bonds with the more electronegative Cl ligands. However, as the effective oxidation state or charge of Ti is increased, the Ti becomes more electronegative, and the ionicity of the bonds is reduced. By contrast, the Ti in $Ti(NMe_2)_4$, where the ligands are relatively donating, should exhibit a lower effective oxidation state. By mixing the two ligand types and producing $Ti(NMe_2)_2Cl_2$ the overall bond enthalpies could then be maximized, as the Ti–Cl bonds in the heteroleptic species maintain a higher degree of ionicity. This is one simple explanation for why the heteroleptic species may be favored over the homoleptic ones when the ligand donor abilities are so discrepant. With other ligands, we could invoke overlap discrepancies, Lewis acidity, etc.

If we consider the available donors to occupy the two protolytically exchangeable coordination sites to Ti in the iminoamination reaction mixture with the $Ti(OArCH_2ArO)(NMe_2)_2$ precatalyst, we can imagine that the donor abilities of the N-donors in solution are comparable to the bis(phenoxide). The NMe_2 sites will exchange with NHPH (anilide) ligands, bridging imides (μ -NPh), or even the iminoamination product (with donor properties presumably somewhere between an amine and an amide). The donor ability of an electron-rich phenol is much closer to

that of an anilide or nacnac-type interaction than the comparisons above (i.e. dpm or Cl^-), where ΔLDP was on the order of 4 or more kcal/mol.

Specifically, a typical phenol LDP value is 11.8-12 kcal/mol, while anilides are typically around 10 kcal/mol. Something like the iminoamination product, if considered independent of sterics, could demonstrate a similar LDP value to an anilide ligand (likely higher due to resonance delocalization). In fact, it seems reasonable that the electronic donor ability would be similar to that of phenoxide. With these similar donor abilities, disproportionation is observed, rapidly generating the homoleptic complexes from initial heteroleptic Ti(IV) species. Thus, when the donor abilities of X^- and A^- ligands available for Ti are similar, it seems like there is no clear driving force for formation of the heteroleptic complex exclusively, and rather a mixture of the homoleptic complexes, the heteroleptic complex, or species somewhere in between, can easily be formed.

These observations are consistent with work performed in the group by Dhvani Kansal. In Dhvani's studies, she examined the equilibrium distribution of tetra(aryloxide)Ti(IV) species with the $\text{Ti}(\text{OArCH}_2\text{ArO})_2$ di(bischelate) complex in solution. This scenario is outlined in Fig. 6.9, below. As mentioned above, we suspected that the equilibrium constants for these ligand redistribution reactions are related to the difference in the donor abilities of the two different ligands. By experimentally determining the K_{eq} values for different X^- ligands with the $(\text{OArCH}_2\text{ArO})$ bischelating ligand and comparing these values to the differences in the LDP values between the chelate and the variable ligand, X^- , we hoped that a correlation could be established. Establishing this sort of relationship, between donor abilities of the ligands and the tendency of a compound to undergo ligand redistribution reactions, would facilitate more educated ancillary ligand selection for Ti(IV) catalysts.

The ligand sets used for these initial studies were carefully matched, as use of a bischelate in combination with a given TiX_4 species means that only 3 different Ti complexes are possible in solution, provided bridging interactions are not observed with the chelate. These complexes are TiX_4 , $\text{Ti}(\text{OArCH}_2\text{ArO})_2$, and $\text{Ti}(\text{OArCH}_2\text{ArO})\text{X}_2$. Also a careful consideration in these systems is the steric protection applied to the aryloxy ligands; when aryloxy or alkoxide ligands are put on Ti, bridging interactions often occur which lead to multinuclear Ti species (i.e. dimers and oligomers). The inclusion of a *tert*-butyl group in the 2-position of the aryloxides ensures that the complexes are monomeric. Keeping the substitution of the aryloxy ligand constant in the 2 and 6 positions of the ring also makes these ligands isosteric. Thus, any changes observed in the equilibrium behavior of the aryloxy ligands can be assigned purely to electronic differences. Additionally, since the determinations of K_{eq} were carried out using ^1H NMR spectroscopy to probe the concentrations of each species in solution, the benefits of the $(\text{OArCH}_2\text{ArO})$ species, described above, were highly useful in quantification of each species.

Dhwani had examined the equilibrium constants for comproportionation (Fig. 6.10) with the tetra(*2-tert*-butyl-4-R-phenoxy)Ti(IV) complexes where $\text{R} = \text{CF}_3, \text{H}, \text{Me}, \text{and Br}$. Her preliminary results showed that, with these similar A^- (OArCH_2ArO) and X^- (*2-tert*-butyl-4-R-phenoxy) ligands (in terms of their donor abilities) all 3 species (Fig. 6.9) coexist in solution, in relatively similar concentrations. This indicates that when the A^- and X^- ligands have similar donor abilities, there is no significant driving force to favor the heteroleptic species, and so a mixture of products is observed. Her results also suggested that as the differences in the donor abilities of the aryloxy and the chelating $(\text{OArCH}_2\text{ArO})$ were enhanced (i.e. *2-tert*-butyl-4- CF_3 -phenol = aryloxy), the equilibrium shifted toward the heteroleptic complex. Unfortunately, Dhwani was not able to finish these studies prior to leaving the group. As the applications of these studies had

become highly relevant to the targeted iminoamination catalyst systems, we decided to expand and finish the studies that Dhvani had begun examining.

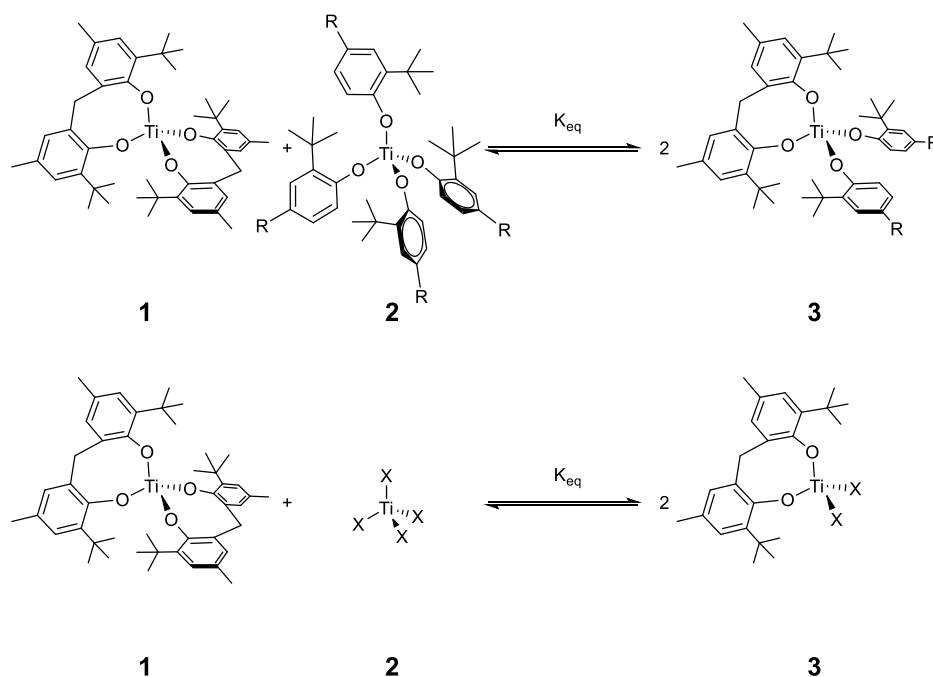


Figure 6.9 The comproportionation reaction monitored by determination of the equilibrium constant K_{eq} . The 3 possible Ti species in equilibrium in these solutions are shown, including both starting materials and the only possible product.

We reexamined the values, for $R = H, Br, Me,$ and CF_3 finding similar K_{eq} values to Dhvani's original values, and expanded the complexes examined to include $R = F, ^tBu,$ and OMe . Additional ligands with dramatically different electronic and steric properties were also pursued, specifically, with $X = NMe_2, O^iPr, I,$ and Cl . With these values for K_{eq} established, we approached building a model. Several possible relationships between the donor ability (LDP), the size (% V_{bur}), and the observed K_{eq} value were considered. Strong graphical evidence suggested that a dependence on the electronic difference between the bischelate and the X^- ligand was second order, given the general parabolic appearance of the plot shown in Fig. 6.10. The values used to perform the data modeling are listed in Table 6.4.

The correlation between K_{eq} and ΔLDP , $(\Delta LDP)^2$, $\Delta(\%V_{bur})$, and $(\Delta(\%V_{bur}))^2$ was evaluated by fitting equations of the general form shown below, in Eq. 6.2, with a least squares approach. Goodness of fit was evaluated by examining plots of the model-predicted vs. the experimental K_{eq} values. Perfect agreement between these two sets of values would be represented by $R^2 = 1$ and a linear equation of $y = x$, so the closer the plot of model-predicted vs. experimental K_{eq} gets to these qualifications, the better the model.

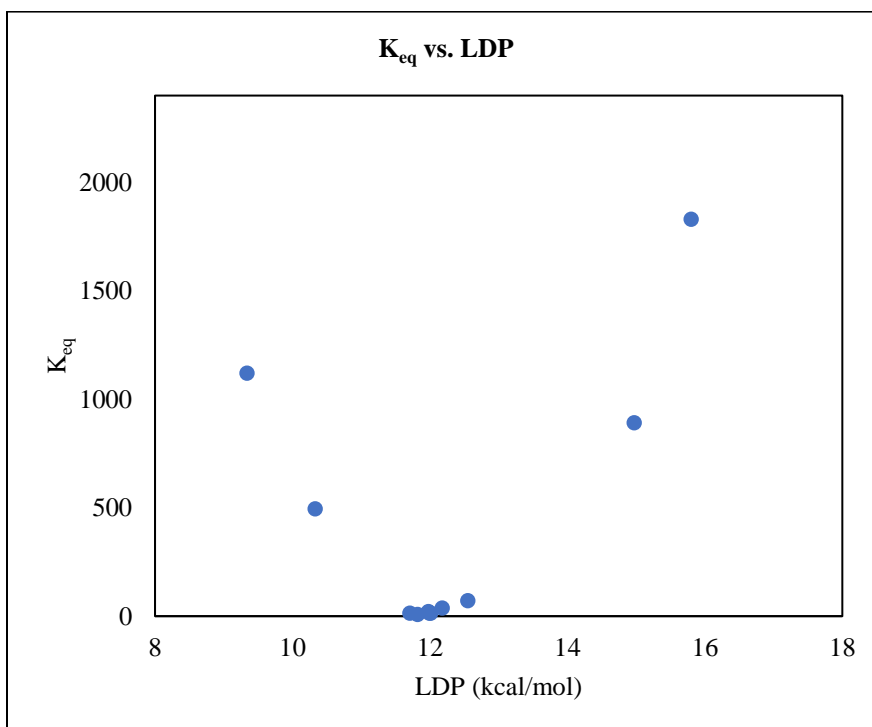


Figure 6.10 Plot of K_{eq} vs. LDP of the X^- ligands in the $Ti(OArCH_2ArO)(X)_2$.

$$K_{eq} = a + b(\Delta LDP) + c(\Delta LDP)^2 + d(\Delta\%V_{bur}) + e(\Delta\%V_{bur})^2 \quad (\text{Eq. 6.2})$$

To establish the impact of each term in Eq. 6.2, several iterations of the least squares fit, were performed. In turns, coefficients c , d , and e were each set to zero, and the least squares fit reapplied (see Experimental for more details). Primarily, these modeling exercises highlight several important aspects of the relationship between K_{eq} and the steric and electronic properties of the X^- ligands.

First, the K_{eq} value is essentially independent of sterics, with the fitted coefficients for $\Delta\%V_{bur}$ or $(\Delta\%V_{bur})^2$ weighted very small in magnitude relative to a , b , and c . Note, when every variable in Eq. 6.2 is included in the fit, the data appears to be “overfitted” as the coefficients no longer make chemical sense and several negative K_{eq} values are calculated. Thus, the coefficients for d and e were fitted independently in turns. Essentially the same quality fit was obtained when either $(\Delta\%V_{bur})$ or $(\Delta\%V_{bur})^2$ were used as the steric parameter; both provided an approximately 0.002 improvement in R^2 , which is over 0.99 with just electronic effects modeled. Collectively these observations suggest that sterics do not have a measurable effect on K_{eq} , and the minute improvement in R^2 observed is simply due to adding another parameter to the least squares fit. In a system with a larger, more rigid bischelating ancillary ligand, or with a dramatic increase in the sizes of the X^- ligands under study, steric influence could reasonably affect the K_{eq} observed. With the ligand selection under study, however, only about 85% of the first coordination sphere is occupied by ligands in any given Ti(IV) complex and the size range spans only a 5% range in $\%V_{bur}$.

Table 6.4 Values used to model the relationship of sterics and electronics to the equilibrium constant for the interconversion of the homoleptic and heteroleptic.

$Ti(OArCH_2ArO)_X_2$		LDP	ΔLDP	$(\Delta LDP)^2$	$\%V_{bur}$	$\Delta\%V_{bur}$	$(\Delta\%V_{bur})^2$	K_{eq} exp.	Error	K_{eq} modeled
X	NMe ₂	9.34	-2.52	6.35	21.9	0.7	0.49	1120	118	1133
	OiPr	10.33	-1.53	2.34	17.4	-3.8	14.44	495	80	491
	I	15.8	3.94	15.52	19.2	-2	4	1830	190	1742
	Cl	14.97	3.11	9.67	16.8	-4.4	19.36	898	179	1029
2-tert-butyl-4-R-phenoxide	tBu	12.01	0.15	0.022	21.4	0.2	0.04	14	4	10
	H	11.98	0.12	0.014	21.7	0.5	0.25	21	5	12
	Me	11.82	-0.04	0.0016	21.2	0	0	8	4	26
	Br	12.18	0.32	0.102	21.3	0.1	0.01	38	6	4
	F	11.99	0.13	0.016	21.9	0.7	0.49	14	4	11
	OMe	11.71	-0.15	0.022	21.6	0.4	0.16	14	3	40
CF ₃	12.55	0.69	0.4761	21.2	0	0	71	11	19	

In fact, when both d and e are set equal to zero we obtained the following fit, dependent exclusively on electronic properties of the X ligand:

$$K_{eq} = 22.0 - 98.6(\Delta LDP) + 136(\Delta LDP)^2 \quad (\text{Eq. 6.3})$$

This fit is plotted with the experimental data in Fig. 6.12, as well as the model-determined values for K_{eq} . If we scale the variables fitted in this equation, we can determine the relative magnitudes of the two coefficients despite the dramatically different ranges for the parameters, ΔLDP and ΔLDP^2 . This indicates the importance of the two terms in determining the K_{eq} . The scaled coefficients are presented in Eq. 6.4.

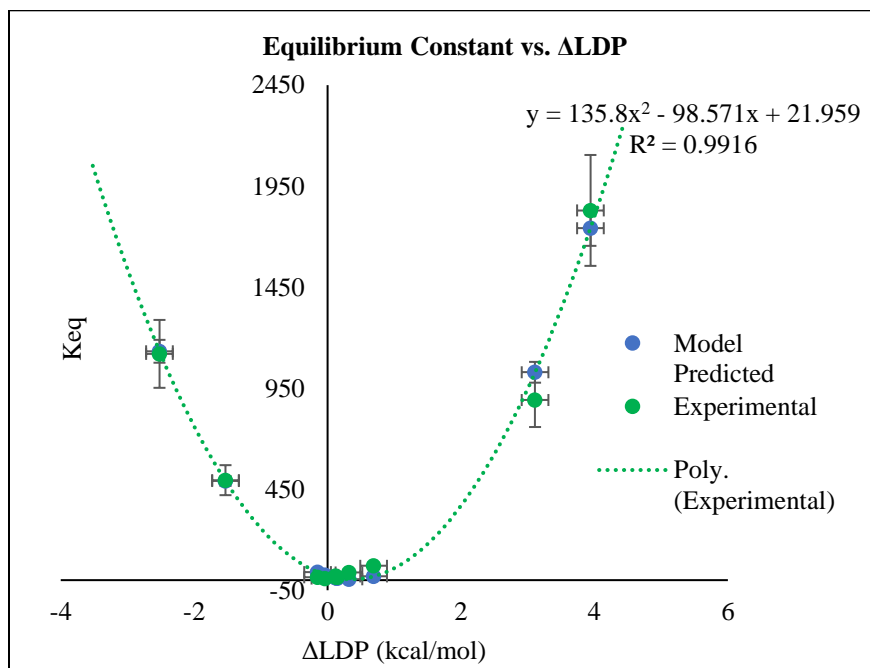


Figure 6.11 A plot showing model-predicted versus experimental data relating the donor ability of a given X^- ligand to the equilibrium constant observed for formation of the heteroleptic species, $Ti(X)_2(OArCH_2ArO)$ (Fig. 6.15).

$$K_{eq} = 1006 - 318(\Delta LDP) + 1054(\Delta LDP)^2 \quad (\text{Eq. 6.4})$$

From the scaled coefficients, we can see that the coefficient of the squared term is much larger in magnitude than the linear term for ΔLDP . This will further exaggerate the nature of the second-order polynomial equation, with the squared term dominating the K_{eq} when ΔLDP is large

and the linear term dominating K_{eq} when ΔLDP is small, i.e. at the vertex where the aryloxy ligands are observed. Based on this model, when the absolute value of ΔLDP is > 0.30 kcal/mol, the second order term exceeds the magnitude of the linear term and will begin to dominate the electronic effects on K_{eq} .

We think that, in theory, this general relationship applies to the equilibrium process of ligand disproportionation with any metal, but that the coefficients for these electronic terms are perhaps characteristics of the metal. With metals that don't typically exhibit disproportionation and comproportionation processes the coefficients modifying the effects of ΔLDP and $(\Delta LDP)^2$ would then be very large (approaching ∞), whereas with other metals that demonstrate similar disproportionation and comproportionation properties to Ti(IV), i.e. high valent U, Zr, or Hf, the general form of Eq. 2 with similar coefficients to those found with Ti(IV) may effectively describe the ligand exchange processes. In this way, we think the correlations discovered here with Ti are likely observed with other metals, as well, and demonstrate the fundamental properties that control these ligand exchange processes. This realization is interesting, and further studies examining these relationships in other metal systems are a continuing interest in the group.

For the iminoamination reaction under study—and the applications of this study to catalyst development—the relationships shown by the model suggest that there is a minimum difference in donor ability for the ancillary ligand and the species that occupy the protolytically exchangeable sites on Ti(IV) during the iminoamination reaction which will maintain catalyst stability in regards to ligand processes. Relative to the (OArCH₂ArO) ligand, we should select a ligand that is less electron rich. Considering the model, something that is > 0.3 kcal/mol higher or lower than the LDP value of the chelated iminoamination product would perhaps offer the greater donor ability sought to increase the proportion of the active Ti-imide species while preventing the ligand

exchange deactivation pathway. Alternatively, something substantially *more* donating may also improve results. For example, a chelating bis(amide) ligand with a high degree of conjugation to reduce basicity, that is sterically protected, may provide the same benefits but with an even faster rate of iminoamination (again via enhanced donor ability facilitating generation of the active species or faster product protonation). These results provide a direction for future ligand-screening progress. Some candidate ligands of interest are shown in Fig. 6.12, below.

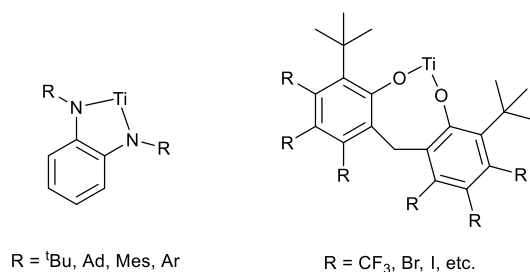


Figure 6.12 Potential ligands of interest that could avoid deactivation via ligand disproportionation as their donor abilities (LDP values) are predicted to be more and less donating than a chelated iminoamination product, potentially disfavoring ligand exchange reactions.

6.6 Conclusions

Obviously, a simple clean rate law with simple first-order dependences are easier to understand and implement than those with complex reaction orders, like the one we have uncovered that describes the process of homogeneous titanium-catalyzed iminoamination. Despite the fractional order in aniline, potentially fractional order in catalyst, the decomposition caused by product, and the conversion-limiting deactivation processes observed throughout kinetic trials, the experimental results from these studies have been highly informative. Because of the complicated rate law, we saw improving catalyst stability and minimizing the potential contribution of catalyst resting states, which persist due to the electron deficiency of the titanium metal center, as the most viable options for improving catalyst performance. Promising results have been observed by pursuing a very easy ancillary ligand switch, indicating the merits of this approach in improving

the practical application of these catalysts to iminoamination as a first step in the production of several functionalized heterocycles.

The observations made with the new catalyst, $\text{Ti}(\text{OArCH}_2\text{ArO})(\text{NMe}_2)_2$, forced us to consider the aspects of ligand properties and design that might lead to the most stable catalysts for this reaction in solution. Systematically approaching the characterization of catalyst stability via ligand exchange reactions correlated to donor ability has allowed for the development of a model system. This model can now guide subsequent adjustments to the ancillary ligands selected to perform the iminoamination reaction. Afterall, in these systems, the primary motivator for achieving a faster rate is to achieve a higher yield. However, if we make a more stable catalyst, higher yields can be achieved regardless of the rate relative to our existing catalyst systems. While shorter reaction times are one of the ultimate goals for targeted catalyst design for iminoamination, a 1-pot-2-step reaction that take 2 days to yield a complex heterocycle is still faster than traditional organic methodology that might take 10 steps to generate the same heterocycle.

6.7 Experimental

General Considerations

Synthesis Considerations

All syntheses and handling of materials were carried out under an inert N_2 atmosphere, either in an MBraun glovebox or by standard Schlenk technique unless otherwise specified. Generally, this includes reaction set-up for catalytic reactions and the preparation of the Ti species, as well as preparations of NMR samples that contain Ti complexes. Column chromatography, GC sample preparation, and the characterization of organic products were performed in air, on the benchtop with solvents handled and stored in air.

Solvents including toluene, diethyl ether, and pentanes, were purchased commercially. These solvents were dried and deoxygenated by sparging with N₂ and passage over an activated alumina column before use. The NMR solvent CDCl₃ was purchased from Sigma-Aldrich and used as received (for routine organic compound characterization) or dried over P₂O₅ and distilled under N₂ prior to use (for titanium complexes). The NMR solvent C₆D₆ was purchased from Sigma-Aldrich and dried over CaH₂; it was then distilled under N₂ prior to use.

All alkynes were purchased commercially (Alfa Aesar) and dried over Na₂SO₄ and distilled under N₂ prior to use. Aniline (and any derivatives) was dried over CaH₂ and distilled under vacuum prior to use. *Tert*-butyl isonitrile (^tBuNC) was prepared according to literature procedures.²⁸ Dodecane was sparged with N₂ prior to use. Materials used for column chromatography, including hexanes, diethyl ether, and triethylamine (TEA), were purchased commercially and used as received. The Ti(dpm)(NMe₂)₂ complex was prepared as previously reported and matched literature ¹H and ¹³C NMR.²

Instrumentation

NMR Routine characterization spectra were obtained using an Agilent DDR2 500 MHz NMR spectrometer equipped with a 5 mm PFG OneProbe operating at 499.84 MHz (¹H) and 125.73 MHz (¹³C). ¹H NMR chemical shifts were referenced to residual CHCl₃ in CDCl₃ as 7.26 ppm, or residual C₆HD₅ in C₆D₆ as 7.16 ppm. ¹³C NMR chemical shifts are reported relative to ¹³CDCl₃ as 77.16 ppm, or (¹³C)C₅D₆ as 128.06 ppm.

The Varian Dbppste_cc (DOSY bipolar pulse pair simulated spin echo convection corrected) pulse sequence was utilized for all experiments where DOSY NMR was used. All spectra were multiplied by a weighted exponential of 10 Hz and baseline corrected before applying DOSY processing. Standard DOSY processing, as supplied by the vendor, was used based on peak

heights and with compensation for non-uniform gradients. For notes on NMR-based determination of K_{eq} , see below.

GC GCMS data was collected on an Agilent 5973 MSD with a 6890N series GC. GCFID data was collected on a Hewlett Packard 6890 series GC system and standardized against dodecane as an internal standard. 3CC products were quantified *in situ* by utilizing GCFID standardized calibration curves generated by quantification of the authentic iminoamination product, isolated from a catalytic reaction mixture. Full characterization data is given below. The hydroamination side product was quantified in a similar manner from previously isolated amine derivatives of the genuine imine product (see Chpt 4). The 4CC product was quantified analogously to the 3CC product.

X-ray All single crystal X-ray structures were collected at the MSU Center for Crystallographic Research. The data was collected on Bruker diffractometers running Cu-K α radiation. The collection data and information about the unit cell, etc. for these structures is provided below.

Synthesis of Iminoamination Product from aniline, 1-octyne, and ^tBuNC:

A 15 mL pressure tube was charged with 62 mg of Ti(dpm)(NMe₂)₂, 1 mL of toluene, and a stir bar. To the stirred solution was added a 1 mL solution containing 186 mg of aniline (2 mmol, 1 equiv) in toluene. This mixture was stirred for 10 min at room temperature over which time the solution went from a transparent bright orange color to an opaque reddish-brown. Then a 1 mL solution containing 184 mg of ^tBuNC (2 mmol, 1 equiv), and 220 mg of 1-octyne (2 mmol, 1 equiv) in toluene, was added to the solution in the pressure tube. The tube was sealed and transferred from the glovebox to a 110 °C oil bath. The tube was heated and stirred for 24 h. The

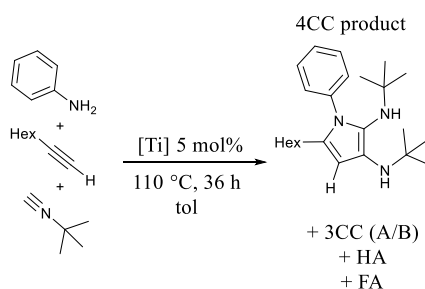
tube was removed from the bath and allowed to cool ambiently. The volatiles were removed by rotary evaporation, and the resulting crude, dark brown oil was separated by column chromatography (Al₂O₃, Hexanes(1% TEA), gradient Et₂O from 0 to 25%). The isolated product was obtained as an orange oil (310 mg, 54%), which proved to be a mixture of regioisomers A and B, shown above. Standard column conditions could not be found that effectively separate the two regioisomers.

¹H NMR (500 MHz, chloroform-*d*) (**A**) 9.97 (s, 1H), 4.72 (d, *J* = 8.0 Hz, 1H), 1.27 (s, 9H), 0.90 (m, 3H); (**B**) 10.83 (s, 1H), 7.77 (d, *J* = 2.8 Hz, 1H), 7.11 (d, *J* = 2.8 Hz, 1H), 1.32 (s, 9H), 0.84 (t, 3H); (**A/B**) 7.33 – 7.26 (m, 4H), 7.04 (d, *J* = 7.7 Hz, 2H), 7.03 – 6.97 (m, 1H), 6.85 – 6.78 (m, 3H), 2.37 (s, 1H), 2.22 – 2.09 (m, 3H), 1.48 (m, 5H), 1.18 (m, 8H). ¹³C NMR (126 MHz, chloroform-*d*) 171.01, 153.80, 151.55, 150.11, 146.87, 142.28, 129.06, 128.43, 122.66, 121.83, 121.38, 119.00, 103.60, 91.79, 52.60, 51.03, 33.68, 33.21, 32.91, 31.93, 31.80, 31.46, 30.36 (d, *J* = 1.9 Hz), 30.31, 29.47, 29.32, 28.74, 28.67, 27.73, 23.69, 22.72, 22.47, 14.15, 14.05. HRMS: QTOF EI (positive ion) calc'd for C₁₉H₃₁N₂: 287.2487; found: 287.2484. EA calc'd for C₁₉H₃₀N₂: C, 79.66; H, 10.56; N, 9.78. Found: C, 79.88; H, 10.44; N, 9.44.

Synthesis of 2,3-diaminopyrrole from aniline, 1-octyne, and 2^tBuNC:

On several occasions, the product mass that corresponds to the coupling of 1 equiv aniline, 1 equiv alkyne, and 2 equiv of isonitrile was observed by GC/MS in reactions catalyzed by homogeneous Ti-catalysts. Typically, the amount of this product was relatively small. However, under certain conditions when reactions were carried out on large enough scales, substantial masses of the 4CC product were noted in various column fractions when isolating the 3CC products by column chromatography.

On one such occasion, a very clean fraction of the 4CC product was isolated from a 2 mmol scale reaction (H_2NPh , $t\text{BuNC}$, 1-octyne) with 5 mol% $\text{Ti}(\text{dpm})(\text{NMe}_2)_2$ as precatalyst. The 4CC product was the first compound eluted from an alumina column, basified with 2% TEA in Hexane. Note from the same column, the 3CC product was also isolated, but as a later fraction with the addition of Et_2O on a gradient from 0-30%. The 4CC product was characterized by GCMS, HRMS, ^1H NMR, ^{13}C NMR, and a few additional 2D NMR techniques. The following structural assignment seems to most closely match the characterization data for this product, in agreement with previous studies by our group.³



Scheme 6.8 Production of 4CC product from iminoamination reaction mixture.

^1H NMR (500 MHz, benzene- d_6) 7.43 (d, $J = 7.1$ Hz, 2H), 7.13 (t, $J = 7.8$ Hz, 2H), 6.97 (t, $J = 7.5$ Hz, 1H), 6.53 (t, $J = 0.9$ Hz, 1H), 2.99 (s, 1H), 2.68 – 2.54 (m, 2H), 2.34 (s, 1H), 1.75 (pentet, $J = 7.7$ Hz, 2H), 1.52 – 1.42 (m, 3H), 1.40 – 1.29 (m, 06H), 1.23 (s, 12H), 0.92 (s, 15H). ^{13}C NMR (126 MHz, benzene- d_6) 142.18, 128.80, 125.41, 125.16, 123.74, 122.06, 121.84, 113.63, 55.46, 54.53, 32.33, 30.66, 30.60, 30.54, 30.07, 26.37, 23.16, 14.41. HRMS: QTOF EI (positive ion) calc'd for $\text{C}_{24}\text{H}_{40}\text{N}_3^+$: 370.3222; found: 370.3218. EA calc'd for $\text{C}_{24}\text{H}_{39}\text{N}_3$: C, 77.99; H, 10.69; N, 11.37. Found: C, 78.09; H, 10.85; N, 11.11.

Synthesis of $[\text{Ti}(\mu\text{-Ntoly})_2(\text{dpm})_2]$: A solution of 50 mg of $\text{Ti}(\text{dpm})(\text{NMe}_2)_2$ (1 equiv) in 1.5 mL of C_6D_6 was prepared and stirred at room temperature. To this solution was added a solution of 34 mg (2 equiv) H_2Ntoly in 0.5 mL of C_6D_6 . The resulting solution immediately began to

darken from light yellow to dark brown. The solution was stirred for 10 minutes at room temperature and was then examined by ^1H NMR. The spectrum shows that one equivalent of H_2NtolyI has reacted with the $\text{Ti}(\text{dpm})(\text{NMe}_2)_2$ while one equivalent remains free in solution. The peak shifts and integral values for the new species approximately matches the formula which contains $[\text{Ti}(\text{dpm})(\text{NtolyI})]$ in those ratios. There is fluxionality with the Ti complex at room temperature, evidenced by the broadness of the peaks for the new species in the ^1H NMR. X-ray quality crystals were grown from a concentrated toluene solution layered with n-hexane and stored at $-35\text{ }^\circ\text{C}$ for 24 h. The compound can also be purified by precipitation from a concentrated $\text{Et}_2\text{O}/\text{n-hexane}$ solution stored at $-35\text{ }^\circ\text{C}$ for 2 d (yield: 30 mg, 58%). The purified compound still presents broad signals by ^1H NMR at room temperature due to rapid haptotropic shifting of the η^1/η^5 pyrrole rings of the dpm ligands. The peaks begin to resolve around $-75\text{ }^\circ\text{C}$.

^1H NMR (500 MHz, $\text{tol-}d_8$, $-75\text{ }^\circ\text{C}$) 7.63 (s, 2H), 6.76 (d, $J = 8.5\text{ Hz}$, 2H), 6.53 (s, 1H), 6.44 (s, 2H), 6.36 (m, 6H), 6.06 (d, $J = 6.2\text{ Hz}$, 2H), 5.82 (s, 2H), 5.65 (s, 1H), 1.97 (d, $J = 17.6\text{ Hz}$, 0H), 1.93 (s, 0H), 1.58 (d, $J = 17.4\text{ Hz}$, 0H). ^{13}C NMR (126 MHz, $\text{tol-}d_8$, $-75\text{ }^\circ\text{C}$) 173.05, 170.55, 158.50, 157.34, 127.15, 126.84, 125.90, 124.54, 122.32, 113.80, 108.45, 45.38, 39.86, 28.70, 28.45. Note, repeated attempts to obtain passing elemental analysis failed to yield adequate results.

Synthesis of $[\text{Ti}(\mu\text{-NtolyI})(\text{OArCH}_2\text{ArO})]_2\cdot\text{HNMe}_2$: A scintillation vial was charged with 100 mg (0.21 mmol, 1 equiv) $\text{Ti}(\text{bisphenoxide})(\text{NMe}_2)_2$, a stir bar, and 2 mL benzene. A separate solution of 23 mg (0.21 mmol, 1 equiv) of H_2NtolyI was prepared in 1 mL benzene. The H_2NtolyI solution was added dropwise to the stirred Ti solution, which resulted in a color change from yellowish orange to dark brown. The solution was stirred for 1 h at room temperature, and the volatiles removed under reduced pressure. This provided powdery dark brown residue, which was

dissolved in a minimal amount of n-hexane. The concentrated n-hexane solution was chilled at -35 °C for 2 d to yield X-ray quality crystals of [Ti(OArCH₂ArO)(μ-Ntolyl)]₂NHMe₂ (41 mg, 39 %).

¹H NMR (500 MHz, benzene-*d*₆) 7.06 – 6.98 (m, 6H), 6.80 (d, *J* = 7.8 Hz, 2H), 3.80 (d, *J* = 14.2 Hz, 1H), 3.36 (d, *J* = 14.3 Hz, 1H), 2.15 (s, 6H), 2.01 (s, 3H), 1.79 (d, *J* = 4.8 Hz, 1.5H), 1.66 (s, 18H). ¹³C NMR (126 MHz, benzene-*d*₆) 161.02, 136.29, 132.93 (d, *J* = 47.4 Hz), 130.26, 129.65, 129.37, 126.11, 121.40, 40.30, 31.30, 21.19, 20.81. EA calc'd for C₆₂H₈₁O₄N₃Ti₂: C, 77.39; H, 9.74; N, 0.0. Found: C, 76.97; H, 9.46; N, 0.10.

Additional Titanium Complexes:

The following Ti complexes were synthesized and fully characterized by Dhvani Kansal: tetrakis(2-*tert*-butyl-4-methyl-phenoxide)Ti(IV), tetrakis(2-*tert*-butyl-4-methoxy-phenoxide)Ti(IV), tetrakis(2-*tert*-butyl-4-bromo-phenoxide)Ti(IV), tetrakis(2-*tert*-butyl-phenoxide)Ti(IV), tetrakis(2-*tert*-butyl-4-fluoro-phenoxide)Ti(IV), and tetrakis(2-*tert*-butyl-4-trifluoromethyl-phenoxide)Ti(IV).

Additionally, the following complexes were prepared according to literature procedures: $\text{Ti}(\text{Cl})_2(\text{OArCH}_2\text{ArO})$, $\text{Ti}(\text{I})_2(\text{OArCH}_2\text{ArO})$, $\text{Ti}(\text{O}^i\text{Pr})_2(\text{OArCH}_2\text{ArO})$, and $\text{Ti}(\text{OArCH}_2\text{ArO})_2$.¹⁸ The recorded ^1H and ^{13}C NMR data matched previous reports, however, the latter 3 complexes had never been structurally characterized. Single crystal X-ray structures were determined with these 3 complexes. Additionally single crystals of the $\text{Ti}(\text{Cl})_2(\text{OArCH}_2\text{ArO})$ were examined by X-ray diffraction, and a matching unit cell to previous structural reports was determined. The X = OⁱPr complex is dimeric in the solid state, but monomeric in solution, according to *in situ* molecular weight calibrations with DOSY NMR. For completeness, $\text{Ti}(\text{I})_2(\text{OArCH}_2\text{ArO})$ was also examined by DOSY NMR, and similarly determined to be monomeric in solution. This complex was also observed as a monomer in the solid state. These results are presented below.

$\text{Ti}(\text{NMe}_2)_2(\text{OArCH}_2\text{ArO})$ was prepared from modification of literature reports.⁴ The new procedure for preparation of this complex is described below. The ^1H and ^{13}C NMR data for this complex matches previous reports.

Synthesis of tetrakis(2,4-di-tert-butyl-phenoxide)Ti(IV): A scintillation vial was charged with 200 mg $\text{Ti}(\text{NMe}_2)_4$ (0.89 mmol, 1 equiv), a stir bar, and 5 mL n-hexane. The vial was chilled in a coldwell cooled with liquid N_2 for 20 min, until the hexane solution was frozen. The vial was warmed ambiently, with stirring, until the solution was just thawed, and a 2 mL toluene solution

of 732 mg 2,4-di-*tert*-butylphenol was added dropwise (3.6 mmol, 4 equiv). The pale yellow solution rapidly turned bright orange. This solution was stirred for 2 h at room temperature, and the volatiles removed in vacuo to yield a powdery orange residue. The residue was rinsed with hexane and dried once more. The residue was dissolved in a minimal amount of toluene and the concentrated solution was stored at -35 °C overnight to yield X-ray quality crystals of $\text{Ti}(\text{OPh}^{2,4\text{-ditBu}})_4$ (589 mg, 76 %).

^1H NMR (500 MHz, benzene- d_6) δ 7.47 (d, $J = 2.4$ Hz, 4H), 7.42 (d, $J = 8.3$ Hz, 4H), 6.95 (dd, $J = 8.3, 2.4$ Hz, 4H), 1.60 (s, 36H), 1.21 (s, 36H). ^{13}C NMR (126 MHz, benzene- d_6) δ 162.29, 145.41, 135.96, 124.70, 123.67, 122.98, 35.43, 34.63, 31.70, 30.57. EA calc'd for $\text{C}_{56}\text{H}_{84}\text{O}_4\text{Ti}$: C, 77.39; H, 9.74; N, 0.0. Found: C, 76.97; H, 9.46; N, 0.10.

Modified Synthesis of $\text{Ti}(\text{OArCH}_2\text{ArO})(\text{NMe}_2)_2$: A scintillation vial was charged with 280 mg of $\text{Ti}(\text{NMe}_2)_4$ (1.25 mmol, 1 equiv), 8 mL of Et_2O , and a stir bar. This solution was chilled in an $\text{N}_2(\text{l})$ coldwell for 10 min. Separately, a solution of 425 mg (1.25 mmol, 1 equiv) of the H_2 (bisphenoxide) ligand was prepared in 2 mL of Et_2O . The chilled Ti solution was stirred, and the ligand solution was added dropwise to it over the course of a few minutes. The solution changed from pale yellow to intense yellow-orange upon addition. The stirred solution was allowed to come to room temperature and stirred for 4 h. The volatiles were removed under reduced pressure to yield a sticky orange oil. The orange oil was dissolve in 2 mL pentane and the volatiles removed once more to give a sparkly orange foam. This foam was rinsed with cold pentane (-35 °C) to give an orange pentane extract and a yellow powder. The pentane extract can be chilled to yield yellow powder (product). Additionally, the yellow powder can be purified by recrystallization from pentane or hexane (-35 °C) to yield 402 mg (68%) of the purified compound. Characterization of the complex matches the previous report.⁴

Examination of Decomposition Pathways with Iminoamination Product and $Ti(dpm)(X)_2$ and a different $Ti(OArCH_2ArO)(NMe_2)_2$ Precatalyst:

To supplement the kinetics-based simulations and shed more light onto the “why” or “how” of the catalyst deactivation event(s), stoichiometric attempts to probe the reactivity of various Ti species that may exist in the catalytic solution were carried out (6.3). These attempts primarily served to elucidate some of the places where catalyst degradation and noninnocence of the product toward the catalyst may arise. The results of these studies were informative and confirm several possible means by which catalyst deactivation may occur.

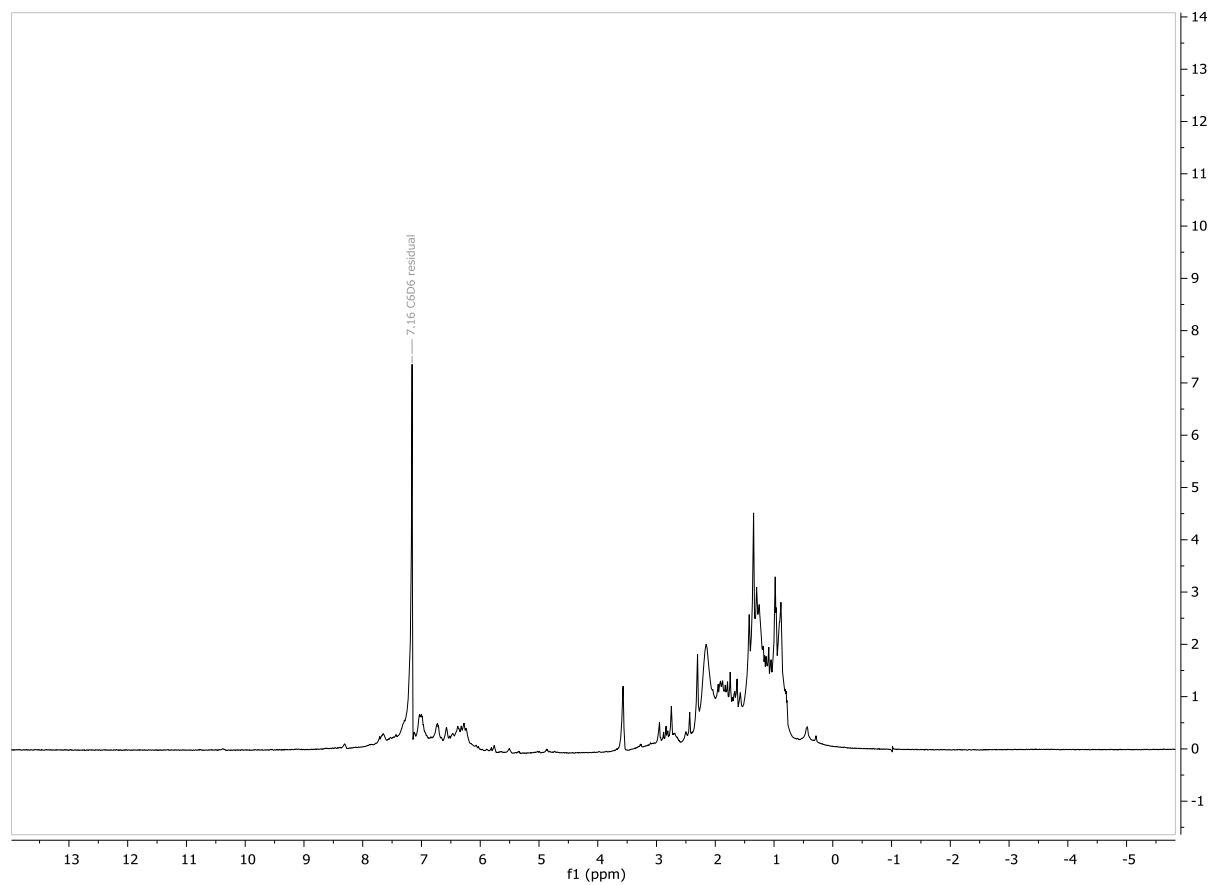


Figure 6.13 ^1H NMR of $\text{Ti}(\text{dpm})(\text{NMe}_2)_2$ and 3CC heated at 80 °C, 40 h in C_6D_6 .

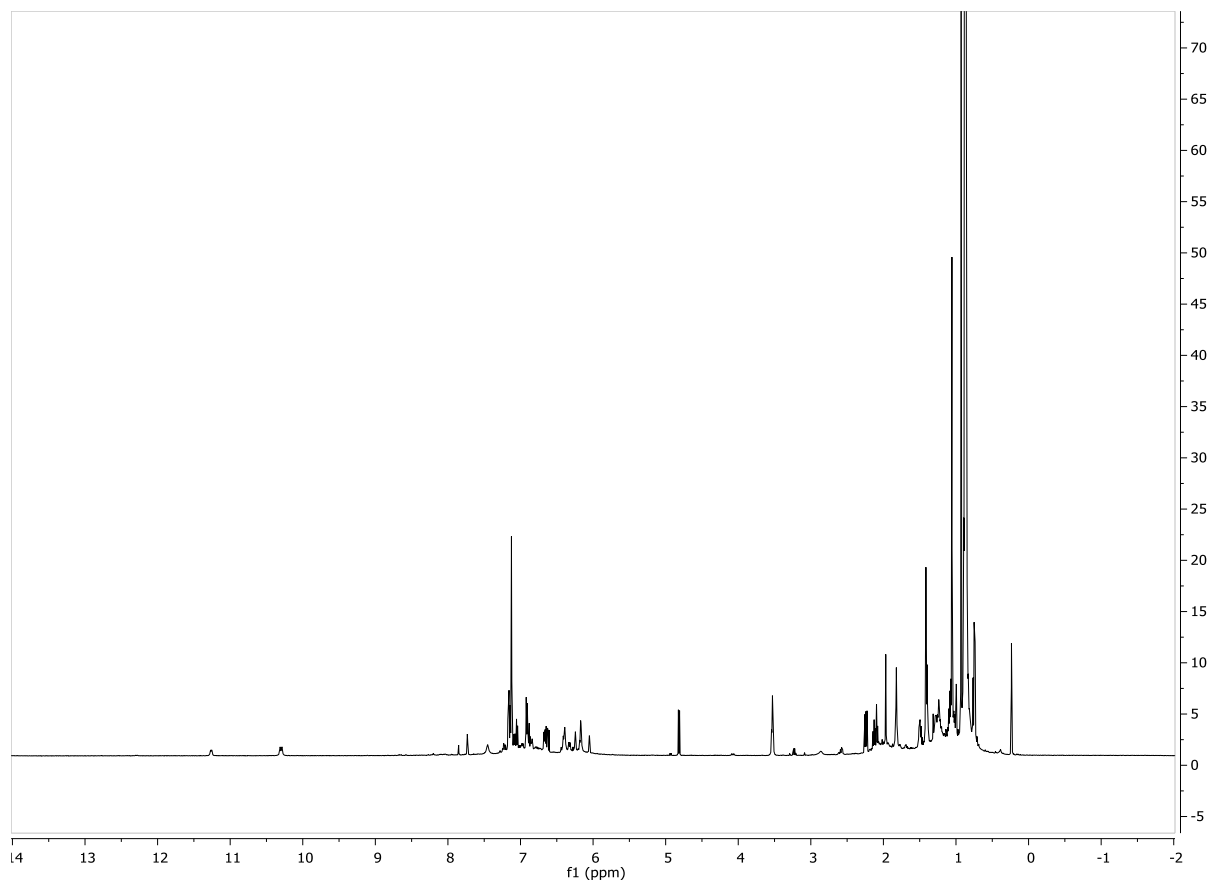


Figure 6.14 ^1H NMR of $[\text{Ti}(\text{dpm})(\text{Ntoly})]_2$, $^t\text{BuNC}$ (xs), and 3CC in C_6D_6 , 80 °C at 6 h.

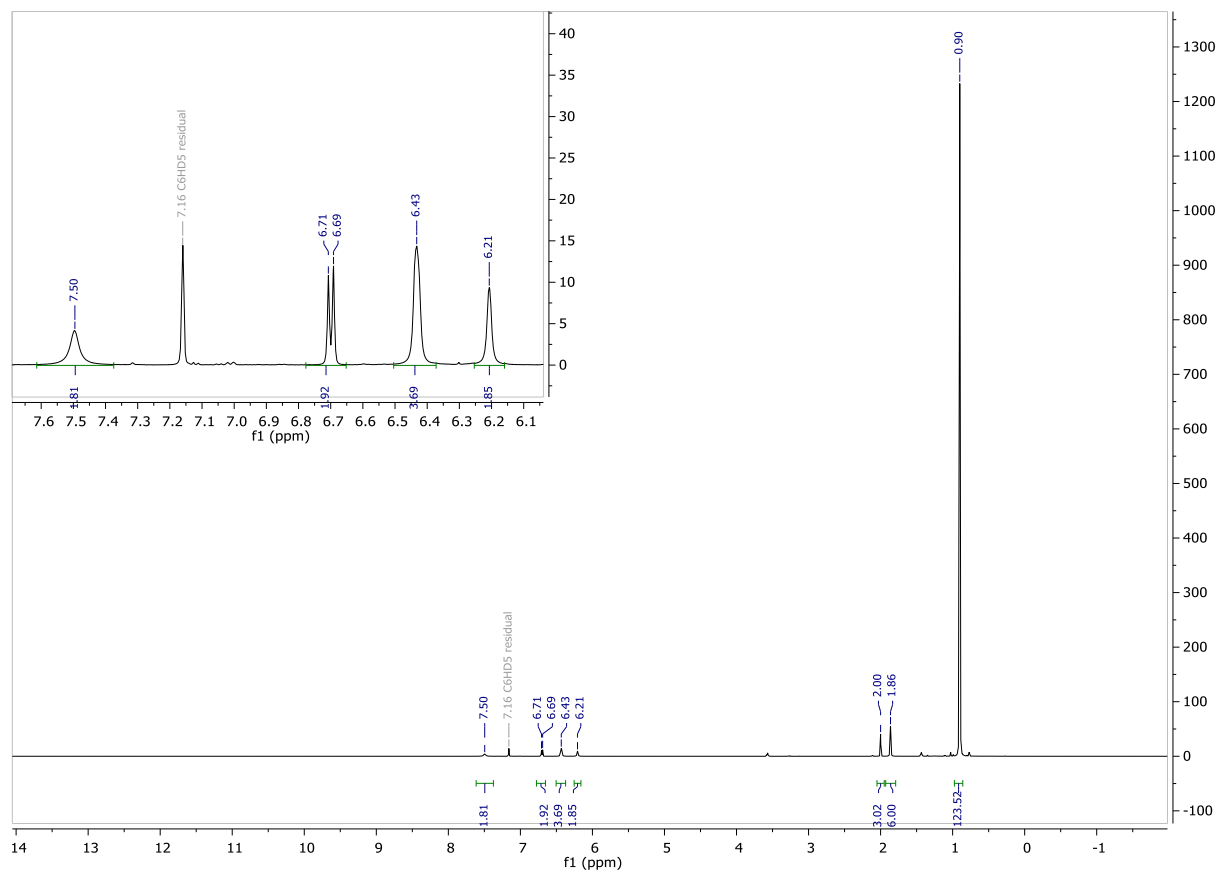


Figure 6.15 ¹H NMR of the [Ti(μ-Ntoly)(dpm)]₂ with ^tBuNC *in situ* in C₆D₆.

¹H NMR (500 MHz, Benzene-*d*₆) 7.50 (s, 4H), 6.70 (d, *J* = 8.0 Hz, 4H), 6.43 (s, 8H), 6.21 (s, 4H), 2.00 (s, 6H), 1.86 (s, 12H).

Stability of [Ti(OArArO)(Ntoly)]^{1/2}(NHMe₂) in-situ: A J. Young tube was charged with 10 mg of [Ti(OArArO)(μ₂-Ntoly)]₂NHMe₂ (which appears to exist mostly as the monomer in solution by ¹H DOSY Molecular Weight Calibration), and 1.0 mL of C₆D₆. The solution was mixed and the tube sealed with a Teflon stopper. The tube was transferred from the glovebox to an 85 °C oil bath and was heated for 16 h. The contents of the tube were examined by ¹H NMR. Several sets of peaks were easily distinguished after heating. The characteristic doublets for the CH₂ linker protons in each of the following species were observed: Ti(OArArO)(Ntoly)·^{1/2}(HNMe₂), Ti(OArArO)₂, and Ti(OArArO)(NMe₂)₂. This also suggests there is at least one more complex in solution, which have distributions of N-based ligands, and lack an (OArArO) fragment as well, i.e. [Ti(Ntoly)_{x-4}(NMe₂)_{4-x}]_n. This experiment, suggests that disproportionation likely changes the catalyst loading in the 3CC reactions over the course of the reaction period—in agreement with ¹H NMR observations of a genuine 3CC reaction with the Ti(OArCH₂ArO)(NMe₂)₂ catalyst.

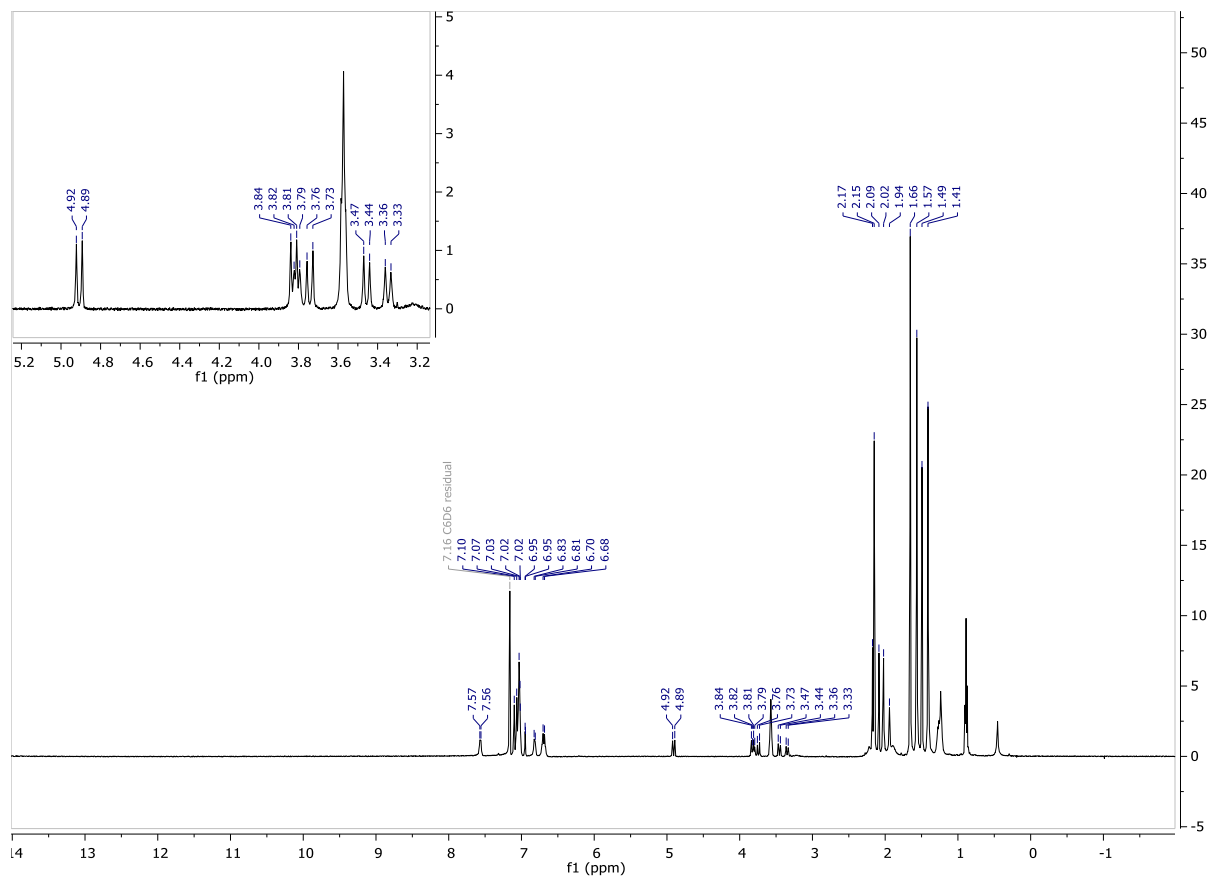


Figure 6.16 ^1H NMR of $[\text{Ti}(\text{OArCH}_2\text{ArO})(\mu\text{-NtolyI})]_2 \cdot \text{NHMe}_2$ after heating 16 h at $80\text{ }^\circ\text{C}$.

In-situ Reactivity of [Ti(OArArO)(Ntoly)]₂ with 3CC: A scintillation vial was charged with 20 mg of the Ti(Ntoly)(bisphenoxide) species and 1.5 mL of C₆D₆. The solution was stirred to ensure complete dissolution of the Ti species. Then, 20 mg of the isomeric mixture of 3CC_k was dissolved in C₆D₆ and added to the Ti solution. The mixture was allowed to sit at room temperature for 10 minutes, and a baseline NMR spectrum was taken, This spectrum is shown in Fig. 6.16 and shows the two isomers of 3CC, as well as the Ti(Ntoly)(OArCH₂ArO).

The solution was then heated in an oil bath in a J. Young tube with a Teflon stopper for 3 h at 85 °C. Another ¹H NMR spectrum was taken and is shown in Fig. 6.17. The starting materials are all still present, however, many of the peaks have decreased in intensity, and a few new peaks are beginning to grow into the baseline of the spectrum. The sample was returned to the oil bath and heating continued for a total of 48 h at 85 °C. The spectrum after 48 h is shown in Fig. 6.18. We can see that one of the 3CC_k isomers (B) has decreased in overall peak intensity. Additionally, a new set of peaks that correspond to the Ti(OArCH₂ArO)₂ disproportionation product are evident in solution.

It is also relevant to note that there is no evidence of free H₂Ntoly in this spectrum. This suggests that the (Ntoly) fragments are bound to the other ½ equivalent of Ti still in solution. This is also likely where the consumed 3CC product is. However, clear peaks that correlate to this species cannot be deciphered from the crowded aromatic and aliphatic regions of this ¹H NMR spectrum. This experiment is another piece of evidence that one possible pathway for decomposition of the catalyst is via ligand disproportionation facilitated directly by interaction with the 3CC product.

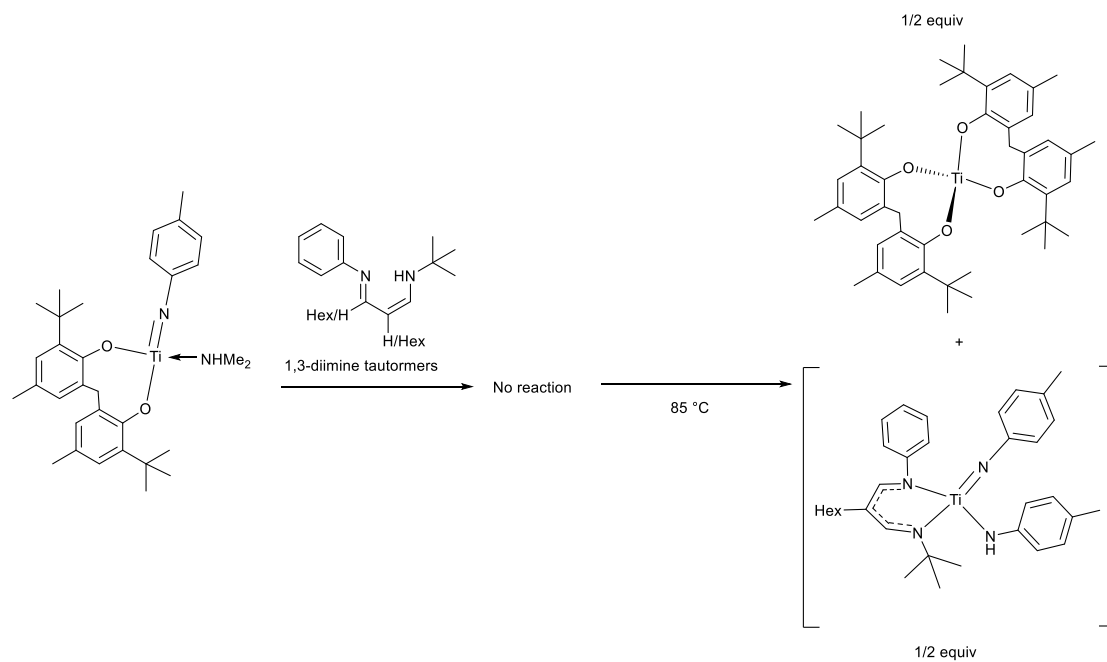


Figure 6.17 Proposed decomposition pathway and final products observed (top) and proposed (bottom) for the Ti-imide species upon heating with the iminoamination product in C_6D_6 .

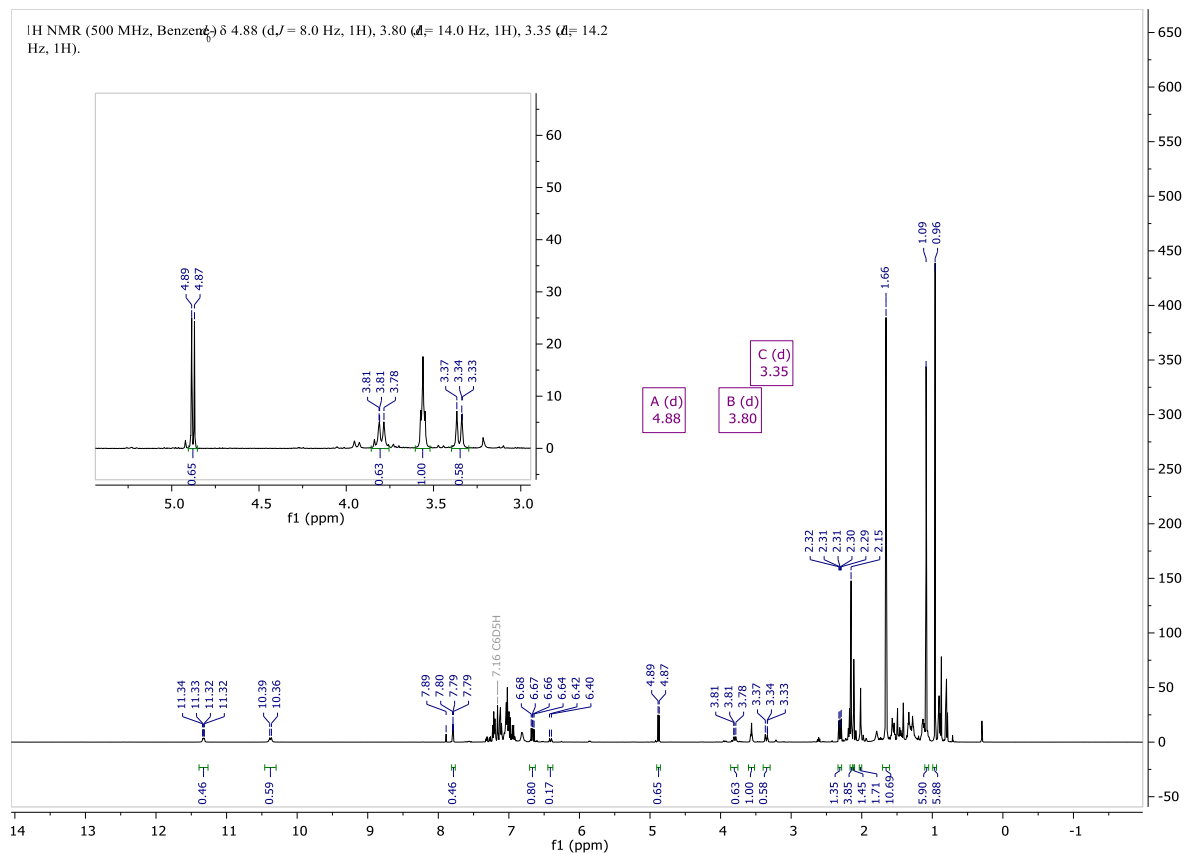


Figure 6.18 $^1\text{H NMR}$ of $3\text{CC(A/B)} + [\text{Ti}(\text{OArCH}_2\text{ArO})(\text{Ntoly})]_2 \cdot \text{HNMe}_2$ heated for 0 h at 85°C —showing no $\text{Ti}(\text{OArCH}_2\text{ArO})_2$.

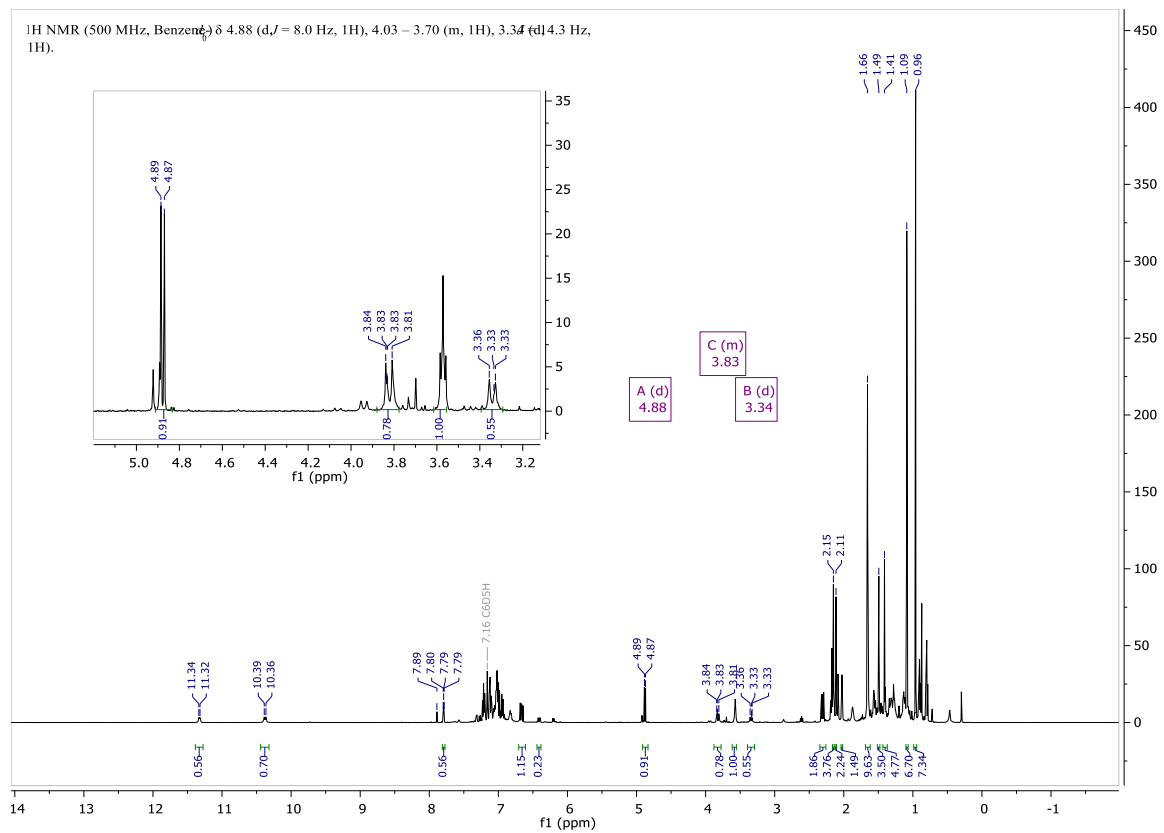


Figure 6.19 ¹H NMR of 3CC(A/B) + [Ti(OArCH₂ArO)(Ntoly)]₂·HNMe₂ heated for 3 h at 85 °C—showing a small amount of Ti(OArCH₂ArO)₂.

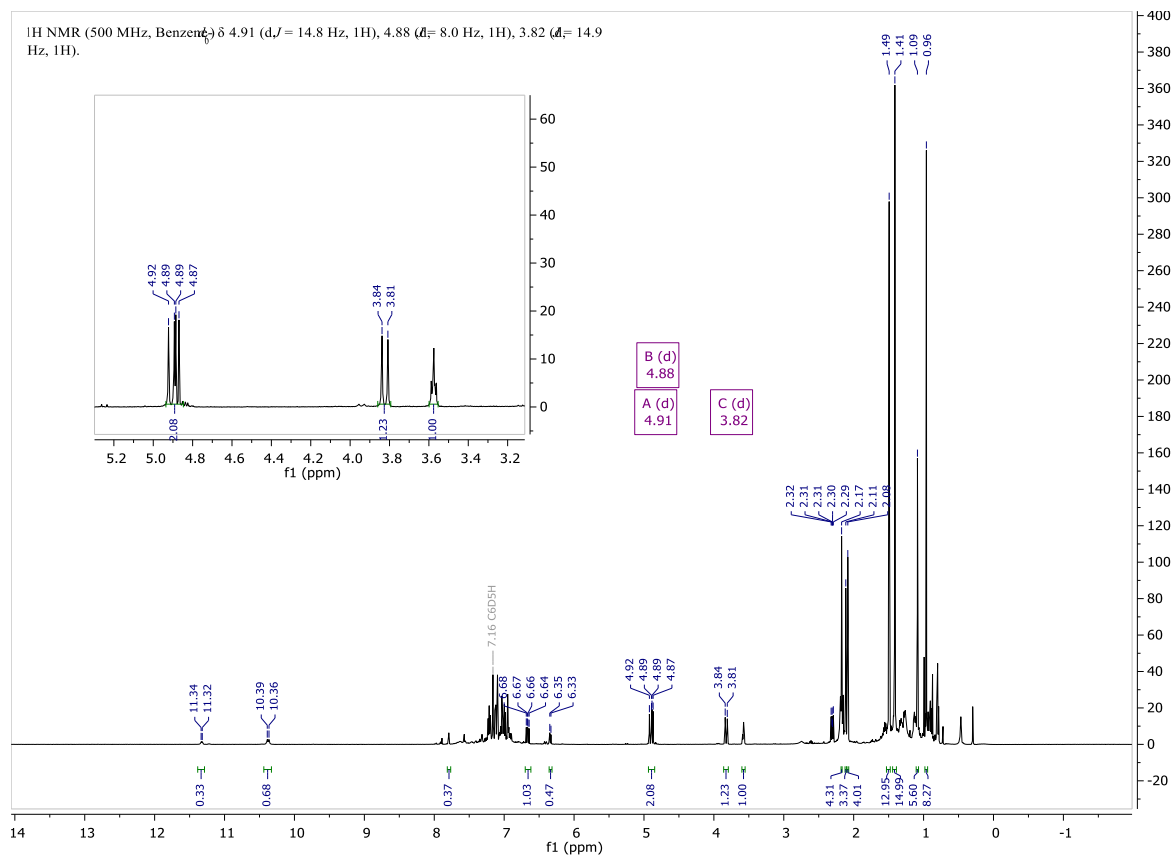


Figure 6.20 $^1\text{H NMR}$ of $3\text{CC(A/B)} + [\text{Ti}(\text{OArCH}_2\text{ArO})(\text{Ntoly})]_2 \cdot \text{HNMe}_2$ heated for 48 h at $85\text{ }^\circ\text{C}$ —showing only $\text{Ti}(\text{OArCH}_2\text{ArO})_2$ as identifiable Ti species.

Iminoamination reaction catalyzed by Ti(OArCH₂ArO)(NMe₂)₂: A 15 mL pressure tube was charged with 47 mg of Ti(OArCH₂ArO)(NMe₂)₂ (0.1 equiv), a stir bar, and 1 mL of toluene. To this solution was added 1 equiv H₂NPh and the solution was stirred for 5 min at room temperature. Then a 1 mL solution of 1 equiv ^tBuNC, 1 equiv 1-octyne, and dodecane (0.0001 mol, 17 mg) in toluene was added to the pressure tube solution. The tube was sealed and transferred from the glovebox to a preheated oil bath (110 °C) and was heated with stirring for 16 h. The reaction solution was analyzed by GC-MS and the amount of iminoamination and other reaction products quantified by GC-FID analysis.

In situ Iminoamination Reaction Catalyzed by Ti(OArCH₂ArO)(NMe₂)₂: A solution containing ferrocene (46.5 mg, 0.05 M internal standard), H₂NPh (93 mg, 0.2 M), 1-octyne (110 mg, 0.2 M), and ^tBuNC (82 mg, 0.2 M) in tol-d₈ (diluted to 5.0 mL) was prepared volumetrically. To 19 mg of the Ti catalyst (0.04 M) 1.0 mL of the prepared solution was added. After complete dissolution of the Ti complex, the solution was loaded into a J-young NMR tube and sealed with a Teflon cap. The tube was heated at 110 °C for 16. The solution was then examined by ¹H NMR (shown below).

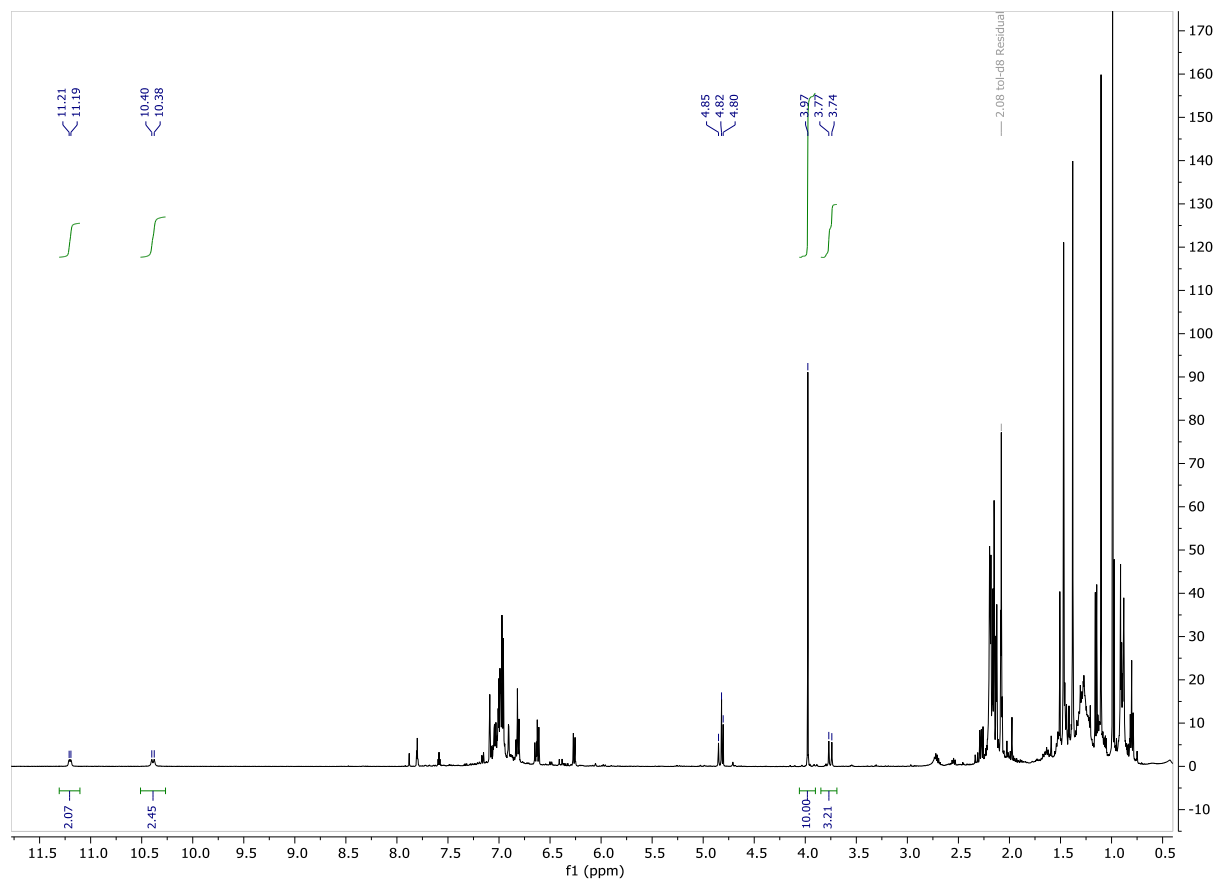


Figure 6.21 ^1H NMR of the iminoamination reaction catalyzed by 20 mol% $\text{Ti}(\text{OArCH}_2\text{ArO})(\text{NMe}_2)_2$ in $\text{tol-}d_8$. Peaks at 11.2 and 10.4 ppm are for the two different regioisomers of the 3CC product. The large singlet at 3.97 ppm is Fc as internal standard. The peak at 3.35 ppm belongs to the $\text{Ti}(\text{OArCH}_2\text{ArO})_2$ disproportionation species.

NMR and GCMS Spectra

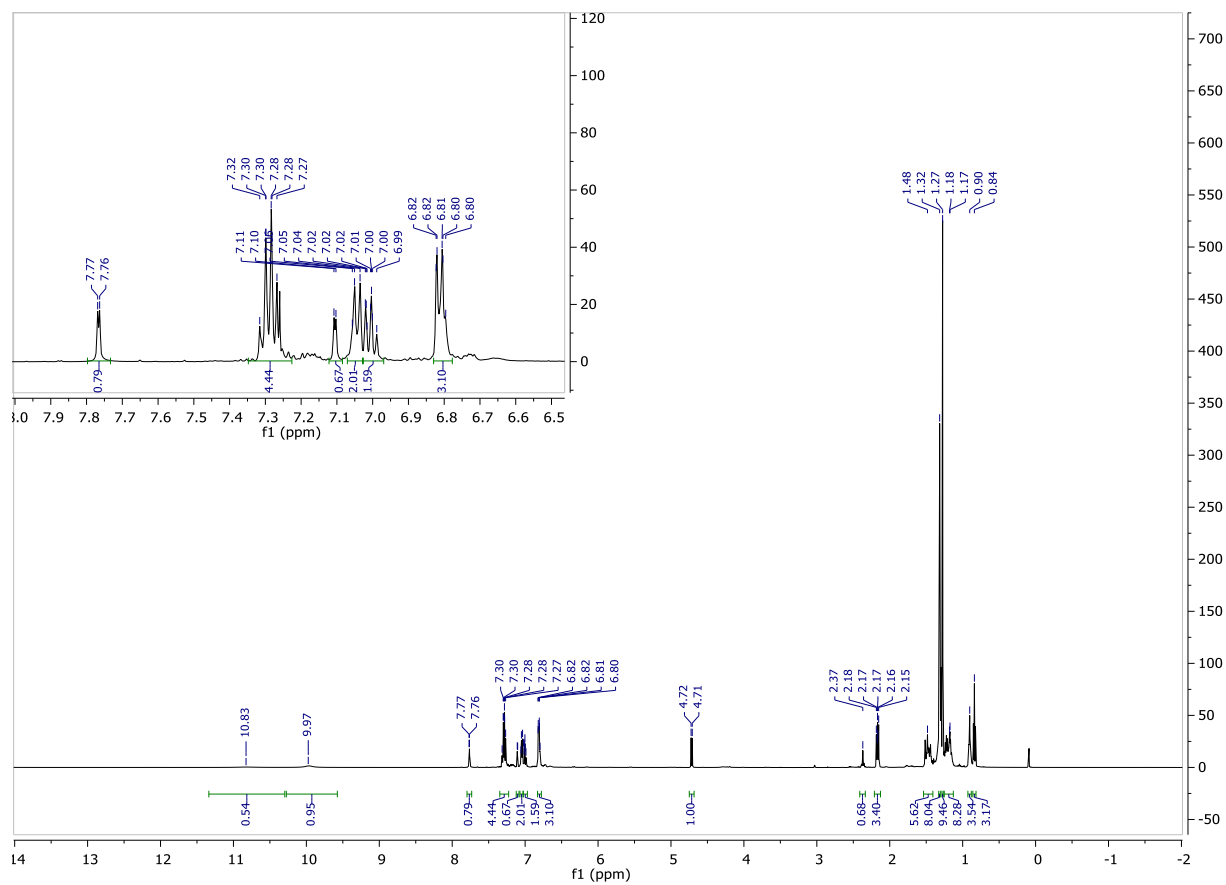


Figure 6.22 ^1H NMR of an isomeric mixture of 3CC(A) and (B) in CDCl_3 .

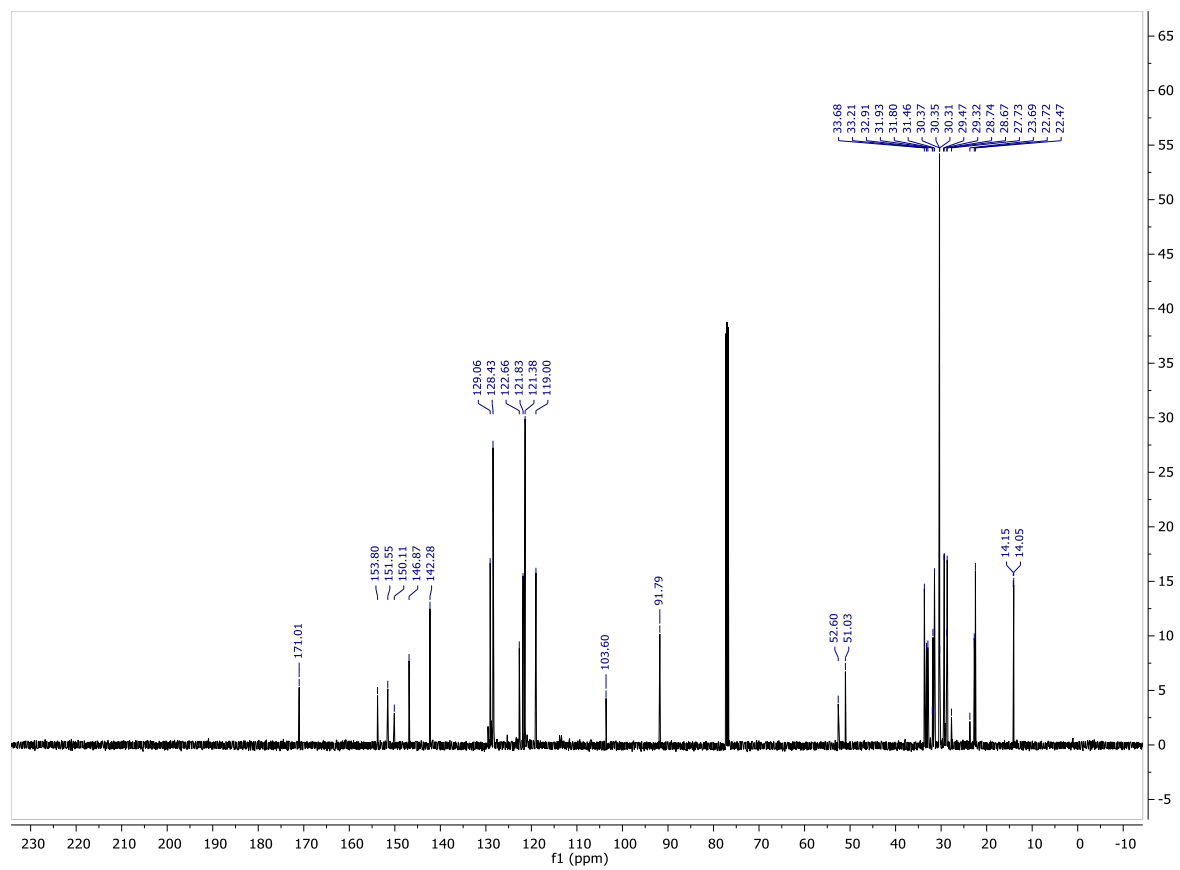


Figure 6.23 ^{13}C NMR of an isomeric mixture of 3CC_k(A) and (B) in CDCl_3 .

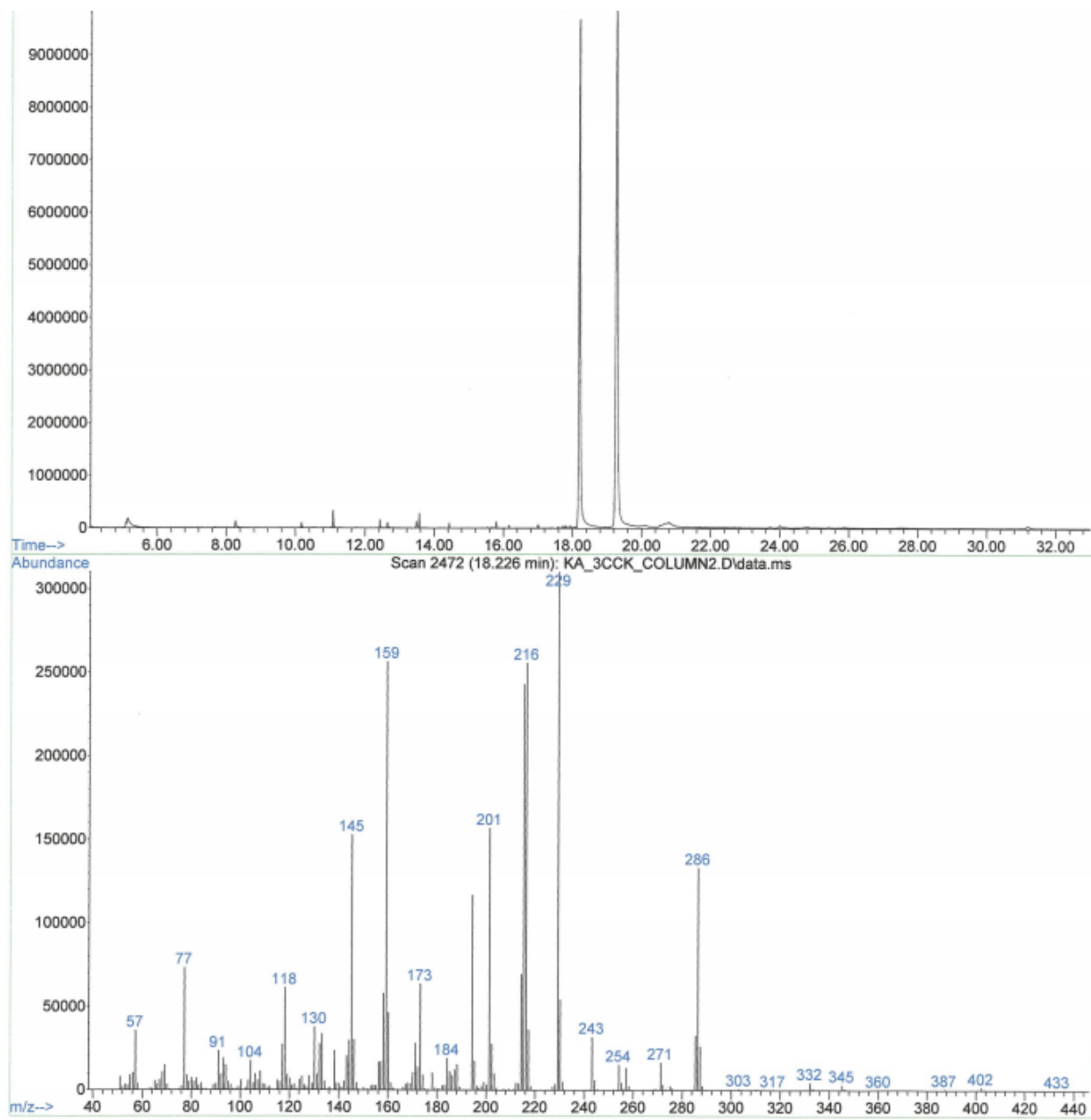


Figure 6.24 GCMS of 3CC isomers A and B; fragmentation pattern for A isomer.

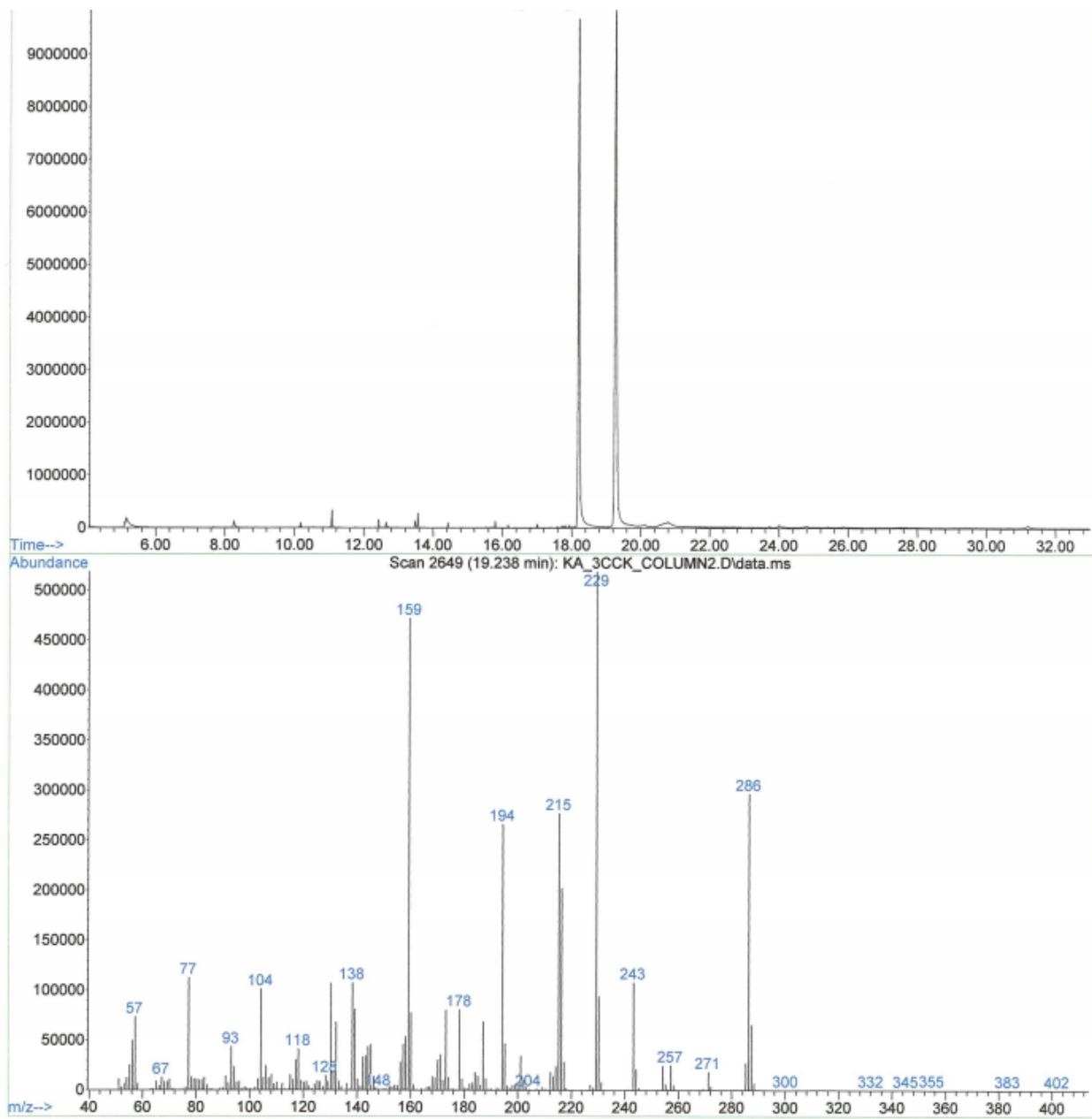


Figure 6.25 GCMS of 3CC isomers A and B; fragmentation pattern for B isomer.

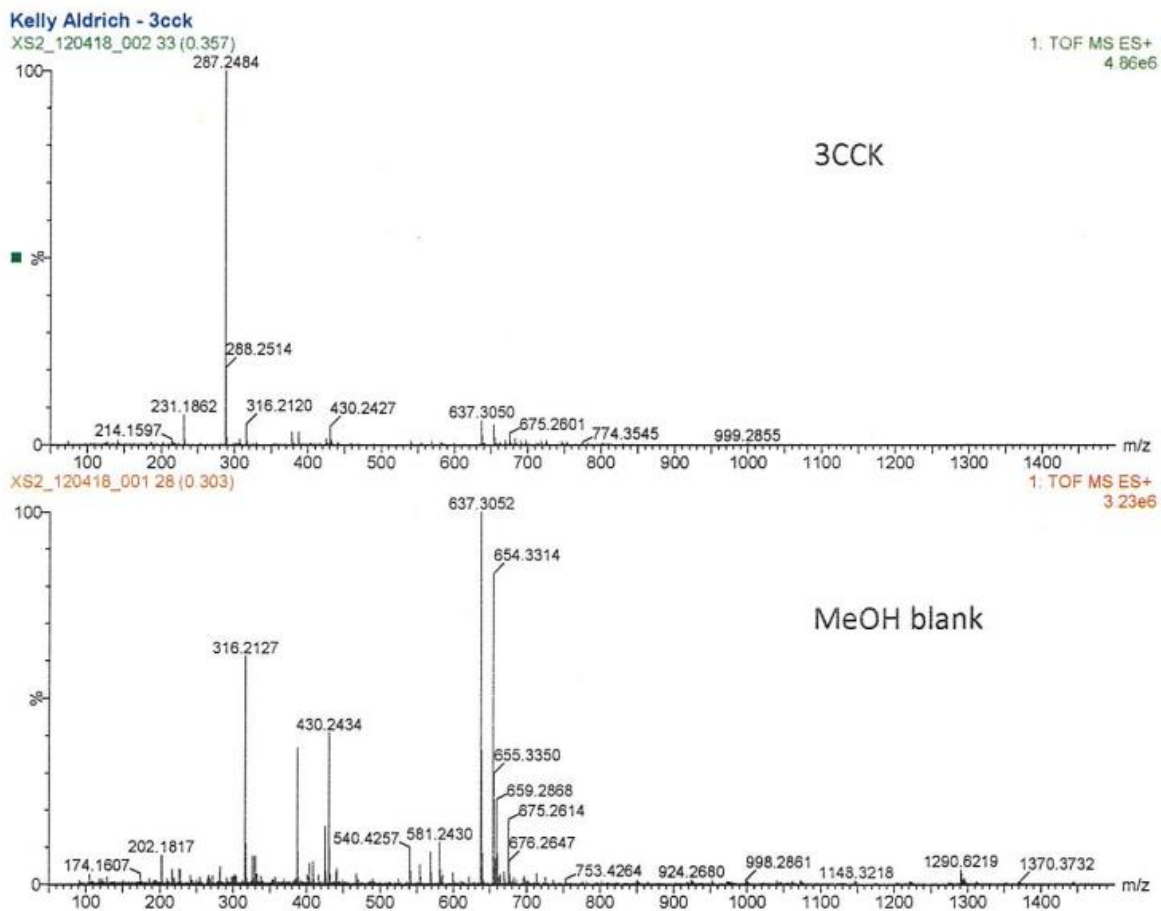


Figure 6.26 HRMS for isomeric mixture of 3CC.

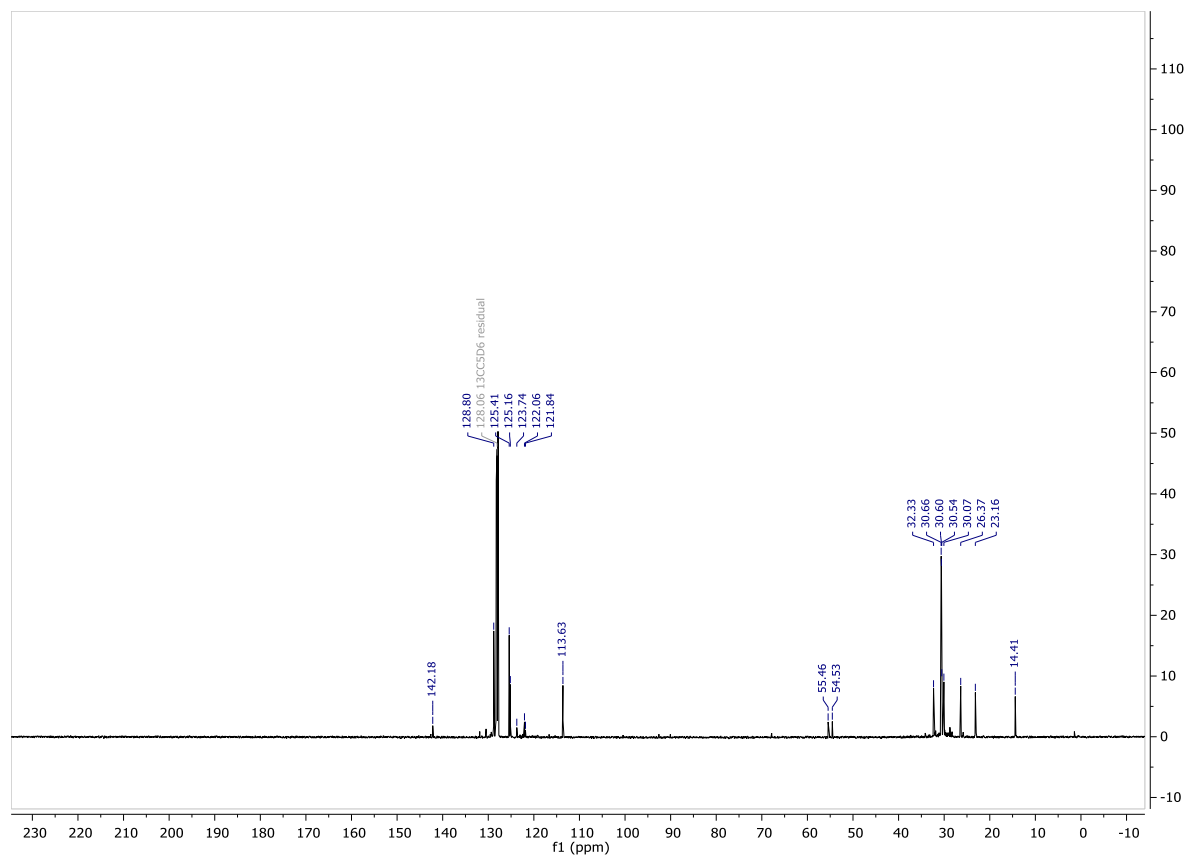


Figure 6.28 ^{13}C NMR of the 4CC product in CDCl_3 .

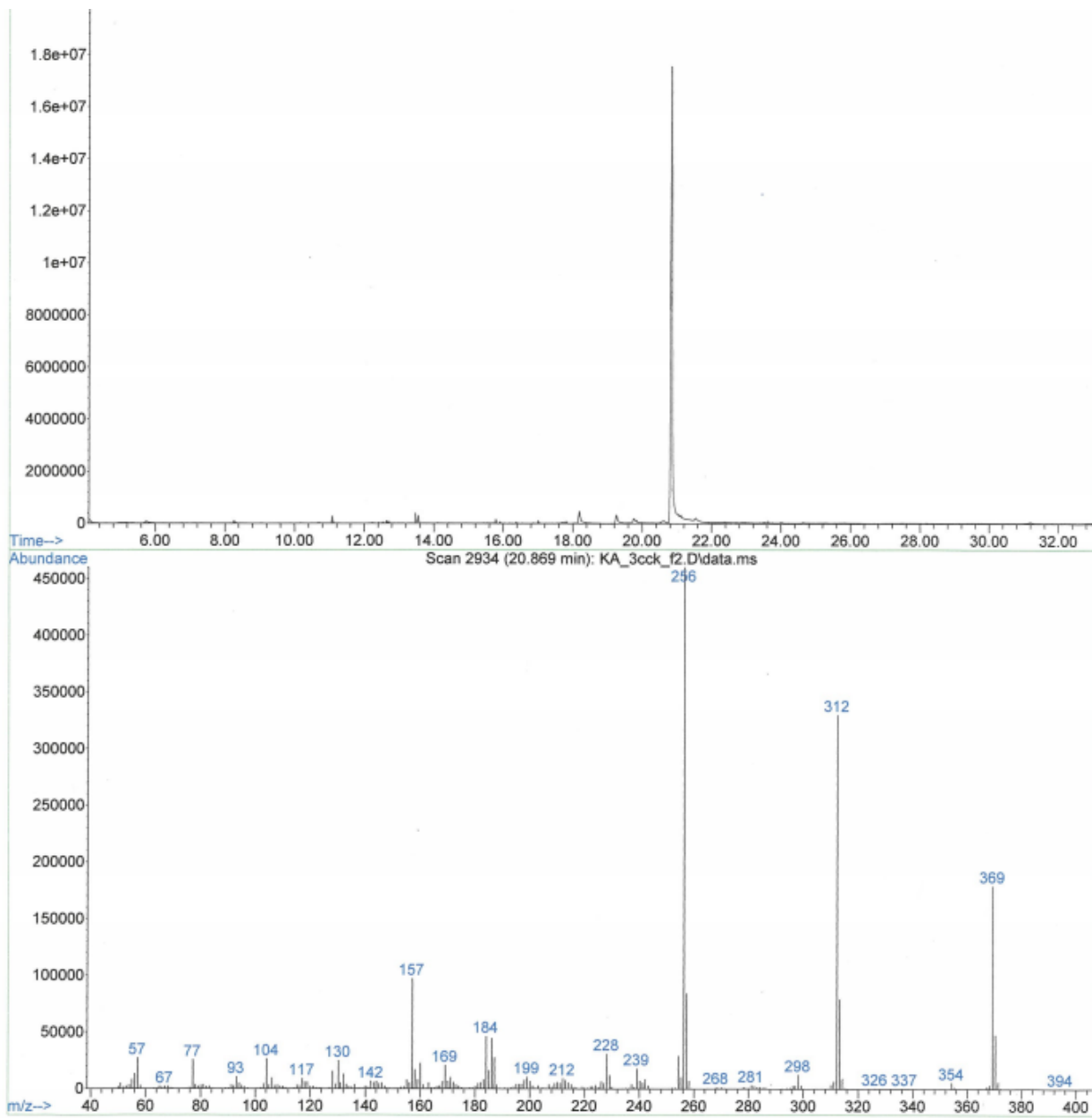


Figure 6.29 GCMS of the 4CC product and MS fragmentation pattern.

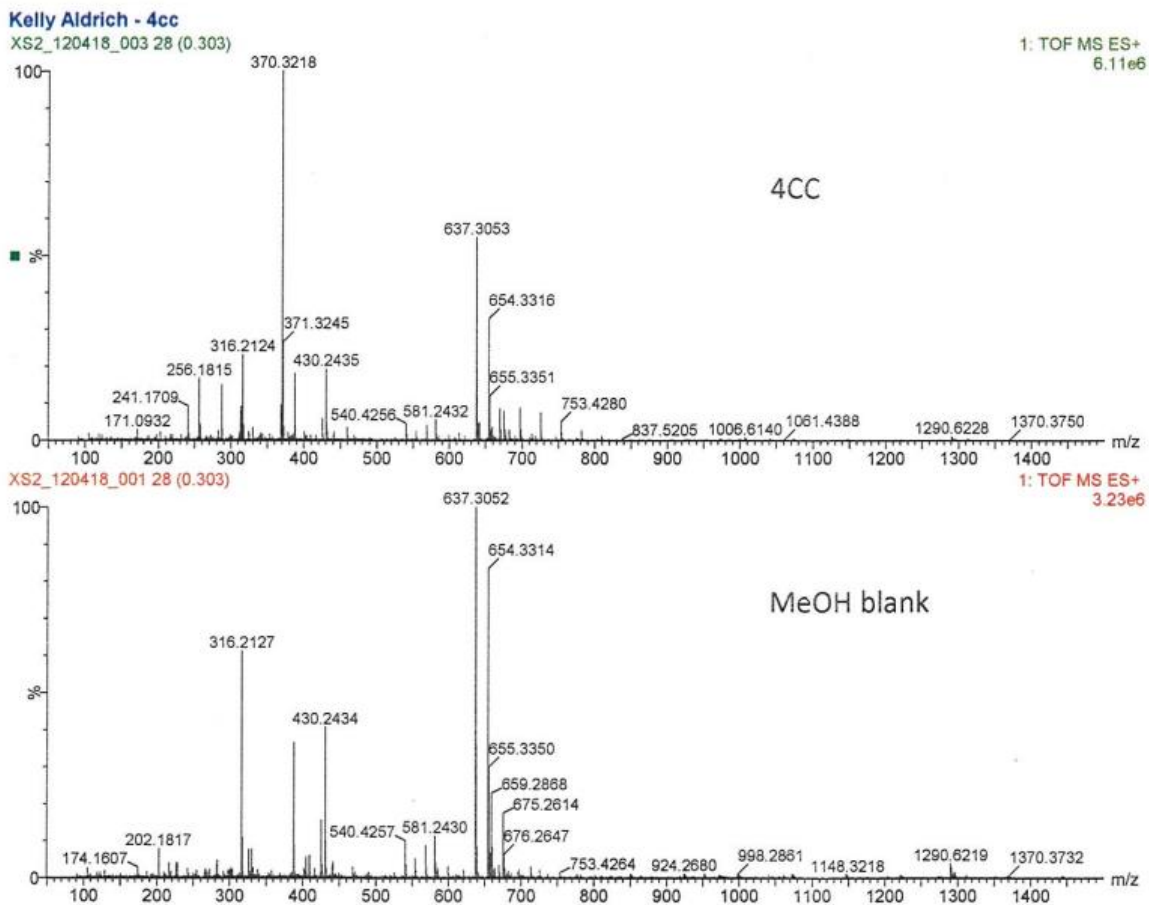


Figure 6.30 HRMS of the 4CC product.

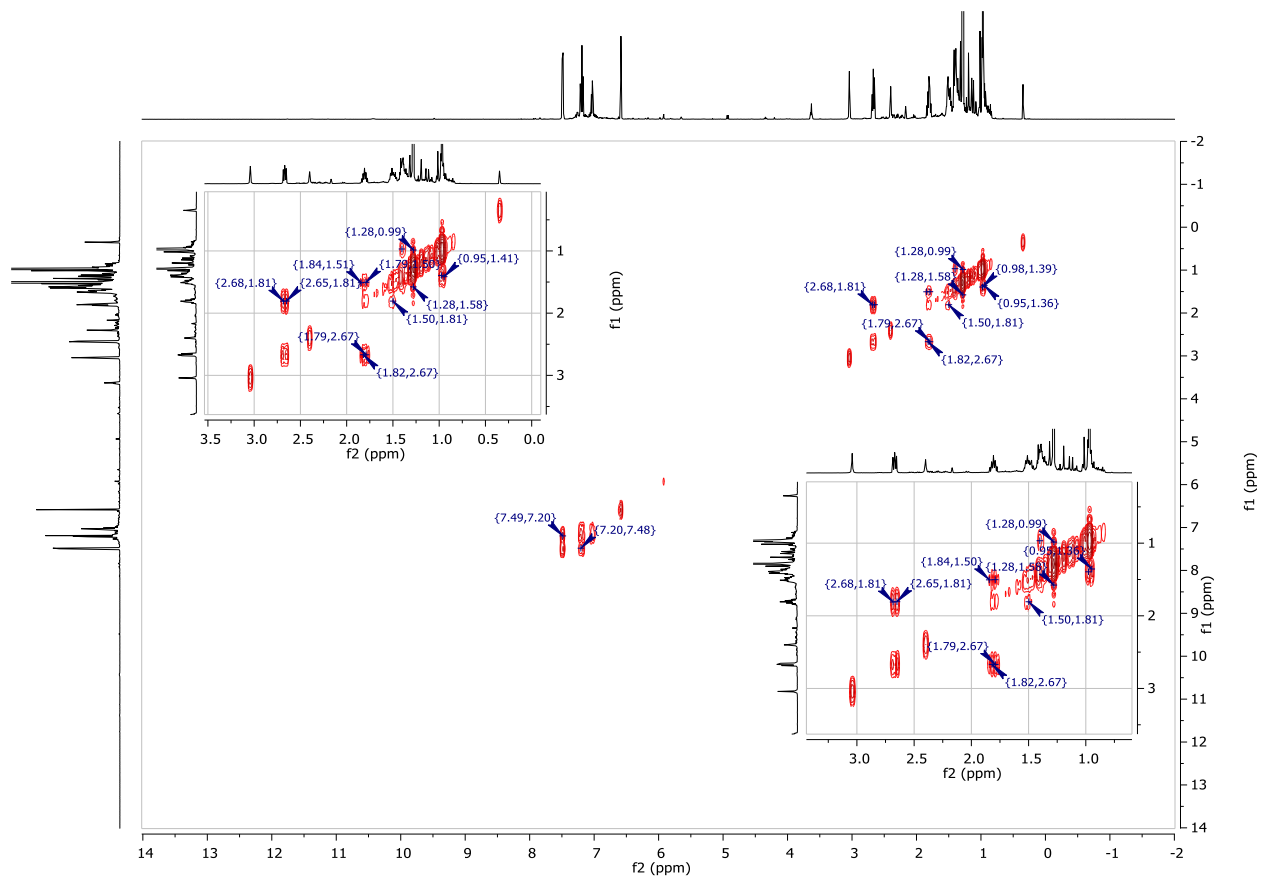


Figure 6.31 gCOSY NMR of the 4CC product in CDCl₃.

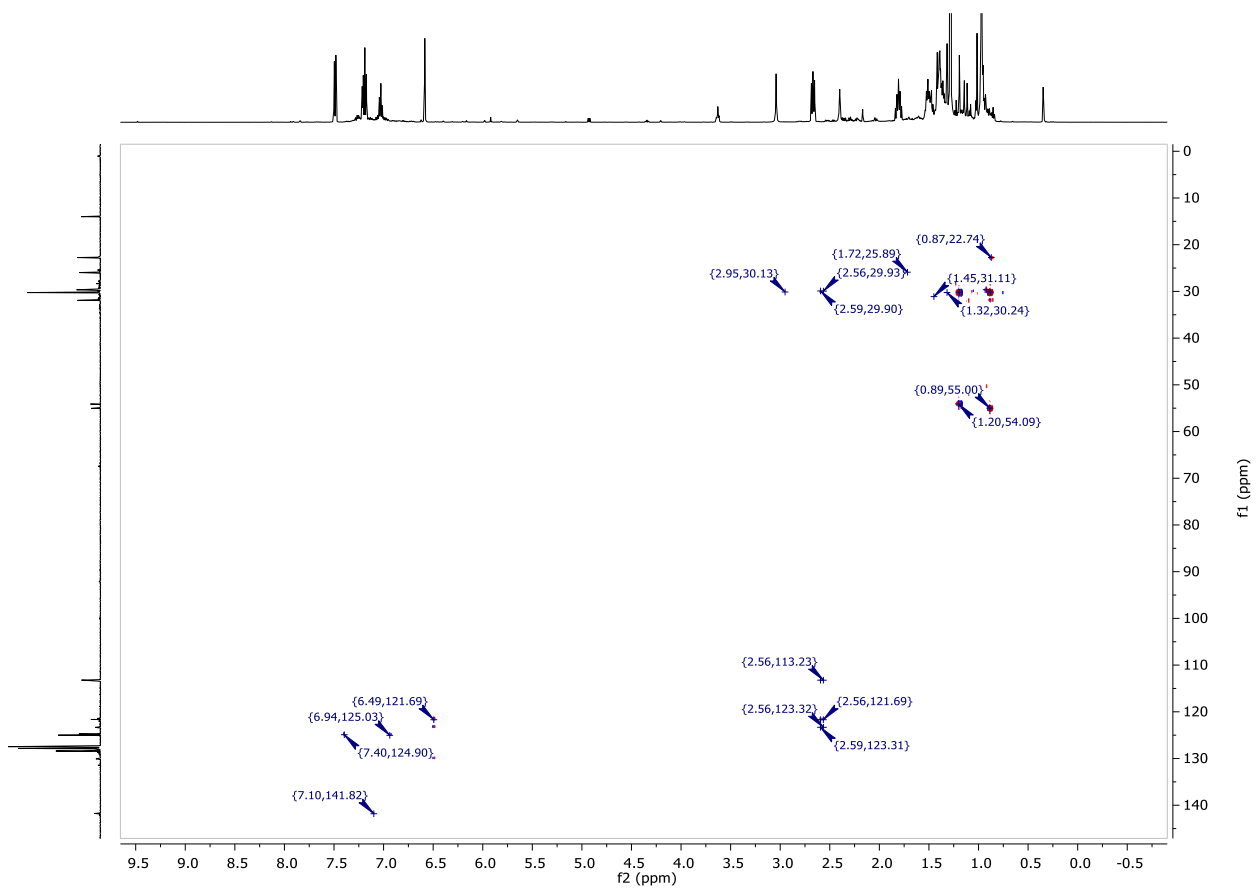


Figure 6.32 HMBC NMR of 4CC in CDCl₃.

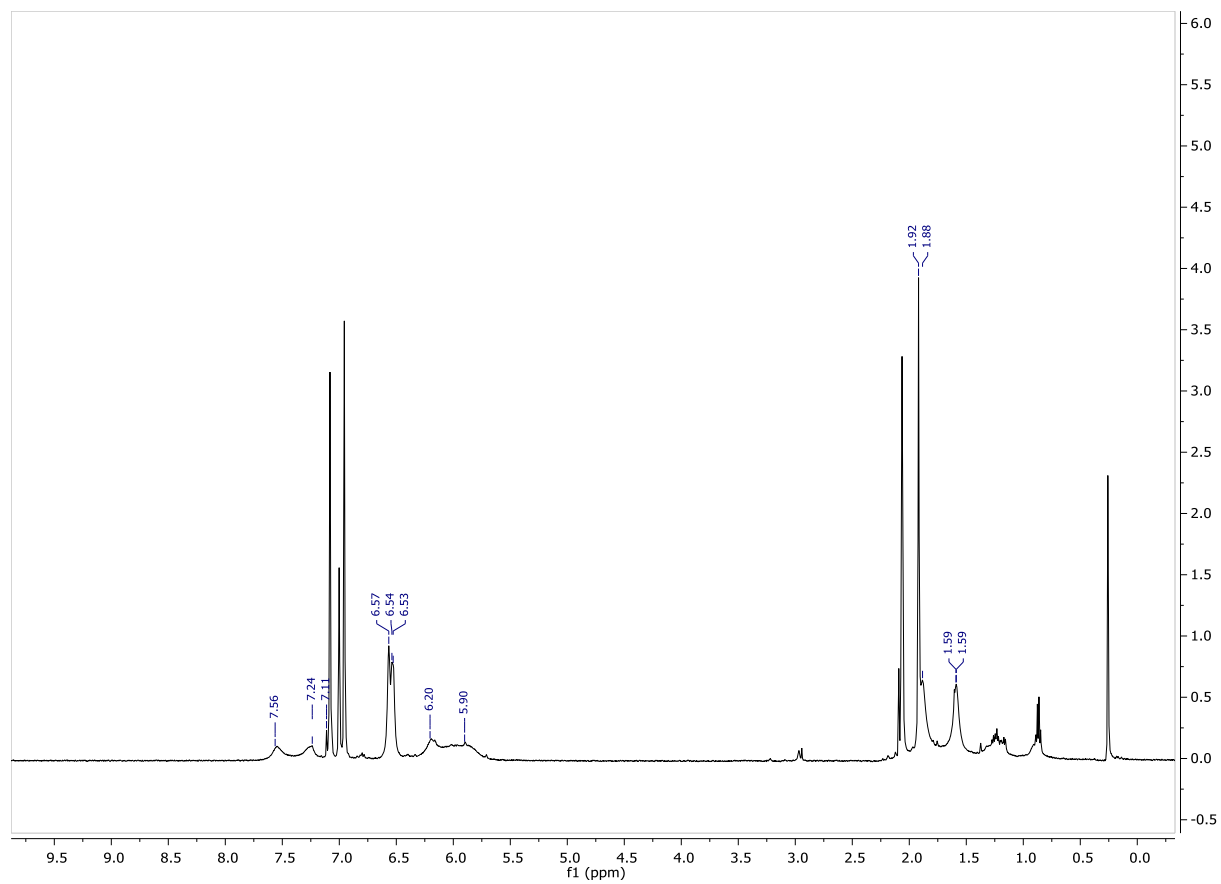


Figure 6.33 ^1H NMR of $[\text{Ti}(\mu\text{-Ntolyl})(\text{dpm})]_2$ in tol-d_8 . (room temperature, high vac grease and hexane impurities)

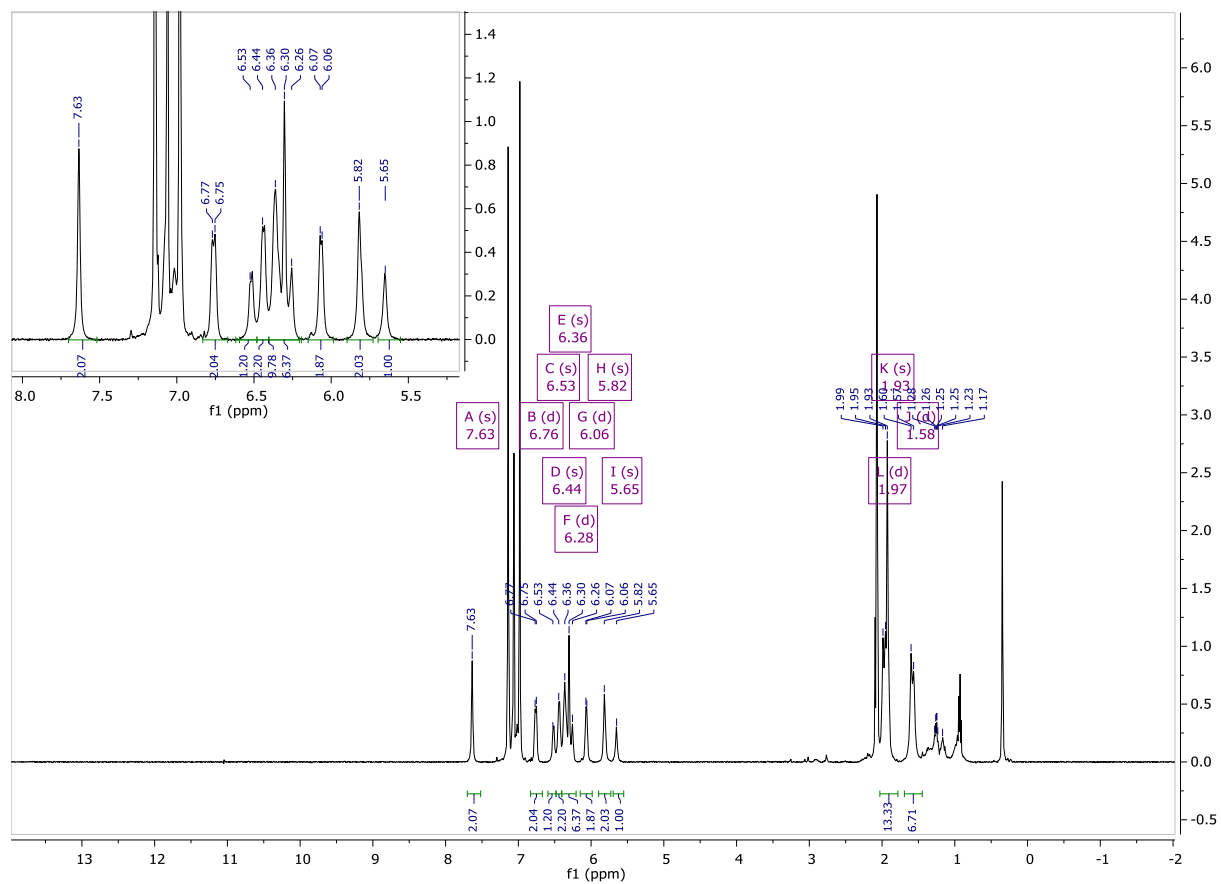


Figure 6.34 ^1H NMR of $[\text{Ti}(\mu\text{-Ntoly})(\text{dpm})_2]$ in $\text{tol-}d_8$. (-75 $^\circ\text{C}$, high vac grease and hexane impurities)

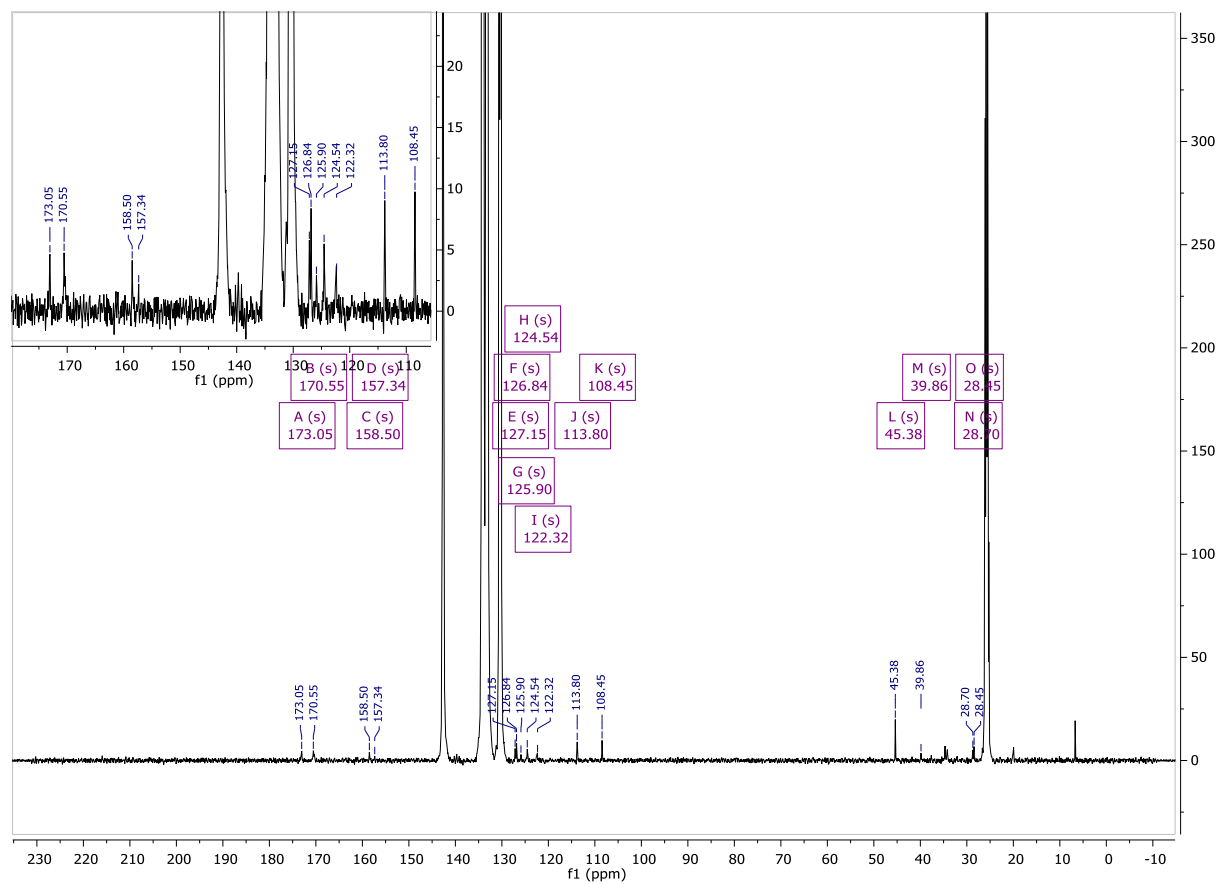


Figure 6.35 ^{13}C NMR of $[\text{Ti}(\mu\text{-Ntoly})(\text{dpm})]_2$ in $\text{tol-}d_8$ (room temperature, high vac grease and hexane impurities)

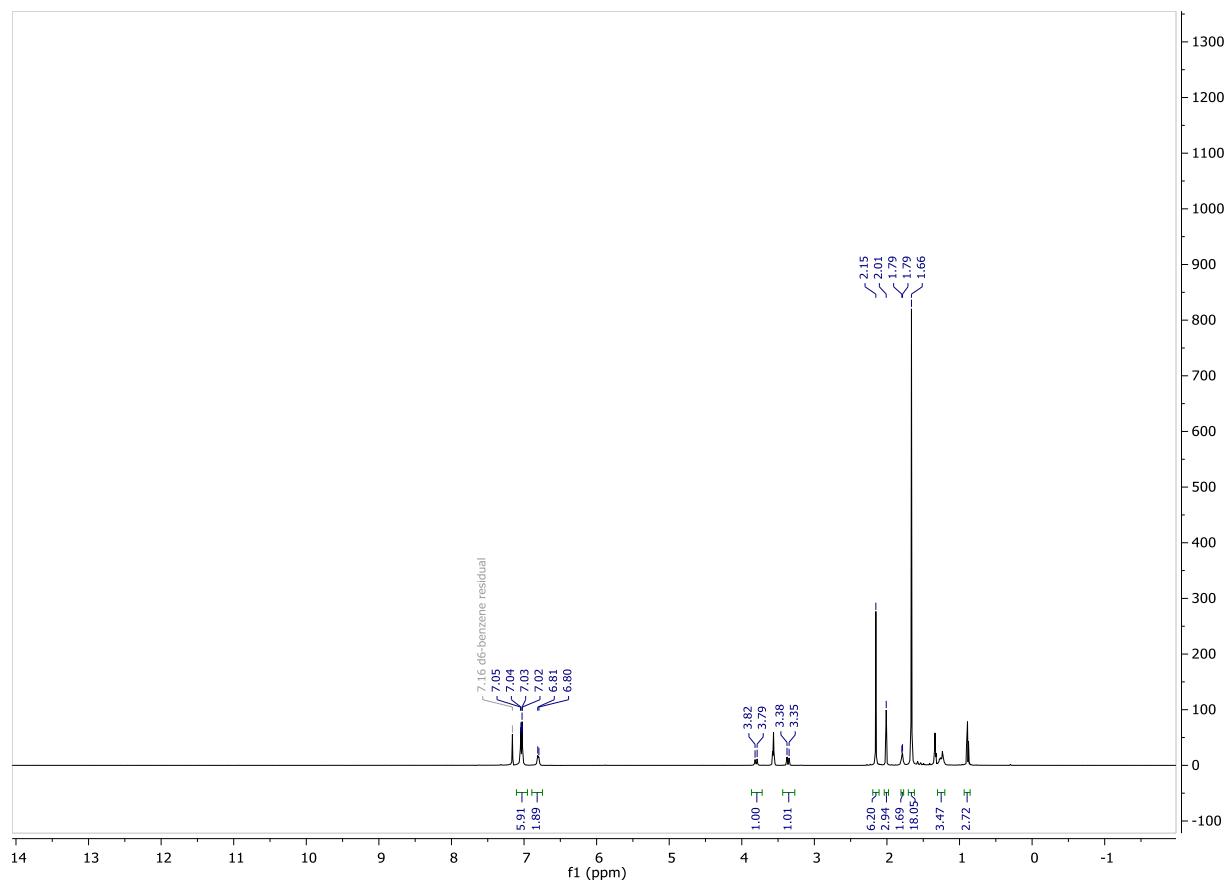


Figure 6.36 ^1H NMR of $[\text{Ti}(\text{OArCH}_2\text{ArO})(\mu\text{-Ntoly})]\cdot\text{HNMe}_2$ in C_6D_6 .

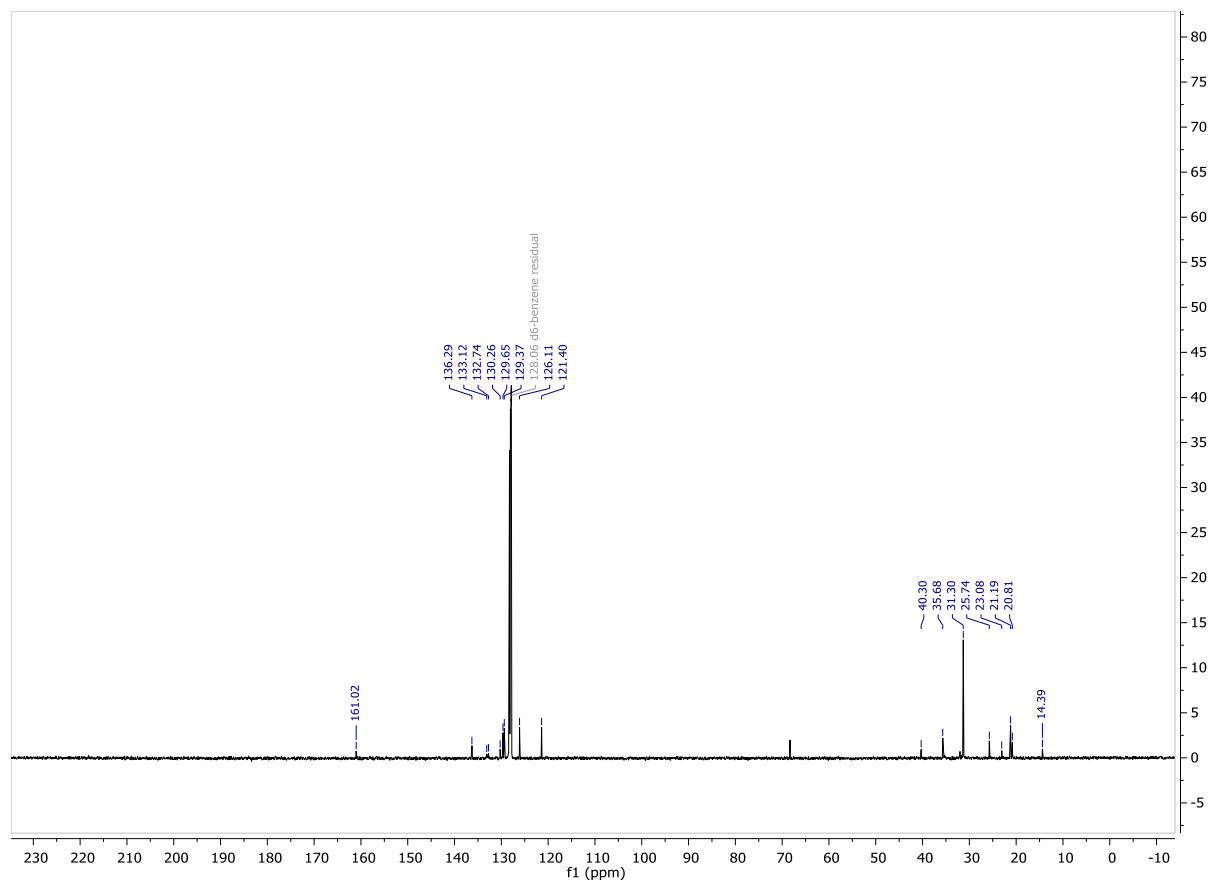


Figure 6.37 ^{13}C NMR of $[\text{Ti}(\text{OArCH}_2\text{ArO})(\mu\text{-Ntolyl})]\cdot\text{HNMe}_2$ in C_6D_6 .

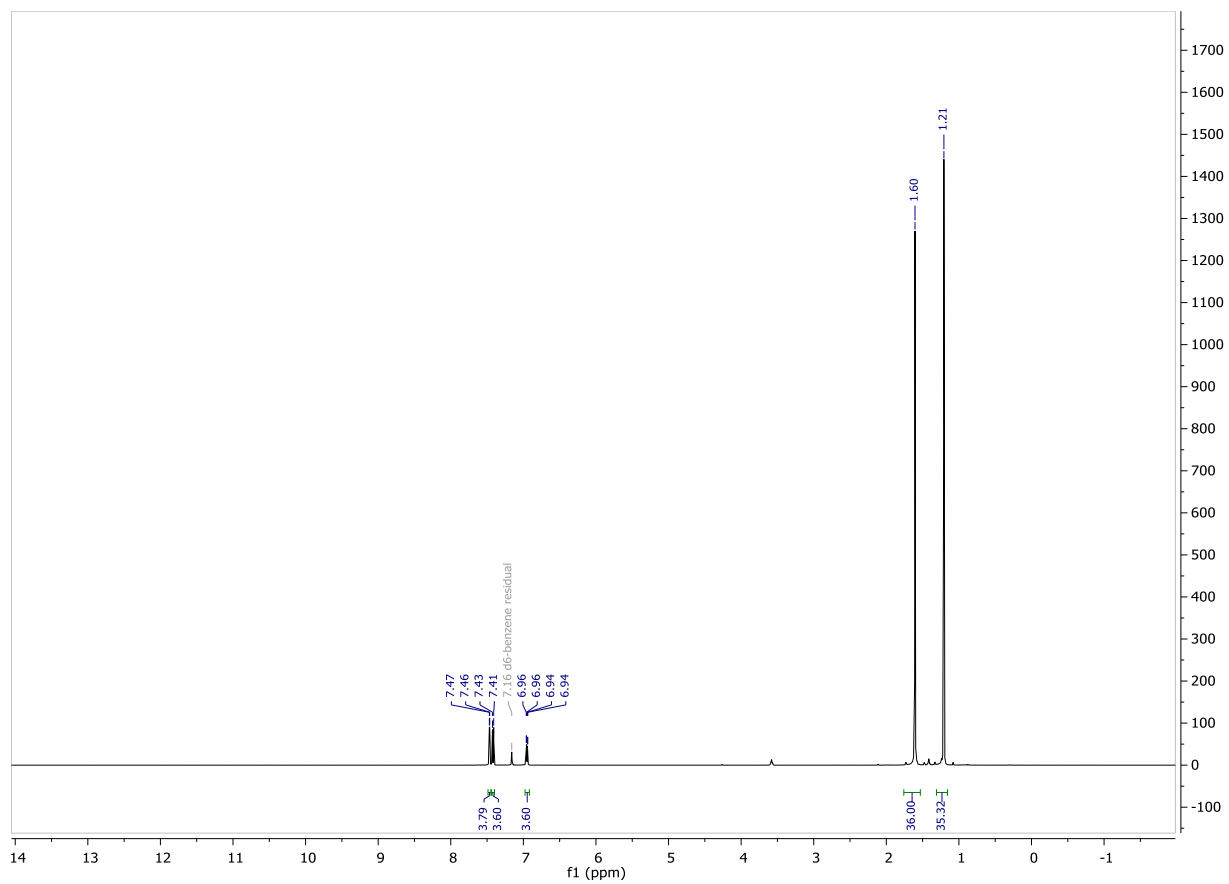


Figure 6.38 ^1H NMR of $\text{Ti}(\text{2,4-di-}i\text{-tert-butyl-phenoxy})_4$ in C_6D_6 .

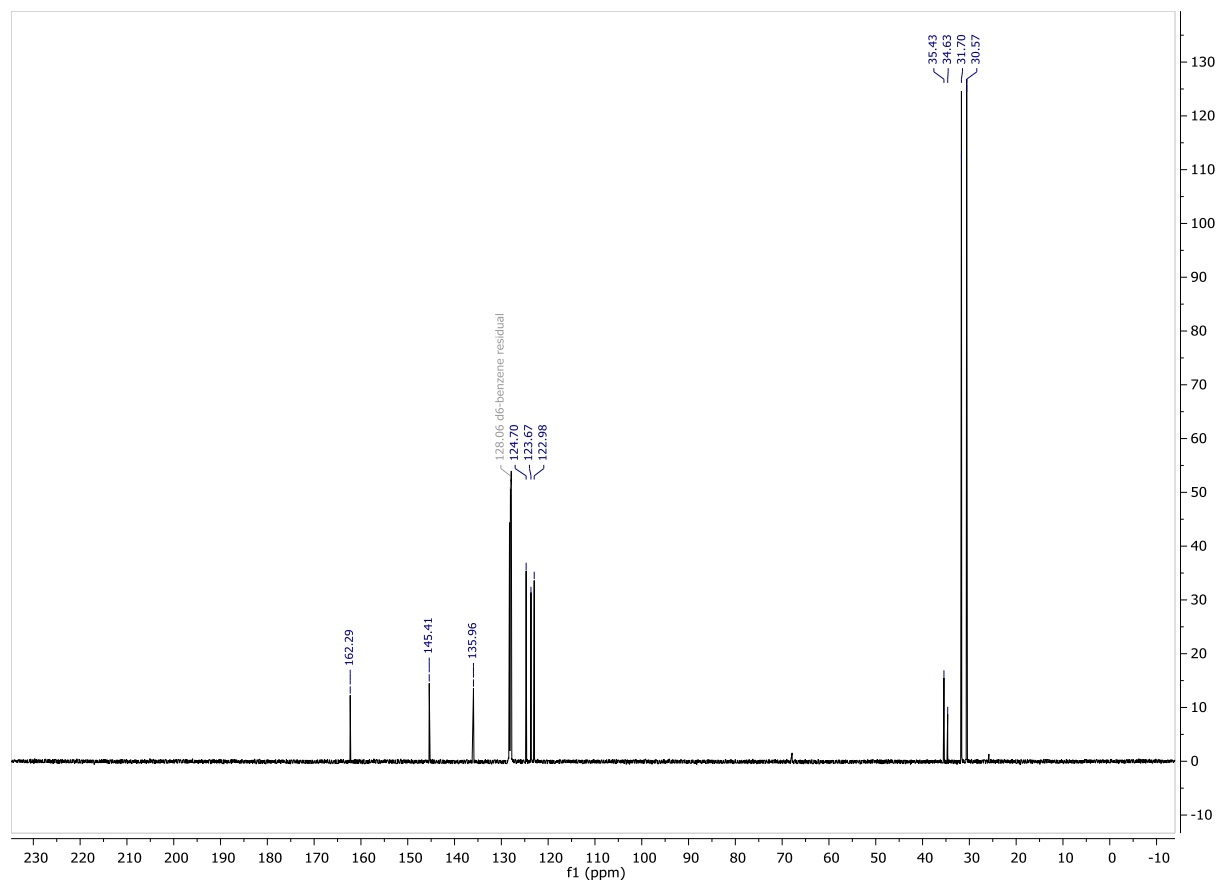


Figure 6.39 ^{13}C NMR of $\text{Ti}(\text{2,4-di-}t\text{-butyl-phenoxy})_4$ in C_6D_6 .

X-ray Structures

[Ti(dpm)(μ -Ntoly)]₂ (KA_10Dec2018)



Figure 6.40 Crystal data and structure refinement for earlyy2.

Identification code	earlyy2
Empirical formula	C ₁₈ H ₁₉ N ₃ Ti
Formula weight	325.26
Temperature/K	173.0
Crystal system	triclinic
Space group	P-1
a/Å	7.7583(3)
b/Å	9.5204(4)

$c/\text{\AA}$	11.4421(4)
$\alpha/^\circ$	70.673(2)
$\beta/^\circ$	88.342(3)
$\gamma/^\circ$	84.629(3)
Volume/ \AA^3	794.01(5)
Z	2
$\rho_{\text{calc}}/\text{g/cm}^3$	1.360
μ/mm^{-1}	4.546
F(000)	340.0
Crystal size/ mm^3	$0.381 \times 0.152 \times 0.123$
Radiation	CuK α ($\lambda = 1.54178$)
2Θ range for data collection/ $^\circ$	8.188 to 136.746
Index ranges	$-8 \leq h \leq 9, -11 \leq k \leq 10, -13 \leq l \leq 13$
Reflections collected	6753
Independent reflections	2787 [$R_{\text{int}} = 0.0877, R_{\text{sigma}} = 0.0758$]
Data/restraints/parameters	2787/0/202
Goodness-of-fit on F^2	1.015
Final R indexes [$I \geq 2\sigma(I)$]	$R_1 = 0.0613, wR_2 = 0.1527$
Final R indexes [all data]	$R_1 = 0.0734, wR_2 = 0.1604$
Largest diff. peak/hole / $e \text{\AA}^{-3}$	0.98/-0.68

[Ti(OArCH₂ArO)(μ-Ntoly)]₂·HNMe₂ (KA_04Dec2018)

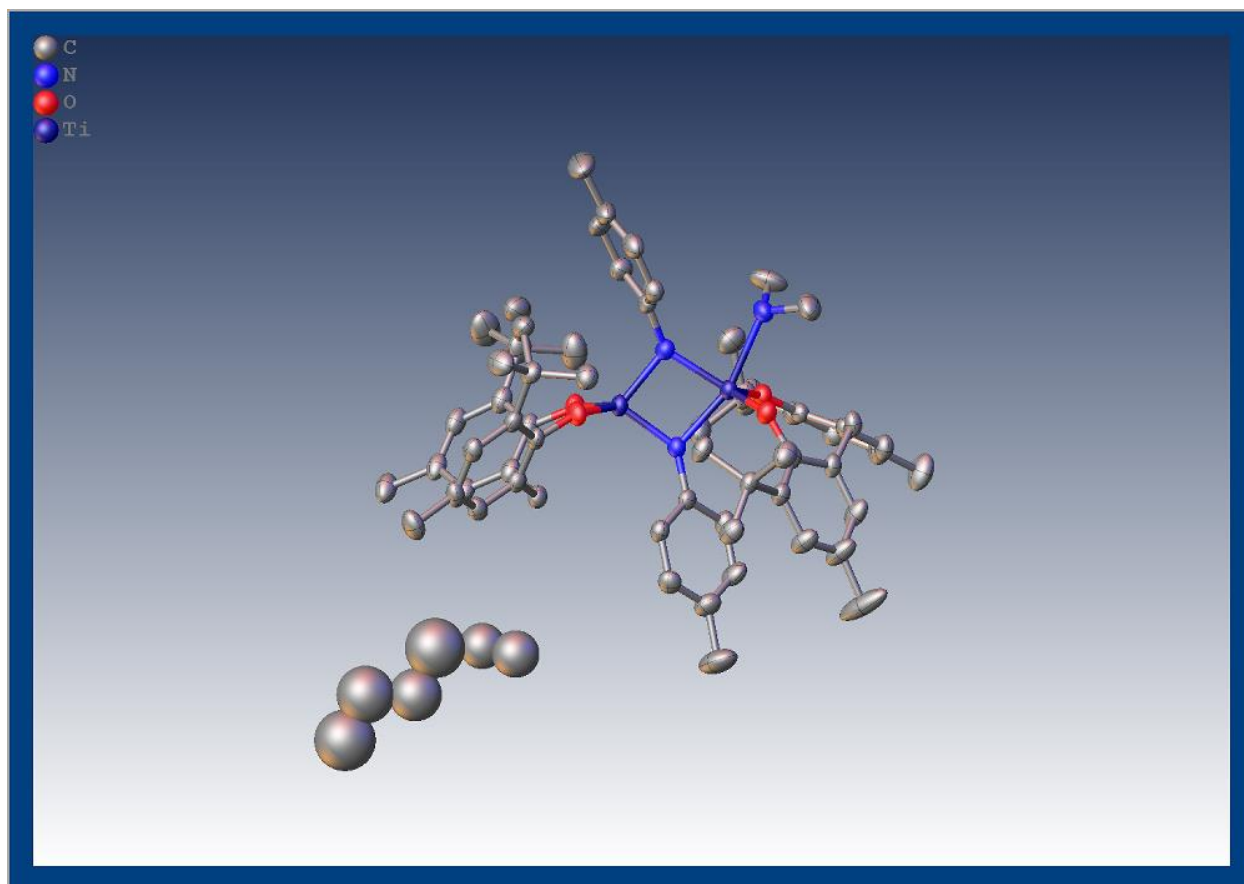


Figure 6.41 Crystal data and structure refinement for c2c_early_a.

Identification code	c2c_early_a
Empirical formula	C _{66.5} H _{91.5} N ₃ O ₄ Ti ₂
Formula weight	1092.72
Temperature/K	173.0
Crystal system	monoclinic
Space group	C2/c
a/Å	34.0256(18)
b/Å	17.3283(7)

$c/\text{\AA}$	25.5196(12)
$\alpha/^\circ$	90
$\beta/^\circ$	121.054(2)
$\gamma/^\circ$	90
Volume/ \AA^3	12890.1(11)
Z	8
$\rho_{\text{calc}}/\text{g/cm}^3$	1.126
μ/mm^{-1}	2.456
F(000)	4700.0
Crystal size/ mm^3	$0.223 \times 0.205 \times 0.16$
Radiation	CuK α ($\lambda = 1.54178$)
2Θ range for data collection/ $^\circ$	5.934 to 136.488
Index ranges	$-40 \leq h \leq 40, -20 \leq k \leq 18, -30 \leq l \leq 30$
Reflections collected	83770
Independent reflections	11770 [$R_{\text{int}} = 0.1037, R_{\text{sigma}} = 0.0513$]
Data/restraints/parameters	11770/14/686
Goodness-of-fit on F^2	1.030
Final R indexes [$I \geq 2\sigma(I)$]	$R_1 = 0.0570, wR_2 = 0.1488$
Final R indexes [all data]	$R_1 = 0.0881, wR_2 = 0.1693$
Largest diff. peak/hole / $e \text{\AA}^{-3}$	0.84/-0.33

Ti(OArCH₂ArO)₂ (KA_06Dec2018CU)

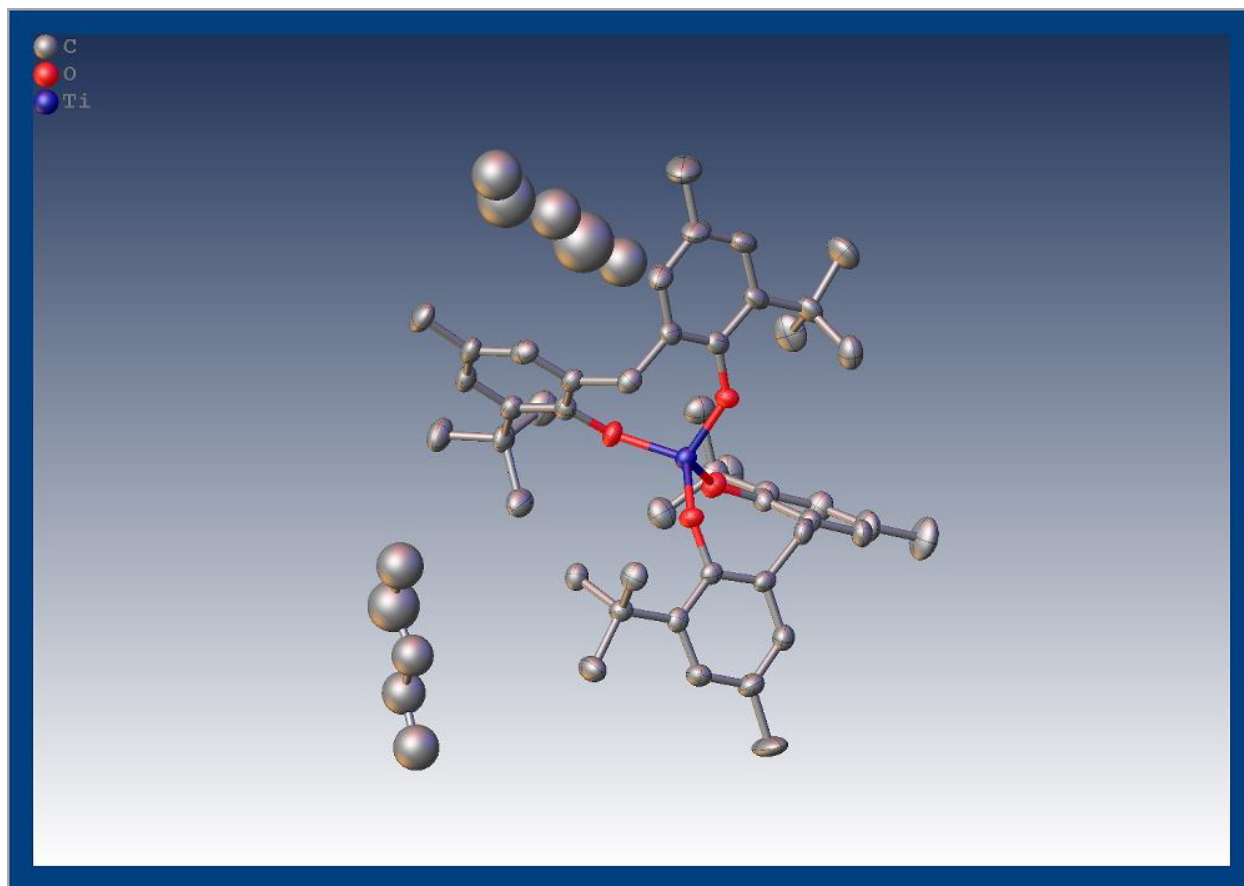


Figure 6.42 Crystal data and structure refinement for p21_c_a.

Identification code	p21_c_a
Empirical formula	C _{35.67} H ₅₂ O _{2.67} Ti _{0.67}
Formula weight	555.37
Temperature/K	173.0
Crystal system	monoclinic
Space group	P2 ₁ /c
a/Å	12.9534(4)
b/Å	21.2798(5)

$c/\text{\AA}$	19.3799(4)
$\alpha/^\circ$	90
$\beta/^\circ$	98.805(2)
$\gamma/^\circ$	90
Volume/ \AA^3	5279.0(2)
Z	6
$\rho_{\text{calc}}/\text{g/cm}^3$	1.048
μ/mm^{-1}	1.665
F(000)	1812.0
Crystal size/ mm^3	$0.193 \times 0.154 \times 0.121$
Radiation	CuK α ($\lambda = 1.54178$)
2Θ range for data collection/ $^\circ$	6.208 to 136.882
Index ranges	$-14 \leq h \leq 15, -25 \leq k \leq 25, -23 \leq l \leq 23$
Reflections collected	29162
Independent reflections	9481 [$R_{\text{int}} = 0.1607, R_{\text{sigma}} = 0.1945$]
Data/restraints/parameters	9481/0/520
Goodness-of-fit on F^2	0.896
Final R indexes [$I \geq 2\sigma(I)$]	$R_1 = 0.0796, wR_2 = 0.1959$
Final R indexes [all data]	$R_1 = 0.1801, wR_2 = 0.2407$
Largest diff. peak/hole / $e \text{\AA}^{-3}$	0.83/-0.32

[Ti(OArCH₂ArO)(OⁱPr)(μ-OⁱPr)]₂ (KA_22Dec218)

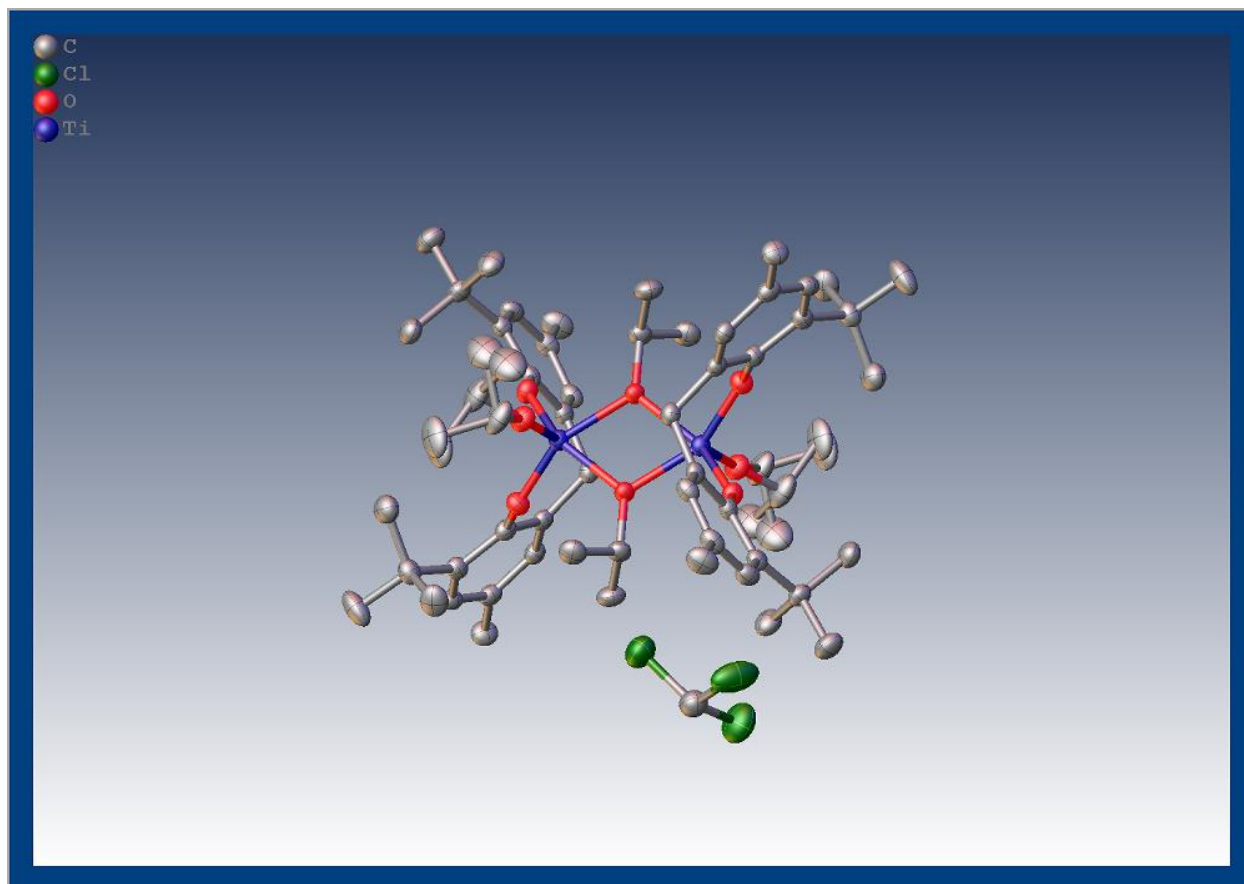


Figure 6.43 Crystal data and structure refinement for rjs.

Identification code	rjs
Empirical formula	C ₃₀ H ₄₅ Cl ₃ O ₄ Ti
Formula weight	623.91
Temperature/K	173.01
Crystal system	triclinic
Space group	P-1
a/Å	11.57250(10)
b/Å	12.38990(10)

$c/\text{\AA}$	13.0612(2)
$\alpha/^\circ$	67.6580(10)
$\beta/^\circ$	80.5460(10)
$\gamma/^\circ$	66.6990(10)
Volume/ \AA^3	1590.67(3)
Z	2
$\rho_{\text{calc}}/\text{g/cm}^3$	1.303
μ/mm^{-1}	4.849
F(000)	660.0
Crystal size/ mm^3	$0.21 \times 0.141 \times 0.107$
Radiation	CuK α ($\lambda = 1.54178$)
2Θ range for data collection/ $^\circ$	7.318 to 136.352
Index ranges	$-13 \leq h \leq 13, -14 \leq k \leq 14, -13 \leq l \leq 15$
Reflections collected	20754
Independent reflections	5629 [$R_{\text{int}} = 0.0697, R_{\text{sigma}} = 0.0519$]
Data/restraints/parameters	5629/6/367
Goodness-of-fit on F^2	1.065
Final R indexes [$I \geq 2\sigma(I)$]	$R_1 = 0.0509, wR_2 = 0.1339$
Final R indexes [all data]	$R_1 = 0.0738, wR_2 = 0.1479$
Largest diff. peak/hole / $e \text{\AA}^{-3}$	0.41/-0.54

Ti(2,4-di-*tert*-butyl-phenoxide)₄ (KA_14Dec2018)

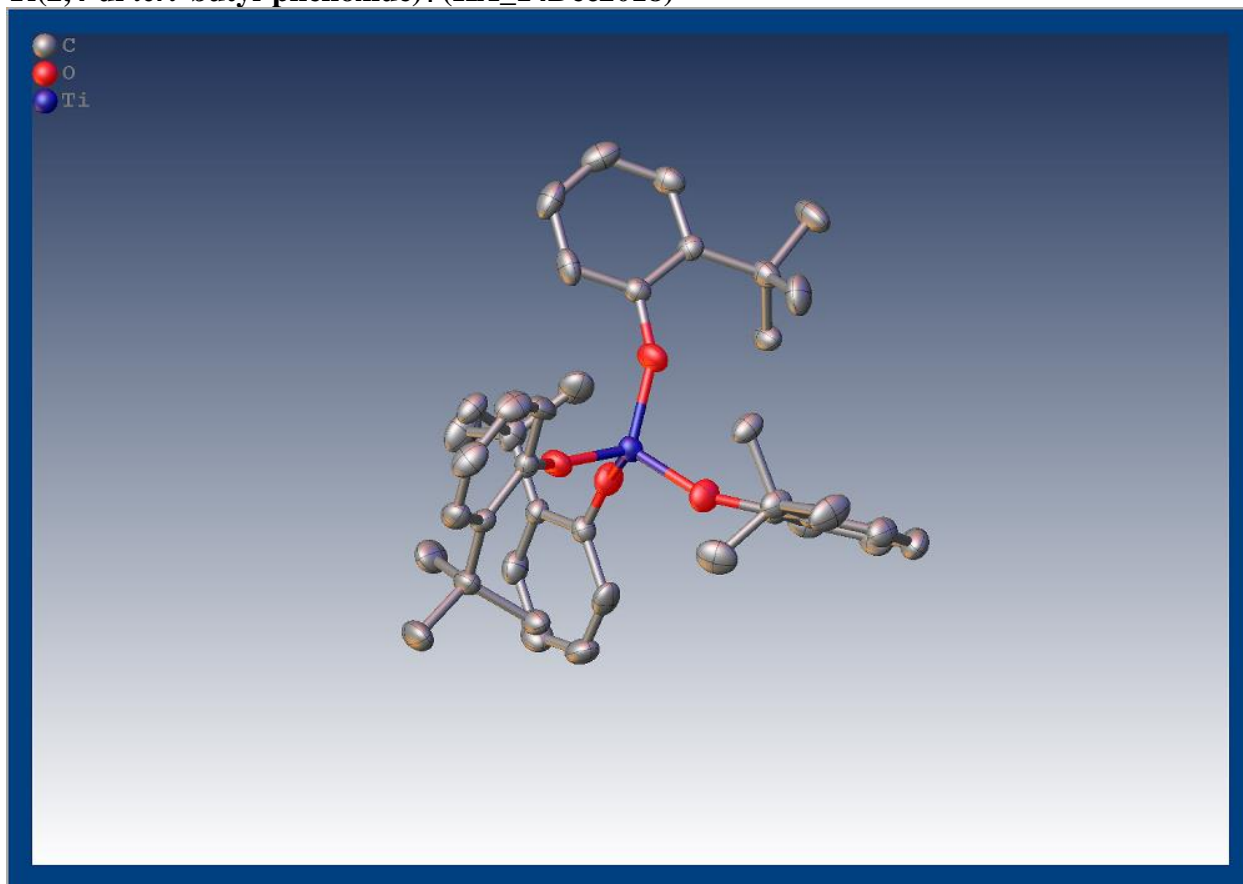


Figure 6.44 Crystal data and structure refinement for uc_a.

Identification code	uc_a
Empirical formula	C ₅₆ H ₈₄ O ₄ Ti
Formula weight	869.13
Temperature/K	172.99
Crystal system	tetragonal
Space group	P-42 ₁ c
a/Å	12.3120(3)
b/Å	12.3120(3)
c/Å	17.7572(8)

$\alpha/^\circ$	90
$\beta/^\circ$	90
$\gamma/^\circ$	90
Volume/ \AA^3	2691.73(18)
Z	2
$\rho_{\text{calc}}/\text{g}/\text{cm}^3$	1.072
μ/mm^{-1}	1.650
F(000)	948.0
Crystal size/ mm^3	$0.315 \times 0.21 \times 0.2$
Radiation	CuK α ($\lambda = 1.54178$)
2 Θ range for data collection/ $^\circ$ 8.74 to 136.512	
Index ranges	$-12 \leq h \leq 14, -14 \leq k \leq 9, -19 \leq l \leq 21$
Reflections collected	9325
Independent reflections	2462 [$R_{\text{int}} = 0.0433, R_{\text{sigma}} = 0.0539$]
Data/restraints/parameters	2462/0/144
Goodness-of-fit on F^2	1.022
Final R indexes [$I \geq 2\sigma(I)$]	$R_1 = 0.0350, wR_2 = 0.0846$
Final R indexes [all data]	$R_1 = 0.0397, wR_2 = 0.0869$
Largest diff. peak/hole / $e \text{\AA}^{-3}$	0.13/-0.39
Flack parameter	0.019(6)

Ti(OArCH₂ArO)₂ (KA_25Jan2019)

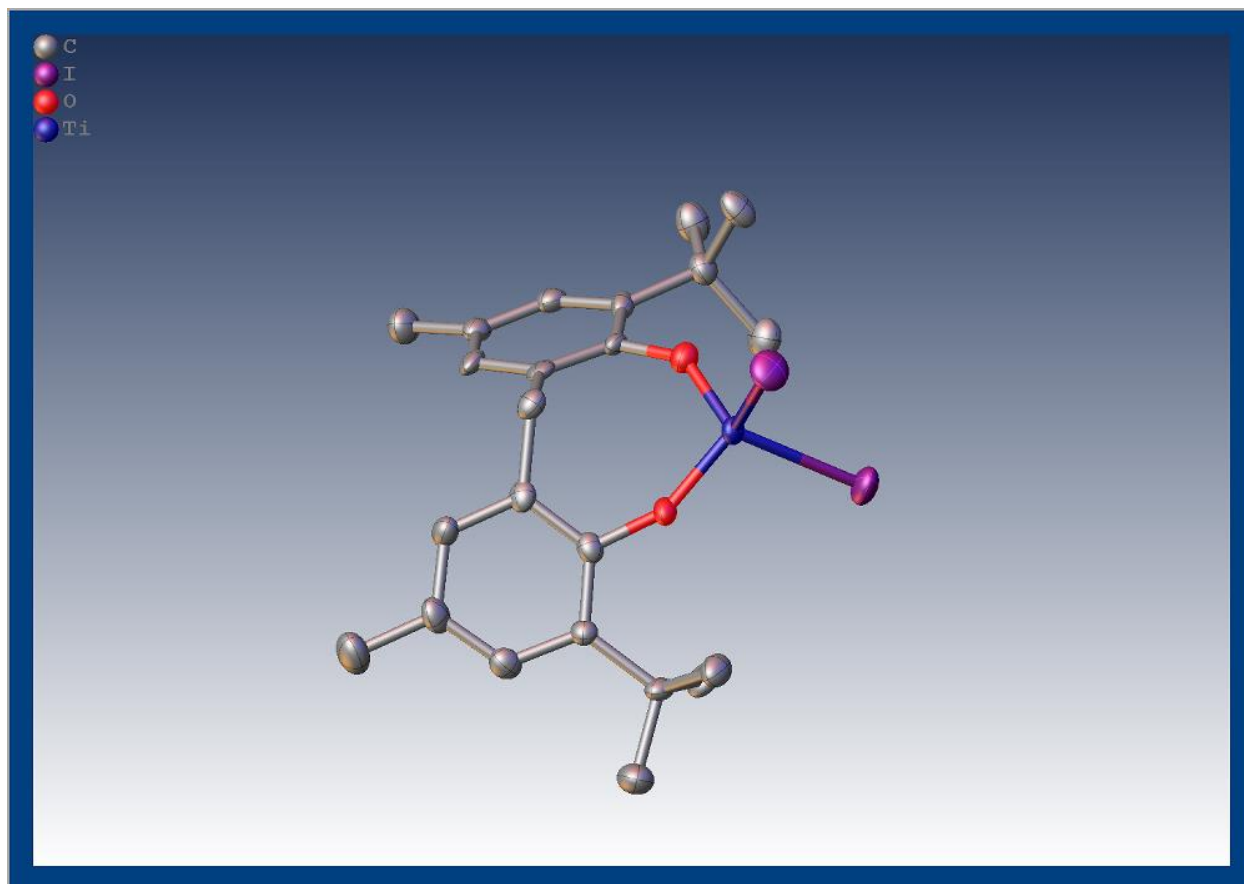


Figure 6.45 Crystal data and structure refinement for early_a.

Identification code	early_a
Empirical formula	C ₂₆ H ₄₀ O ₂ TiI ₂
Formula weight	640.17
Temperature/K	173.0
Crystal system	triclinic
Space group	P-1
a/Å	9.6900(10)
b/Å	9.8844(13)

$c/\text{\AA}$	13.151(2)
$\alpha/^\circ$	90.518(7)
$\beta/^\circ$	92.411(5)
$\gamma/^\circ$	95.161(4)
Volume/ \AA^3	1253.3(3)
Z	2
$\rho_{\text{calc}}/\text{g/cm}^3$	1.6963
μ/mm^{-1}	22.342
F(000)	625.6
Crystal size/ mm^3	$0.161 \times 0.157 \times 0.064$
Radiation	Cu K α ($\lambda = 1.54178$)
2Θ range for data collection/ $^\circ$	8.98 to 136.3
Index ranges	$-11 \leq h \leq 11, -11 \leq k \leq 11, -14 \leq l \leq 15$
Reflections collected	15520
Independent reflections	4410 [$R_{\text{int}} = 0.1065, R_{\text{sigma}} = 0.0869$]
Data/restraints/parameters	4410/0/261
Goodness-of-fit on F^2	1.028
Final R indexes [$I \geq 2\sigma(I)$]	$R_1 = 0.0521, wR_2 = 0.1228$
Final R indexes [all data]	$R_1 = 0.0767, wR_2 = 0.1366$
Largest diff. peak/hole / $e \text{\AA}^{-3}$	1.38/-1.39

Note: an X-ray crystal structure of the $\text{Ti}(\text{Cl})_2(\text{OArCH}_2\text{ArO})$ has been previously reported. Single crystals were grown and examined by X-ray diffraction, providing a matching unit cell to the previous report. The species is monomeric in the solid state.

¹H DOSY NMR Molecular Weight Calibrations

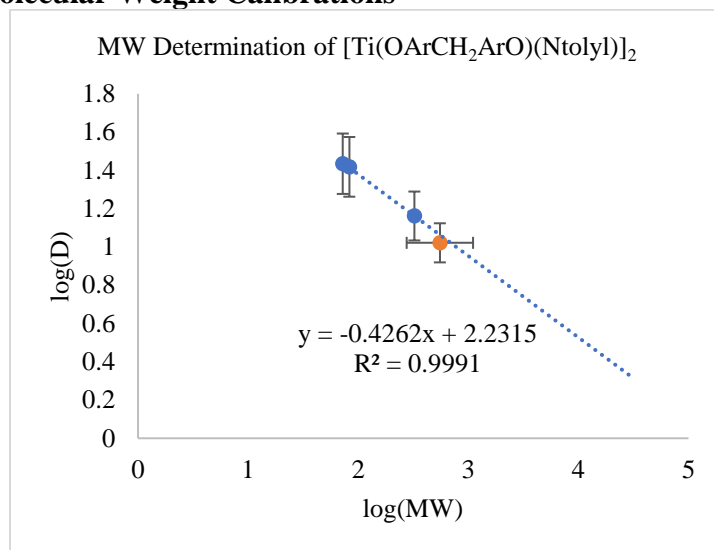


Figure 6.46 DOSY MW determination for $[\text{Ti}(\text{OArCH}_2\text{ArO})(\mu\text{-Ntoly})]_x \cdot 1/2 \text{NHMe}_2$ in C_6D_6 .

Table 6.5 Experimentally determined diffusion coefficients (D) and calculated MW for Ti species for $[\text{Ti}(\text{OArCH}_2\text{ArO})(\mu\text{-Ntoly})]_x \cdot 1/2 \text{NHMe}_2$ in C_6D_6 .

Compound	MW (g/mol)	Log(MW)	D	Log(D)
THF	72	1.86	27.2	1.45
Benzene	83	1.92	26.2	1.41
TMS ₄ Si	321	2.51	14.5	1.12
$[\text{Ti}(\text{Ntoly})(\text{OArCH}_2\text{ArO})]_x$	551 (± 62)	2.74	10.5	1.02

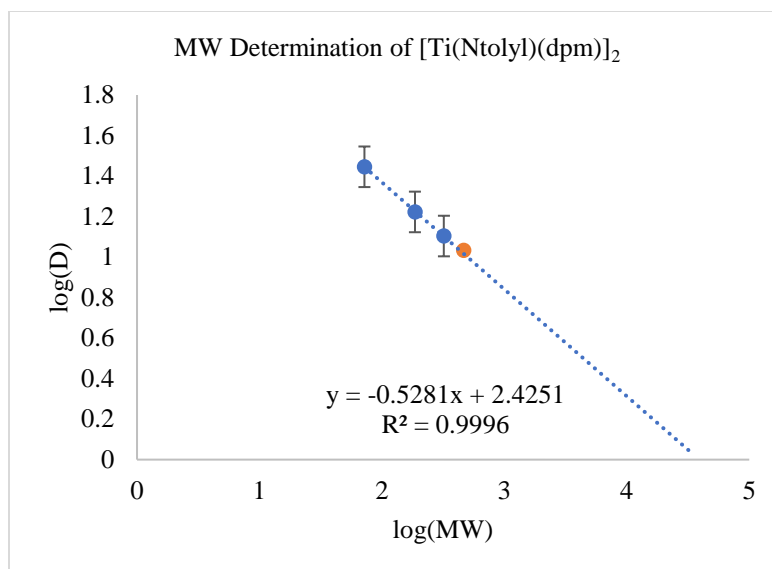


Figure 6.47 DOSY MW determination for $[\text{Ti}(\text{dpm})(\mu\text{-Ntoly})]_x$ in C_6D_6 .

Table 6.6 Experimental determination of diffusion coefficients (D) and calculated MW for Ti species for $[\text{Ti}(\text{dpm})(\mu\text{-Ntoly})]_x$ in C_6D_6 .

Compound	MW (g/mol)	Log(MW)	D	log(D)
bnz	72	1.86	27.9	1.45
Fc	186	2.27	16.7	1.22
TMS ₄ Si	321	2.51	12.7	1.10
$[\text{Ti}(\text{dpm})(\text{Ntoly})]_n$	465 (± 51)	2.67	10.8	1.03

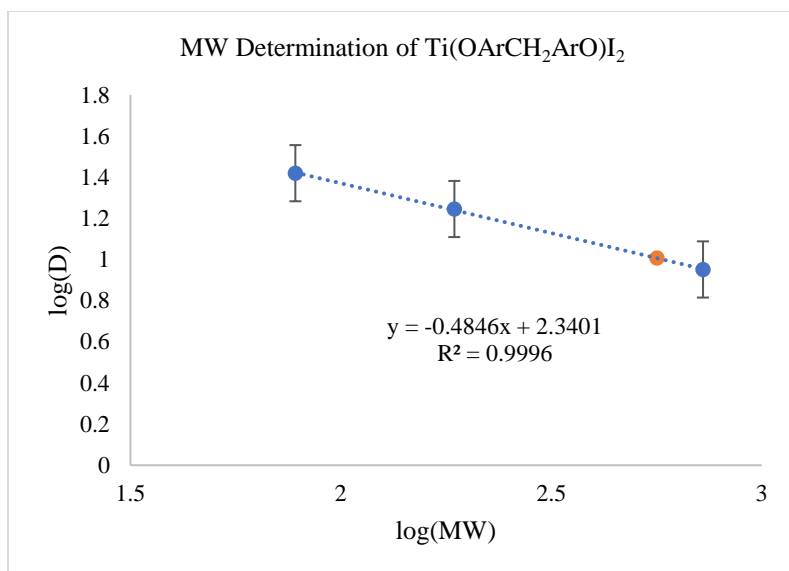


Figure 6.48 DOSY MW determination of $\text{Ti}(\text{OArCH}_2\text{ArO})\text{I}_2$ in C_6D_6 .

Table 6.7 Experimentally determined diffusion coefficients (D) and calculated MW for the Ti species for $\text{Ti}(\text{OArCH}_2\text{ArO})\text{I}_2$ in C_6D_6 .

compound	MW	log(MW)	D	log(D)	Error
Fc	186.04	2.269606	17.61	1.245759	0.25
$\text{C}_6\text{D}_5\text{H}$	78	1.892095	26.29	1.419791	0.58
$\text{Ti}(\text{OArArO})_2$	724.85	2.860248	8.95	0.951823	0.81
$\text{Ti}(\text{OArARrO})\text{I}_2$	563 (±94)	2.750929	10.16	1.006894	0.2
Real monomer weight	638				

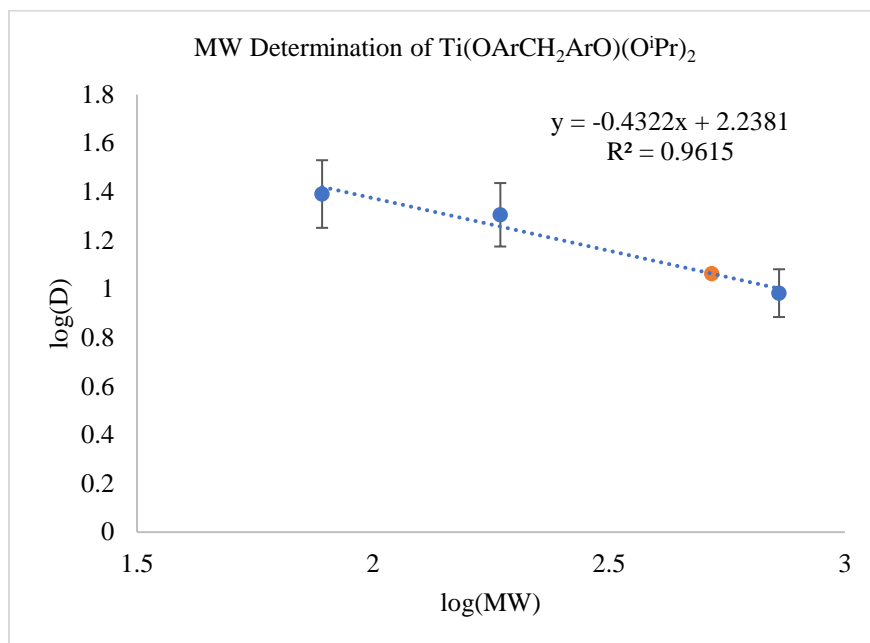


Figure 6.49 DOSY MW determination of $\text{Ti}(\text{OArCH}_2\text{ArO})(\text{O}^i\text{Pr})_2$ complex in C_6D_6 .

Table 6.8 Experimentally determined diffusion coefficients (D) and calculated MW of the Ti species for $\text{Ti}(\text{OArCH}_2\text{ArO})(\text{O}^i\text{Pr})_2$ complex in C_6D_6 .

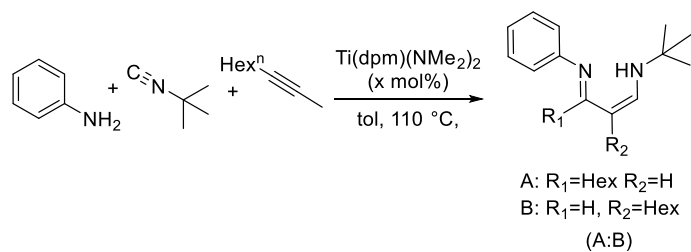
compound	MW	log(MW)	D	log (D)	Error
Fc	186.04	2.269606	20.21	1.305566	0.76
$\text{C}_6\text{D}_5\text{H}$	78	1.892095	24.6	1.390935	0.76
$\text{Ti}(\text{OArCH}_2\text{ArO})_2$	724.85	2.860248	9.62	0.983175	1.4
$\text{Ti}(\text{OArCH}_2\text{ArO})(\text{O}^i\text{Pr})_2$	522.62 (± 74)	2.718186	11.57	1.063333	0.33
Real monomer weight	504				

Kinetic Analysis for Homogeneous Ti(dpm)(NMe₂)₂ Catalyzed Rate Law:

For each set of kinetics conditions examined to determine the rate law, the following general procedure was applied. The specific conditions for each run are listed in Table 1 above.

General Procedure: The following reagents were measured separately by mass: (1) Ti(dpm)(NMe₂)₂ (78-312 mg, 5-20 mol%), (2) dodecane (212 mg, 1.25 mmol, 0.05 M), (3) H₂NPh (465 mg-2.32 g, 5-25 mmol), (4) ¹BuNC (415-830 mg, 5-10 mmol), and (5) 1-octyne (550 mg-2.75 g, 5-25 mmol). In a scintillation vial, the Ti(dpm)(NMe₂)₂ was dissolved in 5 mL toluene, and the dodecane and H₂NPh were added to this solution, causing the solution to change colors from bright orange to dark reddish brown. This solution was stirred at room temperature for 5-10 min and transferred to a 25.0 mL volumetric flask. The ¹BuNC and 1-octyne were added to the flask, and the solution was diluted to 25.0 mL with toluene. This solution was thoroughly mixed and transferred in 1 mL aliquots to sample tubes (generally 10-12 per entry). The tubes were sealed and transferred from the glovebox to a preheated oil bath. The elapsed time from the start of the reaction was recorded each time a sample was removed for GC analysis, ranging from 30 min to 28 h.

The samples were analyzed by GC-MS to look for reaction products and detection of unwanted side products. GC-FID was used to quantify the amounts of 3CC, HA, and FA or 4CC production in each sample based on external calibrations standardized with internal dodecane (0.05 M) from the authentic isolated products, obtained by separation from the organic reaction mixtures. The concentrations of products were used in the graphical analysis of the order of each reactant.¹³



Scheme 6.9 Iminoamination reaction examined under different reaction conditions to probe the rate law and suggest optimal reaction conditions.

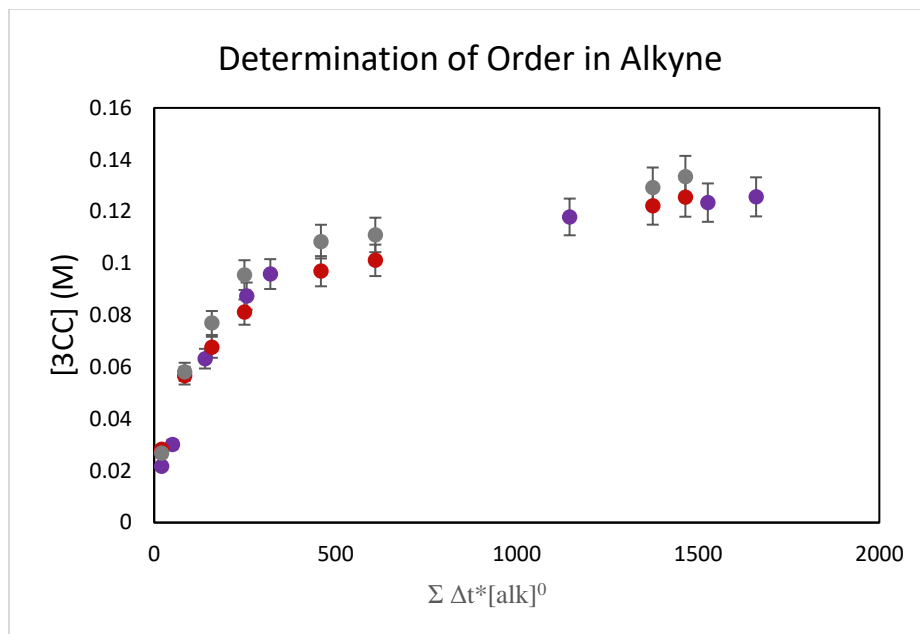


Figure 6.50 The graphical determination of reaction rate dependence on alkyne concentration. Purple spheres = 0.2 M (Entry 3); Red spheres = 1.0 M (Entry 4); Grey spheres = 0.4 M (Entry 5).

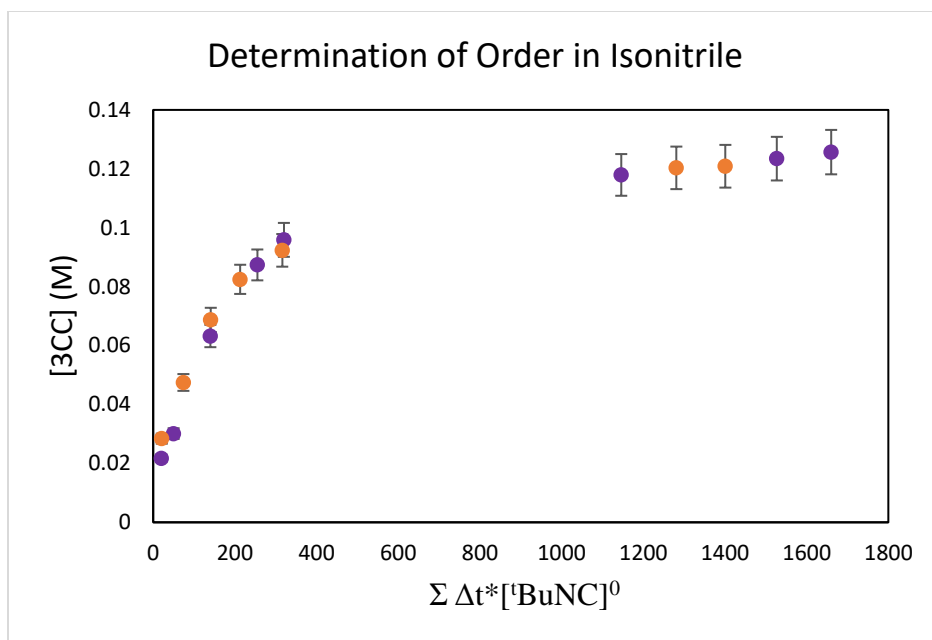


Figure 6.51 The graphical determination of reaction rate dependence on isonitrile concentration. Purple spheres = 0.2 M (Entry 3); Orange spheres = 0.4 M (Entry 6).

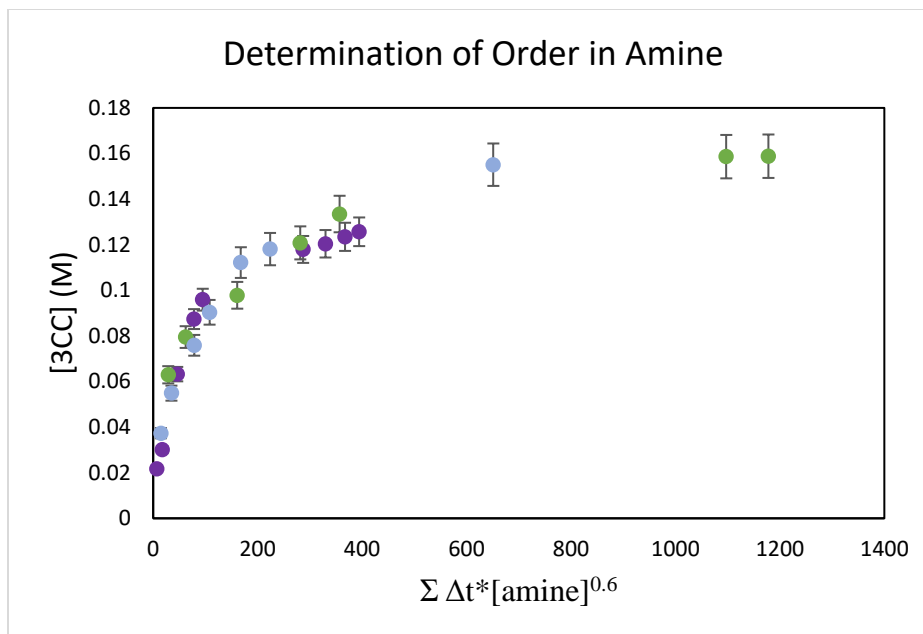


Figure 6.52 The graphical determination of reaction rate dependence on amine concentration. Purple spheres = 0.2 M (Entry 3); light blue spheres = 0.4 M (Entry 7); Green spheres = 1.0 M (Entry 8).

Kinetic analysis of $\text{Ti}(\text{OArCH}_2\text{ArO})(\text{NMe}_2)_2$ catalyzed Iminoamination:

The general kinetic analysis procedure was applied, using the reaction conditions described for Entry 3 above (Table 1). The figures below show a side-by-side comparison of the reaction results with $\text{Ti}(\text{dpm})(\text{NMe}_2)_2$ catalyst,

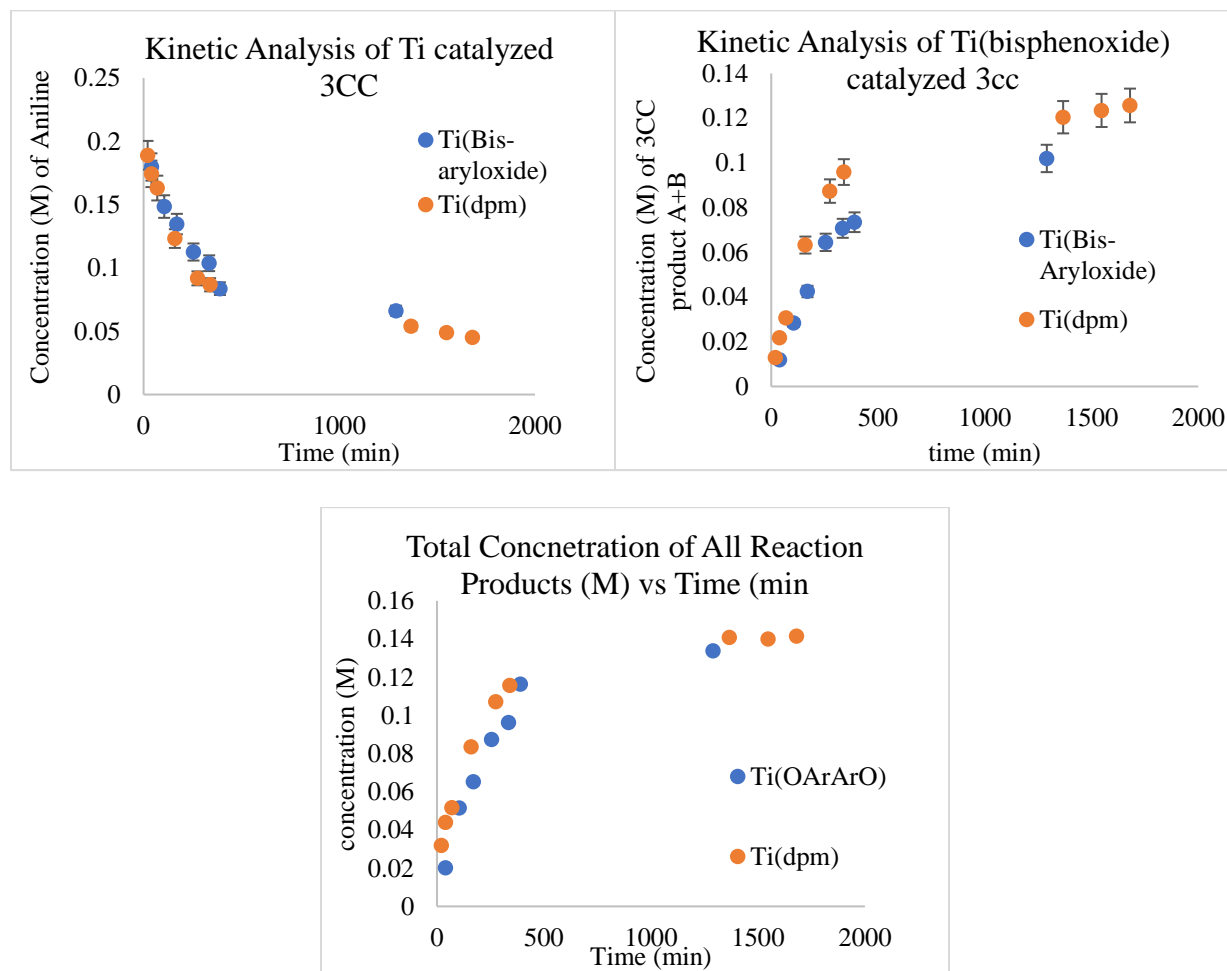


Figure 6.53 Reaction progress of two identical kinetics trials run with $\text{Ti}(\text{dpm})(\text{NMe}_2)_2$ and $\text{Ti}(\text{OArCH}_2\text{ArO})(\text{NMe}_2)_2$. Similar results were obtained with both catalysts under the conditions used for kinetics despite better performance of the $\text{Ti}(\text{OArCH}_2\text{ArO})(\text{NMe}_2)_2$ under normal conditions applied to a typical iminoamination reaction.

K_{eq} determination by ¹H NMR:

The determination of the K_{eq} values for the ligand exchange reactions, of the general form shown in Fig. 6.54 below, were performed by monitoring the concentrations of the 3 species in solution by ¹H NMR. Solutions were prepared in C₆D₆ on the order of 0.025-0.05 M (in titanium). Ferrocene was included as an internal standard. Due to the long T₁ of ferrocene (~30 s) in deoxygenated NMR solvents, the NMR experiments were performed differently from the standard ¹H NMR experiments with d1=150 and gain = 30. The solutions were examined every few days until the integral values of the species in solution had stopped changing.

Once the solution concentrations of the species of interest had leveled off, 3 spectra were taken and averaged. From these triplicate measurements, an error could be assigned to the K_{eq} values calculated, as they will be affected by the error of manual integration in the ¹H NMR. For the following X ligands, the equilibrium processes were initiated from the heteroleptic Ti(X)₂(OArCH₂ArO) species: I⁻, Cl⁻, (OⁱPr)⁻, and (NMe₂)⁻. The Ti(OAr)₂(OArCH₂ArO) species typically begin the ligand exchange processes during isolation from the crude reaction mixture and therefore cannot be isolated free of impurities. For the ligand exchange reactions with the various 2-*tert*-butyl-4-R-phenoxy ligands, the equilibrium exchange process was initiated from the two homoleptic species Ti(OAr)₄ and Ti(OArCH₂ArO)₂ added in equivalent molar amounts to the initial solution.

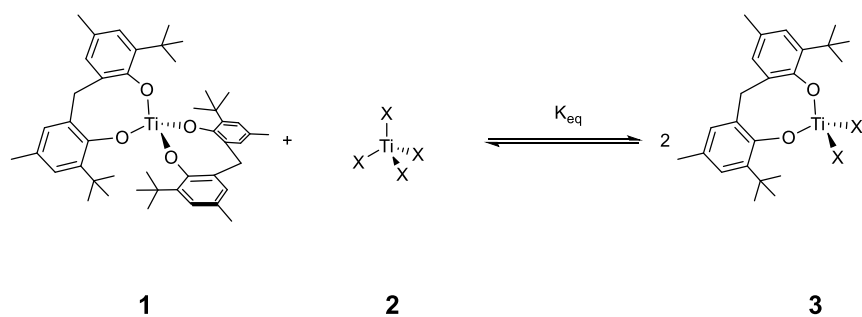


Figure 6.54 Equilibrium ligand exchange reaction used to determine K_{eq} experimentally. For reactions where K_{eq} is small, starting materials 1 and 2 were used. For reactions where K_{eq} was large, 3 could be prepared and isolated cleanly and was utilized in these experiments.

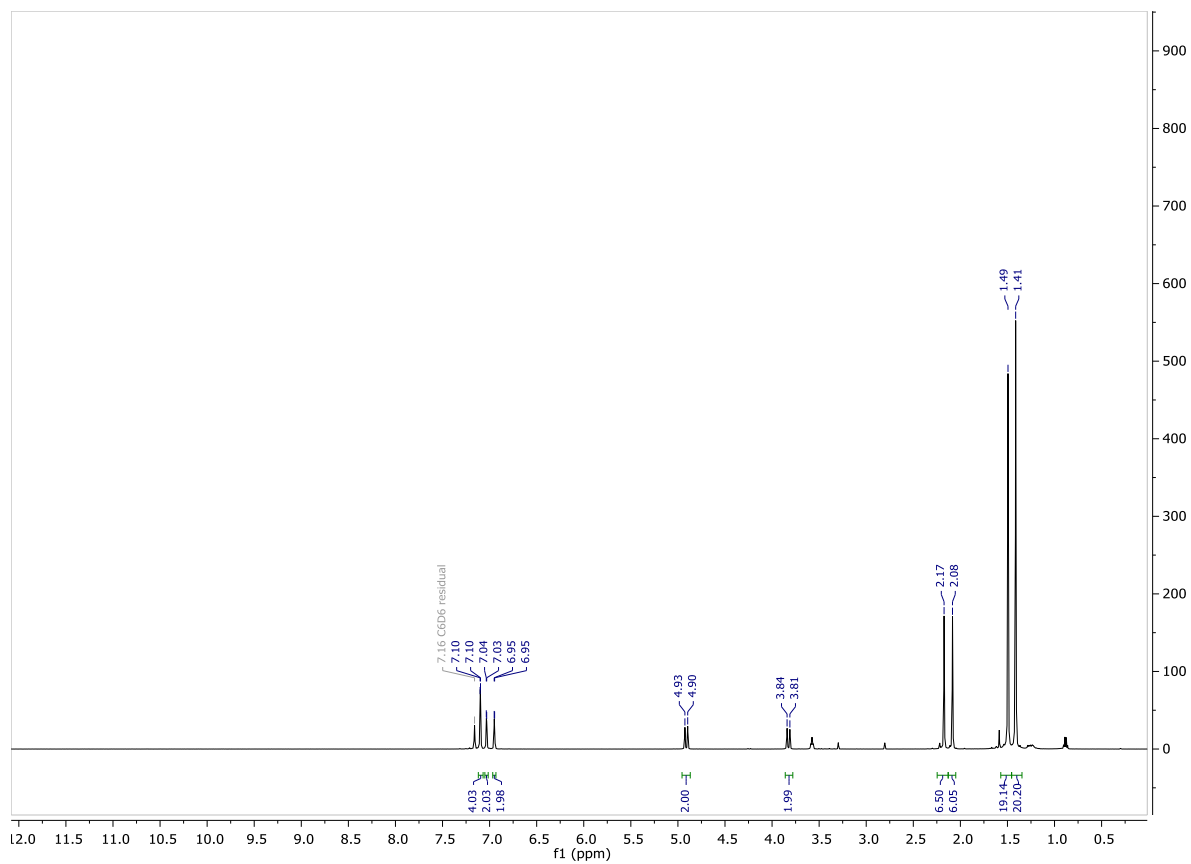


Figure 6.55 ^1H NMR of $\text{Ti}(\text{OArCH}_2\text{ArO})_2$ in C_6D_6 .

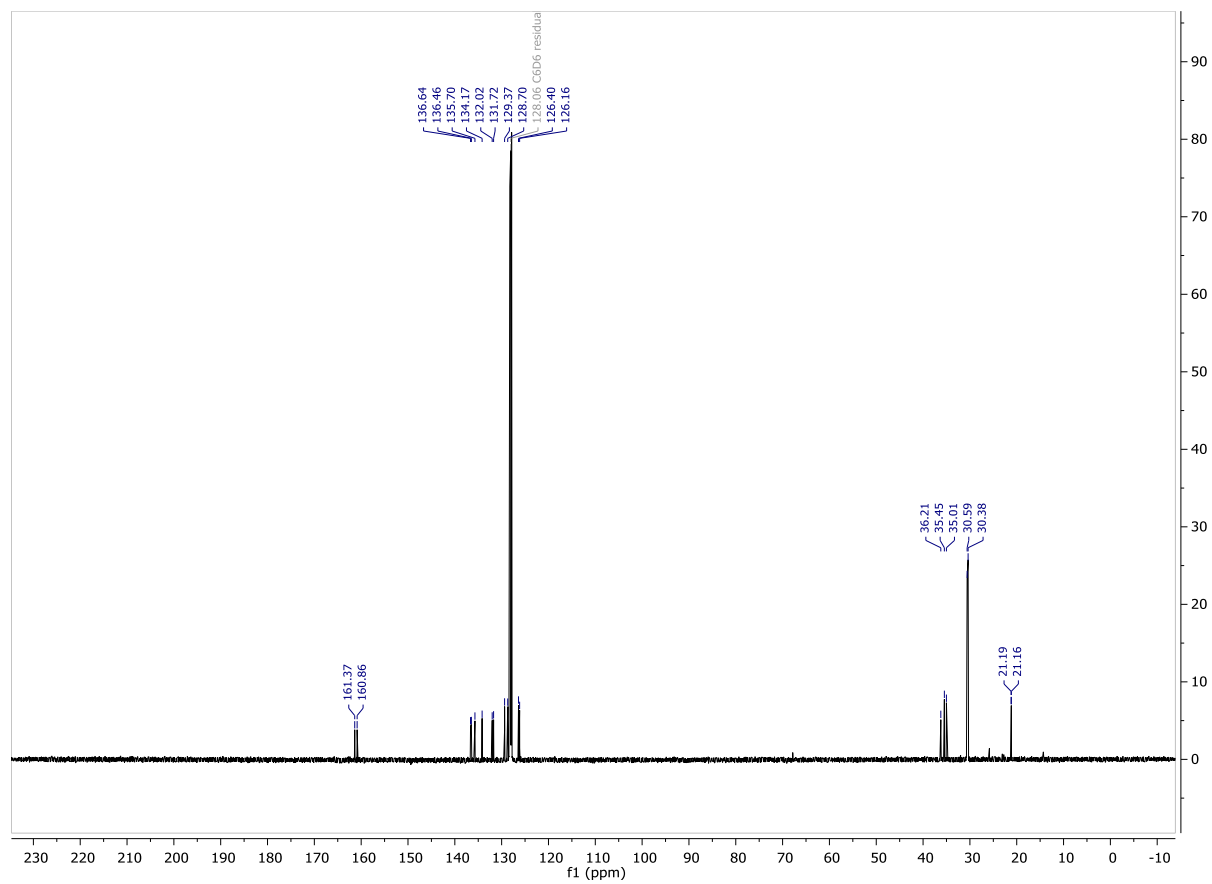


Figure 6.56 ^{13}C NMR of $\text{Ti}(\text{OArCH}_2\text{ArO})_2$ in C_6D_6 .

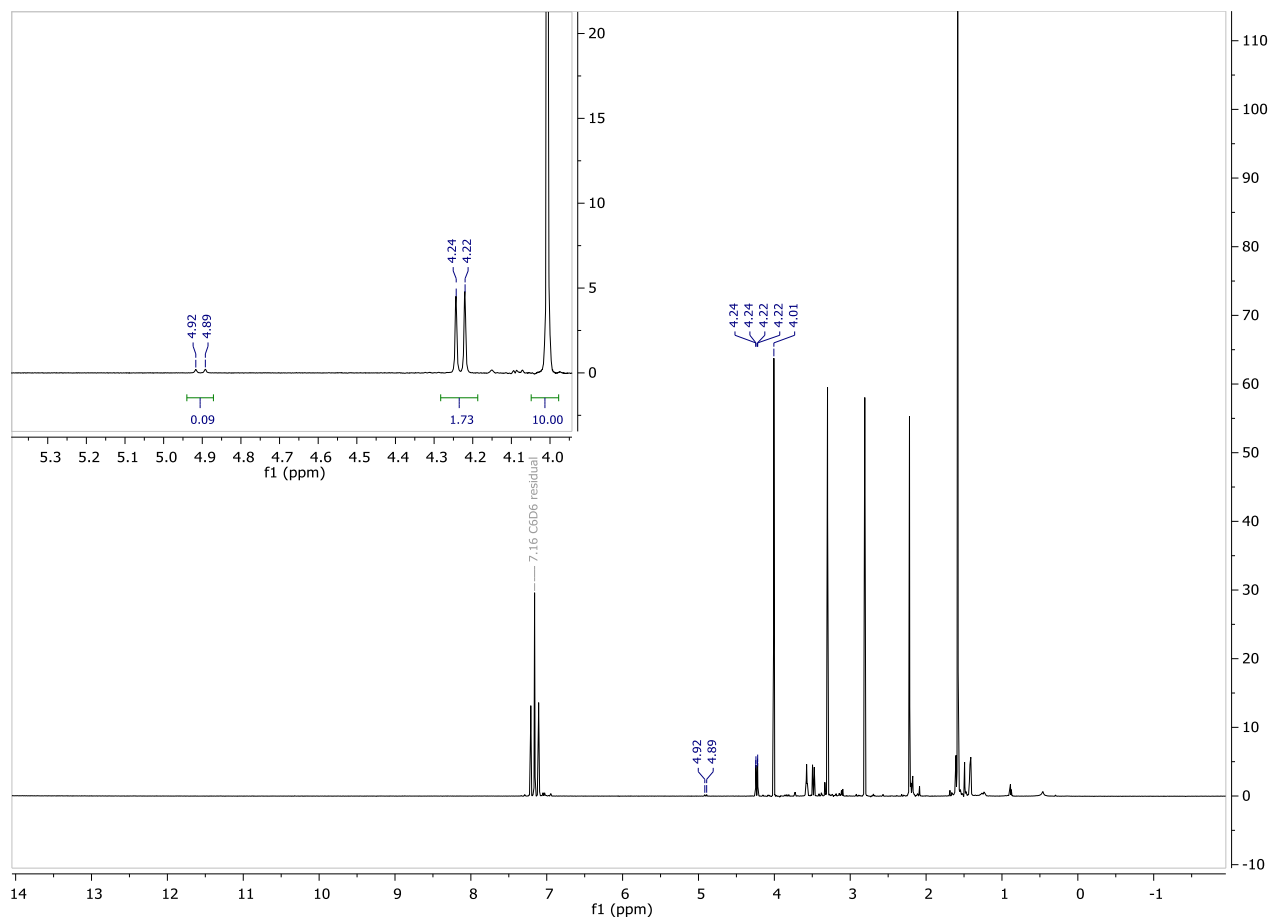


Figure 6.57 ^1H NMR of the equilibrium mixture of $\text{Ti}(\text{NMe}_2)_4$, $\text{Ti}(\text{NMe}_2)_2(\text{OArCH}_2\text{ArO})$, and $\text{Ti}(\text{OArCH}_2\text{ArO})_2$.

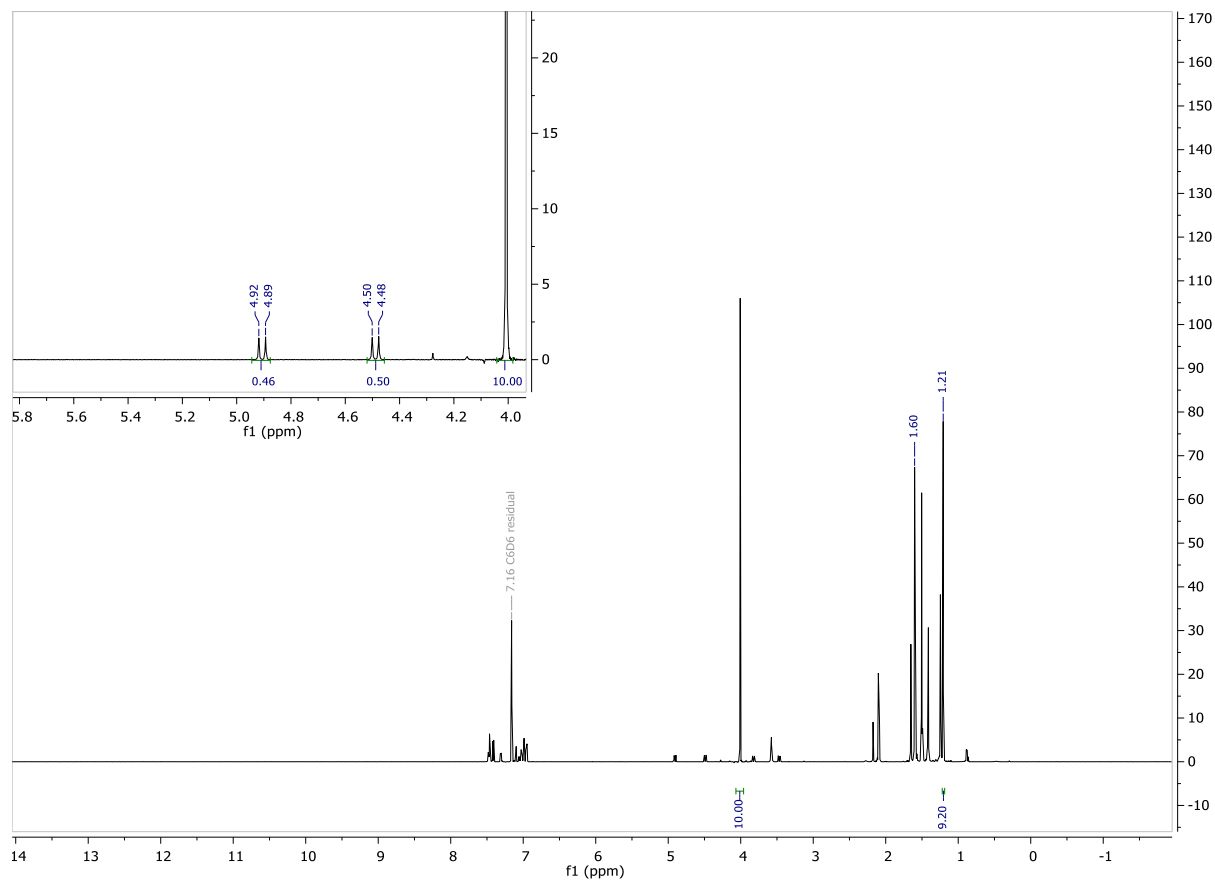


Figure 6.58 ^1H NMR of the equilibrium mixture of $\text{Ti}(\text{OAr}^{4\text{-tert-butyl}})_4$, $\text{Ti}(\text{OAr}^{4\text{-tert-butyl}})_2(\text{OArCH}_2\text{ArO})$, and $\text{Ti}(\text{OArCH}_2\text{ArO})_2$.

Modeling of K_{eq} as a function of sterics and electronics:

Excel was used to perform standard ordinary least squares fits on the desired parameter arrays following the basic matrix equation shown below:

$$[C] = ([A] \cdot [A]^{trans})^{-1}[A]^{trans}[B]$$

Here each array is treated using standard matrix formulas in excel to give final values for the coefficients for the K_{eq} equation in the output array, C. The matrix [A] contains the parameters fitted, in this case LDP and Δ LDP values. The matrix [B] contains the property correlating to the parameters, in this case K_{eq} .

The following combinations of variables were considered and the best overall fit resulted from simple electronic treatment of the K_{eq} data.

Table 6.9 Combinations of parameters examined for fitting the dependence of K_{eq} on Δ LDP and $\%V_{bur}$.

Least Squares Fit Trial	Parameters
1	Δ LDP, $(\Delta$ LDP) ² , $\Delta\%V_{bur}$
2	Δ LDP, $(\Delta$ LDP) ² , $(\Delta\%V_{bur})^2$
3	Δ LDP, $(\Delta$ LDP) ² , $(\Delta\%V_{bur})^2$, $\Delta\%V_{bur}$
4	$(\Delta$ LDP) ² , $\Delta\%V_{bur}$
5	Δ LDP, $(\Delta$ LDP) ²

We noted that while a very slight improvement in the R^2 value for the fitted parameters was noted in Trial 3, several of the calculated K_{eq} values were small negative numbers. This appears to impart no physical meaning to the fit and suggests that the inclusion of all 4 parameters begins to “overfit” the data. Additionally, comparing trials 1 and 2 to trial 4, almost no improvement to the fit is made on including the steric term. It doesn’t appear to be necessary for an accurate fit.

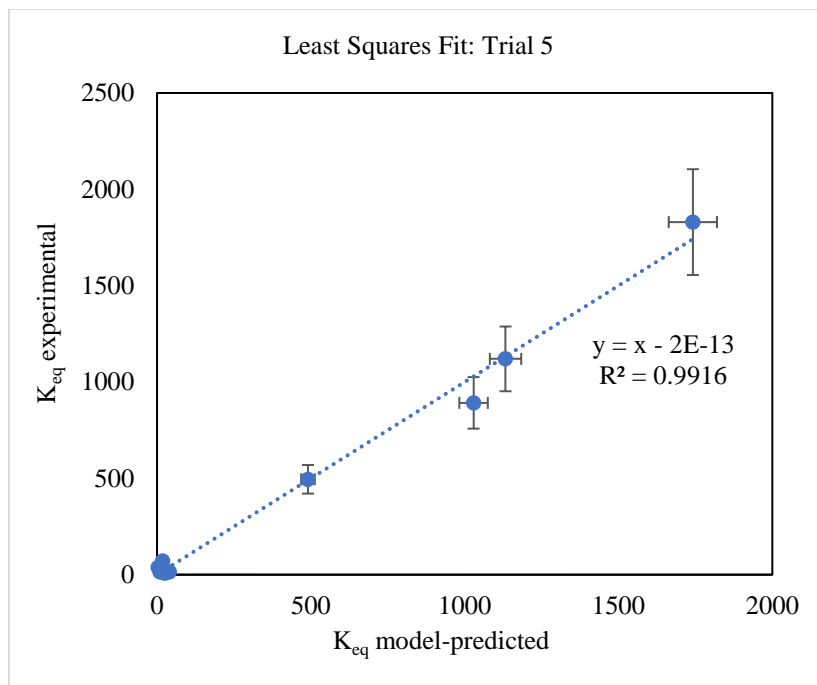


Figure 6.59 Least Squares fit result for predicting K_{eq} from ΔLDP .

REFERENCES

REFERENCES

- (1) Cao, C.; Shi, Y.; Odom, A. L., A Titanium-Catalyzed Three-Component Coupling To Generate α,β -Unsaturated β -Iminoamines. *Journal of the American Chemical Society* **2003**, *125* (10), 2880-2881.
- (2) Odom, A. L.; McDaniel, T. J., Titanium-Catalyzed Multicomponent Couplings: Efficient One-Pot Syntheses of Nitrogen Heterocycles. *Acc. Chem. Res.* **2015**, *48* (11), 2822-2833.
- (3) Barnea, E.; Majumder, S.; Staples, R. J.; Odom, A. L., One-Step Route to 2,3-Diaminopyrroles Using a Titanium-Catalyzed Four-Component Coupling. *Organometallics* **2009**, *28* (13), 3876-3881.
- (4) Billow, B. S.; McDaniel, T. J.; Odom, A. L., Quantifying ligand effects in high-oxidation-state metal catalysis. *Nature Chemistry* **2017**, *9*, 837.
- (5) DiFranco, S. A.; Maciulis, N. A.; Staples, R. J.; Batrice, R. J.; Odom, A. L., Evaluation of donor and steric properties of anionic ligands on high valent transition metals. *Inorganic chemistry* **2012**, *51* (2), 1187-200.
- (6) Bemowski, R. D.; Singh, A. K.; Bajorek, B. J.; DePorre, Y.; Odom, A. L., Effective donor abilities of E-t-Bu and EPh (E = O, S, Se, Te) to a high valent transition metal. *Dalton transactions* **2014**, *43* (32), 12299-12305.
- (7) Aldrich, K. E.; Billow, B. S.; Holmes, D.; Bemowski, R. D.; Odom, A. L., Weakly Coordinating yet Ion Paired: Anion Effects on an Internal Rearrangement. *Organometallics* **2017**, *36* (7), 1227-1237.
- (8) Aldrich, K. E.; Billow, B. S.; Staples, R. J.; Odom, A. L., Phosphine interactions with high oxidation state metals. *Polyhedron* **2019**, *159*, 284-297.
- (9) McDaniel, T. J.; Lansdell, T. A.; Dissanayake, A. A.; Azevedo, L. M.; Claes, J.; Odom, A. L.; Tepe, J. J., Substituted quinolines as noncovalent proteasome inhibitors. *Bioorganic & Medicinal Chemistry* **2016**, *24* (11), 2441-2450.
- (10) Majumder, S.; Gipson, K. R.; Odom, A. L., A Multicomponent Coupling Sequence for Direct Access to Substituted Quinolines. *Organic Letters* **2009**, *11* (20), 4720-4723.
- (11) Majumder, S.; Odom, A. L., Titanium catalyzed one-pot multicomponent coupling reactions for direct access to substituted pyrimidines. *Tetrahedron* **2010**, *66* (17), 3152-3158.
- (12) Dissanayake, A. A.; Staples, R. J.; Odom, A. L., Titanium-Catalyzed, One-Pot Synthesis of 2-Amino-3-cyano- pyridines. *Advanced Synthesis & Catalysis* **2014**, *356* (8), 1811-1822.
- (13) Burés, J., A Simple Graphical Method to Determine the Order in Catalyst. **2016**, *55* (6), 2028-2031.

- (14) Burés, J., Variable Time Normalization Analysis: General Graphical Elucidation of Reaction Orders from Concentration Profiles. **2016**, *55* (52), 16084-16087.
- (15) Rosner, T.; Le Bars, J.; Pfaltz, A.; Blackmond, D. G., Kinetic Studies of Heck Coupling Reactions Using Palladacycle Catalysts: Experimental and Kinetic Modeling of the Role of Dimer Species. *J. Am. Chem. Soc.* **2001**, *123* (9), 1848-1855.
- (16) Pohlki, F.; Doye, S., The Mechanism of the [Cp₂TiMe₂]-Catalyzed Intermolecular Hydroamination of Alkynes. *Angew. Chem. Int. Ed.* **2001**, *40* (12), 2305-2308.
- (17) Walsh, P. J.; Baranger, A. M.; Bergman, R. G., Stoichiometric and catalytic hydroamination of alkynes and allene by zirconium bisamides Cp₂Zr(NHR)₂. *Journal of the American Chemical Society* **1992**, *114* (5), 1708-1719.
- (18) Okuda, J.; Fokken, S.; Kang, H.-C.; Massa, W., Synthesis and Characterization of Mononuclear Titanium Complexes Containing a Bis(phenoxy) Ligand Derived from 2,2'-Methylene-bis(6-tert-butyl-4-methylphenol). **1995**, *128* (3), 221-227.
- (19) Floriani, C.; Corazza, F.; Lesueur, W.; Chiesi-Villa, A.; Guastini, C., Eine empfindliche Sonde für Veränderungen in der Koordinationssphäre von Titan: Achtgliedrige Dioxatitanacyclen und ihre metallorganischen Derivate. **1989**, *101* (1), 93-94.
- (20) Sun, L., Devore, D. D. (Dow Global Technologies, LLC), A process for preparing functional polymers through addition of amino and polymeryl groups to aldehyde moieties. *United States Patent* **2018**, (PCT/US2016/054190).
- (21) Tinkler, S.; Deeth, R. J.; Duncalf, D. J.; McCamley, A., Polymerisation of ethene by the novel titanium complex [Ti(Me₃SiNCH₂CH₂NSiMe₃)Cl₂]; a metallocene analogue. *Chemical communications* **1996**, (23), 2623-2624.
- (22) Mikami, K.; Terada, M.; Nakai, T., Catalytic asymmetric glyoxylate-ene reaction: a practical access to .alpha.-hydroxy esters in high enantiomeric purities. *Journal of the American Chemical Society* **1990**, *112* (10), 3949-3954.
- (23) Mikami, K.; Matsumoto, Y.; Xu, L., Modification of alkoxo ligands of BINOL-Ti ladder: Isolation and X-ray crystallographic analysis. *Inorganica Chimica Acta* **2006**, *359* (13), 4159-4167.
- (24) Mikami, K., T., Masahiro, N. Takeshi, S., Noboru, K., Hidenori (Takasago International Corporation), Process for producing optically active alpha-hydroxycarboxylates. *United States Patent* **1990**, (US4965398).
- (25) van Leeuwen, P. W. N. M., Decomposition pathways of homogeneous catalysts. *Applied Catalysis A: General* **2001**, *212* (1), 61-81.
- (26) Lehn, J.-S. M.; Hoffman, D. M., Synthesis and Structures of Zirconium Amide-Iodide Complexes. *Inorganic chemistry* **2002**, *41* (15), 4063-4067.

- (27) Group, O., Ligand Donor Parameters. *Odom Group Wiki Page* **2012-2019**.
- (28) Gokel, G. W. W., R. P., Weber, W. P., Phase-transfer Hofmann Carbylamine Reaction: *tert*-Butyl Isocyanide. *Organic Syntheses* **1976**, 55, 96.

CHAPTER 7. AN EXPLORATION OF THE SYNTHESIS AND ELECTRONIC PROPERTIES OF RUTHENIUM AND IRON IMIDO COMPLEXES

7.1 Introduction^{9,10}

Imide ligands and metal-nitrogen multiple bonds have been the topic of countless studies over the last 50 years.^{1,2} The group 8 metals have been no exception and their potential for metal nitrogen multiple bond formation has been particularly interesting for several reasons.

- 1) The group 8 metals delineate the “oxo wall.” They are the last group for which several (or any) genuine examples of terminal oxo complexes exist and can be readily synthesized, isolated, and structurally characterized, specifically with octahedral coordination and a *d*-electron count >5 .³ Even today, only a handful of terminal oxo complexes in group 9 have been remotely characterized, some only *in situ*, and all with coordination numbers of 4 or 5.⁴⁻⁶ Last year, the Anderson group published a well-characterized terminal Co(III)-oxo species with basal C_{3v} symmetry. The Co–O bond in this structure, interestingly, is bent, similar to the electronic structure exhibited by many of the Group 8, +2, d^6 imido complexes discussed below with similar electronic structure.⁷ This example highlights, one of the big (indirect) reasons why Fe, Ru, and Os multiple bond character is of interest.

⁹ The work in this chapter is an expansion from initial investigations of Ru–imido chemistry started by Dr. Amrendra Singh while he was a postdoc in the Odom group. His efforts are what first demonstrated the ligand-based-radical character upon oxidation of these species from Ru(II) to Ru(III).

¹⁰ These results have been submitted for publication to *Inorganic Chemistry* as a research article. The manuscript is currently in revision, but was accepted with minor revisions: Kelly E. Aldrich, B. Scott Fales, Amrendra K. Singh, Richard J. Staples, Benjamin G. Levine, John McCracken, Milton R. Smith III, and Aaron L. Odom, “Electronic and Structural Comparisons Between Iron(II/III) and Ruthenium(II/III) Imide Analogs.” **2019**, *accepted* with minor revisions.

Learning about these bonding interactions with group 8 metals stands to provide more information from which analysis of late, low valent metal-ligand multiple bonds, relevant to highly reactive metal-imido, metal-alkylidene, or metal-oxo species in catalytic processes, can be applied.

- 2) Despite the much greater number and diversity of metal-imido compounds that have been synthesized and studied in the last several decades, several big questions about the nature of metal-imide bonds remain. There are some general trends known. For example, when a metal is substantially less electronegative than N, the π -bonding orbitals of the M–N bond is primarily N centered. When the metal becomes more electronegative, this orbital shifts its distribution toward the metal.⁸ The resultant change in electronic structure from specific changes to the property of a metal, and the ability to predict what these changes will do to the reactivity of a metal-imido complex have not been fully developed. One of the simplest trends, which has not been investigated in a systematic way, is what happens to a metal imido bond transcending a group (i.e. Fe, Ru, and Os), and how differences in the metal down a series changed the reactivity. More targeted efforts to establish basic trends stand to provide more rapid information about these types of interactions than random syntheses of various M=NR complexes.
- 3) Fe, Ru, and Os multiple bonds to nitrogen have been repeatedly found in highly active biological systems (i.e. nitrogenase enzyme active site⁹ and cytochrome P450^{10,11}). In many of these systems, highly reactive Fe–N multiple bonds are suspected to be important intermediates within catalytic cycles.¹²⁻¹⁴ However, exact intermediates and mechanism of action in many of these systems is not fully understood. Further study is needed to

completely establish how these enzymes catalyze reactions like N_2 reduction or aminations.

Along the same lines, the Haber Bosch process utilizes solid Fe, Ru, or Os catalysts to reduce N_2 to NH_3 in heterogeneous reactors that operate at high pressures and temperatures.^{15,16} Several mechanisms have been proposed for this reduction process, including the adsorption of both N_2 and H_2 to solid catalysts. Many steps in the process, including intermediates, have become more fully understood over the past several years as advanced spectroscopy techniques have been developed (i.e. Auger electron spectroscopy and SEM). So, while progress has been made to understand these catalysts, and the equilibrium conditions of the process have been thoroughly studied, there isn't much room to improve these catalyst systems further.¹⁵

Practically, we need ammonia for food production, and currently there is no way around the highly energy intensive conditions required to reduce N_2 to NH_3 . Chemically, there should be a way to connect the dots between nitrogenase and the solid catalysts used in the Haber-Bosch process. Thorough investigation of these M–N multiple bonds within discrete organometallic complexes offers a way to gain insight into these immensely important catalytic processes and reduce energy usage to produce ammonia catalytically.

For these reasons, among others, an astounding amount of work has gone into the synthesis and characterization of Fe-imido complexes in the last few decades.¹⁷⁻²² Using careful ligand design, Fe-imido complexes have been synthesized in the +1 to +6 oxidation state; as cationic, neutral, and anionic species; and demonstrating a wide variety of electronic structures. In recent years, two groups have even successfully published the synthesis of three-coordinate Fe-bis(imido) complexes in the +4 and +5 oxidation states.^{23,24}

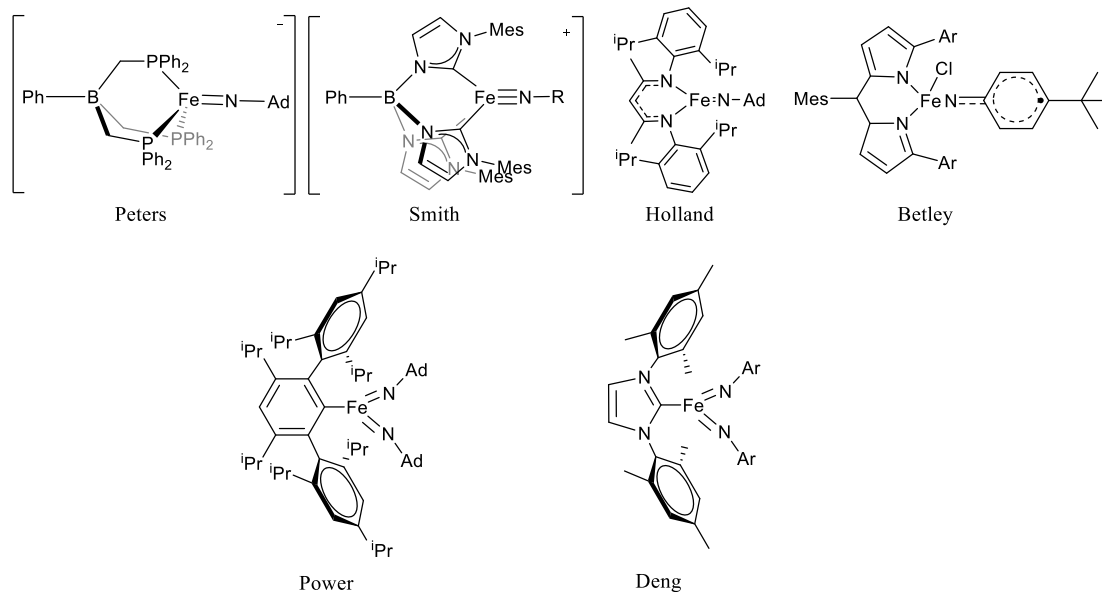


Figure 7.1 Examples of terminal mono- and bis-imido Fe complexes in the literature. Note the prevalence of both bulky and chelating ligands, which stabilize these complexes.²⁰⁻²⁸

There are also several terminal Os-imide complexes known, again, with a variety of oxidation states and ligands. Specifically, Schrock and coworkers have prepared and studied the electronic properties of several bis- and tris(imide) complexes, including $\text{Os}(\text{NAr})_3$, $\text{Os}(\text{NAr})_2\text{O}_2$, $\text{Os}(\text{NAr})_2(\text{PMe}_3)_2$, and $\text{Os}(\text{NAr})_2(\eta^2\text{-alkyne})$ species, in addition to work by Sharpless.²⁹⁻³³ Typically, the preparation of these complexes starts with OsO_4 , which is (relatively for Os) cheap and commercially available. Unfortunately, RuO_4 and FeO_4 materials are not, and so achieving analogous complexes with the congeners is not feasible via the same synthetic routes. As a result, Os-imide complexes have the most well developed high-valent chemistry. Osmium-imide chemistry will be discussed more thoroughly in the following chapter (see Chapter 8).⁸

Lagging behind both Fe and Os imido chemistry is Ru. Very few examples of Ru-imides exist in the literature. Both Schrock and Steedman have examples of Ru(II) mono(imido) complexes; while Schrock's complex is a bridging dimeric species, Steedman's bulky derivative is a monomeric, terminal imido.³⁴⁻³⁶ In 2013, the Odom group published a terminal Ru(II) imido complex, $\text{Ru}(\text{NAr})(\text{PMe}_3)_3$.³⁷ This complex, while interesting due to its unique geometry, reacts

much as one would predict an imido complex in a low oxidation state. The d^6 Ru(II) metal center doesn't enable enough vacant π -orbitals of proper symmetry and orientation to localize the N-ligand's available electron density all in σ and π bonding interactions. This results in a heavily N-centered HOMO, which effectively behaves as a lone pair of electron density on the imide N. The imide moiety, therefore, reacts with strong nucleophilic character.

This electronic structure is also what causes the odd geometry of the complex, where the imide ligand tips toward one of the PMe_3 ligands preferentially, breaking the C_{3v} symmetry of the molecule. The metal orbital participating in the HOMO is the d_z^2 orbital. According to calculations, an 18 kcal/mol stabilization of the HOMO is achieved when the out-of-phase interaction between the Ru d_z^2 orbital and the N σ orbital minimize their overlap (See Experimental, Fig. 7.17). This minimum occurs when the N orbital shifts its orientation, falling into the node of the d_z^2 orbital. The distortion from C_{3v} symmetry is shown in the crystal structure in Fig. 7.2, below.³⁷

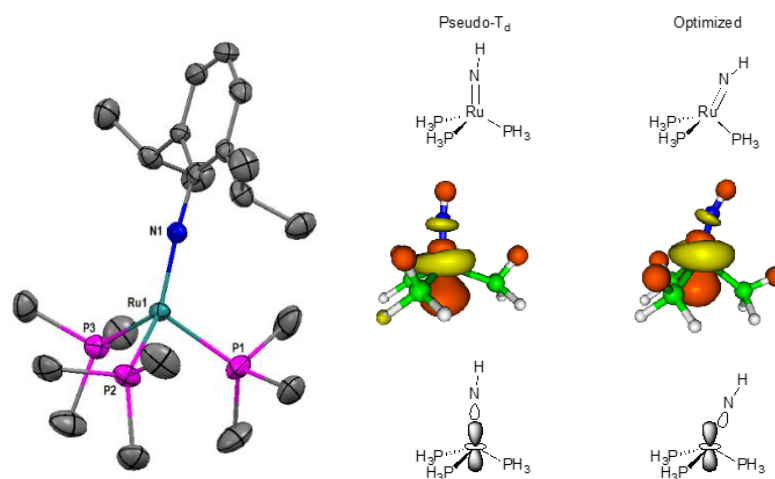


Figure 7.2 (top) X-ray crystal structure of Ru1 with ellipsoids shown at 50% probability and H's omitted for clarity (N = blue, Ru = teal, P = pink). (bottom)

Table 7.1 Table of relevant bond lengths and angles for **Ru1**.

Bond	Angle (°)	Bond	Distance (Å)
Ru1–N1–C1	174.86	Ru1–N1	1.811
N1–Ru1–P1	113.70	Ru1–P1	2.224
N1–Ru1–P2	128.41	Ru1–P2	2.254
N1–Ru1–P3	122.63	Ru1–P3	2.239

Again, while this complex demonstrates an interesting electronic structure, which can be supported and rationalized with experimental and theoretical arguments, it quite possibly raises more questions than it answers. Do Fe and Os analogues impose the same geometric distortion, or do the differences in orbital overlap between metals have an effect? Would a less symmetric basal phosphine set make this more or less likely to occur? Does this electronic structure compromise stability upon oxidation? We lack the fundamental knowledge about the character of M-imido bonds to make these sorts of predictions and assess what affects these changes would have on the reactivity.

A lot of knowledge stands to be gained by synthesizing and characterizing the electronic structure of even very basic Ru-imide complexes. A direct comparison with Fe analogues serves

as a tool to simultaneously examine the bonding differences going down a series. Additionally, given the comparative wealth of knowledge that has been gained by the larger number of terminal Fe–imides published in the past two decades, examining Fe and Ru analogues simultaneously facilitates comparisons with other known complexes. Thus, we set about preparing Fe and Ru analogues of various imide complexes to compare their reactivity, bonding properties, and overall electronics. By employing direct comparison between these congeners, we have gained some insight into the relative instability of Ru-imide complexes, which have helped explain synthetic difficulties associated with targeting these types of molecules.

7.2 Synthesis and Oxidation of Terminal Ru Imido Complexes

The Ru(NAr)(PMe₃)₃ (**Ru1**) complex mentioned above presented an ideal place to start when we first looked at expanding the synthetic chemistry of Ru–imides. Because oxidation state effects on the character of the Ru–N multiple bond was one direction that we wanted to explore with this project, direct chemical oxidation of **Ru1** was attempted. However, this produced an unstable compound, leading to intractable mixtures that were not amenable to purification or additional characterization. Thus, we began looking for ways to stabilize the Ru–imide fragment prior to oxidation.

The complex's phosphine ligands are substitutionally inert to other monodentate phosphines. However, under mild conditions, bidentate ligands can replace the monodentate PMe₃ ligands. When the closest chelating electronic surrogate to PMe₃ was employed for the ligand exchange, dimethylphosphinoethane (dmpe), two equivalents of dmpe add to Ru. This results in the formation of the stable, 5-coordinate, 18-electron Ru(NAr)(dmpe)₂ (**Ru2**) complex shown in Fig. 7.3. This complex is highly insoluble, and produces two enantiomers, which complicated

attempts at further study. We were also interested in retaining the unique geometry of the 4-coordinate Ru-imide, so a different bis-phosphine was selected.

Diphenylphosphinoethane (dppe), when added to $\text{Ru}(\text{NAr})(\text{PMe}_3)_3$, is sterically demanding enough to limit addition of the chelate to Ru to a single equivalent, yielding $\text{Ru}(\text{NAr})\text{dppe}(\text{PMe}_3)$ (**Ru3**) as the only product. This complex was characterized structurally and is shown in Fig. 7.3. The structural properties of **Ru3** are very similar to **Ru1**, with the smallest N1–Ru1–P1 angle measuring 106.52° .

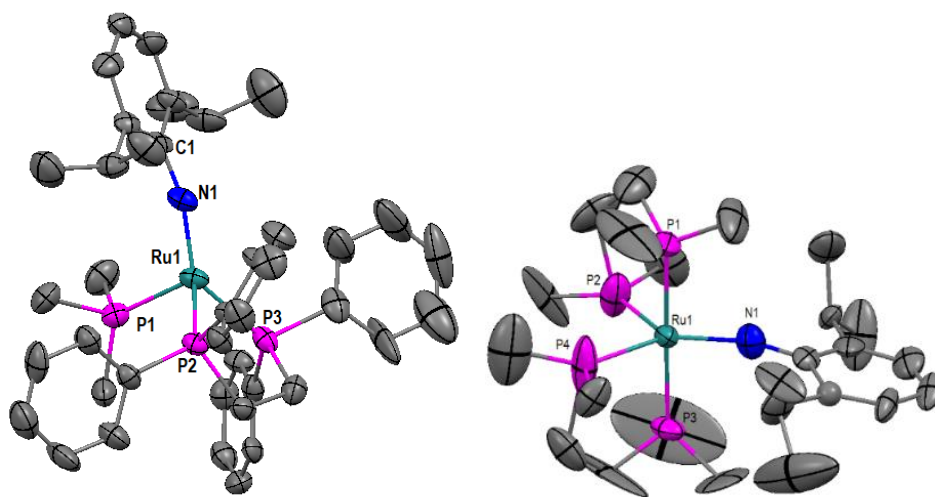
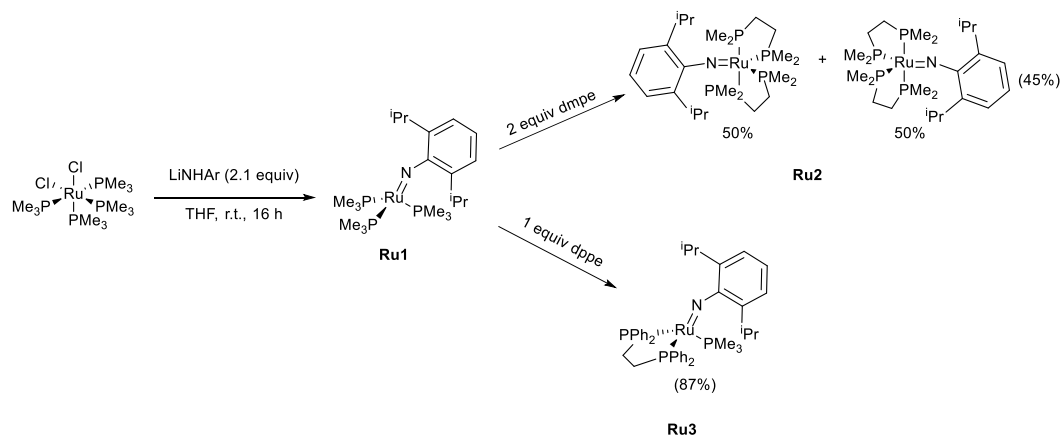


Figure 7.3 (top) Synthetic schemes for the synthesis of **Ru2** and **Ru3**. (bottom) X-ray crystal structure for **Ru3** (left) ($\text{Ru}(\text{NAr})\text{dppe}(\text{PMe}_3)$) and **Ru2** (right); ellipsoids shown at 50% probability, hydrogens omitted for clarity. For **Ru2**, the two enantiomers co-crystallize and are disordered across the axis coincident with the P1–Ru1–P3 bond. Select bond lengths and angles are shown.

Table 7.2 Select bond lengths and angles from the single crystal X-ray structures for **Ru3** and **Ru2**, shown in Fig. 7.3.

Bond	Angle (°)	Bond	Distance (Å)
Ru3			
Ru1–N1–C1	166.65	Ru1–N1	1.808
N1–Ru1–P1	106.52	Ru1–P1	2.237
N1–Ru1–P2	136.68	Ru1–P2	2.277
N1–Ru1–P3	127.03	Ru1–P3	2.239
Ru2			
C1–N1–Ru1	163.82	Ru1–N1	1.921
N1–Ru1–P1	90.32	Ru1–P1	2.301
N1–Ru1–P2	132.34	Ru1–P2	2.317
N1–Ru1–P3	88.70	Ru1–P3	2.323
N1–Ru1–P4	131.30	Ru1–P4	2.317

With **Ru3** isolated and bearing a similar geometry and electronic structure to **Ru1**, attempts to oxidize **Ru3** were undertaken. Amrendra discovered that when **Ru3** and a silver salt (AgSbF_6 or AgBARF_{24}) are combined in a mixed solvent system containing DME and MeCN, oxidation of the **Ru3** occurs. However, this oxidation is accompanied by dimerization of the Ru species via radical *para*-coupling of the Ar fragment, as shown in Fig. 7.4, resulting in **Ru4**.

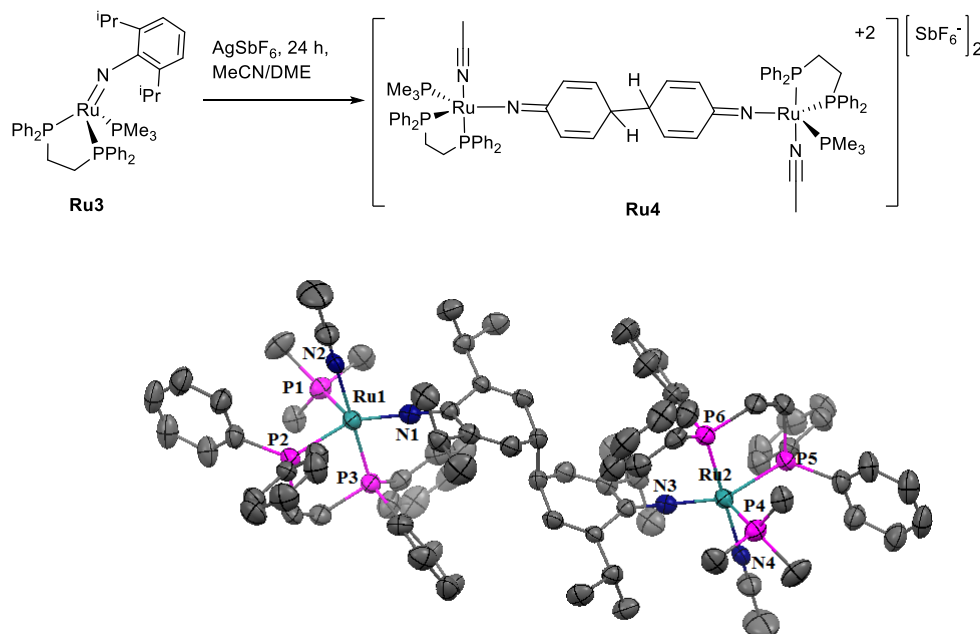


Figure 7.4 (top) Synthetic scheme for the production of **Ru4** from **Ru3** via oxidation with AgSbF_6 (AgBARF_{24} can also be used). (bottom) X-ray crystal structure of the dimeric species with ellipsoids shown at 50% probability; H atoms and disordered counter anion omitted for clarity.

When the same oxidation was performed in the absence of acetonitrile (i.e. only DME is used), a color change occurred, going from dark red to a pinkish-brown color, and the precipitation of Ag^0 was evident. When the Ag^0 was removed by filtration and the filtrate was worked up, an unstable, powdery brown residue was obtained. While the material is not crystalline, and cannot be structurally characterized, several properties have led us to propose the structure shown in Fig. 7.5, $[\text{Ru}(\text{NAr})(\text{PMe}_3)\text{dppe}][\text{SbF}_6^-]$ (**Ru5**). Whereas the **Ru3** precursor is soluble in highly nonpolar organic solvents, the new material is insoluble in most organic solvents; it is sparingly soluble in THF and DME and soluble but reactive with halogenated solvents. The material is also paramagnetic and shows both metal- and ligand-based radical signal by EPR spectroscopy (vide infra). However, thorough EPR analysis of this species was not possible due to the instability of the species, even frozen as a glass in 2-methyltetrahydrofuran.

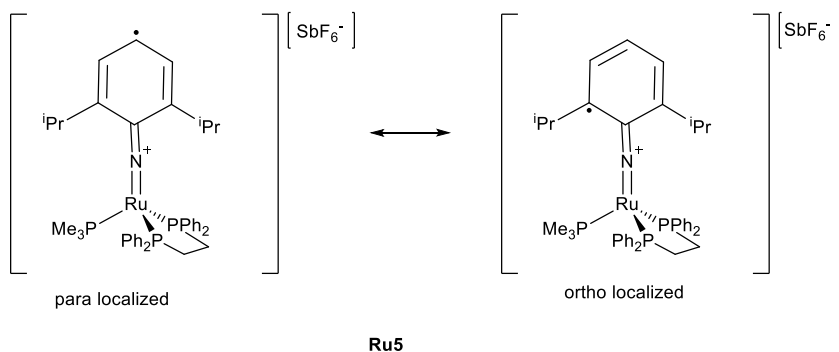


Figure 7.5 Proposed resonance contributors for **Ru5** with radical distribution across the *ortho* and *para* positions of the imide aryl group.

Given the reactivity demonstrated by the Ru species upon oxidation (Fig. 7.4), and the presence of ligand-centered radical signal in the preliminary EPR data, delocalization of the unpaired electron density induced by oxidation appears to spread across the imide ligand fragment. Specifically, resonance localization should put radical character on the metal, nitrogen, and *ortho*- and *para*-carbons of the Ar group. While the *ortho* positions are protected by the isopropyl substituents, the unprotected *para* carbon position appears to destabilize the oxidized complex.

There is precedence in the literature of similar ligand radical character in copper-imide and iron-imide systems, where similar reactivity has been demonstrated.^{20,38,39}

With this experimental evidence for ligand-radical based destabilization, I proposed a switch in the aryl derivative we were using for the imido fragment, adding an additional substituent to the *para* position. Similar efforts had shown significant improvement in the stability of the Fe-imide system published by Betley, et. al.³⁹ where their phenylimido was exchanged for 4-^tBu-phenylimide and stability in the complex dramatically improved. The tri-substituted aniline, 2,4,6-triisopropylaniline, can be readily prepared from 1,3,5-triisopropylbenzene in two steps.⁴⁰ The procedure to attach the more highly substituted aniline to Ru as an imido ligand is then identical to the existing procedure to make **Ru1**. The crystal structure of the resulting Ru(NAr*)(PMe₃)₃ (**Ru1***) is shown in Fig. 7.6. Again, analogous to the pathway to convert **Ru1** to **Ru3**, addition of 1 equiv of dppe to **Ru1*** yields Ru(NAr*)(PMe₃)dppe (**Ru3***). Note, due to the greatly reduced solubility of **Ru3*** relative to **Ru1***, **Ru1*** was not typically isolated. Rather, the synthesis was carried through to **Ru3***, which made purification and removal of the residual equivalent of H₂NAr* easier.

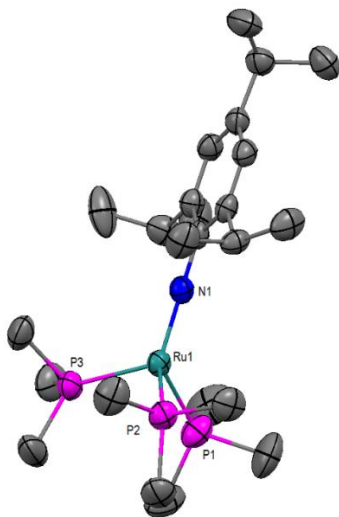
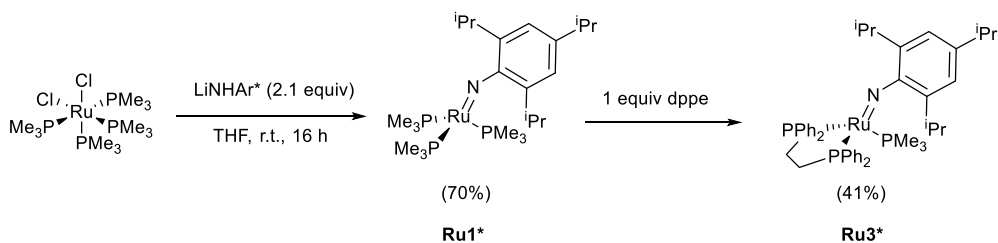


Figure 7.6 Synthesis procedure for **Ru1*** and **Ru3*** from *cis*-RuCl₂(PMe₃)₄ starting material. The crystal structure of **Ru1*** is shown with ellipsoids are shown at 50% probability; H atoms omitted for clarity.

With the potentially more stable **Ru3*** isolated, oxidation of **Ru3*** with AgSbF₆ was performed using DME as the solvent. This reaction resulted in the precipitation of Ag⁰ and a similar color change as was previously noted with oxidation of **Ru3**, going from red to brown. The same structure is proposed for the oxidation product, [Ru(NAr*)(PMe₃)dppe][SbF₆] **Ru5***, as we previously proposed for **Ru5**. Similar properties were noted between the two, with **Ru5*** also demonstrating paramagnetism consistent with one unpaired electron and similar solubility properties. Furthermore, **Ru5*** proved stable enough for more thorough investigation by EPR spectroscopy and was probed at length using this technique. These results are discussed in sections 7.5 and 7.6, below.

7.3 Synthesis and Oxidation of Fe Imide Analogues

In tandem with the development of a more stable Ru-Imido cation, the extension of this chemistry to Fe congeners was also pursued. Starting from FeCl_2 , the addition of excess PMe_3 (6 equiv) leads to the generation of $\text{FeCl}_2(\text{PMe}_3)_4$ *in situ*. This reaction has been previously reported and, like previous reports, we observe that this species is unstable when isolation is attempted. When the crude solution is exposed to reduced pressure, the solution changes color from pale green to brown, and after full removal of volatiles, appears to yield FeCl_2 as a pale orange residue.⁴¹ No NMR signals are observed for the transient species *in situ* due to its high magnetic moment (high spin Fe(II)).

When 2.1 equiv of LiNHAr is added to the *in situ* generated $\text{FeCl}_2(\text{PMe}_3)_4$, a rapid color change is noted, from transparent pale green to opaque dark orange. Upon stirring at room temperature for 24 h, the dark orange color gradually turns to a dull brownish green. This dark green compound is likely $\text{Fe}(\text{NAr})(\text{PMe}_3)_3$ (**Fe1**) based on subsequent reactivity. The terminal Fe(II)-imido was trapped and isolated with chelating phosphines. **Fe1** was also characterized *in situ* by ^{31}P and ^{14}N NMR of the crude reaction mixture, showing singlet shifts in the expected ranges based on observed shifts with **Ru1**. However, like its precursor, it is also unstable under reduced pressure. When we removed the volatiles under reduced pressure, the reaction mixture turned black, and the ^{31}P and ^{14}N NMR signals were no longer observed in the resulting residue.

Upon addition of dppe to the crude $\text{Fe}(\text{NAr})(\text{PMe}_3)_3$ reaction, no color change is noted. However, upon removal of the volatiles, a dark residue remains, which, when washed with hexane and recrystallized from toluene to yield X-ray quality crystals of $\text{Fe}(\text{NAr})(\text{PMe}_3)\text{dppe}$ (**Fe3**). However, the yield of **Fe3** from this reaction is not very high (39%). This is, in part, because there is a second product yielded from this reaction which is a red, powdery substance that provides a

magnetic moment consistent with a high-spin Fe(II) complex ($\mu_{\text{eff}} = 5.42$) (**Fe2**). With the **Fe2** isolated from the crude reaction mixture, X-ray quality crystals could not be grown. However, from additional experiments, including targeted synthesis of the complex we suspected to be **Fe2**, it has been identified as $\text{Fe}(\text{NAr})_2\text{dppe}$. (vide infra, Fig. 7.7)

Attempts to oxidize **Fe3** with AgSbF_6 , much like those to oxidize **Ru3**, outwardly appeared to result in oxidation. However, the oxidized product **Fe4**, was unstable and challenging to purify. Given the improvement that switching to NAr^* offered for the Ru synthesis, we thought it could also improve our synthetic attempts with Fe. Following the same synthetic protocols to go from FeCl_2 to **Fe1** to **Fe3**, we were able to synthesize **Fe1*** and **Fe3***.

As was observed for the synthesis of **Fe3**, in the synthesis of **Fe3*** a second major product is also made. The product is also a dark red, paramagnetic complex, however, it is notably more crystalline than **Fe2**, and X-ray quality single crystals were grown directly from the byproduct isolated from the crude reaction mixture. Thus **Fe2*** was identified as $\text{Fe}(\text{NAr}^*)_2\text{dppe}$ from isolation of the single crystals. Structures and synthetic schemes outlining the syntheses of these Fe analogues of the Ru complexes are shown below in Fig. 7.7.

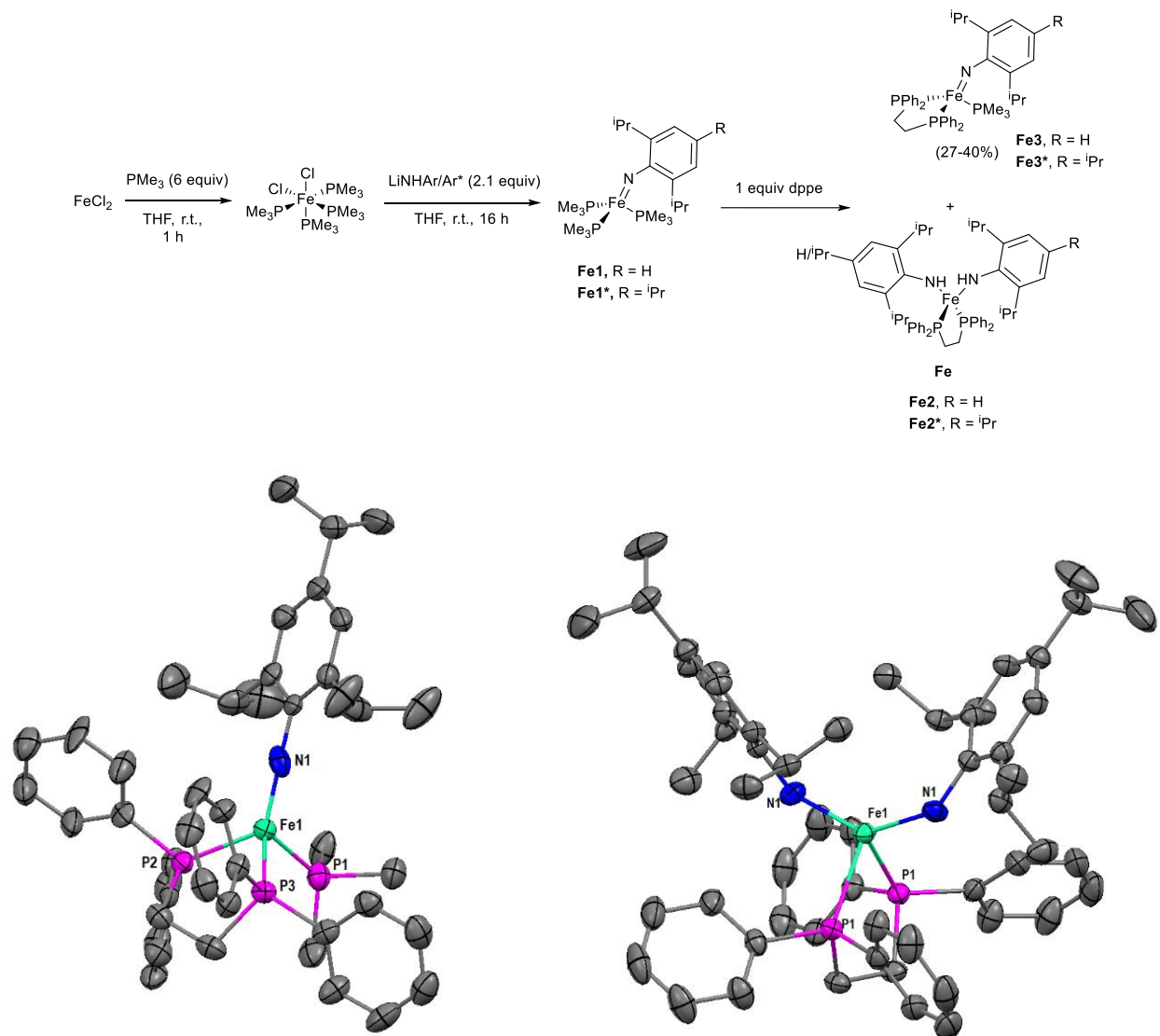


Figure 7.7 (*top*) Synthesis of Fe analogues of Ru-imido complexes, **Fe1**, **Fe1***, **Fe3**, and **Fe3***. The side product, **Fe2/2***, also results from this synthetic route, and is separated from **Fe3/3*** by several extractions and recrystallizations. (*bottom*) Crystal structures of **Fe2*** and **Fe3***; ellipsoids are shown at 50% probability with H atoms omitted for clarity. Note, **Fe2*** crystallizes in the C2/c spacegroup, with the crystallographic 2-fold axis bisecting the N1–Fe1–N1 and P1–Fe1–P1 angles. Thus, half of the molecule is symmetry generated.

Table 7.3 Select bond distances and angles from the single crystal X-ray structures of **Fe3*** and **Fe2*** shown in Figure 7.7.

Fe3*				Fe2*			
Bond	Angle (°)	Bond	Distance (Å)	Bond	Angle (°)	Bond	Distance (Å)
N1–Fe1–P1	111.74	N1–Fe1	1.654	C1–N1–Fe1	138.00	N1–Fe1	1.928
N1–Fe1–P2	132.17	P1–Fe1	2.166	N1–Fe1–P1	105.21	P1–Fe1	2.446
N1–Fe1–P3	122.79	P2–Fe1	2.158	N1–Fe1–N1	135.81	-	-
C1–N1–Fe1	172.09	P3–Fe1	2.161	P1–Fe1–P1	83.21	-	-

With **Fe3*** isolated, oxidation via AgSbF₆ was performed, and while high-spin Fe(III) impurities are sometimes detected by EPR spectroscopy, its enhanced stability allowed for more thorough study of the electronic structure of **Fe4***. The results of these electronic structure investigations are discussed in detail below (7.5 and 7.6).

7.4 Exploration of a Trischelating Phosphine Ligand Platform for Fe and Ru Imides

As shown in the introduction to this chapter, trischelates are a particularly common ligand motif for the synthesis and stabilization of terminal Fe-imides. We thought this type of ligand platform could lead to interesting electronic behavior by inducing more rigid *C*_{3v} symmetry on the imide complexes. Electronically similar phosphine ligands to those in **Fe3** and **Ru3** can be employed for the purpose of reducing differences in the metal-ligand interactions; this focuses analysis on the electronic structure effects due to the 3-fold symmetric chelation.

With Fe, Amrendra had previously shown that this is a straightforward and relatively stable complex to reach, Fe(NAr)⁴P₃ (**Fe5**, ⁴P₃ = (Me₂PCH₂)₃Si(C(CH₃)₃) or triphos). However, his original synthesis of this complex (see experimental) was not reproducible, even in his own hands. I modified his original synthesis of this complex, such that it is analogous to the synthesis of **Fe3/3***, utilizing the chelate to trap *in situ* **Fe1**. This synthesis has proven to be a reproducible and reliable method to yield **Fe5**. With the trischelate, no high-spin Fe(II) bis(amide) species were evident in the reaction mixture.

Oxidation of **Fe5** with 1 equiv of AgSbF₆ results in a color change from dark purple to bright blue, accompanied by the precipitation of Ag^o. X-ray quality crystals of [Fe(NAr)³][SbF₆] (**Fe6**) can be grown from DME layered with hexane at -35 °C. It is interesting to note that **Fe5** shows almost no distortion of the N1–Fe1–P angles, which are close to equivalent. However, upon oxidation, **Fe6** shows the smallest N1–Fe1–P angle (most contracted) noted for any of the structurally characterized Ru or Fe imide complexes that we have structurally characterized. This feature is highlighted in Fig. 7.8.

Table 7.4 Select bond distances and angles for the single crystal X-ray structures of **Fe5** and **Fe6**. Note that **Fe6** has two unique molecules in the asymmetric unit; several of the bond lengths and angles show statistical differences, so both measurements are shown. Images of these structures are shown in Fig. 7.8.

Bond	Angle/Distance (°/Å)
Fe5	
C1–N1–Fe1	178.98
N1–Fe1–P1	121.19
N1–Fe1–P2	121.79
N1–Fe1–P3	124.47
N1–Fe1	1.667
P1–Fe1	2.136
P2–Fe1	2.144
P3–Fe1	2.148
Fe6	
C1–N1–Fe1	167.82/172.51
N1–Fe1–P1	101.46/105.56
N1–Fe1–P2	127.96/130.78
N1–Fe1–P3	133.53/129.47
N1–Fe1	1.653/1.643
P1–Fe1	2.192/2.195
P2–Fe1	2.232/2.232
P3–Fe1	2.235/2.229
P2–Fe1–P3	94.36/93.93
Σ Angles between Fe1, N1, P2, P3	355.85/354.18

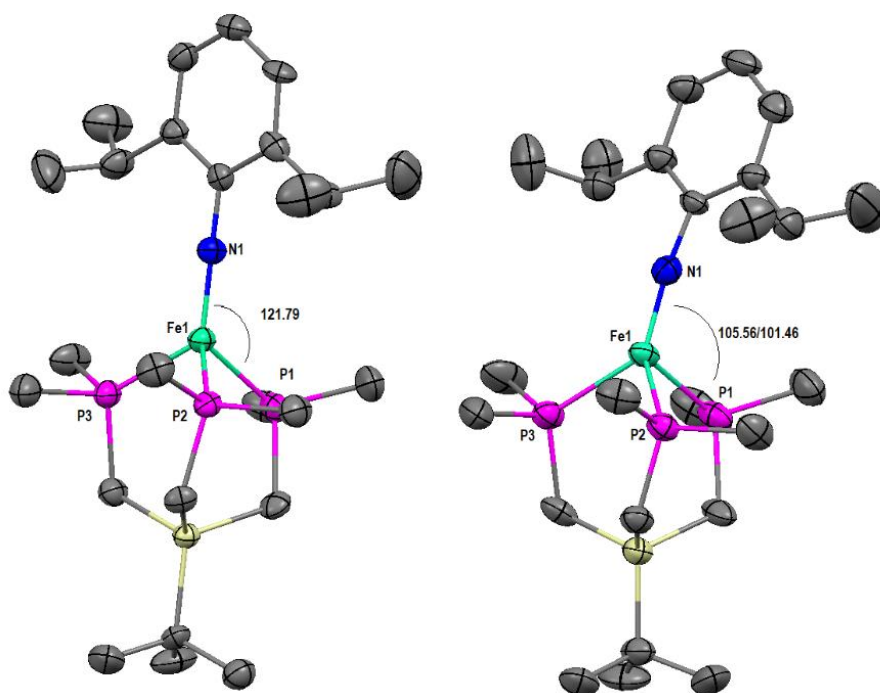
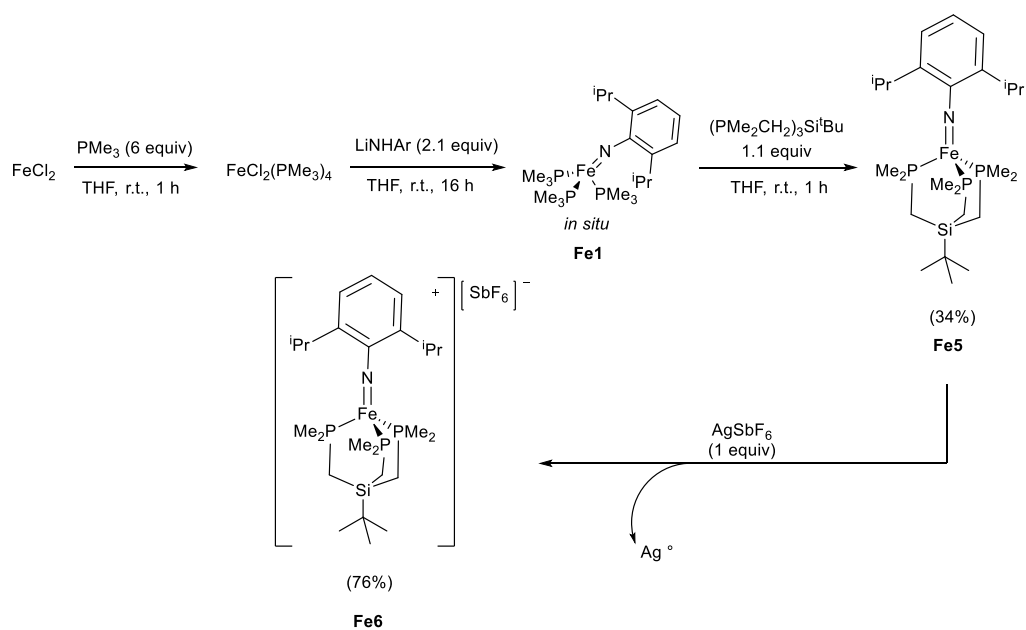


Figure 7.8 Synthesis of **Fe5** and **Fe6** by trapping the unstable **Fe1** with the trischelating $(\text{PMe}_2\text{CH}_2)_3\text{Si}^t\text{Bu}$ ligand. X-ray crystal structures of **Fe5** and **Fe6** are shown for comparison; ellipsoids are shown at 50% probability with H atoms and counteranion (**Fe6**) omitted for clarity.

While several attempts have been made by both Amrendra and myself to replicate a triphos-imido complex with Ru, successful synthesis has never been achieved. These results never

resulted in the clean synthesis of a monomeric, terminal imido complex. Generally, addition of the triphos ligand to a Ru complex (i.e. **Ru1** or *cis*-RuCl₂(PMe₃)₄) results in dozens of new ³¹P signals in the NMR of the crude reaction solution without a clear major product. I suspect this is due to a mismatch in the size of the Ru(II) cation's ionic radius and the pocket size of the triphos ligand when fully coordinated to a metal. This could lead to incomplete chelation between a single ³¹P ligand and a single metal center, giving rise to multiple oligomeric species.

7.5 Characterization of Cationic Ru5*, Fe4*, and Fe6 by EPR Spectroscopy (7.5)¹¹

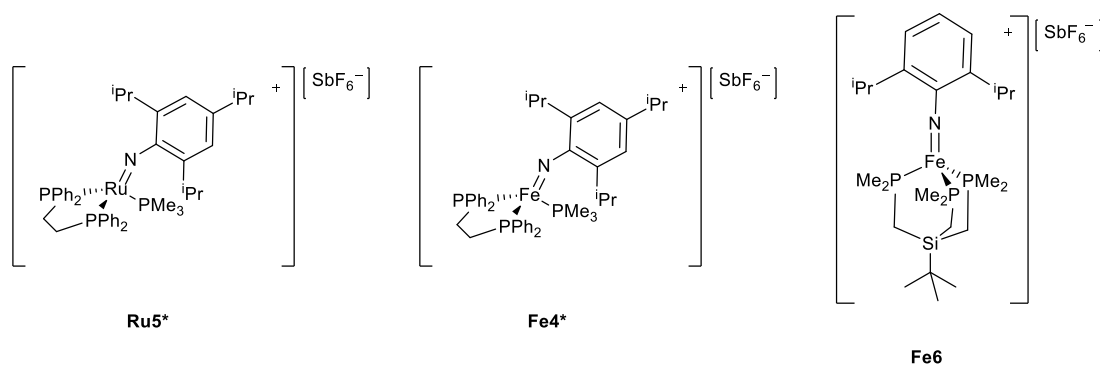


Figure 7.9 M(III) cationic complexes examined by EPR spectroscopy. **Fe6** is reasonably crystalline and has been characterized by single crystal X-ray crystallography. **Ru4*** and **Fe4*** are amorphous. They become oily when exposed to polar ethereal solvents, and attempts at crystallization generally produce powder solids.

EPR spectroscopy is an incredibly useful experimental technique that provides details about the electronic structure of a paramagnetic complex by examining the behavior of the unpaired electron(s). We thought this could provide invaluable insight in characterizing the radical cations **Fe4***, **Fe6***, and **Ru5***, which are all $S = 1/2$ systems. While trying to synthesize and study these compounds, delocalization of the radical was noted in the **Ru5** system (see above, Fig. 7.4 and 7.5). The Fe complexes were also unstable, however, they did not exhibit the same type of radical reactivity as the Ru analogue; in the sense of their radical character, there seemed to be a substantial difference due to the identity of the metal and the basal ligand set. Going into these

¹¹ EPR data was collected and interpreted by Professor John McCracken. He has also provided figures representing the experimental data and simulated spectra for the studies discussed in this section.

experiments, we suspected that, in the Ru systems, substantial delocalization of the radical was spread across the imide ligand's π -system, while the Fe systems were likely simple Fe(III) complexes with metal-localized radicals.

To test this hypothesis, radical complexes were examined by X-band cw-EPR spectroscopy at several temperatures and with several preparations of each compound. These studies proved challenging due to the instability of the species of interest. Even with the addition of a *para*-isopropyl substituent on the imido group's phenyl ring for stability (**Fe4*** and **Ru5***), these complexes decompose within a few days stored at -35 °C as solids. This, coupled with their lack of crystallinity, precluded effective purification. Consequently, some variation was noted from spectrum to spectrum among the different samples prepared for **Fe4*** and **Ru5***. Even small differences, such as the purity of the Ag-salt used in the oxidation or the particular batch of PMe_3 used to generate the starting material, appear to affect the character of **Fe4*** and **Ru5*** after oxidation. By contrast, **Fe6**, which is crystalline and could be reproducibly purified following the oxidation of **Fe5**, provided very consistent EPR spectra from sample to sample.

The spectrum of **Fe4*** originally looked like a composite of low-spin Fe(III) and low-spin Fe(III)-coupled ligand radical. However, the spectrum proved to be simpler than we initially thought. The species of interest in Fig. 7.10a is a bona-fide low-spin Fe(III), $S = \frac{1}{2}$ paramagnet. By studying additional spectra from several preparations of **Fe4***, we were able to determine what was really happening in these samples.

Even when the spectrum appears to be a single species (Fig. 7.10a), a very small impurity of a high-spin Fe(III)-coupled contaminant with paired ligand radical (Fig. 7.10, inset) skews the fit of the first derivative of the absorption spectrum. This contaminant seems to be an impurity, or possibly even a decomposition product from the preparation of **Fe4***. Since the synthesis of **Fe3***

is accompanied by the formation of at least one other Fe species (high spin Fe(II), **Fe2***, Fig. 7.7), co-produced in this one-pot-three-step synthesis, either decomposition of **Fe3*/Fe4*** or contamination from the oxidation product of **Fe2*** seem like possible sources for this impurity. The sample that provided the EPR spectrum highlighted in the inset of Fig. 7.10 came from an oxidation of **Fe3*** to **Fe4*** in which the reaction solution quickly went from the dark green color characteristic of **Fe3*** and **Fe4*** to a dark brownish-grey upon standing. Thus, no **Fe4*** appeared to be present in the sample

The radical contaminant appears to be primarily organic, with a g value of 1.982 and ^{14}N hyperfine coupling ($A_{\text{iso}} = 13.3 \text{ MHz}$; $A_{\text{dip}} = 80.4 \text{ MHz}$), consistent with a π -based radical.⁴² It is important to note that this g-value is lower than what is expected for an *isolated* organic radical (2.0023), thus the paramagnetic character of this species appears to be affected by coupling with a metal ion (Fe(II/III)). Fitting this impurity, whether a side product or decomposition product, accurately and by itself, clarified the nature of subsequent spectra by facilitating improved accuracy of species separation in the spectral simulations. Consequently, the spectra for the two **Fe4*** samples shown in Fig. 7.10a and 7.10b could be fitted with roughly the same results, despite outward differences.

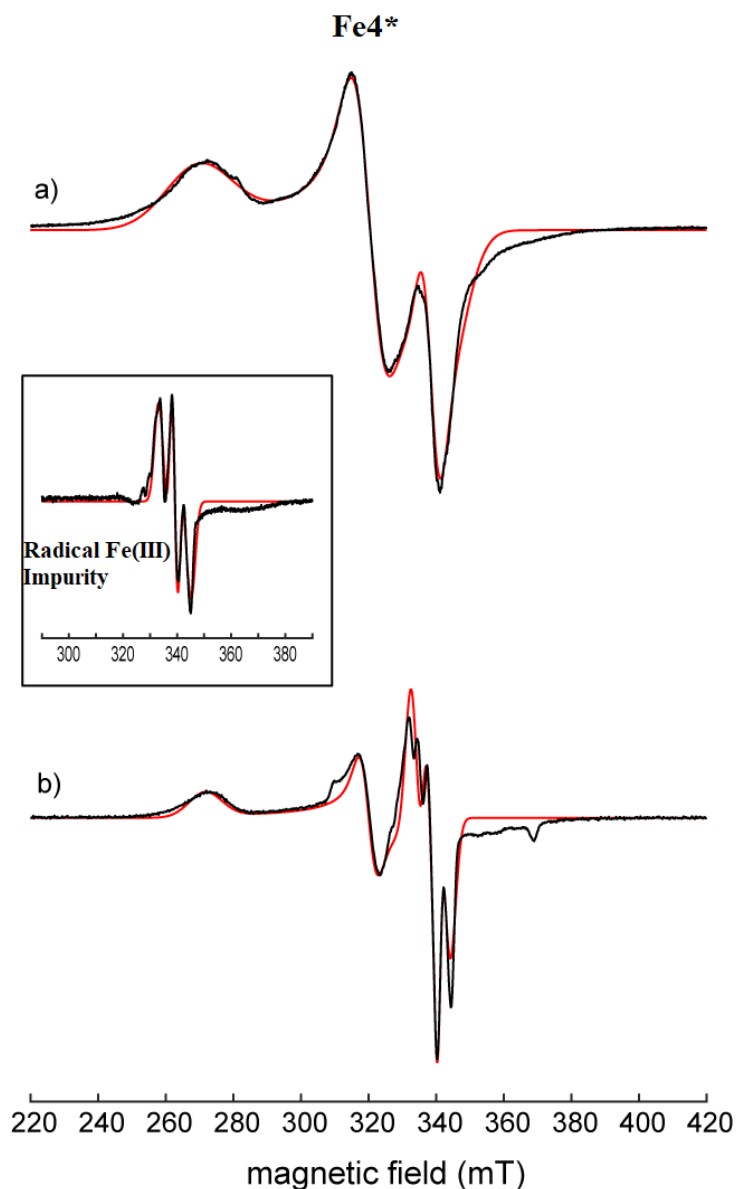


Figure 7.10 EPR spectra (black) of 2 different preparations of **Fe4*** (a and b), utilizing identical synthetic preparations. The insert shows a mixed Fe(III) radical species that seems to form as an impurity (or decomposition product) upon oxidation of Fe3* to Fe4*. The spectrum shown in a is relatively pure, while b shows the Fe(III) mixed radical impurity superimposed on the spectrum of Fe4*. Red traces represent simulated spectra. For more simulation details, see Experimental. Spectra were recorded at 10 K.

In both samples of **Fe4***, similar g-values were calculated which agree with the assignment of **Fe4*** as a low spin Fe(III)-centered paramagnetic species. The g-values were determined as 2.49, 2.10, and 1.96 and 2.47, 2.10, and 1.97, respectively, for the samples in Fig. 7.10a and 7.10b. The major difference between the two spectra is that, in 10b, there is roughly 18% impurity of the

ligand radical species superimposed on the **Fe4*** spectrum. The radical impurity was fitted with $g = 1.982$ and ^{14}N hyperfine couplings of $A_{\text{iso}} = 6.4$ MHz and $A_{\text{dip}} = 78.8$ MHz; these parameters agree quite well with those found in the sample of the radical impurity. These studies of the Fe(III) terminal imide-species, **Fe4*** suggest that the oxidation of the complex results in unpaired electron localization on the metal center. The ligands remain intact, and while the species is unstable, the instability does not likely manifest itself in the type of reactivity exhibited by **Ru5** to produce **Ru4**.

In contrast to **Fe4***, **Fe6**, which is easily recrystallized, does not present impurities in the EPR spectrum and has consistently given a composite spectrum with both metal- and ligand-based radical signal. In both spectra in Fig. 7.11a and 7.11b, there are two sets of features which show low-spin Fe(III) character and organic-imido based radical character with ^{14}N hyperfine coupling with a g -value substantially shifted from an isolated organic radical. The spectrum of **Fe6**, overall covers a narrower magnetic field than **Fe4***. The Fe(III) paramagnetic center was assigned g -values of 2.35, 1.99, and 1.97 in Fig. 7.11a, and 2.36, 2.00, and 1.99 in 10b. Respectively, these Fe(III)-centered contributions to the spectra in the two different samples are 71% and 75% of the total signal observed. The imido-centered radical in Fig. 7.11b provided a g -value of 2.014 and ^{14}N hyperfine couplings of $A_{\text{iso}} = 8.4$ MHz and $A_{\text{dip}} = 76.5$ MHz. In the spectrum, the ^{14}N coupling is not resolved due to large linewidths, which is markedly different from the organic-ligand radical

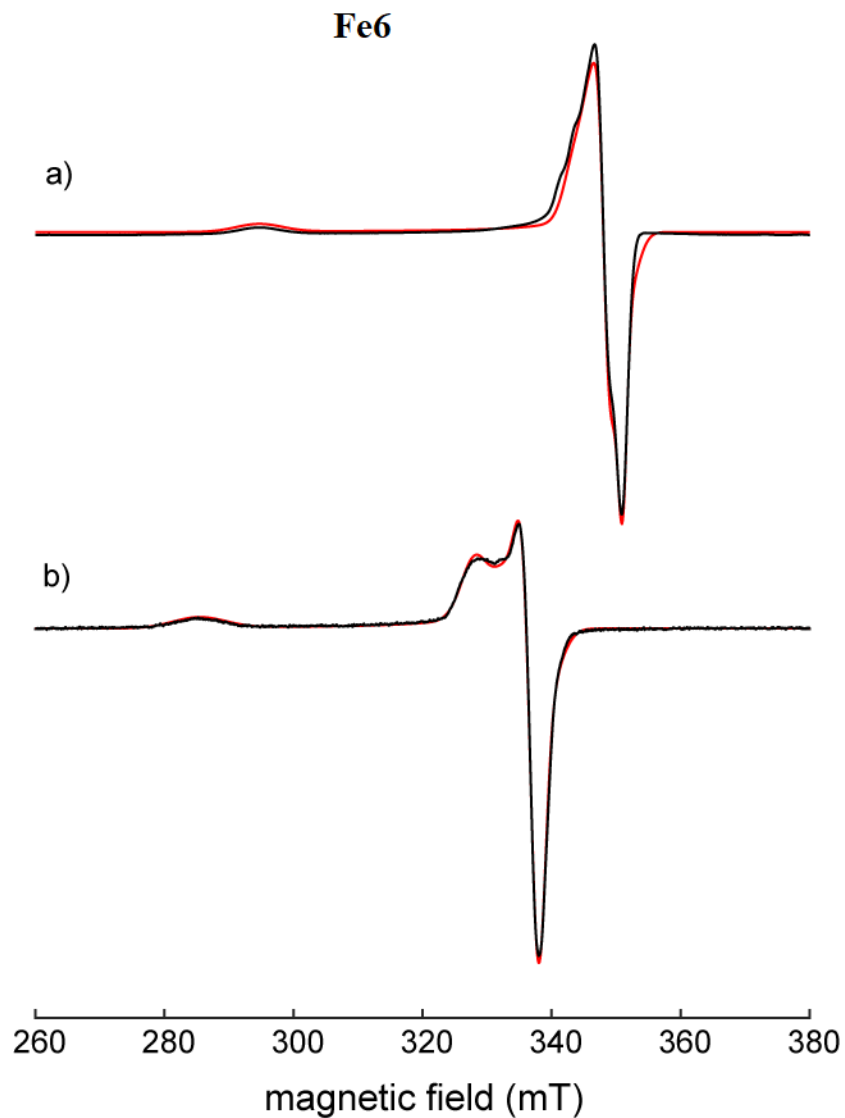


Figure 7.11 EPR spectra of two different preparations of Fe6 (black) and their simulated spectra (red), utilizing identical synthetic methods. Both samples show very similar characteristics, with about 75% Fe(III)-centered character and 25% ligand-centered radical with ^{14}N hyperfine coupling. Two different lineshapes are noted in toluene (top) and 2-methylTHF (bottom), but the radical character has very similar properties in both spectra. Spectra were recorded at 10K

signals observed in the **Fe4*** system (or **Ru5***, below). Also note that the spectrum in Fig. 11a was recorded with **Fe4*** in toluene while the spectrum in Fig. 7.11b was in 2-methylTHF.

While the formality of fitting the EPR spectra might define the spectra for **Fe6** shown in Fig. 7.11a and 7.11b most properly as two different species with separate $S = \frac{1}{2}$ paramagnetic centers, the spectra represents a static mixture of the solution state populations. The “powder”

spectra are recorded for the molecular species frozen in a solid matrix of 2-methylTHF or toluene, and thus the populations observed should be proportional to the solution state populations in terms of where the radical character is delocalized in the molecule. Another way to describe this is that the “two species” corresponding to the two paramagnetic ($S = 1/2$) centers observed in these samples are two electronic ground state resonance contributors of the **Fe6** molecule.

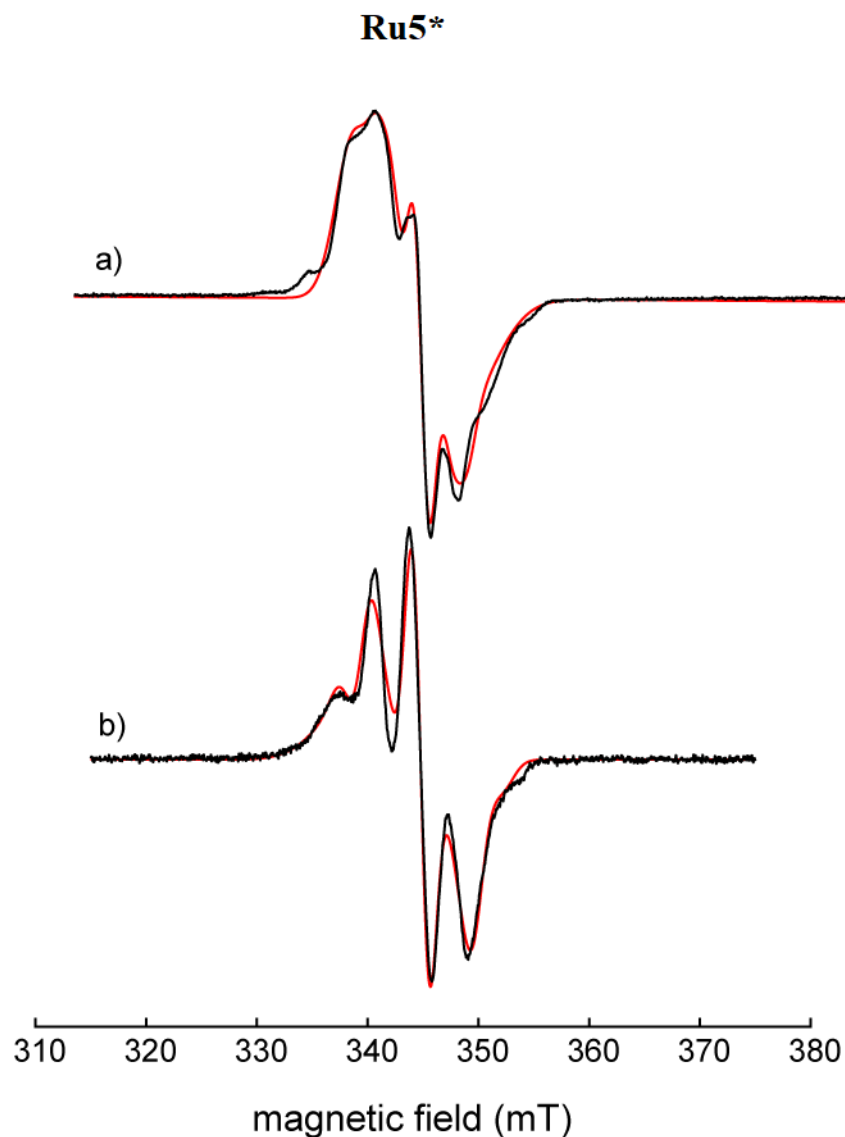


Figure 7.12 EPR spectra of two different samples of **Ru5*** (black) and their simulated spectra (red), utilizing identical synthetic methods. The samples are treated as a composite of two distinct paramagnetic centers—one centered on Ru(III) and one centered on the imide fragment. The two spectra show dramatically different proportions of each radical center in the sample. Spectrum (a) is about 90% Ru(III) and 10% ligand radical, whereas spectrum (b) shows about 30% Ru(III) character and 70% ligand radical. These spectra were taken from different batches of **Ru5***, prepared following the same synthetic procedures. The relative distribution of radical character seems to be affected by synthesis and sample preparation of the compounds.

The paramagnetic behavior of **Fe6** is similar to that exhibited by **Ru5***, however, the relative contributions of the ligand-centered and Ru(III)-centered paramagnets vary substantially from sample to sample. The spectra shown in Fig. 7.12a and 7.12b are, again, from separate preparations of **Ru5***. The two spectra show the same two paramagnetic centers giving rise to the

same sets of signals, but in different proportions. The spectra in Fig. 7.12a is composed of about 90% Ru(III) signal with g -values of 2.06, 2.01, and 1.97, with the remaining 10% originating from a radical contributor with $g = 2.007$ and ^{14}N hyperfine coupling of $A_{\text{iso}} = 4.0$ MHz and $A_{\text{dip}} = 80.6$ MHz. By contrast, the spectra in 11b is only about 30% Ru(III)-centered where $g = 2.05, 2.04,$ and 1.96 and 70% ligand-based radical with $g = 2.0042$ ($A_{\text{iso}} = 15.5$ MHz and $A_{\text{dip}} = 56.6$ MHz). The ligand-based radical's g -value is closer to free electron g -value than those noted in **Fe6** and **Fe4***, demonstrating different orbital angular momentum coupling with the metal. While few literature examples of EPR characterization for low-spin Ru(III) are available, the values determined for Ru(III) are similar to literature reports of Ru(III) paramagnetic centers in zeolites.⁴³

The results of these EPR analyses are summarized in Fig. 7.13, showing the relative distribution of radical character observed in each species. With these analyses in hand, we had additional experimental support for the induction of ligand-radical character in the oxidized **Ru5*** (and **Ru5**) species. We had also observed that with the same ligand set on Fe ($\text{P}_3 = \text{PMe}_3/\text{dppe}$), the radical character stays localized on the metal. This suggests a fundamental difference in the electronic structure in these two systems based on the identity of the metal. Alternatively, with the more rigid and roughly C_{3v} symmetric triphos ligand system ($\text{P}_3 = (\text{Me}_3\text{Si})\text{C}(\text{CH}_2\text{PMe}_2)_3$), some ligand-centered radical character is induced in the Fe(III) system. This suggests that changing the ligand set can induce similar behavior between Fe and Ru(III) metal centers toward their ligands, restoring their electronic structure similarities between the two metals.

The question still remains, what is the most accurate way to describe radical character on the metal versus the ligand in these systems? In both the **Ru5*** and **Fe6** samples, the ligand-centered paramagnetic centers contribute a substantial proportion of the paramagnetic character observed in these compounds. Is the delocalization a reversible delocalization that represents

proportional population of a ground and excited state that lie close in energy? If this is the case, the two paramagnetic centers may still be most aptly discussed as a single species, in which EPR spectroscopy of a frozen solution allows us to view the population ratio of the two distinct electronic states when the solution was prepared.

Is the phenomenon of radical delocalization between the metal and aryl imido ligand an equilibrium process? Alternatively, is delocalization of the radical in the aryl imido π system an irreversible process, resulting in different proportions in different samples that have otherwise indistinguishable characteristics? For example, if the unpaired electron density is shifted to the imide ligand, a geometric distortion of the complex could then pose a barrier to reverse this process. If the process is an equilibrium or irreversible “reaction” in which the metal oxidizes the ligand, external factors like temperature and the age of the sample may result in different populations of the metal- vs. ligand-centered radical states arising from differences in the handling of the complex.

Regardless of the formalism with which we label the behavior of these complexes, the trend was observed that in these species, Ru has the ability to delocalize a great deal of radical character onto the aryl imide ligand (up to 70% was observed). By comparison, the Fe analogue to **Ru5***, **Fe4***, localizes the radical on the metal. On the other hand, in **Fe6**, the unpaired electron is, again, consistently delocalized across both the metal and the imide ligand. This characterization by EPR supports the reactivity observed with Ru, which led to the isolation of **Ru4**. Although the same reactivity was not observed in the Fe systems, these experiments also demonstrate that substantial radical delocalization also occurs in **Fe6**. Thus both the metal and the basal ligand set play significant roles in the electronic behavior exhibited by unpaired electron density in these complexes.

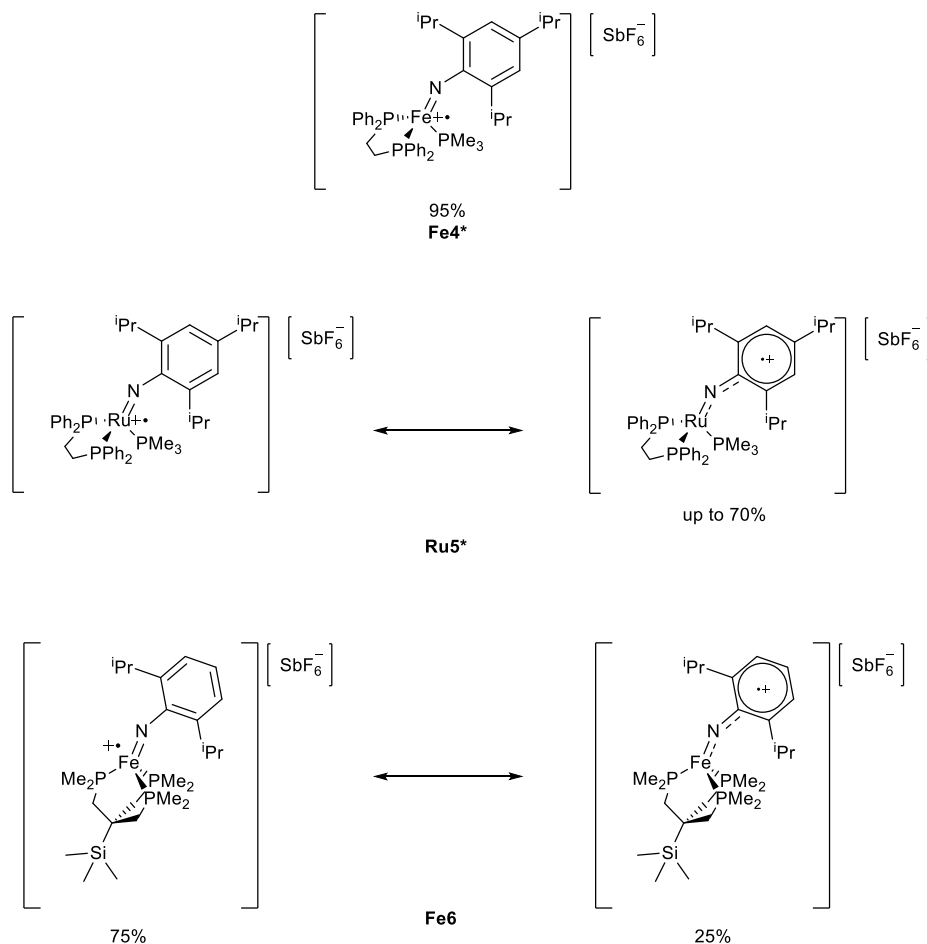


Figure 7.13 The figure shows the radical localization in the **Fe4***, **Ru5***, and **Fe6** cations. Note that with **Fe4***, the cationic species is most accurately described by a single paramagnetic center. However, the **Ru5*** and **Fe6** spectra could only be successfully modeled as a composite of two paramagnetic species, where both a metal- and ligand-centered radical contribute to the entire spectrum.

7.6 Computational Analysis Comparing Fe and Ru Analogues¹²

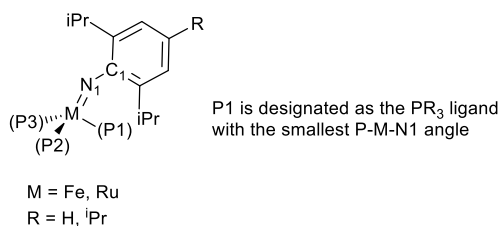
The crystallographic and EPR data for complexes **Fe4***, **Fe6**, and **Ru5*** clearly indicate a wide variance in the amount of radical localization versus delocalization observed in the M(III) cationic imide radicals discussed above. Moller-Plesset second-order perturbation theory (MP2) and multistate complete active space second-order perturbation theory (CASPT2)^{44,45} were applied to investigate the observed differences between the iron and ruthenium complexes. For

¹² Calculations were performed by Professor Ben Levine and his former graduate student, Dr. B. Scott Fales. The results presented here are a summary of their findings based on experimental work in the Odom group.

computational convenience, truncated versions of **Fe1** (Fe(NAr)(PMe₃)₃) and **Ru1** (Ru(NAr)(PMe₃)₃) were approximated with model compounds **Fe7** and **Ru6**: Ph–N=M(PH₃)₃. Computational details are presented in the Experimental section, along with the optimized coordinates.

Table 7.5 Data from the X-ray crystal structures of several Fe and Ru-imide compounds for comparison to the computed optimized structures of **Fe7** and **Ru6**.

Bond (Å)/ Angle (°)	Compound							
	Ru1	Ru1*	Ru3	Fe3	Fe3*	Fe5	Fe6(1) ^b	Fe6(2) ^b
M-N1	1.811(2)	1.817(4)	1.808(6)	1.657(4)	1.653(9)	1.667(3)	1.643(4)	1.653(4)
M-P1	2.224(1)	2.224(1)	2.240(2)	2.156(2)	2.166(4)	2.136(1)	2.232(2)	2.232(2)
M-P2	2.239(1)	2.240(2)	2.240(2)	2.155(2)	2.157(3)	2.144(1)	2.229(2)	2.235(2)
M-P3	2.254(1)	2.253(1)	2.275(2)	2.175(2)	2.162(3)	2.148(1)	2.195(2)	2.192(2)
N1-C1	1.372(4)	1.364(6)	1.388(9)	1.381(5)	1.387(13)	1.372(5)	1.386(6)	1.382(6)
M-N1-C1	174.9(2)	179.9(3)	166.5(5)	171.0(3)	172.1(8)	178.9(4)	172.5(4)	167.8(4)
N1-M-P1	113.69(8)	119.3(1)	106.1(2)	107.2(1)	111.7(3)	121.2(1)	105.6(2)	101.5(2)
N1-M-P2	122.63(8)	121.9(1)	127.7(2)	125.0(1)	122.8(3)	121.8(1)	129.4(2)	128.0(2)
N1-M-P3	128.40(8)	124.5(1)	136.4(2)	130.3(1)	132.2(3)	124.4(2)	130.8(2)	133.5(2)
P1-M-P2	96.47(3)	94.70(6)	97.38(8)	100.77(6)	96.4(1)	93.97(5)	93.93(6)	93.23(6)
P1-M-P3	95.17(3)	95.36(5)	99.20(8)	102.35(6)	102.0(1)	93.88(5)	91.95(6)	93.16(6)
P2-M-P3	93.27(3)	93.99(5)	82.07(8)	86.10(6)	85.4(1)	93.70(5)	93.05(6)	94.36(6)



The experimentally determined structure of **Ru3** (Ru(NAr)dpe(PMe₃)) deviates farther from C_{3v} symmetry than that of **Fe3**, as indicated by a difference in the range spanned by the three N1–M–P angles (30.3° for **Ru3** vs. 23.3° for **Fe3**), as shown in Table 7.5 above. A similar trend is noted in the MP2-optimized structures of **Ru6** and **Fe7**, which have N1–M–P angles spanning

ranges of 9.5° and 3.4°, respectively (Table 7.6). The smaller ranges in these computed compounds relative to **Ru3** and **Fe3** can be attributed to the difference in the ligands. In both **Ru3** and **Fe3** the phosphine ligands are not identical, which likely encourages further deviation from C_{3v} symmetry. For example, consider the ranges observed in the X-ray structures of **Ru1** and **Fe5**, which are 14.7° and 3.2° respectively, where three identical PR_3 ligands are bound to the metal; these values are much more similar to the ranges computed for **Ru6** and **Fe7**.

Table 7.6 N1-M-P angles (°) as optimized at the MP2 level of theory. The range spanned by each set of angles is also given.

Angle	Compounds	
	Ru6	Fe7
N1-M-P1	122.1	121.2
N1-M-P2	122.3	121.6
N1-M-P3	131.6	124.6
Range	9.5	3.4

As described in the introduction, it was previously proposed that the deviation of **Ru1** from C_{3v} symmetry is due to the nature of the HOMO, which is composed of the Ru d_z^2 orbital and a σ -bonding orbital on the aryl imide ligand's nitrogen atom. In this interaction, a deformation of the complex, which shifts the imide ligand off the z-axis and breaks the C_{3v} symmetry of the molecule, stabilizes the HOMO of the complex.⁴⁶ By comparison, the optimized structure of **Fe7** is much more symmetric. Thus, in this configuration, the HOMO (Figure 7.14, top-left inset) is purely antibonding—the aryl-imide fragment remains relatively aligned with the z-axis of the molecule. As the imido ligand moves farther from the C_3 axis (z-axis), as in **Ru6**, the nitrogen atom shifts closer to the node of the metal d_{z^2} orbital. This generates a mixed HOMO with both bonding and antibonding character (Figure 7.14, top-center inset). The partial bonding character is represented by the blue lobe, marked by a green arrow. We can attribute the stronger distortion in **Ru6**, relative to **Fe7**, to the stronger bonding/antibonding interactions associated with second-row transition

metals compared to first-row transition metals in the same group, consistent with increased overlap in second row metals (due to the primogenic effect).

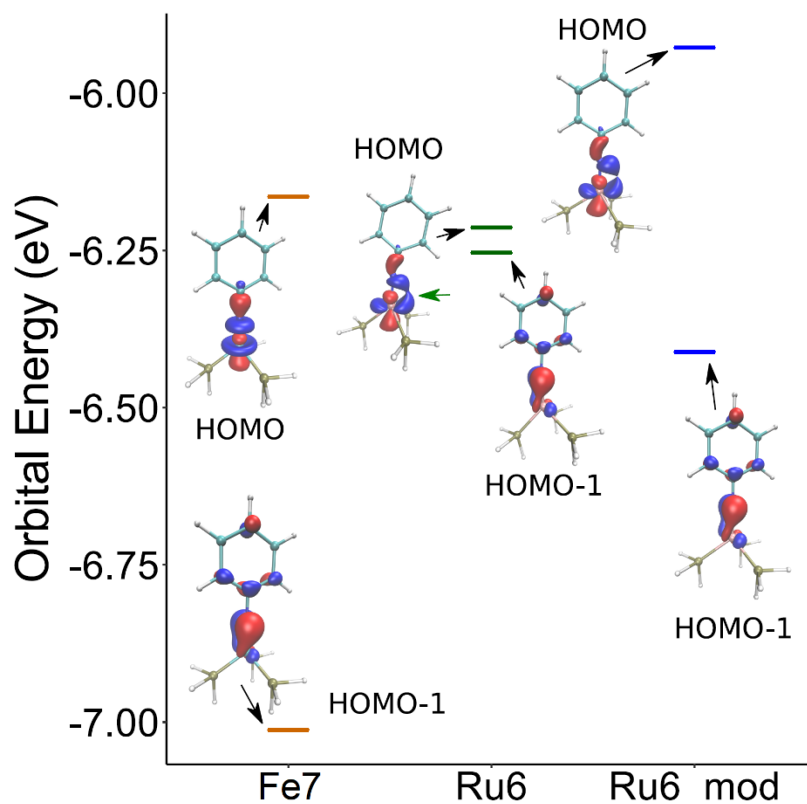


Figure 7.14 The orbital energies (defined as the negative ionization potential, as described in the text) of **Fe7**, **Ru6**, and **Ru6_mod** computed at the CASPT2 level of theory. Insets show the HOMO and HOMO-1 orbitals (SONOs of the cations, as described in the text). A green arrow indicates the bonding lobe of the HOMO of **Ru6**.

These results, therefore, agree with conventional theories and experimental evidence, which supports the accuracy of the orbital description provided by these calculations. With the ground state structures for M(II) compounds established, the balance between M(III) and ligand-centered radical character in **Ru6** and **Fe7** were examined. Experimental EPR results (above) indicate that **Fe4*** is Fe(III) in character, while **Ru5*** demonstrates mixed M(III)/ligand radical character. CASPT2 calculations also suggest that **Ru6** would more likely exhibit ligand-radical character than **Fe7** (Fig. 7.14) and provide a physical explanation for this trend. In **Fe7**, the metal-centered (d_{z^2}) HOMO is 0.85 eV above the HOMO-1 orbital, which has significant population on

the ligand. This large energy gap prevents mixing of the HOMO and HOMO-1 in $[\text{Fe7}]^+$, resulting in an iron-centered radical. In contrast, the HOMO and HOMO-1 of **Ru6** are split by only 0.04 eV. Similar to the **Fe7** case, in **Ru6**, the HOMO-1 orbital also has a large orbital contribution from the imide ligand. Unlike in **Fe7**, the closeness of the energies of the HOMO and HOMO-1 will facilitate mixing of the two orbitals, leading directly to ligand radical character.

These comparisons line up well with the experimental characterization of **Ru5*** and **Fe4***, but the intermediate behavior of **Fe6** remained unexplained. To investigate the relationship between the basal PR_3 ligand set and the HOMO and HOMO-1 energies, a hybrid model complex was generated. **Ru6_mod** was developed by taking the optimized structure of **Fe7** and replacing the central Fe atom with Ru. The bond distances were then altered by rigidly stretching the metal ligand bonds to match the optimized **Ru6** bond lengths (ligand-metal-ligand bond angles and ligand-internal coordinates remain frozen at their **Fe7**-optimized values). This preserved the coordination geometry while preserving realistic orbital overlaps on changing the metal identity.

The results of this exercise are consistent with other calculations. The closer the geometry of the complex to true C_{3v} symmetry, the bigger the energy gap is between the HOMO and the HOMO-1. This energy gap between the HOMO and HOMO-1 is 0.48 eV in the more symmetric **Ru6_mod**, versus 0.04 eV in **Ru6**. The only structural difference between these two models is the ligand orientation, more or less C_3 symmetric. This energy difference is created by a destabilization of the HOMO by 0.29 eV, as well as a simultaneous stabilization of the π -bonding HOMO-1 interaction between Ru and N by 0.16 eV. Thus, the orientation of the P_3 -basal set seems to be crucial in determining the localization of the unpaired electron upon oxidation of these complexes.

What is perhaps most interesting about this finding is that in the Fe system where the P ligands themselves are symmetric, with triphos in **Fe5/Fe6**, the oxidized complex demonstrates

radical character more consistent with distortion from C_{3v} symmetry. This is supported by the heavily distorted solid-state X-ray structure obtained for this complex. With the inherently less symmetric P_3 basal set of PMe_3 and dppe, in **Fe3*/Fe4***, a higher degree of C_3 symmetry is demonstrated upon oxidation.

This conclusion initially seems counterintuitive, as we would expect the triphos ligand to enforce more rigid C_{3v} symmetry. The symmetry of **Fe5** is higher than that of **Fe3** or **Fe3***, for example. However, due to the specific orientations enforced by the chelator—which in the Fe(II) complex maintains symmetric P coordination—the ligand is less adaptable to electronic changes at the metal. When the Fe(II) is oxidized to Fe(III), no subtle shifts in the positions of the P_3 ligands, to stabilize the complex upon oxidation, is possible. As a result, a dramatic distortion of the N1–Fe1–Px bond angles occurs. This results in a more symmetric ligand set producing a less symmetric radical cation, which facilitates ligand radical character. Such a result demonstrates a need for detailed electronic structure studies with M–E multiple bond complexes, as results are often counter to predictions. Based on the small sample size of complexes in this study, it also seems that generalizations about the electronic structures require a far larger sampling of complexes. As the small changes in ligand choice here led to dramatic changes in the character of the complexes examined, it is clear that no single factor dominates the electronic character of these complexes.

7.7 Reactivity Studies with Fe5

Due to the instability of **Fe1**, and our inability to isolate it from the crude reaction mixture, which contains H_2NAr/Ar^* , LiCl, and **Fe2/2***, reactivity studies similar to those undertaken previously with **Ru1**, could not be assessed with the exact Fe analogue. **Fe1** and **Fe5** are likely to possess similar electronic structure, given their 3-fold symmetric tri(alkyl) phosphine basal sets, so reactivity studies were instead pursued with **Fe5**.

If we consider a simple molecular orbital model for this system, applying idealized C_{3v} symmetry, the frontier orbitals are likely an e set of π^* orbitals representing antibonding interaction between the imide N and the Fe d_{xz} and d_{yz} orbitals. The π -bonding orbitals should be more heavily N-centered, making these antibonding orbitals more Fe-centered. This is consistent with the picture for Ru analogues, and in the Fe system, could be even more pronounced; this would be consistent with the periodic trend of weaker orbital overlap among ligands and first row transition metals (i.e. primogenic effect). The electron distribution across these MO's likely imparts nucleophilic character to both the Fe and N in the metal-imide bond. This makes reactivity from either site possible, with specific **Fe5** interactions with substrates influenced by both steric and kinetic factors. A series of reactants with an electrophilic center were combined with **Fe5** to probe its reactivity and begin looking for trends.

Carbon disulfide (CS_2) is an interesting substrate for several reasons. Several plausible possibilities from reaction of this substrate with **Fe5** can be imagined, from a [2+2]-cyclometallated product to a terminal sulfide species. Upon addition of 1 equivalent or a large excess (neat) of CS_2 , dark purple solutions of **Fe5** turn dark red and a maroon colored, microcrystalline solid precipitates. Analysis of the crude solution by GCMS and ^{14}N NMR appears to show production of 2,6-diisopropylthioisocyanate. We propose that the minimally soluble, maroon colored microcrystalline solid is a dimeric or oligomeric Fe(II) triphos species with bridging sulfides. While we were unable to confirm this structurally, the byproduct characterization heavily supports this stoichiometry. It also suggests that both the imide N and the Fe center are directly involved in the reactivity of **Fe5** with CS_2 . This could occur either via a concerted [2+2] cycloaddition process, followed by elimination of $SCNAr$ or potentially by nucleophilic attack of the imide N on the CS_2 C, followed by insertion of S into the N-Fe bond.

This result appears consistent with the results published by Deng, et. al. for the reactivity noted between CS₂ and their Co(NAr)(PMe₃)₃ complex. They report that addition of CS₂ with their Co(NAr)(PMe₃)₃ as a [2+2] cycloaddition. Upon exposure of the metallocyclic compound to wet hexane, SCNAr is liberated in 90% yield.⁴⁷ The accompanying Co-S complex, however, was not isolated or structurally characterized. It would be interesting to determine if **Fe5** can perform a similar reaction with CO₂, or even a carbodiimide, which could demonstrate metathesis with the Fe–N imide fragment.

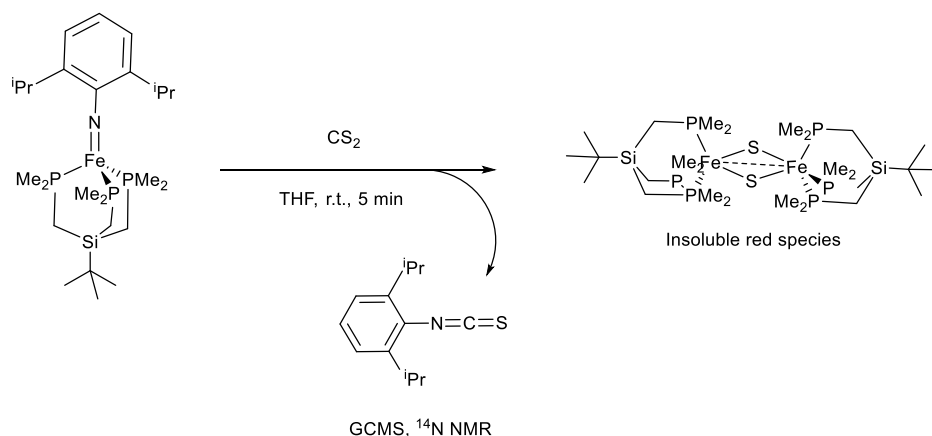


Figure 7.15 Addition of CS₂ to the terminal Fe(II) imide, **Fe5**, results in the production of 2,6-diisopropylphenylthioisocyanate and an insoluble red species proposed to be [Fe(^tP₃)(μ-S)₂].

Another interesting substrate with which **Fe5** reacts is benzaldehyde. Initially, the reaction was performed by combining 1 equivalent of benzaldehyde with 1 equiv of **Fe5**. The reaction solution went from dark purple to bluish green upon addition, and from the reaction solution, crystals of **Fe5** were obtained. The reaction was performed again, by combining 2 equivalent of benzaldehyde with 1 equivalent of **Fe5**. This resulted in a high yield of the chiral, metalocyclic Fe complex, **Fe8**, shown in Fig. 7.16. This reactivity differs from that observed by Deng, et. al. for the Co(NAr)(PMe₃)₃ which simply adds one equivalent of benzaldehyde to the complex to form a κ₂-amidate ligand on Co.

Based on the structural data for **Fe8**, the 7-membered metallocycle is best represented as drawn in Fig. 7.16. The bond lengths indicated double-bond character between N1 and C1, as well as between O1 and C1. The compound is diamagnetic, and lacks a counter ion of any kind, and the structural characteristics of O2 suggest it is a monoanionic ligand. This suggests that O1 is also formally an RO⁻ type ligand and that resonance exists with the adjacent imine nitrogen (N1). This assessment is also supported by the planar orientation of N1, C1 and O1, as well as the observation that this protonation state yields the lowest R1(%) upon refinement of the structure. Addition of H atoms to different portions of the structure reduces the quality of the crystallographic refinement parameters. Also, no clear evidence of a terminal Fe–H is observed by ¹H NMR. This description of the ligand is consistent with a loss of H₂ and suggests that upon interaction of the electrophilic carbon in the benzaldehyde with the imide moiety, a highly reactive Fe species is generated, capable of inducing C–C bond formation (coupling of the benzaldehydes).

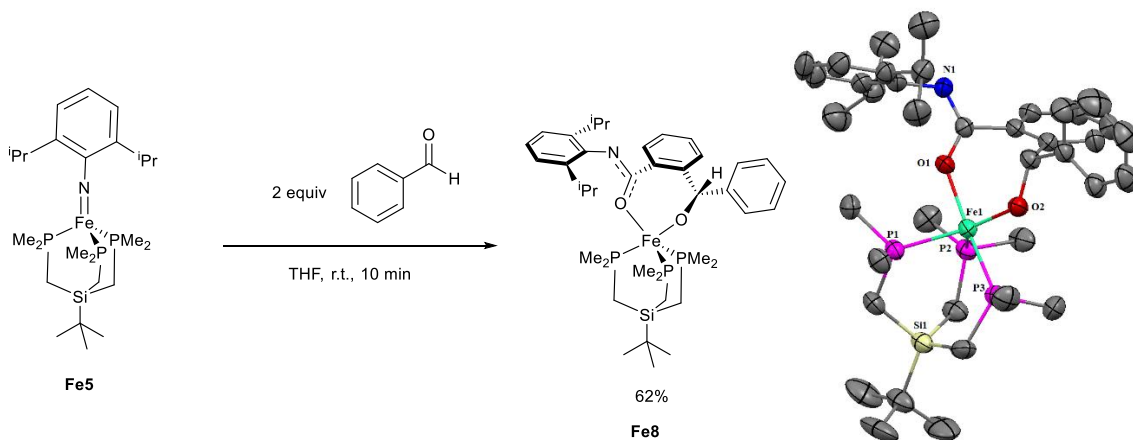


Figure 7.16 Reaction of 2 equivalents of benzaldehyde with **Fe5** produces a metalacyclic species which is chiral, and appears to be diamagnetic, low spin Fe(II). Based on bond lengths and angles in the crystal structure, the two oxygens coordinated to Fe appear anionic, with N1 best described as an imine. This means that loss of H₂ has occurred during the reaction. The crystal structure (*right*) is shown with ellipsoids at 50% probability. H's and one molecule of n-hexane in the lattice were omitted for clarity. (Fe1–O1 = 1.985 Å, Fe1–O2 = 1.858 Å, O1–C1 = 1.291 Å, C1–N1 = 1.297 Å, O2–C9 = 1.416 Å).

One additional type of reaction examined with **Fe5** is imide group exchange with protic H₂NR species. This process is slow but does appear to occur when an excess of H₂NPh is added

(i.e. 10 equiv. of H₂NPh gives about 50% conversion of **Fe5** over the course of 5 days estimated by NMR integrations). However, isolation of the converted product from a solution containing a huge excess of H₂NR was not productive. The imide group has been observed to exchange with 1,1,-dimethylhydrazine at a similar rate in solution, but again, isolation of the resulting hydrazido complex was not achieved from the reaction solution. Specifically, with the hydrazine exchange, it appears to be an equilibrium process, as complete conversion is not noted after extended periods of time or with a large excess of H₂NNMe₂; this, coupled with the relative lability of H₂NNMe₂ and H₂NAr, may prevent separation of the new hydrazido species from the crude reaction solution. However, these reactions demonstrate that these pathways could provide interesting opportunities to generate and study new complexes in solution.

Lastly, we also discovered that 10 mol% **Fe5**, when combined with 1 equivalent of phenylacetylene catalyzes the dimerization of the alkyne into an enyne compound. However, alkyne dimerization and polymerization are not new or particularly difficult reactions to perform, so further optimization or expansion of this reaction was not pursued.

7.8 Conclusions

Examination of a series of Ru(II) and Fe(II) imido complexes has illustrated important geometric and electronic structure differences that result from changes in the metal and phosphine ligand set. In these Ru(NAr)P₃ and Fe(NAr)P₃ complexes, Ru appears to produce more bonding character in the HOMO and results in the geometric distortion of the N1–M–P bond angles. With Fe, the HOMO appears to be more strictly antibonding in nature which prevents the distortion observed with Ru. The basic properties of the metal in these analogues triggers a chain of electronic differences that lead directly to differences in reactivity.

These differences are exacerbated upon oxidation, as highlighted by the behavior of the complexes, **Ru5***, **Fe4***, and **Fe6**. The distortion observed in the Ru structures facilitates mixing of the HOMO and HOMO-1 orbitals, which provides a means of radical delocalization across the metal center and the arylimide ligand. By contrast, in the Fe system (**Fe4***), the HOMO and HOMO-1 have more discrepant energies, and therefore, upon oxidation, unpaired electron density is isolated on the Fe. Intermediate to these two cases is **Fe6**, which shows some amount of ligand-radical character, but not to the extent that was observed with Ru (**Ru5***). In these examples, both changes in the metal (i.e. going from Fe to Ru), and changes that restrict the flexibility of the P₃ basal set elicit a similar distortion of the N1–M–P angles upon oxidation. Through this structural effect, the HOMO and HOMO-1 energies are shifted and mixing between the two orbitals can occur. In both **Fe6** and **Ru5***, this results in partial oxidation of the aryl imide ligand and delocalized radical character. While the resultant electronic structures are similar, the initial cause of the structural distortion in both molecules is very different, and was not something that we predicted when synthetic efforts began.

These results highlight the need for more fundamental studies that probe the electronic structure of M=E complexes, where the character and subsequent reactivity associated with the M=E π - and π^* -orbitals are directly impacted by the properties of the metal changing. Only through systematic studies such as this will understanding of these types of bonds in transition metal complexes develop to the point of providing predictive guidance in designing and synthesizing new complexes.

7.9 Experimental

General Considerations. All manipulations were carried out under inert N₂ atmosphere, either in an Mbraun glovebox or under standard Schlenk techniques. The solvents acetonitrile,

toluene, dimethoxyethane (DME), pentane, and diethyl ether were sparged with nitrogen and passed over an activated alumina column prior to use. The solvents benzene, tetrahydrofuran, and *n*-hexane were dried over sodium-benzophenone ketal radical, refluxed, and distilled under nitrogen prior to use. All deuterated NMR solvents were purchased from Cambridge Isotope Labs. Benzene- d_6 was dried over CaH_2 and distilled under N_2 . The solvents $CDCl_3$ and CD_2Cl_2 were dried over P_2O_5 and distilled under N_2 . Tetrahydrofuran- d_8 and 2-methyltetrahydrofuran (used in the EPR experiments) were dried over Na and distilled under nitrogen. All solvents were stored over 3 Å molecular sieves in a glovebox after purification.

The triphos-ligand (P_3) was prepared according to literature procedures.^{41,48} Trimethylphosphine was purchased from Strem Chemicals, Inc. and used as received. Anhydrous $FeCl_2$ was purchased from Sigma-Aldrich, Inc. and used as received. 2,6-Diisopropylaniline was purchased from Sigma-Aldrich, Inc., distilled under N_2 from CaH_2 , and was stored in the glovebox after purification. 2,4,6-Triisopropylaniline was prepared following literature procedures⁴⁹ and dried by azeotropic removal of water in a Dean-Stark apparatus using benzene. $FeCl_2(dppe)$ was prepared as described in the literature.⁵⁰ $AgSbF_6$ was purchased from Sigma-Aldrich, Inc. and used as received. (Note, the $AgSbF_6$ was dissolved in THF, filtered over Celite, and precipitated with *n*-hexane prior to use if it was substantially darkened in color).

$LiNHAr$ and $LiNHAr^*$ were prepared by addition of 1 equiv of 2.5 M $nBuLi$ in hexanes to a cold ($-78\text{ }^\circ\text{C}$) solution of the respective amine in hexane; after stirring for 2 h and warming to room temperature, the salts were collected by filtration, washed with hexane, and used without further purification.

CS₂ was dried over Na₂SO₄ and distilled under N₂ prior to use. Benzaldehyde, phenyl acetylene, and 1,1-dimethylhydrazine were distilled under N₂ prior to use. 1,1-dimethylhydrazine was stored over 3 Å molecular sieves after distillation.

EPR spectroscopy EPR measurements were made on a Bruker E-680X spectrometer at X-band using a 4122 SHQE-W1 resonator. Cryogenic sample temperatures were achieved using an Oxford ESR-900 cryostat together with an ITC-503 temperature controller. EPR data were simulated using EasySpin 5.2.11 running in the MATLAB 2017b environment.⁵¹

Electronic structure calculations CASPT2 is an inherently many-body theory, making interpretation of its results in terms of intuitive concepts such as orbitals and orbital energies somewhat ambiguous. Here, we define the HOMO of the neutrally-charged species as the singly-occupied natural orbital (SONO) of the ground state of the cation of the same species at the same geometry. The negative of the computed vertical ionization potential can be interpreted as the HOMO energy (Koopmans' theorem). Similar analysis of the excited states of the cation yields orbitals and orbital energies for lower occupied orbitals (HOMO-1 corresponds to the SONO of the first excited state of the cation, and so on). Although one can imagine ambiguities arising in this analysis, in the present work all of the discussed orbitals and orbital energies were completely unambiguous.

Neutral **Ru6** and **Fe7** were optimized at the MP2 level of theory. Vertical ionization potentials are computed as the difference between the MP2 energies of the neutral and the CASPT2 energies of the cations at the neutral-optimized structures. An active space of 7 electrons in 4 orbitals and a state average over 4 states was used for CASPT2 calculations of **Ru6** and **Fe7**. All CASPT2 and MP2 calculations were performed using the cc-pVTZ basis for Fe, the cc-pVTZ-PP basis and effective core potentials for Ru, and the cc-pVDZ basis for all other atoms.⁵²⁻⁵⁵ The

multistate variant of CASPT2⁵⁶ was used for all calculations. All calculations were performed with the MolPro software package.⁵⁷⁻⁶¹ Orbital pictures were created with VMD.⁶²

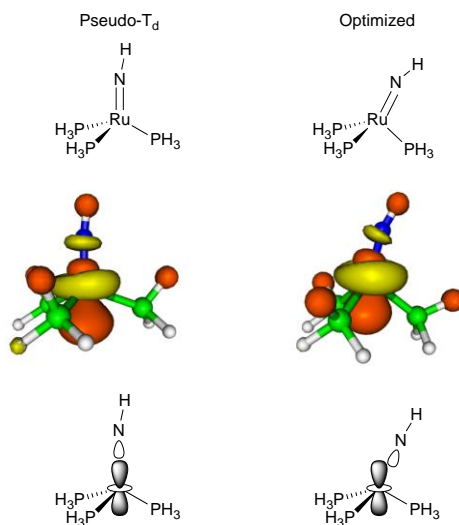


Figure 7.17 Results demonstrating the electronic basis of the distortion of **Ru1** away from C_{3v} symmetry.⁴⁶

Instrumentation

NMR All NMR spectroscopy was performed at Michigan State University's Max T. Rogers NMR Facility. These include a UNITYplus 500 spectrometer equipped with a 5 mm switchable broadband probe operating at 36.12 MHz (^{14}N); a Varian Inova 500 spectrometer equipped with a 5mm pulse-field-gradient (PFG) switchable broadband probe operating at 499.84 MHz (^1H); a Varian Inova 600 spectrometer equipped with a 5 mm PFG switchable broadband probe operating at 599.89 MHz (^1H); and an Agilent DDR2 500 MHz NMR spectrometers equipped with a 5 mm PFG switchable broadband probe operating at 499.84 MHz (^1H), 125.73 MHz (^{13}C), and 202.35 (^{31}P). ^1H NMR chemical shifts are reported relative to residual C_6HD_5 in C_6D_6 as 7.16 ppm. ^{13}C NMR chemical shifts are reported relative to $^{13}\text{C}_6\text{D}_6$ as 128.06 ppm. ^{14}N NMR shifts are referenced to the internal peak for dissolved N_2 in NMR solvent (309.6 ppm vs. external nitromethane as 0 ppm).

X-ray Crystallography All crystallographic data was collected at the Michigan State University Center for X-ray Crystallography. All structures were collected on Bruker AXS instruments operating with either copper or molybdenum radiation sources. Data was collected at 173 K. Structure solutions were typically found using XT Intrinsic Phasing and refined by least squares using Olex software. For further information please see the .cif files provided as supporting information.

Cyclic Voltammetry All electrochemical experiments (CV's) were performed using a CH Instruments Electrochemical Workstation. The standard conditions were to prepare a 5.0 mL solution of 0.2 M TBAPF₆ (387 mg) in THF with 2 mmol of the complex under investigation. The experiments were run in an N₂ atmosphere MBraun glovebox, using a 3-electrode setup. This involved a Pt disc working electrode, Ag/AgNO₃ 0.1M reference electrode in MeCN, and a Pt wire counter electrode. All compounds were internally referenced to the ferrocene/ferrocenium couple as 0 V. Reversibility of events was assigned by observing linear correlation in a plot of (current)² vs. scan rate for a given redox couple.

Notably, the Ru(III) species seemed to react with electrolyte upon dissolution (evidenced by color change and lack of redox waves), thus adequate characterization by cyclic voltammetry could not be obtained.

Uv-vis UV-Vis spectra were collected using an Ocean Optics DH-mini UV-Vis-NIR spectrophotometer in an N₂ glovebox. Experiments were performed in dry THF using a quartz cell. The raw data were fit with OriginPro 9.0 software to obtain accurate peak separation and assignment of maxima assuming gaussian peak shapes.

Improved synthesis of cis-RuCl₂(PMe₃)₄ A 35 mL pressure tube was charged with Ru(COD)Cl₂ (1.00 g, 1 equiv), a stir bar, toluene (10 mL), and PMe₃ (1.60 g, 6 equiv). The tube was sealed inside the glovebox and transferred to a 110 °C oil bath. The solution was stirred for 12 h. Over the reaction time, the solution changed from opaque brown to transparent yellow. The pressure tube was removed from heat and transferred to the glovebox. The reaction solution was concentrated to about 2 mL *in vacuo* to yield large blocky yellow crystals of *cis*-RuCl₂(PMe₃)₄. The remaining reaction solution was decanted from the crystals, and chilled to yield additional product. NMR of the material match published spectra.⁴⁶ Yield: 1.4 g (83%).

Synthesis of RuNAr(PMe₃)₃ (Ru1) **Ru1** was prepared as previously reported,⁴⁶ using *cis*-RuCl₂(PMe₃)₄ as prepared above. Elemental analysis, ³¹P/¹H/¹³C NMR, and the structure from X-ray diffraction were published previously.⁴⁶ UV-vis absorption (THF, 21 °C): 465 nm (3039 cm⁻¹ M⁻¹), 290 (5532 cm⁻¹ M⁻¹), 232 nm (14065 cm⁻¹ M⁻¹). ¹⁴N NMR (benzene-d₆, 36 MHz, 25 °C): 326.3 ppm.

Synthesis of Ru(NAr)(dmpe)₂ (Ru2) A 20 mL scintillation vial was charged with **Ru1** (106 mg, 0.2 mmol, 1 equiv), 5 mL THF, and a magnetic stir bar. To this red-orange solution was added a solution of dmpe (65 mg, 0.4 mmol, 2 equiv) in 2 mL THF, dropwise, at room temperature. The solution was stirred for 4 h, over which time the solution became brownish-yellow in color. The volatiles were removed *in vacuo*, and the residue was rinsed with several small aliquots of *n*-hexane. The solids were then dissolved in a minimum amount of THF and layered with *n*-hexane. The layered solution was stored at -35 °C overnight to yield plate-like green-brown crystals of **Ru2** (52 mg, 45%). NMR: ¹H NMR (500 MHz, benzene-d₆): δ 7.27 (d, *J* = 7.3 Hz, 2H), 6.51 (t, *J* = 7.3 Hz, 1H), 2.87 (septet, *J* = 7.0 Hz, 2H), 1.51-1.38 (m, 4H), 1.34 (dd, *J* = 10.6, 6.9 Hz, 12H), 1.29-1.19 (m, 4H), 1.17 (d, *J* = 8.2 Hz, 6H), 1.10 (t, *J* = 3.2 Hz, 6H), 0.99 (t, *J* = 2.2 Hz, 6H), 0.82

(d, $J = 6.3$ Hz, 6H). ^{13}C NMR (126 MHz, THF- d_8) δ 119.84, 109.28, 108.19, 104.28, 33.33 (m), 30.44, 30.10 (m), 27.78, 25.73, 24.81, 23.73–22.89 (m), 22.39 (d, $J = 12.2$ Hz), 21.06–20.21 (m), 18.97, 13.92. ^{31}P NMR (202 MHz, benzene- d_6): δ 42.88 (t, $J = 14.7$ Hz), 30.76 (t, $J = 14.8$ Hz). ^{14}N NMR (36 MHz, THF): δ 577.0.

Synthesis of Ru(PMe₃)(dppe)(NAr) (Ru3) To a stirred solution of **Ru1** (134 mg, 0.398 mmol, 1 equiv) in THF was added a solution of dppe (164 mg, 0.402 mmol, 1 equiv) in 2 mL of THF. The reaction mixture was stirred for 1 h at room temperature. The volatiles were removed in vacuo, and the dark red solid residue was rinsed with cold hexane (3 x 1 mL). The volatiles were once again removed in vacuo, and the solids were dissolved in a minimal amount of toluene. The concentrated toluene solution was stored at -35 °C overnight to yield flaky, red-orange crystals of **Ru3** (202 mg, 87%). M.p.: 110 °C (dec). NMR: ^1H NMR (500 MHz, benzene- d_6): δ 8.08 (t, $J = 9.9$ Hz, 4H), 7.58–7.51 (m, 4H), 7.13 (s, 3H), 7.12–6.81 (m, 12H), 4.90 (septet, $J = 7.0$ Hz, 2H), 2.02–1.89 (m, 2H), 1.85–1.71 (m, 2H), 1.41 (d, $J = 6.9$ Hz, 12H), 0.60 (d, $J = 9.8$ Hz, 9H). ^{13}C [^1H] NMR (126 MHz, benzene- d_6): δ 133.90 (t), 130.94 (t), 128.97(s), 128.14(s), 122.73(s), 122.31 (d), 120.40 (d), 118.51(s), 30.23 (t), 27.77(s), 26.67(s), 23.65(s), 22.20 (d), 21.97(s). ^{31}P NMR (202 MHz, benzene- d_6): δ 99.31 (d, $J = 21.3$ Hz), 23.65 (t, $J = 21.2$ Hz). ^{14}N NMR (36 MHz, THF): δ 337.6 (s). UV-vis absorption (THF, 21 °C): 472 nm ($3610\text{ cm}^{-1}\text{ M}^{-1}$), 314 ($6576\text{ cm}^{-1}\text{ M}^{-1}$), 272 nm ($16709\text{ cm}^{-1}\text{ M}^{-1}$). Elemental Analysis calc'd for C₄₁H₅₀NP₃Ru: C, 65.59; H, 6.71; N, 1.87. Found: C, 65.07; H, 6.80; N, 1.73.

Synthesis of [Ru(dppe)(PMe₃)(NAr)(NCCH₃)]₂[BAR^F₂₄]₂ (Ru4) A solution of **Ru3** was prepared (60 mg, 0.080 mmol) in 6 mL of a 1:1 (volume: volume) mixture of MeCN and DME. This red-orange solution was stirred at room temperature. A separate solution of AgSbF₆ (30 mg, 0.087 mmol) in 2 mL of MeCN/DME, was added dropwise to the solution of **Ru3**. After addition,

the reaction was stirred for 24 h at room temperature, over which time the reaction solution turned bright purple. The reaction mixture was filtered using Celite as a filtering agent to remove Ag^0 , and the filtrate was concentrated in vacuo. The concentrated filtrate was layered with hexane and stored at $-35\text{ }^\circ\text{C}$ for 3 days to get dark purple crystals of **Ru4** (62.1 mg, 75.6%). M.p.: $140\text{ }^\circ\text{C}$ (dec). NMR: ^1H NMR (500 MHz, CD_2Cl_2): δ 7.92 (s, 8H), 7.64 (t, $J = 8.2\text{ Hz}$, 8H), 7.38 (t, $J = 7.4\text{ Hz}$, 8H), 7.33 (dd, $J = 8.2, 5.2\text{ Hz}$, 12H), 7.27–7.20 (m, 12H), 6.93 (d, $J = 7.4\text{ Hz}$, 4H), 6.91–6.86 (m, 2H), 4.55 (septet, $J = 6.8\text{ Hz}$, 4H), 2.42–2.25 (m, 4H), 2.09 (m, 2H), 2.07–1.95 (m, 4H), 1.18 (d, $J = 6.9\text{ Hz}$, 24H), 0.67 (d, $J = 9.9\text{ Hz}$, 18H). ^{19}F NMR (470 MHz, CD_2Cl_2): δ -62.88 (s). ^{31}P NMR (202 MHz, CD_2Cl_2): δ 99.24 (d, $J = 22.5\text{ Hz}$), 24.43 (t, $J = 22.5\text{ Hz}$). (Note: ^{13}C and ^{14}N could not be obtained due to compound instability in solvents in which it was soluble enough to see NMR signal).

Synthesis of $\text{Fe}(\text{NAr})(\text{PMe}_3)_3$ (Fe1) A 20 mL scintillation vial was charged with FeCl_2 (50 mg, 0.394 mmol, 1 equiv), a magnetic stir bar, and 8 mL of THF. To this off-white suspension, trimethylphosphine (0.25 mL, 2.37 mmol, 6 equiv) was added at room temperature. The mixture was stirred for 1 h, over which time the FeCl_2 dissolved, and the solution changed color from pink to pale aquamarine. After this color change, the solution was chilled ($-78\text{ }^\circ\text{C}$), while a separate solution of LiNHAr (152 mg, 0.827 mmol, 2.1 equiv) in 2 mL THF was prepared. The chilled iron-containing mixture was stirred and to it was added the LiNHAr solution dropwise. Upon addition, the solution turned orange. The solution was allowed to warm to room temperature, and stirring was continued for 18 h, at which point the solution had turned dark green. Attempts to isolate **Fe1** led to decomposition, but the complex is stable in the reaction solution for a few days with a slight excess of PMe_3 present. ^{31}P NMR (127 MHz, THF, $20\text{ }^\circ\text{C}$): δ 38.37 (s). ^{14}N NMR (36 MHz, THF, $20\text{ }^\circ\text{C}$): δ 312.1 (s).

Synthesis of Fe(dppe)(NHAr)₂ (Fe2) (Method A) A clean sample of X-ray quality single crystals could not be obtained from the reaction mixture to synthesize **Fe3**. However, the presence of a red, paramagnetic impurity was noted in this reaction. (Method B) A 20 mL scintillation vial was charged with FeCl₂(dppe) (150 mg, 0.29 mmol, 1 equiv), 4 mL THF, and a stir bar. This mixture was chilled at -78 °C. Separately, a solution of LiNHAr (105 mg, 0.58 mmol, 2 equiv) was prepared in 2 mL of room temperature THF. The chilled suspension of FeCl₂(dppe) was stirred, and the LiNHAr solution was added dropwise. Upon complete addition, the solution was opaque and red in color. The mixture was stirred for 4 h, warming to room temperature. The volatiles were removed in vacuo, resulting in a dark red residue. This residue was extracted with diethyl ether and filtered using Celite as a filtering agent. The filtrate was concentrated in vacuo, and the concentrated solution was stored at -35 °C to yield large, red crystals of **Fe2** (37 mg, 16%). μ_{eff} (benzene-d₆, 25 °C): 5.19 μ_{B} .

Synthesis of Fe(NAr)(PMe₃)(dppe) (Fe3) An in situ generated solution of **Fe1** (30 mg scale FeCl₂) was stirred at room temperature. To this mixture was added dppe (84 mg, 0.21 mmol, 1 equiv) as a solution in 2 mL of THF. The resulting mixture was stirred for 1 h at room temperature. The volatiles were then removed in vacuo, and the resulting dark brown residue was rinsed with hexane (4 mL, discarded). The residue was then extracted with diethyl ether to give a bright green solution. This ether solution was filtered using Celite as a filtering agent, concentrated in vacuo, and stored at -35 °C overnight. This yielded flaky, dark green X-ray quality crystals of **Fe3** (64 mg, 39%). M.p.: 134-135 °C. ¹H NMR (500 MHz, benzene-d₆): δ 8.05 (t, J = 8.7 Hz, 4H), 7.55 (t, J = 8.2 Hz, 4H), 7.34 (t, J = 7.6 Hz, 1H), 7.13 (t, J = 7.4 Hz, 4H), 7.10–7.00 (m, 9H), 6.97 (t, 1H), 4.78 (septet, J = 6.7 Hz, 2H), 1.89 (m, 4H), 1.33 (d, J = 6.8 Hz, 12H), 0.65 (d, J = 8.2 Hz, 9H). ¹³C[¹H] NMR (126 MHz, benzene-d₆): δ 156.53 (s), 141.58 (s), 140.18 (s), 133.84 (d), 130.81 (s),

128.72 (s), 120.94 (s), 120.46 (s), 35.13 (s), 27.00 (s), 23.90 (s), 23.56 (s), 22.32 (s), 21.73 (d). ^{31}P NMR (202 MHz, benzene- d_6): δ 115.16 (d, $J = 6.5$ Hz), 35.11 (t, $J = 6.4$ Hz). ^{14}N NMR (36 MHz, THF): δ 325.6 (s). UV-vis absorption (THF, 21 °C): 591 nm ($2009\text{ cm}^{-1}\text{ M}^{-1}$), 388 ($4471\text{ cm}^{-1}\text{ M}^{-1}$), 298 nm ($13460\text{ cm}^{-1}\text{ M}^{-1}$). Elemental Analysis calc'd for $\text{C}_{41}\text{H}_{50}\text{NP}_3\text{Fe}$: C, 69.79; H, 7.14; N, 1.99. Found: C, 69.40; H, 6.77; N, 1.77.

Synthesis of $\text{Fe}(\text{NAr})^t\text{P}_3$ (Fe5) An in situ solution of **Fe1** (prepared using 100 mg FeCl_2 , 0.79 mmol, 1 equiv) was stirred at room temperature. To the mixture was added $^t\text{P}_3$ (247 mg, 0.79 mmol, 1 equiv) as a solution in 2 mL THF. The reaction solution rapidly changed color from dark green to dark purple upon addition. The resulting solution was stirred for 1 h at room temperature, and the volatiles were removed in vacuo. The resulting black residue was extracted with hexane and filtered using Celite as a filtering agent until the extracts were colorless. The filtrate was then concentrated in vacuo to ~3 mL and stored at $-35\text{ }^\circ\text{C}$ overnight to yield blocky, dark purple X-ray quality crystals of **Fe5** (142 mg, 34 %). M.p.: $196\text{ }^\circ\text{C}$ (dec). ^1H NMR (500 MHz, benzene- d_6): δ 7.15 (dd, $J = 12.4, 4.7$ Hz, 1H), 6.97 (d, $J = 7.5$ Hz, 2H), δ 4.31 (septet, $J = 6.9$ Hz, 2H), 1.66 (m, 18H), 1.38 (d, $J = 7.0$ Hz, 12H), 0.67 (s, 9H), 0.27–0.24 (m, 6H). $^{13}\text{C}[^1\text{H}]$ NMR (126 MHz, benzene- d_6): δ 159.73, 139.51, 122.35, 119.98, 28.26–27.65 (m), 27.41, 26.43, 23.44, 16.76 (q, $J = 5.9$ Hz), 10.74. ^{31}P NMR (202 MHz, benzene- d_6): δ 47.38. ^{14}N NMR (36 MHz, THF): δ 315.2 (s). UV-vis absorption (THF, 21 °C): 632 nm ($2809\text{ cm}^{-1}\text{ M}^{-1}$), 549 ($3327\text{ cm}^{-1}\text{ M}^{-1}$), 383 nm ($7015\text{ cm}^{-1}\text{ M}^{-1}$). Elemental Analysis calc'd for $\text{C}_{25}\text{H}_{50}\text{FeNP}_3\text{Si}$: C, 55.45; H, 9.31; N, 2.59. Found: C, 55.45; H, 9.54; N, 2.61. $E_{1/2}$ (THF, 21 °C, $0\text{V} = \text{Fc}/\text{Fc}^+$): ($\text{Fe}^{+2/+3}$) -0.91 V (rev.).

Synthesis of $[\text{Fe}(\text{NAr})^t\text{P}_3]\text{SbF}_6$ (Fe6) A 20 mL scintillation vial was charged with **Fe5** (40 mg, 0.0727 mmol, 1 equiv), a magnetic stir bar, and 4 mL of DME. This solution was stirred at room temperature. Separately, a solution of AgSbF_6 (25 mg, 0.0727 mmol, 1 equiv) was prepared

in 2 mL DME, which was added dropwise to the stirred solution of **Fe5**. The resulting mixture was stirred for 12 h at room temperature, during which time the reaction solution went from dark purple to bright blue and solid Ag^0 precipitated. The mixture was filtered using Celite as a filtering agent, concentrated to ~3 mL total volume, and layered with 4 mL of hexane. This layered solution was stored at $-35\text{ }^\circ\text{C}$ overnight to yield small, blue X-ray quality crystals of **Fe6** (43 mg, 76%). M.p.: $121\text{ }^\circ\text{C}$ (dec). UV-vis absorption (THF, $21\text{ }^\circ\text{C}$): 624 nm ($3704\text{ cm}^{-1}\text{ M}^{-1}$), 353 ($5463.6\text{ cm}^{-1}\text{ M}^{-1}$), 289 nm ($13031\text{ cm}^{-1}\text{ M}^{-1}$). Elemental Analysis calc'd for $\text{C}_{25}\text{H}_{50}\text{F}_6\text{FeNP}_3\text{SbSi}$: C, 38.63; H, 6.48; N, 1.80. Found: C, 38.60; H, 7.03; N, 1.73. μ_{eff} (THF- d_8 , $25\text{ }^\circ\text{C}$): $2.17\text{ }\mu\text{B}$. $E_{1/2}$, (THF, $21\text{ }^\circ\text{C}$, $0\text{ V} = \text{Fc}/\text{Fc}^+$): ($\text{Fe}^{+2/+3}$) -0.89 V (rev.).

Synthesis of Ru(NAr)(PMe₃)₃ (Ru1*)* To an Erlenmeyer flask was added a stir bar, 200 mg of *cis*- $\text{RuCl}_2(\text{PMe}_3)_4$ (0.410 mmol, 1 equiv), and 20 mL THF to give a pale-yellow solution. This solution was chilled to $-78\text{ }^\circ\text{C}$ and to this cold solution was added a room temperature solution of LiNHAr^* (196 mg, 0.875 mmol, 2.1 equiv) in 3 mL THF dropwise. Upon complete addition, the solution had turned light orange. The reaction mixture was stirred overnight at room temperature to give a viscous dark red solution. The volatiles were removed in vacuo, and the residue was extracted with hexane until the filtrate was colorless. This extract was filtered using Celite as a filtering agent and concentrated in vacuo. The concentrated solution was stored in the freezer for 2-3 d at $-35\text{ }^\circ\text{C}$ to yield blocky, red-orange X-ray quality crystals of **Ru1*** (162 mg, 70%). Note: Due to the NH_2Ar^* generated upon imido production and the high solubility of **Ru1*** in aliphatic solvents, analytically pure compound was obtained by repeated recrystallization from hexamethyldisiloxane. This resulted in a substantially reduced yield of approximately 12%. CHN analysis was taken of these single crystals. For the purposes of utilizing the complex in further reactions, specifically in the subsequent reaction to make **Ru3***, samples of such high purity were

not necessary, and a small amount of the 2,4,6-triisopropylaniline was tolerable in samples of **Ru1***. M.p.: 112.7-114 °C. NMR: ¹H NMR (500 MHz, benzene-d₆): δ 7.04 (s, 2H), 4.42 (septet, J = 7.0 Hz, 2H), 3.03–2.45 (septet, J = 6.9 Hz, 1H), 1.43 (d, J = 7.0 Hz, 12H), 1.33 (d, J = 7.0 Hz, 6H), 1.29 (m, 26H). ¹³C[¹H] NMR (126 MHz, benzene-d₆): δ 139.50 (d), 138.95 (s), 138.32 (s), 132.03 (s), 120.46 (s), 119.62 (s), 34.89 (s), 34.14 (s), 27.97 (s), 26.59 (s), 26.32–25.40 (m), 24.50 (s), 24.20 (s), 23.22 (s), 22.33 (s). ³¹P NMR (202 MHz, benzene-d₆): δ 19.47 (s). ¹⁴N NMR (36.5 MHz, benzene-d₆): 328.0 (s). UV-vis absorption (THF, 21 °C): 459 nm (4808 cm⁻¹ M⁻¹), 338 (5642 cm⁻¹ M⁻¹), 270 nm (14016 cm⁻¹ M⁻¹). Elemental Analysis calc'd for C₂₄H₅₀NP₃Ru: C, 52.73; H, 9.22; N, 2.56. Found: C, 52.79; H, 8.70; N, 2.57.

Synthesis of Ru(NAr)(dmpe)₂ (Ru2*)* This complex was synthesized following the same procedure as **Ru2**. A 20 mL scintillation vial was charged with **Ru1*** (150 mg, 0.27 mmol, 1 equiv), 5 mL THF, and a magnetic stir bar. To this red-orange solution was added a solution of dmpe (85 mg, 0.54 mmol, 2 equiv) in 2 mL THF, dropwise, at room temperature. The solution was stirred for 4 h, over which time the solution became brownish-yellow in color. The volatiles were removed in vacuo, and the residue was rinsed with several small aliquots of *n*-hexane. The solids were then dissolved in a minimum amount of THF and layered with *n*-hexane. The layered solution was stored at -35 °C overnight to yield plate-like green-brown crystals of **Ru2*** (42 mg, 25%). ¹H NMR (500 MHz, Benzene-d₆): δ 7.19 (s, 1H), 7.05 (s, 1H), 3.19 (septet, J = 7.1 Hz, 1H), 2.91 (septet, J = 7.1 Hz, 2H), 1.61 (d, J = 6.9 Hz, 6H), 1.38 (d, J = 6.8 Hz, 12H), 1.35–1.31 (m, 2H), 1.21 (m, 12H), 1.03 (s, 6H), 0.98–0.90 (m, 3H), 0.86 (d, J = 5.5 Hz, 6H), 0.84 (t, J = 1.6 Hz, 3H). ¹³C[¹H] NMR (126 MHz, Benzene-d₆): δ 125.81, 120.42, 118.55, 108.76 (t, J = 8.0 Hz), 34.26, 33.26 (d, J = 17.1 Hz), 30.28, 27.99, 26.56, 25.79 (d, J = 7.5 Hz), 23.92 (dd, J = 13.9, 7.5 Hz), 22.94 (d, J = 8.6 Hz), 22.36, 21.07 (t, J = 7.6 Hz), 19.27, 13.03 (t, J = 13.5 Hz). ³¹P NMR

(202 MHz, benzene-d₆): δ 42.22 (t, $J = 14.5$ Hz), 30.24 (t, $J = 14.7$ Hz). ¹⁴N NMR (36 MHz, benzene-d₆): δ 595.3. Elemental Analysis calc'd for C₂₇H₅₅RuNP₄: C, 52.42; H, 8.96; N, 2.26. Found C, 53.24; H, 9.11; N, 2.27. HRMS(ESI⁺): calc'd, 618.2558; found, 618.2336 (m/z).

Synthesis of Ru(NAr)(PMe₃)(dppe) (Ru3*)* This compound was prepared similarly to **Ru3** starting with a reaction solution of **Ru1*** (0.30 mmol, 1 equiv) and adding dppe (120 mg, 0.30 mmol, 1 equiv). The crude reaction was stirred for ~1 h at room temperature, and then volatiles were removed in vacuo. The sticky red residue was washed with hexamethyldisiloxane (3 × 2 mL), and once again dried in vacuo. The remaining solids were extracted with Et₂O and filtered using Celite as a filtering agent until the extracts were colorless. The Et₂O solution was then concentrated and stored at -35 °C to yield flaky, red crystals of **Ru3*** (98 mg, 41%). Unfortunately, these crystals demonstrate severe full-molecule disorder by X-ray diffraction, and an adequate solution for the data could not be found. M.p.: 188.2-189.6 °C. NMR: ¹H NMR (500 MHz, benzene-d₆): δ 8.18 (t, $J = 7.9$ Hz, 4H), 7.64 (m, 4H), 7.23 (s, 2H), 7.14 (dt, $J = 19.7, 7.3$ Hz, 8H), 7.09–6.96 (m, 4H), 5.01 (septet, $J = 6.7$ Hz, 2H), 2.97 (septet, $J = 6.8$ Hz, 1H), 2.04 (m, 2H), 1.87 (m, 2H), 1.53 (d, $J = 6.5$ Hz, 12H), 1.43 (d, $J = 6.8$ Hz, 6H), 0.70 (d, $J = 9.6$ Hz, 9H). ¹³C[¹H] NMR (126 MHz, benzene-d₆): δ 133.96 (d), 132.74 (t), 130.95 (s), 128.91 (s), 128.67–128.21 (m), 128.08 (s), 127.94 (s), 120.47 (s), 120.16 (d), 34.98 (s), 34.13 (s), 30.29 (t), 27.98 (s), 26.79 (s), 24.50 (s), 24.28 (s), 24.12 (s), 23.73 (s), 22.50–21.88 (m). ³¹P NMR (202 MHz, benzene-d₆): δ 99.84 (d, $J = 21.1$ Hz, 2H), 23.02 (t, $J = 21.2$ Hz, 1H). ¹⁴N NMR (36 MHz, THF): δ 337.2 (s). UV-vis absorption (THF, 21 °C): 465 nm (3053 cm⁻¹ M⁻¹), 330 (8035 cm⁻¹ M⁻¹), 280 nm (10045 cm⁻¹ M⁻¹). Elemental Analysis calc'd for C₄₄H₅₆NP₃Ru: C, 66.65; H, 7.12; N, 1.77. Found: C, 66.46; H, 7.04; N, 1.73. Cyclic Voltammetry: (THF, 21 °C, 0 V = Fc/Fc⁺): E_{1/2}(Ru^{+2/+3}) = -0.58 V (rev.).

Synthesis of [Ru(NAr)(PMe₃)(dppe)]SbF₆ (Ru5*)* A 20 mL scintillation vial was charged with a stir bar, **Ru2*** (50 mg, 0.063 mmol, 1 equiv), and 4 mL DME. This red-orange solution was stirred at room temperature. Separately, a solution of AgSbF₆ (22 mg, 0.063 mmol, 1 equiv) was prepared in 2 mL of DME. The AgSbF₆ was then added dropwise to the solution of **Ru3*** with vigorous stirring. The solution gradually changed from bright red to pinkish-brown, and a precipitate formed on the sides of the vial. The reaction was stirred at room temperature for 24 h, and then filtered using Celite as a filtering agent to remove Ag⁰. The filtrate was concentrated in vacuo to give a brown oil. The oily residue was washed with hexane until the filtrate was colorless. The residue was once again dried in vacuo and was then dissolved in a minimum amount of DME. The DME solution was layered with hexane and stored at -35 °C overnight to yield a fine pinkish-brown powder (34 mg, 53%). The mother liquor was decanted, and the powder was dried in vacuo. The pink-brown powder was assigned as complex **Ru5*** as identified by EPR spectroscopy. M.p.: 147 °C (color change 80 °C). μ_{eff} (THF-d₈, 25 °C): 1.47 μ_{B} . UV-vis absorption (THF, 21 °C): 612 nm (912 cm⁻¹ M⁻¹), 475 (1297 cm⁻¹ M⁻¹), 353 nm (2937 cm⁻¹ M⁻¹), 280 nm (6575 cm⁻¹ M⁻¹). Note: Satisfactory elemental analysis was not obtained for **Ru5*** after several attempts, presumably due to its high sensitivity. Sample masses were noted to change rapidly when sample holders were taken out of the inert atmosphere glovebox and into air, despite our best attempts.

Synthesis of Fe(NAr)(PMe₃)₃ (Fe1*)* This compound was prepared similarly to compound **Fe1** using FeCl₂ (50 mg, 1 equiv), PMe₃ (180 mg, 6 equiv), and LiNHAr* (185 mg, 2.1 equiv). Similarly, it was found to decompose during attempted isolation and could not be separated from the reaction mixture, but the complex is stable for a few days in the reaction solution in the presence of excess PMe₃. ³¹P NMR (127 MHz, THF): δ 43.06 (s). ¹⁴N NMR (36 MHz, THF): δ 320.6 (s).

Synthesis of Fe(dppe)(NAr)₂ (Fe2*)* (Method A) **Fe2*** was recovered as a byproduct from the synthesis of **Fe2*** (vide supra). This was accomplished by extracting the remaining solid residue, after pentane extraction, with diethyl ether, resulting in a red solution. This solution was filtered using Celite as a filtering agent, concentrated in vacuo to ~1 mL, and stored at -35 °C for 4 d to yield large, red X-ray quality crystals of **Fe2*** (26 mg, 7%). (Method B) A 20 mL scintillation vial was charged with FeCl₂(dppe) (100 mg, 0.19 mmol, 1 equiv), 4 mL THF, and a stir bar. This mixture was chilled at -78 °C. Separately, a solution of LiNAr* (69 mg, 0.38 mmol, 2 equiv) was prepared in 2 mL of room temperature THF. The chilled suspension of FeCl₂(dppe) was stirred, and the LiNAr* solution was added dropwise. Upon complete addition, the solution was opaque with a pink color. The mixture was stirred for 4 h, warming to room temperature. The volatiles were removed in vacuo, resulting in a dark red residue. This residue was extracted with diethyl ether and filtered using Celite as a filtering agent. The filtrate was concentrated in vacuo, and the concentrated solution was stored at -35 °C to yield large, red crystals of **Fe2*** (47 mg, 28 %). M.p.: 144.4-146.6 °C. μ_{eff} (benzene-d₆, 25 °C): 5.24 μ_{B} .

Synthesis of Fe(NAr)(PMe₃)(dppe) (Fe3*)* This compound was prepared similarly to **Fe3**. The reaction mixture of **Fe1*** (50 mg, 1 equiv) and dppe (145 mg, 0.95 equiv) was used. After the reaction volatiles were removed in vacuo, the crude residue was extracted with pentane and filtered using Celite as a filtering agent. The filtrate was concentrated in vacuo and stored at -35 °C to yield dark green crystals of **Fe3*** (200 mg, 66%). These crystals were not X-ray quality but were suitably pure for NMR and elemental analysis. X-ray quality crystals were grown from a very dilute solution in *n*-hexane at -35 °C. M.p.: 148.9-150.2 °C. NMR: ¹H NMR (500 MHz, benzene-d₆): δ 8.02 (t, J = 8.6 Hz, 4H), 7.52 (t, J = 8.1 Hz, 4H), 7.09 (d, J = 7.3 Hz, 3H), 7.06–6.96 (m,

8H), 6.93 (t, $J = 7.2$ Hz, 2H), 4.76 (septet, $J = 6.9$ Hz, 2H), 2.81–2.68 (septet, $J = 6.8$ Hz, 1H), 1.84 (m, $J = 36.7, 21.9, 13.8$ Hz, 4H), 1.33 (d, $J = 6.9$ Hz, 12H), 1.27 (d, $J = 6.8$ Hz, 6H), 0.62 (d, $J = 8.3$ Hz, 9H). $^{13}\text{C}[^1\text{H}]$ NMR (126 MHz, benzene- d_6): δ 156.53 (s), 141.58 (s), 140.18 (s), 133.79 (s), 130.81 (s), 128.72 (s), 120.94 (s), 120.46 (s), 35.13 (s), 27.97 (s), 27.00 (s), 24.49 (s), 23.90 (s), 23.56 (s), 22.32 (s), 21.73 (d). ^{31}P NMR (202 MHz, benzene- d_6): δ 115.35 (d, $J = 5.2$ Hz), 34.93 (t, $J = 5.2$ Hz). ^{14}N NMR (36 MHz, benzene- d_6): δ 324.8. UV-vis absorption (THF, 21 °C): 589 nm ($1754 \text{ cm}^{-1} \text{ M}^{-1}$), 404 ($4114 \text{ cm}^{-1} \text{ M}^{-1}$), 301 nm ($11596 \text{ cm}^{-1} \text{ M}^{-1}$). Elemental Analysis calc'd for $\text{C}_{44}\text{H}_{56}\text{FeNP}_3$: C, 70.68; H, 7.55; N, 1.87. Found C, 71.48; H, 7.57; N, 1.75. Cyclic Voltammetry: (THF, 21 °C, 0 V = Fc/Fc $^+$): $E_{1/2}(\text{Fe}^{2/+3}) = -0.75$ V (rev.).

Synthesis of [Fe(NAr)(PMe $_3$)(dppe)]SbF $_6$ (Fe4*)* A 20 mL scintillation vial was charged with **Fe2*** (50 mg, 0.067 mmol, 1 equiv), a magnetic stir bar, and 4 mL of DME. This solution was stirred at room temperature. Separately, a solution of AgSbF $_6$ (23 mg, 0.067 mmol, 1 equiv) was prepared in 2 mL DME. The silver solution was added dropwise to the solution of **Fe3***. The resulting mixture was stirred for 12 h at room temperature, during which time the reaction solution remained dark green and solid Ag 0 precipitated. The mixture was filtered using Celite as a filtering agent, and the solvent was removed in vacuo. This yielded an oily green residue, which was rinsed with 5 mL pentane and dried in vacuo to obtain a powdery green solid of **Fe4*** (32 mg, 49%). M.p.: 110 °C (dec). UV-vis absorption (THF, 21 °C): 584 nm ($1245 \text{ cm}^{-1} \text{ M}^{-1}$), 387 ($2566 \text{ cm}^{-1} \text{ M}^{-1}$), 293 nm ($5233 \text{ cm}^{-1} \text{ M}^{-1}$). μ_{eff} (THF- d_8 , 25 °C): 1.97 μ_{B} . Cyclic Voltammetry: (THF, 21 °C, 0 V = Fc/Fc $^+$): $E_{1/2}(\text{Fe}^{2/+3}) = -0.77$ V (rev.).

NMR Spectra

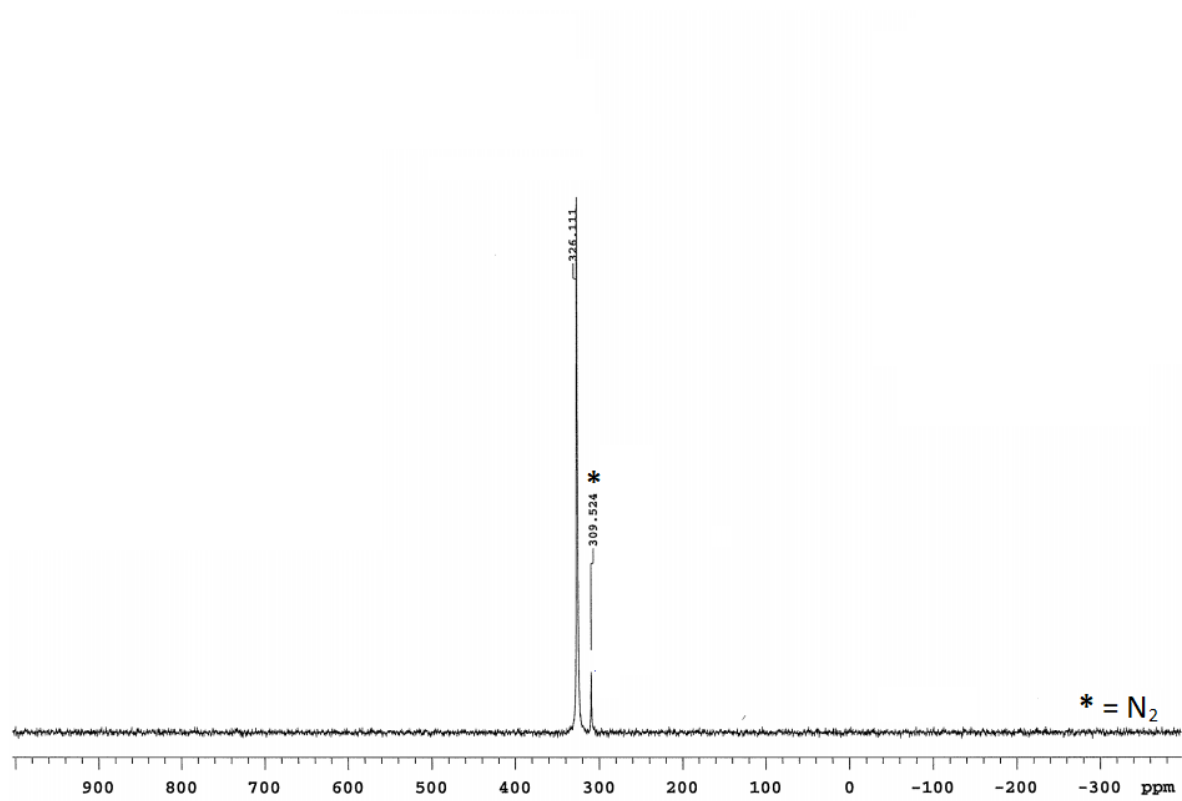


Figure 7.18 ^{14}N NMR of **Ru1** in C_6D_6 .

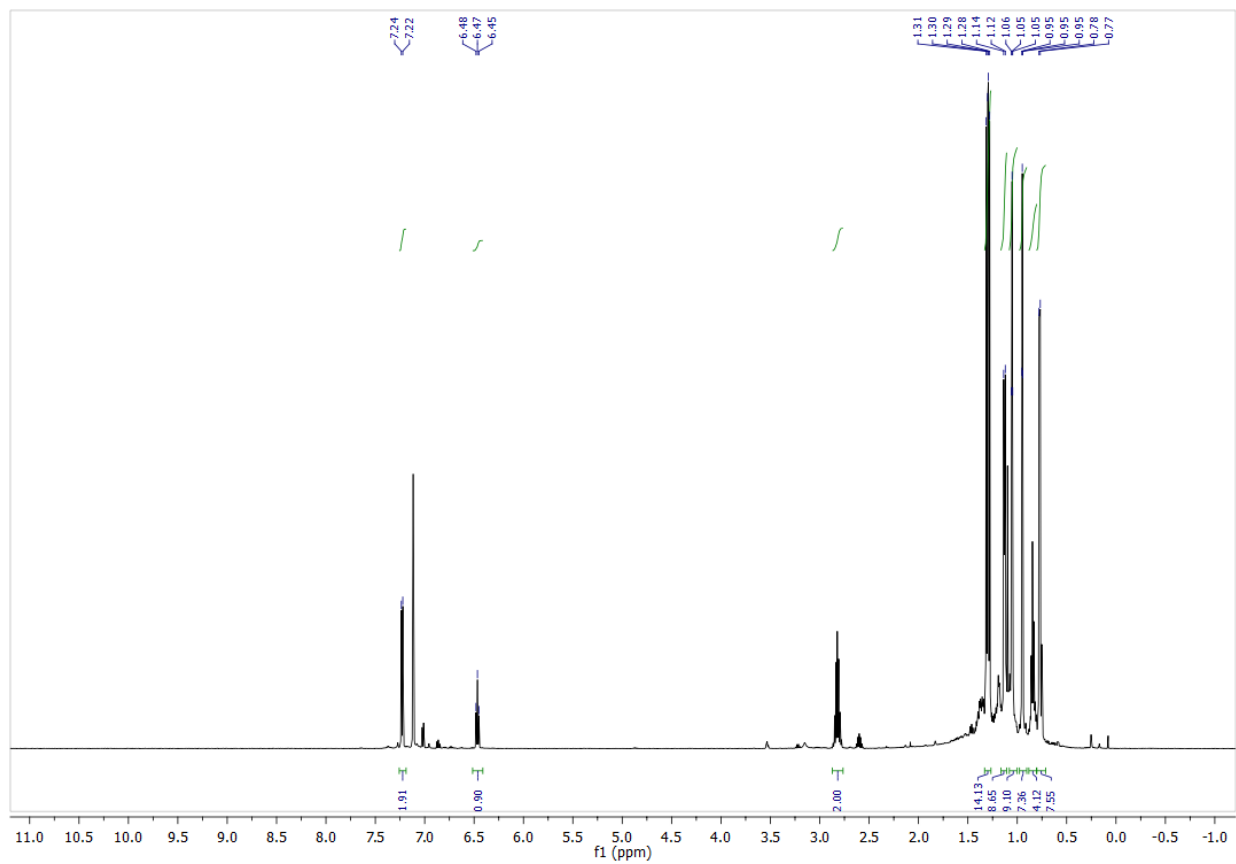


Figure 7.19 ^1H NMR of **Ru2** in C_6D_6 .

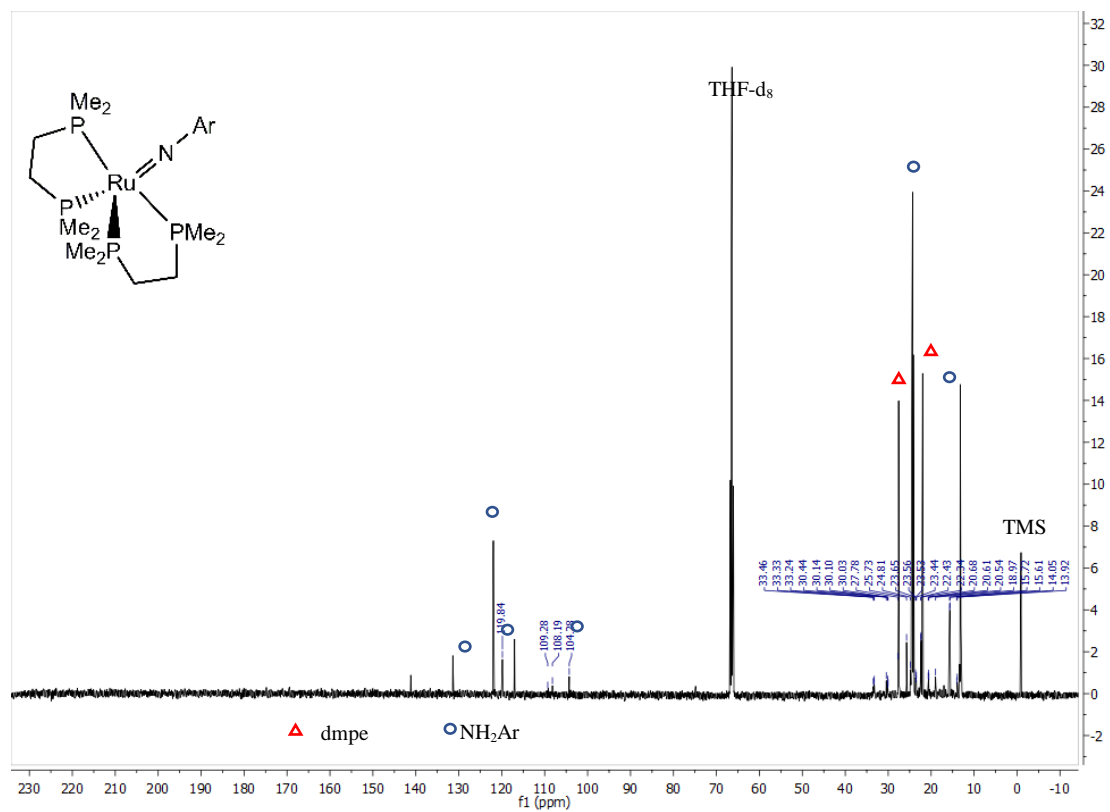


Figure 7.20 ¹³C NMR of **Ru2** in d₈-THF.

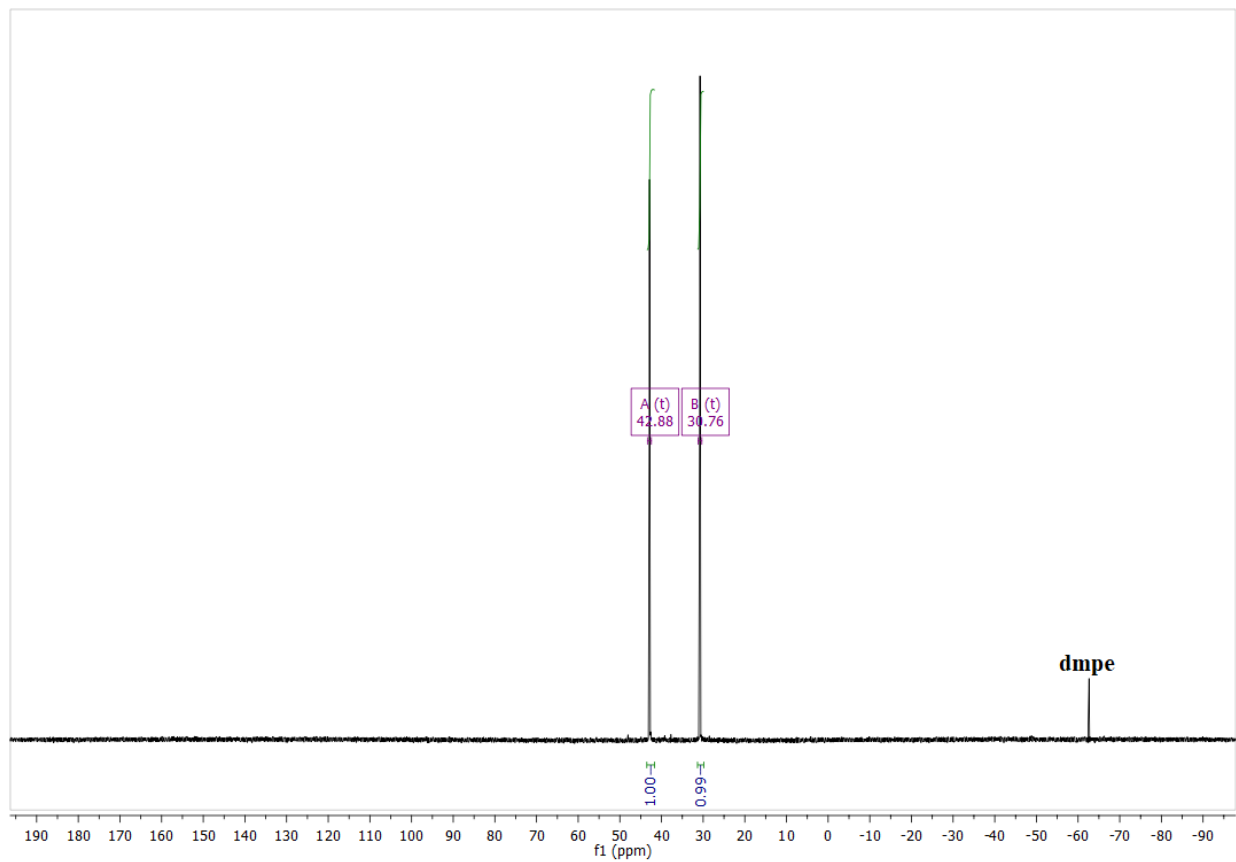


Figure 7.21 ^{31}P NMR of **Ru2** in d_8 -THF.

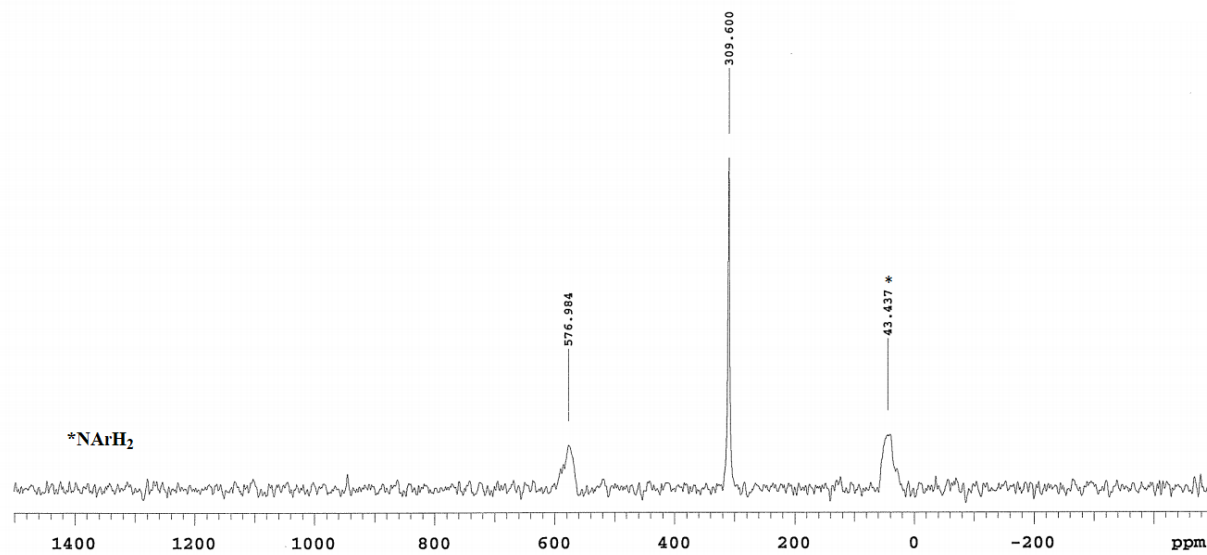


Figure 7.22 ^{14}N NMR of **Ru2** in C_6D_6 .

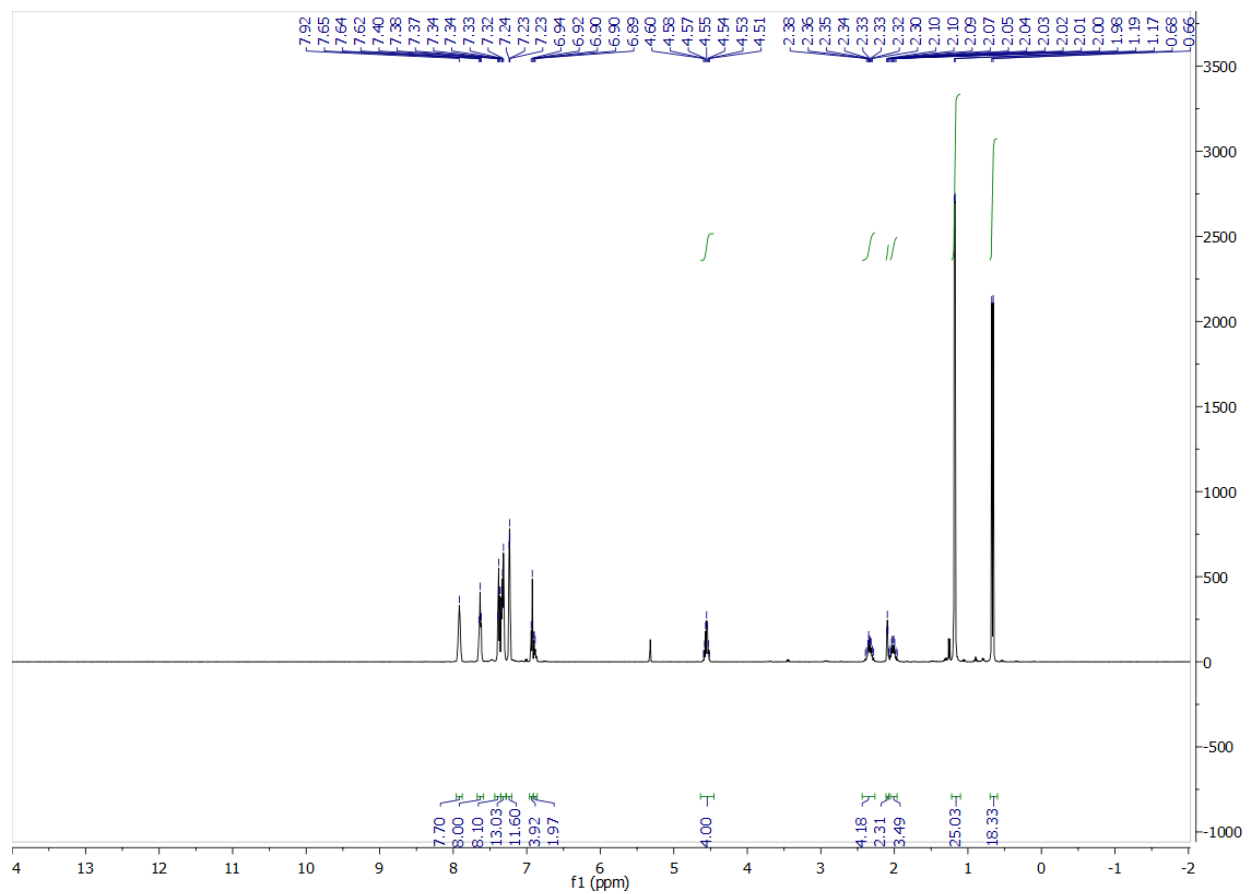


Figure 7.23 ^1H NMR of **Ru4** in CD_2Cl_2 .

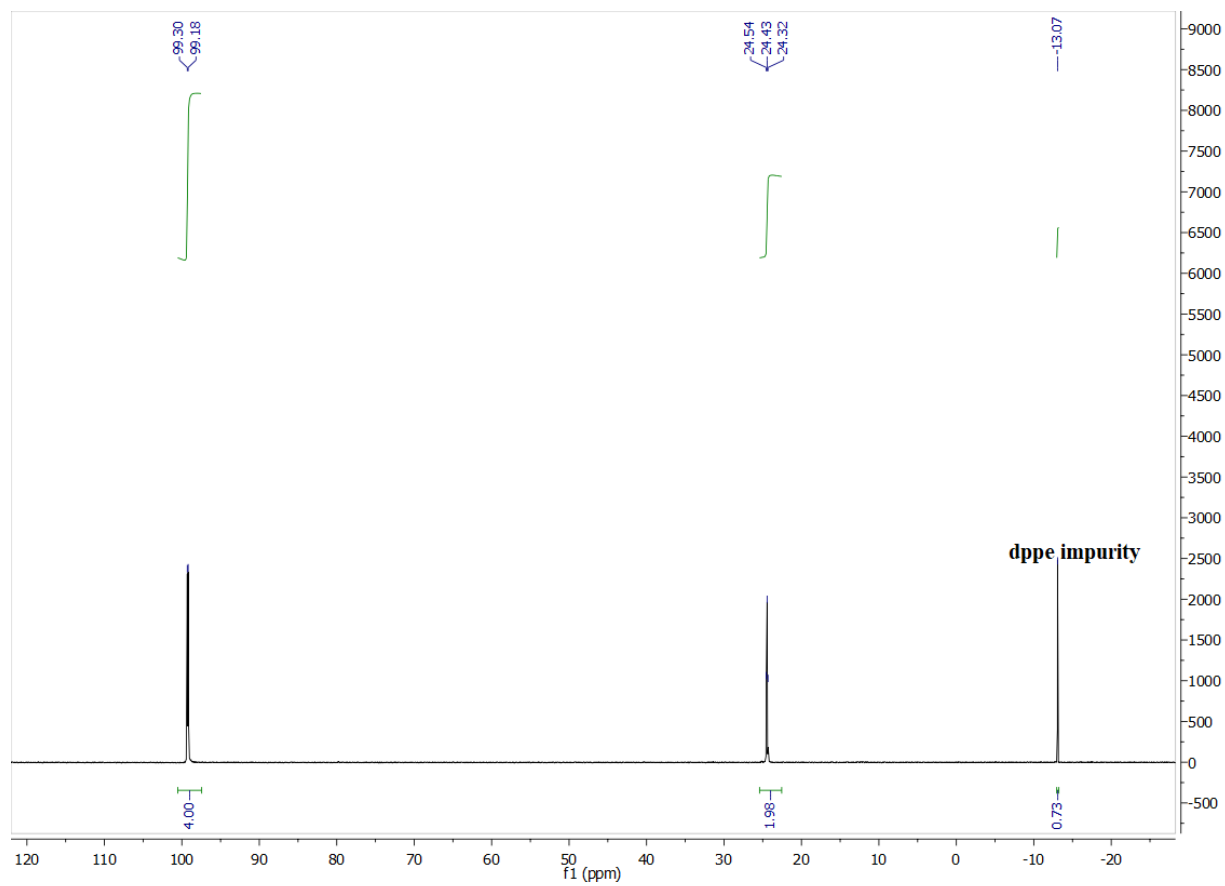


Figure 7.24 ^{31}P NMR of **Ru4** in CD_2Cl_2 .

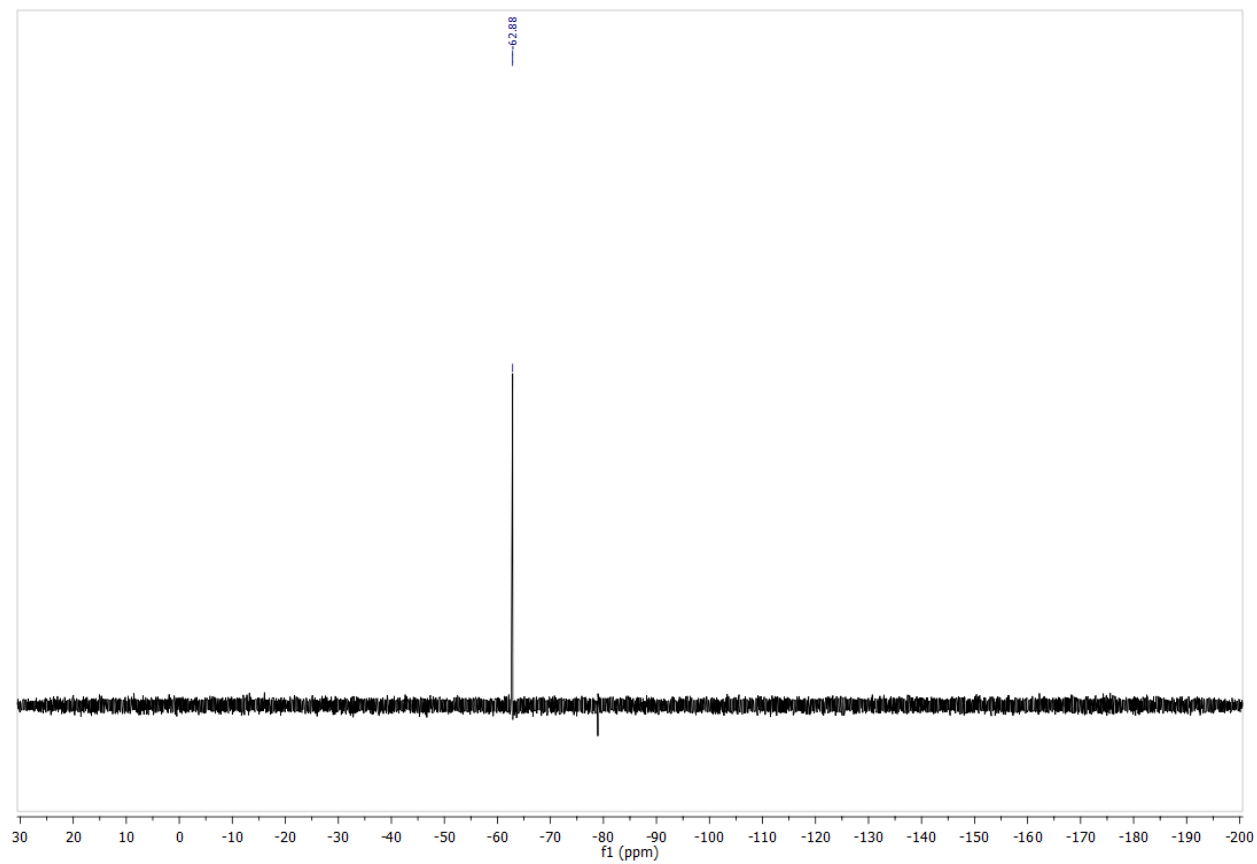


Figure 7.25 ^{19}F NMR of **Ru4** in CD_2Cl_2 .

Note: This complex does not exhibit sufficient solubility in most NMR solvents. While soluble in CD_2Cl_2 , it does slowly react with the solvent. This prevented accurate acquisition of ^{13}C and ^{14}N NMR data for this complex.

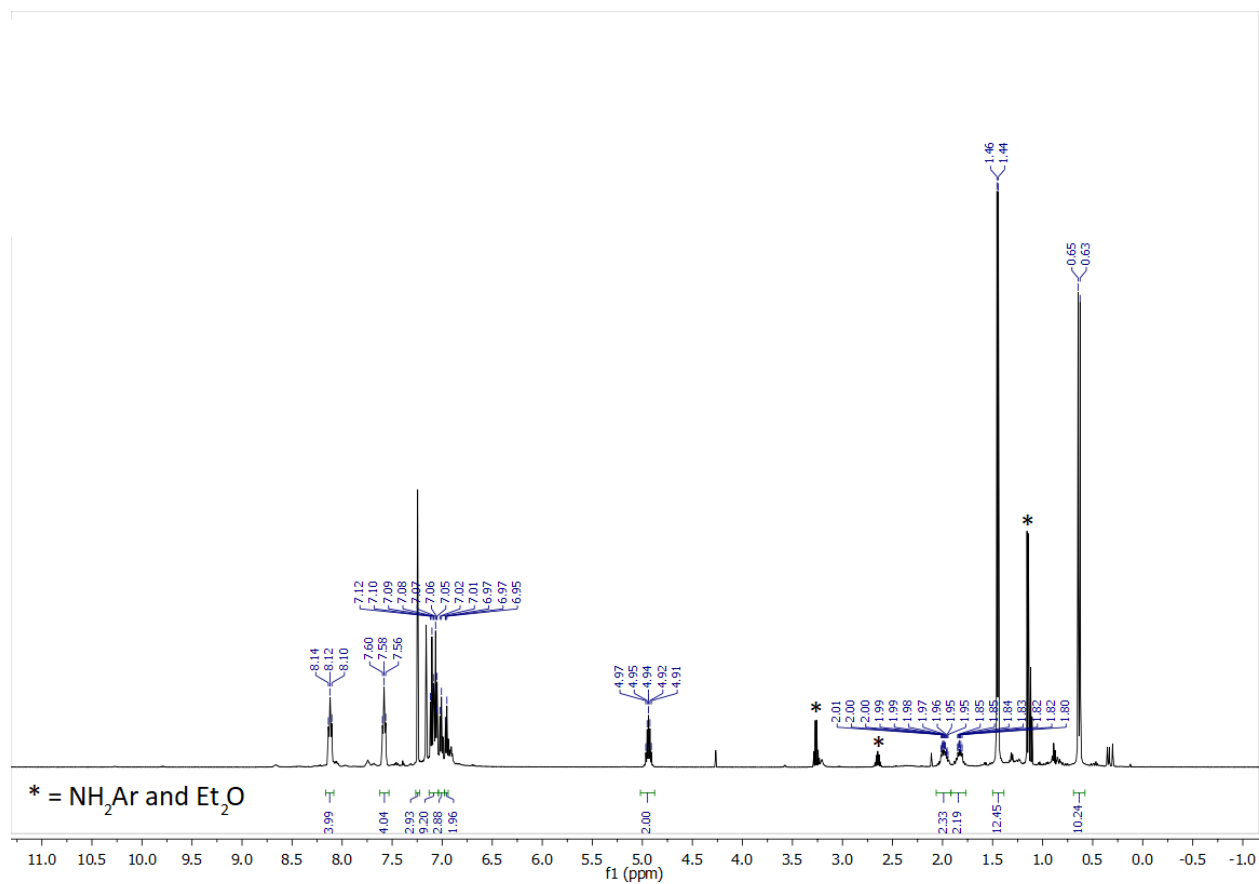


Figure 7.26 ¹H NMR of **Ru3** in C₆D₆.

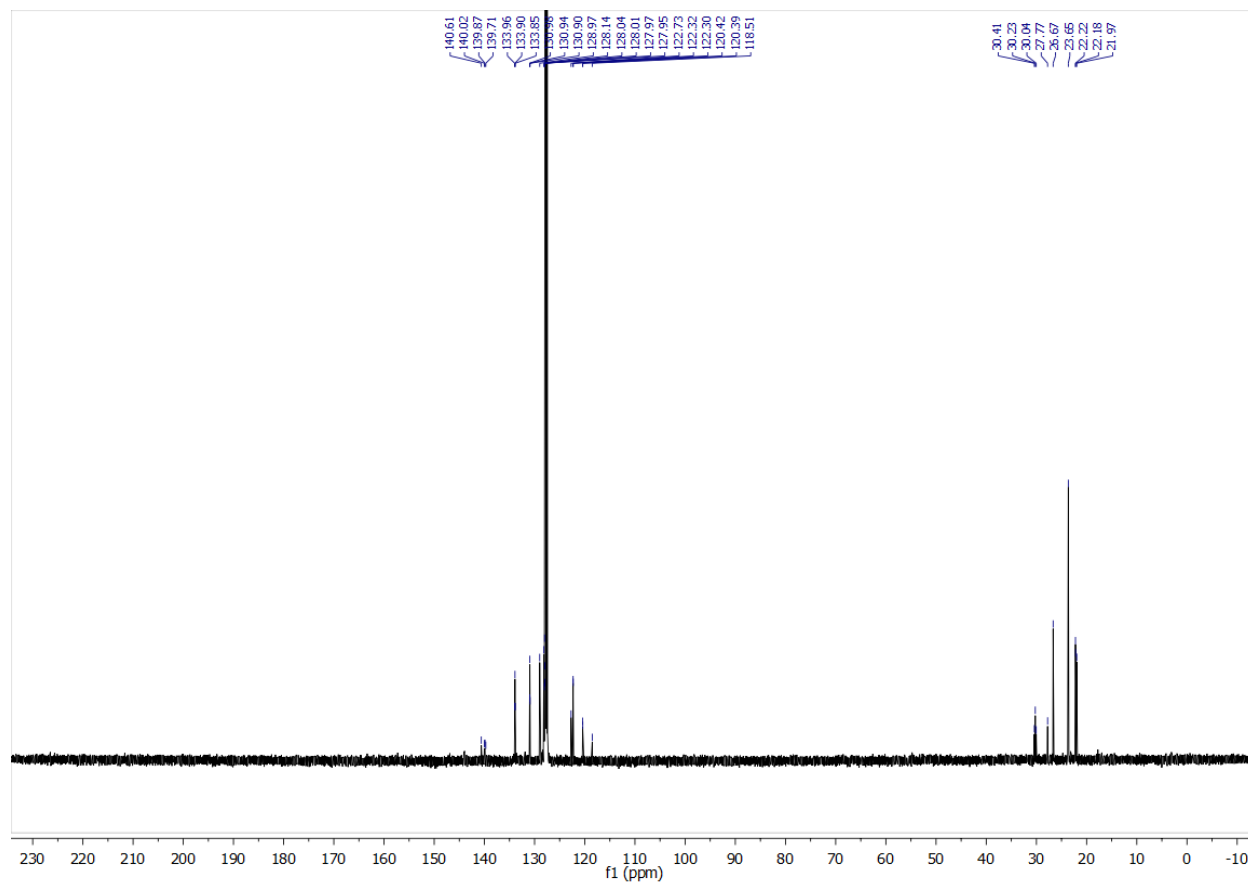


Figure 7.27 ^{13}C NMR of **Ru3** in C_6D_6 .

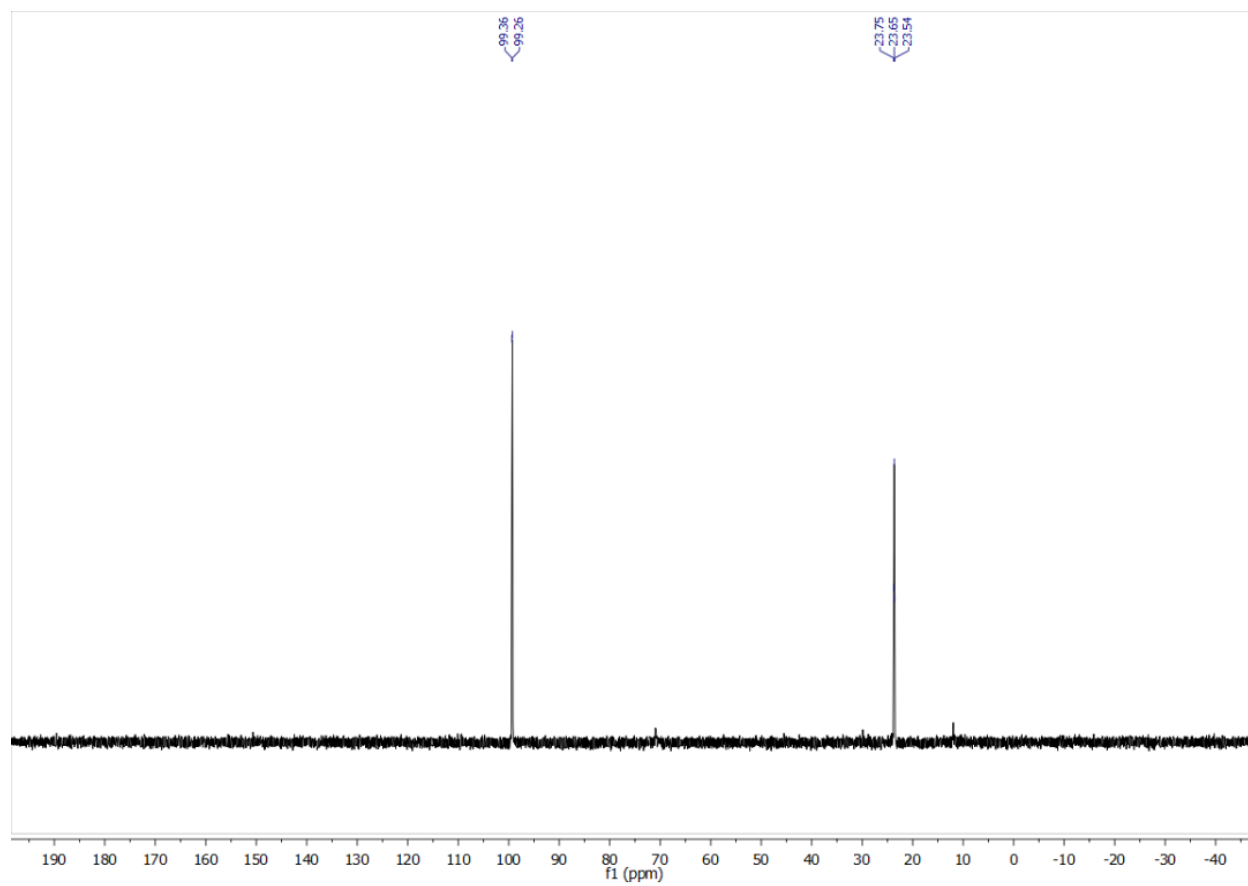


Figure 7.28 ^{31}P NMR of Ru_3 in C_6D_6 .

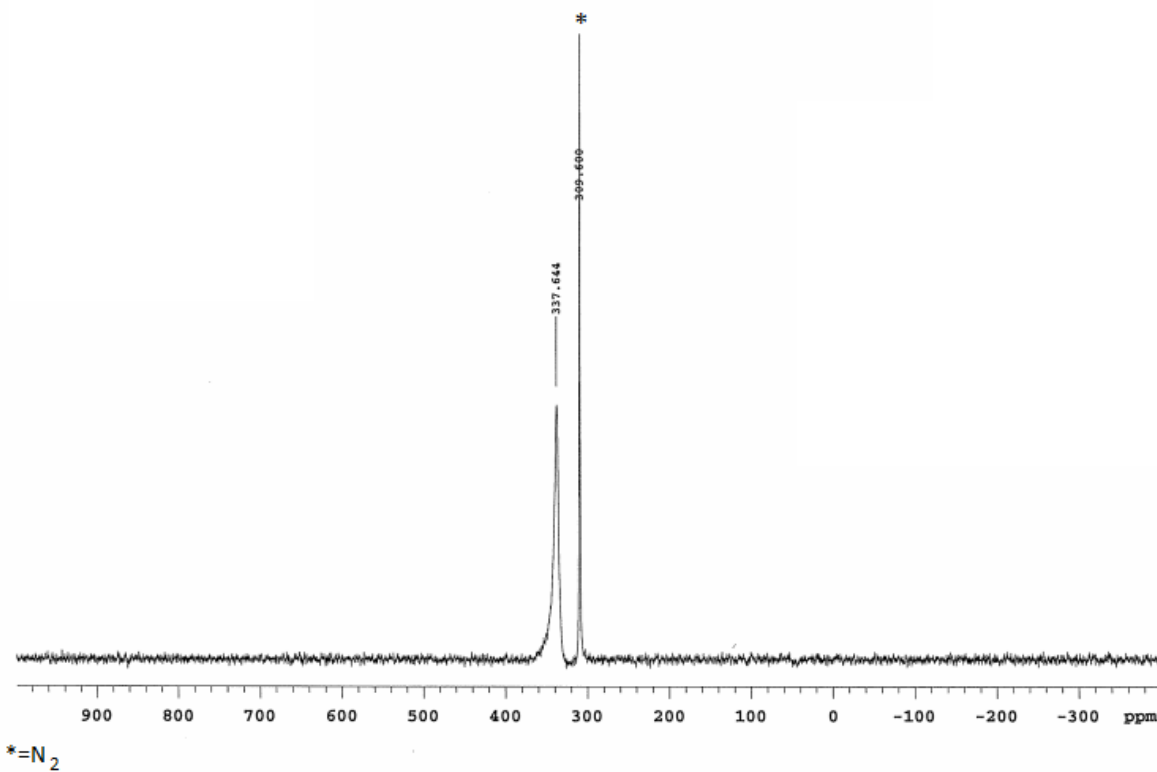


Figure 7.29 ^{14}N NMR of **Ru3** in C_6D_6 .

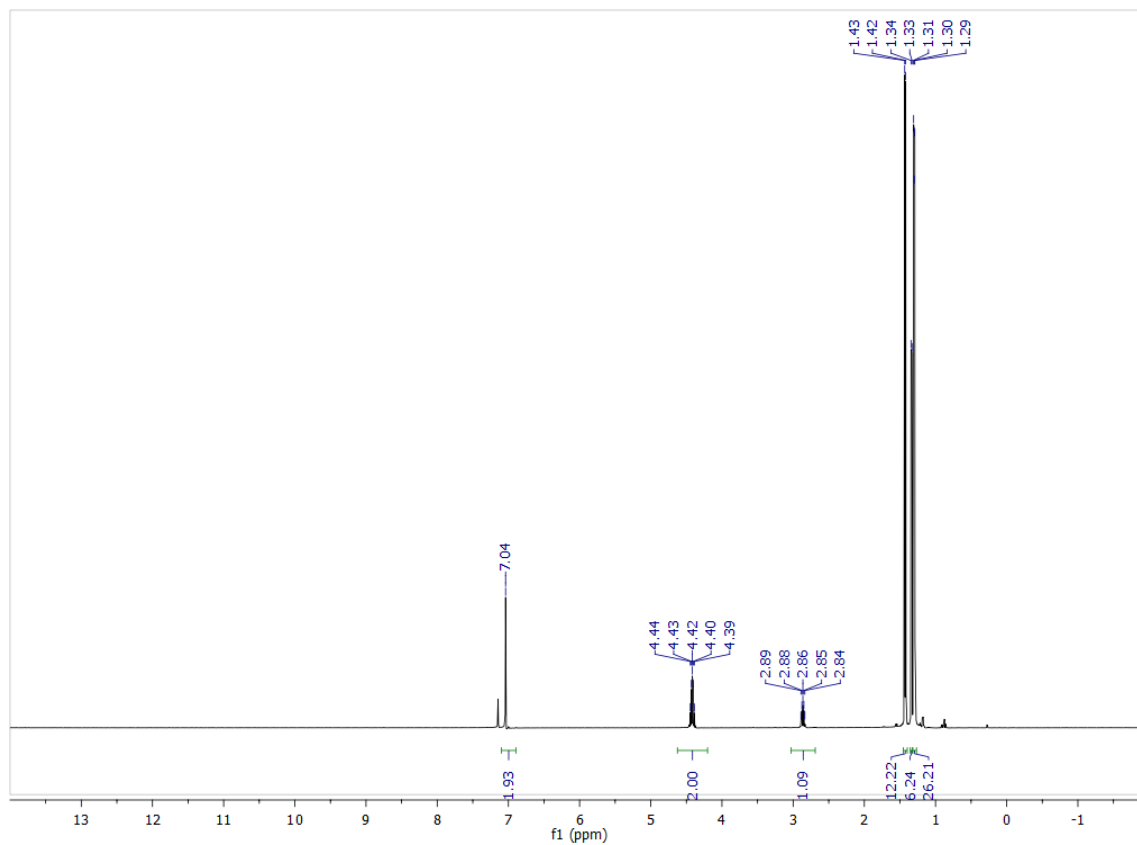


Figure 7.30 ^1H NMR of **Ru1*** in C_6D_6 .

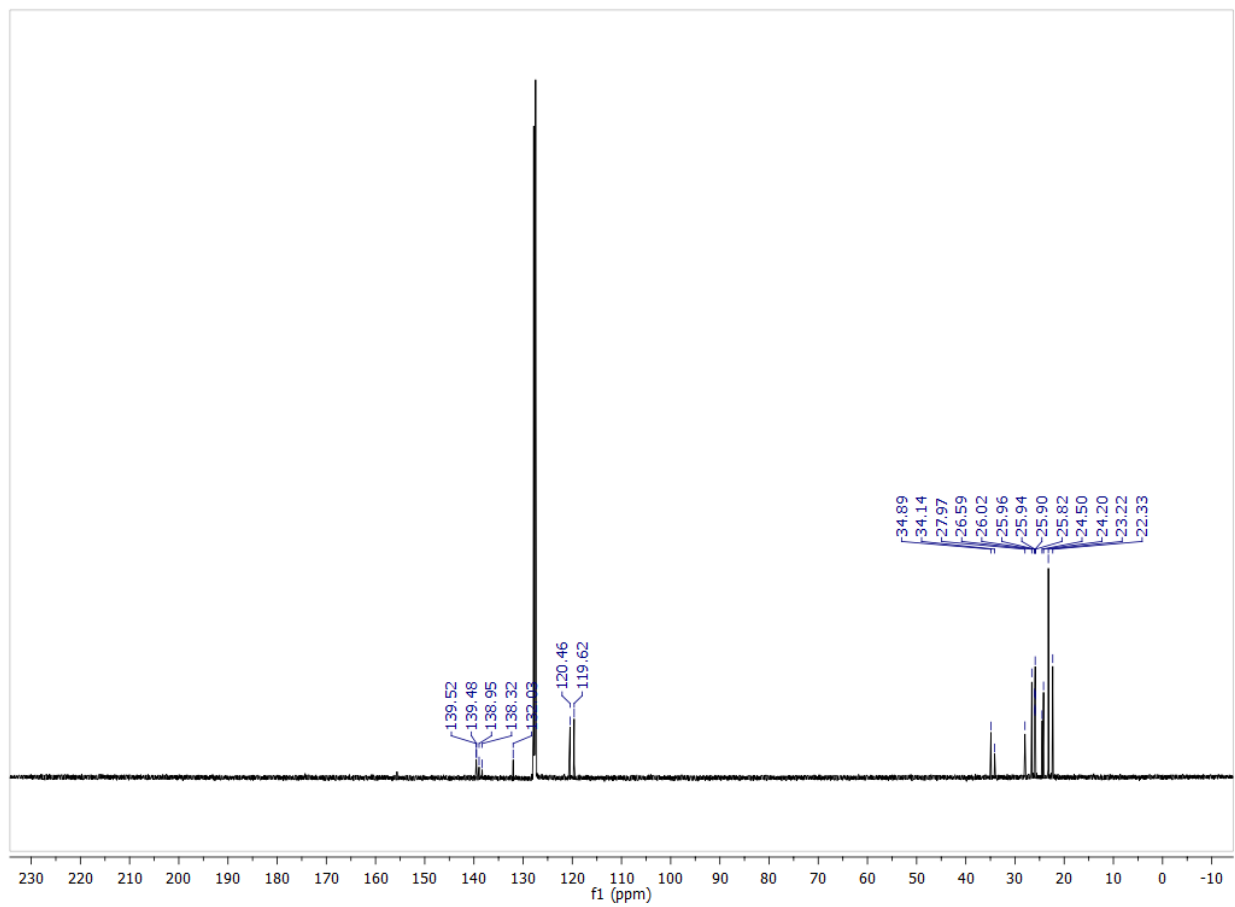


Figure 7.31 ^{13}C NMR of **Ru1*** in C_6D_6 .

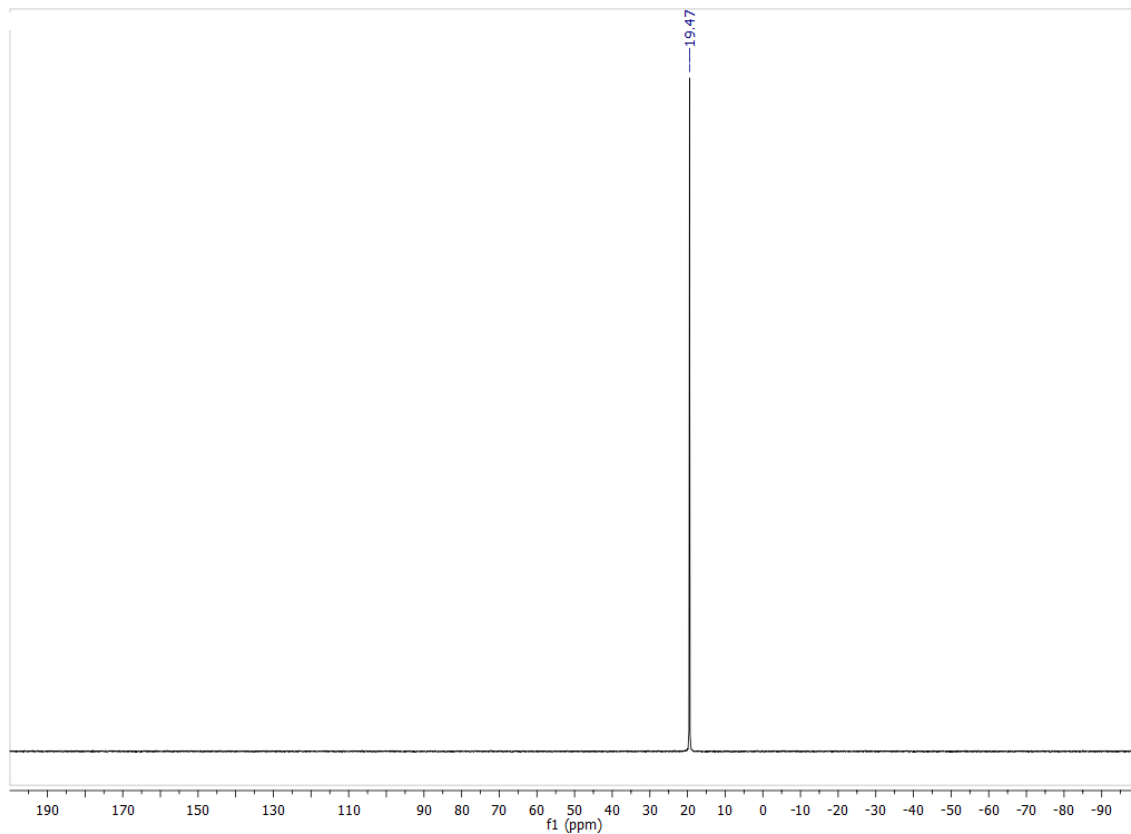


Figure 7.32 ^{31}P NMR of **Ru1*** in C_6D_6 .

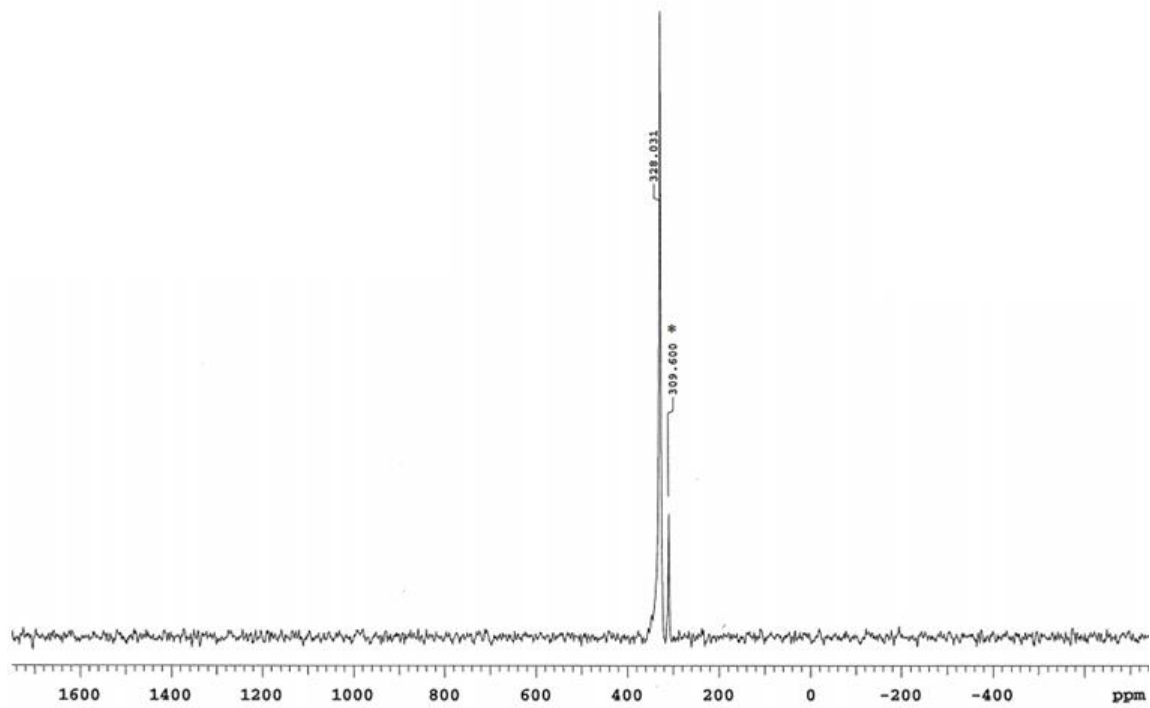


Figure 7.33 ^{14}N NMR of **Ru1*** in C_6D_6 .

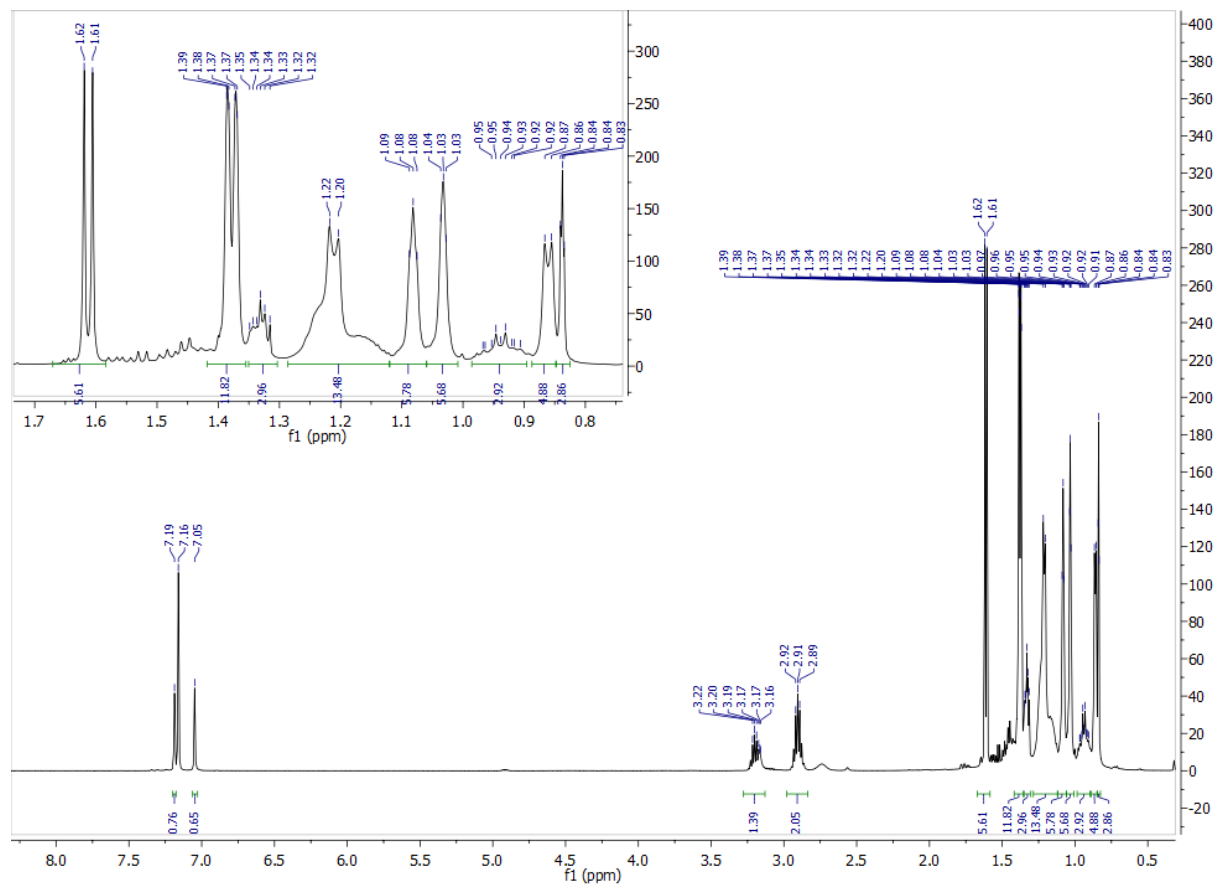


Figure 7.34 ^1H NMR of $\text{Ru}2^*$ in C_6D_6 .

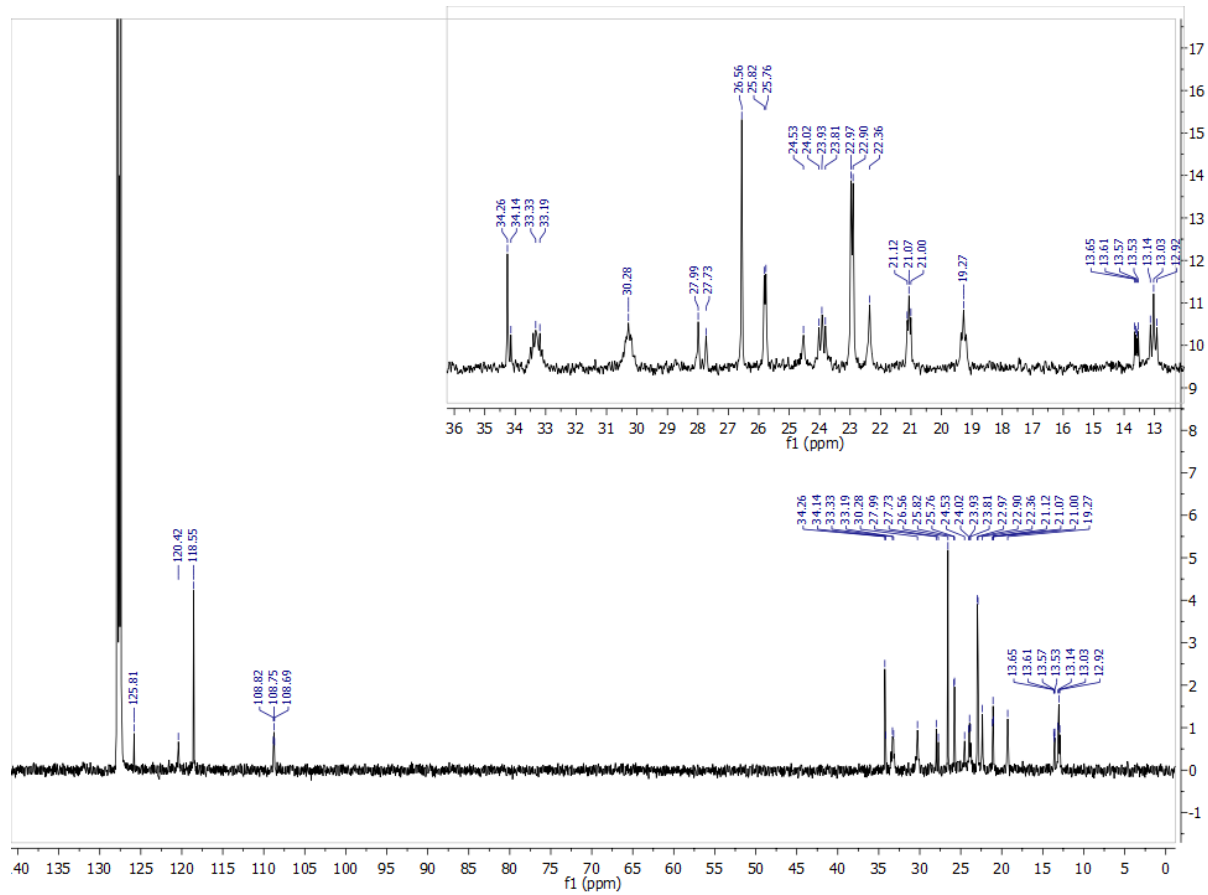


Figure 7.35 ^{13}C NMR of Ru_2^* in C_6D_6 .

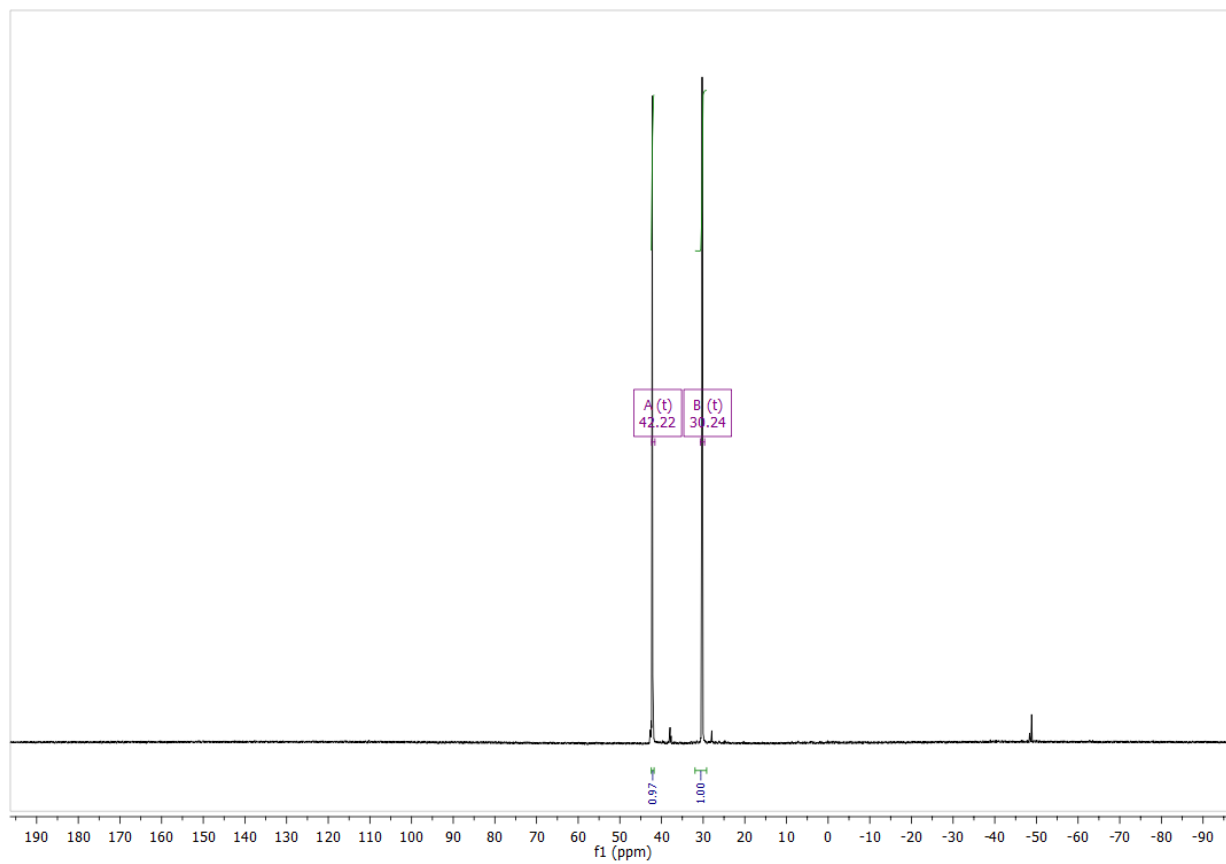


Figure 7.36 ^{31}P NMR of **Ru2*** in C_6D_6 .

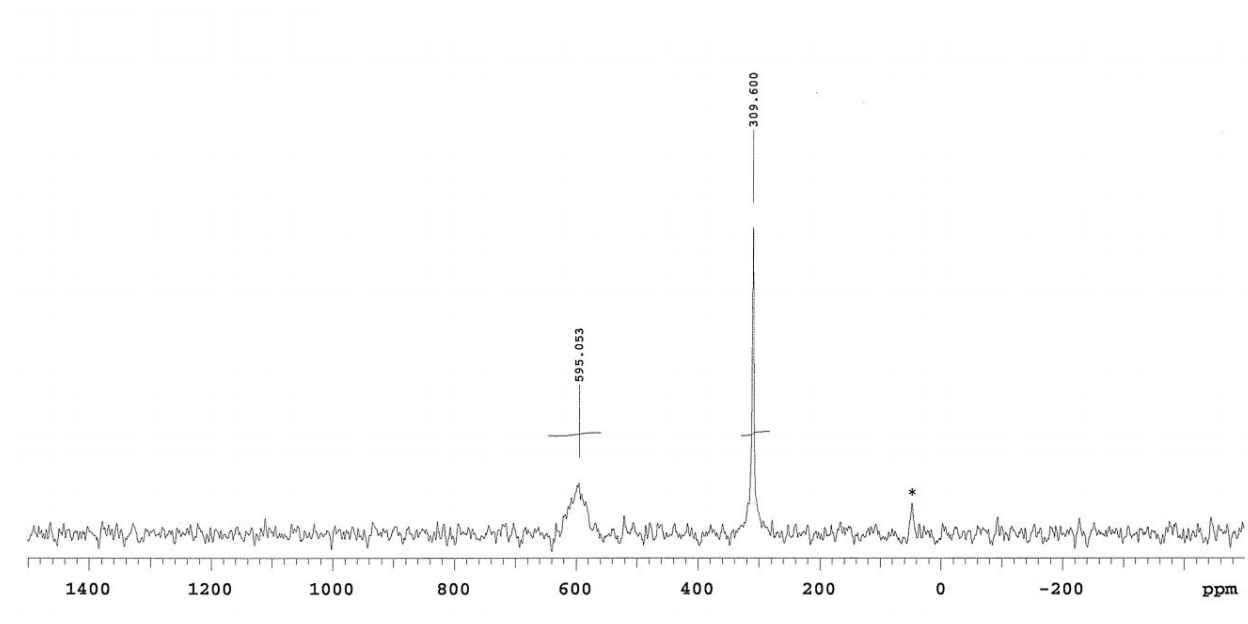


Figure 7.37 ^{14}N NMR of Ru_2^* in C_6D_6 .

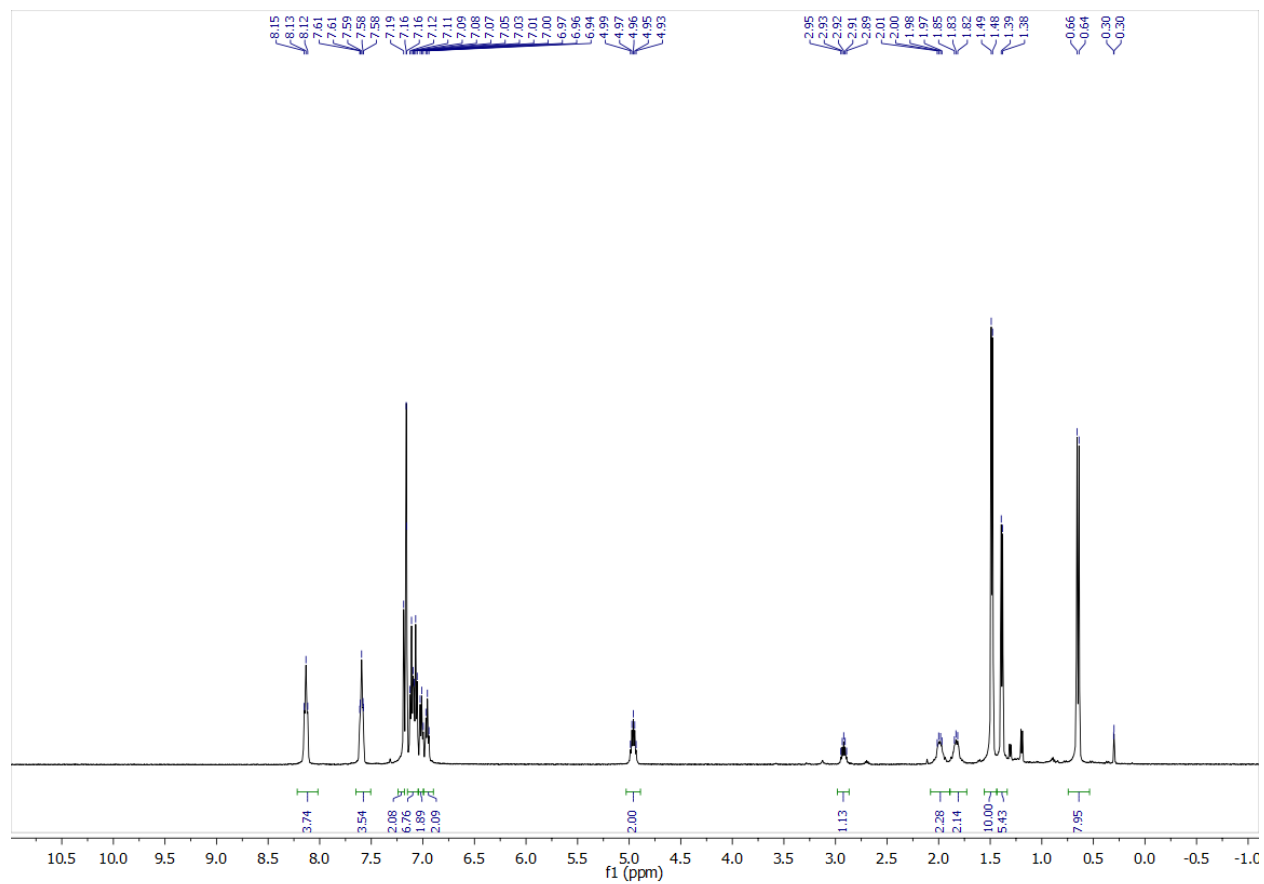


Figure 7.38 ^1H NMR of **Ru3*** in C_6D_6 .

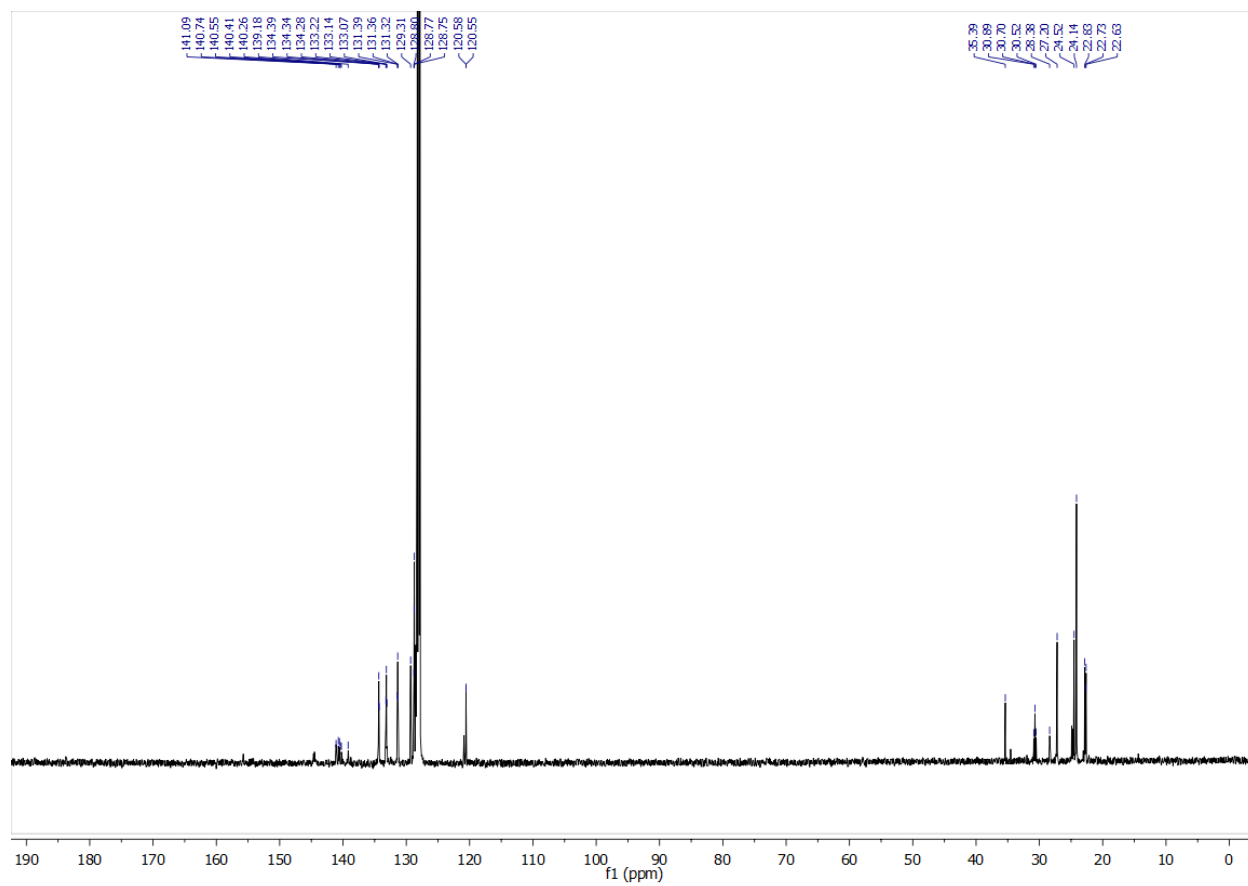


Figure 7.39 ^{13}C NMR of Ru3^* in C_6D_6 .

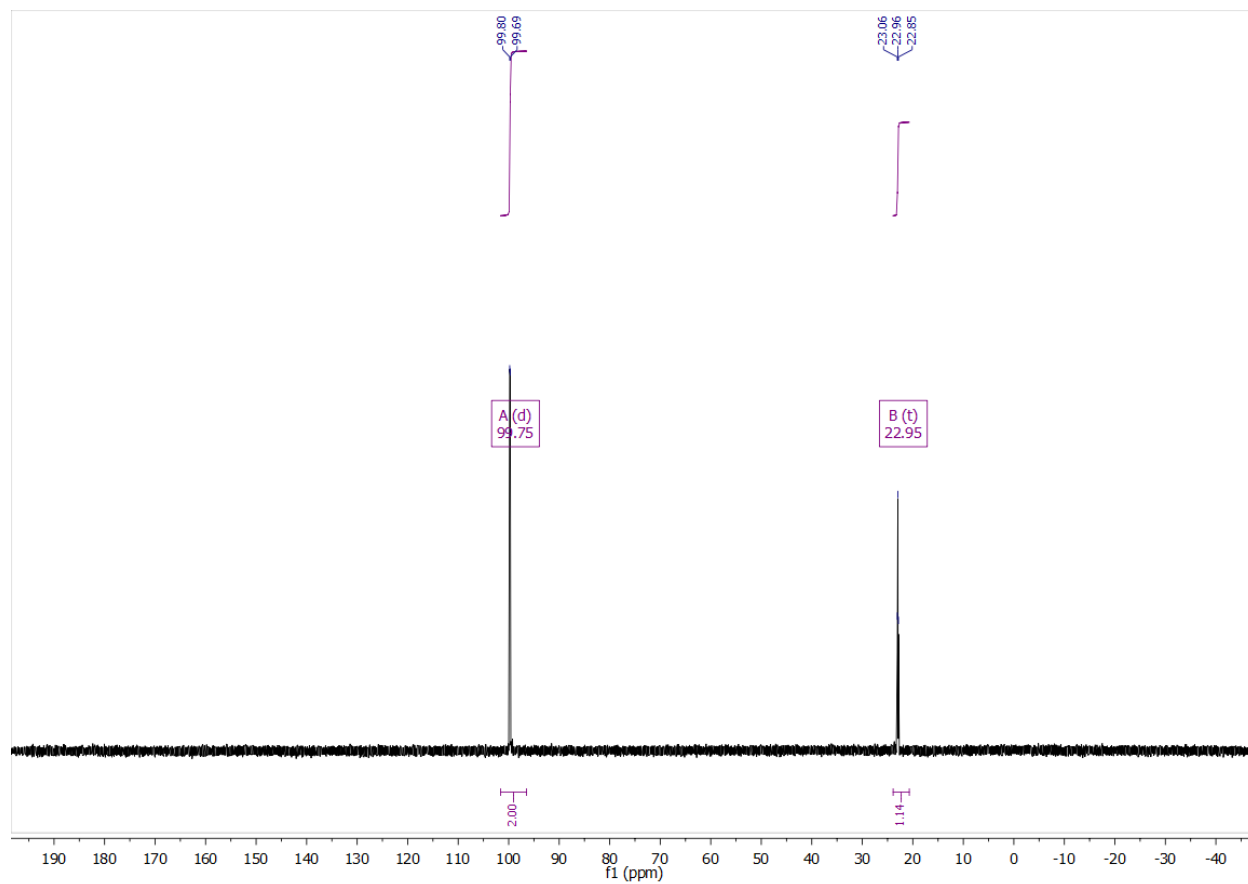


Figure 7.40 ^{31}P NMR of Ru_3^* in C_6D_6 .

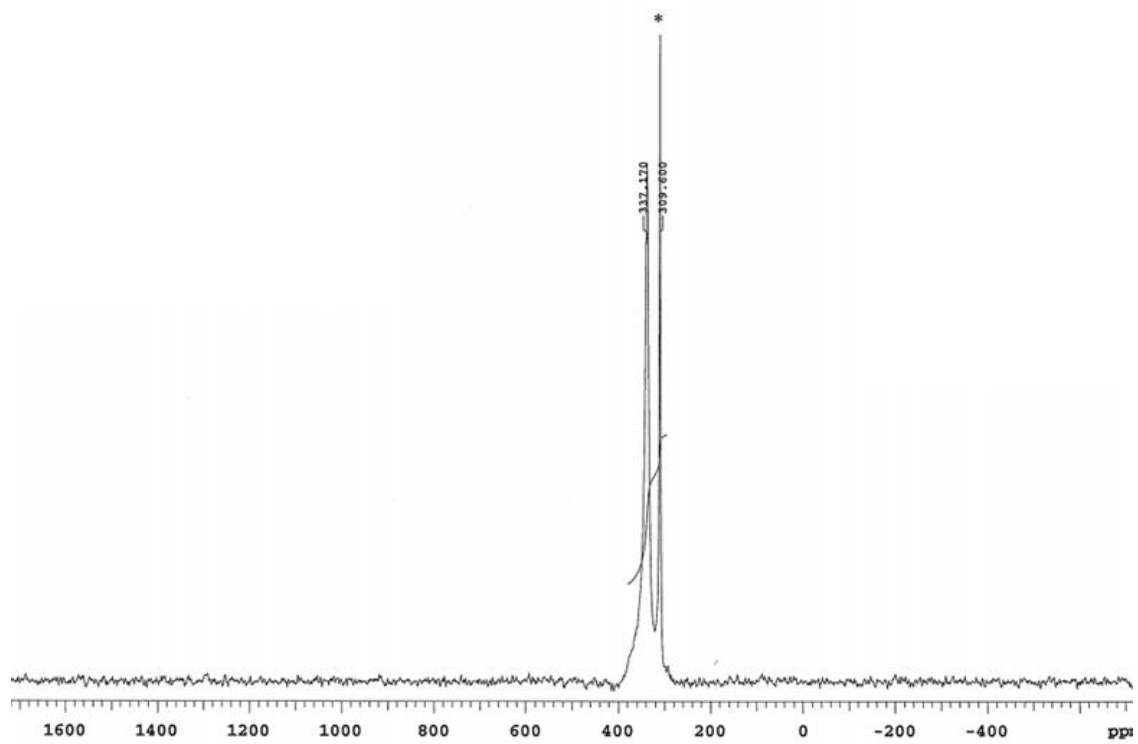


Figure 7.41 ^{14}N NMR of Ru3^* in C_6D_6 .

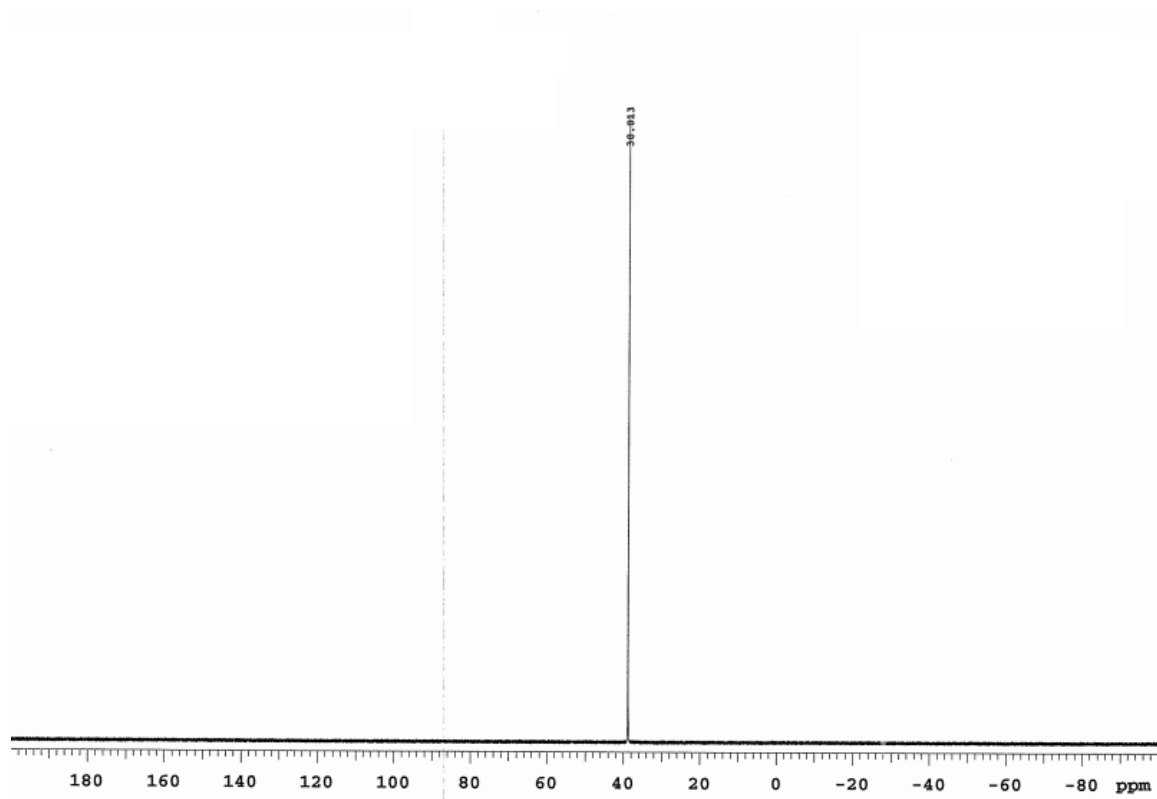


Figure 7.42 ^{31}P NMR of **Fe1** in THF (*in situ*).

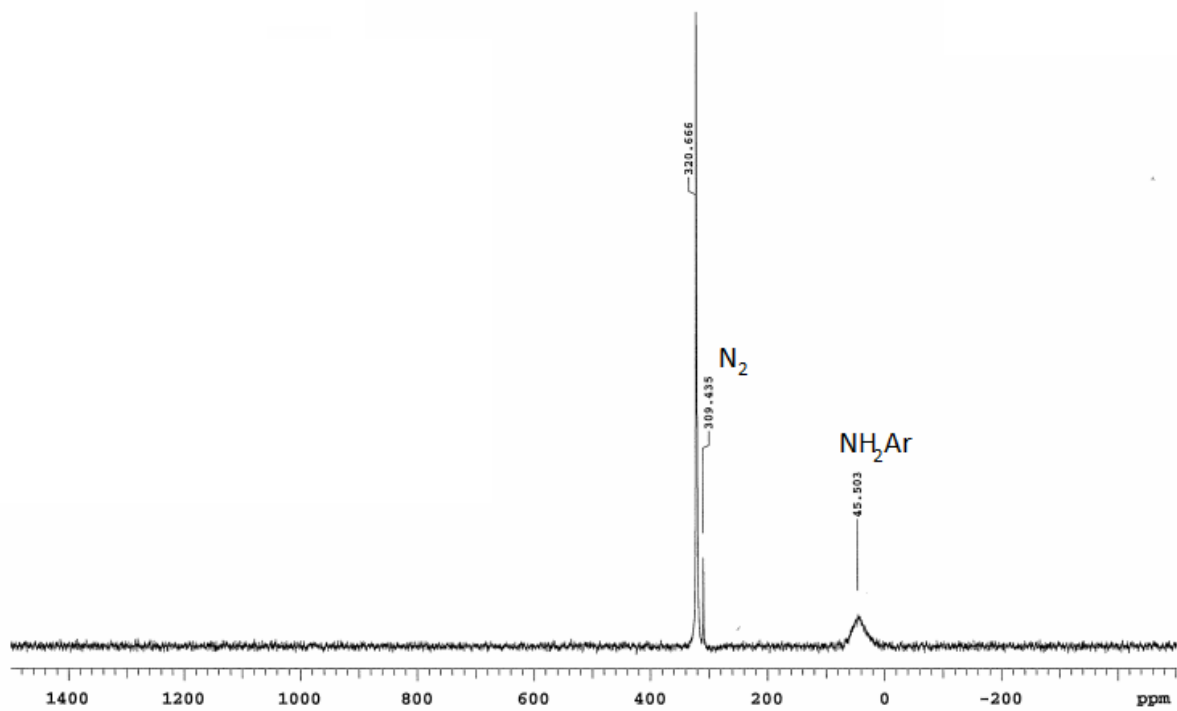


Figure 7.43 ^{14}N NMR of **Fe1** in THF (*in situ*).

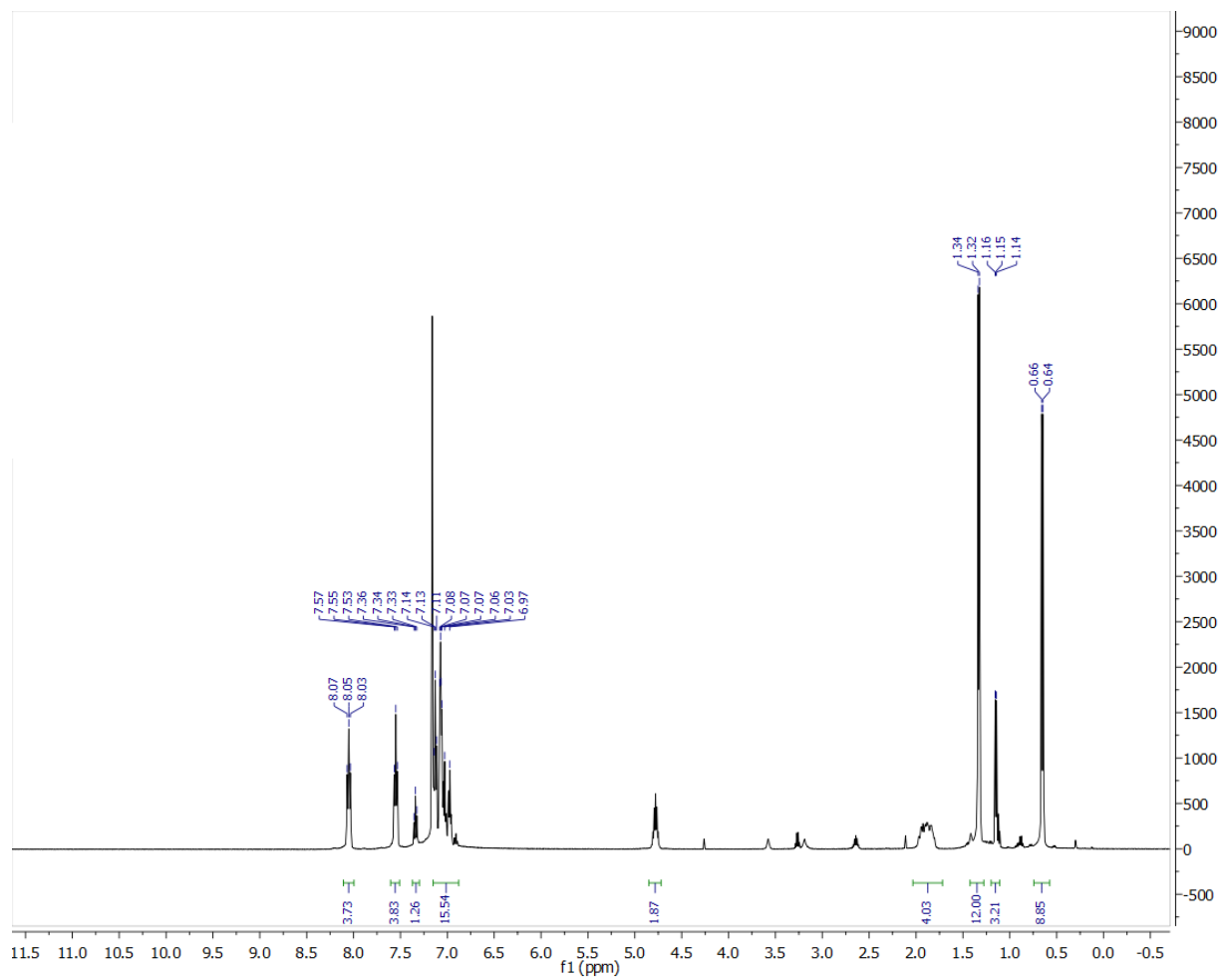


Figure 7.44 ^1H NMR of Fe_3 in C_6D_6 .

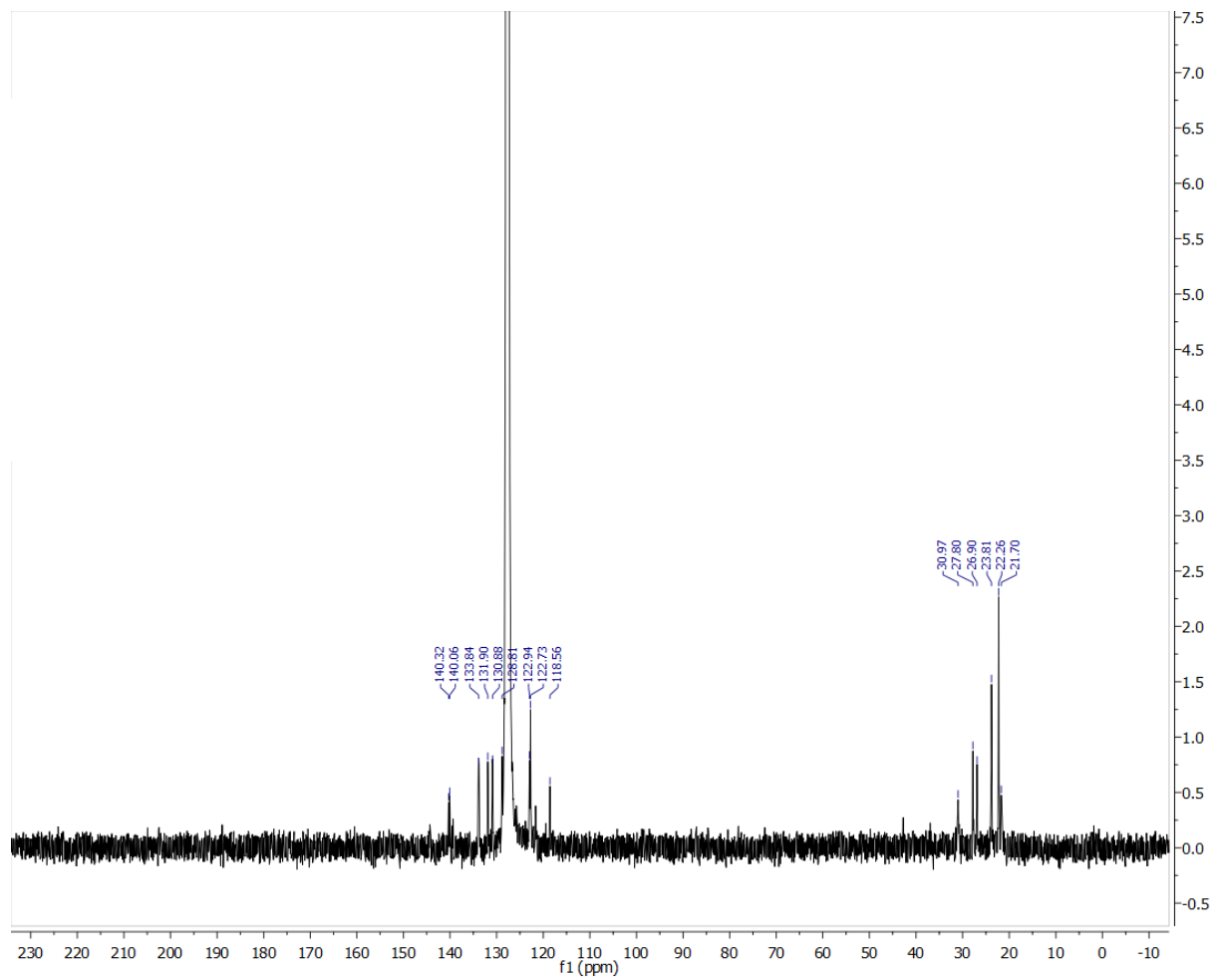


Figure 7.45 ^{13}C NMR of Fe_3 in C_6D_6 .

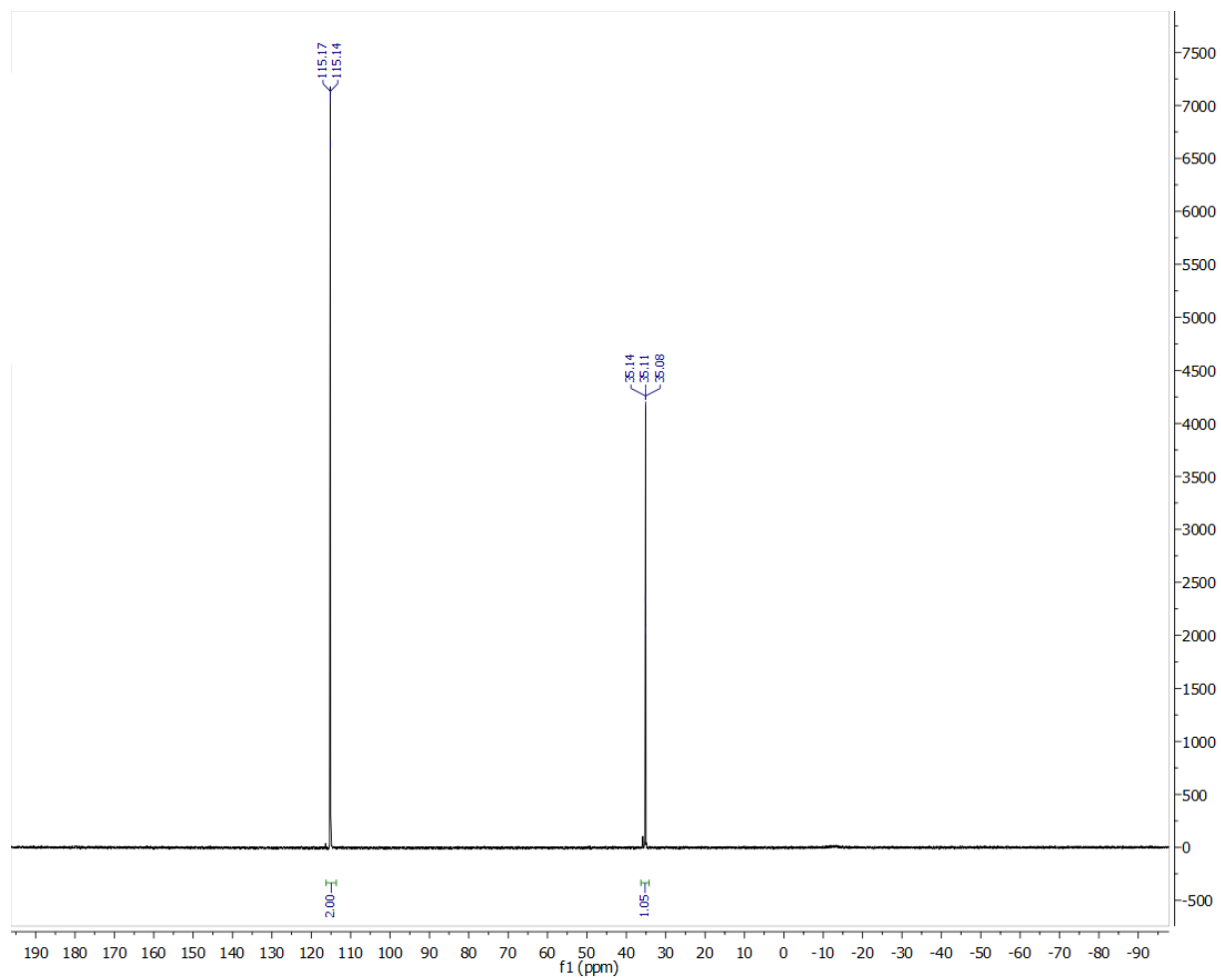


Figure 7.46 ^{31}P NMR of **Fe3** in C_6D_6 .

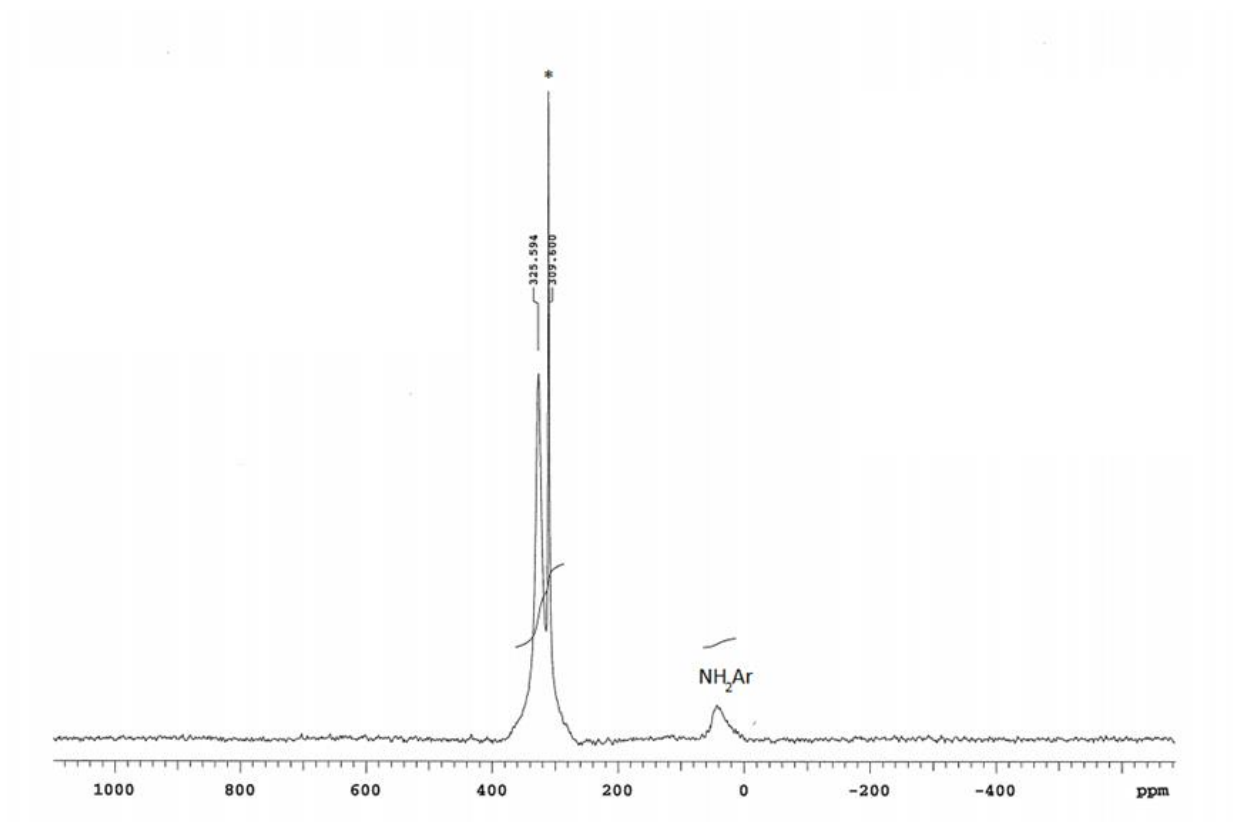


Figure 7.47 ^{14}N NMR of **Fe3** in C_6D_6 .

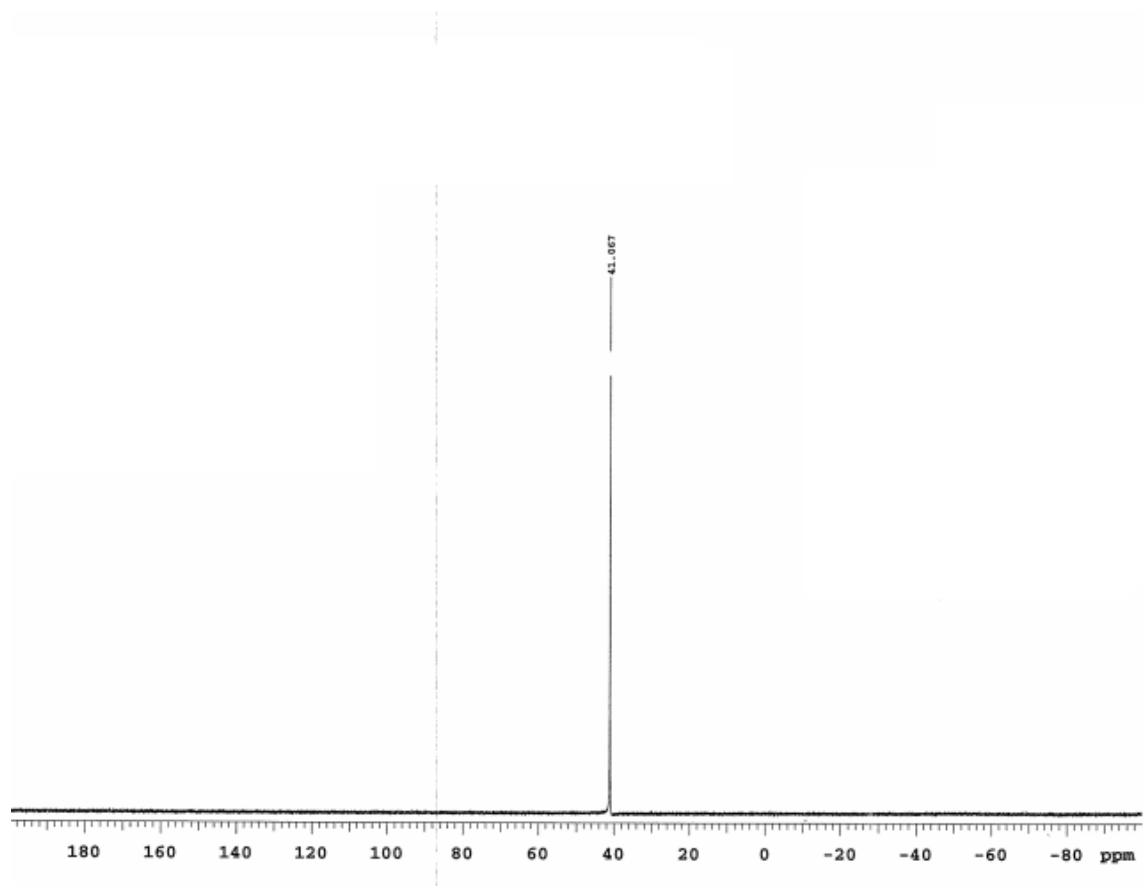


Figure 7.48 ^{31}P NMR of **Fe1*** in C_6D_6 .

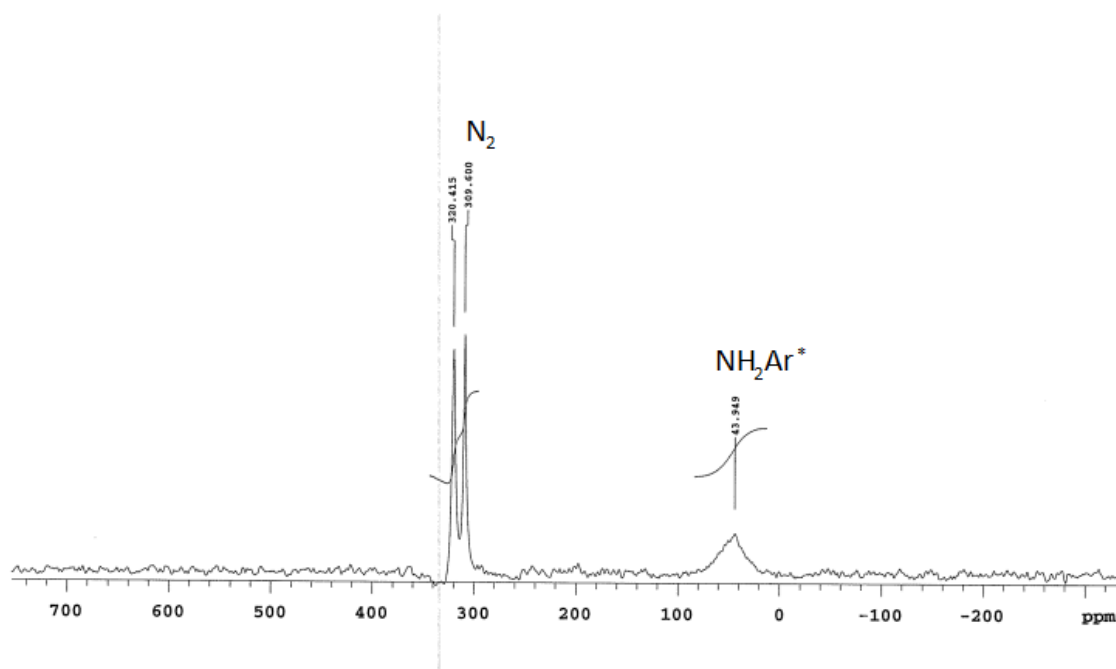


Figure 7.49 ^{14}N NMR of **Fe1*** in C_6D_6 .

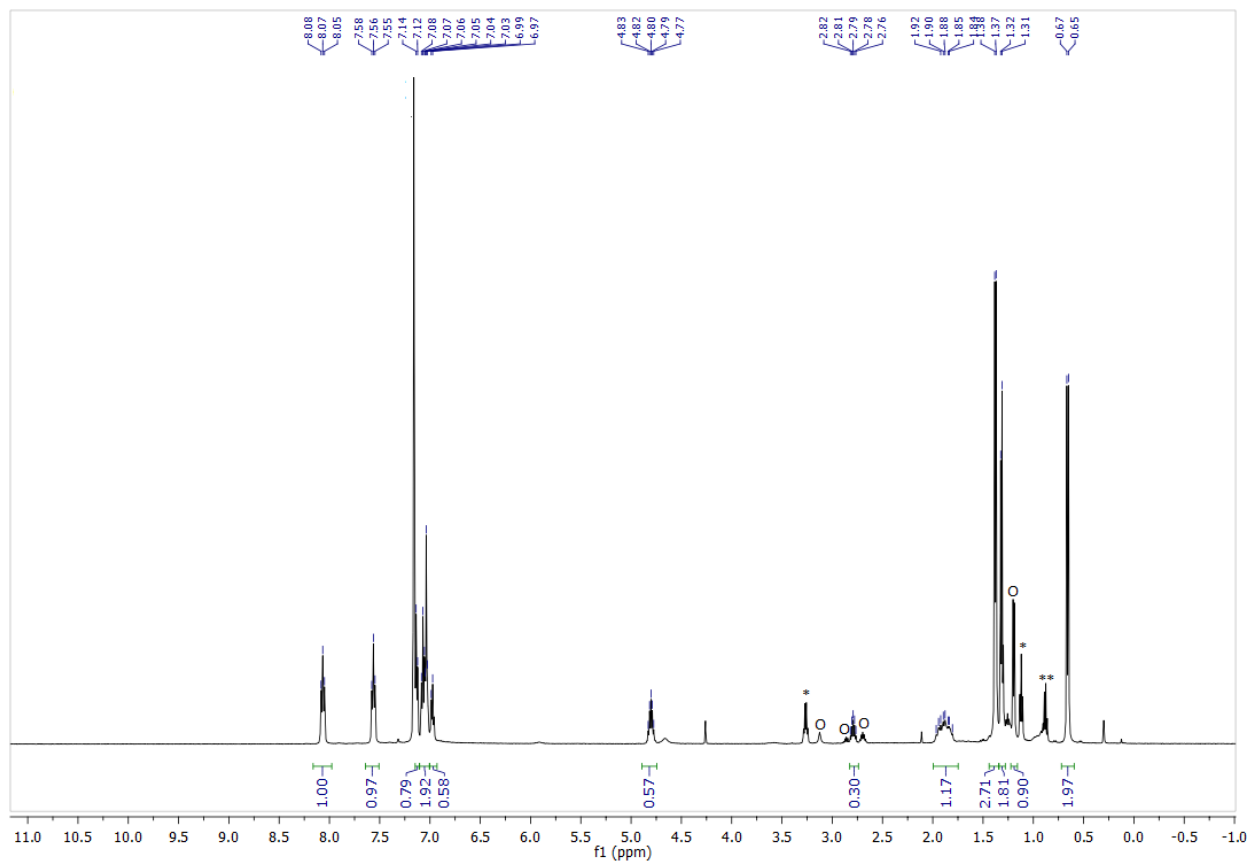


Figure 7.50 ^1H NMR of Fe3^* in C_6D_6 .

$\text{O} = \text{NH}_2\text{Ar}^*$, $*$ = Et_2O , $**$ = n-hexane

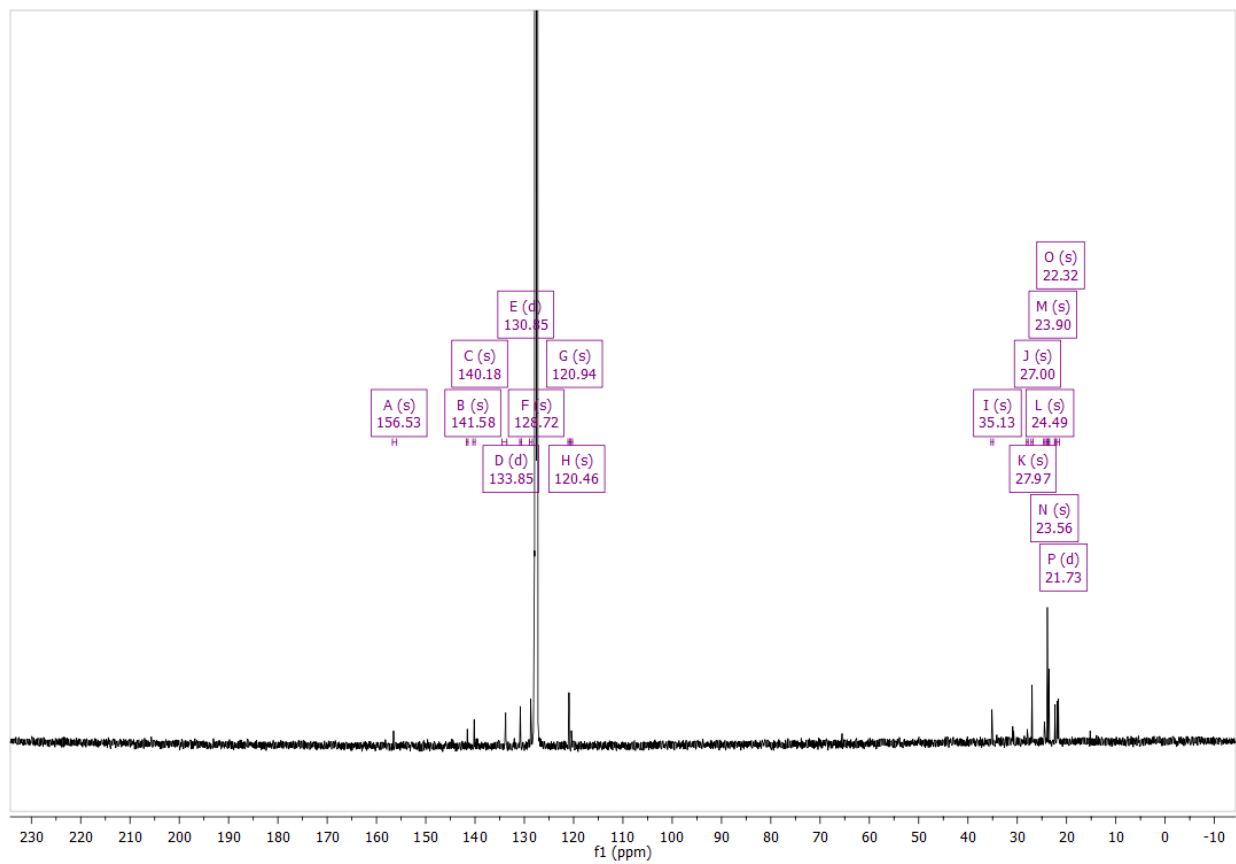


Figure 7.51 ^{13}C NMR of $\text{Fe}3^*$ in C_6D_6 .

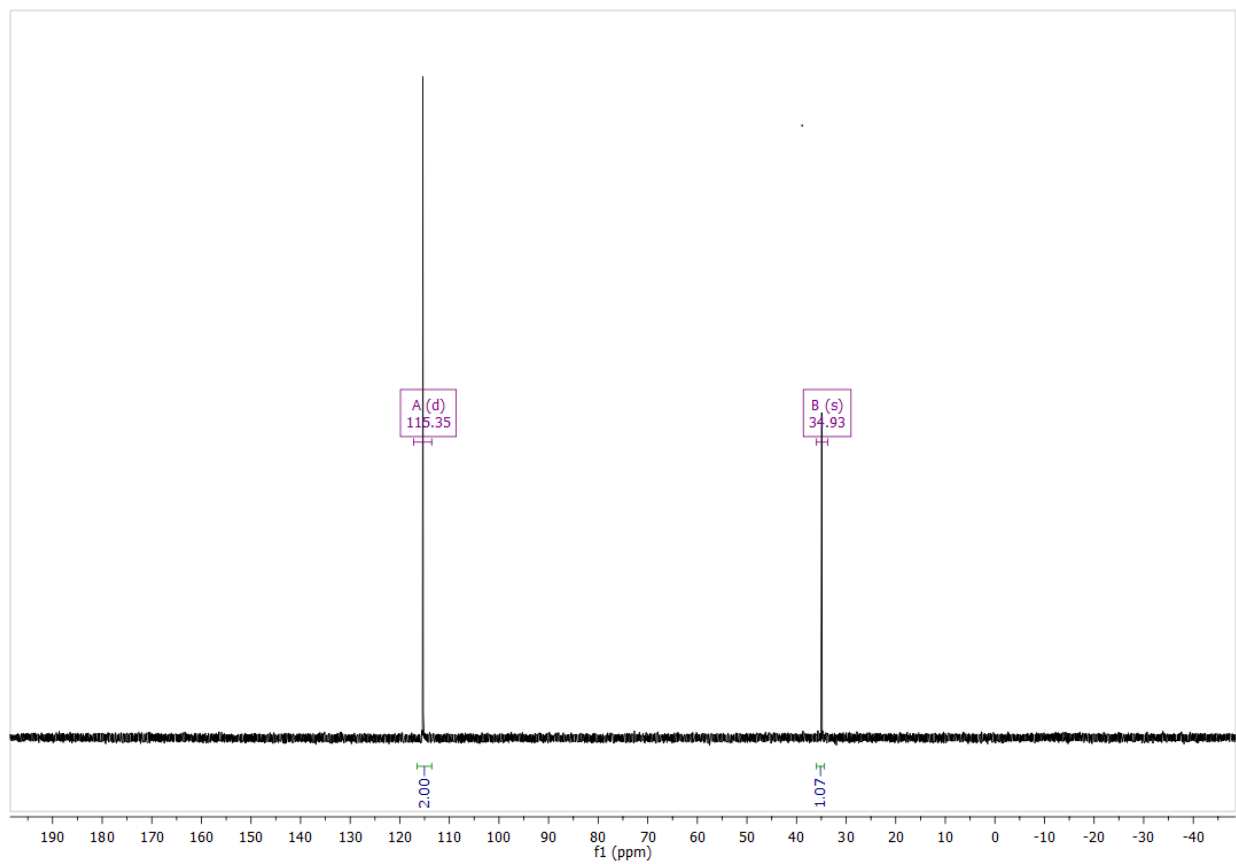


Figure 7.52 ^{31}P NMR of Fe3^* in C_6D_6 .

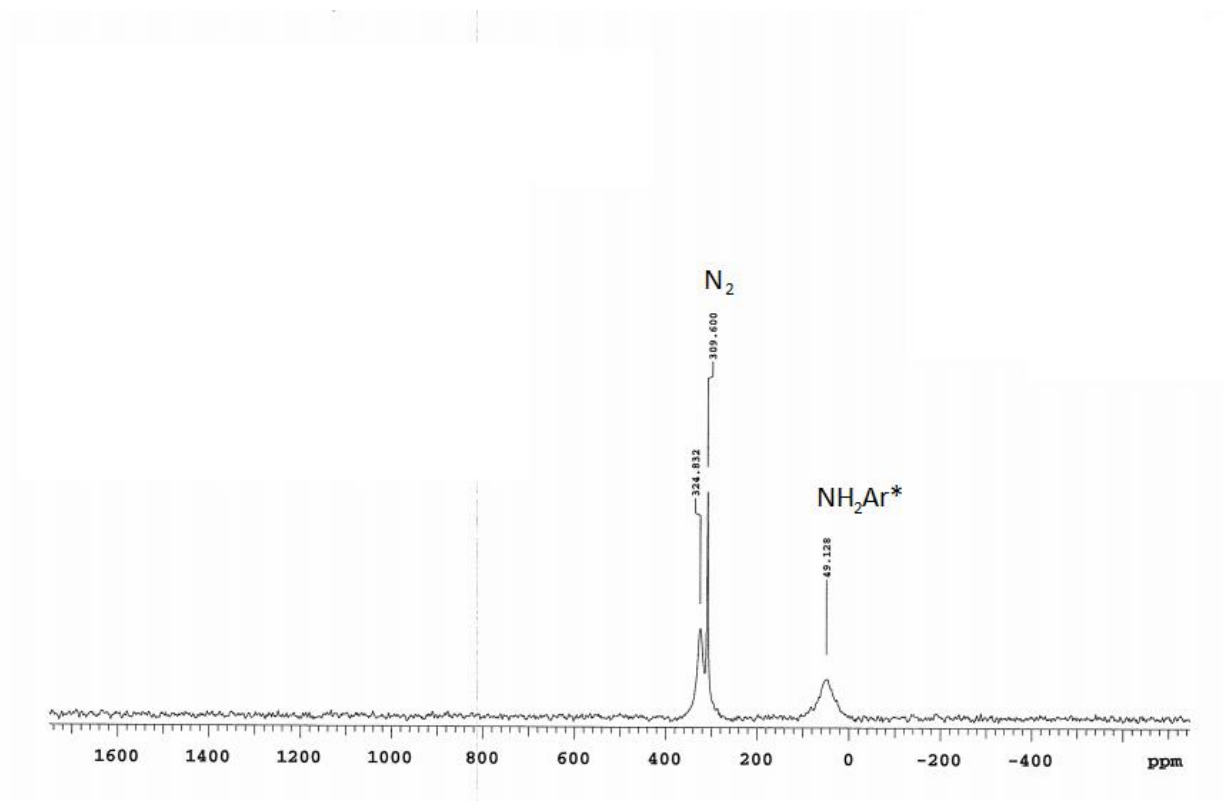


Figure 7.53 ^{14}N NMR of $\text{Fe}3^*$ in C_6D_6 .

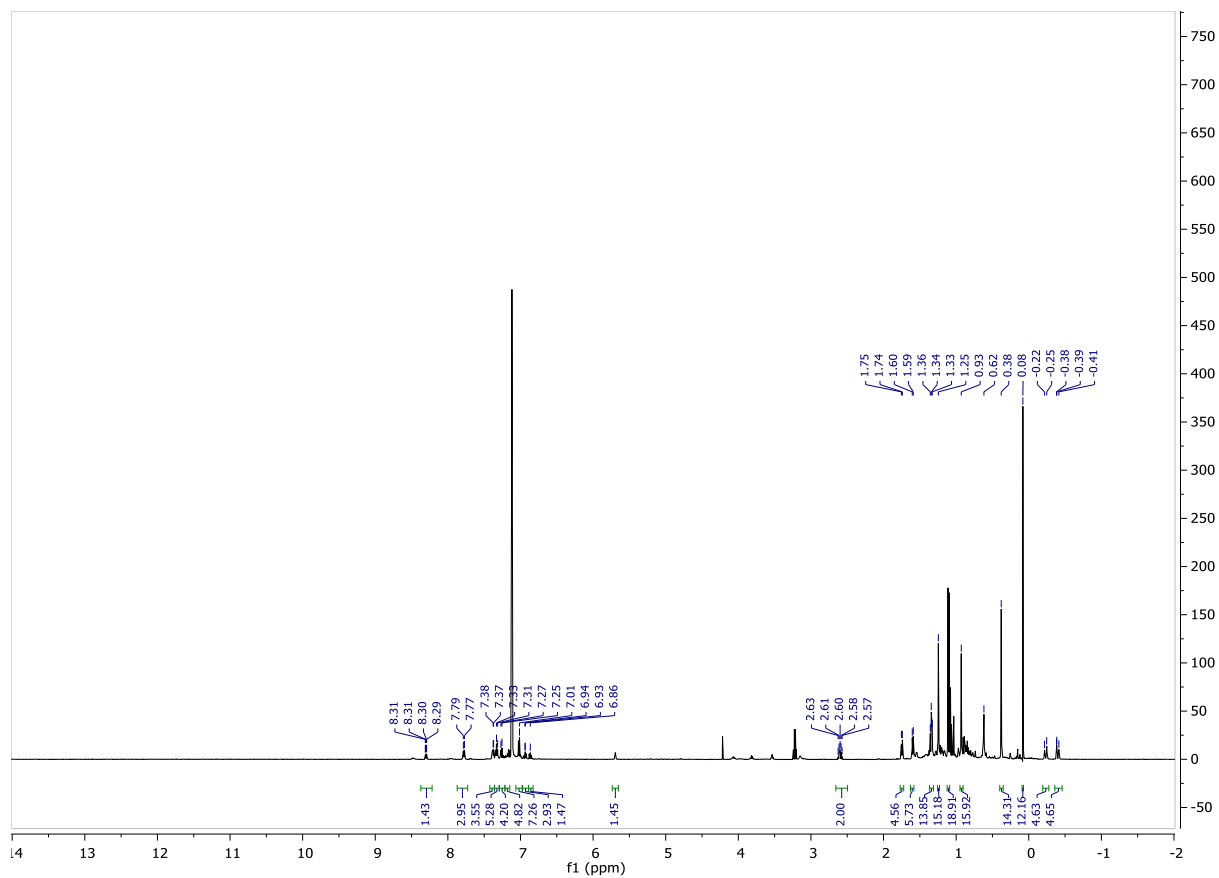


Figure 7.54 ^1H NMR of **Fe8** in C_6D_6 .

Note: This is a crude NMR and the compound is chiral, so full assignment of the spectrum was not attempted.

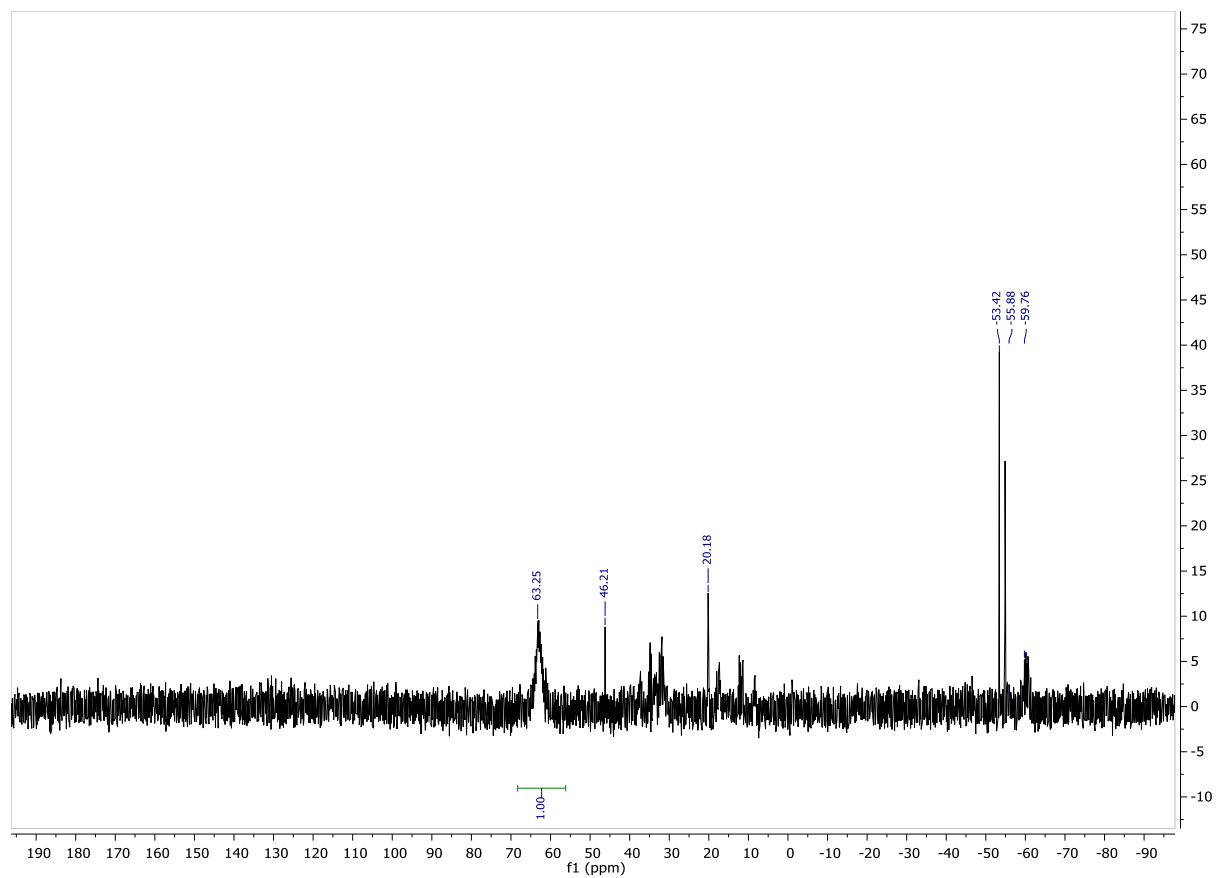


Figure 7.55 ^{31}P NMR of **Fe8** in C_6D_6 .

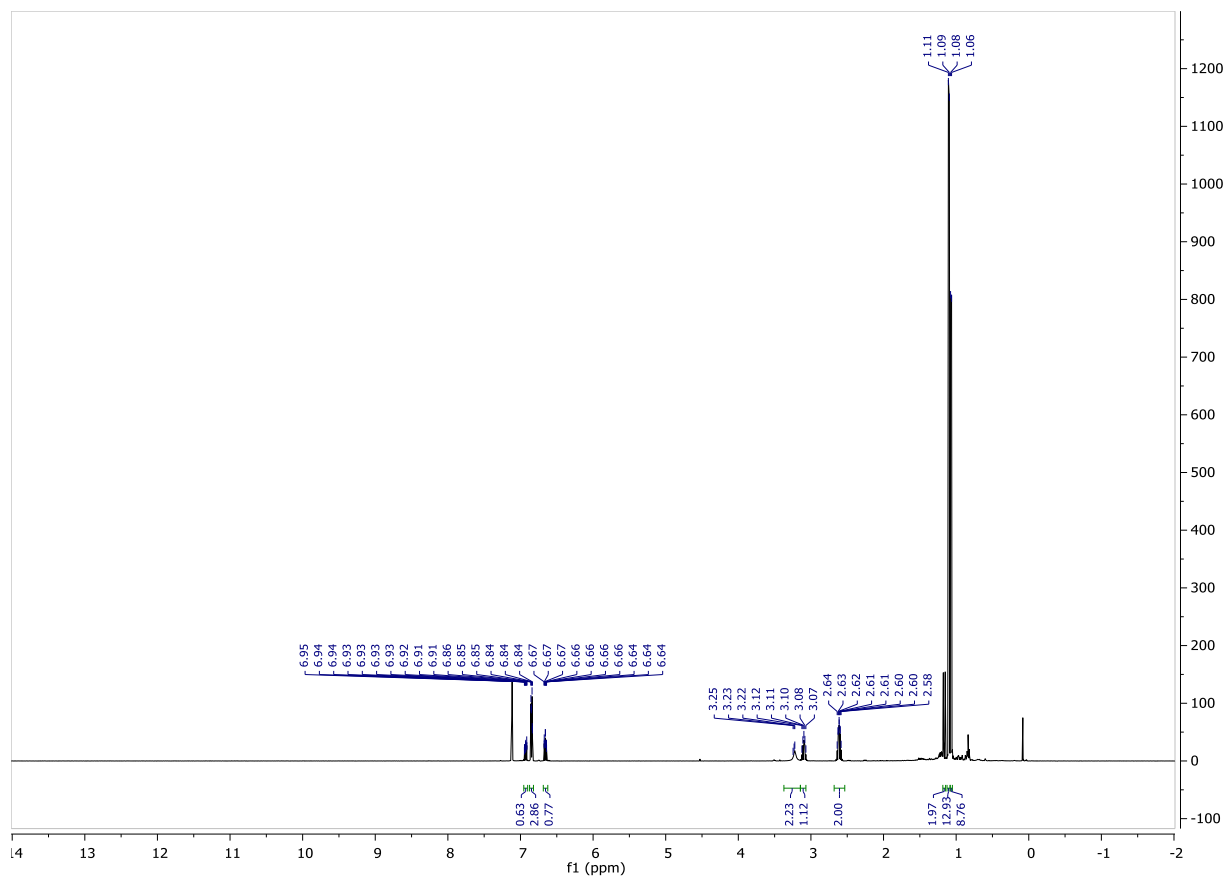


Figure 7.56 ^1H NMR of the C_6D_6 soluble extracts from the reaction of **Fe5** and CS_2 . The ^1H NMR shows H_2NAr and SCNAr .

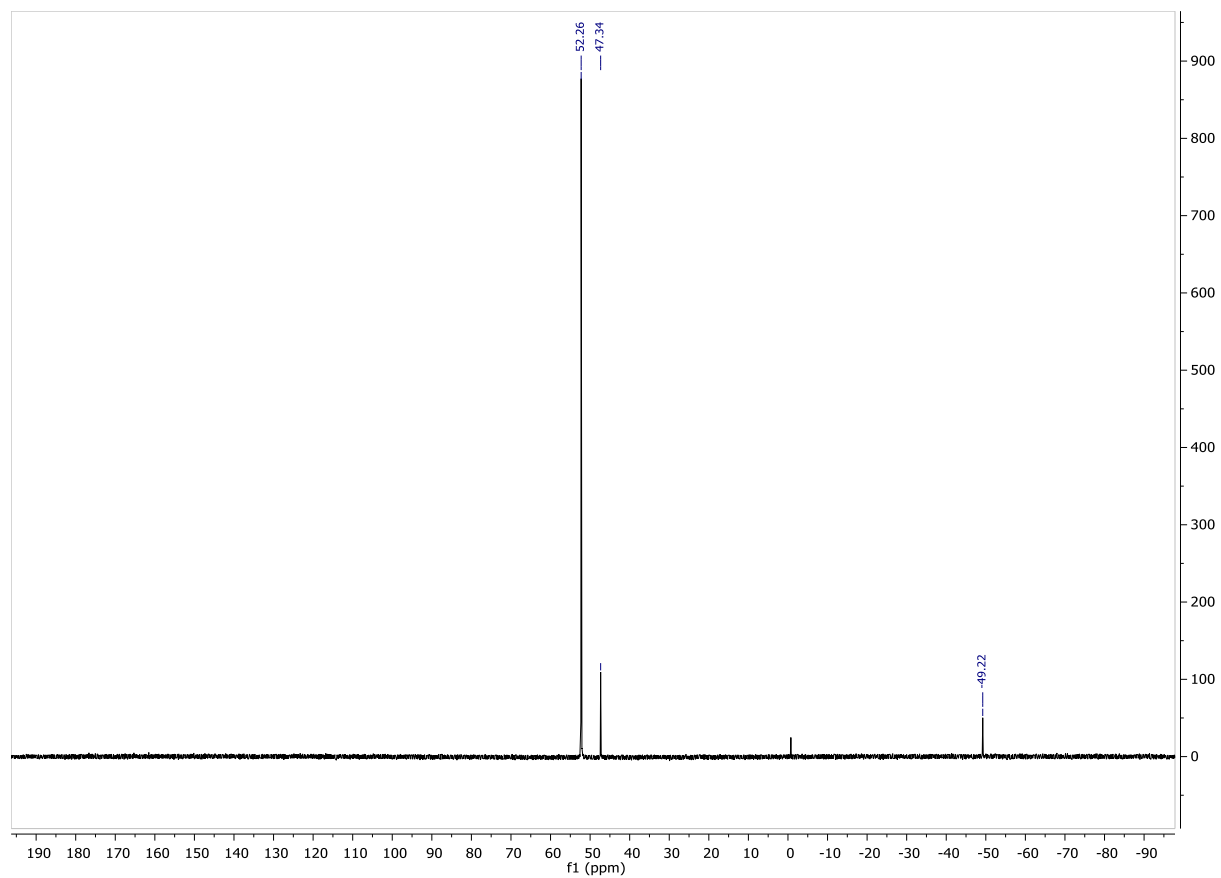


Figure 7.57 ^{31}P NMR of **Fe5** + 1,1-dimethylhydrazine in C_6D_6 . The peak at 47 ppm is the starting **Fe5**. The peak at 52 ppm is a new compound. (-49 is free triphos ligand)

UV-Vis Characterization

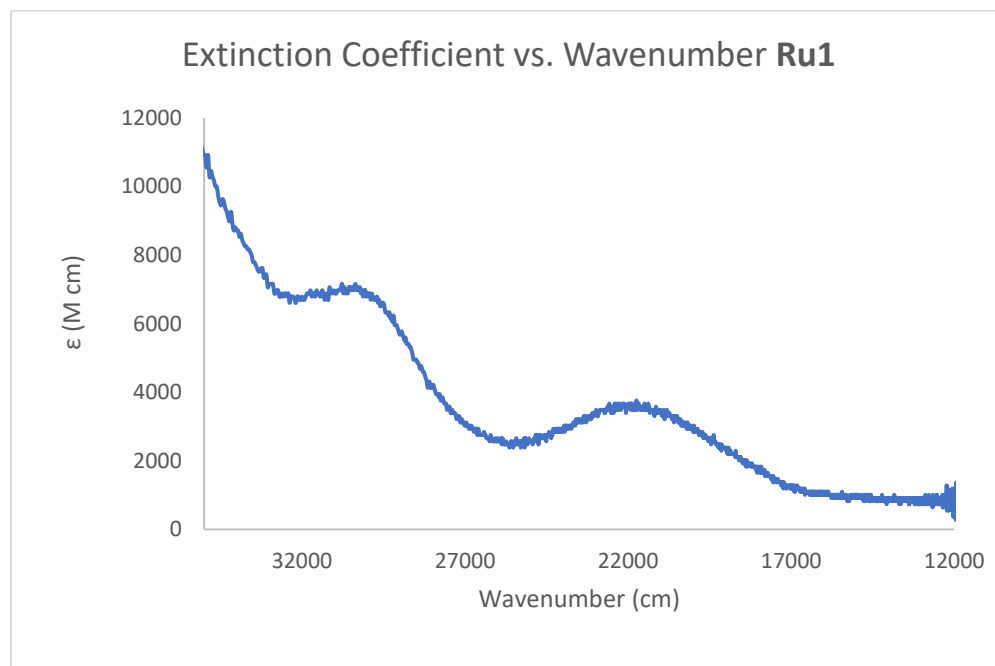


Figure 7.58 0.000109 M, THF

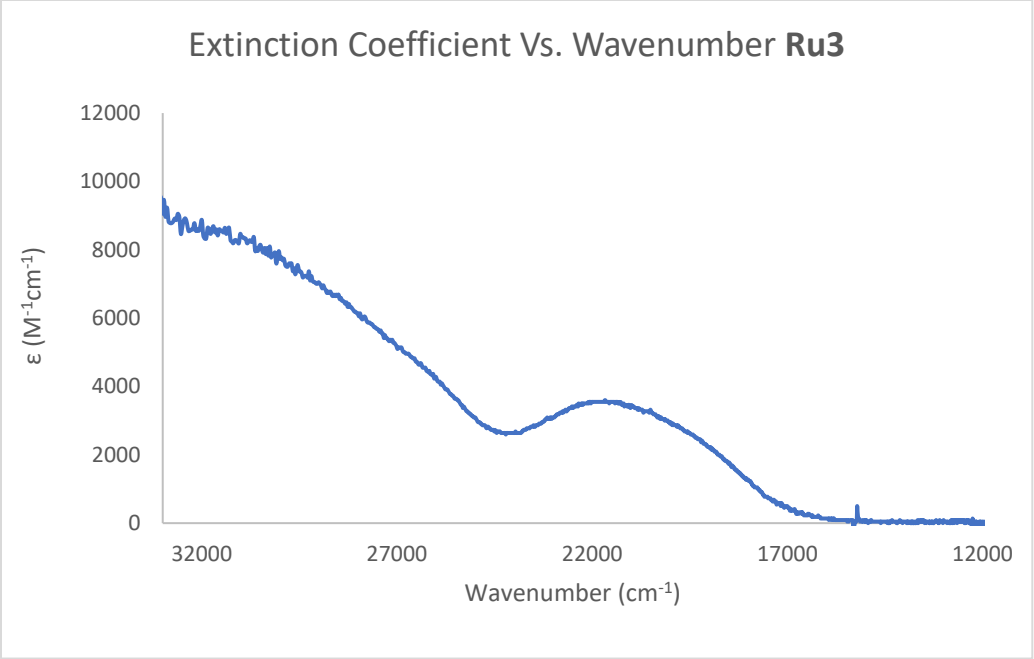


Figure 7.59 0.00022 M THF

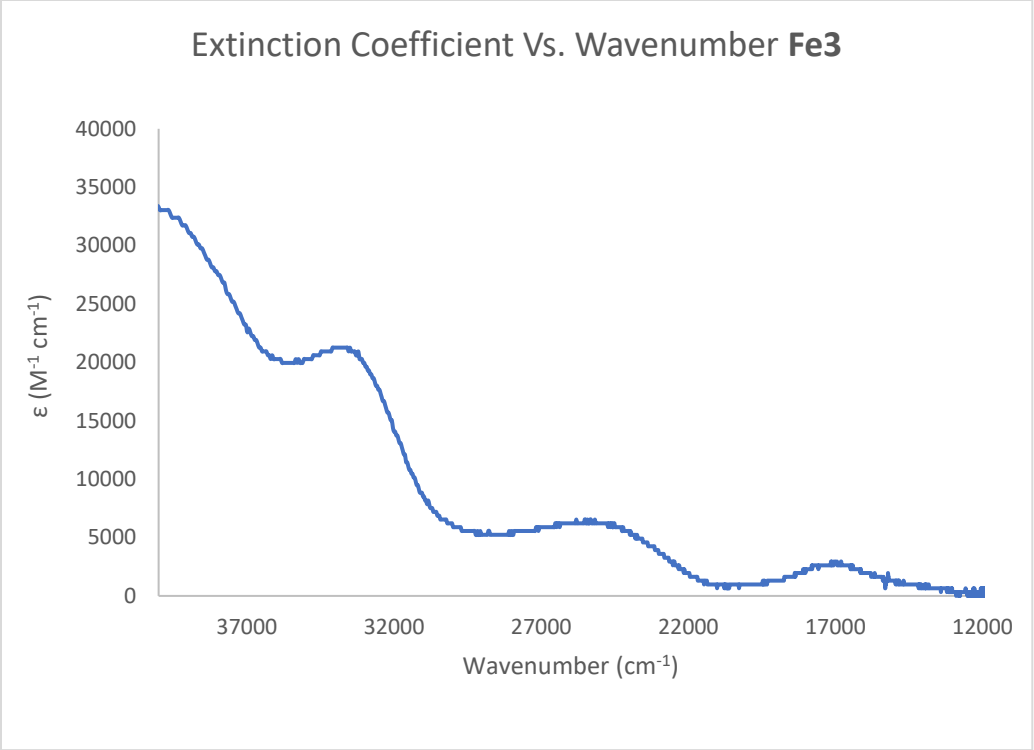


Figure 7.60 0.00031 M, THF

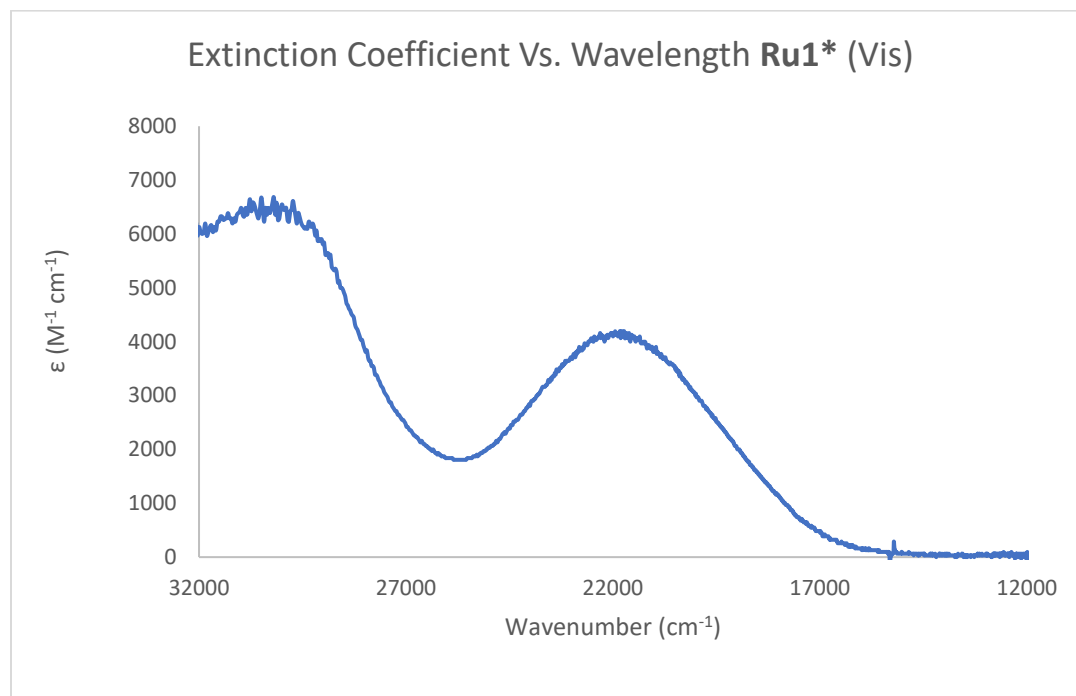


Figure 7.61 0.00031 M, THF

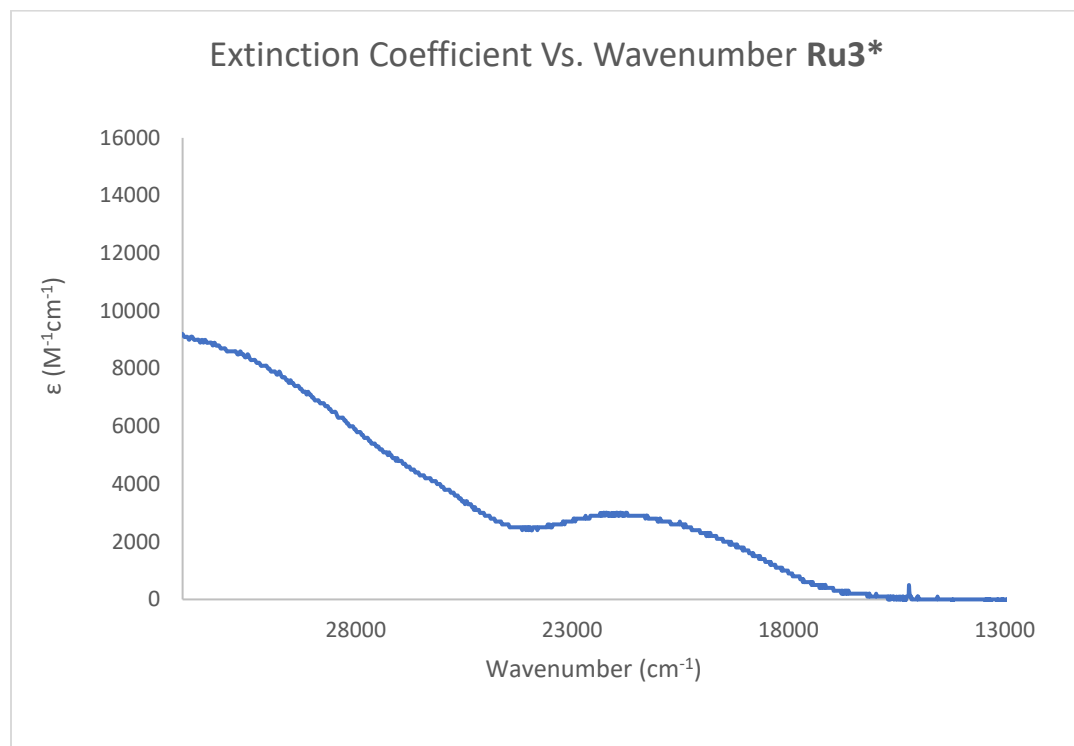


Figure 7.62 0.00010 M, THF

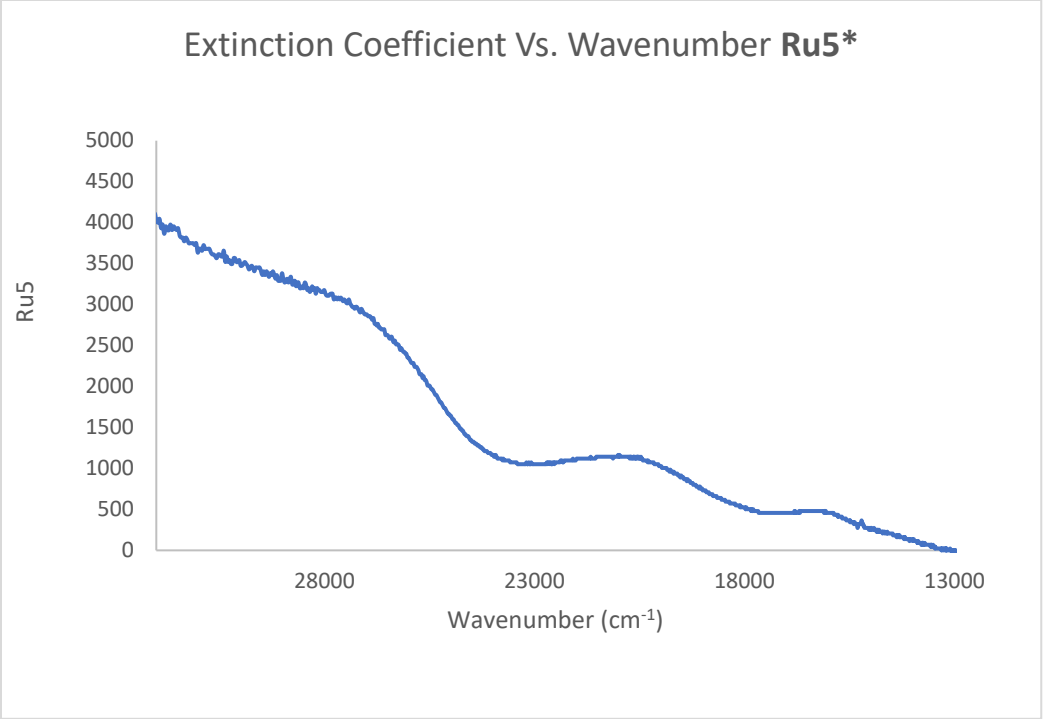


Figure 7.63 0.00044 M, THF

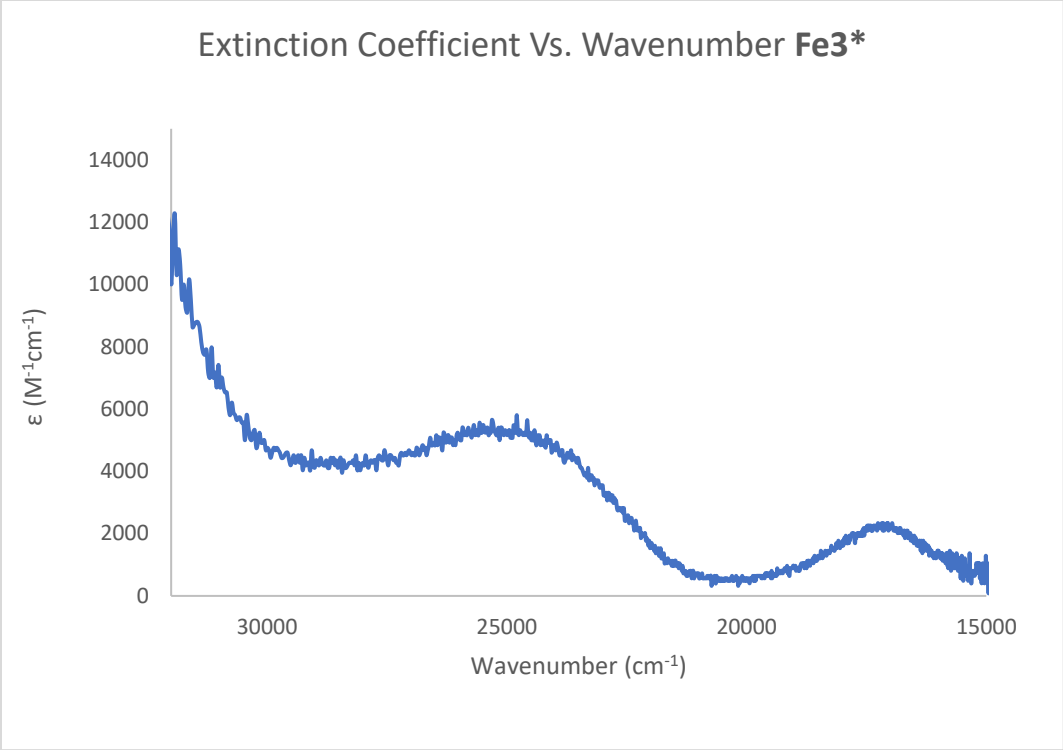


Figure 7.64 0.000068 M, THF

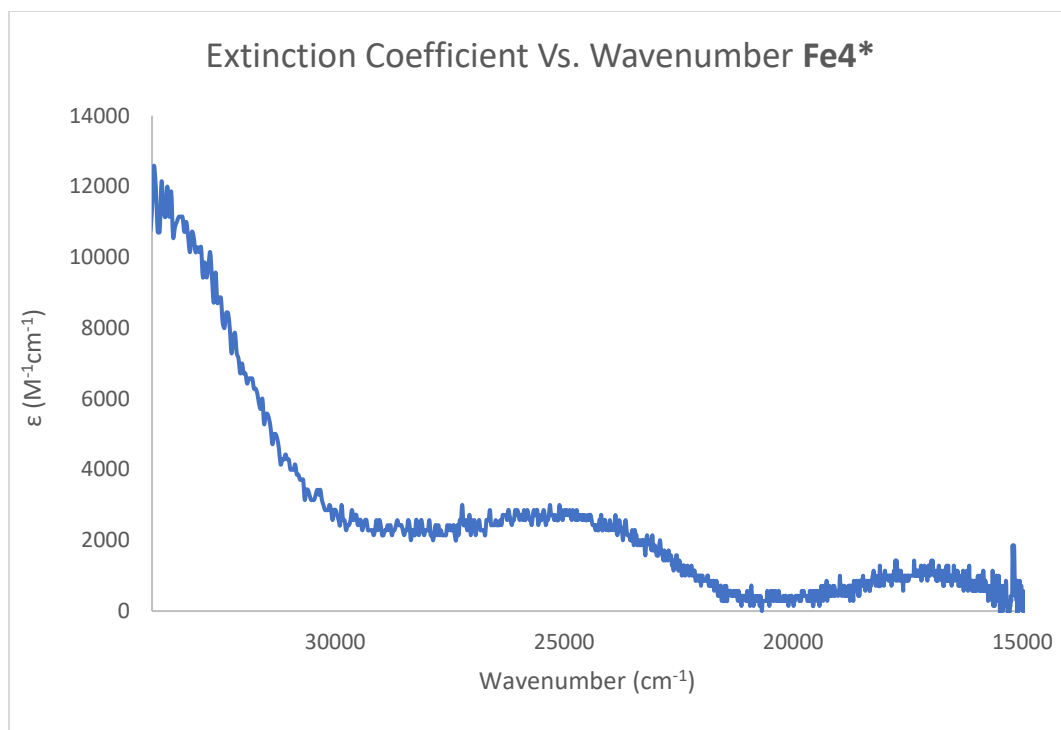


Figure 7.65 0.000071 M, THF

Note: additional features in the UV range of the spectrum for **Fe3*** and **Fe4*** could not be accurately fit, so no ϵ values were assigned for purposes of characterization.

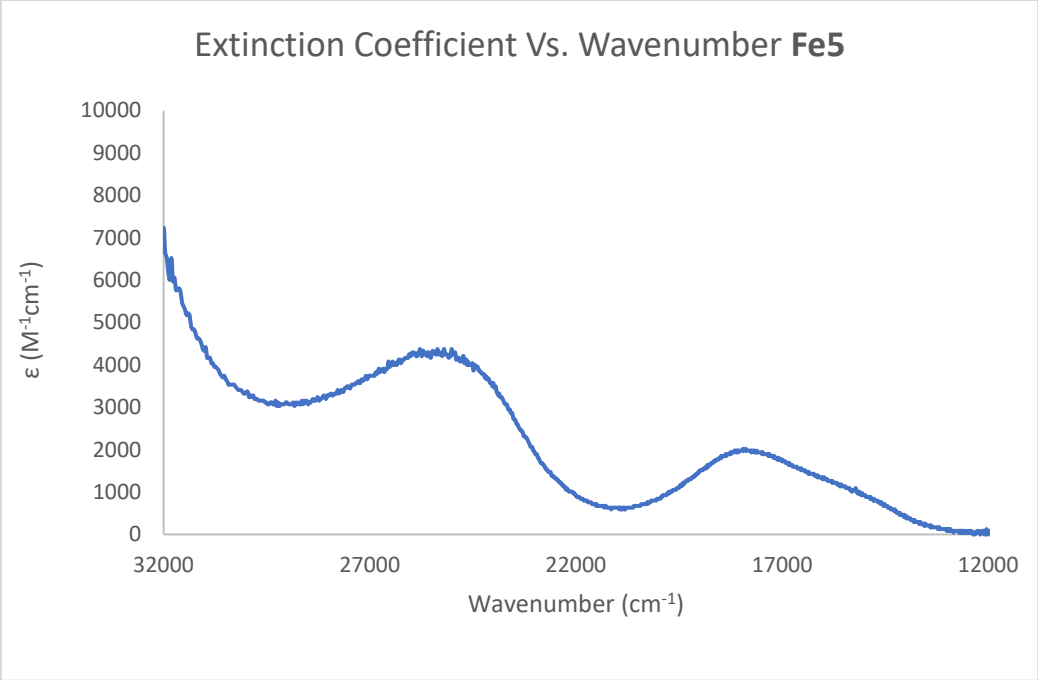


Figure 7.66 0.000238 M, THF

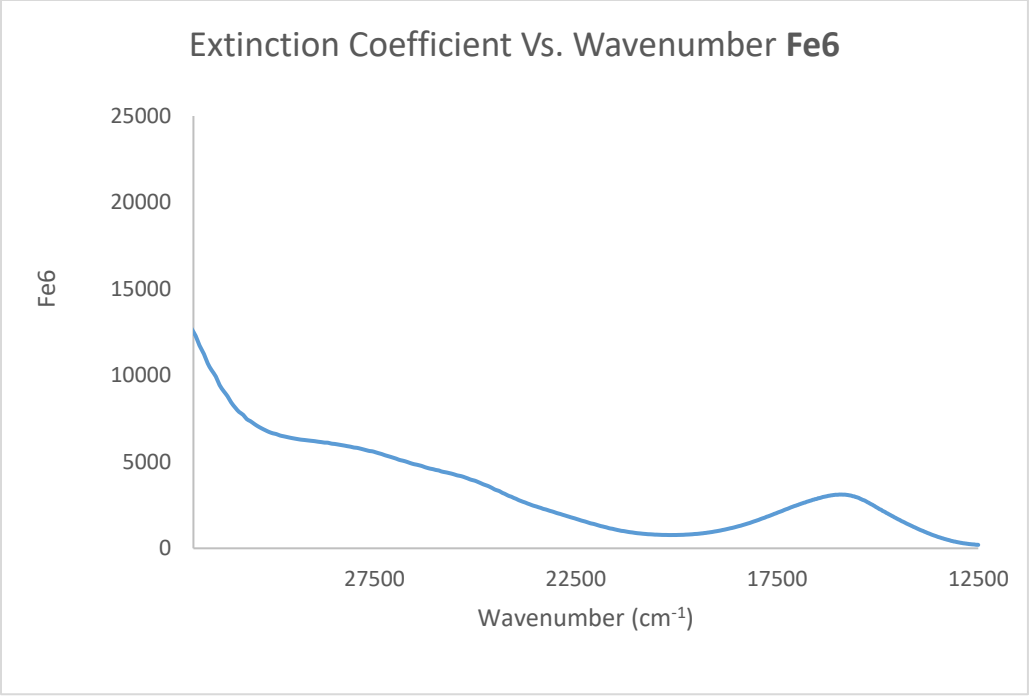


Figure 7.67 0.00016 M, THF

X-Ray Crystallography

The following complexes have been structurally characterized by single crystal X-ray diffraction and their structures deposited in the Cambridge Structural Database: CCDC #'s: 1856951-1856961 (**Ru2**, **Ru2***, **Ru3**, **Ru3***, **Ru4**, **Fe2**, **Fe2***, **Fe3**, **Fe3***, **Fe5**, and **Fe6**).

One additional crystal structure was collected for structure elucidation: **Fe8**. This structure has not been submitted to the CCDC, but the .cif file has been added to the MSU structural database managed by Dr. Richard Staples. Basic structural data, including the unit cell and diffraction data for the structure, is provided below.

Xray-data for Fe5: spacegroup, Pbc_a

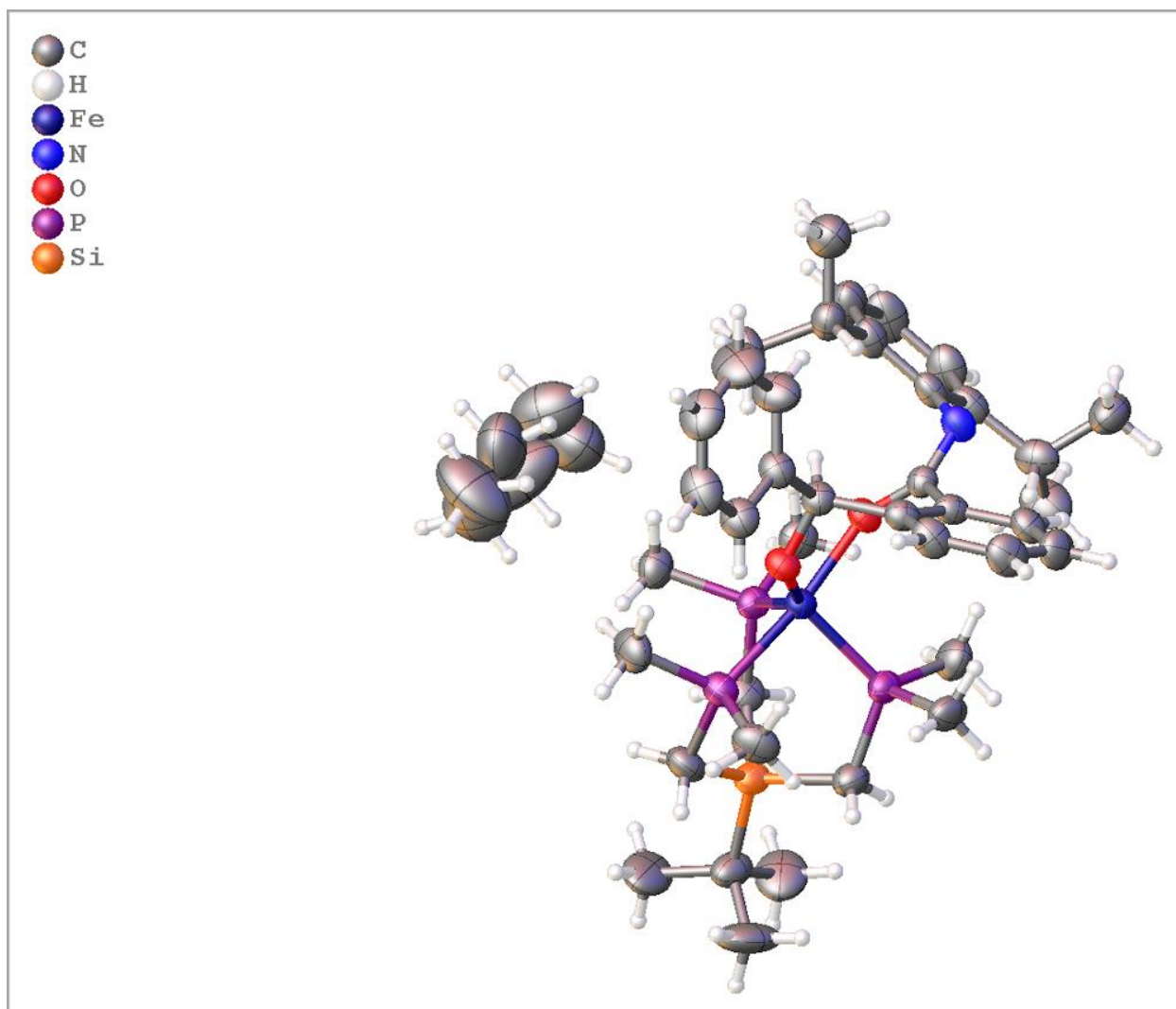


Figure 7.68 Crystal data and structure refinement for Pbc_a.

Identification code	Pbc _a
Empirical formula	C ₃₀ H _{49.33} Fe _{0.67} N _{0.67} O _{1.33} P ₂ Si _{0.67}
Formula weight	621.42
Temperature/K	173.15
Crystal system	orthorhombic
Space group	Pbc _a

a/Å	18.909(2)
b/Å	17.097(2)
c/Å	29.757(3)
α /°	90
β /°	90
γ /°	90
Volume/Å ³	9620.1(19)
Z	12
ρ_{calc} /cm ³	1.287
μ /mm ⁻¹	0.682
F(000)	3864.0
Crystal size/mm ³	0.364 × 0.276 × 0.262
Radiation	MoK α (λ = 0.71073)
2 Θ range for data collection/°	3.484 to 50.744
Index ranges	-21 ≤ h ≤ 22, -20 ≤ k ≤ 20, -35 ≤ l ≤ 35
Reflections collected	61350
Independent reflections	8820 [R _{int} = 0.1333, R _{sigma} = 0.0843]
Data/restraints/parameters	8820/0/493
Goodness-of-fit on F ²	0.923
Final R indexes [I ≥ 2 σ (I)]	R ₁ = 0.0569, wR ₂ = 0.1400
Final R indexes [all data]	R ₁ = 0.0910, wR ₂ = 0.1592
Largest diff. peak/hole / e Å ⁻³	0.75/-0.32

Electrochemical Characterization of M(NAr)(PMe₃)dppe Complexes and Oxidized Species

Fe5 presents a reversible Fe(II/III) couple which appears around -900 mV versus the Fc/Fc⁺ couple. Additionally, there is also a reversible couple, assigned as the Fe(III/IV) redox wave centered at -160 mV. Upon scanning to more highly reducing potentials, a small irreversible anodic wave is noted, which causes the shoulder located on the cathodic wave of the Fe(II/III) couple to grow upon reversal of the current. This is likely an irreversible Fe(I/II) couple. This species is perhaps related to the small redox event centered at roughly -450 mV.

Upon oxidation of **Fe5** to **Fe6** a slight shift is noted in the Fe(II/III) redox wave, however, this process is still electrochemically reversible. The Fe(III/IV) couple, however, has shifted to much higher potentials and is irreversible when starting from the chemically oxidized species, **Fe6**. This suggests that the electronics of **Fe6** (in the +3 state) may be different from the electrochemically oxidized **Fe5**⁺.

Relative to **Fe5** and **Fe6**, the **Fe3*** and **Fe4*** couples are shifted to slightly less reducing potentials. The reversible Fe(II/III) couple is -750 mV relative to Fc/Fc⁺. Further oxidation (Fe(III/IV)) is irreversible, with the onset of a large cathodic wave around 0 V. The oxidized species shows very similar features, with a reversible Fe(II/III) couple at -770 mV vs. Fc and a large irreversible anodic wave, with an onset slightly before 0 V (Fe(III/IV)). This suggests that the species generated by chemical oxidation is similar electronically to that generated by electrochemical oxidation. These species display potentials within agreeable ranges to similar derivatives in the literature.¹

The ruthenium derivative (**Ru3***) demonstrates two reversible couples. The Ru(II/III) couple, is assigned as -580 mV vs Fc. It is interesting to note that this potential is more oxidative than either of the Fe(II/III) redox couples. The Ru(II) is actually *more difficult* to oxidize than the

lighter congeners. This difference in the redox potentials between Ru and Fe could be interpreted as a resistance of Ru(II) to oxidize to Ru(III), or more specifically, that the electron removed from the Ru species originates from an orbital of different make-up than the electrons removed when oxidizing the Fe derivatives. This observation agrees with the experimentally observed ability of the “Ru(III)” to sacrificially oxidize the imido ligand.

It might be expected in simple ligand fields, that the heavier congeners are easier to oxidize relative to lighter ones. For instance, the redox potential to go from Ru(II) to Ru(III) in an aqueous system is reported as 0.24 V (vs. SCE), while the Fe(II) to Fe(III) couple is reported as 0.77 V.² Upon introducing more complicated ligands, however, this trend has been noticeably disrupted. For instance, the series of $M(\text{bpy})_3^{+2/+3}$ couples for $M = \text{Fe, Ru, and Os}$ are reported (vs. SHE) as 1.06 V, 1.27 V, and 0.84 V, respectively.² This same trend is noted comparing hexacyano complexes and their reduction potentials looking down Group VIII, as well. With these traditionally π -accepting ligands, it seems Ru often proves harder to oxidize than Fe.

Comparing the Ru(III/IV) redox potential vs. the Fe(III/IV) potentials, we see that it is intermediate to the two Fe species. While still more positive in potential than the reversible couple for **Fe5**, it is slightly more negative than the onset of the irreversible couple noted for **Fe3***. There is another wave, that appears reversible, but with about half the current density for the Ru(II/III) and (III/IV) couples following the Ru(III/IV) couple. This wave has not been assigned, but could take place on the ligands. Additionally, **Ru5*** appears to react with the electrolyte, thus electrochemical characterization could not be compiled for comparison. While the rest of the species examined were stable enough over the time frame necessary to compile the CV measurements, the solutions often changed color after 12 to 24 hours stored at $-35\text{ }^\circ\text{C}$.

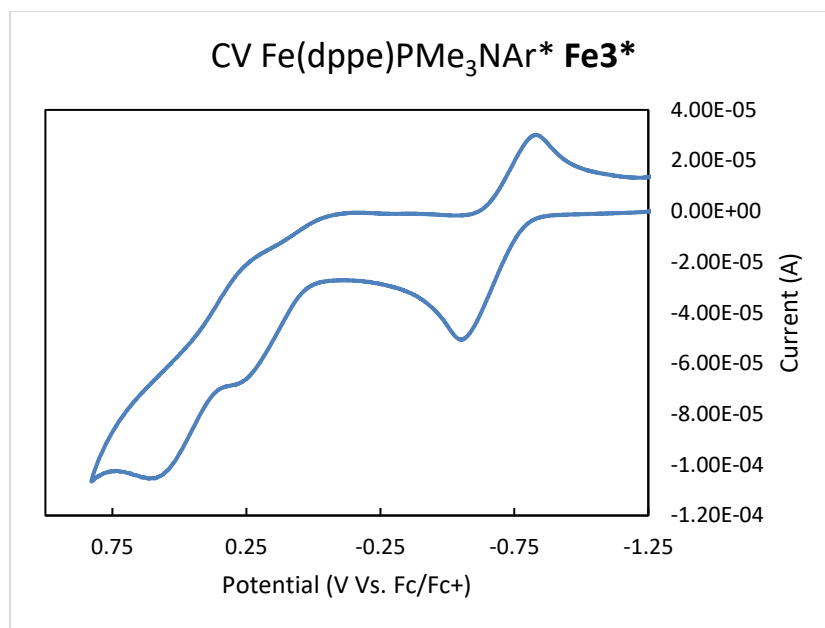


Figure 7.69 CV for **Fe^{3*}** in THF with TBAPF₆ electrolyte.

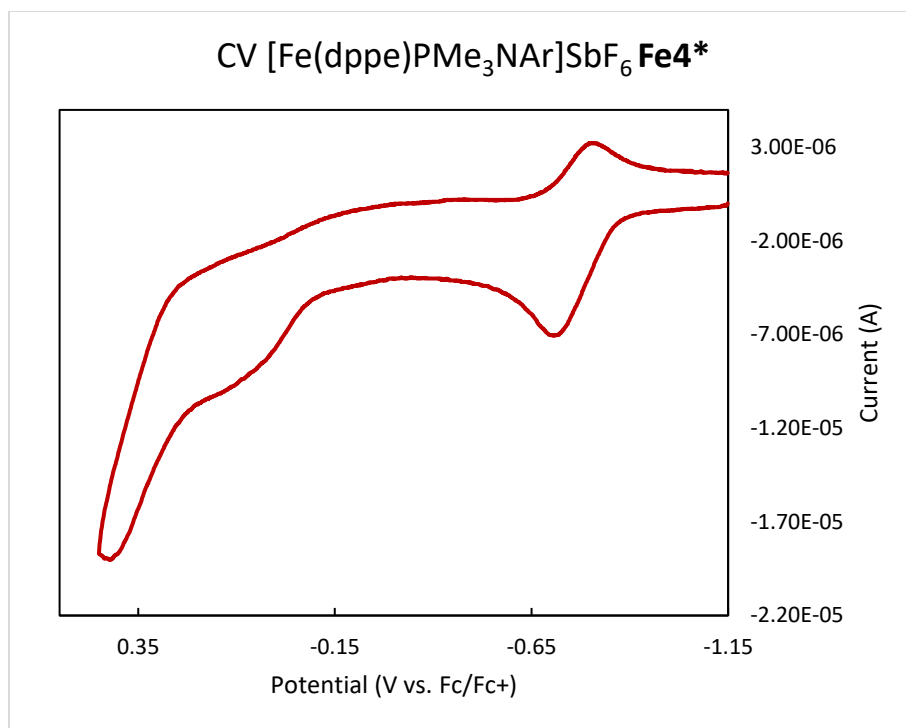


Figure 7.70 CV for Fe₄* in THF with TBAPF₆ electrolyte.

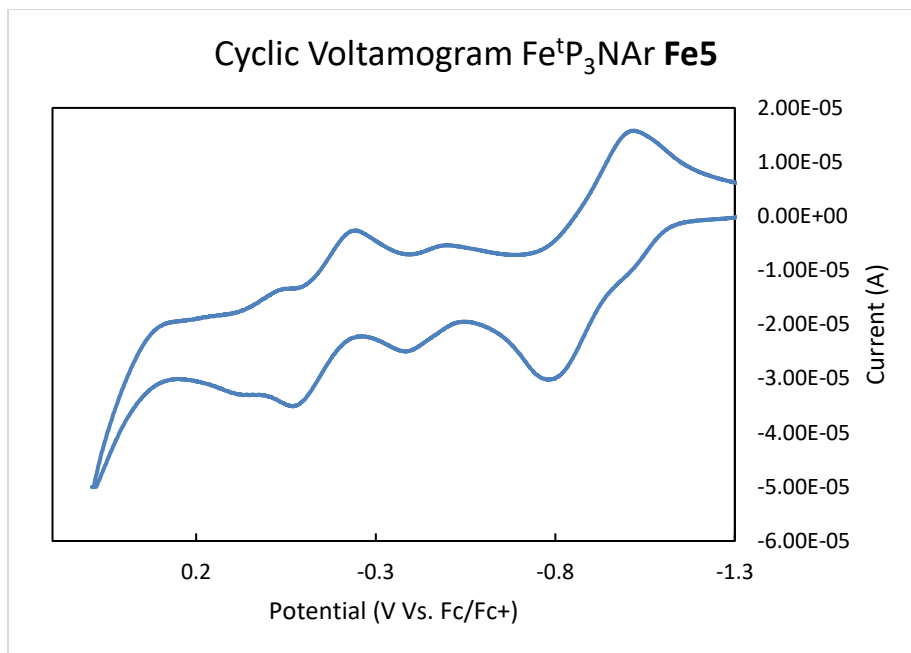


Figure 7.71 CV for **Fe5** in THF with TBAPF6 electrolyte.

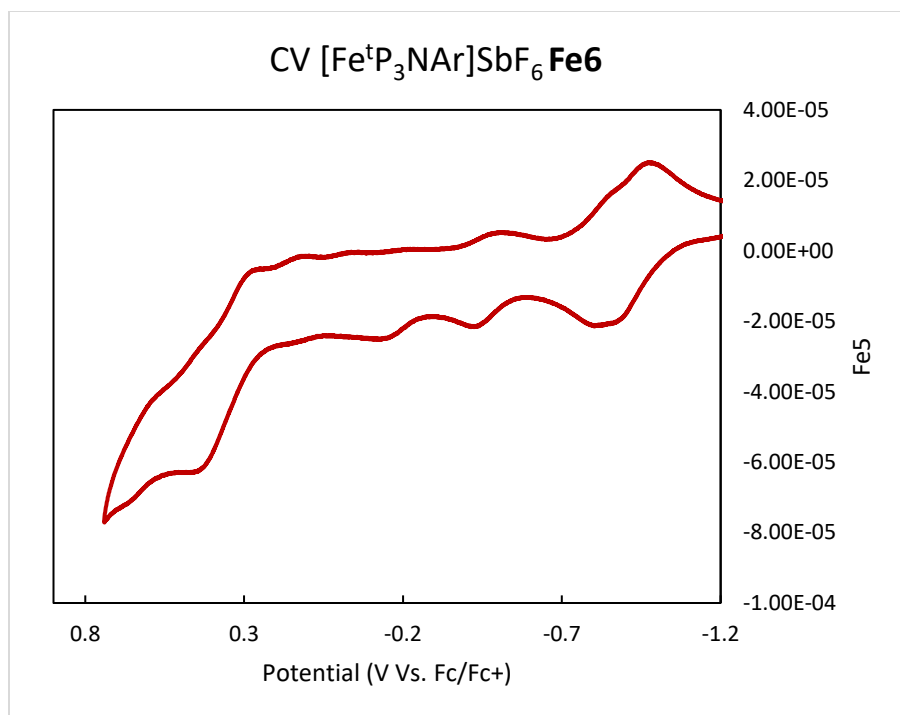


Figure 7.72 CV for **Fe6** in THF with TBAPF6 electrolyte.

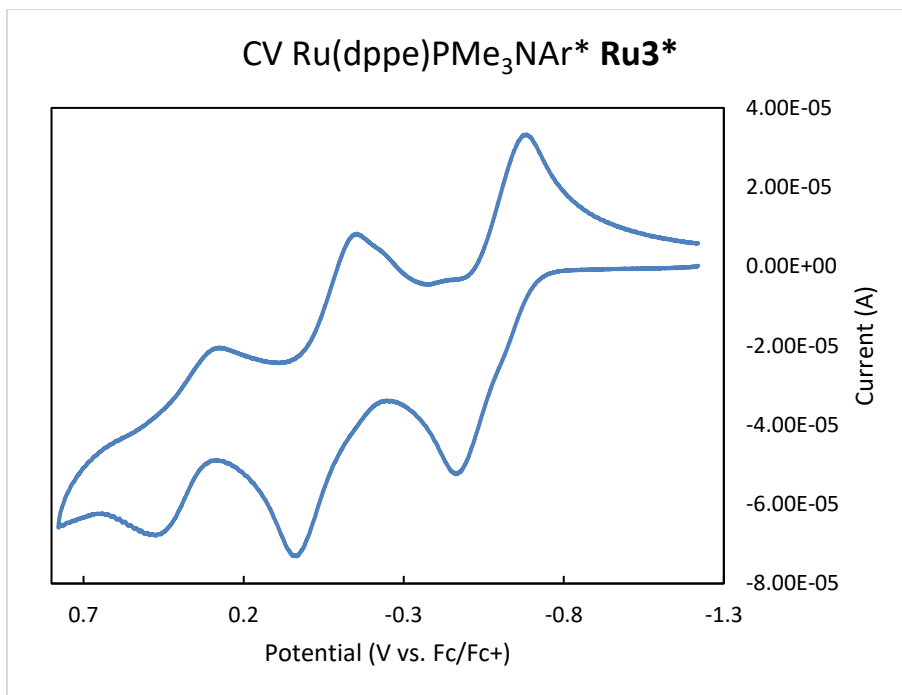


Figure 7.73 CV for **Ru3*** in THF with TBAPF6 electrolyte.

Optimized Geometries for Calculated Model Complexes

RuNPh(PH₃)₃ (Ru6)

25

MP2/CC-PVDZ,RU=CC-PVTZ-PP ENERGY=-1407.58451778

C	0.1333360925	3.3187269145	7.6940896461
C	1.0945904142	3.4428915742	6.6664653368
C	1.2155783789	4.6492344203	5.9420744321
C	0.3737222832	5.7287664983	6.2480304854
C	-0.5841795137	5.6051420981	7.2717808070
C	-0.7046040282	4.4027803033	7.9939087184
N	1.9287940576	2.3700077093	6.3622262914
Ru	2.8658620169	0.9040458595	6.1562339740
P	4.0165815330	0.0118280810	7.8041101187
P	4.5227374948	0.3953028798	4.7667986457
P	1.9324430492	-1.0347768015	5.6992149233
H	4.7166128800	-1.2375641985	7.6776872573
H	5.1051203810	0.7125249397	8.4113773163
H	3.3619280325	-0.3251187642	9.0290989892
H	5.1551494186	-0.8966007301	4.7459173907
H	4.3321299963	0.4717225459	3.3524722093
H	5.7432078795	1.1389309804	4.7856710839
H	2.6867185834	-2.2547449440	5.5991363692
H	0.9311228973	-1.5671271113	6.5691037801
H	1.1939593112	-1.2351195462	4.4913987396
H	1.9699166487	4.7153560325	5.1511410708
H	0.4635209516	6.6659381805	5.6893309016
H	-1.4513206566	4.3117603633	8.7893463376
H	0.0648367387	2.3698921329	8.2366226796
H	-1.2399348407	6.4495085821	7.5079874961

FeNPh(PH₃)₃ (Fe7)

25

MP2/CC-PVDZ,FE=CC-PVTZ ENERGY=-2576.09296549

N	0.1744675944	3.2025124108	7.7043270825
Fe	1.2474484024	3.2243995144	6.6244549027
P	1.6084432519	4.7961179621	5.4847817695
P	1.2288202166	1.9780924698	5.1041275069
P	3.1493705724	2.9327928327	7.0287976816
H	4.1640559345	2.9487028288	6.0027379655
H	3.8833613192	3.7901276860	7.9200903533
H	3.6218627878	1.7158018645	7.6308413911
H	2.6297277134	4.7888878525	4.4654107503
H	0.6024863291	5.3634395462	4.6289181868
H	2.0121438641	6.0607124595	6.0362951427
H	2.2479088317	1.9981756449	4.0825386548
H	1.2848233809	0.5531834685	5.2865755059

H	0.1381534655	1.9275529229	4.1681458281
C	-0.8147099140	3.1630425515	8.7073630985
C	-1.6018977523	4.3046711429	8.9242841282
C	-2.5869252091	4.2651739181	9.9240898017
C	-2.7615073764	3.0918982270	10.6800917287
C	-1.9659809420	1.9540748546	10.4529620705
C	-0.9790043131	1.9863211240	9.4548126361
H	-1.4315494176	5.1957838372	8.3127131456
H	-3.2131148749	5.1418319659	10.1122799995
H	-3.5299972676	3.0635961108	11.4589723303
H	-2.1137969697	1.0492010329	11.0491336039
H	-0.3378296272	1.1250547715	9.2442527352

RuNPh(PH₃)₃ (Ru6_mod)

25

N	0.7392	-0.0191	0.0013
Ru	-1.0127	-0.0024	0.0003
P	-2.2513	-1.8465	0.0066
P	-2.1744	0.9312	-1.6167
P	-2.1788	0.9451	1.6070
H	-3.6219	0.9622	1.6013
H	-2.0811	0.5202	2.9774
H	-2.0542	2.3437	1.9151
H	-3.6906	-1.7518	0.0455
H	-2.2327	-2.8063	-1.0633
H	-2.1778	-2.8365	1.0463
H	-3.6160	0.9147	-1.5539
H	-2.0949	2.3296	-1.9405
H	-2.1207	0.4966	-2.9865
C	2.1485	-0.0126	0.0007
C	2.8291	-1.2397	0.0022
C	4.2332	-1.2327	0.0016
C	4.9208	-0.0056	-0.0005
C	4.2269	1.2181	-0.0020
C	2.8231	1.2180	-0.0007
H	2.2537	-2.1703	0.0039
H	4.7866	-2.1760	0.0028
H	6.0154	-0.0027	-0.0009
H	4.7753	2.1643	-0.0041
H	2.2432	2.1459	-0.0009

REFERENCES

REFERENCES

- (1) Cundari, T. R. Transition metal imido complexes. *J. Am. Chem. Soc.* **1992**, *114* (20), 7879.
- (2) Berry, J. F. TERMINAL NITRIDO AND IMIDO COMPLEXES OF THE LATE TRANSITION METALS. *Comments on Inorganic Chemistry* **2009**, *30* (1-2), 28.
- (3) O'Halloran, K. P.; Zhao, C.; Ando, N. S.; Schultz, A. J.; Koetzle, T. F.; Piccoli, P. M. B.; Hedman, B.; Hodgson, K. O.; Bobyr, E.; Kirk, M. L. et al. Revisiting the Polyoxometalate-Based Late-Transition-Metal-Oxo Complexes: The "Oxo Wall" Stands. *Inorg. Chem.* **2012**, *51* (13), 7025.
- (4) Hay-Motherwell, R. S.; Wilkinson, G.; Hussain-Bates, B.; Hursthouse, M. B. Synthesis and X-ray crystal structure of oxotrimesityliridium(V). *Polyhedron* **1993**, *12* (16), 2009.
- (5) Wang, B.; Lee, Y.-M.; Tcho, W.-Y.; Tussupbayev, S.; Kim, S.-T.; Kim, Y.; Seo, M. S.; Cho, K.-B.; Dede, Y.; Keegan, B. C. et al. Synthesis and reactivity of a mononuclear non-haem cobalt(IV)-oxo complex. *Nature Communications* **2017**, *8*, 14839.
- (6) Hong, S.; Pfaff, F. F.; Kwon, E.; Wang, Y.; Seo, M.-S.; Bill, E.; Ray, K.; Nam, W. Spectroscopic Capture and Reactivity of a Low-Spin Cobalt(IV)-Oxo Complex Stabilized by Binding Redox-Inactive Metal Ions. **2014**, *53* (39), 10403.
- (7) Goetz, M. K.; Hill, E. A.; Filatov, A. S.; Anderson, J. S. Isolation of a Terminal Co(III)-Oxo Complex. *Journal of the American Chemical Society* **2018**, *140* (41), 13176.
- (8) Nugent, W. A., Mayer, J. M. Metal-Ligand Multiple Bonds. *Wiley Interscience* **1987**.
- (9) Peters, J. W.; Szilagyi, R. K. Exploring new frontiers of nitrogenase structure and mechanism. *Current Opinion in Chemical Biology* **2006**, *10* (2), 101.
- (10) Svastits, E. W.; Dawson, J. H.; Breslow, R.; Gellman, S. H. Functionalized nitrogen atom transfer catalyzed by cytochrome P-450. *Journal of the American Chemical Society* **1985**, *107* (22), 6427.
- (11) Singh, R.; Bordeaux, M.; Fasan, R. P450-Catalyzed Intramolecular sp³ C–H Amination with Arylsulfonyl Azide Substrates. *ACS Catalysis* **2014**, *4* (2), 546.
- (12) Hoffman, B. M.; Lukoyanov, D.; Yang, Z.-Y.; Dean, D. R.; Seefeldt, L. C. Mechanism of Nitrogen Fixation by Nitrogenase: The Next Stage. *Chemical Reviews* **2014**, *114* (8), 4041.
- (13) Barney, B. M.; Lee, H.-I.; Dos Santos, P. C.; Hoffman, B. M.; Dean, D. R.; Seefeldt, L. C. Breaking the N₂ triple bond: insights into the nitrogenase mechanism. *Dalton Transactions* **2006**, DOI:10.1039/B517633F 10.1039/B517633F(19), 2277.

- (14) Hohenberger, J.; Ray, K.; Meyer, K. The biology and chemistry of high-valent iron–oxo and iron–nitrido complexes. *Nature Communications* **2012**, *3*, 720.
- (15) Modak, J. M. Haber process for ammonia synthesis. *Resonance* **2002**, *7* (9), 69.
- (16) In *Ullmann's Encyclopedia of Industrial Chemistry*,
DOI:doi:10.1002/14356007.a02_143.pub2 doi:10.1002/14356007.a02_143.pub2.
- (17) Mehn, M. P.; Peters, J. C. Mid- to high-valent imido and nitrido complexes of iron. *J. Inorg. Biochem.* **2006**, *100* (4), 634.
- (18) Moret, M.-E.; Peters, J. C. Terminal Iron Dinitrogen and Iron Imide Complexes Supported by a Tris(phosphino)borane Ligand. *Angew. Chem. Int. Ed.* **2011**, *50* (9), 2063.
- (19) Thomas, C. M.; Mankad, N. P.; Peters, J. C. Characterization of the Terminal Iron(IV) Imides {[PhBPtBu₂(pz⁺)]FeIV:NAd}⁺. *J. Am. Chem. Soc.* **2006**, *128* (15), 4956.
- (20) Iovan, D. A.; Betley, T. A. Characterization of Iron-Imido Species Relevant for N-Group Transfer Chemistry. *J. Am. Chem. Soc.* **2016**, *138* (6), 1983.
- (21) King, E. R.; Hennessy, E. T.; Betley, T. A. Catalytic C–H Bond Amination from High-Spin Iron Imido Complexes. *J. Am. Chem. Soc.* **2011**, *133* (13), 4917.
- (22) Cowley, R. E.; DeYonker, N. J.; Eckert, N. A.; Cundari, T. R.; DeBeer, S.; Bill, E.; Ottenwaelder, X.; Flaschenriem, C.; Holland, P. L. Three-Coordinate Terminal Imidoiron(III) Complexes: Structure, Spectroscopy, and Mechanism of Formation. *Inorg. Chem.* **2010**, *49* (13), 6172.
- (23) Wang, L.; Hu, L.; Zhang, H.; Chen, H.; Deng, L. Three-Coordinate Iron(IV) Bisimido Complexes with Aminocarbene Ligation: Synthesis, Structure, and Reactivity. *J. Am. Chem. Soc.* **2015**, *137* (44), 14196.
- (24) Ni, C.; Fettinger, J. C.; Long, G. J.; Brynda, M.; Power, P. P. Reaction of a sterically encumbered iron(i) aryl/arene with organoazides: formation of an iron(v) bis(imide). *Chem. Commun.* **2008**, DOI:10.1039/B810941A 10.1039/B810941A(45), 6045.
- (25) J.T. Wilding, M.; A. Iovan, D.; A. Betley, T. *High-Spin Iron Imido Complexes Competent for C-H Bond Amination*, 2017.
- (26) Brown, S. D.; Peters, J. C. Ground-State Singlet L₃Fe-(μ-N)-FeL₃ and L₃Fe(NR) Complexes Featuring Pseudotetrahedral Fe(II) Centers. *J. Am. Chem. Soc.* **2005**, *127* (6), 1913.
- (27) Mehn, M. P.; Brown, S. D.; Paine, T. K.; Brennessel, W. W.; Cramer, C. J.; Peters, J. C.; Que, J. L. High-spin and low-spin iron(ii) complexes with facially-coordinated borohydride ligands. *Dalton Transactions* **2006**, DOI:10.1039/B509580H 10.1039/B509580H(10), 1347.

- (28) Bucinsky, L.; Breza, M.; Lee, W.-T.; Hickey, A. K.; Dickie, D. A.; Nieto, I.; DeGayner, J. A.; Harris, T. D.; Meyer, K.; Krzystek, J. et al. Spectroscopic and Computational Studies of Spin States of Iron(IV) Nitrido and Imido Complexes. *Inorg. Chem.* **2017**, *56* (8), 4751.
- (29) Schofield, M. H.; Kee, T. P.; Anhaus, J. T.; Schrock, R. R.; Johnson, K. H.; Davis, W. M. Osmium imido complexes: synthesis, reactivity, and SCF-X.alpha.-SW electronic structure. *Inorg. Chem.* **1991**, *30* (19), 3595.
- (30) Anhaus, J. T.; Kee, T. P.; Schofield, M. H.; Schrock, R. R. Planar "20-electron" osmium imido complexes. A linear imido ligand does not necessarily donate its lone pair of electrons to the metal. *J. Am. Chem. Soc.* **1990**, *112* (4), 1642.
- (31) Wolf, J. R.; Bazan, G. C.; Schrock, R. R. Exchange of oxo ligands in osmium tetroxide with imido ligands in bis(arylimido)bis(tert-butoxo)molybdenum complexes, Mo(NAr)₂(O-tert-Bu)₂. A facile route to Os(NAr)₂O₂ and Os(NAr)₃O and osmium(IV) complexes of the type Os(NAr)₂L₂ (NAr = N-2,6-C₆H₃-iso-Pr₂; L = a phosphine). *Inorg. Chem.* **1993**, *32* (19), 4155.
- (32) Herranz, E.; Sharpless, K. B. Improvements in the osmium-catalyzed oxyamination of olefins by chloramine-T. *The Journal of Organic Chemistry* **1978**, *43* (12), 2544.
- (33) Patrick, D. W.; Truesdale, L. K.; Biller, S. A.; Sharpless, K. B. Stereospecific vicinal oxyamination of olefins by alkylimidoosmium compounds. *The Journal of Organic Chemistry* **1978**, *43* (13), 2628.
- (34) Kee, T. P.; Park, L. Y.; Robbins, J.; Schrock, R. R. Synthesis of the ruthenium imido complexes, [Ru(η -C₆H₆)(N-2,6-R₂C₆H₃)]₂ (R = Pri or Me), and the crystal structure of [Ru(η -C₆H₆)(N-2,6-Pri₂C₆H₃)]₂. *J. Chem. Soc., Chem. Commun.* **1991**, DOI:10.1039/C39910000121 10.1039/C39910000121(2), 121.
- (35) Burred, A. K.; Steedman, A. J. (η -6-p-Cymene)Ru[triple bond, length half m-dash]N(2,4,6-tri-tert-butylphenyl): a monomeric ruthenium(II) complex containing a terminal imido ligand. *J. Chem. Soc., Chem. Commun.* **1995**, DOI:10.1039/C39950002109 10.1039/C39950002109(20), 2109.
- (36) Burrell, A. K.; Steedman, A. J. Synthesis, Structure, and Reactivity of Ruthenium(II) Terminal Imido Complexes. *Organometallics* **1997**, *16* (6), 1203.
- (37) Singh, A. K.; Levine, B. G.; Staples, R. J.; Odom, A. L. A 4-coordinate Ru(II) imido: unusual geometry, synthesis, and reactivity. *Chem Commun (Camb)* **2013**, *49* (92), 10799.
- (38) Bakhoda, A.; Jiang, Q.; Bertke, J. A.; Cundari, T. R.; Warren, T. H. Elusive Terminal Copper Arylnitrene Intermediates. *Angew. Chem. Int. Ed.* **2017**, *56* (23), 6426.
- (39) King, E. R.; Hennessy, E. T.; Betley, T. A. Catalytic C-H bond amination from high-spin iron imido complexes. *J. Am. Chem. Soc.* **2011**, *133* (13), 4917.
- (40) Liu, J.-Y.; Zheng, Y.; Li, Y.-G.; Pan, L.; Li, Y.-S.; Hu, N.-H. Fe(II) and Co(II) pyridinebisimine complexes bearing different substituents on ortho- and para-position of imines:

synthesis, characterization and behavior of ethylene polymerization. *J. Organomet. Chem.* **2005**, *690* (5), 1233.

- (41) Karsch, H. H.; Appelt, A. Functional trimethylphosphane derivatives. 18. Methyl(phosphinomethyl)silanes and methyl(phosphinomethyl)stannanes. *Z. Naturforsch., B: Chem. Sci.* **1983**, *38* (11), 1399.
- (42) Henning, J. C. M. 14N Hyperfine Structure in ESR Spectra of Heterocyclic Anions. **1966**, *44* (5), 2139.
- (43) Oliver, S. W.; Smith, T. D.; Pilbrow, J. R.; Harvey, T. G.; Matheson, T. W.; Pratt, K. C. An ESR study of zeolite-supported ruthenium hydrodenitrogenation catalyst. *Inorganica Chimica Acta* **1986**, *117* (1), L9.
- (44) Andersson, K.; Malmqvist, P. A.; Roos, B. O. 2nd-order Perturbation-Theory with a Complete Active Space Self-Consistent Field Reference Function. *J. Chem. Phys.* **1992**, *96*, 1218.
- (45) Celani, P.; Werner, H.-J. Multireference perturbation theory for large restricted and selected active space reference wave functions. *J. Chem. Phys.* **2000**, *112*, 5546.
- (46) Singh, A. K.; Levine, B. G.; Staples, R. J.; Odom, A. L. A 4-coordinate Ru(II) imido: unusual geometry, synthesis, and reactivity. *Chem. Commun.* **2013**, *49* (92), 10799.
- (47) Liu, Y.; Du, J.; Deng, L. Synthesis, Structure, and Reactivity of Low-Spin Cobalt(II) Imido Complexes [(Me₃P)₃Co(NAr)]. *Inorg. Chem.* **2017**, *56* (14), 8278.
- (48) Thoreson, K. A.; Follett, A. D.; McNeill, K. Synthesis and Characterization of Pentaphosphino Zero-Valent Iron Complexes and Their Corresponding Iron(II)-Chloride and -Hydride Complexes. *Inorganic Chemistry* **2010**, *49* (8), 3942.
- (49) Liu, J. Y.; Zheng, Y.; Li, Y. G.; Pan, L.; Li, Y. S.; Hu, N. H. Fe(II) and Co(II) pyridinebisimine complexes bearing different substituents on ortho- and para-position of imines: synthesis, characterization and behavior of ethylene polymerization. *Journal of Organometallic Chemistry* **2005**, *690* (5), 1233.
- (50) Evans, D. J.; Hitchcock, P. B.; Leigh, G. J.; Nicholson, B. K.; Niedwieski, A. C.; Nunes, F. S.; Soares, J. F. The synthesis of triangulo-trimetal complexes containing both iron(II) and vanadium(II). *Inorg. Chim. Acta* **2001**, *319* (1-2), 147.
- (51) Stoll, S.; Schweiger, A. EasySpin, a comprehensive software package for spectral simulation and analysis in EPR. *Journal of Magnetic Resonance* **2006**, *178* (1), 42.
- (52) Dunning, T. H. Gaussian-basis sets for use in correlated molecular calculations. 1. The atoms boron through neon and hydrogen. *J. Chem. Phys.* **1989**, *90* (2), 1007.
- (53) Woon, D. E.; Dunning, T. H. Gaussian-basis sets for use in correlated molecular calculations. 3. The atoms aluminum through argon. *J. Chem. Phys.* **1993**, *98* (2), 1358.

- (54) Balabanov, N. B.; Peterson, K. A. Systematically convergent basis sets for transition metals. I. All-electron correlation consistent basis sets for the 3d elements Sc-Zn. *J. Chem. Phys.* **2005**, *123* (6), 15.
- (55) Peterson, K. A.; Figgen, D.; Dolg, M.; Stoll, H. Energy-consistent relativistic pseudopotentials and correlation consistent basis sets for the 4d elements Y-Pd. *J. Chem. Phys.* **2007**, *126* (12), 12.
- (56) Finley, J.; Malmqvist, P. A.; Roos, B. O.; Serrano-Andres, L. The multi-state CASPT2 method. *Chem. Phys. Lett.* **1998**, *288* (2-4), 299.
- (57) Celani, P.; Werner, H. J. Multireference perturbation theory for large restricted and selected active space reference wave functions. *J. Chem. Phys.* **2000**, *112* (13), 5546.
- (58) Knowles, P. J.; Werner, H. J. An efficient 2nd-order MC SCF method for long configuration expansions. *Chem. Phys. Lett.* **1985**, *115* (3), 259.
- (59) Werner, H.-J.; Knowles, P. J. A second order multiconfiguration SCF procedure with optimum convergence. *J. Chem. Phys.* **1985**, *82* (11), 5053.
- (60) Werner, H. J. Third-order multireference perturbation theory - The CASPT3 method. *Mol. Phys.* **1996**, *89* (2), 645.
- (61) Werner, H. J.; Knowles, P. J.; Knizia, G.; Manby, F. R.; Schutz, M. Molpro: a general-purpose quantum chemistry program package. *Wires Comput Mol Sci* **2012**, *2* (2), 242.
- (62) Humphrey, W.; Dalke, A.; Schulten, K. VMD: Visual molecular dynamics. *J. Mol. Graph.* **1996**, *14* (1), 33.

CHAPTER 8. PURSUIT OF RUTHENIUM BIS(IMIDO) COMPLEXES AND HIGHER OXIDATION STATES

8.1 Introduction¹³

In 1992 Wilkinson and coworkers published the synthesis of a unique, Ru(IV)(NAr)₂(PMe₃)₂ (**Ru1**), square planar, *d*⁶ complex (Ar = 2,6-diisopropylphenyl).¹ In their original report, they start from *trans*-RuCl₂(PMe₃)₄ and add a significant excess of LiNHAr (3.1 equiv), along with excess PMe₃. The reaction mixture is refluxed for 1 week and produces a red intermediate, which is carried on without isolation. This complex is postulated to be a Ru(II) bis(amide) species. Upon addition of “oxygenated” MeOH to the red intermediate, the reaction solution turns greenish-blue and the Ru(NAr)₂(PMe₃)₂ product was isolated in 16% total yield. Given the ambiguity of the oxidation step in this reaction, the unidentified intermediate product, and the low overall yield of the Ru bis(imido) species, it seems like several other products are likely formed as a result of this synthesis; in our hands, these results have not been reproduced on any scale.

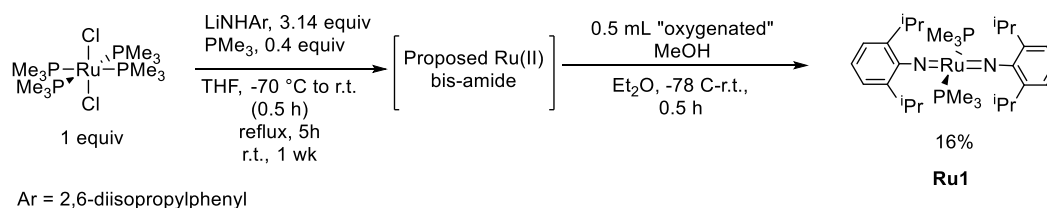


Figure 8.1 The synthetic procedure presented by Wilkinson and coworkers in 1992 which lead to the square planar *d*⁴ Ru species on the right.

For ruthenium, this is a highly unusual complex for several reasons. As mentioned in the previous chapter, there are sparing examples of terminal Ru imido complexes in the literature.

¹³ Portions of this work have been published in the following article: Aldrich, K. E., Odom, A. L., “A Photochemical Route to a Square Planar, Ruthenium(IV)-bis(Imide)”, *Chem Commun*, **2019**, 55(30), 4403-4406.

These include the Ru(II) (NPh^{2,4,6-tri-*tert*-butyl})(η_6 -cymene) complex published by Steedman^{2,3}, as well as the Ru(NAr/Ar*)(PMe₃)₃, Ru(NAr/Ar*)(dmpe)₂, Ru(NAr/Ar*)dppe(PMe₃) complexes that we've discovered.^{4,5} Outside of these complexes, which all have similar ligand electronics, there is **Ru1**,¹ and a few different derivatives of Ru(VI) porphyrin bis(imido) complexes.⁶⁻⁹ It is notable that these reported Ru(VI) bis(imido) complexes are fleetingly stable and highly reactive, sometimes invoked as reactive intermediates.¹⁰ In this way, the chemistry of Ru-imides is highly incomplete, marked with small groupings of electronically similar species with large gaps in the oxidation states, coordination environment, and general diversity observed with other metals that form imido complexes.

Bis(imido)Os analogues with porphyrin ligands can be isolated and studied to the extent of full structural and electronic characterization.^{6,11,12} Mono-imido analogues with Fe have also been reported, and much like the Os examples, are markedly more stable relative to the Ru complexes.^{13,14} Additional examples with Fe-porphyrin cores abound if we expand consideration to nitrides and oxos, due to their biological relevance, and this motivation, as a whole has greatly enriched the chemistry of iron-ligand multiple bonds.¹⁵⁻¹⁷

Access to mid- to high-valent Os imido complexes has been synthetically facilitated from the OsO₄, which is commercially available. The first Os-imido compound synthesized, in fact, was Os(O)₃(N^{*t*}Bu), which can be generated from addition of H₂N^{*t*}Bu to OsO₄.^{18,19} Sharpless' and Schrock's groups have also taken advantage of this synthetic starting point in reaching high valent Os-imido species.²⁰⁻²⁴ Alternatively starting from a low valent Os source can produce terminal imido species as well.¹⁴ Thus, synthetically, a fairly wide variety of these types of species have

¹⁴ Analogous reaction pathway to that presented in Chapter 7 for Ru(NAr)(PMe₃)₃ can be applied to Os(NAr)(PMe₃)₃. However, due to challenging starting material pathways and similarity to the Ru species, full electronic structure studies were not pursued with these derivatives.

been easy to access with Os. Complementary routes for Ru and Fe however aren't typically as diverse.

Some clever routes have been devised to achieve midvalent bis(imido) species with Fe, however these syntheses start from low valent Fe sources and leverage the reducing ability of Fe(I) and Fe⁰ species to transform organic azides into N₂ and imido ligands. Two examples in the last decade have shown that this method, coupled with bulky ancillary ligands, can yield isolable Fe(IV) or Fe(V) bis(imido) complexes which have been fully characterized.^{25,26} These complexes are shown in Fig. 8.2.

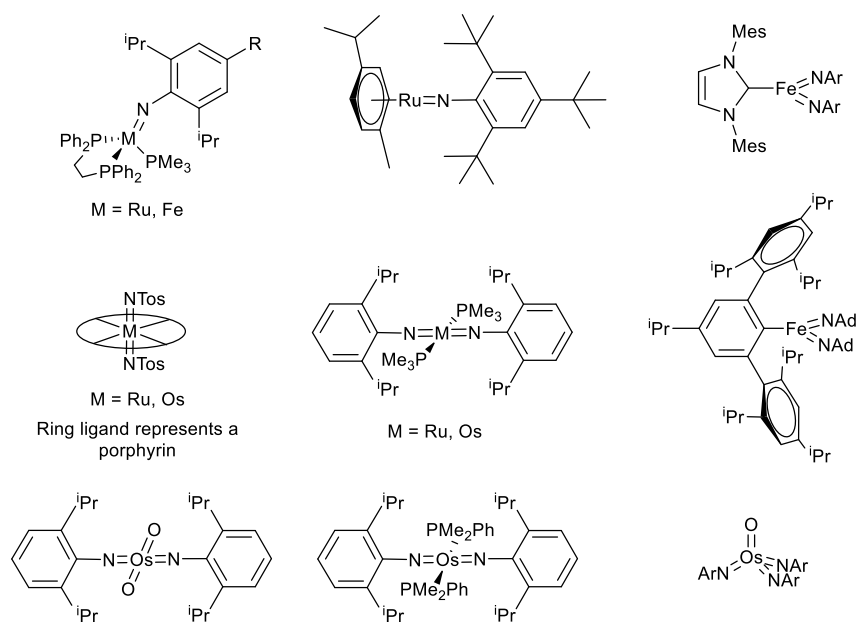


Figure 8.2 Examples of various Group 8 mono- and bis(imido) compounds.

The history of Group 8 imido complexes seems to demonstrate that part of the reason why Ru-imido chemistry isn't as advanced as Os and Fe chemistry in similar directions—the metal-imide chemistry with Ru isn't nearly as varied or numerous in the available examples—is due to synthetic challenges. Certainly, from our attempts to access mid-valent Ru-imido species, this observation seems accurate (Chapter 7). These difficulties seemed even more significant after our attempts to repeat Wilkinson's reported procedure to make **Ru1** failed. Recognizing the lack of

synthetic techniques to access mid- to high-valent Ru-imido species, we set out to explore alternate synthetic pathways to access these complexes.

8.2 Synthesis of Ru and Os κ^2 -diphenylhydrazido Complexes from Azobenzene

We formulated a method of producing higher valent Ru imido complexes that we thought might lead to potentially less reactive intermediates along the pathway to oxidize the metal. As we had previously learned, direct chemical oxidation of an existing low-valent, terminal imido complex tends to produce radical species that are highly unstable (see Chapter 7).

As an alternative, we sought to use ligands that contain N–N bonds that we could harness by attaching them to a low valent Ru complex, and then breaking the N–N bonds in the ligand to generate imide ligands. Breaking N–N bonds in proximity to the metal center could induce an oxidative addition, without requiring the addition of external oxidants or reductants. Rather, heat or light might provide enough energy to induce such reactivity. Similar reactivity has previously been reported with an $\text{Fe}(\text{CO})_3(1,4\text{-diphenyltetrazene})$ species, which upon exposure to light, results in the elimination of N_2 and the formation of a dimeric Fe species $[\text{Fe}(\text{CO})_3]_2(\mu\text{-PhNNPh})$.²⁷ Similarly, this type of reactivity has also been shown using uranium and external reductant.²⁸ This general strategy is shown in Fig. 8.3.

In a way, this is similar to the methods often employed, for example, to produce the Fe bis(imide) complexes shown in Fig. 8.2.^{25,26} In these reactions, a spontaneous redox reaction between the metal and an aryl azide results in oxidation of the metal and formation of imide ligands accompanied by N_2 elimination upon reduction of the azide. Many other metal-imide complexes have also been synthesized using the same technique. However, it requires an extremely reducing metal, often M^{-2} to M^{+1} , or the addition of a strong external reductant such as KC_8 .^{14,29,30}

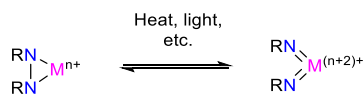


Figure 8.3 Illustration of the synthetic route proposed to access Ru-imido species in mid- to high oxidation states.

As a starting point, we chose to target a κ_2 -hydrazido moiety. Literature procedures have shown that upon addition of excess (4 equivalents) Li to azobenzene in THF, a di-lithiated, 2-electron-reduced species can be generated *in situ*. Addition of this solution of reduced azobenzene to *cis*-RuCl₂(PMe₃)₄ results in the production of the (κ_2 -diphenylhydrazido)Ru(PMe₃)₄ (**Ru2**) complex shown in Fig. 8.4.

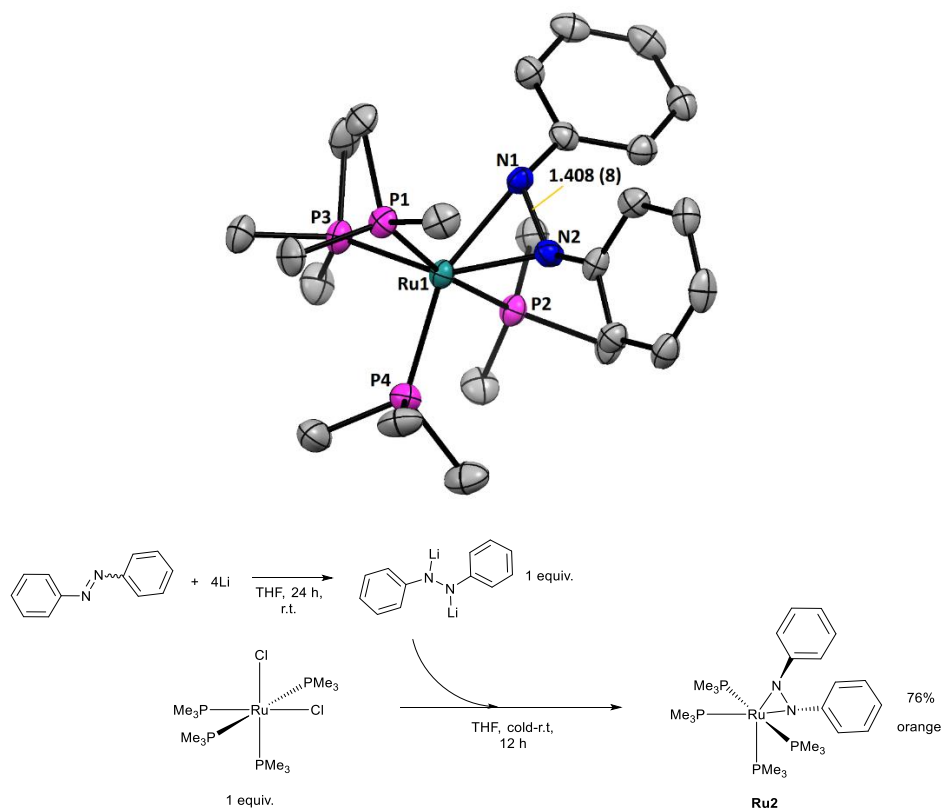


Figure 8.4 (top) The X-ray crystal structure of Ru2 with ellipsoids shown at 50% probability; H atoms and solvent molecule omitted for clarity. (bottom) Synthetic procedure to yield (κ_2 -diphenylhydrazido)Ru(PMe₃)₄ from *in situ* reduced azobenzene and *cis*-RuCl₂(PMe₃)₄. The same procedure can be utilized to produce the Os analogue of this compound.

8.3 Thermal and Photochemical Reactivity of (κ^2 -diphenylhydrazido)Ru(PMe₃)₄

As is evident from the isolation of this complex, spontaneous cleavage of the N–N bond upon addition to Ru does not occur. However, with **Ru2** in hand, we began exploring methods to induce the oxidative addition of the electron density in the N–N bond to the metal. Initially, we examined what happens when the complex is simply heated. Following the reaction by ³¹P NMR, the tightly spaced doublet of triplets, characteristic of **Ru2**, transforms quantitatively into a doublet of doublets (-9.0 ppm, 2P) and a doublet of triplets (-13.9 ppm, 1P), with the loss of 1 PMe₃ ligand.

When the volatiles are removed from the reaction solution, and the resulting dark brown residue is recrystallized, X-ray quality crystals of the *ortho*-C-H activated azobenzene adduct are isolated (**Ru3**). This complex shows a distinct Ru–H resonance by ¹H NMR at -11.39 (triplet of doublets), which presumably occupies the vacant 6th coordination site observed in the single-crystal structure of the complex. Evident from the structure is the dramatic shortening of the N–N bond relative to that distance in **Ru2**, indicating the reformation of a N–N double bond. The Ru1–N1 is also consistent with a dative interaction. Additionally, there is a slight distortion from perfect octahedral geometry, but this is likely a result of the equatorial ligands shifting toward the hydride where the first coordination sphere is less congested. A summary of this reaction and the crystal structure of **Ru3** are shown in Fig 8.5.

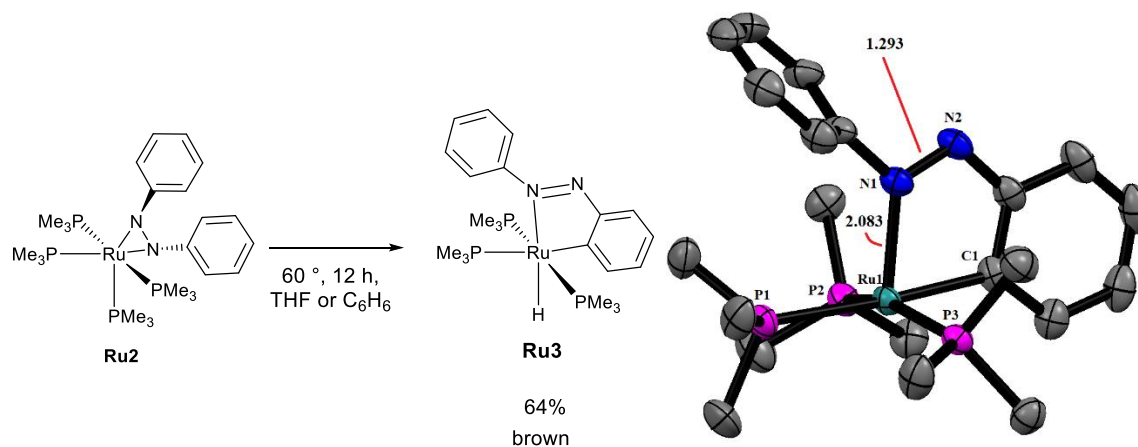


Figure 8.5 The Ru(II) terminal hydride (**Ru3**) species produced upon heating **Ru2**. The single crystal X-ray structure is shown with ellipsoids at 50% probability; H atoms and solvent omitted for clarity.

The same reaction sequence shown above with Ru to produce **Ru2** and **Ru3** was also undertaken with Os. The same reactivity is noted, giving highly similar structural analogues. However, due to scarcity of the *cis*-OsCl₂(PMe₃)₄ and no reliable synthesis found by which to remake the starting material from available Os complexes in the laboratory, further reactivity with Os was not pursued.

Since heating the complex did not yield the desired result, of breaking the N–N bond, we shifted our attention to light-driven reactivity. There are a few examples of this type of photolysis in the literature,²⁷ and we had previously observed that dilute (i.e. NMR) samples of **Ru2** change color from bright orange to dark green when exposed to ambient light. This initial color change was followed by complete decomposition of the sample (i.e. an intractable mixture with several new ³¹P resonances observed).

Intentional photolysis of **Ru2** agrees with qualitative observations. When a solution of **Ru2** in benzene (C₆D₆ or C₆H₆) or THF is exposed to an intense UV-Vis light source (800 W Hg Arc lamp), the solution rapidly goes from orange to green. The green species (**Ru4**) can be identified by new ³¹P resonances, and increases in the size of these new peaks is accompanied by diminishing

peaks for the starting material resonances (**Ru2**). This green species is transient, however, as it rapidly decomposes to **Ru3** at room temperature. Therefore, efforts to characterize **Ru4** have been limited to *in situ* experiments that can be done rapidly or are amenable to low-temperatures, as reduced temperatures appear to dramatically slow the conversion of **Ru4** to **Ru3**.

We know that **Ru4** is diamagnetic and, like **Ru3**, loses one PMe_3 ligand upon formation. The species does not appear to be an alternative C-H activation product, as characteristic ^1H or ^{13}C resonances for Ru-H or Ru-C bonds are not observed in photolysis samples in C_6D_6 . Interestingly, **Ru4** also lacks a ^{14}N NMR resonance. This negative response is very inconclusive, however, as we have noted several other species that contain M-N bonds are often ^{14}N NMR-silent. The quadrupolar relaxation of the ^{14}N nucleus likely broadens these signals to an extent that our instrumentation cannot detect them; this potential broadening could be exacerbated with coupling (i.e. several ^{31}P nuclei or ^{14}N in proximity in the molecule).^{19,31,32}

As mentioned, by ^{31}P NMR two new resonances are observed at 11.0 ppm (td, 1P) and -7.8 ppm (dd, 2P). The integration ratio of 1:2 indicates the presence of a C_2 -axis or mirror plane within **Ru4**, and along with the observation that 1 equiv of unbound PMe_3 (-62.6 ppm), confirms that 3 PMe_3 ligands remain coordinated to Ru. Aside from this spectral data, ^1H and ^{13}C NMR of the *in situ* photolysis solution of **Ru4** agree that there are 3 PMe_3 ligands on Ru, and that the hydrazido fragment is still bound to Ru. However, no clear indication of the geometry or binding properties of the hydrazido fragment are evident.

UV-Vis spectra of the complex, generated *in situ* in THF show distinct new absorbances, accounting for the dramatic color change. A plot of the electronic absorption spectrum is shown in Fig. 8.6 for both **Ru2** and **Ru4**. The differences in these spectra are readily observed, including the absorption feature at $\sim 15,000\text{ cm}^{-1}$, which likely results in the green color of the complex in

solution. While the product, **Ru4**, demonstrates stronger absorbance characteristics over most of the range observed by UV-Vis spectroscopy, relative to the starting material, this does not appear to impact the conversion efficiency of **Ru2** to **Ru4**. *In situ* ^{31}P NMR demonstrates quantitative conversion in relatively short photolytic exposure times. This suggests that the quantum efficiency of photon absorption resulting in the chemical conversion is very high, or that the incident radiation responsible for the chemical transformation is outside of the range of wavelengths examined. Attempts to identify what excitation event may be leading to reactivity using time-dependent DFT did not provide useful insight. Experimentally, this could be examined by repeating the photolysis with band pass filters, to narrow in on the energy of the transformation. However, since full conversion was achieved and product stability precluded our ability to fully structurally characterize **Ru4**, this study was not pursued (see below).

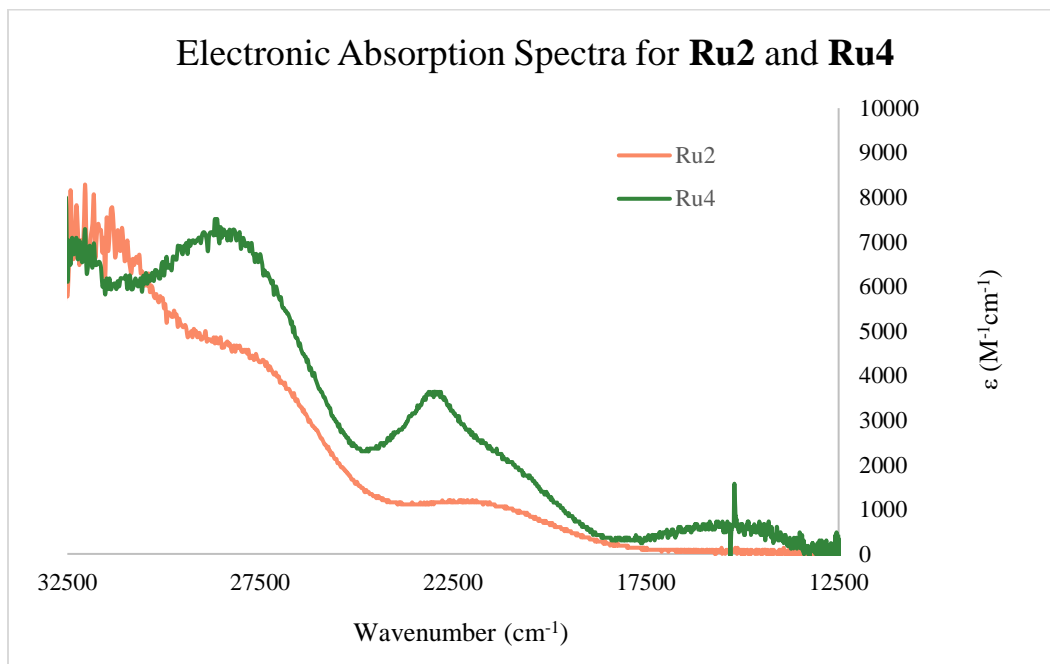


Figure 8.6 Plot of extinction coefficient (ϵ) versus wavenumber for the complexes **Ru2** and **Ru4**. Although the photolysis product absorbs more strongly than the starting material across most of the spectrum, full conversion is still achieved in these photolytic conversions. (Note that the sharp feature at $\sim 15,000\text{ cm}^{-1}$ is due to the light source change in the UV-lamp).

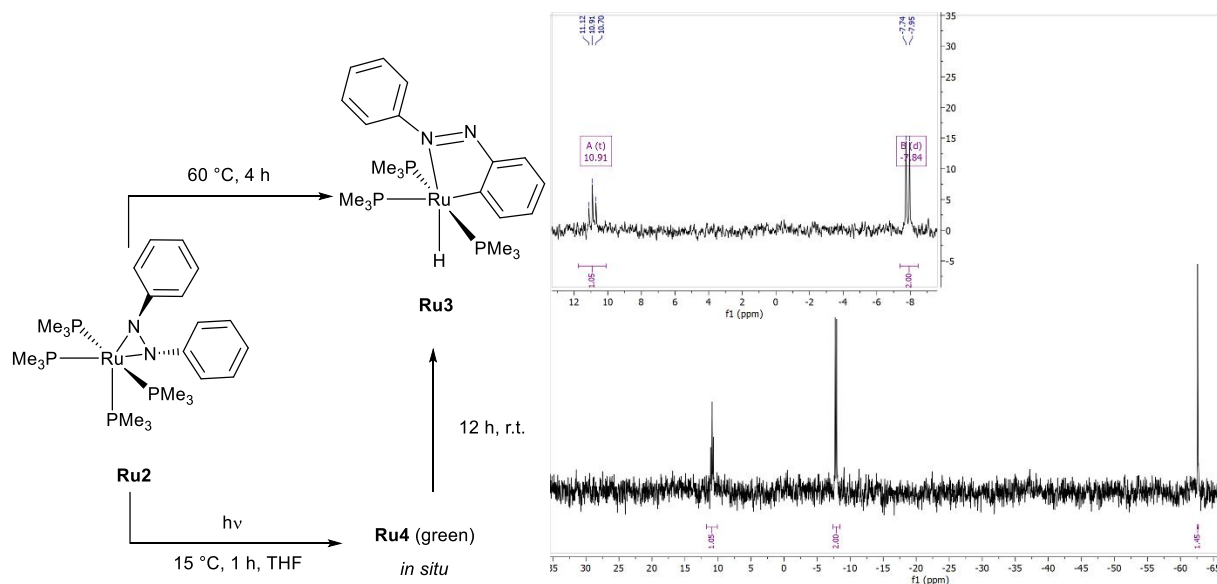


Figure 8.7 (left) Schematic showing the interconversion of **Ru2**, **Ru4**, and **Ru3**. (right) ^{31}P NMR of photolysis solution to generate **Ru4**. The inset shows the new ^{31}P resonances, while the sharp singlet at -62 ppm is free PMe_3 .

To aid in experimental deductions of the possible structure of **Ru4**, we turned to density functional theory. The structures (geometries) of **Ru2**, **Ru3**, and several candidate molecules proposed as **Ru4** were optimized utilizing B3LYP as the functional, LANL2DZ(Ru)/6-311g+(d,p) (C,H,N,P) basis sets, and the CPCM THF solvent model. The ground state single point energies for these optimized complexes were determined, with the same basis set assignments, solvent model, and the B3LYP functional. Using these calculated energies, the ΔG^0 and ΔH^0 of several possible reactions from **Ru2** to **Ru4** were estimated. The results of these calculations are shown in Fig. 8.8.

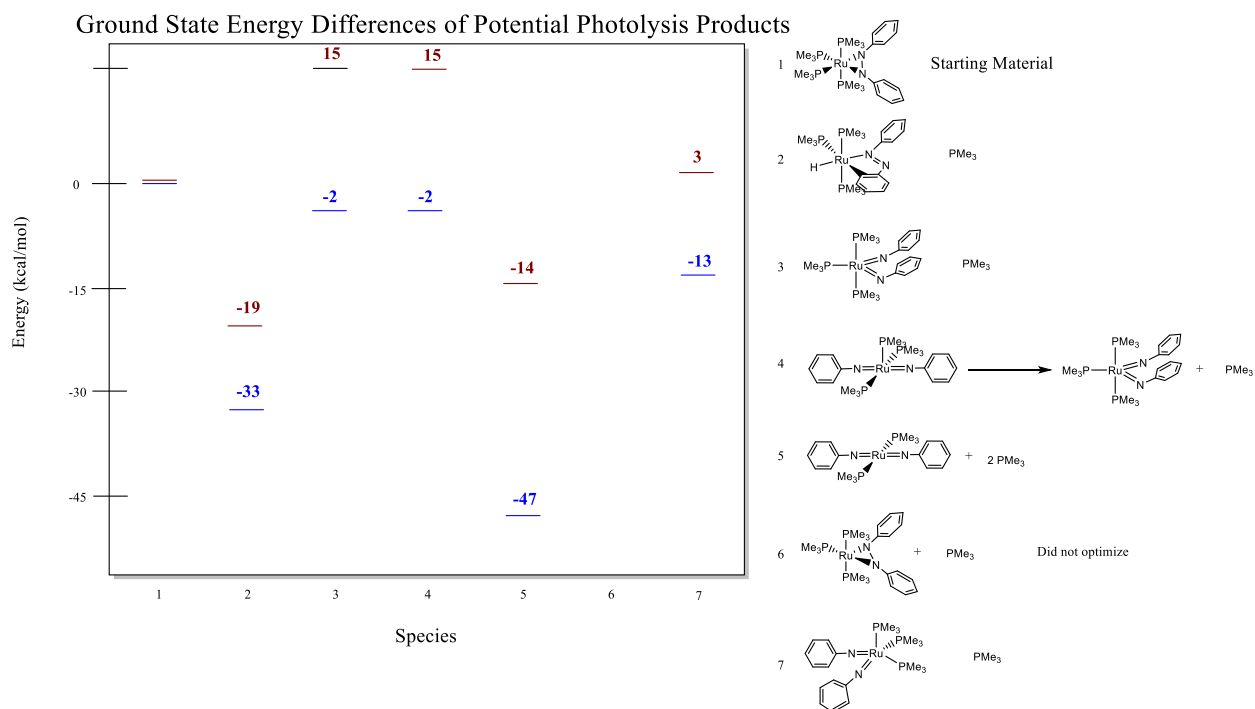


Figure 8.8 Several possible products that were considered in identifying **Ru4**. The chart shows the ΔG (blue) and ΔH (orange) values calculated for the conversion of **Ru2** to the product number listed on the x-axis. Each complex is numbered and shown structurally on the right.

Combined with experimental data, two main possibilities emerge from the options that we have considered thus far. Structure **3** appears to be close to thermal neutral in terms of free energy. It also demonstrates a structure with ^{31}P environments consistent with the NMR spectrum for **Ru4**, making it a probable candidate. The ^{31}P NMR data makes option **5** unlikely, as this structure should present a single ^{31}P NMR resonance. Complex **7** is difficult to predict, as each PMe_3 is unique relative to the positions of the imides; I would predict that this complex would have a single broad resonance and some degree of PMe_3 exchange, or that all 3 positions would have different shifts by ^{31}P NMR. However, it is not obvious that the splitting pattern would match what was experimentally observed. Also note that when a square pyramidal geometry is provided for optimization, with the imido groups either *cis*- or *trans*- they distort until they optimize in alternate geometries. Specifically, as shown for **4**, attempts to optimize a *trans*- $\text{Ru}(\text{NPh})_2(\text{PMe}_3)_3$ complex distorted into the same geometry as **3**, which has two equatorial ($=\text{NPh}$) ligands and a trigonal

bipyramidal geometry. The geometry of **7**, similarly, was started as *cis*-Ru(NPh)₂(PMe₃)₃ but distorted to a geometry intermediate between square pyramidal and TBP geometry.

The other possible structure, aside from **3**, that seems likely from the list above, is **6**. In **6**, the N–N bond of the κ_2 -hydrazido ligand remains intact, but rather the photolysis may dissociate a PMe₃ ligand. This would leave a vacant coordination site on the Ru, generating what would likely be a highly reactive species. The geometry for this structure could not be successfully optimized by DFT, however, so an assessment of the energy change to generate this species from **Ru2** was not possible. The fact that the structure couldn't be optimized makes it seem like it may also be a high-energy intermediate; for example, this species is likely somewhere along the reaction coordinate for the conversion of **Ru2** to **Ru4** or **Ru4** to **Ru3**. Based on the calculations, however, it cannot be directly ruled out.

Collectively, these results do not provide the same strength in structural identity for **Ru4** that we would typically acquire through X-ray crystallography or detailed reactivity studies. The most complete case can be made for **Ru4**'s similarities to **3**, based on the NMR spectra, UV-Vis properties (see below), and calculations. This result certainly encouraged further exploration of this synthetic strategy to produce mid-valent Ru imido complexes. Several efforts were undertaken by which ligand modification was attempted, to try to produce a more stable derivative of **Ru4**. When azobenzene is substituted for 2,2',6,6'-tetramethylazobenzene, however, the addition of the reduced azobenzene species to the Ru metal center results in a mixture of products (many peaks by ³¹P NMR of crude product). Conventional separation techniques did not lead to isolation of the desired product. Similarly, when we tried to add bulk to the phosphine ligands (i.e. switching to PMe₂Ph), a similar result was observed.

The starting molecule for the photolysis, **Ru2**, appears to be very nearly sterically saturated. The space filling model of the single crystal X-ray structure, shown in Fig. 8.9 below illustrates this property well. It seems likely that by adding bulk to the substituents close to the atoms of the first coordination sphere, we've surpassed the steric limits of the octahedral complex. Thus, given the fleeting nature of the complex and the inevitable conversion to the terminal Ru(II) hydride species (**Ru3**), as well as our inability to alter the ligand substitution for enhanced stability, we sought a slightly more tamable ligand as the nitrogen source.

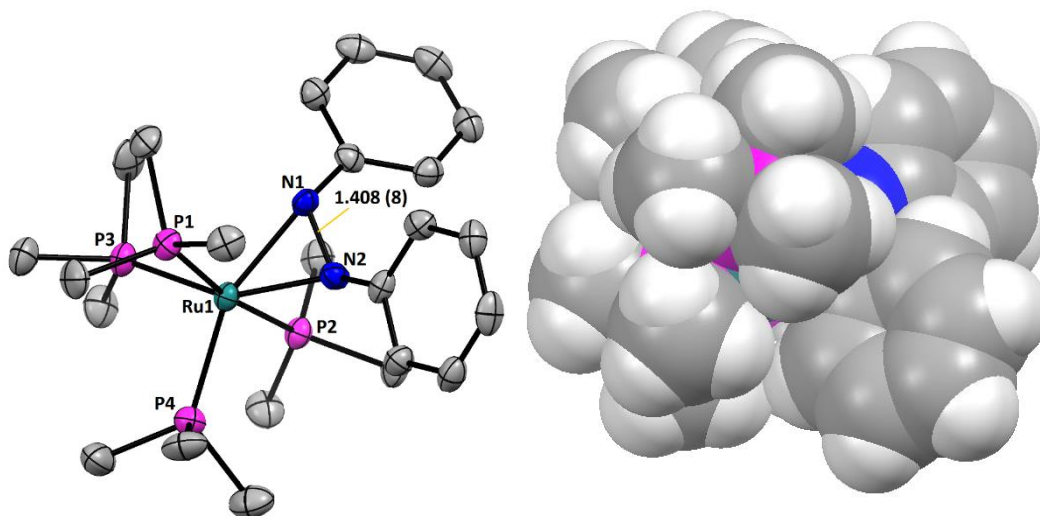


Figure 8.9 The single crystal X-ray structure of Ru2 shown (*left*) with thermal ellipsoids and (*right*) as the spacefilling model with van der Waals radii on all atoms. Notice that essentially none of the central Ru atom is visible from the spacefilling perspective, demonstrating the steric crowding in this molecule.

8.4 Synthesis of Ru(II)(1,4-diaryltetrazene)tris(trimethylphosphine) Complexes

As mentioned in the Introduction (8.1), addition of organic azides to low-valent metals has been shown to lead to spontaneous reduction of the azide and oxidation of the metal. Sometimes this can be achieved by adding an external reductant or simply by heating the reaction.^{14,29,30} When an aryl azide is added to the terminal Ru(NAr)(PMe₃)₃ complex, a spontaneous redox reaction does not occur. Rather, the azide adds cleanly to the existing Ru–N double bond to form a Ru(II)(1,4-

diaryltetrazene)tris(trimethylphosphine) (**Ru5**) complex. Similar complexes with Ru and Ir, with η^6 -arene or Cp ligands respectively, have been published by Wilkinson and Hursthouse in addition to examples with other metals.³³⁻³⁵

This reaction, and subsequent isolation of the tetrazene species, has been achieved with N_3Ar , N_3Mes , and N_3Ar to $Ru(NAr^*)(PMe_3)_3$ (**Ru7**) to yield the symmetric $Ru(1,4-(2,6\text{-diisopropylphenyl})\text{tetrazene})(PMe_3)_3$ (**Ru5**), as well as the asymmetric $Ru(1\text{-mesityl-}4\text{-(}2,6\text{-diisopropylphenyl})\text{tetrazene})(PMe_3)_3$ (**Ru6**) and $Ru(1\text{-(}2,4,6\text{-triisopropylphenyl)-}4\text{-(}2,6\text{-diisopropylphenyl})\text{tetrazene})(PMe_3)_3$ species (**Ru7**), respectively. This scheme is outlined in Fig. 8.10.

Even N_3TMS undergoes the same initial reaction, and a preliminary crystal structure of the $Ru(1\text{-(}2,6\text{-diisopropylphenyl)-}4\text{-trimethylsilyl-tetrazene})\text{tris(trimethylphosphine)}$ (**Ru8**) complex has been obtained. However, the geometry of this species appears fluxional in solution (broad 1H and ^{31}P NMR), and the complex readily decomposes as a solid at room temperature or from exposure to ambient light. It is also worth mentioning that the crystal structure is preliminary because the crystals decompose upon irradiation with X-rays. For these reasons, further study of this species wasn't pursued.

The X-ray crystal structure of **Ru5** is shown in Fig. 8.10, along with an outline showing the general synthesis. The structural characteristics of all 3 complexes, **Ru5-7**, are similar. The base geometry is close to square pyramidal, with the plane defined by N1, N4, P1, P2, and Ru1. The angles residing in the plane sum to a total of 352° . The plane is slightly distorted, as the 4 ligand atoms in the square base flex slightly below the plane; the axial P3 is also tilted slightly away from the bulky Ar groups on the tetrazene ring. If the τ parameter is calculated for the complex—where $\tau = 0$ corresponds to perfect square pyramidal geometry and $\tau = 1$ is trigonal

bipyramidal—it is found to be 0.02. Again, it seems like the distortion from square planar in this structure are primarily a result of steric congestion. This is demonstrated by the spacefilling model of **Ru5**.

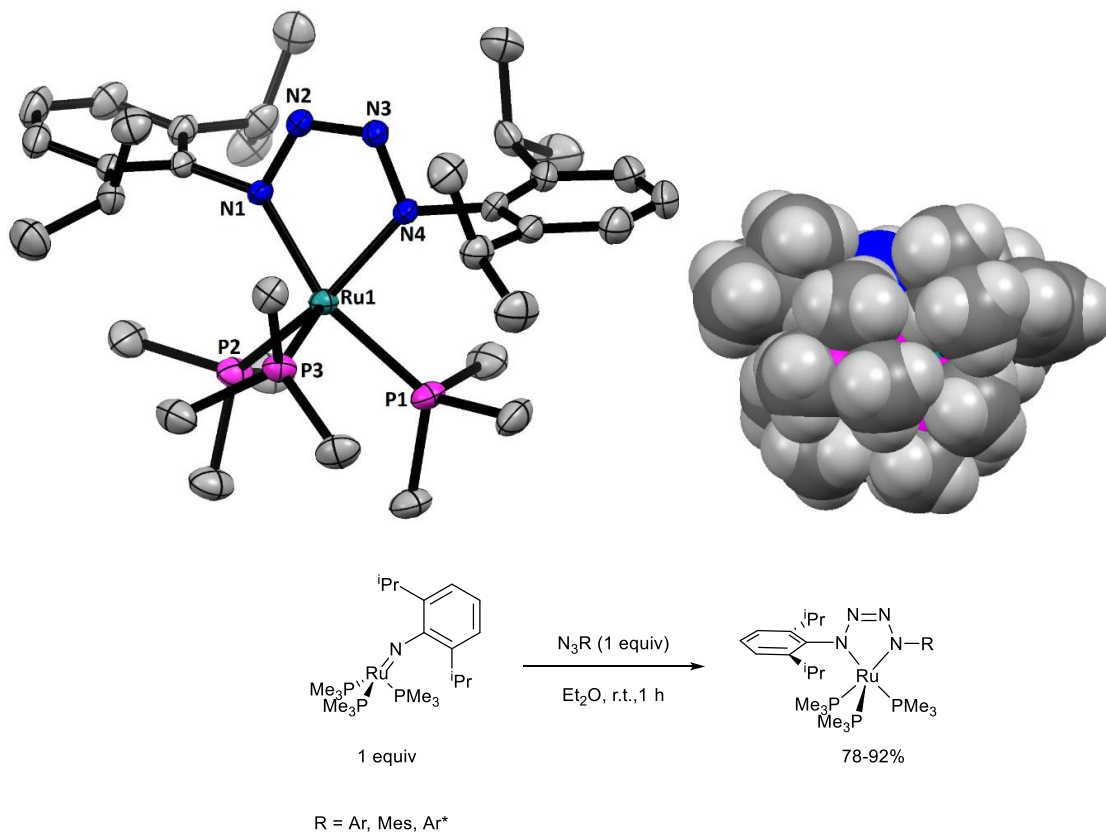


Figure 8.10 (top) Single crystal X-ray structure of **Ru5**. Thermal ellipsoids are shown at 50% probability and H atoms and solvent were omitted for clarity and spacefilling model of **Ru5**. (bottom) General synthetic scheme for making Ru(II) tetrazenes.

Table 8.1 Selected bond distances and angles from the single crystal structure of **Ru5** in Fig. 8.10.

Bond	Distance (Å)	Angle	(°)
Ru1–N1	2.043	N1–Ru1–N4	73.29
N1–N2	1.374	N1–Ru1–P2	95.85
N2–N3	1.274	N4–Ru1–P1	92.82
N3–N4	1.366	P1–Ru1–P2	89.92
Ru1–N4	2.043	P1–Ru1–P3	95.94
Ru1–P1	2.326	P2–Ru1–P3	93.47
Ru1–P2	2.309	N1–Ru1–P2	105.63
Ru1–P3	2.245	N4–Ru1–P1	109.83

8.5 Reactivity of Ru(II)(1,4-diaryltetrazene)tris(trimethylphosphine) Complexes

The goal of reactions with **Ru5-7** is to achieve cleavage of the tetrazene ring accompanied by the elimination of N₂. Initial studies with **Ru5** showed that chemical oxidants and reductants are relatively unreactive with the tetrazene species, even with an excess of oxidant or strong reductant (KC₈) or mild heating (< 50 °C). At higher temperatures, decomposition is noted by ¹H and ³¹P NMR, however, even when alone in solution, **Ru5** decomposes at temperatures over 65 °C. This also demonstrates that **Ru5** doesn't react productively with heat.

With the failures of reductants, oxidants, and thermally driven reactivity, we turned to light-induced reactivity. A 0.002 M solution of **Ru5** in THF was prepared in a Schlenk tube. The reaction was then transferred to a jacketed chiller fitted with a quartz window and the sample was irradiated using a mercury arc lamp. After 8 hours of irradiation at 800 W, the transparent orange solution had begun to darken, after 24 h the solution was opaque and murky green, and after 48 h the solution was dark blue. Crude ³¹P NMR shows that about 25% of the **Ru5** was converted to **Ru1**, Ru(NAr)₂(PMe₃)₂. Upon work-up, a yield of 21% of **Ru1** crystals were obtained, with a small impurity of the phosphine-imine (ArN)PMe₃.

A single crystal X-ray structure of **Ru1** was collected and provided the same unit cell and parameters as were previously reported by Wilkinson, et. al. Note that the crystal structure, as shown in Fig. 8.11 shows the full molecule, but the Ru sits on a crystallographic inversion center. As a result, half of the molecule is symmetry generated.

Repeated recrystallizations of impure **Ru1** appear to remove most of the impurity, however, satisfactory elemental analysis of the material was not obtained. In part, this is due to the limiting masses that can be carried through the photochemical synthesis and the inherent conversion limit. This conversion limit seems to be a direct result of the absorption properties of the product (**Ru1**) and the reactant (**Ru5**). Both complexes absorb strongly across the UV-Vis spectrum. At several points, **Ru1** even absorbs more strongly than **Ru5**. Thus, when a substantial concentration of **Ru1** has accumulated in solution, further conversion of **Ru5** is halted because of the limited penetration depth of the incoming radiation. When the concentration of the photolysis solution is reduced, more decomposition is noted, and the desired yield increase is not achieved. We suspect that this is likely the result of adventitious water in the solvent or the effect of a small leak of air into the Schlenk tube during the 48 h irradiation time. While this doesn't provide an

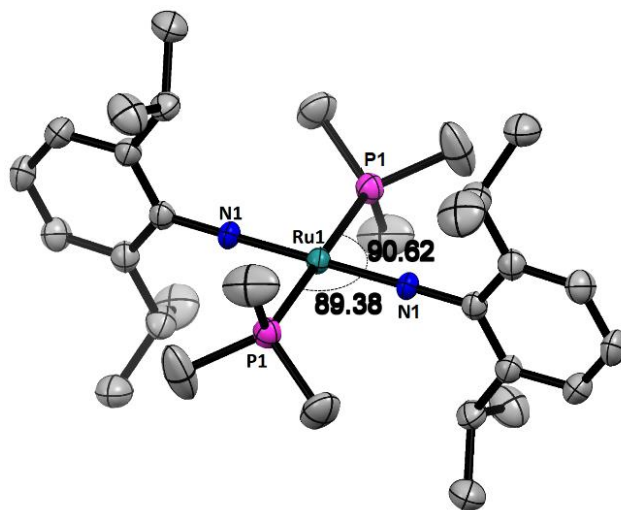


Figure 8.11 Single crystal X-ray structure of Ru(NAr)₂(PMe₃)₂ with ellipsoids shown at 50% probability and H atoms omitted for clarity.

explanation for the additional decomposition observed, lower conversion at lower concentrations could also indicate that a bimolecular mechanism is responsible for the conversion, where the rate would be decreased with a decrease in concentration of **Ru5**. However, given the increased decomposition, we don't want to draw any firm conclusions from this experiment; it simply didn't answer our practical problems.

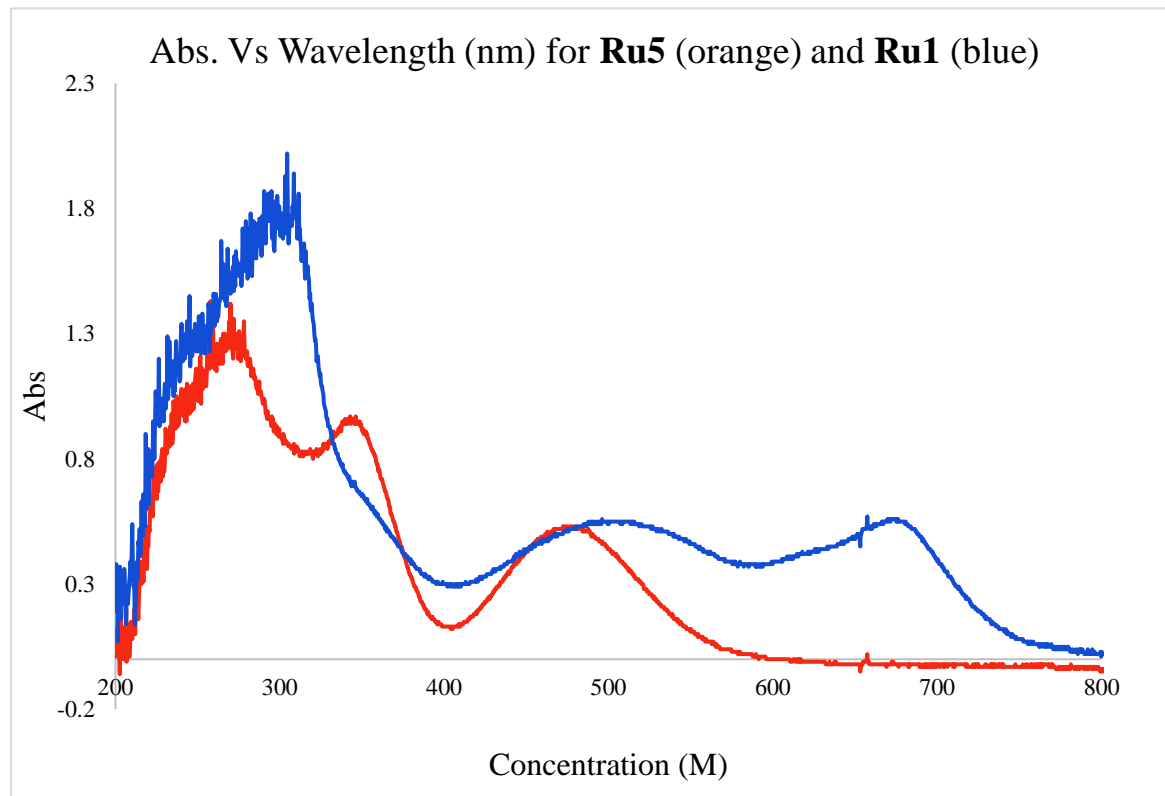


Figure 8.12 Absorption spectra for 0.002 M solutions of **Ru5** (orange trace) and **Ru1** (blue trace) in THF. The strong absorbance of the product (**Ru1**) across the UV-Vis spectrum likely contributes to the conversion limit of 25% in solution.

Similar results were achieved with **Ru7**, with the photolysis solution going from orange to dark green over 24 h and a ^{31}P signal growing in at -22 ppm. However, isolation of the more heavily-substituted $\text{Ru}(\text{NAr})(\text{NAr}^*)(\text{PMe}_3)_2$ (**Ru1***) derivative from the starting material, phosphine-imine byproduct, and small amounts of both anilines, was not productive. **Ru6**, on the other hand, exclusively shows decomposition upon irradiation. A transparent orange solution of **Ru6**, irradiated for 8 h at 800 W, turns pale yellow. A dark precipitate is formed and H_2NMe_3 and

H₂NAr are observed in the crude reaction residue by ¹H NMR. This result highlights a point that will be further illustrated below—that **Ru1** (and proposed **Ru1***) is an anomaly, stabilized by extreme steric protection imparted by the 4 isopropyl groups which point toward the metal. Steric bulk on the aryl imides is necessary to prevent undesired reactivity and even the reduction of an ⁱPr to a Me group in the *ortho* positions can lead to decomposition.

This makes efforts to further improve this reaction pathway challenging. Significant alteration of the ligand electronics is the most straightforward way to change the absorption properties of the product and reactants, which is necessary to overcome the conversion limit. Dramatic stereoelectronic changes, however, are also likely to destabilize the Ru(IV) bis(imido) formation. The same problem we faced with the **Ru2** complex, where ligand manipulations led to undesired reactivity, was encountered again in this system with the tetrazene ligands. Thus, these synthetic challenges prevented the synthesis and isolation of the targeted derivatives for **Ru1**.

8.6 Synthetic Alterations of the Ru Platform: A Larger Phosphine Ligand

Based on the photochemical decomposition of **Ru6**, it seemed like alteration of the aryl group on the imido was detrimental to stability. Instead, we sought to alter the phosphine ligand, going from PMe₃ to the slightly larger PPhMe₂ (TCA of 118 ° and 122°, respectively). Replication of the syntheses to yield *cis*-RuCl₂(PPhMe₂)₄ and Ru(NAr)(PPhMe₂)₃ (**Ru8**) was straightforward and identical to the procedures used to make the PMe₃ derivatives.

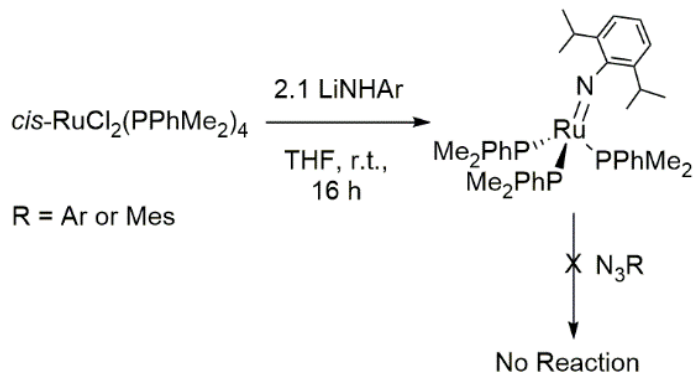


Figure 8.13 Reaction scheme to produce a Ru(II) imide species with bulkier phosphine ligands, PPhMe₂, and subsequent lack of reactivity upon addition of aryl azide.

Upon addition of aryl azide to **Ru8**, however, no reaction occurred. The two species simply coexist in solution without yielding the desired tetrazene species. We suspected that the increase in the size and rigidity of the phosphine ligands lead to steric inhibition that prevented reaction of the Ru species and the azide. The size of the aryl group on the imide was reduced in order to increase the reactivity of the Ru(II) imido. However, this increased the reactivity of the complex too much. Upon addition of 2.1 equiv of LiNHMe₃ to *cis*-RuCl₂(PPhMe₂)₄, the clear yellow solution rapidly turns dark red. After 2 h at room temperature, the red solution turns pink. After work-up, the product recovered is a Ru(II)(κ²-NH(6,4-Me-2-CH₂-Phenyl))(PPhMe₂)₄ (**Ru9**), where C–H activation of one of the *ortho* (-CH₃) groups on the mesityl imide fragment has occurred.

While interesting, these results prevented our attempt to generate a tetrazene species with larger phosphine ligands. Based on these efforts, it seems like producing $\text{Ru}(\text{NR})_2(\text{PR}_3)_2$ complexes with variable substitution will require very careful balancing of the R groups on the imido and phosphine ligands at every step in the synthesis. The promising results that we observed with both the **Ru5** and **Ru7** derivatives certainly suggest that expansion of this synthetic method deserves further exploration. While it may be possible that **Ru1** is special, a “goldilocks” complex, the wider variation in ligand stability observed with related Os-imido complexes suggests that alternate substituent combinations should be accessible.

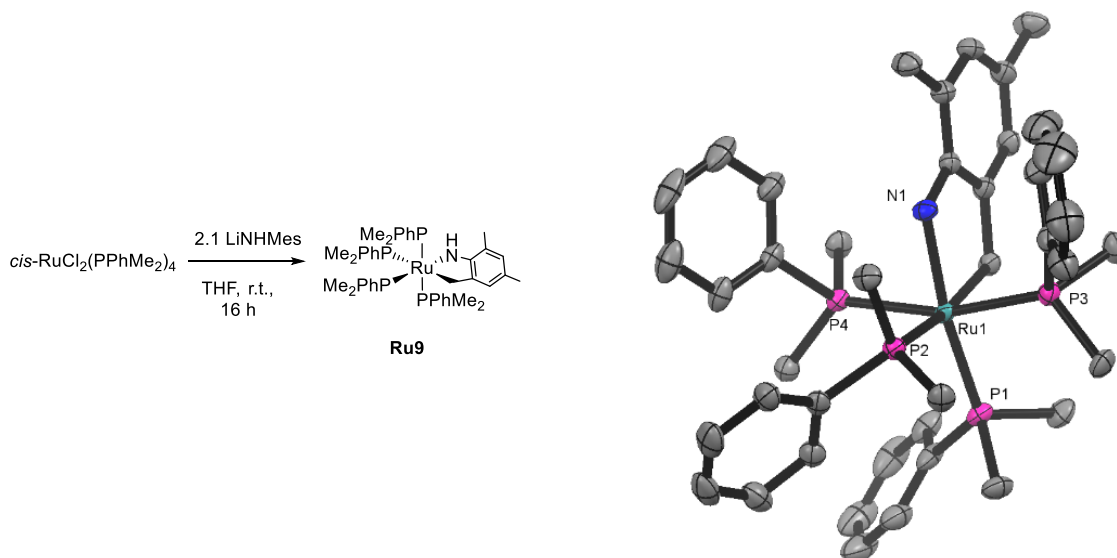


Figure 8.14 The formation of a 6-coordinate, C–H activated mesityl anilide species, resulting from an attempt to generate a terminal $\text{Ru}(\text{=NMe}_s)(\text{PPhMe}_2)_3$.

8.7 A Basic Reactivity Study with Ru1 and Comparison to Known Os Analogues

As mentioned above in the introduction, Schrock and coworkers published several Os bis- and tris(imido) species. Of particular relevance to this work is the synthetic procedure that transforms OsO_4 into $\text{Os}(\text{NAr})_2\text{O}_2$ and finally $\text{Os}(\text{NAr})_2(\text{PMe}_3)_2$, which is outlined below in Fig. 8.15. The $\text{Os}(\text{NAr})_2(\text{L})_2$ derivatives where $\text{L} = \text{PPhMe}_2$, PPh_2Me , and PPh_3 were also synthesized in a similar fashion.

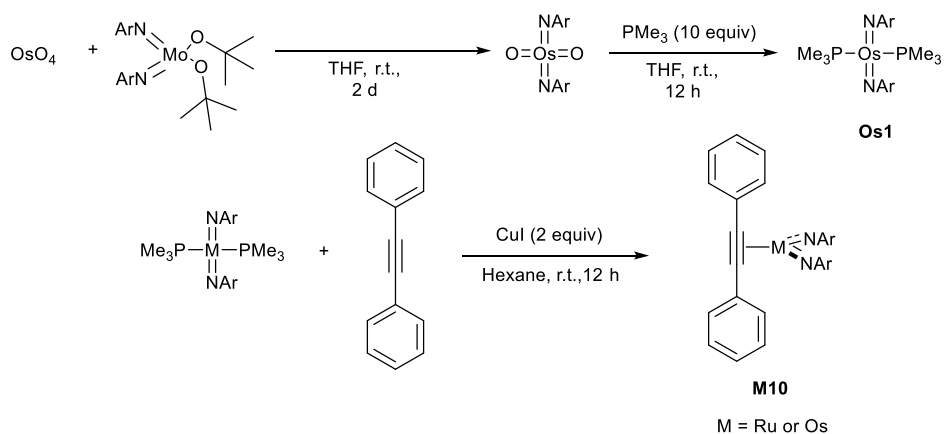


Figure 8.15 Synthetic scheme presented by Schrock and coworkers to produce an $(\eta^2\text{-diphenylacetylene})\text{Os}(\text{NAr})_2$ (**Os10**) complex. It is interesting that the compound doesn't exhibit nucleophilic or electrophilic behavior via interaction of the unsaturated C–C bond participants with the Os–N multiple bond. The same synthetic method was applied to produce **Ru10**.

In addition to electronic structure analysis with these complexes, these studies also explored several basic reaction pathways. One that particularly interested us is the addition of an alkyne to $\text{M}(\text{NAr})_2(\text{PMe}_3)_2$, as shown in the figure. We sought to observe whether this reactivity—simple η^2 -binding of the alkyne to the metal—would be observed with the Ru analogue, as well. Electronically, this is an interesting result. If we think about the nature of the M–N multiple bond, the nature of this bond should be impacted by the oxidation state of the metal. A metal-imide bond in a low oxidation state metal tends to be nucleophilic, with residual electron density on the N, and the σ and π bonds polarized such that the N atomic orbitals constitute more of the bonding MO's. Conversely, as the d -orbital manifold is emptied and the metal gains electronegativity, as occurs in a formally high oxidation state metal, the bonding MO's gain more contribution from the metal orbitals. This tends to saturate more electron density into the M–N bond, making the N less nucleophilic. This facilitates alternate reactivity, such as sigmatropic rearrangements (i.e. cycloaddition of another unsaturated species).

In complexes with similar ligands, but where the Os has maximal valency, like $\text{Os}(\text{NAr})_3\text{O}$ unsaturated C–C bonds can add to the imide nitrogens to form two new C–N σ bonds.

Alternatively, as we have noted with complexes such as $\text{Ru}(\text{NAr})(\text{PMe}_3)_3$, the imide nitrogen is a strong nucleophile, attacking Lewis acidic or electrophilic atoms, such as the Cu in CuI or the central C atom in phenylisocyanate (OCNPh).³⁶ Primarily this seems to differentiate the two diverging reaction pathways, where categorical differences arise depending on the valency of the metal and its relation to the HOMO and LUMO character. Reactivity exhibited by high valent systems, therefore, seems to involve a delocalized orbital spanning the metal and the N of the imide ligand. In low valent systems, on the other hand, the HOMO tends to be nonbonding to antibonding in nature and centered on the N. therefore, reactivity in these complexes is driven by nucleophilic attack of the N atom.

Given these two avenues of M–N double bond reactivity, one might expect that a mid-valent metal-imide complex of this type could react in either manner, depending on the substrate, sterics in the system, etc. Based on the reaction shown in Fig. 8.15, however, neither reactivity is exhibited. In fact, the M–N bonds demonstrate inertness. In this same reaction with **Ru1**, addition of a phosphine scavenger CuI) and an alkyne to **Ru1**, addition of the alkyne results in a color change in the solution. However, by NMR no reaction is evident. Only upon addition of the phosphine-scavenger (CuI) does the alkyne interact with the remaining Ru compound in solution. Because only small amounts of **Ru1** could be isolated, we conducted these investigations *in situ*, examining the reaction by NMR. Both ^{14}N and ^1H NMR present similar spectra to those of the Os analogue; it seems likely that the product of this reaction, therefore, is also the $(\eta^2\text{-PhCCPh})\text{Ru}(\text{NAr})_2$ complex.

The ^{14}N shifts noted for $\text{Os}(\text{NAr})_2(\text{PMe}_3)_2$, $\text{Os}(\text{NAr})_2(\eta^2\text{-PhCCPh})$, and $\text{Os}(\text{NAr})_2(\text{O})_2$ were observed at 283.0, 365.6, and 390.8 ppm, respectively. Across this series, the ^{14}N shifts for the imido moieties increases as the Os becomes more formally oxidized or less electron rich and the

Os–N bonds become, presumably, more covalent. We can see a similar trend with the Ru values, where Ru(NAr)₂(PMe₃)₂ has a shift of 303.3 ppm and Ru(NAr)₂(η²-diphenylacetylene) has a shift of 387.1 ppm. These values follow the trends we would predict based on the electronic factors affecting ¹⁴N NMR shifts.³¹

However, it is interesting to note, that the η²-diphenylacetylene imide shifts for **Ru10** and **Os10** fall closer to those in the Os(NAr)₂(O)₂ complex than **Ru1** and **Os1**. This observation suggests that the η²-alkyne complexes have M–N bonds more similar in character to those in the Os(VIII) complex than the Os(IV) or Ru(IV) complexes, (**Os1/Ru1**) respectively. This change in the ¹⁴N chemical shift suggests a higher bond order or more electron density donation from the imide groups likely occurs in Ru/Os10 than in **Ru/Os1**. Electronically, this may indicate that it's worth considering **Ru/Os10** as M(VI) species. However, this may also be due to the proposed geometry change, whereby the two imide groups may no longer be *trans* to one another. Electronic structure calculations probing charge distribution in the system and bond order between the metal and the η²-PhCCPh to assess these differences would be interesting to pursue.

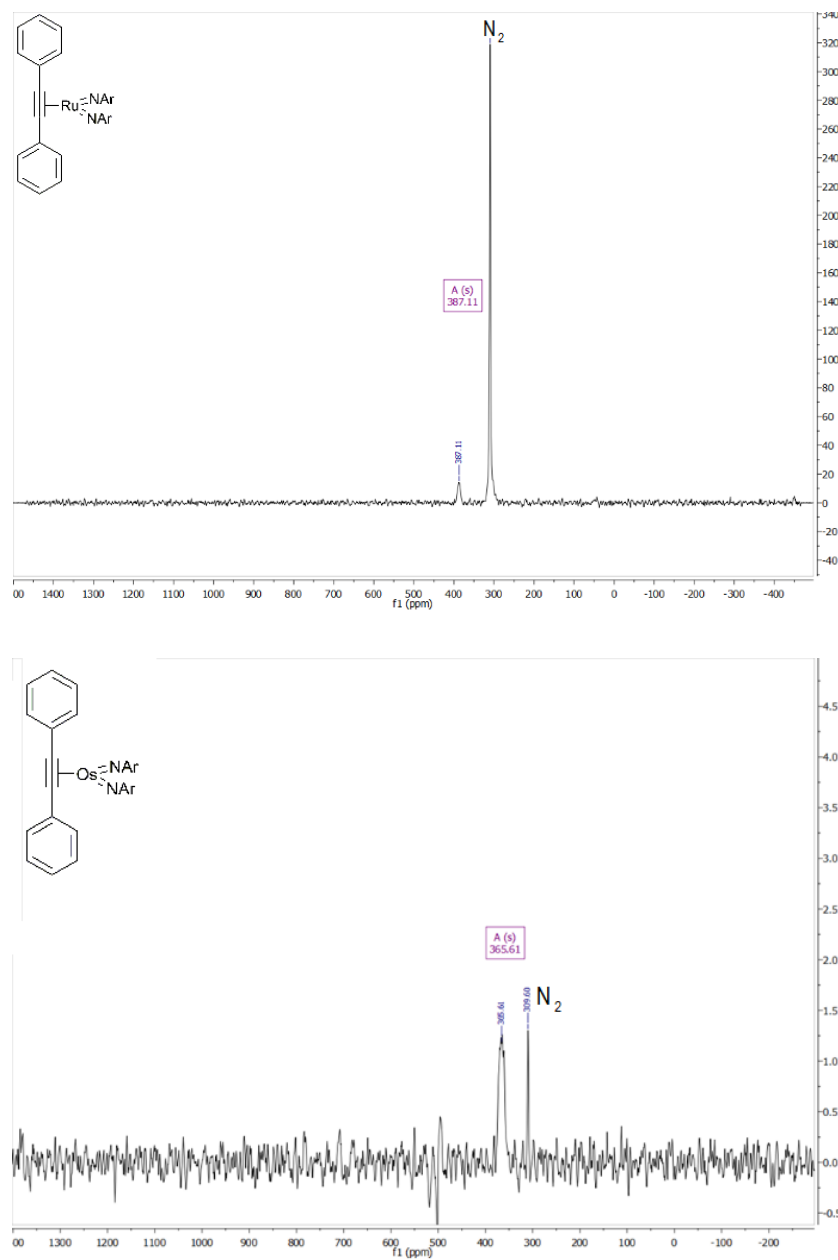


Figure 8.16 ^{14}N NMR of **Ru10** (387.1 ppm) and **Os10** (365.6 ppm).

8.8 Conclusions

In terms of reactivity, it would be very interesting to observe whether or not the inertness observed for $\text{Ru}(\text{NAr})_2(\text{PMe}_3)_2$ (**Ru1**) is from some electronic effect of its middling oxidation state (i.e. midvalency of the metal spreads the HOMO and LUMO across both bond participants, making the metal-imide bond neither nucleophilic or electrophilic), or if this effect is a manifestation of

the sterics needed to prevent C–H activation reactions of the ligands. To that end, continued expansion of synthetic techniques to yield Ru(III)-(V) imides with varied ligand platforms is needed.

As the studies presented here demonstrate, the process of generating midvalent Ru imidos is a delicate synthetic challenge. We have observed C–H activation, total decomposition, and a complete lack of reactivity all as results of very subtle changes to the ligand R groups. While the synthetic strategies that we have discovered here are promising and may be expandable to generate similar complexes (i.e. using slightly different ligand scaffolds with photochemical methods), initial efforts highlight the challenges that face generalization of these processes. Considering analogous chemistry with Fe and Os, it seems that the Ru syntheses are somewhat more sensitive to ligand alteration in terms of finding side reactions and their subsequently high propensity for off-target products.

8.9 Experimental

General Considerations

Synthetic Considerations

All manipulations were carried out under inert atmosphere, either in an N₂ atmosphere MBraun glovebox or using standard Schlenk techniques. The solvents THF and n-hexane were dried over Na and distilled under N₂ prior to use. The solvents toluene, Et₂O, and pentane were dried by passage over activated alumina and sparged with N₂ prior to use. The NMR solvents C₆D₆ and tol-d₈ were dried over CaH₂ and distilled under N₂ prior to used. The solvent hexamethyldisiloxane was dried over CaH₂ and distilled under N₂ prior to use. The azide starting materials N₃Ar, and N₃Mes, were synthesized according to literature procedures.³⁷ However, the purification of the organic azide by silica gel chromatography was omitted, as the crude product

was found to be pure by ^1H and ^{13}C NMR after removal of volatiles. N_3TMS was purchased from Alfa Aesar and used as received. The H_2NAr and H_2NMes were purchased from Oakwood and distilled under vacuum from CaH_2 prior to use. The *cis*- $\text{RuCl}_2(\text{PMe}_3)_4$ starting material, $\text{Ru}(\text{NAr})(\text{PMe}_3)_3$, and $\text{Ru}(\text{NAr}^*)(\text{PMe}_3)_3$ were prepared according to published procedures.^{5 4}

LiNHR salts (where $\text{R} = 2$, -diisopropylphenyl or mesityl) were prepared by adding 2.5 M $^n\text{BuLi}$ (in hexanes, 1 equiv) to a chilled solution (liquid N_2 coldwell) of the respective H_2NR (1 equiv) in hexane. The reaction was warmed to room temperature, while stirring, which resulted in the precipitation of a white to pale yellow powder. This powder was collected by filtration, rinsed several times with n-hexane, and dried under reduced pressure. The powder was used without further purification. It was stored in the glovebox freezer ($-35\text{ }^\circ\text{C}$) to reduce exposure to light. The phosphines PMe_3 and PPhMe_2 were purchased commercially (Strem Chemical Co.) and used as received. They were stored in sealed containers in an N_2 glovebox.

Instrumentation

NMR All NMR data was collected at the Max T. Rogers NMR facility. Routine characterization spectra were obtained using an Agilent DDR2 500 MHz NMR spectrometer equipped with a 5 mm PFG OneProbe operating at 499.84 MHz (^1H), 125.73 MHz (^{13}C), and 202.35 MHz (^{31}P). Additional experiments, including ^{14}N and variable temperature NMR measurements were made using the following instrumentation: a UNITYplus 500 spectrometer equipped with a 5 mm switchable broadband probe operating at 36.12 MHz (^{14}N); a Varian Inova 500 spectrometer equipped with a 5 mm pulse-field-gradient (PFG) switchable broadband probe operating at 499.84 MHz (^1H); a Varian Inova 600 spectrometer equipped with a 5 mm PFG switchable broadband probe operating at 599.89 MHz (^1H). ^1H NMR chemical shifts are reported relative to residual C_6HD_5 in C_6D_6 as 7.16 ppm. ^{13}C NMR chemical shifts are reported relative to

(¹³C)C₅D₆ as 128.06 ppm. ¹⁴N NMR shifts are referenced to the internal peak for dissolved N₂ in NMR solvent (309.6 ppm vs. external nitromethane as 381.6 ppm, which sets NH₃ to 0 ppm).

X-Ray Crystallography All crystallographic data was collected at the Michigan State University Center for X-ray Crystallography. All structures were collected on Bruker AXS instruments operating with either copper or molybdenum radiation sources. Data was collected at 173 K. Structure solutions were typically found using XT Intrinsic Phasing and refined by least squares using Olex software. For further information please see the .cif files provided as supporting information.

Photochemical Reactions Photolysis experiments were carried out using an Oriel Instruments Mercury Arc Lamp (Model # 66921) operating between 450-1000 W. An ≈15 cm H₂O column was used as an IR filter between the lamp and the jacketed chiller, fitted with a quartz window. This reduced the temperature at the quartz window between incoming light and the reaction vessel, which was important for some experiments. A picture of the photolysis set-up is shown below.

UV-Vis Spectroscopy UV-Vis spectra were collected using an Ocean Optics DH-mini UV-Vis-NIR spectrophotometer in an N₂ glovebox. Experiments were performed in dry THF using a quartz cell. The raw data was fitted with OriginPro 9.0 software to obtain accurate peak separation and assignment of maxima.

Synthetic Procedures

In-situ Reduction of PhNNPh A scintillation vial was charged with 176 mg of azobenzene (1 equiv, 1 mmol), a stir bar, and 6 mL of THF. The solution was stirred at room temperature, and 30 mg (4 equiv, 4 mmol) of Li pellets was added to the solution. The solution went from bright,

transparent orange to dark green rapidly. The solution was stirred for 24 h, over which time it turned pale, transparent yellow. Note, solid Li was still present after this time. This solution was stable at room temperature in the presence of excess Li. Full conversion was assumed in calculating stoichiometries.

The same procedure as listed above can be performed with Na in place of Li metal, however, results in a dark brown solution after 24 h, and seems to lead to some reduction when utilized in the subsequent reaction step.

Synthesis of Ru(PhNNPh)(PMe₃)₄ · PhMe (Ru2) A 35 mL pressure tube was charged with 480 mg (1 equiv, 1 mmol) of *cis*-RuCl₂(PMe₃)₄, a stir bar, and 5 mL of THF. To this solution was added a 6 mL solution in THF containing 190 mg (1 equiv, 1 mmol) of reduced azobenzene (Li₂[PhNNPh]). The tube was sealed and removed from the glovebox and heated at 60 °C in an oil bath for 8 h. The pressure tube was cooled and returned to the glovebox, where the THF was removed under vacuum. The dark brown residue was extracted with toluene until the extract was colorless. The toluene extracts were filtered over Celite, concentrated, and n-hexane was layered into the toluene solution. This layered solution was stored at -35 °C for 48 h to yield 415 mg (61 %) of crystals of Ru(PhNNPh)(PMe₃)₄ · PhMe.

A similar procedure can be used with Na₂[PhNNPh], with slight modifications. A scintillation vial was charged with 200 mg (1 equiv, 0.42 mmol) of RuCl₂(PMe₃)₄, a stir bar, and 5 mL of THF. This solution was stirred at room temperature. To the stirred solution, a solution containing reduced azobenzene Na₂[PhNNPh] (originally 75 mg of azobenzene (1 equiv, 0.42 mmol) and 40 mg Na (4 equiv, 1.68 mmol)) was added dropwise; note, the excess sodium in this solution was not transferred to the Ru solution. The reaction solution rapidly changed color from pale yellow to dark brown upon addition of the reduced azobenzene species. The reaction mixture

was stirred for 8 h at room temperature, and the volatiles removed under reduced pressure. The dark brown residue was extracted with toluene until the extracts came off colorless. The toluene extract was then filtered over Celite, and concentrated. The concentrated toluene filtrate was layered with hexane and stored at -35 °C to yield 133 mg (47 %) of crystals of Ru(PhNNPh)(PMe₃)₄ · PhMe. This material had identical properties to that obtained using Li as the reductant above.

¹H NMR (500 MHz, benzene-*d*₆) δ 7.32 (t, *J* = 8.1 Hz, 2H), 7.20 (t, *J* = 7.7 Hz, 2H), 7.06 (d, *J* = 7.5 Hz, 2H), 6.68 (t, *J* = 7.1 Hz, 2H), 6.46 (d, *J* = 8.4 Hz, 2H), 1.08 (d, *J* = 6.4 Hz, 18H), 0.93 (t, *J* = 2.6 Hz, 18H). ¹³C[¹H] NMR (126 MHz, benzene-*d*₆) δ 129.12, 116.69, 116.11, 111.93, 25.02 (d, *J* = 21.2 Hz), 20.35 (t, *J* = 13.5 Hz). ³¹P NMR (202 MHz, benzene-*d*₆) δ -0.92–6.11 (m). Elemental Analysis calculated for RuC₃₁H₅₄P₄N₂: C, 54.78, H, 8.01, N, 4.12; found, C, 54.30, H, 7.95, N, 4.13. UV-vis, λ_{max}: 458 nm (ε = 1295 M⁻¹·cm⁻¹); 340 nm (ε = 3156 M⁻¹·cm⁻¹); 308 nm (ε = 5029 M⁻¹·cm⁻¹).

Synthesis of Ru-H (Ru3) A 35 mL pressure tube was charged with 100 mg of **RuN₂P₄**, a stir bar, and 10 mL of THF. The pressure tube was sealed and transferred from the glovebox to an oil bath and heated at 60 °C for 12 h. The pressure tube was cooled to room temperature and returned to the glovebox, where the THF was removed under reduced pressure, leaving a dark brown residue. The residue was extracted with n-hexane (6 mL), and the extract filtered over Celite. The filtrate was concentrated and stored at -35 °C for 5 days to yield 42 mg (57%) of crystals of **RuH**.

¹H NMR (500 MHz, benzene-*d*₆) δ 8.66–8.61 (m, 1H), 8.45–8.40 (m, 1H), 7.47–7.40 (m, 2H), 7.24 (tdd, *J* = 7.0, 1.7, 1.0 Hz, 2H), 7.16–7.14 (m, 3H), 7.11–7.05 (m, 1H), 0.99 (d, *J* = 5.2 Hz, 9H), 0.90–0.81 (m, 18H), -11.39 (td, *J* = 33.1, 15.4 Hz, 1H). ¹³C[¹H] NMR (126 MHz,

benzene- d_6) δ 147.08, 129.07, 128.92, 128.43, 128.16, 127.94, 127.75, 127.56, 125.94, 125.29, 123.11, 120.98, 23.72 (d, $J = 17.0$ Hz), 22.19–21.57 (td, $J = 13.8, 3.0$ Hz). ^{31}P NMR (202 MHz, Benzene- d_6) δ -8.98 (dd, $J = 29.9, 13.2$ Hz, 2P), -13.86 (td, $J = 29.6, 29.2, 5.5$ Hz, 1P). ^{14}N NMR (36 MHz, benzene- d_6): δ 397.6 (br, s). Elemental analysis calc'd for $\text{RuN}_2\text{P}_3\text{H}_{37}\text{C}_{21}$: C, 49.31, H, 7.29, N, 5.48; found, C, 49.10, H, 7.69, N, 4.82.

Synthesis of TBP cis-Ru(NPh)₂(PMe₃)₃ (Ru4) (in situ) A J.Young tube was loaded with a solution containing 20 mg of RuN_2P_4 in 1 mL C_6D_6 . The tube was sealed with a Teflon stopper and transferred out of the glovebox to the photolysis apparatus. The tube was irradiated with a mercury arc lamp at 800 W in an ice bath (0 °C) for 2 hours. The tube and its contents were then taken for *in situ* measurements. Care was taken to keep the solution cold (-30 °C) for long measurements and while storing the solution to prevent thermal conversion to **Ru3**.

^1H NMR (500 MHz, benzene- d_6) δ 9.70 (s, 2H), 8.78 (d, $J = 7.8$ Hz, 1H), 8.43 (d, $J = 7.4$ Hz, 1H), 7.36–7.30 (m, 2H), 7.25 (td, $J = 7.9, 7.4, 1.5$ Hz, 1H), 7.22–7.17 (m, 3H), 1.36 (d, $J = 7.2$ Hz, 9H), 0.70 (t, $J = 2.9$ Hz, 18H). ^{13}C [^1H] NMR (126 MHz, benzene- d_6) δ 141.95, 132.65, 128.93, 128.67, 128.17, 120.42, 24.24 (dd, $J = 21.0, 3.5$ Hz), 21.21 (t, $J = 13.2$ Hz). ^{31}P NMR (202 MHz, benzene- d_6) δ 10.98 (td, $J = 42.9, 42.4, 6.0$ Hz), -7.83 (dd, $J = 42.6, 7.7$ Hz), -62.61. UV-vis: 636 nm ($\epsilon = 646 \text{ M}^{-1}\text{cm}^{-1}$); 470 nm ($\epsilon = 2149 \text{ M}^{-1}\text{cm}^{-1}$); 435 nm ($\epsilon = 2154 \text{ M}^{-1}\text{cm}^{-1}$); 359 nm ($\epsilon = 6179 \text{ M}^{-1}\text{cm}^{-1}$).

Synthesis of Ru(1,4-bis(2,6-diisopropylphenyl)tetrazene)(PMe₃)₃ (Ru5) A scintillation vial was charged with 150 mg (1 equiv, 0.3 mmol) of $\text{Ru}(\text{NAr})(\text{PMe}_3)_3$, a stir bar, and 5 mL of Et_2O . To this stirred solution, a separate solution containing 60 mg (1 equiv, 0.3 mmol) N_3Ar in 2 mL of Et_2O was added dropwise. After 10 min of stirring at room temperature, a fine orange precipitate had started to form. The reaction was stirred another 2 h at room temperature, at which time the

fine orange powder was collected by filtration and rinsed with n-hexane. The powder was dried under vacuum and found to be analytically pure, giving 120 mg (57 %) of RuN₄P₃. Chilling the original filtrate (-35 °C) resulted in the precipitation of an additional 52 mg (25 %) of RuN₄P₃. X-ray quality crystals were grown from concentrated THF layered with hexane at -35 °C.

¹H NMR (500 MHz, benzene-*d*₆) δ 7.39 (dd, *J* = 8.2, 7.1 Hz, 2H), 7.30 (d, *J* = 7.6 Hz, 4H), 3.15 (p, *J* = 6.8 Hz, 4H), 1.39 (d, *J* = 6.6 Hz, 12H), 1.31 (d, *J* = 6.9 Hz, 12H), 1.01–0.81 (m, 26H). ¹³C[¹H] NMR (126 MHz, benzene-*d*₆) δ 154.58, 145.76, 125.93, 122.41, 27.59, 27.10, 24.50–23.66 (m), 21.83. ³¹P NMR (202 MHz, benzene-*d*₆) δ 6.50. Elemental analysis calc'd for RuC₃₃H₆₁P₃N₄: C, 55.99, H, 8.69, N, 7.92; found, C, 55.46, H, 8.47, N, 7.83. UV-vis, λ_{max}: 478 nm (ε = 2347 M⁻¹cm⁻¹), 349 nm (ε = 4081 M⁻¹cm⁻¹).

Synthesis of Ru(1-(2,6-diisopropylphenyl)-4-mesityl-tetrazene)(PMe₃)₃ (Ru6) The same procedure used for RuN₄P₃ above was used for the preparation of RuN₄^{Ar/Mes}P₃, utilizing 76 mg (1 equiv, 0.15 mmol) Ru(NAr)(PMe₃)₃ and 32 mg N₃Mes (1 equiv, 0.15 mmol). This yielded 79 mg (73 %) of the crude powder. X-ray quality crystals were grown from concentrated THF layered with hexane at -35 °C.

¹H NMR (500 MHz, benzene-*d*₆) δ 7.45–7.36 (m, 1H), 7.30 (d, *J* = 7.6 Hz, 2H), 6.95 (s, 2H), 3.20 (p, *J* = 6.8 Hz, 2H), 2.33 (s, 3H), 2.20 (s, 6H), 1.40 (d, *J* = 6.7 Hz, 6H), 1.30 (d, *J* = 7.0 Hz, 6H), 0.93 (dd, *J* = 4.6, 2.5 Hz, 28H). ¹³C[¹H] NMR (126 MHz, benzene-*d*₆) δ 154.91, 154.52, 145.65, 135.19, 133.79, 128.64, 125.87, 122.51, 27.55, 26.85, 24.28–23.58 (m), 22.03, 20.82, 20.16. ³¹P NMR (202 MHz, benzene-*d*₆) δ 6.43. Elemental analysis calc'd for RuC₃₀H₅₅P₃N₄: C, 54.12, H, 8.33, N, 8.42; found, C, 54.10, H, 8.64, N, 8.19. UV-vis, λ_{max}: 490 nm (ε 2052 M⁻¹cm⁻¹), 339 nm (ε 3796 M⁻¹cm⁻¹).

Synthesis of Ru(1-(2,6-diisopropylphenyl)-4-(2,4,6-triisopropylphenyl)-tetrazene)(PMe₃)₃

(Ru7) A scintillation vial was charged with 70 mg Ru(NAr*)(PMe₃)₃ (0.128 mmol, 1 equiv), 5 mL THF, and a stir bar. This solution was stirred at room temperature, and a solution of N₃Ar (29 mg, 0.128 mmol, 1 equiv) in THF (1 mL) was added to it dropwise. The solution was stirred for 4 h at room temperature, at which point an orangish-red, powdery precipitate had formed. The solution was decanted from the precipitate, and the precipitate was rinsed with hexane and dried. This yielded 68 mg of the crude powder, which was recrystallized from HMDSO to give 24 mg X-ray quality crystals. Additional powder was precipitated from the mother liquor of the reaction by chilling the solution to -35 °C. This provided a total yield of 53 mg (55%).

¹H NMR (500 MHz, benzene-*d*₆) δ 7.39 (dd, *J* = 8.2, 7.0 Hz, 1H), 7.33–7.28 (m, 2H), 7.25 (s, 2H), 3.16 (hept, *J* = 6.7 Hz, 4H), 3.02 (hept, *J* = 7.0 Hz, 1H), 1.46–1.38 (m, 18H), 1.36 (d, *J* = 6.9 Hz, 6H), 1.32 (d, *J* = 6.9 Hz, 6H), 0.97–0.85 (m, 27H). ³¹P NMR (202 MHz, benzene-*d*₆) δ 6.51. ¹³C NMR (126 MHz, benzene-*d*₆) δ 155.02, 152.88, 146.37, 146.17, 145.77, 126.31, 122.80, 120.39, 34.85, 28.05 (d), 27.59 (d), 24.91, 24.68, 24.60 (d), 24.54, 24.47, 22.31 (d), 2.10. Elemental analysis calc'd for RuC₃₆H₆₇P₃N₄: C, 57.66, H, 9.01, N, 7.47; found, C, 57.33, H, 9.04, N, 6.80. UV-vis, λ_{max}: 474 nm (ε 1600 M⁻¹cm⁻¹), 340 nm (ε 3620 M⁻¹cm⁻¹).

Synthesis of Ru(NAr)₂(PMe₃)₂ (Ru1) A 500 mL Schlenck tube, fitted with a Teflon stopper, was charged with 75 mg of RuN₄^{Ar}P₃ (0.11 mmol), a stir bar, and 200 mL of THF. This provided a 5.5 mM solution. The Schlenck tube was sealed and transferred from the glovebox to the photolysis apparatus. The Schlenck tube was submerged in a water-jacketed chiller which maintained a temperature of about 16 °C during the photolysis process.

The jacketed chiller was placed on a stir plate, and in the path of the Hg-Arc lamp, with the quartz window of the jacketed chiller aligned with the lamp. The lamp was then run at 800 W,

irradiating the stirred solution in the Schlenk flask for 48 h. After the photolysis period, the exterior of the Schlenk tube was dried and the vessel was returned to the glovebox. The reaction solution was transferred to a side-arm flask, and the volatiles removed under reduced pressure to provide a tacky, dark brown residue. This residue was extracted with cold n-hexane until the extracts came off colorless. The extracted n-hexane solution was filtered over celite and the filtrate concentrated to about 1 mL. This solution was stored at -35 °C for several days to provide 38 mg of crystals of Ru(NAr)₂(PMe₃)₂, mixed with crystals of RuN₄^{Ar}P₃ and P(NAr)Me₃. To obtain a purer sample of Ru(NAr)₂(PMe₃)₂, 2 more recrystallizations from n-Hex were preformed successively. This sample was utilized to examine the UV-Vis spectrum of the complex and HRMS. Attempts to obtain elemental analysis were unsuccessful.

¹H NMR (500 MHz, benzene-*d*₆) δ 6.93–6.90 (m, 4H), 6.85–6.81 (m, 2H), 4.45 (hept, *J* = 7.0 Hz, 4H), 1.28 (d, *J* = 6.9 Hz, 26H), 1.23 (t, *J* = 2.6 Hz, 19H). ³¹P NMR (202 MHz, benzene-*d*₆) δ -20.90. ¹⁴N NMR (36 MHz, benzene-*d*₆) δ 303.30. UV-vis, λ_{max}: 675 nm (ε 4034 M⁻¹cm⁻¹), 484 nm (ε 1776 M⁻¹cm⁻¹), 344 nm (ε 1997 M⁻¹cm⁻¹), 30 nm (ε 8200 M⁻¹cm⁻¹).

Repeated attempts to obtain passing elemental analysis failed. Given the relatively small scales on which this reaction can be performed, and the product compound isolated, HRMS was instead attempted. A peak for the species shown below was observed by QTOF-HRMS running in positive ion mode: HRMS calc'd for RuNP₂C₁₈H₃₆⁺: 429.1296; found: 429.1096.

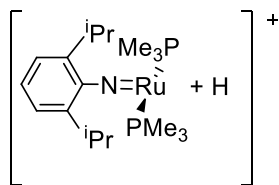
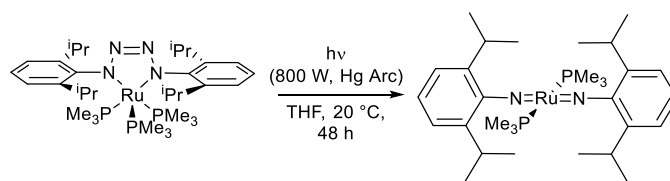


Figure 8.17 Fragment for **Ru1** observed by HRMS.



Scheme 8.1 Photochemical conversion to yield **Ru1** from **Ru5**.

Synthesis of Ru(NAr)₂(η²-Diphenylacetylene) (Ru10) (in situ) A scintillation vial was charged with 12 mg **Ru1** (1 equiv, 0.021 mmol), 5.5 mg diphenylacetylene (1.5 equiv, 0.031 mmol), a stir bar, and 2 mL of C₆D₆. The mixture was stirred at room temperature. To the stirred solution was added 8 mg (2 equiv, 0.042 mmol) of CuI, portionwise. The reaction solution was stirred vigorously for 4 h, over which time it went from deep blue to reddish-purple in color. The reaction mixture was filtered over a pad of Celite, and the filtrate transferred to an NMR tube for *in situ* analysis.

¹H NMR (600 MHz, benzene-*d*₆) δ 8.36 (d, *J* = 7.4 Hz, 4H), 7.22 (t, *J* = 8.6 Hz, 6H), 6.92–6.86 (m, 7H), 3.73 (p, *J* = 6.9 Hz, 4H), 1.14 (d, 28H). ¹³C[¹H] NMR (151 MHz, benzene-*d*₆): δ 200.41. (Note: the full ¹³C NMR spectrum could not be assigned *in situ* due to the presence of excess diphenylacetylene, in addition to other impurities. However, this new resonance noted at >200 ppm is close to the observed ¹³C resonance for the acetylenic carbon in the Os derivative of this molecule previously reported). ¹⁴N NMR (36 MHz, THF-*d*₈) δ 387.11. (Note: Attempts to grow X-ray quality crystals from this reaction solution did not result in the isolation of a new complex.)

Synthesis of Me₃PNAr A scintillation vial was charged with 38 mg of PMe₃ (0.5 mmol, 1.2 equiv), 3 mL of THF, and a stir bar. At room temperature, 78 mg (0.4 mmol, 1 equiv) of N₃Ar was added dropwise, as a solution in 1 mL THF, to the stirred PMe₃ solution. The reactions immediately began to produce bubbles. The reaction was allowed to stir for 4 h, and the volatiles removed in vacuo, resulting in 90 mg (94%) of a powdery, pale yellow residue. The crude product was used without further purification. X-ray quality crystals can be grown from n-hex at -35 °C.

^1H NMR (500 MHz, benzene- d_6) δ 7.24 (dd, $J = 7.6, 1.5$ Hz, 2H), 7.08 (td, $J = 7.5, 2.8$ Hz, 1H), 3.58 (septet, $J = 6.9$ Hz, 2H), 1.34 (d, $J = 6.9$ Hz, 12H), 0.93 (d, $J = 12.0$ Hz, 9H). ^{13}C [^1H] NMR (126 MHz, benzene- d_6) δ 142.51 (d), 128.35, 122.97 (d), 119.72 (d), 28.71, 24.21, 17.61 (d). ^{31}P NMR (202 MHz, benzene- d_6) δ -7.57. Elemental analysis calc'd for $\text{C}_{15}\text{H}_{26}\text{PN}$: C, 71.68, H, 10.43, N, 5.57; found, C, 71.25, H, 9.78, N, 5.61.

Synthesis of cis-RuCl₂(PPhMe₂)₄ A 35 mL pressure tube was charged with 0.506 g $[\text{RuCODCl}_2]_x$ (1.9 mmol, 1 equiv), a stir bar, and 3 mL toluene. The solution was stirred and to it was added 1.4 g PPhMe₂ (9.5 mmol, 5 equiv). The pressure tube was sealed and transferred from the glovebox to a 120 °C oil bath. The pressure tube was heated, with stirring, for 16 h, over which time the opaque, brown suspension turned an orangish-yellow. The pressure tube was removed from heat and cooled ambiently, resulting in the precipitation of copious amounts of yellow solids, which was an assortment of various sized crystals. (Note, from this precipitate, X-ray quality crystals were obtained). When the pressure tube was cooled, it was returned to the glovebox. The mother liquor was decanted, and the solids dried under reduced pressure to yield 1.1 g (80%) of cis-RuCl₂(PPhMe₂)₄.

Once the title compound is precipitated from toluene, it has poor solubility in NMR solvents, as well as most organic solvents. The complex demonstrates marked color changes when dissolved in DMSO- d_6 or MeOD, which seem to correspond to solvent reactivity. Consequently, adequate NMR spectra could not be obtained. The collected precipitate was found to be analytically pure by elemental analysis, without further treatment, and was used in subsequent reactions. The crystals obtained upon cooling were also structurally characterized. Elemental analysis calc'd for $\text{RuC}_{32}\text{H}_{44}\text{P}_4\text{Cl}_2$: C, 53.05, H, 6.12, N, 0.00; found, C, 52.72, H, 6.29, N, 0.06.

Ru(NH-2,4-dimethyl-6-CH₂-phenyl)(PPhMe₂)₄ (Ru9) A scintillation vial was loaded with 124 mg of *cis*-RuCl₂(PPhMe₂)₄ (0.16 mmol, 1 equiv), a stir bar, and 5 mL of THF. In a separate vial, 48 mg of LiNHMe_s (0.34 mmol, 2.1 equiv) was dissolved in THF. This solution was added dropwise to the first solution, with stirring, at room temperature. Upon addition, the solution went from a pale yellow suspension to an intense red solution. The reaction was stirred for 8 h and the volatiles removed under reduced pressure. The residue was extracted with hexane and filtered over celite until the filtrate came out colorless. The reddish-pink filtrate solution was concentrated under reduced pressure and stored at -35 °C for 24 h to yield 46 mg (42 %) X-ray quality crystals.

¹H NMR (500 MHz, benzene-*d*₆) δ 7.34 (s, 1H), 7.20 (t, *J* = 7.2 Hz, 8H), 7.04 (t, *J* = 7.6 Hz, 11H), 6.97 (s, 1H), 4.11 (s, 1H), 2.88 (s, 2H), 2.56 (s, 3H), 2.23 (s, 3H), 1.19 (d, *J* = 4.8 Hz, 24H). ¹³C[¹H] NMR (126 MHz, benzene-*d*₆) δ 162.16, 144.15 (d, *J* = 26.8 Hz), 130.64 (d, *J* = 10.4 Hz), 128.35, 127.98 (d, *J* = 3.5 Hz), 126.41, 120.84, 119.66, 31.98, 21.57, 18.85, 18.13. ³¹P NMR (202 MHz, benzene-*d*₆) δ 7.44. Elemental analysis calc'd for RuC₄₁H₅₅P₄N: C, 62.58, H, 7.05, N, 1.78; found, C, 62.36, H, 7.16, N, 1.85.

Ru(NAr)(PPhMe₂)₃ (Ru8) A scintillation vial was charged with 194 mg (1equiv, 0.25 mmol) of *cis*-RuCl₂(PPhMe₂)₄, a stir bar, and 8 mL of THF. To this stirred solution, a solution of 100 mg (2.1 equiv, 0.52 mmol) LiNHAr in 2 mL THF, was added dropwise at room temperature. The solution rapidly changed color from pale yellow to bright red. The solution was stirred for 16 h at room temperature and the volatiles were removed under vacuum. This yielded a dark red residue which was extracted with n-hexane and filtered over celite until the filtrate came off colorless. The filtrate was concentrated to 2 mL and chilled to -35 °C to give 124 mg (67%) of amorphous crystals, which were not X-ray quality.

^1H NMR (500 MHz, benzene- d_6) δ 7.63 (ddt, $J = 8.8, 4.5, 1.9$ Hz, 6H), 7.22 (s, 3H), 7.08 (t, $J = 7.5$ Hz, 6H), 7.04–6.93 (m, 3H), 4.62 (septet, $J = 6.9$ Hz, 2H), 1.40 (d, $J = 7.0$ Hz, 12H), 1.39–1.36 (m, 18H). ^{13}C NMR (126 MHz, benzene- d_6) δ 157.68, 146.15–143.90 (m), 140.54 (q, $J = 6.2$ Hz), 130.59 (dd, $J = 7.6, 3.7$ Hz), 128.34, 128.14 (dd, $J = 6.1, 3.2$ Hz), 122.78, 120.49, 26.68, 23.99, 23.72–22.74 (m). ^{31}P NMR (202 MHz, benzene- d_6) δ 34.62. Elemental analysis calc'd for $\text{RuC}_3\text{H}_{50}\text{P}_3\text{N}$: C, 62.59, H, 7.30, N, 2.03; found, C, 62.13, H, 7.49, N, 2.11.

Os2-toluene The procedure outlined for the synthesis of **Ru2** was applied to produce analogous Os2, utilizing 200 mg *cis*- $\text{OsCl}_2(\text{PMe}_3)_4$ (0.34 mmol, 1 equiv), 62 mg azobenzene (0.34 mmol, 1 equiv) reduced with 4 equiv Li (10 mg, 1.4 mmol), and 5 mL THF. The reaction solution was dried under reduced pressure to give a brown residue, which was extracted with toluene and filtered over Celite until the filtrate was colorless. The toluene solution was concentrated to 2 mL and layered with n-hexane. Storing the layered solution at -35 °C yielded 110 mg (42%) of X-ray quality orange crystals.

Os3 A pressure tube was charged with 50 mg of Os2, 5 mL of THF and a stir bar. The tube was sealed and heated at 65 °C for 12 h. After this time, the pressure tube was returned to the glovebox and the reaction solution dried under reduced pressure. This yielded a dark brown residue. The residue was dissolved in hexane and recrystallized at -35 °C to yield 21 mg of X-ray quality brown-orange crystals of Os3. ^1H NMR (500 MHz, benzene- d_6) δ 8.73 (d, $J = 7.6$ Hz, 1H), 8.39 (d, $J = 5.7$ Hz, 1H), 8.00 (d, $J = 7.9$ Hz, 1H), 7.37 (d, $J = 7.6$ Hz, 4H), 7.23 (dd, $J = 11.0, 7.4$ Hz, 2H), 7.05 (dd, $J = 16.9, 6.8$ Hz, 3H), 1.15 (d, $J = 6.0$ Hz, 9H), 0.98 (t, $J = 3.6$ Hz, 16H). ^{31}P NMR (202 MHz, benzene- d_6) δ -49.30 (d, $J = 20.5$ Hz), -55.72 (t, $J = 20.7$ Hz). (xtal structure below).

Os(NAr)₂(L)₂ Several compounds originally reported by Schrock, et. al. were synthesized following literature reports for the purpose of examining the ¹⁴N NMR spectra of the complexes. These data provided a useful comparative tool when analyzing the Ru analogues presented here. These compounds include Os(NAr)₂(O)₂, Os(NAr)₂(PMe₃)₂, and (η²-diphenylacetylene)Os(NAr)₂.^{22,23} These complexes matched reported ¹H, ¹³C, ³¹P and X-ray diffraction unit cell parameters provided in the literature.

Computational Analysis All calculations were performed using the MSU HPCC facilities. DFT optimizations and single-point energy calculations were performed using Gaussian09, and data handling was done with GaussView software. For the calculations presented in section 8.3, the following parameters were used in order to optimize structures: initial optimization using PBEPBE functional and a split basis set (cc-pvtz-PP on Ru, 6-311g+(d,2p) on all other atoms, CPCM solvent model using THF polarization). The optimized structures were then reoptimized with the same basis set assignment with the b3lyp functional. From the structures optimized with b3lyp, single-point energy calculations were performed with the structures and ΔH values assigned for the transformation to each proposed species. The coordinates for each optimized, theoretical structure are provided below.

Complex 1

N	1.376900	0.495500	0.677100
N	1.398000	-0.500300	-0.358600
C	2.182600	1.624300	0.528600
C	2.053900	-2.691300	-1.149800
H	1.155000	-2.717100	-1.750800
C	4.377200	-2.614200	0.390100
H	5.278400	-2.575900	0.991900
C	4.142300	-3.720200	-0.436800
H	4.849500	-4.537500	-0.485200
C	2.965700	-3.740600	-1.205600
H	2.760700	-4.585200	-1.853500
C	2.810600	3.844700	1.354900

H	2.633700	4.664600	2.041200
C	1.991600	2.721700	1.410500
H	1.190700	2.666300	2.134500
C	3.255700	1.714000	-0.396300
H	3.438700	0.885500	-1.063500
C	3.472900	-1.552800	0.459700
H	3.673800	-0.708000	1.101900
C	2.276900	-1.559400	-0.314700
C	3.861900	3.926500	0.425400
H	4.498100	4.800700	0.386600
C	4.072100	2.848000	-0.440800
H	4.882600	2.885300	-1.159700
Ru	-0.607000	-0.031200	0.004400
P	-2.031600	-1.659800	-1.106000
C	-3.931700	-1.553600	-1.091300
H	-4.286500	-1.590700	-0.064000
H	-4.355800	-2.388600	-1.648300
H	-4.251500	-0.619000	-1.546100
C	-1.778000	-1.968600	-2.968500
H	-2.048100	-1.088100	-3.541800
H	-2.406500	-2.802100	-3.280100
H	-0.736400	-2.216700	-3.159000
C	-1.848800	-3.465500	-0.536600
H	-0.797600	-3.742700	-0.523800
H	-2.386200	-4.116000	-1.225500
H	-2.266300	-3.581500	0.458200
P	-0.550000	-1.253800	2.147100
C	-0.147400	-0.136500	3.622400
H	0.740000	0.436000	3.371700
H	0.034000	-0.747400	4.506100
H	-0.974400	0.541000	3.821400
C	0.767400	-2.586500	2.408400
H	0.673800	-3.352100	1.642700
H	0.632400	-3.030700	3.394400
H	1.752500	-2.140000	2.330700
C	-2.039900	-2.212600	2.853000
H	-2.978700	-1.777600	2.528700
H	-1.990700	-2.197800	3.941100
H	-1.991900	-3.246100	2.519200
P	-2.383800	1.432800	0.850300
C	-3.733400	0.841700	2.058900
H	-4.306700	0.035700	1.607600
H	-4.400200	1.673900	2.281100
H	-3.287000	0.491000	2.985100
C	-3.538100	2.369200	-0.341200
H	-2.957400	2.970500	-1.033900

H	-4.189500	3.023000	0.237300
H	-4.146400	1.664300	-0.901800
C	-1.770700	2.934700	1.846100
H	-1.246000	2.598100	2.736200
H	-2.620600	3.550300	2.139000
H	-1.087700	3.522400	1.238100
P	-0.397500	1.342300	-2.038500
C	-1.864500	1.565900	-3.248000
H	-2.780300	1.172300	-2.821000
H	-1.646700	1.042900	-4.176600
H	-2.000200	2.623300	-3.468300
C	0.085800	3.164100	-1.809200
H	-0.709800	3.696100	-1.291800
H	0.245200	3.620000	-2.785900
H	0.995100	3.223600	-1.220000
C	0.934100	0.806700	-3.270400
H	1.892500	0.796200	-2.765200
H	0.951100	1.499200	-4.111600
H	0.711500	-0.196500	-3.624800

Complex 2

Ru	0.349600	0.437100	0.451000
N	-0.215700	-0.897200	-1.134200
C	3.498300	0.127200	0.015400
H	3.685600	0.853200	0.795700
C	2.158400	-0.204000	-0.310600
N	0.734300	-1.549000	-1.761000
C	-1.531100	-1.272200	-1.588600
C	-4.100300	-1.953300	-2.479800
H	-5.092800	-2.215600	-2.819800
C	-2.439100	-0.270000	-1.947100
H	-2.127500	0.761000	-1.881800
C	2.016100	-1.186800	-1.340600
C	-3.716700	-0.609900	-2.397200
H	-4.408200	0.170700	-2.684900
C	4.404300	-1.438700	-1.625500
H	5.257600	-1.895300	-2.109100
C	4.590400	-0.467000	-0.621600
H	5.596900	-0.182400	-0.337200
C	-1.905300	-2.619500	-1.690600
H	-1.192700	-3.386400	-1.426100
C	3.112800	-1.798900	-1.984500
H	2.925100	-2.538000	-2.753300
C	-3.189900	-2.955000	-2.125200

H	-3.477700	-3.995900	-2.189200
P	-1.945700	1.049100	1.396500
C	-3.174700	2.267000	0.592200
H	-2.751600	3.267200	0.598100
H	-4.101100	2.266400	1.166200
H	-3.388900	1.971300	-0.430600
C	-1.954800	1.846800	3.123500
H	-1.418200	1.224400	3.831900
H	-2.979600	1.991000	3.466000
H	-1.454200	2.811100	3.056800
C	-3.168200	-0.386900	1.665700
H	-3.460300	-0.775300	0.693100
H	-4.051500	-0.035500	2.198700
H	-2.697900	-1.186000	2.232200
P	0.658200	-1.317200	2.137400
C	2.442300	-1.652900	2.669600
H	3.031800	-1.959400	1.812100
H	2.450800	-2.435700	3.427200
H	2.866400	-0.739500	3.079300
C	0.125200	-3.071600	1.653100
H	-0.949900	-3.094700	1.489300
H	0.390200	-3.777800	2.439600
H	0.630000	-3.348000	0.729900
C	-0.104000	-1.189400	3.870600
H	0.271700	-0.289200	4.351800
H	0.190800	-2.060000	4.455100
H	-1.187500	-1.144200	3.821300
P	0.681600	2.412900	-0.934100
C	-0.536500	3.864600	-1.012200
H	-1.489000	3.528100	-1.411400
H	-0.130100	4.644200	-1.656000
H	-0.684900	4.263400	-0.011200
C	0.912300	2.082400	-2.785700
H	1.730100	1.378100	-2.916400
H	1.136800	3.011000	-3.309600
H	0.002100	1.646000	-3.190800
C	2.264100	3.376800	-0.559700
H	2.208700	3.763500	0.455100
H	2.373300	4.201300	-1.263500
H	3.116000	2.708800	-0.640400
H	1.033900	1.385800	1.629800

Complex 3

Ru	0.002200	0.490300	-0.024600
N	-1.632000	-0.033900	-0.773800

C	-2.555800	-1.053500	-0.697100
C	-3.780400	-0.879700	0.015100
C	-2.412600	-2.263400	-1.439600
C	-3.421300	-3.224600	-1.459000
H	-3.275400	-4.131400	-2.034200
C	-4.784300	-1.846200	-0.024500
H	-5.702800	-1.676400	0.525100
C	-4.619100	-3.031600	-0.755000
H	-5.400200	-3.779400	-0.778700
N	1.707500	0.123900	-0.707000
C	2.710300	-0.814900	-0.606900
C	2.673200	-2.043700	-1.330500
C	3.909100	-0.529900	0.113400
C	4.988600	-1.411600	0.098400
H	5.884700	-1.158500	0.653100
C	3.757800	-2.918700	-1.326500
H	3.692700	-3.842900	-1.888800
C	4.928700	-2.617300	-0.615300
H	5.768800	-3.298400	-0.620900
H	3.971500	0.401500	0.662000
H	1.783400	-2.276600	-1.901500
H	-1.502200	-2.415000	-2.005500
H	-3.924000	0.034100	0.577500
P	-0.036200	2.082500	-1.978900
C	-0.090100	1.054100	-3.557600
H	-0.090600	1.699800	-4.434900
H	-0.990600	0.447200	-3.537300
H	0.781100	0.404800	-3.573600
C	1.445100	3.202400	-2.328200
H	2.345900	2.598800	-2.250800
H	1.492000	4.008000	-1.599600
H	1.368700	3.625900	-3.328700
C	-1.503600	3.243600	-2.251400
H	-1.504900	4.033600	-1.503000
H	-2.418300	2.663200	-2.157200
H	-1.453800	3.690200	-3.243600
P	0.054900	-1.350300	1.576600
C	1.520900	-1.437200	2.769800
H	1.430700	-2.330700	3.386300
H	2.440500	-1.480300	2.192200
H	1.543700	-0.560100	3.408800
C	-1.412300	-1.495100	2.761800
H	-1.496000	-0.600300	3.373000
H	-2.322200	-1.610000	2.178500
H	-1.275300	-2.360900	3.408300
C	0.101900	-3.109800	0.889900

H	-0.775400	-3.281600	0.273600
H	0.998400	-3.232600	0.289000
H	0.114600	-3.815800	1.719600
P	-0.189700	2.228500	1.724700
C	0.721400	3.841400	1.355500
H	0.573100	4.536200	2.180600
H	1.781900	3.633900	1.236900
H	0.337100	4.283300	0.441200
C	-1.971900	2.814900	1.943200
H	-2.576400	1.988900	2.308600
H	-2.001700	3.638100	2.655400
H	-2.360600	3.141200	0.982800
C	0.349800	1.961900	3.516200
H	-0.179400	1.122100	3.955600
H	1.420000	1.774900	3.545600
H	0.126100	2.861600	4.087400

Complex 5

Ru	-0.000000	0.000000	0.000000
N	-1.778300	0.053400	-0.000300
C	-3.146300	0.078900	-0.000200
C	-3.879100	0.081000	-1.218000
C	-3.878500	0.103200	1.217700
C	-5.271200	0.128000	1.209900
H	-5.809000	0.146500	2.149200
C	-5.271700	0.105800	-1.209900
H	-5.810000	0.107000	-2.149100
C	-5.979400	0.129200	0.000100
H	-7.060600	0.148100	0.000200
N	1.778300	-0.053400	0.000300
C	3.146300	-0.078900	0.000200
C	3.879200	-0.081000	1.218000
C	3.878500	-0.103200	-1.217800
C	5.271100	-0.128000	-1.210000
H	5.808900	-0.146500	-2.149300
C	5.271700	-0.105800	1.209800
H	5.810100	-0.106900	2.149000
C	5.979400	-0.129200	-0.000200
H	7.060600	-0.148100	-0.000300
H	-3.330500	0.063700	-2.150200
H	-3.329500	0.103000	2.149800
H	3.329400	-0.103100	-2.149800
H	3.330600	-0.063700	2.150200
P	-0.140000	-2.473300	0.005700

C	-1.161000	-3.223900	1.404900
H	-1.214100	-4.306500	1.296300
H	-2.163300	-2.803300	1.376200
H	-0.699200	-2.973500	2.357300
C	1.472500	-3.442200	0.117300
H	1.980400	-3.185900	1.043900
H	2.112200	-3.173400	-0.719600
H	1.267700	-4.511500	0.094700
C	-0.960500	-3.231100	-1.517100
H	-0.371700	-2.985300	-2.398100
H	-1.956900	-2.809700	-1.627700
H	-1.028700	-4.313300	-1.412000
P	0.140000	2.473300	-0.005700
C	1.161000	3.223900	-1.404900
H	1.214100	4.306500	-1.296200
H	2.163300	2.803300	-1.376200
H	0.699200	2.973500	-2.357300
C	-1.472500	3.442200	-0.117300
H	-1.980400	3.185900	-1.043800
H	-2.112200	3.173400	0.719600
H	-1.267700	4.511500	-0.094600
C	0.960500	3.231100	1.517200
H	0.371800	2.985300	2.398100
H	1.956900	2.809700	1.627700
H	1.028800	4.313300	1.412100

Complex 7

1 Ru1	0.1356	-0.2803	-0.2874 Ru
2 P2	1.1889	-2.5286	-1.1188 P
3 N3	1.8559	0.3107	-0.8835 N
4 C4	2.5006	1.5038	-0.6044 C
5 C5	3.9228	1.5678	-0.7427 C
6 C6	1.8285	2.7263	-0.2967 C
7 C7	2.5354	3.9223	-0.1484 C
8 H8	1.9937	4.8394	0.0709 H
9 C9	4.6187	2.7619	-0.5695 C
10 H10	5.7008	2.7736	-0.6736 H
11 C11	3.9322	3.9531	-0.2721 C
12 H12	4.4764	4.8841	-0.1453 H
13 C13	1.2924	-2.3011	-2.9942 C
14 H14	1.8559	-3.1180	-3.4572 H
15 H15	1.7853	-1.3464	-3.1915 H
16 H16	0.2814	-2.2699	-3.4114 H
17 C17	0.5212	-4.3057	-1.0275 C

18 H18	-0.5199	-4.3393	-1.3570 H
19 H19	0.5874	-4.6760	-0.0007 H
20 H20	1.1196	-4.9556	-1.6752 H
21 C21	3.0015	-2.8552	-0.6867 C
22 H22	3.0726	-3.2605	0.3264 H
23 H23	3.5403	-1.9074	-0.7391 H
24 H24	3.4385	-3.5704	-1.3916 H
25 H25	4.4524	0.6529	-0.9948 H
26 H26	0.7493	2.7101	-0.2028 H
27 N27	-1.0173	1.0163	-0.9037 N
28 P28	-2.0987	-1.6684	0.3500 P
29 P29	0.7992	-0.3290	2.0578 P
30 C30	-2.1422	1.7837	-0.7437 C
31 C31	-3.1119	1.8830	-1.7859 C
32 C32	-2.3547	2.5654	0.4308 C
33 C33	-4.2282	2.7069	-1.6476 C
34 H34	-2.9572	1.3072	-2.6936 H
35 C35	-3.4686	3.3977	0.5449 C
36 H36	-1.6208	2.5104	1.2288 H
37 C37	-4.4186	3.4739	-0.4857 C
38 H38	-4.9539	2.7604	-2.4549 H
39 H39	-3.6016	3.9894	1.4470 H
40 H40	-5.2855	4.1198	-0.3886 H
41 C41	-0.6002	-0.0775	3.3005 C
42 H42	-1.2726	-0.9374	3.2942 H
43 H43	-0.1753	0.0375	4.3030 H
44 H44	-1.1621	0.8215	3.0372 H
45 C45	1.6143	-1.8971	2.7326 C
46 H46	0.9817	-2.7626	2.5207 H
47 H47	2.5859	-2.0319	2.2508 H
48 H48	1.7581	-1.8062	3.8145 H
49 C49	2.0216	0.9760	2.6607 C
50 H50	2.1951	0.8241	3.7309 H
51 H51	2.9658	0.8877	2.1208 H
52 H52	1.6119	1.9738	2.4931 H
53 C53	-3.5822	-0.8016	1.1556 C
54 H54	-3.2988	-0.4110	2.1357 H
55 H55	-3.9087	0.0286	0.5267 H
56 H56	-4.4076	-1.5122	1.2730 H
57 C57	-2.9292	-2.2912	-1.2354 C
58 H58	-3.8338	-2.8627	-1.0017 H
59 H59	-3.1945	-1.4289	-1.8536 H
60 H60	-2.2369	-2.9222	-1.7986 H
61 C61	-2.0701	-3.2549	1.3937 C
62 H62	-1.2952	-3.9339	1.0344 H
63 H63	-1.8651	-3.0044	2.4385 H

64 H64 -3.0416 -3.7577 1.3358 H

PMe₃

P	0.000500	-0.000700	-0.594000
C	1.553900	-0.537500	0.275800
H	1.802100	-1.556900	-0.021400
H	2.378500	0.110500	-0.022700
H	1.447700	-0.499800	1.362100
C	-0.311100	1.613900	0.275100
H	0.447100	2.338800	-0.022300
H	-1.285100	2.004000	-0.021600
H	-0.289300	1.502800	1.361500
C	-1.243400	-1.075600	0.275300
H	-2.249400	-0.780300	-0.024300
H	-1.095200	-2.114600	-0.020200
H	-1.160000	-0.999700	1.361700

Spectral Data for Complexes

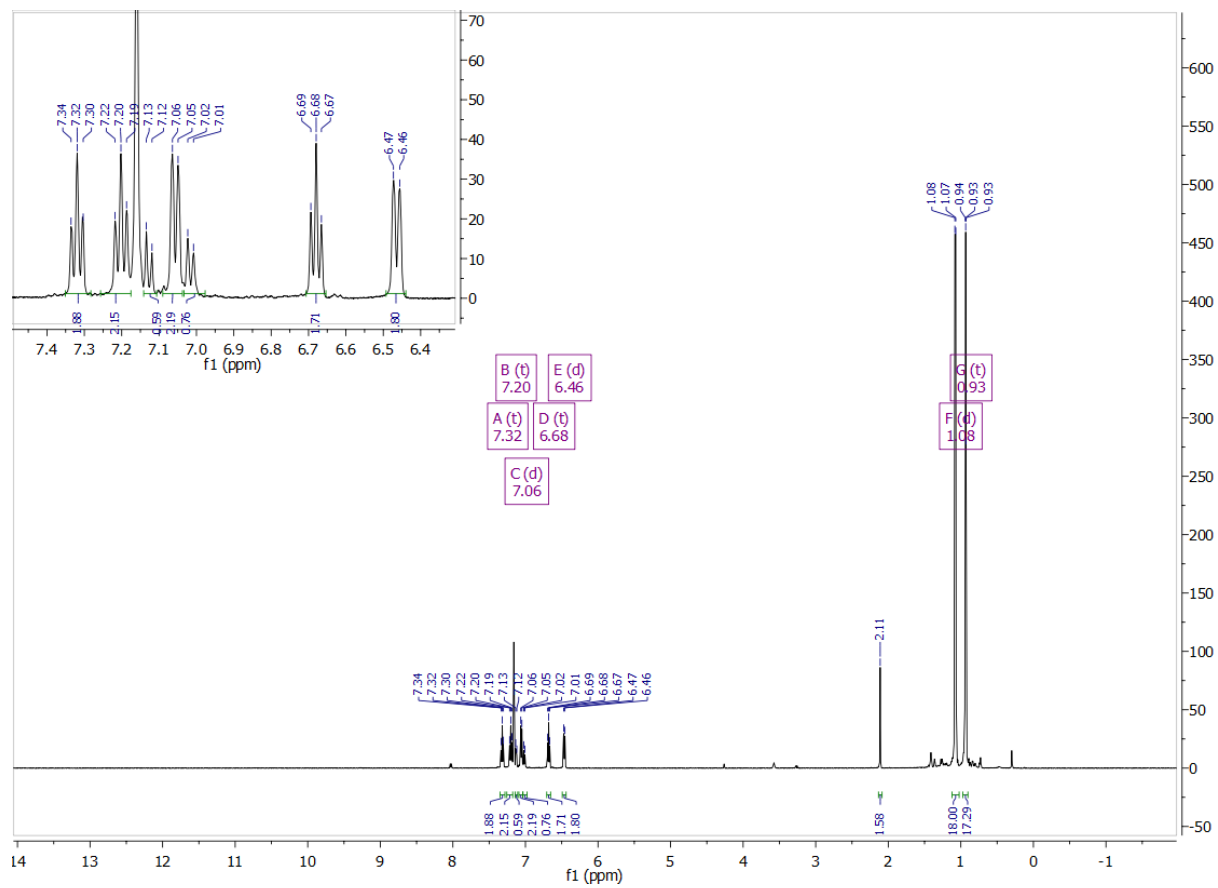


Figure 8.18 ^1H NMR spectrum of $\text{Ru}(\text{PhNNPh})(\text{PMe}_3)_4 \cdot \text{PhMe}$ (**Ru2**) in C_6D_6 .

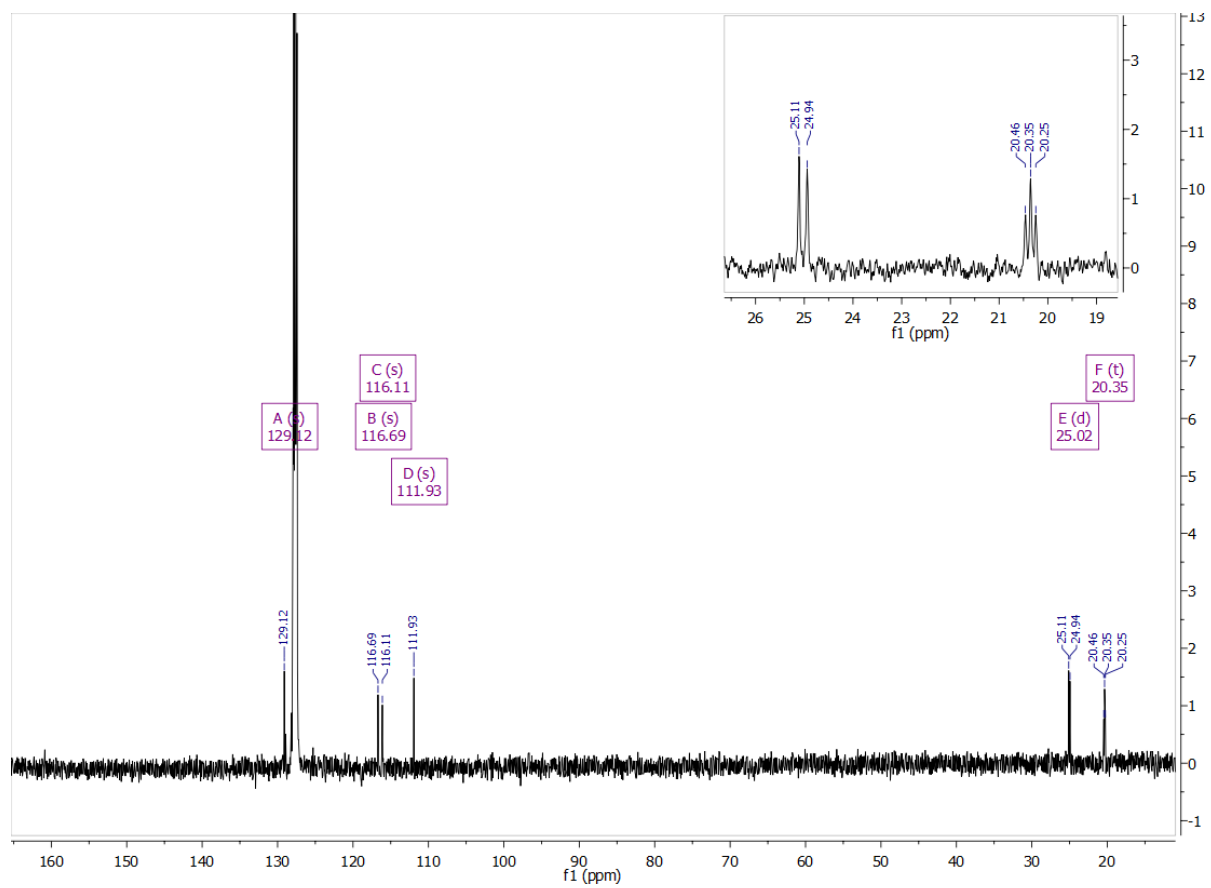


Figure 8.19 ^{13}C NMR spectrum of $\text{Ru}(\text{PhNNPh})(\text{PMe}_3)_4 \cdot \text{PhMe}$ (**Ru2**) in C_6D_6 .

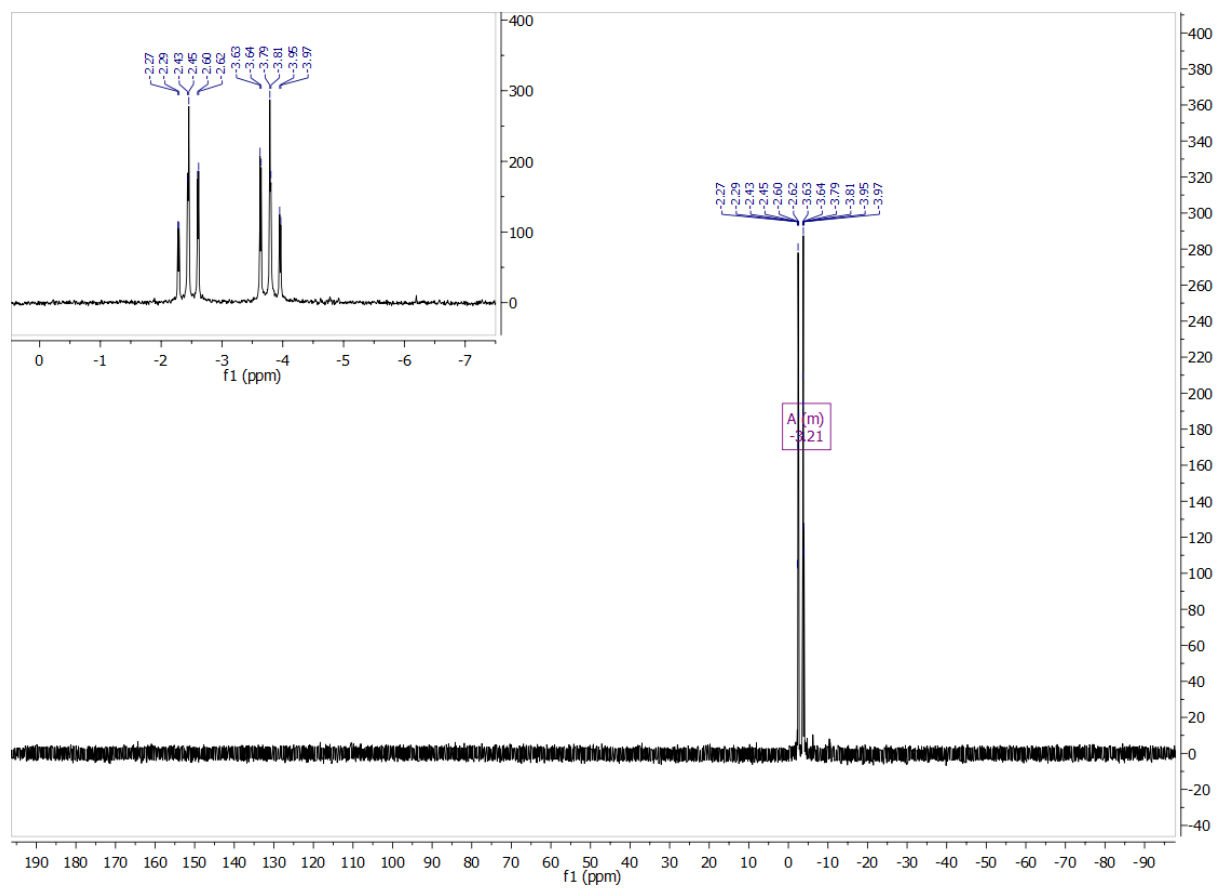


Figure 8.20 ^{31}P NMR spectrum of $\text{Ru}(\text{PhNNPh})(\text{PMe}_3)_4 \cdot \text{PhMe}$ (**Ru2**) in C_6D_6 .

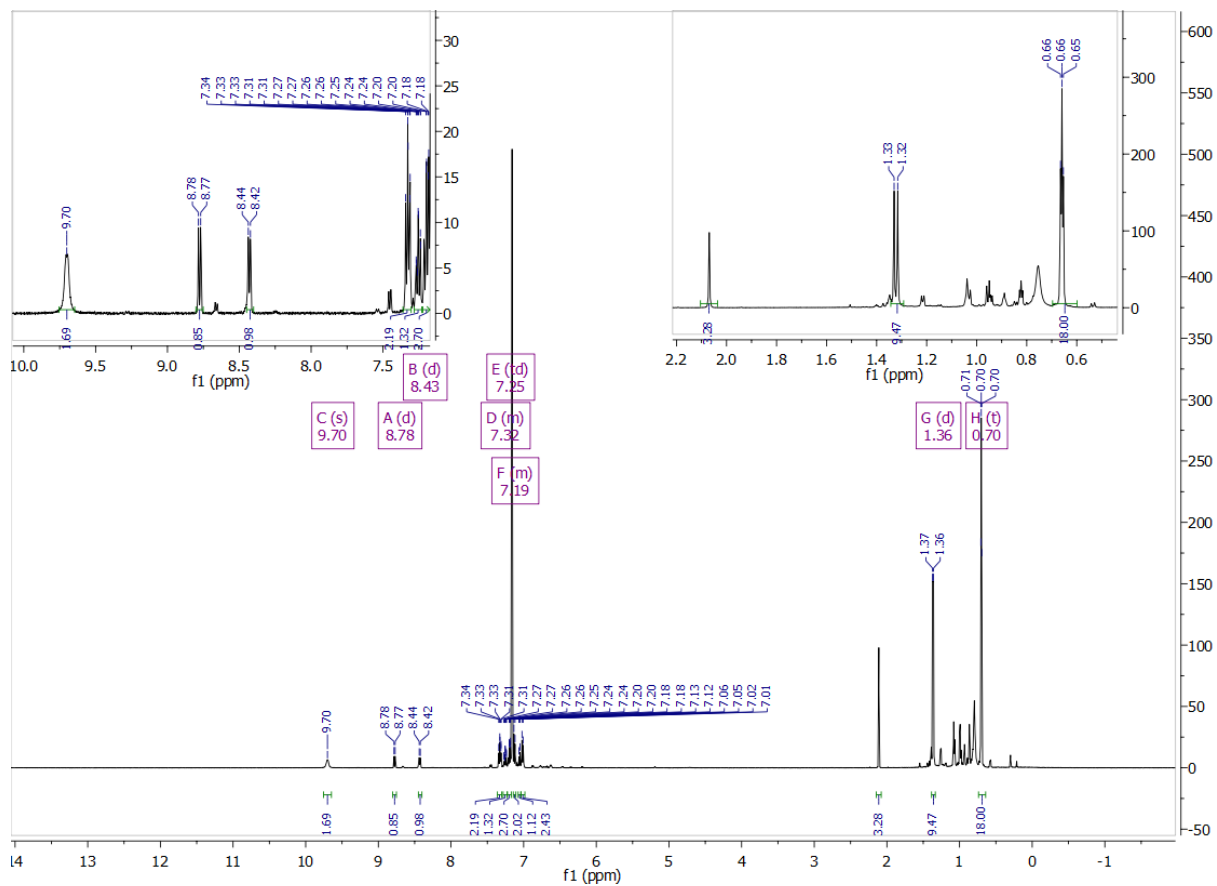


Figure 8.21 ^1H NMR spectrum of **Ru4** (in situ) in C_6D_6 .

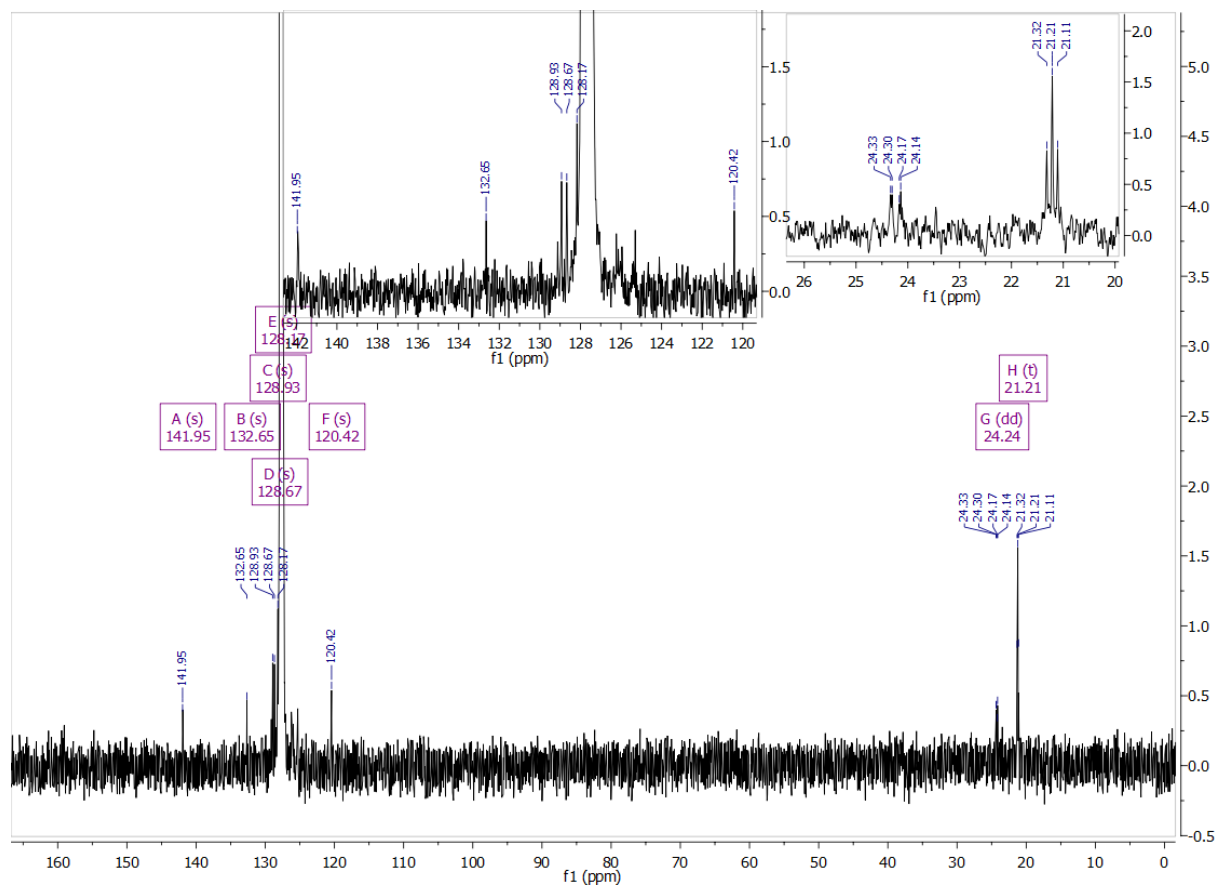


Figure 8.22 ^{13}C NMR spectrum of **Ru4** (in situ) in C_6D_6 .

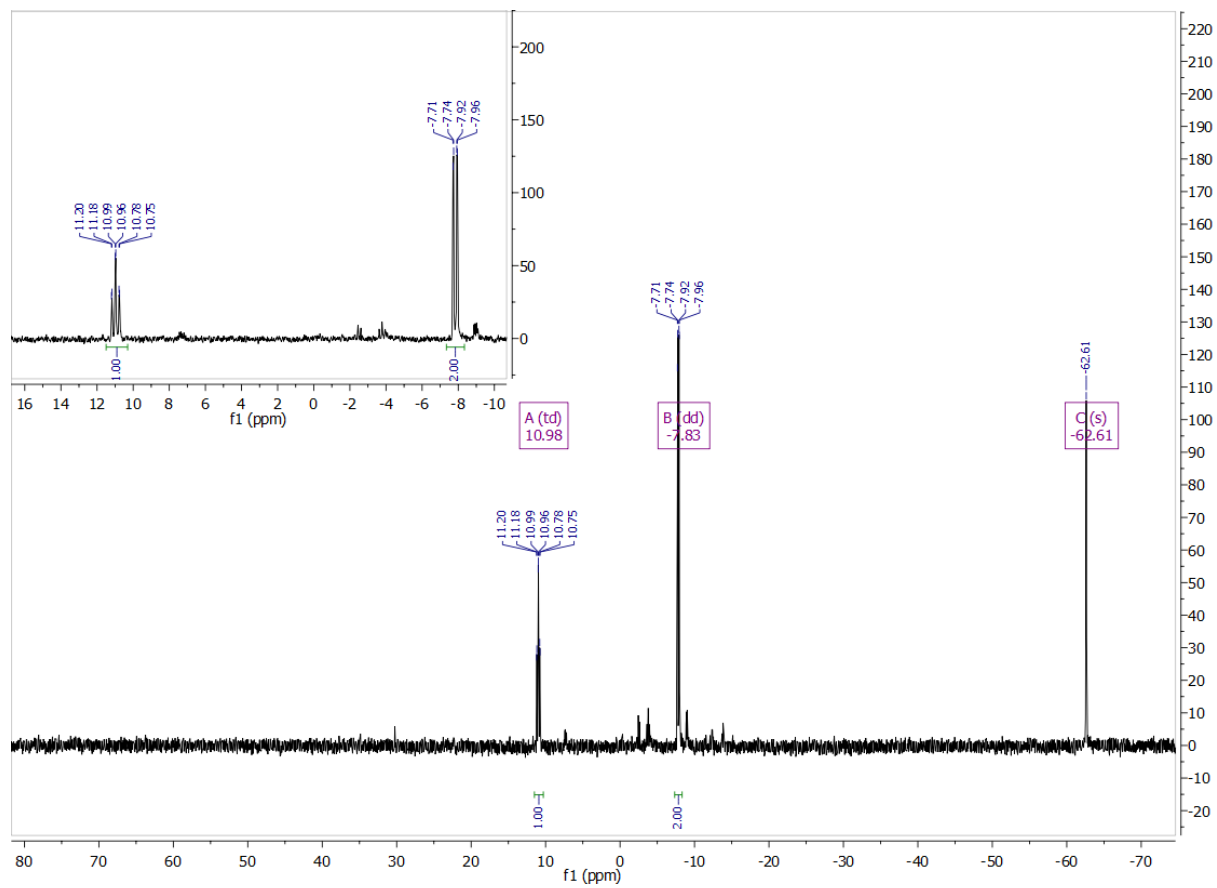


Figure 8.23 ^{31}P NMR spectrum of **Ru4** (in situ) in C_6D_6 .

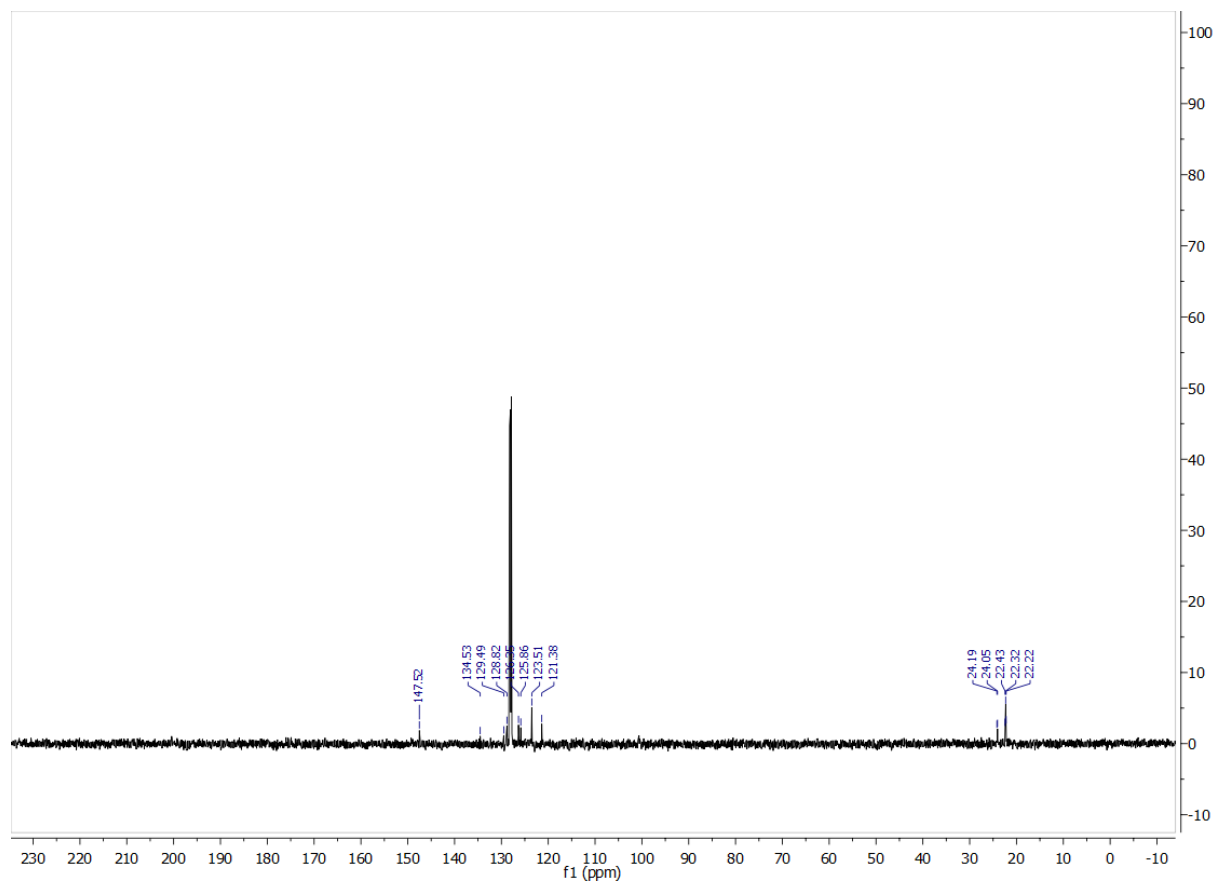


Figure 8.25 ^{13}C NMR spectrum of **Ru3** in C_6D_6 .

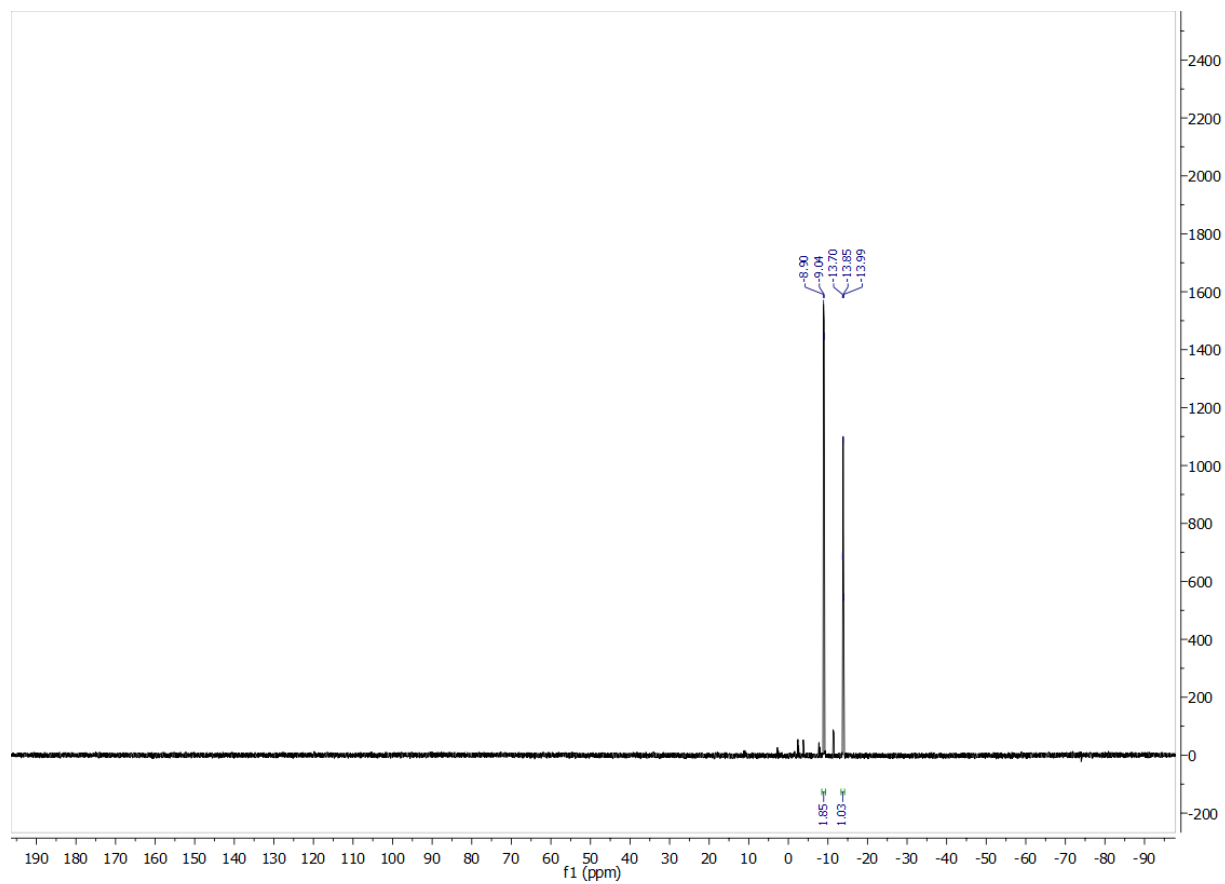


Figure 8.26 ^{31}P NMR spectrum of **Ru3** in C_6D_6 .

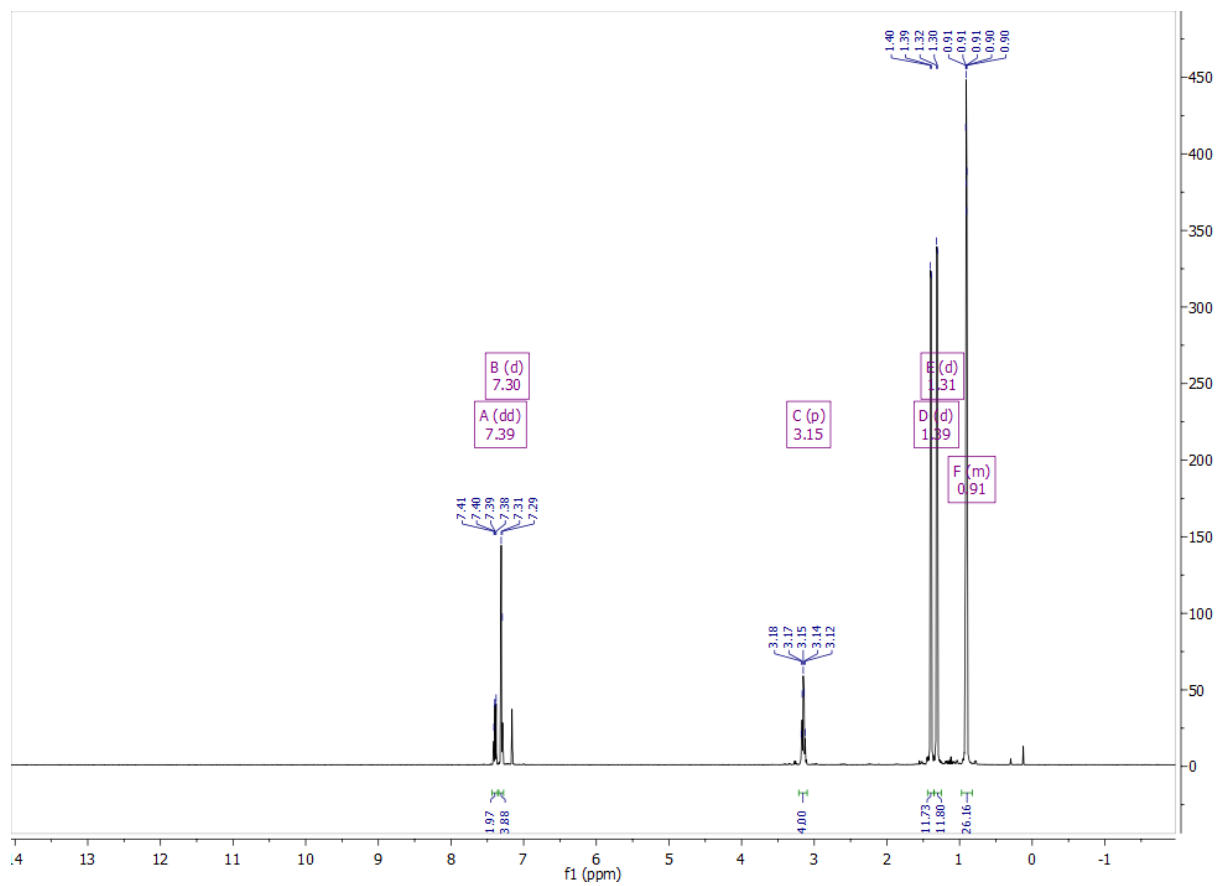


Figure 8.27 ^1H NMR of **Ru5** in C_6D_6 .

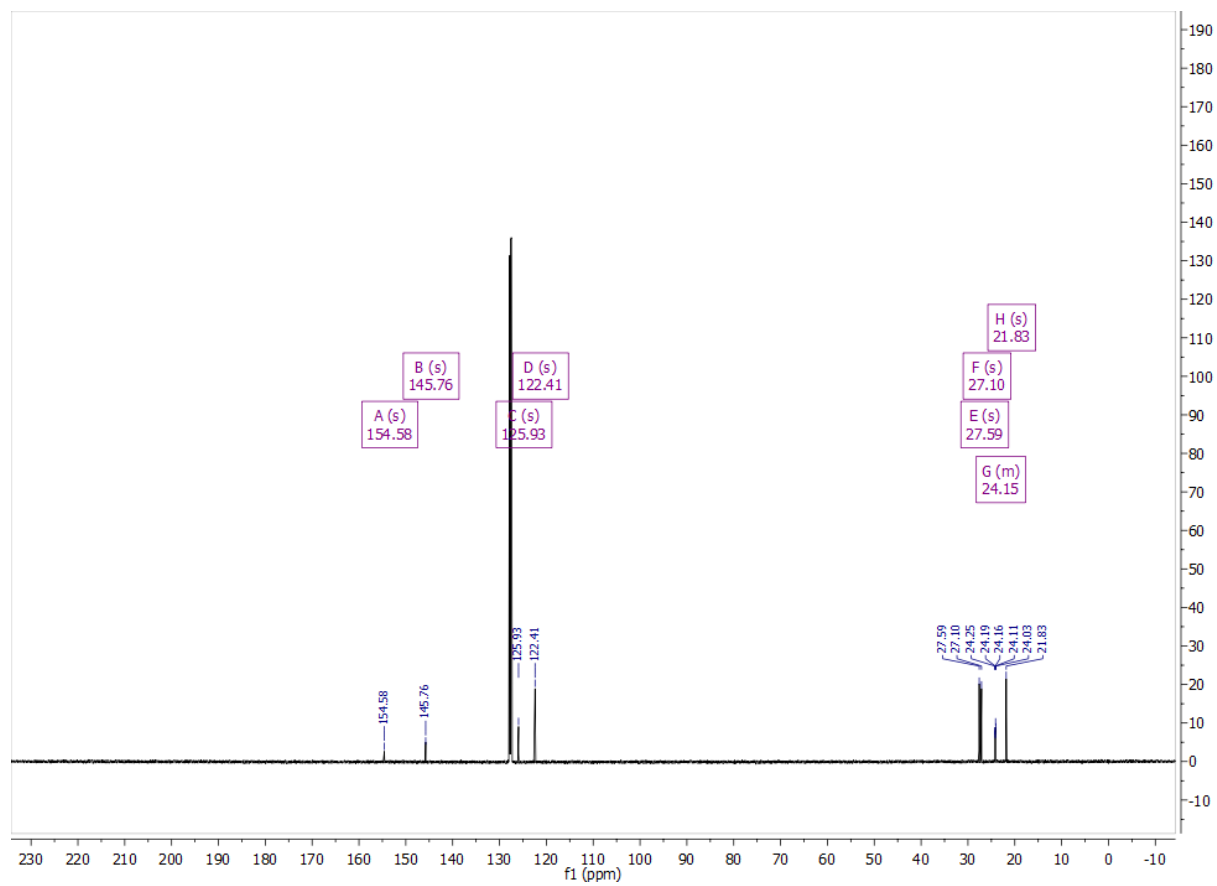


Figure 8.28 ^{13}C NMR of **Ru5** in C_6D_6 .

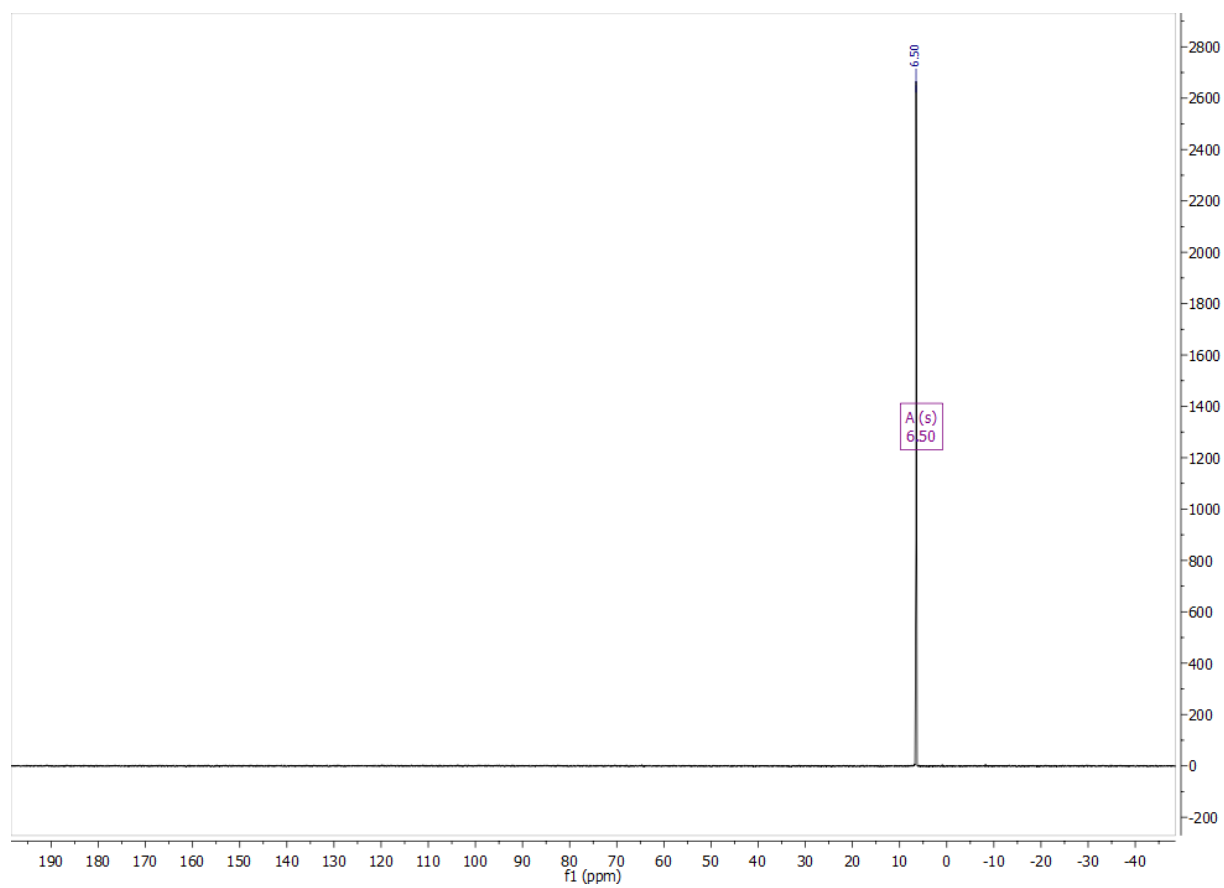


Figure 8.29 ^{31}P NMR of **Ru5** in C_6D_6 .

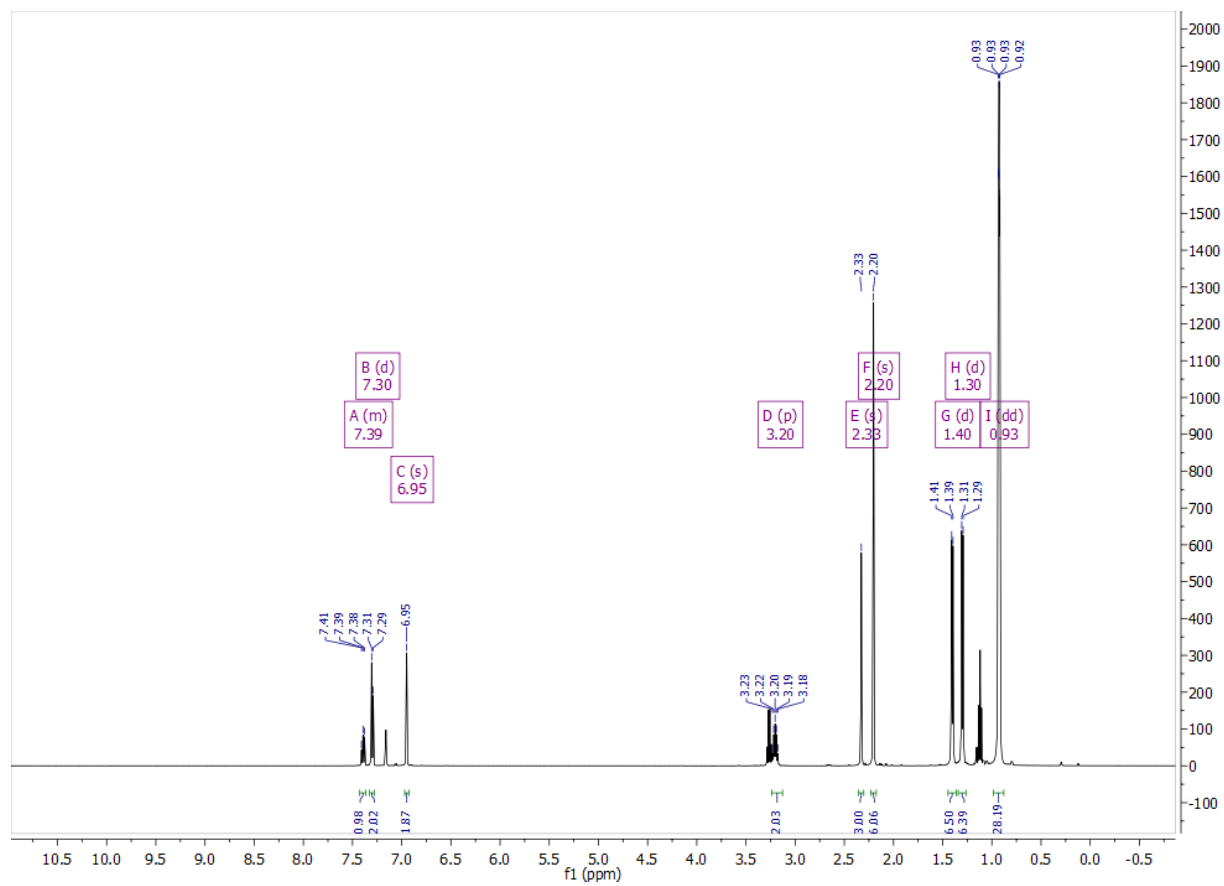


Figure 8.30 ^1H NMR of **Ru6** in C_6D_6 .

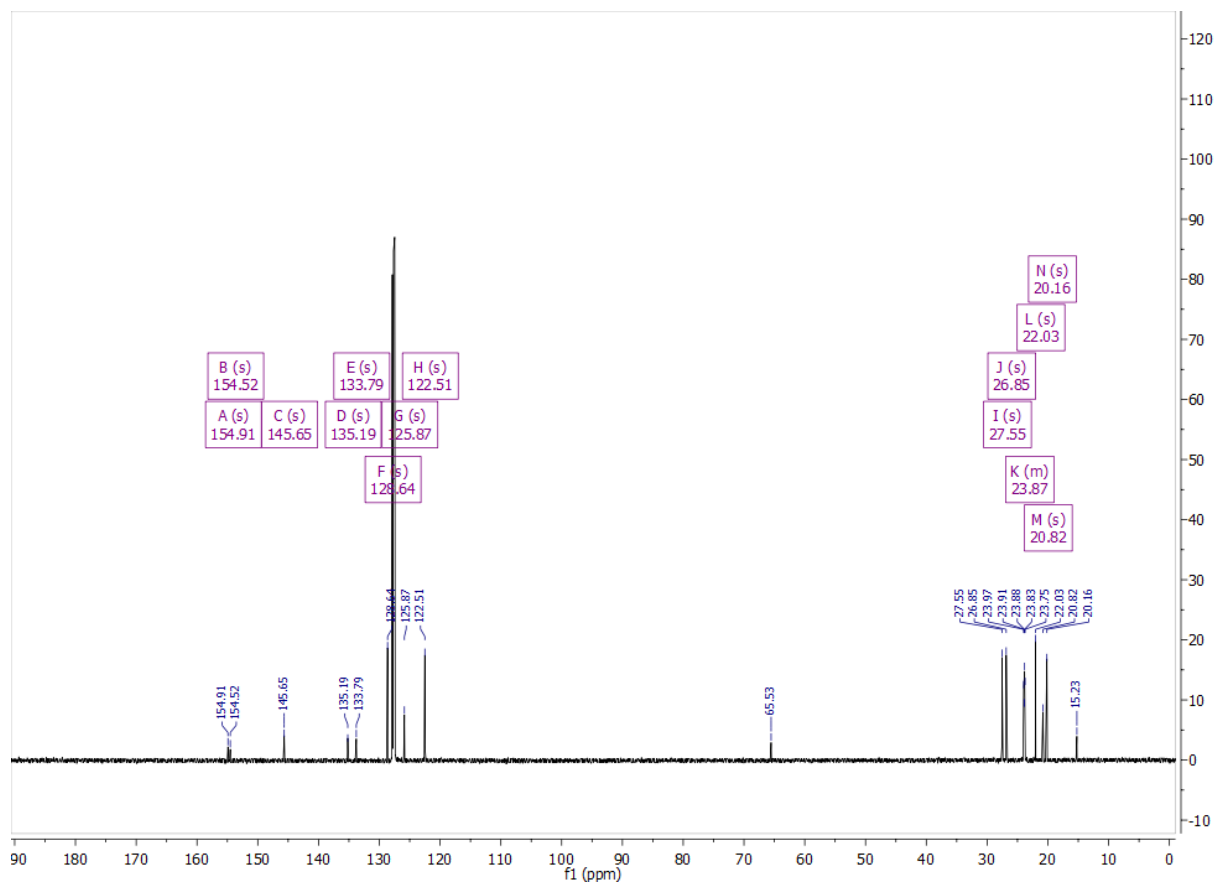


Figure 8.31 ^{13}C NMR of **Ru6** in C_6D_6 .

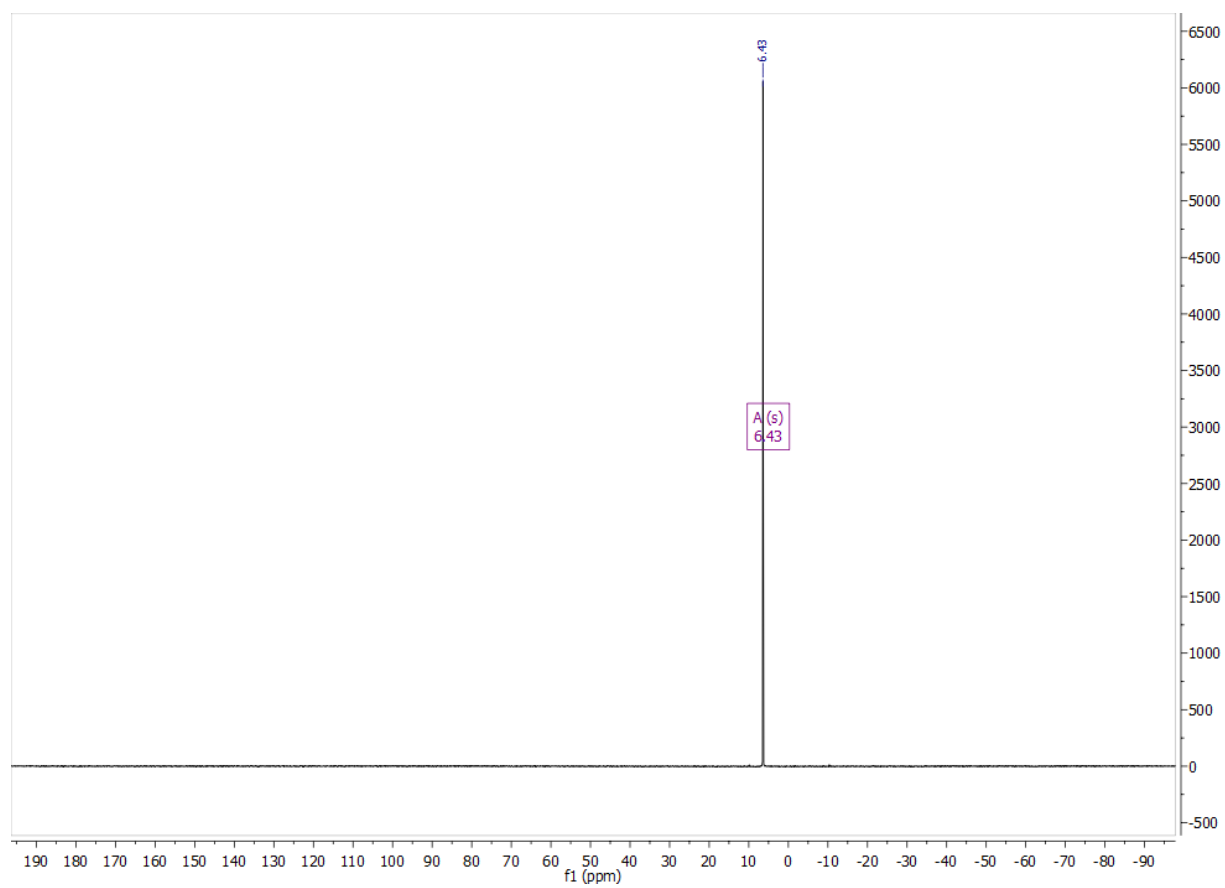


Figure 8.32 ^{31}P NMR of **Ru6** in C_6D_6 .

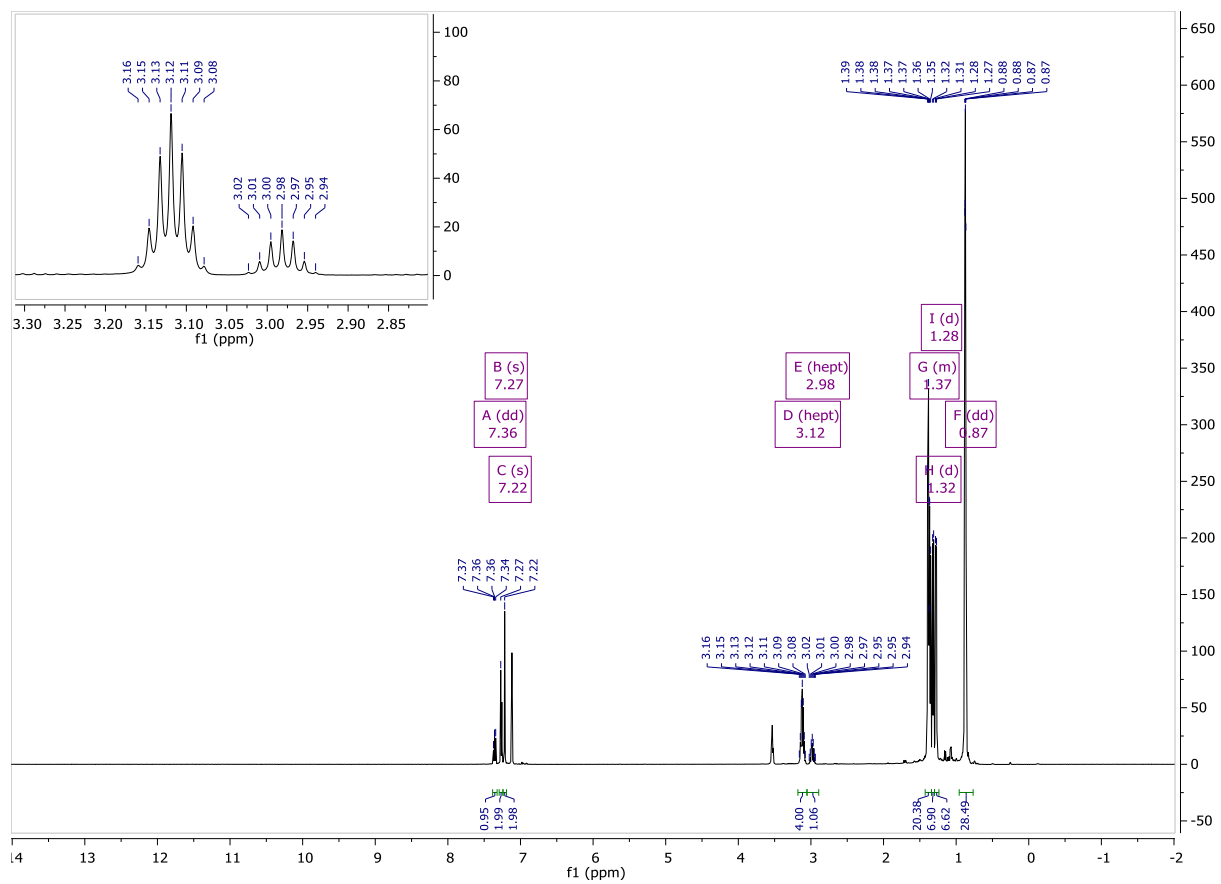


Figure 8.33 ^1H NMR of **Ru7** in C_6D_6 .

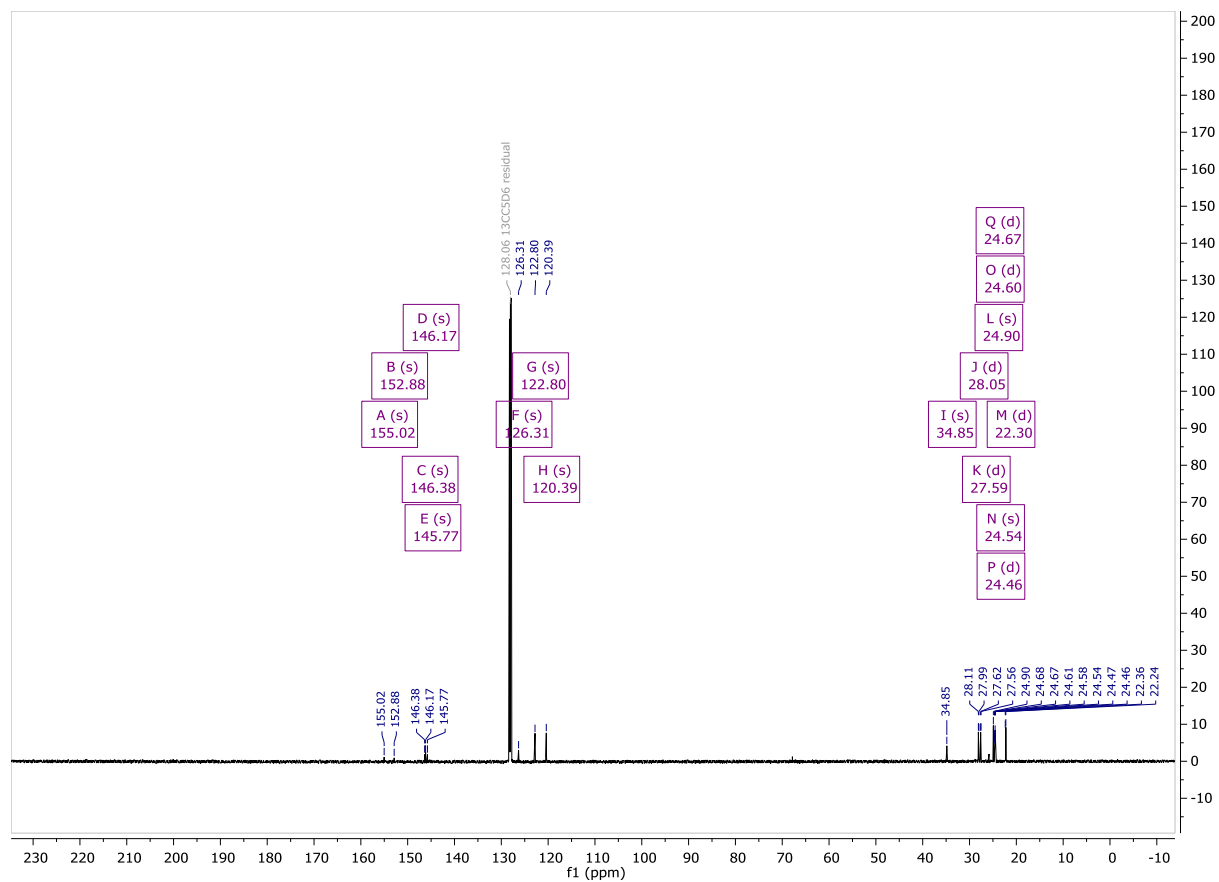


Figure 8.34 ^{13}C NMR of **Ru7** in C_6D_6 .

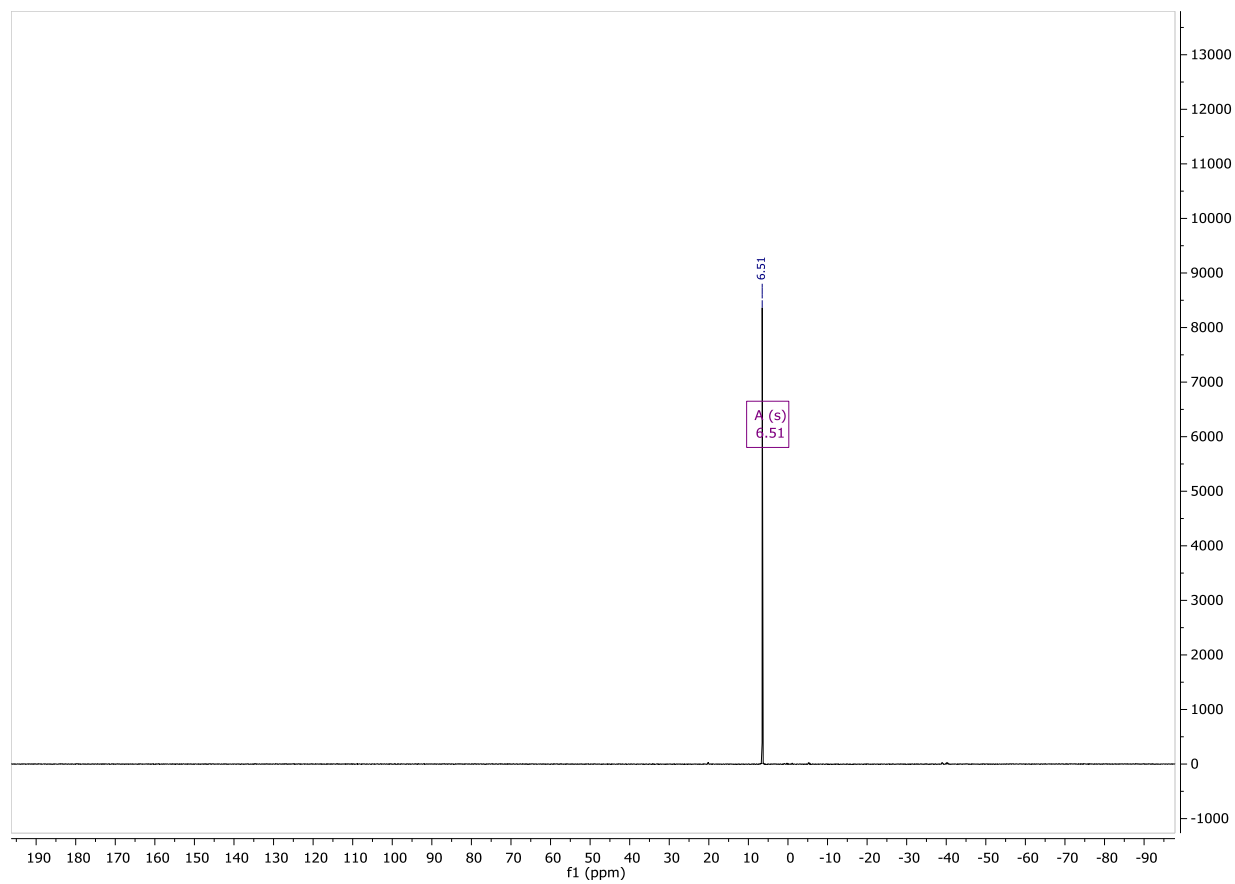


Figure 8.35 ^{31}P NMR of **Ru7** in C_6D_6 .

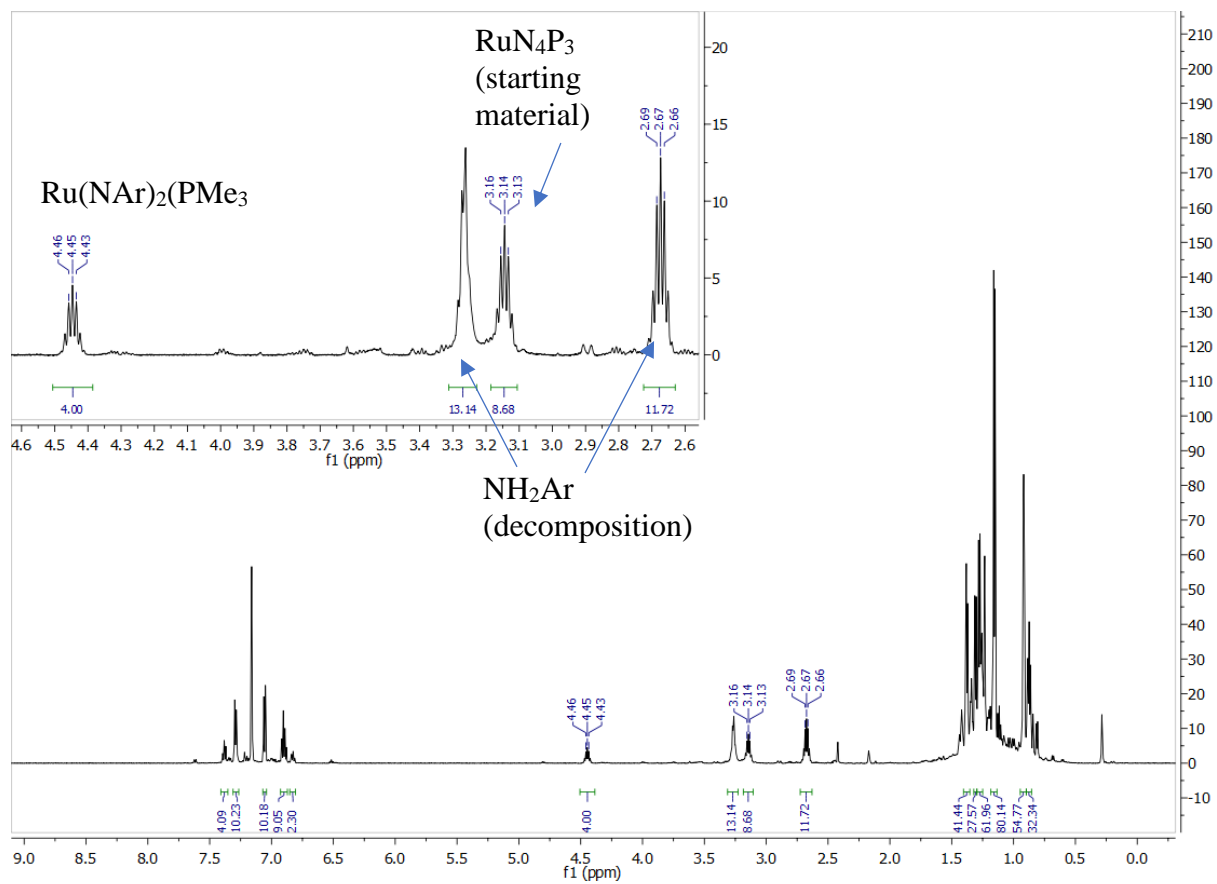


Figure 8.36 ^1H NMR of photolysis reaction containing a mixture of **Ru1**, **Ru5** (starting material), and H_2NAr (decomposition byproduct).

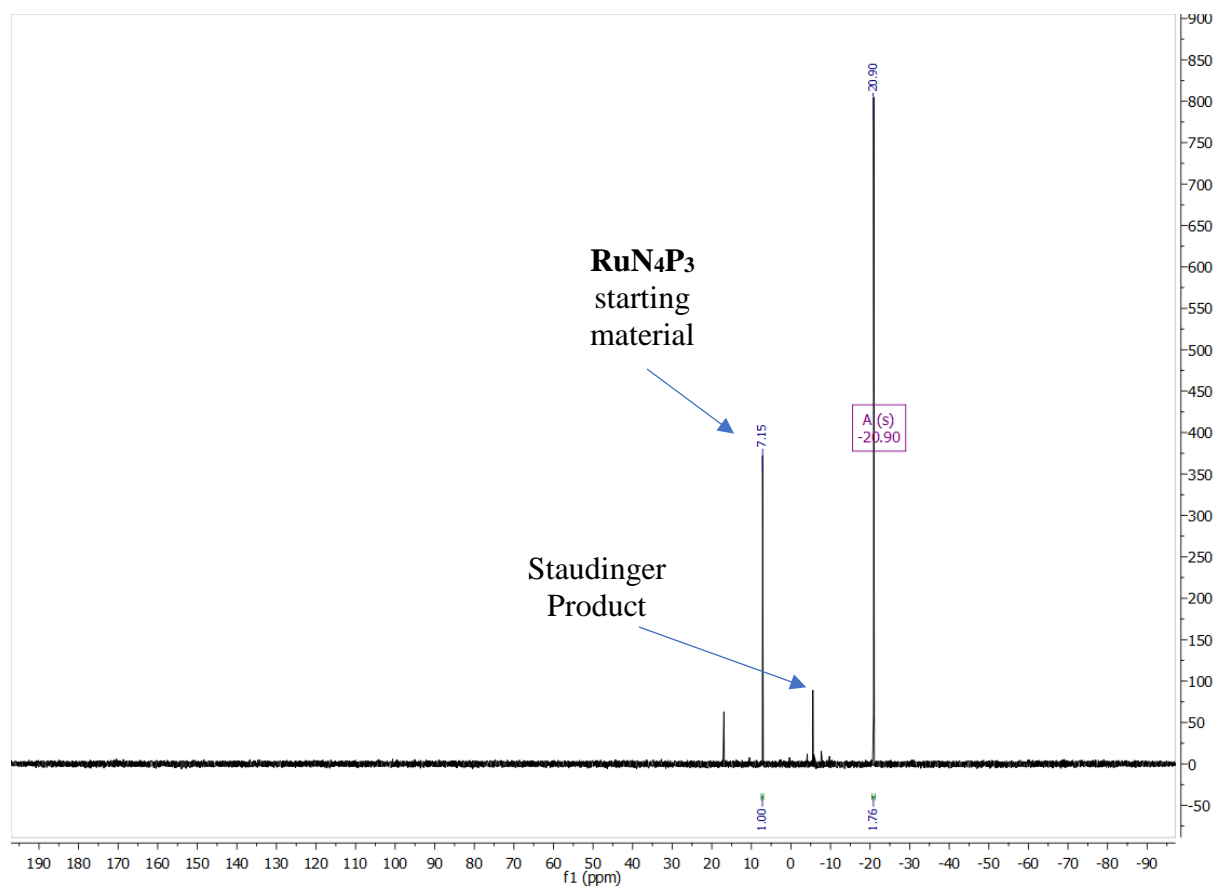


Figure 8.37 ^{31}P NMR spectrum of **Ru1**(after extraction and repeated recrystallization) in C_6D_6 .

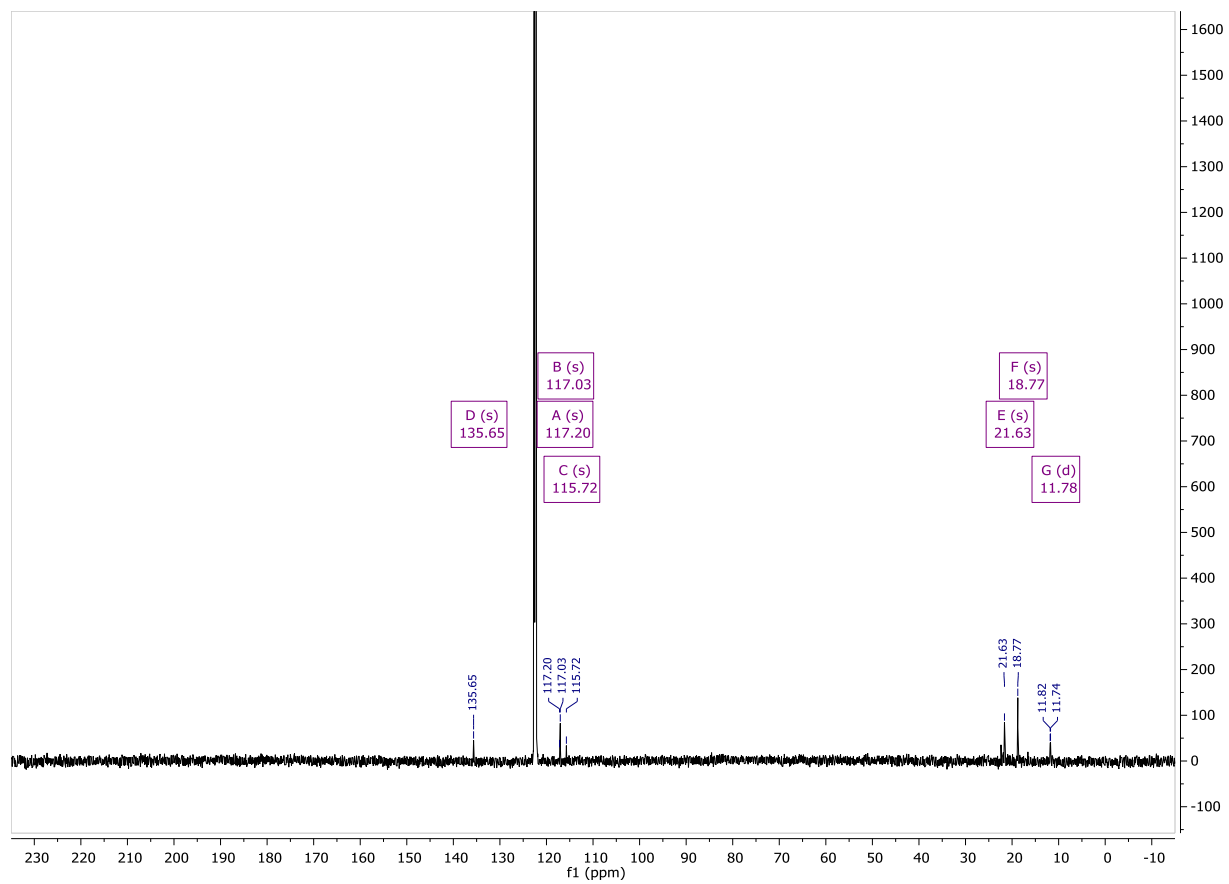


Figure 8.38 ^{13}C NMR spectrum of **Ru1** in C_6D_6 .

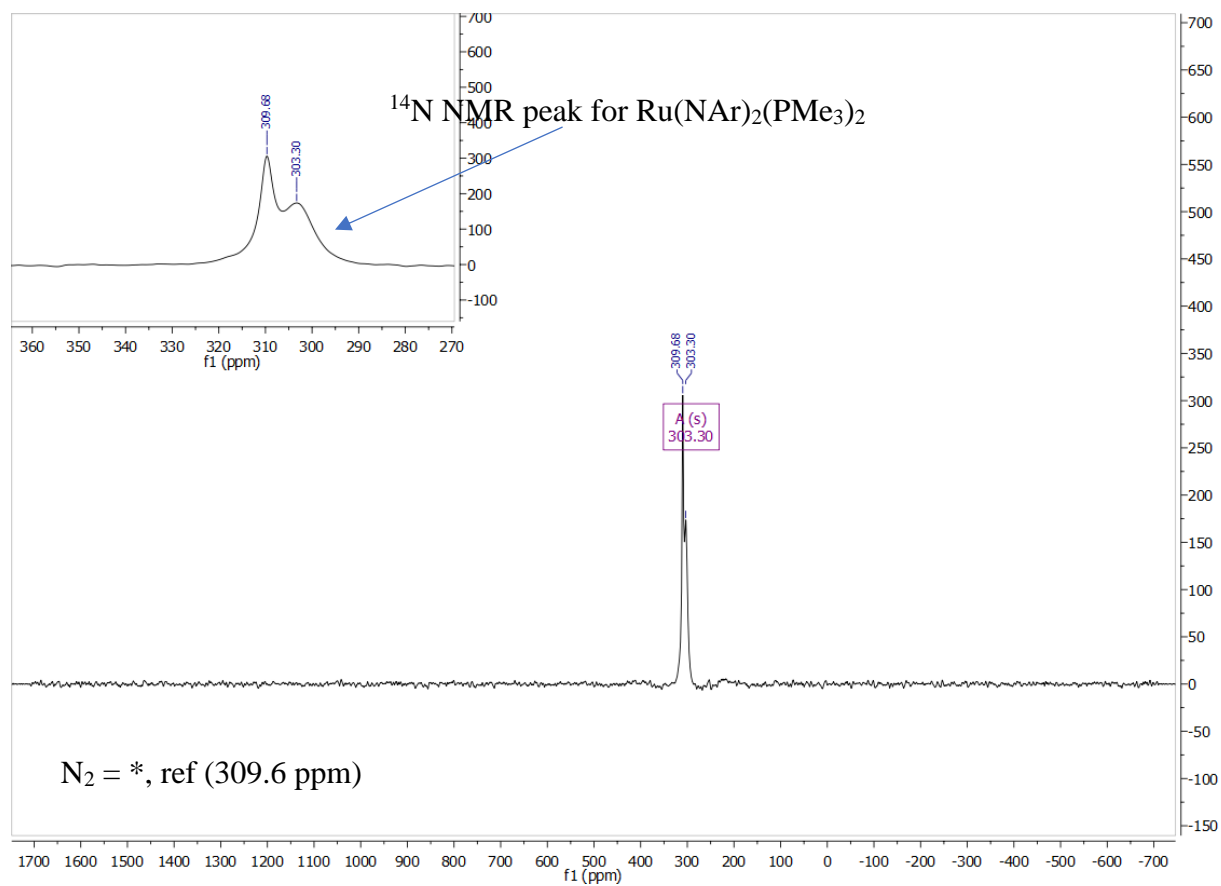


Figure 8.39 ^{14}N NMR of **Ru1** in C_6D_6 .

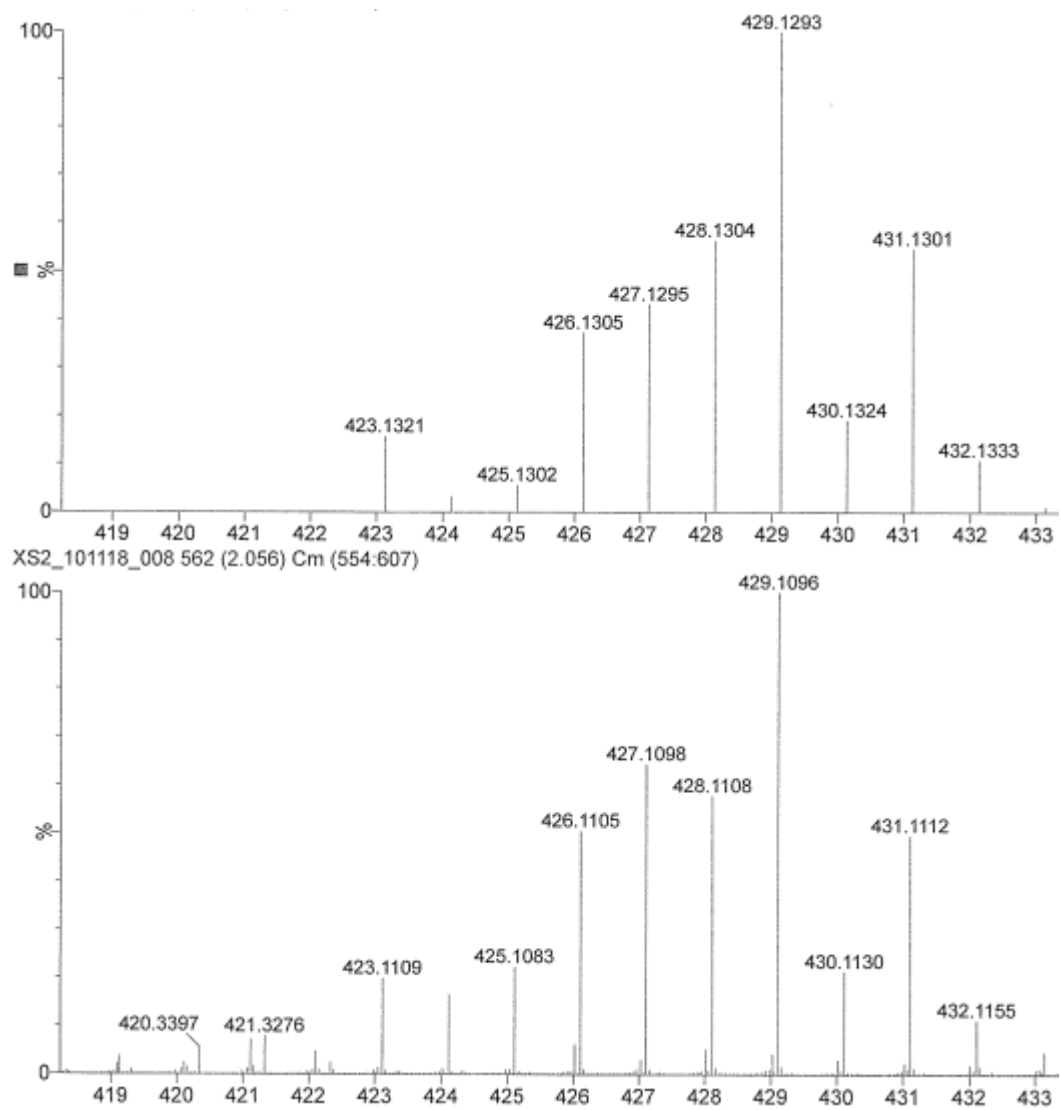


Figure 8.40 QTOF-HRMS fragmentation patterns (top) calculated and (bottom) experimental for **Ru1**.

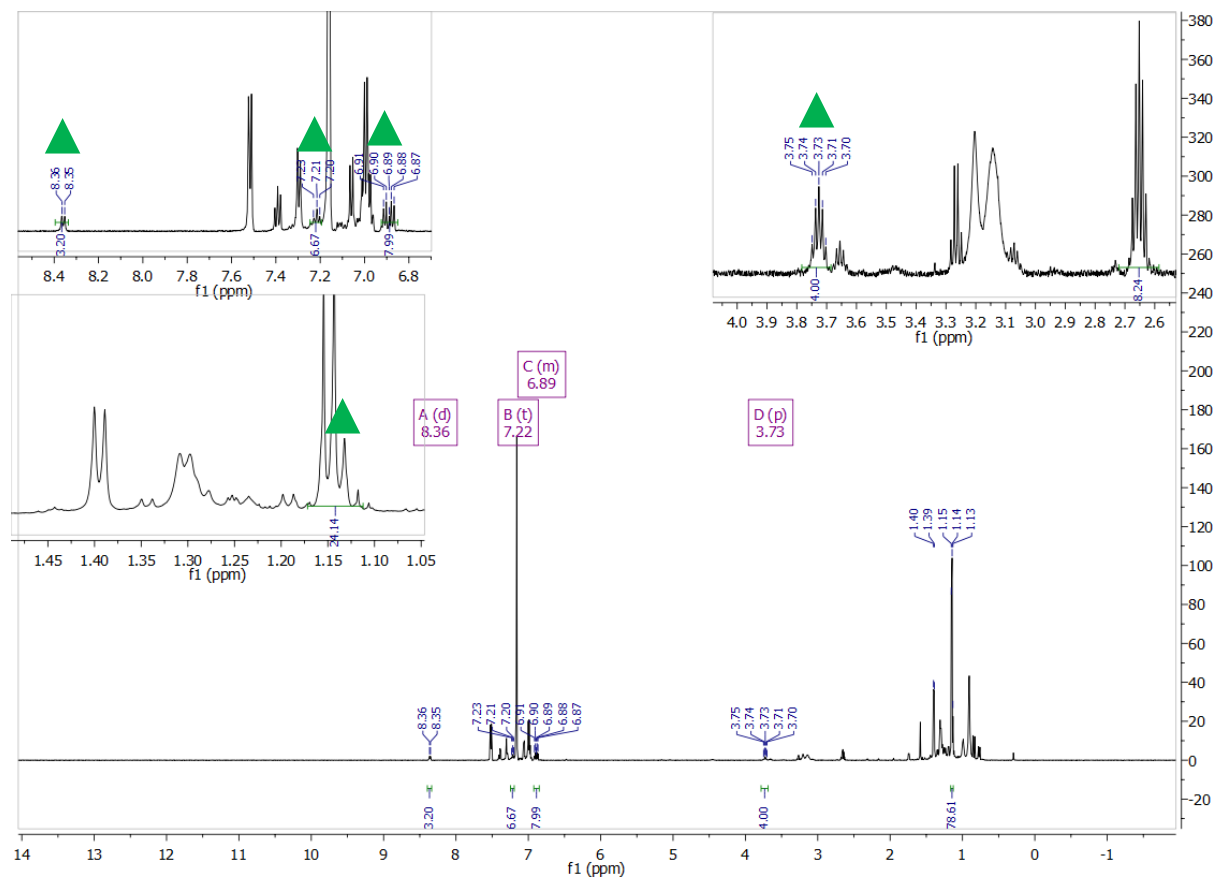


Figure 8.41 ^1H NMR spectrum of $\text{Ru}(\text{NAr})_2(\eta^2\text{-diphenylacetylene})$ containing diphenylacetylene (excess) and H_2NAr impurities.

Note: in the above spectrum, peaks assigned with multiplet values and denoted by green triangles correspond to the title complex formed *in situ*. The peaks noted match very closely the splitting pattern and chemical shifts of those reported for the osmium analogue of this complex by Schrock, et. al.²³

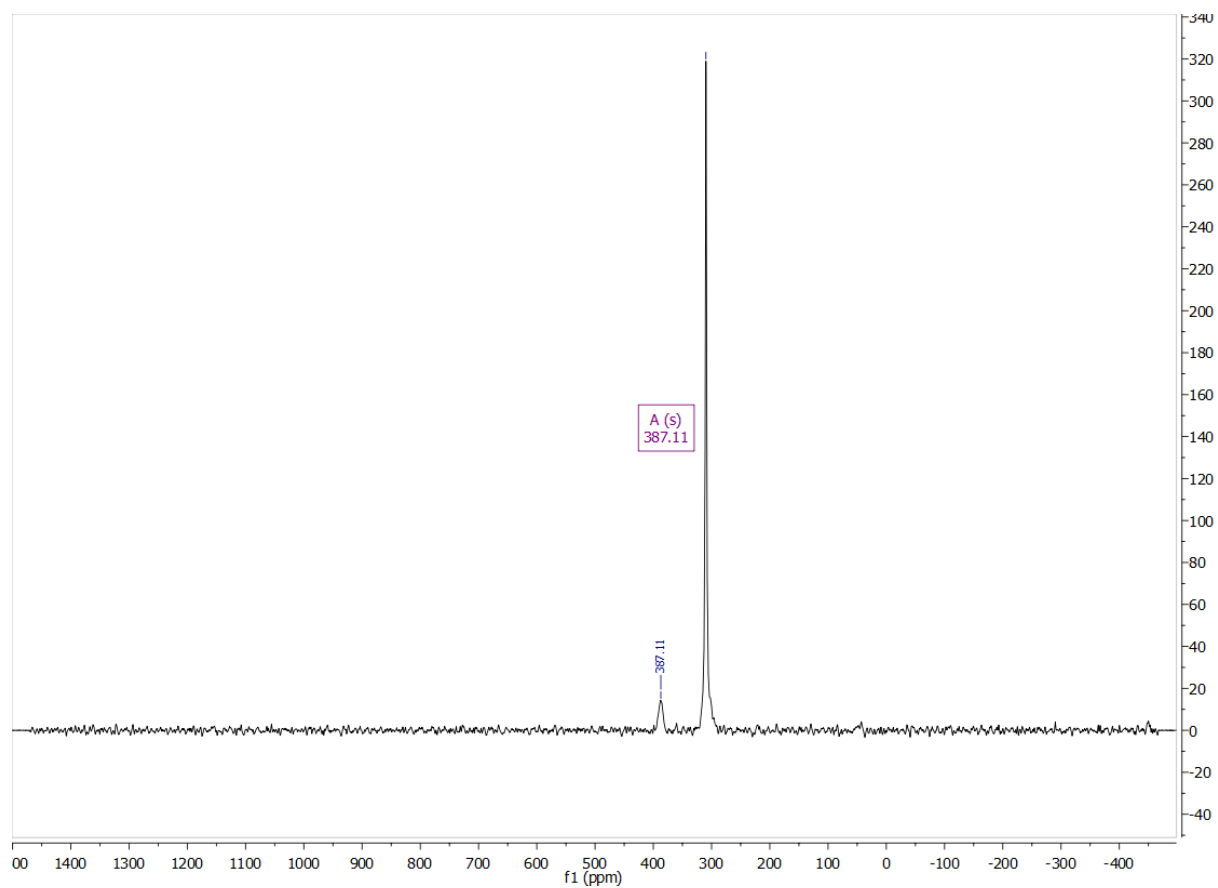


Figure 8.42 ^{14}N NMR spectrum of $\text{Ru}(\text{NAr})_2(\eta^2\text{-diphenylacetylene})$ in C_6D_6 (in situ).

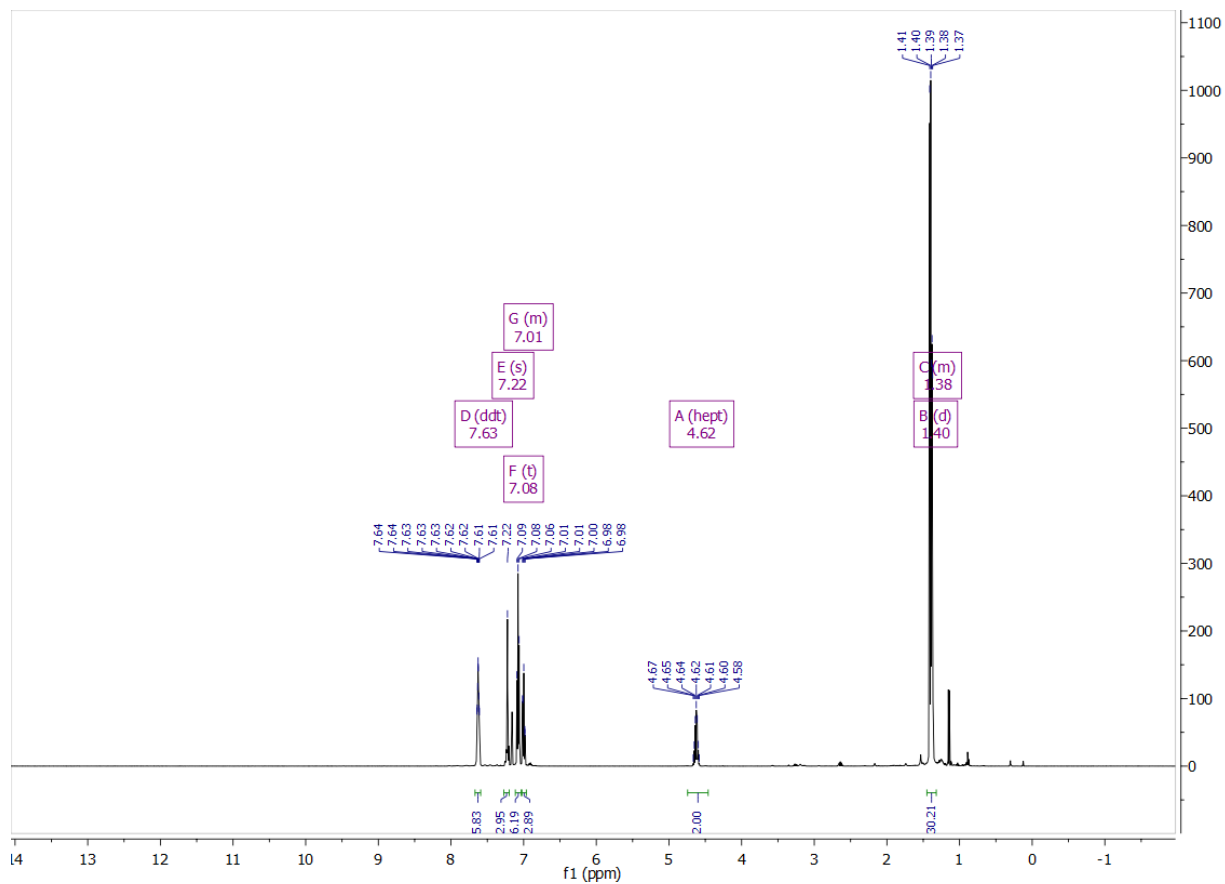


Figure 8.43 ^1H NMR of **Ru8** in C_6D_6 .

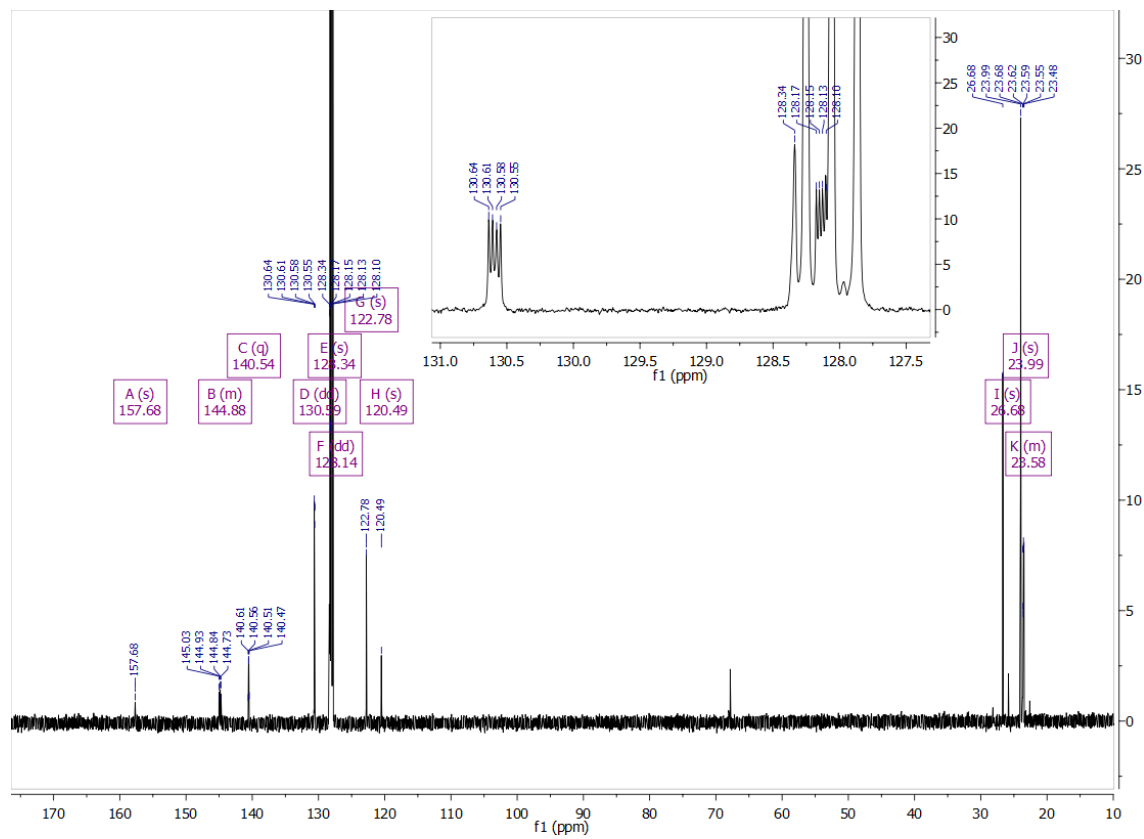


Figure 8.44 ^{13}C NMR of **Ru8** in C_6D_6 .

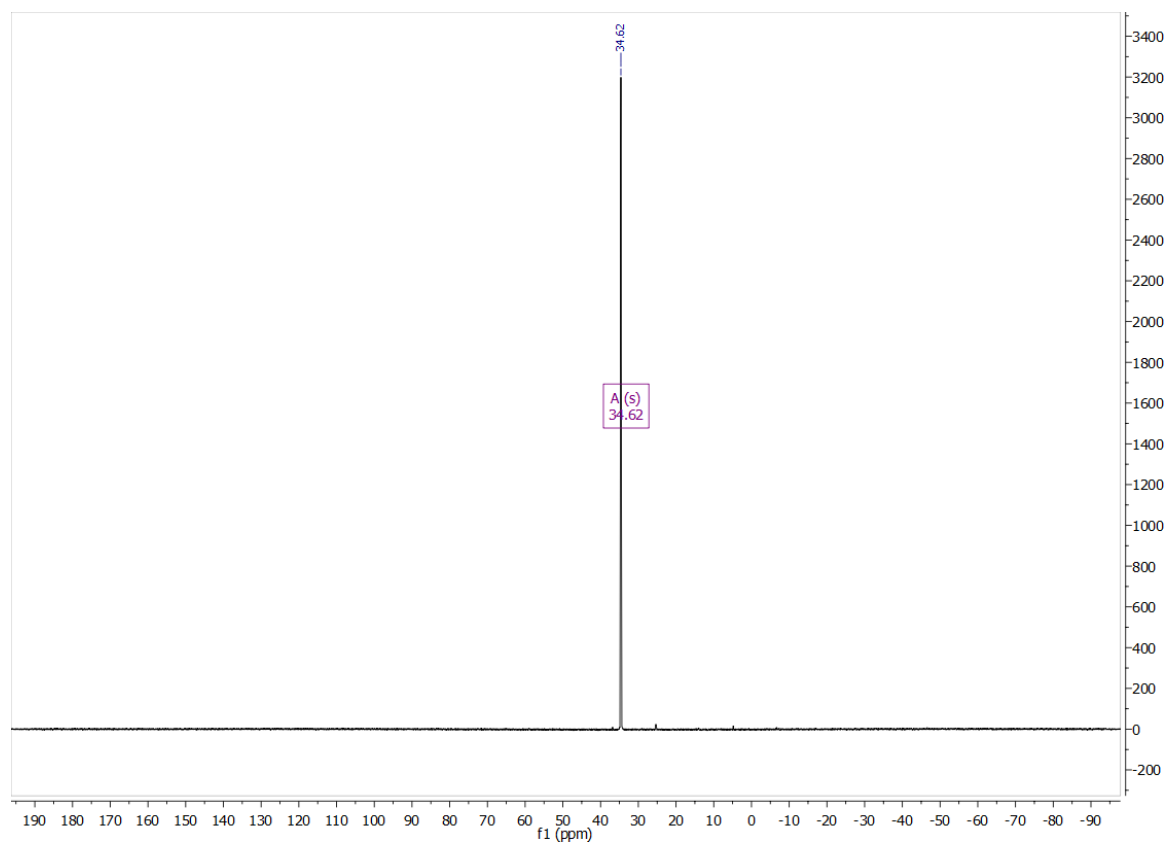


Figure 8.45 ^{31}P NMR of **Ru8** in C_6D_6 .

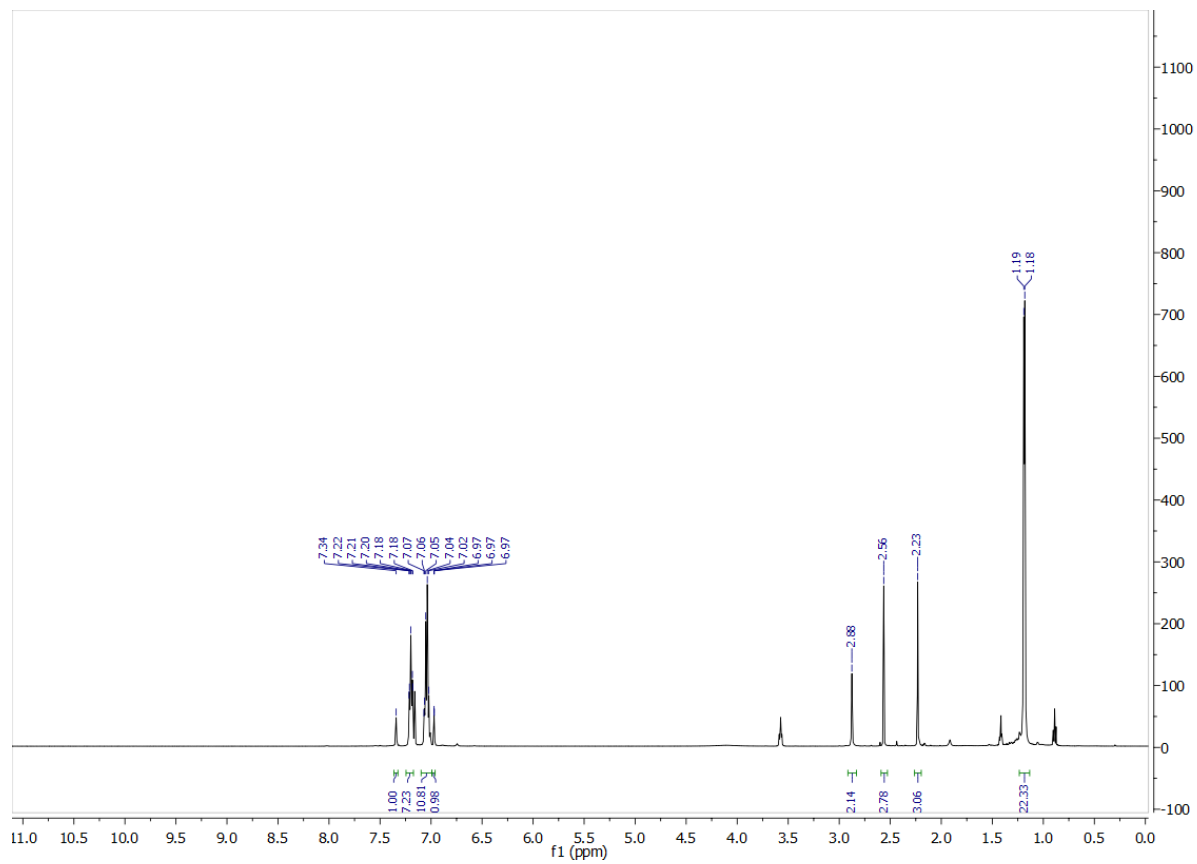


Figure 8.46 ^1H NMR of **Ru9** in C_6D_6 .

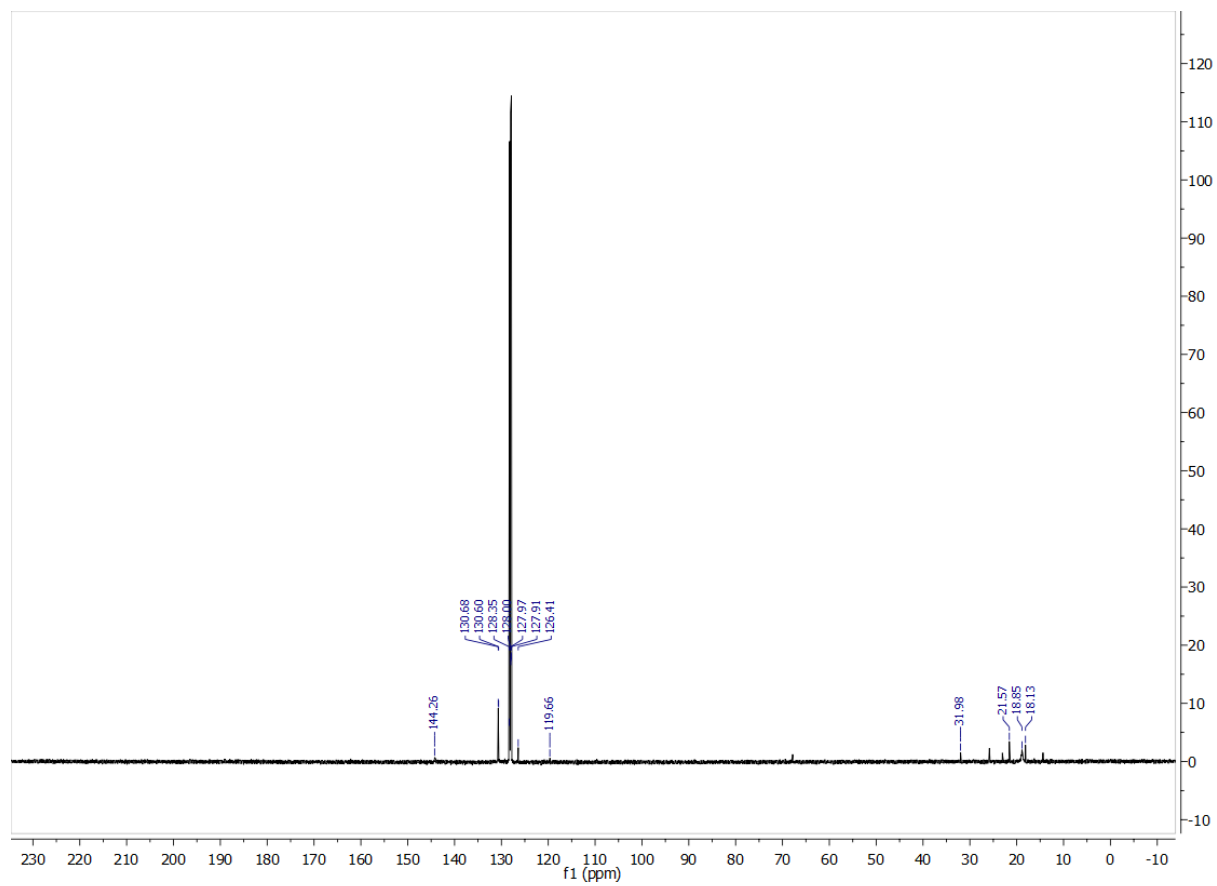


Figure 8.47 ^{13}C NMR of **Ru9** in C_6D_6 .

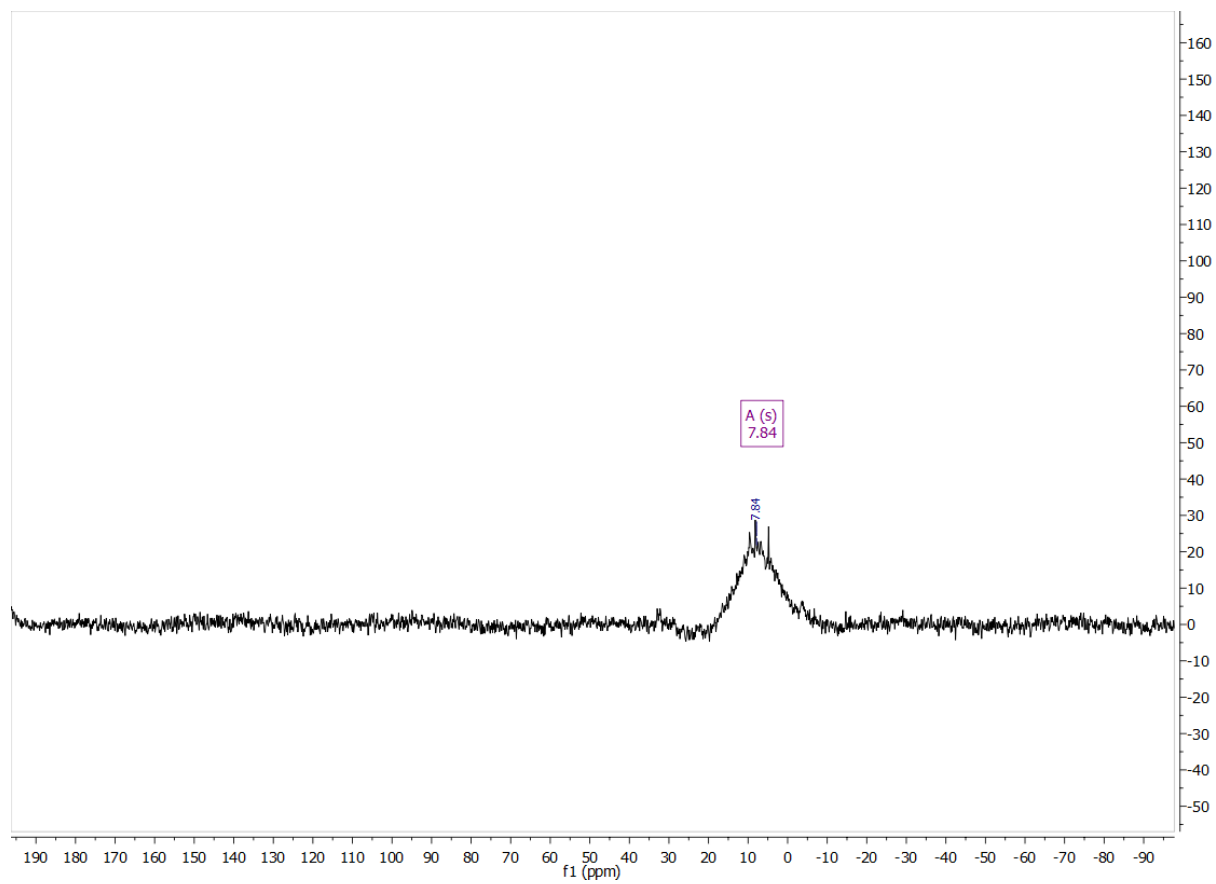


Figure 8.48 ^{31}P NMR of **Ru9** in C_6D_6 .

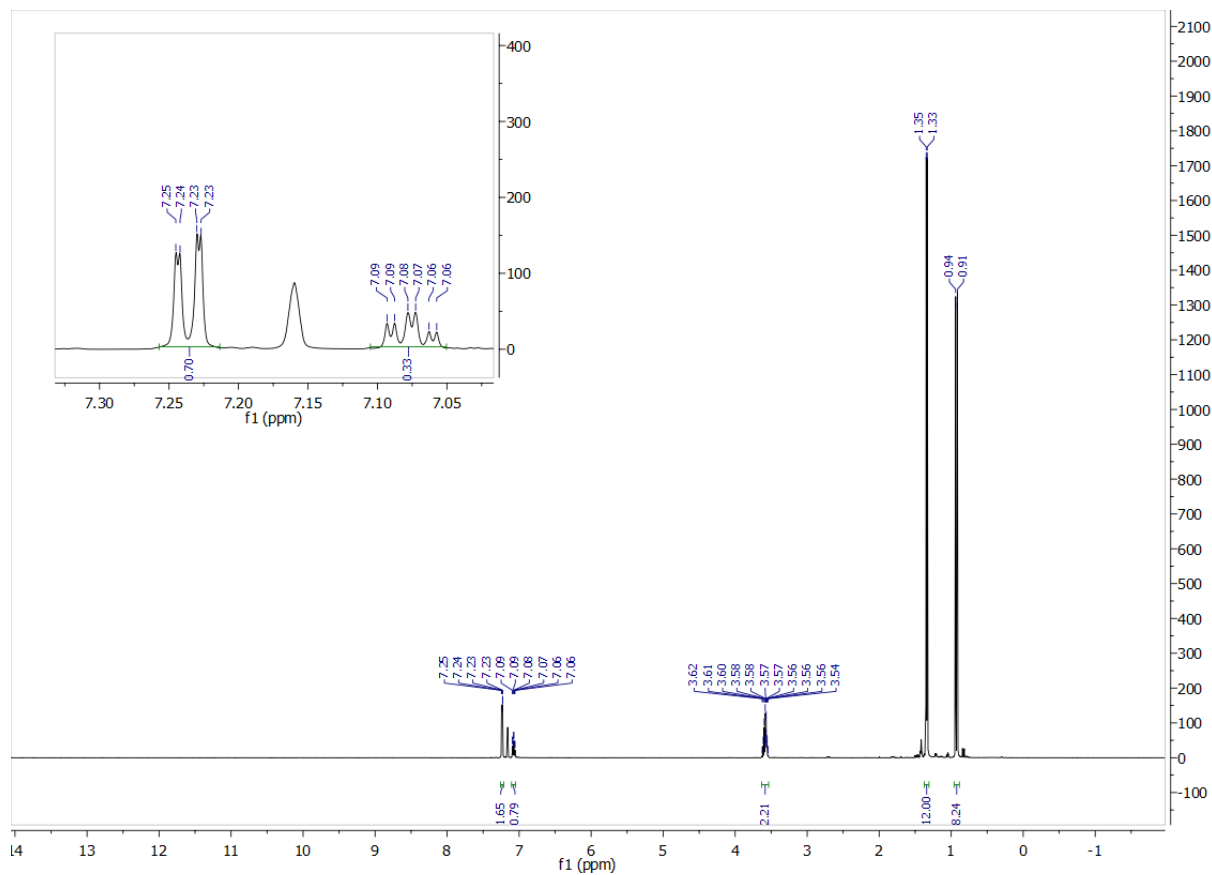


Figure 8.49 ^1H NMR of ArNPMe_3 in C_6D_6 .

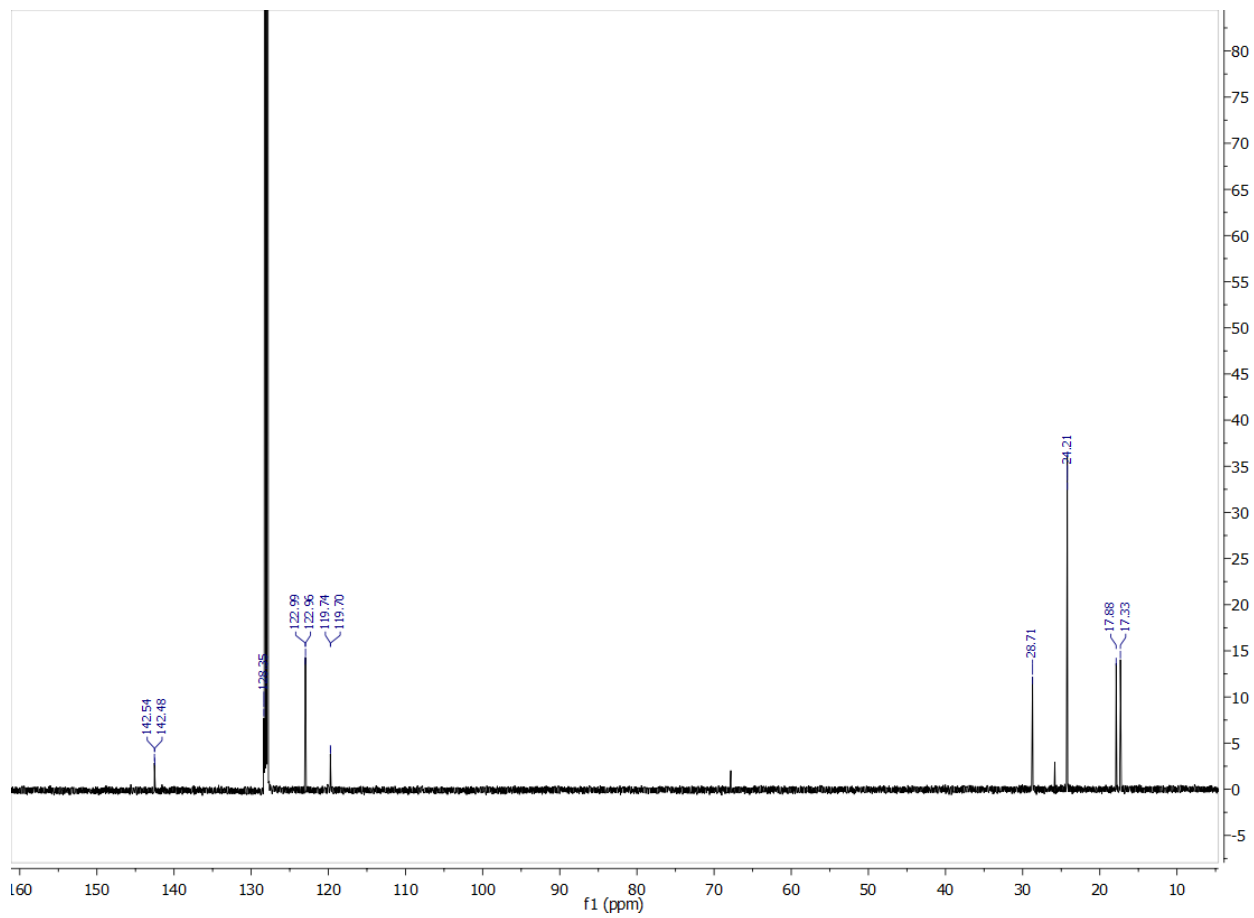


Figure 8.50 ^{13}C NMR of ArNPMe_3 in C_6D_6 .

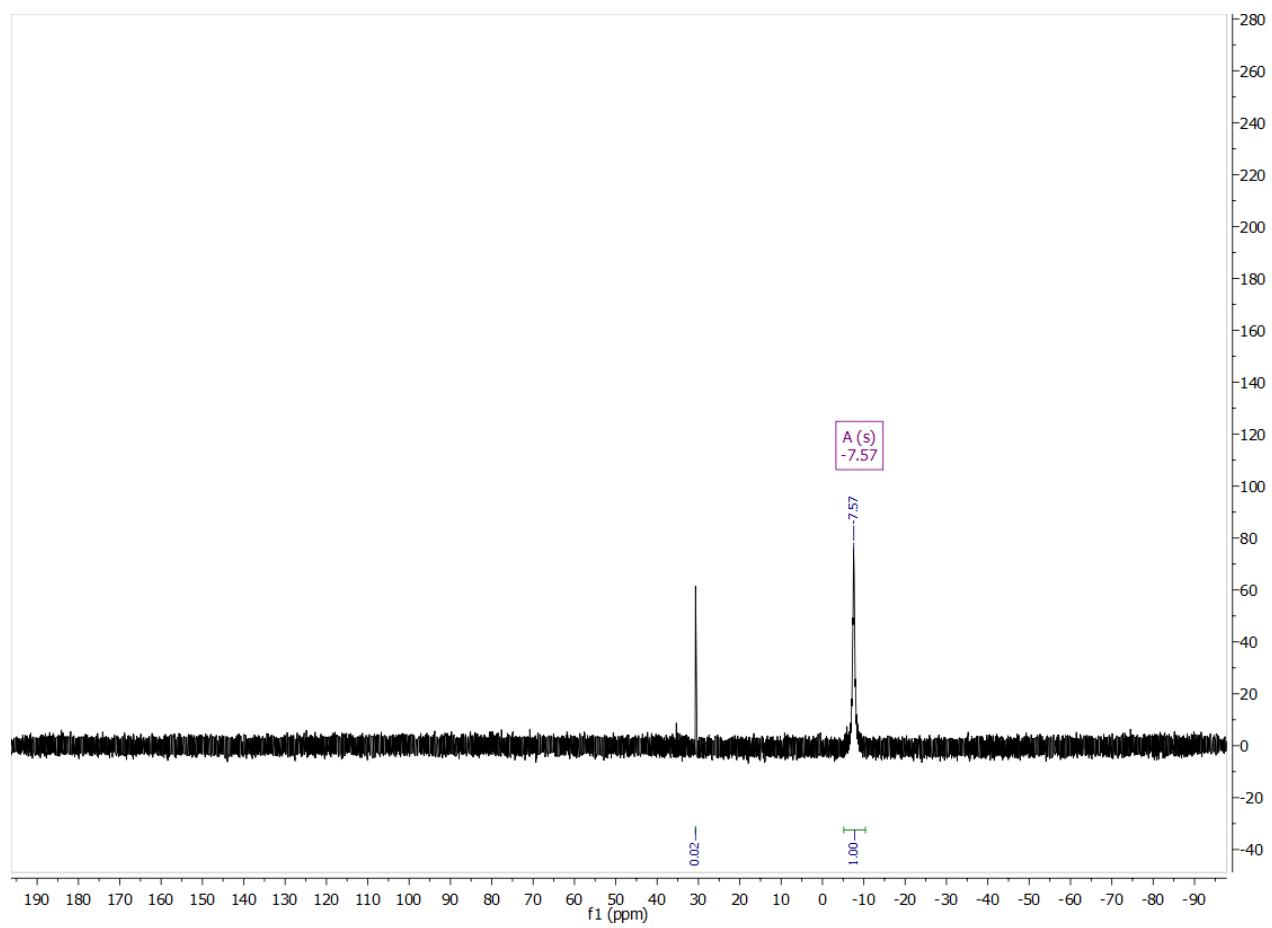


Figure 8.51 ^{31}P NMR of ArNPMe_3 in C_6D_6 .

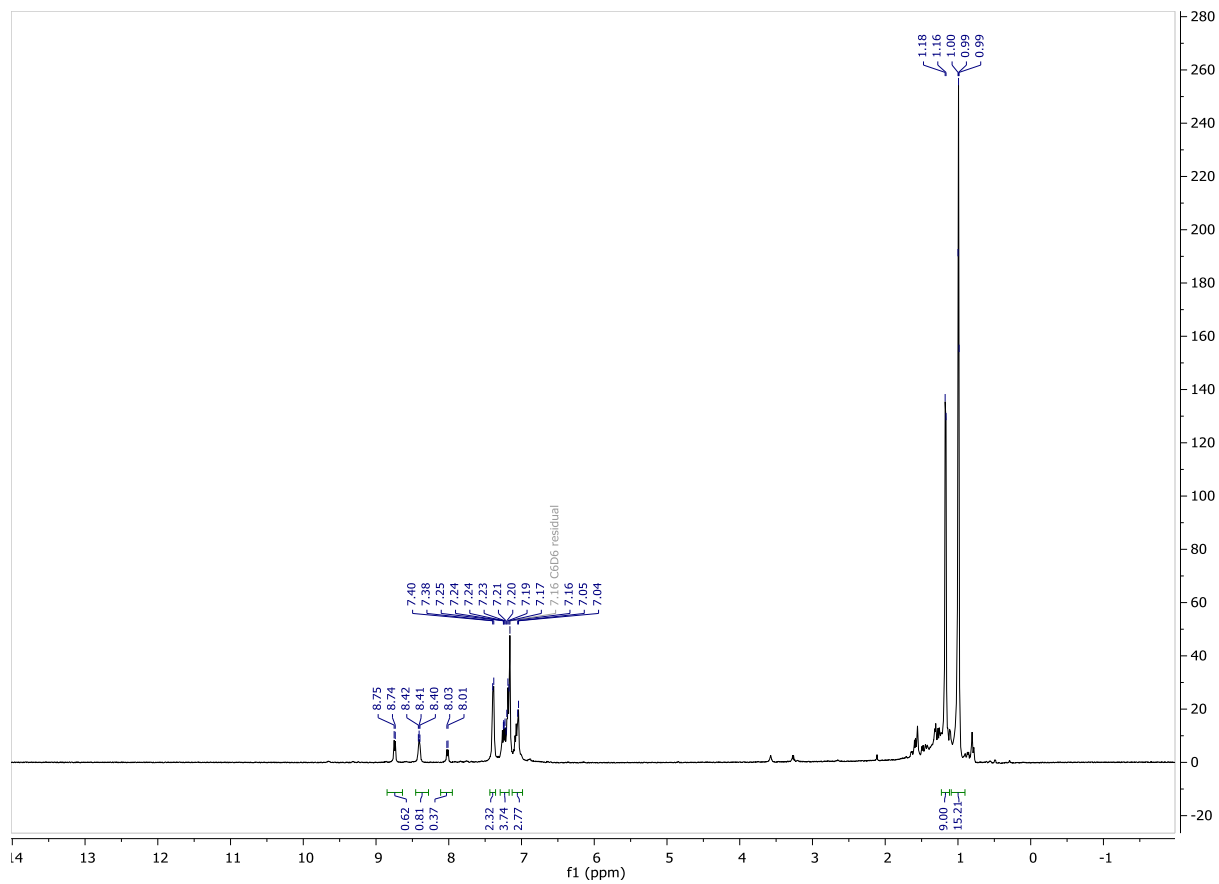


Figure 8.52 ^1H NMR of **Os3** in C_6D_6 .

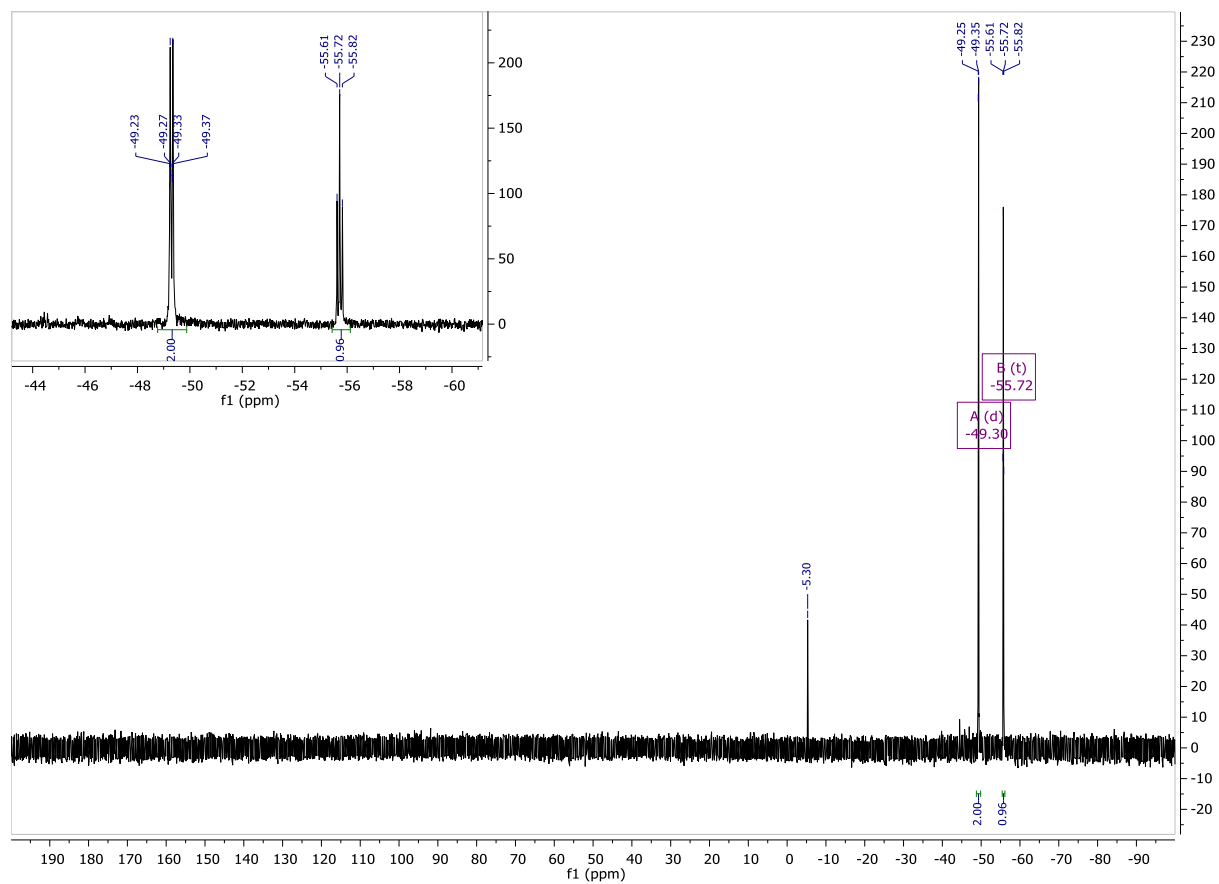


Figure 8.53 ^{31}P NMR of Os_3 in C_6D_6 .

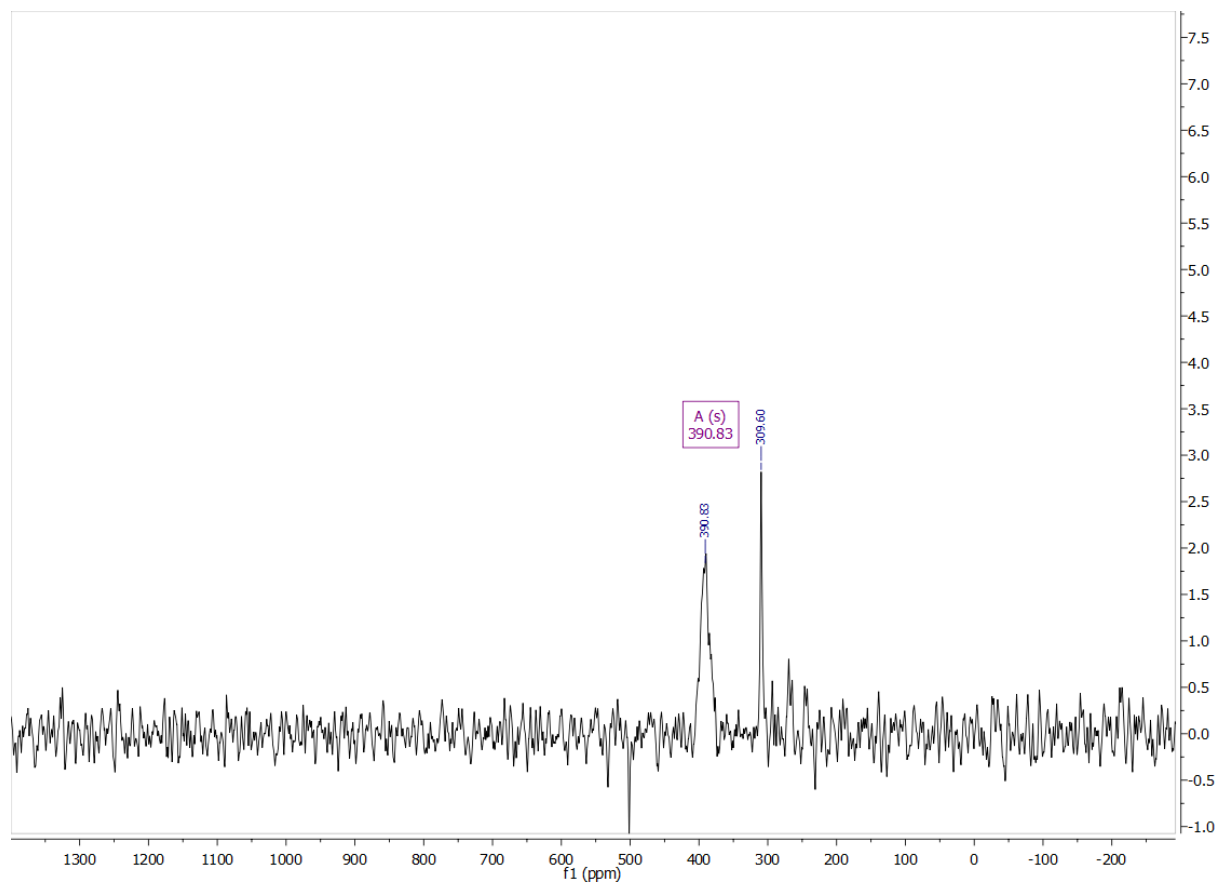


Figure 8.54 ^{14}N NMR of $\text{Os}(\text{NAr})_2(\text{O})_2$.

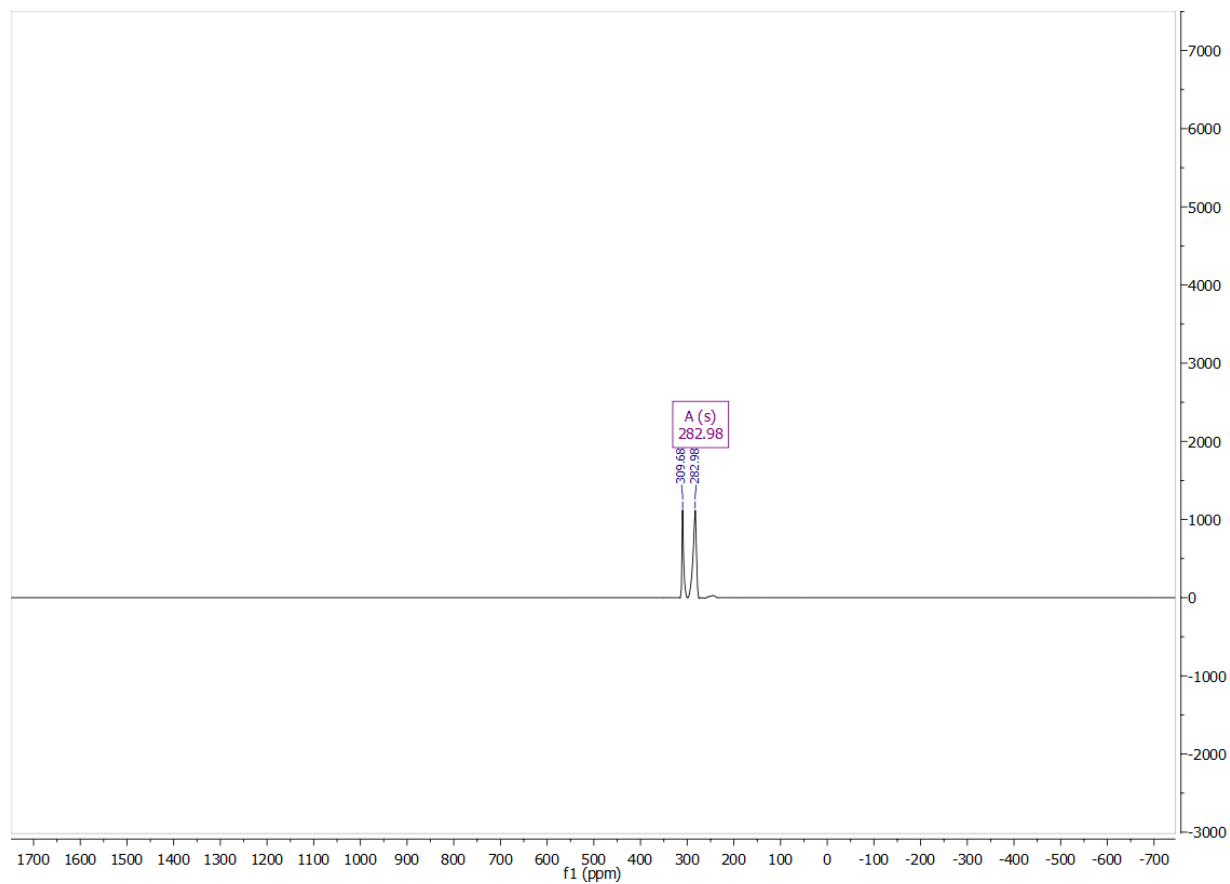


Figure 8.55 ^{14}N NMR of $\text{Os}(\text{NAr})_2(\text{PMe}_3)_2$.

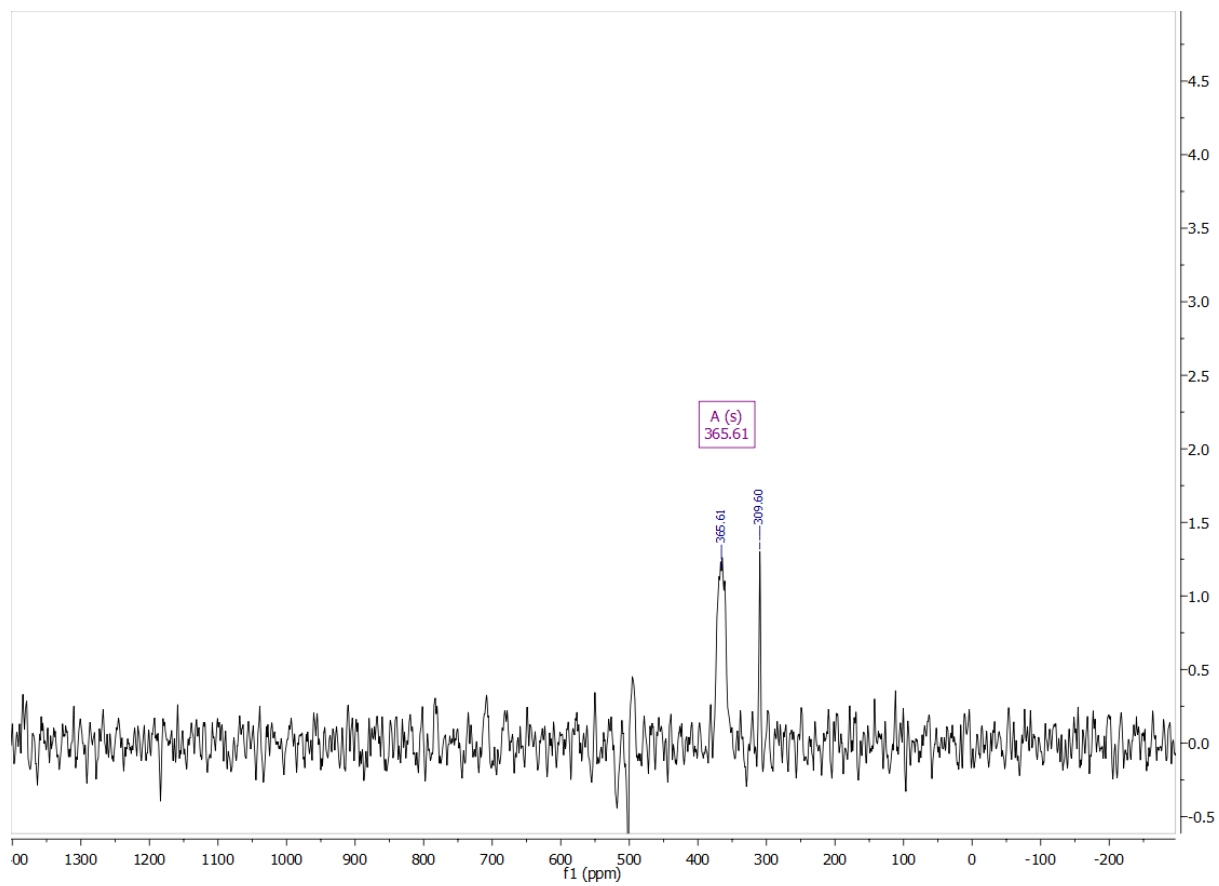


Figure 8.56 ^{14}N NMR of $\text{Os}(\text{NAr})_2(\eta_2\text{-diphenylacetylene})$.

UV-Vis Spectroscopy of Several Ru Complexes

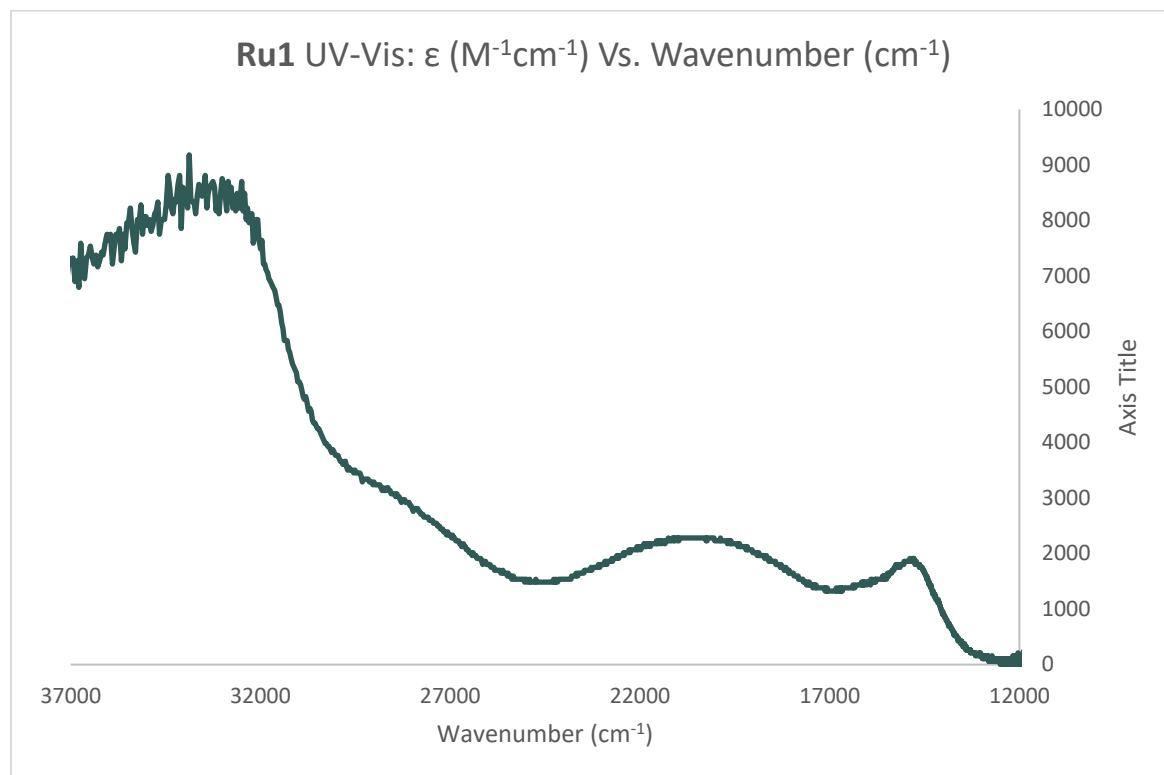


Figure 8.57 Plot of ϵ vs wavenumber for **Ru1** (0.000188 M in THF).

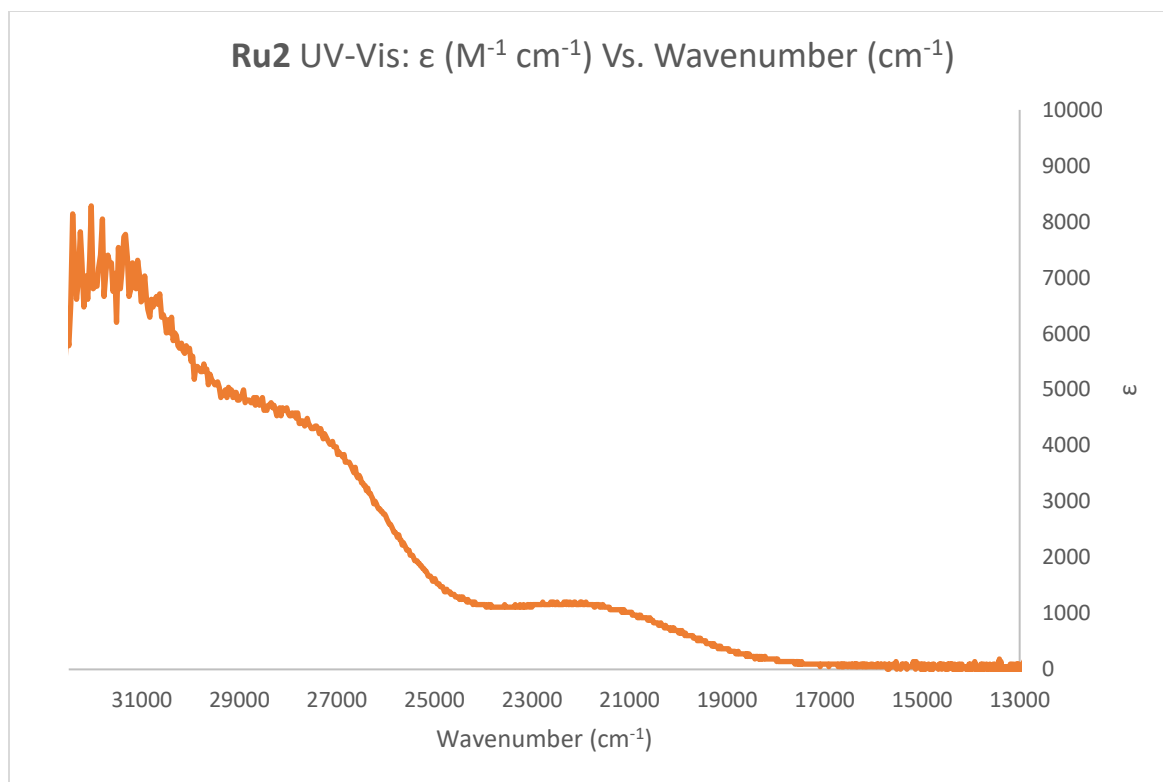


Figure 8.58 Plot of ϵ vs wavenumber for **Ru2** (0.00023 M in THF).

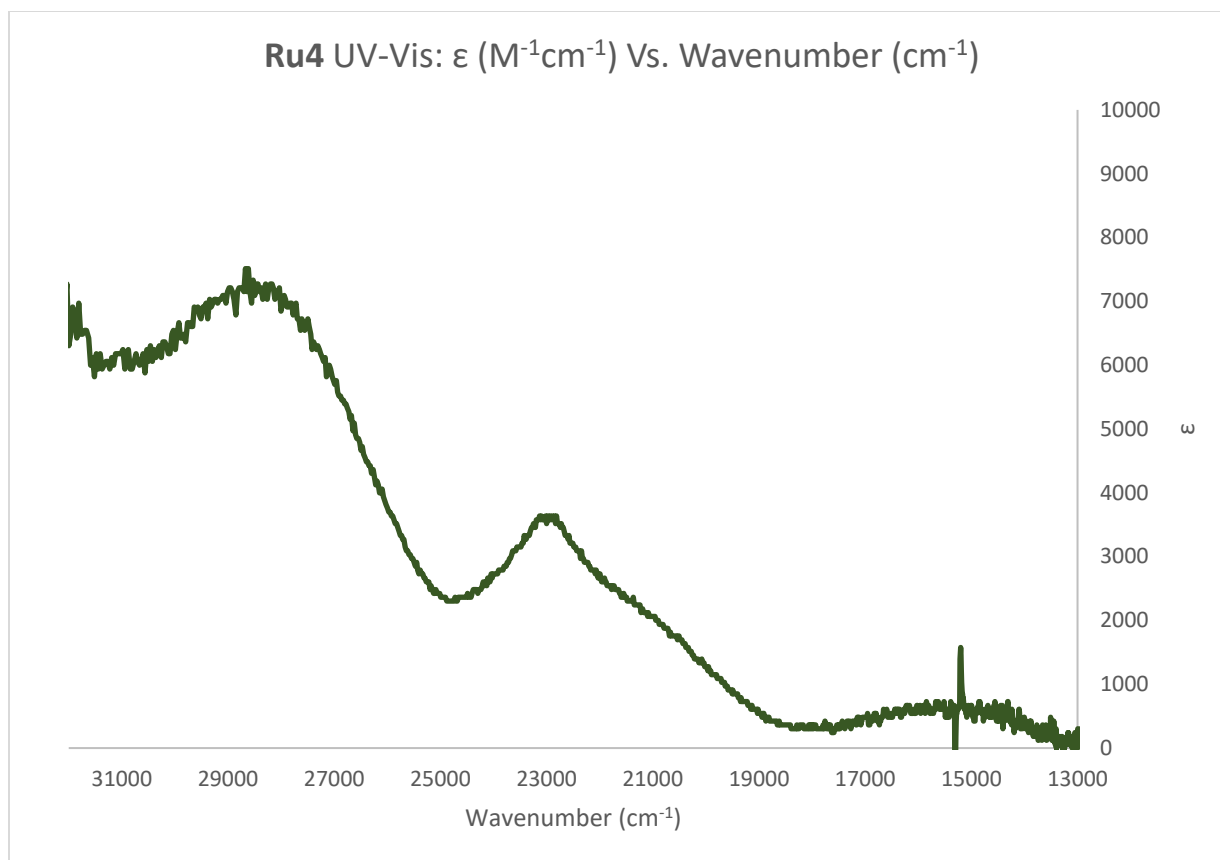


Figure 8.59 Plot of ϵ vs wavenumber for **Ru4** (0.00019 M in THF).

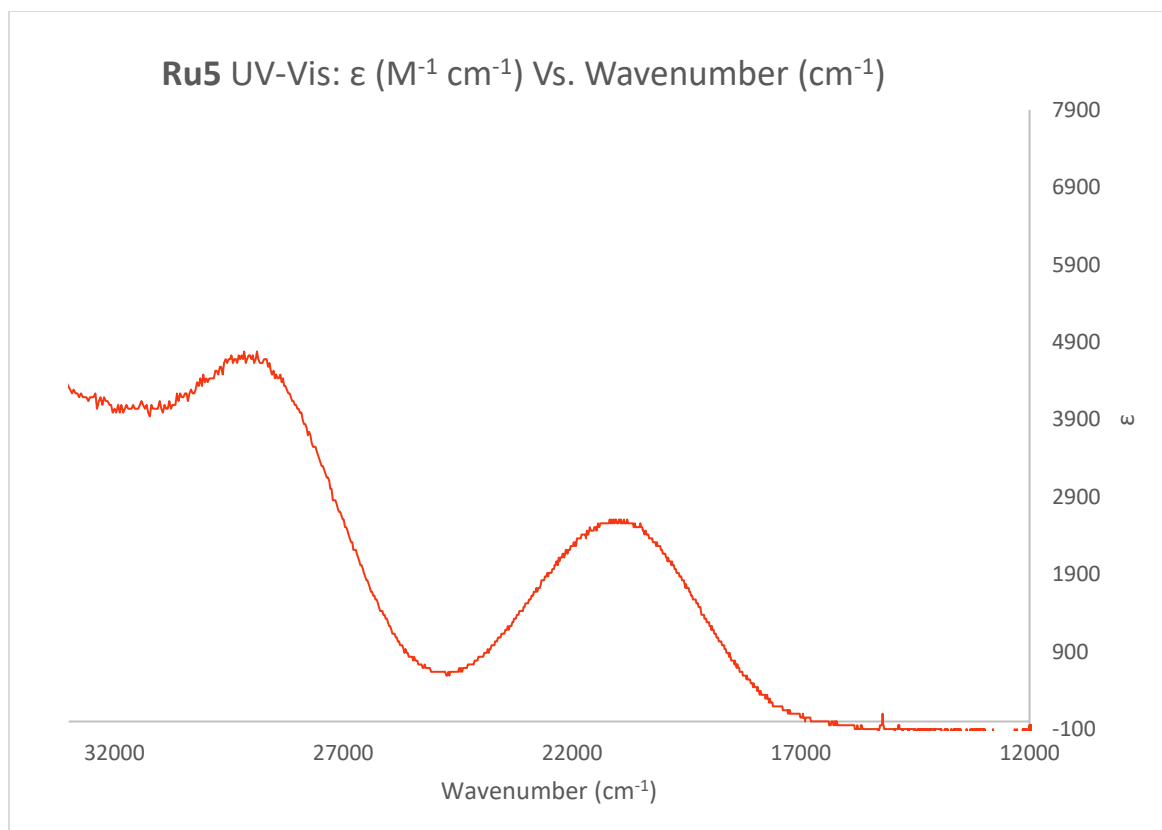


Figure 8.60 Plot of ϵ vs. wavenumber for **Ru5** (0.000203 M in THF).

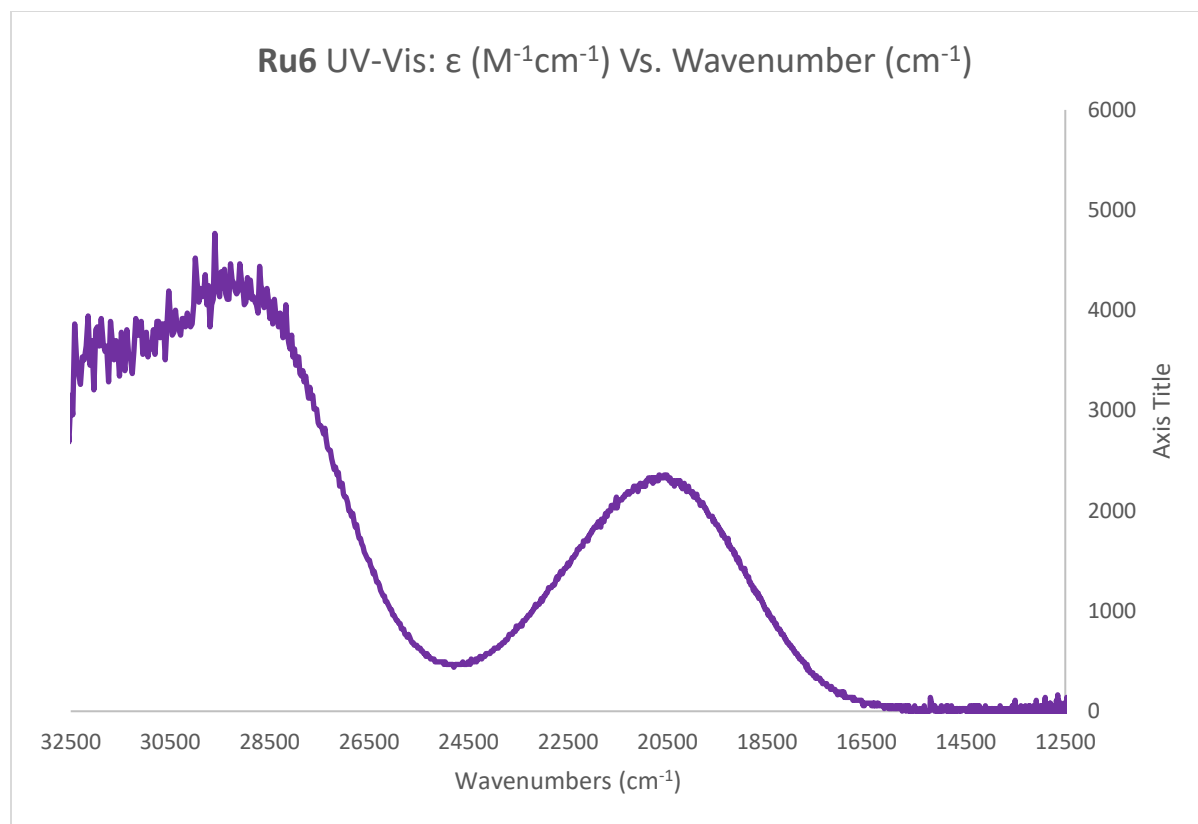


Figure 8.61 Plot of ϵ vs wavenumber for **Ru6** (0.00030 M in THF).

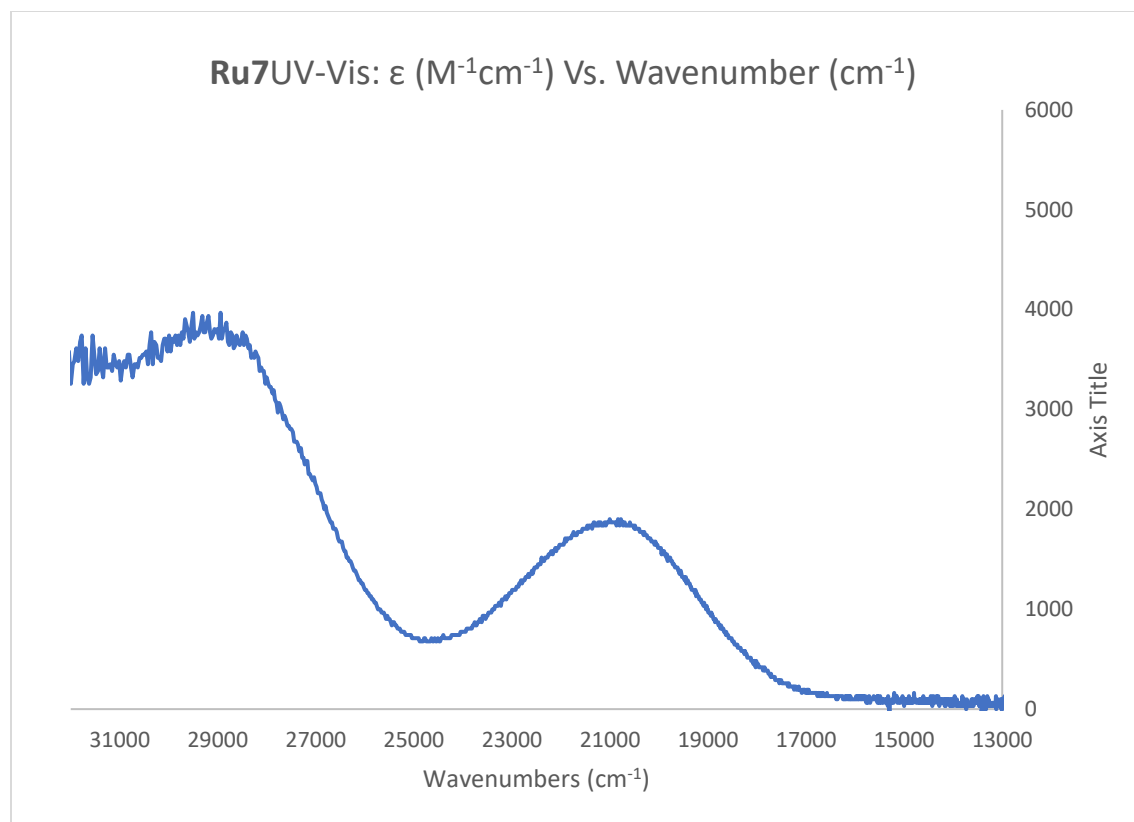


Figure 8.62 Plot of ϵ vs wavenumber for **Ru7** (0.00031 M in THF).

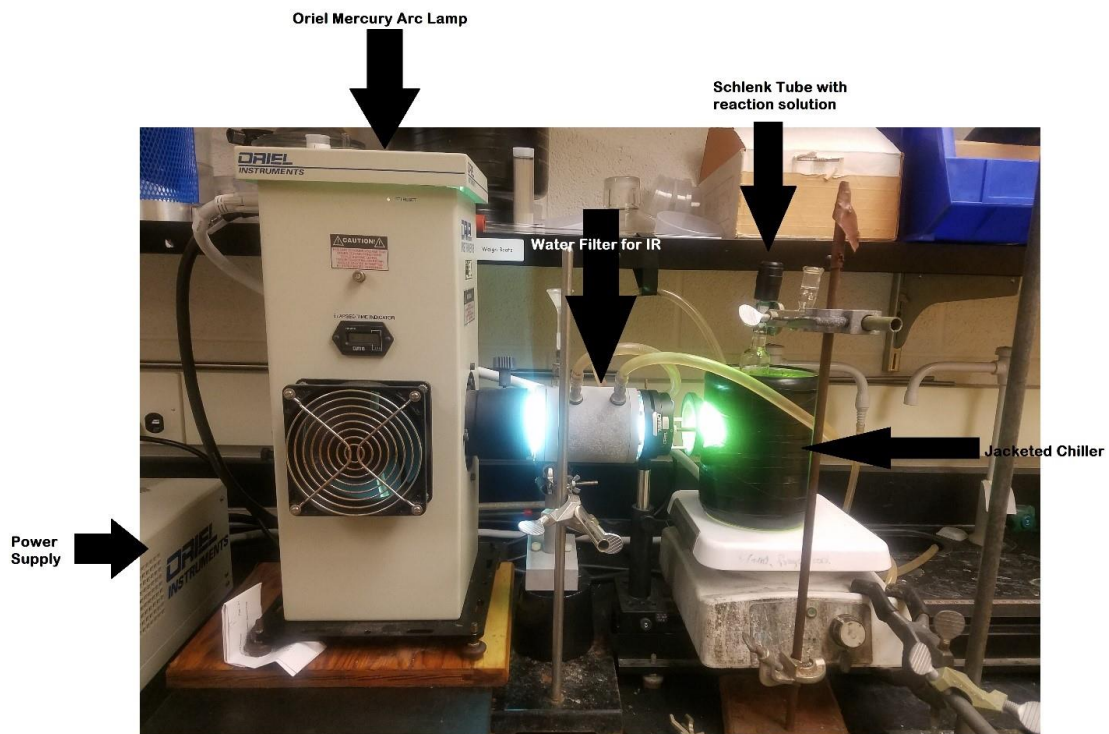


Figure 8.63 Photochemical irradiation setup utilizing a mercury arc lamp.

Crystallographic Data

The following molecules have been characterized by single crystal X-ray crystallography, and their structures deposited in the Cambridge Structural Database: **Ru1**, **Ru5-7**, **Ru9**, P(NAr)Me₃ and *cis*-RuCl₂(PPhMe₂)₄ (CCDC 1895000-05 and 1895272).

Additional molecular structures have been collected for several other compounds included above, but their structures not deposited in the Cambridge Structural Database. Information about these structures is given below. The .cif files have been added to the MSU Structural Database managed by Dr. Staples.

Ru2

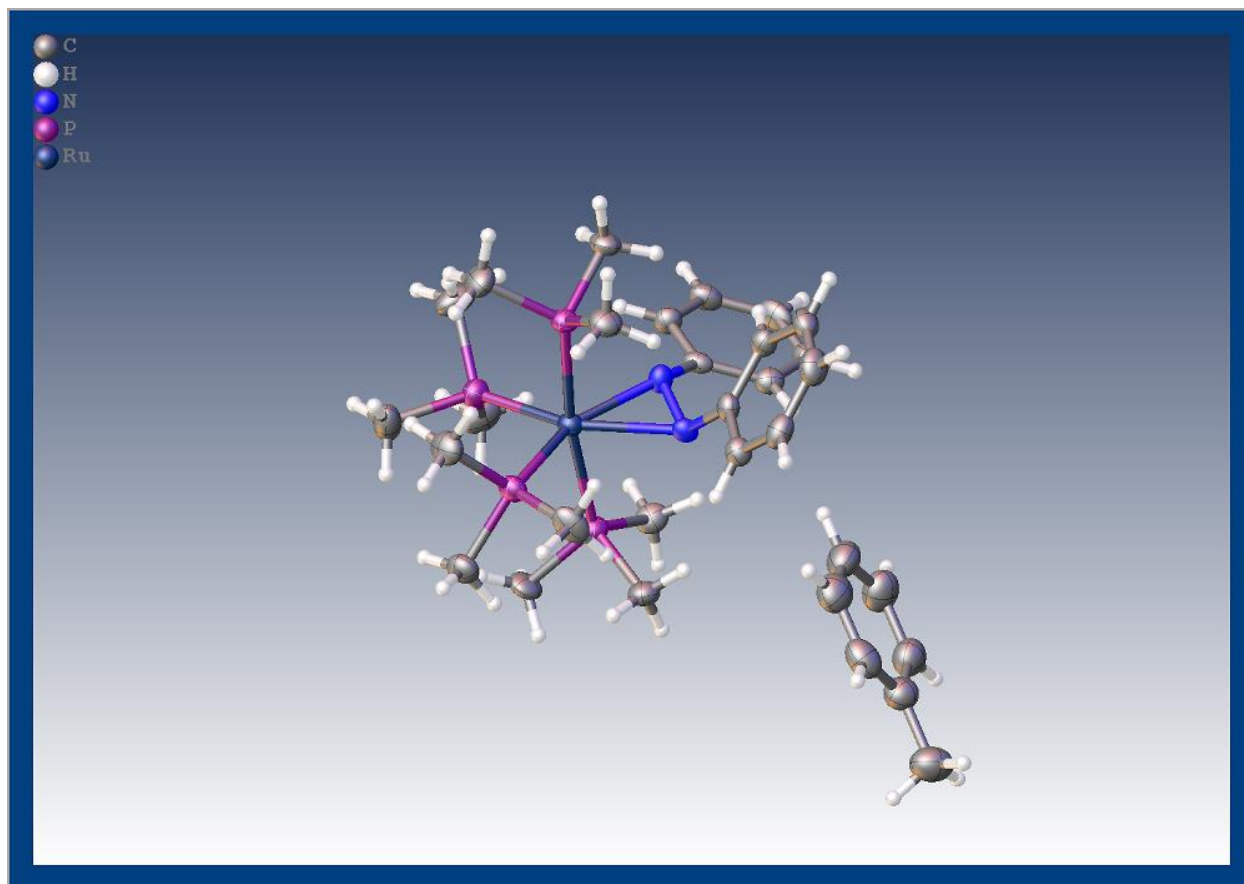


Figure 8.64 Crystal data and structure refinement for p21c.

Identification code	p21c
Empirical formula	$C_{31}H_{54}N_2P_4Ru$
Formula weight	679.71
Temperature/K	173.15
Crystal system	monoclinic
Space group	$P2_1/c$
a/Å	10.1433(17)
b/Å	26.868(4)

$c/\text{\AA}$	12.584(2)
$\alpha/^\circ$	90
$\beta/^\circ$	98.261(3)
$\gamma/^\circ$	90
Volume/ \AA^3	3393.8(9)
Z	4
$\rho_{\text{calc}}/\text{g/cm}^3$	1.330
μ/mm^{-1}	0.673
F(000)	1432.0
Crystal size/ mm^3	$0.174 \times 0.083 \times 0.05$
Radiation	MoK α ($\lambda = 0.71073$)
2Θ range for data collection/ $^\circ$	3.604 to 50.784
Index ranges	$-12 \leq h \leq 12, -32 \leq k \leq 32, -15 \leq l \leq 15$
Reflections collected	28322
Independent reflections	6224 [$R_{\text{int}} = 0.1249, R_{\text{sigma}} = 0.1130$]
Data/restraints/parameters	6224/0/367
Goodness-of-fit on F^2	1.026
Final R indexes [$I \geq 2\sigma(I)$]	$R_1 = 0.0602, wR_2 = 0.1260$
Final R indexes [all data]	$R_1 = 0.1153, wR_2 = 0.1520$
Largest diff. peak/hole / $e \text{\AA}^{-3}$	0.93/-0.48

Ru3

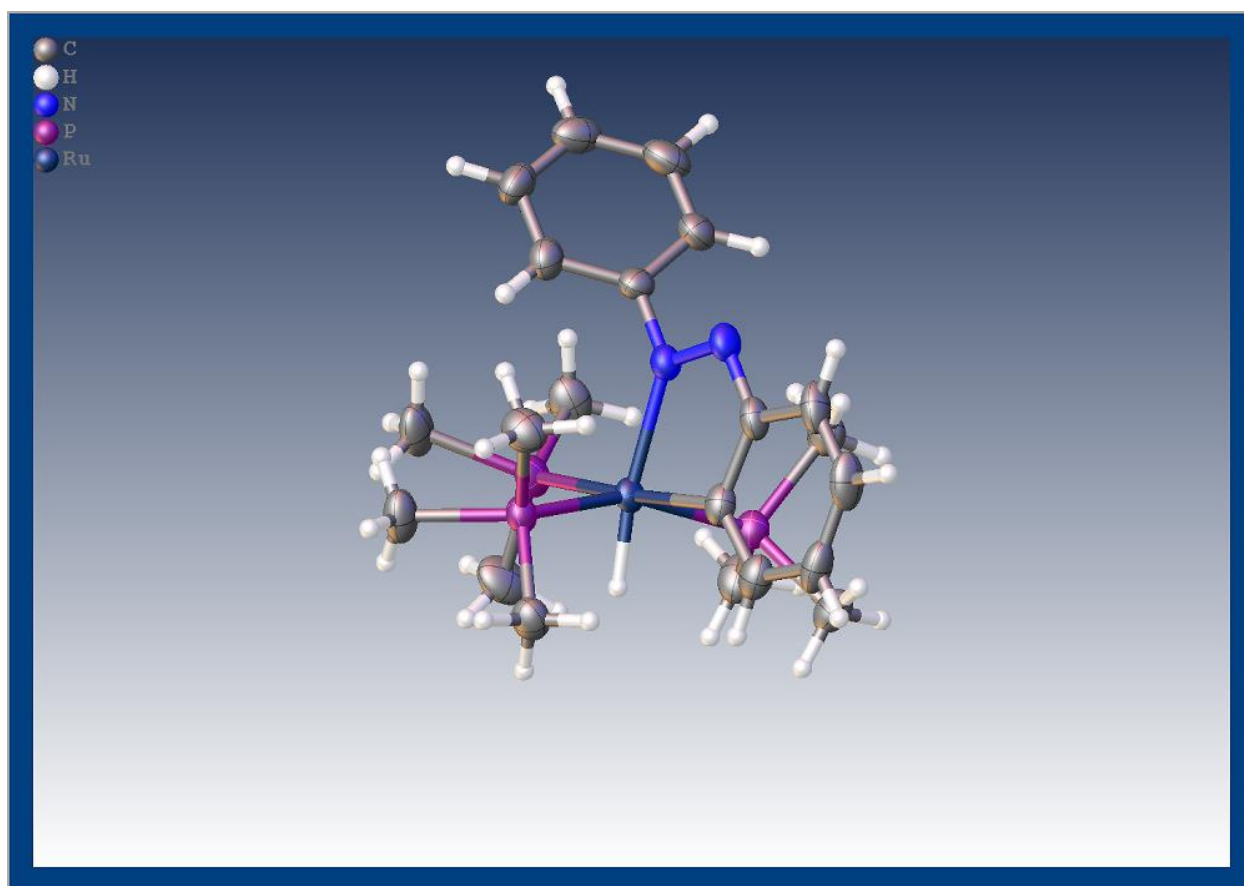


Figure 8.65 Crystal data and structure refinement for early_a.

Identification code	early_a
Empirical formula	C _{10.5} H _{18.5} NP _{1.5} Ru _{0.5}
Formula weight	255.76
Temperature/K	173.0
Crystal system	triclinic
Space group	P-1
a/Å	9.1159(8)
b/Å	11.8325(11)

$c/\text{\AA}$	12.4414(10)
$\alpha/^\circ$	77.950(5)
$\beta/^\circ$	79.242(5)
$\gamma/^\circ$	70.487(6)
Volume/ \AA^3	1227.04(19)
Z	4
$\rho_{\text{calc}}/\text{g/cm}^3$	1.3844
μ/mm^{-1}	7.074
F(000)	534.9
Crystal size/ mm^3	$0.189 \times 0.12 \times 0.089$
Radiation	Cu $K\alpha$ ($\lambda = 1.54178$)
2Θ range for data collection/ $^\circ$	7.32 to 144
Index ranges	$-10 \leq h \leq 11, -14 \leq k \leq 13, -15 \leq l \leq 14$
Reflections collected	13254
Independent reflections	4445 [$R_{\text{int}} = 0.0550, R_{\text{sigma}} = 0.0539$]
Data/restraints/parameters	4445/1/257
Goodness-of-fit on F^2	1.026
Final R indexes [$I \geq 2\sigma(I)$]	$R_1 = 0.0460, wR_2 = 0.1123$
Final R indexes [all data]	$R_1 = 0.0571, wR_2 = 0.1201$
Largest diff. peak/hole / $e \text{\AA}^{-3}$	1.70/-0.57

Os2

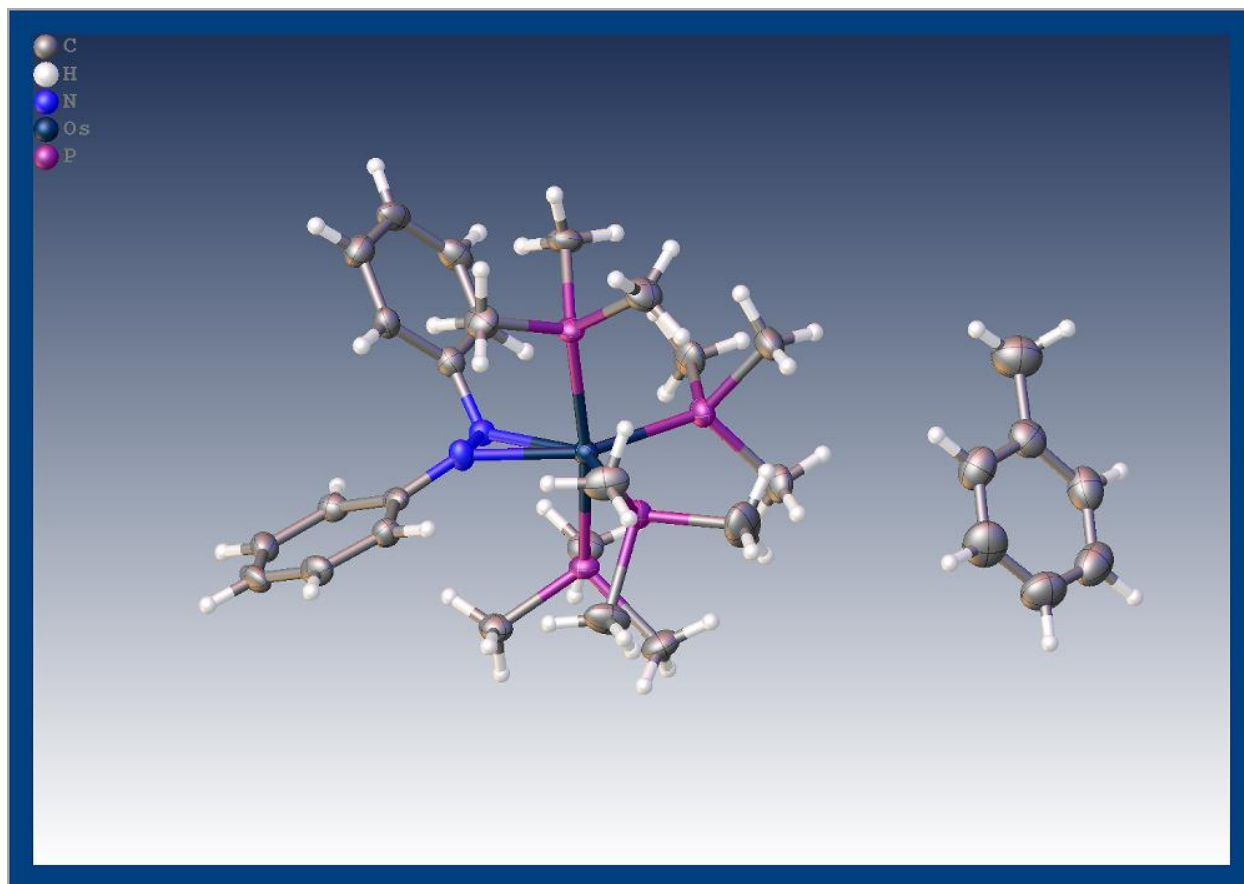


Figure 8.66 Crystal data and structure refinement for KA_OsBisImido.

Identification code	KA_OsBisImido
Empirical formula	C ₃₁ H ₅₄ N ₂ OsP ₄
Formula weight	768.91
Temperature/K	173.15
Crystal system	monoclinic
Space group	P2 ₁ /c
a/Å	10.1721(10)
b/Å	26.872(3)

$c/\text{\AA}$	12.6014(13)
$\alpha/^\circ$	90
$\beta/^\circ$	98.3670(10)
$\gamma/^\circ$	90
Volume/ \AA^3	3407.8(6)
Z	4
$\rho_{\text{calc}}/\text{g/cm}^3$	1.4985
μ/mm^{-1}	3.954
F(000)	1558.0
Crystal size/ mm^3	N/A \times N/A \times N/A
Radiation	Mo K α ($\lambda = 0.71073$)
2Θ range for data collection/ $^\circ$	3.04 to 50.74
Index ranges	$-12 \leq h \leq 12$, $-32 \leq k \leq 32$, $-15 \leq l \leq 15$
Reflections collected	25327
Independent reflections	6213 [$R_{\text{int}} = 0.0618$, $R_{\text{sigma}} = 0.0564$]
Data/restraints/parameters	6213/0/351
Goodness-of-fit on F^2	0.887
Final R indexes [$I \geq 2\sigma(I)$]	$R_1 = 0.0296$, $wR_2 = 0.0637$
Final R indexes [all data]	$R_1 = 0.0425$, $wR_2 = 0.0727$
Largest diff. peak/hole / $e \text{\AA}^{-3}$	1.96/-0.85

Os3

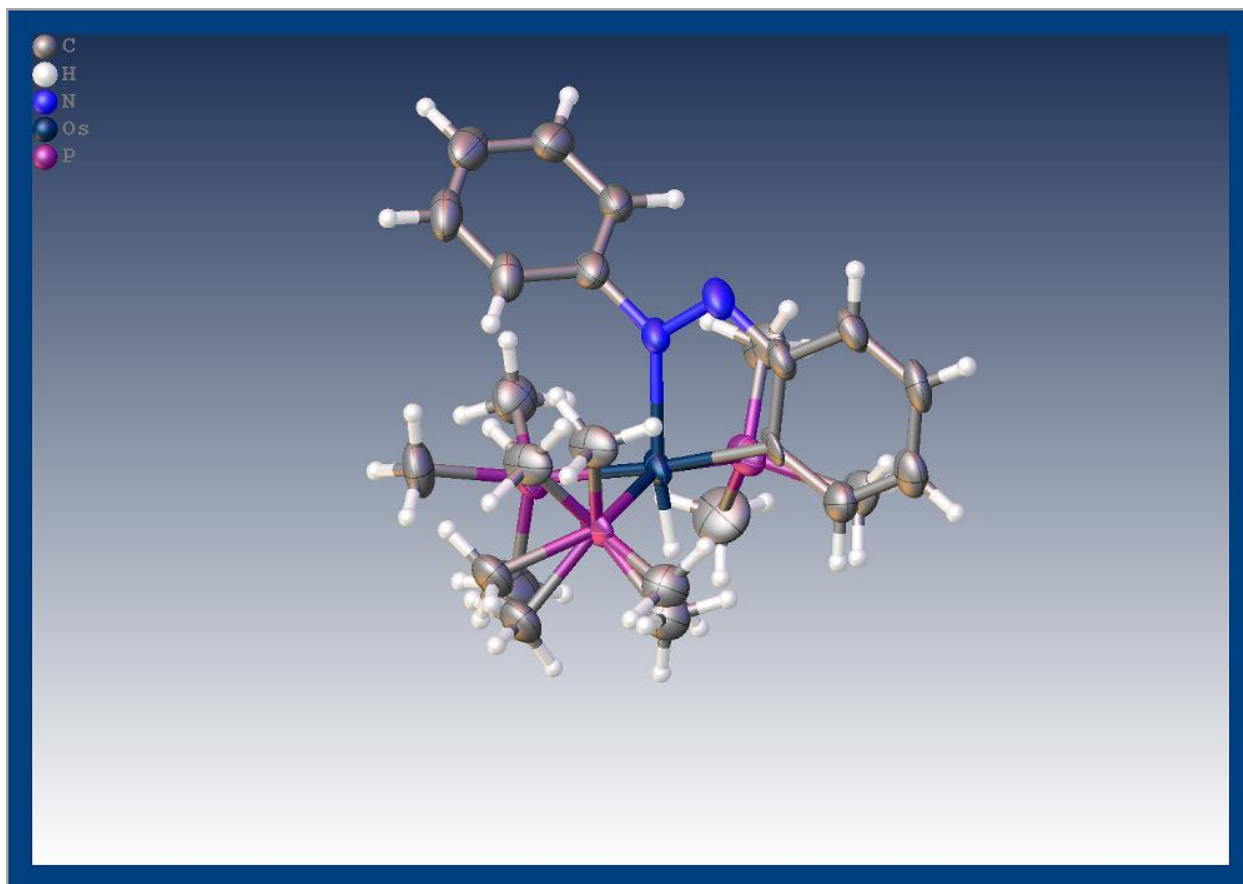


Figure 8.67 Crystal data and structure refinement for smalltwin5.

Identification code	smalltwin5
Empirical formula	C ₂₁ H ₃₇ N ₂ OsP ₃
Formula weight	600.63
Temperature/K	173.15
Crystal system	triclinic
Space group	P-1
a/Å	9.2309(12)
b/Å	11.8060(16)

$c/\text{\AA}$	11.8841(16)
$\alpha/^\circ$	78.4871(16)
$\beta/^\circ$	74.9609(16)
$\gamma/^\circ$	81.8801(17)
Volume/ \AA^3	1220.1(3)
Z	2
$\rho_{\text{calc}}/\text{g/cm}^3$	1.635
μ/mm^{-1}	5.431
F(000)	596.0
Crystal size/ mm^3	$0.225 \times 0.209 \times 0.132$
Radiation	MoK α ($\lambda = 0.71073$)
2Θ range for data collection/ $^\circ$	3.536 to 50.956
Index ranges	$-10 \leq h \leq 11, -13 \leq k \leq 14, 0 \leq l \leq 14$
Reflections collected	5185
Independent reflections	5185 [$R_{\text{int}} = ?$, $R_{\text{sigma}} = 0.0515$]
Data/restraints/parameters	5185/258/267
Goodness-of-fit on F^2	1.086
Final R indexes [$I \geq 2\sigma(I)$]	$R_1 = 0.0440, wR_2 = 0.0938$
Final R indexes [all data]	$R_1 = 0.0544, wR_2 = 0.0983$
Largest diff. peak/hole / $e \text{\AA}^{-3}$	1.87/-1.75

REFERENCES

REFERENCES

- (1) Danopoulos, A. A.; Wilkinson, G.; Hussain-Bates, B.; Hursthouse, M. B. Synthesis and X-ray crystal structure of trans-bis(2,6-diisopropylphenylimido) bis-(trimethylphosphino)ruthenium(IV): The first structural determination of a terminal imido ruthenium compound. *Polyhedron* **1992**, *11* (22), 2961.
- (2) Burred, A. K.; Steedman, A. J. ([small eta]6-p-Cymene)Ru[triple bond, length half m-dash]N(2,4,6-tri-tert-butylphenyl): a monomeric ruthenium(II) complex containing a terminal imido ligand. *J. Chem. Soc., Chem. Commun.* **1995**, DOI:10.1039/C39950002109 10.1039/C39950002109(20), 2109.
- (3) Burrell, A. K.; Steedman, A. J. Synthesis, Structure, and Reactivity of Ruthenium(II) Terminal Imido Complexes. *Organometallics* **1997**, *16* (6), 1203.
- (4) Singh, A. K.; Levine, B. G.; Staples, R. J.; Odom, A. L. A 4-coordinate Ru(II) imido: unusual geometry, synthesis, and reactivity. *Chem Commun (Camb)* **2013**, *49* (92), 10799.
- (5) Aldrich, K. E. F., B. S.; Singh, A. K.; Staples, R. J.; McCracken, J.; Levine, B.; Smith, M. R.; Odom, A. L. . *Inorganic chemistry* **2019**.
- (6) Smieja, J. A.; Shirzad, K.; Roy, M.; Kittilstved, K.; Twamley, B. Unusual Bis(imido)metalloporphyrins. The synthesis of M(4-R-TPP)(NC₆H₄NO₂)₂ (M=Ru, R=H; M=Os, R=Cl) and structural study of the osmium derivative. *Inorganica Chimica Acta* **2002**, *335*, 141.
- (7) Law, S.-M.; Chen, D.; Chan, S. L.-F.; Guan, X.; Tsui, W.-M.; Huang, J.-S.; Zhu, N.; Che, C.-M. Ruthenium Porphyrins with Axial π -Conjugated Arylamide and Arylimide Ligands. **2014**, *20* (35), 11035.
- (8) Au, S.-M.; Huang, J.-S.; Yu, W.-Y.; Fung, W.-H.; Che, C.-M. Aziridination of Alkenes and Amidation of Alkanes by Bis(tosylimido)ruthenium(VI) Porphyrins. A Mechanistic Study. *Journal of the American Chemical Society* **1999**, *121* (39), 9120.
- (9) Leung, S. K.-Y.; Tsui, W.-M.; Huang, J.-S.; Che, C.-M.; Liang, J.-L.; Zhu, N. Imido Transfer from Bis(imido)ruthenium(VI) Porphyrins to Hydrocarbons: Effect of Imido Substituents, C–H Bond Dissociation Energies, and RuVI/V Reduction Potentials. *Journal of the American Chemical Society* **2005**, *127* (47), 16629.
- (10) Zardi, P.; Pozzoli, A.; Ferretti, F.; Manca, G.; Mealli, C.; Gallo, E. A mechanistic investigation of the ruthenium porphyrin catalysed aziridination of olefins by aryl azides. *Dalton Transactions* **2015**, *44* (22), 10479.
- (11) Au, S.-M.; Fung, W.-H.; Huang, J.-S.; Cheung, K.-K.; Che, C.-M. Synthesis, Spectroscopic Properties, and Reactivities of Bis(tosylimido)osmium(VI) Porphyrin Complexes.

X-ray Crystal Structure of [OsVI(TPP)(NSO₂C₆H₄-pCH₃)₂] (TPP = Tetraphenylporphyrinato). *Inorganic chemistry* **1998**, 37 (26), 6564.

- (12) Leung, S. K.-Y.; Huang, J.-S.; Zhu, N.; Che, C.-M. Reactivity of Dioxoosmium(VI) Porphyrins toward Arylhydrazine. Isolation of Hydrazidoosmium and Amidoosmium Porphyrins. *Inorganic chemistry* **2003**, 42 (22), 7266.
- (13) Dey, A.; Ghosh, A. "True" Iron(V) and Iron(VI) Porphyrins: A First Theoretical Exploration. *Journal of the American Chemical Society* **2002**, 124 (13), 3206.
- (14) Cramer, S. A.; Hernandez Sanchez, R.; Brakhage, D. F.; Jenkins, D. M. Probing the role of an FeIV tetrazene in catalytic aziridination. *Chem. Commun.* **2014**, 50 (90), 13967.
- (15) Hohenberger, J.; Ray, K.; Meyer, K. The biology and chemistry of high-valent iron-oxo and iron-nitrido complexes. *Nature Communications* **2012**, 3, 720.
- (16) Mehn, M. P.; Peters, J. C. Mid- to high-valent imido and nitrido complexes of iron. *J. Inorg. Biochem.* **2006**, 100 (4), 634.
- (17) Mahy, J. P.; Battioni, P.; Mansuy, D. Formation of an iron(III)-porphyrin complex with a nitrene moiety inserted into an iron-nitrogen bond during alkene aziridination by (tosylimidoiodo)benzene catalyzed by iron(III) porphyrins. *Journal of the American Chemical Society* **1986**, 108 (5), 1079.
- (18) Clifford, A. F., Kobayashi, C. S. *130th National Meeting of the American Chemical Society* **1956**, 50R.
- (19) Nugent, W. A., Mayer, J. M. Metal-Ligand Multiple Bonds. *Wiley Interscience* **1987**.
- (20) Patrick, D. W.; Truesdale, L. K.; Biller, S. A.; Sharpless, K. B. Stereospecific vicinal oxyamination of olefins by alkylimidoosmium compounds. *The Journal of Organic Chemistry* **1978**, 43 (13), 2628.
- (21) Herranz, E.; Sharpless, K. B. Improvements in the osmium-catalyzed oxyamination of olefins by chloramine-T. *The Journal of Organic Chemistry* **1978**, 43 (12), 2544.
- (22) Wolf, J. R.; Bazan, G. C.; Schrock, R. R. Exchange of oxo ligands in osmium tetroxide with imido ligands in bis(arylimido)bis(tert-butoxo)molybdenum complexes, Mo(NAr)₂(O-tert-Bu)₂. A facile route to Os(NAr)₂O₂ and Os(NAr)₃O and osmium(IV) complexes of the type Os(NAr)₂L₂ (NAr = N-2,6-C₆H₃-iso-Pr₂; L = a phosphine). *Inorg. Chem.* **1993**, 32 (19), 4155.
- (23) Schofield, M. H.; Kee, T. P.; Anhaus, J. T.; Schrock, R. R.; Johnson, K. H.; Davis, W. M. Osmium imido complexes: synthesis, reactivity, and SCF-X.alpha.-SW electronic structure. *Inorg. Chem.* **1991**, 30 (19), 3595.
- (24) LaPointe, A. M.; Schrock, R. R.; Davis, W. M. Imido/Oxo Exchange between Osmium and Tantalum as a Route to Os(NAr)₂R₂ and OsO(NAr)₂R₂ Complexes (NAr = N-2,6-i-

Pr₂C₆H₃; R = CH₂CMe₃, CH₂CMe₂Ph, CH₂SiMe₃) and Attempts To Induce α -Hydrogen Abstraction To Give Alkylidene Complexes. *Organometallics* **1995**, *14* (6), 2699.

(25) Wang, L.; Hu, L.; Zhang, H.; Chen, H.; Deng, L. Three-Coordinate Iron(IV) Bisimido Complexes with Aminocarbene Ligation: Synthesis, Structure, and Reactivity. *J. Am. Chem. Soc.* **2015**, *137* (44), 14196.

(26) Ni, C.; Fettinger, J. C.; Long, G. J.; Brynda, M.; Power, P. P. Reaction of a sterically encumbered iron(i) aryl/arene with organoazides: formation of an iron(v) bis(imide). *Chem. Commun.* **2008**, DOI:10.1039/B810941A 10.1039/B810941A(45), 6045.

(27) Hansert, B.; Vahrenkamp, H. Preparation, structure, and some reactions of the elusive azobenzene complex [Fe₂(CO)₆(μ -Ph₂N₂)]. *Journal of Organometallic Chemistry* **1993**, *459* (1), 265.

(28) Kiernicki, J. J.; Higgins, R. F.; Kraft, S. J.; Zeller, M.; Shores, M. P.; Bart, S. C. Elucidating the Mechanism of Uranium Mediated Diazene N=N Bond Cleavage. *Inorg. Chem.* **2016**, *55* (22), 11854.

(29) Lin, K.-M.; Wang, P.-Y.; Shieh, Y.-J.; Chen, H.-Z.; Kuo, T.-S.; Tsai, Y.-C. Reductive N–N bond cleavage and coupling of organic azides mediated by chromium(i) and vanadium(i) β -diketiminates. *New Journal of Chemistry* **2010**, *34* (8), 1737.

(30) Gehrman, T.; Lloret Fillol, J.; Wadepohl, H.; Gade, L. H. Synthesis, Characterization, and Thermal Rearrangement of Zirconium Tetraazadienyl and Pentaazadienyl Complexes. *Organometallics* **2012**, *31* (12), 4504.

(31) Mason, J. *Multinuclear NMR*; Plenum Press: New York [etc.], 1987.

(32) Mason, J. Nitrogen nuclear magnetic resonance spectroscopy in inorganic, organometallic, and bioinorganic chemistry. *Chem. Rev.* **1981**, *81* (3), 205.

(33) Danopoulos, A. A.; Wilkinson, G.; Sweet, T. K. N.; Hursthouse, M. B. Reactions of imido complexes of iridium, rhodium and ruthenium. *J. Chem. Soc., Dalton Trans.* **1996**, DOI:10.1039/DT9960003771 10.1039/DT9960003771(19), 3771.

(34) Heyduk, A. F.; Blackmore, K. J.; Ketterer, N. A.; Ziller, J. W. Azide Addition To Give a Tetra-azazirconacycle Complex. *Inorg. Chem.* **2005**, *44* (3), 468.

(35) Cowley, R. E.; Bill, E.; Neese, F.; Brennessel, W. W.; Holland, P. L. Iron(II) Complexes with Redox-Active Tetrazene (RNNNR) Ligands. *Inorg. Chem.* **2009**, *48* (11), 4828.

(36) Singh, A. K.; Levine, B. G.; Staples, R. J.; Odom, A. L. A 4-coordinate Ru(ii) imido: unusual geometry, synthesis, and reactivity. *Chem. Commun.* **2013**, *49* (92), 10799.

(37) Park, J. Y.; Kim, Y.; Bae, D. Y.; Rhee, Y. H.; Park, J. Ruthenium Bisammine Complex and Its Reaction with Aryl Azides. *Organometallics* **2017**, *36* (18), 3471.